17th International Conference on Sustainable Energy Technologies

21st to 23rd August 2018, Wuhan, China

Sustainable Energy Technologies for Eco Cities and Environment

Conference Proceedings Volume 4

Proceedings of the
17th International Conference on
Sustainable Energy Technologies – SET 2018
21st to 23rd August 2018, Wuhan China

Sustainable Energy Technologies for Eco Cities and Environment

Volume 4

Edited by

Professor Saffa Riffat, Dr Yuehong Su,
Professor Defu Liu and Professor Yingjiang Zhang

SET 2018 Admin Support
Department of Architecture and the Built Environment
Faculty of Engineering, University of Nottingham

Supported by the Conference Organising Committee:

Chair: Professor Saffa Riffat
Professor Liu Defu
Professor Zhang Yingjiang
Dustin Chen
Amy Long
Zeny Amante-Roberts
Dr Yuehong Su

Reference to a conference paper:

To cite a paper published in these conference proceedings, please substitute the highlighted sections of the reference below with the details of the article you are referring to:

Author(s) Surname, Author(s) Initial(s), 2018. 'Title of paper'. In: Riffat, Su, Liu & Zhang. ed., **Sustainable Energy Technologies for Eco Cities and Environment**: Proceedings of the 17th International Conference on Sustainable Energy Technologies, 21-23 August 2018, Wuhan, China. University of Nottingham: Buildings, Energy & Environment Research Group. Volume X, pp XX-XX. Available from: nottingham-repository.worktribe.com/ [Last access date].

ISBN-13 9780853583271

Version: 26.02.2019

Foreward

The 17th International Conference on Sustainable Energy Technologies was a significant international academic conference in the domain of world sustainable energy technologies with a theme of *Sustainable Energy Technologies for Eco Cities and Environment*. The conference aimed to provide a forum for the exchange of latest technical information, the dissemination of up-to-date research results, and the presentation of major issues that may shape future directions of human society, such as sustainable energy technology research, its application and energy security.

Held from August 21st to August 23rd, 2018, in Wuhan, China, the conference was a collaboration between the World Society of Sustainable Energy Technologies (WSSET) and the Hubei University of Technology. World-renowned experts and scholars in the area, representatives of prominent enterprises and universities attended to discuss new developments and achievements in the field, as well as promoting academic exchange, application of scientific results, university-industry collaboration and government-industry collaboration.

The papers contained in these proceedings focus on topics such as Energy Storage for the Age of Renewables; Research, Innovation and Commercialisation in Sustainable Energy Technologies; Integrating Planning & Policy, Architecture, Engineering & Economics; Energy and Environment; Engineering Thermo-physics; and Systemic Change for Cities.

Over 300 delegates from 27 countries attended SET2018; over 400 abstracts were received and 251 papers have been published in the conference proceedings. The proceedings have therefore been divided into four volumes. I hope you enjoy as much as I did the breadth of work you will find in this book.

We would like to thank all participating authors for their contributions to both the conference and to the publishing of this book. We are also indebted to our international scientific committee for their advice and seemingly endless review of papers. We would also like to thank unreservedly Celia Berry, Zeny Armante-Roberts, Amy Long, Dustin Chen for their tireless efforts in making SET2018 one of the most successful conferences we have held. Also a huge thanks to our sponsors PCM Products Ltd., Solar Ready Ltd., Positive Homes, Hubei Provincial Department of Education, Oxford University Press and MDPI.

Professor Saffa Riffat
Chair in Sustainable Energy Technologies
President of the World Society of Sustainable Energy Technologies
SET 2018 Chairman

CONTENTS

Paper Reference # List of Papers Page Number

301: Design framework for the development of dual heat recovery system in photo-voltaic powered air conditioning systems

Koketso MADITSI[1], Timothy LASEINDE[2]

[1] University of Johannesburg, Johannesburg, 201446621@student.uj.ac.za
[2] University of Johannesburg, Johannesburg, otlaseinde@uj.ac.za

Energy regeneration through heat recovery is practically possible for maximizing energy obtained from the sun, by recovering and reusing the heat that is typically lost within energy dependent electrical equipment's. The study is aimed at developing an efficient and cost effective heat recovery system, which is an improvement to existing variants. Solar thermal systems utilise flat plates or evacuated tube collectors which absorb the heat from the sun. Similarly, Photo-Voltaic (PV) systems absorb solar irradiation to generate electricity. A combination of both technologies results in Solar Photo-Voltaic Thermal (PV/T) systems wherein thermal plates or liquid contained tubes cool PV collectors resulting in increased efficiency. The PV cooling mechanism is important because excessive heat in PV panels generates high resistance, which impedes the performance of the solar cell and in the process, results in lower efficiency. PV/T systems are currently sold at relatively high cost and their availability is limited. The study focuses on the development of a dual heat recovery system for harnessing both the heat build-up on the PV plates and the heat generated from the heat exchanger exhaust outlet of a solar air-conditioning system, by incorporating electro-thermal generators and Peltier devices for the optimisation process. The research is sectioned into design, prototype development, and a testing phase. The focus of this paper is to share the design phase of the project. The design highlighted herein is a cost effective and highly efficient PV/T model with a different heat absorption approach in comparison to conventional PV/T systems. The heat recovery system design is complete and is currently undergoing extensive tests to complete the testing and optimisation phase.

Keywords: Heat Recovery, PV/T, PVT, Photovoltaic thermal, Peltier fan, Design

1. INTRODUCTION

The energy sector is globally going through a transition because of increasing demand for cleaner energy. Renewable sources of energy are widely being promoted, which calls for more research on how best to maximise the energy potential of these greener sources (Da Rosa, 2005). The energy emitted by the sun is about 3.8 x 1023 kW whereas only about a third of this is received on the earth surface, which is estimated at about 1.2 x 1014 kW (Ramos, et al., 2017). Notwithstanding, the fraction received on earth is not fully harnessed due to a lot of system inefficiencies through heat losses. This unlimited amount of energy during sunny days may be collected using various collection methods of the irradiance. Solar energy can play important role in the Heating Ventilation and Air Conditioning (HVAC) systems of buildings, by the application of solar absorption systems in combination with heat recovery systems, which can generate both heat and electricity for heating and cooling of residential buildings, shipping vessels, commercial facilities and industries (Martinez, et al., 2018).

Energy regeneration through heat recovery is also practically possible for maximising energy obtained from the sun, by recovering and reusing the heat that is typically lost within solar energy dependent electrical equipment's. Hybrid Photovoltaic Thermal (PV/T) collectors generate heat and electricity simultaneously in one module as presented in Figure 1. The basic idea behind the PV/T concept is to utilise more of the solar radiation by also harvesting the waste heat that is generated in Photo Voltaic (PV) modules. In a PV/T collector, a thermal absorber and the photovoltaic cells are integrated into a single module (Kalogirou & Tripanagnostopoulos, 2007). The solar radiation that is not absorbed by the cells for electricity production and not lost to the surroundings is transferred to the thermal absorber positioned at the back (rear) of the module. Working fluid such as air and liquids transports the heat away from the PV cells, and the heat lost by the PV module is the heat gained by the cooling medium. As a result, both heat and electricity are generated from the same panel. Hybrid PV/T technologies may be implemented within local energy systems to cover a large fraction of the corresponding heat demands at high efficiency, low cost and with low associated emissions therefore, enabling the emergence of such distributed systems (Ramos, et al., 2017). The proposed solar technology is motivated by the need to utilise both electrical and thermal output from the combined technology and since solar air conditioning system uses both of these outputs, there may be a huge demand for this technology based on economic considerations and factors associated with environmental impacts of this clean energy system (Hormazabal, et al., 2016).

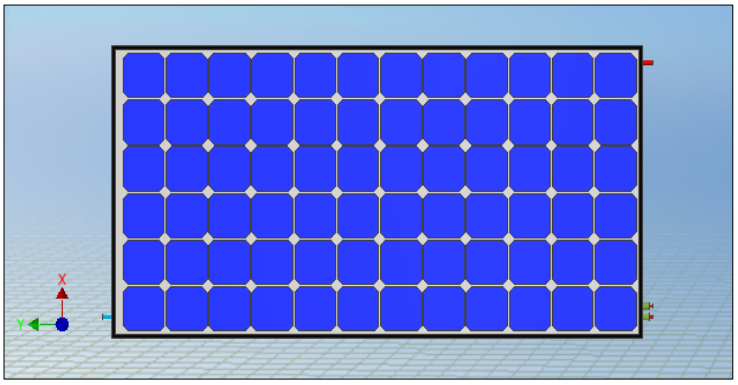

Figure 1: Solar PV/T module

There is a significant drop in efficiency of solar PV panels due to high surface temperature, which impedes the performance of the cells, and in the process, lowers the thermal and electrical output of the electricity and heat produced from PV systems (Sorensen, 2007). Current cooling methods of the solar cells are effective for electricity production for low temperature application but ineffective and less efficient for heat generation (Thorpe, 2011). The exhaust air leaving the air conditioning system outlet escapes at a temperature significant enough for re-utilization processes. Some methods applied for energy reutilization have proven to be highly efficient (Sorensesn & Katic, 2003). In this research, the improvement in efficiency of PV output and the re-utilization of the exhaust air temperature is desirable, to develop a more efficient and cost effective heat recovery system for capturing the excessive heat loss from both the exhaust airflows of an air conditioning system and from the panel of the PV system. The combined heat may be fed back into a system that will convert the captured heat into a source of energy that will be useful to the solar air conditioning unit. The study followed an exploratory method, which involved an extensive and intensive literature review followed by the design phase. The Non-Destructive Testing (NDT) of materials and generation of simulations using TRNSYS computer software for simulations are beyond the scope of this research and this approach focuses more on the complete system design including the energy efficiency within the air conditioning system. However, the study presented focused more on the design of a PV/T system with different heat absorption to conventional PV/T systems and ANSYS was adopted in the research in place of TRNSYS.

2. LITERATURE REVIEW

Literature on air-cooled PV/T technologies suggest that hybrid solar electric-thermal systems produce both electricity and heated air, which has the potential of generating two to three times more energy than a standalone PV system without a cooling medium (Donwell, 2016). In some cases, air-cooling may achieve more electricity with an estimated 25% more cost efficiency, based on some PV/T manufactures (ART solar (Pty) Ltd). The two solar technologies in one footprint offset both heating and electricity costs, while also increasing the PV performance by up to 10% by cooling the panels. Other technologies available for PV cooling are the separate solar thermal systems using water as the cooling medium, and the solar electric concentrated systems using oil and other highly concentrated chemical mix (Jager et al., 2014).

PV/T systems are usually designed to meet 30% of the heating load because they operate at lower temperatures and have lower thermal efficiencies than traditional flat-plate or evacuated-tube collectors (Moss, et al., 2018). PV module generally achieve between 6 to 20% efficiency if not optimised in terms of installation. The inclination to face the direction of the sun, shading based on positioning, cooling of the panel as the surface temperature rises, and the type of panel design greatly contribute to the efficiency obtained. Higher efficiencies are a function of rightly putting measures in place to optimise the system in terms of the aforementioned factors. These measures may include rightly inkling the panels to face South and installing a solar tracking positioning system that rotates the panel in the direction of the sun as the sun moves from the East to the West in a normal day. The application of a cooling medium as proposed in this research also improves the efficiency of the panels (Cozzini, 2012). The lost energy, estimated to be between 80 to 94% of incident solar radiation, is mostly converted to heat and a greater portion of this energy can be used to satisfy thermal heating loads (Sorensesn & Katic, 2003). Another measure for improving efficiency of the PV modules is the installation of this array away from obstructions such as buildings, trees, and high structures, which cast shadows and reduces the irradiance absorption (Lynn, 2010).

According to the Imperial report in London (Ramos et al., 2017), solar cells in PV collectors suffer lower temperature stresses, which are known causes that increases the possibilities of major PV system failure due to cell breakage, encapsulation, discolouration and delamination. Figure 2 illustrates this relationship where the module efficiency decreases in warm environment and increases in cool environment based on an experiment carried out on the selected panels for the research. This emphasises the need to keep the module as cool as possible.

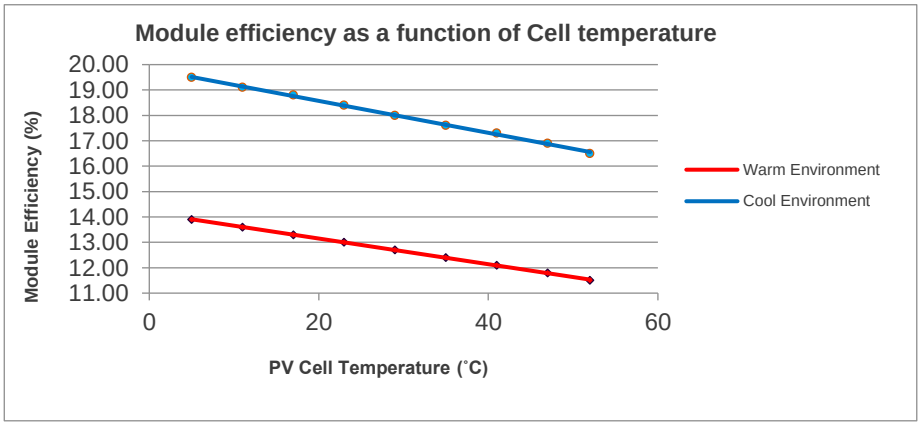

Figure 2: Comparative Cell Temperature over Module Efficiency

High surface temperature on the PV panel induces the solar cell to overheat and in the process, the efficiency of electrical output decreases and this is because of the vibrations caused by solar radiations, which further impedes the electrons already freed during sunlight to electricity conversion (Dean et al., 2015). The research carried by Dean and McNutt suggests that weather has special effects on the performance of PV cells. The photons from the sun radiation sometimes do not have sufficient energy to free electrons from the material surface of the absorber depending on the weather. The location/position of the sun gives rise to temperature difference on the panel surface thus the panel must be positioned in a way that will direct the radiations towards the transparent screen and to the absorber. Alternative solutions are the parabolic concentrators, which concentrates the sun radiation towards the receiver (Jager et al., 2014).

The Peltier fans are special kind of fans, which uses a heat sink in between the extracting and exhausting surfaces. The smaller fan draws heat from a conditioned space and transfers the heat to the bigger fan underneath which exhaust the heated air on the other side of the conditioned space. This “Peltier Effect’’ results in cooling on one side and heating on the other side. They typically consume around 30 – 90 Watts of the electrical output depending on the size (Tahakkar, 2016).

Thermoelectric generators are devices, which generates electrical current directly from the heat source. They use the temperature of the thermoelectric materials of the hot and cold side. As the heat from the hot site piles up, the electrons

and poles from the PN junction gets excitations, this effect induces electrical field for the flow of charge with the circuit connected at the cold side of the generator. For better conversion of heat to electricity, it is significant for thermoelectric materials to have low thermal conductivity and high electrical conductivity as to accommodate the temperature rise to the cool side, which increases the electrical resistance hence, lowering the output produced (Jensen et al., 2010). It is mandatory for the cool side to be maintained for a considerable temperature difference of the thermoelectric materials. Typical conversion efficiency for these devices are approximated to be around 5 -8%, with this mentioned, these devices are suitable for low power applications (BCS, 2008). These devices may be integrated in the proposed PV/T model in this study, to power the low energy consumption Peltier fans for maximum optimisation of the electrical output produced by the PV alone.

3. METHODOLOGY

The study followed an exploratory method, which involved holistic review of past works from literature, followed by the design of a model using Autodesk Inventor Professional. The design was developed based on lapses of current systems identified in literature. There were numerous options to consider, however; the approach selected was partially based on simulation results carried out driven by software, and partly based on physical evaluation of different components and designs of existing heat recovery systems. The testing involved the use of predictive simulations carried out by ANSYS and solid works. Currently, the research is in the final testing phase wherein physical tests to validate the simulation results of the design phase of the project being presented in this paper. The results obtained will be further validated using Comsol Multiphysics algorithms, which is a virtual experimentation application. The model will also undergo material alteration to determine the most efficient heat recovery material that will be recommended for final prototype development.

3.1. Data sources

Required information were sourced from local manufactures of Photovoltaic (PV) panels, which involved sites visits to study the full geometry of the PV modules and their operations. Numerous manufactures confirmed the conclusive literature that PV modules remains inefficient with increasing panel temperature, especially in South Africa where the ambient temperature can reach as high as 50ºC. The study on optimisation process then began where the use of the Peltier fans were studied in detail. The modified Peltier fan is used in this study to recover the heat from the PV module. Conference proceedings, journal articles and books were major sources of information that contributed to the model developed in the research.

3.2. Waste heat recovery in the presented PV/T system

The PV module alone is a heat liberating system and without proper system design, this heat may be lost to the surrounding environment. The design presented recovers some of this heat to a maximum by cooling off the panel while extracting and exhausting this heat from the panel surface and the surrounding. Energy from the sun may come in different forms of rays and some of this are absorbed by the PV cells while others builds up heat to the panel surface. The heat or rays not absorbed by the PV module are absorbed by the thermal absorber positioned at the rear of the PV module. The absorber transfers this heat by conduction to the liquid-contained tubes underneath which in turn, partly cools the module. The design presented accommodates a modified Peltier fans which is held by a transparent glass below the PV layer. A small fan extracts excess heat from the PV layer and exhaust it to the absorber in the second compartment, this cools the first compartment to the maximum and provides the second compartment with excess heat which is concentrated more on the centre of the absorber. The liquid-contained tubes are then designed in such a way that more of these tubes are concentrated on the centre for maximum heat collection. The result is a PV/T system with an improved electrical efficiency and higher liquid temperature outlet.

3.3. ANSYS simulations

ANSYS software was used to predict the cooling effect of the panel. The software requires having all numerical and operational boundary conditions of the proposed model. The 3 Dimensional model from Inventor was imported into ANSYS simulation environment where thermal properties such as thermal conductivity, convective heat coefficient, heat flux, rotational speed, ambient and surface temperature were defined after meshing the geometry. This cooling effect helped in generating the graphs of module efficiency as a function of cell temperature. The last step was used together with the PV efficiency equation defined later under numerical interpretations.

3.4. SolidWorks simulations

Thermal and flow analysis was performed using the above-mentioned software which followed an approach similar to the procedure taken using ANSYS. The flow analysis carried out on the Peltier fan served the purpose of generating information that showed the nature of the extraction process from the proposed geometry. This helped identifying regions exposed to high thermal conduct with the surface. Thermal analysis was also used to predict the areas where high thermal

exposure exists by entering the necessary boundary conditions as mentioned in ANSYS simulation above. The predictive simulations explained in this section are further elaborated under the result section.

4. RESULTS AND DISCUSSIONS

This section provides an overview of the whole design where drawings, tables, simulations and graphs, provide a clear design of the proposed PV/T model.

4.1. 3-Dimensional model

The design was carried out using Autodesk Inventor Professional. Figure 3 shows different layers of the PV/T system of which the design specifications are presented in Table 1. The frontal layer (upper portion) shown in Figure 3 is the glazing of the PV module. The Peltier fan is positioned at the centre of the module where its light weight is held by the hard transparent glass which also accommodates the radiation not absorbed by the PV cells. The liquid transporting tubes underneath the thermal absorber are designed in such a way that they accommodate excess heat produced by the fan.

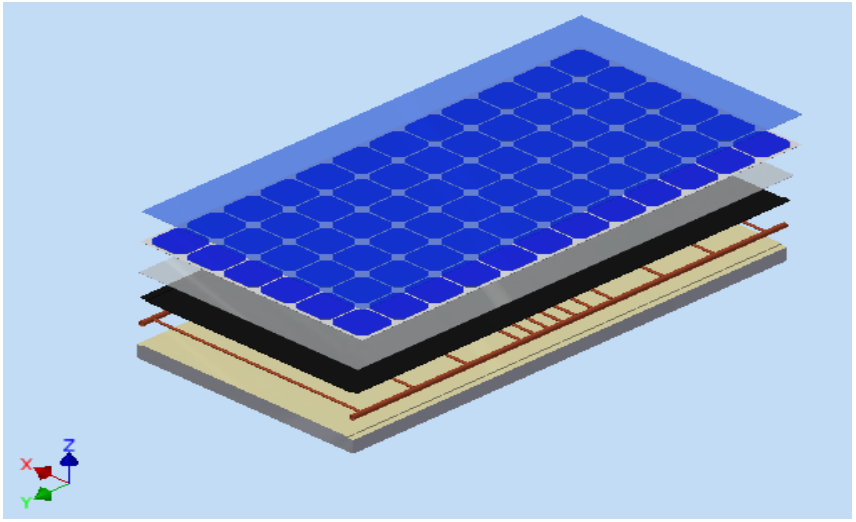

Figure 3: PV/T layers

Table 1: Design specifications

Component	Material	Dimensions (mm)	Thermal Conductivity (W/m.K)
PV outer cover	Glass	1586 x 800 x 2	0.96
PV module	Mono-Silicon	1586 x 800 x 2	148
Cell	Mono-Silicon	125 x 125 x 2	148
Frame	Aluminium	1606 x 820 x 10	237
Peltier fan	Thermoplastic	D100 and D180 x 30	-
Anti-reflective cover	Glass	1566 x 780 x 2	0.96
Insulation	Styrofoam	1566 x 780 x 60	0.003
Tubes	Copper	D20 and D10 x 2	401
Case	Aluminium	1606 x820 x 220	237
Absorber	Copper coated	1566 x 780 x 60	401

Table 2: Operational conditions

Maximum Operating Temperature	150 ºC
Maximum Operating Pressure	22 bar
Water Flow Rate	80 litres/hour
Nominal Power	200W

Figures 4 and 5 illustrates the inside design of the PV/T module and shows the positioning of the Peltier unit. There is an allowance between the Peltier fans and the PV glass. Similarly, underneath the bigger fan, the same allowance exists to allow heat distribution to the absorber.

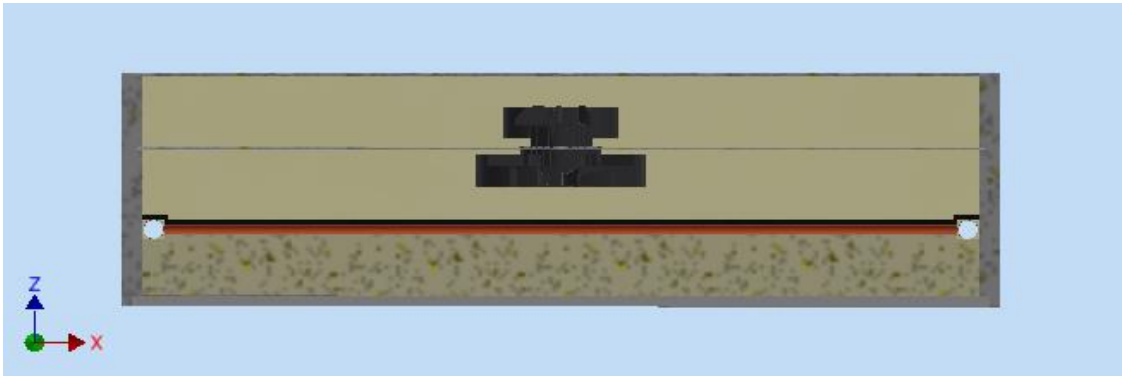

Figure 4: Sectioned wide view

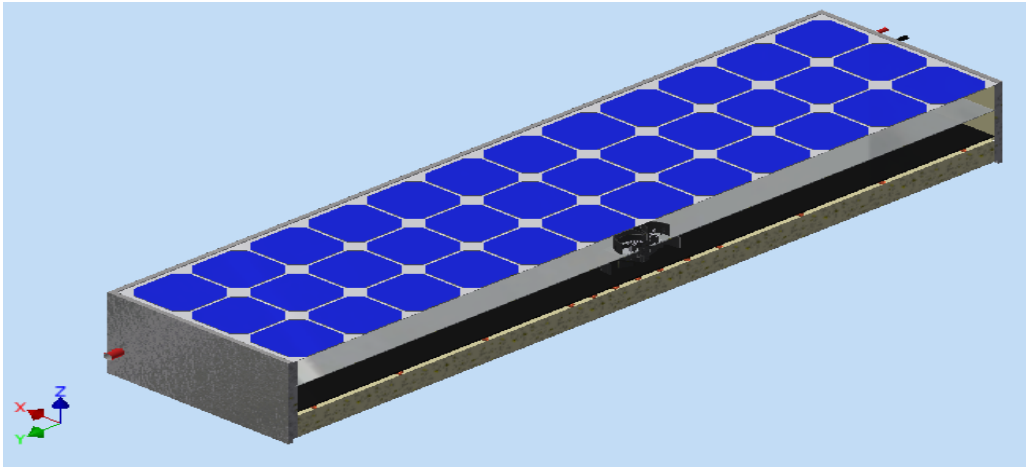

Figure 5: Angled sectioned view

Figure 6 illustrates the Peltier fan developed for cooling the surface cells and drawing the heat absorbed downwards towards the absorber area and the tubes, positioned directly under the absorber layer. Figure 7 shows the section view AA of the PV/T model for better illustration of the components making out the whole unit.

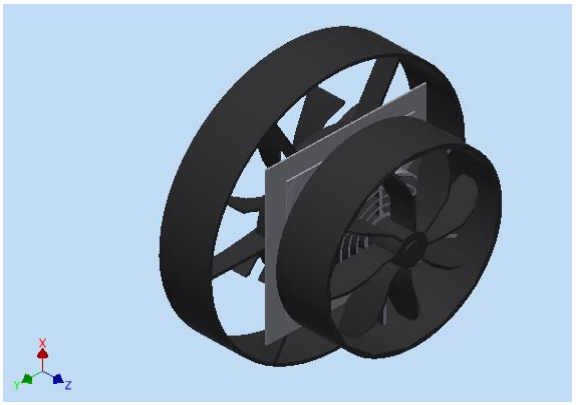

Figure 6: The modified Peltier fans

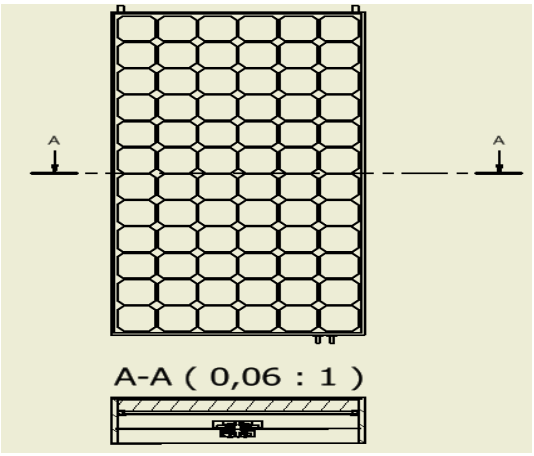

Figure 7: Model section view

4.2. Flow and thermal analysis

Flow analysis

The fan extracts heat from the PV module, in the process cooing it and transferring the heat using the Peltier effect to the absorber which in turn transfer the heat to the liquid contained tubes underneath. Figure 8 illustrates this effect where the maximum temperature lines are shown over the panel surface and the absorber area.

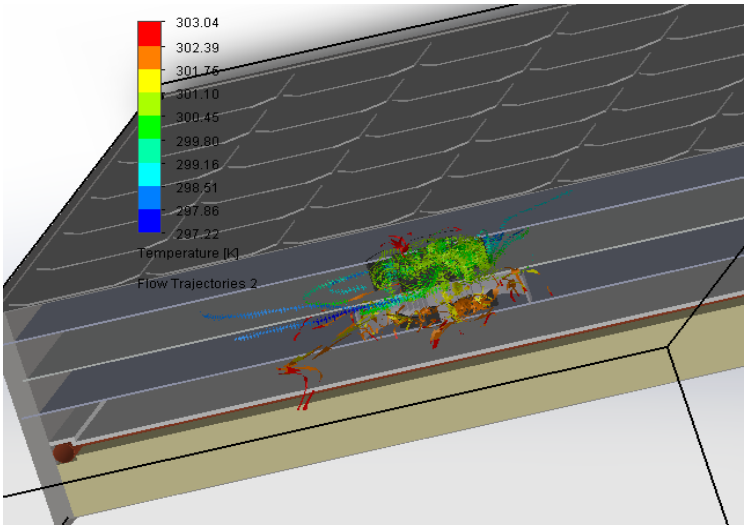

Figure 8: Flow Analysis in SolidWorks

Thermal analysis

The analysis in Figure 9 on the thermal absorber compartment shows that heat is concentrated more around the centre than the sides. Hence, more heat is transferred to the centre due to the positioning of the Peltier fan. Both of the designs incorporate the tubing system with more tubes concentrated on the centre for maximum thermal collection. As such, the centre of the tubes is ideal for positioning the thermal generator for maximum efficiency. This is important because the Peltier fan shall be powered by the electric energy generated by the thermoelectric generator.

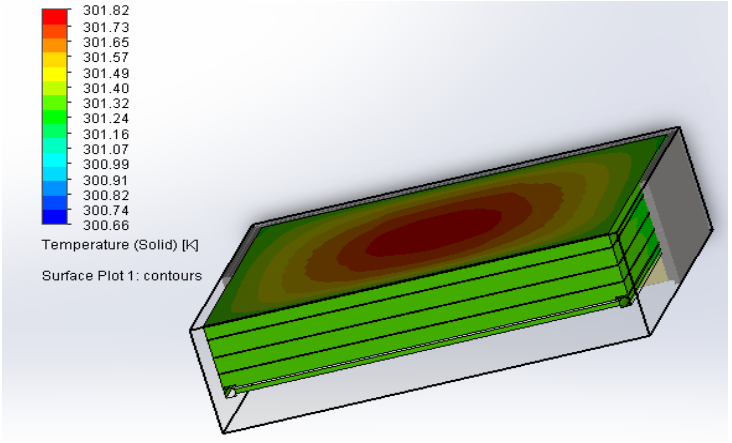

Figure 9: Thermal Analysis in SolidWorks

4.3. Graphical and numerical interpretation

Design 1

The design shown in figure 8 uses a timer where the Peltier is to extract heat from the PV module and cool the cells within a certain time range and after that time, the fan automatically draws heat until the time expires. The graph below showed that as the module is cooled after every 3 minutes of fan shutoff, the efficiency of the module fluctuates by a small percentage. The proposed design ensures that the module operates at a higher efficiency as compared to conventional PV or PV/T operating at the same temperature.

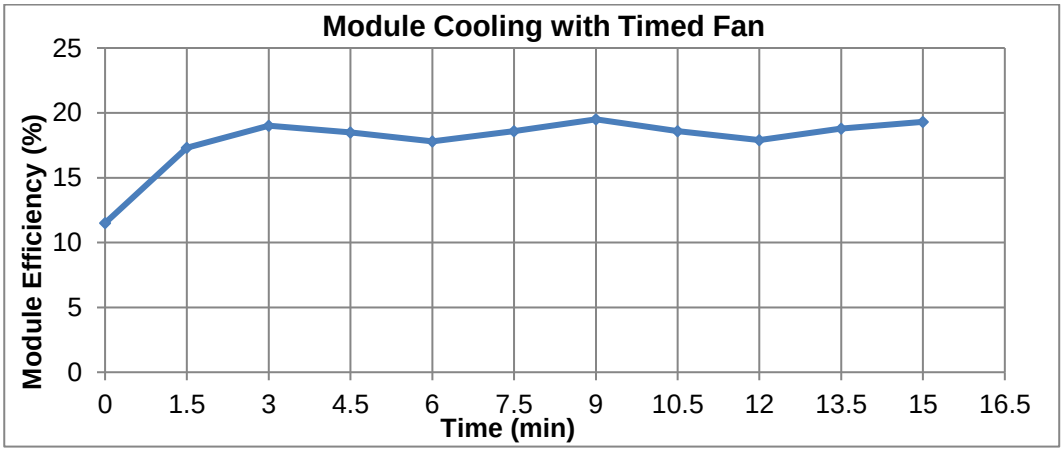

Figure 10: PV timed cooling

Design 2

The design for Figure 11 below uses a continuous cooling process where the Peltier extracts heat from a module without using a timer. The fan rotates at a certain speed to maintain the efficient cell operating temperature within the PV compartment. The graph in Figure 11 shows that by using this design, the efficiency of the module in terms of electricity generated is almost constant. The slight fluctuations witnessed in design 1 as shown in Figure 10 is eliminated by this design. The efficiency remained high irrespective of the time range as shown. The challenge of design 2 is how to effectively maintain the rotational speed of the fan to avoid overcooling or undercooling. The incorporation of a thermostat is currently

being considered, however; because the temperature is different across layers and within each layer, this may not be ideal. Furthermore, as efficient as this option is in design 2, the possibility of early failure (damage) of the Peltier fan is eminent due to constant operation.

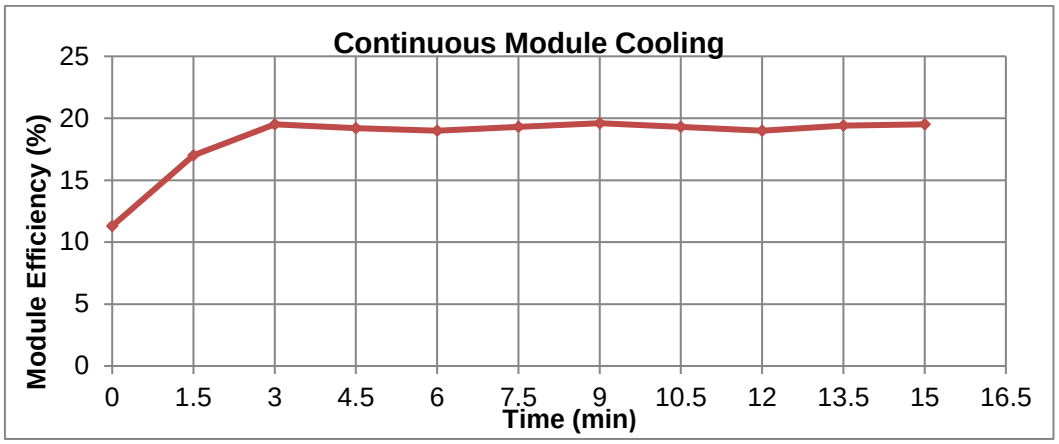

Figure 11: Continuous module cooling

Equation 1 below was used together with the predictions from ANSYS to generate the graphs above. Equation 2 may be used to calculate the thermal output of the PV/T system with known quantities of the fluid inlet and outlet. The proposed model is an efficient electrical and thermal output. Depending on the panel and ambient temperature of the environment, the thermal output may be so high such that the system integrates the thermal storage tank for domestic heating (Eastop & McConkey, 1993).

$$\eta_{module} = \frac{(PV/T)\ power\ output\ in\ kW}{A_{module}}$$

Equation 1: The electrical efficiency of the PV/T module

$$\eta_{thermal} = \frac{m \times C_p \times (t_{outlet} - t_{inlet})}{A_{PV/T\ module}}$$

Equation 2: The thermal efficiency of the PV/T module

Where:

- η = Electrical and thermal efficiency (%)
- m = mass flow rate of air (kg/s)
- C_p = specific heat capacity of air (1.012 kJ/kgK)
- t = outlet and inlet tube temperatures (ºC)
- A = Area of the module (m^2)

5. CONCLUSIONS

The model presented has a high thermal and electrical output. It uses the Peltier effect to cool the PV panel and exhaust that heat into the absorber. Design 1 uses a timer to control the cooling fans of the Peltier connected to the PV module while design 2 uses continuous cooling without a timer. Design 2 yielded maximum desirable results as it maintained the efficiency of the module, but this was factor dependent which is to be avoided by using Design 1 as it is controlled by the timer and also yielded maximum results with small fluctuations. The initial electrical efficiency for both of these designs from the numerical analysis is approximately 11%, at time 0 second before the integration of the cooling systems. Design 1 after 15 minutes of predictive testing resulted in a range of electrical efficiency between 11.5% and 19.5% and for design 2, the range was between 11.3% and 19.5%.This emphasises the need to implement Design 1 with less implications as opposed to Design 2, as both of these designs can reach an electrical efficiency as high as 19.5%. The testing phase of the physical prototype is currently on for further validating the model designs illustrated in this paper. The prototype is currently being tested using different environmental temperature conditions across South Africa, different solar irradiation variants, and different materials. Since reliability is a major component considered in engineering design, the longevity of the two designs will be considered using a lifecycle assessment approach. As a recommendation, researchers can consider testing this system in summer and comparing the obtained results with winter conditions, which is currently beyond the scope of this research.

6. REFERENCES

BCS, I., 2008. [Online] Available at: https://www1.eere.energy.gov/manufacturing/intensiveprocesses/pdfs/waste_heat_recovery.pdf [Accessed 06 May 2018].

Cozzini, M., 2012. *Solar Cell Cooling and Heat Recovery In a Concentrated Photovoltaic System ,* Tronto, Italy : Renewable Energy and Technology Institute.

Da Rosa, A., 2005. *Fundamentals of renewable energy processes.* San Diego: Elsevier Academic Press.

Dean, J., McNutt, D. & Lisell, L., 2015. *Photovoltaic-Thermal New Technology Demonstration ,* United States : National Renewable Energy Labaratory.

Donwell, P., 2016. [Online] Available at: https://www.uky.edu/bae/sites/www.uky.edu.bae/files/Chapter%207%20Heating%20Ventilation%20Air% 20Conditioning.pd [Accessed 01 February 2018].

Eastop, T. & McConkey, A., 1993. *Applied Thermodynamics for Engineering Technologists.* United Kingdom: Longman Group.

Hormazabal, N., Gillett, M. & Ford, B., 2016. The perfomance and in-use experience of low to zero carborn technologies in an experimental home. *International journal of low carborn technologies ,* 11(3), pp. 283 - 295.

Jager, K., Olindo, I. & Smets, A., 2014. *Solar Energy fundametals, technology and systems.* Netherlands : Delft University of Technology .

Jensen, K., Messick, D. & Verzosa, J., 2010. *Google Scholar.* [Online] Available at: https://harding.edu/olree/2009-10/senior%20design%20-%20final%20reports/thermoelectric%20generator/thermoelectric_generator_-_final_report.pdf [Accessed 21 June 2018].

Kalogirou, S. & Tripanagnostopoulos, 2007 . Photovoltaic Thermal (PV/T) Collectors. *Applied Thermal Engineering ,* 27(8-9), pp. 1259 - 1270.

Lynn, P., 2010. *Electricity from Sunlight - An Introduction to Photovoltaics.* United Kingdom : John Wiley & Sons Ltd .

Martinez, P., Ruiz, J., Kaiser, A. & Lucas, M., 2018. Experimental study of energy and exergy peformance of plastic mesh evaporative pad used in air conditioning applications. *Applied Thermal Engineering,* Volume 138, pp. 575 - 685.

Moss, R., Shire, G., Honshall, P. & P.C, J., 2018. Design and fabrication of a hydroformed absorber for an evacuated flat plate solar collector. *Applied Thermal Engineering,* Volume 138, pp. 456 - 464.

Ramos, A., Guarracino, I. & Mellor, A., 2017. [Online] Available at: https://www.imperial.ac.uk/media/imperial-college/grantham-institute/public/publications/briefing-papers/2679_Briefing-P-22-Solar-heat_web.pdf [Accessed 01 February 2018].

Sorensen, B., 2007 . Photovoltaic Conversion . In: *Renewable Energy Conversion, Transmisson and Storage .* USA : Elsevier Academic Press , pp. 94 - 126.

Sorensesn, B. & Katic, I., 2003. [Online] Available at: http://citeseerx.ist.psu.edu/viewdoc/download?doi=10.1.1.552.8832&rep=rep1&type=pdf [Accessed 25 January 2018].

Tahakkar, M., 2016 . *A report on Peltier thermoelectric cooling module ,* s.l.: s.n.

Thorpe, D. (., 2011. *Solar Technology - The earthscan expect guide.* New York : Earthscan .

304: A numerical study of mixed convection within a liquid flowing on an open horizontal channel

Shenglin QUAN, Jiayue ZHAO, Fei MENG, Qinggang QIU, Shengqiang SHEN

Dalian University of Technology, Key Laboratory of Desalination Dalian, Liaoning Province,116024, slquan@dlut.edu.cn

The study of mixed convection in a horizontal channel with a free upper surface is not only able to guide the design and optimisation of many industrial applications, such as heat exchangers, evaporative cooling devices, but also beneficial for further understanding the nature of liquid flowing instability. By using the software of FLUENT, this paper presents a numerical study of laminar mixed convection in a horizontal channel with a uniformly heating bottom and a free upper surface where fluid convects with air. The temperature of sidewalls are both constant. The results showed that in the range of the dimensionless numbers we studied, the secondary flow of liquid is in the form of longitudinal rolls. The rolls appear near the sidewalls of the channel. As the liquid flows, the rolls gradually appear in the centre of the channel. The occurrence of longitudinal rolls improves the local heat transfer coefficient. The increase of Reynolds number lengthens the entrance region, and also strengthens the overall heat transfer. The variation of Biot number has almost no effect on the heat transfer near the sidewalls, but in the central region, the local Nusselt number increases with Biot number.

Keywords: Laminar mixed convention, Longitudinal rolls, Horizontal channel, Free surface

1. INTRODUCTION

The phenomenon of film flow widely exists in industrial fields like desalination, distillation, falling film evaporation and so on. When film flows in the horizontal channel with heated bottom, a secondary flow will be generated by the change of body force which causes by temperature gradient of the film. Under a certain range of Reynolds number, the secondary flow is in the form of longitudinal rolls (the axis of the rolls is parallel to the direction of the main flow) and begins to bifurcate and return back to the heated wall by shear force, whose structure is similar to mushrooms. Under certain conditions, buoyancy of the liquid causes the development of longitudinal rolls, which constitutes the first stage of the transition towards to turbulence and enhances heat transfer (Imura, 1978). It is found that the flow pattern and heat transfer of the film depend on Rayleigh number, Reynolds number, Prandtl number and the aspect ratio (1992).

In some literatures, the mixed convection in horizontal channels have been studied by experiment and simulation. Mori and Uchida (1966) found the longitudinal rolls of air heated in the parallel-plate channel. The mechanism of the secondary flow in the bottom-heated, above-cooled channel was studied in literatures (Chang, 1997; Chiu, 1987; Gau, 1999; Maughan, 1990), and the results demonstrated that the longitudinal rolls are triggered near the side walls of the channel in the inlet region and then move toward the centre, as shown in Figure 1. At high Rayleigh number, Benderradji et al. (2008) observed other initiation mechanism of longitudinal rolls in the horizontal channel heated below. The mechanism combines the lateral wall effect with the high vertical temperature gradient at the lower position of the channel, and pairs of rolls are simultaneously formed throughout the whole area of it. Ostrach and Kamotani (1975) experimented with the fully developed airflow between isothermal plates and indicated that the rolls become irregular when Re=38 and Ra>8000. Based on the propagation theory, Kim et al (2003) analysed the critical condition of the onset of longitudinal rolls versus Prandtl number in Poiseuille flow uniformly heated below. The result showed that the starting position of the secondary flow moves downwards with an increase of Prandtl number and Reynolds number. For water and air, this result is consistent with the experimental data. Lahcen Bammou (2013) used numerical simulation method to prove that the wavelength of the local Nusselt number of liquid decreases with the increase of Biot number in the open horizontal channel which has adiabatic sidewalls.

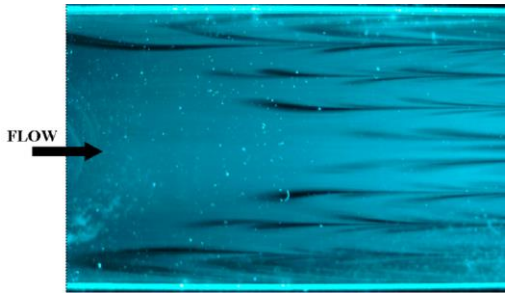

Figure 1: The flow pattern of air mixed convention in the horizontal channel

Over the years, scholars have studied the mixed convection of water or air in closed channels deeply, but it is very rare for free-surface laminar mixed convection studies. In actual industrial equipment, forced convection, natural convection, buoyancy convection, and marangoni convection often coexist at the same time, driving fluid motion and flowing more complex. In this paper, the numerical simulation method is used to study the laminar mixed convection of water in a rectangular horizontal channel which has free upper surface and uniformly heated from below. The influence of Reynolds numbers and Biot numbers on the flow is analysed. It may provide a certain theoretical basis to practical engineering.

2. PHYSICAL AND MATHEMATICAL MODELS

The physical model used in this subject is a rectangular horizontal channel, as shown in Figure 2. The size is length L = 50cm, width W = 10cm, depth d = 1cm. The upper surface is free surface, and is in contact with air, the surface heat transfer coefficient is h, the lower surface is heating surface whose temperature is Th. The left and right sidewalls is adiabatic or constant temperature vertical wall, the water flow through the channel with velocity v, the inlet temperature T = Tc, ambient temperature T0 = Tc. For simplicity, it is assumed that: 1) the liquid is incompressible Newtonian fluid, the density satisfies the Boussinesq approximation; 2) the free surface is not deformed, According to the Davis (1987) when $Cr = \rho\gamma\alpha/\sigma H << 1$ (where ρ is the density, γ is the kinematic viscosity, α is the thermal diffusivity), the deformation of the liquid surface can be ignored, that can be considered the height of the liquid is same in any point .3) takes into account the thermalcapillary force effect (Marangoni effect) at the free surface , and the other surfaces are non-slip boundary conditions; 4) Flow is laminar which velocity is low.

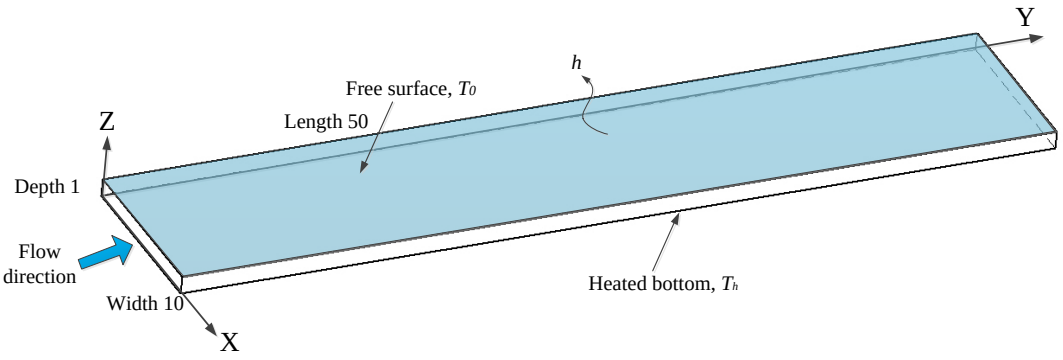

Figure 2: Physical model

Defining the non-dimensional temperature $\theta=(T-T_0)/(T_h-T_0)$. Using these assumptions and dimensionless variables, the equations governing the conservation of mass, momentum and energy can be expressed in the following form:

Boundary conditions are as follows:

At the free surface (Z=1, 0<X<W, 0<Y<L/d)

$$\frac{\partial V_x}{\partial Z}=-\frac{Ma}{Pe}\frac{\partial \theta}{\partial X},\ \frac{\partial V_y}{\partial Z}=-\frac{Ma}{Pe}\frac{\partial \theta}{\partial Y},\ V_Z=0,\ \frac{\partial \theta}{\partial Z}=-Bi\,\theta \tag{1}$$

At the bottom surface (Z=0, 0<X<W/d, 0<Y<L/d)

$$\vec{V}=\vec{0},\theta=1 \tag{2}$$

At the side walls (X=0 和 X=W/d, 0≤Z≤1, 0≤Y≤L/d)

$$T=T_W \tag{3}$$

At the inlet (Y=0)

$$V_X=V_0,V_Y=V_Z=0,\theta=0 \tag{4}$$

Where $Ma=\frac{\partial\sigma}{\partial T}\frac{\Delta TH}{\mu\alpha}$, $Pe=\frac{U_m H}{\alpha}$ is Ma number and Pe number.

The fundamental equations are discretised by the finite volume method. For the diffusion term and the convective term, second-order central difference and second-order upwind scheme are used respectively. And SIMPLE method is used for the pressure-velocity correction. In order to test the grid convergence, different grids are simulated and calculated under the condition of Re = 10, Bi = 30, Ra = 4200, Ma = 500 and Γ = 10. The results of the maximum speed of the outlet is shown in Table 1. Obviously, the 100X × 400Y × 50Z grid is the most appropriate for accurate simulation in this paper.

In order to verify the correctness of the results, we compared the results with those in same conditions in the literature (Zhou, 2015). The results are shown in Figure 3. It can be seen from figure 3 that the two curves are in good agreement, which indicates that the results are reliable.

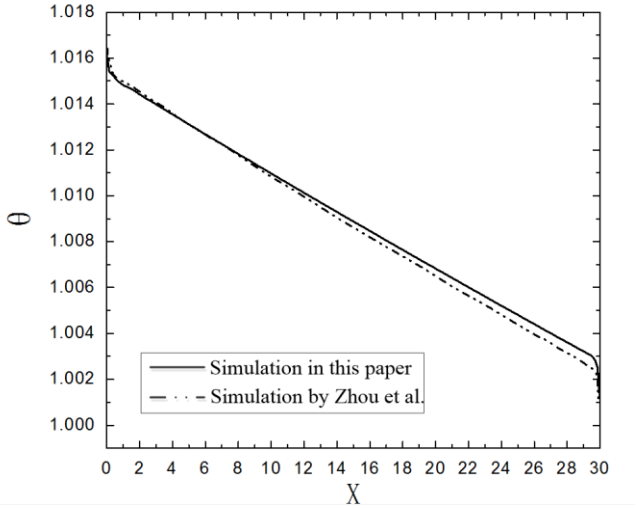

Figure 3: Comparison of temperature distribution

Table 1. Mesh-independence check Re=10，Bi=30，Ra=4200，Ma=500 和Γ=10

grid (X×Y×Z)	200×50×25	400×100×50	800×200×100
vmax	1.83×10-3	1.78×10-3	1.76×10-3

3. RESULTS AND DISCUSSION

Figure 4 shows the contours of the stream function at cross section Y = 40 when Re = 10, Bi = 30, Ra = 4200 and Ma = 500. All subgraphs are obtained when both sidewalls are at constant temperatures except Figure 4(a) which is the case when the walls are thermal-insulated. From Figure 4(a)~(d), we can see that the direction of longitudinal rolls near the same side in the case of adiabatic sidewalls is opposite to that in the case of constant temperatures. This is because that for adiabatic sidewalls, due to the presence of the boundary layer near the sidewalls where heat accumulating triggers the fluid temperature increase, i.e. the fluid temperature gradually decreases from sidewalls to centre. Furthermore, the higher the fluid temperature, the greater the buoyancy force, which results the generation of longitudinal rolls. When sidewalls are at constant temperature, the direction of fluid temperature gradient is opposite to that in the case of adiabatic sidewalls, so that the direction of rolls in the same wall is opposite to that in adiabatic case. But the increasing sidewall temperature makes the fluid temperature gradient smaller and smaller, which results that the volume of rolls reduces.

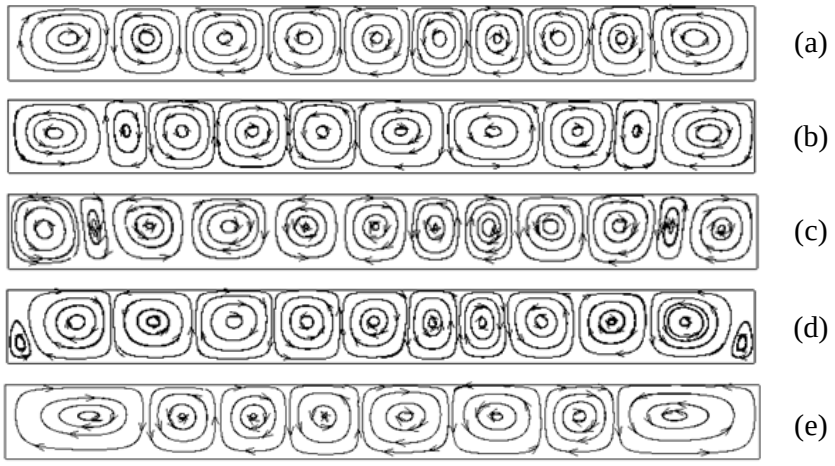

Figure 4:The 2D stream function field at cross section Y=40 when Re=10, Bi=30, Ra=4200 and Ma=500 (a. adiabatic side walls, b-e. dimensionless temperatures of side walls are：0,1/3,2/3,1，respectively).

Therefore in the same cross-sectional size, the number of longitudinal rolls increases. If the sidewall temperature continues to rise, the direction of fluid temperature gradient will be changed, i.e., being consistent with the adiabatic case, see Figure 4(e). In this case, the longitudinal flow direction also changes.

Figure 5 shows the variation of Nusselt number near the bottom when Re = 10, Bi = 30, Ra = 4200 and Ma = 500. It can be seen from Figure 5(a) that in the middle region of the channel transverse (Y=40), the local Nusselt number Nul under the different sidewall conditions are all similar to a sinusoidal function changed with the x-coordinate, and the amplitudes of Nul in different condition in this region are much the same. However, in the near wall area, when the wall temperature is lower than bottom, Nul there decreases with the increase of the dimensionless sidewall temperature. This is because the lower dimensionless sidewall temperature, the lager temperature gradient near the wall where the buoyancy force becomes more obvious, which means that natural convection there is enhanced gradually. However, when the sidewall temperature is same to bottom temperature, the temperature gradient there approaches to zero and thus Nul approximately equals zero too. Figure 5(b) demonstrated the longitudinal variation of the transversally averaged Nusselt Nutav under different sidewall conditions. It can be seen from the figure that with the augment of Y, Nutav first decreases sharply and then grows to reach a peak before falling again slightly. This is because the inlet region is characterised by force convection. And after a short distance from the entrance, due to the development of longitudinal rolls, natural convection increases, and therefore Nutav increases. In the entrance region, as can be seen, Nutav is consistent in different sidewall cases. However, with the augment of Y, the higher dimensionless sidewall temperature, the smaller temperature gradient at the channel cross section where the natural convection weakens, and thus Nutav decreases.

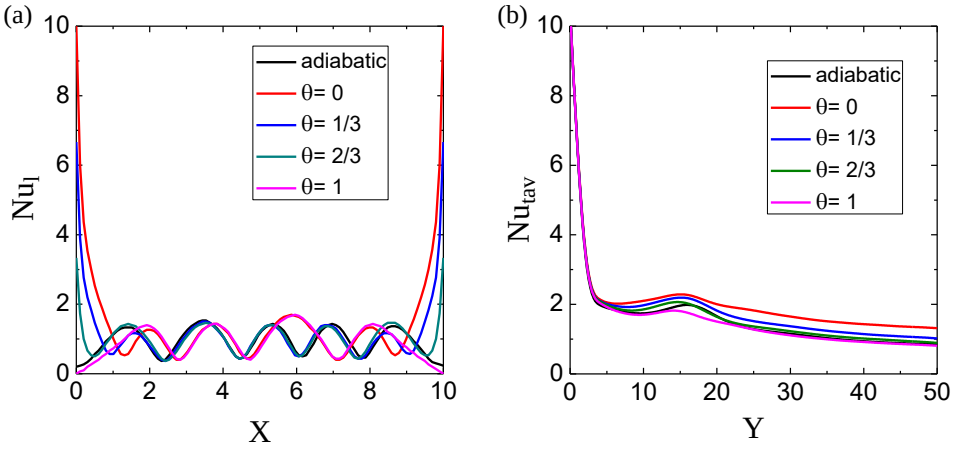

Figure 5: When Re=10, Bi=30, Ra=4200 and Ma=500. (a) the transverse variation of the local Nusselt number at Y=40; (b) the longitudinal variation of the transversally averaged Nusselt number.

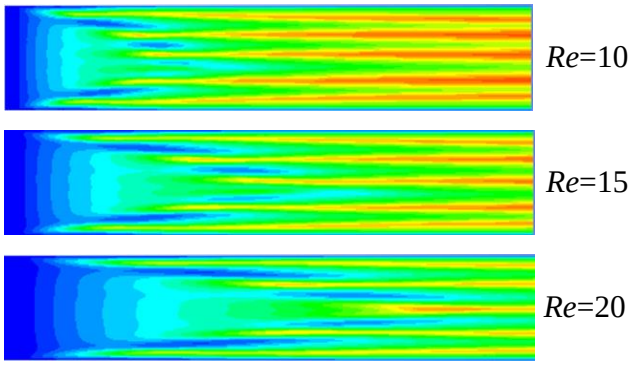

Figure 6: The reduced temperature field □ on the free surface for different Reynolds numbers when the dimensionless temperatures of side walls are 1/3 (Bi=30, Ra=4200 and Ma=500).

Figure 6 shows the change of dimensionless temperature field in free surface at different Reynolds numbers when dimensionless sidewall temperature is 1/3. It can be seen that with the increase of Reynolds number, the onset position of longitudinal rolls in fully developed area gradually moves backward while the number of rolls is not affected by Reynolds number. This is consistent with the results of adiabatic sidewall in literature (Bammou 2013). It can be seen from Figure 7 that the local peak of Nu_{tav} in cross-section moves backwards as Reynolds number increases, which is also due to the moving backward of the full development zone. However, different with that Nu_{tav} after the local peak has no variation with Reynolds number in adiabatic sidewall case which is shown in Bammou (2013), Nu_{tav} in that region grows monotonically as Reynolds number augments when dimensionless sidewall temperature is 1/3. This is because the fluid heat transfer is enhanced with the increase of Reynolds.

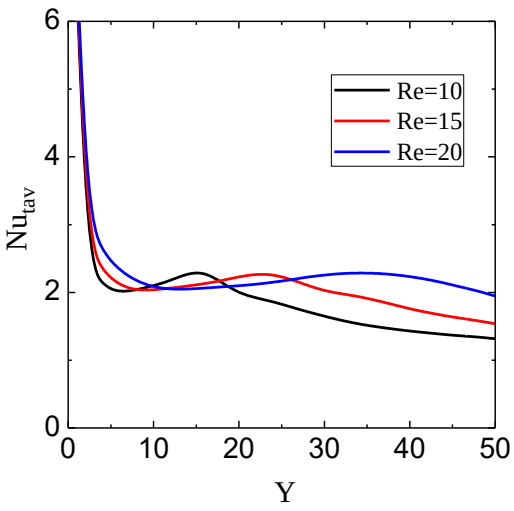

Figure 7: The longitudinal variation of the transversally averaged Nusselt number for different Reynolds numbers when Bi=30, Ra=4200, Ma=500 and the dimensionless temperatures of side walls are 1/3.

Figure 8 shows the variation of Nusselt number with Biot number when dimensionless sidewall temperature is 1/3, *Re* = 10, *Ra* = 4200 and *Ma* = 500. From Figure 8(a), we can see that Biot number has no effect on the local Nusselt number Nu_l at the near wall. However, in the central region, Nu_l increases with Biot number. This is because the increase of Biot number makes temperature gradient below the free surface increases, thereby enhancing the heat transfer effect. But Biot number has no effect on the number and positions of Nu_l peaks. As shown in Figure 8(b), the positions of local peaks of Nu_{tav} under different Biot numbers are same. But in *Y* direction after the peaks

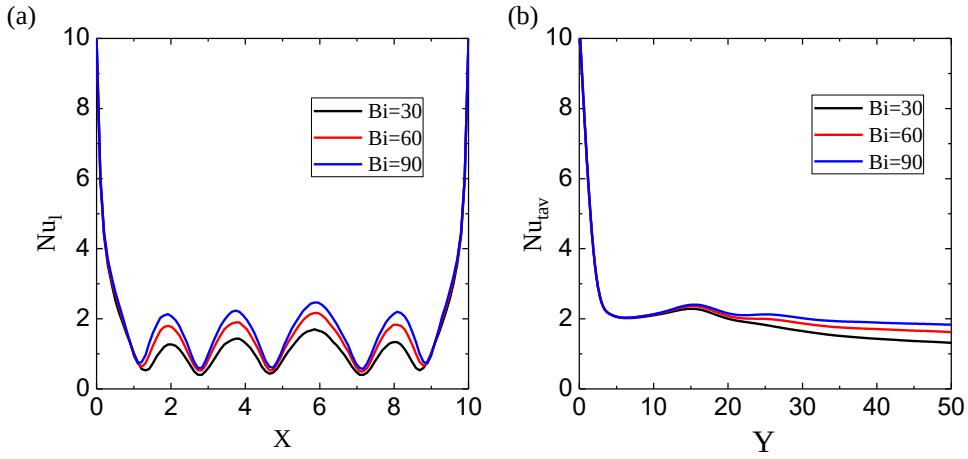

Figure 8: When Re=10, Ra=4200, Ma=500 and the dimensionless temperatures of side walls are 1/3, for different Biot numbers: (a) the transverse variation of the local Nusselt number at Y=40; (b) the longitudinal variation of the transversally averaged Nusselt number.

4. CONCLUSION

In this paper, through numerical simulation of the three-dimensional hydromechanics basic equations and FLUENT software, the effects of different sidewall temperatures, Reynolds numbers and Biot numbers on the laminar mixed flow in a rectangular channel with a free upper surface and a heating bottom are studied. The main conclusions are as follows:

1) When the sidewall temperature is lower than the bottom heating temperature, the rotational direction of longitudinal rolls formed near the sidewall is opposite to that in adiabatic or same temperature with bottom cases. And meanwhile, Nul near sidewalls decreases with the increase of sidewall temperature, which is same with the variation of Nutav in the full development region.

2) With the increase of Reynolds number, the onset of longitudinal rolls is gradually shifted backwards in the fully developed region, but the number of rolls is not affected by Reynolds number. And Nutav in the area behind the local peak increases gradually due to the increase of Reynolds number.

3) Biot number has almost no effect on Nutav near the side walls. However, in the central region, Nutav augments with Biot number. And the position of local peak of Nutav under different Biot numbers are same. However, in the region beyond the position of local peak, Nutav augments with the increase of Biot number.

5. ACKNOWLEDGEMENT

Supports from National Natural Science Foundation of China (No. 51376035) and the Fundamental Research Funds for the Central Universities (DUT17ZD226) for this research are acknowledged with thanks.

6. REFERENCES

Bammou L, El Omari K, Blancher S, Le Guer Y, Benhamou B, and Mediouni T. 2013. A. Numerical study of the longitudinal thermoconvective rolls in a mixed convection flow in a horizontal channel with a free surface. [J]. Int J. Heat Fluid Flow, 42: 265–277.

Benderradji A, Haddad A, Tahe, R, Médale M, Abid C, and Papin, F. 2008. Characterization of fluid flow patterns and heat transfer in horizontal channel mixed convection [J]. Heat and Mass Transfer, 44: 1465–1476.

Chang M Y, Yu C H, and Lin T F. 1997, Changes of longitudinal vortex roll structure in a mixed convective air flow through a horizontal plane channel: an experimental study [J]. Int J. Heat Mass Transfer, 40:347-363.

Chiu K-C and Rosenberger F. 1987, Mixed convection between horizontalplates-I. Entrance effects [J]. Int J. Heat Mass Transfer, 30: 1645-1654.

Davis, S. 1987, Thermocapillary instabilities [J]. Annual Review of Fluid Mechanics, 19: 403–435.

Gau C, Liu S W, Huang T M, and Aung W. 1999, Secondary flow and enhancement of heat transfer in horizontal parallel-plate and convergent channels heating from below [J]. Int J. Heat Mass Transfer, 42: 2629-2647.

Imura H, Gilpin R, and Cheng K, 1978, K. An experimental investigation of heat transfer and buoyancy induced transition from laminar forced convection to turbulent free convection over a horizontal isothermally heated plate [J]. Int J. Journal of Heat Transfer, 100: 429–434.

Kim M C, Chung T J, and Choi C K. 2003. The onset of convective instability in the thermal entrance region of plane Poiseuille flow heated uniformly from below [J]. Int J Heat Mass Transfer, 46:2629–2636

Maughan J R and Incropera F P, 1990, Regions of heat transfer enhancement for laminar mixed convection in a parallel plate channel [J]. Int J. Heat Mass Transfer, 33: 555-570.

Mori Y, and Uchida Y. 1966, Forced convection heat transfer between horizontal flat plate [J]. Int J Heat Mass Transf, 9:803–817.

Oosthuizen P H, and Monaghan P F. 1992, Free Convective Flow in a Vertical Non-rectangular Cavity with a Cooled Flat Upper Surface, Natural/Forced Convection and Combustion Simulation [J]. Proc. 2nd International Conference on Advanced Computational Methods in Heat Transfer, 2: 192–208.

Ostrach S, and Kamotani Y. 1975, Heat transfer augmentation in laminar fully developed channel flow by means of heating from below [J]. Int J. Journal of Heat Transfer, 97: 220–225.

Zhou Y. 2015. Research on Marangoni-Thermocapillary Convection in a Shallow Rectangular Liquid Pool with the Bidirectional Temperature Gradients [D]. Chongqing: Chongqing University.

305: Research on the compensation mechanism and effects of low carbon operating costs of enterprises under the constraint of carbon emission reduction

Defa WANG [1], Ling LIU [2]

[1] Hubei Collaborative Innovation Centre for High-efficiency Utilization of Solar Energy, Hubei University of Technology, 674804321@qq.com
[2] School of Economics and Management, Hubei University of Technology,2066175546@qq.com

The rapid development of human industry over the past 200 years has enabled us to seize unprecedented material wealth while failing to avoid environmental problems such as depletion of resources, muddy air, warming of climate, and pollution of water sources. Under the background of the increasingly serious global environmental problems, the green economy model of energy conservation, emission reduction and low carbon development has been put on the agenda and has been widely recognised by the international community. As the world's largest emitter of greenhouse gases, China is also actively seeking response measures. This paper starts from the externalities of low-carbon operations and selects listed companies in the heavily polluted A-shares industry from 2013 to 2016 to use spss19.0 software for empirical analysis to explore the compensation effect of market compensation and government subsidies on low-carbon businesses. With the aid of regulatory variables, the analysis of the regional and property rights nature of the carbon emission reduction pilots will influence the company's access to market compensation and government subsidies.

Through analysis of empirical results, it is believed that companies can obtain compensation for their low-carbon business activities from the government and the market. In the current market environment, due to the imperfection of the carbon trading market, its role has not been fully realised. Government compensation is still the main means of regulation. Although state-owned enterprises can obtain more compensation from the government, relatively less compensation is obtained from the market.

Keywords: low-carbon management, externality theory, carbon emissions, environmental issues, cost compensation

1. INTRODUCTION

The world warming is a common problem faced by humans in the 21st century. Since the industrial revolution, the impact of human activities on the climate has gradually increased. In particular, developed countries have used a large amount of fossil energy, resulting in rising CO_2, increasing the concentration of CO_2 in the air, and accelerating the rate of global temperature rise. In the past 100 years, the average annual temperature in China has increased by 0.5-0.8°C, especially in the past 50 years. China's future climate warming trend will further intensify. Scientists in China have predicted through research that compared with 2000, China's average temperature will increase by 1.3 to 2.1°C by 2020 and by 2.3 to 3.3°C by 2050. Climate warming indirectly intervenes in the natural ecosystem and brings to our production and life challenges that cannot be overestimated (China Clean Development Mechanism Network).

As China is currently in a critical period of rapid industrialization and urbanization, the construction of large-scale infrastructure has become an impending trend. The large amount of energy consumed and continued to rise cannot be changed within a short period of time, resulting in a continuous increase in carbon emissions. At present, more than 80% of China's CO_2, more than 70% of smoke and 90% of SO_2 originate from corporate coal. The coal-based energy consumption structure has brought severe environmental pollution to China, but this energy structure cannot be replaced in the near term or even for a long time. The backwardness of software and hardware leads to a higher CO_2 emission per unit of GDP in China than in developed countries. The energy consumption of major production processes and products is higher than that of other countries in the world by nearly one third. China's dependence on energy continues to increase with the development of the economy, energy issues become increasingly acute, and low-carbon environmental protection has become an inevitable requirement for China's development.

2. THEORETICAL BASIS

2.1. Theory of externalities

Externality theory is one of the theoretical foundations of sustainable development. It was first proposed by welfare economist Pigou (2013). On the basis of Marshall's "internal economy" and "external economy" theory, Pigou believes that when the private marginal income does not equal the social marginal revenue, the activity will have an impact on the society; that is, the microscopic entities in the market may cause damage to third parties or society during the transaction, but this damage is not Contained in the transaction costs of both parties, leading to society cannot achieve Pareto optimal state. As for the theory of externalities, Pigou's "Pigou's tax" suggests that the government should play a role in subsidizing enterprises that have positive externalities and taxing companies that have negative externalities. The amount of subsidies or taxes should be equal to the marginal gain or loss of the positive externality of the producer. Externalities are divided into positive and negative aspects. The positive externality is that the social marginal income is greater than the private marginal revenue, the economic activity will bring favourable social influence to the society; the negative externality is that the social marginal benefit is smaller than the private marginal benefit, and the economic activity will bring adverse influence to the society (Wang, 2012).

2.2. Cost compensation theory

Marx pointed out in " Capital " that the value of commodities W, the surplus value M, and the capital value C + V, the formula is W = C + V + M. Cost is the unity of production cost and compensation value. Cost is both a measure of consumption value and a basic limit of compensation.

The concept of cost compensation changes with the extension of the concept of cost. Under the influence of the concepts and goals of sustainable development, people from all walks of life generally realised that enterprises cannot exploit natural resources free and unrestrained in pursuit of economic interests, nor can they pursue economic benefits at the expense of the environment, but should pursue economic interests, Balanced development of the three goals of social interests and environmental benefits. In the face of the current world-wide shortage of resources, environmental pollution, frequent disasters, soil erosion, land desertification and other more and more serious reality, people should realise that these problems have not been resolved scientifically for a long time. One of the important reasons is that some cost theories lack a cost theory that is understood and defined in terms of natural capital scars and human activities. From the perspective of large-cycle cost theory, the composition of cost should be the sum of the cost of natural resources, materialised labour, and consumption of living labor. Cost compensation only includes the consumption or expenditure of these three aspects, and ultimately it can make the human society and nature complete a virtuous cycle (Fu, 2001).

2.3. Low carbon operating cost compensation mechanism

Government compensation

Given the current reality in our country, government compensation is still the most effective way in existence.

Financial transfer payment is one of the main measures of government compensation. Mainly refers to the fact that part of the public revenue that is unpaid is under the micro-economy or subordinate (sibling) government, and they have the right to deal with it. As a special subsidy, the financial payment transfer is a general term for the central fiscal expenditure and horizontal disbursements between local governments. The funds allocated for the transfer must be used for specific projects and be used for special purposes. The representative countries of the system are the United States and Germany.

Carbon tax is one of the common ways of government compensation. As a kind of indirect taxation, the carbon tax can influence consumers' consumption behaviour to a certain extent, mainly as follows: a certain amount of tax is levied on every ton of carbon emissions, and in the case of constant energy efficiency and energy varieties, it is equivalent to raising the commodity price on the basis of the original price. When commodity prices rise, consumers do not have to change their spending budget, there are only two options, either reduce the consumption of goods, or choose low-carbon alternatives. Second, change producers' production behaviour. When Consumers change their behaviours, it will then affect the producers; it will then affect the producer. The producer will either increase product competitiveness or increase energy efficiency. The ultimate goal is to reduce carbon emissions.

Market compensation

Based on the classification of “beneficiaries”, the current market compensation mainly includes the following two types: One-point transactions are one-to-one transactions. This model can well meet the needs of single-income objects, single situations, and single ecological function compensation (Zhou, 2010). For example, given that forests conserve water and maintain soil and water, they can prevent ~~of~~ the occurrence of siltation, thus prolonging the life of reservoirs, hydropower stations, and embankments, it can be seen that the beneficiaries of this ecological function are the water conservancy and hydropower departments, so they should be compensated for the main body of forest rights; Market trading, such as trading of emission rights and eco-labels. Under this model, there is less government intervention, and buyers and sellers of ecological services trade directly in the market. The EU's ecolabel is a typical example of this approach. As an indirect payment method, after the relevant national agencies conduct a rigorous review, the compliance products are given the “green” mark. Such products can be more expensive than other products, and some customers receive higher payments to purchase such products (Cai, 2012). Eco-labelling can influence the generation of consumer behaviour to a certain extent, thereby promoting the improvement and development of green industry (Wu, 2009).

3. RESEARCH HYPOTHESIS

3.1. Market compensation and government compensation

As to the theory of externality, the "Pigou tax" proposed that the government should play a role in providing subsidies to enterprises that have positive externalities and to impose taxes on enterprises that have negative externalities. "Kos theorem" thinks that as long as the property right can be defined in the market, when the transaction cost is zero, the result can be reached to the Pareto optimal by bargaining. The "Kos theorem" is a market plan to solve externalities. It shows that the government is not the only way to solve the market failure caused by externalities. The practice of market economy countries also proves that the market is the most effective way to allocate resources.

Manhong Shen (2011) explains the essence of low carbon economy, and thinks that the economic essence of carbon emission is negative externality, and the economic essence of carbon emission reduction is positive externality. Low carbon management is a new management model with low energy consumption, low emission and low pollution. Low carbon technology and energy saving technology are used to develop low carbon products and industries and reduce carbon dioxide emissions. This is a positive externality. To solve the externalities of low carbon management, we should combine government regulation and market allocation organically.

Based on the above theory, the hypothesis 1 is proposed：

H1：Low carbon business can obtain cost compensation from the market and the government.

The market compensation mode mainly includes carbon emissions trading, water rights, energy consumption, emissions trading, eco label system and derivative financial products. Carbon emission right is the amount of surplus carbon emission from enterprises to develop low carbon management because of technology improvement. The enterprises with difficult emission reduction can buy these quotas through the carbon trading market, so as to obtain the right to discharge the amount of carbon dioxide. Emission rights, water rights and energy use rights and carbon emission rights have similar meanings. The eco label system is the authoritative certification of the European Union in order to encourage the production and consumption of "green products" in Europe. Product label certification in the European Union can increase the added value of the product and win a larger consumer group, although it is 20%~30% higher than the average price.

At present, the market compensation models that enterprises can obtain are mainly green product certification, carbon emission trading and carbon financial products. However, since the authority of green product certification has not been fully established in the commodity market, the carbon trading market is still in the primary stage and the calculation of

carbon distribution and accounting for carbon accountings still not available. To be perfect, the scope of the development is very limited. The government as the maker, the guarantor and the supervisor of policy is responsible for guiding, promoting and supporting the low carbon development of the enterprises. So it is easier for the enterprises to obtain the corresponding subsidies from the government in the early stage of low carbon management.

Based on the above theory, the hypothesis 2 is proposed:

H2: Under the current market environment, the government's compensation for the low carbon business cost is higher than that of the market.

3.2. Regionally

Since 2010, the National Development and Reform Commission (NDRC), in order to actively respond to climate change, has explored the model of low carbon economic development, and decided to determine eight cities including Guangdong, Hubei, Liaoning, Shaanxi and Yunnan provinces and Tianjin, Chongqing, Hangzhou, Xiamen, Shenzhen, Guiyang, Nanchang and Baoding as the low carbon pilot provinces. Compared with non-pilot areas, carbon trading market is established in some pilot areas, and enterprises can get compensation from carbon market transactions. The government requires enterprises in the pilot area to formulate supporting policies to support low carbon green development, Including implementing low carbon emission system, data system and management system as well as promoting low carbon green lifestyle and consumption patterns. This increases the input cost of the enterprises further, and accordingly the government may give more compensation.

Based on the above theory, the hypothesis 3 is proposed:

H3: Compared with the non-pilot areas, the market compensation level in the pilot area is higher than the government compensation level.

3.3. Property right

State-owned enterprises control the economic lifeline of the state. They are the embodiment of the will and interests of the state and play a role in regulating the various aspects of national economic development. Because of the special nature of the state-owned enterprises, the government has more stringent requirements for the state-owned enterprises, hoping them to bear more social responsibility. Therefore, the government tends to tilt the limited resources to the state-owned enterprises. Although private enterprises also carry out low carbon management, their primary purpose is to pursue profit, the state-owned enterprises Should take the role of take the role of exemplary lead, and not only pursue profits. From this perspective, the compensation of private enterprises from the market will be higher than that of state-owned enterprises. To be fair, the government needs to give more compensation to state-owned enterprises.

Based on the above theory, the hypothesis 4 is proposed:

H4: Compared with private enterprises, state-owned enterprises get more compensation from the government.

4. EMPIRICAL MODEL

4.1. Index selection

Tobin Q. The low carbon operation and social responsibility of the company will enable the company to gain a good reputation and image, thereby enhancing the performance of the enterprise. From a market perspective, compensation for low carbon business cost will ultimately be reflected in enterprise value. The Tobin Q value is a common market index to measure the performance of the enterprise. Its advantage is that it takes account of the book value and the market value, as well as equity and debt, and can reflect the value of the company more comprehensively.

Market Compensation (MC). Considering the imperfection of the carbon trading market and the availability of the data, when the market compensation index is selected, the compensation amount produced by the model of carbon emission rights mentioned earlier is not adopted. Based on the EU's ecological label system, although the cost the "green product" will increase in the process of circulation, the income will increase high degree corresponding. Market compensation is part of the income generated by the green product that reflects the current unit cost and exceeds the cost of the previous unit cost.

The calculation formula is as follows:

$$MC = \frac{I_n / C_n}{I_{n-1} / C_{n-1}} - 1$$

Where:

In- the operating income of the n year

Cn- the operating cost of the n year

Government Compensation (GC). This article takes the natural logarithm of the amount of the government subsidy. Government subsidies are usually are usually arisen by enterprises engaging in industries or projects that conform to national policies, or involving technological innovation. The losses due to those developments are subsidised by the government.

The name of variables, code and definition is given in Table 1:

Table 1: Definition of variables

Variable Type	Variable Name	Variable Code	Variable Definition
Dependent variable	Tobin Q Value	TOB	The measurement of the market the market value of the enterprise and reflect the compensation level of the cost of the enterprise
Independent variables	Market Compensation	MC	Same as above
	Government Compensation	GC	The natural logarithm of government subsidies
Control variable	Whether or not the State-owned Enterprises	Gov	If the enterprise is state-owned, then 1, otherwise 0
	Whether or not the Pilot Area	Reg	If the area is pilot, then 1, otherwise 0.
	Asset Liability Ratio	Lev	Total assets divided by total liabilities
	Whether disclosing social responsibility report	CSR	The current disclosure of social responsibility is 1, otherwise 0
	Asset Scale	Size	Natural logarithm of asset
	Rate of Return on Common Stockholders' Equity	ROE	The ratio of net profit to average net assets
	Tax Burden	Tax	Sum of additional and income taxes divided by total assets
	Revenue	Rev	Natural logarithm of revenue

4.2. Data sources

Taking 2013 to 2016 as the sample period, the listed companies in heavily polluting industries are selected. The selection of heavy pollution industry is mainly based on the "guide to disclosure of environmental information of listed companies" published by the Ministry of environmental protection in 2010 and the classification of CITIC industry, It includes thermal power, steel, coal, chemical, building materials, paper, textile and pharmaceutical industries. The financial data are from the CSMAR database, excluding ST, *ST company's observations, data outliers and data missing samples, and we obtained 5384 samples. SPSS19.0 and Excel2016 were used to analyse the data.

4.3. Empirical model

Equation 1: to test H1 and H2

$$TOB_{it} = \beta_1 + \beta_2 MC_{it} + \beta_3 GC_{it} + \beta_4 CSR_{it} + \beta_5 Lev_{it} + \beta_6 ROE_{it} + \beta_7 Tax_{it} + \beta_8 Rev_{it} + \beta_9 Gov_{it} + \beta_{10} Reg_{it} + \mu_{it}$$

Equation 2: to test H3

$$TOB_{it} = \delta_1 + \delta_2 MC_{it} + \delta_3 GC_{it} + \delta_4 Reg + \delta_5 MC_{it} * Reg + \delta_6 GC_{it} * Reg + \delta_7 Gov + \delta_8 CSR_{it} + \delta_9 Lev_{it} + \delta_{10} ROE_{it} + \delta_{11} Tax_{it} + \delta_{12} Rev_{it} + \omega_{it}$$

Equation 3: to test H4

$$TOB_{it} = \alpha_1 + \alpha_2 MC_{it} + \alpha_3 GC_{it} + \alpha_4 Gov + \alpha_5 MC_{it} * Gov + \alpha_6 GC_{it} * Gov + \alpha_7 Reg + \alpha_8 CSR_{it} + \alpha_9 Lev_{it} + \alpha_{10} ROE_{it} + \alpha_{11} Tax_{it} + \alpha_{12} Rev_{it} + \varepsilon_{it}$$

i=natural numbers

α，β，δ =the coefficient of variable

μ_{it}，ε_{it}，ω_{it}= random error

5. EMPIRICAL ANALYSIS

5.1. Collinearity diagnosis

If there is collinearity, the result will be distorted or difficult to estimate accurately, so the data need first to do a collinearity diagnosis before the empirical analysis. The correlation coefficient between the company size, income scale, debt ratio,

TOB and government compensation is greater than 0.5, and there is a certain degree of collinearity. To further examine the severity of the collinearity between the explanatory variables, this paper uses the variance factor (VIF) method. If the variance inflation factor (VIF) is less than 5, it indicates that there is no multicollinearity among the variables; if VIF is greater than or equal to 5 and less than 10, the model has more serious collinearity; when VIF is greater than 10, the model has serious multi-coexistence Linear. As shown in Table 2, there is a more serious collinearity between the size of enterprises and the size of income. The reason is that these variables are all functions of corporate assets. When conducting empirical analysis, the impact of the scale of income is not considered, because it represents the profitability and scale of the company, and overlaps with the indicators of firm size and net asset value.

Table 2: Collinearity analysis among variables

Variable	Tolerance	VIF
MC	0.990	1.010
GC	0.606	1.650
Reg	0.990	1.011
GOV	0.819	1.222
CSR	0.813	1.231
Size	0.180	5.553
Lev	0.611	1.637
Rev	0.180	5.571
Tax	0.881	1.135

5.2. Market and government compensation effects

Table 3 shows the regression results of Equation 1. The coefficients of market compensation (MC) and government compensation (GC) are 0.941 and 6.275. Respectively both are significantly related at the 1% level, indicating that the low-carbon business of the company can obtain from the government and the market. Corresponding cost compensation, hypothesis 1 is proved. The coefficient of market compensation (MC) is less than the coefficient of government compensation (GC), which shows that under the circumstances that the low-carbon economy market is not perfect, government compensation dominates, and its compensation effect is more obvious than market compensation. Hypothesis 2 is proved.

It is worth mentioning that CSR coefficient is 0.134 and there is a significant correlation at the level of 1%, that is, corporate disclosure of social responsibility report can better enable enterprises to obtain cost compensation if enterprise carries out low-carbon business operations. The tax burden is significantly and positively related to corporate cost compensation, which indicates that the more taxes the company pays, the more social responsibility it undertakes, and the more it can receive government subsidies. There is a significant positive correlation between the indicators of the low-carbon emission reduction pilot area (Reg) and the compensation effect of the low-carbon operating cost of the company, which shows that the national low-carbon pilot program has begun to play its role.

Table 3: Regression results of Equation 1

Variable	Coefficient	T Value	Sig
MC	0.941***	6.460	0.000
GC	6.275***	4.066	0.000
Reg	0.214***	4.739	0.000
GOV	-0.221***	-4.739	0.000
CSR	0.134***	2.675	0.007
Size	-63.296***	-25.637	0.000
Lev	-2.279***	-18.259	0.000
ROE	0.667***	3.985	0.000
Tax	8.562***	7.685	0.000
F value		370.972	
Adjust R		0.382	

5.3. Effect of regional and property rights of enterprise

In order to further study the compensation effect of low carbon business cost of enterprises, this paper uses two variables of the carbon emission reduction pilot and the property of the enterprise to divide the sample with the independent variables, and analyse the cost compensation effect of the market and the government on the enterprises of different regions and different property rights.

Table 4: Regression results of Equation 2

Variable	Coefficient	T Value	Sig
MC	0.894***	5.177	0.000
GC	7.036***	3.946	0.000
Reg	0.599	1.351	0.177
MC*Reg	0.164	0.522	0.602
GC*Reg	-2.362	-0.876	0.381
CSR	0.135***	2.703	0.007
Size	-63.479***	-25.592	0.000
Lev	-2.278***	-18.245	0.000
ROE	0.671***	4.007	0.000
Tax	8.561***	7.683	0.000
F value		303.564	
Adjust R		0.382	

From the regression results of Equation 2, it can be seen that after the interaction item is added, there is no relationship between the regional variable itself and the dependent variable, and the interaction terms of market compensation, government compensation, and regional variables are not significant, indicating that the enterprise has low-carbon operations from the government. There is little relationship between the cost-compensation obtained by the market and whether it is a low carbon pilot area. On one hand, it may be because there are few samples in the pilot area and it is not representative; on the other hand, the market compensation chosen in this paper is mainly due to the operation of commodity trading, so the carbon trading market is not reflected. Although the interaction items are not significant, from the perspective of the coefficient, the degree of market compensation in the pilot areas is higher than the government compensation. Hypothesis 3 is proved.

Table 5: Regression results of Equation 3

Variable	Coefficient	T Value	Sig
MC	1.192***	7.535	0.000
GC	2.311	1.206	0.228
GOV	-1.706***	-4.016	0.000
MC*GOV	-1.607***	-4.201	0.000
GC*GOV	9.120***	3.556	0.000
CSR	0.136***	2.717	0.007
Size	-65.298***	-26.105	0.000
Lev	-2.212***	-17.648	0.000
ROE	0.783***	4.653	0.000
Tax	8.694***	7.821	0.000
F value		307.881	
Adjust R		0.385	

From the regression results of Equation 3, it can be seen that the regression coefficient of the nature of property rights and cost compensation effect is - 1.706, which is significant at the level of 1%. The total cost compensation obtained by state-owned enterprises is lower than that of private enterprises. The interaction between government compensation and property right is significantly positively correlated at the level of 1%. The interaction between market compensation and the nature of property rights is significantly and negatively correlated at the level of 1%, which means that compared to private enterprises, state-owned enterprises are obtained more from the government. The cost of compensation is higher than that of private enterprises, but the compensation obtained from the market is weakened. Hypothesis 4 is proved.

6. CONCLUSIONS AND RECOMMENDATIONS

6.1. Research conclusions

First, the paper elaborates from the perspective of low-carbon operation and cost compensation including externality theory, cost compensation theory, sustainable development theory, environmental Kuznets curve theory, and cleaner production theory. The paper analyses the domestic policy, size and future of carbon market of China and abroad. The theoretical basis of science, strong policy guarantees, and good market conditions show the inevitability of companies taking a low carbon road.

Second, listed companies carrying out low-carbon operations and disclosing social responsibility reports are assumed to take social responsibilities. They build up good market reputation and obtain more benefits from the market, thus they are compensated for their cost. The government provides guidelines to encourage enterprises to carry out low-carbon development. Subsidies to enterprises can relieve the financial pressure the financial pressure on corporate R&D investment. On the other hand, it also compensates for the cost of low-carbon operations.

Third, under the circumstances that the carbon trading market has not well developed, government subsidies are still the key to the cost recovery of enterprises. Market compensation is only a supplementary measure.

Fourth, compared to private enterprises, state-owned enterprises, due to their unique nature and positioning, can receive more compensation from the government, but their compensation form the market is reduced.

6.2. Policy suggestions

In order to enable more enterprises to be involved in the low-carbon operation to achieve emission reduction targets, the paper proposes the following suggestions:

Guiding and encouraging low-carbon business operations, in the initial stage of the carbon trading market, appropriate macro-control policies should be used to promote the development of carbon finance. In terms of financial policy, we can increase financial subsidy for low-carbon industries and reduce the VAT rate for low-carbon projects and carbon finance businesses. The establishment of a sound financial and taxation policy, even if it is an old-style, can also promote the operation of the market and become a benign incentive measure. UK has shows that there is a certain degree of complementarity between carbon tax and carbon trading, and the former's bindingness can promote the latter. In terms of financial policy, the lending quotas for carbon-financing projects should be raised. And interest rates should be given a preferential treatment for this loan. Higher interest rates should be set for high-carbon projects to increase their loan costs, the preferential policies are to guide the financial institution's business to tilt toward carbon finance projects. In foreign exchange management, a green channel for carbon finance should be established, and overseas “low-carbon capital” should be actively introduced into the domestic low-carbon industry.

Accelerating the development of the carbon trading market. In terms of resource allocation, the government is more of a regulatory and supervisory role, and the market should play a decisive role. To promote the development of a low-carbon economy, we should rely more on the market, reducing the government's direct allocation of resources, and ensure a healthy and orderly operation of the carbon market. The carbon trading market should adopt innovative trading mechanisms to reduce transaction costs through using the financial attributes of carbon trading quotas to find effective carbon prices and guide companies in carbon asset management and production optimisation. Through carbon-financing innovation, we can allocate the capital to the carbon market and provide companies with more emission reduction funds. Relevant departments strengthen the supervision of carbon-financing access thresholds, risk rating and the supervision of various types of low-carbon financial services, projects, and products, so that the targeted and well-documented businesses and institutions can gain access. Secondly, carbon financial supervision authorities regulate and define their business scope according to the nature and characteristics of different financial institutions. Third, relevant departments strengthen the risk control of carbon- financing loans. Market risk, credit risk and policy risk should be under controllable limits for financial institutions. Relevant departments establish low-carbon loan capital composition and adequacy ratios and the monitoring of various financial indicators of commercial banks' low-carbon loans. Strengthening and improving information disclosure systems among different financial regulatory agencies. Sharing mechanisms and using early warning mechanisms to create a good external environment for reducing carbon financial risks.

Improving the construction of carbon accounting system. As part of the market economy, companies should establish carbon accounting system for their carbon-related activities, whether they are participating in domestic or world trade. The establishment of this system can provide statistics of carbon emissions, and it can also retrieve relevant data on carbon signs and carbon trading. As a kind of economic activity, carbon trading should be recorded, supervised and provide feedback by means of the carbon accounting system. Such a system should be implemented as soon as possible to avoid becoming a victim of “green trade barriers”.

7. ACKNOWLEDGEMENT

This paper is a periodical achievement of the "Research on the Compensation Path and Efficiency of Low Carbon Operation Cost Based on Pareto Improvement", which is supported by Soft Science Project of Hubei Province. (No. 2018ADC048).

8. REFERENCES

Cai W. Environmental Finance Law [J]. Western Law Review 2012, (1): 15-23

China Clean Development Mechanism Network. http://www.ccchina.org.cn/

Fu G. Thinking about Modern Most Compensation [J]. Finance and Accounting Monthly, 2001(06): 4-5.

Pigou AC. Welfare Economics [M]. China Press, 2013.

Wang S. An Overview of Externality Theory [J]. Economic Perspectives, 2012(27):52-53.

Wu J, Jiang Q. Carbon Labelling in International Trade [J]. International Economic Cooperation, 2009(7):82-85.

Zhou J. A Review of China's Low-carbon Economy and Carbon Finance Research [J]. Financial Science, 2010 (5): 17-23.

306: Analysis of seasonal variation of carbon concentration in china based on satellite remote sensing monitoring

Lanlan ZHANG[1, 2,] Jinye ZHANG[1, 2*]

[1] *School of Science, Hubei University of Technology, Wuhan 430068;*
[2] *Hubei Collaborative Innovation Center for High-efficiency Utilization of Solar Energy, Hubei University of Technology, Wuhan 430068;*
**Corresponding author: zhangjinye@hbut.edu.cn*

Global warming has a serious impact on the global ecosystem, politics and economy. Carbon dioxide (CO_2) is one of the major greenhouse gases. In this paper, CO_2 concentration in China were analysed by using CO_2 concentration data from GOSAT and ground monitoring, respectively, as well as the auxiliary data such as population density and vegetation distribution in different provinces provided by the "2014 China Statistical Yearbook". The spatial distribution of carbon concentration is obtained by using kriging interpolation. Annual average carbon concentration was about 402.75ppmv. CO_2 concentration had obvious seasonal variation. It was higher in spring and winter than that in summer and autumn. It was 399.74ppmv in summer and 404.82ppmv in autumn. The fluctuation of CO_2 was more severe in summer. In space, it was higher in the northeast and was lower in the northwest.

Keywords: Remote sensing monitoring; GOSAT; Carbon dioxide; Seasonal variation

1. INTRODUCTION

In January 2018, the National Oceanic and Atmospheric Administration (NOAA) and NASA notified that the global land and sea temperatures have risen by 1°C compared to the 20th century. In order to better monitor the global temperature changes, the Intergovernmental Panel on Climate Change (IPCC) have been established. It has published five assessment reports. The fourth assessment report pointed out that the rise of atmospheric CO_2 concentration was one of the most important factors causing global temperature rise (IPCC, 2007).

At present, there are two main methods for monitoring CO_2 concentration. Atmospheric background monitoring had the advantages of high accuracy, instant access, and easy access. However, the distribution of stations was not uniform and there was great uncertainty for future climate prediction. Wang et al. (2002) founded that the average annual growth rate of CO_2 was 1.59 $\mu L / L$ in China from 1991 to 2000. Zhou et al. (2004) concluded that the distribution and growth trend of CH_4 concentrations was provided by Mt.Waliguan station was consistent with consistent with the monitoring results of 30°N~60°N.

With the rapid development of remote sensing technology, remote sensing monitoring had become the main method for monitoring atmospheric CO_2 distribution. In 2002, the United States launched successfully the Aqua satellite equipped with an AIRS. Maddy et al. (2008) founded that the error of tropospheric CO_2 concentration that monitored by AIRS and on-board was less than 0.5% within ±65° latitude. On July 2, 2014, the "Orbital Carbon Observer 2" (OCO-2) was successfully developed by NASA. D Wunch et al. (2016) founded CO_2 concentration was provided by OCO-2 and Total Carbon Column Observing Network (TCCON) had good agreement, and the RMS difference was less than 1.5 ppmv. On January 23, 2009, Japan launched GOSAT successfully. It was jointly developed by Japan Aerospace Exploration Agency (JAXA), Environmental Studies (NIES) and Ministry of the Environment (MOE). GOSAT satellites had higher inversion accuracy for near-surface carbon concentrations. O Uchino et al. (2012) found that the difference between TCCON data and GOSAT data can be reduced by making full use of the solar irradiance database. Lei et al. (2010) concluded that XCO_2 and XCH_4 are high in provinces with high population density, strong human activities, or large farmland coverage by analysing GOSAT data.

According to the global carbon project data, in 2017, the consumption of coal, oil, and natural gas has increased by 3%, 5%, and 12% in China, respectively, and the total carbon emissions increased by 3.5%. Therefore, the study of the temporal and spatial distribution and seasonal variation of CO_2 concentration has important reference significance for dealing with climate change and establishing carbon emission reduction plans.

2. ANALYSIS OF CARBON CONCENTION IN CHINA

2.1. Validation of GOSAT data

The accuracy of the carbon concentration was inversed by GOSAT is higher than that of other satellites in near the ground. Therefore, the temporal and spatial distribution of carbon concentration in China was analysed by using GOSAT data. Fitting the Carbon Data were monitor by GOSAT and Mt.Waliguan station by Least Square Method. Fitting results was shown in Figure 1. The trend line equation was as follows:

Equation 1: The trend line equation.

$$y = 1.165x - 61.04$$

Figure 1 showed that GOSAT CO_2 data and ground-based observations data had good consistency, and the correlation coefficient was 0.65. CO_2 concentration had obvious seasonal variation. It was low in summer, and was high in spring.

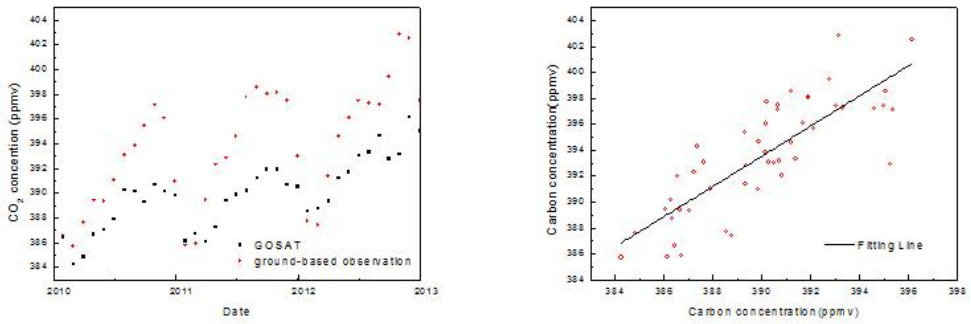

(a) *(b)*

Figure 1: Comparison of CO_2 concentration from ground-based observation and GOSAT

2.2. Seasonal variation of carbon concentration in China

The temporal and spatial distribution of carbon concentration in 2106 was analysed. CO_2 concentration values were inversed by short-wave infrared radiation values. The inversion model was as follows:

Equation 2: Inversion model.

$$Y = F\left(x, b\right) + \varepsilon$$

Where:

F = a forward model
Y = observation values
x = atmospheric parameters
b = a series of input parameters for correction
ε = a variety of errors

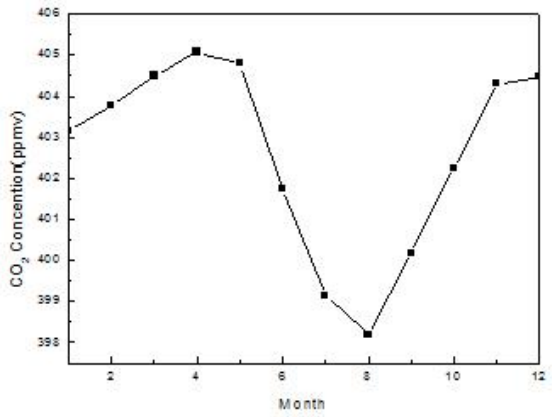

Figure 2: Time series of carbon concentrations in China in 2016

In Figure 2, carbon concentration had obvious seasonal variation. It was low in summer, and was high in spring. It was reduced from April to August, and was the smallest in August, which was 398.19ppmv. It was increased in other month, and was the largest in April, which was 405.07ppmv. The monthly changes of carbon concentration in summer and autumn were more dramatic than that in spring and winter.

CO_2 concentration is closely related to the photosynthesis of plants and human activities. In summer, the CO_2 absorbed by vegetation through photosynthesis was greater than that emitted by human activities. CO_2 concentration began to decrease. Photosynthesis of plants closely relate to the temperature. In autumn and winter, plants enter a dormant period. The CO_2 absorbed by plants through photosynthesis was less than that emitted by human activities, CO_2 concentration began to increase.

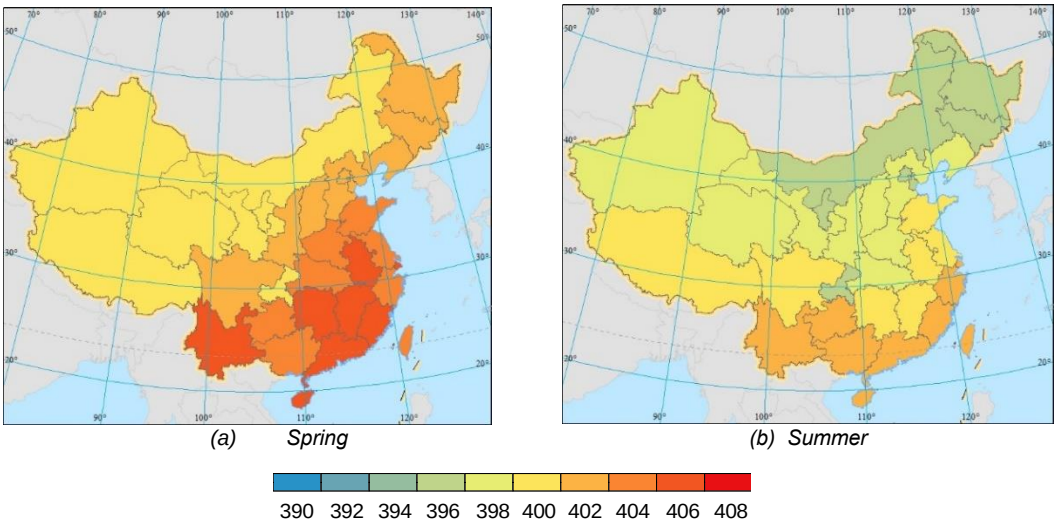

(a) Spring *(b) Summer*

Figure 3: Spatial distribution of carbon concentration in China in different seasons

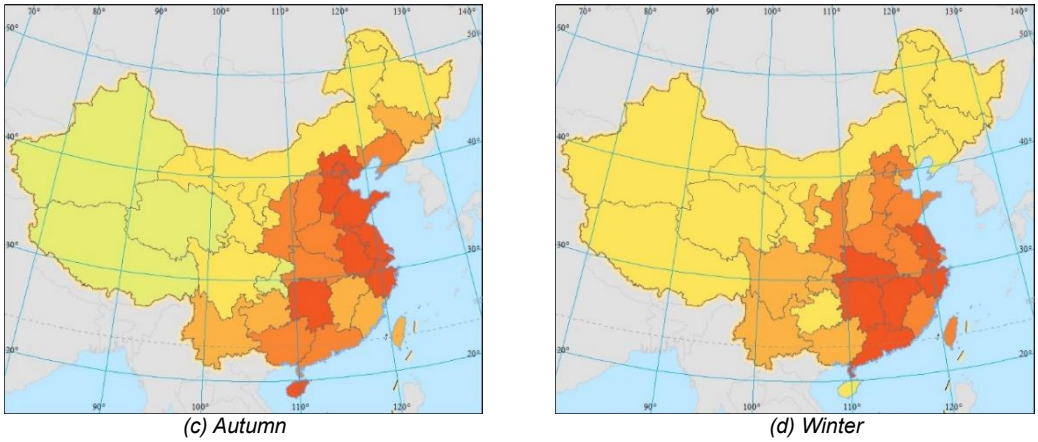

Figure 3: Spatial distribution of carbon concentration in China in different seasons

Figure 3 and Table 1 were the distribution and values of CO_2 concentration in different seasons in China. Carbon concentration In Figure 3, CO_2 concentration was low in the Northwest and was high in the Southeast in different season. It was low in summer and was high in spring, which was consistent with the results in Figure 2. The monthly changes of carbon concentration in coastal areas were more dramatic pronounced than that in inland areas.

Terrestrial ecosystems are diverse, which include forest ecosystems, grassland ecosystems, desert ecosystems, wetland ecosystems, and farmland ecosystems. According to the distribution of vegetation in China, the ecosystems in the Southeast Coast, Central China, North China, and Northeast China belong to the forest ecosystems, while in the northwest, they belong to desert ecosystems and grassland ecosystems. Schwartz et al. (2013) found that the underlying surface of the forest has the strongest carbon storage capacity. Forest ecosystems can absorb more carbon dioxide through photosynthesis in the same environment. Photosynthesis of plants closely relate to the temperature. As the latitude increases, the types of forest vegetation are different. The change of CO_2 concentration has difference.

Table 1: CO_2 concentrations in China's provinces in different seasons

Area	CO_2 Concentration（ppb）			
	Spring	Summer	Autumn	Winter
Beijing	404.95	397.63	403.77	404.40
Tianjin	404.63	397.91	403.31	403.37
Shanghai	406.14	403.21	403.24	405.24
Chongqing	404.31	398.06	400.22	402.81
Hebei	404.53	398.44	403.17	404.20
Shanxi	404.47	399.37	402.75	403.62
Liaoning	404.40	398.84	402.76	401.82
Jilin	404.27	397.68	401.96	401.66
Heilongjiang	404.11	396.79	401.18	401.35
Jiangsu	405.70	400.40	403.56	405.68
Zhejiang	405.65	401.94	403.29	405.69
Anhui	405.86	401.55	401.89	404.73
Fujian	405.87	397.63	403.77	404.40
Jiangxi	405.88	400.31	402.07	405.73
Shandong	405.75	400.57	403.37	404.86
Henan	405.32	398.39	402.90	405.04
Hubei	405.59	398.91	402.73	405.96
Hunan	406.28	400.64	403.28	406.17
Guangdong	406.17	401.49	405.14	402.00
Hainan	406.85	398.53	400.64	402.37
Sichuan	404.81	400.93	401.41	403.12
Guizhou	405.54	401.12	402.31	402.49
Yunnan	406.19	401.41	401.69	403.60
Shaanxi	404.65	399.53	402.42	404.18
Gansu	402.41	398.53	400.64	401.51
Qinghai	401.14	399.39	399.78	402.37
Tibet	401.81	400.82	400.15	401.59
Guangxi	405.44	401.20	402.51	403.90
Inner Mongoria	402.87	397.32	400.74	401.89
Ningxia	402.40	398.14	400.97	402.98
Xinjiang	402.14	398.39	400.47	402.39
Hong Kong	408.28	399.87	409.01	407.03
Taiwan	405.55	401.39	402.05	405.21

Figure 4 showed the comparison of carbon concentrations in different climate zones with forests as underlying surfaces. In different climatic zones, the carbon concentration had the same seasonal variation, it was smaller in summer and was larger in spring. In cold temperate deciduous forest areas and temperate coniferous mixed forest areas, the change of carbon concentration was more violently. It was relatively weak in the tropical monsoon forests and rainforest regions, which was consistent with the results in Figure 3.

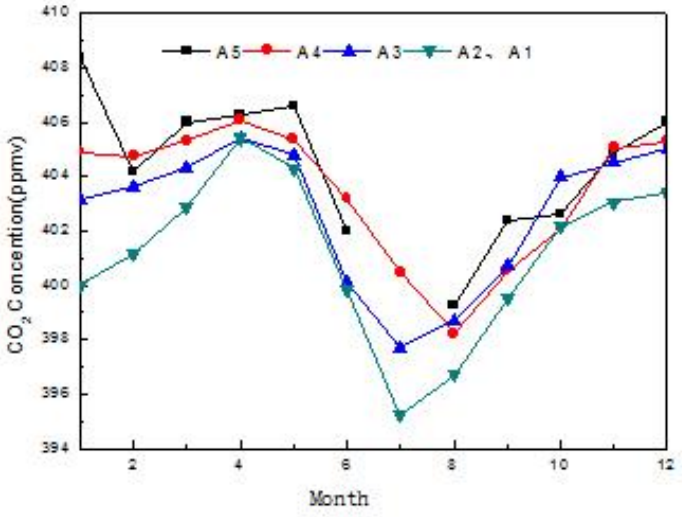

Figure 4: Comparison of CO_2 concentration in forest ecosystems in different climatic zones (A1: Cold temperate deciduous coniferous forest, A2: temperate coniferous broadleaved mixed forest, A3: warm temperate deciduous broad-leaved forest, A4: subtropical evergreen broad-leaved forest, A5: tropical monsoon forest, rainforest)

3. CONCLUSION

The seasonal variation of CO_2 concentration in China in 2016 was analysed based on GOSAT data. The main conclusions were as follows:

(1) Through fitting analysis, GOSAT data and ground-based observations data had good consistency, the correlation coefficient was 0.65.

(2) CO_2 concentration in China had obvious seasonal variation. It was low in summer and was high in spring. The monthly changes of carbon concentration in summer and autumn were more dramatic.

(3) It was low in the Northwest and was high in the Southeast in different season. The monthly changes of carbon concentration in coastal areas were more dramatic pronounced than that in inland areas. In different climatic zones, the carbon concentration had the same seasonal variation characteristics.

4. ACKNOWLEDGEMENTS

The author are grateful for CO_2 data provided by GOSAT project and WDCCG. This project was supported by the Hubei Collaborative Innovation Center for High-efficiency Utilization of Solar Energy, Hubei University of Technology (HBSKFZD2016002 and HBSDY201502).

5. REFERENCES

IPCC, 2007. Climate Change 2007: Synthesis Report. Contribution of Working Groups I, II and III to the Fourth Assessment Report of the Intergovernmental Panel on Climate Change [Core Writing Team, Pachauri, R.K and Reisinger, A.(eds.)]. IPCC, Geneva, Switzerland.

Lei, L., Liu, Q., Zhang, L., Liu, L., & Zhang, B. (2010). A preliminary investigation of coand chconcentration variations with the land use in northern china by gosat. 1141-1144.

Maddy, E. S., Barnet, C. D., Goldberg, M., Sweeney, C., & Liu, X. (2008). Co 2, retrievals from the atmospheric infrared sounder: methodology and validation. *Journal of Geophysical Research Atmospheres, 113*(D11), -.

Schwartz, M. D., Hanes, J. M., & Liang, L. (2013). Comparing carbon flux and high-resolution spring phenological measurements in a northern mixed forest. *Agricultural & Forest Meteorology, 169*(169), 136-147.

Uchino, O., Kikuchi, N., Sakai, T., Morino, I., Yoshida, Y., & Nagai, T., et al. (2012). Influence of aerosols and thin cirrus clouds on the gosat-observed co2: a case study over tsukuba. *Atmospheric Chemistry & Physics, 11*(7), 3393-3404.

Wang, G., Wen, Y., Kong, Q., Ren, L., & Wang, M. (2002). Co2 background concentration in the atmosphere over the Chinese mainland. Chinese Science Bulletin*, 47*(14), 1217-1220.

Wunch, D., Wennberg, P. O., Osterman, G., Fisher, B., Naylor, B., & Roehl, C. M., et al. (2017). Comparisons of the orbiting carbon observatory-2 (oco-2) xco2 measurements with tccon. *Atmospheric Measurement Techniques, 10*, 1-45.

Zhou, L., Jinlong, L. I., Tang, J., Wen, Y., & Zhang, X. (2004). Variations of background atmospheric methane at mt.waliguan, china. *Acta Scientiae Circumstantiae*.

307: A distributed AGC method based on system compensation for multi-area interconnected power systems with high penetration of photovoltaic system

Xilin ZHAO[1], Jingjing HE[2], Bo FU[3]

[1] Department of Electrical and Electronic Engineering, HuBei University of Technology, Wuhan, zhaoxl@mail.hut.edu.cn
[2] Department of Electrical and Electronic Engineering, HuBei University of Technology, Wuhan, 1223312730@qq.com
[3] Department of Electrical and Electronic Engineering, HuBei University of Technology, Wuhan, fubofanxx@mail.hbut.edu.cn

The presence of distributed generation in modern power system renders the traditional automatic generation control (AGC) strategies more challenging. The penetration of renewable energy causes the power output to be affected by environment greatly. For example, when PV system is included in a power grid, the power output variation of the PV system will affect the balance between load and resource of the power system. However, the power output variation of the PV system is unavoidable for the environmental uncertainty. An improved AGC method is proposed in this paper to reduce the negative impacts of the photovoltaic power uncertainty and high fluctuation. Firstly, the power output characteristic of PV array is discussed, and multi-area power system model is built with high penetration of photovoltaic (PV) system. Then, in order to analyse the influence of PV power output uncertainty and fluctuation on AGC, the AGC performance with different power fluctuation caused by different maximum power point tracking (MPPT) method is indicated. Furthermore, a compensation unit is designed and introduced to eliminate the adverse effect of PV power output on AGC. Finally, based on the distributed model predictive control (DMPC) theory, taking the step load as perturbation variables, a two-area interconnected power grid AGC dynamic model with two PV systems is shown as an example to testify the proposed method. The simulation results show that the proposed method can guarantee the good dynamic response performance of AGC system under the condition of high fluctuation and uncertainty of PV system, and the feasibility and effectiveness of the proposed method is also verified.

Keywords: Automatic generation control (AGC); photovoltaic power; interconnected power grid;

1. INTRODUCTION

Automatic Generation Control (AGC) is designed to minimise frequency deviations and to maintain the system frequency close to its scheduled value when there is a load and resource variation in power systems (Rahman, 2016; Liu, 2015; Chávez, 2015). As an important research field in power system operation and control, AGC technique is developed both practically necessary and theoretically interesting. Therefore, many AGC strategies have been proposed as in numerous references, for example, proportional integral differential (PID) (Saikia, 2015; Sahu, 2013; Mohanty, 2016), sliding mode control (SMC) (Mi, 2013), self-adaptive control (Khooban, 2015), and robust control (Yao, 2017) etc.

At present, due to the large scale of power grid and the high penetration of renewable energy, research on the AGC is more challenging. Majority renewable energy outputs such as photovoltaic, wind generation usually tend to be uncertain because of natural and meteorological conditions. Thus, many of the research on AGC for modern power system focus on the control approach for AGC in the presence of renewable energy.

The presence of renewable energy will lead to the complexity of AGC implementation due to the impact of external environment. This issue also raises concern on the modeling of renewable energy system under AGC (Chang-Chien, 2014). Thus, some AGC methods have been researched according to the building of the model of hybrid energy system. Xu et al. (2016) proposed a dynamic gain-tuning control (DGTC) method for AGC with effects of wind resources, which the PI control parameters can be automatically and dynamically calculated according to different disturbances in a power system. Basit et al. (2017) described an algorithm to control the active power balance through automatic generation control process with wind power integration of large scale. Rahman et al. (2017) proposed an optimal-based PID controller for AGC of a two-area hybrid thermal system with solar and wind turbine. Obviously, the power output of most renewable energy resources is affected by the environment. In order to improve the efficiency of energy conversion, the maximum power point tracking (MPPT) technique is indispensable. But the aforementioned references did not discuss the problem about the influence of renewable power output on AGC when MPPT strategy is carried out.

This paper is organised as follows. After introducing the background of the research, the PV system model and the model configurations of two-area interconnected AGC system are analysed in Section 2. In Section 3, principle of MPC and the impact of MPPT results in PV system are analysed. In order to reduce the impact of PV power output on AGC, a compensation unit is designed and introduced. In Section 4, a numerical example is provided, which illustrates the effectiveness of the proposed method. Finally, a conclusion is provided in Section 5.

2. DISTRIBUTED AGC SYSTEM MODEL

2.1. Photovoltaic system model

The PV array is assembled by PV cells according to the voltage and power demand. A PV cell is a semiconductor device which can absorb energy of sunlight, and convert it into electric energy through photoelectric effect. The typical equivalent circuit of PV cell is shown in Figure 1.

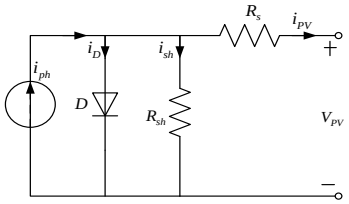

Figure 1: Equivalent Model of PV Cell.

The output characteristic of PV cell is given as (Villalva, 2009):

$$i_{PV} = i_{ph} - i_D - i_{sh} = i_{ph} - i_o\left(e^{\frac{q\left(v_{pv}+i_{PV}R_s\right)}{AKT}} - 1\right) - \frac{v_{pv}+i_{PV}R_s}{R_{sh}}, \quad (1)$$

where i_{PV}, and v_{PV} are the output current and voltage respectively, i_{ph} is the photocurrent, i_D is the diode junction current, i_o is the reverse saturation current, q is the electronic charge, K is the Boltzmann constant, T is the PV cell temperature, A is the diode factor, R_s and R_{sh} are the PV cell series and parallel resistance respectively.

Then, the power output is given by

$$P_{PV} = v_{PV} i_{PV} . \tag{2}$$

2.2. AGC system model building

A large power system is usually divided into several subsystems which are connected by the tie-lines for efficient operation and control. The subsystems represent interconnected regional power grid. Without loss of generality, a two-area interconnected power system with penetration of PV system and time delay among different areas is considered as an example for design and analysis purposes. The system model is shown in Figure 2.

In the model, T_{gi} is the time constant of the governor for area i; T_{ti} is the time constant of the generator for area i; K_{ri} is the reheat coefficient of the steam turbine for area i; T_{ri} is the reheat time constant for area i; R_i is the speed regulation parameter for area i; B_i is the frequency bias factor for area i; M_i is the rotary inertia of assembling unit for area i; D_i is the damping coefficient of load for area i; ΔP_{ti} is the change in turbine output for area i; ΔP_{ri} is the change in thermal power output of reheat steam turbine generator sets for area i; ΔX_{gi} is the change in valve position of the governor for area i; ΔP_{ci} is the control variable of controller for area i; ΔP_{Li} is the load changes for area i; Δf_i is the frequency deviation for area i; ΔP_{t12} is the tie-line power flow for area i; T_{12} is the power system synchronizing coefficient; ACE_i is the area control error for area i; I is the light intensity; P_{DSE} is the PV power output.

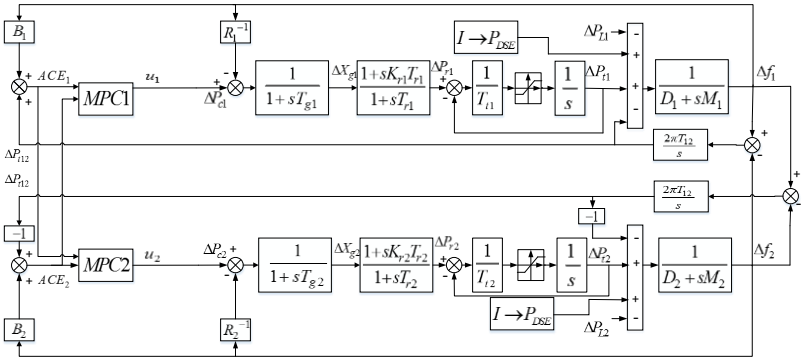

Figure 2: Two-area interconnected power grid AGC dynamic model.

When describing ith regional power grid with subscript i (i=1,2,...,n), the state-space equations of each region is given by

$$\dot{X}_i(t) = A_{ii} X_i(t) + B_{ii} U(t) + F_{ii} W_i(t) + \sum_{i \neq j} \left(A_{ij} X_j(t) + B_{ij} U_j(t) + F_{ij} W_j(t) \right)$$

$$Y_i(t) = C_{ii} X_i(t), \tag{3}$$

$$(i = 1, 2, \cdots, n;\ j = 1, 2, \cdots, n)$$

where $X_i \in R^n$, $U_i \in R^m$, $W_i \in R^k$, $Y_i \in R^r$ are the system state variables, control variables, disturbance variables and output variables of the ith region respectively with appropriate dimensions. $X_j \in R^n$, $U_j \in R^m$, $W_j \in R^k$, $Y_j \in R^r$ are the system state variables, control variables, disturbance variables and output variables of the jth region adjacent to the ith region. A_{ii}, B_{ii}, F_{ii}, C_{ii}, A_{ij}, B_{ij}, F_{ij}, respectively, are the parameter matrices with appropriate dimensions. In which,

$$X_i = \left[\Delta f_i \quad \Delta P_{ti} \quad \Delta P_{ri} \quad \Delta X_{gi} \quad \Delta P_{tij} \right]^T \quad Y_i = \left[ACE_i \quad \Delta f_i \quad \Delta P_{tij} \right]^T$$

$$U_i = \left[\Delta P_{ci} \right] \quad W_i = \left[\Delta P_{Li} \right]$$

$$\boldsymbol{A}_{ii}=\begin{bmatrix} \frac{-D_i}{M_i} & \frac{1}{M_i} & 0 & 0 & \frac{(-1)^i}{M_i} \\ 0 & \frac{-1}{T_{ti}} & \frac{1}{T_{ti}} & 0 & 0 \\ \frac{-K_{ri}}{R_i T_{gi}} & 0 & \frac{-1}{T_{ri}} & \frac{1}{T_{ri}}-\frac{K_{ri}}{T_{gi}} & 0 \\ \frac{-1}{R_i T_{gi}} & 0 & 0 & \frac{-1}{T_{gi}} & 0 \\ \sum_j 2\pi T_{ij} & 0 & 0 & 0 & 0 \end{bmatrix} \quad \boldsymbol{A}_{ij}=\begin{bmatrix} 0 & 0 & 0 & 0 & 0 \\ 0 & 0 & 0 & 0 & 0 \\ 0 & 0 & 0 & 0 & 0 \\ 0 & 0 & 0 & 0 & 0 \\ -2\pi T_{ij} & 0 & 0 & 0 & 0 \end{bmatrix}$$

$$\boldsymbol{C}_{ii}=\begin{bmatrix} B_i & 0 & 0 & 0 & (-1)^{i+1} \\ 1 & 0 & 0 & 0 & 0 \\ 0 & 0 & 0 & 0 & 1 \end{bmatrix} \quad \boldsymbol{B}_{ii}=\begin{bmatrix} 0 & 0 & \frac{K_{ri}}{T_{gi}} & \frac{1}{T_{gi}} & 0 \end{bmatrix}^T \quad \boldsymbol{F}_{ii}=\begin{bmatrix} \frac{-1}{M_i} & 0 & 0 & 0 & 0 \end{bmatrix}^T$$

$$\boldsymbol{B}_{ij}=\boldsymbol{B}_{12}=\boldsymbol{B}_{13}=\boldsymbol{B}_{21}=\boldsymbol{B}_{23}=\boldsymbol{0}_{5\times 1} \qquad \boldsymbol{F}_{ij}=\boldsymbol{F}_{12}=\boldsymbol{F}_{13}=\boldsymbol{F}_{21}=\boldsymbol{F}_{23}=\boldsymbol{0}_{5\times 1}$$

Traditional centralised controllers are becoming less reliable and more difficult to deal with the distributed control system. The distributed MPC is thus designed based on the system model to maintain the system frequency at the scheduled value.

Owing to the physical and mechanical limitations, the generation rate constraint (GRC) of 3% per minute is considered in this paper. For optimising purpose, the objective function is determined by

$$\min \boldsymbol{J}_{AGC}=k_1\left(\boldsymbol{R_S}-\boldsymbol{ACE}\right)^{\boldsymbol{T}}\left(\boldsymbol{R_S}-\boldsymbol{ACE}\right)+k_2\left(\boldsymbol{f_S}-\boldsymbol{\Delta f}\right)^{\boldsymbol{T}}\left(\boldsymbol{f_S}-\boldsymbol{\Delta f}\right) \tag{4}$$

where $\boldsymbol{R_S}$ is the expected output of ACE, $\boldsymbol{f_S}$ is the expected output of Δf, k_1 and k_2 are weighting coefficients which are set to 0.5 in this paper.

3. DESIGN OF THE CONTROL APPROACH FOR AGC SYSTEM

3.1. Background of model predictive controller

MPC is widely recognised as a favorite technique, for this model based control strategy uses a predicted sequence of system response to establish an appropriate control response by minimizing an objective function. It also can be an effective method for AGC due to its characteristics. Considering the following discrete-time system

$$\begin{aligned} x(k+1)&=\boldsymbol{A}x(k)+\boldsymbol{B}u(k) \\ y(k)&=\boldsymbol{C}x(k) \end{aligned}, \tag{5a}$$

subject to:

$$\begin{aligned} u_{\min}&=u(k)\le u_{\max} \\ y_{\min}&\le y(k)\le y_{\max} \end{aligned}, \tag{5b}$$

where $x \in R^n$, $u \in R^m$ and y $\in R^s$ are the state, input and output variables with correspond dimension, respectively.

Generally, the objective function is designed as a quadratic function about the deviation between expected value and predicted value of the system response. The control object is to minimise the objective function which can be written as follows:

$$\boldsymbol{J}=\left(\boldsymbol{R}_S-\boldsymbol{Y}\right)^T\left(\boldsymbol{R}_S-\boldsymbol{Y}\right), \tag{6}$$

where $\boldsymbol{R}_S$ is the expected output of the system, $\boldsymbol{Y}$ is the output sequence in prediction horizon.

At each sampling instant, the optimisation problem is solved to obtain the optimal control sequence as

$$\boldsymbol{U}^* = \left[u^*(k) \quad u^*(k+1) \quad \cdots \quad u^*(k+N_c-1) \right]^T , \tag{7}$$

where N_c is the control horizon, k is the sampling time instant. Only the first element in the control sequence is carried out to the system during the control process.

Corresponding to the optimal control sequence, the predictive sequence of state variables and output can respectively be obtained as

$$\boldsymbol{X} = \left[X(k_i+1|k_i) \quad X(k_i+2|k_i) \quad \cdots \quad X(k_i+N_P|k_i) \right]^T , \tag{8}$$

$$\boldsymbol{Y} = \left[Y(k_i+1|k_i) \quad Y(k_i+2|k_i) \quad \cdots \quad Y(k_i+N_P|k_i) \right]^T , \tag{9}$$

where N_P is the prediction horizon.

3.2. Impact analysis of MPPT results

The power output of PV array will definitely impact the AGC performance. In fact, the power output is not only determined by environmental status, but also influenced by MPPT approach. Owing to the fact that the environment cannot be controlled, the affect of MPPT result to AGC performance need to be discussed. When the environment changes, for example, light intensity reduces from 800W/m^2 to 600W/m^2, and then returns to 800W/m^2, the power output with different MPPT approach is shown in Figure 3. Where Figure 3(a) corresponds to the conventional P&O method, Figure 3(b) corresponds to the MPC based MPPT method which proposed in Zhang (2014).

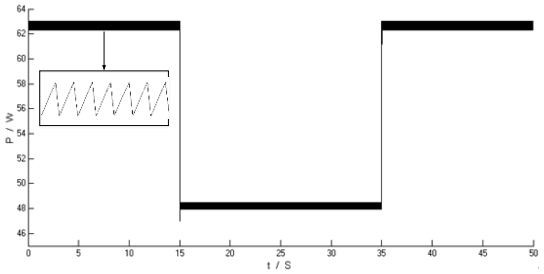

(a) conventional P&O method

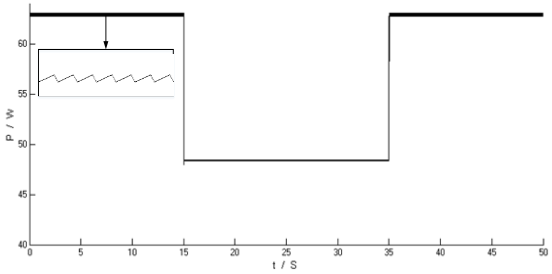

(b) MPC based MPPT method

Figure 3: Power output with different MPPT approach.

Figure 3 indicates that different MPPT methods will yield different fluctuation degrees of the power output amplitude. In order to analyse the effect of the fluctuation to the AGC system, the waveform in Figure 3 is chosen as an example of the power output of PV system, the AGC performance of area 1 is shown in Figure 4.

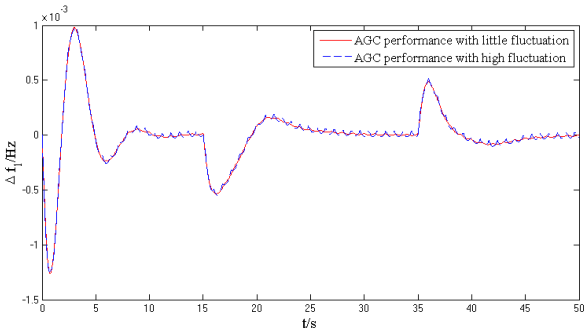

Figure 4: Response curve of Δf1 with different fluctuation degrees.

Figure 4 manifest that fluctuation of the power output of PV system will more or less cause fluctuation of AGC result. The less fluctuation PV system output has, the better AGC performance is. In other words, better MPPT effect will be conducive to the improvement of AGC performance.

3.3. System compensation strategy

Conventionally, when traditional MPC is applied separately, it is mainly applicable in the process of slow dynamic changes in the larger sampling period, which involves a large amount of computation and time consuming. Therefore, considering the introduction of cascade compensation unit can enhance the system stability and performance, it is necessary to add a unit to the original system. The compensation unit is designed as

$$G_c(s) = \frac{ms+n}{s+q}. \tag{10}$$

The design mode possess diversity, in the case of q=0, G_c(s) is equivalent to a PI controller; when q=0 and n=0, G_c(s) is equivalent to a proportional link.

In order to pursue the best control effect, the particle swarm optimisation (PSO) is applied to obtain the optimal solution of the parameters of the compensation unit, so as to avoid or reduce the influence of the photovoltaic power uncertainty on the AGC.

The way to compensate for the system is shown in Figure 5.

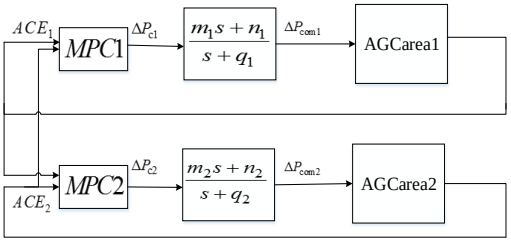

Figure 5: System block diagram after compensation.

As shown in Figure 5, the compensation unit is added between the controller and the actuator to achieve compensation for the controller. The compensation unit includes six parameters m_1, n_1, q_1, m_2, n_2, q_2 which is optimised through particle swarm optimisation (PSO) for global optimisation.

After compensation, the system state variables, control variables, disturbance variables and output variables are as below respectively

$$X_i = \left[\Delta f_i \quad \Delta P_{ti} \quad \Delta P_{ri} \quad \Delta X_{gi} \quad \Delta P_{t12} \quad \Delta P_{comi}\right]^T \quad Y_i = \left[ACE_i \quad \Delta f_i \quad \Delta P_{t12}\right]^T$$

$$U_i = \left[\Delta P_{ci}\right] \quad W_i = \left[\Delta P_{Li}\right]$$

4. NUMERICAL EXAMPLE

In this paper, the studied system is simulated based on Matlab/Simulink. The controller is realised by means of MPC toolbox, and the prediction horizon N_P is set to 10, control horizon N_c is set to 5. Sampling period is set to 0.01s. Detailed parameters are shown in Table 1. The optimal parameters of the compensation unit for step load perturbation are shown in Table 2.

Table 1: Simulation parameters of dynamic model of two-area interconnected AGC system

parameter	area 1	area 2
M_i	11	12.5
D_i	2.75	2.0
B_i	28	19
R_i	0.04	0.06
K_{ri}	0.3	0.4
T_{gi}	0.15	0.1
T_{ri}	11	9
T_{ti}	0.2	0.3
T_{12}	0.85	

Table 2: Parameters optimal solution under step signal

parameter	Optimal solution
m_1	5.187 793 973 963 098
n_1	4.591 708 935 793 283
q_1	0.763 401 703 669 231
m_2	5.107 249 768 899 896
n_2	6.428 451 138 599 305
q_2	0.579 802 457 772 249

Without loss of generality, in the simulation, the light intensity at region 1 and region 2 is assumed the same form as in Figure 3. Compare the system performance with compensation and without compensation. Assuming the step load perturbationΔP_{L1} is 0.04 pu MW, andΔP_{L2} is 0.02 pu MW. The output response of Δf of the two areas is shown in Figure 6. Where Figure 6(a) is the response for the PV output obtained by MPC-based MPPT approach which was proposed in Zhang (2014) and has little power output fluctuation, Figure 6(b) is the response for the PV output obtained by conventional P&O MPPT approach which has more power output fluctuation.

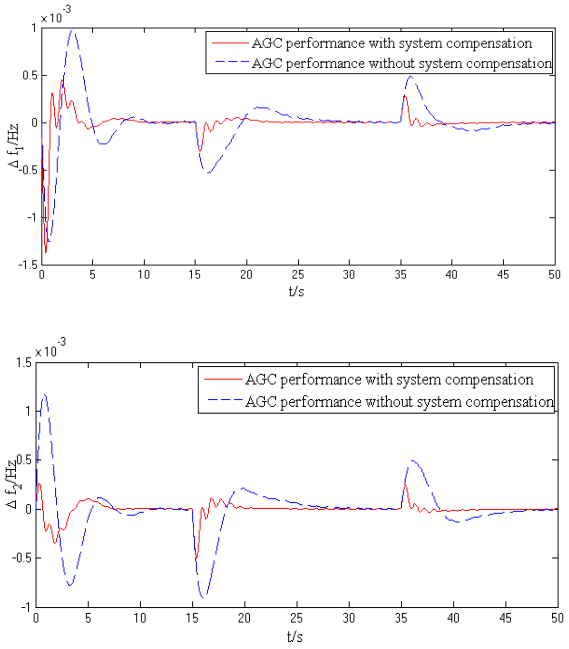

Figure 6: The step response curve ofΔf for different MPPT approaches and control methods

(a) PV output obtained by MPC-based MPPT approach

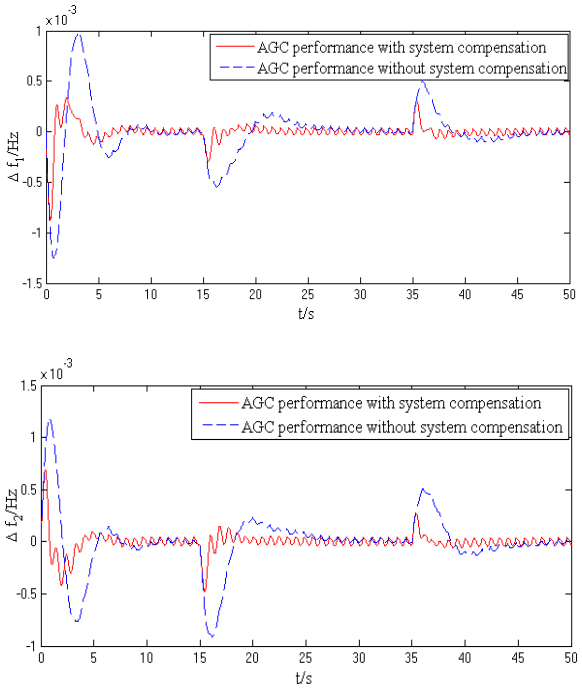

Figure 6: The step response curve ofΔf for different MPPT approaches and control methods

(b) PV output obtained by conventional P&O MPPT approach

The results reveal that different MPPT approach will cause the different fluctuation of PV output, and the fluctuation will lead to the difference in performance of AGC. In addition, it indicate that the system with compensation have better performance in settling time and overshoot than the system without compensation. Consequently, the research on the appropriate method for advanced MPPT approach and system compensation unit deserve to be concerned.

5. CONCLUSION

In this paper, a distributed model predictive AGC method is presented for the multi-area power systems with penetration of PV system. As an example, the model of an IEEE 39-bus system with 2 areas, 10 machines and 2 PV systems is constructed. The comparison of AGC performance with different fluctuation degrees caused by different MPPT methods is exhibited. The comparison indicates that the degree of fluctuation can impact the AGC performance. The feasibility and effectiveness of the proposed method is verified on the uncertainty treatment of the power output of the PV system.

6. ACKNOWLEDGEMENTS

The research team members thank for the support by the National Natural Science Foundation of China, (Grant No. 51379081), and the Scientific Research Foundation for the Returned Overseas Chinese Scholars, State Education Ministry (Grant No. [2014]1685).

7. REFERENCES

Basit A, Hansen A D, Sørensen P E, et al. “Real-time impact of power balancing on power system operation with large scale integration of wind power”. *Journal of Modern Power Systems & Clean Energy*, 2017, 5(2):1-9.

Chang-Chien L, Sun C, Yeh Y. “Modeling of Wind Farm Participation in AGC”. *IEEE Transactions on Power Systems*, 2014, 29(3):1204-1211.

Chávez H, Baldick R, Matevosyan J. “The Joint Adequacy of AGC and Primary Frequency Response in Single Balancing Authority Systems”. *IEEE Transactions on Sustainable Energy*, 2015, 6(3):959-966.

Khooban M H, Niknam T. “A New Intelligent Online Fuzzy Tuning Approach for Multi-area Load Frequency Control: Self Adaptive Modified Bat Algorithm”. *International Journal of Electrical Power and Energy Systems*, 2015, 71:254-261.

Liu S, Liu P X, Saddik A E. “Modeling and Stability Analysis of Automatic Generation Control over Cognitive Radio Networks in Smart Grids”. *IEEE Transactions on Systems*, *Man*, *and Cybernetics: Systems*, 2015, 45(2):223-234.

Mi Y, Fu Y, Wang C, et al. “Decentralized Sliding Mode Load Frequency Control for Multi-area Power Systems”. *IEEE Transactions on Power Systems*, 2013, 28(4):4301-4309.

Mohanty P K, Sahu B K, Pati T K, et al. “Design and analysis of fuzzy PID controller with derivative filter for AGC in multi-area interconnected power system”. *IET Generation Transmission & Distribution*, 2016, 10(15):3764-3776.

Rahman A, Saikia L C, Sinha N. “AGC of Dish-Stirling Solar Thermal Integrated Thermal System with Biogeography based Optimised Three Degree of Freedom PID Controller”. *IET Renewable Power Generation*, 2016, 10(8):1161-1170.

Rahman A, Saikia L C, Sinha N. “Automatic generation control of an interconnected two-area hybrid thermal system considering dish-stirling solar thermal and wind turbine system”. *Renewable Energy*, 2017, 105:41-54.

Sahu R K, Panda S, Rout U K. “DE optimized parallel 2-DOF PID controller for load frequency control of power system with governor dead-band nonlinearity”. *International Journal of Electrical Power & Energy Systems*, 2013, 49(1):19-33.

Saikia L C, Das S K, Dash P, et al. “Multi Area AGC with AC/DC Link and BES and Cuckoo Search Optimized PID Controller”. *In: Proceedings of the 2015 Third International Conference on Computer, Communication, Control and Information Technology (C3IT), West Bengal, India*, 7-8 *February* 2015:1-6. *New York*: *IEEE*.

Villalva M G, Gazoli J R, Filho E R. “Comprehensive approach to modeling and simulation of photovoltaic arrays”. IEEE Transactions on Power Electronics, 2009, 24(5) , pp. 1198-1208.

Xu Y, Li F, Jin Z, et al. “Dynamic Gain-Tuning Control (DGTC) Approach for AGC with Effects of Wind Power”. *IEEE Transactions on Power Systems*, 2016, 31(5):3339-3348.

Yao E, Wong V W S, Schober R. “Robust Frequency Regulation Capacity Scheduling Algorithm for Electric Vehicles”. *IEEE Transactions on Smart Grid*, 2017, 8(2):984-997.

Zhang J, Domínguez-García A D. “On the Impact of Communication Delays on Power System Automatic Generation Control Performance”. In: Proceedings of the 2014 North American Power Symposium (NAPS), Pullman, Washington, 7-9 September 2014:1-6. New York: IEEE.

308: Hydrogen generation properties of Al-Bi-NaCl composites

Chen CHEN[1,2],Shijie DONG[1,2],Yufei ZUO[1,2], Xiaohan XU[1,2], Cheng CHEN[1,2], Zhen CHEN[1,2],Ping LUO[1,2*]

[1]Hubei Provincial Key Laboratory of Green Materials for Light Industry, Hubei University of Technology, Wuhan 430068 P. R. China
[2]Collaborative Innovation Center of Green Light-weight Materials and Processing. Hubei University of Technology Wuhan 430068 P. R. China
[*] Corresponding author: blueknight_0930163.com

Al-Bi-NaCl composites was prepared by ball milling. Firstly, Al-5%Bi-10%NaCl was used as the research object to study the effect of milling time on the hydrogen production performance of Al-5%Bi-10% NaCl composites. Then, the content of Bi and NaCl was changed appropriately to carry out the ball milling experiment. The influence of the content of Bi and NaCl on the hydrogen generation performance was investigated. Finally, the Al-4%Bi-4%NaCl composites with the highest hydrogen production efficiency was obtained under the milling parameters of milling time of 11h, milling speed of 360r/min and ball-to-material ratio of 10:1. The hydrogen yield of composites material was 1156 ml/g in 1 h. X-ray diffraction (XRD), scanning electron microscopy (SEM) and energy dispersive X-ray spectroscopy (EDS) were used to analyse the phase, morphology and element distribution of the composites. The results show that there is no new phase formation in the ball milling process. Al, Bi, and NaCl are only mechanically mixed. The Bi is uniformly distributed in the composites material. The corrosion effect of the micro-cell generated between Al-Bi is the key to promote the reaction of Al with water.

Keywords: composites; ball milling; milling time; hydrogen production

1. INTRODUCTION

The massive use of fossil fuels by humans has led to increasingly serious environmental pollution. Clean energy has attracted people's attention. Hydrogen as a high calorific value, non-polluting and resource-rich fuel has been favored by people. It is regarded as the most promising energy in the 21st century (Deng, 2010; López-Miranda, 2016). Traditional methods of hydrogen production include decomposition of fossil fuels and water electrolysis. Although both of them are relatively mature, fossil fuels are not renewable and the hydrogen which is decomposed from fossil fuels is not of high purity. High-purity hydrogen can be obtained by water electrolysis, but it consumes a lot of energy. Both of these methods of hydrogen production don't meet the theme of green development. At present, new methods for hydrogen production include hydrogen production from biomass, photolytic water and metal matrix composites. Hydrogen production from metal matrix composites has obvious advantages because it can solve hydrogen storage and transportation problem. Therefore, in recent years, more and more attention has been paid to the hydrogen production of aluminum-based materials (Razavi-Tousi, 2016; Shmelev, 2016).

Aluminum is abundant on the earth and its price is low, which is in line with the theme of green development. Its hydrogen storage capacity is very strong, and the hydrogen density of Al (the hydrogen production of unit mass materials) can reach 11.1% (Yang, 2016). 1g of aluminum completely reacts with water at 25°C and 1 standard atmospheric pressure, theoretically it can produce 1358ml of hydrogen, and the hydrogen has high purity and its by-products are non-pollution. Current hydrogen production methods for the reaction of Al with water include ball milling (Guan, 2017; Razavi-Tousi, 2013; Jia, 2014; Razavi-Tousi, 2016; Chen, 2014), smelting (Wang, 2010; Wang, 2012; Huang, 2015), alkaline solutions (Sun, 2017; Sun, 2017; Yang, 2014), and liquid metal catalysts (Tan, 2016; Yang, 2016; Yuan, 2016). The key of the reaction of Al with water is to destroy the oxide film covered on the aluminum surface. The reaction in the alkaline solution can effectively destroy the aluminum oxide film. However, the alkaline solution is corrosive and can corrode the equipment. Woodall et al. (Ziebarth, 2011; Woodall, 2009) found that Ga and Ga alloys can effectively destroy the aluminum oxide film, and Al-Ga-In-Sn alloys can react with water to produce hydrogen at low temperature because the formed low-melting eutectic component is distributed on the surface of aluminum and can promote the reaction of Al with water. However, Ga and In are rare and expensive on the earth, so the cost of the system is high. Fan Meiqiang et al (2008), (2007) added Bi and other inorganic salts to the aluminum powder, and then increased the activity of the aluminum matrix composites by mechanical ball milling, thereby increasing the hydrogen yield. Xu Fen et al. (2014) added Bi to Al-SnCl2 composites and made the hydrogen production rate near 100% by the ball milling method because of the micro-cell corrosion effect between Bi and Al. Liu Yuheng et al. (Liu, 2017) used Al-20%Bi composites prepared by gas atomization to react with distilled water at room temperature, it exhibits good hydrolysis properties and the conversion rate could reach 100%. It can be seen that inexpensive metal Bi can effectively promote the reaction of Al with water, and it has an inestimable role in hydrogen production.

Based on previous studies, this paper continues to explore the role of metal Bi in hydrogen production. By optimising the distribution ratio of components and improving the parameters of ball milling, a more cost-effective aluminum-based hydrogen production material was obtained.

2. EXPERIMENTAL

2.1. Material preparation

The purity of the aluminum powder is 99%, the particle size is approximately 75~150μm; the NaCl is an analytically pure AR; the purity of the Bi powder is 99.99%, and the particle size is approximately 75μm. Fistly, put 20g different proportion of raw materials and 200g corundum balls into the ball milling pot. Then, the open-mouthed ball milling pot was placed in a vacuum glove box, Extract the air in the glove box so that the vacuum gauge reaches a reading of about 0.085 Mpa and then argon is injected into the glove box. Finally, the Al-Bi-NaCl composites was prepared by a QM-3SP2 planetary ball mill.

2.2. Hydrogen production performance test

The device for measuring hydrogen is shown in Figure 1. A certain amount of tap water is added to the sealed reactor. After the reactor is heated to 25°C in a water bath, 1 g of the prepared aluminum matrix composites is added into the reactor. The hydrogen produced by the reaction is led out from the top of the reactor. After drying, the hydrogen is collected with displacement of water. The volume of water removed from the measuring cylinder is the volume of hydrogen. In order to obtain accurate results, each composite was examed to hydrogen production 3 times.

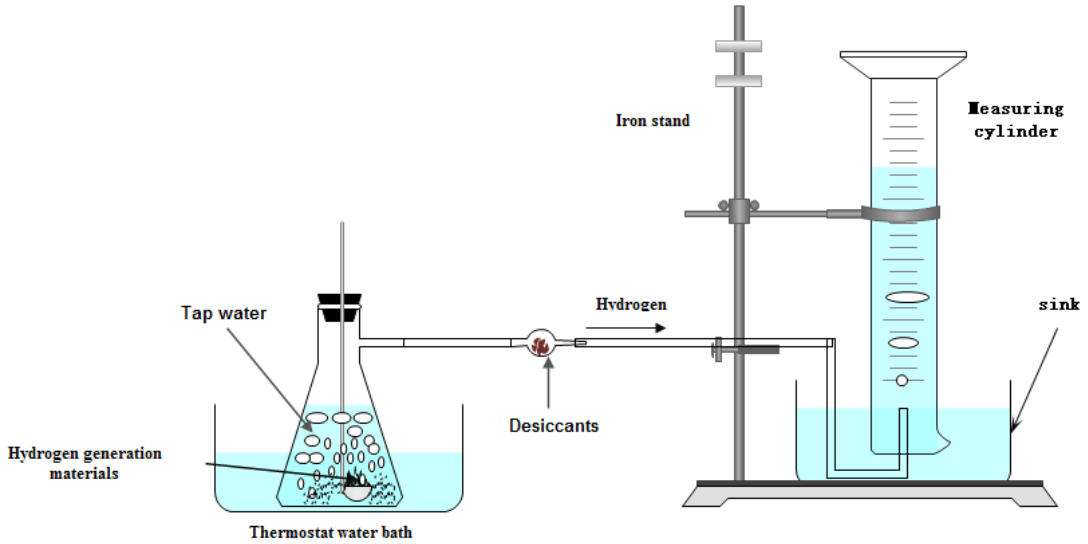

Figure 1: Hydrogen production plant schematic

2.3. X-ray diffraction and scanning electron microscope analysis

The X-ray diffraction (XRD) measurements were performed to investigate the crystallographic structure using a Bruker D8 Discover X-ray diffractometer with Cu Kα radiation (λ = 1.5418 Å). The SEM images were collected by a JEOL-7100F microscope at an acceleration voltage of 20 kV.

3. RESULTS AND DISCUSSION

3.1. Effect of milling time on hydrogen production performance of composites

Taking Al-5%Bi-10% NaCl as the research object, the rotational speed of the ball mill is 360r/min, and the ratio of ball to material is 10:1. The effect of milling time on the hydrogen production performance of the composite material is studied. Figure 2 shows the hydrogen production performance of composites with 3h, 6h, 9h, 11h, 13h ball milling time. It can be seen that as the milling time increases, the hydrogen production capacity of composites gradually increases. This is because the increase in ball milling time leads to the material being refined, the defects increased, and the oxide film on the surface of the Al powder is sufficiently destroyed (Chen, 2013). The hydrogen yield of the composite material with a ball milling time of 11 h was approximately 1070 ml. Although continue to extend the ball milling time to 13 hours, the hydrogen yield is basically the same as that of ball milling for 11 hours. Figure 3 shows the morphology of the Al-5% Bi-10% NaCl composites at different milling times. One can see that with the increase of ball milling time, the morphology of composites has undergone three stages of change: large particles (average particle size of 100μm) → flakes → small fragments (average particle size of 25μm). In other words, this composite material is gradually refined. When the ball milling time is 3 h, the sheet-like morphology appears in the composite material. That is because the ball milling time is short, there is also a part of Al powder that is a spherical particle (average particle diameter 100 μm). When the milling time was increased to 6 hours, the spherical Al powder became all sheetlike. As the milling time increased to 9 hours, most of the sheet composites were shredded into small particles. When the ball milling time increased to 11 hours, all the sheet composite materials were shredded into small particles with an average particle size of about 25 μm. After increasing the milling time to 13 hours, the morphology of the composite material did not change much. This is because NaCl has the effect of preventing cold welding, resulting in no agglomeration of Al powder (Yolcular, 2017). In order to further see the morphology of the Al-5% Bi-10% NaCl composites, an 11-hour ball mill composite was subjected to a higher SEM test. The results are shown in Figure 4. One can see that the composite material is a lamellar structure, which means that the surface area of the composite increases and the defects increase, so the hydrogen production rate and hydrogen yield of the composite material increase. The results obtained from Figures 3 and 4 are in accordance with Figure 2 which shows that the ball milling time is the best for 11 hours of hydrogen production.

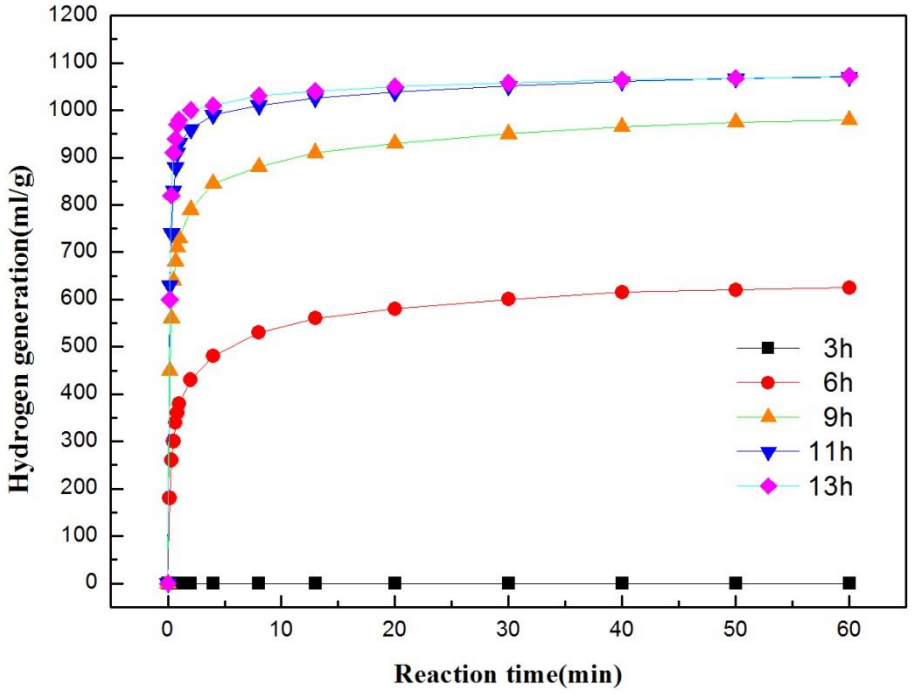

Figure 2: Hydrogen-producing performance curve of composites reacting with water for 1 h under different milling time

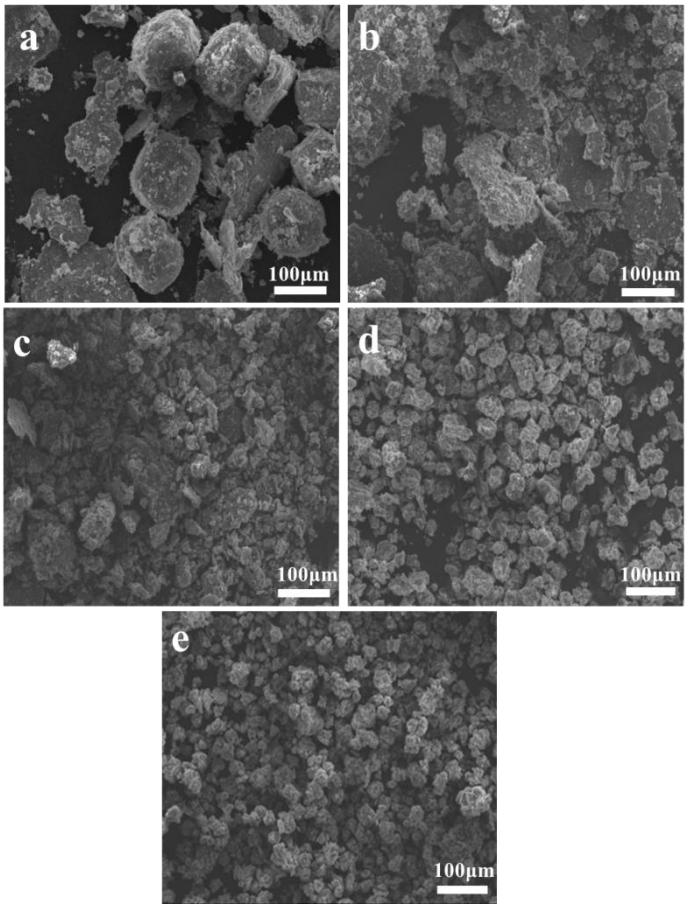

Figure 3: SEM image of ball-milled Al-5%Bi-10%NaCl material (a) 3h, (b) 6h, (c) 9h, (d) 11h, (e) 13h

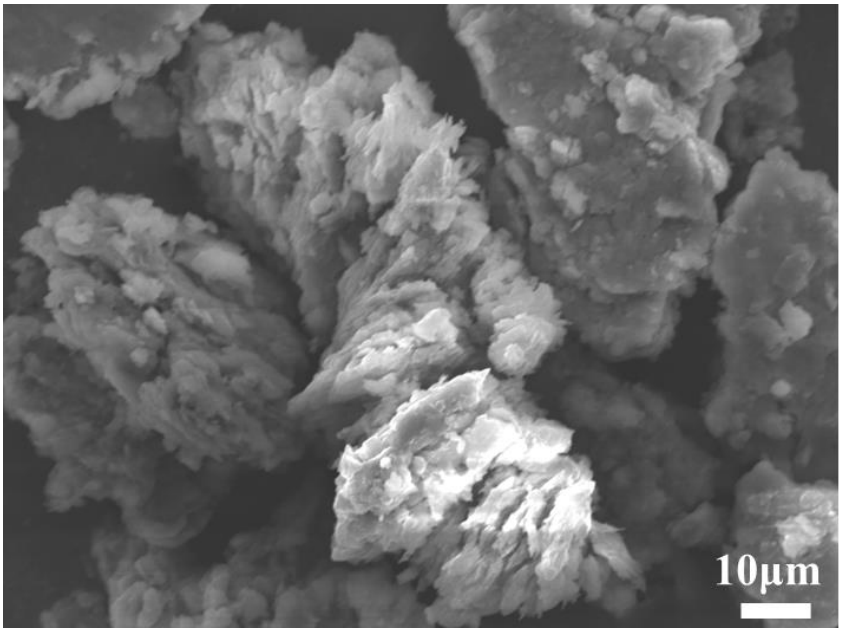

Figure 4: 1000X SEM image of Al-5%Bi-10% NaCl composites with 11 hour ball milling time

3.2. Effect of Bi content on hydrogen production performance of composites

Under the milling time is 11 hours, the ball milling speed is 360r/min, and the ball-to-material ratio is 10:1 for the ball milling parameters, Al-X%Bi-10%NaCl (X is 0, 1, 2, 3, 4, 5 , 6 and 7) was investigated to explore the effect of Bi content on the hydrogen production performance of composite materials. From Figure 5, One can see that when no Bi is added, the composite material does not generate hydrogen basically; with the addition of Bi, the composite material starts to generate a small amount of hydrogen; when 2% Bi is added, the composite material reacts for 1 hour to produce approximately 100ml hydrogen; When the content of Bi reaches 3%, the hydrogen production of the composite material has been greatly changed, and hydrogen yield has risen to about 980ml, which means that there is a critical point. When the content of Bi increases to a certain amount, the effect of Bi to promote the reaction of Al with water is activated. We know that the standard electrode potential of Al is -1.662 V, and the standard electrode potential of Bi is +0.216 V. During the reaction process, micro-battery corrosion occurs between Al and Bi, in which Bi is used as the cathode and Al as the anode (Fan, 2007). And we should note that when the Bi content is 4%, hydrogen yield has basically reached its maximum. From the viewpoint of cost savings, it is best to select the Bi content of 4%, and the hydrogen yield is approximately 1070 ml/g.

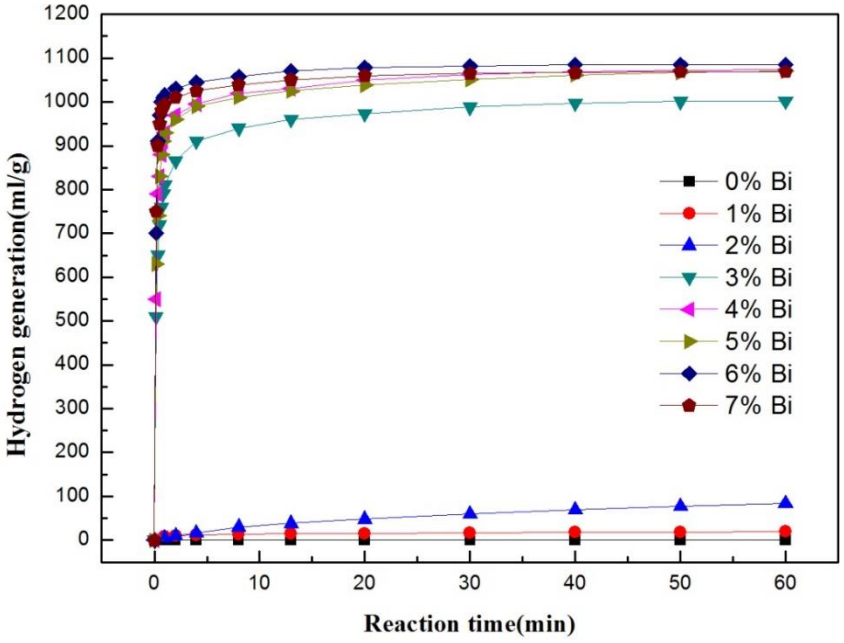

Figure 5: Hydrogen production performance curves of composites with different Bi contents

3.3. Influence of NaCl content on hydrogen production performance of composites

Under the milling time is 11 hours, the ball milling speed is 360r/min, and the ball-to-material ratio is 10:1 for the ball milling parameters, Al-4%Bi-Y%NaCl (Y is 0, 2, 4, 6, 8 and 10) was investigated to explore the effect of NaCl content on the hydrogen production performance of composite materials. From Figure 6, it can be seen that when NaCl is not added, the resulting composite material does not substantially generate hydrogen. This is because the oxide film on the Al powder surface is difficult to be destroyed due to the lack of NaCl assisting action. With the addition of NaCl, the composites starts to generate hydrogen, and the hydrogen yield increases greatly. When the NaCl content is 4%, the maximum hydrogen yield of the composites in one hour is 1156 ml/g. As the NaCl content continues to increase, although the rate of hydrogen production has increased, the hydrogen yield has decreased. This is because the increase of NaCl makes the composite particles finer, more defects, which makes more violent reaction. The increase of NaCl content will also reduce the relative content of Al, so the hydrogen yield decreases. The final choice of Al-4%Bi-4%NaCl is the best ratio.

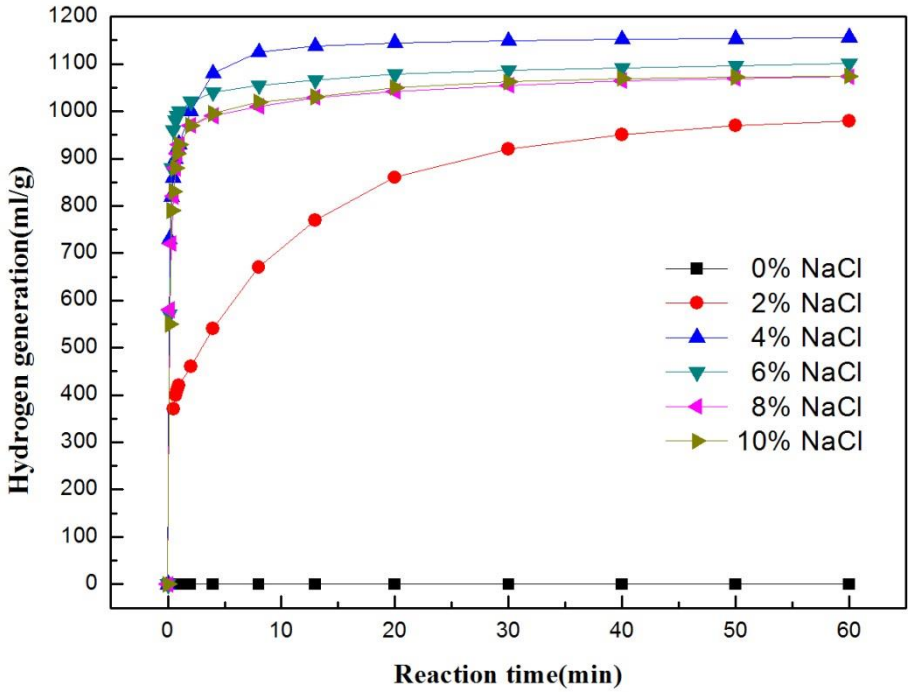

Figure 6: Hydrogen production performance curves of composites at different NaCl contents

3.4. Phase and micromorphology analysis of composites

Figure 7 shows the X-ray diffraction (XRD) analysis of the Al-4% Bi-4% NaCl composite obtained by ball milling and compared with the diffraction of raw Al powder, Bi powder and NaCl powder. One can see that the diffraction peaks of the ball milled Al-Bi-NaCl composites do not migration and no new diffraction peaks appear. It shows that after ball milling, Al, Bi, and NaCl are only mechanically mixed, no new phase is formed and no solid solution is formed. Figure 8 shows the energy dispersive X-ray spectrum analysis of the composites. It can be seen that NaCl and Bi are evenly distributed in the composites. The uniform distribution of NaCl on the surface of Al powder can effectively prevent Al powder from agglomerating. The uniform distribution of Bi contributes to its better formation of micro-primary cells with Al.

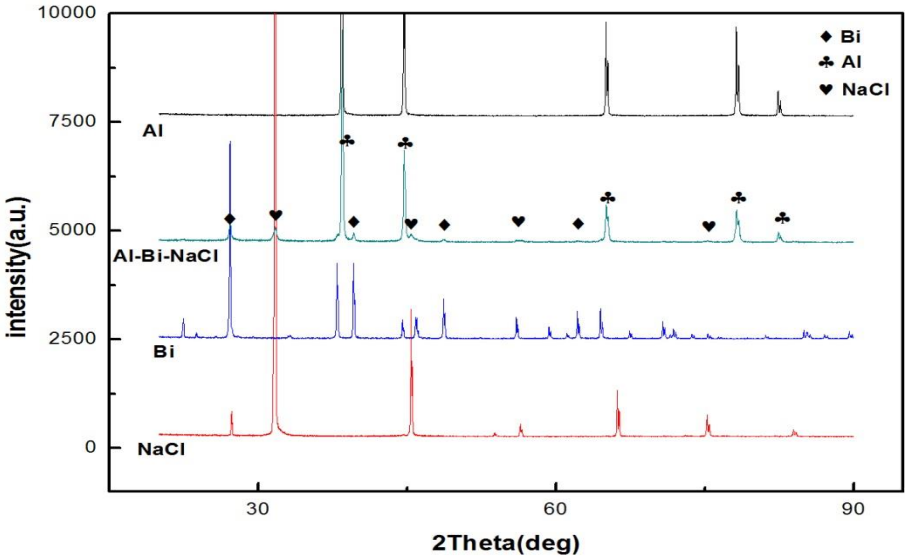

Figure 7: X-ray diffraction patterns of composites

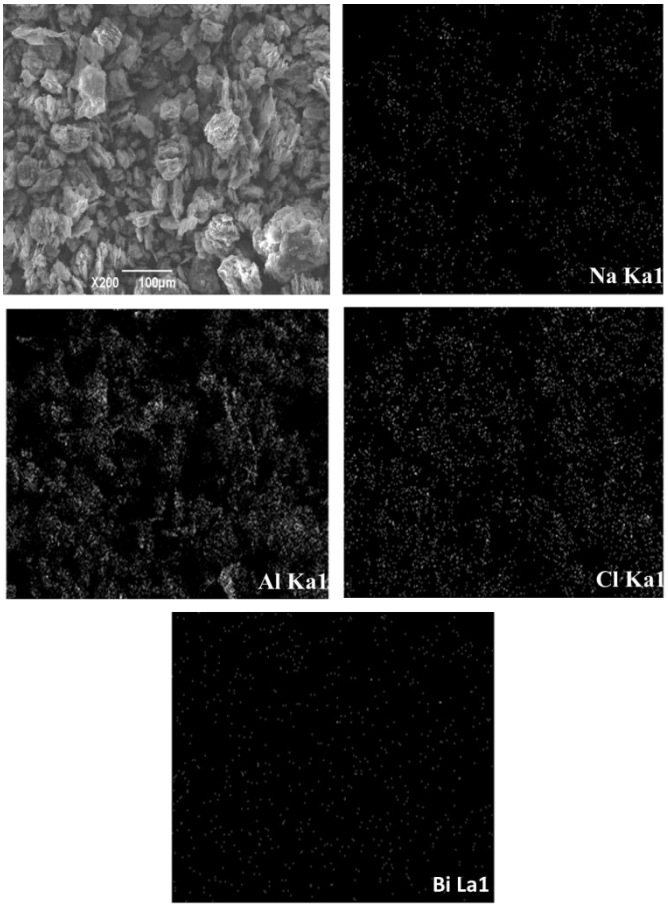

Figure 8: EDS pictures of composites

4. CONCLUSION

In this paper, the effects of milling time, Bi content and NaCl content on the hydrogen production performance of Al-Bi-NaCl composites were investigated. The results show that they have a very large impact on the hydrogen production performance of composites. Both Bi and NaCl are indispensable and need to reach a certain amount to have a significant effect on the hydrogen production performance of the composites. Taking into account the hydrogen production performance and economic benefits of composite materials, Al-4% Bi-4% NaCl was selected as the optimal ratio. When the ball milling time is 11h, the ball milling speed is 360r/min, and the ball-to-material ratio is 10:1, the hydrogen yield of

Al-4%Bi-4%NaCl composite material after reacting with water for 1 hour is 1156ml/g, and the maximum hydrogen production rate is about 4294ml/(g.min). X-ray diffraction (XRD) analysis of the as-prepared Al-Bi-NaCl composites revealed that Al, Bi, and NaCl were only mechanically mixed and neither formed a new phase nor formed a solid solution. The microstructure of Al-Bi-NaCl composites was analysed by SEM. The results showed that the composites were gradually refined with the increase of milling time, and the lamellar composites have good hydrogen production performance. EDS was used to analyse the distribution of elements in the composites. The results show that Bi is uniformly distributed in the composites and the micro-cell corrosion effect between Al-Bi plays an important role in the hydrogen production performance of the composites.

5. ACKNOWLEDGEMENTS

This work was financially supported by the National Natural Science Foundation of China (Grant No. 51771071).

6. REFERENCES

Chen XY, Zhao ZW, Hao MM, et al. 2013. Research of hydrogen generation by the reaction of Al-based materials with water. Journal of Power Sources,222:188-195.

Chen XY, Zhao ZW, Liu XH, et al. 2014. Hydrogen generation by the hydrolysis reaction of ball-milled aluminium–lithium alloys. Journal of Power Sources,254(15):345-352.

Deng ZY, Tang YB, Zhu LL, et al. 2010. Effect of different modification agents on hydrogen-generation by the reaction of Al with water. International Journal of Hydrogen Energy,35(18):9561-9568.

Fan MQ, Xu F, Sun LX. 2007. Hydrogen Generation by Hydrolysis Reaction of Ball-Milled Al−Bi Alloys. Energy & Fuels,21(4):2294-2298.

Fan MQ, Xu F, Sun LX et al. 2008. Hydrolysis of ball milling Al–Bi–hydride and Al–Bi–salt mixture for hydrogen generation. Journal of Alloys and Compounds,460(1-2):125-129.

Guan X, Luo P, Dong SJ. 2017. Hydrogen production using aluminum-based materials prepared by mechanical milling. International Journal of Modern Physics B,31(16-19):1744019.

Huang TP, Gao Q, Liu D, et al. 2015. Preparation of Al-Ga-In-Sn-Bi quinary alloy and its hydrogen production via water splitting. International Journal of Hydrogen Energy,40(5):2354-2362.

Jia YY, Shen J, Meng HX, et al. 2014. Hydrogen generation using a ball-milled Al/Ni/NaCl mixture. Journal of Alloys and Compounds,588(10):259-264.

Liu YH, Liu XJ, Chen XR et al. 2017. Hydrogen generation from hydrolysis of activated Al-Bi, Al-Sn powders prepared by gas atomization method. International Journal of Hydrogen Energy,42(16).

López-Miranda JL, Rosas G. 2016. Hydrogen generation by aluminum hydrolysis using the Fe2Al5 intermetallic compound. International Journal of Hydrogen Energy,41(6):4054-4059.

Razavi-Tousi SS, Szpunar JA. 2013. Effect of structural evolution of aluminum powder during ball milling on hydrogen generation in aluminum–water reaction. International Journal of Hydrogen Energy,38(2):795-806.

Razavi-Tousi SS, Szpunar JA. 2016. Modification of the shrinking core model for hydrogen generation by reaction of aluminum particles with water. International Journal of Hydrogen Energy,41(1):87-93.

Razavi-Tousi SS, Szpunar JA. 2016. Effect of addition of water-soluble salts on the hydrogen generation of aluminum in reaction with hot water. Journal of Alloys and Compounds,679:364-374.

Shmelev V, Nikolaev V, Lee JH, et al. 2016. Hydrogen production by reaction of aluminum with water. International Journal of Hydrogen Energy,41(38):16664-16673.

Sun YL, Sun R, Zhu BZ, et al. 2017. Effects of additives on the hydrogen generation of Al-H2O reaction at low temperature. International Journal of Energy Research,41(14):2020-2033.

Sun R, Zhu BZ, Sun YL. 2017. The effect of NiCl2 and Na2CO3 on hydrogen production by Al/H2O system. International Journal of Hydrogen Energy,42(6):3586-3592.

Tan SC, Gui H, Yang XH, et al. 2016. Comparative study on activation of aluminum with four liquid metals to generate hydrogen in alkaline solution. International Journal of Hydrogen Energy,41(48):22663-22667.

Wang W, Chen DM, Yang K. 2010. Investigation on microstructure and hydrogen generation performance of Al-rich alloys. International Journal of Hydrogen Energy,35(21):12011-12019.

Wang W, Zhao XM, Chen DM, et al. 2012. Insight into the reactivity of Al–Ga–In–Sn alloy with water. International Journal of Hydrogen Energy,37(3):2187-2194.

Woodall JM. 2009. Aluminum: a safe, economical, high energy density material for energy storage, transport and splitting water to make hydrogen on demand. School of Electrical and Computer Engineering, Discovery Park, Purdue University, West Lafayette, IN 47906, USA.

Xu F, Sun LX, Lan XF, et al. 2014. Mechanism of fast hydrogen generation from pure water using Al–SnCl2 and bi-doped Al–SnCl2 composites. International Journal of Hydrogen Energy,39(11):5514-5521.

Yang Y, Gai WZ, Deng ZY, et al. 2014. Hydrogen generation by the reaction of Al with water promoted by an ultrasonically prepared $Al(OH)_3$ suspension. International Journal of Hydrogen Energy,39(33):18734-18742.

Yang WJ, Liu XW, Liu JZ, et al. 2016. Thermogravimetric analysis of hydrogen production of Al–Mg–Li particles and water. International Journal of Hydrogen Energy,41(19):7927-7934.

Yang XH, Yuan B, Liu J. 2016. Metal substrate enhanced hydrogen production of aluminum fed liquid phase Ga–In alloy inside aqueous solution. International Journal of Hydrogen Energy,41(15):6193-6199.

Yolcular S, Karaoglu S. 2017. Activation of Al powder with NaCl-assisted milling for hydrogen generation. Energy Sources, Part A: Recovery, Utilization, and Environmental Effects,39(18):1919-1927.

Yuan B, Tan SC, Liu J. 2016. Dynamic hydrogen generation phenomenon of aluminum fed liquid phase Ga–In alloy inside NaOH electrolyte. International Journal of Hydrogen Energy,41(3):1453-1459.

Ziebarth JT, Woodall JM, Kramer, RA, et al. 2011. Liquid phase-enabled reaction of Al–Ga and Al–Ga–In–Sn alloys with water. International Journal of Hydrogen Energy,36(9):5271-5279.

309: Lightweight design of 7MW permanent magnet direct drive wind generator

Zhenyu WU[1], Xinwei LUO[1], Ling LI[2]

[1] School of Mechanical Engineering, Hubei University of Technology, Wuhan,430068
[2] Wuhan Puhui Ocean Optoelectronic Technology Co., Ltd., Wuhan,430223

For the permanent magnet direct drive wind generator, the volume and weight of the motor have a great influence. As far as the general rule is concerned, no matter what kind of electromechanical device, if the volume, weight or speed is very large, it will inevitably cause a series of mechanical problems. In this paper, the mechanical mechanism design of generator is chosen as the research direction to solve the lightweight problem of generator. Therefore, in this paper, the author first introduces the overall structure of permanent magnet direct drive wind generator. After that, the structure of the motor is designed with light weight from the motor parts, which partly reduces the weight of the motor. Then, a structure to resist stator deformation is designed in this paper. By directly installing a certain number of double-head bolts on the base and shell to increase the radial strength, the electromagnetic force and gravity are offset while the strength of the motor base is strengthened, and the weight of the motor is reduced effectively. Finally, three kinds of structures are selected by the control variable method. The analysis results show that the optimised structure has better anti-deformation effect and better strength effect than that of increasing plate thickness. The new anti-stator deformation structure not only solves the problem of overweight problem of the motor base, but also strengthens the strength of the frame and prevents it from deforming.

Keywords： lightweight design; permanent magnet direct drive generator; anti-stator deformation

1. INTRODUCTION

Permanent magnet direct drive generator has become the most promising wind power generation (Bianchi, 1996) because of its advantages of high power density, high efficiency, high reliability and low maintenance cost (Barr, 2002). But with the increase of the motor power rating, the volume and weight of the motor become one of the factors restricting the market of this kind of motor, bringing great difficulties to the manufacture, assembly, transportation and installation of the motor (Shrestha, 2013). The reason why large permanent magnet direct drive wind turbine is large in size and heavy in mass is: in addition to produce effective material of electromagnetic torque, large wind generator also includes the structure of the transmission torque material (Shrestha, 2013). In order to overcome the torque load without plastic deformation or fracture and ensure that the deformation at the air gap of the generator does not exceed the allowable value, the rigid strength index greatly increases the size and weight of the structure, these account for about 2/3 of the total weight of the generator and is key factor in determining the overall weight of the generator (McDonald, 2008).

For large generators, the stator core is installed on the base, that is, the base is the support structure of the stator core, so it is the main component of bearing and transmitting torque and supporting the end cover. So that it can withstand all kinds of mechanical force, electromagnetic force without harmful deformation in processing, transportation, lifting, split valve placement and operation. Considering the electromagnetic performance of the motor, the air gap between the stator and rotor is generally only a few millimetres or so (Colli, 2012). Once the air gap changes, it will seriously affect the overall performance of the motor. Factors that result in the change of air gap, in addition to the deformation of stator iron core due to electromagnetic force, another important reason is that the strength of the stator core is not strong enough (Polinder, 2006). Therefore, under the action of strong electromagnetic force, the seat is deformed, thus changing the length of the air gap. So effective mechanical structure design must be taken to improve the strength of the stator frame, especially improve the tensile strength of frame. For large wind generator, one approach to improve the strength of the stand is to increase the thickness of the plate. Another is to weld a considerable number of stiffeners to improve the strength of the base on the outer surface of the base (Wu, 2015). Although these two approaches can improve the strength of the frame, to prevent the severe deformation, but also will increase the volume and weight of the whole.

In view of the fault of heavy stator mounting base at present, a new structure scheme against stator deformation is put forward, the scheme combines the structure and assembly characteristics of the fixed parts of the generator set and sets up anti deformation parts in specific parts. In solving the problems of large size and bulky structure of the stator base of wind generator at the same time, the tensile strength of the stator base is improved significantly, and the deformation of the stator base is effectively prevented in various power generation situations.

2. GENERAL SCHEME OF PERMANENT MAGNET DIRECT DRIVE WIND DRIVEN GENERATOR

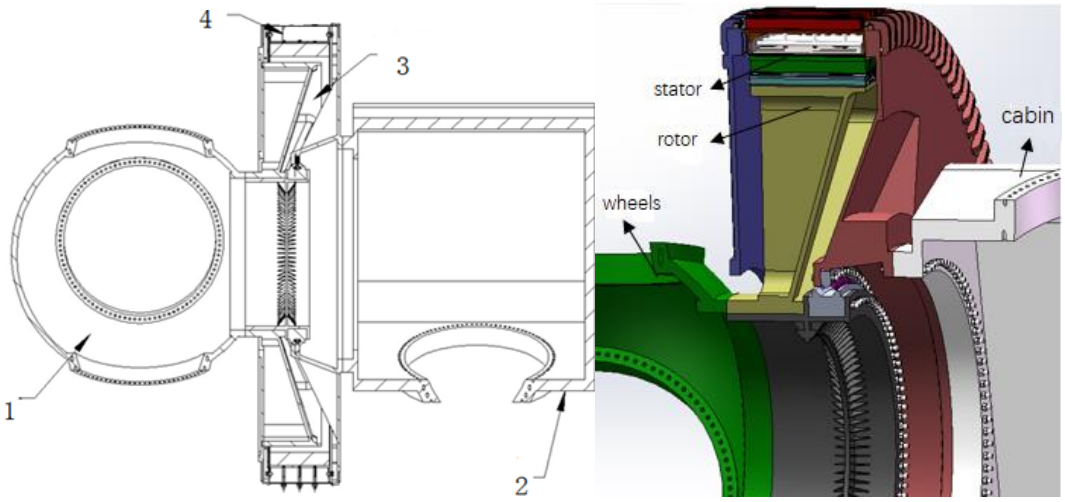

Figure 1: Mechanical structure of 7MW Wind generator

The main parameters of the 7mw permanent magnet direct drive wind generator prototype are shown in Table 1. As shown in Figure 1, it is mainly composed of wheel 1, cabin 2 rotor 3 and stator 4.

Table 1: main parameters of 7MW prototype

	Parameter	numerical value		Parameter	numerical value
Stator	numerical value	216/180	rotor	outer diameter (mm)	7676
	outer diameter (mm)	8044		inner diameter (mm)	7508
	inner diameter (mm)	7690		Lamination length (mm)	1156
	Lamination length (mm))	1156		yoke thickness (mm))	73
	yoke thickness (mm)	37		silicon steel sheet material	50WW470
	Groove depth (mm)	140		permanent magnet material	N42SH
	Slot width (mm)	56		permanent magnet type	V type
	Material	50WW470		permanent magnet thickness (mm)	32
Air gap length (mm)		7	structural internal	inner rotor	

At the same time, the inner structure of the wind generator is the single bearing of the rotor in the horizontal shaft. This structure abandoned the dual bearing structure of the conventional motor and only used a double-row tapered roller bearing with a larger diameter to bear the shaft and radial load. The stator base and rotor yoke of the generator are connected directly to the inner and outer rings of the bearing through tapered support respectively. The hub is connected to the other side of the outer ring of the bearing. This allows the generator rotor, bearing outer ring and hub to form a synchronous rotating whole. Since the spindle is eliminated, the generator structure becomes simple and compact. The weight of the structural material is greatly reduced.

The bearing adopts double roller angular contact bearing, which can bear large radial force and axial force. At the same time in the motor, using a bearing can reduce weight, compact structure size compared with the dual bearing system. As shown in Figure 2, the through hole of the inner and outer ring of the bearing can be connected with the shaft part and the stator part respectively through the bolt, which plays the role of supporting the transition.

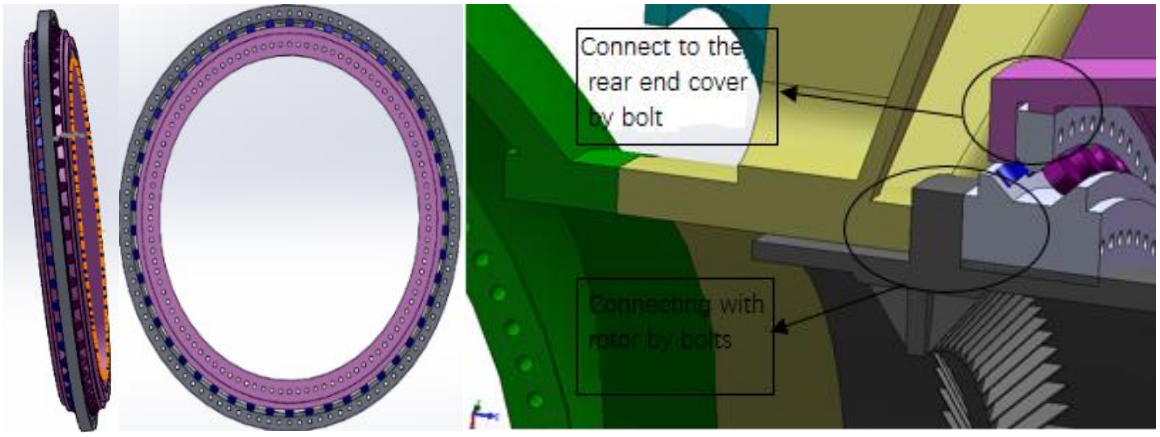

Figure 2: Bearing interface

3. PRINCIPLES OF THE DEVICE

For the fixed part of the generator set, the whole structure is subject to strong electromagnetic force in addition to its own gravity. The electromagnetic force is composed of radial force perpendicular to the stator core tooth surface and tangential force tangent to the stator core tooth surface. Accordingly, in addition to the deformation of the stator core, the stator core is connected with the stator base through the coordination between the mortise and tenon groove, so the electromagnetic force of the stator core is transmitted to the stator base through the connection part between them, causing the deformation of the stator base.

Therefore, a certain number of specially machined double-headed screws are installed between the chassis and the base. Through the hole in the shell, one end of the double-headed screw column is screwed to the seat through a thread connection, and the other end is locked to the shell with a nut. As long as the nut is screwed, there will be relative movement between the stud and the nut, and a tension will be generated at the joint between the stand and the stud. The direction of

this tensile force is always opposite to that of the radial component force of the electromagnetic force, the main force that causes the deformation of the base. So, the force can offset part of the radial component of the electromagnetic force, at the same time also can counteract gravity component in radial direction, then improve the tensile strength and reduce the deformation of the machine base in radial direction.

According to the principles described in the previous section, as long as there is a relative motion between the stud and the nut, the tension at the joint between the base and the stud will offset the radial force of gravity and the electromagnetic force in the motor to reduce radial deformation of chassis.

4. SPECIFIC IMPLEMENTATION MODE

Figure 3 is a schematic diagram of the main mechanical structure of a generator unit with anti-stator deformation function

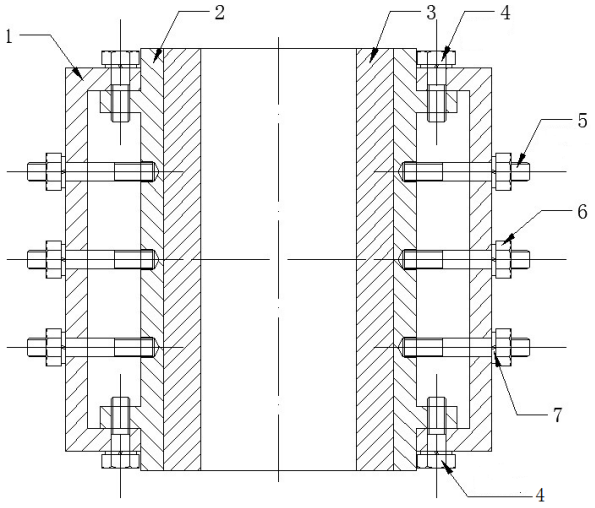

Figure 3: Schematic diagram of anti-stator deformation structure
1 - chassis; 2 -- stator base; 3 -- stator core; 4 -- connection bolts; 5 -- double-headed stud; 6 - nut; 7 – gasket

In particular, the upper and lower ends of the chassis 1 and the stator base 2 are connected to the flange face by a plurality of connecting bolts running through the flange face The stator iron core 3 is provided with a plurality of tenon grooves along its circumferential direction, through which the tenon slots are meshed with the corresponding tenons set on the stator base 2. Stator winding can be fixed on stator core 3. As shown in figure 3, considering that the stator outer diameter of a large wind turbine is usually more than 8 m, so the stator core and winding can be divided into 54 equal parts in its circumferential direction, each of which is fixed by the tenon groove on the core and the tenon of the stator base 2. Similarly, the flange faces of the upper and lower ends of the stator base 2 are connected with that of the chassis 1 by 54 specifications, such as the connecting bolt 4 of the M20, and these connecting bolts are arranged in a uniform way along the circumference of the flange face and symmetrical up and down.

In addition, as one of the most critical improvements, in the middle region between the upper and lower ends of the chassis 1 and the stator base 2, multiple double studs 5 are uniformly arranged along the circumferential direction of the casing 1 (for example, 108 are also provided). The specification is M42, one end of each double end stud 5 runs through the chassis along the radial direction of the casing 1 and is tightened on the stator base 2 through the thread structure, the other end is locked on the outer surface of the chassis 1 through nut 6 and gasket 7.

5. OPTIMISATION EXPRIMENTS VERIFICATION

The feasibility and anti-deformation effects of the structure are verified by the following three groups of experiments. The first two groups did not adopt anti-deformation structure, and the thickness of the base plate was 10mm and 50mm respectively. The third group of experiments adopted anti-deformation structure and set the thickness of the bottom plate to 30mm.Because of the circular symmetry of the entire structure, it takes a 1/54 segment to be the object of the study. In the finite element analysis model, the actual working condition can be simulated only by applying a certain amount of racial tension on the screw hole of the machine base. Therefore, the solid model of double screw and nut cannot be seen in the finite element model.

Firstly, the structural scheme is not adopted. The plate thickness of the stator stand is 10mm. The radial deformation of the stator stand under the action of gravity and electromagnetic force is shown in figure 4(a). Because the thin plate and the small stiffness, the core is deformed 0.152 mm.

Next, with the same boundary conditions, the plate thickness of the chassis is increased to 50mm. As shown in Figure 4(b), the deformation is obviously improved because of the increase of the base thickness, the maximum deformation is very small, only 0.074 mm.

All the above discussions are to increase the stiffness of the chassis by increasing the thickness of the base plate, without adopting the structural scheme proposed in the paper. These methods not only increase the stiffness of the chassis, but also increase the weight of the base. Therefore, consideration is given to appropriately increasing the plate thickness of the base to 30mm and adopting the scheme of anti-deformed stator proposed in this paper. The deformation of the assembly is shown in the Figure 4(c), and the deformation has reached the level of 50mm plate thickness. It can be seen that, without changing the shape size, material and plate thickness of stator core and base, the deformation of the whole frame is close to zero deformation if the structural scheme is adopted in this paper. When the structural scheme of this paper is not adopted, the deformation of stator stand is close to zero only at the flange face connected with the chassis, while there is a large amount of deformation at other positions. The simulation results show that the proposed structure can improve the tensile strength of the base and improve the deformation of the base on the basis of reducing the thickness of the plate.

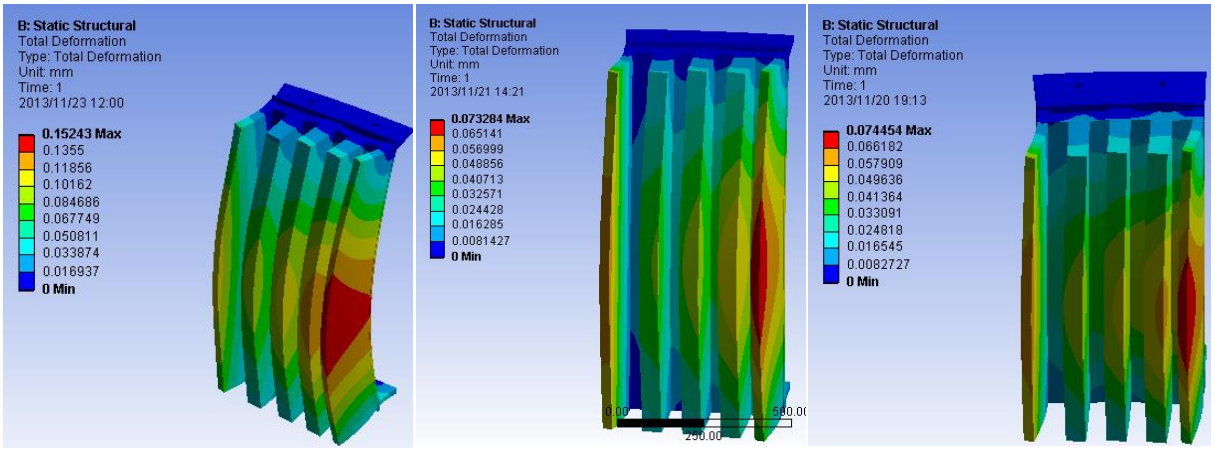

(a) 10mm (b) 50mm (c) 30mm+ this scheme

Figure 4: Radial deformation of stator core and frame assembly

6. CONCLUSION

For the large permanent magnet direct drive wind generator, single bearing and inner rotor structure can make the generator structure simple and compact, thus reducing the weight of structural materials. Moreover, the new anti-stator deformation structure in this paper has a good effect on reducing the overweight of generator base. By installing a certain number of specially machined double-ended studs between the housing and the base, the stress on the stator base in the direction of diameter can be effectively reduced, thus the deformation of the base can be restrained. The simulation experiments results show that the optimised structure has better anti-deformation effect and better strength effect than that of increasing plate thickness. The new anti - deformation structure improves the tensile strength of the stator base while solving the problems of large volume and heavy structure, and the stability of the machine base is increased.

7. ACKNOWLEDGEMENTS

This work was supported in part by the Hubei Province Natural Science Foundation under Grant 2017CFB324, Science and Technology Supporting Program of Educational Commission of Hubei province under Grant D20171404 and Doctoral Researching Funding under Grant BSQD2015016.

8. REFERENCES

Barr D. 2002. Modern Wind Turbines: A Lubrication Challenge [J]. Machinery Lubrication Magazine, 46(9):30-35.

Bianchi N, Lorenzoni A., 1996, Permanent magnet generators for wind power industry: an overall comparison with traditional generators [C]. IEEE Conf. on Opportunities and Advances in International Power Generation, Durham, UK, 49-54.

Colli V D, Marignetti F, Attaianese C. 2012. Analytical and multiphysics approach to the optimal design of a 10MW DFIG for direct-drive wind turbines [J]. IEEE Trans. Ind. Electron, 59(7):2791-2799.

McDonald A S. 2008, Structural analysis of low speed, high torque electrical generators for direct drive renewable energy converters [D]. School of Engineering & Electronics, University of Edinburgh.

Polinder H, van der Pijl F F A, de Vilder G J, et al., 2006, Comparison of direct-drive and geared generator concepts for wind turbines [J]. IEEE Trans. Energy Conversion, 21: 725-733

Shrestha G, Polinder H, Bang, D J et al., 2013. Review of energy conversion system for large wind turbines[C]. in Proc. 2013 Eur. Wind Energy Conf., 1-10.

Shrestha G, Polinder H, Bang D J, et al., 2013. A new concept of weight reduction of large direct drive machine [C]. in Proc. 2013 Int. Conf. Electr,1-6.

Wu Z.Y, Qu R.H, Li J., et al., 2015. Structure optimization of rotor supporting of permanent magnet direct drive synchronous generators for large wind turbine based on genetic algorithm and finite element method. IEEE International Electric Machines & Drives Conference (IEMDC). USA: IEEE.

310: Feasibility study of biogas energy generation from refuse dump in a community- based distribution in Nigeria

Ogbene G. IGBUM[1], Sunday ADOGA[2], Andrew C.ELOKA-EBOKA[3], Ekani OTIKWU[4]

[1, 2 & 4] *Department of Chemistry, Benue State University, Makurdi, Nigeria ogbenebenny@yahoo.com*
[3] *Discipline of Mechanical Engineering, University of KwaZulu-Natal, Durban, South Africa, fatherfounder@yahoo.com*

In this survey, three different wastes generated were combined in a locally fabricated digester and each singly loaded in respective digesters to generate energy in the form of biogas with an anticipation of redistribution for a community-based use. The biodegradability test of the substrates were studied ab initio by evaluating for ash and moisture contents, C/N ratio, biochemical oxygen demand and chemical oxygen demand for maize chaff, watermelon and cassava peels. The results showed 2.85, 0.66 and 2.40 % for ash content, 11.18, 93.22 and 70.26% for moisture content, 12.10, 15.10 and 19.10% for C/N ratio, 155.07, 131.96 and 113.79 ppm for BOD, and 240.00, 212.00 and 264.00 ppm for the substrates respectively. From the results, maize chaff with the highest ash content, has the least bio-degradable (organic) matter, while watermelon, with the least ash content, has the highest biodegradable matter. The moisture content results for maize chaff and water melon were below and above the optimum value of "60 – 80" % and this confirmed the low biogas volume produced when used alone. The ideal C/N ratio for anaerobic digestion is between "20:1 and 30:1". A comparison of these sets of values from the study showed that the C/N ratios obtained from the research work are below the optimum values of the C/N ratios and could be responsible for the poor biogas yield for the disjoined substrates. The biogas volume of 2100 mL was produced at the end of the retention time for the combined substrates and, was higher compared with the 18, 25 and 29 milliliters (mL) produced for maize chaff, watermelon and cassava peels, (the disjoined) substrates respectively. In this study, the COD value for each substrate is higher than the corresponding BOD values. Hence, co-digestion of unavoidable food wastes is economic and, a potentially viable option to generate alternative renewable energy for rural community-based use.

Keywords: Energy generation, wastes, biogas, biodegradability and rural community.

1. INTRODUCTION

Energy generation remains one of the biggest challenges of developing or third world counties like Nigeria. About 80 million (44.4%) out of 180 million Nigerians living in 8000 villages across the country lack access to electricity according to World Bank report for sustainable energy to all (The World Bank, 2016). Lack of access to electricity to stimulate small and medium scale enterprises in rural communities is believed to be a major factor responsible for rural - urban migration (internal migration) and the lingering emigration crises across the globe. In this study, wastes generated from three different feed stocks namely: watermelon, maize chaff and cassava peels dumped at Rail way market, Wadata market/gari processing plant and Naka road respectively in Makurdi metropolis, Benue State of Nigeria were used to generate biogas for utilisation. These unavoidable wastes are produced daily due to lack of adequate disposal system, poor transportation network and improper waste management system in the country. Four 25–litre laboratory scale galvanised anaerobic reactors, known as digesters in the work were fabricated locally for this research study. The digesters have four openings each, one serving as the inlet of the substrates, the second for the biogas outlet, while the third was for the removal of the slurry. The fourth opening was made on the cover through which a thermometer was permanently attached for temperature measurement. The gas outlet was connected to two Buchner flasks which served as purification chambers containing 20% NaOH and 20% lead acetate solutions each for the removal of CO_2 and H_2S respectively, as adopted by Dahusi (2013). The Buchner flasks were then connected to a 500ml measuring cylinder filled with water and inverted in a big beaker supported with a retort stand for measuring the volume of gas produced by water displacement method as seen in Figure 1.

Figure 1: Fabricated digesters and experimental set – up

2. MATERIALS AND METHODS

The substrates (cassava peels, maize chaffs and watermelons) were homogenised with mortar and pestle to increase the surface area in order to hasten up the digestion. A mixture consisting of about 12 kg of each food waste and water was prepared by mixing them in a ratio of 1:1 W/V to make approximately 30 liters of slurry. Each of the reactors (digesters) was filled to three - quarters of its volume (19000 ml), and three of the reactors were fed with maize chaffs, watermelon and cassava peels each, while the fourth reactor was fed with a mixture of the three substrates.

The digestion was allowed for 60 days in a batch fermentation mode. The physicochemical and biodegradability analyses of the substrates were evaluated before and after digestion using standard procedures (APHA and AWWA, 2012).

3. RESULTS

Parameters analysed include ambient and slurry temperature of the reactors for different substrate, slurry pH, moisture content, ash content, organic carbon, total nitrogen, biochemical oxygen demand (BOD), chemical oxygen demand (COD) and volume of biogas produced from each digester. These are presented in Table 1.

Table 1: Percentage proximate composition of substrates

Parameters (%)	**Food wastes**		
	MC	***WM***	***CP***
Ash	2.85±1.50[b]	0.66±0.12[a]	2.40±0.61[b]
Moisture	11.18±0.18[a]	93.22±0.27[c]	70.26±1.86[b]
Carbon	70.64±0.76[b]	59.91±1.08[a]	60.21±0.98[a]
Nitrogen	5.93±0.06[b]	3.87±0.03[a]	3.08±0.05[a]
C/N ratio	12.10	15.10	19.10

*Values are mean ± standard deviation. Superscripts with same alphabet denote values within the same range at P ≤ 0.05 for maize chaff (**MC**), watermelon (**WM**) and cassava peels (**CP**) respectively.*

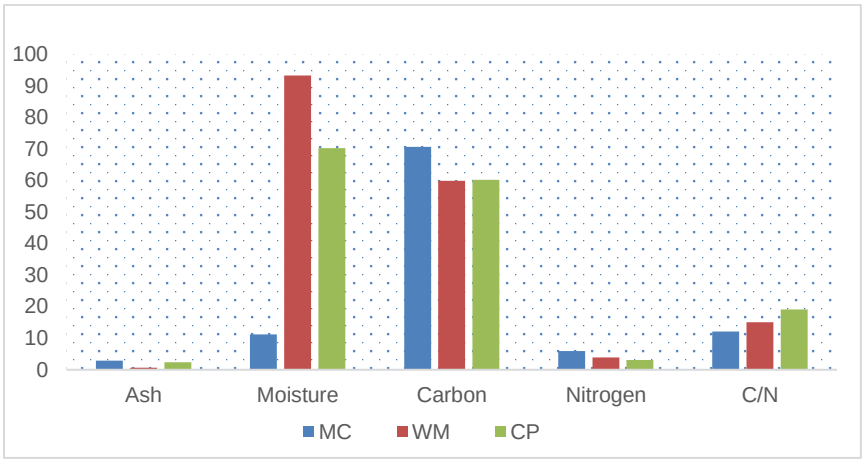

Figure 2: Substrates proximate composition variation chart

Table 2: Substrates biochemical and chemical oxygen demand

Parameters (%)	**Food wastes**		
	MC	***WM***	***CP***
BOD	155.07±1.96c	131.96±3.01b	113.79±3.85a
COD	240.00±4.00b	212.00±4.00a	264.00±4.00c

*Values are mean ± standard deviation. Superscripts with same alphabet denote values within the same range at P ≤ 0.05 for maize chaff (**MC**), watermelon (**WM**) and cassava peels (**CP**) respectively.*

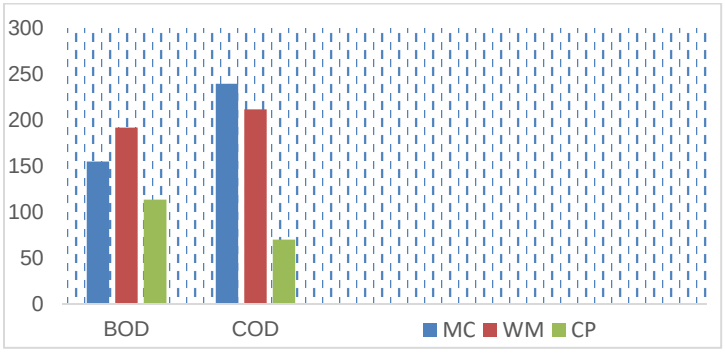

Figure 3: Substrates biochemical and chemical oxygen demand variation chart

Table 3: Weekly pH of the slurry

Weeks	MC	WM	CP	CS
1	5.20	4.76	4.83	-
2	3.88	4.39	3.84	3.85
3	3.89	4.65	3.99	3.86
4	3.76	4.74	3.73	3.97
5	3.85	4.94	4.10	4.09
6	3.81	4.94	4.60	4.16
7	3.88	5.12	4.30	4.27
8	3.77	5.06	3.81	4.30

Key: CS (Combined Substrates)

Table 4: Volume of biogas produced and the percentage yield

Food Wastes/Reactors	Volume of biogas (ml)	% Yield
Maize chaff(R1)	18.00	0.09
Water melon(R2)	25.00	0.13
Cassava peels (R3)	29.00	0.15
Combined food waste R4)	2100.00	11.05

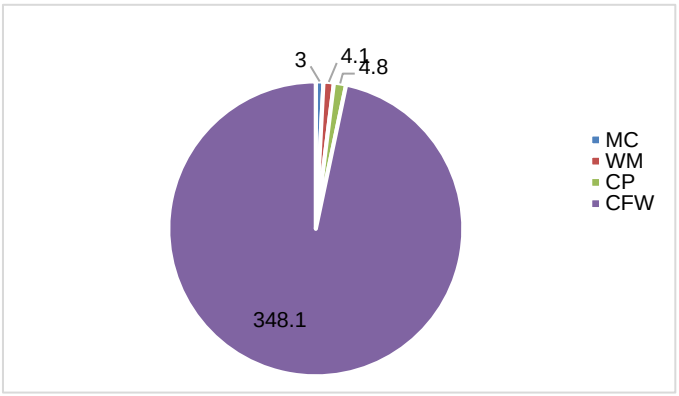

Figure 4: Substrates biogas volume chart

4. DISCUSSION

The bio-degradability tests of the substrates are as shown in Tables 1 and 2 and in Figure 2. Table 1 shows the percentage ash, moisture, carbon and nitrogen contents of the substrates. From the table, maize chaff, watermelon and cassava peels have 2.85 ±1.50%, 0.66±.0.12% and 2.40± 0.61% ash content respectively. It is evident from the results that maize chaff has the highest percentage ash content but with the least bio-degradable (organic) matter, while watermelon has the least ash content with the highest organic matter.

The percentage moisture content study of the substrate showed that watermelon has the highest moisture content of 93.22±0.27%, followed by cassava peels with 70.26 ±1.86%. Maize chaff is the least with 11.18± 0.18%. Comparing these results with the optimum value of moisture content of 60-80%, Khalid (2011) indicated in is study that it is evident that maize chaff and watermelon may not produce much biogas since their values are below and above the optimum range respectively, cassava peels whose value falls within the range may produce more biogas under the same conditions. The carbon contents of the substrates are presented in Table 1. This also shows some variations in the percentage content. Maize chaff has a carbon content of 70.64±0.76%, watermelon has 59.91 ±1.08%, while that of cassava peels is 60.21±0.98%. From these, maize chaff has the highest percentage carbon while watermelon has the least. The implication of which is that high amount of biogas yield is anticipated from maize with high composition of carbon.

The table further shows values for percentage nitrogen content of the substrates: maize chaff has a nitrogen content of 5.93 ±0.06%, watermelon has 3.87 ±0.03% and cassava peels have 3.08 ±0.05% as also the carbon to nitrogen ratios: 12:1, 15:1 and 19:1 for maize chaff, watermelon and cassava peels respectively. The carbon to nitrogen ratio expresses the relationship between the quantity of carbon and nitrogen present in the substrates. Materials with different carbon to nitrogen ratios differ widely in their yields of biogas.

The ideal carbon to nitrogen ratio for anaerobic digestion is between 20:1 and 30:1 according to studies of Yadvika (2004), Khalid (2011) and Poliafico (2007). A comparison of these sets of values shows that the C/N ratios obtained from this study are below the optimum values of the C/N ratios and could be responsible for the poor biogas yields for individual substrate. When the C/N ratio is lower than the ideal values, nitrogen will be liberated and it will accumulate in the form of ammonia and will raise the pH value of the slurry in the digester. This is not an ideal situation. pH value higher than 8.5

(alkaline) are toxic to the methanogenic bacteria in the slurry (Poliafico, 2007) and the cumulative effect of this is the low generation of biogas. However, if the C/N ratio is higher than the ideal range, biogas production will be low. This is because the nitrogen will be consumed rapidly by the methanogenic bacteria for meeting their protein requirements and will no longer react with the leftover of carbon remaining in the material. In such a case of high C/N ratio, the gas production can be improved by adding nitrogen in form of cattle urine or by fitting latrine to the plant according to Fulford (1988). Materials with high C/N ratio typically are residues of agricultural plants. Materials having low C/N ratio could be mixed with those having high C/N ratios so as to bring the average C/N ratio of the mixture to a desirable level. Human excreta, duck dungs, chicken dungs, and goat dungs are some of the materials which typically have low C/N ratios.

The BOD and COD values of the substrates as presented in Table 2 indicate that maize chaff has a BOD of 155.07±1.96 ppm and COD of 240.00±4.00 ppm, watermelon has BOD of 131.96± 3.01 ppm and COD of 212.00±4.00 ppm, while those of cassava peels are 113.79±3.85 ppm and 264.00±4.00 ppm respectively. BOD and COD are indicative of the degree of both biological and chemical decompositions that are taking place in the digesters. The COD gives a precise estimation of the organic (degradable) material content of the sample. The results showed that the COD value for each of the substrates is higher than that of the corresponding BOD as observed in Table 2 and Figure 3. This is in agreement with the earlier work of Curry in 2012 where he reported that higher values of COD than BOD are favourable for anaerobic digestion, hence more biogas production. Therefore in this context, maize chaff, watermelon and cassava peels are good substrates for anaerobic digestion for the production of biogas. The characterisation results suggest that mixing the food wastes is necessary to provide a nutrient balanced feedstock for anaerobic digestion.

The pH data presented in Table 3 shows the values of the weekly pH of the slurry for the period of eight (8) weeks. The pH values showed initial fall to a more acidic level before assuming gradual increase. The pH of the maize chaff dropped from 5.20 to 3.88 and that of watermelon were from 4.76 to 4.39. Cassava peels fell from 4.83 to 4.84. The initial drop in pH is important since activities of aerobes and facultative aerobes are essential in producing relevant acidic metabolites, which are acted on by methanogenic bacteria to yield methane. According to similar studies, microorganism involved in anaerobic bio digestion requires neutral or mildly alkaline environment, as a too-acidic or too-alkaline environment will be detrimental to them (Buren, 1983). The acidic environment of the digester accounts for the low biogas production. The pH value of a digester depends on the ratio of acidity and alkalinity and the carbon dioxide content in the digester, the determining factor being the density of the acids (Buren, 1983).

The pH requirements of the groups of microorganisms participating in anaerobic digesters differ. While acidogenic bacteria can perform well when the pH is above 5, methanogenic bacteria require a minimum pH value of 6.2. Anaerobic bacteria especially the methanogens are sensitive to the acid concentration within the digester and their growth can be inhibited by acidic conditions. During digestion, the two processes of acidification and methanogenesis require different pH levels for optimal process control. The retention time of the digestate affects the pH value and in a batch reactor, acetogenesis occurs at a rapid pace (Kanger, 2013). Acetogenesis can lead to accumulation of large amount of organic acids resulting in pH below 5. Initially, pH decreased as organic matter undergoes acetogenesis, but methanogens rapidly consume those acids increasing pH and stabilizing digester performance. Due to their sensitivity to acid conditions, excessive generation of acid can inhibit methanogens. Reduction in pH can be controlled by the addition of lime, recycled filtrate obtained during residue treatment (Poliafico, 2007).

The biogas production process from co-digestion of food wastes was investigated for the samples under study. The individual biogas yields were recorded in Table 4 and in Figure 4. The biogas volume produced at the end of the retention time for combined substrates was the highest at 2100.00 mL, while for disjoined substrates were 18.00 mL, 25.00 mL and 29.00 mL for maize chaff, watermelon and cassava peels respectively. The higher biogas yield for the combined food wastes is in concord with a similar work by Kanger in 2013 which reported that co-digestion of substrates resulted in higher biogas yields.

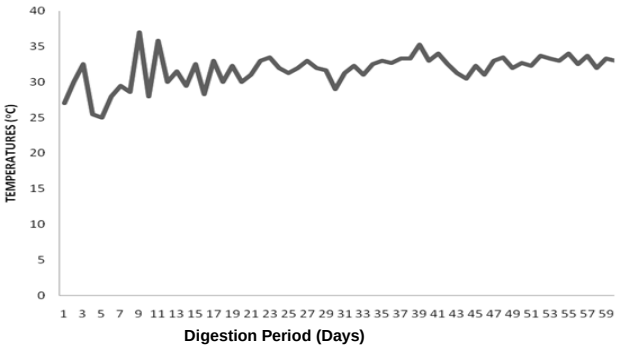

Figure 5: Average Daily Ambient Temperatures

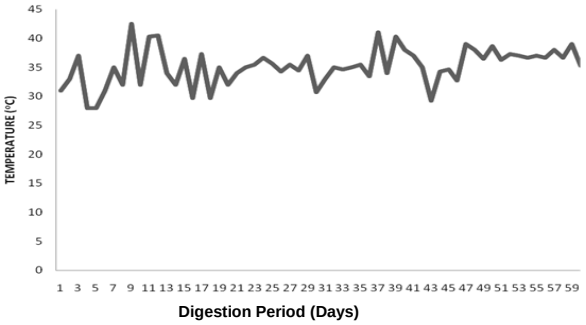

Figure 6: Average Temperatures of maize chaff (Reactor 1)

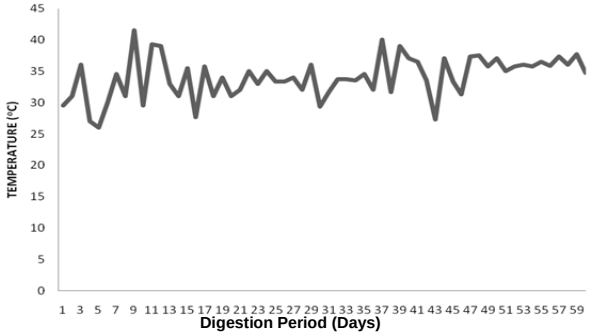

Figure 7: Average Temperatures of watermelon (Reactor 2)

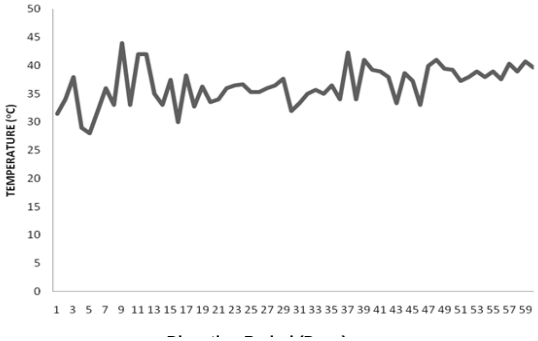

Figure 8: Average Temperatures of Cassava peels (Reactor 3)

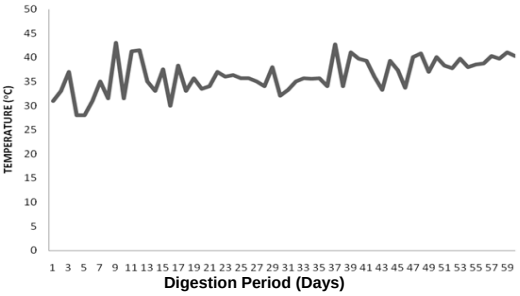

Figure 9: Average Temperatures of combined food wastes (Reactor 4)

Figures 5- 9 showed the ambient and slurry temperatures of the four reactors. The results show that the temperatures of the slurry were gradually higher than the corresponding ambient temperatures. Bacterial activities in the digesters may have caused the increase in temperature. It was observed from the study that bio-digestions in the reactors predominantly occurred within the mesophilic temperature range (30^{o}C to 38^{o}C), although there were some cases of temperatures fluctuations below and above the range, as seen in the figures. Temperature is a critical environmental factor affecting digester's performance. It affects the physical and physicochemical properties of compounds present in the digester and the kinetics and thermodynamics of biological processes (Gustavsson, 2011). Anaerobic bacteria communities can endure temperatures ranging from below freezing to above 57.2^{o}C but they thrive best at temperatures of about 36.7^{o}C (mesophilic) and 54.4^{o}C (thermophilic). Bacterial activity and thus biogas production falls off significantly between about 39.4^{o}C and 51.7^{o}C and gradually from 35 to 0^{o}C. To optimise the digestion process, the digester must be kept at a consistent temperature as rapid changes will upset bacterial activity as observe by Carcelon (2002). In order to reach

optimum operating temperatures (30 to 37^{o}C), some measures must be taken to insulate the digester. Straw or shredded tree bark can be used around the outside of the digester to provide insulation (VITA, 1980).

5. CONCLUSION

Biogas production from maize chaff, watermelon, cassava peels and a combination of the three substrates was carried out using batch fermentation mode for a retention time of 60 days. It is evident from the result that biogas yield was enhanced by co- digestion of the substrates. Co-digestion of the selected food wastes significantly increased biogas volume produced and eco-friendly sludge was as well formed. The study is part of waste to wealth strategy adopted in developing country like Nigeria to generate energy and to mitigate waste accumulation and its disturbing environmental effects and challenges.

6. REFERENCES

Buren, V. (1983). A Chinese Biogas Manual Popularization Technology. Country side. Intermediate technology Publications Ltd.

Carcelon, J. and Clark, J. (2002). Methane Biogas from Anaerobic Digesters. The US Environmental Protection Agency, the US department of Agriculture and the US Department of Energy. pp. 64 – 68.

Curry, N. and Pillay, P. (2012). Biogas prediction and design of a food waste to energy system for the urban environment. Renew. Eenergy 41:200-209.

Dahusi, S.O and Oranusi, U.S. (2013). Co- digestion of Food Waste and Human Excreta for Biogas Production. Dept of Biological Sciences, Covenant University, Ota, Nigeria. *British Biotech. J*. 3 (4): 485-499.

Fulford, D. (1988). Running of Biogas Program Handbook, Intermediate Technology Publication London.

Gustavsson J., Cederberg C., Sonesson U., van Otterdijk R. and Meybeck A. (2011). FAO. Global Food Losses and Food Waste – Extent, Causes and Prevention. Rome.

Kanger, K. (2013). Biogas production under co- digestion of food waste with sewage sludge. A bachelor science thesis, Department of Geography, university of Tartu.

Khalid, A., Arshad, M., Anjum, M., Mahmood, T., Dowson, L. (2011). The anaerobic digestion of solid organic waste. Waste Manage. 31:1737-1744.

Khalid, A., Arshad, M., Anjum, M., Mahmood, T., Dowson, L. (2011). The anaerobic digestion of solid organic waste. Waste Manage. 31:1740-1744.

Poliafico, M. (2007): Anaerobic digestion: decision support software. Master's thesis, department of civil, structural and environmental engineering. Cork institute of technology, Cork Ireland.

Standard Method for the Examination of Water and Wastewater, 20th Edition (jointly published by American Public Health Association (APHA), American water works Association (AWWA) and water Environment Federation (WEF): (2012).

The World Bank (2016). World Bank Sustainable Energy for All (SE4ALL) database from the Global Tracking Framework led jointly by the World Bank, International Energy Agency and the Energy Sector Management Assistance Program.

Volunteers in Technical Assistance (VITA) (1980). 3 – Cubic Metre Biogas Plant. A const. Manual VITA.

Yadvika, S., Sreekrishnan, T.R., Kohi, S. and Rana, V. (2004). Enhancement of biogas production from solid substrate using different techniques – a review – Bioresource Technol. 95 (1): 1-10.

311: Spring MVC based power new energy basic date management and analysis system

Shuai HUANG [1], Li ZHU[2], Yuanxin LE[3]

1 Hubei Key Laboratory for High-efficiency Utilization of Solar Energy and Operation Control of Energy Storage System, Hubei University of Technology, Wuhan, 430068, P. R. China, 1428329744@qq.com
2 Hubei Key Laboratory for High-efficiency Utilization of Solar Energy and Operation Control of Energy Storage System, Hubei University of Technology, Wuhan, 430068, P. R. China, julianabiding@126.com
3 Hubei Key Laboratory for High-efficiency Utilization of Solar Energy and Operation Control of Energy Storage System, Hubei University of Technology, Wuhan, 430068, P. R. China, 1853664183@qq.com

With the energy shortage in the world, people's consciousness of low carbon, environmental protection and energy saving has been raised gradually, and the exploration of human beings is slowly turning to new energy, especially renewable energy. New energy is renewable energy based on current new technologies, such as solar energy, wind energy and so on. These sources of energy were already being used by our ancestors, but the way they were converted into secondary energy and then reused was something that had never been done before. Therefore, the new energy in this paper is not only renewable energy, but also energy based on new technology. The research object of this paper is wind farm and photovoltaic power station which convert wind energy and light energy into electric energy. The system platform developed in this paper provides statistics and analysis of the power data of the fan in each wind farm or the photovoltaic panel in the photovoltaic station. This paper is a new energy basic data display and analysis system based on Spring MVC framework of B / S architecture, and uses Oracle database technology to manage a large number of new energy data. In this paper, the requirements of the system are analysed and designed in detail. The functions of the system are basic information, data statistics, advanced application and system management module. The system has a good operating interface, easy for users to input, query, modify, delete, import, guide, analysis and so on.

Keywords: new energy; electric energy; statistical chart; analysis; Spring MVC

1. INTRODUCTION

In the field of energy transmission, every country has made great efforts to strengthen the optimal allocation of resources, improve the interaction and cooperation ability of energy transportation system, in order to ensure the safe transmission of energy. Large capacity transmission technology such as UHV, safe and stable operation technology of large power grid, grid connection technology of renewable energy generation and smart grid technology are the core contents of the technological revolution in the field of energy transmission. In the field of energy consumption, various countries are constantly improving the efficiency of energy use, mainly in the field of transportation to achieve the replacement of oil. And high-efficiency energy-saving technology, the new energy vehicle technology represented by electric vehicles, has a broad market prospect. In the future, a new round of energy technology revolution will be a technological innovation as the guide, electric power as the centre, energy system intelligence as the direction, to optimise the energy structure, improve the efficiency of energy sources, promote energy saving and consumption reduction, and share social resources. To achieve sustainable development as the goal of the depth of change. Overall, the development of new energy and smart grid will become an important driving force of the new energy technology revolution.

As the main technology of power technology, smart grid is characterised by automation, information and interaction. Automation refers to the automation level of power network production, operation, dispatch and management, which depends on the advanced automatic control strategy. Informatization refers to the high integration, sharing and utilization of real-time and non-real-time information, which is supported by the communication information platform and the fusion of information flow and power flow and traffic flow. Interaction refers to the realization of two-way information communication between power grid and power supply, power facilities and power users, which can adjust adaptively to achieve the best state of system operation. With the rapid development of computer technology and computer network technology, various power system software came into being. With the continuous improvement of software development and power system automation, the technical level of power software is constantly updated and improved.

At present, at home and abroad, there are many software for power data analysis, which are different according to the functional focus of the user industry, calculation methods, model interface, are not the same, And the traditional power generation technology data analysis platform is mainly studied, but the integration of emerging energy data is still insufficient.

With the development of power system more and more complex and powerful, accurate calculation and analysis has great guiding significance for power network operation management. At present, the power system has a large scale and rapid development, its calculation data covers a wide range, the total amount of data is large, and changes quickly, so the data collection and maintenance are required. However, there are many problems in management and maintenance, such as: the data source is not clear, the reliability of data uniqueness is poor, the existing power network parameters can not directly generate the calculation data file, the data file needs to be made manually, and the efficiency is low. When the electric power workers screen and produce the data, they lack the support of the application platform and have a lot of workload. These problems have a serious impact on the quality and effectiveness of power system calculation and analysis data.

Based on this background, this management and analysis platform, which is specially customised for the new power energy data, is developed. The power workers can import the data into the system according to the unified template, and the system will automatically aggregate and calculate according to the algorithm. Get the results that users want and make it easy for all users to share data and export reports. The platform has strong practicality and reliability, and has very strong popularization significance.

1.1. Research contents

According to all the wind farms and photovoltaic power stations in the country, we can access the data in the basic data management and analysis system of power new energy at any time in different regions, so that we can share the data. The data is mainly imported into the management and maintenance by the people with the right of data maintenance in the region, and then the data can be analysed and managed by the people in the range of the data.

Through the information collected from wind farms and photovoltaic power stations in various regions about the basic information and generating power of various fans and photovoltaic panels, they are regularly uploaded to the system. The system classifies according to assigned regional data dictionaries. Row data summary, displayed in the form of pie chart, streamline chart, etc., so that users can clearly see the power generation situation of each power plant, and can also make the summary chart according to the needs of the users, according to the area or date, Category and other categories of summary analysis charts export excel charts, so that users can easily get summary reports.

2 INTRODUCTION TO SYSTEM DEVELOPMENT TOOLS

2.2. Introduction to Java language

Java is a widely used object-oriented development language. Originated in 1991, Sun Microsystems' Jame Gosling, Bill Joe and others developed a software called Oak for interactive operation on consumer electronics such as television, oven, etc. Because the CPU used on these appliances are diverse, and C languages can only compile specific platforms, so to solve this problem, portable, Platform independent programming language, Java came into being (Lu).

The World Wide Web has become one of the most popular programming languages. On the other hand, Java has also promoted the development of the World Wide Web. Java itself some characteristics are inseparable, mainly have the following several characteristics (Moran).

1. Portability: through portability, programmers do not have to worry about different platforms, can concentrate on development system.

2. Object-Oriented: Java is a complete object-oriented programming language that inherits most of the features of C and C but is more concise and reliable.

3. Multithreading: can take advantage of multiple processors to bring better interactivity and real-time, making Java suitable for server development.

4. Robustness: Java removed pointers, increased memory protection, is a strong type of language.

5. Distributed: Java provides class libraries to support network programming, uses class libraries to handle TCP / IP protocols, and provides a mechanism for communication between distributed objects (Moran).

The birth of Java has historical significance, is the product of the times progress, not only promoted the development of the World Wide Web, but also subverted the software industry. It can be used on many platforms, which makes Java portability very strong, can be developed and used on any platform, and has the requirements of reusability, scalability, plug and play and other distributed computing patterns. It has a profound impact on both software industry and industry. Software has changed from development-centreed to service-centric. Enterprises should see business opportunities in e-commerce and reshape themselves (Zhang).

2.3. Spring MVC development framework

Spring MVC is a development framework, based on Web applications lightweight development framework. Spring MVC uses the idea of MVC (Model View Controller) architecture pattern to decouple the responsibilities of the web layer. The same is also based on the request-driven, that is, using the request-response model (Yang).

Spring MVC develops the Web layer with the following characteristics: support restful style, static resource, flexible URL mapping to page controller, flexible localization, principal parsing, etc. Naturally integrated with the Spring framework; very easy to integrate with other graphical technologies, such as Velocity, Fire Marker, etc.; provides strong contract programming support for conventions greater than configuration; provides strong data validation, Formatting and data binding mechanisms; simple Web-tier unit testing; very flexible data validation, formatting and data binding mechanisms; simple handling of exceptions (Zhao).

Spring Web MVC framework is a request-driven Web framework. It also uses the front-end controller pattern to design and distribute to the corresponding page controller (action / processor) according to the request mapping rules (Bi).

The specific execution steps are as follows:

1. First, the user sends the request-> the front-end controller, According to the request information (such as URL), the front-end controller decides which page controller should be selected for processing and delegates the request to it, that is, the control logic part of the previous controller.Steps 1, 2 in figure 1;

2, After the page controller receives the request, carries on the function processing, first needs to collect and bind the request parameter to an object, this object in Spring Web MVC calls the command object, and carries on the verification, Then the command delegates the image to the business object; after processing, it returns a Model And View (model data and logical view name).3, 4, 5 steps in the figure;

3,The front-end controller recovers control, then selects the corresponding view to render according to the returned logical view name, and passes in the model data for view rendering. 6, 7 steps in the figure;

4, the front-end controller takes back control again and returns the response to the user,8 steps in the figure; this is the end of the whole.

As shown in the following figure：

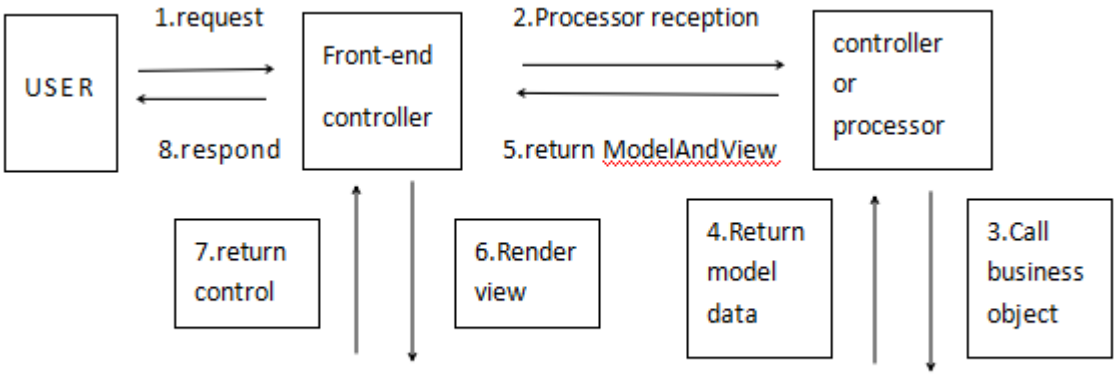

Figure 1: Spring MVC framework for processing the request flow chart

2.4. Construction of spring MVC development environment

This paper takes Windows platform as an example to build Spring MVC development environment, build JDK 1.6 + Spring 3 development environment and background database system Oracle environment. The build process is described as follows:

1. Install JDK 1.6 at the following download address:

http://download.oracle.com/otn/java/jdk/6u25-b06/jdk-6u25-windows-x64.exe

2. Install directly after download. After installation, configure the environment variables as follows:

JAVA_HOME

C:\Program Files\Java\jdk1.6.0_25

Path

%JAVA_HOME%\bin;%JAVA_HOME%\lib\dt.jar;%JAVA_HOME%\lib\tools.jar;

3. View the installation results. Windows environment, use the command cmd to enter the command window, and then enter the command: java -version return.

4. Install Oracle. The download address is ： http://www.oracle.com/technetwork/database/enterprise-edition/downloads/112010-win32soft-098987.html

5. Create a database. Use PLSql software to manage, create a new table space as TBSSTENERGY, use the name of the energy, password 123

6. Jar packages needed to introduce Spring MVC

7. Write the key code in the Spring MVC configuration file, applicationContext.xml.

3. SYSTEM ANALYSIS

3.1. Feasibility analysis

The following is a study on the feasibility of the Spring MVC based power new energy basic data management and analysis system, in order to better manage and display and analyse the power data, It is an important and meaningful practice to analyse wind farm data in a more convenient way, to check every index of wind farm at a glance, and to realise the application value according to the theoretical basis.

The following three aspects are analysed:

1. Economic feasibility: the development of the system can greatly reduce the integration of electric field data in the power sector, and upload all the data to the system in a certain format. Can be visually displayed on the interface, At the same time, support for exporting data, data management, view and share provides a great convenience, staff do not use excel or other software for complex power data analysis and calculation, The system provides the corresponding algorithm.

2. Technical feasibility: this paper uses Spring MVC development framework, is a very easy to use lightweight development frame, the technology is very mature, has been widely used; the database uses Oracle technology used by large enterprises to guarantee a large amount of information management. Oracle database is the world's leading data system.

3. Operational feasibility: because the system is B / S structure, the interface design is simple and easy to use, do not need to install software on the client, make the operation friendlier.

3.2. User type analysis

Because the statistical management of the new energy data of electric power is still in the traditional manual survey method, the amount of data is huge and the classification is various. If you want to see all the data information, it is very difficult, so there is a demand for such a digital display platform which is of great significance to the analysis of basic data for new energy sources. System administrators can upload and manage all data, assign users, have permission to upload local electric field data, view the underlying data and final statistics, download the corresponding reports and create subusers. The administrator has all authority, data dictionary and system operation log function and can change all electric field information at will. The common users have the same permission to upload local electric field data, they can view the basic data and the final statistical results, and download the corresponding reports, but they do not have the function of deleting electric field data and creating subusers. Because the system, mainly a demonstration and analysis of the new energy data of electric power, does not have a manipulation function, it is only a process of making the data clear and clear so there is no division of the types of users. Are query users at the same level?

3.3. Functional requirements analysis

1. User management - For user rights, specific permissions include viewing, modifying, deleting, creating users by administrators, users can upload local electric field information, view all electric field information and power generation summary table, also can download summary report, do not have delete modification function. This function can only be accessed by logging in as a user with set permissions.

2. Electric field database management - Users with administrator rights can delete electric field data uniformly on this page, and other function modules of the system do not provide data deletion function. Non-administrator user rights users, can not operate delete function, and can only view their own uploaded electric field data information.

3. Data dictionary - Preserve the hierarchical relationships between regions and provinces in the system, as well as specific constants in the system. Provide add, delete, change function

4. Data input - Can be collated through the standard template wind farm, photovoltaic power station data upload to the database.

5. Personalisation parameter setting - The user sets the parameters of the system according to their own requirements, including password modification and so on.

6. System operation log - Record system update log, including software and hardware update, database operation (import, export) and so on.

7. Wind farm basic data - The basic information of the wind farm can be displayed in the form of a table; the selected wind farm information can be screened by the conditions (the screening conditions include the dispatching side / station side, the province of the network, the city in which the wind farm is located, the owner); You can edit the data.

8. Time series data of wind farm - The historical actual power data of wind farm are displayed in the form of graph and text; there are two ways to query: (1) after screening condition query and display specific wind farm (selection conditions include dispatching side / station side, network province, Located in the city, owner); (2) through the name of the wind farm query and display.

9. Basic data of photovoltaic power station - The basic information of wind farm can be displayed in the form of tables; the selected wind farm information can be selected through conditional screening (screening conditions include dispatching side / station side, network province, local city, owner); the data can be edited.

10. Time series data of photovoltaic power station - Displaying historical actual power data of wind farms in the form of graphics and words; there are two ways to query: (1) after having passed the screening conditions and displaying specific wind farms (the selection conditions include the dispatching side / station side, the network province, the prefecture and the city, the selection conditions include the dispatching side / station side, the province of the network, and the local city, Owner); (2) through the name of the wind farm query and display.

11. Basic information statistics = The forecast total capacity of wind power is displayed in the form of tables, and the total capacity of wind power forecast in each network province is shown separately at the dispatching end and the station end, and through the screening conditions (dispatching side / station side, network province, prefecture, city, etc.), Owner), in the form of graph (pie chart or bar chart) plus table to show the number of wind farms that meet the screening conditions, and predict the capacity.

12. Mutual comparison of wind farm output - All wind farms in the region, multiple wind farms on any date of the output comparison, in the form of a table display comparison results (the specific comparison indicators are power maximum, minimum, maximum change rate, minimum change rate, daily cumulative maximum electricity generation, Minimum daily cumulative generating capacity).

13. Power error statistics - A column chart showing the mean root mean square error (RMS) of all wind farms / photovoltaic plants in the provinces at a certain time (optional, default is last month); The mean value of root mean square error of each wind farm in a certain period of time in the province is shown in the form of a bar chart, and the detailed statistical value of prediction accuracy of a particular area and a particular wind farm is displayed in the form of a table through selection.

14. Advanced application - According to the screening conditions, the target electric field is displayed. The screening conditions include wind farm / photovoltaic power station, dispatching side / station side, network province, location, owner, grid connection time, modeling time, data length, data time (to be added); Click on the results of the query and the page displays the details of the electric field.

4. DATABASE REQUIREMENT ANALYSIS

Database design, in addition to some necessary object creation, also takes into account forward-looking design based on the actual situation and possible changes of the system throughout the life cycle of the system, to meet the needs of all aspects of the life cycle of the system.

The database is the core part of constructing the comprehensive display and analysis platform of the new energy basic data. According to the characteristics of the new energy basic data type is complex, the data amount is huge, the database design and deployment should consider the high availability factor. Fast response to high concurrent requests, high availability of servers with high concurrent requests, and requirements for different levels of user access security. In order to meet these requirements, the database system uses the Oracle database kernel to adopt multithreading, multi-process architecture, supports the massive data storage management, the system is safe and reliable and the business request of quick response.

In the design of database object based on massive data, the efficiency of database is the most important problem. Different database optimisation methods, such as index, database partition and so on, are adopted for different quantity of data.

5. SYSTEM MANAGEMENT MODULE

The system management module mainly realises electric field data management, data dictionary, data import, user management, personalisation parameter setting and system operation log function module as shown in Figure 2 below.

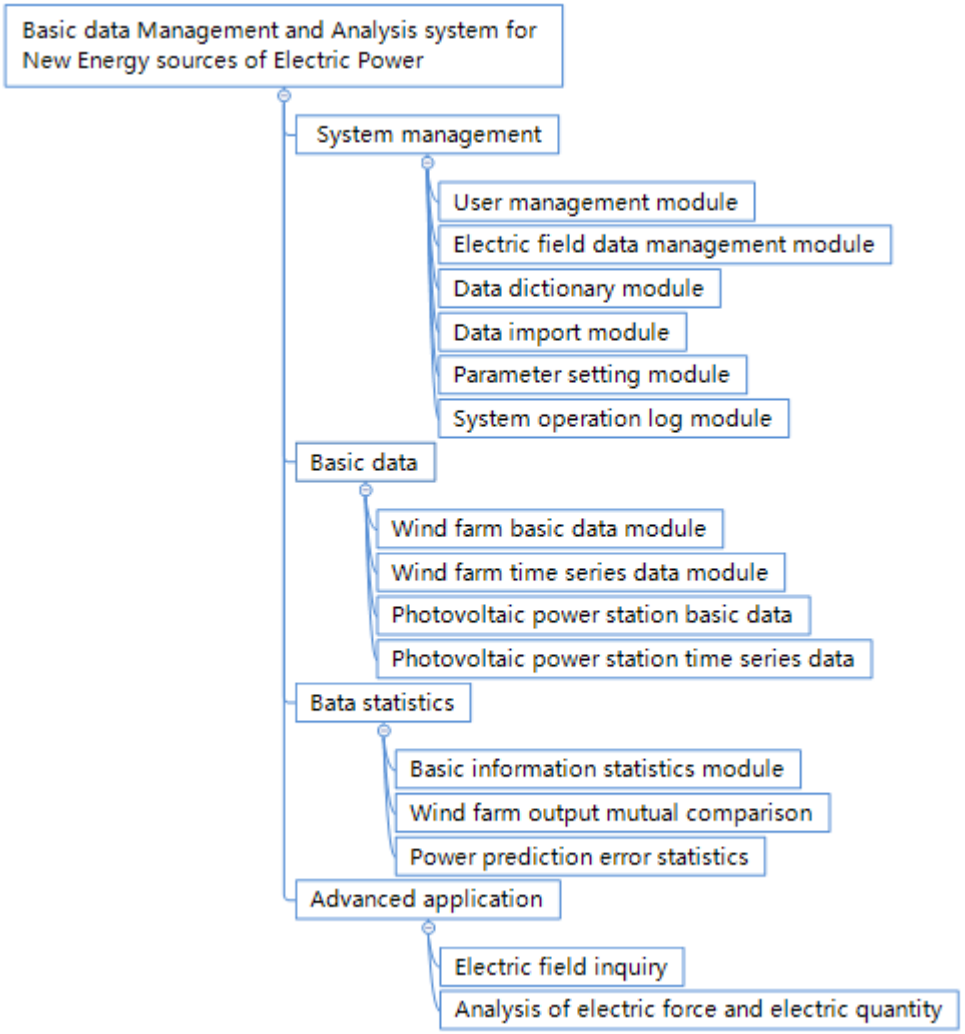

Figure 2: The system function module structured chart

5.1. User management module

User management only administrators have permission to use, mainly to add users, passwords and other basic information. In addition, according to the user name can be conditional combination, retrieval of user information. You can also edit and delete users.

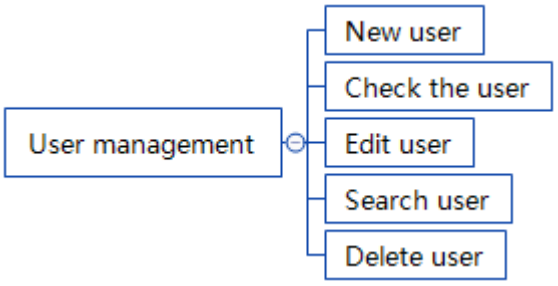

Figure 3: User management module structured chart

5.2. Electric field data management module

Because each electric field has a lot of data, so set up the electric field data management module, the administrator user can delete the data of each electric field in batches under this page. When deleted, all data related to the wind farm in the system are deleted. Users can also add and modify electric field information and search and view electric field information.

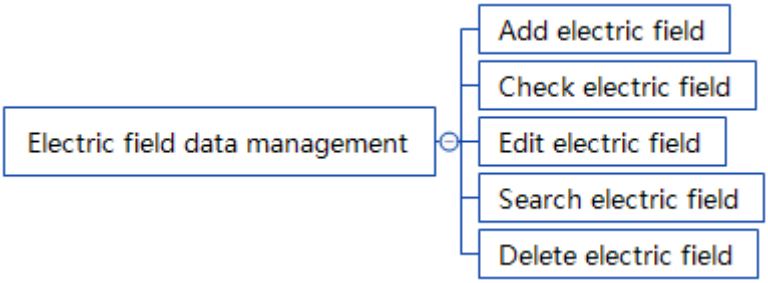

Figure 4: The electric field data management module structured chart

5.3. Data dictionary module

The data dictionary module manages the constants in the system, including the addition, deletion, modification of the code type and the addition, deletion and modification of the code value.

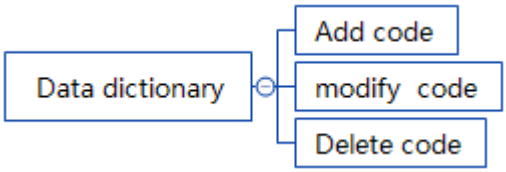

Figure 5: Data dictionary module structured chart

5.4. Data import module

The data import module provides the interface for the electric field data input, the user can upload the electric field single data file, also can upload the compressed package, this compressed package contains all the item data files of the electric field, The file format of the data and the file content format system provide the template. The user can successfully import the electric field data into the system database according to the template format. The system provides the function of automatically emptying the server cache for uploading files. To ensure that the server users upload files do not pile up, when the server operation exception, users can also manually empty.

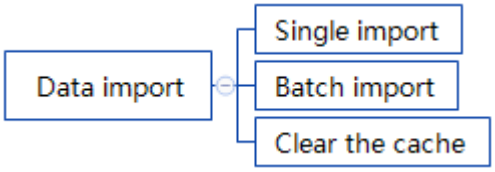

Figure 6: Data import module structured chart

5.5. Parameter setting module

The personalisation parameter setting module provides the user to modify his login password and login user name.

5.6. System operation log module

The system operation log module provides administrator users with the ability to view and delete user action logs in the system.

5.7. Basic date module

The basic data module provides the basic data of wind farm, the timing data of wind farm, the basic data of photovoltaic power station and the time sequence information of photovoltaic power station.

5.8. Wind farm basic data module

The basic information module of wind farm includes basic information of wind farm and query function of detailed information of wind farm. Users can search and analyse the names of wind farms through their own network province, city and electric field.

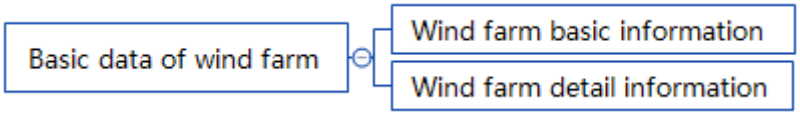

Figure 7: Wind farms basic data module structured chart

5.9. Wind farm time series data module

The time series data module of wind farm includes the query and analysis of actual power data and predicted power data.

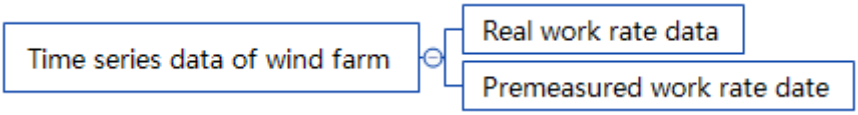

Figure 8: Wind farm time-series data module structured chart

5.10. Photovoltaic power station basic data and time series data

The basic information module of photovoltaic power station includes basic information of photovoltaic power station and detailed information query function of photovoltaic power station. The user can inquire and analyse the name of the photovoltaic power plant through the grid province, the city and the electric field name.

The time series data module of Photovoltaic power station includes the query and analysis of actual power data and predicted power data.

5.11. Data statistics module

The data statistics module realises the graphical statistics and report statistical analysis of electric field data in the system, which is convenient for users to look up and analyse, including statistics of basic information, mutual comparison of wind farm output and error statistics of power prediction.

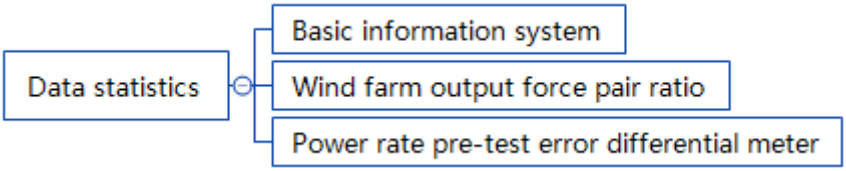

Figure 9: Data statistics of the sub-module structured chart

5.12. Basic information statistics module

The basic information statistics module includes wind power forecasting capacity statistics, fan statistics, photovoltaic prediction capacity statistics and photovoltaic panel statistics sub-modules. In the statistical function of wind power forecasting capacity, the statistics of wind farm forecasting capacity is carried out according to all regions and provinces of the country, and the statistics function of fan is based on the basic information of wind turbine manufacturers. In the statistical function of photovoltaic prediction capacity, according to all regions and provinces of the country, the forecast capacity of photovoltaic power station is reported and counted. The statistical function of photovoltaic panel is to report the basic information of photovoltaic panel according to the cell manufacturer.

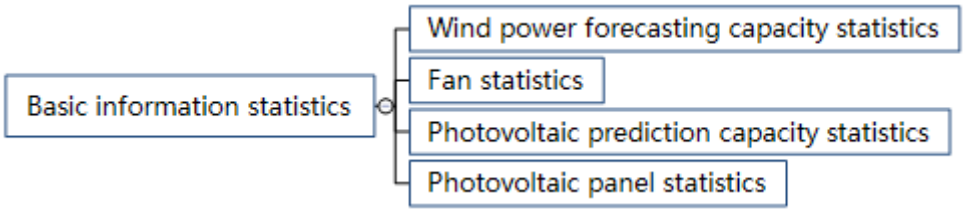

Figure 10: Basic statistical information module structured chart

5.13. Wind farm output comparison

Wind farm output comparison modules include daily, monthly, year-to-year and custom wind power. Under this function, several wind farms can be selected by day, month by month, year by year and custom analysis according to their network province, city and electric field name. The comparative items include the name of wind farm, installed capacity, maximum power, minimum power, average power, accumulative electricity quantity, maximum change rate, peak and valley difference, power variance and equivalent utilization hours.

5.14. Power prediction error statistics

The power error statistics module includes prediction error time interval analysis, prediction error time-by-time analysis and prediction error analysis month by month. Under this function, several wind farms can be selected according to their network province, city and electric field name to calculate and analyse the prediction error. The average absolute error, root mean square error, correlation system and the proportion of error less than 20% of the electric field are calculated. The prediction error analysis shows the root mean square error of the selected electric field in the form of a histogram.

5.15. Advanced application

Advanced applications include target electric field query and power quantity analysis submodule. The target electric field query is a whole local electric field checking function, the input key word can carry on the electric field global fuzzy search. Electric power analysis module is based on the selection of network province, city, electric field name, find the electric field on the day of generation of detailed information.

6. CONCLUSION

This paper mainly introduces the design and implementation of the basic data management and analysis system for power new energy in detail, and makes the development of the system with Spring MVC framework. This paper takes the system development as the main line, introduces the Java language in turn, Spring MVC framework some basic points and the technology. The foreground is mainly developed with javascript technology and jQuery plug-in is used to realise the front interface.

The main contents of this paper are as follows:

1. Research Java Web project related development and application technology, including Java script syntax, Spring MVC architecture, the use of jQuery plug-in, And Oracle database technology.

2. Based on the requirement analysis of the system function, the design of the system function module and database is carried out.

7. ACKNOWLEDGEMENTS

This research was supported by National Natural Science Foundation of China (61471162, 61501178, 61571182, 11605051, 41601399, 61601177); Program of International science and technology cooperation (2015DFA10940); Science and technology support program (R & D) project of Hubei Province (2015BAA115); PhD Research Startup Foundation of Hubei University of Technology (BSQD13029, BSQD13032, BSQD14028, BSQD14033); Open Foundation of Hubei Collaborative Innovation Center for High-Efficiency Utilization of Solar Energy (HBSKFZD2015005, HBSKFTD2016002).

8. REFERENCES

Bi Y. Research on key Technologies of Communication Middleware for Smart Grid [D]. Shandong University.

Lu X. Design and implementation of client of Power supply Network Analysis platform [D]. Xi'an University of Science and Technology.

Moran. Development and Application of Intelligent Storage and Analysis platform for important data of TD-SCDMA Core Network [A]. China Association of Science and Technology, Tianjin Municipal people's Government. The 13th Annual meeting of China Association of Science and Technology-Proceedings of the China Wisdom cities Forum [C]. China Association of Science and Technology, Tianjin Municipal people's Government.

Yang Z. Research on Smart Grid data processing and Application [D]. Hunan University.

Zhang H. Research on data Storage in Large-Scale Smart Grid [D]. Liaoning University.

Zhao H. Design and implementation of data acquisition platform for power network service [D]. University of Electronic Science and Technology.

315: Influence of Lignin model compound on cellulase hydrolysis of Avicel

Congxin CHEN[1], Lan YAO[1], Long XIONG[1], Jianshen FU[2], Haitao YANG[1]*,

1. Hubei University of Technology ,School of Material & Chemical Engineering, Wuhan 430068, 508087268@qq.com
2. Guangxi Chesir Pearl Material Co. Ltd

Lignin is the second most abundant biopolymer on earth, and a kind of renewable resource in nature. It plays important roles in biofuel production, as it could form non-productive adsorption with cellulase. Due to the structural complexity of lignin, limited result was obtained so far. The dehydrogenation polymer (DHP) was usually used to study the features of lignin, whose structure was simpler than that of lignin. In this study, new method was employed to synthesise coniferin. The yield based on the starting reactant was 51.44%, which was 19.67% higher than the traditional method. Furthermore, Guaiacyl-type lignin polymer models (DHP) were prepared from coniferin by Zutropfverfahren (ZT) and Zulaufverfahren (ZL) with ß-glucosidase, peroxidase and glucose oxidase. The DHPs were characterised by GPC, FT-IR, and HSQC. The molecular weights of ZT and ZL DHP were 2032 and 2332 g/mol. FT-IR analysis and Semi-quantitative analysis by 2D HSQC NMR indicated that typical lignin structures such as β-5, β-O-4 and β-β existed in DHP and ZT DHP had higher content of β-β and C-H than ZL DHP. Finally, the DHP were added to Avicel to determine its effect on glucose release. The results showed that in the presence of ZT and ZL DHP, the cellulose conversion of avicel are 26.35% and 29.32% when the cellulase loading was 50 FPU/g cellulose, while the cellulose conversion of avicel is 37.16% without DHP. It is found that molecular weight and PDI of DHPs were negatively correlated with cellulase hydrolysis of Avicel. And DHP with higher content of β-β and C-H had great effect on cellulase hydrolysis of Avicel. The results could broaden horizon of lignin-cellulase complex and decrease the cost of biofuel production accordingly.

Keywords: lignin, coniferin, dehydrogenation polymer, enzymatic hydrolysis, avicel

1. INTRODUCTION

Lignin is one of the main components of the plant cell wall. Its structural composition is complex. It is important to plant as it involves in mechanical support, transportation of water ,resistance to bacterial invasion and other important biological function (Guo et al., 2001; Taherzadeh and Karimi, 2008; Weng and Chapple, 2010).There are three precursors of lignin: coniferyl alcohol, sinapyl alcohol and p-coumaryl alcohol (Guo et al., 2014). These three precursors were polymerised to form guaiacum, syringa and P-hydroxyl phenyl lignin monomers, respectively ,which were composed of C-C bonds (β-β, β-5,β-4,5-5) and C-O bonds (including β-O-4, 4-O-5, α-O-4) and other disorderly combinatorial linkages to form a complex macromolecular lignin (Frits, 2009).

In bioethanol production process, lignin has an inhibitory effect on cellulase digestion, which greatly reduces the conversion of cellulose to glucose (Berlin et al., 2006; Nakagame et al., 2011; Lu et al., 2016). Ko et al. found that 50–60% activities of cellobiohydrolase and endoglucanase from Tri-choderma reesei were retained after incubation with lignin isolated from liquid hot water pretreated hard wood chips (Ko et al., 2015). Qin found that when exposed to lignin-derived phenols, cellulase inhibition occurs immediately and causes a steady loss of enzyme activity as the length of exposure to phenols increases (Ximenes et al., 2011; Qin et al., 2016). Q Chengrong used atomic force microscopy to examine the binding force between cellulase enzymes and cellulose and the lignin hydrophobic group (-OH, -COOH), finding that the binding force of cellulase to the hydrophobic end groups of lignin was on average 43% higher than that of cellulose (Qin et al., 2014). However, Wu found that the lignin obtained by pretreating bamboo with ethanol promoted the hydrolysis of cellulose (Wu et al., 2016). A large number of studies have been conducted to investigate the effect of lignin on cellulase, but due to the complex structure of lignin, the mechanism of the effect of lignin on cellulase has not been explained in full detail.

The lignin dehydrogenation polymer (DHP) was a good model for studying the structure and reaction properties of natural lignin in plants (Brunow, 1995; Ralph et al., 2004; Ralph et al., 2010). In 1939 K.Freundenberg (Freudenberg, 1939) synthesised dehydrogenated polymers by coniferyl alcohol and laccase in the presence of oxygen. The results revealed that the structure was similar to that of spruce milled wood lignin. Later, the peroxidase/H_2O_2 system was introduced. However, the water-solubility of coniferyl alcohol was relatively poor, which was contrary to its transportation in plants as a raw material. Therefore, In 1955 K.Freundenberg proposes the synthesis of a lignin dehydrogenation polymer using monolignol glucoside as precursor. When radioactive coniferin was administered to those growing trees, lignin became radioactive too. N. Terashima conducted the biopolymerization of lignin dehydrogenation polymers in a peroxidase/H_2O_2 system using coniferyl alcohol and coniferin as precursors by the ZT method. The results showed that the structure of these polylignols from coniferin were more closely to that of native lignin than polylignols prepared by the conventional method from coniferyl alcohol (Terashima, 1996). Various p-glucocoumaryl alcohol, coniferin and syringing specifically labeled with 3H, 14C, or enriched with 13C have been fed to a variety of plants including ginkgo, pine, spruce, magnolia, lilac, poplar, oleander, wheat, etc., and the lignin formation process and structure of the labeled lignins were examined by nondestructive methods including double labeling techniques, microautoradiography, and difference NMR spectroscopy focusing on differences between 13C-enriched and unenriched specimens in solid and in solution state. The structure of the labeled lignin showed the same characteristic features as the untreated lignin (Fukushima and Terashima, 1990; Xie and Terashima, 1994; Eglinton et al., 2000; Terashima et al., 2009; Yao et al., 2016).

In this paper, the lignin precursor coniferin was synthesised, and then DHPs were prepared from coniferin by the action of ß-glucosidase and peroxidase, with hydrogen peroxide generated in situ through the action of oxygen and glucose oxidase on the glucose liberated from the coniferin by *ZT* and *ZL* method. The structure of DHP was characterised by FT-IR, GPC and NMR. Finally, the influence of DHP on the cellulase hydrolysis of Avicel was studied to explain the mechanism of lignin inhibitory effects on enzymatic hydrolysis.

2. MATERIALS AND METHODS

2.1. Materials

Cellulase, β-glucosidase, glucose oxidase and peroxidase were purchased from Sigma Corporation; diisobutyl aluminum hydride and diethyl malonate were purchased from Aladdin Biochemical Technology Co., Ltd.; vanillin, bromine , Glucose, acetic acid, sodium acetate, anhydrous ethanol, toluene, pyridine, dichloroethane and ethyl ether were obtained from Sinopharm Group Chemical Reagent Co., Ltd.

2.2. Synthesis of Coniferin

The synthetic way of coniferin was shown in Figure 1. Vanillin and brominated tetra-O-acetyl-α-D glucose underwent substitution reaction to obtain tetra-O-acetyl-α-D vanillin glucoside, which was then condensed with monoethyl malonate to get tetra-O-acetyl-β-D-glucosides of ferulic ethyl ester. Last, ferulic ethyl ester was reduced and deacetylated by diisobutyl aluminum hydride to yield coniferin. The yield based on the starting reactant was 51.44%, which was 19.67% higher than the traditional method as shown in Figure 2.

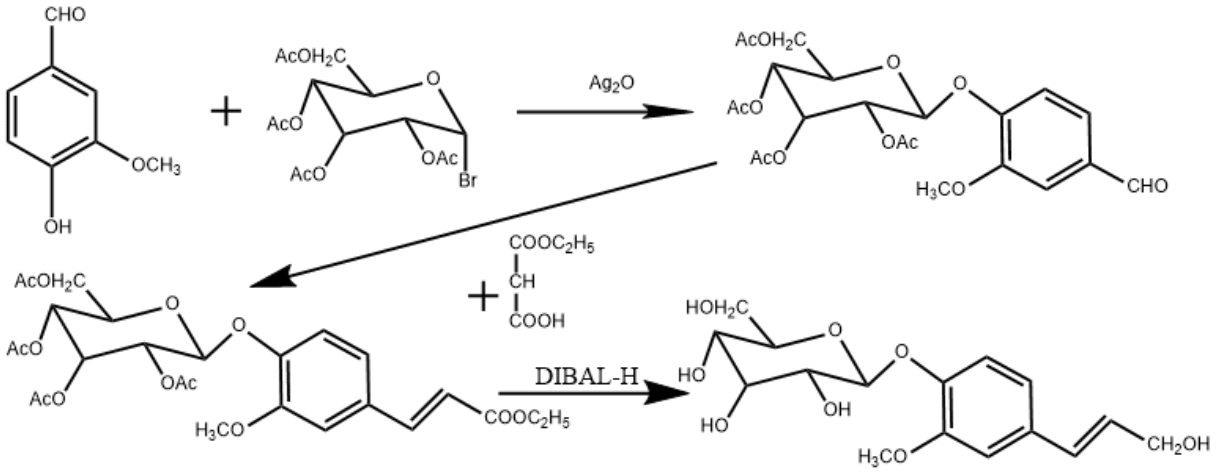

Figure 1: Improved synthetic method for coniferin

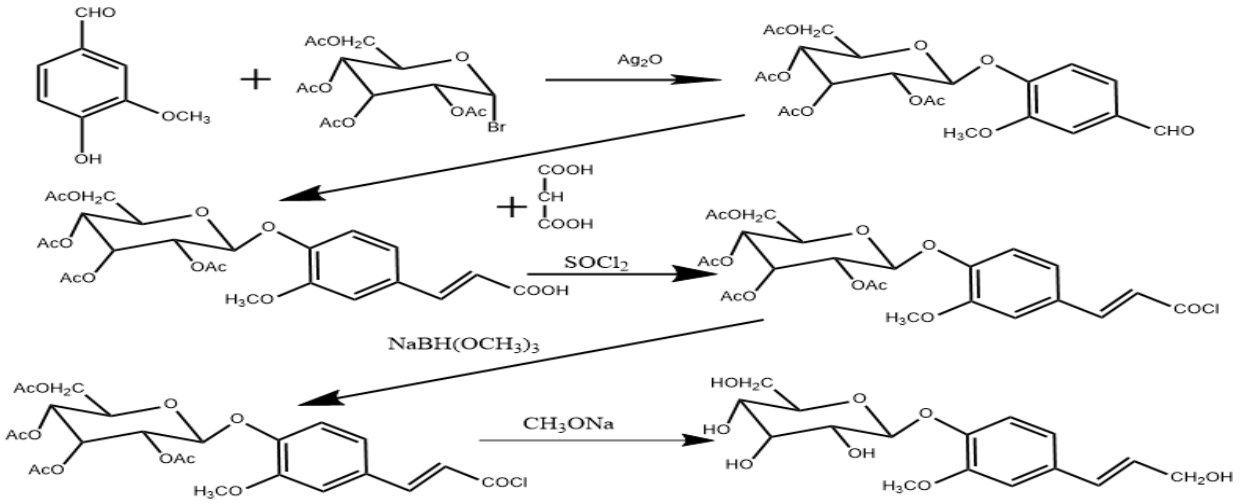

Figure 2: Traditional synthetic method for coniferin

2.3. Preparations of DHPs

End-wise polymerization (ZT DHP)

The coniferin (500mg) was dissolved in 36 ml acetic acid/sodium acetate buffer (0.2M, pH = 4.8).This solution was then pumped over a period of 24h into 14ml buffer solution containing 10.2 mg of β-glucosidase (*from almond, 9.1 U/mg, sigma*), 15.8 mg of glucose oxidase (*Type II: From Aspergilus niger, 19,290 units/g*) and 1mg of peroxidase (*TypeII: from horseradish, 200 units/mg, sigma*). After the addition was completed, 14.47 mg of β-glucosidase, 15.83 mg of glucose oxidase and 1.027 mg of peroxidase were further added to the solution. The reaction temperature was 30°C and the reaction time was 94 hours. During the reaction, clean air filtered by activated carbon was passed through. After the reaction was completed, the mixture was centrifuged to obtain a solid, which was then repeatedly washed with deionised water twice. For further purification, the dried DHP was dissolved minimum quantity of 1,2-dichloroethane-ethanol mixture (2:1, v/v) and precipitated in diethyl ether. The precipitated DHP was recovered by centrifugation, washed 3 times with diethyl ether and dried. 142mg of purification DHP was obtained, the yield was 53.96%.

Bulk polymerization (ZL DHP)

The coniferin (500mg) was dissolved in 36 ml of 0.2 M acetic acid/sodium acetate buffer (pH = 4.8). And 10.2 mg of β-glucosidase (*from almond, 9.1 U/mg, sigma*), 15.83 mg of glucose oxidase (*Type II: From Aspergilus niger, 19,290 units/g*) and 1.027 mg of peroxidase (*TypeII: from horseradish, 200 units/mg, sigma*) were added to the solution. After 9h , 14.47 mg of β-glucosidase, 15.83 mg of glucose oxidase and 1.027 mg of peroxidase were further added to the solution. The reaction temperature was 30°C and the reaction time was 94 hours. During the reaction, clean air filtered by activated

carbon was passed through. The following procedure was the same as mentioned above. 134mg of purification *DHP* was obtained, the yield was 50.92%.

2.4. Influence of DHP on cellulase hydrolysis of Avicel

80mg Avicel and 20mg *DHP* were hydrolyzed at a consistency of 2% (w/v) in acetate buffer (50 mM, pH 4.8) at 50 °C under continuous agitation at 150 rpm for 72 h in a shaking incubator. Hydrolysis of 100 mg Avicel was used as the control. Cellulase loading was 50 filter paper unit (*FPU*) per gram of cellulose. Liquid samples were centrifuged at 10,000 rpm for 10 min, and the supernatant was used for glucose release analysis by HPLC method.

2.5. Analysis procedures

FT-IR determination

The FT-IR spectra were obtained from 4000 to 500 cm $^{-1}$ using a FTIR spectroscopy Thermofisher Nicolet 360. A total of 64 scans at 2 cm^{-1} resolution were signal averaged and stored.

Molecular weight determination

To measure the molecular weights of each lignin fraction, gel permeation chromatography (GPC) analysis was conducted. Prior to the analysis, *DHP* samples were acetylated. In brief, the oven-dried lignin (5 mg) was dissolved a 1:1 (v/v) mixture of acetic anhydride/pyridine mixture (1.00 mL) and stirred at room temperature for 24 h. The mixture was dropped into 10 ml of diethyl ether and centrifuged to get the solid. The molecular weight distributions of the *DHP* acetate were analysed on a Shimadzu LC-20AD HPLC system equipped with Shim-pack GPC-803D column and a UV detector, using THF as the mobile phase (1.0 mL/min) with injection volumes of 25uL Polystyrene standards were used for calibration.

2D-HSQC spectroscopy of DHPs

Dry *DHP* samples (~50 mg) were dissolved in DMSO-d_6(0.4 mL).Two-dimensional (2D) ^{1}H– ^{13}C heteronuclear single quantum coherence (HSQC) NMR experiment was conducted at 298 K using a Bruker AVIII 400-MHz spectroscopy with a 5-mm Broadband Observe probe (5-mm BBO 400 MHz W1 with Z-gradient probe, Bruker). The analysis was conducted with a Bruker standard pulse sequence ('hsqcetgpsi2') and the following parameters: spectral width of 11 ppm in F2 (^{1}H) with 2,048 data points and 190 ppm in F1 (^{13}C) with 256 data points; 96 scans and 1s interscan delay.

3. RESULTS AND DISCUSSION

3.1. FT-IR determination

Figure 3 shows Infrared spectroscopy of *DHPs*. Signal assignment and relative intensities in the FTIR spectra of *DHP*s are shown in Table 1. FT-IR spectra of ZT and ZL samples showed strong absorbance at around 3410 cm^{-1} from –OH stretching, as well as signal at 2920 cm^{-1} of –CH stretching vibration. It was obvious that there were strong signal from aromatic ring at 1600 cm $^{-1}$, 1510 cm^{-1} and 1423 cm^{-1}, indicating that the structure of *ZT* and *ZL DHP* is similar to that of lignin. Furthermore, ZT DHP has higher absorption intensity at each characteristic peak than ZL DHP. It was found that ZT DHP has more obvious absorption intensity than ZL DHP at 2937cm^{-1} of C-H stretch in methyl and methylene groups, 1035.58cm^{-1} of Aromatic C-H in plane deformation G and 862.02cm^{-1} of Aromatic C-H out of plane bending.

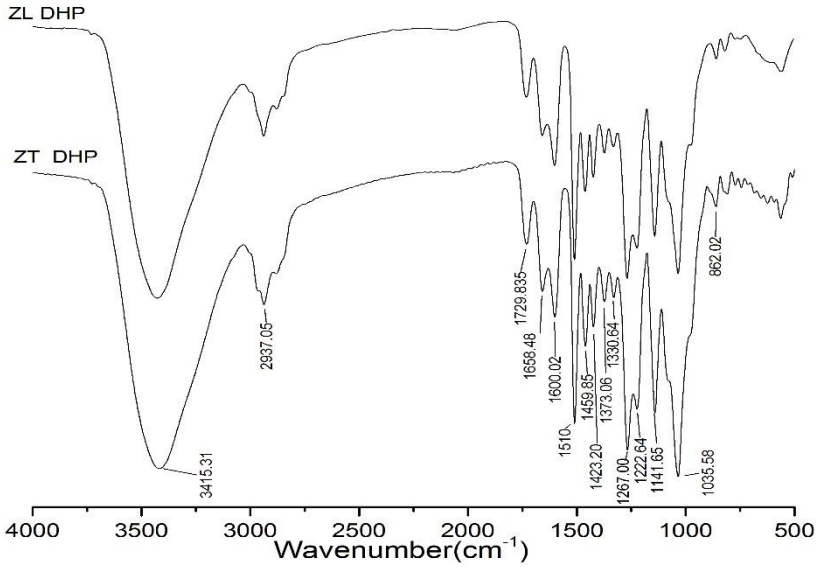

Figure 3: Infrared spectroscopy of ZL DHP and ZT DHP

Table 1: Assignments of FTIR spectrum of, ZT and ZL DHP

Assignments	Wavenumber cm^{-1}	ZT DHP	ZL DHP
O-H stretch	3415.31	1.14	1.15
C-H stretch in methyl and methylene groups	2937.05	0.61	0.51
C=O stretch in unconjugated ketone	1729.83	0.42	0.36
C=O stretch in conjugated ketone	1658.48	0.57	0.51
Aromatic skeletal vibrations plus C=O stretch	1600.62	0.65	0.63
	1510.00	1.00	1.00
C-H deformations	1459.84	0.75	0.73
Aromatic sketetal vibrations	1423.20	0.69	0.67
Aromatic skeletal vibrations O-H stretch	1373.06	0.60	0.58
Aromatic C-O stretching	1267.00	1.08	1.07
C-C plus C-O plus C=O stretch	1222.64	0.95	0.95
Aromatic C-H stretching	1141.65	0.96	0.91
Aromatic C-H in plane deformation G	1035.58	1.17	1.05
Aromatic C-H out of plane bending	862.02	0.30	0.20

The relative intensity was calculated as the ratio of the intensity of the band to the intensity of band at 1510cm^{-1}

3.2. Molecular weight determination

The results of molecular weights and polydispersity of *DHP* samples were shown in Table 2.The *ZT DHP* has lower Mw (2032g/mol) than *ZL DHP* (2332g/mol).The polydispersity index (*PDI*)of *ZL DHP* was relatively low(<1.5),which implies that the distribution of *ZL DHP* was narrow.

Table 2: Weight average, number average molecular weights and polydispersity index of DHP samples.

	Mn	Mw	polydispersity index
ZT DHP	974	2032	2.086
ZL DHP	1692	2332	1.378

3.3. 2D-HSQC determination of *ZT* and *ZL DHP*

Aromatic and aliphatic regions of 2D ^{13}C-^{1}H HSQC spectra for the *DHPs* sample were shown in Figure.4. The NMR spectra showed typical lignin structural features, further confirming that the *DHPs* can be used as lignin model compound.

In the aromatic region of δ_C/δ_H100-135/5.5-8.5, prominent correlation signals for lignin syringyl (S) and guaiacyl (G) units along with *p*-hydroxyphenyl benzoate (PB) substructure could be observed. In Figure 4, only guaiacyl substructure was found, which were from G_2, G_5 and G_6 at δ_C/δ_H111.1/6.93, δ_C/δ_H115.7/6.96 and δ_C/δ_H119.2/6.86, respectively in the ZT and *ZL DHP* NMR spectrum.

The main signals in the aliphatic region of lignin δ_C/δ_H50-90/2.5-6.0 were from $-OCH_3$ (δ_C/δ_H55.7/3.69), β-O-4, β-β and β-5. The signals for β-O-4 substructure were well resolved for C_α/H_α, C_β/H_β, and C_γ/H_γ correlations observed around δ_C/δ_H 71.71/4.76, 84.37/4.31 and 60-64/3.4-4.2. The crosspeak of phenylcoumaran substructure (β-5) from α-position was at δ_C/δ_H87.50/5.50. Along with these interunits, signals from α, β and γ-position of resinols (β-β) can be observed at δ_C/δ_H85.58/4.63,54.17/3.05 and 71.44/4.13.

According to the quantitative analysis results of these DHPs inter-unit linkages from Table 3. It was found that the main substructure in the *ZT DHP* was β-β substructures (45.69%), then β-5(30.68%) and β-O-4(23.63%) substructures, while in the *ZL DHP*,the most relative quantity was β-O-4(39.19%), followed by β-β (31.92%) and β-5(28.89%) subunit. It is clear that *ZT DHP* contains more β-β structures than *ZL DHP*.

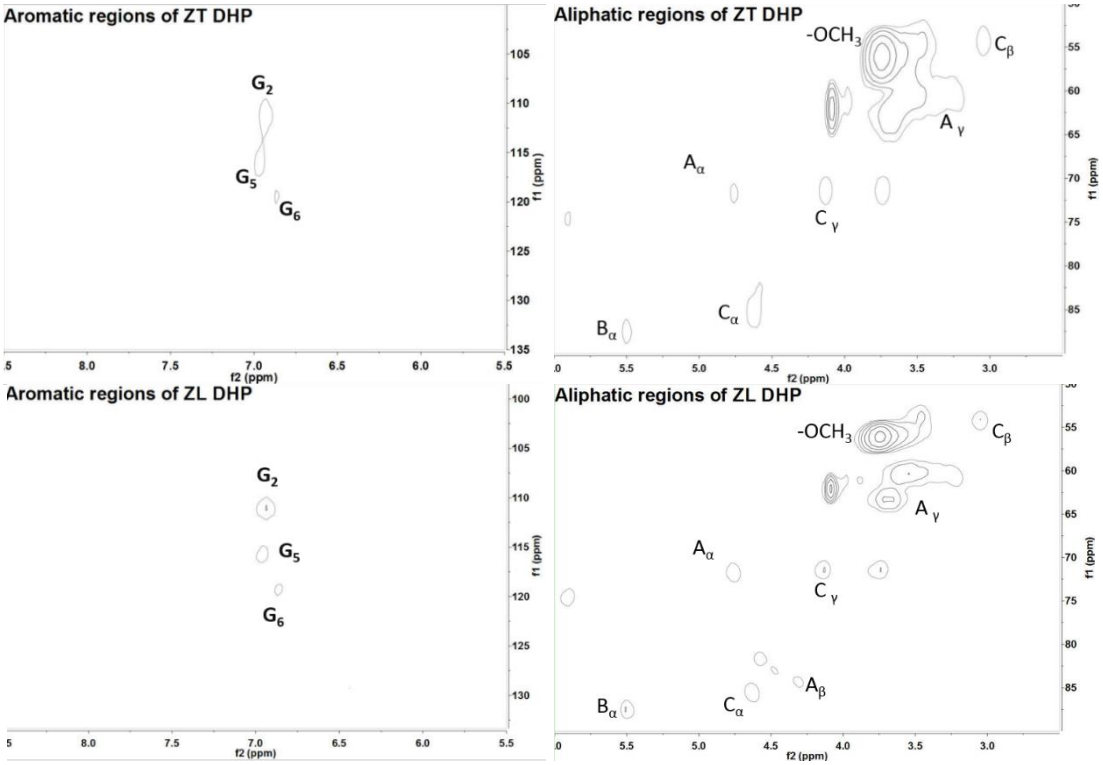

Figure 4: Aromatic (left) and aliphatic (right) region of a ^{13}C-^{1}H HSQC spectrum of ZT and ZL DHP: (A) β-O-4 alkyl-aryl ethers; (B) phenylcoumarane; (C) resinols;

Table 3: Quantitative information of the DHPs in the HSQC spectra.

Lignin substructure	ZT DHP	ZL DHP
β-O-4	23.63%	39.19%
β-5	30.68%	28.89%
β-β	45.69%	31.92%

The amount of specific interunit linkage was expressed as percentage of total side chain.

3.4. Effects of DHP on hydrolysis in enzymatic saccharification of Avicel

To elucidate the roles of *ZT* and *ZL DHP* in the enzymatic digestibility, the effects of *ZT* and *ZL DHP* on enzymatic hydrolysis of Avicel were investigated. The Figure 5 was showed that the addition of *ZT* and *ZL DHP* decreased the 72h glucose yields of Avicel obviously from 37.16% to 26.35% and 29.32%, respectively.

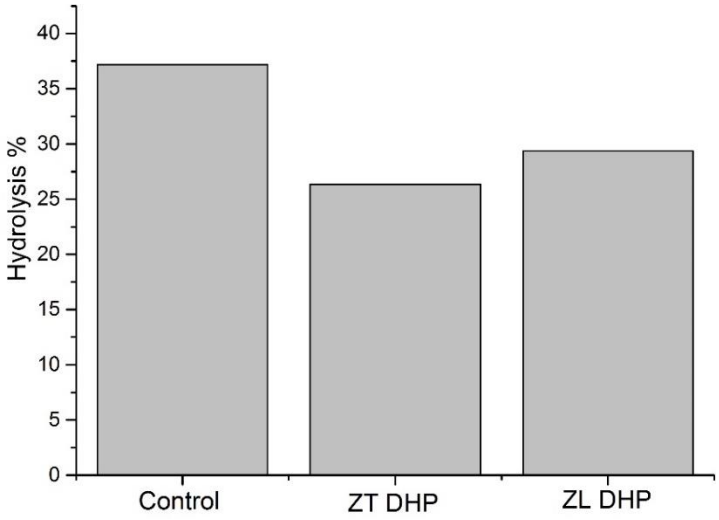

Figure 5: Cellulose conversion of Avicel with or without DHP

It was known that lignin typically is an inhibitor to enzymatic saccharification and can remarkably decrease enzyme efficiency through electrostatic, hydrophobic, hydrogen bonding interactions and non-productive binding, as described previously (Rahikainen et al., 2013; Vermaas et al., 2015; Yang et al., 2017; Yao et al., 2018b).As Lignin with low molecular weight and PDI has a stronger linkage with cellulose endonucleases(Yao et al., 2018a), *ZT DHP* with lower molecular weight and PDI than *ZL DHP* exhibited greater inhibitory effect on Avicel . The analysis of FT-IR indicated that the C-H bond in DHP has a negative effect on cellulose hydrolysis. According to NMR analysis of the *ZL* and *ZT DHP*, it can be speculated that the β-β structure of *DHP* has a more inhibitory effect on cellulase.

5. CONCLUSION

The structural characteristics of *ZT* and *ZL DHP* were elucidated by FT-IR, GPC and NMR. Results showed that molecular weight and PDI of DHPs were negatively correlated with cellulase hydrolysis of Avicel.At the same time, it was found that structural features of DHPs had great effect on cellulase hydrolysis of Avicel. Combining FT-IR and NMR analysis, *ZT DHP* had higher content of β-β and C-H than *ZL DHP*. Both DHPs like lignin showed strong inhibitory effect on cellulase saccharification, during which *ZT DHP* presednted more pronounced effect on cellulase inhibition than *ZL DHP*. Analysis of the structural content of the DHPs indicated that the β-β and C-H structure plays an important role in inhibiting the enzymatic hydrolysis of cellulase.

6. REFERENCES

Berlin, A., Balakshin, M., Gilkes, N., Kadla, J., Maximenko, V., Kubo, S., Saddler, J., 2006. Inhibition of cellulase, xylanase and beta-glucosidase activities by softwood lignin preparations. Journal of Biotechnology 125, 198-209.

Brunow, G., 1995. Oxidative Coupling of Phenols and the Biosynthesis of Lignin, ACS Symposium Series, pp. 131-147.

Eglinton, T.I., Goñi, M.A., Boon, J.J., Hage, E.R.E.V.D., Terashima, N., Xie, Y., 2000. Incorporation of 13C-labeled coniferyl alcohol into developing Ginkgo biloba L. lignin revealed by analytical pyrolysis and CuO oxidation in combination with isotope ratio monitoring-gas chromatography-mass spectrometry. Holzforschung 54, 39-54.

Freudenberg, K., 1939. Lignin. Springer Vienna.

Frits, P.D.V., 2009. A win-win technique of stabilizing sand dune and purifying paper mill black-liquor. Journal of Environmental Sciences 21, 488-493.

Fukushima, K., Terashima, N., 1990. Heterogeneity in formation of lignin. XIII. Formation of p-hydroxyphenyl lignin in various hardwoods visualized by microautoradiography. Journal of Wood Chemistry & Technology 10, 413-433.

Guo, D., Chen, F., Inoue, K., Blount, J.W., Dixon, R.A., 2001. Downregulation of caffeic acid 3-O-methyltransferase and caffeoyl CoA 3-O-methyltransferase in transgenic alfalfa. Impacts on lignin structure and implications for the biosynthesis of G and S lignin. Plant Cell 13, 73.

Ko, J.K., Um, Y., Park, Y.C., Seo, J.H., Kim, K.H., 2015. Compounds inhibiting the bioconversion of hydrothermally pretreated lignocellulose. Applied Microbiology & Biotechnology 99, 4201-4212.

Lu, X., Zheng, X., Li, X., Jian, Z., 2016. Adsorption and mechanism of cellulase enzymes onto lignin isolated from corn stover pretreated with liquid hot water. Biotechnology for Biofuels 9, 118.

Nakagame, S., Chandra, R.P., Kadla, J.F., Saddler, J.N., 2011. Enhancing the enzymatic hydrolysis of lignocellulosic biomass by increasing the carboxylic acid content of the associated lignin. Biotechnology & Bioengineering 108, 538-548.

Qin, C., Clarke, K., Li, K., 2014. Interactive forces between lignin and cellulase as determined by atomic force microscopy. Biotechnology for Biofuels,7,1(2014-04-17) 7, 65.

Qin, L., Li, W.C., Liu, L., Zhu, J.Q., Li, X., Li, B.Z., Yuan, Y.J., 2016. Inhibition of lignin-derived phenolic compounds to cellulase. Biotechnology for Biofuels 9, 70.

Rahikainen, J.L., Martinsampedro, R., Heikkinen, H., Rovio, S., Marjamaa, K., Tamminen, T., Rojas, O.J., Kruus, K., 2013. Inhibitory effect of lignin during cellulose bioconversion: the effect of lignin chemistry on non-productive enzyme adsorption. Bioresour Technol 133, 270-278.

Ralph, J., Brunow, G., Harris, P.J., Dixon, R.A., Schatz, P.F., Boerjan, W., 2010. Lignification: are lignins biosynthesized via simple combinatorial chemistry or via proteinaceous control and template replication Recent Advances in Polyphenol Research 1, 36-66.

Ralph, J., Lundquist, K., Brunow, G., Lu, F., Kim, H., Schatz, P.F., Marita, J.M., Hatfield, R.D., Ralph, S.A., Christensen, J.H., 2004. Lignins: Natural polymers from oxidative coupling of 4-hydroxyphenyl- propanoids. Phytochemistry Reviews 3, 29-60.

Taherzadeh, M.J., Karimi, K., 2008. Pretreatment of Lignocellulosic Wastes to Improve Ethanol and Biogas Production: A Review. International Journal of Molecular Sciences 9, 1621-1651.

Terashima, N., 1996. New Preparations of Lignin Polymer Models under Conditions that Approximate Cell Wall Lignification. II. Structural Characterization of the Models by Thioacidolysis. Holzforschung - International Journal of the Biology, Chemistry, Physics and Technology of Wood 50, 9-14.

Terashima, N., Akiyama, T., Ralph, S., Evtuguin, D., Pascoal Neto, C., Parkås, J., Paulsson, M., Westermark, U., Ralph, J., 2009. 2D-NMR (HSQC) difference spectra between specifically 13C-enriched and unenriched protolignin of Ginkgo biloba obtained in the solution state of whole cell wall material. Holzforschung 63, 379-384.

Vermaas, J.V., Petridis, L., Qi, X.H., Schulz, R., Lindner, B., Smith, J.C., 2015. Mechanism of lignin inhibition of enzymatic biomass deconstruction. Biotechnology for Biofuels 8, 217.

Weng, J.K., Chapple, C., 2010. The origin and evolution of lignin biosynthesis. New Phytologist 187, 273-285.

Wu, K., Shi, Z.J., Yang, H., Liao, Z., Yang, J., 2016. Effect of Ethanol Organosolv Lignin from Bamboo on Enzymatic Hydrolysis of Avicel. Acs Sustainable Chemistry & Engineering 5.

Xie, Y., Terashima, N., 1994. Selective carbon 13-enrichment of side chain carbons of ginkgo lignin traced by carbon 13 nuclear magnetic resonance. Journal of the Japan Wood Research Society.

Ximenes, E., Kim, Y., Mosier, N., Dien, B., Ladisch, M., 2011. Deactivation of cellulases by phenols. Enzyme & Microbial Technology 48, 54.

Yang, H., Sun, S., Chen, H., Qiang, Y., Elder, T., Tu, M., 2017. Stimulation and inhibition of enzymatic hydrolysis by organosolv lignins as determined by zeta potential and hydrophobicity. Biotechnology for Biofuels 10, 162.

Yao, L., Chang, G.Y., Meng, X., Li, M., Pu, Y., Ragauskas, A.J., Yang, H., 2018a. A structured understanding of cellobiohydrolase I binding to poplar lignin fractions after dilute acid pretreatment. Biotechnology for Biofuels 11, 96.

Yao, L., Chen, C., Zheng, X., Peng, Z., Yang, H., Xie, Y., 2016. Determination of Lignin-Carbohydrate Complexes Structure of Wheat Straw using Carbon-13 Isotope as a Tracer. Bioresources 11.

Yao, L., Yang, H., Chang, G.Y., Meng, X., Pu, Y., Hao, N., Ragauskas, A.J., 2018b. Characteristics of Lignin Fractions from Dilute Acid Pretreated Switchgrass and Their Effect on Cellobiohydrolase from Trichoderma longibrachiatum. Frontiers in Energy Research 6.

316: An overview of holistic approach to achieve net zero energy residential building retrofit

Ke QU[1], Xiangjie CHEN[2], Saffa B. RIFFAT[3]

[1] *Ke Qu, Department of Architecture and Built Environment, Faculty of Engineering, University of Nottingham, University Park, NG7 2RD Nottingham, UK, ezxkq@nottingham.ac.uk*

[2] *Xiangjie Chen, Department of Architecture and Built Environment, Faculty of Engineering, University of Nottingham, University Park, NG7 2RD Nottingham, UK, ezzxc1@nottingham.ac.uk*

[3] *Saffa B. Riffat, Department of Architecture and Built Environment, Faculty of Engineering, University of Nottingham, University Park, NG7 2RD Nottingham, UK, Lazsbr@nottingham.ac.uk*

This review focus on the holistic approach technologies and strategies of energy-efficient residential building retrofitting. Besides, energy balance between both energy demand side and renewable energy supply side are discussed with the integration of different renewable energy technologies, such as advanced insulation, high efficient heat pump, solar aided energy system, combined heat and power plants, dynamic control strategies. Moreover, this review especially focused on the retrofitting problems and challenges of traditional residential buildings which is mostly built before 1960s, which accounts for 14.5% of the overall CO_2 emission based on 2015 levels. Combined with these retrofit technologies, several reference residential building cases in Europe are analysed, indicating six main problems from pre-retrofit simulation to retrofit operation process that obstacle the retrofitting performance. To bridge the performance gaps, this review discussed the building performance simulation models and optimisation algorithms. The optimisation function have mathematical characters of multi-objective, multi-variability, multi-disciplinary, multi-constrained (4M) with discrete, non-linear characteristics. Applying the optimisation strategies model is an essential to build a deep understanding between building performance simulation (BPS) and building performance optimisation (BPO), which help engineers to make an optimised holistic retrofitting decisions.

Keywords: traditional residential building, retrofit optimisation, holistic approach, NZEB, performance gap

1. INTRODUCTION

The European Commission had set climate strategies for 2020, 2030 and 2050 in their relatively climate and energy packages. For a promising future, according to climate and energy package action, there are three main steps: 1) by the end of 2020, greenhouse gas emission will be reduced by at least 20% compared with 1990 level (Capros, 2012); 2) For the mid-term, by the end of 2030, greenhouse gas emission should be reduced 40% compared with 1990 level (Höglund-Isaksson, 2010); 3) For the long-term, by the end of 2050, the target of the greenhouse gas emission is to cut 80% based on 1990 level (European Commission, 2011), which implies that at least an average of 2% of greenhouse gas emission reduction must be realised to fulfil the final target. Take the UK for example, the UK government set itself a 60% reduction of carbon dioxide target on 2000 levels by 2050. And the residential sector accounts for around 23% of the UK's total energy consumption (DBEIS, 2017). As it is calculated, 63% of properties were built before 1960s, which is also categorised to the historic and traditional buildings. That means these kinds of dwellings accounts for 14.5% of overall greenhouse gas emission by 2015 levels. To be more visually understand the meaning of 80% of greenhouse gas emission reduction, a specific example is a must. Taking the CO_2 emission as an example, according to statistics, the averaged emissions baseline in 1990s level is about $97\,\mathrm{kg}CO_2/m^2 \cdot year$, which is taken from a semi-detached house with area of $80m^2$ (Change, 2015). If the target is set to reduce 80% of the emissions, the final CO_2 emission value will be no more than $19.4\ \mathrm{kg}CO_2/m^2 \cdot year$ in 2050. If the target is set to reduce 90% of the emissions, the final CO_2 emission value will be no more than $9.7\ \mathrm{kg}CO_2/m^2 \cdot year$ in 2050.

The first concept of ZEB goes back to the 1970s. Esbensen and Korsgaard (1977) describe the Experimental Zero Energy Building. It denoted that the Zero Energy House is dimensioned to be self-sufficient in space heating and domestic hot-water supply during normal climatic conditions (Esbensen and Korsgaard, 1977). It was 2007 when a broad discussion about ZEB began because of the increased concern about climate change and energy resource shortages. The UK was the first country to provide an original definition of zero carbon homes in late 2006. According to the definition, a "zero carbon home" has zero net emissions of carbon dioxide from all energy use in the home including heating, lighting, hot water and all other energy use (DCLG, 2006). At the same time, a discussion about the definition of Zero Energy Building occurred in the USA, which is defined as follows: A net zero energy building is a residential or commercial building with greatly energy needs reduced through efficiency gains such that the energy needs can be supplied with renewable technologies (Torcellini, 2006).

From a global perspective, the International Energy Agency (IEA) has provided two definitions, for Net Zero Energy and Zero Carbon Buildings. Net Zero Energy Buildings address that these buildings are energy-neutral over a year period. Zero Carbon Building address that these buildings are carbon-neutral over a year period, which do not use energy that results in net carbon dioxide emissions. In addition, most definitions only include operational energy, ignoring the embodied energy, which consists all of the processes associated with the production of a building because of the absence of an efficient and accurate methods to calculate the embodied energy. ZEB categories according to the produced energy amount:

I. Energy Plus building
II. Autonomous Zero Energy Building
III. Net Zero Energy Building
IV. Near Zero Energy Building

2. HEAT PUMP SYSTEMS COMBINED WITH SOLAR ENERGY

2.1. Solar boosted heat pump

Solar PV panels can convert solar energy to electricity output with efficiency of approximately 15%, and the balance of the solar energy dissipated into environment as thermal heat. Thus, we can use the waste solar thermal heat and the electricity from the PV panels to boost the work of Heat pump systems. Especially, during cold ambient periods, the solar thermal collector can collect the low-grade heat from the incident solar energy, and serves as an evaporator to boost the temperature of the working fluid in the evaporator. In this way, the heat pump cycle can transfer heat from low-grade solar collector to thermal storage in a form of high temperature. Sankey diagrams can calculate the energy performance of the PV/thermal boosted Domestic water heating. In the calculation, the COP of the direct solar boosted heat pump can reach up to 4.2, and the system efficiency up to 3.64 (Harrison, 2017). According to the recent literatures, there are two main approaches that emerged in the commercial market:

I. Direct expansion SB-HPWH system

For the direct-expansion approach, refrigerant is circulated directly through the solar collectors (O'Dell et al., 1984, Y.W. Li, December 2007, Ito et al., 1999, Ito et al., 2005, Kuang and Wang, 2006, Chow et al., 2010). And the absorber of the solar collector becomes evaporator directly. However, the main risks are the leakage of traditional refrigerants and high installation cost.

II. Indirect SB-HPWH system

For the indirect solar boosted-heat pump system, the working principle is similar to direct ones, the solar collector is connected to the evaporator of heat pump as heat exchanger in the close system. This is especially used in much colder areas where the antifreeze heat transfer fluid cannot be directly contact with the cycle of domestic water storage (Kong et al., 2018, Y.W. Li, December 2007, Chow et al., 2010, Kuang and Wang, 2006). Although the installation is simplified, there are the additional components, such as the electric heat pump and the heat exchanger. The example of (a) direct and (b) indirect SB-HPWH configurations are shown in Figure 1 (Harrison, 2017).

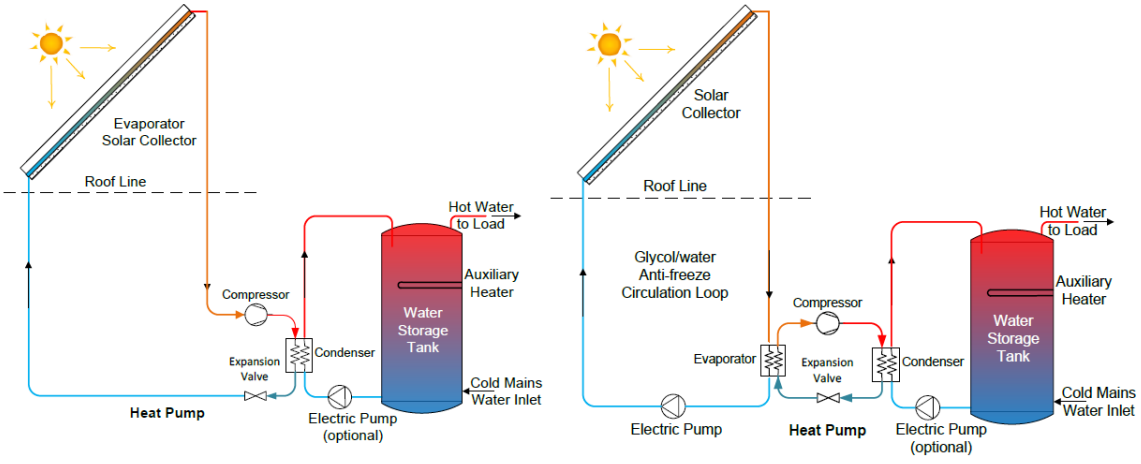

Figure 1: The example of (a) direct and (b) indirect SB-HPWH configurations

2.2. Dual-mode or Tri-mode heat pump solar collector

To realise the reliable supporting of the thermal energy for both the space heating and domestic water heating by renewable energy. Jacob van Berkela, Onno Kleefkensb and Felix Lacroixc put forward a novel control strategy for connection of PV/thermal solar collector, ground heat source to one heat pump systems depending on the heat demand of the users. The configuration of the connection system is shown in Figure 2.

Overall efficiencies for GSHPs are inherently higher than that of the air source heat pumps, because ground temperatures are relatively stable and higher than the mean air temperature in winter and lower in summer. The majority of heat pump output temperature is ranged in 50-55℃, and no more than 65℃. Commercially used products usually performance with COP of 4 in space heating, and COP of 2.75 in domestic water heating. Also, the lifespan of GSHP is expected to be 20-25 years, and the ground coil will lasts for 50 years. One of the main challenges is the cost of such GSHP systems. Taking the example of SLINKY systems. The capital costs for horizontal installed ground source to water heat pump systems will cost around 600-1150£/KW, and 850-1500£/KW for vertical installed systems.

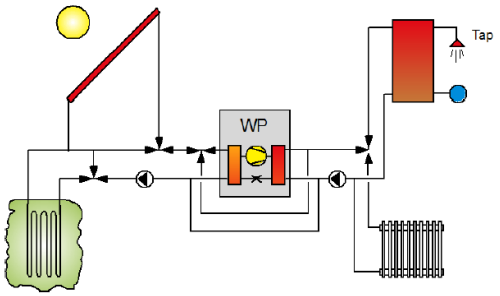

Figure 2: configuration of the connection of PV/Thermal collector and ground source heat exchanger system

3. OTHER HYBRID SYSTEMS

3.1. Hybrid photovoltaic and thermal PV/T technology

Photovoltaic is been widely used recently in different applications with an electricity efficiency in markets arranging from 12%-19% (Wikipedia, 2018) for inorganic PV panels, and 3%-15% (Yu, 2014) for organic photovoltaic panels. Company SUNPOWER can produce a type of solar cell with high efficiency, which is up to 21.5% (Sunpower, October 2015). Besides, there are three main problems that challenge the development of PV panels: (1) Relatively high initial investment and low electricity output; (2) Dust and other particles that accumulated on the surface of the panels will reduce the electricity efficiency; (3) Overheating of the PV panels will result in electricity degradation. The efficiency of a solar cell declines by about 0.25%-0.5% for every 1 degree Celsius increase in temperature (Nižetić et al., 2016).

Many investigations have been made to explore the solutions to both dust accumulations and cooling technologies. Besides common improvements, there is a possibility to improve the overall performance of PV panels by integrating the PV and thermal collector, which is also called the PV/T technologies. According to the results, there is an improvement of 16.3% of the overall increase in electricity output (Nižetić et al., 2016). The water-based PV/thermal technology, which enhanced solar electrical and thermal efficient by 9.1% and 42%, respectively (Zhang et al., 2013). In another study, a simple passive automatic cooling and cleaning system using thin film of water is developed for standalone PV system (Elnozahy et al., 2015). This study figures out a 29% increase in electricity fields, together with 45.5% and 39% reduction in temperatures of the front and rear faces of the module, respectively. Besides, current PV/Thermal cost are approximately 3-5 times that of standard PV modules, however it is expected that these prices will drop as volume and competition increases in the market (Harrison, 2017).

3.2. Solar collector combined domestic water heating

The solar energy from the sun reaches the earth in the radiation form. When the radiation is absorbed by surface of solar collector, it transfers and stored as thermal heat, and usually stored with the water heating. As we know, solar water heating is the cheapest storage method, which will replace almost 20% of heat consumption for a family. Literatures (Jayamalathi, January 2012, Bhowmik and Amin, 2017) indicate that the flat solar collector usually have 50% of thermal efficiency without reflector, and 60% of thermal efficiency with reflectors. Thus, the overall efficiency of the flat plate solar collector is increased approximately 10% by using the reflector. Another investigation to improve its efficiency is focused on solar radiation concentration, which is also called as concentrating solar collectors. And it will reaches a higher temperature level. A typical concentrated solar collector typically has a collector, tracking system, absorber, heat transferring liquid and an energy storage system.

3.3. Hybrid CHP systems

Another innovative hybrid CHP systems for high temperature heating plant in existing buildings are investigated by Livio de Santoli, Gianluigi Lo Basso and Benedetto Nastasi (de Santoli et al., 2017). To produce high temperature heat water along with the electricity generation, four types of energy plants were designed and compared. They are listed as below:

I. Separated generation, Figure 3(a)
II. Traditional CHP and boiler, Figure 3(b)
III. Combined CHP and 2-stage heat pump system, Figure 3(C)
IV. Combined CHP, CO_2-HP, PV/T and boiler system, Figure 3(d)

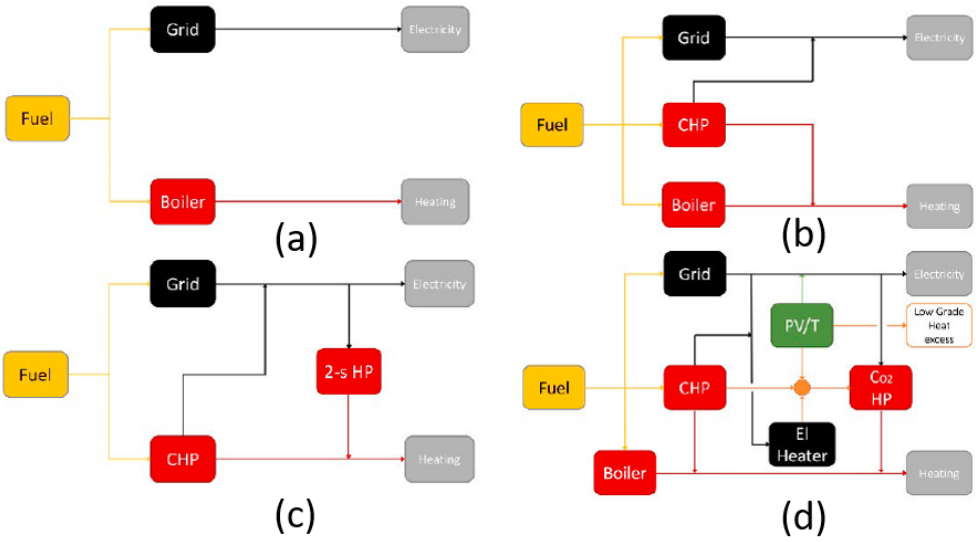

Figure 3: four types of energy plants

The first energy scenario is composed by separated heat and electricity parts, which is directly support electricity from grid and heat from boiler. The second energy scenario is composed by traditional CHP systems, which means that CHP and grid together support electricity, and boiler together with the waste heat of CHP to support heat. The third energy scenario is composed of grid, CHP and two-stage heat pump. The CHP can drive partial or total two-stage heat pump to support heat to the users. And partially generated electricity along with grid electricity to support electricity to users. In the fourth energy scenario, it is more complicated, with an addition boiler as a back-up, CHP waste heat along with CO_2 heat pump to realise heating requirement. At the same time, the hybrid PV/T solar collector will support the low-grade heat requirement of the CO_2 heat pump. With increasing of the PV/T heat production, the electric heater will operate within the thermal storage device to support the operation of the CO_2 heat pump. Similar to the third scenario, electricity is supported by grid electricity, CHP and PV panels. The experiment results indicate that when PV/T contributes 80% of the total energy as heat to drive the low-grade CO_2 heat pump, the equivalent primary energy of the whole systems can be reduced by 68.35%.

4. UNCERTAINTIES OF BUILDING ENERGY PERFORMANCE RELIABILITY

During the process of building retrofit towards net zero energy buildings concept, recognition of optimisation is a necessary improvement for complex NZEBs. Form the abstracted mathematically perspective, this kind of optimisation is even more difficult and time-consumption, regarding multi-disciplinary systems including passive and active envelop insulation, daylight, natural ventilation, HVAC, heat and electricity storage, micro-CHP, biomass boiler, heat pump, PV, PV/T, solar collector, and micro- wind turbines and so on. Therefore, the optimisation of historic and traditional residential building energy-efficient retrofitting can be concluded with the following mathematical properties of multi-objective, multivariate, multi-disciplinary, multi-constrained (4M) with discrete, non-linear characteristics. And analysis of these characters is crucial for developing a deep understand of integrating building performance simulation (BPS) and building performance optimisation (BPO).

Nowadays, the popular optimisation algorithms can be classified into three main areas: (1) enumerative algorithms, (2) deterministic algorithms, (3) stochastic algorithms. Especially, in the last decades, genetic algorithms (GA) and evolutionary algorithms (EA) are the most efficient stochastic algorithms for the optimisation problems in building energy design (Congradac and Kulic, 2009, Attia et al., 2013, Meyarivan, 2002). Literatures also mentioned many BPO tools namely GenOpt, MATLAB, modeFrontier, Topgui, EnergyPlus and so on (Attia et al., 2013, Wu et al., 2017).

Many literatures mentioned that there is often a significance performance between the simulated energy prediction and the operational measured energy pre- and post- building retrofit. This performance gap has become an increased concern recently with the requirement of large amount of energy efficient building retrofitting, especially for those house owners with self-funded building renovation. As house owners, they are wondering what kind of the energy level that their house could reach with a reasonable investment before energy retrofitting, and what it exactly will be after the renovation. With the development of automated meter reading technology, the performance gap becomes more and more visible, which help us make a better understanding of the cause of this phenomenon. As can be seen in the retrofit case study, there are lots of new development of monitor technologies, such as cheap sensors, radio-frequently identification (RAFID) tags, and ubiquitous positioning, which can provide high resolution results to measure the operational energy performance. There are three main categories that cause the performance gap: the design stage, the construction stage, the operational stage

(de Wilde, 2014), which can be summarised in the following parts. And in many cases, there is a combination of several issues.

In design stage, the main problems are: (1) Inefficient communication about performance targets for the future building between clients and design team; (2) Inefficient energy saving systems; (3) Fundamental uncertainties, such as actual weather condition, occupancy schedule, internal heat gains, and plug loads (4) Inefficient alignment between design and prediction

In construction stage, the main problems are: (1) Insufficient attention to both insulation and airtightness; (2) Potential risks for the creation of thermal bridges that can change the overall performance; (3) Actual construction does not meet specification

In operational stage, the problems are: (1) uncertainties in experimental data; (2) Occupant behaviours are often different from the design stage; (3) Lack of standardization and continuity of monitoring, analysis, and control throughout the building life cycles

Therefore, there are two main prediction methods: Firstly, one of the most used prediction method is first-principle model. According to the known building physics and building systems, a physical model is developed, which will be translated into a computational model. And once it is solved, the prediction is generated. Plus, there is also more precise prediction with more details, which develops into dynamic energy simulation. The dynamic means the indoor and outdoor conditions will vary dynamically with a time step in simulation. The second prediction method is black box approach. This is based on developing input parameters and output parameters without explicitly modelling the system and physical processes. This approach is broadly known as machine learning and covers techniques such as regression analysis, artificial neural networks, and support vector machines. And the training data can be supported by either experimental tests or first-principle model. Thus, further investigation is proposed to develop a solid approach on model calibration:

I. Further quantify the performance gap range dependent on the time and contextual factors.
II. Taking into account the uncertainties to specific simulations, and making sensitivity analysis.
III. Capturing measured data that can not to be fully predicted, decompose the performance gap and making a further study.
IV. Deep study of machine learning approaches will provide a better baseline for a much accurate prediction based on first-principle simulation.
V. Deep study of large sets of buildings, where each building has specific prediction and experiment data on the similar design or similar performance.

5. CASE STUDY RESEARCH AND RETHINKING

This review collected and investigated eight different residential retrofitted cases, except for the case 7, which is an efficient energy-plus constructed recently as zero energy building in German. The investigated cases mainly focus on residential buildings that is funded by the house owners of European countries, including Denmark, UK (England and Wales), Belgium, German and Finland (Figure 4). The UK cases represent western north-Atlantic climate. The Denmark and Finland cases represent northeast subarctic and tundra climates. And the German and Belgium cases represent central continental climate. However, for these cases, there is a lack of collection of south mediterranean climate such as Italy and Croatia. Furthermore, these cases contain four European residential building typologies, including single-family houses (detached or semi-detached house), terraced houses, multi-family houses, and apartment blocks.

These cases implied several different levels of retrofit technologies, including element retrofitting and holistic retrofitting. From the investigation of these cases, many lessons can be concluded and described as below:

I. In case 1, a saving of about 50% on the energy consumption for heating confirms that there is a large potential for achieving energy saving in the insulation part of the building stock through renovation as the first step of building retrofit before applying other active and renewable energy measures.
II. Only focus on the simple economic and energy savings achieved through renovation, there will be a problem of neglecting the increased market value of the house
III. Without enough consideration and prediction of indoor environment quality in both case 2 and case 3, pollutions such as CO_2 concentration will easily exceed the standard, which will not meet the satisfy standard of the house owners. Although the energy performance is much better than before the renovation, the indoor environment is poorer than before.
IV. As the analysis in case 5, with considering of primary energy consumption to be compensated by production on site, the retrofitted dwellings should need a large amount of sustainable energy supplied by generator, such as thermal heat collector, PV panels, wind turbines, micro-CHP. However, take the example of PV panels only. If all compensated energy has to be suppled in this case, it need 77 m^2 totally in case 5. Whereas, there is no enough places for PV panels to mount on the pitched roofs.

V. Another problem with zero energy building concept is the time lag between primary energy consumption and renewable energy production, as is shown in case 5. However, case 6 tried to solve this problem with battery storage and on-grid and off-grid strategies. The results indicate the investment of battery is still high.

VI. Case 8 indicates that a domestic scale CHP is not the best approach to realise NZEB in Finland. However, applying local shared biomass CHP is a better solution, because of its high overall efficiency and power to heat ratio in the large scale system.

VII. Among case 1 and case 6, energy performance gaps occurred in different scales. A further deep understanding of the performance gaps is urgent and significant to improve the reliability of the post-retrofit performance. The performance gaps is described is Figure 4 for each cases.

6. CONCLUSION AND FUTURE WORK

This literature review focus on the holistic approach of energy-efficient residential building retrofitting. It begin with the basic introduction of CO_2 emissions target in 2015 and UK residential building market stocks, which especially stressed dwellings built before 1960s that accounts for 14.5% of the overall CO_2 emission based on 2015 emission levels. Then the review discussed different ZEB definitions and their characters. Furthermore, the energy demand side is been analysed with the application of current building envelop insulation and the advanced future materials. Then, the renewable energy supply side is been analysed with the on-site and off-site renewable energy technologies, including heat pump, solar energy, combined heat and power plants. Moreover, this review especially focused on the retrofitting problems of historic and traditional buildings which is mostly built before 1960s. To solve these problems, the building performance simulation and optimisation is introduced and discussed. The optimisation of historic and traditional residential building energy-efficient retrofitting has the mathematical properties of multi-objective, multivariate, multi-disciplinary, multi-constrained (4M) with discrete, non-linear characteristics. To have a deep understand of integrating building performance simulation (BPS) and building performance optimisation (BPO), it is essential to build dynamic mathematical model under different condition limitations.

Case number	Case name	Building details	Retrofit measures	Energy performance	Gap level	Payback time	Reference
1	Danish single-family house	Built in 1965, single-family house, 160m^2, 2-4occupants	New gas boiler, electrical convectional heater, heat pump, wood burning, MVHR, LED	Final energy consumption reduced by 23% Heating consumption after retrofitting reduced by 53%	+5%	Payback time 36 years	[26, 27]
2	Danish 3 multi-story apartment blocks	Built in 1969, apartment blocks, 5293m^2, 66 flats	District Heating, MVHR, air supply control, daylight, energy saving bulb with auto-off control, PV systems(30,000KWh/year)	Heating consumption after retrofitting reduced by 31.5%	+27%	Payback time 14 years	[28]
3	Low energy retrofit in UK – a Victoria solid wall house	Built in Pre-1919, 76.9m^2, 2 occupants, end-terraced house	High efficiency boiler, MVHR, LED, Daylight, passive clothes drying, Solar PV, Solar thermal collector	CO_2 emissions reduced by 43% (reduced from 40 to 23 $(kgCO_2)/m\text{^}2 \cdot yr$	+28%	Not mentioned	[29]
4	Low energy retrofit in UK – a Modern 1990s cavity wall	Built in 1992, 84m^2, 2-4 occupants, mid-terraced house	High efficiency boiler, natural ventilation, LED, passive clothes drying, Solar PV, daylight, solar thermal collector	CO_2 emissions reduced by 40% (reduced from 76 to 46 $(kgCO_2)/m\text{^}2 \cdot yr$	+34%	Not mentioned	[30]
5	Energy efficient retrofit of an end of the row house in Belgium	Built in 1957, 78.3m^2, 2 occupants, self-detached house	High efficiency with built-in pump, a stack driven ventilation system, small electrical radiator in the loft room, 2.75m2 solar boiler with remained electrical boiler, 120l water tank, programmable thermostat, 8.7m2 PV panels	Final energy reduced by 67% in space heating, 48% in DHW	+27.7 %	Payback time: 19 years	[31]
6	Five energy retrofit houses in South Wales	Built in Pre1919, 1950s, 1960s and 2000s, 67-86m^2, 2-5 occupants, semi-detached houses	2.5-4.5KWp PV panels, 4.8-18KWp lead acid battery/ 2-3.97KWp lithium-ion battery, gas boiler/combi-boiler, MVHR	CO_2 emissions reduced arranging from 49%-74% Final total energy consumption reduced arranging from 15%-52% Energy saving improved with up to 56% reduction in space heating and up to 84% reduction in electricity	-15.3%	Payback time: 50-60 years	[32]
7	Efficient House Plus in Berlin	130m^2, 2 storeys, single-family detached, 4 occupants	98m^2 PV panels (efficiency 15%), 73m^2 thin-film PV (efficiency 12%) Central heating system with air-to-water heat pump, floor heating systems, mechanical ventilation with 80% heat recovery, auto switch-off smart control system, 40KWh buffer battery (second hand battery cells)	Energy use: total final energy consumption will be 61.1KWh/$m\text{^}2 \cdot yr$ Electricity surplus will be 4.5KWh/$m\text{^}2 \cdot yr$ Photovoltaic energy generation will be 65.5KWh/$m\text{^}2 \cdot yr$	Not mentioned	Not mentioned	[33]
8	Two single family NZEB in Finland	150m^2, one story house, single-family detached, 4 occupants	4 modules-2.874m^2 each solar plate collector, PV modules 93Kwh/m^2a 100KWe Direct Combustion Indirect Fired Gas Turbine Ground Source heat pump 1KW thermal boiler+50Lwater storage 500L hot water tank for both space heating and DHW Radiator heating using both hot water and electricity	Compared with standalone house, total heating demand of passive house decreased by 57%, and total electric demand decreased by 5%, DHW reduced by 35.3% and 47.2% relatively, in standalone and passive house.	Not mentioned	Not mentioned	[34]

Figure 4: Case study collection

This overview also summarised eight reference residential building cases in Europe. There cases indicate many real problems that obstacle the retrofitting performance. These performance gaps from simulation and construction are discussed and formed into future works. With the reduction of the performance gaps, the retrofit process will get a more optimised solution, which help to achieve a higher energy level certificate.

In future work, the following aspects need to be further investigated:

I. Explore an efficient and accurate method to calculate the embodied energy

II. Develop holistic energy efficiency retrofitting strategies for the whole building, results in the optimisation to reduce energy consumption refers to the integration of renewable energy systems, avoiding the oversize of the system.

III. More attention should be focused on visual, fabric and culture value characters of historic and traditional buildings, to get a better understanding of the performance gap with calibration from the measurement-based methodology.
IV. In the northern countries of Europe, utilizing on-site solar energy as a renewable energy resources to achieve annual balance of NZEB may face many obstacles, such as the mismatching between the energy production and consumption with the limited area of roof and façade, especially in the dense city areas. This situation encourages the investigation of using micro and small-scale biomass-based combined heat and power systems as energy systems to achieve NZEB balance. Thus, there should be a criteria between on-site and off-site decision.
V. The difficulty of defining a building retrofit boundary when CHP systems are combined as a retrofit technology.
VI. Understanding the occupancy behaviours before renovation may positively affects the post-retrofitting performance reliabilities.

7. REFERENCES

Attia, S., Hamdy, M., O'brien, W. & Carlucci, S. 2013. Assessing gaps and needs for integrating building performance optimization tools in net zero energy buildings design. *Energy and Buildings,* 60**,** 110-124.

Bhowmik, H. & Amin, R. 2017. Efficiency improvement of flat plate solar collector using reflector. *Energy Reports,* 3**,** 119-123.

Capros, P., Tasios, N, De Vita, A., Mantzos, L., Parousos, L. 2012. Technical report accompanying the analysis of options to move beyond 20% GHG emission reductions in the EU by 2020: Member State results. European Commission.

Change, D. O. E. C. 2015. UK progress towards GHG emissions reduction targets.

Chow, T. T., Pei, G., Fong, K. F., Lin, Z., Chan, A. L. S. & He, M. 2010. Modeling and application of direct-expansion solar-assisted heat pump for water heating in subtropical Hong Kong. *Applied Energy,* 87**,** 643-649.

Congradac, V. & Kulic, F. 2009. HVAC system optimization with CO2 concentration control using genetic algorithms. *Energy and Buildings,* 41**,** 571-577.

DCLG 2006. Zero Carbon Non-domestic Buildings: Phase 3 Final Report, Department of Communities and Local Government. Code for Sustainable Homes, Department for Communities and Local Government, London, UK

Department for Business, Energy & Industrial Strategy. 2017. Annex: 2015 UK greenhouse gas emissions, final figures. Statistical Release: National Statistics. Department for Business, Energy & Industrial Strategy, London UK.

De Santoli, L., LO Basso, G. & Nastasi, B. 2017. Innovative Hybrid CHP systems for high temperature heating plant in existing buildings. *Energy Procedia,* 133**,** 207-218.

De Wilde, P. 2014. The gap between predicted and measured energy performance of buildings: A framework for investigation. *Automation in Construction,* 41**,** 40-49.

Elnozahy, A., Rahman, A. K. A., Ali, A. H. H., Abdel-Salam, M. & Ookawara, S. 2015. Performance of a PV module integrated with standalone building in hot arid areas as enhanced by surface cooling and cleaning. *Energy and Buildings,* 88**,** 100-109.

Esbensen, T. V. & Korsgaard, V. 1977. Dimensioning of the solar heating system in the zero energy house in Denmark. *Solar Energy,* 19**,** 195-199.

European Commission. 2011. A Roadmap for moving to a competitive low carbon economy in 2050. European Commission.

Harrison, S. 2017. The Potential and Challenges of Solar Boosted Heat Pumps for Domestic Hot Water Heating. *12th IEA heat pump conference.*

Höglund-Isaksson, L., Winiwarter, W., Wagner, F., Klimont, Z., Amann, M. 2010. Potentials and costs for mitigation of non-CO2 GHG emissions in the European Union until 2030.

Ito, S., Miura, N. & Takano, Y. 2005. Studies of Heat Pumps Using Direct Expansion Type Solar Collectors. *Journal of Solar Energy Engineering,* 127**,** 60-64.

Ito, S., Miura, N. & Wang, K. 1999. Performance of a heat pump using direct expansion solar collectors 1Paper presented at the ISES Solar World Congress, Taejon, South Korea, 24–29 August 1997.1. *Solar Energy,* 65**,** 189-196.

Jayamalathi, P. S. C. S. January 2012. Performance improvement study of solar water heating system. *ARPN Journal of Engineering and Applied Sciences*.

Kong, X., Sun, P., Li, Y., Jiang, K. & Dong, S. 2018. Experimental studies of a variable capacity direct-expansion solar-assisted heat pump water heater in autumn and winter conditions. *Solar Energy,* 170**,** 352-357.

Kuang, Y. H. & Wang, R. Z. 2006. Performance of a multi-functional direct-expansion solar assisted heat pump system. *Solar Energy,* 80**,** 795-803.

Meyarivan, K. D. A. P. S. A. T. 2002. A fast and elitist multiobjective genetic algorithm: NSGA-II. *IEEE, Transactions on Evolutionnary Computation*.

Nižetić, S., Čoko, D., Yadav, A. & Grubišić-Čabo, F. 2016. Water spray cooling technique applied on a photovoltaic panel: The performance response. *Energy Conversion and Management,* 108**,** 287-296.

O'Dell, M. P., Mitchell, J. W. & Beckman, W. A. 1984. Design Method and Performance of Heat Pumps With Refrigerant-Filled Solar Collectors. *Journal of Solar Energy Engineering,* 106**,** 159-164.

Sunpower October 2015. SunPower TM X-Series Data Sheet. *In:* Sunpower (ed.).

Torcellini, P., Pless,S., Deru, M., Crawley, D., 2006. Zero Energy Buildings: A Critical Look at the Definition. National Renewable Energy Laboratory and Department of Energy, US.

Wikipedia. 2018. *Photovoltaics* [Online]. Wikipedia. Available: https://en.wikipedia.org/wiki/Photovoltaics#Efficiency [Accessed].

Wu, R., Mavromatidis, G., Orehounig, K. & Carmeliet, J. 2017. Multiobjective optimisation of energy systems and building envelope retrofit in a residential community. *Applied Energy,* 190**,** 634-649.

Li, Y. W., Wang. R. Z., Wu, J. Y., Xu, Y. X. December 2007. Experimental performance analysis on a direct-expansion solar-assisted heat pump water heater. *Applied Thermal Engineering,* 27.

Yu, J. Z., Y.; Huang, J. 2014. Towards High Performance Organic Photovoltaic Cells: A Review of Recent Development in Organic Photovoltaics. *Polymers,* 6**,** 2473-2509.

Zhang, X., Zhao, X., Shen, J., Hu, X., Liu, X. & Xu, J. 2013. Design, fabrication and experimental study of a solar photovoltaic/loop-heat-pipe based heat pump system. *Solar Energy,* 97**,** 551-568.

317: An improved low pressure steam operated adsorption cycle

Pressure swing adsorption cycle

Doskhan YBYRAIYMKUL[1], Muhammad WAKIL SHAHZAD[2], Muhammad BURHAN[3], Kim Choon NG[4]

[1] *Water Desalination and Reuse Centre, King Abdullah University of Science & Technology, Thuwal, 23955-6900, Saudi Arabia, doskhan.ybyraiymkul@kaust.edu.sa*
[2] *Water Desalination and Reuse Centre, King Abdullah University of Science & Technology, Thuwal, 23955-6900, Saudi Arabia, muhammad.shahzad@kaust.edu.sa*
[3] *Water Desalination and Reuse Centre, King Abdullah University of Science & Technology, Thuwal, 23955-6900, Saudi Arabia, muhammad.burhan@kaust.edu.sa*
[4] *Water Desalination and Reuse Centre, King Abdullah University of Science & Technology, Thuwal, 23955-6900, Saudi Arabia, kimchoon.ng@kaust.edu.sa*

Over the last century, fresh water and cooling demand have been increased tremendously due to improved living standard, industrial and economic development. The conventional air-conditioning and refrigeration processes consume 15% of total global electricity and it is expected to increase any fold due to harsh weather conditions. In terms of fresh water supplies, the current 38 billion m3 per year desalination capacity is projected to increase to 54 billion m3 per year by 2030, 40% more compared to 2016. The current business as usual trend of cooling and desalination is not sustainable due to high energy consumption and CO2 emissions.

In contrast, the adsorption (AD) cycle operate at low-grade waste heat or renewable energy and produce fresh water and cooling simultaneously. The major bottleneck of conventional thermally driven AD cycle is its large foot print and capital cost due to complex packed bed arrangements. We proposed pressure swing adsorption cycle (PSAD) that can utilise low-pressure steam (2-5 bar) for regeneration using thermal vapor compressor (TVC). In this paper, an experimental investigation on PSAD has been presented. It was demonstrated successfully that primary steam at 3-5 bar pressure can regenerate silica gel at less than 1 kPa using correctly designed TVC system. The proposed system will reduce CAPEX and OPEX due to simple design and operation.

Keywords: Adsorption cycle, Pressure swing, Thermal vapor compressor, Adsorption desalination

1. INTRODUCTION

Demand for fresh water and cooling is increasing due to population growth and industrial development, so portable water need becomes major issue in many countries as available fresh-water resources are limited (Gude, 2017; Alaei, 2018; Shahzad, 2017; Ng, 2018; Khawaji, 2008). Almost 70% of global water use is referred to agriculture, evidently population growth will increase water demand extremely. In order to partially satisfy needs currently 38 billion m3 per year water is desalinated, and it is expected increasing of desalination capacity to 54 billion m3 per year by 2030, 40% more compared to 2016 (Ng, 2018). However, the total water demand is already higher than the sustainable level (Ng, 2013). On the other hand, cooling provided by conventional vapor-compression refrigeration systems are challenged due to the ozone depletion potential (ODP) and global warming potential (GWP) caused by the halogenated refrigerants. Adsorption cooling is one of the most attractive technology for cooling applications, because it is environmentally friendly: zero ODP, zero GWP (Anupam, 2011). Adsorption cooling system uses adsorbents such as silica gel to adsorb and desorb a water vapor by changing temperature or pressure. Notable works have been done on temperature swing adsorption cooling systems (Thu, 2013; Wang, 2005; Ng, 2006; Chua, 1999; Li, 2014; Thu, 2017; Saha, 2006; Ng, 2012; Chua, 2004; Saha, 2003; Palodkar, 2017), and pressure swing adsorption cooling is still developing (Palodkar, 2017; Anupam, 2016). Categories of the available desalination methods are shown in Figure 1.

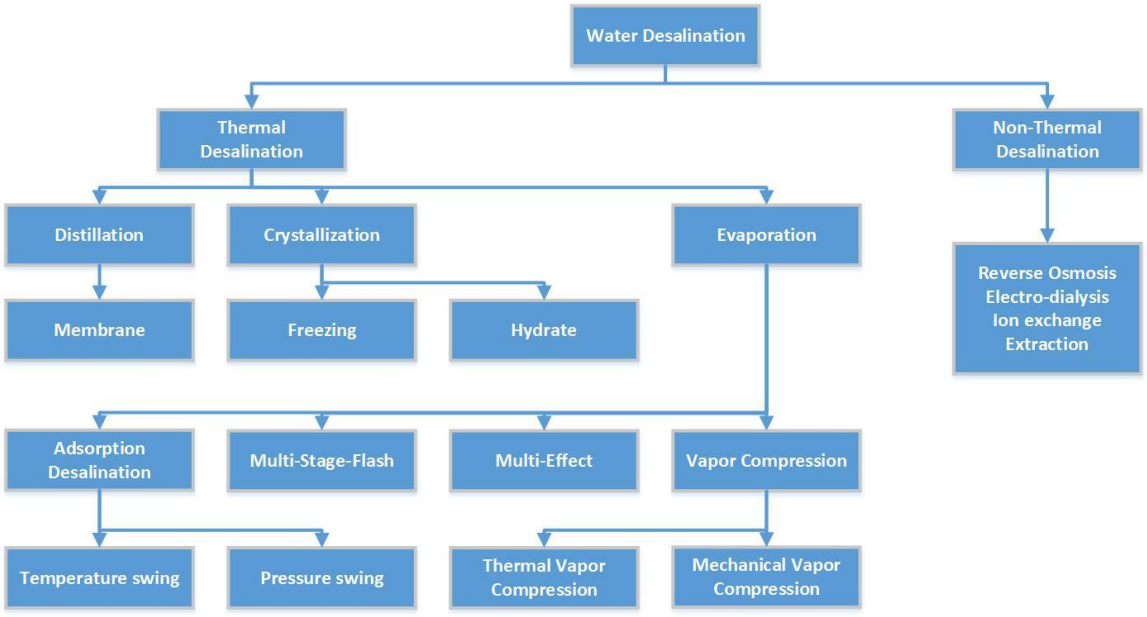

Figure 1: The categories of desalination processes.

One of the most developing desalination method is TVC with combination of other methods. Al-Juwayhel et al. (1997) theoretically analysed TVC with single effect evaporation by steady state model. Theoretical model considered salinity of water, demister effect and boiling point evaluation. Dessouky et al. showed that the performance ratio for the four single-effect vapor compression systems had values higher than one. The Multi Effect Distillation (MED) is frequently advised as an efficient thermal desalination technology. Hybrid of MED and TVC is modelled and analysed in many paper (Liu, 2017; Cipollina, 2017; Kouhikamali, 2011; Ettouney, 1999; Kamali, 2008). El-Dessouky et al analysed MED-TVC system and concluded that performance ratio declined with increase of the boiling temperature and compression ratio (Ettouney and El-Dessouky, 1999). Liu et al. (2017) investigated influence of the area ratio on the ejector efficiencies, and concluded that mixing efficiency played a more important role in ejector performance than other parts efficiencies of elector.

We proposed pressure swing adsorption cycle (PSAD) that can utilise low-pressure steam (2-5 bar) for regeneration using thermal vapor compressor (TVC). The ejector is main part of the PSAD-TVC, so performance of PSAD-TVC system depends on performance of ejector. The main advantage of steam ejector is increasing of vapor pressure without spending of mechanical energy. Application of ejectors is one of the highly reliable solution for compressing vapor comparing to mechanical compressors due to no moving parts, simple construction, stable operation and easy maintenance. Piston compressors are not reliable for high volume flow rate which is typical feature to large desalination plants. COP of ejector is almost proportional to ER, which is ratio of entrained mass flow rate to motive steam mass flow rate, and it is the important feature to investigate.

2. PSAD-TVC SYSTEM FOR DESALINATION AND COOLING

Recent studies on thermal desalination were focused on many hybrid technologies, especially multi-effect desalination (MED) with thermal vapor compression (TVC), MED with adsorption desalination (AD) and etc. Current system consists of

pressure swing adsorption desalination combined with thermal vapor compressor. System produces two useful effects such as fresh water and cooling with only utilizing low-pressure steam (2-5 bar).

2.1. Experimental setup

Figure 2 shows schematic diagram and pictorial view of the designed TVC-AD system. System consist of 2 AD beds, 2 ejectors, boiler, condenser, evaporator, distillate tank, AD cooling water tank. Ejectors, tanks, evaporator and condenser were made from stainless steel in order to eliminate corrosion in system. Falling-film evaporator composed of tube bundle, water circulation apparatus such us pump, tube and nozzles. Connection tubes of high temperature steam flow, ejectors, and steam header were thermal insulated with fiberglass, meanwhile low temperature parts such as AD beds, evaporator and condenser were thermal insulated with foam rubber. Both materials have satisfying thermal insulation properties. Pressure of evaporator is measured with pressure sensors (Yokogawa) which have an accuracy ±0.125 kPa. Vapor temperature in evaporator is measured with 10 kΩ thermistor (±0.15 °C). Other temperatures are measured with Pt 100 RTD (±0.15 °C).

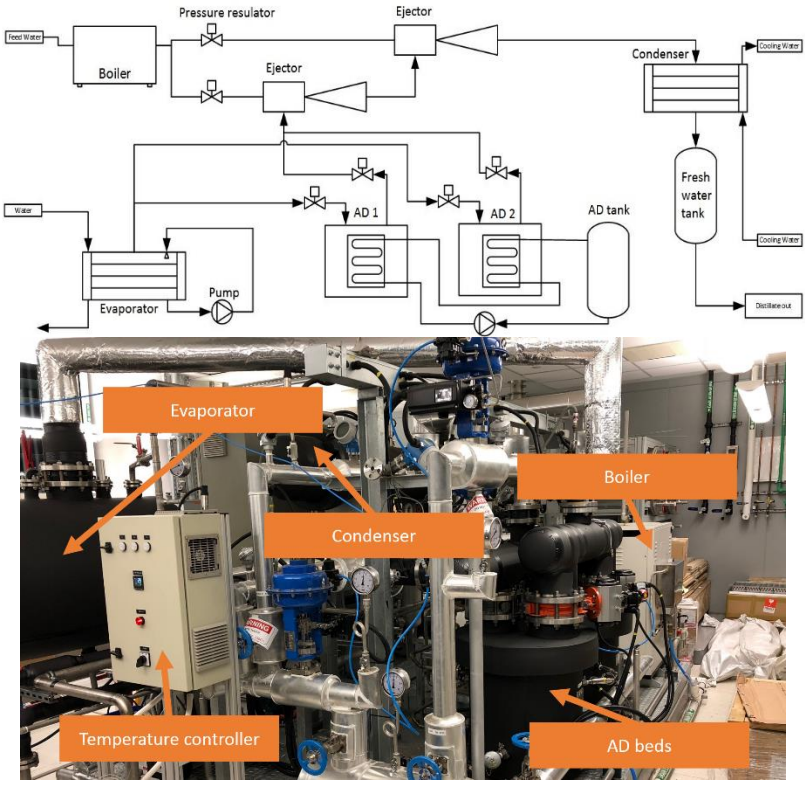

Figure 2: Schematic diagram and pictorial view of the designed TVC-AD

2.2. PSAD-TVC process description

Main part of the system is the boiler, which maintains desired maximum steam pressure. Two electrical pressure regulator, which are installed after the boiler, control inlet pressure to ejectors (motive steam pressure). Serially connected ejector are able to achieve up to 1 kPa in suction line with motive steam from 2-5 bar. Discharge pressure of ejector depends on motive steam and suction pressure. Discharged steam form ejectors goes to condenser and condensed fresh water accumulates in distillate tank. When distillate tank will be filled excess fresh water is diverted to drain by pump. PSAD-TVC system operates as a 2-bed mode, where one of AD bed works as adsorber and second one works as desorber. AD vessels were embedded with Type RD silica gel, as the adsorption uptake of silica gel and other characteristics meet requirements. Water circulated through coils in the AD in order to regulate temperature of adsorbent bed. Water vapor from evaporator goes to one of the AD bed, meanwhile, another AD bed is discharged by ejectors. Coefficient of performance (COP) of ejector is proportional to entrainment ratio (ER), which is ratio of entrained mass flow rate to motive steam mass flow rate, and it is the important feature to investigate:

$$COP = \frac{\dot{m}_m(h_m - h_d)}{\dot{m}_e(h_e - h_d)} = ER\frac{(h_m - h_d)}{(h_e - h_d)}$$

3. RESULTS AND DISCUSSION

Temperature profiles of adsorbent beds of the PSAD-TVC are illustrated in Figure 3. Temperature of silica gel changes from 19 C to 31 C, while charging cycle, and decrease from 31 C to 19 C at discharging cycle.

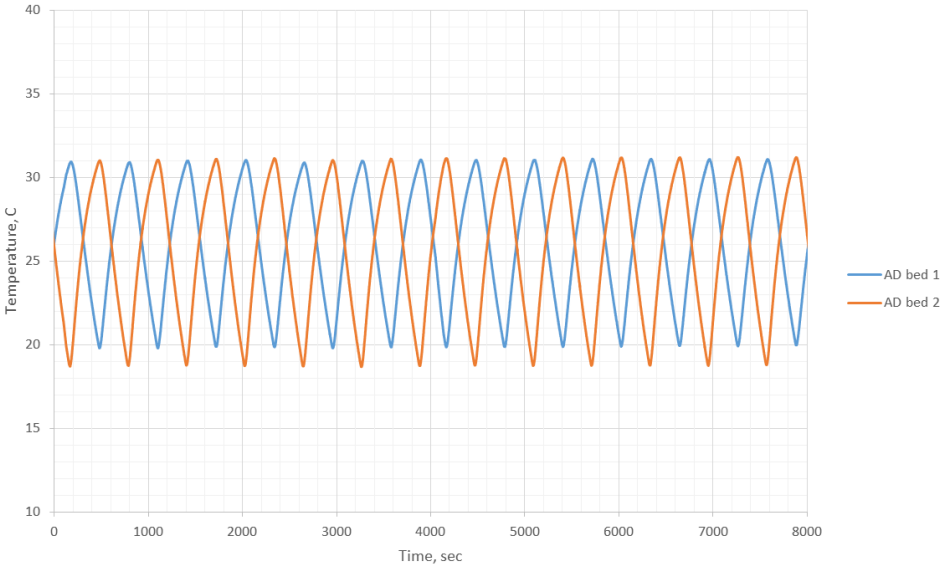

Figure 3: Temperature profiles of adsorbent beds

Pressure of motive steam was 2 barg, suction pressure was around 1 kPa, discharge pressure changed from 6 to 7 kPa. Pressure profile of adsorbent bed of PSAD-TVC system are imaged Figure 4. AD bed pressure was increased form 0.5 kPa to 2.5 kPa while adsorption cycle. Average water production rate was around 2 LPM. As we can see that PSAD-TVC system works stably for 10 hours, in order to show temperature change between adsorption and desorption cycles. Temperature is changing form 22 C to 18 C. cooling the system, meanwhile water inlet temperature of evaporator is 26 C.

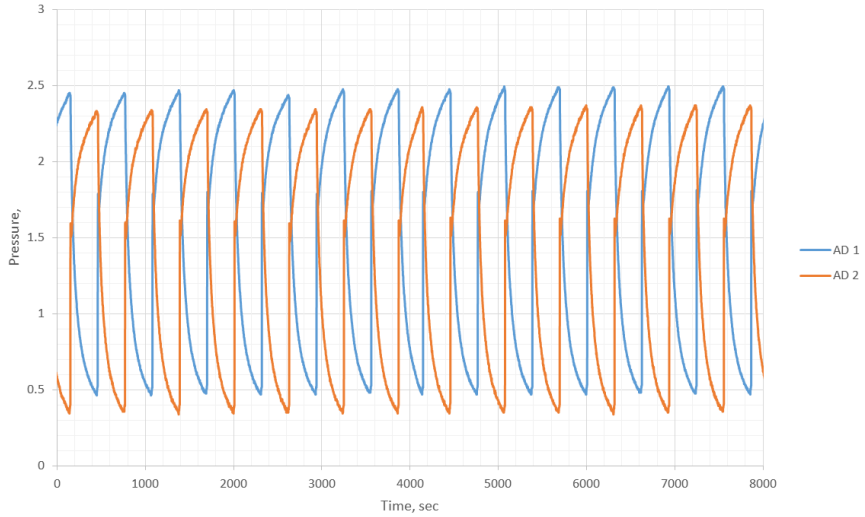

Figure 4: Pressure profiles of adsorbent bed

Figure 5 shows results of changing of ER depending of motive steam pressures of two stage TVC system. Higher ER can be achieved at the lowest motive steam pressures 1 barg. Decreasing motive steam pressure of first TVC increases ER at all motive steam pressures of second TVC, however decreasing motive steam of second TVC at 4 barg of first TVC decreases ER, this could be due to critical back pressure of first TVC.

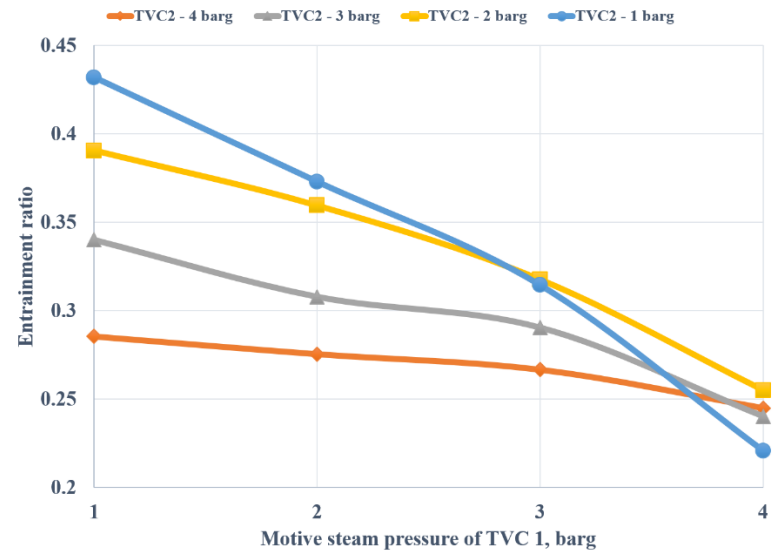

Figure 5: Variation of entrainment ratio

4. CONCLUSION

Experimental result demonstrated in above section shows that PSAD-TVC system works stably and produces portable water and cooling simultaneously. The proposed system has best thermodynamic synergy with CCGT plants where low-pressure bleed steam can be utilised more efficiently to produce cooling and water. It was demonstrated successfully that primary steam at 3-5 bar pressure can regenerate silica gel at less than 1 kPa using correctly designed TVC system. The proposed system will reduce CAPEX and OPEX due to simple design and operation.

5. REFERENCES

Alaei Shahmirzadi MA, Hosseini SS, Luo J, Ortiz I.2018.Significance, evolution and recent advances in adsorption technology, materials and processes for desalination, water softening and salt removal, Journal of Environmental Management. 215, 324–44.

Al-Juwayhel F, El-Dessouky H, Ettouney H.1997.Analysis of single-effect evaporator desalination systems combined with vapor compression heat pumps, Desalination. 114(3), 253–75. Anupam K, Chatterjee A, Halder GN, Sarkar SC.2011.Experimental investigation of a single-bed pressure swing adsorption refrigeration system towards replacement of halogenated refrigerants, Chemical Engineering Journal. 171(2), 541–8.Shahzad MW, Burhan M, Ang L, Ng KC.2017.Energy-water-environment nexus underpinning future desalination sustainability, Desalination. 413, 52–64.

Anupam K, Palodkar A V, Halder GN.2016.Experimental study on activated carbon--nitrogen pair in a prototype pressure swing adsorption refrigeration system, Heat and Mass Transfer. 52(4), 753–61.

Chua HT, Ng KC, Malek A, Kashiwagi T, Akisawa A, Saha BB.1999.Modeling the performance of two-bed, sillica gel-water adsorption chillers, International Journal of Refrigeration. 22(3), 194–204.

Chua HT, Ng KC, Wang W, Yap C, Wang XL.2004.Transient modeling of a two-bed silica gel–water adsorption chiller, International Journal of Heat and Mass Transfer. 47(4), 659–69.

Cipollina A, Agnello M, Piacentino A, Tamburini A, Ortega B, Palenzuela P, et al.2017.A dynamic model for MED-TVC transient operation, Desalination. 413, 234–57.

Ettouney H, El-Dessouky H.1999.Single-Effect Thermal Vapor-Compression Desalination Process: Thermal Analysis, Heat Transfer Engineering. 7632(July),.

Gude VG.2017.Desalination and water reuse to address global water scarcity, Reviews in Environmental Science and Biotechnology. 16(4), 591–609. Khawaji AD, Kutubkhanah IK, Wie J-M.2008.Advances in seawater desalination technologies, Desalination. 221(1–3), 47–69.

Journal of Heat and Mass Transfer. 60, 143–55. Ng KC, Thu K, Kim Y, Chakraborty A, Amy G.2013.Adsorption desalination: An emerging low-cost thermal desalination method, Desalination. 308, 161–79.

Kamali RK, Abbassi A, Sadough Vanini SA, Saffar Avval M.2008.Thermodynamic design and parametric study of MED-TVC, Desalination. 222(1–3), 596–604.

Kouhikamali R, Mehdizadeh MSM.2011.Process investigation of different locations of thermo-compressor suction in MED–TVC plants, Desalination. 280(1–3), 134–8.

Li A, Ismail A Bin, Thu K, Ng KC, Loh WS.2014.Performance evaluation of a zeolite–water adsorption chiller with entropy analysis of thermodynamic insight, Applied Energy. 130, 702–11.

Liu J, Wang L, Jia L, Wang X.2017.The influence of the area ratio on ejector efficiencies in the MED-TVC desalination system, Desalination.

Ng KC, Wang X, Lim YS, Saha BB, Chakarborty A, Koyama S, et al.2006.Experimental study on performance improvement of a four-bed adsorption chiller by using heat and mass recovery, International Journal of Heat and Mass Transfer. 49(19–20), 3343–8.

Ng KC, Thu K, Saha BB, Chakraborty A.2012.Study on a waste heat-driven adsorption cooling cum desalination cycle, International Journal of Refrigeration. 35(3), 685–93.

Ng KC, Shahzad MW.2018.Sustainable desalination using ocean thermocline energy, Renewable and Sustainable Energy Reviews. 82, 240–6.

Palodkar A V, Anupam K, Roy Z, Saha BB, Halder GN.2017.High pressure adsorption isotherms of nitrogen onto granular activated carbon for a single bed pressure swing adsorption refrigeration system, Heat and Mass Transfer. 53(10), 3155–66.

Saha BB, Koyama S, Kashiwagi T, Akisawa A, Ng KC, Chua HT.2003.Waste heat driven dual-mode, multi-stage, multi-bed regenerative adsorption system, International Journal of Refrigeration. 26(7), 749–57.

Saha BB, Koyama S, Choon Ng K, Hamamoto Y, Akisawa A, Kashiwagi T.2006.Study on a dual-mode, multi-stage, multi-bed regenerative adsorption chiller, Renewable Energy. 31(13), 2076–90.

Thu K, Kim Y-D, Myat A, Chun WG, NG KC.2013.Entropy generation analysis of an adsorption cooling cycle, International

Thu K, Yanagi H, Saha BB, Ng KC.2017.Performance investigation on a 4-bed adsorption desalination cycle with internal heat recovery scheme, Desalination. 402, 88–96.

Wang X, Chua HT, Ng KC.2005.Experimental investigation of silica gel–water adsorption chillers with and without a passive heat recovery scheme, International Journal of Refrigeration. 28(5), 756–65.

319: Digestibility and cellulose ultrastructure changes of populus variant during different pretreatments

Lan YAO, Congxin CHEN, Long XIONG, Fangke ZHENG, Haitao YANG

Hubei Provincial Key Laboratory of Green Materials for Light Industry, Hubei University of Technology, Wuhan, 430068, China. yaolislan1982@aliyun.com

Leading pretreatment technologies based on dilute sulfuric acid, liquid hot water, alkali and organosolv were applied to Populus variant. The remaining solids after each pretreatment were hydrolyzed by cellulase to glucose. Mutant poplar exhibited higher accessibility and glucose yield after four different pretreatments. Composition analysis, FTIR-ATR, gel permeation chromatography (GPC) and cross polarization/magic angle spinning carbon-13 nuclear magnetic resonance (CP/MAS 13C-NMR) techniques were employed to elucidate structural transformations of poplars during the leading pretreatments. Composition analysis and FTIR-ATR results revealed that hemicellulose and lignin were removed to variant extent during pretreatment. GPC analysis showed that DP of cellulose was decreased the most after dilute acid pretreatment, followed by organosolv, alkali and liquid hot water pretreatment. Cellulose crystallinity index analysed by CP/MAS 13C-NMR indicated that CrI was increased after pretreatment and was comparable between different pretreatment methods. The results also demonstrated that organosolv pretreatment resulted in the most decrease of recalcitrance of poplar to obtain the lowest pretreatment yield and the highest glucose yield in the process of enzymatic hydrolysis. Among the tested properties of poplar, lignin removal during pretreatment and cellulose accessibility were the most important features that associated with glucose release from the Populus.

Keywords: Populus, pretreatment, biomass recalcitrance, cellulose accessibility

1. INTRODUCTION

Lignocellulose based bioethanol is attracting more and more attention due to renewable energy need and environmental concerns. The process of bioethanol production typically involved pretreatment, cellulase hydrolysis, fermentation and ethanol purification (Meng et al., 2016). Lignocellulose is mainly composed of (1) cellulose, a linear homopolymer composed by D-glucose formed into crystalline and amorphous region (Sun et al., 2014a); (2) hemicellulose, as matrix substance, is an amorphous branched heteropolymer of glucose, xylose, galactose, arabinose and mannose (Pu et al., 2008); (3) lignin, different from carbohydrate, is a heterpolymer of cross-linked phenylpropane units (syringyl, guaiacyl and p-hydroxyphenyl) (Ragauskas et al., 2014). Natural recalcitrance of biomass is a major barrier of cellulase attack for glucose release. Among the four steps, pretreatment is a necessity to reduce recalcitrance of biomass to increase glucose yield in the following process (Mosier et al., 2005a). Different pretreatments have different mechanisms which would affect the ultrastructure of pretreated biomass and the generation of co-products (Sun et al., 2014b).

Dilute acid pretreatment (DAP) is the most studied pretreatment method, during which most of hemicellulose could be removed (Kim et al., 2014). It has been applied to various species of biomass and has been tried on industrial scale production (Yao et al., 2010; Cao et al., 2012; Dien et al., 2006). Although digestibility of pretreatment lignocellulose is increased, lignin could form droplets on the surface of cellulose when pretreatment temperature is higher than 120 oC (Selig et al., 2007), which shows adverse effect on glucose release by physical barrier and non-productive binding (Yao et al., 2017, 2018a, 2018b). DAP could also change cellulose ultrastructure, such as increase of crystallinity index (CrI) and crystallite dimension (Sun et al., 2014b).

Hydrothermal pretreatment, also called liquid hot water (LHW) pretreatment, is one of the most promising pretreatment methods as it is environment friendly and cost effective (Mosier et al., 2005b). One of the major advantages is complete hemicellulose dissolution during hot water pretreatment. Similar to DAP, dissolved hemicellulose could form organic acid (Mosier et al., 2005a), which promotes the reduction of the degree polymerization of cellulose when pretreatment temperature is higher than 170 °C (Yang and Wyman, 2008). Cellulose accessibility is increased after LHW pretreatment, at the same time, minimal inhibitor is formed (Li et al., 2014).

Alkaline pretreatment (Alkali) is well known for its lignin targeting. Compared to DA and LHW pretreatment, alkali pretreatment shows more capability in disrupting lignin structures, and cleavage of ester bonds between lignin and hemicellulose (Yang et al., 2016). More importantly, the reduction of this crosslinking tends to increase the accessibility of pretreated biomass to enzymes (Chen et al., 2013). Numerous researches have evaluated the application of alkali pretreatment on the following digestibility of various lignocelluloses. Most of them reported near-theoretical sugar yields (Jin et al., 2013).

Organosolv pretreatment is a well-known delignification method. The organosolv pretreatment could remove substantial amounts of lignin by the cleavage of β-aryl ether bonds via either acidolysis or homolytic cleavage (Nakagame et al., 2011). The beneficial effect of organosolv pretreatment on subsequent cellulase hydrolysis has been explored in numerous previous studies (Santo et al., 2018; Guo et al., 2015). This pretreatment might be more expensive than some other pretreatment methods, but can generate lignin-derived value-added products which could be applied in many fields (Nagy et al., 2009; Pan et al., 2006).

It has been revealed that cellulose ultrastructure, mainly cellulose degree of polymerization (DP) and crystallinity index (CrI), shows great effect on cellulase hydrolysis (Hallac and Ragauskas, 2011; Hall et al., 2010). Populous variant has been tested and applied in studying gene function and biomass recalcitrance (Meng et al., 2016; Yoo et al., 2017). It has also been demonstrated that natural variants displayed differently in digestibility from their control counterparts. In the past, studies on Populus natural variant showed that low recalcitrant Populus natural variants showed higher sugar yields after hydrothermal pretreatment (Meng et al., 2016). Low lignin content, low cellulose DP, high cellulose accessibility and S/G ratio favor glucose release from Populus (Yoo et al., 2017). However, comparison of different pretreatment methods on cellulose ultrastructure and the following sugar release was not reported, especially for poplar variant with low content of lignin. The structural related-factors in these natural variants which are correlated with Populus recalcitrance are still unclear. Recent studies demonstrated that poplar with low content of lignin modified by modern molecular biotechnology could achieve improved accessibility (Mansfield et al., 2012; Van Acker et al., 2014). Although the impact on these modifications from an economic perspective is currently unknown, it gives us a new method to overcome the problem.

In the present study, populous variant with less lignin content (BESC 131) was chosen as the raw material. Digestibility of pretreated populous was evaluated and compared. Cellulose was isolated from populous variant, and their physicochemical characteristics were determined by GPC, ATR-FTIR and CP/MAS 13C-NMR to elucidate pretreatment mechanism of changed cellulose ultrastructure and improved glucose release.

2. MATERIALS AND METHODS

2.1. Materials

Four year old Populus Trichocarpa (BESC-131) was provided by Oak Ridge National Laboratory, TN. Cellulase (from *Trichoderma reesei* ATCC 26921), β-glucosidase (from *Aspergillus niger*) and antibiotics (Antibiotic Antimycotic Solution, A5955) were purchased from Sigma. Papers exceeding the page limit will need to revised and resubmitted.

2.2. Pretreatment

Dilute acid pretreatment (DA): Dilute sulfuric acid (0.5% w/w) was employed to pretreat *Populus* (liquid/solid was 20) at temperature of 170 ^{o}C for 2 h. Pretreatment was conducted in a stirred Parr 1 L reactor (Model 4842, Parr Instrument Co., IL, USA). After being submerged in a cold water bath to stop the pretreatment, the pretreated residue was obtained by vacuum filtration and was washed with deionised water until pH being neutral. Liquid hot water pretreatment (LHW): *Populus* (liquid/solid was 20) was pretreated at temperature of 180 ^{o}C for 44 min. Alkaline pretreatment (Alkali): *Populus* (liquid/solid was 20) was pretreated by Sodium hydroxide (1% w/w) at temperature of 120 ^{o}C for 1h. Organosolv pretreatment (OS): *Populus* (liquid/solid was 8) was pretreated by aqueous ethanol (v/v: EtOH/H_2O=65/35) with sulfuric acid (1.0 wt %) as catalyst. The pre-treatments were conducted at 180°C for 60 min. The pretreated *Populus* was washed with warm (60°C) ethanol/water (0.65:0.35, 3×200 mL).

2.3. Cellulase hydrolysis

Populus was hydrolyzed at 2% (w/v) in 0.05 M acetic acid-sodium acetate buffer (pH 4.8) at 150 rpm and 45 oC for 72 hours. Cellulase and β-glucosidase loading was 25 U/g and 50 U/g. Antibiotics was added at 10 ml/L. Liquid samples at different intervals were taken to analyse glucose content by high performance Liquid chromatography (Angilent Technologies 1200 series). 10.00 mM HNO3 was used as the eluent. Flow rate was 0.6 ml/min.

2.4. Analytical method

Composition analysis

Populus were treated hydrolyzed by 72% sulfuric acid and then 4% dilute acid based on the National Renewable Energy Laboratory protocols (determination of carbohydrates and lignin content in biomass) (NREL, Golden, CO, USA) to get insoluble Klasson lignin and dissolved sugars. The monosaccharide was analysed by high performance Ion chromatography (Dionex ICS-3000).

GPC analysis

Cellulose isolated from *Populus* by peracetic acid and sodium hydroxide was mixed with anhydrous pyridine and phenyl isocyanate at 70 oC for 48 h to get cellulose tricarbanilate. The molecular weight distributions of the cellulose tricarbanilate were analysed on an Agilent GPC SECurity 1200 system equipped with four Waters Styragel columns (HR0.5, HR2, HR4, HR6). THF was used as the mobile phase (1.0 mL/min). Molecular weights (Mn and Mw) were calculated by Polymer Standards Service WinGPC Unity software (Build 6807).

ATR-FTIR analysis

PerkinElmer Spectrum 100 FTIR spectrometer (Perkin-Elmer Inc., Wellesley, MA, United States) was employed to analyse structural features of *Populus*. Spectra were obtained by 64 scans accumulation from 4,000 to 500 cm−1 at 4 cm−1 resolution.

CP/MAS 13C-NMR analysis

Bruker DSX-400 spectrometer (Bruker, Billerica, MA, United States) was used to carry out the Solid-state NMR determination at frequencies of 100.55 MHz. CP/MAS experiments utilised a 5 μs (90°) proton pulse, 1.5 ms contact pulse, 4.0 second recycle delay and 8 K scans.

2.5. Simons' staining

Direct Orange 15 (CAS:1325-35-5) and Direct Blue 1 (CAS 2610-05-1) was employed to study cellulose accessibility of Populus , which were obtained from Pylam Products Company, Inc. Briefly, Populus (100 mg) was mixed with 1 mL phosphate buffer (0.3 M, pH 6.8), 1 mL NaCl solution (1%), and 1 mL of dye mixture (Direct Orange 15: Direct Blue 1=1:1,

with increasing concentration). After being absorbed constantly, the absorbance of the supernatant solution was determined by PerkinElmer UV-Vis Lambda at 455 nm and 624 nm, respectively. Specifications

3. RESULTS AND DISCUSSION

3.4. Solid recovery and composition analysis of Populus variant after pretreatments

The solid recovery after various pretreatment was determined and compared. It was obvious to find that organosolv pretreatment left the least amount of solid residue, suggesting that more hemicellulose and lignin was removed by organic solvent, which was also indicated by Figure1. The solid yield of different pretreatment was decreased by the following order: Alkali (86%) >LHW (76%) >DAP (67%) >OS (53%). The glucan loss was less than 20% for all pretreatment methods. Alkali pretreatment caused the least effect on glucan. Hemicellulose removal is beneficial for the following cellulase hydrolysis, as indicated by previous studies (Zhang et al., 2012). DA, LHW and OS showed more ability for hemicellulose removal than Alkali pretreatment, which only removed less than 30% of hemicellulose. As lignin could adversely affect cellulase attack, the remove of lignin was an important aim of pretreatment (Yang et al., 2016). The four leading pretreatment method exhibited different lignin removal capability. Organosolv pretreatment removed most of lignin (94%), followed by Alkali (24%), LHW (5%) and DAP (2%). The great ability of dissolving and removing both of hemicellulose and lignin could explain the lowest pretreatment yield of organosolv pretreatment.

The chemical compositions were determined as presented in Table 1. From the composition analysis, it can be found that the Populus mutant shows higher content of glucan, lower content of lignin and xylan, being compared with the standard poplar (data not shown). Great difference of composition of Populus can be observed after being pretreated by different methods. Basically, glucan content was increased after pretreatments, due to various removal extents of hemicellulose and lignin. Most of hemicelluloses were degraded during DAP and LHW pretreatment process, indicated by low xylan content and totally removed arabinan and galactan in pretreated residue. Alkali pretreatment removed part of hemicellulose (xylan, arabinan and galactan) and lignin. Most of lignin was recovered after the organosolv pretreatment, which resulted in the highest content of glucan.

Table 1: Composition analysis of pretreated Populus after different pretreatments (%)

	Glucan	Xylan	Arabinan	Galactan	Mannan	Lignin
Raw	51.66	12.82	0.40	0.69	1.94	20.81
DAP	63.91	0.21	0.00	0.00	0.18	30.29
LHW	57.09	1.93	0.00	0.00	0.52	25.91
Alkali	58.31	11.04	0.22	0.30	0.30	18.30
OS	90.94	3.07	0.00	0.00	1.07	2.34

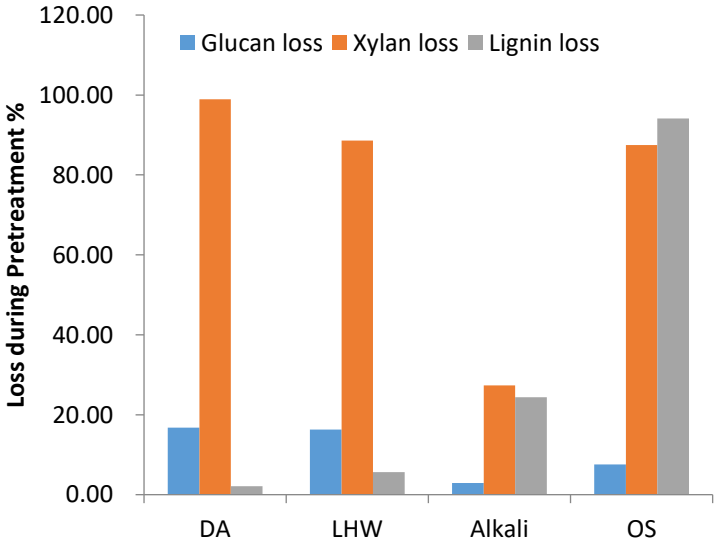

Figure 1: Loss of various components (B) during different pretreatment process

3.2. Sugar release analysis

Populus were hydrolyzed by cellulase and β-glucosidase with solid loading of 2% (w/v) at 45 oC. Figure 2 showed that glucose was released at a high rate during the first 4h, then at a reduced rate until 48h. Cellulose conversion of Populus

variant varied from 26.8% to 86.3%. The organosolv pretreated Populus variant showed the highest glucose yield, the other three pretreatment methods were comparable. Furthermore, xylose was the second largest amount of monosaccharide released from pretreated Populus. The cost of bioethanol could be reduced significantly if xylose was fermented to ethanol effectively. The amount of sugar obtained during cellulase hydrolysis process based on raw material was presented in Table 2. It was obvious to find that glucose release was greatly improved after pretreatment, which was increased from 0.14g/g to 0.45g/g after OS pretreatment, followed by Alkali, DA and LHW was comparable. Due to extensive remove of xylan during DA, LHW and OS pretreatment (as shown in Figure1B), xylose release after cellulase degradation was not much improved, even decreased after DA pretreatment. The glucose+xylose yield was increased in the following order: Raw<DA<LHW< Alkali<OS.

The most increased extent of glucose release after organosolv pretreatment was mainly due to the extensive remove of xylan (87%) and lignin (94%), making more cellulose exposed for cellulase attack. Earlier studies showed that structure of lignicellulosic materials would become loosen after OS pretreatment, which was caused by dissolution of lignin and hemicellulose, thus, could promote the adsorption of fungi cellulase onto pretreated residue (Koo et al., 2011). Populus variant after Alkali pretreatment got the second most amount of sugar release, which was 0.42g/g. During Alkali pretreatment, almost the same amount of xylan (27%) and lignin (24%) was removed. It was reported that during alkaline pretreatment the ester linkages between xylan and lignin was saponifed, and resulted in lignin dissolution. Lignin removal would increase cellulose accessibility to cellulase and decrease non-productive adsorption of cellulases to lignin during enzymatic hydrolysis (Sun and Cheng, 2002). DA and LHW pretreated Populus showed comparable glucose and xylose release. These two pretreatment methods both involve similar mechanism, including hemicellulose solubilization and partially delignifcation on various extents. Compared with LHW pretreated Populus variant, which removed 87% of xylan and 6% of lignin, although nearly 99% of xylan and 2% of lignin were depolymerised and solubilised during DAP, a little bit more sugar was obtained from LHW pretreated Populus variant. It was suggested that lignin removal was much more important than that of xylan to improve digestibility of biomass.

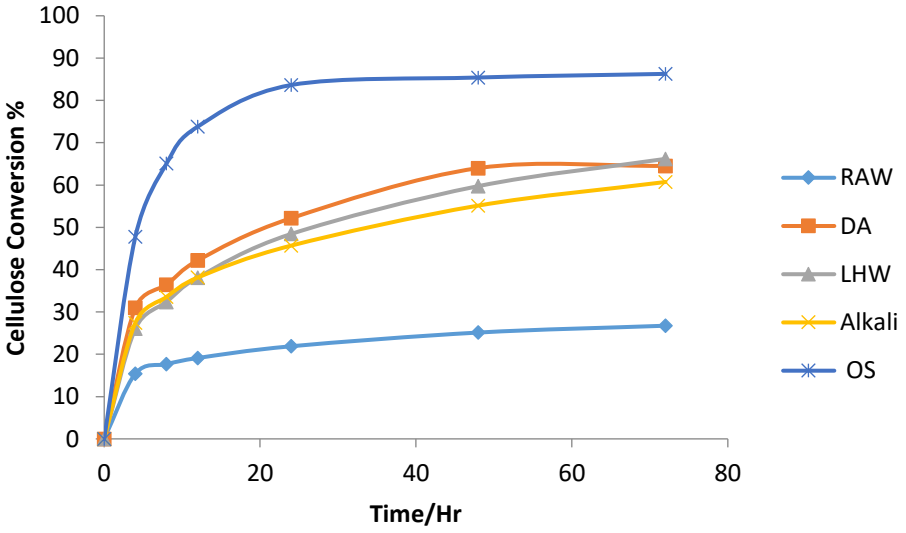

Figure 2: Cellulose conversions of Populus during 72 hours of enzyme hydrolysis

Table 2: Monosaccharide release from Populus variant during cellulase hydrolysis process

Sample	Amount g/g raw material		
	Glucose	Xylose	Glucose+Xylose
BESC 131	0.14	0.02	0.16
BESC 131-DA	0.28	0.01	0.29
BESC 131-LHW	0.29	0.02	0.31
BESC131-Alkali	0.34	0.08	0.42
BESC 131-OS	0.45	0.03	0.48

3.3. GPC analysis

It was reported that the molecular weight of cellulose could affect cellulase hydrolysis. On one hand, shorter cellulose chain is beneficial for enzyme attack, on the other hand, more reducing ends in cellulose with lower molecular weight is easier for exoglucanase to release cellobiose (Pan et al., 2007). Number average molecular weight (Mn), weight average molecular weight (Mw) and the degree of polymerization (DP) of celluloses from Populus was determined by GPC and the

results were shown in Table 3. It was found that DP of cellulose was decreased drastically after all kinds of pretreatment process. Cellulose from DA pretreated biomass showed the lowest molecular weight and DP. The following are organosolv, LHW and alkali pretreated Populus. The improved sugar release after pretreatment was partly due to cellulose molecular weight reduction, which was in accordance with previous studies (Hu et al., 2012; Pu et al., 2013). OS pretreated Populus showed the highest cellulose conversion, but DP of cellulose was not the lowest. The cellulose conversion after various pretreatments was decreased by OS>DA=LHW> Alkali, while that of cellulose DPw was LHW > Alkali > OS > DA. To be specific, DA and LHW pretreated Populus showed similar cellulose conversion, but Mw of cellulose from LHW pretreated Populus was almost as 3 times as that of cellulose from DA pretreated Populus. It was suggested that molecular weight of cellulose does have effect on cellulase hydrolysis performance, but that effect is limited.

Table 3: Molecular weight and degree of polymerization of cellulose in Populus

Sample	Mn	Mw	DPn	DPw	PDI
RAW	343640	1858600	662	3581	5.4
DA	49689	178750	96	344	3.6
LHW	87846	553890	169	1067	6.3
Alkali	90701	495500	175	955	5.5
OS	64341	384300	124	740	6.0

3.4. ^{13}C CPMAS NMR analysis

^{13}C CPMAS NMR spectroscopy was employed to compare the relative intensity of the ultrastructural components within cellulose fibrils from native and pretreated *Populus*. Cellulose is composed by crystalline and amorphous regions. The two regions exhibit totally different reaction rate during cellulase hydrolysis process. Generally, crystalline region is much more difficult to be degraded by cellulase than amorphous region (Liu et al., 2017). The C4 region extends over a chemical shift range of 80-92 ppm. Signals assigned to cellulose amorphous domains appear as broad while that of crystalline domains are sharper (Foston, 2014; Pu et al., 2006). It was indicated that crystalline region accounted for more than a half in native Populus, as shown in Figure4B. Earlier researches revealed that pretreatments under high pressure could disrupt inter and/or intra hydrogen bonding of cellulose and resulted in changed crystalline structure (Mosier et al., 2005a). As shown in Figure4B, cellulose crystallinity index (CrI) was slightly increased after pretreatment, indicating that part of amorphous region was destroyed or/and transformed during pretreatments. Organosolv and alkali pretreated Populus showed the lowest CrI, followed by LHW and DAP. Although OS and Alkali pretreated Populus showed similar CrI, which was 60%, sugar release was different. Be consistent with previous results, as an indicator of biomass recalcitrance, CrI did not show any correlation with glucose release from pretreated biomass (Meng et al., 2016; Brienzo et al., 2014).

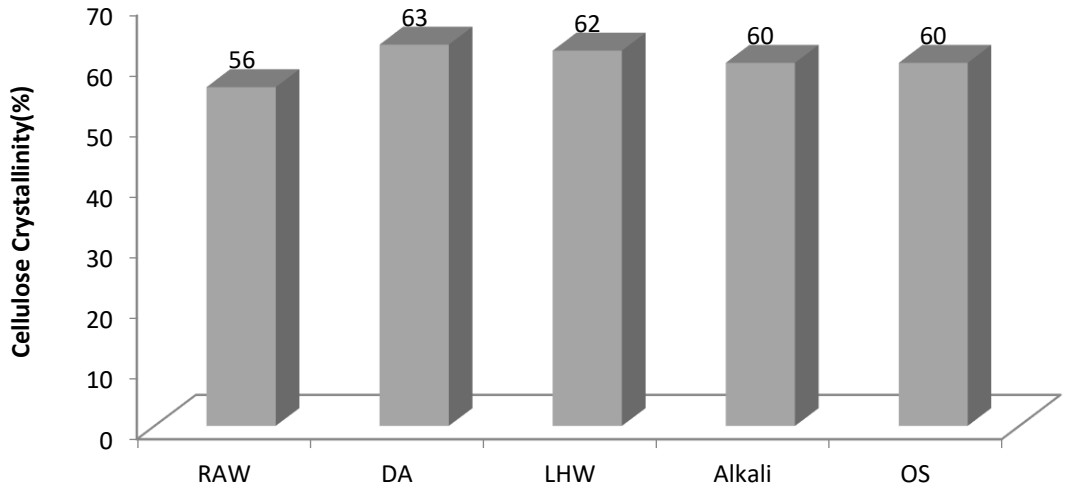

Figure 4: Cellulose crystallinity index of cellulose (B) from Populus

The relative intensity of the cellulosic ultrastructural components, including cellulose crystalline allomorphs, para-crystalline cellulose and cellulose fibril surface, and their changes after various pretreatments were shown in Figure5. It was analysed by a seven-peak model and a least-squared non-linear fit of the C4-carbon region in the 13C CP/MAS spectrum. It was

indicated that after different pretreatments, generally, the content of para-crystalline was increased at various extent, which is a form of cellulose that is ordered between crystalline and amorphous cellulose (Ioelovich et al., 2010). In addition, cellulose Iα content was decreased, accompanied by increase of I(α+β) content. This was in accordance with previous studies, which suggested preferential degradation and/or transformation of cellulose Iα into cellulose Iβ during pretreatment process under high pressure (Sun et al., 2014a, 2014b). Furthermore, relative proportion of amorphous (i.e., accessible and inaccessible fibril surfaces) cellulose was decreased, indicating of favored hydrolysis of amorphous cellulose over that of crystalline cellulose during pretreatment process. The results were also confirmed by crystallinity index analysis, which was increased after pretreatment. Comparing effect of different pretreatments on the ultrastructure changes, it was found that DA pretreated Populus contained the most of para-crystalline cellulose, which was due to the preferential degradation/removal of amorphous cellulose under acidic conditions (Foston and Ragauskas, 2010). Populus pretreated by Alkali showed the most percentage of Iβ, suggesting that more cellulose Iα was converted into cellulose Iβ under alkali conditon.

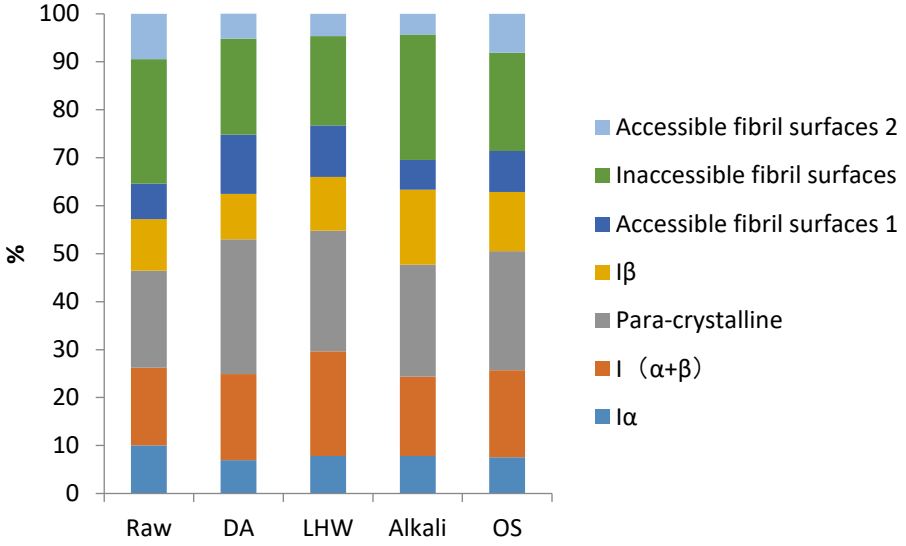

Figure 5: Relative percentage of cellulose crystalline allomorphs, para-crystalline cellulose and cellulose fibril surface in the pretreated poplar solids

3.5. Simons' staining analysis

The changes of cellulose accessibility to cellulase caused by various pretreatments were also evaluated. Simons' staining method is commonly applied to analyse cellulose accessibility to cellulase by Direct Blue (DB) 1 and Direct Orange (DO) 15 (Meng et al., 2016). The two dyes show different molecular size and maximum UV absorption wavelengths, populate different surfaces of cellulose during staining. The total maximum adsorbed DO 15 and DB 1 dye is a strong indicator of the ease of attack by cellulases (Chandra et al., 2008). As shown in Table 4, pretreated Populus variant exhibited increased cellulose accessibilities to cellulase, compared with raw material. Organsolv pretreated Populus variant showed the highest cellulose accessibility, followed by Alkali, LHW and DA. It was found that pretreated Populus with the most Simons' staining ability also exhibited the most sugar release during cellulase hydrolysis process. It was noted that the accessibility of cellulose was increased in the same order with sugar release, DA<LHW<Alkali<OS, suggesting that cellulose accessibility is a good indicator of digestibility of pretreated Populus by cellulase attack. Previous researches also indicated that positive correlation was observed between cellulose accessibility and digestibility of biomass (Meng et al., 2016; Yoo et al., 2017).

Table 4: The maximum amount of direct orange and blue dye adsorbed by Populus during Simons' stain

Substrate (Populus)	Maximum adsorbed orange dye (mg/g sample)	Maximum adsorbed blue dye (mg/g sample)	Total adsorbed dye (mg/g sample)
Raw	17.1	24.3	41.4
DA	23.5	29.4	52.9
LHW	27.9	32.2	60.1
Alkali	34.4	37.5	71.9
OS	29.0	51.5	80.5

4. CONCLUSION

Key features related to biomass recalcitrance, including cellulose DP, ultrastructure and accessibility were compared after DA, LHW, Alkali and OS pretreatment on a comprehensive analysis of Populus for biofuel production. Composition analysis revealed that lignin and/or hemicellulose was removed variously during pretreatment. OS pretreatment removed the most amounts of lignin and hemicellulose and got the most sugar release by cellulase hydrolysis. Cellulose DP results showed that cellulose was degraded at different extent during pretreatment process. DA pretreated solid residue exhibited the least cellulose DP, followed by OS. 13C CPMAS NMR analysis indicated that cellulose CrI was slightly increased. Para-crystalline cellulose was increased and cellulose Iα was converted into cellulose Iβ after pretreatments. Lignin removal, combined with the changes of cellulose features were important to improved digestibility of Populus, especially the increased cellulose accessibility were the most important factors that related to biomass recalcitrance.

5. REFERENCES

Brienzo M, Ferreira S, Vicentim MP, Souza WD, Sant'Anna C, 2014. Comparison Study on the Biomass Recalcitrance of Different Tissue Fractions of Sugarcane Culm. *Bioenergy Res*, 7 (4), 1454-1465.

Cao S, Pu Y, Studer M, Wyman C, Ragauskas A, 2012. Chemical transormations of Populus trichocarpa during dilute acid pretreatment. *Rsc Adv*., 2, 10925-10936.

Chandra R, Ewanick S, Hsieh C, Saddler J, 2008. The characterization of pretreated lignocellulosic substrates prior to enzymatic hydrolysis, part 1: a modified Simons' staining technique. *Biotechnol. Prog.,* 24, 1178–1185.

Chen Y, Stevens M, Zhu Y, Holmes J, Xu H, 2013. Understanding of alkaline pretreatment parameters for corn stover enzymatic saccharification. *Biotechnol. Biofuels,* 6, 1–10.

Dien B, Jung H, Vogel K, Casler M, Lamb J, Iten L, Mitchell R, Sarath G, 2006. Chemical composition and response to dilute-acid pretreatment and enzymatic saccharification of alfalfa, reed canarygrass, and switchgrass. *Biomass Bioenerg,* 30, 880–891.

Foston M, Ragauskas A, 2010. Changes in lignocellulosic supramolecular and ultrastructure during dilute acid pretreatment of Populus and switchgrass. *Biomass Bioenerg*, 34,1885–1895.

Foston, M., 2014. Advances in solid-state NMR of cellulose. Curr. Opin. Biotech. 27, 176-184.

Guo Y. Zhou J, Wen J, Sun G, Sun Y, 2015. Structural transformations of triploid of *Populus tomentosa Carr*. ligninduring auto-catalyzed ethanol organosolv pretreatment. *Ind Crop Prod*, 76, 522–529.

Hallac B, Ragauskas A, 2011. Analysing cellulose degree of polymerization and its relevancy to cellulosic ethanol. *Bioruels Bioprod Biorefin.,* 5 (2), 215-225.

Hall M, Bansal P, Lee J, Realff J, Bommarius A, 2010. Cellulose crystallinity-a key predictor of the enzymatic hydrolysis rate. *Febs J*, 277 (6),1571-1582.

Hu F, Ragauskas A, 2012. Pretreatment and Lignocellulosic Chemistry. *Bioenergy Research*, 5 (4),1043-1066.

Ioelovich M, Leykin A, Figovsky O, 2010. Study of cellulose paracrystallinity. *Bioresource*, 5,1393–1407.

Jang S,Kim H, Jeong H, Kim J, Yeo H, Choi I, 2016. Effect of ethanol organosolv pretreatment factors on enzymatic digestibility and ethanol organosolv lignin structure from Liriodendron tulipifera in specific combined severity factors. *Renew. Energ*., 87, 599-606.

Jin Y, Huang T, Geng W, Yang L, 2013. Comparison of sodium carbonate pretreatment for enzymatic hydrolysis of wheat straw stem and leaf to produce fermentable sugars. *Bioresour. Technol,* 137, 294–301.

Kim I, Lee B, Park J, Choi S, Han J, 2014. Effect of nitric acid on pretreatment and fermentation for enhancing ethanol production of rice straw. *Carbohyd.Polym.,* 99, 563-567.

Koo BW, Kim HY, Park N, Lee SM, Yeo H, Choi IG, 2011. Organosolv pretreatment of Liriodendron tulipifera and simultaneous saccharifi cation and fermentation for bioethanol production. *Biomass Bioenerg* 35, 833–1840.

Li X, Lu J, Zhao J, Qu Y, 2014. Characteristics of corn stover pretreated with liquid hot water and fed –batch semi-simultaneous saccharifcation and fermentation for bioethanol production. *PLoS One*, 9(4):e95455.

Liu Z, Inokuma K, Ho S, Riaan H, Willem H, Tomohisa H, Akihiko K, 2017. Improvement of Ethanol Production From Crystalline Cellulose via Optimizing Cellulase Ratios in Cellulolytic Saccharomyces cerevisiae. *Biotechnol. Bioeng.*, 114,1201-1207.

Meng X, Pu Y, Yoo C, Li M, Bali G, Park D, Gjersing E, Davis M, Muchero W, Tuskan G, Tschaplinski T, Ragauskas A, 2016. An In-Depth Understanding of Biomass Recalcitrance Using Natural Poplar Variants as the Feedstock. *ChemSusChem*, 9, 1–13.

Mosier N, Wyman C, Dale B, Elander R, Lee YY, Holtzapple M, Ladisch M, 2005a. Features of promising technologies for pretreatment of lignocellulosic biomass. *Bioresour Technol*, 96,673–686.

Mosier N, Hendrickson R, Ho N, Sedlak M and Ladisch MR, 2005b. Optimization of pH controlled liquid hot water pre-treatment of corn stover. *Bioresource Technol*, 96:1986–1993.

Nagy M, David K, Britovsek G., Ragauskas A, 2009. Catalytic hydrogenolysis of ethanol organosolv lignin. *Holzforschung* 63 (5), 513–520.

Nakagame S, Chandra R, Sadller J, 2011. The influence of lignin on the enzymatic hydrolysis of pretreated biomass substrate. In: In: Zhu, J.Y., Zhang, X., Pan, X.J. (Eds.), Sustainable Production of Fuels, Chemicals, and Fibers from Forest Biomass1067. American Chemical Society, New York, pp. 145–167.

Pan X, Kadla J, Ehara K, Gilkes N, Saddler J, 2006. Organosolv ethanol lignin from hybrid poplar as a radical scavenger: relationship between lignin structure, extraction conditions, and antioxidant activity. *J. Agric. Food Chem.*, 54 (16), 5806–5813.

Pan X, Xie D, Kang K., Yoon S, Saddler J, 2007. Effect of organosolv ethanol pretreatment variables on physical characteristics of hybrid poplar substrates. *Appl. Biochem. Biotech.,* 137, 367-377.

Pu Y, Ziemer C, Ragauskas A, 2006. CP/MAS C-13 NMR analysis of cellulase treated bleached softwood kraft pulp. *Carbohyd. Res*., 341, 591-597.

Pu YQ, Zhang DC, Singh PM, Ragauskas AJ, 2008. The new forestry biofuels sector. *Biofuels Bioprod Biorefining*, 2,58–73.

Pu Y, Hu F, Huang F, Davison BH, Ragauskas AJ. 2013. Assessing the molecular structure basis for biomass recalcitrance during dilute acid and hydrothermal pretreatments. *Biotechnol. Biofuels*, 6 (1):15-27.

Ragauskas AJ, Beckham GT, Biddy MJ, Chandra R, Chen F, Davis MF, Davison BH, Dixon RA, Gilna P, Keller M, Langan P, Naskar KA, Saddler JN, Tschaplinski TJ, Tuskan GA, Wyman CE, 2014. Lignin valorization: improving lignin processing in the biorefnery. *Science*, 344,709–818.

Santo E, Rezende A, Bernardinelli D, Jr P, Curvelo S, deAzevedo R, Guimarães G, Polikarpov I, 2018. Structural and compositional changes in sugarcane bagasse subjected to hydrothermal and organosolv pretreatments and their impacts on enzymatic hydrolysis. *Ind Crop Prod*, 113, 64–74.

Selig MJ, Viamajala S, Decker SR, Tuker MP and Himmel ME, 2007. Deposition of lignin droplets produced during dilute acid pre-treatment of maize stems retards enzymatic hydrolysis of cellulose. *Biotechnol .Prog.*, 23,1333–1339.

Sun Q, Foston M, Meng X, Sawada D, Pingali V, O'Neill M, Li H, Wyman E, Langan P, Ragauskas J, Kumar R, 2014a. Effect of lignin content on changes occurring in poplar cellulose ultrastructure during dilute acid pretreatment. *Biotechnol. Biofuels*, 7,150-163.

Sun Q, Foston M, Sawada D, Pingali V, O'Neill M, Li H, Wyman E, Langan P, Pu Y, Ragauskas A, 2014b. Comparison of changes in cellulose ultrastructure during different pretreatments of poplar. *Cellulose,* 21, 2419–2431.

Sun X, Xu F, Sun R, Fowler P, Baird M, 2005. Characteristics of degraded cellulose obtained from steam-exploded wheat straw. *Carbohyd. Res.*, 340 (1), 97-106.

Sun Y, Cheng J, 2002. Hydrolysis of lignocellulosic materials for ethanol production: A review. *Bioresour Technol* 83:1–11.

Yang B and Wyman CE, 2008. Pre-treatment: The key to unlocking low-cost cellulosic ethanol. B*iofuels Bioprod Bioref,* 2, 26–40.

Yao L, Yue J, Zhao J, Dong J, Li X, Qu Y., 2010. Application of acidic wastewater from monosodium glutamate process in pretreatment and cellulase production for bioconversion of corn stover – Feasibility evaluation. *Bioresour. Technol.*,101, 8755-8761.

Yao L, Yang H, Yoo C, Meng X, Li M, Pu Y, Ragauskas A, Sykes R, 2017. Adsorption of cellobiohydrolases I onto lignin fractions from dilute acid pretreated *Broussonetia papyrifera*. *Bioresour. Technol.,* 244, 957-962.

Yao L, Yoo C, Meng X, Li M, Pu Y, Ragauskas A, Yang H, 2018a. A structured understanding of cellobiohydrolase I binding to poplar lignin fractions after dilute acid pretreatment. *Biotechnol Biofuels*, 11,96-106.

Yao L, Yang H, Yoo C, Meng X, Pu Y, Hao N, Ragauskas A, 2018b. Characteristics of lignin Fractions from Dilute acid Pretreated switchgrass and their effect on cellobiohydrolase from *Trichoderma longibrachiatum. Frontiers in Energy Research*, 6,1-9.

Yang H, Xie Y, Zheng X, Pu Y, Huang F, Meng X, Wu W, Ragauskas A, Yao L, 2016. Comparative study of lignin characteristics from wheat straw obtained by soda-AQ and kraft pretreatment and effect on the following enzymatic hydrolysis process*. Bioresour. Technol.,* 207, 361–369.

Yoo C, Yang Y, Pu Y, Meng X, Muchero W, Yee K, Thompson O, Jr Rodriguez M, Bali G, Engle N, Lindquist E, Singan V, Schmutz J, DiFazio S, Tschaplinski T, Tuskan G, Chen J, Davison B, Ragauskas A, 2017. Insights of biomass recalcitrance in Populus trichocarpa natural variants for biomass conversion. *Green Chem.,* 19, 5467-5478.

Zhang J, Tang M, Viikari L, 2012. Xylans inhibit enzymatic hydrolysis of lignocellulosic materials by cellulases. *Bioresour. Technol.*, 121, 8–12.

320: Investigation of the possibility re-using retired batteries from EV for office building

Xiaojing HAN[1], Shuli LIU[1,2],*,Ashish SHUKLA[2], Liu YANG[1], Yongliang SHEN[1], Ming SONG[1]

1 School of Mechanical and Vehicular Engineering, Beijing Institute of Technology, China
2 School of Energy, Construction and Environment, Coventry University, Coventry, CV1 2FB, UK
**Corresponding Author: Shuli.Liu@coventry.ac.uk*

Currently, fast development of the electric vehicles (EVs) technology has potential to replace the fuel-oil driven conventional vehicles to solve energy, economic and ecological issues. Having increased number of EVs will produce more power batteries at the end of their service life though still useful for other purposes. Therefore, there is big market for the retired electrochemical batteries from EVs for energy storage systems at various scales. The aim of the paper is to analyse the technical and economic potential of fully utilising these retired power batteries for their secondary life. When these batteries reach the 70%-80% of their initial capacities, they do not meet the energy and power requirements for electric vehicles, but they can still generate considerable benefits if they are properly used in applications with lower current rates, such as grid and buildings as the energy storage systems (ESSs). In order to investigate the available value of the retired power batteries, performance tests and theoretical calculation has been carried out. As case study office building, has been used to study the feasibility of retired batteries. Due to the structure of regulated energy price in Beijing, the results show that although the energy consumption increase by 942.5 kWh every year, the cost will save $916.74. However, if the retired power batteries from Nissan Leaf will be used in a single room of 100 m^2 office building, having occupancy of 10 staff, the total battery cost is $3304.90. The cost of retired power batteries can be covered completely in approximate 4 years and can provide cost savings further on from 5th year. This will be a new and promising direction of development for energy sustainability and environment conservation in the future.

Keywords: Retired batteries; Office building; Energy storage; Feasibility analysis

1. INTRODUCTION

The rapid development of electric vehicles has replaced conventional fuel-oil transportation. This is mainly because of concerns about environmental quality and energy issues arising from greenhouse gas emissions. In response to the energy and environmental issues in the automotive field, the Chinese government has promoted different types of city buses and private cars for public transportation. The government has also induced more governmental subsidies and stimulating policies since 2008. The number of Chinese electric vehicles, such as hybrid electric vehicles, plug-in hybrid electric vehicles and battery electric vehicles has reached nearly 579,000 in 2017. This brings China ranking first around the world in the use of EVs. Several governments around the world have set up decisive policies and stimulating plans, such as tax incentives to consumers and financial supports for automakers. This is to attract more consumers adopt electric vehicles (Shafiei et al., 2015: page 615). The targets set for different penetration scenarios from low to high in the near future have been achieved. Depending on type of electric vehicles, these factors including sales price, types of EVs, gasoline and electricity prices, governmental subsidies and stimulating policies provided more choices to consumers (Shokrzadeh et al., 2016: p703).

The future of electric transportation as a potential solution in solving energy and climate issues has been studied in depth (Brown et al., 2010: page 3797). However, the growing number of retired power batteries from EVs has led to severe issues of re-using them in the view of economy, human health and ecology. For example, when the effective charging capacity of retired power batteries falls below 80% they cannot be used in EVs. However they are still in good performance when they are discarded and has been studied in some countries. Though in many cases, these retired power batteries are often discarded at the end of their life cycle. This leads to great waste resource and environment pollution.

During the cycle life of power batteries from electric vehicles, retired power batteries can be re-used in applications for energy storage system at end of their automotive life. Many technologies and applications of ESS (energy storage system) have been analysed using renewable energy. Until now, many applications have been studied to investigate the potential of energy storage technologies among these applications (Eyer et al., 2010: page 322). Utility grid combined with retired power batteries has played a significant role in load shifting and peak shaving, which has been used for energy storage system several years ago. As we all know, these retired power batteries from EV need to be collected, tested, classified, reconfigured and repacked for new energy storage applications. The significant work is to estimate the effective remaining life of retired power batteries at the beginning of secondary life applications, i.e., the vehicular SOH (state of health), and to predict the battery degradation rate in secondary life applications before being re-used. After disassembling these retired power batteries from EV and removing the batteries packs, the retired power batteries packs would be entered secondary use life for energy storage system.

The most significant considerations, before applying these retired power batteries for energy storage system are: (1) whether these retired power batteries can be successfully used in other applications, such as buildings; and (2) how long these retired power batteries can serve consumers from feasible and economic perspectives. To date, the scope of second use applications, the feasibility, and popularity of these energy storage applications has not widely been investigated in China. The objective of this paper is to re-use these retired power batteries and to apply them in office buildings for energy storage system. Based on the regulated energy price in Beijing, the economic feasibility and benefits of retired power batteries from EV into proper applications has not yet been comprehensively investigated. By battery degradation testing and a series of cost calculations, feasibility analysis of retired batteries will be illustrated in this paper.

2. RESEARCH

2.1. Precious research

Energy storage technology at the beginning of the late 19th century refers to the storage of electrical energy through conversion to other forms of energy (Tusiani et al., 2007: page 15). This is suggested as one possible direction of second use applications of retired power batteries from EV. Re-using of retired power batteries from EV at end of automotive of life has been investigated in literature. In a pioneering study, they (Ahmadi Leila et.al, 2014: page 64) investigated the environmental feasibility of re-using electric vehicle batteries at their automotive end-of-life into stationary applications in a parameterised life cycle model. Authors (Ahmadi Leila et.al, 2014: page 9) also analysed the energy efficiency of Li-ion battery packs for secondary use. The technology of re-using Li-ion batteries for energy storage system to balance demand and supply of electricity has also been studied. A series of simulations were used for the analysis and investigation of cost savings from reused batteries packs for peak-shifting (Heymans et al., 2014: page 22). Sathre Roger et.al, (2015: page 82) studied the energy and climate effects of second-life use of electric vehicle batteries to enable the expansion of intermittent renewable electricity supply. Rooftop photovoltaic systems combined with lithium-ion battery storage are raised. Based on the theory of battery energy storage, the techno-economic feasibility of integrated PV-battery storage systems has been investigated in the article (Uddin et al., 2017: page 20). The economic viability of second use batteries from electric vehicles for load shifting and peak shaving in residential applications is analysed and the impacts of residential storage systems on the electricity market are further investigated in the paper (Madlener et al., 2017: page 3806). As well, the technical and economic feasibility of retired power batteries is assessed in support of residential sector by s series of battery performance and simulations (Assunção et al., 2016: page 120). The second life batteries from EVs have been explored by the academia and the industry to reduce the costs of original EV (Martinez-Laserna et al., 2018: page 701).

Recovery of lithium metal through recycling from power batteries can be an alternative and feasible option to meet demand and supply for sustainable energy systems (Swain B, 2016: page 401). Among many aforesaid options use of retired EVs power batteries for office buildings has not be investigated in detail and is focal point of the current research.

2.2. Application of battery second use

The main innovation of the paper is about the investigation of re-using retired power batteries in office building at daytime for energy storage system to solve the high-energy consumption costs. It is a significant breakthrough that retired power batteries from EV will be successfully used in office building for energy storage system. The objective is to protect these retired power batteries from being thrown away by finding accessible ways so that more retired power batteries from EV can be reused when they still have the potential of secondary recycling. A greater quantity of retired power batteries should preferably be reused instead of being sent to their final disposal, such as landfills. Considering these aspects, the study focuses on the development of re-using retired power batteries for energy storage system, such as utility grid, office building and other fields.

EV adoption and availability of retired power batteries from EV will rise alongside an evolving energy storage system, including increasing amounts of renewable electricity sources. This paper investigates the feasibility whether second-life use of retired power batteries can provide electricity storage role for office building at daytime, such as electricity demand of building during the high-energy consumption. With the structure of regulated energy prices, energy storage technology greatly improves the energy efficiency and saves cost in various scales.

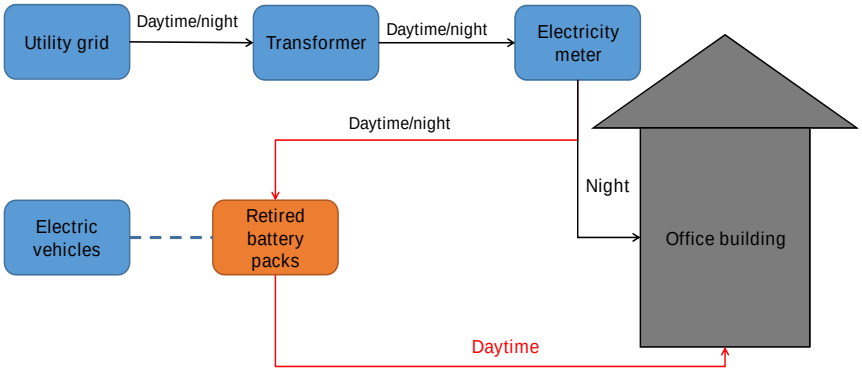

Figure 1: process of energy consumption for a single room of office building

Considering the benefits of second-life of power batteries to adjust diurnal energy supply, so we expand applications of intermittent renewable energy storage. As shown in Figure 1, retired battery packs is reused for office building at daytime, which store energy from utility grid mostly at evening hour. As shown in Figure 3, due to the regulated energy price, period between 23:00 and 06:00 is key phase of the lowest energy price. This is the most feasible and economic energy storage period. High energy consumption is mainly supplied in the period between 10:00 and 14:00 at daytime, at the highest energy price, which is nearly 4 times of the lowest one. Energy storage demand at valley time is strongly needed and better serve consumers during day time. Although coal-fired electricity is used in China, these retired power batteries may, in principle, be applied in other scenarios where coal-fired power is more common, which can meet lower requirements and use for load shifting and peak shaving. The proposed application technology will be tested and investigated whether retired power batteries in office building can meet the demand and save cost. This development direction will be popular among office buildings in the near future. Using governmental subsidies and stimulating policies and further cooperation from government will prove more useful in implementing this technology for more cost savings in near future.

3. FEASIBILITY ANALYSIS

3.1. Battery performance analysis

Battery degradation is one of the most significant factors for different types of electric vehicles. All power batteries from EVs experience calendar aging, a gradual decomposition of the electrolyte for a given temperature over the life of the power batteries (Christophersen et al., 2007: page 1002). However, the continuous long-time operating of EV batteries

accelerates their degradation especially if the thermal cycling is not closely controlled. Battery degradation mostly includes capacity and power fade. Capacity fade is mainly by the migration resistance of lithium-ion between the cathode and anode (Cheng et al., 2017: page 1602). Power fade is due to a gradual increase in internal impedance that decreases available power. More specifically, for different types of electric vehicles, both capacity fade and power fade each have two reasons. For capacity fade (Ahmadi et al., 2014: page 65): (1) a reduction in capacity indicates large state-of-charge swings; (2) battery capacity is corresponding to charge-depleting range of the automotive. Considering the capacity fade, (1) the minimum and the maximum high voltage but limits will be achieved at lower battery discharge and charge currents respectively; (2) a further reduction in useable battery capacity as a given power will require additional current to compensate for a lower terminal battery voltage (Arora et al., 1998: page 3647). Lithium-ion batteries degrade during utilization in different ways that are not easily tested or well predicted. It is impossible to predict accurately voltage of charge and discharge, effective charging capacity of power batteries from different types of electric vehicles. One significant issue is to analyse the value of retired batteries due to degradation. In the article (Debnath et al., 2014: page 582), the model of capacity degradation of an EV battery is shown. Such research results show that the maximum allowed degradation for the automobile use was 70% of the battery original capacity, giving 5871 cycles for applications, remaining capacity of 30% after automobile usage, giving 4500 cycles, which ensures 3600 deep cycles (Debnath et al., 2014: page 583). Based on the effective cycle number, these retired power batteries can be reused for energy storage system and achieve their residual value in the long run.

Battery packs with regular extreme state of charge cycles or extreme temperature issues will be possible to have more degradation, and potentially more single cell failures, than one that has suffered from less extreme usage. Thus, these battery packs with more extreme stress conditions would need more testing for secondary energy storage system. The next is to transport the collected retired power batteries and gather them in a processing plant. Then according to different capacity of each single cell of battery pack, classification is operated precisely and seriously. Because of consistency and suitability of retired power batteries from EV, collected battery packs would be tested for a series of operations after disassembling, such as electrochemical testing, degradation testing and testing of the integrity of the cooling plates (Ahmadi et al., 2014: page 64).Due to choice and preference from consumers, retired power batteries from EV that experience 20% degradation in capacity or power fade will be considered to end their useful life and will be replaced by new power batteries. That means significant potential for prolonging their lifetime and for reducing economic value and energy investments that can be offset original cost of power batteries. In this paper, these tested retired battery packs will be reused for office building application.

Accordingly, it is reasonable to (take into consideration) think about the potential whether these retired power batteries from electric vehicles can applied in some places for energy storage system, taking into consideration the health of the retired power batteries; the cost of collecting. A retired product discount factor considered to be valuable, which price is $38 to $132 per kWh (Heymans et al., 2014: page 27), can be reused and whether customers is willing to pay for this; and the alternative value of recycling. Based on considerations above, customers can still accept retired power batteries as energy storage system in the long run. The retired batteries have been successfully reused in some scenarios, such as utility grid, electricity supply of buildings and so on, which received good results and make demonstration projects in many countries. Actually the value of reusing reconfigured batteries packs, availability of products and popularity of customers have not formed a large scale in Beijing of China, which need joint efforts of the governments and customers to realise the goals.

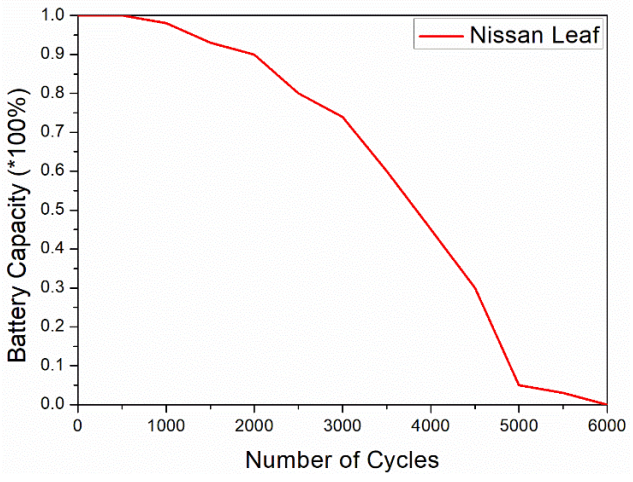

Figure 2: Degradation in % of the reused retired battery (Assunção et al., 2016 : p126)

Considering the battery degradation, a series of performance test will be made. As shown in Figure 2, the result shows that the capacity degradation for the reused retired battery, with 16.8kWh, a daily cycle and corresponding life time were considered for the analysis. The definition of the minimum value for which the batteries is still able to guarantee the technical benefits was defined as 25% of reference storage system of 9.32 kWh, being therefore 2.33kWh (Assunção et

al., 2016: page 125). As a result, for the reused large battery (Nissan Leaf), its lifespan was 13.5 years(Assunção et al., 2016: page 127).Considering the requirements of second application, the retired power batteries has taken a series of performance tests and can meet the energy storage system with lower current rates again. In this paper, battery packs from Nissan Leaf will be reused for office building energy storage, thus greatly solving energy demand at daytime.

3.2. Economic analysis

To understand the economic effectiveness of the retired battery packs for energy storage system, it is useful to calculate the present cost of the energy consumption in a single room of office building, which can be compared to the cost of operating system with retired battery packs for at least 4 years. The most significant issue is cost savings for consumers, focusing on benefits how much these retired battery packs application can bring about, a series of investigations will be analysed in the following. The energy consumption appliances in a single room of office building have been listed in Table 1, according to usage time and the power of different elements, a series of calculations will be made to assess the cost due to regulated energy prices of commercial electricity in a single room of office building.

Table 1: Basic parameters of different appliances in a single room of office building

Profiles	Power (W)	Number	Energy consumption time
Air conditioner	1060W	1	08:00-18:00
Light	20W	6	08:00-18:00
Computer	290W	10	08:00-18:00
Printer	295W	1	08:00-18:00
Water dispenser	420W	1	08:00-18:00

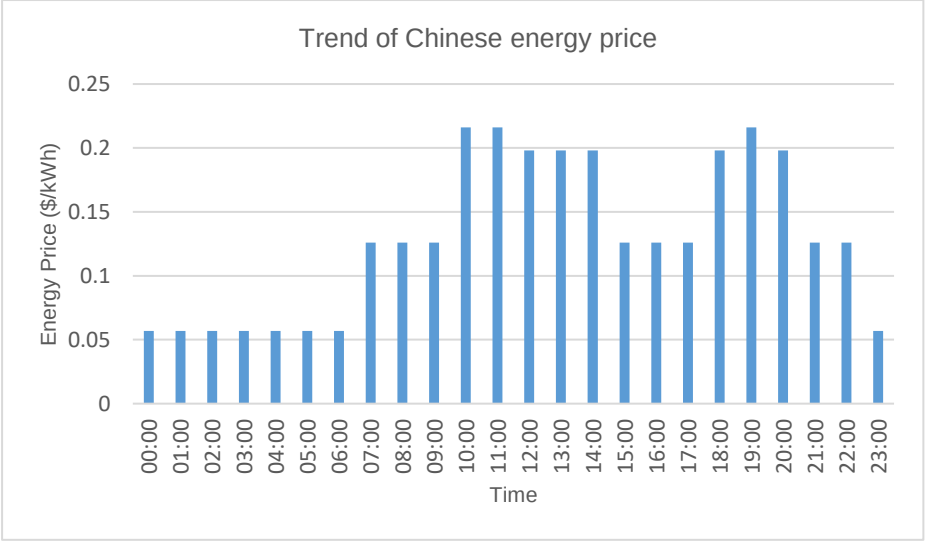

Figure 3: Energy consumption price of office buildings at different time (Data from State Grid)

According to 2017 commercial electricity implementation standards, regulated energy prices range from approximately $0.057 to $0.216 per kWh. To maximise the potential savings to the consumer, the charging and discharging periods must be chosen in accordance with the lowest and highest energy pricing, respectively. As shown in Figure 3, due to the structure of the regulated price in Beijing, which the lowest price of commercial electricity is nearly 4 times of the highest one, considering this occasion, using electricity during the periods outside of the minimum and maximum energy prices actually saves cost. Therefore, the availability of retired battery packs as energy storage system brings new chance for shifting 7 hours (at least 23:00-06:00) value of energy, thus greatly contributing to the load shifting and peak shaving in office building. The structure of regulated price relates to the demand for energy especially in Beijing, a big city of energy consumption in China. Therefore, the structure of regulated price will promote the popularity of retired batteries for cost savings.

The annual energy costs for office buildings is a big fee, basically energy consumption from continuous operating appliances. Energy consumption and predicted consumption with battery at different time are presented in Figure4, the highest energy consumption is between 8:00 and 18:00, with the same energy consumption of 4.795 kWh/hour, excluding from energy consumption of 2 kWh/hour between 12:00 and 13:00. Normally the work time is between 8:00 and 12:00 in the morning, and between 13:00 and 18:00 in the afternoon, the lunch time is 12:00-13:00, workday is between Monday and Friday, it usually takes a staff 9 hours every day. In Figure 4, load shifting for the hourly pricing periods of office building one day, as shown in Figure3, is illustrated.

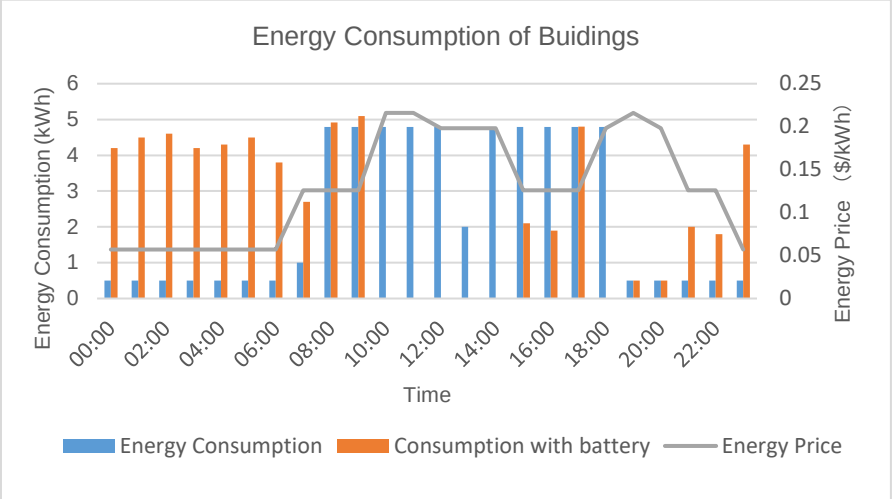

Figure 4: Example of average hourly energy consumption in one day of office buildings

Due to the lower evening energy prices shown in Figure4, the battery packs store energy at evening time is predicted by a series of analysis. The energy capacity of battery packs are sufficient enough to cover the entire period of peak pricing. The retired power batteries can store energy from grid during the lowest energy prices, which will be applied in office building during highest energy prices. As shown in Table 2, the energy consumption of different occasion is presented, the energy storage system increases energy consumption by 6.6% and annual energy use by 15180 kWh, however, the cost saving by $3.67 every day shown in Table 3.

Table 2: Typical energy consumption data for a single room of office buildings

	Typical consumption (kWh/day)	Consumption with battery (kWh/day)	Increase in energy consumption with battery (%)
Everyday	56.95	60.72	6.6

Table 3: Cost savings under regulated energy price

	Energy consumption cost ($/day)	Energy consumption cost with battery ($/day)	Cost savings ($/day)
Total	10.54	6.87	3.67

Data is calculated based on the 22 days per month, not including holiday (at least 14 days), the energy consumption increase by 942.5 kWh every year, however, the cost will save $916.74. However, if the retired power batteries with capacity of 63 kwh will be used in a single room of office building of approximate 100 m^2, holding 10 staff in it, the battery cost is totally $3304.90 (based on $49.23/kWh in this paper), that means we can recover the cost in about 4 years.

Considering the high cost of new power battery, the pricing clearly stands in the purchase of retired battery, which range in value from $38 to $132 per kWh (Heymans et al., 2014: page 27). Although high cost of retired battery packs and energy consumption rising, the cost has decreased greatly in the long run, after 5 years, retired power batteries can bring benefits. As shown in Table 4, compared with small capacity of Citroen C0, retired power batteries from Nissan Leaf with capacity of 16.8 kWh at second life are selected, such battery packs are needed for energy storage in office building, with the structure of regulated energy price, it is estimated that cost savings can cover the cost of retired battery packs in approximate 4 years, however, the residual capacity still can meet the requirement in 5th year, which will greatly benefit from retired battery packs for consumers in the long run.

Table 4: Remaining capacity of the battery from EV, considering 70% degradation of its initial capacity (Assunção et al., 2016: page 122)

Electric Vehicle	Initial capacity(kWh)	2nd Life Capacity (kWh)	Capacity in the 5th year(kWh)	Capacity in the 10th year (kWh)
Nissan Leaf	24	16.8	15.46	10.92
Citroen C0	14.5	10.15	9.12	5.1

3.3. Environmental and safety analysis

Before reusing battery packs for energy storage, it is significant to learn about the safety risks. Retired power battery tends to thermal runaway, which leads to fires or explosions (Heymans et al., 2014: page 26). When the temperature is between

13°C and 150°C, spontaneous reactions can happen between the electrolyte and cathode (Balakrishnan et al., 2006: page 403). To avoid various risks, it is necessary to consider the possible shortages between building and battery energy storage, as well as the fires and explosions associated with battery.

The technology of battery energy storage benefits environment by shifting energy demand from coal to clean energy, thus greatly reducing the non-greenhouse gas emissions. The study (Ahmadi et al., 2014: page 69) is purposefully restrained in its consideration of environmental impacts, focusing only on potential CO_2 emissions as a significant and broad based indication of environmental performance. Electric vehicles, compared with internal combustion engine with gasoline, reduces the main greenhouse gases (CO_2, N_xO) emissions, thus improving the air quality and environment conservation. However, the disposal problems of power batteries have gradually appeared. Although recycling of them have successfully been applied in some fields for energy storage system. The completely scrapped batteries will be a series of mechanical and chemical disposal. Wastes, such as Lithium-ion batteries, have the potential to release toxic elements to water supplies if disposed of on the land in an uncontrolled occasion. Due to this reason, most countries require protective measures for landfills that receive hazardous wastes or garbage. By intercepting, collecting, and properly treating leachate before it can reach the underlying and surrounding environment, groundwater resources are preserved, protecting human health and reducing the financial burden on the water treatment.

4. DISCUSSION

4.1. Implication for economy

The presented results have shown that investigation in second-use battery storage systems are profitable for the consumers of office building under certain circumstances. For an annual increase of energy consumption by 6.6% and energy use by 15180 kWh, however, the cost will save $916.74. The cost of retired battery is $38 to $132 per kWh, the capacity of more 60 kWh is needed for a single room of office building, the whole investment is a big cost. However, it is estimated that cost savings can cover the cost of retired battery packs in approximate 4 years. Due to the structure of regulated energy price in Beijing, consumers can benefit from these retired battery packs in the 5^{th} year. The economic feasibility has been illustrated in this paper, if the governmental subsidies and some stimulating policies can support the recycling of retired batteries, the benefits and popularity for consumers will greatly improve in the future.

4.2. Implication for the technology

Energy storage technology has successfully been applied in grid, residential house and other fields, based on the advanced technology, retired battery applications will be involved in various scales in the near future. Although applications of energy storage system have not formed a large scale in China. However, the government has already begun to address the issue of recycling of retired batteries from EV a few years ago, some research institutes and universities have conducted substantive analysis and feasible investigation of the technical performance of retired batteries. Every battery pack consists of hundreds of single cell, performance test and battery installation will consume a lot of manpower and material resources, advanced technologies and efficiency is the key to success. Based on mature technologies, these tested and assembled battery packs will better be reused in lower demand situations to meet the energy storage of consumers.

4.3. Implication for the environment

Compared with traditional internal combustion engine vehicles, electric vehicles have solved energy, economic and ecologies issues. EV adoption in China has been popular among consumers since 2008. Further the government subsidies and stimulating policies, the sales of new energy electric vehicles have exceeded 500,000 in 2017. This brings china, ranking first in the world, thus reducing the non-greenhouse emissions and improving the air quality and environment conservation. However, the disposal problems of power batteries have gradually appeared. Although recycling of them have successfully been applied in some fields for energy storage system, the completely scrapped batteries will be a series of mechanical and chemical disposal. Wastes, such as Lithium-ion batteries, have the potential to release toxic elements to water supplies if disposed of on the land in an uncontrolled occasion. Due to this reason, most countries require protective measures for landfills that receive hazardous wastes or garbage. By intercepting, collecting, and properly treating leachate before it can reach the underlying and surrounding environment, groundwater resources are preserved, protecting human health and reducing the financial burden on the water treatment.

5. CONCLUSION

In this paper, a promising application of using retired power batteries for a single room of office building has been investigated. A series of performance tests and economic analysis have illustrated the feasibility of energy storage system with lower current rates. Storing energy at evening hours of the lowest price periods and supplying for the peak time resulted in significant savings. Some of the key conclusions from the current study are as follows;

- Based on the 22 days per month, not including holiday (at least 14 days), the energy consumption increase by 942.5 kWh, however, the cost will save $916.74 every year;
- It is estimated that if the retired power batteries with capacity of 63 kwh will be used in a single room of office building of approximate 100 m^2, having oppupancy 10m2/person, the total battery cost is $3304.90 (based on $49.23/kWh);
- Pay back periods for the retired power batteries is approximately 4 years;
- Re-using retired power batteries from EV will extend the cycle lifetime, reduce waste resource and cost savings. The proposed method is viable from technological, economic and ecological perspectives. This will be a new and promising direction of development for energy sustainability and environment conservation in the future.

6. REFERENCES

Ahmadi L, Yip A, Fowler M, et al., (2014), "Environmental feasibility of re-use of electric vehicle batteries", Sustainable Energy Technologies & Assessments, Vol. 6, p.64-74.

Ahmadi L, Fowler M, Young S B, et al., (2014), "Energy efficiency of Li-ion battery packs re-used in stationary power applications", Sustainable Energy Technologies & Assessments, Vol. 8,p.9-17.

Arora P, White RE, Doyle M, (1998), "Capacity fade mechanisms and side reactions in lithium-ion batteries"，J Electrochem Soc ,Vol.145, p.3647.

Assunção A, Moura P S, Almeida A T D, (2016), "Technical and economic assessment of the secondary use of repurposed electric vehicle batteries in the residential sector to support solar energy"， Applied Energy, Vol.181, p.120-131.

Balakrishnan P G, Ramesh R, Kumar T P, (2006), "Safety mechanisms in lithium-ion batteries", Journal of Power Sources, Vol.155, p.401-414.

Brown S, Pyke D, Steenhof P, (2010), "Electric vehicles: The role and importance of standards in an emerging market", Energy Policy, Vol.38, p.3797-3806.

Cheng J L, Xin-Hai L I, Wang Z X, et al., (2017), "Mechanism for capacity fading of 18650 cylindrical lithium ion batteries", Transactions of Nonferrous Metals Society of China, Vol.27, p.1602-1607.

Christophersen J P, Hunt G L, Ho C D, et al.,(2007), " Pulse resistance effects due to charging or discharging of high-power lithium-ion cells: A path dependence study",Journal of Power Sources, Vol. 173,p.998-1005.

Debnath U K, Ahmad I, Habibi D, (2014), "Quantifying economic benefits of second life batteries of gridable vehicles in the smart grid", International Journal of Electrical Power & Energy Systems, Vol.63,p.577-587.

Eyer J M, Corey G P,(2010) ,"Energy storage for the electricity grid: benefits and market potential assessment guide : a study for the DOE Energy Storage Systems Program", Geburtshilfe Und Frauenheilkunde, Vol. 45,p.322-5.

Heymans C, Walker S B, Young S B, et al., (2014), "Economic analysis of second use electric vehicle batteries for residential energy storage and load-levelling", Energy Policy, Vol. 71,p.22-30.

Madlener R, Kirmas A,(2017)," Economic Viability of Second Use Electric Vehicle Batteries for Energy Storage in Residential Applications ", Energy Procedia, Vol. 105,p.3806-3815.

Martinez-Laserna E , Gandiaga I, Sarasketa-Zabala E, Badeda J, Store D-I,Swierczynski M, Goikoetxea A, (2018), "Battery second life: Hype, hope or reality? A critical review of the state of the art", Renewable and Sustainable Energy Reviews, Vol.93,p.701-718.

Shafiei E, Davidsdottir B, Leaver J, et al., (2015), "Comparative analysis of hydrogen, biofuels and electricity transitional pathways to sustainable transport in a renewable-based energy system", Energy, Vol. 83,p.614-627.

Shokrzadeh S, Bibeau E, (2016), "Sustainable integration of intermittent renewable energy and electrified light-duty transportation through repurposing batteries of plug-in electric vehicles", Energy, Vol. 106,p.701-711.

Sathre R, Scown C D, Kavvada O, et al., (2015)," Energy and climate effects of second-life use of electric vehicle batteries in California through 2050", Journal of Power Sources, Vol. 288,p.82-91.

Swain B, (2016), "Recovery and Recycling of Lithium: A Review", Separation & Purification Technology, Vol.172,p.388-403.

Tusiani M D, Shearer G, (2007), "LNG: a nontechnical guide", PennWell.

Uddin K, Gough R, Radcliffe J, et al., (2017), "Techno-economic analysis of the viability of residential photovoltaic systems using lithium-ion batteries for energy storage in the United Kingdom", Applied Energy, Vol. 206,p.12-21.

321: Feasibility analysis of solar heating system in rural areas in China

Yongliang SHEN[1], Shuli LIU[1,2]*, Ashish SHUKLA[2], Liu YANG[1], Xiaojing HAN[1], Ming SONG[1]

[1] School of Mechanical and Vehicular Engineering, Beijing Institute of Technology, China, shenyl0104@163.com
[2] School of Energy, Construction and Environment, Coventry University, Coventry, CV1 2FB, UK, Shuli.Liu@coventry.ac.uk
**Corresponding Author: Shuli.Liu@coventry.ac.uk*

The most rural areas in China are rich in solar energy providing potential for energy-saving, emission-reduction, enhancing life quality of life for rural residents. However, advanced solar technologies for heating purpose has not been widely used because the high capital cost requirements. This paper presents the current status on solar energy heating technologies applied in rural areas for China. Paper also investigates solar energy collecting system, thermal energy storage, heating terminal, auxiliary heat source and analyse the methods to increase the efficiency while keeping the cost minimal. China has four major climatic zone and it has been found that solar heating can be applicable and reduce the cost in all four regions. Four heating models of regions were given in paper for reference in engineering application with the cost of 2131, 3055.6, 4075.6 and 2661.2 yuan/a respectively. It presents the adaptability strategy of some potential equipment's will depend on the economic development in rural areas of China.

Keywords: solar energy; rural areas; heating system; cost

1. INTRODUCTION

China has abundant solar energy, annual sunshine hours of its two-thirds areas is greater than 2200 hours and the total solar radiation on the surface is more than 4190MJ/m^2, which is equivalent to 17000 billion ton of coal (Zhao, 2013: page 1). Solar energy technologies, including solar photovoltaic system and solar heating system, have been widely used domestically and abroad because of its low pollution and endless supply. However, there are several factors affecting solar energy utilization technologies development, such as low efficiency and high cost.

In 2016, the per capita housing construction area of rural residents in China is 45.8 m^2, with an average annual growth of 5.4%. In China, building energy consumption has been up to 40% since 1990–2014 in the nation's total energy use (Zeng, 2017: page 145). Currently coal is one of main source of energy for building energy consumption accounting for 8.14 billion tons i.e. 19.12% of the total energy consumption in the country (Ding, 2017: page 58). When coal is used as the main fuel for heating, the coal consumption is up to 30~40 kgce / (M^2·a) because of poor thermal insulation performance and low efficiency of heating system. This is 1.5 to 2 times the energy consumption of urban heating (Huang, 2017: page 19). This shows that by improving the system efficiency and replacing coal with clean energy e.g. solar provides huge potential for energy use reduction. Therefore, the solar energy utilization technology will be applied to rural heating, with great potential for energy saving, emission reduction and broad prospects. In 13th Five-Year plan, the Energy Bureau of the national development and Reform Commission pointed out that by 2020, more than 3 million demonstration projects of solar heating and heating in rural buildings were promoted throughout the country.

This paper aims two main parts: current status of solar heating system in China and feasibility analysis of solar heating system in rural areas in China, which present the heat collecting and thermal energy storage technologies, heating terminal and auxiliary heat source applied in China's rural areas.

2. CURRENT STATUS OF SOLAR HEATING SYSTEM IN CHINA.

2.1. Passive solar heating system

Several study has been reported on the use of passive solar heating system in Inner Mongolia, Beijing, Xinjiang, Tibet etc. (Meng, 2002: p316; Zheng, 1983: page 115; Dong, 2014: pages 37-38; Wang, 2008: page 130), which illustrated that:

- The passive solar house can increase the indoor temperature by 5-10°C in the heating season;
- Indoor thermal performance is closely related to wall insulation and thermal storage materials; and
- Cities with higher average temperature or higher sunshine rates can utilise passive heating system to meet thermal comfort requirements.

In recent years, phase change materials (PCMs) has been widely used in thermal storage research of passive solar houses in rural areas in China. Comparative analysis of heating wall with inner PCM and traditional heating wall was done by Zhang et al. (Zhang, 2010: pages 29-30) in rural area of north China. $Na_2HPO_4 \cdot 12H_2O$ was embedded in cement mortar can absorbed the excess heat and stored it. The author shown that the average temperature of the heating wall surface with PCM can reached to 360K.

Kang, a commonly used heating terminal in rural areas in China, has been studied along with passive solar houses in recent years. Chen et al. (Chen, 2006: page 24) studied the indoor thermal environment of rural residences in a coupled heating pattern of passive solar-collected wall and oven kang combination in rural area in Dalian, China. The correlation coefficient (mean value 0.753) under the coupling effect was significantly higher than that of Kang only (the average value was 0.323). The indoor air temperature reached to 20-22°C under the coupling effect, while 16-18°C under the Kang only. From the cost point of view, although the initial investment of the former increased by 10%, it can save about 50% of the heating coal in winter every year.

The biggest problem with passive solar house is the overheated indoor temperature in summer. In order to study the solution to the problem (Zhu, 2015: Page 58-59) in Dalian, northeast zone of China, did the experiment of the influence of colour changed on thermal performance of passive solar house. Venetian blind as the absorber board, its colour is changed by manual operation that the black pieces outward in the winter and the white ones outward in the summer. The result was that the indoor air temperature can reached 10°C or more in winter because of the passive heating effect of solar wall and decreased to 25°C or less because of the absorber board with white colour.

2.2. Active solar heating system

Taking a village in Beijing as an example, Zhang (Zhang, 2006: page 5) analysed the feasibility of active solar heating in rural areas in northern China. The author shown that using low-temperature hot water floor heating system for active solar heating can reduce energy consumption by 80%, which is similar to 1t of coal.

Huo (Huo, 2013: pages 53, 58-59) used rock and soil as heat storage materials and low-temperature hot water floor radiant heating systems to achieve a solar heating rate of 60 -76% during the heating period in the Beijing mountainous region and avoided the problem of low solar energy density and the inability to heat at night and on rainy days. In addition, the solutions to the above problems were proposed:

- Auxiliary electric heating;
- Heating with conventional energy; and
- Cross-seasonal heat storage.

Under the water tank volume of 300m^3, A (collector area) /V (regenerative water volume) in the 0.1-0.4 range conditions, Zhao (Zhao, 2013: page 218) utilised cross-seasonal heat storage technology to achieved solar energy guarantee rate of 31-54% in second year in Tianjin.

- Combined heating with other new exploitable energy sources

PCMs also can be used in active solar heating system (Figure 1). The several authors studied the effect of PCM on the heat transfer performance of floor heating system (Zhang, 2006: pages 59-66; Feng, 2011: page 56) and concluded that:

- The factors influencing the heat transfer performance of the floor are phase change temperature and the amount of PCM; and
- The energy storage ratio of the stabilised PCM floor is 16% to 21% more than that of the concrete floor.

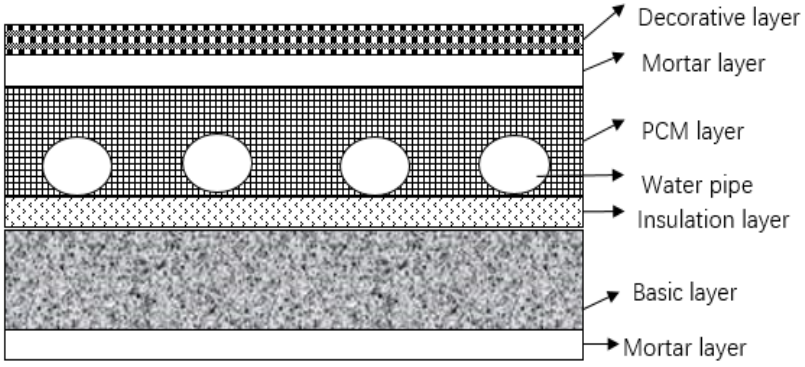

Figure 1: Each layer structure of low temperature hot water floor heating system [18] (Feng, 2011: Page 53)

A solar heating system is designed by Jing et al. (Jing, 2006: page 114). By combining the heat storage tank with the Kang, low-temperature hot water heating system can be used for heat storage and heating in winter and providing hot water in summer by regulating valve switch. In the overcast or rainy weather, the furnace can provide heat instead of solar energy. Water tank with a volume of 1.57 m^3 will be needed to storage heat when the temperature of water change by 5°C. Absolutely, there is plenty of space for a heat storage tank in cold areas in China.

The comparison of thermal performance (warming rate, cooling rate, heat storage capacity, average indoor temperature and PMV value) between solar kang and traditional kang was studied by Feng et al (Feng, 2016: pages 539-540). The author presented that temperature fluctuations of solar kang was smaller than that of traditional kang. In addition, the average indoor temperature increase of 3.28°C and the warming rate and cooling rate were 5.17°C/h and 3.01°C/h, which were less than that of traditional kang 8.57°C/h and 4.58°C/h. The total heat storage capacity of solar Kang is 1273w, which is higher than that of traditional Kang 1148w. What's more, the PMV value was -0.5, which absolutely meets human thermal comfort needs. In addition, the thermal capacity and thermal conductivity on thermal performance of a solar kang system was carried out by Yang et al. 2014. The simulation results illustrated that:

- Reducing the convective heat transfer resistance has little influence on kang body's energy storage; and
- More solar heat can be stored and less can be released to the room with the larger thermal capacity by changing the thickness of the upper kang plate. Larger thermal conductivity can helped to increase the heat release to the room.

3. FEASIBILITY ANALYSIS OF SOLAR HEATING SYSTEM IN RURAL AREAS IN CHINA

Through the technical and economic analysis of the related technologies including heat collection, storage and terminal, combined with the characteristics of Chinese regional architecture. Research seek the better solar energy heating model in rural areas for China. The analysis results can provide a theoretical basis for the promotion and utilization of solar heating system in rural areas in the future.

3.1. Solar collector

At present, the most common solar collector in the market includes flat plate collector, vacuum tube collector and compound parabolic collector, and their instantaneous thermal efficiency formula is (Liu, 2012: page 169):

$$\eta = a - \frac{b}{I}(t_f - t_a) \quad (3\text{-}1)$$

$$I = J_T/(3.6S_Y) \quad (3\text{-}2)$$

$$T^* = T* = (t_f - t_a)/I \quad (3\text{-}3)$$

Where, –a and b are the coefficients related to the type of solar collector;

–t_f and t_a are fluid temperature and outdoor temperature,°C;

–I is annual average sunshine intensity, W/m^2;

–J_T is average daily radiation, MJ/(m^2·d); and

–S_Y is average sunshine hours, h.

Based on previous studies and data of solar collector from China's market, the empirical formulas for thermal efficiency of various collectors were obtained, summarised in Table 1 and Figure 2 (Liu, 2009: page 50; Dong, 2013: page 45; Wan, 2012: page 96; Wang, 2012: page 88).

Table 1: The instantaneous efficiency of various collectors

Classification	Formulas
Flat plate collector	$\eta_1 = 0.732 - \frac{5.86}{I}(t_f - t_a)$
Evacuated tubular collector	$\eta_2 = 0.659 - \frac{2.796}{I}(t_f - t_a)$
Compound parabolic collector (Concentration ratio 1.5, non-tracking)	$\eta_3 = 0.689 - \frac{1.365}{I}(t_f - t_a)$

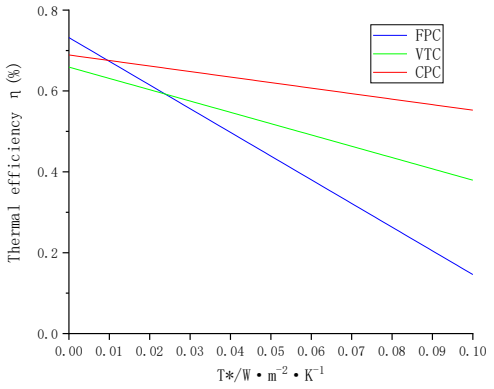

Figure 2: The efficiency curve of solar collectors

The heating areas in China were divided into four regions based on the conditions of the solar radiation and the climate, and the weather conditions of heating season in various regions are summarised in Table 2. Assuming that the heating water temperature of the inlet of collector t_f is 50°C, thermal efficiency of solar collectors can be acquired from the curve, which are summarised in Table 2.

Table 2: Weather conditions of heating season in various regions of China and thermal efficiency

Region	Areas in China	J_T	S_Y/h	t_a/°C	I	T*	Thermal efficiency
Ⅰ	Southwest China: The large part of the Tibet; The southern part of Shaanxi Province.	21.7	8.1	1.1	744	0.066	η_1=34.52% η_2=47.45% η_3=59.89%
Ⅱ	Northwest China: Ningxia; Xinjiang; Qinghai Province; Shaanxi Province; Gansu Province.	17.8	7.5	-8.3	659	0.088	η_1=21.63% η_2=41.30% η_3=56.89%
Ⅲ	Northeast China: Heilongjiang Province; Jilin Province; Liaoning Province.	14.8	6.5	-18.4	633	0.108	η_1=9.91% η_2=35.70% η_3=54.12%
Ⅳ	North China: Hebei Province; Shanxi Province; Shandong Province; Beijing, Tianjin; The part of Inner Mongolia.	14.5	5.8	-2.6	694	0.076	η_1=28.66% η_2=44.65% η_3=58.53%

The required areas of the solar collectors can be calculated according to (3-4), and the cost of various solar collectors (Table 3) can be obtained from market (Liu, 2012: page 44; Zhu, 2004: page 54; Cen, 1981: page 64).

$$A_c = \frac{86400 Q_H f_1}{J_T \eta (1-\eta_L)} \tag{3-4}$$

$$Q_H = q_v V (t_n - t_a) A \tag{3-5}$$

Where: - A_c is the collecting areas, m^2;
- Q_H is energy consumption of building heating, W;
- f_1 is solar energy guarantee rate, 0.3-0.8;
- η_L is the heat loss efficiency of hot water storage tank and pipeline, 0.2-0.3;
- q_v is volume heat index, 0.87 W/(m^3·°C) ;
- A is heating load adjustment coefficient of rural building, A=0.65;
- t_n is indoor temperature, t_n=16°C.

Table 3: Cost calculation of solar collectors

Region	Q_H	f_1	Collecting areas/m2			Unit Price (yuan/m2)	Total price		
			FPC	ETC	CPC		FPC	ETC	CPC
Ⅰ	2528	0.70	27.2	19.8	15.6	FPC:590 ETC:450 CPC:680	16048	8910	10608
Ⅱ	4122	0.60	74.0	38.7	26.7		43660	17415	18156
Ⅲ	5836	0.55	252.2	70.0	41.7		148798	31500	28356
Ⅳ	3155	0.50	43.7	28.1	20.9		25783	12645	14212

Assuming that the three collectors have a service life of 20 years, 10 years and 10 years respectively. The thermal efficiency and cost of various solar collectors are summarised according to the four regions, shown in Figure 3. Considering the cost, efficiency and the influence of heat collecting areas on the convenience of installation, the better selection of solar collectors in different regions is displayed in the Table 3.

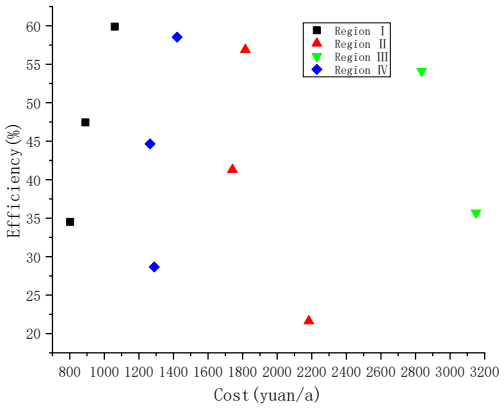

Figure 3: The thermal efficiency and cost of various solar collectors

Table 3: The selection of solar collector for various regions.

Region	Selection	Collecting areas/m^2	Efficiency	Cost/(Yuan/a)
I	Evacuated tubular collector	19.8	47.45%	891
II	Compound parabolic collector	26.7	56.89%	1815.6
III	Compound parabolic collector	41.7	54.12%	2835.6
IV	Compound parabolic collector	20.9	58.53%	1421.2

Although, the thermal efficiency of solar collectors are also related to the wind speed, fluid velocity and the temperature of hot water and the cost is related to the market, the overall trend is the same as the results.

3.2. Heat storage system

Because of the intermittent nature of the solar radiation, the solar collecting system cannot operate all the time. Therefore, when the solar radiation is sufficient, the part of heat obtained by the solar collecting system is supplied for heating directly to meet the user's needs; the remaining part needs to be stored and supplied to the user when there is no solar radiation. A few common heat storage devices will be analysed in the following paper.

Heat storage water tank

The cost and performance of the water tank is governed by the capacity, which can be calculated from Table 4 according to the formal research and engineering experience (Liu, 2012: page 48).

Table 4: The capacity of heat storage tank (Liu, 2012: Page 48)

The model of system	Small heating system	Short-term system	Seasonal system
The capacity of tank (L/m^2)	40~100	50~150	1400~2100

Because the system only meet the need of heating, the capacity of tank prefer to 50L/m^3 for easy to install. The capacity of water tank needed for heating system in various regions is summarised in Table 5. From this table, the size of these water tanks can be fully applied to the building to store heat. There are no specific budget calculations of water tanks because of the significant low proportion of its cost in the heating system.

Table 5: The capacity of heat storage tank of various regions

Region	The areas of solar collector (Table 3)	The capacity of tank (L)
I	19.8	990
II	26.7	1335
III	41.7	2085
IV	20.9	1045

Soil and stone heat storage

Soil is suitable for thermal storage because of its low thermal conductivity and high heat capacity, which is about 1kw·h/(m^{3}·°C). However, soil thermal storage will reduce the shear strength of the soil, which may cause ground subsidence, and the heat storage temperature should be limited to between 20°C-40°C (Zhang, 2000: Page 23). Therefore, auxiliary heat source may need to increase the temperature for heating, generally is heat pump. There is usually enough space in rural areas, especially in frontier cold area, to achieve soil seasonal heat storage.

Stone also can be the favorable material to store the heat because of its heat capacity with about 0.6 kw·h/(m^{3}·°C), which is slightly lower than soil. Similar to soil thermal storage, this method requires multiple holes in the stone to form heat storage capacity, so its structure is complex and difficult to utilise. At present, the way of stone thermal storage in rural areas in China has not been widely applied in engineering.

PCM heat storage

Compared with other thermal storage materials, the only drawback of phase change materials is that the price is too high, so they have not been widely applied in buildings. Paraffin as a better organic phase change material (moderate density, wide range of melting points without supercooling phenomenon, stable chemical properties and cheaper price, its application in building has been widely studied in passive heating system, which are shown in Table 6. In addition, some inorganic PCMs were mainly studied in active heating system that all shown reliable thermal performance (Zeng, 2017: pages 146-151).

Table 6: Applications and price of PCMs.

PCM	Applied technology	Applied position	Price (Yuan/t)
Paraffin	Passive system	Brick ; Cement, concrete and gypsum; Wall.	4000
Common inorganic materials	Active system	Heat pump; Radiant floor.	3000-4000

The only drawback is that the price is higher than ordinary materials. However, considering the maintenance and operation in the later, applying PCMs does not have obvious disadvantage compared to the initial investment. Yu Dan et al. (Yu, 2005: page 38) designed a combined phase change thermal storage unit using paraffin as a phase change material. The thermal efficiency of storage and discharge was increased by 30% to 40%, and the cost was only less than 2,000 yuan per year. Therefore, PCM can be used in passive solar houses to save the cost of solar collectors in regions where solar radiation is abundant.

Heating terminals

Because of the high cost of capillary radiation that is not suitable for use in rural areas, only the thermal performance analysis and economic analysis are carried out on the radiator, low temperature floor radiation, fan coil and solar Kang. Exergy efficiency and the cost of these heating terminals were usually be used to select the better terminals, the results shown in Table 7 (Zu, 2010: page 7; Pan, 2018: page 43). It has been found that radiant floor heating has advantages both in terms of thermal performance and economy.

Table 7: Exergy analysis of heating terminals (Zu, 2010: page 7; Pan, 2018: page 43).

Terminal	Inlet exergy kJ/kg	Outlet exergy kJ/kg	Profit exergy kJ/kg	Exergy efficiency (%)	Initial investment	Cost yuan/m^{2}·a
Radiator	34.45	19.25	15.2	44.1	2500	21.11
Fan coil	10.50	6.03	4.47	42.6	4500	19.5
Floor radiation	2.74	0.70	2.04	74.5	8000	17

Auxiliary heat source

The auxiliary heat source, an important part of the solar heating system, plays a significant role in continuous cloudy days or at night, and the principle of selection is the cost. The parameters of some typical auxiliary heat source under the condition of heat load with 5000W are shown in the Table 8 (Zhang, 2012: page 48).

Electric heating with the high operating costs is not suitable for use in the rural areas (Table 8). On the contrary, both air source heat pump and water source heat pump have higher thermal efficiency and smaller operating cost.

Table 8: Comparison of auxiliary heat sources (24h per day and 120 day per year) (Zhang, 2012: page 48).

	Air source heat pump	Water source heat pump	Electric heating
COP	3.0	5.0	0.95
Energy	Electric	Electric	Electric
Heat value	3600 kJ/kw	3600 kJ/kw	3600 kJ/kw
Consumption	1.67kw/h	1kw/h	5.26kw/h
Initial investment (yuan/m^2)	44.53	90	0
Operation cost (yuan/h)	1.08	0.65	3.42
All cost (yuan/a)	3333 (24h)/ 870 (5h)	2322 (24h)/ 840 (5h)	9849.5 (24h)/ 2052 (5h)

Selection of heating mode

Based on the above results, the economy of solar heating and conventional energy heating have been compared. Assuming that the 20 durable years of heating terminals and auxiliary heat source for solar heating and ignoring the maintenance costs of various equipment. The operation costs are only caused by auxiliary heat source (Table 9). It has been found that the cost of solar heating is significantly less than the conventional energy heating apart from the Region Ⅱ and region Ⅲ. This is mainly because of the low outdoor temperature and less solar radiation. However, solar heating projects will receive government subsidies and can save a lot of conventional energy. Therefore, the better heating mode for different regions can be selected according to the estimated results in the Table 10.

Table 9: The cost comparison of solar heating and of conventional energy heating

	Region Ⅰ	Region Ⅱ	Region Ⅲ	Region Ⅳ	Conventional heating
Initial investment (yuan)	25910	35156	45156	31212	17000
Operation cost (yuan/a)	390	390	390	390	1872
All cost (yuan/a)	2131	3055.6	4075.6	2661.2	2722

Table 10: Selection of heating mode.

Region	Mode	Cost (yuan/a)
Ⅰ	ETC + Water tank + low-temperature water floor radiation + Water source heat pump/ Passive solar heating	2131.0
Ⅱ	CPC + Water tank + low-temperature water floor radiation + Water source heat pump/ Passive solar heating	3055.6
Ⅲ	CPC + Water tank + low-temperature water floor radiation + Water source heat pump	4075.6
Ⅳ	CPC + Water tank + low-temperature water floor radiation + Water source heat pump	2661.2

4. CONCLUSION

The analysis of the appropriate solar heating mode in rural areas in China led to the following conclusions given below:

- Several solar heating technologies has been investigated and research prove their feasible application for rural areas. However, due to high cost use of some advance technologies have been badly impacted.
- Even though high initial investment in solar heating systems, it is possible to recover the additional investment due to low operation cost. This makes solar energy technology more lucrative for masses and need further promotion.
- The climate conditions in northern China are very complicated. Different regions should use different heating technologies and devices to ensure that the thermal performance of the entire system is optimised with minimal cost.
- PCM heat storage technology can be utilised in economically affluent areas. However, due to high cost technology might take further research before its use for rural areas.

5. REFERENCES

Cen H, 1981.The calculation of the solar energy guarantee rate f. Acta Energiae Solaris Sinica, 61-70.

Chen B, Zhuang Z, Yang W, 2006. Indoor thermal environment of rural residences in a coupled heating pattern of passive solar-collected wall and oven-kang combination. Heating Ventilating & Air Conditioning, 20-24.

Ding Y, 2017. China's building energy consumption research report shows that carbon emission reduction has entered the total control stage. Architectural Design Management, 58.

Dong C, 2013. Analysis and Study on thermal efficiency of trough solar collector. North China Electric Power University.

Dong L, 2014. Simulation study on indoor thermal environment of passive solar house heat stored by thick-and-heavy envelope. Shihezi University.

Feng G, Huang K, Chen Q, Liu Q, Lu M, 2011. Experimental research on hot water heating system with phase change energy storage floor. Journal of Chongqing University, 34(S1):52-57.

Feng G, Wang Q, Li G et al., 2016. Study on Solar KANG Heating System for Cold Areas. Procedia Engineering, 146:536-540.

Huang J, Chen J, 2017. The feasibility of solar regional heating in China. District Heating, 18-25.

Huo J, 2013. Study on several problems of direct utilization of solar energy in mountainous buildings in Beijing. North China University of Technology.

Jing F, Wang J, Zhang X, 2006. Solar kang heating system for cold areas. Low Temperature Architecture Technology, 113-114.

Liu B, Zhu D, Chen Y, 2012. Discussion on the present situation and development trend of rural heating in northern China. Science & Technology Information, 168-169.

Liu G, 2009. Efficiency analysis of evacuated tubular collector and flat collector. China Appliance Technology, 50-51.

Liu S, 2012. Study on solar heating system in rural area of Hebei. Hebei University of Engineering.

Meng C, Ba T, Ma G, 2002. A Simple Method for Optimizing and Sizing of Indirect Passive Solar Heating Elements. Energy Conservation Technology, 311-319.

National Bureau of Statistics of the People’s Republic of China. http://www.stats.gov.cn/

Pan L, Xu Z, Yang Q, 2018. Analysis on different terminal form of household air-source heat pump heating systems. Heating Ventilating & Air Conditioning,40-43.

People's Republic of China 2017 national economic and social development statistical bulletin. http://www.stats.gov.cn/tjsj/zxfb/201802/t20180228_1585631.html

Urban historical weather query. http://www.tianqi.com/

Wan S, 2012. Discussion on annual average heat collection efficiency of solar collectors in Shanghai area. Water & Wastewater Engineering, 95-98.

Wang J, Wang J, Li K, 2012. Thermal performance of a new type of concentrating CPC heat pipe vacuum tube collector. Yangtze River Delta Energy Forum, 577-583.

Wang L, 2008. Study on the heating of passive solar building in Tibet. Southwest Jiaotong University.

Yang M, Yang X, Wang Z et al., 2014. Thermal analysis of a new solar kang system. Energy & Buildings,531-537.

Yu D, Song Y, Cao Y, 2005. Feasibility of applying multiple phase change materials on a new solar energy heating system. China Construction Heating & Refrigration, 37-39.

Zeng C, Liu S, Shukla A, 2017. Adaptability research on phase change materials based technologies in China. Renewable & Sustainable Energy Reviews,145-158.

Zhang K, Yu L, 2000. The Technology of Thermal Storage to Utilize Solar Energy. BUILDING ENERGY & ENVIRONMENT, 22-26.

Zhang K, 2012. Selection and discussion of auxiliary heat source for solar heating system. Heating & Refrigeration, 46-48.

Zhang Q, Di H, Lin K, 2006. Simulation on the thermal performance of hydraulic floor heating modular with shape-stabilized. Journal of Engineering Thermophysics, 641-643.

Zhang S, Ren N, 2006. Investigation and Analysis on Solar Energy Housing of Small Towns in North Area. South Architecture,52-55.

Zhang X, Feng G, Feng G, 2010. Comparative Analysis of Heating Wall with Inner PCM and Traditional Heating Wall in Rural Area of North China. Building Energy & Environment, 27-30.

Zhao J, Qu H, Cui J, 2008. Simulation of solar energy central heating system with seasonal thermal storage. Acta Energiae Solaris Sinica, 214-219.

Zhao N, 2013. Research of appropriate technology of renewable energy in new rural residential construction in Shandong district. Shandong Jianzhu University.

Zheng M, Fan G, Yang Y, 1983. Passive solar heating test of Beijing traditional flat house. Acta Energiae Solaris Sinica, 113-116.

Zhu J, Chen B, 2015. Experimental study on thermal response of passive solar house with color changed. Renewable Energy, 55-61.

Zhu W, Zhang W, Xin L, 2004. An estimate method of heating and heat load in rural residential building. Renewable Energy, 51+54.

Zu W, Zuo T, Wang D, 2010. Application of enthalpy analysis method in selection of end heating mode. Shandong civil building society academic conference on thermal power Specialized Committee.

322: Performance analysis of an air-to-air energy recovery system for building applications in hot-humid environment

Fatin Zafirah MANSUR[1], Mardiana Idayu AHMAD [2], Saffa RIFFAT[3]

[1]Environmental Technology Division, School of Industrial Technology, Universiti Sains Malaysia, 11800 Penang Malaysia, zafirahmj8@gmail.com
[2]Environmental Technology Division, School of Industrial Technology, Universiti Sains Malaysia, 11800 Penang Malaysia, mardianaidayu@usm.my
[3]Department of Architecture and Built Environment, Faculty of Engineering, University of Nottingham, NG7 2RD University Park, Nottingham, United Kingdom

The aim of this study is to evaluate the performance of a hydrophilic membrane-based energy recovery system in terms of efficiency and recovered energy for potential building applications in hot-humid environment. Experimental investigations are carried out under controlled conditions in Energy and IEQ Testing Unit located in School of Industrial Technology, Universiti Sains Malaysia. Tests are performed under different airflow rates range from 1.0 to 3.0 m/s, intake air temperature of 28°C, 31°C, 35°C, 40°C) and intake relative humidity of 70%, 75% and 80%. The efficiency and recovered energy of the system are calculated and evaluated by adopting calculation method by ASHRAE Standard. From the study, the effect of operating parameters denotes that the effect of airflow rate on the system results in a decrease in efficiency as the airflow rate increase. The increase of airflow rate causes the increment in recovered energy. The system indicates that as the intake air temperature (T_{in}) increases, efficiency and recovered energy also increase. Effect of intake relative humidity (RH_{in}) exhibits a decline in efficiency when the intake relative humidity (RH_{in}) increases. Additionally, as the relative humidity increases, the recovered energy of the system remains constant.

Keywords: air-to-air energy recovery system; hot-humid environment; performance; building applications

1. INTRODUCTION

World energy consumption is growing rapidly due to the increasing energy demand by emerging and developed economies. As a result, the over-reliance on the fossil fuels (coal, oil, natural gas) as primary energy sources has already raised concern over energy supply difficulties, diminishing of energy resources and environmental impacts. As it was identified that building services of HVAC systems account for 50% of the total building energy consumption, hence there is a need to combat this phenomenon. Thus, the air-to-air energy recovery system was introduced as an important component of energy efficient technology in buildings that assists in reducing the energy consumption. Recent developments of air-to-air energy recovery system has heightened its application of the air-to-air energy recovery system in all types of the building that recognised having the potential in reducing the energy consumption and providing good indoor air quality (Zhang et al., 2000). However, the latest finding of its application in the hot-humid environment shows contrasting results as there still has been little discussion of the air-to-air energy recovery application in hot-humid environment. This is due to the fact that hot-humid environment are still conventionally using a large amount of electrical energy for cooling system operating purpose (Rasouli, et al., 2013). To date, there have been little agreements on the air-to-air energy recovery system is prevalently designed for cold climate area and also country with both summer and winter season (Roth, 2013). There are also several studies of the system that were carried out in hot-humid environment, however the report found a weakness as it used the complex run-around type of the air-to-air energy recovery system (Hemingson, et al., 2011).

While some studies show that the utilization of the system in reducing the energy consumption eventually gives advantage both on the environmental and economic benefits analysis, there is still inadequate studies which pinpointed its application in terms of the effect for both factors especially in the hot-humid environment. A number of researchers have reported the efficient performance of the air-to-air energy recovery system in hot-humid environment (Jadhav, & Lele, 2015), however, the existing account failed to identify whether the study was conducted based on the experimental approach or merely on numerical study. Therefore in such situation, it is crucial to explore an air-to-air energy recovery system that could recover or transfer both heat and mass to be used for building applications by experimental outdoor design of air conditions based on hot-humid environment. This paper aimed to investigate the performance of an air-to-air energy recovery system that able to recover both sensible and latent heat. It is hoped that these findings could give an important contribution to the field of air-to-air energy recovery especially to its application in the hot-humid environment.

2. METHODOLOGY

The operant conditions involved in this study are temperature, relative humidity and air velocity. In order to obtain the accurate testing results and investigate the relationship between the air temperature, relative humidity, and air velocity with the air-to-air energy recovery efficiency, two air condition control systems are set up in this experiment to obtain steady and appropriate intake as well as exhaust air streams. One will be controlling the intake air conditions, the other one is for the return air from indoor space, where air temperature is controlled according to ANSI/ASHRAE Standard 55, 2003. For the whole, the measurement for temperature, relative humidity and air velocity are taken in the air-to-air energy recovery system can be seen in Figure 1. As the measurement of the sensors are sensitive to where it is placed in the air-streams; hence the sensors are placed as close as possible to the inlets and outlets of the air-to-air energy recovery system (Hilmersson, & Paulsson, 2006). This is to prevent as little influence as possible from the surrounding.

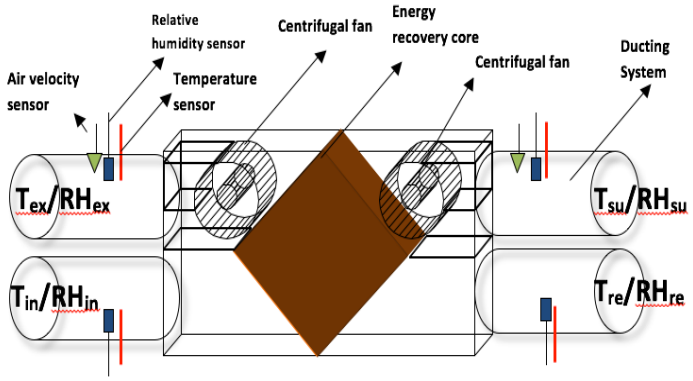

Figure 1: The measurement point for each operant condition in the air-to-air energy recovery system

For the temperature measurement, the intake air temperature (T_{in}) at 28°C, 31°C, 35°C and 40°C are regulated in a control chamber. Meanwhile, the return air temperature (T_{re}) from indoor space is controlled at about 24°C (ANSI/ASHRAE Standard 55, 2003).The temperature measurement consists of:

- Two (2) points thermocouples in the supply air before entering the core or intake air, T_{in}
- Two (2) points of thermocouples in the supply air after entering the core or supply air, T_{su}
- Two (2) points of thermocouples in the return air, T_{re}
- Two (2) points of thermocouples in the exhaust air, T_{ex}
- Four (4) points of thermocouples in the insulated room, T_{IR}
- Four (4) points of thermocouples in the indoor space/room, T_{IS}

Relative humidity measurement in the air-to-air energy recovery system is taken using a relative humidity and temperature transmitters with analogue output (model: Delta Ohm). This device can measure both temperature and relative humidity levels. The relative humidity can be measured from 0 to 100% with the measuring accuracy of ± 2% (10 to 90% RH), and ± 2.5% in the remaining range. In addition, the temperature measurements using PT100 sensor type recorded a measuring range of -40 to +60°C with the accuracy of ± 0.2°C, ± 0.15% of the measured data. These devices were located at each air duct referring to Figure 3.6, which are:

- One (1) point at the supply air before entering core or intake air, RH_{in}
- One (1) point at the supply air after entering core or supply air, RH_{su}
- One (1) point at the return air inside, RH_{re}
- One (1) point at the exhaust air after entering core, RH_{ex}

Meanwhile, the relative humidity measurement in the insulated room (RH_{IR}) and indoor space (RH_{IS}) are measured using the Hobo ZW series-wireless sensor. It was located at the centre of the insulated room (RH_{IR}) and indoor space (RH_{IS}). The accuracy of temperature measurement is ± 0.21°C from 0 to 50°C (± 0.38°F; from 32 to 122°F); relative humidity: ± 2.5% from 10 to 90% typical, max. ± 3.5% and analog channel: ± 1.544 mV plus 2% of reading typical. The experiment is conducted in an indoor space with the relative humidity (RH_{IS}) is controlled at 54% (ANSI/ASHRAE Standard 55, 2003) and the intake relative humidity (RH_{in}) is tested at 70%, 75%, 80%.

In airflow measurement, a hand-held hot wire anemometer with an accuracy of ± 3% reading, ± 0.05 m/s is used to measure the velocity of airstream at intake and exhaust stream at the same location as the temperature and relative humidity measurement. In order to obtain accurate air velocity measurement in the circular air duct, log-Tchebycheff method was applied following a suggestion made by Zhou (2005).

Data collection is carried out using a data logger, DT800 connected to a computer. In this study, there are 20 connections made at the analog channels that include the temperature (16 sensors) and relative humidity sensors (4 sensors) with DeLogger™ 5 Pro Software. The performance of the system based on outdoor design air conditions is recorded in the form of efficiency and recovered energy. The data are computed at equal airflow rate at both intake and exhaust stream by adopting the established formula in several studies (Al-Waked et al., 2015; Moffitt et al., 2012; Mardiana et al., 2011; Liu et al., 2010; ANSI/ASHRAE Standard 84, 1991). Meanwhile, the recovered energy is calculated by adopting the principal of rate of energy transfer which depends on the rate and direction of the heat and moisture transfer in relation to the total surface area (Liu and Niu, 2014; ASHRAE, 2003).

3. RESULTS AND DISCUSSION

3.1. Temperature and relative humidity profiles

Figure 2(a) presents temperature profiles of the intake air temperature (T_{in}), supply air temperature (T_{su}), return air temperature (T_{re}) and exhaust air temperature (T_{ex}) at 28°C and 70% with the airflow rate fixed at 1.0 m/s when passing through the air-to-air energy recovery unit. It is clearly observed that the intake air temperature (T_{in}) eventually drops after passing through the air-to-air energy recovery system. The supply air temperature (T_{su}) is reduced with a difference of about 3°C. It can be seen that the return air temperature (T_{re}) reaches its peak at minutes of 35, 55, 70 and 115, however, the temperature recorded remains at 24°C. Additionally, the exhaust air temperature (T_{ex}) shows its highest peak at minute of 65 and the average temperature is recorded about 30°C. This happens might be due to uncertainties of the airflows at that particular time.

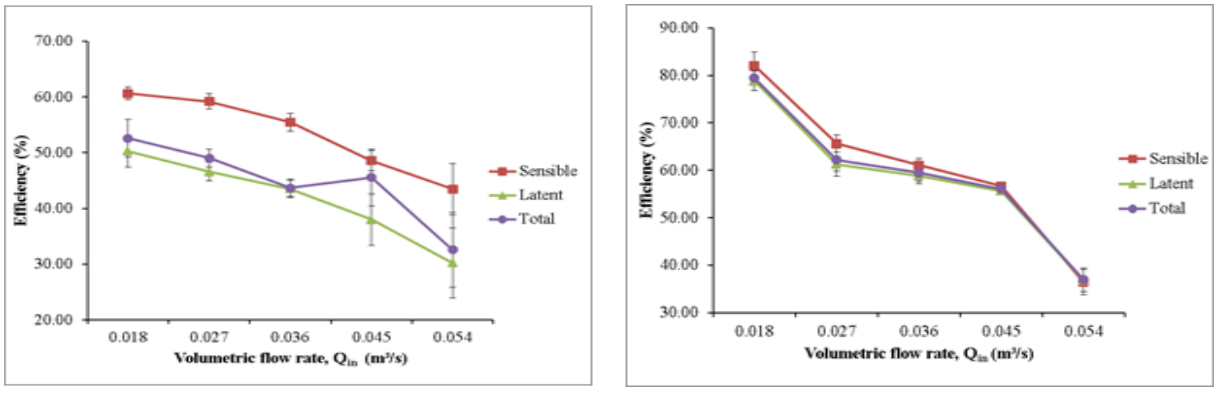

(a) (b)

Figure 2: (a) Temperature profiles of the system at 1.0 m/s, 28°C and 70%; (b) Temperature profiles of the system at 1.0 m/s, 28°C and 75%

Figure 2(b) shows another temperature profiles at 28°C and 75% with intake air velocity (V_{in}) fixed at 1.0 m/s. All supply air temperature (T_{su}) and return air temperature (T_{re}) lies under the intake air temperature (T_{in}). The average reading of supply air temperature (T_{su}) recorded is at 26.12°C and barely reduces about 9% from the intake air temperature (T_{in}). In addition, return air temperature (T_{re}) and exhaust air temperature (T_{ex}) show a fluctuation pattern of temperature reading and the average is calculated at 22.99°C and 28.39°C, respectively.

3.2. Relative humidity profiles

The relative humidity profile at intake air temperature (T_{in}) of 28°C, intake relative humidity (RH_{in}) of 70%; and intake air velocity (V_{in}) of 1.0 m/s can be seen in Figure 3. It can be seen that the reading is dropped below 70% which are about 10% reduction from the beginning. This might be due to the uncertainty errors of the airflow rate or the intake air temperature (T_{in}) that occurs during the investigation. This result is also in good agreement with Aarnes (2012), which suggests that airflow rate on the supply air side is decreased as time passes by. The relative humidity at the exhaust and return are approximately similar and is recorded with the average of 57%.

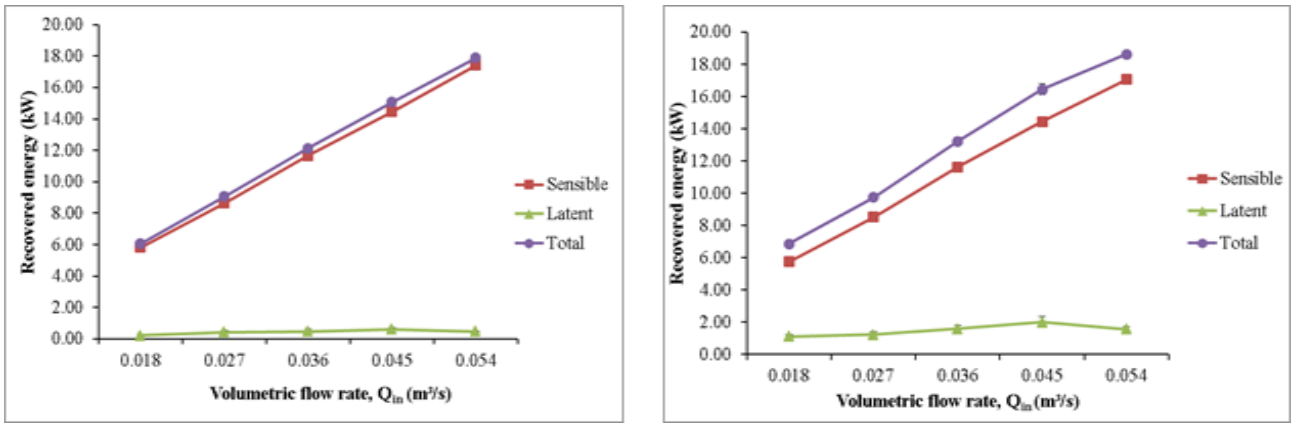

Figure 3: (a) Relative humidity profiles at 1.0 m/s, 28°C and 70%; (b) Relative humidity profiles at 1.0 m/s, 28°C and 75%

Figure 3 (a) and (b) shows the relative humidity profiles of the intake air temperature (T_{in}) at 28°C, intake relative humidity (RH_{in}) of 70% and 75%, respectively; and intake air velocity (V_{in}) at 1.0 m/s. It is noticeable that the supply relative humidity (RH_{su}), return relative humidity (RH_{re}), and exhaust relative humidity (RH_{ex}) are lower compared to the intake relative humidity (RH_{in}). This indicates that the energy recovery system has the potential in dehumidifying the incoming fresh air before being released into the indoor space to meet its requirements (Zhou et al., 2007). Initially, supply relative humidity (RH_{su}) decreases about a maximum percentage of 13%. However, the reduction percentage reduces about 10% towards the end. In addition, the average reading of return relative humidity (RH_{re}) and exhaust relative humidity (RH_{ex}) are recorded at 52.75% and 55.49%, respectively. Exhaust relative humidity (RH_{ex}) displays an increment as time passes by and shows a fluctuation trend at minutes of 30, 60 and 105. Based on the figure, the reduction of supply relative humidity (RH_{su}) at intake relative humidity (RH_{in}) of 75% shows a better reduction value with the average of 11% compared to intake relative humidity (RH_{in}) of 70%, which is calculated about 9% of relative humidity. Hence, this system is able to reduce the relative humidity level before being released into the indoor space.

3.3. Effects of airflow rate on performance

The system performance is tested at the volumetric flow rate from 0.018 to 0.054 m^3/s. Table 1 and Table 2 display the recorded temperature and relative humidity. Data are collected at the intake relative humidity (RH_{in}) of 80% with different temperatures of 31°C (Table 1) and 40°C (Table 2) correspondingly. It can be clearly seen from both tables that the intake air temperature (T_{in}) and intake relative humidity (RH_{in}) are declining after passing through the system.

Table 1: The tested temperatures and relative humidity at 31°C and 80%

T_{in} = 31.00°C, RH_{in} = 80.00%					
Intake air velocity, V_{in} (m/s)	1.0	1.5	2.0	2.5	3.0
Volumetric flow rate, Q_{in} (m^3/s)	0.018	0.027	0.036	0.045	0.054
Mass air flow rate, M_{a1} (kg/s)	0.021	0.031	0.042	0.052	0.063
Intake air temperature, T_{in} (°C)	31.08	30.90	29.89	31.07	29.99
Supply air temperature, T_{su} (°C)	27.55	26.75	26.64	27.48	27.77
Return air temperature, T_{re} (°C)	25.26	23.89	24.03	23.68	24.88
Exhaust air temperature, Te_x (°C)	31.14	30.00	29.02	31.48	30.12
Intake relative humidity, RH_{in} (%)	80.32	80.1	79.91	81.81	80.57
Supply relative humidity, RH_{su} (%)	80.20	76.82	76.06	79.94	78.99
Return relative humidity, RH_{re} (%)	70.87	56.33	54.00	56.86	58.63
Exhaust relative humidity, RH_{ex} (%)	73.54	55.57	65.56	65.32	69.19

Based on Table 1, both the maximum temperature difference (ΔT) and humidity ratio difference (Δω) are 0.027 m^3/s at 4.15°C and 5.76 g/kg, respectively. It is also found that the temperature difference (ΔT) and humidity ratio difference (Δω) are ranging from 2.22 to 4.15°C and 3.08 to 5.76 g/kg, respectively. An average of 11% is calculated on temperature difference (ΔT) while humidity ratio difference (Δω) is recorded at the average of 20%.

Table 2: The tested temperatures and relative humidity at 40°C and 80%

T_{in} = 40.00°C, RH_{in} = 80.00%					
Intake air velocity, V_{in} (m/s)	1.0	1.5	2.0	2.5	3.0
Volumetric flow rate, Q_{in} (m^3/s)	0.018	0.027	0.036	0.045	0.054
Mass air flow rate, M_{a1} (kg/s)	0.020	0.030	0.041	0.051	0.061
Intake air temperature, T_{in} (°C)	40.31	39.85	39.89	39.88	40.13
Supply air temperature, T_{su} (°C)	27.55	30.42	30.73	31.16	34.93
Return air temperature, T_{re} (°C)	24.76	25.48	24.89	24.49	25.86
Exhaust air temperature, Te_x (°C)	37.80	40.23	40.38	39.99	44.98
Intake relative humidity, RH_{in} (%)	80.32	80.10	79.91	81.81	80.57
Supply relative humidity, RH_{su} (%)	70.20	76.82	78.06	78.94	78.99
Return relative humidity, RH_{re} (%)	51.87	51.33	53.99	50.86	48.63
Exhaust relative humidity, RH_{ex} (%)	73.54	55.57	65.56	65.32	69.19

Table 2 displays that the highest temperature difference (ΔT) and highest humidity ratio difference (Δω) are recorded at 12.76°C and 23.06 g/kg, respectively. The temperature difference (ΔT) is found ranging from 5.2 to 12.76°C. Meanwhile, the humidity ratio difference (Δω) is calculated at 10.66 to 23.06 g/kg. It is found that as the airflow rate escalates, the temperature difference (ΔT) and humidity ratio difference (Δω) decreases.

Airflow rate on efficiency

In order to investigate the performance of the system more thoroughly, the sensible efficiency (ε_{sen}), latent efficiency (ε_{lat}), and total efficiency (ε_{tot}) are calculated using the data presented in Table 1 and Table 2. Figure 4(a) plots the efficiency at intake air temperature (T_{in}) and intake relative humidity (RH_{in}) of 31°C and 80%, respectively. Meanwhile, Figure 4(b) presents the efficiency at intake relative humidity (RH_{in}) of 80% and intake air temperature (T_{in}) of 40°C. It is revealed that the efficiency decreases as the airflow rate increases. The highest efficiency is achieved at sensible efficiency (ε_{sen}) of 60.65% at 0.018 m^3/s. It is also observed that the sensible efficiency (ε_{sen}) shows a constant decrease of efficiency as it approaches the highest airflow rate. In contrast, latent efficiency (ε_{lat}) has the lowest efficiency ranging from 30.23 to 50.29%. The minimum latent efficiency (ε_{lat}) is found to be 30.23% at 0.054 m^3/s. Furthermore, at 0.018 to 0.036 m^3/s, the value of latent efficiency (ε_{lat}) and total efficiency (ε_{tot}) become almost identical. Although the total efficiency (ε_{tot}) at 0.045

m^3/s is extremely accelerated by 4% recorded at 45.55%, latent efficiency (ε_{lat}) and total efficiency (ε_{tot}) at the 0.054 m^3/s are simultaneously recorded at approximately of 30.23% and 32.59%, respectively.

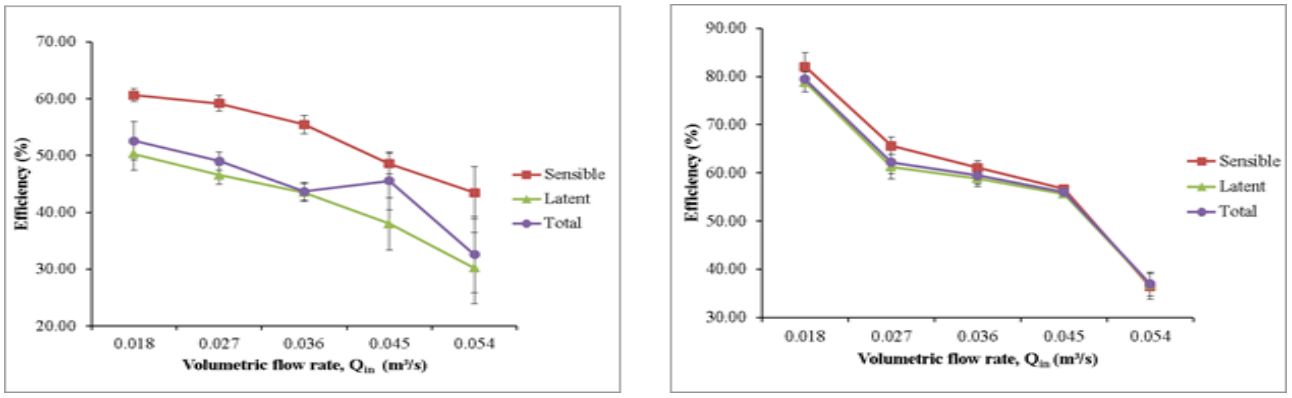

(a) (b)

Figure 4: (a) Results of efficiency at 31°C and 80%; (b) Results of efficiency at 40°C and 80%

Based on Figure 4(b), it can be seen that the efficiency drops as the airflow rate increases. The highest sensible efficiency (ε_{sen}) is found at 0.018 m^3/s with 82.06%. The latent efficiency (ε_{lat}) and total efficiency (ε_{tot}) indicate almost similar value as the airflow rate increases which ranging from 36 to 53.50%. The minimum latent efficiency (ε_{lat}) and total efficiency (ε_{tot}) are spotted at 0.054 m^3/s with 37%. As predicted by Zhang (2007), the sensible efficiency (ε_{sen}) is particularly over than latent efficiency (ε_{lat}) as it is recognised that the mass transfer resistance is larger than heat transfer resistance. Besides, total efficiency (ε_{tot}) showed a similar trend to that of latent efficiency (ε_{lat}), which indicates that mass transfer is leading over the heat transfer (Min and Su, 2010). It appears that the effect of airflow rate on efficiency is supported by the concept of residence time (Pastor et al., 2011). The slower the airflow rate, the higher the residence time and the larger the heat and mass transferred into the energy recovery core. Previous study done by Liu (2008) explains that this trend happens due to the process of convective heat transfer to the formula of airflow speed (power of negative); leading to the perpendicular of efficiency against airflow rate. Meanwhile, the minimum range of latent efficiency (ε_{lat}) also occurs because of the moisture across energy recovery core become more aggravated as the airflow rate increases, which leads to the reduction of efficiency (Liu, 2008).

Airflow rate on recovered energy

The effect of the airflow rate on the recovered energy (q) is also calculated based on Table 1 and 2. It is apparent that airflow rate affects the recovered energy of the system and results in the value of recovered energy that is parallel to the airflow rate. Figure 5(a) with the intake relative humidity (RH_{in}) of 80% and intake air temperature (T_{in}) of 31°C indicate that the highest recovered energy is achieved at 0.054 m^3/s with the amount of 17.89 kW.

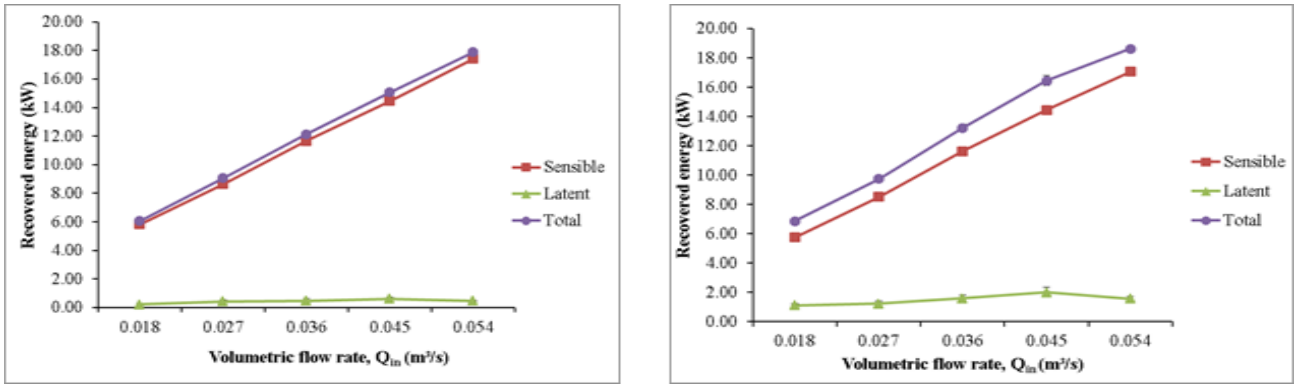

(a) (b)

Figure 5: (a) Results on recovered energy at 31°C and 80%; (b) Results of recovered energy at 40°C and 80%

Another case of recovered energy at 40°C and 80% is illustrated in Figure 5(b). It indicates that the latent recovered energy (q_{lat}) is lower compared to the sensible recovered energy (q_{sen}) and the total recovered energy (q_{tot}). The latent recovered energy (q_{lat}) shows an inconsistent trend when the value starts to drop by 22% at 0.054 m^3/s. Moreover, the sensible recovered energy (q_{sen}) is found to be below the total recovered energy (q_{tot}) with the maximum and minimum values

recorded at 0.054 m^3/s (17.05 kW) and 0.018 m^3/s (5.74 kW), respectively. Meanwhile, the highest total recovered energy (q_{tot}) (63.19%) is achieved at 0.054 m^3/s. From the figure, it can be seen that the recovered energy is parallel to the airflow rate. The increasing of airflow rate has led to the increasing of the recovered energy (q). In contrast, the efficiency decreases with the increasing of airflow rate (Li et al., 2007). The maximum recovered energy recorded is 0.054 m^3/s while the minimum recovered energy is at 0.018 m^3/s. These are in good agreement with the study carried out by Min et al., (2010) that reported the increment of airflow rate has aided in the increasing of total heat transfer rate. Both sensible recovered energy (q_{sen}) and total recovered energy (q_{tot}) possess nearly identical ranges.

4. CONCLUSION

In conclusion, the air-to-air energy recovery system tested in this study is capable of reducing the conditions of fresh outdoor in relation to air temperature and relative humidity before being introduced into an indoor space. The performance of air-to-air energy recovery system is determined and it is found that the temperature is reduced from 2.75°C to 12.76°C. Furthermore, in the perspective of relative humidity reduction, the system is able to decrease the humidity ratio from 18 to 25 kg/kg. In addition, the investigation on the effects of operating parameters towards the performance of the system using outdoor air conditions demonstrate that the operating parameters affects the performance of the system. It is therefore concluded from this study that as the airflow rate increases, the efficiency and the recovered energy also increases.

5. ACKNOWLEDGEMENTS

The authors would like to thank Fundamental Research Grant Scheme (FRGS), Ministry of Education Malaysia as well as the Department of Architecture and Built Environment, University of Nottingham, United Kingdom and Universiti Sains Malaysia, Penang Malaysia for the research support in relation to this project.

6. REFERENCES

Aarnes, S.M., 2012. *Membrane Based Heat Exchanger*. Norwegian University of Science and Technology. Available at: http://ntnu.diva-portal.org/smash/record.jsf?pid=diva2:566164.

Al-Waked, R., Nasif, M.S., Morrison, G. & Behnia, M., 2015. CFD simulation of Air to Air Enthalpy Heat Exchanger: Variable Membrane Moisture Resistance. *Applied Thermal Engineering*. Available at: http://linkinghub.elsevier.com/retrieve/pii/S1359431115002914.

ANSI/ASHRAE Standard 55, 2003. Thermal Environmental Conditions for Human Occupancy. *American Society of Heating, Refrigerating and Air-Conditioning Engineers, Atlanta GA*.

ANSI/ASHRAE Standard 84, 1991. Method of Testing Air-to-Air Heat / Energy Exchangers. *ASHRAE Standard*, 8400.

ASHRAE, 2003. Air-To-Air Energy Recovery. In *2000 ASHRAE (American Society of Heating Refrigerating and Air-Conditioning Engineers) Systems and Equipment Handbook*. Available at: https://cours.etsmtl.ca/mec735/Documents/Notes_de_cours/2012/Hiver_2012/recuperation_ASHRAE.pdf.

Hemingson, H.B., Simonson, C.J. & Besant, R.W., 2011. Steady-state performance of a run-around membrane energy exchanger (RAMEE) for a range of outdoor air conditions. *International Journal of Heat and Mass Transfer*, 54(9–10), pp.1814–1824. Available at: http://dx.doi.org/10.1016/j.ijheatmasstransfer.2010.12.036.

Hilmersson, A. & Paulsson, U., 2006. *Analysis of an Energy Recovery Ventilator*. Halmstad University.

Jadhav, T.S. & Lele, M.M., 2015. Engineering Science and Technology , an International Journal Theoretical energy saving analysis of air conditioning system using heat pipe heat exchanger for Indian climatic zones. *Engineering Science and Technology, an International Journal*, 18(4), pp.669–673. Available at: http://dx.doi.org/10.1016/j.jestch.2015.04.009.

Li, Z., Yanhua, L., Yiping, W. & Jianguo, K., 2007. Study on the performance of a fresh air heat exchanger. , vol.I, pp.426–30.

Liu, J., Li, W., Liu, J. & Wang, B., 2010. Efficiency of energy recovery ventilator with various weathers and its energy saving performance in a residential apartment. *Energy and Buildings*, 42(1), pp.43–49.

Liu, S., 2008. *A Novel Heat Recovery / Desiccant Cooling System*. University of Nottingham.

Liu, X.P. & Niu, J.L., 2014. An optimal design analysis method for heat recovery devices in building applications. *Applied Energy*, 129, pp.364–372. Available at: http://www.sciencedirect.com/science/article/pii/S0306261914005194.

Mardiana, A.I. & Riffat, S.B., 2011. An experimental study on the performance of enthalpy recovery system for building applications. *Energy and Buildings*, 43(9), pp.2533–2538. Available at: http://dx.doi.org/10.1016/j.enbuild.2011.06.009.

Mikkonen, L., 2013. *Air - to - Air Energy Recovery*, Greensettle.

Min, J. & Su, M., 2010. Performance analysis of a membrane-based energy recovery ventilator: Effects of membrane spacing and thickness on the ventilator performance. *Applied Thermal Engineering*, 30(8–9), pp.991–997. Available at: http://dx.doi.org/10.1016/j.applthermaleng.2010.01.010

Min, J. & Su, M., 2011. Performance analysis of a membrane-based energy recovery ventilator: Effects of outdoor air state. In *Applied Thermal Engineering*. pp. 4036–4043.

Moffitt, R., Murphy, J. & Stanke, D., 2012. *Air-to-Air Energy Recovery*, Moffitt, R., Murphy, J. & Stanke, D., 2012. *Air-to-Air Energy Recovery*

Pastor, R., Miravete, G.E. & Lemcoff, N., 2011. A Modeling Study to Determine the Effectiveness of an Energy Recovery Ventilator (ERV). In *2011 COMSOL Conference*. Boston.

Rasouli, M., GE, G., Simonson, C.J. & Besant, R.W., 2013. Uncertainties in energy and economic performance of HVAC systems and energy recovery ventilators due to uncertainties in building and HVAC parameters. *Applied Thermal Engineering*, 50(1), pp.732–742. Available at: http://dx.doi.org/10.1016/j.applthermaleng.2012.08.021.

Roth, B., 2013. *Building Energy Recovery, dPoint Technologies*, Vancouver. Available at: www.dpoint.ca.

Zhang, L., 2007. Heat and mass transfer in a cross-flow membrane-based enthalpy exchanger under naturally formed boundary conditions. *International Journal of Heat and Mass Transfer*, 50, pp.151–162.

Zhang, Y., Jiang, Y., Zhang, L.Z., Deng, Y. & Jin, Z., 2000. Analysis of thermal performance and energy savings of membrane based heat recovery ventilator. *Energy*, 25(6), pp.515–527.

Zhou, C., 2005. *Estimation of volumetric flow rate in a square duct: Equal area versus log-Tchebycheff methods.* University of Windsor.

324: The choice of financing path for China's renewable energy companies under the framework of low-carbon economy

Lanlan LI[1], Bin XU[2]

1 School of Economics and Management, Hubei University of Technology，Wuhan City, Hubei Province, China, 2051750516@qq. com

2 School of Economics and Management, Hubei University of Technology ， Wuhan City, Hubei Province, China,501938801@qq.com

Renewable energy not only has the advantages of low-carbon and cyclic renewable, but also has the disadvantages of high cost, low efficiency, and high investment risk. Therefore, broadening its financing channels and controlling risks have become key issues in the development of the renewable energy industry. In addition to traditional financing such as bank credit, the renewable energy industry can also use the carbon finance market for financing. However, for renewable energy companies, especially small and medium-sized enterprises, the existing carbon trading model is not conducive to their financing development. This article first analyses China's renewable energy financing system. Then, from the aspects of product and trading mechanism, we analyse the operation mechanism of carbon financial market. Finally, it analyses the product features and operating modes of related companies, such as high-emission companies and financial institutions. The article classifies renewable energy companies according to their size. Analyse the characteristics of enterprises of different sizes, and determine the corresponding financing model according to their characteristics. Large companies can use government special funds, clean development mechanisms, and carbon trading markets for financing. Due to its own scale defects, the above financing methods are not suitable for SMEs. This article has designed a financing model for tripartite participation based on carbon trading platform and green finance.

Keywords: low-carbon, renewable energy companies, green finance

1. INTRODUCTION

In 2017, the total global renewable energy investment amounted to 279.8 billion U.S. dollars (excluding large-scale hydropower). China's investment amounted to US$126.6 billion, which represented a year-on-year increase of 31% and a global share of 45% (Global Renewable Energy Investment Trends, 2018). In general, the development of the renewable energy industry requires huge financial support. At present, the financing path for China's renewable energy industry is divided into direct financing and indirect financing.

1.1. Direct financing

Direct financing is government special funds or social direct investment. Kou Zhaohui (Kou, 2014: pages 8-13) believes that China's renewable energy industry has a single source of financing, with government-specific funds as the mainstay, and finally through financial support and tax incentives, it will eventually return to guide various enterprises, residents, and other social investors to invest. Luo Chengxian (Luo, 2016: pages 9-26) analysed the California renewable energy quota system (RPS) and combined with the current situation of China's industry, that China's renewable energy industry can learn from the California development model, policy-led, clearly divided renewable energy power supply and consumption goals Recycling RPS electricity is sold in a unified manner and the electricity sales subsidy policy is implemented. Gong Piqin, Li Xiyang (Gong, Li, 2017: pages 22-29) adopted the ternary tree model of real option method to measure the net present value (NPV) and real option value (ROV) of investment in three types of renewable energy power generation projects, and analysed the price of railings (prices refer to benchmarking prices) with or without policy subsidy for renewable energy power projects of them. These indicates that the volatility of carbon prices increases the value of real options for renewable energy projects, but will delay the time for companies to invest in the project. At the same time, policy subsidies will promote its development.

1.2. Indirect financing

Indirect financing is through carbon finance market financing and bank credit, issuance of stocks and bonds. However, China's renewable energy industry has developed late and its related financial innovation capacity is insufficient. Therefore, financial products are scarce, and it is difficult for related companies to raise funds through this method. In 2005, the "Kyoto Protocol" took effect, which marked the development of the world economy into a low-carbon model. The signing of the "Paris Agreement" in 2015 enabled the gradual transition of mandatory emission reductions to voluntary emission reductions. In order to comply with the requirements of the world's low-carbon development model, China has established a number of regional carbon trading markets. In December 2017, the nationwide carbon trading market (power industry) was completed, and the total carbon emissions reached more than 3 billion tons, which is China's renewable energy source. Industrial development has opened up new financing channels.

Feng Nan (Feng, 2016: pages 62-82) researched and analysed the operating mechanism of the international carbon financial market, saying that carbon emission rights are products with special public attributes. Carbon finance is an important economic means to support emission reduction behaviours. It can integrate funds and reduce social transaction costs. Han Longxi and other scholars (Han, Zhai, Zhang, Gao,2015: pages 21-35) researched the opportunities for renewable energy GHG emission reduction in China and pointed out that at present, China's awareness of energy conservation and emission reduction is enhanced, renewable energy resources are abundant, and emission reduction transactions can promote the development and development of renewable energy technologies, but also The existence of the initial implementation of the mechanism was due to insufficient experience, resulting in a low registration rate, inadequate third-party service agencies, and inconsistent transaction platforms. At the same time, the distribution of carbon emission rights in China is mainly through the quota system, and renewable energy companies originally had less carbon emissions than other companies, so they have less carbon emission rights, which is not conducive to their financing through carbon trading. Zou Jiayu (Zou, 2017: pages 96-97) proposed the way of bargaining and pricing of carbon trading from the perspective of the international carbon trading market. First of all, China needs to establish an authoritative carbon trading information platform to promote the flow of trading information. Secondly, it actively promoted the binding of RMB and carbon emission rights and enhanced the circulation of RMB in international carbon trading platforms. Finally, vigorously develop the carbon trading market, including its market size, product type, and carbon financial derivatives.

Most of the above studies directly analyse the financing model of renewable energy industries or projects from the perspective of government or financial system. This paper will use carbon finance and green finance as the basis to analyse the financing model of tripartite cooperation between renewable energy companies, financial institutions and high-emission companies. The fifth national financial work conference in China proposed the establishment of a real economy for financial services, with the focus on establishing green finance. Pan Xiquan (Pan, 2018: pages 32-37) analysed the current situation of China's green financial system and proposed that China's current green financial system is still not perfect and related financial product innovation is insufficient. Therefore, there is a great demand for green financial products, which provides a new source of financing innovation and development opportunities for renewable energy companies.

2. RENEWABLE ENERGY ENTERPRISE FIANCING BASIS

Before analysing the financing models of the three parties involved in renewable energy companies, it is necessary to analyse the actual conditions of their financing. Specifically, the financing base includes both the carbon financial market and the green finance.

2.1. Carbon financial market

In 1997, the "Kyoto Protocol" for the first time traded carbon dioxide emissions as a commodity to deal with global greenhouse gas emissions. In 2011, the National Development and Reform Commission printed and issued the Circular on Launching the Pilot Work of Carbon Emission Trading, followed by the establishment of seven regional carbon trading markets such as Beijing and Tianjin, and the preliminary establishment of China's carbon trading market. The carbon emission rights are allocated according to the company's past carbon emissions, while the renewable energy industry itself is a low-carbon emission industry. Although it can integrate funds through clean development mechanisms (CDM)[1], renewable energy projects, etc. The financing method is also limited by various factors, such as the product type of the company and the size of the company. In short, the carbon financial market just provides a financing platform for renewable energy companies, and the specific financing method relies on the technological innovation of the company or the financial product innovation produced in cooperation with the financial enterprise.

2.2. Green finance

Green finance refers to investment and financing activities that generate environmental benefits in terms of water resources, soil, etc., and promote sustainable social development. Different from traditional financial activities, green finance considers environmental benefits as one of investment financing options and assessment targets. However, it currently involves limited fields, mainly in financial sectors such as banks, green finance related products, green bonds, green credit, and PPP financing project. Liu Yongjun (Liu, 2017: pages 76-78) believes that the "two-type" society and the increase in government investment make the green and low-carbon economy enter an era of development, which can integrate large-scale funds for green companies and projects. At the same time, banks, as the leading players in green finance, have certain compulsion. Although they can increase support for the development of green projects, they also limit the product innovation and scale of green finance. Therefore, the green financial model is more effective in the early stage of development, but after the early stage, the state should appropriately relax relevant regulations, increase the degree of participation of enterprises, and increase the ability to innovate in green financial products. Taking Ant Financial as an example, this company uses the tree-planting approach (The Ant Forest) to reward users with green living, and fulfills its social responsibilities in this way. On this basis, companies and residents can establish another green financial model with a carbon emission authority bridge.

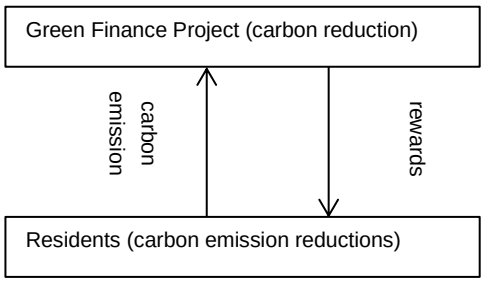

Figure 1: Green finance project financing model

Daily life produces a large amount of carbon dioxide. As shown in Figure 1, green financial projects connect with residents' green lives through carbon emissions, incentives, and other means. Through this approach, they can be motivated. Specifically, financial companies can record users' carbon emission reductions in a certain way and reward a certain amount of currency or daily necessities. An enterprise can acquire carbon emissions by means of carbon emissions, and acquire funds.

3. ANALYSIS OF THE FINANCING PATH FOR THE PARTICIPATION OF THREE PARTIES IN RENEWABLE ENERGY COMPANIES

Renewable energy companies mainly rely on solar energy, wind energy, and biomass energy to produce electricity. The related technologies started later than other industries, and they require high technology and equipment. Therefore, their

[1]The clean development mechanism is the Annex I to the COP3 (Kyoto meeting) of the UN Conference of the Parties to the United Nations Framework Convention on Climate Change (UNFCCC). It refers to a mechanism for the implementation of a part of the emission reduction commitments by the contracting parties abroad. It is usually Refers to the purchase of carbon emissions from developed countries in developing countries.

investment costs are high, the recovery period is longer and the risks are greater. In terms of the above, renewable energy companies have a single mode of financing, relying mainly on national special funds, financial subsidies, and some other investments. Fiscal subsidies refer to electricity price subsidies or tax incentives for the renewable energy industry. However, the size of the companies varies, and their financing methods will also differ.

3.1. Large renewable energy companies' financing path

Large-scale renewable energy companies have sufficient liquidity and have the advantage of technological innovation. Their financing paths are mainly divided into the following three areas:

(1) Government special funds

During the formulation of the “Twelfth Five-Year Plan”, climate change has aroused widespread concern in the world. It has become the largest limiting factor and constraint condition for China's development both at home and abroad. Therefore, energy conservation and emission reduction have become the core target of national development. As one of the policies, this country has established a special fund for renewable energy development. The larger the scale of renewable energy companies, the more abundant the funds and talents they have, the ability to support the company to carry out some large-scale renewable energy projects, and its emission reduction effect will be more obvious, so the government special funds will also More oriented to large-scale renewable energy companies, the specific performance of non-repayable donations, loans and other interest subsidies. Taking Shanghai as an example, the “Support Measures for Special Funds for the Development of Renewable Energy and New Energy in Shanghai” clearly stipulates that the key areas supported by Shanghai's support funds include the wind power projects, large-scale light and heat utilization projects approved by the Municipal Development and Reform Commission and 100 kilowatts and above of solar photovoltaic power generation.

(2) Clean development mechanism

The signing of the "Kyoto Protocol" has caused many countries to undertake certain carbon emission reduction obligations. This imposes more obligations on emission reductions by developed countries, and it takes longer to fulfill obligations. This has led to the development of the Clean Development Mechanism (CDM). The mechanism allows Annex I Parties (developed countries) to the Kyoto Protocol to purchase capital-related or technically validated emission reductions (CERs) from non-Annex I countries (developing countries). In order to fulfill the emission reduction obligation, the company conducts transactions for emission reductions. As of August 2016, the National Development and Reform Commission approved a total of 3,733 new energy and renewable energy CDM projects with emission reductions of 459,401,583 tons, accounting for 58.74% of total CDM project emission reductions. This shows that the Clean Development Mechanism is renewable to China. The development of energy companies provides a better financing platform. In addition, large-scale renewable energy companies are more likely to develop more energy-saving and emission-reduction projects through the company's technology and financial support. Therefore, it is easier to obtain larger-scale investment funds through this mechanism.

(3) Carbon trading platform

The carbon trading platform is an expansion of the carbon financial market products and trading mechanism following the Clean Development Mechanism. The platform emphasises the financialization of carbon emission rights more and companies have more options. For small-scale renewable energy sources, first of all, enterprises are more likely to acquire carbon trading qualifications; secondly, due to economies of scale and technological innovations, they can increase their emission reductions per unit, so that more carbon emission rights can be traded. Get investment funds.

Take Hubei Energy Group Co Ltd company for example, from the pilot operation of Hubei carbon trading in 2014 to 2016, the company generated a total revenue of more than 20 million yuan RMB through the innovation of emission reduction technology. It can be seen from this that large-scale renewable energy enterprises have more advantages in technological innovation and can integrate funds through the carbon trading platform.

3.2. Financing paths for small and medium renewable energy enterprises

Affected by the nature of the industry, renewable energy companies are more difficult to integrate funds. Compared with large-scale renewable energy companies, special government funding preferences and investment preferences have reduced the financing channels for small and medium-sized renewable energy companies. Based on the above-mentioned green finance project financing model and combining carbon emission rights requirements of high carbon emission companies, a new financing model for small and medium-sized renewable energy companies will be constructed to promote the joint development of renewable energy companies, high-emission companies and financial institutions.

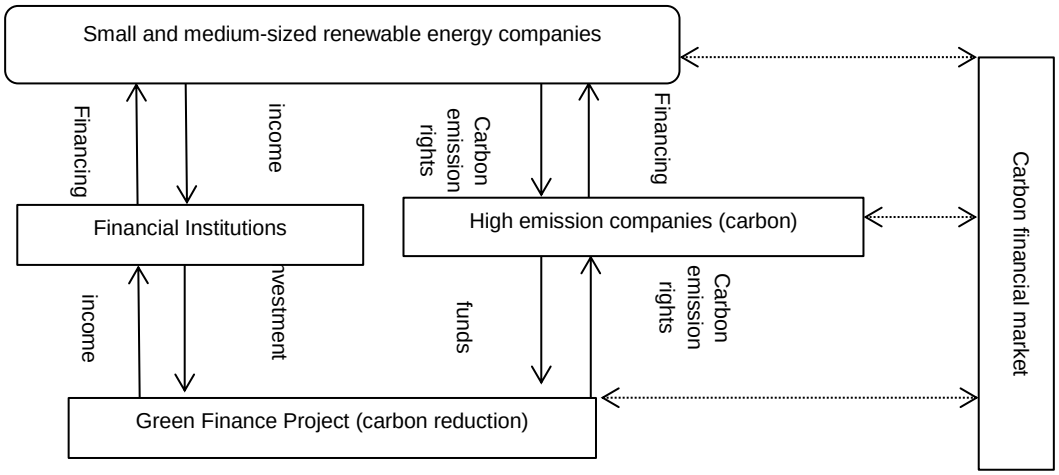

Figure 2: Tripartite participation in renewable energy enterprise financing model

As shown in Figure 2, small and medium-sized renewable energy companies, carbon-emitting companies, financial institutions, and green finance projects form a cycle of capital and carbon emission rights. High-emission companies, such as some industrial manufacturing companies, generate large quantities of carbon dioxide during the production process due to the limitations of the industry's own production model. After the country implements the carbon trading system, companies must bear certain obligations to reduce carbon emissions. For sustainable development, these companies need to purchase carbon emission rights or expand other carbon reduction channels. In this model, renewable energy companies have low-carbon production and transfer their carbon emission rights to high carbon emission companies. The company can also collect carbon emissions from residents' lives through green finance projects. In addition, financial institutions can carry out financial innovations, expand the scope and business scope of small and medium-sized renewable energy companies and green financial projects (carbon emission reduction), and increase investment returns. Renewable energy companies can incorporate certain funds through financial institutions.

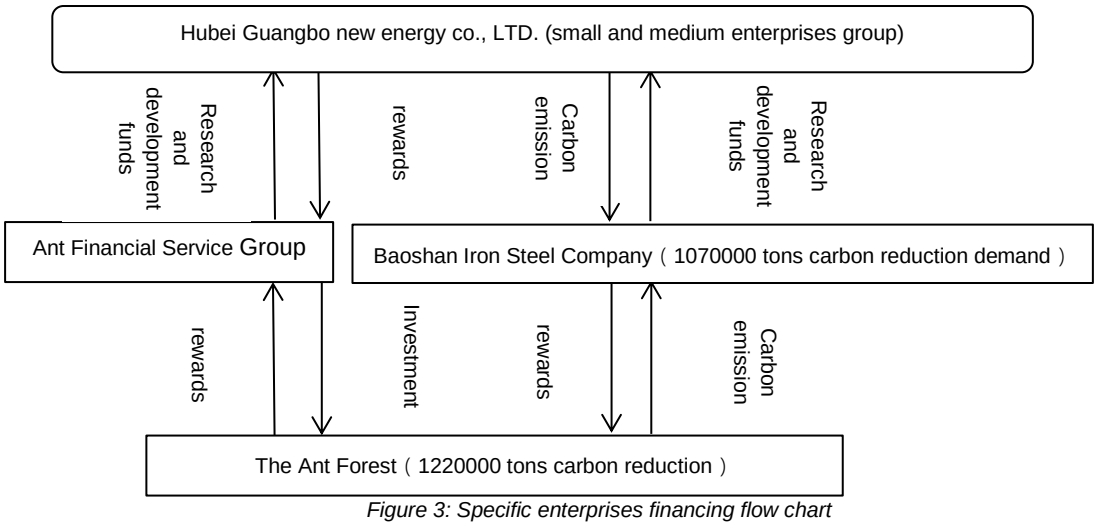

Figure 3: Specific enterprises financing flow chart

Take Hubei Guangbo new energy limited company, Baoshan Iron Steel Company[2] and Ant Financial Service Group as an example. Hubei Guangbo new energy limited company is mainly engaged in R & D and manufacturing of solar and wind energy equipment. The registered capital of the company is 3 million RMB, and it is a small enterprise. Due to the small scale of enterprises and large demand for R & D funds, the company has a large demand for financing. Baoshan Iron and Steel Group is mainly engaged in power transmission and transportation related business of steel manufacturing, with a larger emission reduction quota. The company produced 1070000 tons carbon quota gap in 2016 and bought quotas from the carbon market through CCER (enterprise initial carbon emissions quotas) in 2017 to make up for the gap from the carbon market, with a total cost of up to 26560000 yuan RMB. At the same time, the green public welfare project ant forest is under the ant Financial Services Company.

[2]By the end of 2016, Baoshan iron and Steel Group and Wuhan iron and steel (Group) have implemented joint reorganization. Baoshan iron and Steel Group Co., Ltd. was renamed as China's Bao Wu Iron and Steel Group Co., Ltd., as the reorganised parent company, Wuhan iron and steel (Group) company, as a whole, became its wholly owned subsidiary.

From 2016 "online" to 2017, the number of users more than 230 million, to obtain a total of 1220000 tons of green life reduction emission reduction, planting real trees 10250000, planting total area of more than 160000 Mu. The green life reduction is enough to make up for the carbon quota gap of Baoshan Iron and Steel Group.

When three enterprises form a circulation circle with the above model, Baoshan Iron and Steel Group can buy carbon emissions from Hubei Guangbo new energy Co., Ltd., and can also obtain a small amount of "reward" to obtain residents' life reduction. The cost of the method is far less than 26560000 yuan RMB, which can save a lot of money for Baoshan Iron and Steel Group. Ant Financial Service Group can earn social benefits through the ant forest. Hubei Guangbo new energy Co., Ltd. can obtain investment from Ant Financial Service Group, and on the other hand, it can sell carbon emission rights to Baoshan Iron and steel company. In general, this mode can generate a large amount of capital flow, and can provide funds for many small and medium-sized renewable energy enterprises.

The renewable energy industry itself has high technical development requirements. It has a large initial investment and long payback period. Small and medium-sized enterprises are subject to scale restrictions. Under normal circumstances, their liquidity is small, which will hinder their normal operation and investment funds. The above three-party financing model is a dynamic circulatory system. Small and medium-sized renewable energy companies and high-emission companies can also obtain funds directly from the system in addition to the carbon financial market, and collect people’s daily lives. The scope of carbon emission reduction involves a wide range, a large number of people, and the overall dispersion. Therefore, the carbon reduction will also be relatively stable, and it can promote the normal operation of the entire cycle. In short, the renewable energy industry, the green financial industry, and the high-carbon emission manufacturing and manufacturing industries can directly promote low-carbon rapid development, whether they are direct impacts or external effects.

4. CONCLUSION

This paper analyses the financing path for renewable energy companies of different sizes. However, the specific classification is not perfect and needs to be adjusted later.

5. REFERENCES

Feng Nan, 2016.Research on the operation mechanism of international carbon financial market. Jilin: Jilin University, 62-82.

Global Renewable Energy Investment Trends, 2018

Gong Piqin, Li Xiyang, 2017.Research on the investment value and investment timing of renewable energy under the carbon trading mechanism. Population, Resources and Environment, 27 (3), 22- 29.

Han Longxi, Yan Jiajia, Zhang Lin, Gao Qi.,2015.Opportunities and Challenges of China's Renewable Energy Greenhouse Gas Emissions Trading . Ecological Economy, 2, 31-35.

Interim Measures for the Administration of Renewable Energy Development Special Funds

Kou Zhaohui, 2014.Research on Carbon Financial Support for Renewable Energy Development in China. Qingdao : Qingdao University, 8-13.

Liu Yujun, 2017. Status Quo of Green Finance Development, Problems Needing Attention and Suggestions. Finance and Economics, 1, 76-78.

Luo Chengxian, 2016.Renewable energy quota system in California, USA and its enlightenment to China. Chinese and foreign energy, 21 (12),19-26.

Pan Xiquan, 2018.China's green financial system construction: realistic problems and coping mechanisms. Financial Education Research, 1, 32-37.

Zou Jiayu, 2017.Research on Low Carbon Economy Based on Carbon Financial System. Commercial Economy,11,96-97.

326: A preliminary performance diagnosis of a ground source heat pump system under the winter operation mode in Hefei

Xin MENG[1], Hao WANG[2], Wei HE[1]*, Zhongting HU[1]

[1]Department of Building Environment and Equipment, Hefei University of Technology, Tunxi Road 193, hefei, China, hwei@hfut.edu.cn
[2]Anhui Provincial Architectural Design and Research Institute, Fanhua Road 7699, Hefei, China, 42204109@qq.com

The application and performance of ground source heat pump (GSHP) system in a community named Kexuejiayuan of Hefei, China are reported in this study. Based on the field test and operation record analysis of the GSHP system, it is found that the system has the problems of improper equipment matching and lacking of a reasonable operation strategy. The average temperature difference at the load side is 4.2°C. But the temperatures of the inlet and outlet water are both lower than the set value. The average temperature difference at the source side is obviously unsatisfying with the design condition. Soil heating capacity appeared to be insufficient during January and February while the load decreased to a lower level in March. The operating efficiency of the single pump on the load side and the source side of the system can reach 80% and 72%, respectively. In the condition of three-pump parallel operation, the test proved that there must be a significant parallel flow loss. Except for the existing problems, the system has great potential for energy saving and energy saving reform can be carried out. Combining with the actual situation of the project, the reform proposal is offered from the aspects of system match, monitoring and control systems, etc., aiming to optimise the performance of ground source heat pump. Concerning about the reduction of soil heating capacity in winter, the system can be supplemented with solar heating equipments. Formulating a reasonable operation strategy in separated period is also a viable way to reduce energy consumption.

Keywords: ground source heat pump, operation diagnosis, energy saving reform

1. INTRODUCTION

Geothermal energy is a kind of practical and competitive clean energy characterised by environmental protection and low pollution, which can significantly reduce the consumption of fossil fuels and ecological destruction in the process of fossil fuel mining, and improve the natural environment and ecological environment. Since 2010, China has become the world's largest emitter of green house gas (Liu, 2015: page 559). The requirements of air pollution prevention and improvement of the proportion of renewable energy consumption provide a critical opportunity for development of geothermal energy.

Actually, with abundant reservation of geothermal energy, China is one of the earliest countries utilizing geothermal energy (Zhu, 2015: page 468). Heat pump technology is mainly used in the utilization of shallow geothermal energy. With a stable average annual growth rate in China, it has been applied cover the whole country (Hou, 2018: page 405). At present, with the maturation of ground source heat pump technology, China has become the largest country with heat pump direct-use installed capacity and also the largest annual energy use country with heat pumps (Lund, 2016: page 67).

However, there are still many constraints in the development of ground source heat pump, including low level of resource exploration, imperfect management system, high initial investment and the policy etc. In actual operation condition, the efficiency of the GSHP system largely depends on the control of the operation and the optimisation of design. In order to offer improvement proposals, it is an effective way by investigating on the operation of the ground source heat pump system by experimental study (Xia, 2017: page 70-80) or studying on an onsite case (Naicker, 2018: page 429-442).

In order to ensure the efficient operation of the ground source heat pump system of a community, in this paper, the field test and operation record analysis of a GSHP system of a residential area was reported as well as a preliminary energy saving strategy. This paper analysed the performance of the system by conducting field tests and collecting the operational data and it came to a conclusion that the system has the energy-saving potential. Some preliminary schemes was put forward to promote the system performance. With the implement of strong supportive policy measures of Chinese government and further research on geothermal energy, ground source heat pumps will be more popular in China with higher efficiency.

2. SYSTEM DESCRIPTION

2.1. Description of the project

The Kexuejiayuan Community is located in Hefei, China, with a total construction area of 226,600m^2, including a residential construction area of 190,888m^2, public buildings of 7,820m^2 and other public residential buildings of 27,892m^2(Figure 1). The project adopts a ground source heat pump air-conditioning system, which uses a double U-shaped vertical buried pipe, with a 100-meter-deep single well and a fan coil at the end. The temperature difference on the source side is controlled at about 5°C, and the water supply temperature on the load side meets the user's demand of 26°C in summer and 18°C in winter. The heating season runs from November 20 to March 20 of the following year with a designed cooling load of 7500kW. The cooling season runs from May 20 to September 20 with the heating load of 4600kW. It has been about six years since the system was put into use.

Figure 1: The Kexuejiayuan Community

2.2. Description of the GSHP system

The GSHP system is made up with ground source heat pump units, water pumps and other equipments as shown in Figure 2. The system consists of 5 ground source heat pump units operating in parallel. In actual operation process, only 3 units are turned on in extreme weather conditions whether in winter or summer. The unit to be turned on is manually controlled by the operator according to the outdoor environment and indoor load conditions. The air-conditioning side uses 5 water pump units with 1 unit spared, and the source side uses 3 water pump units with 1 unit spared. The unit starts according to the operation of the heat pump unit. The frequency of the pump is manually adjusted by the operator empirically. The system is equipped with two cooling towers for peak regulation during summer and maintaining the heat balance at the source side. It was used during the cooling period in summer of 2016. Unexpectedly, the cooling towers are extremely close to residential buildings. Excessive noise may affect people's lives therefore the cooling towers cannot continue to be used normally.

The original automatic control system of the project expired due to the expiration of the maintenance period, and the automatic control company stopped its technical support. Although there was no obvious failure in the terminal automatic control system equipment and the automatic control communication line, no automatic control and system monitoring functions could be realised at present due to the interruption of the connection with the closed automatic control host. There is an urgent need to solve this problem through the repair of the automatic control system.

The system currently completely relies on the experience of the operating personnel to manually control the system and record the daily operating data.

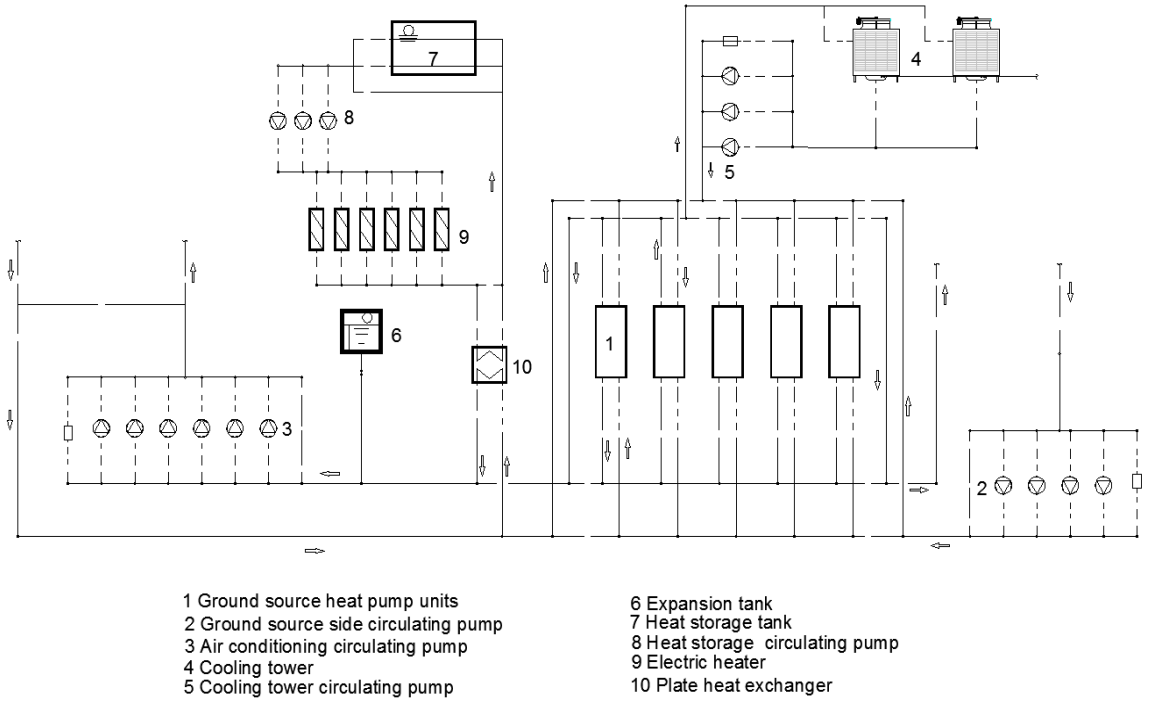

Figure 2: The system layout

3. SYSTEM OPERATION DIAGNOSIS

In order to further understand the actual performance of the system, thus providing basis for and energy-saving work, the field test of the system operation is carried out as follows: 1) Operation parameters tests of part of the system equipment; 2) Collecting and analysing the operation records.

3.1. Field tests of GSHP performance and circulating pump performance

Test conditions: The system starts a heat pump unit, corresponding to a chilled water circulating pump and a cooling water circulating pump. The pump frequency is 41Hz.

Under actual operating conditions (at the end of winter operating condition), the test of the performance of a single heat pump unit was conducted from 9:00 to 10:00. The results are shown in Table 1. The average temperature difference at the

user side is 4.2°C, which is close to the set temperature difference of 5°C. But the inlet and outlet temperatures at the user side are all 5°C lower than the set value. The average temperature difference at the source side is 2.0°C, which has a clear difference between the set temperature. The measured unit performance coefficient COP was 3.83, which was 83% of the unit's rated COP 4.6. But the actual power was lower than the rated value by nearly 30%. At the end of the winter season, the soil temperature drops, resulting in the lack of source-side heating capacity and leading to a decrease of the load-side heating power, and also a decrease in the temperature difference between the source and load side, which results in a reduction in the input power of the heat pump unit. However, because it is not in the rated condition, the COP value decreases compared with the rated value.

Table 1: Performance test results of ground source heat pump units

Category	Rated Value	Measured Value
Ground source inlet temperature (°C)	12	11.3
Ground source outlet temperature (°C)	7	9.3
User inlet temperature (°C)	40	36.4
User outlet temperature (°C)	45	40.6
Source side flow (m^3/h)	/	285
User side flow (m^3/h)	/	198
Heating capacity of the unit (kW)	1634	965.6
Heat pump unit input power (kW)	355	252.3
Average Coefficient Of Performance	4.6	3.83

Under the actual operating conditions (single water pump running both on the source side and load side), the performance of the pump was tested. The operating efficiency of the single pump on the load side and the source side of the system reached 80% and 72%, respectively. The test results are shown in Table 2.

Table 2: Performance test results of circulating water pumps

Category	Load side circulation pump		Source side circulation pump	
	Rated Value	Measured Value	Rated Value	Measured Value
Flow Rate （m^3/h）	187	198	346	285
Power （kW）	37	18.2	55	20.51
Efficiency （%）	-	0.80	-	0.72

The system can only open up to 3 heat pump units corresponding with circulating water pumps in extreme weather. In the test, the number of pump to be turned on was increased one by one. Record the flow rate of each condition separately and compare them with the rated flow to judge the parallel loss of the pump flow.

The results are shown in Figure 3. The load side circulation pump can meet the rated requirements in single and two parallel operating conditions, with no significant parallel loss. In the case of three parallel operating conditions, the increased water flow of a single pump is only 64% of the rated value, and there is a certain parallel loss. Actually, the parallel losses of the design of the three parallel operating conditions can be foreseen from the analysis of the pump characteristics. The flow rate when one pump is working alone is greater than the water flow of each pump when working in parallel. That is, when two pumps are operated in parallel, the flow rate cannot be multiplied more than when the single pump is operated. This phenomenon is obvious when multiple pumps are connected in parallel.

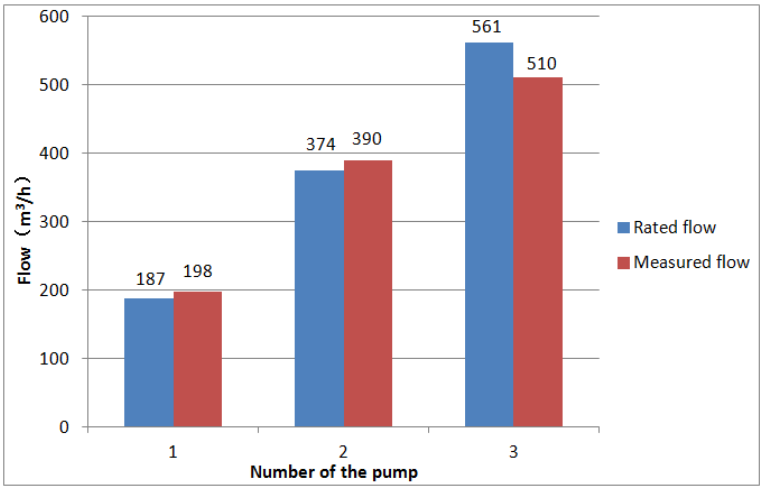

Figure 3: Test result of parallel flow rate of circulating pump on load side

3.2 Statistical analysis of temperature and power consumption

Based on the summary data of temperature in Figure 4, during the 2016-17 winter operating conditions, the source side outlet water temperature is basically maintained at 10 ~ 15 °C, inlet water temperature between 5 ~ 10 °C, basically able to meet the requirement of 7/12°C design condition. The inlet and outlet water temperatures at the source side continued to decrease over the entire heating season, reflecting the fact that the soil temperature was continuously declining, reaching a minimum in February, and the soil temperature began to rise in March. The load side of the outlet water temperature is maintained between 40 ~ 45 °C, the inlet water temperature between 32 ~ 37 °C, slightly lower than the design requirements of 45/40 °C. Especially, the inlet water temperature is lower than the design value, resulting that the temperature difference between the inlet and outlet water is larger than the design requirement in load side. It is necessary to consider whether the load side is in the “small-flow, large-temperature-difference” operating state. At the same time, it is necessary to investigate the indoor thermal comfort of users and comprehensively determine the operating mode that suits the current system status.

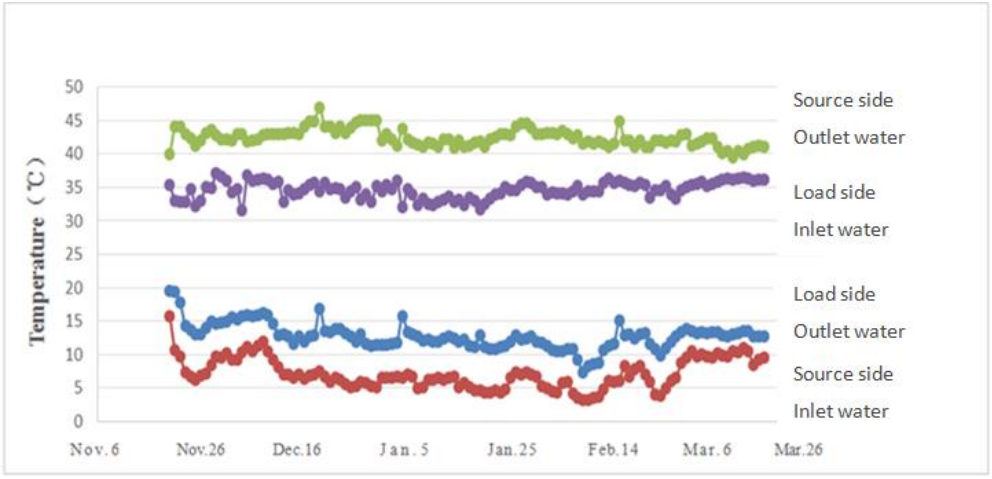

Figure 4: Daily average temperature statistics of source side and load side during the 2016-2017 heating season

The monthly average temperature difference between inlet and outlet water in the source side and load side during the heating season is shown in Figure 5. The trend of temperature difference basically conforms to the peak load period from November to January and gradually decreases in February and March. But at the same time, there remains three problems: (1) In December, the temperature difference between the source side and load side appeared anomalous, indicating that in the operating conditions during this period, the source side and load side of the system may have problems in matching the heat source with the transmission system; (2) Insufficient soil heating capacity during January and February; (3) The load decreased to a lower level in March.

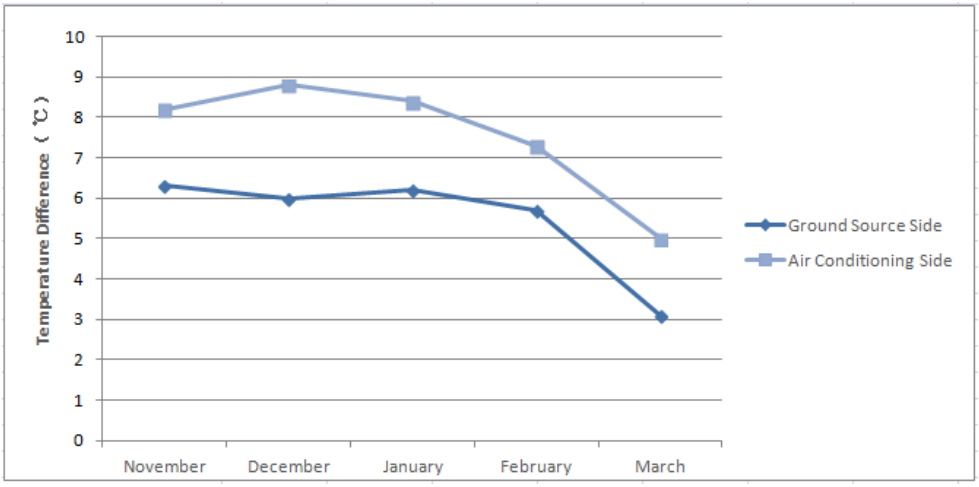

Figure 5: Monthly average temperature difference statistics of source side and load side during the 2016-2017 heating season

According to the statistics of the electricity consumption in the heating season in Figure 6 and Figure 7, the high-load period is from late December to early February. At the beginning of heating in November, the entire building is “preheated” and energy consumption is higher. Therefore, when formulating the system winter operation strategy, it can be roughly considered as following period: warm-up period (11.20-11.30), transition period (12.1-12.20), high-load period (12.20-2.10), and end-of-heating period (2.10-3.20).

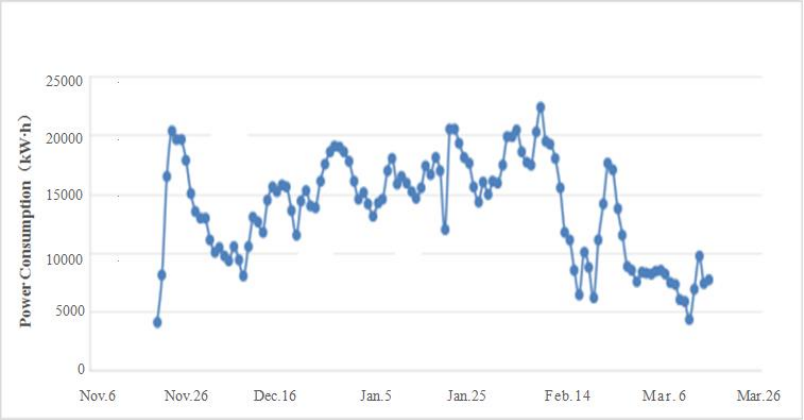

Figure 6: Power consumption statistics of the system in 2016-2017 heating season

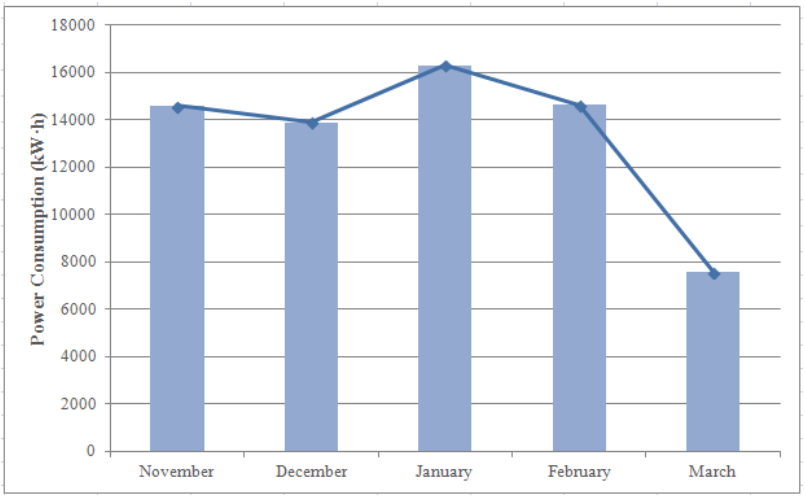

Figure 7: Monthly average power consumption statistics of the system in 2016-2017 heating season

3.3. Analysis of test results

1) Under the test conditions (a single heat pump corresponding to a single water pump), the efficiency of heat pump unit is lower than the rated value, and the power is relatively low;

2) The temperature difference of the heat pump unit between inlet and outlet water on the source side is relatively low compared with the design value, and the outlet water temperature on the load side is also relatively low. However, the test is conducted during the end of the heating season and the load is extremely low, therefore more tests must be conducted in higher load condition to make comprehensive judgments;

3) The single pump performs well. In the conditions of three pumps operating in parallel, the test proved that there must be a significant parallel flow loss.

3.4. Analysis of operation record

1) As the load is in an ever-changing state, the current operation strategy of the load side of the system may be in a state of "small flow and large temperature difference" for a certain period of time. Further investigation and analysis of terminal balance and indoor effects are required;

2) According to temperature difference statistics on both sides of the load and source, the system may have problems in matching the heat source with the transmission and distribution system during the high load operation period;

3) For winter conditions, the operation period can be divided according to energy consumption statistics and load conditions. A reasonable operation strategy can be divided into different time divisions to reduce energy consumption;

4) Existing information on the existence of operational record statistics lacks of integrity, such as: system flow, the number of opened devices, the frequency of equipment operation, thus creating obstacles to judging the status of the system and the cause of the problems.

4. SYSTEM ENERGY SAVING REFORM

The system can only open up to 3 heat pump units at the same time since being put into use, and the number is judged by the operating personnel and controlled manually. The frequency conversion pump is used in the transmission and distribution system, but it lacks an automatic control system. The pump frequency is manually adjusted by the operating personnel according to experience. Due to the design intent, the system is equipped with cooling towers to assist the heat dissipation in summer to maintain the balance of the ground source temperature. However, the cooling tower is no longer able to be used because residents' complaint about the excessive noise during the operation. The original automatic control system stops service and causes the lost of automatic control functions and system status parameter monitoring functions.

Based on the actual operation situation of the system, field test results and analysis of operation records, the following energy-saving schemes are proposed:

1) Divide the time period according to the energy consumption statistics and load situation, and formulate a reasonable operation strategy in time division to reduce energy consumption;

2) Concerning of the reduction of soil heating capacity in winter, it can be supplemented with solar heating systems;

3) Transform the automatic control system, restore the monitoring of the system state parameters, and rely on the automatic control system to execute the operating strategy;

4) According to temperature difference both in the sides of the air conditioning and the ground source, solve the problem in matching the heat source with transmission and distribution system;

5) Perform a full hydraulic balance adjustment of the entire heating and air conditioning system;

6) Carry out the energy-saving rectification of the original construction system which failed to meet the current specifications exists in the original system.

In addition, after combining with the energy saving diagnostic conclusions of the monitoring and control system, the energy management system was added to implement the sub-category measurement. Also the monitoring and control of basic energy-using equipment in the system was enhanced.

However, due to the complexity of practical engineering, the energy-saving effect of the proposed strategies have not been certificated yet. Further research should be carried out during subsequent operation.

5. CONCLUSION

In this paper, in order to optimise the ground source heat pump system in the KeXueJiaYuan community of Hefei, the ground source heat pump system was field tested and the operation performance was analysed. It turns out that the ground source heat pump system equipments of this project are not properly matched with the load and lacks of a reasonable operation strategy, thus causing the system to operate in an energy inefficient state. The system has large potential for energy saving program and is suitable for energy saving transformation. Preliminary strategies for system transformation was put forward to guide to operation of the system, aiming to adjust the system operation strategy, which can strengthen the energy management of the project. To evaluate the performance of system with improved operation schemes, more research should be done in analysing the COP and energy consumption in the future.

The project is the first large-scale project to promote the use of renewable energy for heating and air conditioning in Anhui Province, China. As in actual operation of GSHP system, problems like low operating efficiency and mismatch of energy between demand and supply exist. The research of system performance presented by this paper can be a reference for other project. The thought of implementing energy-saving strategy will contribute to the popularization and application of renewable energy in similar projects. It will also be a scientific guidance for the development of the ground source heat pump in the region.

6. REFERENCES

Hou, J, Cao, M, & Liu, P, 2018. Development and utilization of geothermal energy in china: current practices and future strategies. Renewable Energy, 125, 401-412.

Lund, J W., Boyd, T L., 2016. Direct utilization of geothermal energy 2015 worldwide review. Geothermics, 60, pp. 66-93.

Liu, X, Lu, S, Hughes, P, & Cai, Z, 2015. A comparative study of the status of GSHP applications in the United States and China. Renewable & Sustainable Energy Reviews, 48, 558-570.

Naicker, S S., & Rees, S J., 2018. Performance analysis of a large geothermal heating and cooling system. Renewable Energy, 122, 429-442.

Xia, L, Ma, Z, Mclauchlan, C, & Wang S., 2017. Experimental investigation and control optimization of a ground source heat pump system. Applied Thermal Engineering, 127, 70-80.

Zhu, J, Hu, K, Lu, X, Huang, X, Liu, K, & Wu, X, 2015. A review of geothermal energy resources, development, and applications in china: current status and prospects. Energy, 93, 466-483.

328: A global maximum power point tracking method for PV arrays under partially shaded conditions

Jian PAN[1], Jiacheng LI[2], Kun LI[3]

[1] Jian Pan, Hubei University of Technology, jpan12@126.com
[2] Jiacheng Li, Hubei University of Technology, 2423878729@qq.com
[3] Kun Li, Hubei University of Technology, 834435731@qq.com

For the study of maximum power point tracking (MPPT) control, many existing research methods can exhibit effective output which depend on uniform solar irradiance. However, multiple peaks can be exhibited on the characteristic curve of the PV array under partial shading conditions (PSC) due to the effect of the bypass diode. In this case, the efficiency of the conventional MPPT methods are limited and the others are difficult to apply in engineering due to cost issues. In this paper, an improved hysteresis comparison method that combines with a constraint function is proposed. The performance of the proposed method is validated through MATLAB/Simulink simulations.

Keywords：MPPT; PSC; multiple peaks; constraint function

1. INTRODUCTION

In the photovoltaic power generation system, it is important to perform maximum power point tracking of the photovoltaic array to stably output at the maximum power because the characteristic curve of the PV array is nonlinear. The tracking accuracy and speed are the main factors of the effectiveness of MPPT. There are a mountain of MPPT methods that have been proposed, such as open-circuit voltage method, perturbation and observation (P&O), incremental conductance (INC), and so on. These methods can effectively track the maximum power point of the PV array at an appropriate step size and are easy to apply which only limited to uniform lighting conditions. However, the weather environment will easy to change in the actual process. The characteristics of the PV array will show multiple peaks especially in the partial shadow conditions. In this case, the traditional MPPT will be trapped in the local maximum power point (LMPP) which will greatly reduces the tracking efficiency. Therefore, it is of great significance to track global maximum power point (GMPP) tracking under partially shaded conditions.

At present, many researchers have conducted research on MPPT under PSC. Hassan, et al. (2017) propose a high performance neuro-fuzzy indirect wavelet-based adaptive MPPT control. This method combines the advantages of self-learning ability of neural network, reasoning ability of fuzzy control, and the localised characteristics of wavelet analysis. It achieves the purpose of quickly tracking the maximum power point. This method can decrease the weight of the lengthy pre-learning but it need a large amount of training data to make the weight appropriate. The most popular among these algorithms which has found extensive use for GMPPT under PSC is the particle swarm optimisation (PSO) algorithm due to its simplistic nature. Many modifications have been proposed to the conventional PSO (CPSO) to make it much more suited to GMPPT purposes (Ishaque, 2014; Jhang, 2014; Ishaque, 2012). In Wu (2018), a PSO algorithm combines with open-circuit voltage method was proposed to track the GMPP. The method firstly finds the voltage range of the maximum power point through power closed-loop control, and then tracks the maximum power point by using PSO or 0.8 times open circuit point pressure method respectively when the voltage range is small or large. However, this method passes the experience. The formula to select the appropriate voltage range, and the open circuit voltage method also belongs to an approximate calculation, which will undoubtedly reduce the tracking accuracy. In Ram (2017),the author present a new robust, mutated and fast tracking leader PSO (LPSO) method which add a large number of programs on the basis of PSO algorithm. This method can differentiate between local and global maximum power points to make it much more suited to GMPPT purposes but the algorithm is complex to apply to the Photovoltaic industry. In Sen (2018), a modified particle velocity-based PSO (MPV-PSO) algorithm is proposed. This method can eliminate the inherent randomness in the conventional PSO algorithm and the need for tuning the weight factor, the cognitive and social acceleration coefficients. But the introducing of adaptive values make the tracking speed down. To simplify the controller, the author present a fast tracking method using I-V curve in Ghasemi (2018). It divides the P-U curve into sever regions and compares the maximum power points of these different regions to find the GMPP. The disadvantage of this method is that the tracking accuracy will decrease under the influence of the approximate simulation of the I-U curve.

In the paper, a fast and simple GMPPT method under PSC is proposed. The characteristics of the PV array under mismatch conditions are introduced in Section Two. Section Three introduces the hysteresis comparison method and compares it with other methods. By analysing the characteristics curve of the PV array under PSC, a constraint function is introduced to specify the change direction of the operating point so that the changed operating point can accurately fall within the voltage range to which the global maximum power point belongs. The global maximum power point is then tracked by the hysteresis comparison method. Section Four analyses the simulation results of the proposed method with another conventional method. The feasibility of the proposed method is proved by comparison. Section Five gives a brief summary of this paper.

2. PV ARRAY CHARACTERISTIC CURVE UNDER PSC

Figure 1 shows the circuit topology of PV system. The current of the PV array is boosted by the Boost circuit to supply the load. However, due to the non-linear output power of the PV cell, the output power is not stable. Therefore, the MPPT control of the PV array is required to make it run stably at the maximum power point to improve the photoelectric conversion efficiency. For this reason, this paper first analyses the photovoltaic array.

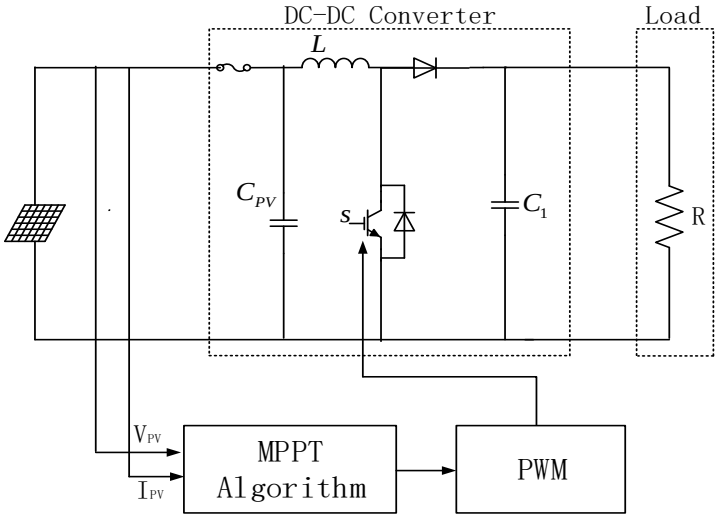

Figure 1: Architecture of PV system with MPPT

Solar cells consist of monocrystalline silicon which converts light energy into electrical energy through the photoelectric effect. The equivalent model is shown in Figure 2. And the PV cell output current I is present by equation 1.

Equation 1: the PV cell output current I

$$I = I_{PH} - I_0[e^{\frac{q(U_R+IR_S)}{AKT}} - 1] - \frac{U_R + IR_S}{R_{SH}}$$

Where：

- I_{PH} = photocurrent
- I_D = junction current of PN junction
- R_S = equivalent resistance of the semiconductor material
- R_{SH} = defective current due to loss of semiconductor material

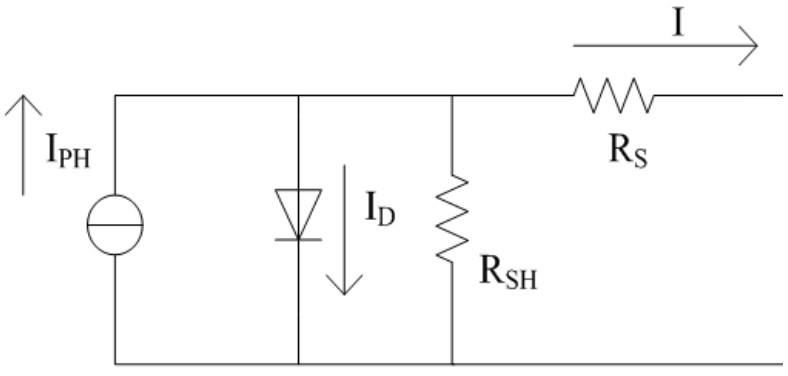

Figure 2: PV cell equivalent circuit

PV array consists of multiple PV modules connecting in series and in parallel where a single PV module comprises several PV cells. Therefore, the output of the PV array is related to the working state of each cell. When the operating conditions of these individual batteries are different, the PV array will experience a mismatch operation. There are many reasons that lead to mismatch conditions. For example, trees, clouds, etc. obscure the sunlight and cause photovoltaic panels to receive uneven irradiation.

Figure 3(a) is the schematic of PV array when PV module are exposed to different irradiation. To prevent energy loss of mismatched cells that generated by the rest modules of the parallel branch, each PV module is connected in parallel with a bypass diode and protected by it. At the same time, a shielding diode is connected in series with each parallel branch to

prevent the influence of the different working conditions of the photovoltaic module. Under normal circumstances, the bypass diode does not work; but when the PV array is exposed to non-uniform irradiation, the current generated by the photovoltaic module in the shadow will decrease with the reducion of the irradiation. Some of the current that flow through the module will flow into the bypass diode in the meantime, preventing the battery from being damaged due to excessive current. And the shielding diode are similar to the bypass diode.

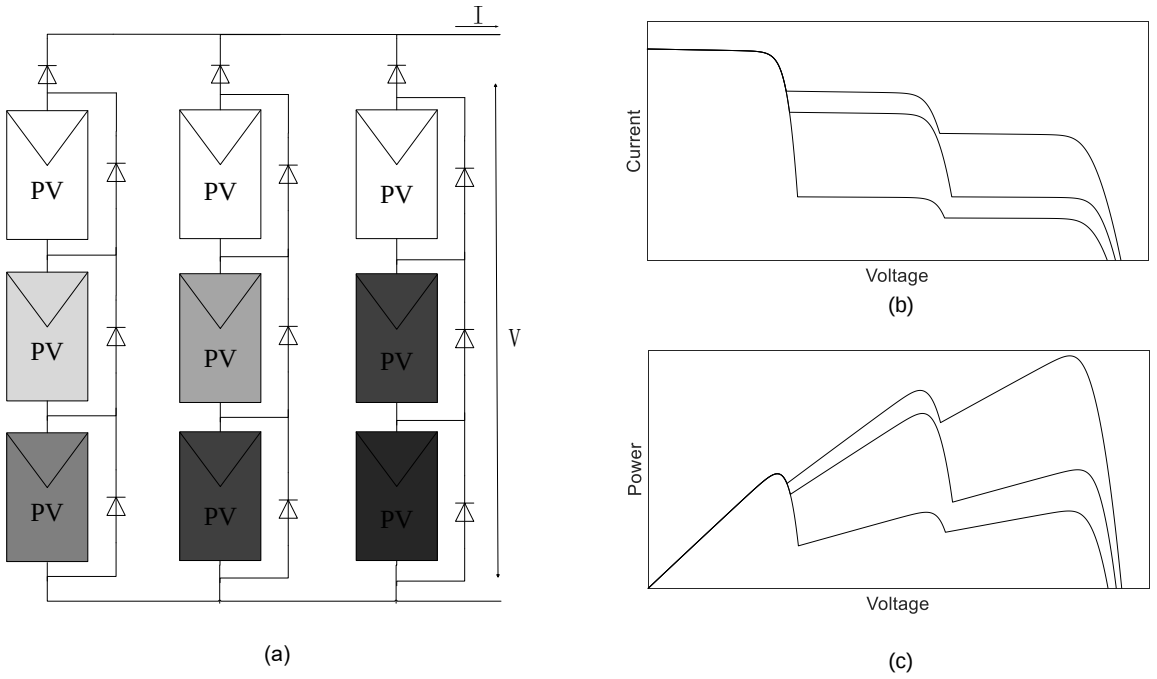

Figure 3: The characteristic curves of PV array under PSC
(a) the schematic of PV array under PSC (b)I-U curve (c)P-U curve

There is only one maximum power point in the characteristic curve of the photovoltaic array under uniform irradiation condition. However, when the photovoltaic array get into the mismatch condition, multiple local maximum power points will occur that caused by the combination of the bypass diode and the shield diode. Figures 3(b) and (c) respectively show the I-U and P-U characteristic curves of the photovoltaic array under PSC. As shown in Figure 3, when PSC occurs, a part of the current which flow into the shaded photovoltaic module flows through the bypass diode at the same time, resulting in multiple peaks in the P-V characteristic curve.

3. THE PROPOSED GMPP TRACKING METHOD

3.1. Work process of the proposed method

As shown in Figure 4, the basic idea of the GMPPT method proposed in this paper is that the working point decreases from point A to B caused by the current drops when the irradiation changes from uniform to non-uniform. Then the work point is repositioned to point C according to the constraint function. And the maximum power point, D, will be tracked again. According to the assumption of this method, it must firstly determine whether the PV array is exposed to non-uniform irradiation condition, and the determination equations are showed as follows (Ji, 2011).

Equation 2: PSC occurrence conditions

$$\Delta V_{PV} = \left| V_{PV(n)} - V_{PV(n-1)} \right| \le \Delta V_{\text{set}}$$

$$\frac{\Delta I_{PV}}{I_{PV(n-1)}} = \left| I_{PV(n)} - I_{PV(n-1)} \right| \le \Delta I_{\text{set}} \approx \frac{I_{PV(n-1)}}{N_{PM}}$$

Where：

- ΔV_{set} = the upper limit value of the step-size
- N_{PM}= the number of the PV module string in parallel
- $V_{PV(n)}$ = the value of the PV voltage at nth moment
- $I_{PV(n)}$ = the value of the PV current at nth moment

When the above equation is satisfied, the operating point is changed according to Equation 3, and it is repositioned to the voltage range where the global maximum power point is located. Finally, the GMPP will be tracked again using the adaptive step-size hysteresis comparison method.

Equation 3: PSC occurrence conditions

$$V_{next} = \frac{V_{oc}}{I_{sc}} I_{pv(n)}$$

3.2. Adaptive step-size hysteresis comparison method

The traditional hysteresis comparison method is to form a hysteresis loop (Peng 2018) by equidistantly taking two points those are on the left and right hands of the operation point within a certain voltage range. By comparing the power of the work point and the other two points, the direction of the next moment of operation is determined to perform maximum power point tracking. When the working point power relation satisfies the hysteresis condition, it operates at a constant voltage and does not perform dynamic tracking. It can prevent the occurrence of the power oscillation. When the working point power relationship jumps out of the hysteresis range, the working point is disturbed to achieve dynamic tracking.

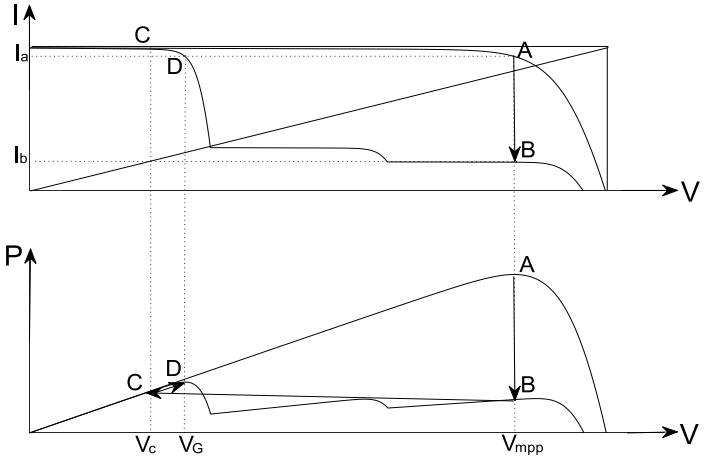

Figure 4: concept of the proposed MPPT method

The proposed method uses adaptive step-size hysteresis comparison method to track MPP. It sets the adaptive step-size disturbance based on the traditional hysteresis comparison method, which avoids the oscillation problem caused by disturbance observation method, open-circuit voltage method and others. The adaptive step-size disturbance request to adjust the disturbance step size in real time. When the step-size is farther away from the maximum power point, the step-size will be large to track the MPP rapidly. When the maximum power point is reached, the disturbance step-size is small, so as not to generate too much oscillation. Assuming that the voltage at the kth moment is V_{kT_P}, and the power is P_{kT_P}. Then the voltage at the (k+1)th moment should satisfy the following equation.

Equation 4: the voltage value at (k+1) moment

$$V_{(k+1)T_P} = V_{kT_P} \pm \Delta x$$

Equation 5: the value of the step-size

$$\Delta x = N\left(\left|\frac{P_{kT_P} - V_{(k-1)T_P}}{V_{kT_P} - V_{(k-1)T_P}}\right| + m\right)$$

Where：

- Δx = the step-size at (k+1) moment
- N = scale factor
- m= Ideal factor

To prevent the system from falling into an infinite loop under the effect of the hysteresis control, a m-fold proportional factor is added to the conventional adaptive step size method. Equation 6 can be derived from Equations 4 and 5.

Equation 6 : the voltage value at (k+1) moment

$$V_{(k+1)T_P} = V_{kT_P} \pm N\left(\left|\frac{P_{kT_P} - V_{(k-1)T_P}}{V_{kT_P} - V_{(k-1)T_P}}\right| + m\right)$$

From Equation 6, the size of the next disturbance step can be determined. Applying this equation to the hysteresis comparison method and then gain the adaptive step-size hysteresis comparison method. The algorithm flow chart is shown in Figure 5.

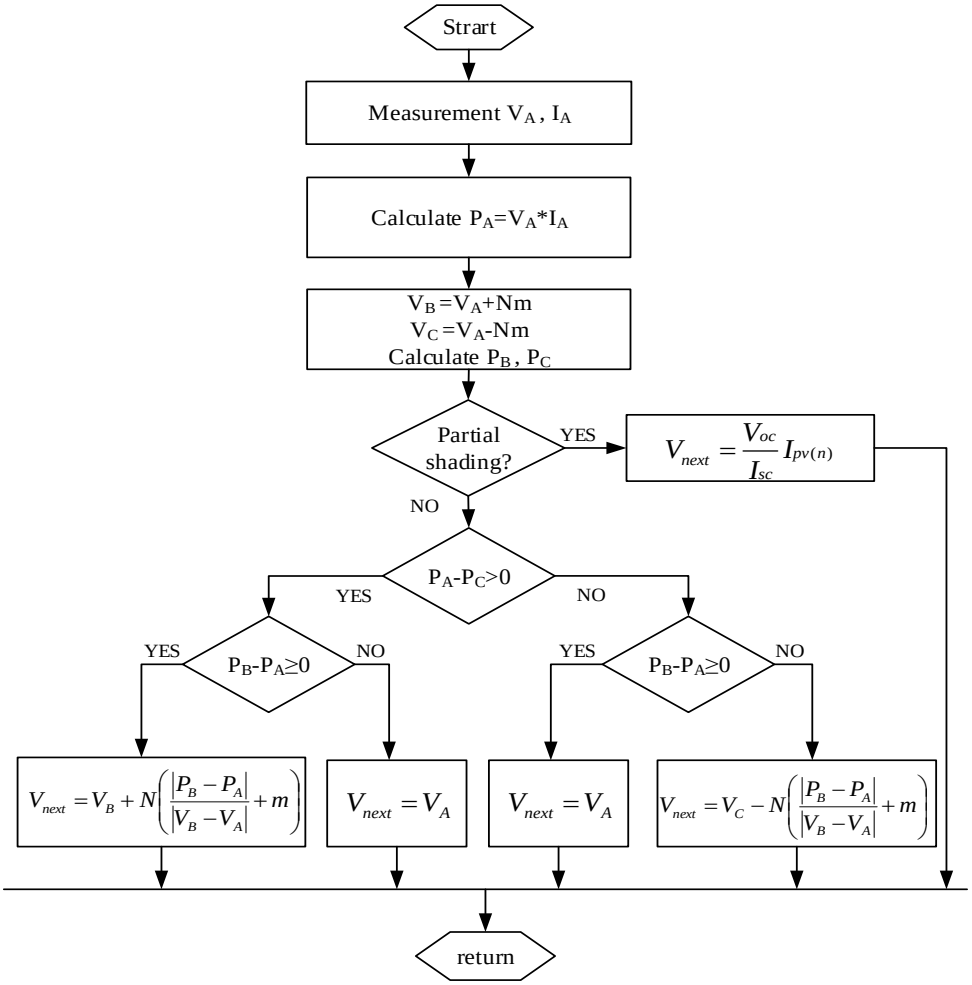

Figure 5: Block diagram of the proposed method

As shown in Figure 5, the proposed method firstly calculates the power of point A by sampling the voltage and current of it, and regards point A as the working point. Then, use the above formula to obtain points B and C. Secondly, it judges whether the system is under uneven irradiation according to equation 2 and 3. Finally, the maximum power point is tracked by the adaptive step-size hysteresis comparison method with the corresponding processing.

4. SIMULATION ANALYSIS

In order to verify the correctness of the proposed method, a PV system with MPPT module is built on MATLAB/Simulink. The Parameters of PV system circuit and PV cell、PV module under uniform irradiation condition are show in the table 1 and 2.

From the analysis of the Section Three, it can be seen that when the irradiation change slowly, the operating point will reduce from the original maximum power point to the high voltage range. At this time, GMPP may also be within this interval, so the traditional MPPT will gain the possibility to track the GMPP.

Table 1: Simulation Parameters of The Boost Converter

Parameters	Symbol	Value	Units
PV capacitor	C_1	500	μH
Converter side inductance	L	60	μF
Net side inductance	C_1	100	μH

Table 2: Simulation Parameters of The PV module

Parameters	Symbol	Cell	Module	Units
Open-circuit voltage	C_{pv}	24.5	73.5	V
Short-circuit current	I_{sc}	2.8	2.8	A
Maximum Power	P_{mpp}	51.36	154.08	W
Maximum Power voltage	V_{mpp}	21.4	64.2	V
Maximum Power current	I_{mpp}	2.4	2.4	A

To avoid this case, the simulation uses rapidly changing irradiation when setting environmental conditions. Figure 6 (a), (b) shows the I-U curve and P-U curve of PV array under PSC. In Figure 6 (a), the irradiance of the partially shaded PV module is respectively reduced from 1000W/m^2 to 300W/m^2 and 200W/m^2. In Figure 6 (b), we can see that there are two PV module under uneven irradiation and the photovoltaic arrays show three peaks where the GMPP is about 57W.

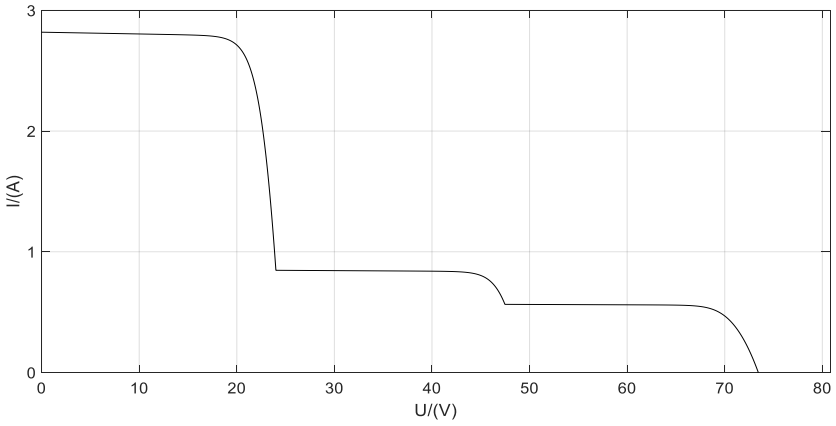

(a)I-U curve

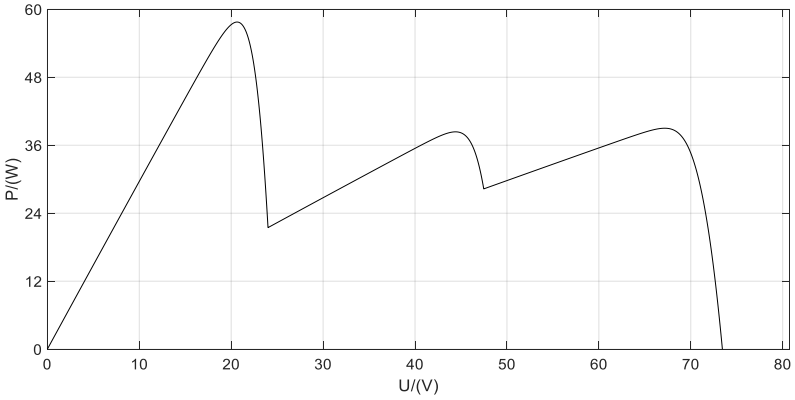

(b) P-U curve

Figure 6: The characteristic of the PV array under PSC

Figure 7 shows the performance of the proposed method and the conventional P&O under PSC when the irradiance rapidly changes. Figure 7(a) shows the output power of the proposed method. The output power eventually stabilises at about 55.3W when PSC occurs, and the power loss is about 3%. Figure 7(b) shows the output power of the conventional P&O method. The output power eventually stabilises at about 36.7W when PSC occurs, and the power loss is about 35%. The figure shows that the tracking speed are fast for both of the methods which tracked the MPP within 0.02s.

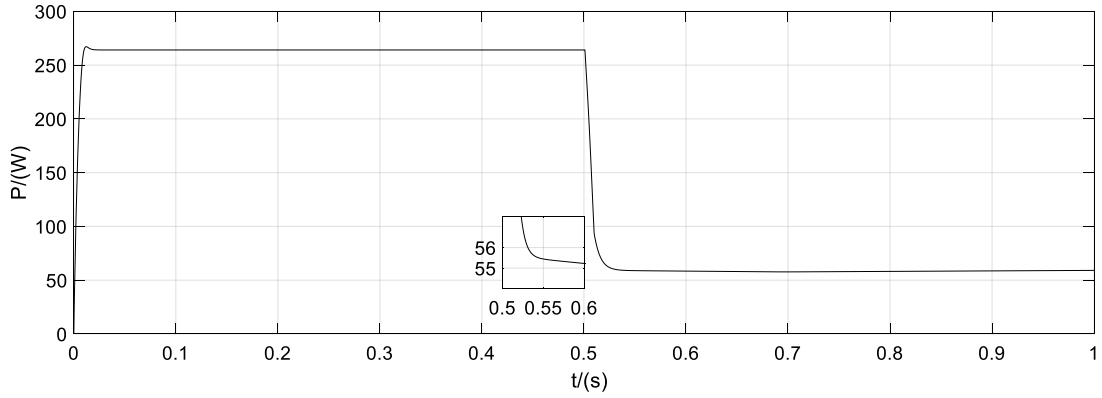

(a) the output power of the proposed method

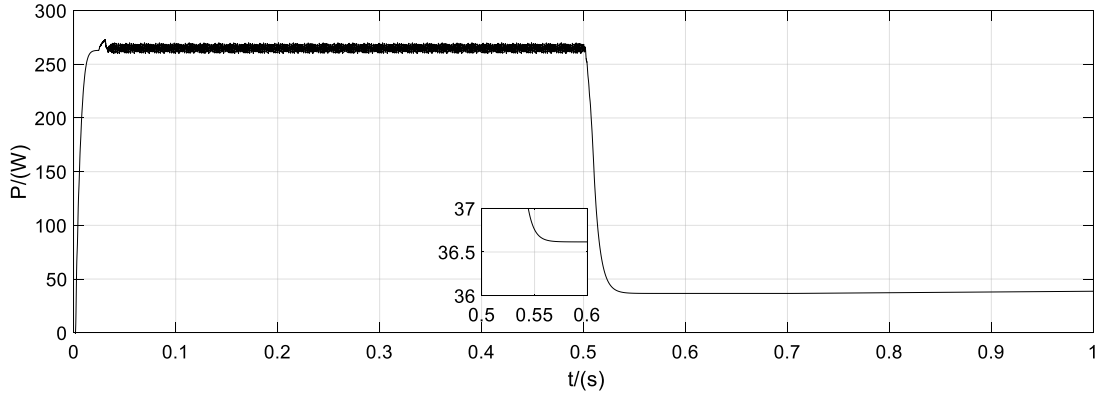

(b) the output power of the conventional P&O

Figure 7: The performance of the MPPT method under PSC

Compared with Figures 7(a) and (b), we can see that the traditional P&O method can not accurately track the GMPP of the PV array under PSC with rapidly changing irradiation, and the power dither is obvious. The proposed method can effectively track the GMPP under both uniform irradiance condition and PSC where the tracking speed is fast and the accuracy is high.

5. CONCLUSION

In this paper, the MPPT control is combined with the adaptive step-size and hysteresis comparison method. A constraint function is designed to successfully solve the multi-peak optimisation problem of photovoltaic arrays caused by uneven irradiation. The method can accurately and rapidly track the global maximum power point of the PV array under both uniform irradiation and PSC. At the same time, it improves the power dither problem of the conventional maximum power point tracking method. The result of MATLAB simulation shows that the tracking accuracy of this method reaches 97%. It successfully verifies the effectiveness of this method.

6. REFERENCES

Esra, T, Chapman P, 2007. Comparison of photovoltaic array maximum power point tracking techniques [J]. IEEE Trans. Energy Convers. 22, (2), pp. 439-449

Ghasemi M A, Ramyar A, et al., 2018. MPPT Method for PV Systems Under Partially Shaded Conditions by Approximating I–V Curve[J]. IEEE Transactions on Industrial Electronics. 65, (5), pp. 3966-3975

Hassan, Syed-Zulqadar, Li, Hui, Kamal, Tariq, Arifoglu, Ugur, Mumtaz, Sidra, Khan, Laiq, 2017. Neuro-Fuzzy Wavelet Based Adaptive MPPT Algorithm for Photovoltaic Systems[J]. Energies.10,394-410.

Ishaque, K, Salam, Z, 2012. A deterministic particle swarm optimization maximum power point tracker for photovoltaic system under partial shading condition[J]. IEEE Trans. Ind. Electron. 60, (8), pp. 3195–3206

Ishaque, K, Salam, Z, Amjad, M, et al., 2014. An improved particle swarm optimization (PSO)-based MPPT for PV with reduced steady-state oscillation[J]. IEEE Trans. Power Electron.. 27, (8), pp. 3627–3638

Jhang, J.H., Tian, I.S, 2014. A maximum power point tracking method based on perturb-and-observe combined with particle swarm optimization[J]. IEEE J. Photovolt. 4, (2), pp. 626–633

Ji J-H, Jung D-Y, et al., 2011. A Real Maximum Power Point Tracking Method for Mismatching Compensation in PV Array Under Partially Shaded Conditions[J]. IEEE Transactions on Power Electronics. 26, (4), pp. 1101–1109

Peng, B-R, Ho, K-C, et al., 2018. A Novel and Fast MPPT Method Suitable for Both Fast Changing and Partially Shaded Conditions[J]. IEEE Transactions on Industrial Electronics. 26, (4), pp. 3240–3251

Ram, J P, Rajasekar, N, 2017. A new robust, mutated and fast tracking LPSO method for solar PV maximum power point tracking under partial shaded conditions[J]. Applied Energy. 201,pp. 45-59

Sen T, Pragallapati N, 2018. Global maximum power point tracking of PV arrays under partial shading conditions using a modified particle velocity-based PSO technique[J]. IET Renewable Power Generation. 12, (5), pp. 555-564

Sokolov M, Shmilovitz D, 2008. A modified MPPT scheme for accelerated convergence[J]. IEEE Trans. Energy Convers. 23, (4), pp. 1105–1107

Wu, Z, Jiang, Z, et al., 2018. An improved global MPPT method based on power closed-loop control [J]. Power System Protection and Control. 46, (1), pp. 57-62

329: Design, development and testing of a novel power-augmented cross-axis-wind-turbine

Wen Tong CHONG[1,a], Wan Khairul MUZAMMIL[1,b], Kok Hoe WONG[1,c], Bernard Lip Huat SAW[2], Yung Jeh CHU[1,d], Xiao Hang WANG[1,e], Chin-Tsan WANG[3]

[1] *Department of Mechanical Engineering, Faculty of Engineering, University of Malaya, 50603 Kuala Lumpur, Malaysia,*
[a] *Corresponding author: chong_wentong@um.edu.my,* [b] *khairulm@siswa.um.edu.my,*
[c] *raymond_wong86@hotmail.com,* [d] *chujeh2022@gmail.com,* [e] *wangxiaohang2011@163.com*
[2] *Lee Kong Chian Faculty of Engineering and Science, University of Tunku Abdul Rahman, Malaysia, sawlh@utar.edu.my*
[3] *Department of Mechanical and Electro-Mechanical Engineering, National Ilan University, Taiwan, ctwang@niu.edu.tw*

The horizontal-axis-wind-turbine (HAWT) is popular in the wind power industry nowadays due to its high power extraction capability. However, the HAWT has some complications due to high turbulent, low speed and changing direction of wind, which inhibits its full performance. Some vertical-axis-wind-turbine (VAWT) designs were able to function well under these wind conditions but they usually produce less power compared to HAWT. Thus, a new type of wind turbine design is proposed to overcome the weaknesses of HAWT and VAWT namely the cross-axis-wind-turbine (CAWT). The CAWT has three vertical and six horizontal blades, which interacts with horizontal and vertical wind. The vertical wind is generated by introducing a deflector or an omni-directional shroud to direct the oncoming horizontal wind towards the horizontal blades. The shroud consists of stacked ring-like deflecting planes supported by vertical webs and an inverted funnel-shaped base. It was designed to produce vertical wind components from any horizontal wind direction. The performance of the shroud was investigated by using a computational fluid dynamics (CFD) software, which showed significant vertical wind component located at the top of the proposed shroud. Experiments using deflectors to guide the oncoming airflow upward were designed to test the CAWT performance with various inclination angles (from 30 to 45°, with 5º increment). The experiments were also conducted with different pitch angles to identify the characteristics of the horizontal blades of the CAWT. A conventional H-rotor VAWT was tested under the same experimental conditions for benchmarking purposes. The results showed that the CAWT produced significant improvements in power output and rotational speed performance compared to the VAWT. It was found that the CAWT's peak power coefficients (integrated with the 45° deflector) were increased significantly by 103 to 175 % at different tip speed ratios for various horizontal blade pitch angles. The study showed that the proposed CAWT was able to achieve maximum RPM of up to 112% higher than that of the VAWT counterpart as well as better starting behaviour. These preliminary findings show the potential of CAWT for future applications in many locations, creating significant opportunities for wind energy devices.

Keywords: Cross-axis-wind-turbine; Efficiency; Power augmentation; Urban energy system; Wind energy

1. INTRODUCTION

Increasing demand for energy attracts interests of the worldwide researchers on the renewable energy field. As the fossil fuel reserves are depleting, renewable energy could play an important role in energy generation and management. Since 1970s, development of wind turbine technologies saw the evolution of wind turbine designs, strategies and concept brought forward by researchers to optimise the performances of rotors. The most well-known lift-type vertical-axis-wind-turbine (VAWT) that has been used since the 1930's is the Darrieus wind turbine. Invented by G.J.M. Darrieus, airfoil profile was adopted in the blades of the wind turbine to mimic the wings of birds that has the minimum resistance in forward motion and capable of exploiting maximum available amount of energy by using the traversing thrust of the blades (Darrieus, 1931). Patented in 1931, Darrieus described two major configurations for the wind turbine, curved and straight blades. Over the years, the original two configurations of lift-type wind turbine have evolved into several variations. The development of the curved-blade configuration has evolved into phi-rotor or also known as the egg-beater rotor due to its similarity in geometry. Meanwhile, two different variations of the straight-blade Darrieus turbine have been developed since the 1970's; notably the variable-geometry (Musgrove-rotor) rotor and variable-pitch (Giromill) rotor. The Musgrove-rotor employed blade-reefing mechanism to limit the speed of the rotor in high wind speed conditions (Mathew, 2006). In its early development, the Musgrove rotor showed good potentials, which led to the building of several large-scale rotors (rated 100 kW). However, due to the complexity of the blade-reefing mechanism and large concrete structure needed to support the rotor result in high production cost and maintenance of the turbine. On the other hand, the giromill is an H-rotor Darrieus wind turbine with variable pitch blades to maintain the angle of attack of the wind interacting with the blades relatively constant in the upwind and downwind regions of the rotor. The method of controlling the pitch blade produced comparable power coefficient as the horizontal-axis-wind-turbine (HAWT). Nevertheless, the mechanism that controls the pitch angle proves costly and unreliable which was difficult to maintain. Therefore, the giromill was abandoned for the much simpler and cost-effective H-rotor (Sjokvist and Eriksson, 2013). The H-rotor is a fixed-pitch straight-blade wind turbine that uses a direct-drive generator to provide better cost efficiency since it is positioned near to the ground. Due to the large-scale cyclic torque of the fixed-pitch blade, the rotor shaft is exposed to torsional stress caused by vibration. Therefore, requiring stronger and lighter shaft. Later, the helical H-rotor was developed with a reported power coefficient of 0.3 at tip speed ratio, λ of 3 (van Bussel et al., 2004). The geometry of the helical H-rotor blades distributes the torque uniformly around its circumference, which reduces cyclic forces and lowers the noise level.

Wind energy is recognised as a potential source for free, clean and inexhaustible energy, especially for use in urban cities where it is urged to place wind turbines closer to populated areas due to the decreasing number of economic sites (Wagner et al., 1996). In general, wind farms use large HAWT with long blades, which would generate noise and vibration that are not suitable for urban use. In recent years, small wind turbines have been employed in urban areas for local off-grid applications. Building integrated wind turbines (BIWTs) have shown that the use of wind turbines on buildings has great potential to provide renewable energy and therefore reducing the dependencies on fossil fuel reserves (Balduzzi et al., 2012). However, incorporating wind turbines into buildings possesses several key issues that hinder a wider acceptance of the technology, i.e. concerns on the vibration and noise generated by the wind turbine rotors that would affect the building and its occupants, the visual impact of the rotating turbines on the appearance of the buildings and public safety (Grant et al., 2008). The complex nature of urban winds requires wind turbines that are designed to receive wind from various directions. Moreover, urban winds are generally erratic, insubstantial and inconsistent due to the many obstacles (e.g. buildings and other obstructions); creating blockages that can reduce wind turbine performances (Abohela et al., 2013). Hence, necessitating wind turbines with good self-starting characteristics. Also, researchers over the years have explored the possibilities of augmenting wind flow from the surroundings to increase the oncoming wind speed before it interacts with the turbine blades (Chong et al., 2013). By applying venturi effect, the augmented wind that flows in between buildings, guide-vanes or baffles experiences an increase in velocity, and therefore its' kinetic energy. Moreover, thoroughly designed guide-vanes could guide the oncoming wind flow to an optimum angle of attack of the blades, hence improving the wind turbine performance.

For a wind energy generation system to be installed in urban areas, several factors need to be considered, i.e. blade failures, noise levels, visual impacts, structural issues, and electromagnetic interference (Oppenheim et al., 2004). Over the years, the HAWTs have been demonstrated to be very effective in generating electricity from the wind. However, the need for a yaw mechanism, the large tower structure supporting the heavy nacelle and the high level of noise hinder the use of HAWTs in urban environments. Due to the disadvantages of the HAWT, the VAWT is deemed to be more suitable to be used in urban areas due to their smaller size and the advantage of producing energy nearer to the consumer (on-site energy generation). Moreover, the VAWT is lighter and safer, and it does not require a yaw mechanism to rotate the VAWT to face the wind direction. Therefore, they can be operated by winds coming from any horizontal direction. Despite the VAWTs general superiority in comparison with the HAWT, the VAWT also has its disadvantages such as the relatively lower efficiency of the Savonius rotor and the poor self-starting capability of the Darrieus rotor.

Due to these various disadvantages of both the VAWT and the HAWT, the main objective of the current study to overcome the drawbacks of both the VAWT and the HAWT by proposing a new type of wind turbine called the cross-axis-wind-turbine (CAWT). The CAWT can extract wind energy from the horizontal and vertical directions by employing the use of airfoil as struts. In addition, the use of deflectors to guide the approaching wind towards the horizontal blades of the CAWT and the overall performance of the new wind turbine against a conventional VAWT are being investigated. The focus of the current paper is to give an overview of the effects of the deflectors to augment the oncoming wind and direct the airflow towards

the central area of the CAWT. For further reading, detailed discussion and investigation of the CAWT can be referred in (Chong et al., 2017a; Chong et al., 2017b; Chong et al., 2016).

2. DESCRIPTION OF THE NOVEL CROSS-AXIS-WIND-TURBINE

The wind characteristics in urban areas are significantly influenced by the roughness of urban settings where there are large densities of high-rise buildings. This produces more complex wind characteristics, where the separation of wind flow is influenced by the buildings in response to the strong multi-directional wind in urban environments. The CAWT has the advantage for turbine performance in a multi-directional wind of urban areas as it can extract wind energy from the horizontal and vertical wind directions. Furthermore, the CAWT can potentially replace the conventional VAWT for urban wind energy system due to its ability to extract wind energy irrespective of the direction of the wind, therefore enhancing the power performance output. The CAWT has three main vertical blades that are connected to six untwisted horizontal blades via specially designed connectors. This arrangement forms the cross-axis-wind-turbine, and it differs from the conventional VAWT where the airfoil-shaped struts will be able to produce lift from the interaction of the vertical airflows. The advantage of the CAWT is its ability to function with airflows coming from the horizontal and vertical directions (see Figure 1), to maximise the wind energy potential.

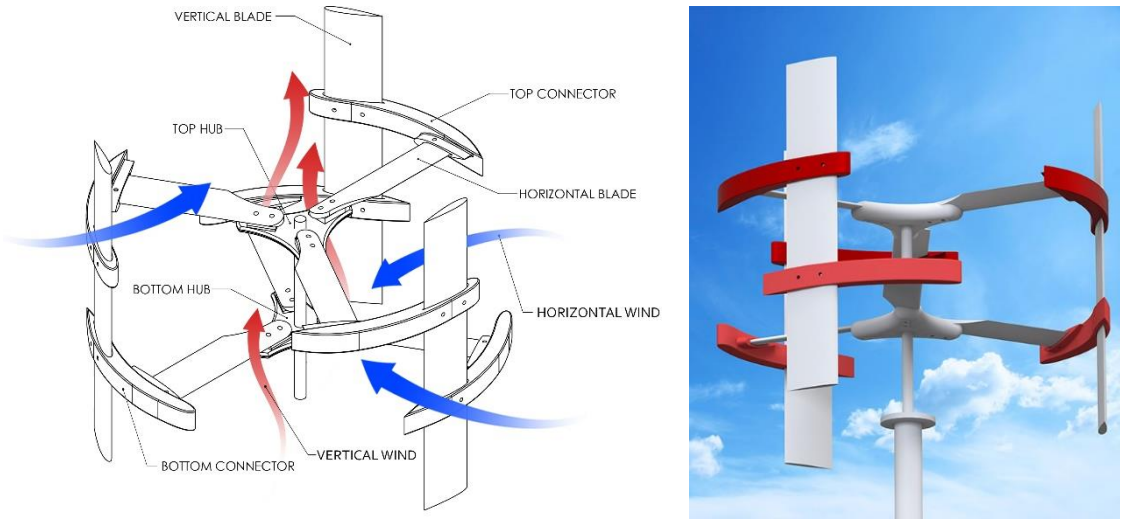

Figure 1: The general arrangement of the cross-axis-wind-turbine

The horizontal blades act as the radial arms of the CAWT, connecting the hub to the vertical blades. The upper and lower hubs are attached to a central shaft. In total, there are six connectors to link the vertical and horizontal blades together. The current study seeks out the effect of the horizontal blades at different angles on the overall performance of the wind turbine. The design philosophy of the CAWT is to use any vertical wind to interact with the lower and upper horizontal blades to create a larger interaction area (swept area) between the winds and the airfoil. Furthermore, the airfoil-shaped arms enhance the self-starting ability of the CAWT and improve the performance of the entire wind turbine by utilising most of the available energy from the oncoming wind.

2.1. Cross-axis-wind-turbine prototype and lab-scale experimental setup

A summary of the CAWT experimental parameters is presented in Table 1. For the present work, a small lab-scale 350 mm diameter CAWT was designed, fabricated and integrated with deflectors to investigate its feasibility. The purpose of the experiment is to gauge the performance of the CAWT and compare it against a conventional three-bladed H-rotor VAWT having the same dimensions (i.e., rotor diameter, vertical blade height, chord length) and tested under the same experimental conditions. The experimental setup consists of an array of nine blower fans and an experimental rig where the CAWT prototype is fixed with a dynamometer controller system. A regime of lab-scale experiments was conducted based on the bare and deflector integrated CAWT configurations with different horizontal blade pitch angles. Bare and deflector integrated H-rotor VAWTs were also tested for benchmarking purposes.

Wind speed measurements were taken downstream of the fan array, at the centre of the test section by using an anemometer. The wind speed measurements were taken over a 3 x 3 grid of equally spaced points covering a 1.0 m x 1.0 m cross-section at 3.5 m downstream. Careful measurements were taken to reduce uncertainties. The average wind speed for the study was measured to be V_∞ = 4.5 ± 0.2 m/s. The experimental rig with deflector (Figure 2) was placed at 3.5 m downstream of the fan array. The deflectors with different angles (30° to 45°, with 5° increment) were placed about 50 mm

away from the central axis of the wind turbines. The deflectors guide the oncoming wind and direct the wind upward to the wind turbines. In the study, four different configurations of the CAWT varies in the pitch angle of its horizontal blades (illustrated in Figure 3 and shown in Table 1). The horizontal blades are pitched downward and directly interact with the deflected wind. The deflector's height, h_d and length, l_d dimensions were varied and limited to 350 mm, which is equal to the diameter of the CAWT rotor. Therefore, the maximum deflector angle for the current study was limited to 45°. Furthermore, the deflector's distance from the bottom of the turbine generator, y_d was set to 50 mm. The wind turbines performances were logged using a dynamometer system in which the recorded parameters for the study are the electrical power, voltage, current, and turbine rotational speed. All the parameters taken from the wind turbines integrated with deflectors were also recorded for bare wind turbines (without deflectors). This is to compare the performance of all the wind turbine configurations.

Table 1: The parameters of the study

Parameters	CAWT	VAWT
Rotor radius, *R* (mm)	175	175
Number of vertical blade, *N*	3	3
Vertical blade height, *h* (mm)	300	300
Vertical blade chord length, *c* (mm)	50	50
Vertical blade pitch angle, β (°)	0	0
Number of horizontal blade, *B*	6	-
Horizontal blade length, l_b (mm)	150	-
Horizontal blade chord length, c_b (mm)	34	-
Horizontal blade pitch angle, β_b (°)	0, 5, 10, 15	-
Profile of airfoil	NACA0015	

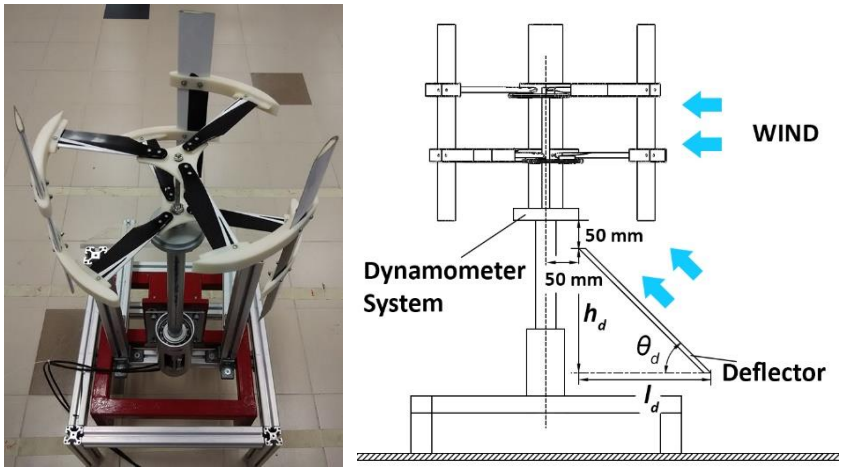

Figure 2: The cross-axis-wind-turbine prototype with the experimental rig

As mentioned, the configuration of the CAWT varies in the pitch angle of its horizontal blades. Figure 3 (left) shows one-third of the CAWT, which consists of one vertical blade and two horizontal blades linked by the top and bottom connectors. Various CAWT configurations were used based on the pitch angle, β_b throughout the experiment. The top and bottom connectors were carefully designed to support the vertical and horizontal blades without sacrificing much on the aerodynamic losses incurred by their shapes. The basic design of the connector resembles the form of a vertical blade, with leading and trailing edges on the curved outline of the connector considering the aerodynamic properties of the connectors and their effects. As shown in Figure 3 (right), the vertical blades are inserted through the vertical blade slots of the connectors. Whereas, the horizontal blades are inserted into the horizontal blade slots of the connectors. The top connector can be identified by the position of the vertical blade slot near to the leading edge of the connector, and the vertical blade slot for the bottom connector is positioned near to the trailing edge of the connector.

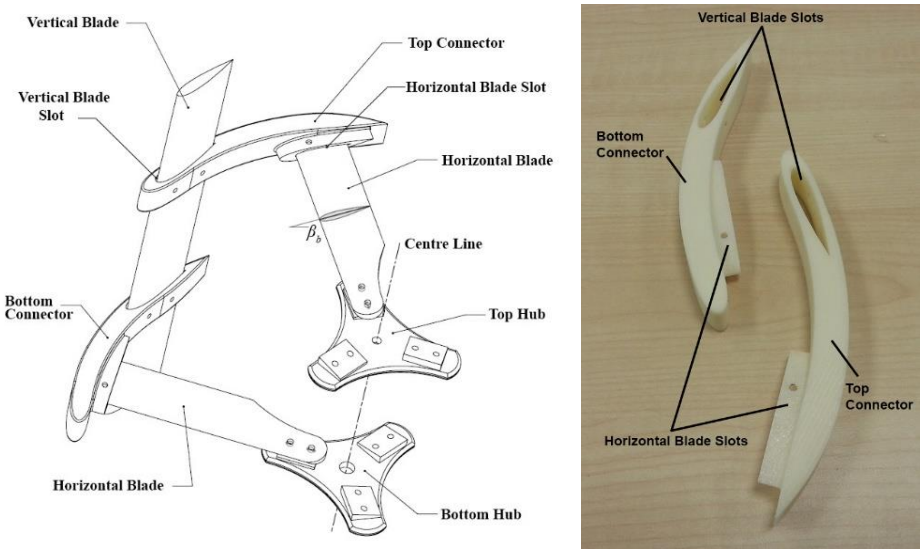

Figure 3: An illustration of the CAWT prototype showing the connectors, hubs, and blades (left), and the fabricated connectors for the CAWT (right).

2.2. Performance evaluation

To evaluate the performance of the wind turbines, the power coefficient and torque coefficient are presented quantitatively. The power coefficient, C_P is used to assess the capability of power generation for a wind turbine. Defined as the ratio of the shaft power, P generated from the wind turbine to the power available in the wind:

Equation 1: Power coefficient of the wind turbine.

$$C_P = P / (0.5 \rho A V_\infty^3)$$

Where:

C_P = coefficient of power delivered by wind turbines

P = wind turbine power output (W)

ρ = density of air (1.225 kg/m^3)

A = turbine swept area (m^2)

V_∞ = wind speed (m/s)

Torque coefficient, C_Q is used to determine the mechanical torque generated by the wind turbine. It is defined as:

Equation 2: Torque coefficient of the wind turbine.

$$C_Q = T / (0.5 \rho A R V_\infty^2) = C_P / \lambda$$

where λ is the tip speed ratio, defined by the ratio of the mean blade tip speed to the approaching wind velocity. The ratio is calculated by:

Equation 3: Tip speed ratio of the wind turbine.

$$\lambda = \omega R / V_\infty$$

Where:

ω = angular velocity (rad/s)

R = wind turbine radius (m)

3. RESULTS AND DISCUSSION

3.1. The effect of deflectors on the performance of the CAWT

Different aerodynamic effects are observed when the inclination angle of the deflectors is varied. Detailed power coefficients of the 15° and 0° pitch angle CAWTs integrated with different deflectors are shown in Figures 4 and 5, respectively. By analysing the data, it was found that the 15º pitch angle CAWT has the best performance. Moreover, it is

observed that by augmenting the approaching wind flow with different inclination angle of deflectors, both the CAWTs have a range of peak power coefficients from 0.0529-0.0785. It is inferred that the deflector guides the deflected airflow towards a better angle of attack as seen by the horizontal blades, therefore better power output is expected. Moreover, the deflected airflow also covers the horizontal blades in the downstream region, therefore creating higher potential of wind energy extraction. From the experiment, the CAWT's peak power coefficients were increased significantly by 103 to 175 % at different tip speed ratios for various horizontal blade pitch angles when compared to their VAWT counterpart (integrated with the 45º deflector). For further analysis, the data shown in Figure 4 for the 15° pitch angle CAWT integrated with deflector having an inclination angle of 45° produced the highest coefficient of power, C_P = 0.0785 at a tip speed ratio of 0.93. In contrast, the bare three straight-bladed VAWT produced a maximum power coefficient of 0.0339 at a tip speed ratio of 0.59. This shows that there is a significant improvement on the power output of the 15° pitch angle CAWT compared to the conventional VAWT where the CAWT produces power 2.3 times higher than the power generated by the VAWT. Note that the graph trend for the bare 15° pitch angle CAWT is almost analogous to that of the VAWT suggesting that without the deflector, the performance of the CAWT is somewhat comparable to the conventional VAWT during operation, although the tip speed ratio range is smaller. Similarly, in Figure 5, the general trend of the CAWT performance with pitch angle of 0° increases when the inclination angle of the deflector is increased. The maximum coefficient of power, C_P = 0.0578 at a TSR of 0.7 produced by this CAWT configuration was generated when the turbine is integrated with the 45° deflector.

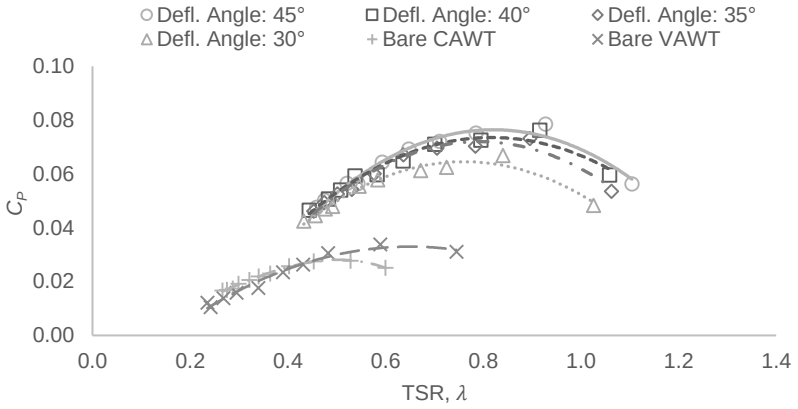

Figure 4: Power coefficient against tip speed ratio for the CAWT (horizontal blade pitch angle 15°) integrated with deflector having inclination angles, θ_d = 30°, 35°, 40°, and 45°. For comparison purposes, the bare CAWT and VAWT power performances are also shown.

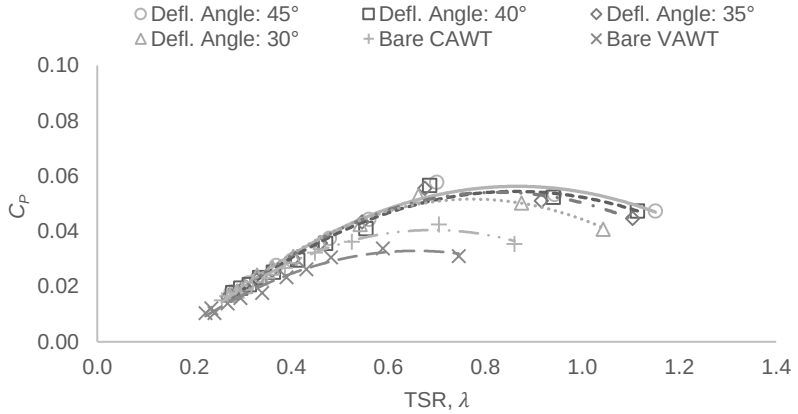

Figure 5: Power coefficient against tip speed ratio for the CAWT (horizontal blade pitch angle 0°) integrated with deflector having inclination angles, θ_d = 30°, 35°, 40°, and 45°. For comparison purposes, the bare CAWT and VAWT power performances are also shown.

One of the most challenging issues associated with wind energy, in particular, the VAWT, is the self-starting capability of the system. For a wind turbine designed to be used in areas experiencing low wind speed, i.e. urban areas and tropical countries, it is essential to conceive a system that can self-start. As mentioned, Darrieus wind turbines have poor self-starting capability compared to the drag-driven Savonius rotor. Over the years, researchers have demonstrated that a proper Darrieus VAWT design can ensure self-starting by lightly loading the turbine, ensuring an optimum number of blades or by exploiting the unsteady tangential force components along the Darrieus turbine circumference (Hill et al., 2009, Worasinchai et al., 2015). Rotor geometry, i.e. chord-to-diameter (c/D) ratio and aspect ratio (AR), is very important in starting performance. Both the CAWT and the VAWT used in the experiment has the same c/D and AR values (0.14 and 6, respectively), and therefore they are geometrically related. With a c/D ratio of 0.14, Worasinchai et al. (2015) have shown

that unsteady tangential force can be generated due to a reduced frequency that drives the rotor to self-start. However, the solidity of the machines, in particularly the VAWT, can affect the rotor performances. Unlike the VAWT, the CAWTs use the airfoil-shaped struts to exploit the lift forces. Based on the experiments, this design is advantageous in producing higher torque output. As shown in Figures 6 and 7, the torque coefficients of 15° and 0° pitch angle CAWTs integrated with 45° and 35° deflectors increased significantly as compared to their VAWT counterparts. The maximum torque coefficients produced in the range between 0.0719-0.1085 for both CAWT configurations, which is 13-71% higher than the bare VAWT (C_Q = 0.0634). The data suggest that the CAWTs are able to self-start even at lower tip speed ratio, which demonstrates the potential of replacing the conventional VAWT for use in low wind speed regions.

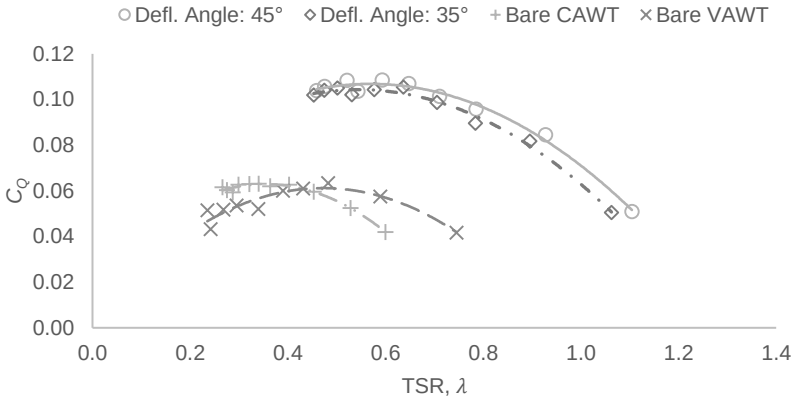

Figure 6: Torque coefficient against tip speed ratio for the CAWT (pitch angle 15°) integrated with deflector having inclination angles, θ_d = 35° and 45°. For comparison purposes, the bare CAWT and VAWT power performances are also shown.

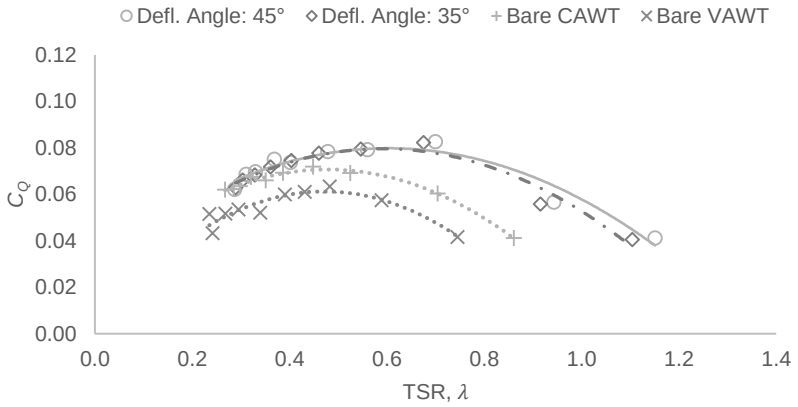

Figure 7: Torque coefficient against tip speed ratio for the CAWT (pitch angle 0°) integrated with deflector having inclination angles, θ_d = 35° and 45°. For comparison purposes, the bare CAWT and VAWT power performances are also shown.

The rotational speed performances for the wind turbines were taken after a duration of 240 s at a free-running condition where the rotors were only subjected to inertia and bearing friction. Based on the experimental findings, the CAWT with various blade pitch angles integrated with the same deflectors as the VAWT recorded an increased performance in rotor rotational speed by up to 112 %. By analysing the data between the deflector integrated CAWTs and the bare VAWT as shown in Figure 8, the trends of the rotational speed for the wind turbines are steadily increasing and then stabilised after reaching a steady state. For the 15° pitch angle CAWT, by integrating the turbine with the 45° deflector, rotational speed of 348 RPM was obtained, which is the highest rotor rotational speed for the 15° CAWT. In comparison, the bare VAWT recorded a stabilised rotational speed of 240 RPM. Interestingly, the rotational speed of the bare 15° pitch angle CAWT is lower than that of the bare VAWT and some of the other CAWT configuration with lower pitch angles. This may be due to the additional drag produced by the high pitch angle of the horizontal blades without the presence of the deflectors. Therefore, impeding the rotational speed of the bare CAWT. The effect of pitch angles on bare configurations of CAWTs is also evident in the torque coefficient graphs shown in Figures 6 and 7, in which the range of tip speed ratio for the bare 15° pitch angle CAWT is smaller than the conventional VAWT. For brevity, some data from the experiment are tabulated in Table 2, which shows the peak power coefficient, torque coefficient, and rotor rotational data.

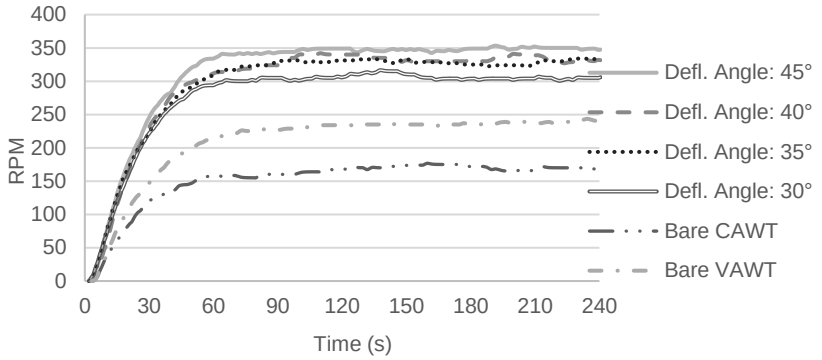

Figure 8: Rotational speed of the CAWT (pitch angle 15°) integrated with deflector having inclination angles, θ_d = 30°, 35°, 40°, and 45°. The bare CAWT and VAWT rotational speed trends are also shown for comparison purposes.

Table 2: Peak power coefficient, torque coefficient, and rotor rotational data

	Rotor		Parameter			Change (%)		
			C_P	C_Q	RPM	C_P	C_Q	RPM
Bare	VAWT		0.0339	0.0634	240	-	-	-
	CAWT	0°	0.0425	0.0719	266	25	13	11
		5°	0.0440	0.0721	258	30	14	8
		10°	0.0363	0.0717	212	7	13	(12)
		15°	0.0277	0.0631	168	(18)	(0.5)	(30)
35° Deflector	VAWT		0.0281	0.0569	205	-	-	-
	CAWT	0°	0.0556	0.0822	349	98	45	70
		5°	0.0675	0.0918	384	140	61	87
		10°	0.0694	0.1029	326	147	81	72
		15°	0.0732	0.1050	334	161	85	63
45° Deflector	VAWT		0.0285	0.0581	204	-	-	-
	CAWT	0°	0.0578	0.0827	363	103	42	78
		5°	0.0724	0.0936	433	154	61	112
		10°	0.0774	0.1044	413	172	80	102
		15°	0.0785	0.1085	348	175	87	70

3.2. Application and impact of the study

Wind augmentation has been shown to increase the performance of wind turbines. Based on the study with deflectors, it was found that the deflectors enhance the power output of the CAWT by creating skewed wind flows to guide the oncoming wind upward to interact with the CAWT rotor. Also, based on the experimental analysis of bare CAWT, without the deflector, the performance of the CAWT is worse than the deflector integrated CAWTs. In the case of the bare 15° pitch angle CAWT, it was found that the turbine performance drops by 18% when compared to the bare VAWT (refer to Figure 4). To illustrate the potential of using a power-augmentation device with the CAWT, a preliminary computational fluid dynamics (CFD) study was conducted to simulate the ability of a shroud to augment the oncoming wind. The shroud consists of stacked ring-like deflecting planes supported by vertical webs and an inverted funnel-shaped base. It was designed to produce vertical wind components from any horizontal wind direction. The wind velocity was set at 8 m/s, with k-omega SST as the turbulence model. Significant vertical wind component located at the top of the proposed shroud was observed as shown in Figure 9.

One example of incorporating the existing studies in a large-scale real-world application is in the offshore wind industry. Wind turbines in offshore applications have been deployed in large-scale wind energy production (Borg and Collu, 2015, Vasel-Be-Hagh and Archer, 2017). Similarly, the CAWT has the potential to be deployed to harness offshore wind energy as illustrated in Figure 10. The shroud can be employed as the floating platform for the CAWT, in which the oncoming wind can be induced and guided towards the CAWT. Without the shroud, the pitching and rolling motion of the sea waves can also induce periodic tilt angle with respect to the oncoming horizontal wind component, which in turn would interact with the horizontal blades of the CAWT. Moreover, the rapidly changing sea motion with highly varying wind conditions at sea

may increase the power output of the bare CAWT. However, the use of the shroud as a platform means the operation of the CAWT is more stable due to the better buoyancy effect of the shroud and its lower centre of gravity.

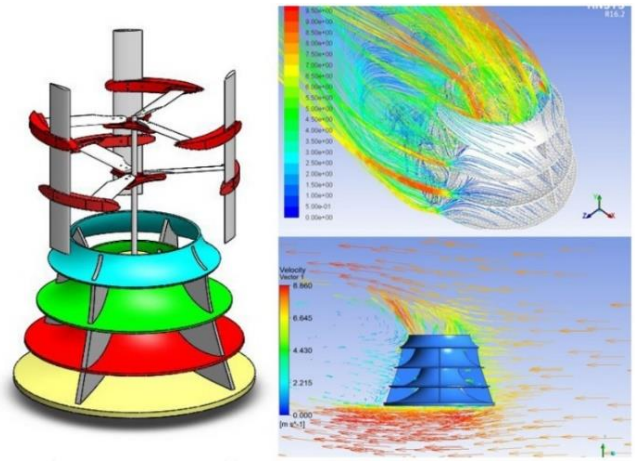

Figure 9: Preliminary CFD study of a shroud for future integration with the CAWT (Chong et al., 2017b)

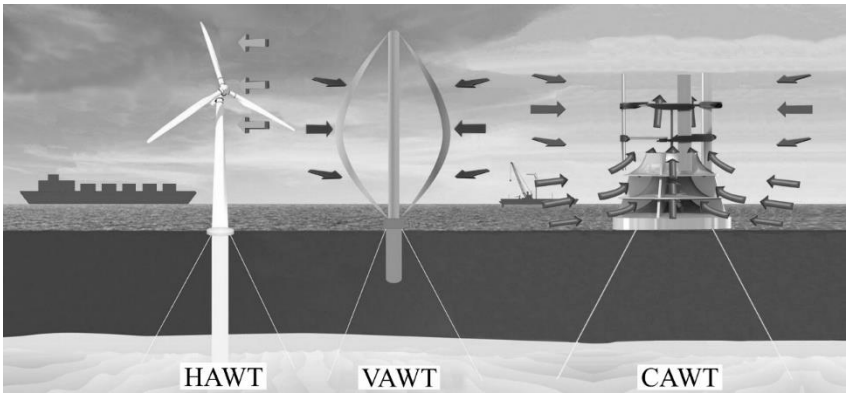

Figure 10: Illustration of the proposed CAWT with shroud in offshore application (Chong et al., 2017b)

4. CONCLUSION

This paper describes the design and experimental analysis of a novel cross-axis-wind-turbine integrated with deflectors. The wind turbine consists of vertical and horizontal blades to enhance its potential power output. The use of deflectors guides the wind flow and increases the wind speed to enhance the performance of the rotor. The concept of the wind turbine has been proven to be feasible even with low TSR response characteristics. With the presence of the deflector as a power-augmentation device, the interaction of the skewed wind flow with the airfoil struts creates a new possibility in the design of wind turbines. In addition, further research is required to draw a more comprehensive conclusion on the design concept, since the experimental prototypes are small and there are many more research opportunities can be carried out to optimise the rotor. Nevertheless, from the experimental study, the CAWT outperforms the conventional straight-bladed VAWT. The CAWT takes advantage of the simple principle of extracting oncoming wind energy from both the horizontal and vertical directions. By creating a larger swept area for the wind to interact with, the power output can also be improved. From the study, the optimum CAWT configuration set was found to be the 45° angle deflector integrated with the 15° horizontal pitch angle CAWT where the maximum coefficient of performance is 2.3 times higher than that of the one produced by the bare conventional VAWT. By integrating both turbines with the 45º deflector, the CAWT's peak power coefficients were increased significantly by 103 to 175 % at different tip speed ratios for various horizontal blade pitch angles when compared to their VAWT counterpart. In addition, the maximum rotational speed of the CAWT increased by up to 112%. Better starting behaviour was also observed where the torque coefficient is higher by 13 to 71% compared to the bare VAWT. Here, the airfoil-shaped struts and the deflector have shown to have potentially beneficial roles in the power extraction from the wind flow. Lastly, further research and development can optimise the concept for a better diffusion of wind energy technology in many locations, providing alternative energy with sustainable source.

5. ACKNOWLEDGEMENT

The authors would like to thank the University of Malaya for the research grants allocated (RU018G-2016). Special appreciation is also credited to the Malaysian Ministry of Higher Education, MOHE for the Prototype Research Grant Scheme (PR005-2016) and the *Geran Sanjungan Penyelidikan* (MO003-2014). The authors would also like to thank the

Centre for Research Grant Management Unit, the University of Malaya for the Postgraduate Research Grant (PG052-2014A).

6. REFERENCES

Abohela, I., Hamza, N. & Dudek, S. 2013. Effect of roof shape, wind direction, building height and urban configuration on the energy yield and positioning of roof mounted wind turbines. *Renewable Energy,* 50**,** 1106-1118.

Balduzzi, F., Bianchini, A., Carnevale, E. A., Ferrari, L. & Magnani, S. 2012. Feasibility analysis of a Darrieus vertical-axis wind turbine installation in the rooftop of a building. *Applied Energy,* 97**,** 921-929.

Borg, M. & Collu, M. 2015. Frequency-domain characteristics of aerodynamic loads of offshore floating vertical axis wind turbines. *Applied Energy,* 155**,** 629-636.

Chong, W. T., Fazlizan, A., Poh, S. C., Pan, K. C., Hew, W. P. & Hsiao, F. B. 2013. The design, simulation and testing of an urban vertical axis wind turbine with the omni-direction-guide-vane. *Applied Energy,* 112**,** 601-609.

Chong, W. T., Gwani, M., Tan, C. J., Muzammil, W. K., Poh, S. C. & Wong, K. H. 2017a. Design and testing of a novel building integrated cross axis wind turbine. *Applied Sciences,* 7**,** 251.

Chong, W. T., Muzammil, W. K., Gwani, M., Wong, K. H., Fazlizan, A., Wang, C. T. & Poh, S. C. The development and testing of a novel cross axis wind turbine. 3rd AUN/SEED-Net Regional Conference on Energy Engineering, 2016 Yogyakarta, Indonesia. AIP Publishing, 030003.

Chong, W. T., Muzammil, W. K., Wong, K. H., Wang, C. T., Gwani, M., Chu, Y. J. & Poh, S. C. 2017b. Cross axis wind turbine: Pushing the limit of wind turbine technology with complementary design. *Applied Energy,* 207**,** 78-95.

Darrieus, G. J. M. 1931. *Turbine having its rotating shaft traverse to the flow of the current*.

Grant, A., Johnstone, C. & Kelly, N. 2008. Urban wind energy conversion: The potential of ducted turbines. *Renewable Energy,* 33**,** 1157-1163.

Hill, N., Dominy, R., Ingram, G. & Dominy, J. 2009. Darrieus turbines: the physics of self-starting. *Proceedings of the IMechE Part A: Journal of Power and Energy,* 223**,** 21-29.

Mathew, S. 2006. *Wind energy: fundamentals, resource analysis and economics,* New York, Springer.

Oppenheim, D., Owen, C. & White, G. 2004. Outside the Square: Integrating Wind into Urban Environments. *Refocus,* 5**,** 32-35.

Sjokvist, S. & Eriksson, S. 2013. Study of demagnetization risk for a 12 kW direct driven permanent magnet synchronous generator for wind power. *Energy Science & Engineering,* 1**,** 128-134.

Van Bussel, G. J. W., Mertens, S., Polinder, H. & Sidler, H. F. A. The development of Turby, a small VAWT for the built environment. Global wind energy conference, 2004 Chicago, USA.

Vasel-Be-Hagh, A. & Archer, C. L. 2017. Wind farm hub height optimization. *Applied Energy,* 195**,** 905-921.

Wagner, S., Bareiss, R. & Guidati, G. 1996. *Wind turbine noise,* Berlin, Springer.

Worasinchai, S., Ingram, G. & Dominy, R. 2015. The physics of H-Darrieus turbine starting behavior. *Journal of Engineering for Gas Turbines and Power,* 138.

331: Heat transfer and resistance characteristics of supercritical cyclohexane in a vertical mini-tube

Tianhui LI[1], Zhuqiang YANG[2], Bo ZHANG[3]

[1] Tianhui Li, Dalian University of Technology, Dalian, P R China, litianhui@mail.dlut.edu.cn
[2] ZHUQIANG Yang, Dalian University of Technology, Dalian, P R China, yangzhuqiang@dlut.edu.cn
[3] BO Zhang, Dalian University of Technology, Dalian, P R China, zhangbo@dlut.edu.cn

With an increasing of March number of the near space aircraft, the effect cooling method is becoming a main factor for the development of engine. A regenerative active cooling, using hydrocarbon fuel as coolant flowing through the mini-tube, is proposed and verified prospectively. To overcome the uneven thermal load as the flight condition change, the flow and heat transfer process under the design condition should be studied. The conclusion affects firsthand on the heat exchange process and ultimately act on the engine design. Thus, the cyclohexane as a typical hydrocarbon was test at supercritical pressure in a vertical tube and its heat transfer and pressure characteristics were obtained in an upflow and downflow respectively. The experiment condition covered a range of heat flux from 158 to 450kw/m^2, pressure from 4.5 to 5.5MPa, inlet temperature from 30 to 70°C *and the test stainless tube owned length of 0.36 to 0.79m and hydraulic diameter 1.0 to 2.0mm. The results shown that buoyancy and viscous force has a significant effect on the heat transfer characteristics in the vertical tube, leading to the effect of heat transfer of upflow is better than that of downflow. Meanwhile with the increase of pipe inner diameter the heat transfer was weakened. Conversely, with the increase of pipe length, the heat transfer coefficient is further enhanced. In experiments, hydrodynamic characteristics was also conducted and found that the onset of the static instability is significant to the heat transfer characteristics. In the outlet of the tube, when the static instability occurred, the heat transfer weakening also occurred at the same time.*

Keywords: Heat transfer; Supercritical; Vertical; Mini-tube

1. INTRODUCTION

As the most prospective candidates for the scramjet propulsion systems, the hydrocarbon fuel has attracted increasing attention of the world (Pezzella, 2011). To overcome the high heat load of the engine surface, the regenerative cooling method adopts hydrocarbon fuels to flow through parallel multiple mini-tube (Liu, 2013; Zhou, 2014; Liang, 2017; Guo, 2017) Hydrocarbon fuels has been studied by the U.S military to uncover the mechanisms of flow and heat transfer or coking characteristics. However, the researches involve national military and strategic development plans, most relative results are confidential, and the few available data for publication.

In Edwards (1993) for hydrocarbon fuels, scholars mainly focus on the coke instabilities and thermal instabilities. Flow instabilities and heat transfer characteristics have few attentions. For the purposed of studying the effect of thermal cracking and coking on heat transfer, Liu (202) conducted experiments with aviation kerosene. The results showed that in the high temperature section, the amount of coke was the main factor that determines the heat transfer mode. Ward (2004) proposed the concept of PPD (Proportional Product Distribution) for slight thermal cracking. It assumed that the ratio of one product to the other was fixed, and a simplified mechanism model for n-decane and n-dodecane was proposed. Experiments were conducted by Brad under supercritical pressure, JP-7 and MCH was used and obvious oscillations in pressure and temperature were observed. The oscillations occurred when the wall temperature was greater than pseudo-temperature and compared pressure was below 1.5 (Hitch, 2015; Hitch, 2013). Hines and Wolf (1962) had experimentally investigated RP-1 and Diethyl cyclohexane in horizontal tube under supercritical pressure, and they found that as the heat flux increasing, the oscillation frequency of wall temperature increasing. This kind of oscillation can be eliminated when system pressure increased. Zhou (2011) focused their attention on heat transfer deterioration, the result showed that the specific heat capacity, thermal conductivity and viscosity had less contribute to heat transfer deterioration. However, the dramatic change in density play a main role in heat transfer. Dang (2013) through numerical simulation of RP-3 in the study of convection heat transfer. However, the cause of the abnormal decrease in turbulent kinetic energy is not clear yet. Urbano (2009 & 2013) investigated pressure drop had influence on the thermal properties of methane and found that the heat transfer deterioration mainly occurs when the near wall fluid is abruptly heated to pseudo-temperature. The great change of density caused the turbulent diffusion weakened, which caused the heat transfer to deteriorate. Xu (Zhang, 2013; Zhu, 2013) held the view when the bulk fluid under the critical temperature, the effect of pressure can be negligible; as the bulk temperature exceeded the critical temperature, pressure drop increased sharply with mass flow decreased.

As buoyancy and thermal acceleration play important roles in the heat transfer deterioration of the supercritical pressure fluids, some mature criteria are proposed. Deng (2012) and Zhang (2012) conducted a series of experiments of RP-3. The former believed that when $Bo^*<6*10^{-6}$, the effect of buoyancy is significant, while the latter pointed out when $Bo^*<1.6*10^{-10}$ and $Kv<1.5*10^{-8}$, the heat transfer deterioration happened. Jiang (Wang, 2015; Liu, 2014) proposed when $Bo^*>2*10^{-7}$, the buoyancy effect is non-negligible; when $Kv<1.5*10^{-8}$, the effect of thermal acceleration is non-negligible.

Based on the existing research results, it can be concluded the hydrocarbon fuels have complicated thermal properties, the applicability of the classical criteria has been severely challenged, and the heat transfer characteristics in different geometric design dimensions are not discussed in detail. The effect of buoyancy on heat transfer in different flow directions need to be further discussion. Therefore, the main task of this paper is achieved in terms of the following three aspects: 1. to explore the effect of flow directions on heat transfer characteristics in vertical mini-tubes, analyse the change in boundary layer. 2. to further investigate the effect of length and inner diameter on the heat transfer characteristics.

2. EXPERIMENTAL SYSTEM AND DATA PROCESSING

2.1. Experimental system

Figure 1 shows the experimental system, which includes two fuel tanks, a piston pump, a control valve, a volume flow meter, two sets of AC power systems, a preheater section, a test section, a water cooler, a back pressure valve, a fuel container, an electronic balance and a data acquisition system. The test section is made of stainless steel tubes with inner diameters of 1.0-2.0 mm, outer diameters of 2.0-3.0 mm and lengths of 0.36-0.79 m. The preheater section and test section are insulated and wrapped with glass wool to reduce heat loss.

The working fuel is cyclohexane with a purity of 99.5% and is heated to the required inlet temperature in the preheater section, and continue to be heated in the test section. Then, the fuel is cooled using a water cooler and recollected by the other tank. All the experiments are conducted with variable mass flow rates, system pressures, inlet temperatures and heat fluxes. In each individual experiment, the wall temperature, bulk temperature and hydrodynamic characteristics curves (pressure drop-mass flow rate curves) are obtained under the constant system pressure, inlet temperature and heat flux. All the experimental conditions are shown in Table 1. During the experiment, in order to ensure safety and avoid the thermal cracking of the fuel, the outlet temperature of the bulk fluid was controlled within 420°C and the wall temperature should not exceed 540°C.

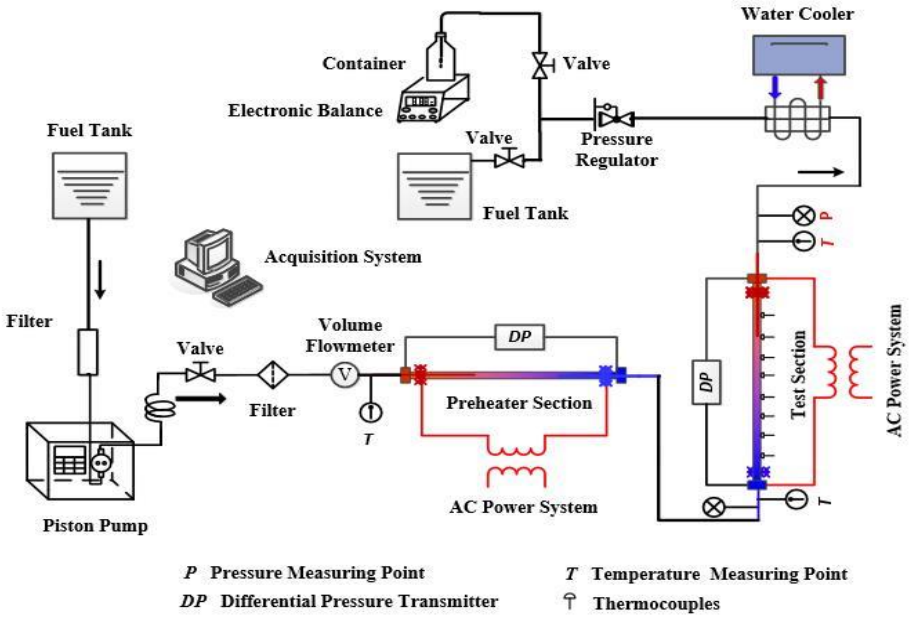

Figure 1: Schematic diagram of the experimental system

Table 1: The experimental conditions.

Parameters	Ranges
System pressure/MPa	4.5
Inlet pressure/°C	30-70
Heat flux/kW/m^2	158-450
Tube length/m	0.36,0.60,0.79
Tube inner diameter/mm	1.0,2.0
Flow direction	Upflows, downflows

2.2. Data reduction and uncertainty analysis

The heat transfer coefficient *h* is defined as follows:

$$h = \frac{q}{T_{wi} - T_b} \tag{1}$$

In the formula, q is the heat flux of the tube wall; T_{wi} is the wall temperature; T_b is bulk temperature.

The heat flux transformed through the outside surface of the heated test section is obtained from Eq. (2):

$$q = \frac{IU - Q_{loss}}{1000\pi DL} \tag{2}$$

where, IU is the total heat power; D and L are the outer diameter and heated length of the test section respectively; Q_{loss} is the heat loss. The heat loss at different wall temperatures was tested by a pre-experiment and the result is shown in Figure 2. The heat loss from the test section is less than 6% of the total power input.

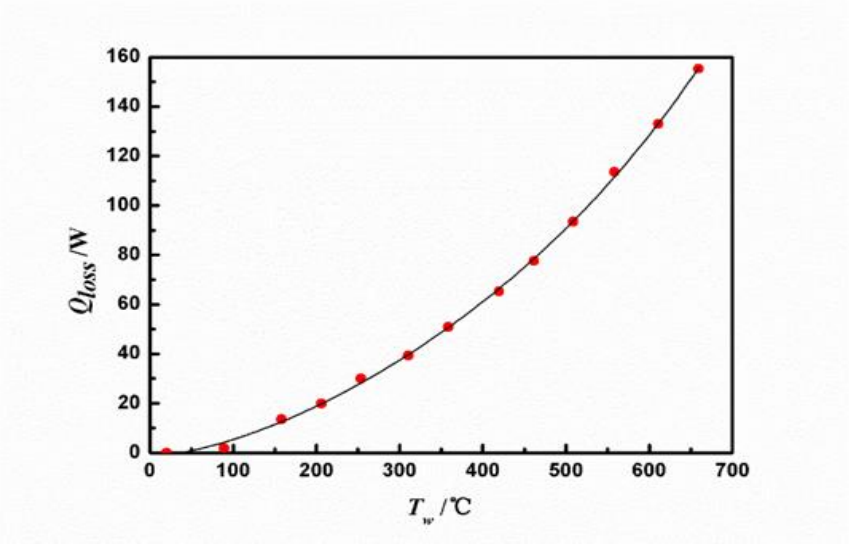

Figure 2: Heat loss at different wall temperatures.

Table 2: Uncertainties of the experimental parameters.

Measurement parameters	Uncertainty (%)
Bulk temperature	0.76
Heat flux	1.40
Mass flow rate	1.91
Pressure	0.42
Differential pressure	3.83

3. RESULTS AND DISCUSSION

3.1. Effect of flow direction on heat transfer in vertical tubes

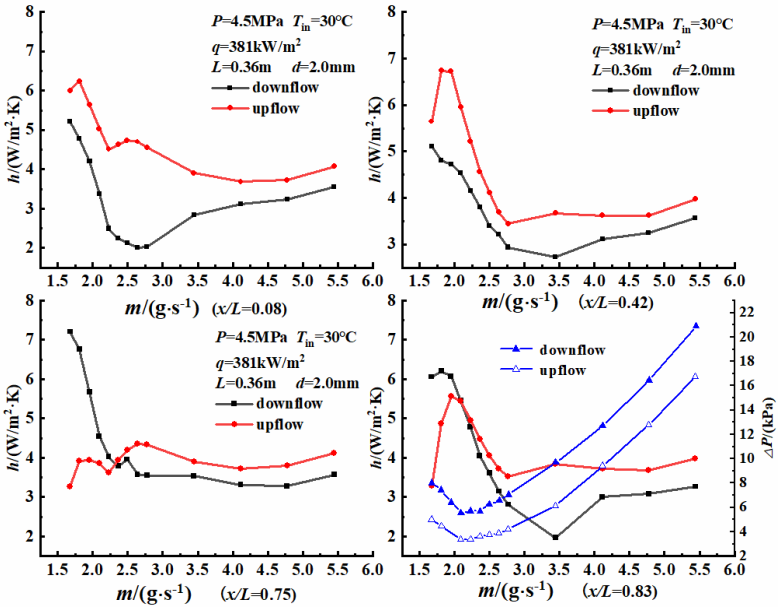

Figure 3: Variation of heat transfer coefficient along length of the tube for different flow directions.

(●■:left axis ▵▲: right axis)

In order to study the difference of heat transfer characteristics of vertical tube in different flow directions, a stainless steel tube with length 0.36m and inner diameter of 2.0mm was selected for experiments at q=381kW/m^2. Upflow and downflow for the vertical tube were selected. Under the same experiment conditions, the results are illustrated in Figure 3.

It shows that any position of the tube, for the downflow, with the decrease of the mass flow rate, the heat transfer coefficient suddenly increases, and the heat transfer enhanced. The mass flow corresponding to the sudden increase of the heat transfer coefficient is in the range of 2.6-3.5g/s; unlike the downflow, for the upflow, after the heat transfer coefficient increased, as the flow rate further decreases, the upflow heat transfer coefficient decreased, and the heat transfer will be weakened. The corresponding mass flow is about 1.9g/s. It shows that the upflow heat transfer is always better than the downflow before the heat transfer weakening occurs. Moreover, the heat transfer weakening has a more significant effect on the outlet of the tube, so that the upflow heat transfer coefficient is smaller than the downflow.

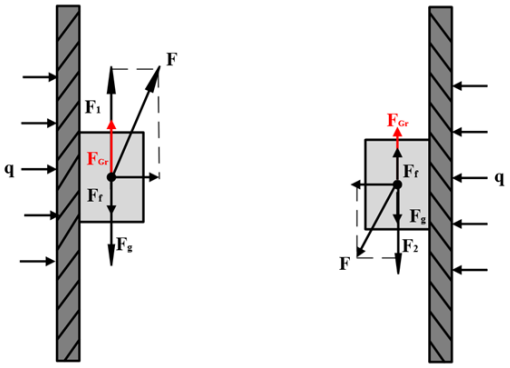

(a) upflow (b)downflow

Figure 4. Analysis of force acting on near-wall fluid in vertical pipe

For the upflow, as the mass flow decreased, the buoyancy effect is more pronounced in the boundary layer. As shown in the Figure 4(a), because the buoyancy is consistent with the flow direction, the near-wall fluid moves axially under the combined effect of the buoyancy and axial velocity to form a boundary layer, making it more difficult for the near-wall disturbances to be transmitted to the bulk flow. As the thickness of the modal boundary layer increases along the length of the tube, the temperature of the fluid in the boundary layer is high, the corresponding specific heat capacity is small, the thermal conductivity is small, and the heat transfer is weakened, which is the cause of the decrease of the heat transfer coefficient. In addition, the weakening of the heat transfer causes the temperature of the near wall fluid to exceed the pseudo-critical temperature, while the temperature of the main stream has not reached the pseudo-critical temperature. This lead to the fluid properties undergoes significant changes. Furthermore, the most significant change in physical properties is near the outlet of the tube which is the cause of flow static instability (it can be verified from the graph of x/L=0.83). As the mass flow decreases, the pressure difference between the inlet and outlet of the tube decreases. When the bulk flow temperature reaches the pseudo -critical temperature and the wall temperature exceeds the pseudo -critical temperature, the flow instability will occur in the tube, resulting in pressure difference increasing. As showed in the last graph in Figure3. When the mass flow is relatively large, due to the low temperature in the bulk flow, the physical properties change of the fluid near the wall are small, so the buoyancy at the near wall can be ignored and the heat transfer effect is good.

For the downflow, when the mass flow is small, the buoyancy, for the downflow, is opposite to the flow direction in the boundary layer when the mass flow is small, leading the fluid incorporation increased, turbulence and heat transfer improved, as indicated in Figure 4(b). Therefore, the heat transfer of downflow is enhanced.

3.2. Effect of inner diameter on heat transfer in vertical tubes

As shown in Figure 5, under the same conditions, the larger the inner diameter of the tube, the effect of the heat transfer worse. For the upflow, the heat transfer weakening at 1.0 mm inner diameter is more pronounced than that of 2.0 mm, and heat transfer weakening also occurs in downflow at 1.0 mm inner diameter. Corresponding to the same mass flow, the smaller the tube diameter is, the flow rate of the fluid is greater. In the forced convection, the larger the flow rate lead the heat transfer effect better. Therefore, 1.0mm tube heat transfer effect is better than 2.0mm tube. For downflow, due to the viscous force, the distribution of turbulent velocity in the cross-section is parabolically distributed. However, the gravity weakens the viscous force, making the distribution of velocity more uniform. The velocity gradient decreases owing to the effect of viscous forces. For upflow, because of gravity, the effect of viscous forces near the wall increases, so that the distribution of cross-sectional velocity is uneven. That is, the velocity gradient becomes larger which lead the heat transfer effect better than that of upflow.

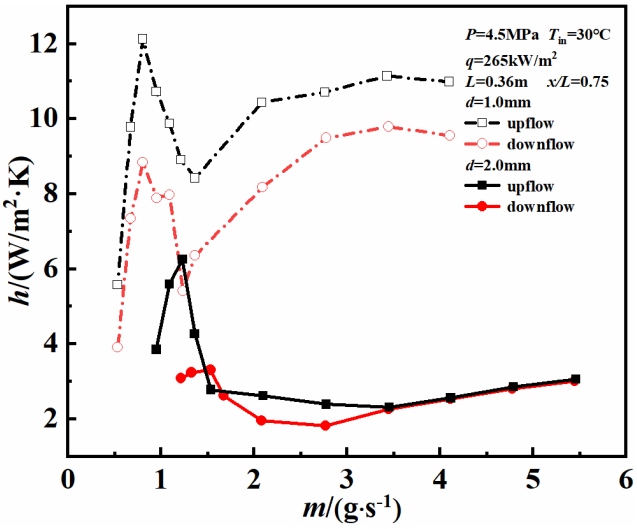

Figure 5: Variation of heat transfer coefficient along length of the tube for different flow directions.

Whether it is a 1.0 mm tube or a 2.0 mm tube, heat transfer weakening occurs at a fixed corresponding mass flow. Considering the hydrodynamic characteristics of supercritical fluids, take the 1.0mm tube as an example. As shown in Figure 6, the blue part is the curve of hydrodynamic characteristic corresponding to the1.0mm tube. The lowest point of the curve represents the onset of the static instability. Combination of wall temperature and bulk flow temperature, it shows that at the onset of instability, the fluid temperature has not reached the pseudo-critical temperature, however, the wall temperature has reached the pseudo-critical temperature, leading the temperature of near wall fluid higher than that of bulk flow. In this area, the thermal conductivity decreases, and the specific heat capacity rises, fluid properties change greatly. Therefore, the heat transfer process is weakened.

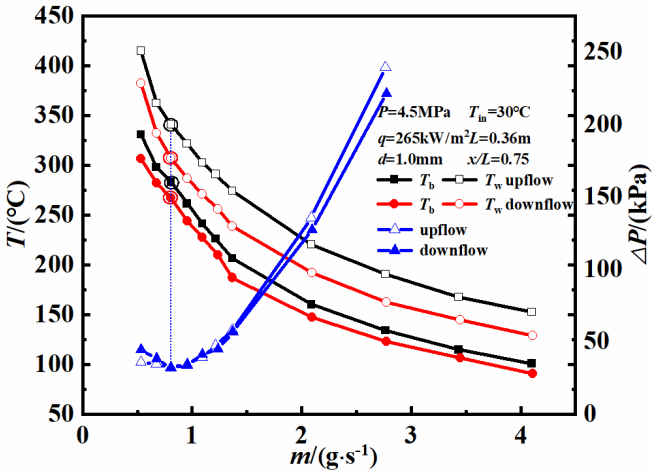

Figure 6: Tb and Tw variation with m and the hydrodynamic characteristics at the x/L=0.75 of the test tube

(●○■□:left axis ◿▲: right axis)

3.3. Effect of tube length on heat transfer in vertical tubes

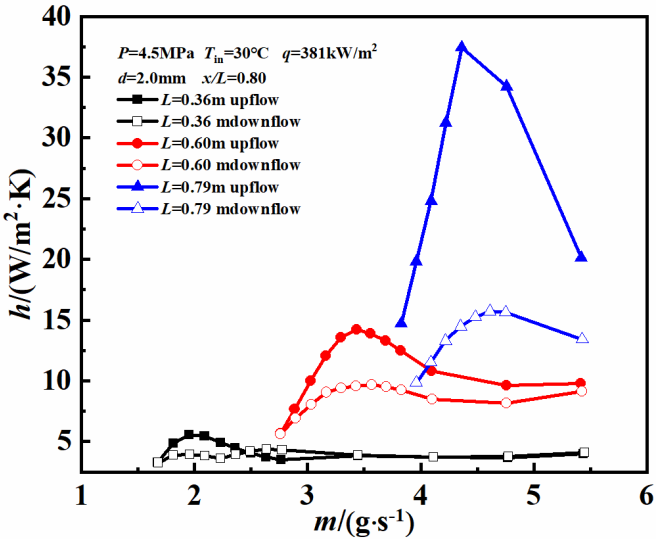

Figure 7: Variation of heat transfer coefficient with different length of the tubes for different flow directions.

In order to determine the effects of tube lengths on the heat transfer characteristics, we selected stainless steel tubes with lengths of 0.36m, 0.60m, 0.79m, and inner diameter is 2.0 mm in different flow directions. The results are illustrated in Figure 7. For the same relative cross-sectional position, e.g. *x/L*=0.80. As the tube length increases, the mass flow corresponding to the heat transfer weakening moves to a higher mass flow rate. With the length of the tubes increase, heat transfer coefficient increases. This is because the longer the tube is, the larger the flow rate at the same *x/L*. With the increase of the flow rate, the heat transfer effect is better. Therefore, with the increase of the tube length, the value of the heat transfer coefficient is greater.

Moreover, the tube with different lengths all have heat transfer weakening phenomenon. This is because of as the mass flow decreasing, the temperature of the bulk flow and the near wall fluid become higher, and when the wall temperature reaches the pseudo-critical temperature, the main flow temperature is still below the pseudo-critical temperature, and the properties of the fluid change drastically. For near wall fluid with low thermal conductivity, heat transfer is weakened. Due to the tube lengths are different, with the increase of the tube length, the greater the heat absorption of the tube at the same heat flux. Therefore, corresponding to the fluid at the pseudo-critical region, the heat transfer weakened point is moved to a higher mass flow.

4. CONCLUSIONS

The heat transfer characteristics in vertical tubes under supercritical conditions were experimentally determined. Effects of the pipe length, inner diameter and flow directions were considered. The conclusions are as follows:

1. For upflow, at the same conditions, the heat transfer effect is better than downflow. Because of buoyancy and viscous force, the variation of heat transfer coefficient along length of the tube for different flow directions is different. When the mass flow decreased to the onset of static instability, the heat transfer of upflow weakened. As the value of *x/L* become greater, the heat transfer weakening will also appear in the downflow.

2. Under the same conditions, in vertical tubes, as the inner diameter of the tube decreased, the heat transfer coefficient increased. The value of the mass flow rate at heat transfer weaken point is consistent with the onset of static instability.

3. It has been verified that at the same *x/L*, an increased tube length leading the heat transfer coefficient higher. At the onset of static instability, the mass flow rate consisted with heat transfer weaken point moved to the higher mass flow rate.

5. ACKNOWLEDGEMENTS

This project was supported by the National Nature Science Foundation of China (51606030), China Postdoctoral Science Foundation (2016M591429) and the Fundamental Research Funds for the Central Universities

6. REFERENCES

Dang G X, Zhong F Q, Chen L H, et al. Numerical investigation on flow and convective heat transfer of aviation kerosene at supercritical conditions[J]. Science China Technological Sciences, 2013, 56(2):416-422.

Deng H, Zhu K, Xu G, et al. Heat transfer characteristics of RP-3 kerosene at supercritical pressure in a vertical circular Tube[J]. Journal of Enhanced Heat Transfer, 2012, 19(5):409-421.

Edwards T. USAF supercritical hydrocarbon fuels interests[C]// Aerospace Sciences Meeting. 1993.

Guo Y, Bi Q, Liu Z, et al. Experimental investigation on thermal-hydraulic characteristics of endothermic hydrocarbon fuel in 1 mm and 2 mm diameter mini-channels[J]. Applied Thermal Engineering, 2017, 122.

Hines W S. Pressure Oscillations Associated With Heat Transfer to Hydrocarbon Fluids at Supercritical Pressures and Temperatures[J]. Ars Journal, 1962, 32(3):361-366.

Hitch B, Karpuk M, Hitch B, et al. Experimental investigation of heat transfer and flow instabilities in supercritical fuels[C]// Joint Propulsion Conference and Exhibit. 2013:489-98.

Hitch B, Karpuk M. Enhancement of heat transfer and elimination of flow oscillations in supercritical fuels[C]// Aiaa/asme/sae/asee Joint Propulsion Conference and Exhibit. 2015.

Liang C, Wang Y, Jiang S, et al. The comprehensive study on hydrocarbon fuel pyrolysis and heat transfer characteristics[J]. Applied Thermal Engineering, 2017, 117:652-658.

Liu B, Wang X, Zhu Y, et al. Experimental study on convective heat transfer of n-decane in micro-circular tube under supercritical pressure [J] Journal of Engineering Thermophysics, 2014, 35(1):114-118.

Liu Z H, Bi Q C, Yong G, et al. Hydraulic and Thermal Effects of Coke Deposition during Pyrolysis of Hydrocarbon Fuel in a Mini-Channel[J]. Energy & Fuels, 2012, 26(6):3672–3679.

Liu Z, Bi Q, Guo Y, et al. Convective heat transfer and pressure drop characteristics of near-critical-pressure hydrocarbon fuel in a minichannel[J]. Applied Thermal Engineering, 2013, 51(1-2):1047-1054.

Pezzella G. Aerodynamic and aerothermodynamic trade-off analysis of a small hypersonic flying test bed[J]. Acta Astronautica, 2011, 69(3):209-222.

Urbano A,Pizzarelli M,Nasuti F. Numerical analysis of transcritical fluids heating in liquid rocket engine cooling channels[y].The Journal ofAerospace Science,2009,88(1-2):20.30

Urbano A, Nasuti F. Parametric Analysis of Heat Transfer to Supercritical-Pressure Methane[J]. Journal of Thermophysics & Heat Transfer, 2013, 26(2):450.

Wang X, Liu B, Zhu Y, et al. Experimental study on convective heat transfer of RP-3 in a thin circular tube under supercritical pressure[J]. Journal of Engineering Thermophysics, 2015, 36(2):360-365.

Ward T, Zabarnick S, Ervin J, et al. Simulations of Flowing Mildly-Cracked Normal Alkanes Incorporating Proportional Product Distributions[J]. Journal of Propulsion & Power, 2004, 20(3):394-402.

Zhang C, Xu G, Gao L, et al. Experimental investigation on heat transfer of a specific fuel (RP-3) flows through downward tubes at supercritical pressure[J]. Journal of Supercritical Fluids, 2012, 72(9):90-99.

Zhang C, Xu G, Deng H, et al. Investigation of flow resistance characteristics of endothermic hydrocarbon fuel under supercritical pressures[J]. Propulsion & Power Research, 2013, 2(2):119-130.

Zhou W, Bao W. Deterioration in Heat Transfer of Endothermal Hydrocarbon Fuel[J]. Journal of Thermal Science, 2011, 20(2):173-180.

Zhou W, Yu B, Qin J, et al. Mechanism and influencing factors analysis of flowing instability of supercritical endothermic hydrocarbon fuel within a small-scale channel[J]. Applied Thermal Engineering, 2014, 71(1):34-42.

Zhu, Kun, Xu, et al. Flow frictional resistance characteristics of kerosene RP-3 in;horizontal circular tube at supercritical pressure[J]. Experimental Thermal & Fluid Science, 2013, 44(1):245-252.

333: Indirect evaporative cooler for energy recovery in some coastal cities in China

Yi CHEN[1], Hongxing YANG[2]

1 Faculty of Science and Technology, Technological and Higher Education Institute of Hong Kong, Hong Kong, China. yichen@vtc.edu.hk

2 Renewable Energy Research Group (RERG), Department of Building Services Engineering, The Hong Kong Polytechnic University, Hong Kong, China. hong-xing.yang@polyu.edu.hk

Indirect evaporative cooler (IEC) is a sustainable and high-efficient cooling device which has been widely used in hot and dry regions around the world. Recent studies indicate that the IEC can also be used as a high-efficient energy recovery device in a central air-conditioning (A/C) system in hot and humid regions. An IEC is installed before an air handling unit (AHU) to pre-cool the fresh air by recovering the cooling capacity from the exhaust air from air-conditioned rooms. The fresh air would be cooled and dehumidified by the IEC because of possible condensation. Therefore, the energy consumption of the chiller is reduced as part of the cooling load is removed by IEC. The IEC energy recovery system is particular suitable for 100% fresh air A/C system, in which cool and dry exhaust air can be fully used as secondary air in an IEC. The energy performance of IEC energy recovery system in three developed cities (Hong Kong, Guangzhou and Shanghai) along the coast of China is evaluated. The numerical model of IEC considering three possible operating states (non-condensation, partial condensation and total condensation) condensation is developed The model is then incorporated into Trnsys for year-around simulation. The results show that the IEC energy recovery system can reduce 28.1% to 31.6% energy consumption in a central air-conditioning system with 100% fresh air supply in the above cities. The IEC almost operates under condensation state in hot and humid summer season. Compared with conventional rotating heat recovery wheel, the IEC energy recovery system stands out for its low energy consumption, easy maintenance and cross contamination free. It breaks the regional limitation of IEC application and extends the application to hot and humid regions, with great energy saving and commercialization potential.

Keywords: indirect evaporative cooler; energy recovery; energy saving; numerical simulation; coastal cities

1. INTRODUCTION

Indirect evaporative cooler (IEC) is a sustainable cooling device which produces cooled air based on water evaporation rather than vapour compressor. It receives increasingly attention in the field of building energy conservation for its high efficient, low energy consumption, pollution-free and easy maintenance features. The most commonly used plate-type IEC consists of alternative wet and dry channels separated by thin plates. The water sprayed into the wet channels forms a water film and cools the separating wall with the aid of water evaporation under the reversed secondary air flow. The primary/ fresh air in the adjacent wall is then sensibly cooled without moisture added.

As the evaporation rate is higher under lower humidity, IEC is widely used in hot and dry regions in the past decades (Krüger, 2010). However, in recent years, researchers propose the IEC can be acted as a high efficient energy recovery device in hot and humid regions (Chen, 2015). In this system, an IEC is installed before an air handling unit (AHU) to pre-cool the hot and humid fresh air using cool and dry exhaust air from the air-conditioned room as secondary air. The IEC energy recovery system is particular suitable for 100% fresh air A/C system, in which cool and dry exhaust air can be fully used as secondary air in an IEC. The schematic diagram of IEC energy recovery system is shown in Figure 1. Unlike the conventional sensible cooling case, due to the high humid fresh air, condensation from fresh air is very likely to occur in the primary air channels. For example, the fresh air of 30°C and 70% RH has a dew-point temperature of 23.9°C. The secondary air of 25°C and 50% RH has a wet-bulb temperature of 13.9°C, much lower than 23.9°C. Under this case, condensation will occur at the place where the plate surface temperature is lower than the dew point temperature of the fresh air. The fresh air is therefore cooled and dehumidified.

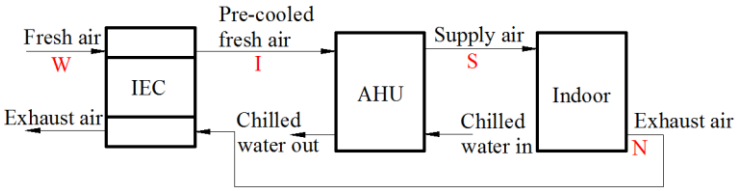

Figure 1: Schematic diagram of IEC energy recovery A/C system

The heat and mass transfer process in IEC with condensation is much more complex than that of non-condensation. In order to evaluate the performance of IEC energy recovery system in hot and humid regions, a model of IEC considering possible condensation is essential to facilitate the system simulation. However, current modelling work focus on IEC without condensation (Cui, 2014). Besides, year round performance of the system with condensation in IEC is seldom reported.

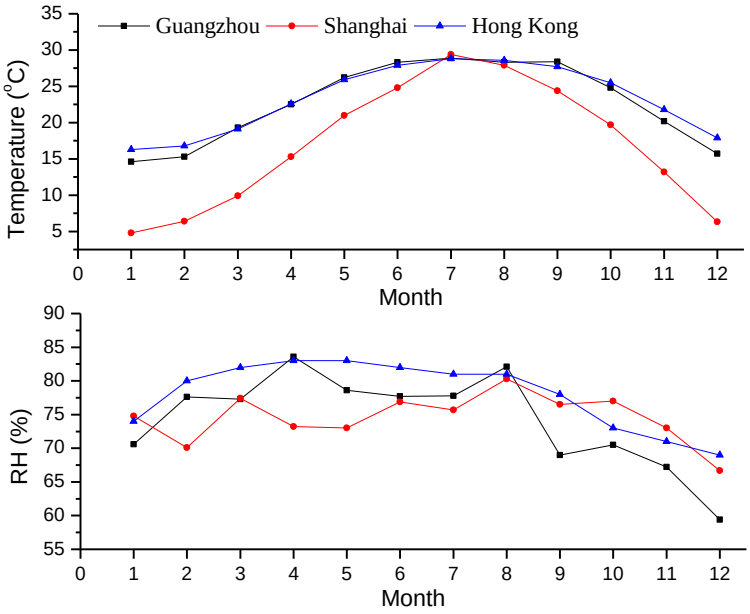

Figure 2: Year round ambient temperature and humidity in three cities

In this study, three typical coastal cities in China are selected, including Hong Kong, Guangzhou and Shanghai. The three cities is highly developed with strong economic strength. Hong Kong and Guangzhou locate in the southern coastal of China, and Shanghai locates in the eastern coastal of China. Year round ambient temperature and humidity in the three cities is shown in Figure 2. Guangzhou and Hong Kong have similar weather condition in term of temperature, but Hong

Kong has relative higher humidity all year around. The temperature varies greatly in Shanghai from month to month. All the three coastal cities have the hot and humid summer, which is our particular research focus for IEC application. As a developed city, the energy consumption of cooling system is tremendous. The IEC energy recovery can provide a sustainable solution to reduce the energy consumption of the cooling system and contribute to a lower carbon city.

In this paper, the simulation model of IEC and IEC energy recovery A/C system are firstly introduced. Case study has been carried out in Hong Kong, Guangzhou and Shanghai, respectively. The IEC operating state and energy saving potentials are evaluated.

2. SIMULATION MODEL

The IEC model considering condensation has been developed by self-programmed MATLAB code. A case has been selected and annual cooling load was simulated by Trnsys software in Hong Kong, Guangzhou and Shanghai. The output parameters including indoor temperature, indoor humidity, and hourly cooling load were exported to MATLAB code to simulate the annual performance of IEC energy recovery system.

2.1. IEC model

The heat and mass transfer process of IEC involves with evaporation and condensation is established by modified ε-NTU method (Hasan, 2012). Maclaine-Cross & Bank (1981) proposed a calculation method for the heat transfer coefficient on the wet surface by assuming the enthalpy of the moist air is in direct proportion to the wet-bulb temperature. In that way, the ε-NTU method can be applied on wet surface by introducing two revised parameters: heat transfer coefficient of the wet surface α_w and specific heat capacity of the wet surface c_{pw}, calculated as:

$$\alpha_w = \alpha\left(1+\frac{h_{fg}}{c_p e}\right) \qquad (1)$$

$$c_{pw} = c_p + \frac{h_{fg}}{e} \qquad (2)$$

By adopting the revised α_w and c_{pw}, the heat capacity ratio and efficiency of crossflow IEC can be used as Equation (3) and (4).

$$Cr = \frac{(c_{pw}m)_{\min}}{(c_{pw}m)_{\max}} \qquad (3)$$

$$\varepsilon = \frac{1-\exp\left[-NTU\cdot(1-Cr)\right]}{1-Cr\cdot\exp\left[-NTU\cdot(1-Cr)\right]} \qquad (4)$$

Under partial condensation, the turning point separates the heat exchange area into dry part and wet part. On the turning point, the plate surface temperature must be equal to the dew point temperature of the fresh air, so the heat balance equation is as follows.

$$a_{w,p}\cdot\left(t_{p,turn}-t_{p,dew}\right) = a_{w,s}\cdot\left(t_{p,dew}-t_{wb,s,turn}\right) \qquad (5)$$

$$t_{pl,turn} = t_{p,dew} \qquad (6)$$

2.2. IEC energy recovery system

The sensible and latent heat recovered by IEC can calculate by obtaining the outlet air parameters as Equation (7) and (8).

$$Q_{sen} = m_p c_p (t_{out} - t_{in}) \qquad (7)$$

$$Q_{lat} = h_{fg} m_p (\omega_{in} - \omega_{out}) \qquad (8)$$

The pre-cooled fresh air is further cooled and dehumidified by an AHU. The cooling load of AHU can be calculated as Equation (9).

$$Q_{AHU} = Q_{load} - (Q_{sen} + Q_{lat}) \qquad (9)$$

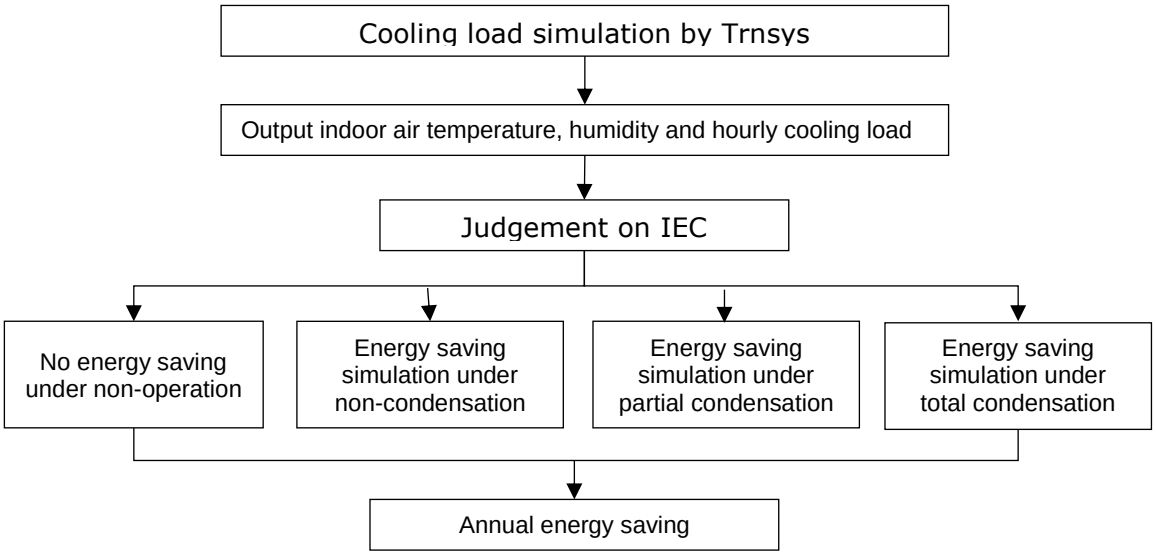

Figure 3: Simulation flow chart

The simulation flow chart of the IEC energy recovery system is shown as Figure 3. Firstly, the year-round cooling load of a building is simulated by Type 56 - TRNBuild multi-zone building module in Trnsys, a kind of powerful software used for building energy simulation. Hourly indoor air temperature, humidity and cooling load can be exported from Trnsys and read by Matlab code of IEC. Before simulation of energy saving by IEC, a programme is needed to make a judgement on the IEC operating states, including non-operation, non-condensation, partial condensation and total condensation. Then, the according energy saving can be simulated under each operating state.

The non-operation state refers to non-business hours or ventilation hours in transition months. The non-condensation state occurs when fresh air is not humid. The partial condensation refers to the humid fresh air condensate on part of the primary air channel. The total condensation takes place when the fresh air is extremely humid that condensation happens in the whole primary air channel.

2.3. Simulation parameters

The simulation parameters of IEC configuration and air-conditioning system settings are listed in Table 1.

Table 1: Simulation parameters

Parameters	Value
IEC length (*L*)	1.0m
IEC width (*Z*)	1.0m
IEC channel gap (*s*)	5mm
Channel pairs (*n*)	100
Supply air temperature from AHU (t_{sup})	14°C
Indoor temperature setting (t_n)	24°C
Indoor humidity setting (RH_n)	60%
Secondary air to primary air ratio	1.1

The studied case is a wet market. The wet market selling fish, meat and chicken together with vegetables will distribute smelling and moisture, the air from central air-conditioning can not be reused and circulated, so 100% fresh air air-

conditioning system is adopted. The one-floor trade region has a total area of 260 m^2 and average height of 6.7m. The detail of heat gain from building envelope, lighting, equipment, people and wet source are listed in Table 2. The schedule of lighting, equipment and occupant is from 8:00 to 20:00.

Table 2: Heat sources in wet market

Building envelope	U-value (W/m^2·°C)	Absorption coefficient
- external wall	2.89	0.8
- partition	2.64	_
- roof	0.495	0.8
- floor	2.341	_
Lighting	Wattage(W/m^2)	Ballast
- overhead lighting	20	1
- task lighting	2.2	1
Equipment	Wattage(W/m^2)	_
- electrical equipment	40	_
Occupant	Occupancy	Activity level
- Seller and customer	142	light work
Wet source	Area(m^2)	Evaporation rate (kg/h)
- water surface	36	78.5

3. RESULTS AND DISCUSSION

The year round cooling load, IEC operating state and energy saving in Hong Kong, Guangzhou and Shanghai are analysed respectively as follows.

3.1. Year round cooling load

The monthly sensible and latent cooling load in the three cities is shown in Figure 4. It can be seen that Hong Kong has the largest sensible load and latent load because of its high temperature and humidity. The load profile of Guangzhou is very similar with Hong Kong. Shanghai experiences with large fluctuation of cooling load in a year, with cooling season from April to October. All the three coastal cities have a large latent load because of its humid climate and a constant evaporation source in the wet market.

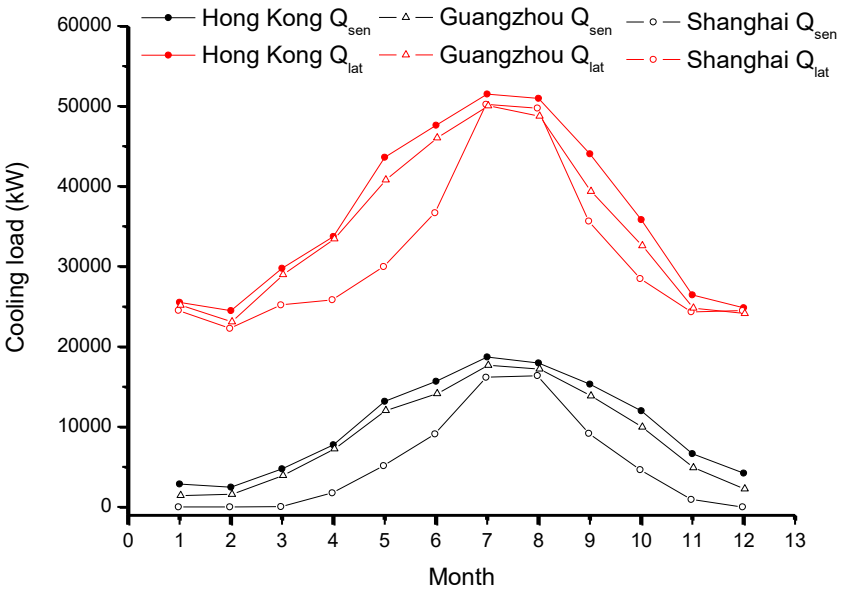

Figure 4: Year round cooling load in three cities

3.2. Year round IEC operation states

When IEC energy recovery system is used in hot and humid regions, there could be four operating state of IEC: non-operation, non-condensation, partial condensation and total condensation. Non-condensation state occurs when the inlet fresh air is dry and the dew point temperature is always lower than the plate surface temperature. Total condensation state occurs when the inlet fresh air is very humid that the dew point temperature is higher than the plate surface temperature at the beginning of the inlet air side. In the partial condensation state, the condensation is not taking place at first until at one point the plate surface temperature is equal to the dew point temperature of the air.

Figure 5 shows the year round IEC operation states in three cities. It can be seen that condensation tends to occur in summer in all three cities. In Hong Kong, the IEC almost operates under partial condensation or total condensation in June, July and August. The condensation state accounts for 95.8% of operating hours in June, 95.2% in July and 95.2% in August. The situation is quite similar in Guangzhou, with condensation state accounts for 72.2% of operating hours in June, 84.2% in July and 89.4% in August.

However, the condensation hours is Shanghai is relatively shorter than that of Hong Kong and Guangzhou. The condensation mostly occurs in July and August and total condensation only takes up for 4.1% and 4.4%, respectively. The reason is that Shanghai is less humid than that of Hong Kong and Guangzhou. In transition seasons like March, April, October and November, non-condensation dominates the operating state. Therefore, mainly sensible load can be reduced by IEC pre-cooling in transition seasons.

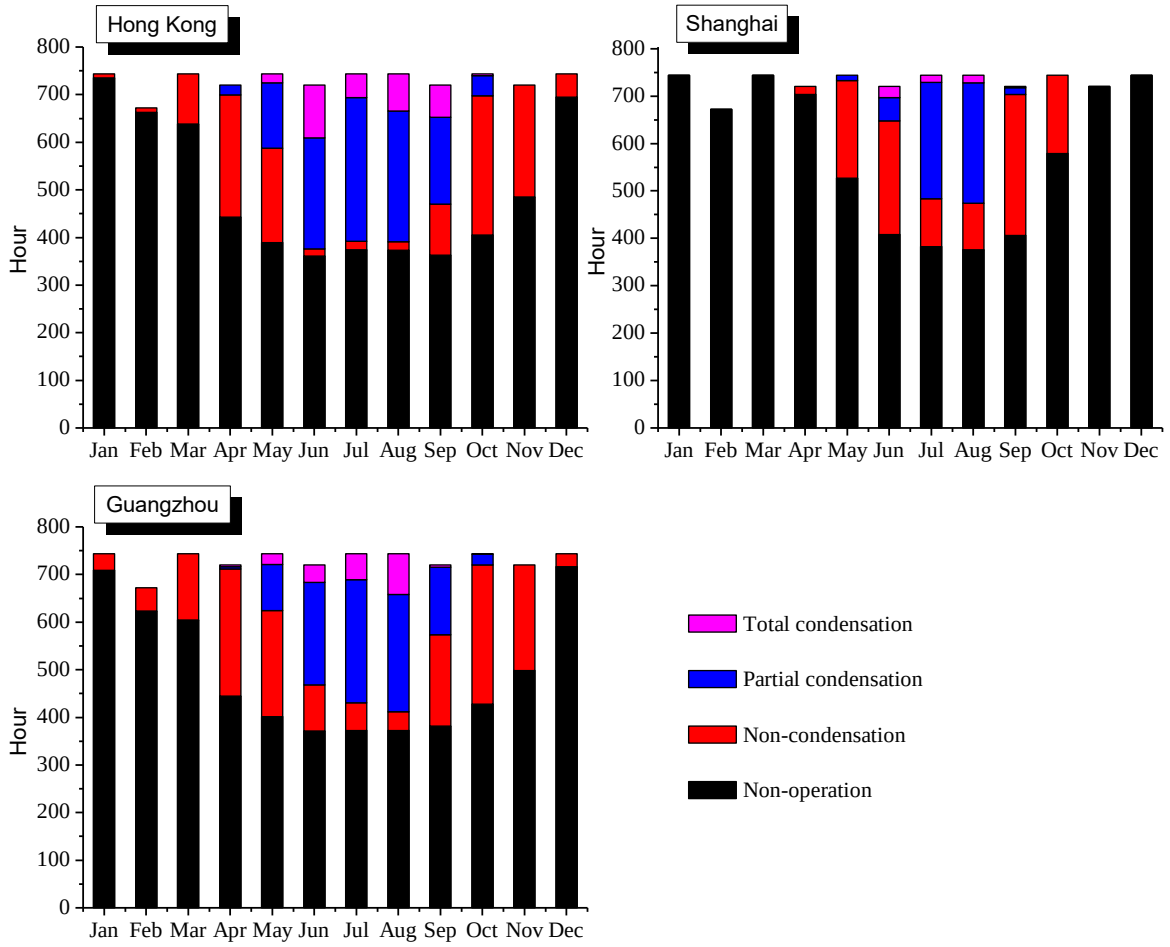

Figure 5: Year round IEC operation states in three cities

3.3. Year round energy saving

Because of possible condensation takes place in IEC, both the sensible load and latent load can be reduced by IEC. The year round energy saving by IEC in the three cities is shown in Figure 6. The energy saving is summer is much larger than that of other months because of higher ambient temperature and latent load saving by condensation. In Hong Kong, the latent energy saving accounts for 58.3%, 53.1% and 55.1% of total monthly saving in June, July and August. The latent energy saving accounts for a smaller proportion in Guangzhou and Shanghai. In Guangzhou, the latent energy saving

accounts for 42.7%, 44.7% and 50.7% of total monthly saving in June, July and August. In Shanghai, the latent energy saving accounts for 22.5%, 43.5% and 48.6% of total monthly saving in June, July and August. Therefore, the latent load saving takes up an important role in energy recovery in coastal cities. The condensation can not be neglected in order to accurately predict the energy performance of IEC.

In this case, the total energy saving by IEC in a year is 8.11×10^4 kWh in Hong Kong, 4.47×10^4 kWh in Shanghai and 8.10×10^4 kWh in Guangzhou. The original annual cooling loads without IEC in the above three cities are 2.61×10^5 kWh, 1.59×10^5 kWh and 2.57×10^5 kWh. Therefore, the energy saving ratio is calculated to be 31.1% in Hong Kong, 28.1% in Shanghai and 31.6% in Guangzhou.

Apart from direct load reduction, adopting IEC for energy recovery can provide other benefits .Firstly, compared with conventional rotating heat recovery wheel, the IEC energy recovery system stands out for its low energy consumption, easy maintenance and cross contamination free. Secondly, the capital investment of the chiller can be reduced because of peak load reduction. In this case, the original A/C system without IEC is 132 kW, but with IEC is 97 kW. The peak load is therefore reduced by 26.5%.

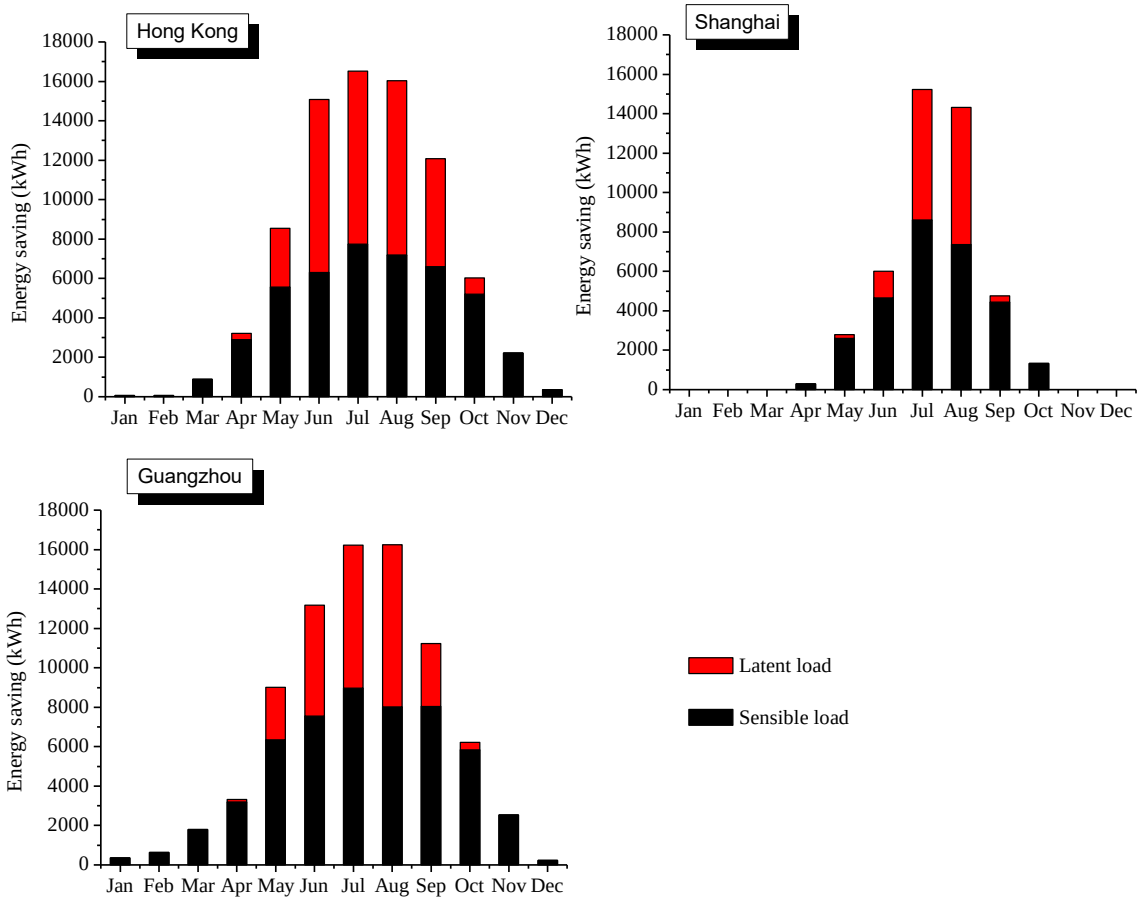

Figure 6: Year round energy saving in three cities

4. CONCLUSION

The performance of indirect evaporative cooler (IEC) for energy recovery in an air-conditioning system is evaluated for three coastal cities in China. The IEC energy recovery technology breaks the regional limitation of IEC application and is proved to have great energy saving potential in hot and humid coastal regions. The main conclusions from the study is summarised as follows:

1. In hot and humid coastal cities, condensation is very likely to occur. Therefore, both the sensible and latent load can be reduced by adopting IEC energy recovery.
2. Condensation tends to occur in summer, when temperature and humidity is high. In Hong Kong, the condensation of IEC accounts for 95.2% to 95.8% of operating hours in June, July and August. The condensation hours is Shanghai is relatively shorter than that of Hong Kong and Guangzhou because of less humid weather. The total condensation only takes up for 4.1% and 4.4% in July and August, respectively.

3. The energy saving is summer is much larger than that of other months because of higher ambient temperature and latent load saving by condensation. In Hong Kong, the latent energy saving accounts for 58.3%, 53.1% and 55.1% of total monthly saving in June, July and August. In Shanghai, the latent energy saving accounts for 22.5%, 43.5% and 48.6% of total monthly saving in June, July and August. Latent energy saving plays an important role in humid regions.
4. The energy saving ratio by IEC is 31.1% in Hong Kong, 28.1% in Shanghai and 31.6% in Guangzhou.

5. NOMENCLATURE

Q	heat transfer rate, W
Cr	heat capacity ratio
NTU	number of heat transfer units
c_p	specific heat capacity, J/kg·°C
c_{pw}	modified specific heat, J/kg·°C

Greek symbols

α	heat transfer coefficient, W/m^2·°C
α_w	modified heat transfer coefficient, W/m^2·°C

Subscripts

p	primary/fresh air
s	secondary air
w	wet region or water
wb	wet-bulb temperature
in	inlet air
e	slope of the saturated moist air
h_{fg}	heat capacity of vaporization, J/kg
m	air flow rate, kg/s
n	number of air channels
t	temperature, °C
ω	moisture content of air, kg/kg
ε	wet-bulb efficiency
out	outlet air
pl	plate
$turn$	turn point of condensation region
sen	sensible heat
lat	latent heat

6. REFERENCES

Chen, Y., Luo, Y., & Yang, H*. (2015). A simplified analytical model for indirect evaporative cooling considering condensation from fresh air: Development and application. Energy and Buildings, 108, 387-400.

Cui, X., Chua, K. J., Yang, W. M., Ng, K. C., Thu, K., & Nguyen, V. T. (2014). Studying the performance of an improved dew-point evaporative design for cooling application. Applied Thermal Engineering, 63(2), 624-633.

Hasan, A. (2012). Going below the wet-bulb temperature by indirect evaporative cooling: Analysis using a modified ε-NTU method. Applied Energy, 89(1), 237-245

Krüger, E., González Cruz, E., & Givoni, B. (2010). Effectiveness of indirect evaporative cooling and thermal mass in a hot arid climate. Building and Environment, 45(6), 1422-1433.

Maclaine-Cross, I. L.; Banks, P. J. A general theory of wet surface heat exchangers and its application to regenerative evaporative cooling. Journal of heat transfer, 1981, 103.3: 579-585.

335: Thermal impact zone of a river water source heat pump system in a main tributary of Yangtze River

Yifei LV [1], Jun LU [1], Ling XIE [1], Liyue ZENG [1], Zhenyong QIAO [2]

[1] *Key laboratory of the Three Gorges reservoir Region's Eco-Environment, Ministry of Education, Chongqing University, Chongqing, China 400044. yifei3706@gmail.com; lujun66@vip.sina.com; cquxieling@cqu.edu.cn; soriyoshi91@163.com;*

[2] *Sichuan Institute of Architectural Science, Chengdu City, Sichuan Province, China 610000; qzymail@163.com*

Temporal and spatial temperature distribution in flow regime is vital for the survival of aquatic biota. As Water Source Heat Pump System (WSHP) is gaining wider application, especially in regions with abundant water resources, water discharge of the WSHP system may induce pollution to river flow regime, which may lead to the outbreak of blue-green algae and consequently threaten the survival of other hydrobios. While the characteristics of thermal discharge into seashore and stagnant waterbody are widely investigated, the thermal impact pattern of WSHP to river flow is less acknowledged. Therefore, this paper studies this phenomenon. This paper used numerical simulations to obtain spatial temperature characteristics of the thermal impact zone of a case study of WSHP system's water discharged into river flow for three worst-case scenarios. For both warm and cold discharge, the shallow water regime is found to be the most affected zone. The water body that sustains temperature difference of 1°C extends about 5m for warm discharge and 2m for cold discharge in depth. However, this zone extends along the riverbank about 80m for warm discharge and 4260 m for cold discharge. This paper introduces a procedure for a preliminary assessment of how the thermal discharge from WSHP systems might threaten the freshwater fishes from a spatial point of view, and this may be a starting point of achieving the microscopic understanding or forecasting of thermal impact of anthropogenic thermal discharge to river flows. This work is fundamental to improve the strategic decisions on WSHP system's design and operation.

Keywords: Water Source Heat Pump System; thermal discharge; water body; CFD

1. INTRODUCTION

Temperature in natural flow regimes is a significant environmental driver for aquatic biota in regulating their spawning and migration behaviours (Wang et al., 2014; Fenkes et al., 2016; Crossin et al., 2008; Paragamian and Kruse, 2001; Eliason et al., 2011; Basiez et al., 2011; Marcy, 1971). In this regard, for freshwater fish, temperature tolerance of different species has been widely studied (Dudgeon, 1992; Wang and Wang, 1994; Liang and Sun, 2003). But because of global warming and anthropogenic water discharge, the habitats for aquatic biota are facing more and more threats.

Common anthropogenic thermal pollution sources in rivers are from thermal plants, sewage treatment plants, and HVAC systems. The attention was firstly placed at the cooling water discharge from thermal plants (Holland et al., 1974; Brandt, 1993; Teixeira et al., 2008) because of their enormous cooling demands. However, since the promotion of energy efficient heating and cooling systems for domestic and public constructions, Surface Water Source Heat Pump system is gaining much more application than before, especially in riverside cities. Water intake and discharge design are important aspects of WSHP systems. Currently, the focus is mainly on the optimisation of water intake (Wang et al., 2012; Russo et al., 2011), which may result in significant difference in system operation efficiency. In China, temperature alteration in the retention water body of WSHP systems should not exceed 2°C in summer and 1°C in winter within a week. But the consideration for thermal hazard is much more discussed in heat pump systems utilizing lake or underground water, and not carefully considered for rivers because of the continuous moving and mixing of the flow. River water is neigher significantly stratified nor stagnant. But on the other side, the mixing rather than conduction and convection dominates, which means the response of thermal impact might be transferred quickly to downstream because of the mixing and momentum transferring. In this consideration, the spatial characteristics of the impact region should also be investigated, to make sure the temperature within the shallow water areas along the drainage site has no big impact on the fish.

Some public buildings' WSHP systems start to operate in cooling mode and discharged warm water in late spring or early summer, which means the drainage water starts to increase in both temperature difference and flow rate. This could be problematic because this period overlaps the spawning period of most riverun fishes, which means the biggest threaten from this kind of thermal pollution could be that to the spawning and larva survival of riverine fishes. For a large building complex, to meet the huge cooling requirement, either the temperature difference between the inlet and outlet water or the discharged flow rate would be much larger.

This paper focuses on estimating spatial characteristics of the thermal impact zone of WSHP system's exhaust water to river flow under typical HVAC operation conditions. We performed numerical analysis to obtain the flow characteristics of thermal discharge and discussed assumptions of possible hazard from WSHP systems' thermal pollution to flow regime in a temporal and spatial way.

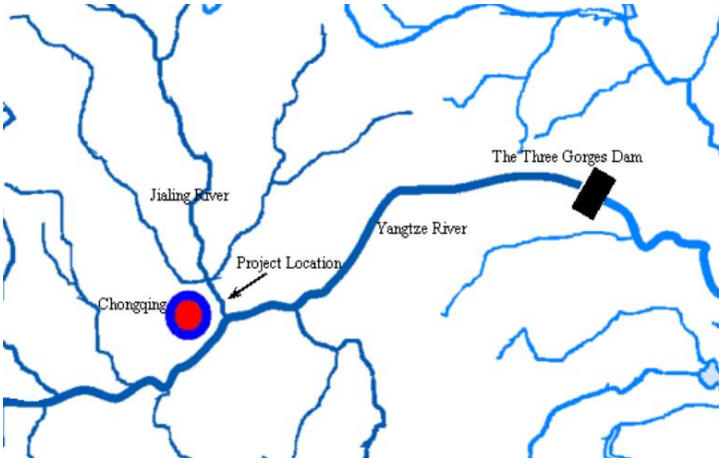

Figure 1: Site location of the WSHP project

2. METHODOLOGY

2.1. Studied area and the WSHP system

The WSHP system serves a 364000 ㎡ building complex in a business district in central Chongqing, a large Chinese inland city along the lower reaches of Jialing River, which is a main tributary of the Yangtze River. As shown in Figure.1, Jialing River originates in southwest China's Sichuan Province and runs 1,345 kilometres before its confluence with the Yangtze River. Currently, in Jialing River, a total of 151 species of fish inhabit the river, of which 51 species are typical of the Yangtze River. Most of the fishes are carps, which are highly adaptive to the extreme environment, though decades ago carps only form the second largest population in the Jialing River regime. The protection of spawning spots is critical to the

conservation of fish population. For this purpose, the government has taken steps to protect fish spawning. For example, each year the authorities drop larvae into the river to adjust the fish population, but fish are still declining in this flow regime because of environmental changes. According to Wang (2012), two factors were significantly positive when correlated with egg abundance: one was increasing rate of the river flow (flood amplitude), and the other was river clearance. In this regard, accurate prediction of the extent to which the flow regime might be affected by WSHP drainage should be carefully estimated.

Annual water intake flow of the WSHP system is approximately 8.25 million m³, the maximum water intake period is in July, and the cooling supply season is from May to September. The transitional season is from March to May, when the HVAC system only supply domestic water and cooling on some of the days.

2.2. Possible worst-case scenarios

We introduced a worst-case scenario analysis of the discharge's thermal impact based on annual variations of river flow rate and WSHP discharge. For both warm and cold-water discharge, the worst-case scenario may occur when river water flow rate is small and WSHP discharge is large.

Water flow data (Figure 2) were obtained from Chang Jiang Water Resources Commission of the Ministry of Water Resources. The minimum flow rate of the target flow regime occurs during December and March from 2010 to 2013. The flow rate slightly rises in early summer in May and increases continuously from June till it reached a maximum in July (for 2010, 2012 and 2013). From August to November, flow rate of the river gradually declines until it reaches the minimum and almost maintains a minimum level till April. The common spawning season for carps are from March to June, and for catfish March to July, bleekers June to August. Riverside floodplains are also important locations of river shrimp activities, especially in April when they start spawning and stay in the weeds among the shallow water.

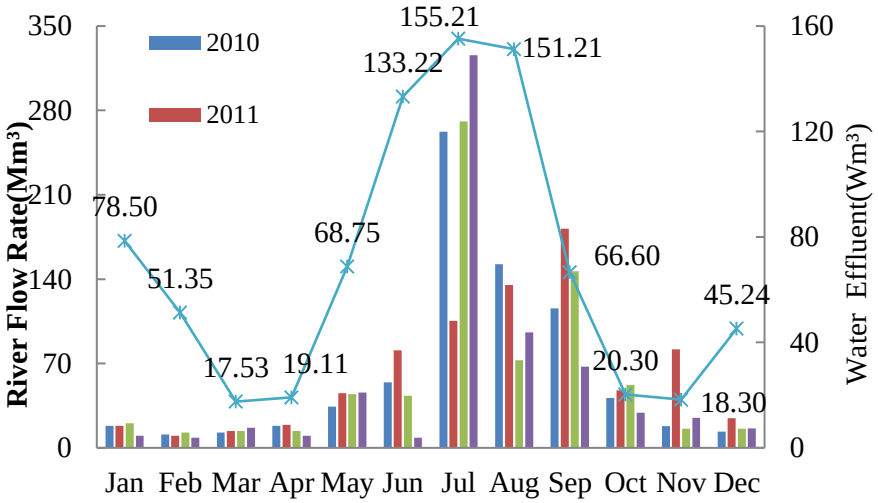

Figure 2: Annual variation of river flow rate and water discharge

The flow rate of WSHP discharge follows a similar pattern compared with river flow. For heating mode of WSHP system in winter, in January, heating load demand is the highest and the cooling water discharge reaches the maximum, which may be an extreme scenario of cold water thermal impact. While for cooling mode of the WSHP system, from June to September, the discharge flow rate retains a relatively high level. June is the summer months with inferior river flow rate, but at the same time the drainage flow rate maintains a relatively high level. In this consideration, June is the possible period that worst-case scenario might appear in cooling period of WSHP system. For transitional season of WSHP system, from March to May, the flow rate maintains a minimum level in March and April. The water discharge is almost equal in this two months. The water body temperature is slightly lower in March, which means a larger temperature difference exists. In Jialing River, carps dominate in both species and amount, and the percentages of both exceed 60%. Water temperature declines of 2 °C–4 °C in March, April and May (a critical period for gonad development) was the principal reason for the observed spawning delay. The variable most associated with spawning timing was the arrival date of the cumulative temperature. In this regard, March is chosen as our studied case for transitional operation season of the WSHP system.

A collection of river flow data and WSHP discharge condition for the 3 worst-case scenarios is summarised in Table 1.

Table 1: Boundary conditions of numerical simulation in 3 worst-case scenarios

Scenario	HVAC operation mode	Water surface elevation （m）	Discharge water temperature (°C)	River water temperature(°C)	Discharge flow rate (m^3/h)	River flow velocity (m/s)
A	Summer	169.12	34	26	4400	1.11
B	Transitional	160.05	6.6	12.66	800	0.27
C	Winter	160.05	6.6	11.6	2600	0.27

2.3. Numerical simulation setup and validation

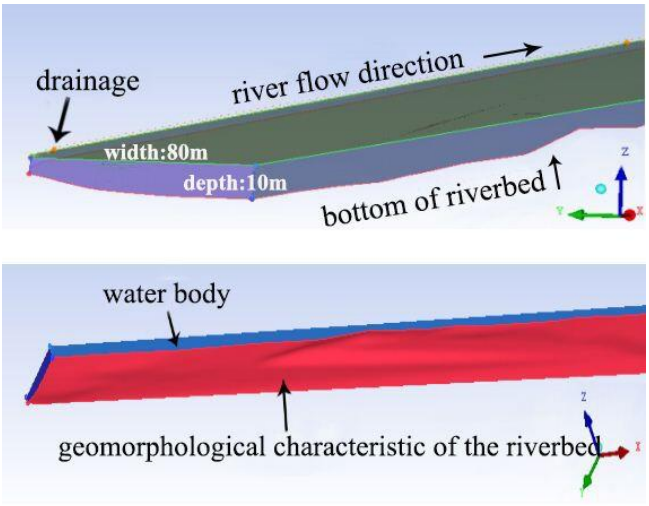

Figure 3: Model setup

GIS elevation data was transferred into geomorphological characteristic of the riverbed structure, as shown in figure 3. Meshes at the bank and the river bottom have been refined. Several assumptions are made for a simplified simulation:

- Based on the mixing characteristics of river flow, the inlet temperature in our model is supposed to have no stratification and maintain a uniform temperature between the surface and bottom (Wang et al., 2012; Russo et al., 2011; Xu et al., 2015; Jones, 2013).
- Cohesive non-slip and heat-insulation conditions are applied at river bank and bottom;
- Water surface is treated as a steel lid and the normal velocity equals 0.
- The model only considered flow dispersion without considering heat transfer with the surrounding

This simulation model is generated by extracting the elevation of the Jialing River from the calculation domain, and the CAD plug-in generates a three-dimensional model of the river bottom based on the underwater topographic map of the engineering section from the Yangtze River Hydrographic Bureau. Then, the ICEMCFD is introduced to establish a calculation model and divide the grid. After establishing the three-dimensional model of the whole river channel, the three-dimensional model after the establishment is used to measure the average cross-sectional area of the whole river section, the average dry-water period is about 425.8 m^2, and the wet season is about 3550 m^2. The convergence criteria are continuity equation 1e-5, velocity equation 1e-4, energy equation 1e-6; k, e equation 1e-3; temperature monitoring points tend to be stable; flux reports check flow balance to ensure strict convergence.

3. RESULTS AND DISCUSSION

3.1. Spatial characteristics of WSHP thermal discharge

Numerical simulations of the temperature distribution around the water discharge have been carried out under 3 worst-case scenarios, as discussed in 2.2. As an example, for Scenario A, the temperature distribution along streamlines start from the discharge is depicted in Figure 4. Temperature of thermal discharge decreases significantly after warm discharge (34°C) enters river water body. Iso-surfaces (Figure 4) of different temperature (5°C, 4°C, 3°C, 2°C, 1°C) above the river water temperature were obtained from the numerical simulation results.

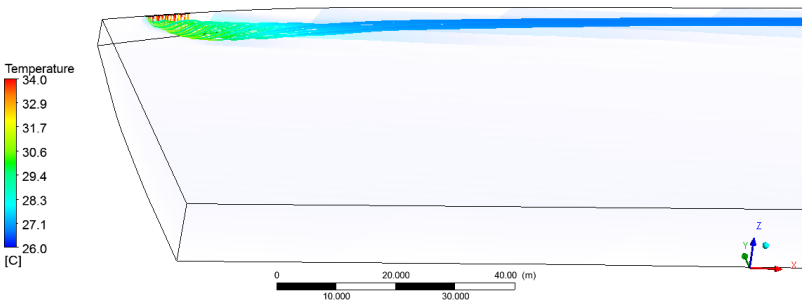

Figure 4: Temperature distribution along streamlines starts from the discharge site in Scenario A

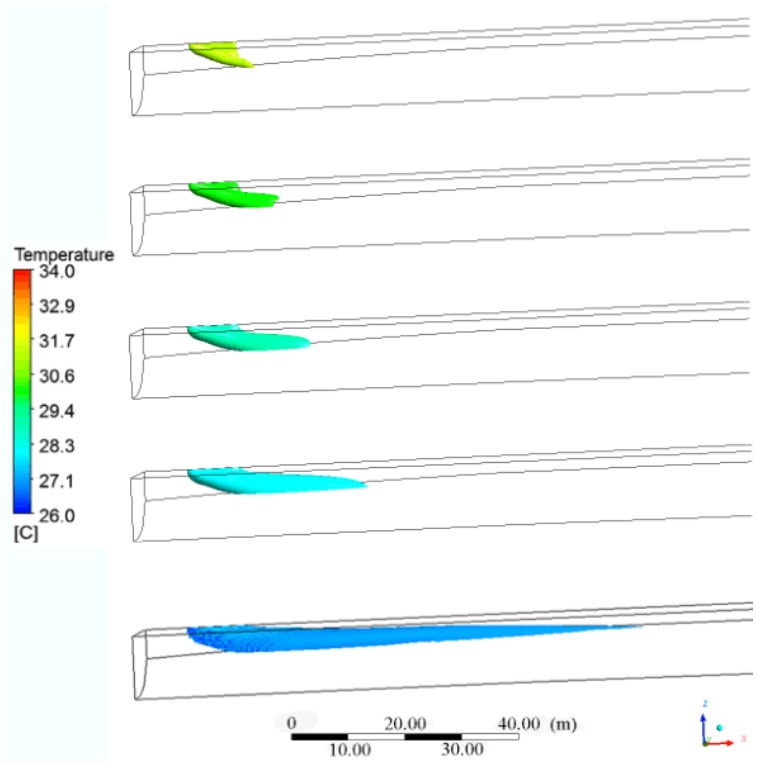

Figure 5: Isothermal-volume of different temperature differences in Scenario A (5°C, 4°C 3°C 2℃, 1°C)

In our analysis, isothermal-volume represents the total volume of water of which the temperature has been altered as a consequence WSHP water discharge. For Scenario A, temperature of discharged water is 5°C above river water, and the isothermal-volumes indicate the water body volumes that exhibit temperature differences between affected water body and original river water body (5°C, 4°C, 3°C, 2°C, 1°C for Scenario A and 4°C, 3°C, 2°C, 1°C for Scenario B, C). As the temperature of discharge decreases rapidly after it enters the river and the isothermal volumes temperature differences higher than of 5°C are very small to be noticed and can be neglected, only the iso-surfaces of temperature differences lower than of 5°C are provided.

Table 2: Isothermal-volume of the affected flow regime in 3 worst-case scenarios

	Scenario	Temperature alteration of river water				
		5℃	4℃	3℃	2℃	1℃
Iso-volume (m^3)	A	30.2	65	119.5	217.4	594.7
	B	——	106.5	320.3	1346	9189
	C	——	444.6	2194	12770	26910
Iso-volume /Total affected water body volume (%)	A	2.9%	6.3%	11.6%	21.2%	57.9%
	B	——	1.0%	2.9%	12.3%	83.8%
	C	——	1.1%	5.2%	30.2%	63.6%

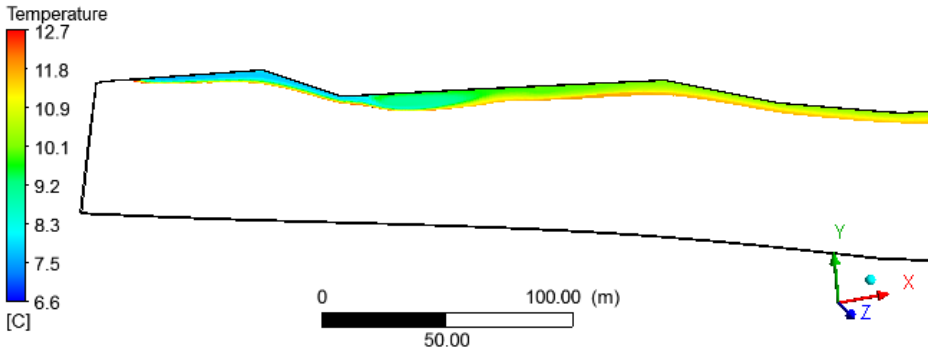

Figure 6: Isothermal-volume of the affected waterbody regime in Scenario B

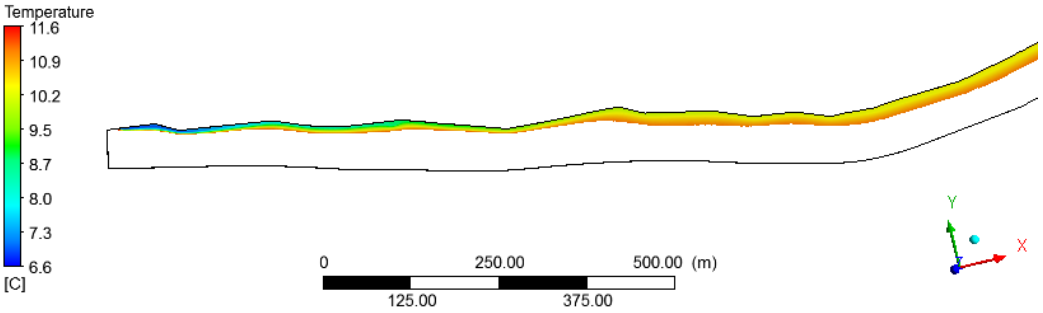

Figure 7: Isothermal-volume of the affected waterbody regime in Scenario C

Isothermal-volumes of each temperature differences for the 3 worst-case scenarios are summarised in Table 2. In high water level season in summer, the isothermal-volume of 1℃ temperature difference is 594.7m³ and the isothermal-volume of temperature difference higher than 1℃ is 432.1 m³, accounting for 1.5% of the total river water volume within the affected water regime. In low water level season (Figures 5 and 6), the isothermal-volume of temperature difference below 2℃ is 10535m³ for transitional season and 39680m³ for winter, respectively. The isothermal-volume of temperature difference higher than 2℃ is 426.8m³ for transitional season and 2638.6 m³ for winter, accounting for 3.2% and 1.5% of the total river water volume within the affected regime. Above all, the affected range of water discharge is limited and regions of large temperature difference tend to be concentrated around the drain. The influence of drainage to the river temperature is mainly concentrated on the scope of 1℃. The percentage of 1℃ isothermal-volume takes up 57.9% (summer), 83.8% (temperature variation) and 63.6% (winter) of the total affected flow regime that has been altered in temperature.

3.2. Extent of temperature alteration in different directions

Table 3: Extent of temperature alteration in x (river flow direction), y (river width), z (river depth) directions

Extent of temperature alteration	Scenario	Temperature alteration of river water				
		5	4	3	2	1
x (m)	A	12.2	16.3	21.9	31.9	79.7
	B	——	180	362.4	677.2	3125
	C	——	438.6	944.7	2650	4260
y (m)	A	1.9	2.6	3.1	3.9	4.7
	B	——	1.8	2.3	4.3	6.5
	C	——	5.7	6.4	7	14.1
z (m)	A	4.6	4.7	4.7	4.8	4.8
	B	——	0.7	0.8	1.4	2
	C	——	1.2	1.3	1.5	2.1

The extent to which river water could be affected in each direction is an important spatial indicator of environmental influence estimation. A collection of the extent of temperature alteration in the river flow direction, river width and river depth are provided in table3. The thermal polluted zone in high water level scenario (Scenario A, length: 12.2m/5℃ ~ 79.7m/1, width: 1.9m/5 ~ 4.7m/1) is the smallest, while the thermal polluted zone in low water level scenario in winter (Scenario C, length: 438.6m/4℃ ~ 4260m/1℃, width: 5.7m/4℃ ~ 14.1m/1℃) suffer thermal impact most. Summer drainage has a smaller density and floats on the surface which improves thermal heat dissipation while winter drainage flows towards the downstream and the diffusion distance is longer. Another reason for the significant difference in affected length could be that mixing is much weaker than in Scenario B and C because the background flow rate of river is much smaller. In summary, the thermal polluted range is limited, and regions of large temperature difference tend to be concentrated around the drain. As for the depth of the affected regime, summer (4.6m/5℃~4.8m/1℃) drainage has a maximum affected depth due to its high river water level and larger discharge flow rate. In contrast with the transition season (Scenario B, 0.7m/4℃ ~ 2.0m/1℃), winter (Scenario C, 1.2m/4℃ ~ 2.1m/1℃) drainage's influence is deeper due to the higher amount of water discharge and lower temperature of river water.

3.3. Possible threats to spawning and larvae

The discharge of the modelled project is significantly lower compared to the water discharge of a power station, in which case the temperature might rise 4-12℃ just below the discharge point and 4-8℃ or more 2 km downstream, in winter.

A similar assessment of the larvae and spawn survival rates near the exhausts of Daya Bay Nuclear Plant has been made by observation in (Wang and Wu, 1994). According to their findings, the huge amount of discharged water is found to have minimum impact on the total population of spawn and larvae, the species construction of fishes in this area is slightly altered. This is due to a comprehensive result of biological adaption and a balance of the increase and decrease of different fish populations. Similar conclusions for benthic fishes are in (Teixeira, Neves and Araújo, 2009).

In our cases, the effect of discharge from WSHP systems are even much smaller than in a power station case. However, other side effects to fish surviving that are induced by thermal impact exists, such as the outbreak of the blue-green algae, the oxidation and the clearance of water. The overall effect of these factors is still unclear, because temperature increase may promote spawning, or cause the outbreak of blue-green algae, as the rate of oxygen absorption increases.

Thermal impact assessment should also be species-specific. For example, with one discharge opening, the shallow water flow regime beside the bank is the most possible target area of thermal impact. In this way, the fishes that lay their eggs among water weed in shallow water may face possible threats to spawning and larvae surviving. Additionally, most species are sensitive to temperature differentials in the range of 1-2°C, particularly in their spawning seasons. So geometry and dimension of exhaust construction should be designed within consideration of the activity area of nearby aquatic biota, such that the thermal impact would not bring negative effect to long time fish population in the water body. Another issue that should be considered is the main species in the target flow regime, for example, cold water fishes are more sensitive to high water temperature and are more fragile to high temperature and even a slight change in river channel may lead to habitat loss (Rahel, Keleher and Anderson, 1996).

4. CONCLUSIONS

In this study, a worst-case scenario analysis has been introduced in the thermal impact of water discharge based on annual variations of river flow rate and WSHP discharge. The isothermal-volume has been utilised to represent the total volume of water of which the temperature has been altered as a consequence WSHP water discharge. The extent of temperature alteration in 3 directions: river flow direction, river width and river depth has been calculated. According to analysis of the above indices, our conclusions can be summarised as:

Although the total thermal impact area is minimal compared to the water body, the shallow water flow regime beside the bank is the most possible target area of thermal impact.

During low water period, due to small depth of flow near the banks, the impact area is much larger and longer compared to high flow period.

Environmental impact assessment of projects that may cause thermal shock to nearby water body should follow specific riverbed geometry and water flow characteristics.

This work introduces a procedure for a preliminary assessment of how the thermal discharge from WSHP systems might threaten the freshwater fishes from a spatial point of view. This may be a starting point of achieving the microscopic understanding or forecasting of thermal impact of anthropogenic thermal discharge to river flows.

5. ACKNOWLEDGEMENTS

This work is sponsored by National Science Foundation of China (No.51708054, No.51478058) and TheNational Key R& D Program of China (2016YFC0700703)

6. REFERENCES

Brandt, S.B., 1993. The Effect of Thermal Fronts on Fish Growth: A Bioenergetics Evaluation of Food and Temperature. Estuaries 16, 142–159.

Crossin, G.T., Hinch, S.G., Cooke, S.J., Welch, D.W., Patterson, D.A., Jones, S.R. m., Lotto, A.G., Leggatt, R.A., Mathes, M.T., Shrimpton, J.M., Van Der Kraak, G., Farrell, A.P., 2008. Exposure to high temperature influences the behaviour, physiology, and survival of sockeye salmon during spawning migration. Canadian Journal of Zoology 86, 127–140.

Dudgeon, D., 1992. Endangered ecosystems: a review of the conservation status of tropical Asian rivers. Hydrobiologia 248, 167–191.

Eliason, E.J., Clark, T.D., Hague, M.J., Hanson, L.M., Gallagher, Z.S., Jeffries, K.M., Gale, M.K., Patterson, D.A., Hinch, S.G., Farrell, A.P., 2011. Differences in Thermal Tolerance among Sockeye Salmon Populations. Science 332, 109–112.

Fenkes, M., Shiels, H.A., Fitzpatrick, J.L., Nudds, R.L., 2016. The potential impacts of migratory difficulty, including warmer waters and altered flow conditions, on the reproductive success of salmonid fishes. Comparative Biochemistry and Physiology Part A: Molecular & Integrative Physiology 193, 11–21.

Fish and River Pollution - J. R. Erichsen Jones - Google Books

Holland, W.E., Smith, M.H., Gibbons, J.W., Brown, D.H., 1974. Thermal Tolerances of Fish from a Reservoir Receiving Heated Effluent from a Nuclear Reactor. Physiological Zoology 47, 110–118.

Liang, L., Sun, X., 2003. Mapping cold tolerance strain on genetic linkage map of common carp. Journal of Dalian Fisheries University.

lin, shaojin, Zhan, H., 2000. Effects of thermal effluent on fish eggs and larvae in waters near daya bay nuclear plant. Journal of Tropical Oceanography 44–51.

Marcy Jr., B.C., 1971. Survival of Young Fish in the Discharge Canal of a Nuclear Power Plant. J. Fish. Res. Bd. Can. 28, 1057–1060.

Paragamian, V.L., Kruse, G., 2001. Kootenai River White Sturgeon Spawning Migration Behavior and a Predictive Model. North American Journal of Fisheries Management 21, 10–21.

Rahel, F.J., Keleher, C.J., Anderson, J.L., 1996. Potential habitat loss and population fragmentation for cold water fish in the North Platte River drainage of the Rocky Mountains: response to climate warming. Limnology and Oceanography 1116–1123.

Russo, S.L., Taddia, G., Baccino, G., Verda, V., 2011. Different design scenarios related to an open loop groundwater heat pump in a large building: Impact on subsurface and primary energy consumption. Energy and Buildings 43, 347–357.

Teixeira, T.P., Neves, L.M., Araújo, F.G., 2009. Effects of a nuclear power plant thermal discharge on habitat complexity and fish community structure in Ilha Grande Bay, Brazil. Marine Environmental Research 68, 188.

Wang, X., Wu, D., 1994. Studies on the criteria of water temperature for major cultured freshwater fishes.

Wang, Y., Wong, K.K.L., Liu, Q., Jin, Y., Tu, J., 2012. Improvement of energy efficiency for an open-loop surface water source heat pump system via optimal design of water-intake. Energy and Buildings 51, 93–100.

338: Preliminary study of effects of primary and back pressure on performance of supersonic ejector driven by compressed air

Ahmed AL-NUAIMI[1], Mark WORALL[2], Saffa RIFFAT[3]

[1] Faculty of Engineering, University of Nottingham, Nottingham, NG7 2RD, ahmed_i1974@yahoo.com
[2] Faculty of Engineering, University of Nottingham, Nottingham, NG7 2RD, lazmw@exmail.nottingham.ac.uk
[3] Faculty of Engineering, University of Nottingham, Nottingham, NG7 2RD, lazsbr@exmail.nottingham.ac.uk

The ejectors have some advantages such as simple, reliable and no moving parts. They can be used in air-conditioning and refrigeration application. Six different ejectors use air as working fluid in this study were proposed and tested experimentally. The Variable Area Ratios of Ejectors (A3/At) were used with range from 10.68 to 30.62. The aim of this study was to investigate these ejectors under variation of primary pressure (1.5–6.0 brag) brag and adjustable spindle position from 0 to -25 mm.

Two groups of ejectors (A and C) were categorised based on the type of nozzle. The effect of Variation of primary pressure (Pp) on entrainment ratio was carried out at different spindle positions. Furthermore, the effect of Variation of back pressure (Pb) on entrainment ratio (ω) was tested under range of primary pressure (3-4.5 brag). At maximum primary pressure (6.0 brag), the entrainment ratios (ω) of ejector (A A) were 0.35, 0.21 and 0.14 for spindle positions (-25mm), (-15mm) and (-5mm), respectively. While, the maximal entrainment ratios (ω)obtained from ejector (C C) are 0.32, 0.35 and 0.39 for spindle positions (-15mm), (-20mm) and (-25mm), respectively

The results show the maximal value for performance of ejector CC is higher than ejector AA about 11.4 %. The ejector (C B) has highest entrainment ratios (ω) about 0.43 compared with the rest of ejectors in groups (A) and (C) at maximum primary pressure (6.0 brag) and adjustable spindle position (-25mm). Group A is more proper for higher values of back pressure, whilst, Group C is more suitable for high performance of ejector.

Keywords: Ejector, Air-conditioning and refrigeration, Entrainment ratio, Adjustable spindle ejector, Variable area ratios

1. INTRODUCTION

The climate changes in the world has created an important tendency to develop or discover modern technologies in renewable energy. Low grade energy is a significant option can obtain it from different sections such as solar energy, waste heat, internal combustion engines and industrials. Ejectors work with low grade energy in refrigeration system and cooling system. Their advantageous are simple, reliable and no moving parts. The Theoretical and Experimental Studies have been highlighted by many researchers to study ejector and its effect in various kinds of proposed cycles.

In theoretical studies, most of researchers have presented a mathematical model in terms of one dimensional model and CFD model. A 1D model analysis (one-dimensional ejector theory) presented initially by Keenan, (Keenan, Neumann, & Lustwerk, 1950), then this model modified by Eames, Aphornratana & Haider (1995). Furthermore, a 1D model validated analytical results by using different ejectors geometry experimentally with R141b as working fluid (Huang, 1999). Moreover, a study investigated the performance of the solar-driven ejector refrigeration system using iso-butane (R600a) as the working fluid. The authors examined the influence of the operating conditions and the solar collector types on the system's performance by dynamic simulation (Pridasawas & Lundqvist, 2007). An ejector cooling system (ECS) using six fluids propane, butane, iso-butane, R152a, R123 and R134a, was achieved with one-dimensional mathematical model of ejector. The results showed the COP of the system decreased from high to low as follow: R290, R152a, R134a, R600a, R600 and R123 respectively. The range of generation temperature from 70 C to 95 C, which are appropriate temperatures for thermal cooling systems, provides the best performance when use of R290 in an ECS (Roman & Hernandez, 2011). For more realistic results, several of researchers applied computational fluid dynamics (CFD) method on the ejector to investigative the performance and design. Chan et al. (2010) used CFD method to study the performance of an actual ejector operated with Propane. A CFD simulation presented for a supersonic ejector using R245fa as a working fluid in a refrigeration system (Scott, Aidoun, Bellache & Ouzzane, 2008). A comparison between experimental and thermotical (CFD) was presented on supersonic air ejector. For off-design predictions, two turbulence models (K-e and k-w-sst) were used to compare their results with experiments. K-e was shown a good agreement with experimental result as compared with less agreement was obtained from k-w-sst. these two models showed an issue related to entrainment ratio (ω) ,whereas no matching results under range of operating conditions (Hemidi, Henry, Leclaire, Seynhaeve & Bartosiewicz, 2009a). The same authors presented the CFD of wide range of operation of supersonic air ejector to investigate an issue in previous study. The findings showed a good result for entrainment ratio (ω) does not mean a clearly matching with local flow properties. For this point, both of sonic line and Mach number proposed as key factor to explain the relationship between entrainment ratio (ω) and local flow properties. Finally, this key helps to assign the place of critical section where the ejector become choked (Hemidi, Henry, Leclaire, Seynhaeve & Bartosiewicz, 2009b). Furthermore, several studies have investigated adjustable spindle nozzle in terms of theoretical and experimental. Movable spindle nozzle was presented to change the nozzle throat and consequently the mass flow rare will change. Spindale nozzle influences the performance of ejector. The highest values for entrainment ratio (ω) and COP (0.34 and 0.323 respectively) can be indicated when the spindle position is 8 mm (Ma, Zhang, Omer & Riffat, 2010). As for turbulence models in CFD, Standard k-ε model, Renormalization-group (RNG) k-ε model and k-ω sst model were used in an adjustable ejector (Lin et al., 2013).

The literature review above indicates that there are many studies on the ejectors theoretically and experimentally. The aim of this paper is to investigate six different types of ejectors under variation of adjustable spindle position, primary and back pressures. According to nozzle and constant area section, two nozzles and three different constant area sections were carried out in this study. In the present study, the working fluid is air to test six different ejectors. Furthermore, adjustable spindle position range between 0 (fully closed) and -25 mm (fully open) to change mass flow rate in inlet primary.

2. EXPERIMENTAL INVESTIGATIONS

Ejectors have been used in cooling systems for long time. They were not preferred in refrigeration system because of their low coefficient of performance. However, the ejectors have some advantages such as simple, reliable, no moving parts. Moreover, several heat sources using these devices for instance waste heat, solar energy, geothermal energy, and biomass products to drive refrigeration system or to generate electricity. Furthermore, reducing the pollution in comparison with fossil fuel power plants.

2.1. Description of the test rig

The rig consists two main components (compressor and ejector) connected by copper and nylon pipes as well as joints such as valves, flow meters, filter, oil level, and other measurements devices. Figure 1 shows a simple circuit diagram of ejector cycle. Air is compressed from air supply source in the lab to the main line before relief valve.

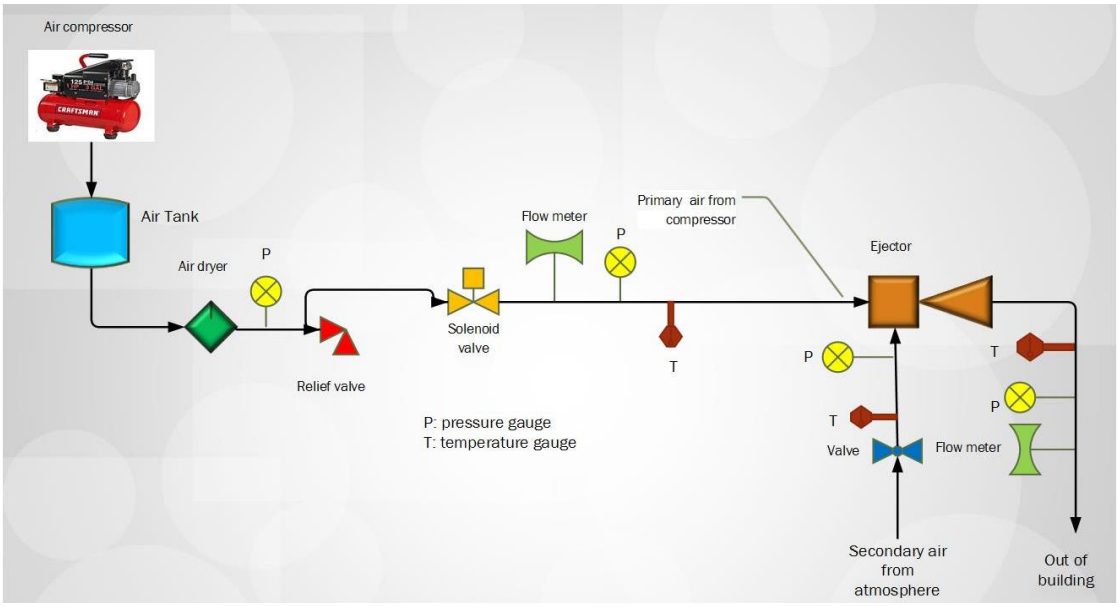

Figure 1: A simple circuit diagram of ejector cycle.

In this cycle, the air is supplied to a nozzle in the ejector at high pressure (primary pressure) to expand to the pressure of surroundings, this will lease the air flow from low pressure side (suction pressure). Both of two streams are mixed and recompressed to exhaust line to atmospheric environment. Figure 2 shows the experimental setup of rig.

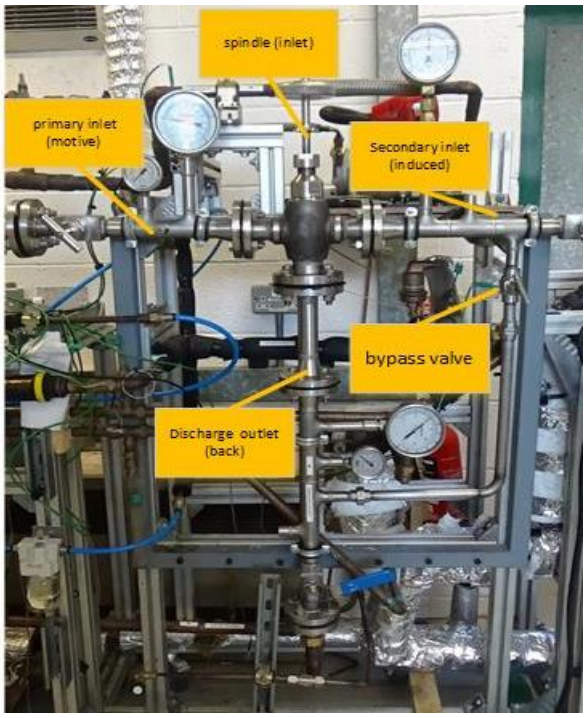

Figure 2: Experimental setup of rig.

Toward to measure the motive, induced and back temperatures, pressures and flow rates, varies instrumentation devise were installed and as listed in Table 1. The pressure transmitter PT5-30M (Pressure range: 0 … 30barg) was used to measure the gauge pressure of primary inlet, with accuracy of 0.1%. While the pressure transmitters PT5-7M (Pressure range: -0.08 … 7barg) was used to measure the gauge pressure of secondary inlet and back pressure outlet, with accuracy of 1%. Temperatures were measured by K type thermocouples (model RS No. 397-1488). The Flowmeters (model RMC) were installed to determine the flow of air in the ejector in inlets and outlet.

Table 1: instrumentation of rig.

Items	Model	Accuracy Full Scale (FS)	Range
Pressure transmitter	PT5-30M	1%	0 … 30barg
Pressure transmitter	PT5-7M	1%	-0.08…….7 brag
Thermocouples K type	RS No. 397-1488	±1.5°C	0°C……+1100°C
Flow meter	RMC	2%	54°C

2.2. Variable area ratios of ejector specifications

To check Verification of theoretical analysis can use the present model by testing 6 different Variable Area Ratios of Ejector. Proposed ejectors and their parts are shown in Figure 3.

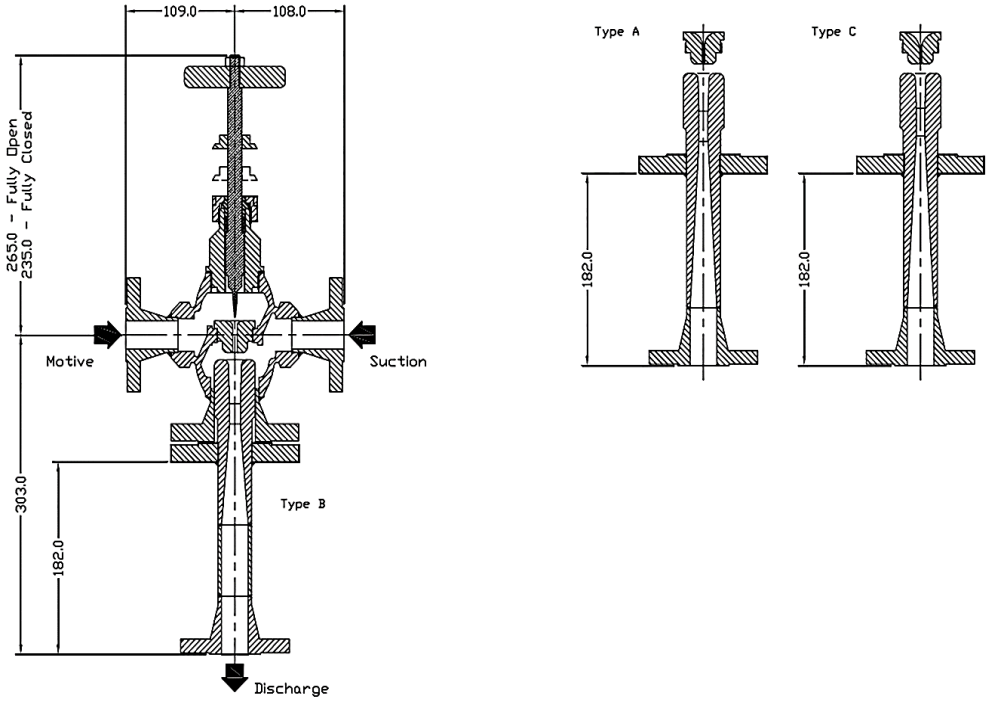

Figure 3: Diagram of ejector designed.

This figure depicts two types of nozzles, the main dimensions of three types of constant area sections (including discharge) and an adjustable primary throat which ranges from 0 (fully closed) to -25 mm (fully open). In addition to, it shows two separate internal sets of nozzles (A), and (C) with a spindle that allows the operator to vary primary mass flow. The motive, suction and discharge connections are 1" ASME B16.5 150lb WN flanges and for easy changing of constant area sections. These parts are designed and fabricated to use them in the experimental tests.

Table 2: Specifications of the nozzles.

Nozzle	Throat diameter, dt (mm)	Exit diameter, dpl (mm)	Apl/At
A	2.60	3.22	1.53
C	1.93	2.0	1.55

The two types of nozzles (A) and (C) are designed and manufactured in the testing. Specifications of the nozzles are detailed in Table 2. Three types of constant area sections are listed in Table 3. Six different Variable Area Ratios of Ejectors (A3/At) are tested in this experiment and they range from 10.68 to 30.62. For simplicity, ejector (A A) refers to the ejector includes type of nozzle A and type of constant-area section A.

Table 3: Types of ejector model.

Constant area section		Ejector specification			
Serial no.	Diameter(mm)	A3/At (with nozzle A)		A3/At (with nozzle C)	
A	9.08	10.68	AC	19.39	CC
B	10.68	12.19	AA	22.13	CA
C	8.60	16.87	AB	30.62	CB

2.3. Test procedure

Experimental tests were carried out under range of primary pressure from 1.5 to 6.0 brag and an ambient temperature. Through individually test of ejectors, monitoring was carried out by matching pressure gauge of primary and value from data taker (D80) under small increments in primary pressure (0.5 brag each step). Logging was carried out over data received from (D80) for inlet secondary and outlet discharge (back) pressures under each primary pressure point. In addition to, flow rates for all inlet and outlet were measured manually by flow meter device (Flow meter RMC). In this work, entrainment ratio and area ratio are the main dimensionless parameters were used. These parameters can be expressed by the fowling equations.

Equation 1: Entrainment ratio of ejector.

$$\omega = \frac{\dot{m}_p}{\dot{m}_s}$$

Where:

$\dot{m}_p$= mass flow rate of inlet primary (Kg/s)

$\dot{m}_s$ = mass flow rate of inlet secondary (Kg/s)

Equation 2: Area ratio of ejector.

$$A_r = \frac{A_2}{A_t}$$

Where:

A_2 = constant area section (m^2)

A_t = throat nozzle area (m^2)

3. RESULTS AND DISCUSSION

The main parameters in this test are primary pressure (*Pp*) at the inlet of nozzle, secondary pressure (*Ps*) at inlet of suction chamber and back pressure (*Pb*) at out of diffuser port. The experimental results were used to investigate the effects of main parameters, area ratio and adjustable spindle position on performance of each type of ejector (*ω*).

3.1. Effect of variation of primary pressure

The effect of variation primary pressure for group (C) of ejectors and under adjustable spindle position (-25mm) is shown in Figure 4 and Figure 5. The mass flow rate in inlet primary ($\dot{m}_p$) increases, resulting in reduce of entrainment ratio (ω) since increases in the primary pressure (*Pp*) leads to higher expansion of the primary flow from the primary nozzle. As presented in figure 4 which consists of group (C), ejector (C B) has the larger value of the entrainment ratio (ω) about 0.43 and followed by ejector (C A) and ejector (C C) approximately 0.40 and 0.39, respectively. Furthermore, figure 5 which includes of group (A) shows that the ejectors (A B), (A A) and (AC) based on the same relationship have the same behaviour of group (C). In these figures, the area ratio of six different ejectors is proportional with the entrainment ratio (ω), the reason for this, when area ratio increases, the flow in mixing stream increases as well and results in high entrainment ratio (ω) at choked state in induced flow.

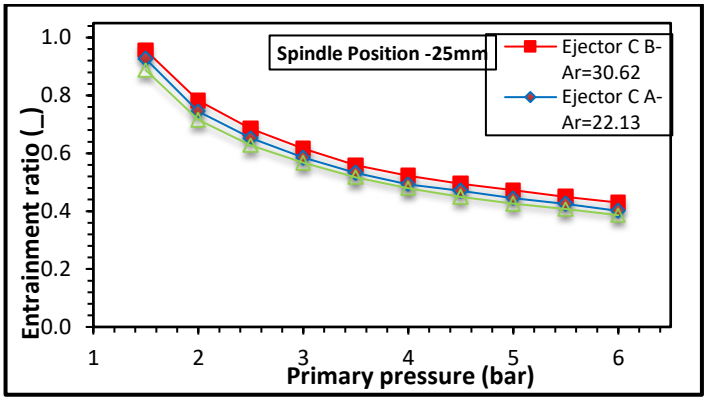

Figure 4: variation of primary pressure for group C of ejector.

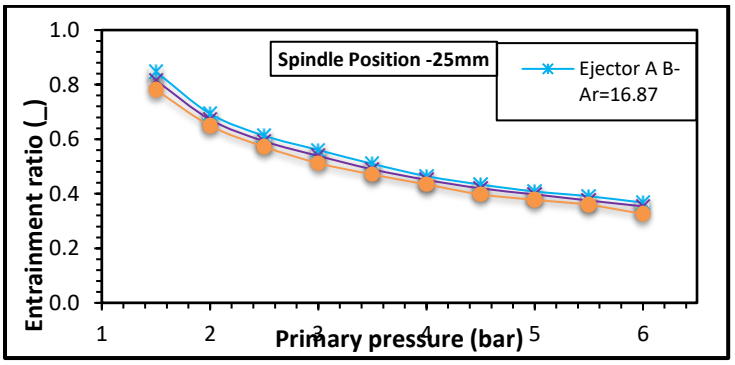

Figure 5: variation of primary pressure for group A of ejector.

3.2. Effect of variation of back pressure

In Figure *6*6 (a and b), the effect of Variation of back pressure (*Pb*) on entrainment ratio (ω) for six different ejectors is shown under range of primary pressure (3-4.5 brag). Figure 6 (a) illustrates Variation of back pressure on entrainment ratio for six different ejectors under primary pressure (Pp) = 3.0 brag. It shows the highest to lowest values of entrainment ratios (ω) are 0.62, 0.59, 0.57, 0.57, 0.55 and 0.52 for ejectors (C B), (C A), (C C), (AB), (AA) and (AC) respectively. It can be shown two groups of ejectors, group (C) with highest values of entrainment ratio (ω) and group (A) with lowest values. In figure 6 (b), a similar behaviour can see for all ejectors under primary pressure (*Pp*) = 4.5 bar, but there is increasing in range of back pressure. In addition to, ejector (C B) has the highest values also (0.50) as compared with the other ejectors under (*Pp*) = 4.5 brag. Moreover, the ejector (AA) displays a largest critical back pressure among all ejectors. This latter ejector can use for high back pressure in various application, but the ejector (CB) can apply in high performance applications.

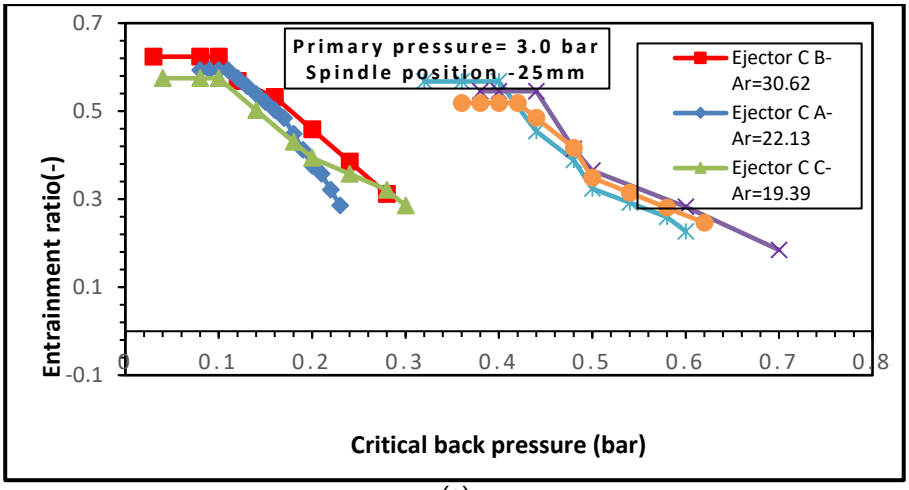

(a)

Figure 6a: Variation of back pressure on entrainment ratio (ω) for six different ejectors -- Pb=3.0 bar

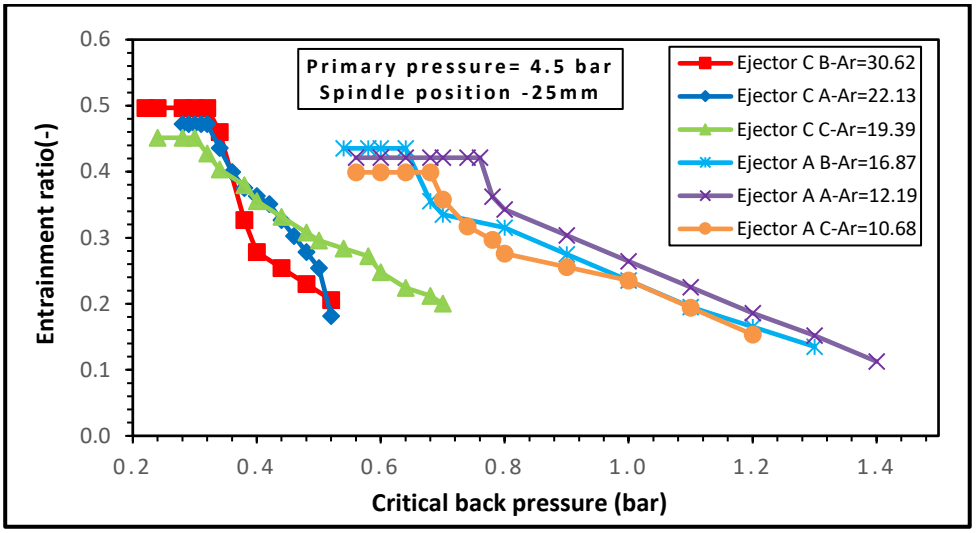

(b)

Figure 6b: Variation of back pressure on entrainment ratio (ω) for six different ejectors -- Pb=4.5 bar.

3.3. Effect of variation of adjustable spindle position

Figure 7 shows the effect of variation of adjustable spindle positions on entrainment ratio (ω) for ejector (A A). The entrainment ratio (ω) lines for ranges of primary pressure (1.5-6.0 brag) were carried out to compare under different spindle positions. The entrainment ratio (ω) increases when spindle increases under the same primary pressure. For example, the (ω) is 0.48, 0.60 and 0.84 as spindle positions are (-5mm), (-15mm) and (-25mm) under 1.5 brag. The reason for that, when the adjustable spindle position moves forward, the cross-section area of primary nozzle decreases and leads to decreases in mass primary flow. Consequently, this results in reduced of the entrainment ratio (ω) when spindle moves forward from (-5mm) to (-25mm). On the other hand, the (ω) decreases nonlinearly when spindle position and primary pressure *(Pp)* increase. It can be seen clearly reduce in (ω) for spindle positions under ranges 1.5-3.0 brag of primary pressure (*Pp*). After that, increasing in (*Pp*) leads to a relatively small reduce in (ω) for spindle positions at (*Pp*) 3.0-6.0 brag, here it is the entrainment ratios (ω) are 0.35,0.21 and 0.14 at maximum primary pressure (6.0 brag) for positions (-25mm), (-15mm) and (-5mm), respectively. While at 4.0 brag, the ratios are 0.21, 0.28 and 0.45 for spindle positions (-5mm), (-15mm) and (-25mm), respectively.

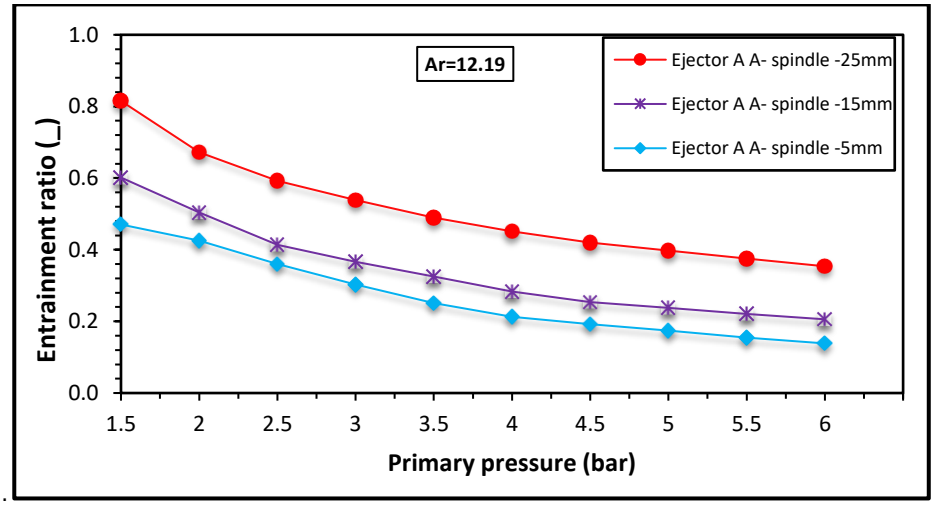

Figure 7: Effect of variation of spindle positions on entrainment ratio (ω) for ejector (AA).

Regard to ejector (CC), it has the same tendency when increases spindle position from (-15mm) to (-25mm) as shown in Figure 8. It shows that the entrainment ratio(ω) under variation in primary pressure (1.5-6.0 brag) is larger than ejector (A A) when use the same spindle position. At primary pressure (*Pp*)= 6.0 brag, the maximal entrainment ratios (ω) obtained from this figure are 0.32, 0.35 and 0.39 for spindle positions (-15mm), (-20mm) and (-25mm), respectively. While at (*Pp*)= 4.0 brag, the ratios are 0.38, 0.42 and 0.46 for spindle positions (-15mm), (-20mm) and (-25mm), respectively.

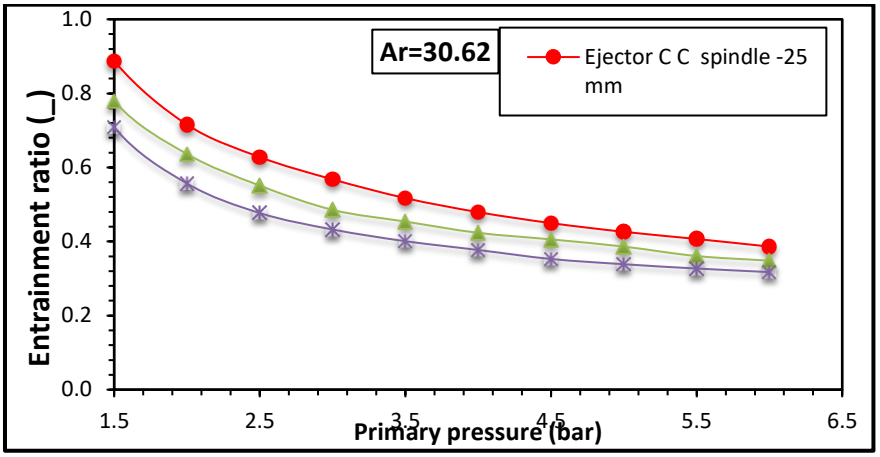

Figure 8: Effect of variation of spindle positions on entrainment ratio (ω) for ejector (CC).

4. CONCLUSION

In the present study, we carried out tests for six different ejectors to estimate the effects of primary pressure, and back pressure on entrainment ratio under variation of area ratio and spindle position. Testing was carried out on two groups of ejectors based on nozzle type, group (A) consists of ejectors (A A), (AB) and (A C) while group (C) consists of ejectors (C B), (C A) and (CC). The effect of primary pressure for each group of ejectors on the (ω) under adjustable spindle position (-25mm) was investigated. Furthermore, the effect of back pressure (*Pb*) on entrainment ratio (ω) for six different ejectors was examined under range of primary pressure (3-4.5 brag). The results show the Ejector (C B) has the highest value of (ω) about 0.43 and the lowest value is 0.33 for ejector (A C) at the maximum primary pressure (*Pp*) (6.0 brag). Ejector (AA) presents the larger value of critical back pressure (Pb^*) approximately (0.76 brag) and entrainment ratio (ω) (0.42) amongst ejectors at primary pressure Pp (4.5 brag).

5. REFERENCES

Eames, I. ., Aphornratana, S., & Haider, H. (1995). A theoretical and experimental study of a small-scale steam jet refrigerator. *International Journal of Refrigeration*, *18*(6), 378–386. https://doi.org/10.1016/0140-7007(95)98160-M

Hemidi, A., Henry, F., Leclaire, S., Seynhaeve, J. M., & Bartosiewicz, Y. (2009a). CFD analysis of a supersonic air ejector. Part I: Experimental validation of single-phase and two-phase operation. *Applied Thermal Engineering*, *29*(8–9), 1523–1531. https://doi.org/10.1016/j.applthermaleng.2008.07.003

Hemidi, A., Henry, F., Leclaire, S., Seynhaeve, J. M., & Bartosiewicz, Y. (2009b). CFD analysis of a supersonic air ejector. Part II: Relation between global operation and local flow features. *Applied Thermal Engineering*, *29*(14–15), 2990–2998. https://doi.org/10.1016/j.applthermaleng.2009.03.019

Huang, B. (1999). A 1-D analysis of ejector performance. *International Journal of Refrigeration*, *22*(5), 354–364. https://doi.org/10.1016/S0140-7007(99)00004-3

Keenan, J., Neumann, E., & Lustwerk, F. (1950). An investigation of ejector design by analysis and experiment. ASME Journal of Applied Mechanics, 72:299–309. *Journal of Applied Mechanics*, *17*, 299.

Lin, C., Cai, W., Li, Y., Yan, J., Hu, Y., & Giridharan, K. (2013). Numerical investigation of geometry parameters for pressure recovery of an adjustable ejector in multi-evaporator refrigeration system. *Applied Thermal Engineering*, *61*(2), 649–656. https://doi.org/10.1016/j.applthermaleng.2013.08.033

Ma, X., Zhang, W., Omer, S. A., & Riffat, S. B. (2010). Experimental investigation of a novel steam ejector refrigerator suitable for solar energy applications. *Applied Thermal Engineering*, *30*(11–12), 1320–1325. https://doi.org/10.1016/j.applthermaleng.2010.02.011

Pridasawas, W., & Lundqvist, P. (2007). A year-round dynamic simulation of a solar-driven ejector refrigeration system with iso-butane as a refrigerant. *International Journal of Refrigeration*, *30*(5), 840–850. https://doi.org/10.1016/j.ijrefrig.2006.11.012

Roman, R., & Hernandez, J. I. (2011). Performance of ejector cooling systems using low ecological impact refrigerants. *International Journal of Refrigeration*, *34*(7), 1707–1716. https://doi.org/10.1016/j.ijrefrig.2011.03.006

Scott, D., Aidoun, Z., Bellache, O., & Ouzzane, M. (2008). CFD Simulations of a Supersonic Ejector for Use in Refrigeration Applications. *Refrigeration And Air Conditioning*, 1–8.

343: Research on moving object detection based on RPCA

Min LIU[1], Zhao ZHANG[2], Sheng HU[3], Juan WANG[4]

[1] Hubei Key Laboratory for High-efficiency Utilization of Solar Energy and Operation Control of Energy Storage System, Hubei University of Technology, Wuhan, 430068, P. R. China, Liu_Min@mail.hbut.edu.cn
[2] Hubei Key Laboratory for High-efficiency Utilization of Solar Energy and Operation Control of Energy Storage System, Hubei University of Technology, Wuhan, 430068, P. R. China, 717126483@qq.com
[3] Hubei Key Laboratory for High-efficiency Utilization of Solar Energy and Operation Control of Energy Storage System, Hubei University of Technology, Wuhan, 430068, P. R. China, shenghu@hust.edu.cn
[4]Hubei Key Laboratory for High-efficiency Utilization of Solar Energy and Operation Control of Energy Storage System, Hubei University of Technology, Wuhan, 430068, P. R. China, happywj@hbut.edu.cn
*corresponding author

As a key technology for assisting driving, the detection of moving targets can warn vehicle drivers of the possibility of collisions with nearby obstacles and provide powerful technical support for avoiding traffic accidents. However, when traditional motion detection algorithms are used in the detection of moving objects in automobiles, it is difficult to ensure real-time performance in complex scenes and high detection accuracy. To solve this problem, this paper proposes a moving object detection algorithm based on RPCA. Firstly, using the maximum similarity between two adjacent frames in the surveillance video, this similarity is expressed as an observation matrix with low rank, and then the low-rank background in the video is recovered from the matrix. Secondly, because there is a lot of redundant information between adjacent frames, the improvement of the construction of RPCA observation matrix reduces the spatial complexity of the observation matrix. Finally, the frame difference method is combined with RPCA to detect the moving target, and the significant area of the moving target is improved. The experimental results show that the algorithm achieves good experimental effect in different scenarios and can accurately extract the moving objects in the video. Compared with the classic three-frame difference method, background subtraction method and traditional method based on RPCA, the detection effects were improved by 54.32%, 36.63% and 2.73%, respectively. Moreover, by reducing the space complexity of the RPCA algorithm, the complexity of the detection algorithm is reduced, thereby reducing the energy consumption of the automobile, reducing the carbon emission, and improving the environmental protection and economy of the automobile.

Keywords: Moving object detection; RPCA; Assisted driving

1. INTRODUCTION

With economic development, vehicle ownership is increasing rapidly, causing increasingly serious traffic problems, such as frequent traffic accidents, traffic jams and the resulting increase in travel time and energy consumption, air and noise pollution. The transportation problem also caused the limited use of the city's limited land resources and energy, the reduced attractiveness of the public transport system, and the decline in operating efficiency, which seriously affected the quality of human life and brought serious consequences to the environment, economy, and society. Moreover, all countries in the world are affected by environmental pollution and shortage of oil, and it is urgently necessary to shift from the traditional model of polluting and energy-saving to the low-emission, low-energy, low-carbon economic model to achieve a harmonious development of the economic environment and society. Recently, new energy is gradually being applied to automobiles, and related technologies for new energy vehicles have also been rapidly developed (Antúnez, 2017). Among them, the detection of moving targets (Jazayeri, 2011; Takemura, 2013), as a key technology of new energy vehicles, is of great significance for assisting safe driving of automobiles.

Traditional methods of motion detection include background subtraction, frame difference and optical flow methods. The moving object detection algorithm applied to automobiles not only requires real-time performance but also requires high accuracy. The background subtraction method has high sensitivity to environmental changes and is greatly affected by the background. The frame-difference method (Qiu-Lin, 2011) is prone to produce voids when extracting the motion area, and cannot extract the target foreground very well. The optical flow method has a large amount of calculation and takes a long time. It does not apply in the case of harsh real-time requirements. Wright et al. (2008) proposed the low rank and decomposition theory of matrices, which decomposes a matrix into a form of a low rank matrix and a sparse matrix sum. This theory is also called RPCA (Robust Principal Component Analysis) (Gao, 2014; Dang, 2015). Due to the large similarity between adjacent frames in the surveillance video, this similarity can be expressed as the low rank of the observation matrix formed by the video frame as a column vector, low rank-based matrix and sparse decomposition of moving target detection. The method is to use this feature to recover the low-rank background in the video from the matrix and extract the motion foreground.

In this paper, a detection method based on the improved RPCA and three-frame difference method is proposed according to the requirements of vehicle motion object detection. In this method, video information is extracted from every frame, frame-by-frame extraction is performed on the video image, low-rank and sparse decomposition of the matrix is performed, and a low-rank background frame is obtained. Then, the background of the current frame extracted by the RPCA is used as the intermediate frame of the three-frame difference method, and is adjacently inter-differentially with the previous frame of the current video frame and the video current frame, so that the three-frame difference method is used in the detection of the moving object. Avoid the effects of background pixels.

This method mainly improves the detection method of moving target in two aspects:

（1）The current video image data has a large amount of data and needs to occupy a large amount of storage and bandwidth resources. At the same time, due to the large amount of data, automotive electronic processing resources and energy consumption increase. However, many vehicles are equipped with embedded platforms. The platform itself has the problems of limited resources such as computing and storage. Moreover, as the video information increases, the number of frames contained therein increases. If you place them in the same matrix at this time, the dimension of the matrix will be too large. When you do the matrix low rank and sparse decomposition, the complexity will increase, so the use of frame extraction will reduce the space complexity of the algorithm and save memory space. At the same time, it can also reduce the requirements for automotive embedded platforms, thereby reducing energy consumption.

（2）By combining the three-frame difference method with RPCA, the background of the video current frame constructed by RPCA is used as the inter frame difference between the intermediate frame of the three-frame difference method and the previous frame and the current video frame of the current video frame. The three-frame difference method avoids the problem of unsatisfactory detection effect caused by the background pixel points in the detection process of moving objects, and eliminates the phenomenon of “holes”.

2. THE OVERVIEW OF RPCA

The RPCA problem is mainly to recover a matrix L that originally had low-rank characteristics from a linearly related matrix D. where $D = L + E$, E is an arbitrary size error matrix or noise matrix，and D is caused by noise contamination of the original matrix L (Cutler 1999). RPCA is an optimisation of classical PCA theory. The following is the principle and problems of PCA:

Is an efficient tool for high-dimensional data processing, analysis, compression, and visualization, PCA (Principal Component Analysis) has a wide range of applications in science and engineering. Assuming that the given high dimensional data depends on the linear subspace of a lower dimensional data, the main purpose of PCA is to be able to estimate this low dimensional subspace effectively and accurately. Assuming that the data matrix is stored in a large matrix

$D \in R^{m \times n}$, the mathematical model is used to estimate the low-rank matrix L in a low-dimensional space, and the difference between L and D is required to be minimal, so there are the following constrained optimisation models:

Equation 1: constrained optimisation models:

$$\min \|E\|_F \quad , \quad s.t \quad rank(L) \le r$$

Where:

$\|\bullet\|_F$ = the Frobenius norm of the matrix and the maximal singular value of $\bullet$

L = Low rank matrix

r = the target dimension of the final desired subspace and $r << \min(m,n)$

In the case where the original noise is contaminated, the PCA can solve the low rank matrix when the noise is small, but when the noise is large, the PCA will be affected even if it affects only a small part of the elements in the matrix. In order to solve this problem, Candes et al. (1999) proposed Robust PCA to solve the problem that some elements of the low-rank matrix are seriously damaged. RPCA assumes that in a matrix D with larger data, a matrix D is given, and $D = L + E$ where L and E are both unknown, where L is a low-rank matrix and E is a sparse matrix. Figure 1 shows the principle of matrix low-sparse sparse decomposition: Matrix D can be seen as a sum of a matrix L and a matrix E .

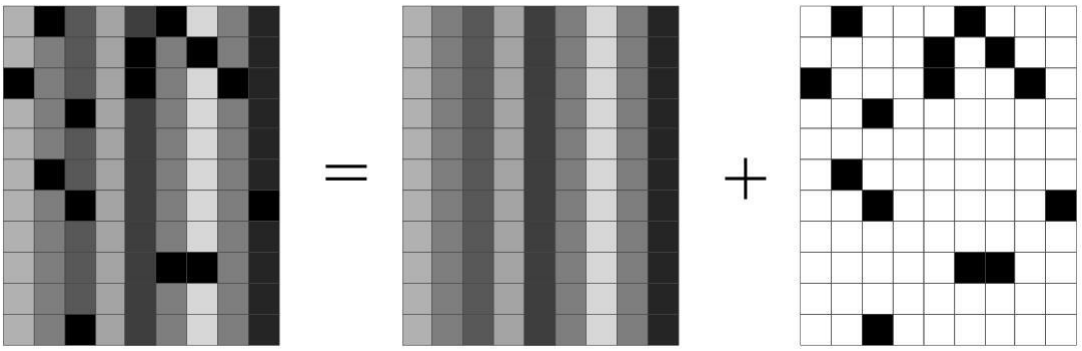

Figure 1: Matrix low-sparse sparse decomposition principle

For this definition, find the matrix with the smallest rank that can generate the matrix, and set the error matrix to be sparse. This problem can be expressed as:

Equation 2: RPCA decomposition:

$$\min_{L,E} rank(L) + \gamma \|E\|_0$$

Where:

γ = To control the ratio of low rank matrix to sparse matrix

L = Low rank matrix

E = Error matrix

Where $D = L + E$, the parameter γ is used to control the ratio of the low rank matrix to the sparse matrix. The above equation is a highly non-convex optimisation problem that can be relaxed and transformed into an easily solved problem. Relaxation of the ℓ^0 norm to the ℓ^1 norm relaxes $rank(L)$ to the nuclear norm $\|L\|_* = \sum_i \sigma_i(A)$, so the above equation is optimised to the following problem.

Equation 3: Relax L to the nuclear norm:

$$\min_{L,E} \|L\|_* + \gamma \|E\|_1$$

Where:

γ = To control the ratio of low rank matrix to sparse matrix

L = Low rank matrix

E = Error matrix

According to the above optimisation problem, even if there are large errors or outliers, the method can still recover the original matrix problem.

3. IMPROVED RPCA AND FRAME DIFFERENCE METHOD

In terms of real-time performance, the frame difference method has absolute advantages, but the algorithm is too simple and results in poor detection results, and it cannot effectively extract the motion area. For the accuracy in the dynamic context, the RPCA-based method can recover the low-rank background from the video image well through matrix low-rank and sparse decomposition, and has good adaptability to the dynamic environment. Therefore, this paper combines the two methods to meet the requirements of the detection of the motion area during the running of a car.

3.1. The principle of improved methods

Traditional moving object detection methods based on matrix low-rank sparse decomposition are directly decomposed for matrix data composed of video sequences. In actual situations, a video segment is composed of at least several hundred frames or thousands of frames. Therefore, the amount of observation matrix data obtained will be very large, and the configuration requirements for the computer will be high, which is not conducive to practical applications. At the same time, considering that the time interval between adjacent frames is extremely short, there is a lot of redundant information in the information between adjacent frames. Therefore, this paper improves the construction of the traditional RPCA observation matrix, and constructs the observation matrix through two-frame interval extraction, as shown in Figure 2.

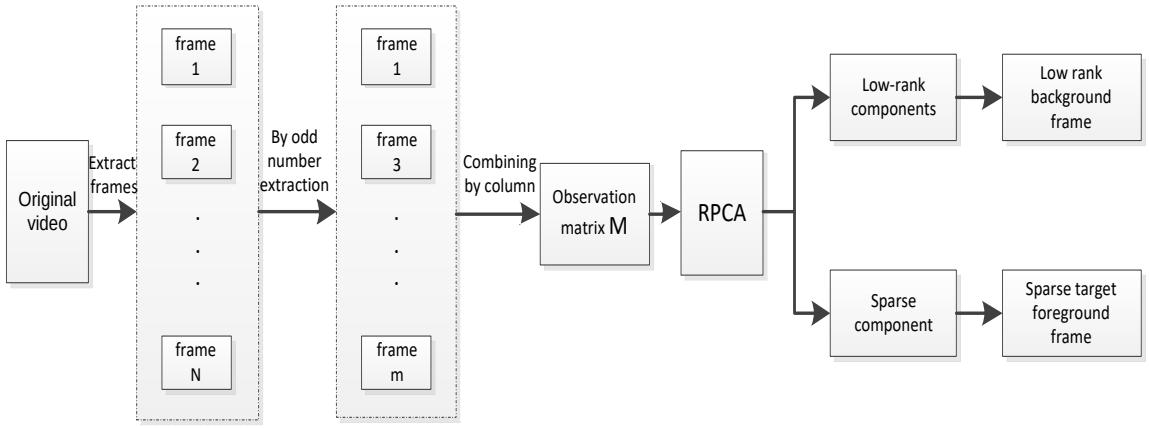

Figure 2: RPCA observation matrix construction method

Suppose there are a total of N frames of images in a video, and select the m frames in equal intervals. Then, each frame of the m frame images is arranged into a matrix M in columns, and the matrix M is subjected to an augmented Lagrangian algorithm to solve the low-rank sparse matrix, and the low-rank component L and the sparse component E of the image are obtained.

Second, the low-rank background of RPCA recovery is superior to the robust performance of the dynamic environment. Therefore, the background of the current frame into which the RPCA is decomposed is used as the intermediate frame of the three-frame difference method, and the difference between the previous frame and the current frame of the video in the current frame of the video is performed. Then the differential image after difference is processed and processed to obtain the binary image of the moving object. Figure 3 is a flowchart of a design method. The K-frame background is obtained by the low rank decomposition of RPCA.

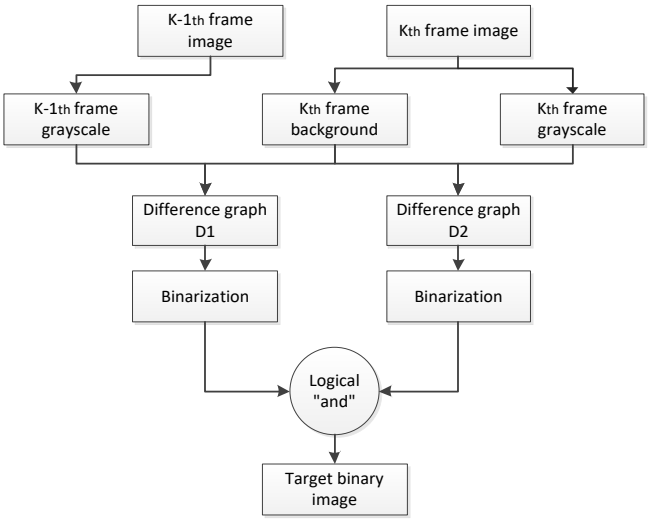

Figure 3: Improved RPCA and three-frame difference flow chart

3.2. Algorithm

The improved algorithm steps are as follows.

---

algorithm 1：

Input：Video frame

Output：Moving target area binary map

For $t=1$ to N

Extract （I_1， $I_3 \ldots I_k \ldots I_m$） frames from odd frames Make up the observation matrix by column M.

Low-rank background map I_k' of video frame I_k is constructed by a low rank sparse decomposition of the matrix based on RPCA, denoted as I_2.

End for

For $t=1$ to N

(1) Grayscale processing of I_{k-1} and I_k frames， and record grayscale images as I_1 and I_3.

(2) Using formula $diff1=\left|I_1(x,y)-I_2(x,y)\right|$ and formula $diff1=\left|I_3(x,y)-I_2(x,y)\right|$ to get difference images I_1' and I_3'.

(3) Binary operation of the difference graph results in I_1'' and I_3''.

(4) Perform a logical AND of the two-valued difference binary graph.

$$f(x,y)=\begin{cases}0, & I_1''(x,y)\cap I_3''(x,y)=0\\ 1, & I_1''(x,y)\cap I_3''(x,y)=1\end{cases}$$

(5) Finally get the binary map of the moving target area

End for

---

4. EXPERIMENTAL

The experimental part was tested using the surveillance video sequences in two dynamic scenes in the Vision standard video library, which were Office videos and People videos. By these two video simulated vehicle during traveling, the detection process to pedestrians.

Figure 4: Test video raw grayscale frames

The algorithm and the other three methods are used for these two video scenes, namely the frame difference method, background subtraction, and the traditional method based on RPCA. The experiment selects the 42nd frame of the Office, and the 37th frame of the People performs the experiment and compares it with the true annotation of the corresponding video frame (GroundTruth).

(a)Ground Truth (b) Frame difference method (c) Background subtraction (d)RPCA (e) The algorithm in this paper

Figure 5: The 42nd frame of the Office

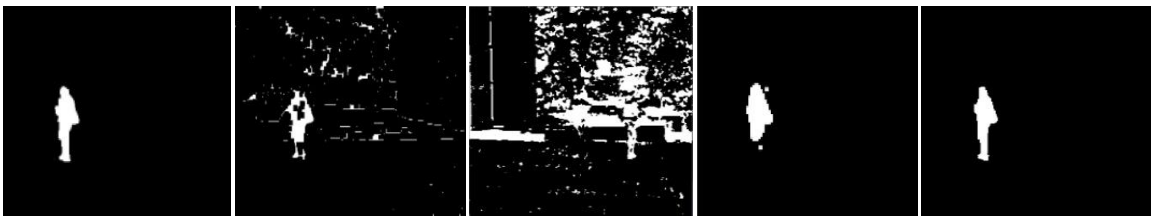

(a) Ground Truth (b) Frame difference method (c) Background subtraction (d) RPCA (e) The algorithm in this paper

Figure 6: The 37th frame of the People

It can be seen from the experimental test results that the frame difference method has a poor detection effect, and a large number of holes appear in the moving object. This is because the dynamic change scene will affect the detection result. The background subtraction method is more sensitive to dynamic scenes, and the background changes cause larger errors. RPCA-based traditional methods tend to extract larger foreground regions, although they eliminate interference from dynamic backgrounds. The algorithm in this paper is more complete than the above methods. The detected motion area is more complete, and there is no dynamic background interference. It meets the requirements of target detection in the car driving process. According to the experimental results, it can be seen that the algorithm of this paper can recover the advantages of low-rank background better in dynamic scenes due to the combination of RPCA method. By combining with the frame difference method and using the low-rank background as an intermediate frame, the effectiveness of the detection in the dynamic scene is better improved, and a more accurate motion area can be detected under the interference of eliminating the dynamic background.

In order to further ensure the reliability of the improved algorithm in the foreground extraction accuracy, this paper introduces the accuracy rate R_A for quantitative analysis. As shown in Equation 4. It reflects the ratio of the pixels of the video image correctly divided into the background and the foreground. The larger the value, the better the effect.

Equation 4: accuracy:

$$R_A = \frac{N_{TP} + N_{TN}}{N_{TP} + N_{FP} + N_{FN} + N_{TN}}$$

Where:

N_{TP} = The number of pixels that are detected in the real foreground

N_{FP} = The real background is falsely checked as the number of pixels in the foreground

N_{FN} = The number of pixels in which the true foreground is falsely detected as the background

N_{TN} = The number of detected real background pixels

Table 2: The value of R_A (%)

Video sequence	Three-frame difference method	Background subtraction	RPCA	The algorithm in this paper
Office	10.67	19.45	83.06	83.07
People	55.55	34.83	75.59	80.56
Avg	33.11	27.14	79.325	81.815

5. CONCLUSION

This article focuses on a series of researches on the motion detection algorithm in the process of driving a new energy vehicle. Firstly, the RPCA low-rank sparse decomposition of moving target detection method is analysed. Secondly, on the basis of these studies, aiming at the characteristics of real-time and accuracy when the vehicle is in the running process, the conventional method is improved. The motion detection is performed by combining the advantages of the RPCA algorithm and the frame difference method. Finally, the improved method is compared with three-frame difference method, background subtraction method and traditional RPCA algorithm. Through experimental comparison and analysis, the improved algorithm not only reduces the complexity of the algorithm, but also reduces energy consumption. In addition, good experimental results can be obtained in different scenes, and the moving objects in the video can be accurately extracted. While satisfying real-time performance, the detection result of the moving target in the driving scene of the automobile is more accurate than the traditional method.

6. REFERENCES

Antúnez, C. S., Franco, J. F., Rider, M. J., & Romero, R. (2017). A new methodology for the optimal charging coordination of electric vehicles considering vehicle-to-grid technology. IEEE Transactions on Sustainable Energy, 7(2), 596-607.

Cao, X., Yang, L., & Guo, X. (2016). Total variation regularized rpca for irregularly moving object detection under dynamic background. IEEE Transactions on Cybernetics, 46(4), 1014-1027.

Cutler, R., & Davis, L. (1999). Real-time periodic motion detection, analysis, and applications. Computer Vision and Pattern Recognition, 1999. IEEE Computer Society Conference on (Vol.2, pp.332 Vol. 2). IEEE.

Dang, C., & Radha, H. (2015). Rpca-kfe: key frame extraction for video using robust principal component analysis. IEEE Transactions on Image Processing A Publication of the IEEE Signal Processing Society, 24(11), 3742.

Gao, Z., Cheong, L. F., & Wang, Y. X. (2014). Block-sparse rpca for salient motion detection. IEEE Transactions on Pattern Analysis & Machine Intelligence, 36(10), 1975-87Gool, L. V. (2012). Pedestrian detection at 100 frames per second. IEEE Conference on Computer Vision and Pattern Recognition (Vol.157, pp.2903-2910). IEEE Computer Society.

Huang, S. C. (2011). An advanced motion detection algorithm with video quality analysis for video surveillance systems. IEEE Transactions on Circuits & Systems for Video Technology, 21(1), 1-14.

Jazayeri, A., & Tuceryan, M. (2011). Vehicle detection and tracking in car video based on motion model. IEEE Transactions on Intelligent Transportation Systems, 12(2), 583-595.

Joshi, K. A., & Thakore, D. G. (2012). A survey on moving object detection and tracking in video surveillance system. International Journal of Soft Computing & Engineering, 2(3).

Kumar, M. S., & Revankar, S. T. (2016). Development scheme and key technology of an electric vehicle: an overview. Renewable & Sustainable Energy Reviews, 70.

Li, H., Zhang, Y., Wang, J., Xu, Y., Li, Y., & Pan, Z. (2015). Inequality-constrained RPCA for shadow removal and foreground detection. Ieice Trans.inf. & Syst, 98(6), 1256-1259.

Mao, X., Xue, Y. L., Li, Z., Huang, K., & Lv, S. W. (2009). Robust facial expression recognition based on rpca and adaboost. IEEE, 62(2), 113-116.

Qiu-Lin, L. I., & Jia-Feng, H. E. (2011). Vehicles detection based on three-frame-difference method and cross-entropy threshold method.Computer Engineering, 37(4), 172-174.

Sermanet, P., Kavukcuoglu, K., Chintala, S., & Lecun, Y. (2013). Pedestrian Detection with Unsupervised Multi-stage Feature Learning.Computer Vision and Pattern Recognition (pp.3626-3633). IEEE.

Takemura, S., Bharioke, A., Lu, Z., Nern, A., Vitaladevuni, S., & Rivlin, P. K., et al. (2013). A visual motion detection circuit suggested by drosophila connectomics. Nature, 500(7461), 175-181.

Wright, J., Yang, A. Y., Ganesh, A., Sastry, S. S., & Ma, Y. (2008). Robust face recognition via sparse representation. IEEE Transactions on Pattern Analysis & Machine Intelligence, 31(2), 210-227.

Yamada, T., Hayamizu, Y., Yamamoto, Y., Yomogida, Y., Izadinajafabadi, A., & Futaba, D. N., et al. (2011). A stretchable carbon nanotube strain sensor for human-motion detection. Nature Nanotechnology, 6(5), 296-301.

Yao, M. H., Jie, L. I., & Wang, X. B. (2013). Solar cells surface defects detection using rpca method. Chinese Journal of Computers, 36(9), 1943-1952.

Zhou, X., Yang, C., & Yu, W. (2013). Moving object detection by detecting contiguous outliers in the low-rank representation. IEEE Transactions on Pattern Analysis & Machine Intelligence, 35(3), 597-610.

344: Future cities: visions of new generation on sustainability concepts and models

Fa LIKITSWAT

Department of Landscape Architecture, Faculty of Architecture and Planning, Thammasat University, Rangsit Center, Pathum Thani 12121, Thailand, Email: flikitsw@ap.tu.ac.th

To create sustainable cities for unpredicted and uncertain futures, this requires and involves broader range of disciplines. The consequences from the past generation are created our living conditions within the cityscape, while the cities have the influences in shaping the next generations' way of lives. One of the key challenges to shape our future cities are not only changing our behaviours but also redesigning and restructuring built environment to be liveable and sustainable urban forms. Based on empirical evidences from Life and Sustainability classes at Thammasat University, this paper critically evaluates sustainability concepts and models of sustainable future cities from the young generations' perspectives. Zero energy, quality of life, green infrastructure, resilience city, and combined approach were five main concepts to further explore and discuss. The method of the study is to analyse and discuss on the students perceptions and learning outcomes on sustainable concepts and models. By using built environment module as an example, the data was collected from 1,735 undergraduate students on fall semester of 2016 and 35 selected group projects were closely re-examined. The result illustrates that most of the students were familiar with two concepts on quality of life and green infrastructure. However, there were not easy to develop the cities' visionaries based on the concept of quality of life. The relationship between new generations' perceptions on sustainability concepts and the conceptualised prototypes or models of future cities from their understandings was debated with socio-economic perspectives. To promote resilience learners with in the uncertainty changing environment, it requires creativity and imagination to support scientific literacies. Finally, this paper concludes on shaping critical minds and strong decision makers of young generations as next decade sustainability drivers visioning on future cities.

Keywords: *Future cities, Sustainability, New generation, Quality of life, Green infrastructure*

1. INTRODUCTION

Sustainable cities for futures must be designed by broader range of disciplines. Sustainability solution must be focussed on consumption habits, lifestyle goals, and value systems thus these strongly involved with ecological paradigm shifted in political thinking, economic activities, and educational systems (Savage, 2006). Most of metropolitan areas around the world are situated in the low lying landscape, which might lead to the risk and vulnerability from unforeseen climate related factors. While some of the metropolitan have been engaged in multiple levels of initiatives promoting and upgrading urban infrastructures and services. The vision on creating better environmental, social and economic conditions and enhancing cities' attractiveness and competitiveness – sustainable cities become a new norm of the urban planning and environmental design challenge. Future cities also required ability to adapt with uncertain future risk and events.

The urgency for educational practice nowadays is how to teach the next generation to be fully responsive, politically, socially, ecologically, and historically, towards sustainable way of living. It would need to cause major shift in attitude. We need to create more open-minded generalists who can see the complexity connections instead of narrowed-minded specialists. Life and sustainability class at Thammasat University is offered the opportunities for multi-disciplinary students to shape and share their ideas on sustainability issues and long term goals. This course emphasises on the dynamic inter-connectedness of nature, consumerism and lifestyle, built-environment and energy consumptions and well as trends of global and Thailand environment situation. It is also review on environmental conflicts and transformation towards sustainable lifestyles. Life and sustainability is divided into three modules; 1) environmental science, 2) built environment, and 3) economic related issues. Within this paper use the content from second module, built environment, as a case study.

To create new frameworks for Life and sustainability, specifically for built environment module, some critical questions and issues frequently were asked and discussed. This aimed to provoke interactivity for the students learning process. How to demonstrate and interpret complexity of sustainability reality and address its critical matter? How to shape the students to have critical minds and get ready to be strong decision makers with visionary perspective? Finally, how to stimulate and elevate sustainability design concept to the students in this chaotic physical world? These questions were discussed and further developed to be the course frameworks. Sustainable built-environment module course objective are: 1) to understand natural dynamics and how it effect the built environment, 2) to realise the natural issues and impact on human lives, and 3) to raise questions and discuss on our way of lives and creation of sustainable future in built environment. To envision the future city, future generation need to sharp their visions, ideas, and values on how the future should be. In order to redesign and restructuring the physical environment, new opportunities on the concepts and models of sustainable cities should be explored.

2. METHODOLOGY

The method of the study is to analyse and discuss on the students perceptions and learning outcomes on sustainable concepts and models. Based on empirical evidences from Life and Sustainability classes at Thammasat University, this paper critically evaluates sustainability concepts and models of sustainable future cities from the young generations' perspectives. The survey aims to pretesting on the personal understanding on sustainability concepts in built environment module. The teaching team designed a series of questionnaires to tackle on basic understanding related to sustainability issues and aspects. This process would allow instructors to be able to understand the basic knowledge of the particular group of students and set ways to guild and develop further discussions and findings.

2.1. Methodology

The main steps of this study included: 1) Identifying four concepts of sustainability – to match with course outline on sustainable built environment. 2) Collecting data from surveys and team projects – to understand both personal perceptions and team decisions on sustainability concepts and models, as well as their visionaries for developing future cities. 3) Analysing the result – to re-examine and redefine the visions on future cities from new generation's perspective and collaboration.

Figure 1 outlines the survey design and methodology underpinning this study. First of all, four key concepts were identified by adjusting to the course outline and embedding various models on sustainable developments. Since it was not simple to define the concepts and models of sustainable future cities, the process on reviewing sustainable development and environmental planning literatures from the international scholars and experts were quite crucial. Secondly, the survey and project assignment on creating future city were launched before the lesson begins. Lastly, this paper discussed on the vision of future generation on sustainable future cities using the result from the survey and sample from the selected projects.

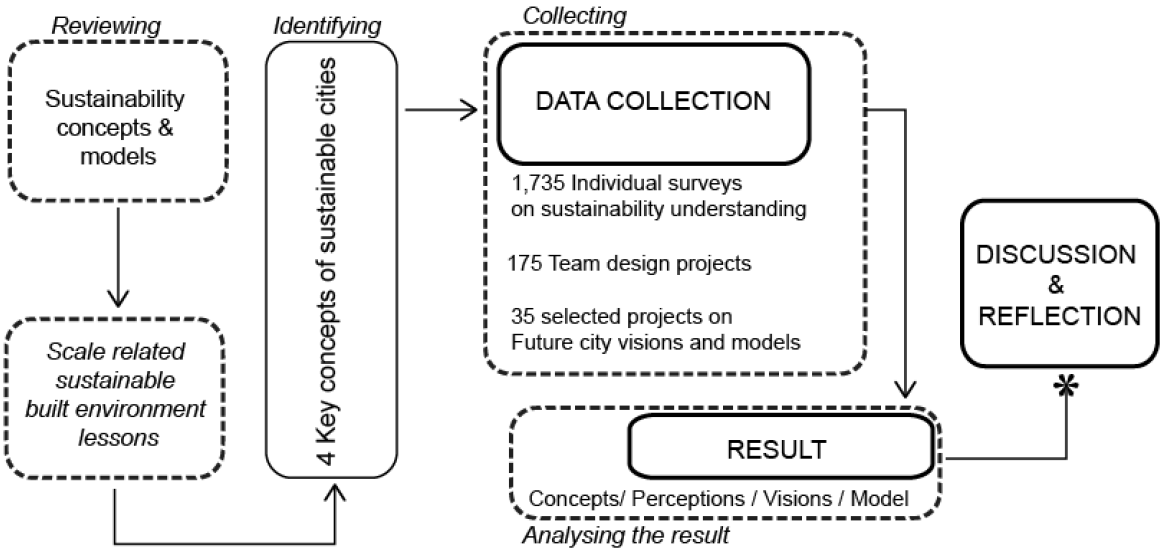

Figure 1: Methodology mapping

2.2. Data collection

By using built environment module as an example, the data was collected from 1,735 undergraduate students on fall semester of 2016 from 10 different faculties. From diverse background and multi-disciplinary including Faculty of Law, Business School, Faculty of Political Science, Faculty Social Administrations, Faculty of Liberal Arts, Faculty Journalism and Mass Communication, Faculty of Science and Technology, Faculty of Dentistry, Faculty of Fine and Applied Arts, and Faculty of Learning Science and Education, the classes were separated to three sections. The data were collected from section 1 of 455 surveys, section 2 of 482 surveys and section 3 of 789 surveys.

Figure 2: Future city design exhibition

Right after the survey was launched, a group of 8 to 10 students were challenged to design and future city based from their group discussion and collaborative processes. The assignment was guided and encouraged students to carefully develop their ideas and reframing shared visions within the team working processes. Within 5 to 6 weeks, each team came up with the visions and city design for their future living. From 175 team projects on visioning future city designs, only 20 percent of their works were pinned down and selected. By picking on qualitative samples focussing on the strong visioning as well

as clear graphic representation works on the future city designs, 35 selected group projects were closely re-examined and exhibited to the public view.

Figure 3: Future city design -- project samples

3. CONCEPTS AND MODEL OF SUSTAINABLE CITIES

Cities are islands of built environment within a global ecosystem of natural landscape (Savage, 2006), secondary organised and composed building, vegetation, road, infrastructure, and agricultural land. How can we create sustainable city in the future? Can the new city portrayed and mimicked the ecosystem services and functions? These questions still remain for discussion and developing the innovation to create the better built environment – better second nature.

3.1. Literature review

Nature of each city is dynamic, with the scale, size, population density, and aged history. The challenges which each city have faced depends on their sizes and levels of developments. Small sized upper income nations are facing with population decline, competing globally, and economic restructuring, while small sized developing nations are facing weak economies, lack of basic public services, and weak urban governances. In the case of large cities, upper income nations are facing aging infrastructure and population, inequality and social cohesion, and increasing competition for global leadership. In contrast, with the large upper income states, large lower income nations are dealing with inadequate infrastructure for transportation, traffic congestion, population housing and urban slums, demographic challenging, socioeconomic inequality, and environmental problems. Future city requires not only a multi-disciplinary approach addressing the urban challenges facing in the emerging cities, but also employs integrated environment technologies, comprehensive urban development, fiscal sustainability, and good governance to ensure and bringing in the quality of life to global citizens. Five dimensions which should be further explored including: promoting economic growth, employing the infrastructure, providing social services, minimizing poverty, and protecting the environment (Riffat, Powell & Aydin, 2016).

With principle of sustainable and ecological design, Jabareen defined distinctive four urban forms including: 1) compact cities, 2) the eco-city, 3) neotraditional development, and 4) urban containment. Each schemes and forms of sustainable cities are quite unique in term of density, diversity, mixed land use, compactness, sustainable transportation, passive solar design, and greening or ecological design. Also, the core concept of sustainable urban form should emphasised on conservation on energy consumption, controlled and reduced waste and pollution, reduced automobile uses, and preservation of open space and sensitive ecosystems as well as liveable and community and cultural environment (Jabareen, 2006).

New sustainable urbanism and emerging cities especially in the urban sprawl areas, the activities and planning should be reprogrammed and redesigned with the new perspectives. The new development trends should be involved with both socio-economic and ecological concerns connecting the new development form with multifunction landscapes toward the sustainable urbanism. The future development should proposed landscape design guideline emphasizing on private sectors' plans and initiatives with in these four characteristics: 1) New urban development form, 2) Storm water management and open space design, 3) Urban and peri-urban agriculture, and 4) Flexible mobility and route options (Likitswat, 2018).

Even cities face different issues and scales of challenges, the concepts to tackle with sustainability challenges were already explored. ‘Sustainable city' is quite broad concept, it gains the most frequent category of academic literature. The other city and model concept related to sustainability such as 'Smart city', 'Digital city', 'Eco city' , ' Green city', 'Low carbon city', 'Knowledge city’, and ‘Resilient city’ were also in the spotlight. While the concept of ‘Intelligent city’, ‘Ubiquitous city’, ‘Liveable city ', and 'Information city ' were relatively new (Jong et.al., 2015).

3.2. Scale related sustainable built environment lessons

Course contents are divided to four topics and lesson related to scale of built-environment: human scale, neighbourhood and community scale, city scale, and landscape scale. First lesson upon human related scale, the content involves sustainable and unsustainable architectures, most of the time questioning about appropriateness and compatibility of vernacular or international design of architectures locally and globally. Also, it provided the principle knowledge of the active versus passive design for the building energy consumption approach which quite important for the real challenges. Secondly, in the neighbourhood and community related scale, the question on identity of the community as well as quality of life was raised. Sense of community, safety and security issues, cultural landscape with in socio-cultural and heritage perspective locally were also the key challenges. Thirdly, in the city related scale, the talk illustrates the ability to cope with the other risks and natural disasters, earth quake for instance. These structures reviewed the conflicts of our unsustainable lifestyles and the choices we have made to expand the built-environments, as well as the possibility to make the cities become more friendly, supporting equality to human the other living organisms and having ability to cope with uncertain crises or disasters. Lastly, in the landscape related scale, the concept of landscape as green infrastructure were adopted and explored. Since most of the cities were building up on the flood plains, most cities are exposed of vulnerability to flooding conditions without realizing that the wet conditions were quite normal and natural. Landscapes as green infrastructures increase the adaptability of the cities to those risks and playing as crucial roles in making the cities become more resilient. Landscape ecology plays as hidden principle for these contents-- how to maintain the natural factors to co-exist in the built environment patches. The paradigms of anthropocentrism versus egocentrism are the main concepts to be challenged showing a different way of thinking and living sustainably (Likitswat, 2016).

3.3. Key concepts of sustainable cities

By categorizing sustainability concept and model literacies and matching with class dynamic and lessons, the author concluded four key concepts of sustainable cities including: ' Zero energy ', ' Quality of life ',' Resilience city ' , and ' Green infrastructure '. Four key concepts of sustainability were synthesised and identified as following along the class dynamic which related to scale in physical human engineered environment different. 1) ' Zero energy ' related to personal or building scale is the main concept for sustainable architecture class. 2) ' Quality of life ' related to neighbourhood and community scale, is the main concept for sustainable neighbourhood and community class. 3) ' Resilience city ' related to city scale ranged from small, medium, large, or mega city, is the main concept for city and climate adaptation class. 4) ' Green infrastructure ' related to landscape scale ranged from rural to urban landscape, is the main concept for sustainable landscape class.

Table 1: Concepts and model of sustainable cities

Scale	Life and sustainability Built-environment lessons	Model of sustainable cities	Key concepts of sustainable cities
Personal Building	Sustainable architecture	Smart city Digital city Low carbon city	' Zero energy '
Neighbourhood Community	Sustainable neighbourhood and community	Intelligent city Liveable city	' Quality of life '
Small city Large city Mega city	Cities and climate adaptation	Resilient city Disaster resilient cities Climate adaptation city	' Resilience city '
Landscape	Sustainable landscape	Eco city Green city Blue green city	' Green infrastructure

Table 1 provides a summary of the four key concepts of sustainable cities related to scale, lesson form the Life and Sustainability class, as well as model of sustainable city in general terms. These four key concepts were further used as a guideline for pretesting questionnaires and developing future city visioning and projects.

4. RESULT

To understand personal perceptions and background knowledge on concepts and models of sustainable future cities, those four key concepts were literally selected from the survey before actual class begins to test out the fresh ideas form the learners' perspectives. They can pick either one or more than one terms which could lead to sustainable concept in future urban and built environment design. This process aims to get the fresh ideas of new generation, avoiding to dominate their perspectives absorbing the lesson learn in the class dynamic. The first survey shown that close to 50 percent of the students confirmed that the concepts of ' quality of life ' and ‘green infrastructure’ were common from their understandings. About 20 percent of students said that ' zero energy ' concepts were quite known. And only 10 percent of them get the idea about the concept of ' resilience city '. The result illustrates that most of the students were familiar with two concepts on ' green infrastructure ' and ' quality of life '. While the concept of ' zero energy ' and ' resilience city ' were quite far away from the majority perception of sustainability concepts and models. The level of terms' understanding of sustainability concepts from all three sections were also on the similar direction.

Table 2: Perception on sustainability concepts

Classes and surveys / Concepts	Section 1 455 surveys	Section 2 482 surveys	Section 3 789 surveys	Total 1735 surveys	Total Percentage
' Zero energy '	144	117	145	376	21.70%
' Quality of life '	210	200	359	769	44.30%
' Resilience city '	58	51	87	187	10.80%
' Green infrastructure	186	227	375	788	45.40%

Table 2 illustrates new generation's perceptions surveying from the group of student at Thammasat University on sustainability concepts.

Next, group project assignment on designing future city was assigned. Four concepts of sustainable cities were used as the example of sustainability concepts including zero energy, quality of life, green infrastructure, and resilience city. Students were challenged to create group discussion, work across their disciplines, and design the future cities. The design should come from team decisions on sustainability visionaries, as well as for developing models of future cities.

The finding from 35 samples of sustainable future city design projects connected to the students' perceptions from the first survey. Most of the teams used and amplified the concepts of green infrastructure and further developed as their visions for the future city design schemes. However, there were not easy to develop the cities' visionaries based on the concept of quality of life as their main ideas. The concept of quality of life were embedded and used as sub concept on their city design models whether within green infrastructure, combined approach, zero energy, or resilience city.

Table 3 demonstrates the relationship between five concepts and approaches behind the visionaries and development models. Five concepts of sustainable cities were explored including zero energy, quality of life, green infrastructure, resilience city, and combined approach. The visionaries from the new generations' future city designs were quite complex not only purposing the idea of physical designs but also some of the schemes were highlighted on social interactions and new stand on quality of life. These are examples of the visionaries and new city models: Forest city, Green city, Happiness city, Creative city, and liveable city. The shared visions could shape and generate the discussion among the students to collaborate and work on future cities and scenario designs together.

Table 3: Visions on future cities from 35 selected projects

Concept of future city	Number of projects (percent)	Visions / Models (samples)	Keywords / Explanations
Green infrastructure	12 (34%)	Forest city Green city	Green economy, Quality of life, Ecosystems services, Blue green network, Green building, Green design, Ecological planning • A strategically planned network of natural and semi natural areas with other environmental features designed and managed to deliver a wide range of ecosystems service. • This blue and green networks can improve environmental conditions and quality of life. • It also supports a green economy and creates job opportunities
Combined approach	10 (28%)	Green + Energy city Zero Energy + Transportation	Alternative energy resources, Environmental friendly, Incorporate natural systems • The city design based on combined concepts of sustainability. • The design focussed on technological innovations and infrastructures.
Zero energy	8 (23%)	Zero energy city Electric city	Net zero building, Zero automobile, Clean energy, Alternative public transformation • This scheme promotes net zero building, and passive energy conservation design. • It also highlights on clean energy resources and public transportation services.
Quality of life	3 (8%)	Happiness city Creative city Liveable city	Creativity, Public services, Lifelong learning, Alternative transportation systems, Pedestrian friendly, Social welfare • Built environment which can promote work life balance, happiness, and better lifestyles. • The design focussed on creativity, connectivity, and social interactions and engagements.
Resilience city	2 (5%)	Resilience city	Adaptation, resilience citizens, adaptive infrastructure • The city with ability to adapt and cope with several natural disasters such as flooding and earthquake. • Smart and adaptive infrastructure which can recovered after shocks or stresses.

5. DISCUSSION AND REFLECTION

There should be several ways to tackle and design for sustainable future cities even the term sustainability itself still broad and generic. This paper attempted to redefine the concept of sustainability which related to the sense of scale in built environment, ranged from human to landscape scales. Four concepts including: zero energy, quality of life, resilience city, and green infrastructure were used as the key concepts to challenge the students working in team, discussing and developing their shared visionaries. The term 'green infrastructure' was in the top rank to perceive as concepts of sustainability and used to develop the future city designs. The term 'quality of life' also gain the most popularity vote at the beginning, while only a few groups had borrowed this concept to create the main visions in their city design schemes. The concept of ' quality of life ' was used as a sub concept, instead of the main one. 'Combined approach' were also proposed to compromise at least two main concepts, mostly binding 'green infrastructure' and 'zero energy', before stating out the visionaries for the city designs. However, the concepts 'resilience city' were not often recognised and selected as the sustainability with this group of students.

The terms 'green infrastructure' and 'quality of life' are wildly understood, thus these can be used as the common languages to building up the discussions on sustainable future city development. Since these two concepts still be debatable and open up some rooms to further discussed, this study suggested that they should be used as main focuses and core principles in future built environment design. The questioning on living standard for the future generation still remains from generation to generation. The other key concepts which are missing in this study including, cultural heritage, local context, sense of place and fair governance should also be explore in the future study. The relationship between new generations' perceptions on sustainability concepts and the conceptualised prototypes or models of future from their understandings should be also debated with socio-economic perspectives. To promote resilience learners (Sterling, 2010) with in the uncertainty changing environment, it requires creativity, imagination, and discussion to support scientific literacies. Shaping critical minds and strong decision makers of young generations to envision on future cities and learn to adapt with future scenarios are crucial for promoting next decade sustainability drivers.

6. REFERENCES

Baxter, W, Grossman, N, Wegner, N, 2016. A Call to Action Thailand and the Sustainable Development Goals. 1. Singapore: Editions Didier Millet.

Grunewald, K, Bastian, O, 2017, Special Issue: “Maintaining Ecosystem Services to Support Urban Needs”, Sustainability. 9, 1647.

Jabareen, Y, 2006. Sustainable Urban Forms Their Typologies, Models, and Concepts, Journal of Planning Education and Research, 26, 38-52.

Jickling, B, Wals, A, 2008. Globalization and environmental education: looking beyond sustainable development. Journal of Curriculum Studies. 40 (1), 1-21.

Jong, M, Joss, S, Schraven, D, Zhan, C, Weijnen, M, 2015. Sustainable–smart– resilient–low carbon–eco–knowledge cities; making sense of a multitude of concepts promoting sustainable urbanization. Journal of Cleaner Production, 109, 25-38.

Lehmann, S, 2016, Sustainable urbanism: towards a framework for quality and optimal density?. Future cities and environment, 2,8.

Likitswat, F, 2016. Incorporating Sustainability for General Education at Thammasat University : XL class challenges on built environment module. 2016 Education for Sustainability Asia Conference. National Institute of Education, Nanyang Technological University.

Likitswat, F, 2018. Landscape Transformations Towards Sustainable Urbanism: The Case of Rangsit, Bangkok PeriUrban. Built Environment Research Associates Conference 9, Faculty of Architecture and Planning, Thammasat University.

Riffat, S, Powell, R, Aydin, D, Future cities and environmental sustainability. Future cities and environment. 2:1.

Salem, D, 2016. Visions for Urban Landscape Sustainability, Past, Present and Future. European Journal of Sustainable Development, 5 (3), 419-432.

Savage, V, 2006. Ecology matter: sustainable development in Southeast Asia. Sustain Sci, 1, 37-63.

Sterling, S. 2010, Learning for resilience, or the resilient learner? Toward a necessary reconciliation in a paradigm of sustainable education. Environmental Education Research. 16, 511-528.

345: An experimental study on thermomagnetic heat engine driven by gadolinium rotor

Yeongmin KIM[1], Jongin KIM[2], Sungho MOON[3], Young Soo LEE[4], Sang Hoon LIM[5]
Wongee CHUN[6]

[1] Department of Nuclear and Energy Engineering, Jeju National University, Jeju 63243, Republic of Korea, km820426@jejunu.ac.kr
[2] Department of Nuclear and Energy Engineering, Jeju National University, Jeju 63243, Republic of Korea, whddls5228@naver.com
[3] Department of Nuclear and Energy Engineering, Jeju National University, Jeju 63243, Republic of Korea, msh0616@naver.com
[4] Thermal Energy Conversion Laboratory, Korea Institute of Energy Research, Daejeon 34129, Republic of Korea, yslee@kier.re.kr
[5] Department of Nuclear and Energy Engineering, Jeju National University, Jeju 63243, Republic of Korea, shlim@jejunu.ac.kr
[6] Department of Nuclear and Energy Engineering, Jeju National University, Jeju 63243, Republic of Korea, wgchun@jejunu.ac.kr

A novel design of gadolinium based thermomagnetic generator to scavenge low grade thermal energy into electrical energy is presented. Gadolinium(Gd) is one of the distinct material whose Curie temperature is nearly room temperature and this makes a Gd based thermo-magnetic engine a good candidate to harness available waste heat from power plants, HVAC systems and etc. This paper introduces the development of such an engine, where its design and construction is experimentally explored. A series of tests were carried out by changing the temperature of water streams so the difference between them varies from 20℃ to 45℃. A maximum power of was 29.4mW was measured when the temperature difference between the hot and cold streams of water was maintained at 45℃, which complies with the thermodynamics principle.

Keywords: Gadolinium, Heat engine, Mechanical energy, Thermal energy, Thermodynamics principle

1. INTRODUCTION

The path to the sustainable energy is a long one. Using low temperature difference engines to generate electricity from low-grade waste heat can make some good contribution to realise this dream. In our everyday life, from fans to washing machines and other kind of household and commercial appliances, we can easily see the possibility of drawing useful work if suitable means are applied. In recent years, it has become an attractive option for energy harvesting due to the advancement in materials engineering and nano technology. Especially, harvesting energy from low temperature differential (LTD) heat sources has attracted many researchers and a variety of systems were developed in this regard.

Shaislamov and et al. developed a Tribo-Electric Nano-Generator (TENG) that can generate electricity from a freely rotating disk driven by a LTD heat engine. They were able to produce an effective open circuit voltage of 105 V and a short circuit current of about 1.2 μA, which was capable of charging a commercial 4.7μF capacitor and lighting a commercial green LED. However, an important issue related to the published TENG need to be addressed, and that is about very low short circuit current of the existing TENG in harnessing low grade thermal energy. It might be useful to apply different kinds of electric generators in converting thermal energy into mechanical energy and eventually into electrical energy as one scheme is short of delivering the maximum output. Also, development of a mechanical unit (rotor or turbine), that readily converts thermal energy into mechanical energy with as little loss as possible, is crucial to fully exploit the low-grade heat sources.

Here we present a simple basic design, where heat energy from LTD heat sources can readily converted into mechanical power and eventually electrical energy. The major focus is made on the working principle of a heat engine, which is driven by harnessing the magneto-caloric effect of a material called, “Gadolinium (Gd).” Gd is a typical material (chemical element), which demonstrates a magneto-caloric effect such that the intensity of magnetism varies with temperature. Gadolinium exhibits the property of ferromagnetism at 20°C or lower and paramagnetic properties at temperatures of 20°C or higher. Taking advantage of this peculiar feature, the basic component of an electro-magnetic generator (Gd rotor) is designed and experimentally tested for its performance of converting heat energy to mechanical power.

2. DESIGN AND CONSTRUCTION OF GD ROTOR

As aforementioned, a simple rotor has been designed and built based on the concept of applying the magneto-caloric effect of Gd, Gd rotor. The Gd rotor is cylindrical shaped which mainly consists of sixteen Gd blocks and a bar magnet (neodymium bar magnet). The distance between the neodymium magnets and the rotating shaft was set to be less than 1 mm. Each Gd block has the shape of a cube with dimensions of 1 cm × 1 cm × 1 cm in size processed from Gd of 99.9% purity. On one side of the rotor, a neodymium bar magnet of 10 cm × 2.5 cm × 1 cm was placed such that the distance between the bar magnet and Gd blocks was maintained within 1mm. Two streams of hot water and a stream of cold water arranged at an interval of 120° were constantly flown over Gd blocks changing their magnetic property between ferromagnetic and paramagnetic. This change in the magnetic property of Gd blocks interacting with the bar magnet resulted in rotational motion of the rotor and eventually the conversion of thermal energy into mechanical energy (power generation). Maximum torque generation depends on how fast the magnetic property of Gd blocks is changing between ferromagnetic and paramagnetic.

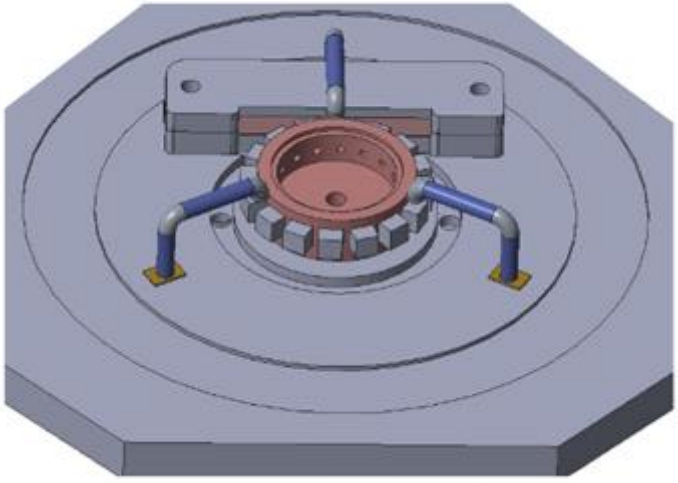

Figure 1: Schematic design of a Gd rotor

Figure 2 shows the refined a Gd block used in this work, where Figure 3 shows the Gd rotor actually constructed in our laboratory.

Figure 2: A Gd block

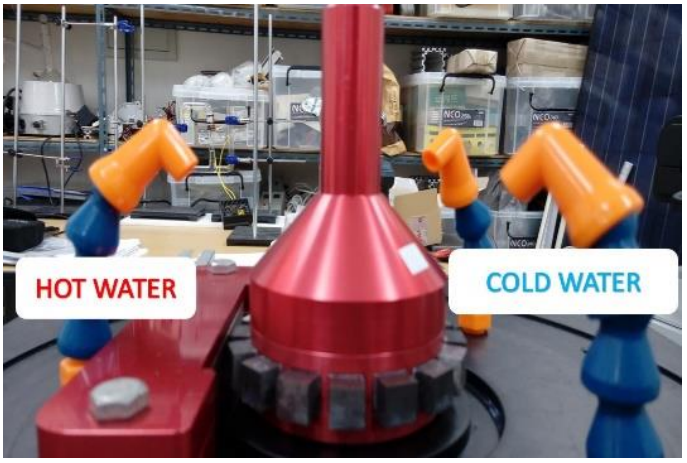

Figure 3: Gd rotor ("heart" of the thermo-magnetic generator)

3. EXPERIMENTAL RUN AND PERFORMANCE MEASUREMENTS

As shown in Figure 1, three water jets at 1200 apart are used where one hot water and two cold water jets provide heat energy and withdraw heat energy from the Gd rotor as it turns. That is, the rotor perfectly realises the classical thermodynamic principle of Kelvin-Planck statement as it converts heat energy to mechanical power. The RPM of Gd rotor was monitored and its output was calculated using the basic work formula of force x distance. Temperature differences of the applied water jets were 20℃, 30℃, 40℃ and 45℃ for the operation of the Gd rotor. As for the cold water jet, the water from mains is used which remained close to 20℃. A flow rate of 300 ml /min was maintained for the water jets as it flows through a 3.8 mm diameter tube. Weights were attached to the rotating shaft of the Gd rotor to determine its mechanical output as the temperature of the hot water jet and the mass changes during the operation. The weights used were 5g, 10g, 20g, and 50g.

4. RESULTS AND DISCUSSION

Table 1 and Figure 4 present the variation in the rotational speed (in RPM) of the Gd rotor as it is driven by the water jets impinging on Gd blocks with changes in load(weight) and temperature differential of the jets applied. As shown, the RPM output increases as the temperature difference between jets becomes larger from 25 to 45 degrees. Equation 1 gives the relation between and RPM and the linear speed of the Gd rotor as it spins. The highest RPM of 111.9 was recorded at the temperature differential of 45 degrees and when the applied load was 50g. Meanwhile, the lowest RPM of 74.4 was measured at 25 degrees and 50g, respectively. In general, the larger the temperature difference between jets, the larger the observed RPM was. It also can be seen that different RPMs can be developed depending on the load even when operated under the same temperature difference between jets.

Equation 1: Relation between and RPM and the linear speed of the Gd rotor as it spins

$$rpm = \frac{V \times 60}{2\pi r}$$

Where:

- V = linear speed of rotor (m/s)
- r = radius of rotor (m)

Table 1: RPM measured for variations in temperature difference between jets and applied weight (load)

	Mass of weights[g]	RPM
ΔT=25°C	20	99.1
	50	74.4
ΔT=35°C	20	108.9
	50	100.1
ΔT=45°C	20	114.5
	50	111.9

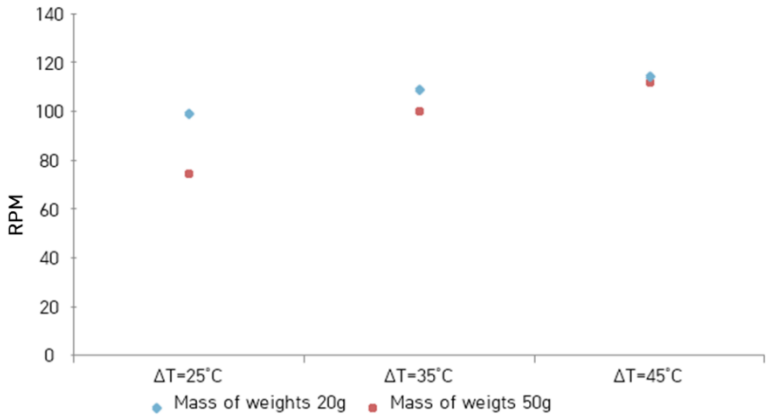

Figure 4: Graphical representation of changes in RPMs in response to variations in temperature difference between jets and applied weight (load).

Table 2 and Figure 5 show the performance of the Gd rotor in terms of mechanical power output under the same operational conditions described above. Equation 2 gives the simple relation that exists between the mechanical power and the measured values of linear speed and load. Similar to RPMs, as witnessed above, the output increases as the temperature difference between the water jets grows larger. The highest output of 57.42 mW was observed at the temperature difference 45°C with applied load of 50 g. In contrast, the lowest output of 20.34mW was recorded for the temperature difference of 25 °C and load of 20g. In general, the mechanical power output was proportional to the temperature difference and the applied weight (load).

Equation 2: Simple relation that exists between the mechanical power and the measured values of linear speed and load $PW = F \times V = mg \times V$

Where:

- m = mass of weights (kg)
- g = Gravitational acceleration (m/s²)
- V = linear speed of rotor (m/s)

Table 2: The effect of applied weight and temperature difference between water jets on mechanical output of Gd rotor

	Mass of weights [g]	Mechanical output [mW]
ΔT=25°C	20	20.34
	50	38.18
ΔT=35°C	20	22.35
	50	51.36
ΔT=45°C	20	23.5
	50	57.42

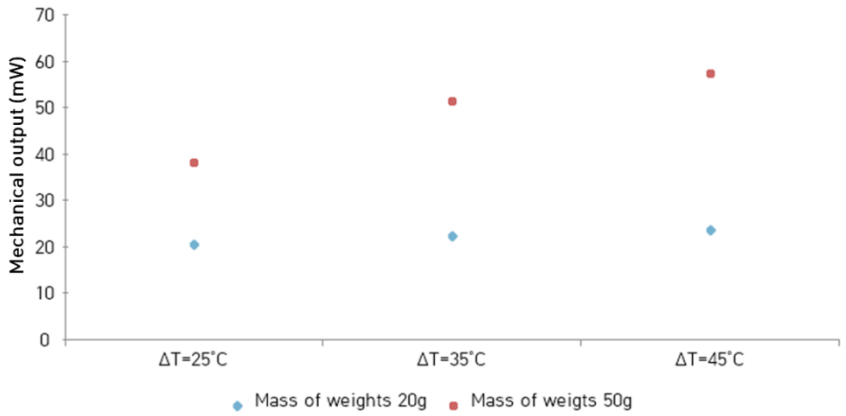

Figure 5: Graphical representation of the effect caused by changes in applied weight and temperature difference between water jets on mechanical output of Gd rotor

5. CONCLUSION

This work explores the performance of a heat engine capable of converting low-grade thermal energy into mechanical power by taking advantage of the magneto-caloric effect of gadolinium (Gd). A simple but effective rotor (Gd rotor) was designed and constructed to examine the effects of what deems major variables in the operation of the rotor. Experimental results indicate that more power could be developed if larger temperature differences were present between the jets applied to drive the Gd rotor (agreeing well with the fundamental principle of thermodynamics). It is, however, interesting to note that the mechanical power output was not just proportional to the temperature difference between jets but also increased with the applied weight (load).

6. ACKNOWLEDGEMENTS

This work was supported by the National Research Foundation of Korea (NRF) and the Korea Institute of Energy Technology Evaluation and Planning (Grant No. 2017R1A2A1A05001461, 2018R1A2B2008542 and 20172010000850).

7. REFERENCES

Chun W. G. et al., 2012. Acoustic waves generated by a TA (ThermoAcoustic) laser pair. *Energy,* 45(1), 541-545.

Jack C., 2012. The Elements: The New Guide to the Building Blocks of Our Universe.

Park J. W., 2012. Chemical element in cast.

Shaislamov U. et al., 2017. Hybrid operation of triboelectric nanogenerator for electricity generation by a low-temperature differential heat engine. *International Journal of Energy Research,* DOI: 10.1002/er/3709.

Wang Z. L., 2013. Triboelectric Nanogenerators as New Energy Technology for Self-Powered Systems and as Active Mechanical and Chemical Sensors. *ACS Nano,* 7(11), 9533–9557.

Wang Z. L., 2014. Triboelectric Nanogenerators as New Energy Technology and Self-Powered Sensors-Principles. Problems and Perspectives. *Faraday Discussions,* 176, 447-458.

348: A voltammetric study on the atomic layer deposition of selenium and antimony on platinum electrode

Yuan CHEN[1,2,3], Huicheng HUANG[1,2,3], Zhishun WEI[1,2,3], Ying CHANG[1,2,3], Annie PRADEL[4], Pascal BOULET[5], Marie-Christine RECORD[6, *]

[1] *Hubei Provincial Key Laboratory of Green Materials for Light Industry, Hubei University of Technology, Wuhan, Hubei 430068, China*
[2] *Collaborative Innovation Center of Green Light-weight Materials and Processing, Hubei University of Technology, Wuhan, Hubei 430068, China*
[3] *School of Materials and Chemical Engineering, Hubei University of Technology, Wuhan, Hubei 430068, China*
[4] *CNRS, ICGM UMR 5253, ChV, CC1503, Université de Montpellier, F-34095, France*
[5] *Aix-Marseille Univ, CNRS, MADIREL, Marseille, France*
[6] *Aix-Marseille Univ, Université de Toulon, CNRS, IM2NP, Marseille, France, m-c.record@univ-amu.fr*

The present paper is a detailed study on the atomic layer deposition of selenium and antimony on platinum electrode by electrochemical atomic layer epitaxy (EC-ALE). Voltammetry and coulometry experiments were performed in this work to investigate the electrochemical behaviours of selenium and antimony on the polycrystalline platinum electrode. The results show that on Pt substrates Se ions can directly form a UPD layer with full coverage without the formation of bulk Se. The total Faradaic charge of the UPD Se is calculated to be 924 μC cm^{-2}. A SbO^+ species adsorbed Pt electrode is obtained by introducing the fresh Sb solution continuously into the electrochemical cell. The irreversibly adsorbed SbO^+ species begin to desorb when the potential is more positive than 0.50 V (vs Ag/AgCl). The reduction potential of irreversibly adsorbed SbO^+ to metallic Sb atoms amounts to 0.11 V (vs Ag/AgCl). After the irreversibly adsorbed SbO^+ species are reduced to metallic Sb, Sb atoms can be further deposited onto this Sb-modified Pt electrode in the way of UPD to increase the coverage of the metallic Sb monolayer. The UPD potential of antimony on the Sb-modified Pt electrode amounts to −0.07 V (vs Ag/AgCl). Finally, a Sb monolayer with the depositing charge 981 μC cm^{-2} is obtained. Now the alternative deposition of Sb-Se compound by EC-ALE method is under study.

Keywords: Sb_2Se_3; Electrochemistry deposition; EC-ALE; Atomic layer; Absorption

1. INTRODUCTION

Sb_2Se_3, a member of V-VI group semiconductors, is the unique intermediate compound in the Sb-Se equilibrium phase diagram (Ghosh, 1993: page 753). Sb_2Se_3 is a semiconductor with a layered crystal structure (space group Pnma; n°62) in which each Sb atom and each Se atom is bound to three atoms of the opposite kind that are held together by weak secondary bonds (Madelung, 1992: page 446). Not only does Sb_2Se_3 itself be a fine thermoelectric material at room temperature (with Seebeck coefficients of 46.2 and 18.3 µV/K for the polycrystalline and amorphous Sb_2Se_3 thin films (Rajpure, 1999: page 1079)), but it is also an important component of the solid solutions $(Bi, Sb)_2(Te, Se)_3$, which are regarded as the best and, in fact, the only materials used for cooling (Xiao, 2006: page 25). In addition, it also has promising applications in several other fields such as optoelectronic, photovoltaic and batteries. Consequently, both elaboration and characterisation of this compound have been largely studied (see for example Ref. (Fernández, 2000: page 202; Rajpure, 1999: page 1079; Xue, 2008: page 351; Yu, 2010: page 1258; Wang, 2013: page 1)).

Miniaturization of the devices requires the use of thin films which are usually prepared by physical vapor deposition methods. In our previous work (Chen, 2015: page 2399), a thin film of Sb_2Se_3 compound was obtained successfully on polycrystalline gold electrode via the route of Electrochemical Atomic Layer Epitaxy (EC-ALE) technique, which was put forward by J. Stickney (Gregory, 1991: page 543) and was proved to be a valid approach to control these parameters for the deposition of chalcogenide compounds on metallic substrates (Lister, 1996: page 153; Zhu, 2005: page 5465; Foresti, 2005: page 6900; Chen, 2015: page 2399). This method is based on the alternate underpotential deposition (UPD) of atomic layers of the elements that form the compound, in a cycle that can be repeated as many times as desired. The major advantage of this method is that the individual steps of each cycle can be investigated and optimised independently.

It is generally known that the substrate plays an important role in the process of electrodeposition. Therefore, how the substrates of different materials affect the processes of underpotential deposition is very important and significative. Platinum has always been of particular interest owing to its electrocatalytic properties and is also widely used as a substrate material in the studies of electrodeposition. However, in the field of EC-ALE, only a few studies utilised Pt as the substrates, which respectively reported the EC-ALE of Sb_2Te_3 (Yang, 2006: page 4599), Bi_2Te_3 (ZHU, 2005: page 4041) and Bi_2Se_3 (Xiao, 2009: page 6821) on Pt electrodes. As we know so far, there is no result reported in the literature concerning the electrodeposition of Sb_2Se_3 thin film on Pt electrode by EC-ALE method.

This paper, as a preliminary study, is devoted to investigating the atomic layer deposition of selenium and antimony on the polycrystalline platinum electrode and to provide the electrodeposition parameters for the subsequent alternate EC-ALE process. The irreversible adsorption and reversible underpotential deposition (UPD) behaviours of Sb on Pt electrode are studied in detail because they have not been fully understood so far according to the literature so far and they affect the obtaining of the high-coverage Sb atomic layer. In this work, the electrochemical behaviours of Sb and Se on the polycrystalline Pt electrode are studied by means of cyclic voltammetry and coulometry. Thanks to the flexibility of the EC-ALE equipment, the work led to a better understanding of the electrochemical behaviour of Sb on Pt electrode. A method to obtain a metallic Sb monolayer with higher coverage on Pt electrode was determined. Now the alternative deposition of Sb-Se compound by EC-ALE method is under study.

2. EXPERIMENTAL

2.1. Solutions and chemicals

Solutions are prepared using ACS reagent grade or higher-grade chemicals (Sigma-Aldrich, Inc., USA) and deionised water (Milli-Q 18.2 MΩ·cm, Merck KGaA, Darmstadt, Germany). Three different solutions are used in this study. The antimony solutions contain 0.05 mM Sb_2O_3 (99.999%) as reactant and 0.2 M Na_2SO_4 as supporting electrolyte. The pH of these solutions is 1.0. The selenium solutions consist of SeO_2 (99.999%) and Na_2SO_4, at pH 1.0, with concentration of 0.5 mM and 0.2 M, respectively. Supporting electrolyte solutions, with same pH and ionic strength as the ones of deposition solutions, are used as blank solutions to rinse the cell. The pH values of the solutions are adjusted with H_2SO_4. Just before the beginning of each series of measurements, all the solutions are freshly prepared and then degassed for 30 min with high purity Ar gas (Ar Bip, O_2 < 10 ppb, Air Products and Chemicals, Inc., France), which is bubbled into the solution. All experiments are performed at room temperature with solution maintained under Ar atmosphere.

2.2. Substrates

Platinum substrates are used as working electrodes. They consist of quartz slides, coated with 200 nm thick platinum films (99.9% pure) by electron beam physical vapor deposition. Under the Pt film, a thin layer of Cr (25 nm) is deposited to improve adhesion of platinum onto quartz. The platinum substrates are pretreated as follows: they are firstly annealed at 375 °C for 18 h at 10^{-6} Torr in sealed glass tubes and then soaked in hot nitric acid for 5 min. Before each experiment, cyclic voltammetry (CV) scanning (repeated 25 times) of the Pt substrate in 0.1 M H_2SO_4 solution is performed with potential scan from −0.27 to 1.20 V to clean and check the substrate. The CV curve of the Pt electrode in 0.1 M H_2SO_4 is shown in Figure 1.

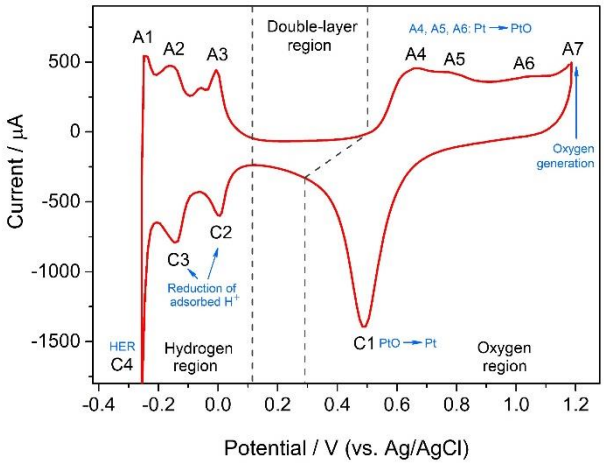

Figure 1: Cyclic voltammogram of the Pt electrode in 0.1 M H_2SO_4. The scanning rate is 100 mV/s.

In Figure 1, three potential regions may be defined from the CV of Pt, i.e. the oxygen region (0.50 to 1.20 V), the double layer region (0.12 to 0.50 V) and the hydrogen region (−0.27 to 0.12 V). In the oxygen region, the anodic peaks A4, A5 and A6 correspond to the oxidation of the platinum to PtO (Jerkiewicz, 2004: page 1451), while the cathodic peak C1 corresponds to the reduction of PtO to Pt. The potential where peak A7 appears corresponds to the beginning of the oxygen generation. In the hydrogen region, the peaks C2 and C3 correspond to the reduction of a monolayer of adsorbed hydrogen ions, while the peaks A2 and A3 correspond to its oxidative desorption. By integrating the peaks C2 and C3 in corresponding I-t curve of CV, the electric charge of the adsorbed hydrogen is calculated to be 796 μC after deducting the charge of double layer. Thus, the real area of the Pt electrode is estimated to be 3.79 cm^2 by taking the value of 210 μC cm^{-2} as a reference (Trasatti, 1991: page 353). The peaks C4 and A1 correspond to the generation and oxidation of hydrogen respectively.

2.3. Electrochemical testing equipment

All electrochemical experiments are performed with the EC-ALE equipment developed by us and depicted in our previous work (Chen, 2014: page 55; Chen, 2015: page 2399). The electrochemical flow cell is close to those described by Stickney's (Flower, 2002: page 273) and Zhu-Yang's (Zhu, 2005: page 4041) working groups. A platinum sheet (Sigma-Aldrich, Inc., USA) is used as counter electrode in the electrochemical cell. All electrochemical potential values are measured with respect to the potential of an Ag/AgCl electrode (3.0 M NaCl, 0.209 V vs. standard hydrogen electrode (SHE), Ametek, Inc., USA) as a reference. The atomic layer deposition of Se and Sb elements was studied electrochemically by means of cyclic voltammetry and coulometry.

3. RESULTS AND DISCUSSION

3.1. Selenium electrochemical behaviour on Pt

Figure 2a and Figure 2b show the cyclic voltammetry (CV) curves of the polycrystalline Pt electrode in 0.5 mM SeO_2 + 0.2 M Na_2SO_4 solution (pH 1.0), successively scanned from 1.06 V to various potential limits (see curve legend in the figures) at a scanning rate of 20 mV/s. As the cathodic scan limit moves from 0.55 V to 0.30 V, a reductive peak C1 (at 0.48 V) and two oxidative peaks A3 (at 0.90 V) and A2 (at 0.74 V) appear successively. The current density of peak A3 reaches its limit when the cathodic scan limit is 0.3 V. The peak A2 seems to keep on increasing when the cathodic scan limit moves further to 0.10 V. However, one can find from Figure 2b that the peak A2 has reached its limit. The increasing of peak A2 in Figure 2a during the cathodic scan limit moving from 0.30 V to 0.10 V should be due to the overlapping by peak A1. Consequently, the reductive peak C1 and oxidative peaks A3 and A2 are associated with the UPD of Se and its anodic stripping, which corresponds to the reaction Equation 1.

Equation 1: Reaction of UPD of Se and its stripping. $HSeO_3^- + 5H^+ + 4e^- \leftrightarrow Se_{(UPD)} + 3H_2O$

The total integrated Faradaic charge of the anodic stripping peaks A3 and A2 is 924 μC cm^{-2}, which is near to the value of 910 μC cm^{-2} corresponding to the stripping charge density of Se UPD layer and oxidation of surface Pt, as reported by Santos and Machado (Santos, 2004: page 203). The same experiment processing and voltammetric phenomena between this study and the literature (Santos, 2004: page 203) indicate that the Se deposition of peak C1 is close to one UPD layer. Compared with the results in our previous paper (Chen, 2015: page 2399) about the electrochemical behaviours of Se on Au, one can find that on Pt substrates Se ions can directly form a total UPD layer without the formation of bulk Se, suggesting that in kinetics the UPD process of Se is faster on Pt substrates than that on Au substrates. This also indicates

that to form a total UPD layer on Pt substrate a rinsing process for cleaning the redundant bulk Se is needless. The results above prove that Se element has different UPD behaviours on different material substrates.

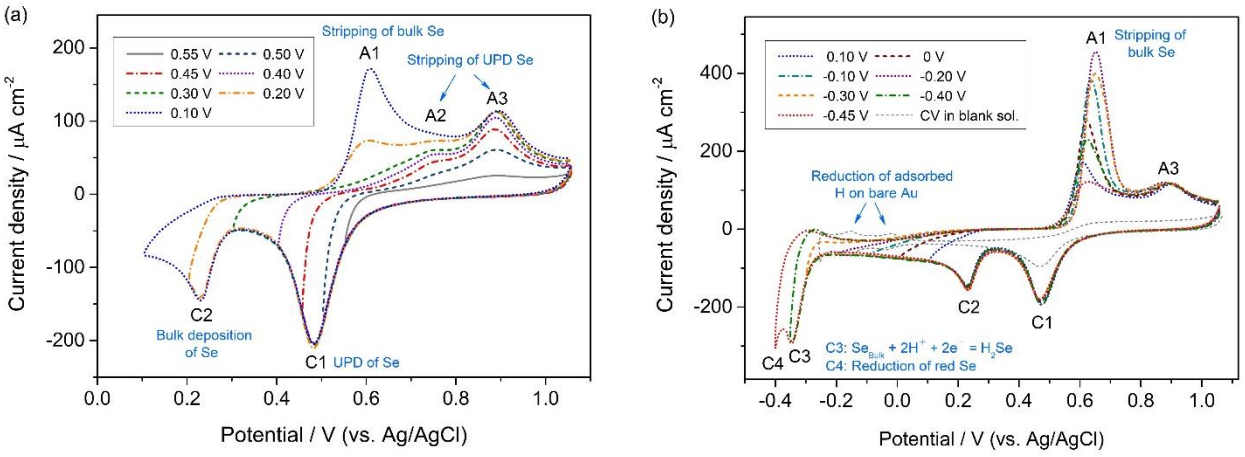

Figure 2: Cyclic voltammograms of Pt electrode in a 0.5 mM SeO_2 + 0.2 M Na_2SO_4 solution (pH 1.0). The cathodic potential limits are: (a) 0.55 V, 0.50 V, 0.45 V, 0.40 V, 0.30 V, 0.20 V and 0.10 V; (b) 0.10 V, 0 V, −0.10 V, −0.20 V, −0.30 V, −0.40 V and −0.45 V, respectively. Used as control, the gray dashed curve in (b) is the cyclic voltammogram of Pt electrode in blank solution with the scanning potential from 1.06 V to −0.26 V. The scanning rate is 20 mV/s.

When the electrode is further scanned negatively to 0.20 V, an additional reductive peak C2 and an oxidative stripping peak A1 appear. As the cathodic scan limit moves more negatively, the oxidative stripping peak A1 continually increases and reaches a maximum when the cathodic scan limit is −0.20 V, indicating that the peak C2 corresponds to the 3-D bulk deposition of Se and the peak A1 corresponds to its stripping, which corresponds to the reaction Equation 2.

Equation 2: Reaction of 3-D bulk deposition of Se and its stripping. $HSeO_3^- + 5H^+ + 4e^- \leftrightarrow Se_{(bulk)} + 3H_2O$

When the cathodic limit of cyclic voltammetry scanning is more negative than −0.20 V, an additional reduction peak C3 is observed at −0.34 V. Furthermore, A1, the stripping peak of bulk Se, decreases with the moving towards more negative cathodic limits. As already discussed in our previous work (Chen, 2015: page 2399), the C3 peak should correspond to the reduction of bulk Se to H_2Se, which is soluble. The reaction is shown as Equation 3.

Equation 3: Formation of H_2Se. $Se_{(bulk)} + 2H^+ + 2e^- \leftrightarrow H_2Se$

The reductive stripping of bulk Se leads to the decrease of the A1 peak. Similar as the situation discussed in the previous work (Chen, 2015: page 2399) on Au electrode, once H_2Se is formed, the two species $HSeO^{3-}$ and H_2Se coexist in the cell and lead to a subsequent chemical reaction (Equation 4) by which red Se is formed. The last cathodic peak C4 should correspond to a further reduction, namely that of red Se.

Equation 4: Formation of red Se. $HSeO_3^- + 2H_2Se + H^+ \leftrightarrow 3Se_{(red)} + 3H_2O$

The gray dashed curve in Figure 2b, used as control, is the cyclic voltammogram of Pt electrode in blank solution with the scanning potential from 1.06 V to −0.26 V with the same scanning rate. It is worthwhile to note the following two details: (i) the reductive peak of PtO locates at the same position as the peak C1, indicating that the peak C1 is actually the overlapping of the reductive peak of PtO and the UPD peak of Se, and this observation coincides with that reported in literature (Santos, 2004: page 203); (ii) in the CV curves of Pt electrode in Se solution, the reductive peaks of adsorbed hydrogen ions (see peaks C2 and C3 in Figure 1) are not observed. The reason is that before entering hydrogen region, the Pt electrode is already covered by UPD and bulk Se, without bare Pt exposed to the solution, thus the characteristic reductive peaks of adsorbed hydrogen cannot be observed.

3.2. Antimony electrochemical behaviour on Pt

In the current electrochemistry, there are two methods to form atomic monolayers of various metals: the underpotential deposition method and the immersion method (Herrero, 1994: page 101; Jung, 1997: page 277; Wu, 2000: page 3683). The principles of both methods are distinct from each other. In the underpotential deposition method, a simple immersion of an electrode into a solution does not lead to any interaction between the depositing species and the electrode surface. To induce an interaction, a cathodic potential is generally applied, and the surface concentration of the deposited element is determined by the applied potential. In the immersion method, on the contrary, a strong or irreversible adsorption of a

depositing species is achieved upon immersion, and the surface concentration of the deposited species is determined by the contact time and the concentration of the adsorbing species. Since the irreversibly adsorbed species generally retains its oxidation state in solution, an application of a cathodic potential is needed to reduce the adsorbate to the metallic element.

In our previous work (Chen, 2015: page 2399), when the working electrodes are Au substrates, the irreversible adsorption of Sb species in solutions (SbO^+) also happens. However, the irreversible adsorption process on Au substrate is completed immediately when the Sb solution is introduced into the electrochemical cell. This can be proved by the observation that the OCV (open circuit voltage) reaches a stable value in a very short time (less than 1 s). In addition, the reductive peak of the irreversibly adsorbed SbO^+ usually hides in the UPD peak of Sb when the potential of the Au electrode is scanned negatively in Sb solution (YAN, 2004: page 843). Therefore, in the EC-ALE studies that focus on obtaining the metallic Sb monolayer of full coverage on Au substrates, usually the irreversible adsorption process is not discussed separately.

However, the irreversible adsorption process of Sb species on Pt electrode is quite slow in kinetics. Thus, in EC-ALE study, the irreversible adsorption behaviour of Sb on Pt electrode should be investigated separately because the amount of irreversibly adsorbed Sb species will affect the subsequent UPD process. J.M. Feliu et al. (Herrero, 1994: page 101; Feliu, 1988: page 149), M.J. Weaver et al. page (Wu, 2000: page 277; Sun, 1990: page 205) studied the irreversible adsorption behaviour of Sb species by immersing simply Pt electrode in a solution containing SbO^+ ions at the OCV, but these studies focused on the electrocatalytic properties of Sb modified Pt electrode towards the oxidative reaction of a variety of organic molecules. In these literatures, the Pt electrode was not fully covered by Sb atoms because only the irreversible adsorption process was involved, but not combined with the UPD process. As we know so far, the method of obtaining a metallic Sb monolayer of full coverage on Pt electrode has not been previously reported. In this section, the irreversible adsorption process of Sb on Pt electrode was firstly studied. Subsequently, the UPD behaviour of Sb on the Pt electrode, which was pre-adsorbed by Sb was investigated.

Irreversible adsorption behaviour of Sb on Pt electrode

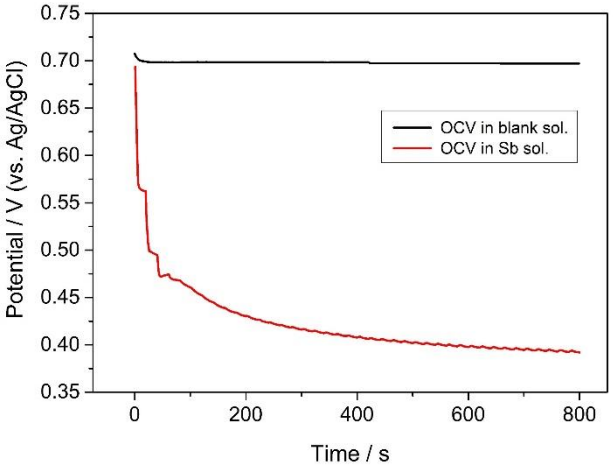

Figure 3. The varying of the OCV of Pt electrode during the irreversible adsorption process of Sb (red curve), where the Sb solution is introduced into the electrochemical cell; kept flowing for 5 s and then kept stable for 15 s as one cycle; totally 40 cycles are performed. The black curve shows the varying of the OCV of Pt electrode in a control experiment, where the blank solution is used instead of the Sb solution.

According to the literatures mentioned above (Herrero, 1994: page 101; Feliu, 1988: page 149; Kizhakevariam, 1994: page 183; Wu, 2000: page 277; Sun, 1990: page 205), antimony can adsorb irreversibly on Pt surface by immersing simply Pt electrode in a solution containing SbO^+ ions at the OCV. Two advantages of this irreversible adsorption may be stated as, (i) the coverage of Sb_{ad} can be easily controlled by the time of immersing and the concentration of the Sb solution; (ii) the Sb_{ad} modified Pt electrode can be studied in a solution free of SbO^+ ions. In this study, the aim is to obtain a metallic Sb monolayer of full coverage on Pt electrode, so the first step is to obtain as much as possible the irreversibly adsorbed Sb species on Pt electrode. Thus, we design the following experimental procedure to adsorb adequate Sb species on a clean Pt electrode:

(i) Before the beginning of the experiments, the clean Pt electrode is placed in the electrochemical cell filled with blank solution. (ii) The Sb solution is introduced into the electrochemical cell and kept flowing for 5 s. Then the Sb solution is kept stable for 15 s. (iii) The step (ii) as a cycle is repeated totally for 40 times, and the varying of the OCV of Pt electrode during this process is shown as the red curve in Figure 3. (iv) As control, a similar experiment procedure is performed as steps (i) to (iii), but during the whole process the blank solution is used instead of the Sb solution. The varying of the OCV of Pt electrode during this process is shown as the black curve in Figure 3.

From the results shown in Figure 3, one can see that the OCV of Pt electrode decreases continuously in the Sb solution, indicating that Sb species (SbO^+) are indeed adsorbed irreversibly on Pt electrode. Before the beginning of the experiments, the clean Pt electrode is kept in the electrochemical cell filled with blank solution, where the OCV is approximately 0.70 V. The high OCV is due to the chemical oxygen O_{chem} adsorbed on Pt electrode in an acid solution environment according to the literature (Jerkiewicz, 2004: 1451). When the Sb solution is introduced into the cell, the SbO^+ species are irreversibly adsorbed on Pt and replace the adsorbed chemical oxygen O_{chem}, leading to the structural change of the double-layer on the surface of Pt electrode. The structural change of the double-layer leads to the change of OCV. Therefore, the decrease of the OCV demonstrates the occurring of the irreversible adsorption of Sb species.

The OCV of Pt electrode in Sb solution approximately reaches a plateau after 800 s (40 cycles), indicating that the amount of irreversibly adsorbed Sb species reaches a maximum. This observation also illustrates that the irreversible adsorption process of Sb species on Pt substrate is slow in kinetics, or in other words, the process of replacing O_{chem} by SbO^+ species is slow in kinetics.

After the irreversible adsorption process of Sb species is achieved on Pt substrate, the next step is to study the redox properties of the adsorbed Sb species. The investigation is performed as follows, and for the sake of clarity, this experimental process is also shown in Figure 4a.

(i) After the irreversible adsorption process of SbO^+ species is achieved on the Pt electrode, the cell is rinsed with blank solution for 25 s (from point A to B in Figure 4a), and during this time no potential is applied, the voltage showed between point A and B is the OCV. (ii) A cyclic voltammetry scanning is performed from the OCV for 7 cycles (after point B). The cathodic and anodic scanning limits are −0.26 V and 1.06 V, respectively.

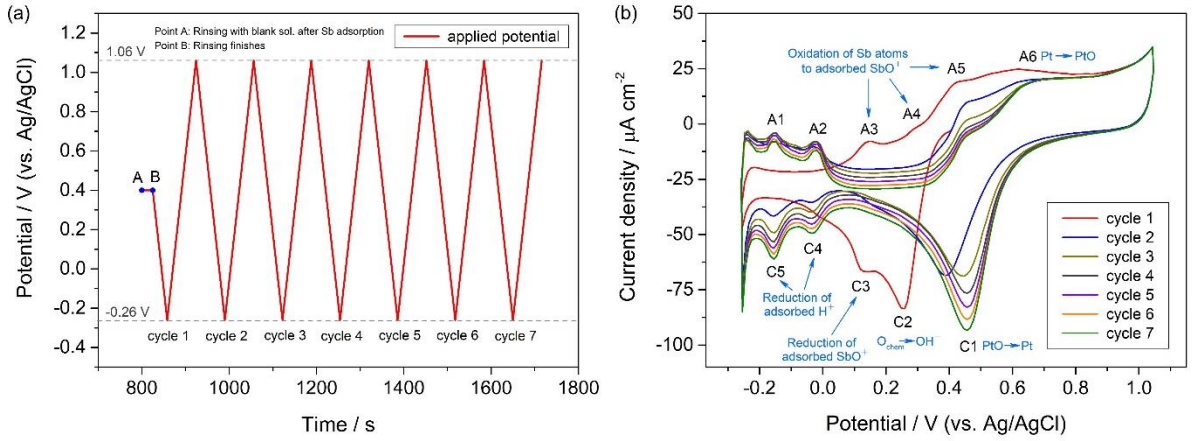

Figure 4: The cyclic voltammetry experiment of the Pt electrode (adsorbed with Sb species) in blank solution: (a) the experimental process and (b) the results of CV scanning. The scanning rate is 20 mV/s.

In Figure 4a, one can observe that the OCV keeps stable around 0.40 V during the rinsing process with blank solution (between point A and B), indicating that the adsorption process of Sb species is irreversible and the adsorbed species is stable on Pt substrate. Figure 4b shows the voltammograms of the Pt electrode (adsorbed with Sb species) in blank solution. The peak C1 corresponds to the reduction of PtO to Pt, and the peak A6 corresponds to the oxidation of Pt. The peaks C4 and C5 correspond to the reduction of a monolayer of adsorbed hydrogen ions, while the peaks A1 and A2 correspond to its oxidative desorption.

In the voltammogram of cycle 1 (Figure 4b), two reductive peaks C2 and C3 appear at 0.27 V and 0.11 V respectively. Because the cycle 1 is scanned from the OCV where the current is zero, the peak C2 should be regarded as the reductive peak of the adsorbed oxygen O_{chem} on Pt substrate to H_2O. This assumption is accordant with the literatures (WU, 2000: 3683; Herrero, 1994: 101; Feliu, 1988: 149), in which the results showed that the irreversibly adsorbed Sb species cannot reach a full coverage on the Pt electrode. In other words, the Sb species cannot replace all the O_{chem} on the Pt electrode, so the reductive peak of O_{chem} can still be observed. At the end of cycle 1, the potential is scanned to a very positive potential (1.06 V), where all the O_{chem} will form the oxide PtO with Pt (Jerkiewicz, 2004: page 1451). That is why from cycle 2, only the peak C1 which corresponds to the reduction of PtO to Pt can be observed. The peak C3 should correspond to the reduction of adsorbed SbO^+ to metallic Sb atoms, while the peaks A3, A4 and A5 are the oxidative peaks of Sb atoms back to SbO^+ species. It is worthwhile to note that when the Sb atoms are just oxidised to SbO^+, the SbO^+ species will still adsorb on the Pt substrate, but not desorb (or strip) into the solution if the potential is not extremely positive. This is also the point by which the irreversible adsorption distinguishes from UPD (Jung, 1997: page 277). The observation of the peak C3 and its oxidative peaks is similar as the results reported in the literature (Wu, 2000: page 3683).

In addition, in the voltammogram of the cycle 1, one can see that the peak C5 is almost completely inhibited and the current intensity of the peak C4 is very low. The inhibition of the reduction of adsorbed hydrogen ions should be attributed to the covered Sb atoms, which occupy a part of sites on Pt electrode. When the scan is performed from the cycle 2 to the cycle 7, the voltammograms show that the peak C3 and A5 decreases greatly, and the oxidative peaks A3 and A4 disappear completely, indicating that the amount of the adsorbed Sb species on the surface of Pt substrate decreases. The reason should be that in the end of cycle 1, the very high potential (1.06 V) leads to the desorption of SbO^+ species. As mentioned above, when the Sb atoms are just oxidised to SbO^+, the SbO^+ species will still adsorb on the Pt substrate, but not strip into the solution. However, the adsorbed SbO^+ species cannot stand the extremely positive potential such as 1.06 V, where the strong electric field make the positively charged SbO^+ species desorb into the solution. In addition, the continuously increase of the peaks C4/A2 and C5/A1 also indicates that the amount of adsorbed Sb species decreases on the surface of Pt substrate, because there are more and more sites available on Pt electrode for hydrogen adsorption.

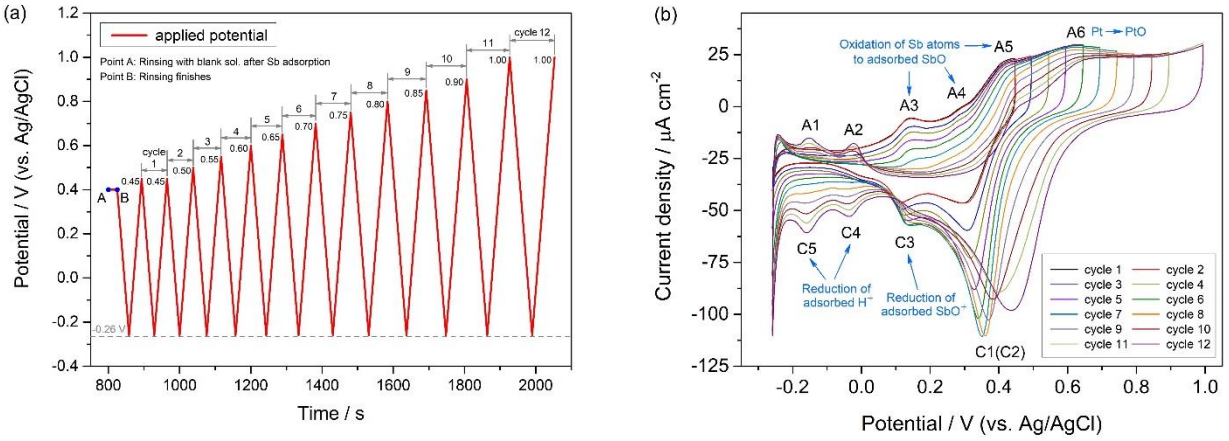

Figure 5: The cyclic voltammetry experiment of the Pt electrode (adsorbed with Sb species) in blank solution: (a) the experimental process and (b) the results of CV scanning. The scanning rate is 20 mV/s.

To confirm the assumption that the decrease of the adsorbed Sb species amount on the surface of Pt substrate is due to the desorption of adsorbed SbO^+ at a very positive potential, another cyclic voltammetry experiment is performed as follows, and for the sake of clarity, this experimental process is also shown as Figure 5a.

(i) After the irreversible adsorption process of SbO^+ species is achieved on the Pt electrode, the cell is rinsed with blank solution for 25 s (from point A to B in Figure 5a), and during this time no potential is applied, the voltage showed between point A and B is the OCV. (ii) A cyclic voltammetry scanning is performed for 12 cycles with the same cathodic scanning limit −0.26 V but different anodic scanning limits.

Figure 5b shows the voltammograms of the Pt electrode (adsorbed with Sb species) in blank solution with different anodic scanning limits. One can see that the voltammograms of the cycle 1 and the cycle 2 are highly coincident with each other, illustrating that at the potential of 0.45 V, i.e. the anodic scanning limit of the cycle 1, the SbO^+ species that are formed by oxidation of metallic Sb can still adsorb on the surface of Pt electrode without stripping. The peaks A3, A4 and A5 start to reduce from the cycle 3 to cycle 12, suggesting that when the potential is equal or more positive than 0.50 V, i.e. the anodic scanning limit of the cycle 2, the adsorbed SbO^+ species begin to desorb into the solution. When the anodic scanning limit is moved to 1.0 V, the voltammogram of cycle 12 shows that the peak C3 and A5 decreases greatly, and the oxidative peaks A3 and A4 disappear completely, similar to the observation in Figure 4b. In addition, the continuous increase of the peaks C4/A2 and C5/A1 also indicates that the amount of the adsorbed Sb species decreases on the surface of Pt substrate from cycle 3 to cycle 12.

The peak C3 seems to increase firstly and then decrease. Actually, this phenomenon is caused by the overlapping with the increasing peak C1 (C2). Along with the anodic scanning limit moving positively, more and more Pt atoms are oxidised to PtO and the amount of the adsorbed oxygen O_{chem} decreases (forming PtO with Pt), so the reductive peak C1 (C2) increases continuously and moves positively, or in other words, the peak C2 evolves to be the peak C1 during the CV process. Therefore, the peak C3 actually is continually decreasing during the CV process when the overlapping with the peak C1 (C2) is deducted.

The experimental results in Figure 5b prove that the decrease of the amount of adsorbed Sb species on the surface of Pt substrate is due to the desorption of SbO^+ species at a relatively positive potential. In the corresponding I-t curve of the voltammogram of cycle 2, the total Faradaic charge of the anodic peaks A3, A4 and A5 is integrated to be 377 μC cm^{-2}, which correspond to the redox charge of irreversibly adsorbed SbO^+ species on Pt electrode.

The voltammogram of cycle 1 in Figure 4b shows that the reductive current of adsorbed hydrogen does not disappear completely (see peak C4 in Figure 4b), indicating that there are still some unoccupied sites on the surface of Pt electrode after the reduction of the irreversibly adsorbed SbO^+ to metallic Sb. Therefore, there is chance for further depositing Sb underpotentially on the Pt electrode covered by metallic Sb atoms that are reduced from adsorbed SbO^+ species. For the sake of convenience, we call the Pt electrode covered by metallic Sb atoms that are reduced from adsorbed SbO^+ species as Sb-modified Pt electrode. To study the UPD behaviour of antimony on a Sb-modified Pt electrode, the experiments are performed as follows, and the corresponding experimental process is also shown as Figure 6a.

(i) After the irreversible adsorption process of SbO^+ species is achieved on the Pt electrode, the cell is rinsed with blank solution for 25 s (from point A to B in Figure 6a), and during this time no potential is applied, the voltage showed between point A and B is the OCV. (ii) In blank solution, the Pt electrode adsorbed with SbO^+ species is scanned from the OCV to −0.26 V and then scanned back to 0.04 V, and the scanning performed in this step is labelled as cycle 1 (from point B to C in Figure 6a). (iii) The potential of the Pt electrode is maintained at 0.04 V, while the Sb solution is introduced to the cell and kept flowing for 25 s. (iv) Subsequently, the electrode is scanned from 0.04 V to −0.26 V and then scanned back to 0.45 V. The scanning performed in this step is labelled as cycle 2. (v) The electrode is scanned from 0.45 V to −0.26 V and then scanned back to 0.45 V. The scanning performed in this step is labelled as cycle 3. (vi) The potential of the Pt electrode is maintained at 0.45 V, while the blank solution is introduced again to the cell and kept flowing for 25 s. (vii) In blank solution, the electrode is scanned from 0.45 V to −0.26 V and then scanned back to 0.45 V. The scanning performed in this step is labelled as cycle 4.

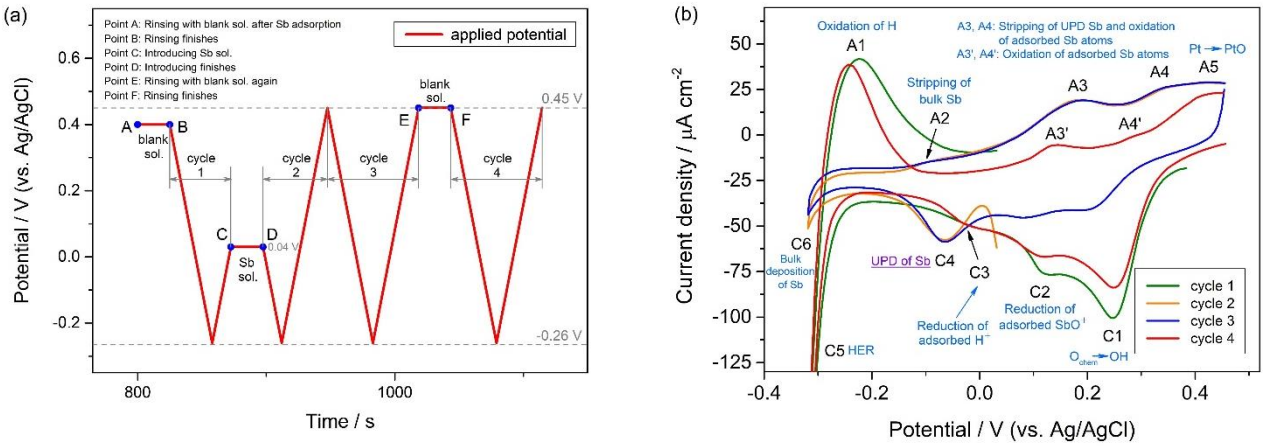

Figure 6: The voltammograms of the Sb-modified Pt electrode in the blank solution and Sb solution (b) and the experimental process (a). Four groups of scanning, cycles 1, 2, 3 and 4, are performed one after another. The cycles 1 and 4 are performed in the blank solution, and the cycles 2 and 3 are performed in the Sb solution. The scanning rate is 20 mV/s.

The voltammograms of the cycles 1, 2, 3 and 4 are shown in Figure 6b. For the cycle 1, when the potential moves positively, the scanning is stopped at 0.04 V. From Figure 5b one can see that in the anodic branch of the voltammogram of every cycle, when the potential is 0.04 V, the peak A2 finishes but the peak A3 does not start, or in other words, the oxidation of the adsorbed hydrogen finishes but the oxidation of the metallic Sb does not begin. Therefore, in cycle 1, when the scanning is stopped at 0.04 V in blank solution, all of the hydrogen atoms on the Pt electrode are oxidised but the Sb species can still remain in the metallic state. The voltammogram of the cycle 1 is similar to those shown in Figure 4b and Figure 5b.

Subsequently, the Sb solution is introduced into the cell, while the potential of the electrode is maintained at 0.04 V during the process of changing solutions. Then the CV scanning of the cycle 2 and cycle 3 are performed successively. In the voltammogram of cycle 2, a new reductive peak C4 is observed at −0.07 V, which corresponds to the UPD of Sb on the Pt electrode. The oxidative peaks A3 and A4 increase obviously and the increased parts should be attributed to the oxidative stripping of the Sb UPD. It is worthwhile to note that the peaks C3 in the CV curves of cycle 2 and cycle 3 nearly disappear, indicating that there is almost no site available for the adsorption of H species. This observation also suggests a higher coverage of Sb monolayer. In addition, in cycle 1 the peak C5 corresponds to the generation of hydrogen, and A1 is the oxidative peak of the peak C5. However, the peaks C5 and A1 cannot be observed in the curves of cycle 2 and cycle 3, but a new pair of redox peaks C6 and A2 appears, which correspond to the bulk deposition of Sb and its oxidative stripping, respectively.

To confirm that the peak C4 is the UPD peak of Sb and the increased parts of the peaks A3 and A4 correspond to its oxidative stripping, after the scanning of cycle 3 finishes, the cell is rinsed by the blank solution and then the scanning of cycle 4 is performed. Dramatically, the voltammogram of cycle 4 in Figure 6b shows that the peak C4 disappears and the

peaks A3 and A4 decrease to the similar intensity as the ones in the curve of cycle 1 in Figure 5b. In addition, the peaks C3, C5 and A1 reappear, but the peaks C6 and A2 cannot be observed. As mentioned above, distinct from the irreversibly adsorbed Sb species, when the UPD Sb atoms are oxidised to SbO^+ ions, these formed SbO^+ ions will directly dissolve into the solutions. Thus, during the process of rinsing with the blank solution after cycle 3 at 0.45 V, the UPD Sb will be oxidised to SbO^+ ions which will be rinsed out of the cell. However, the SbO^+ species that come from the irreversible adsorption will still adsorb on the surface of the Pt electrode, because the results in Figure 5b prove that the irreversibly adsorbed SbO^+ species will not desorb at the potential 0.45 V. As a result, when the potential is scanned negatively in cycle 4, there is no SbO^+ ion existing in the solution. Therefore, the disappearance of the peak C4 and the decrease of the peaks A3 and A4 illustrate that they are related to the UPD of Sb. The Faradic charge of UPD Sb is calculated to be 604 μC cm^{-2} by integrating the increased parts of the peaks A3 and A4 in the corresponding I-t curve of cycle 4. Combined with the reductive charge of irreversibly adsorbed SbO^+ species, which is 377 μC cm^{-2}, finally a Sb monolayer with the depositing charge 981 μC cm^{-2} is obtained.

4. CONCLUSIONS

Voltammetry and coulometry experiments were performed in this work to investigate the electrochemical behaviours of selenium and antimony on the polycrystalline platinum electrode. The following conclusions were obtained:

(i) Comparing with the results obtained on Au substrates, Se element has different UPD behaviours on Pt substrates. On Pt substrates Se ions can directly form a UPD layer with full coverage, and the total Faradaic charge of the UPD Se is calculated to be 924 μC cm^{-2}. (ii) A Pt electrode adsorbed irreversibly with SbO^+ species is obtained by introducing the fresh Sb solution continuously into the electrochemical cell. The irreversibly adsorbed SbO^+ species begin to desorb when the potential is more positive than 0.50 V. The reduction potential of irreversibly adsorbed SbO^+ to metallic Sb atoms amounts to 0.11 V and the Faradic charge of this process is integrated to be 377 μC cm^{-2}. (iii) After the irreversibly adsorbed SbO^+ species are reduced to metallic Sb, Sb atoms can be further deposited onto this Sb-modified Pt electrode in the way of UPD to increase the coverage of the metallic Sb monolayer. The UPD potential of antimony on the Sb-modified Pt electrode amounts to −0.07 V. The Faradic charge of UPD Sb is calculated to be 604 μC cm^{-2}. (iv) Combined with the reductive charge of irreversibly adsorbed SbO^+ species, finally a Sb monolayer with the depositing charge 981 μC cm^{-2} is obtained. Now the alternative deposition of Sb-Se compound by EC-ALE method is under study.

5. ACKNOWLEDGEMENTS

The authors gratefully acknowledge the financial support for this work from Hubei Provincial Key Laboratory of Green Materials for Light Industry (201710A06) and Chutian Scholars Program of the Hubei Province of China.

6. REFERENCES

Chen Y, 2014. A voltammetric study of the underpotential deposition of cobalt and antimony on gold. *Journal of Electroanalytical Chemistry*, 724 (19), 55.

Chen Y, 2015. Underpotential deposition of selenium and antimony on gold. *Journal of Solid State Electrochemistry*, 19(8), 2399.

Feliu JM, 1988. ChemInform abstract: new observations of a structure sensitive electrochemical behavior of irreversibly adsorbed arsenic and antimony from acidic solutions on Pt (111) and Pt (100) orientations. *Journal of Electroanalytical Chemistry*, 256 (1), 149.

Fernández AM, 2000. Preparation and characterization of Sb_2Se_3 thin films prepared by electrodeposition for photovoltaic applications. *Thin Solid Films*, 366 (1), 202.

Flowers JR, 2002. Atomic layer epitaxy of CdTe using an automated electrochemical thin-layer flow deposition reactor. *Journal of Electroanalytical Chemistry*, s524-525 (02), 273.

Foresti ML, 2005. Ternary CdS_xSe_{1-x} deposited on Ag (111) by ECALE: synthesis and characterization. *Langmuir the ACS Journal of Surfaces & Colloids*, 21 (15), 6900.

Ghosh G, 1994. The Sb-Te (antimony-tellurium) system. *Journal of Phase Equilibria*, 15 (3), 349.

Gregory B, 1991. Electrochemical atomic layer epitaxy (ECALE). *Journal of Electroanalytical Chemistry & Interfacial Electrochemistry*, 1991, 300 (91), 543.

Herrero E, 1994. Poison formation reaction from formic acid on Pt (100) electrodes modified by irreversibly adsorbed bismuth and antimony. *Journal of Electroanalytical Chemistry*, 368 (1-2), 101.

Jerkiewicz G, 2004. Surface-oxide growth at platinum electrodes in aqueous H_2SO_4: reexamination of its mechanism through combined cyclic-voltammetry, electrochemical quartz-crystal nanobalance and Auger electron spectroscopy measurements. *Electrochimica Acta*, 49 (9), 1451.

Jung G, 1997. Two electrochemical processes for the deposition of Sb on Au (100) and Au (111): irreversible adsorption and underpotential deposition. *Journal of Electroanalytical Chemistry*, 436 (1-2), 277.

Kizhakevariam N, 1994. Structure and reactivity of bimetallic electrochemical interfaces: infrared spectroscopic studies of carbon monoxide adsorption and formic acid electrooxidation on antimony-modified Pt (100) and Pt (111). *Surface Science*, 310 (1-3), 183.

Lister TE, 1996. Formation of the first monolayer of CdSe on Au (111) by electrochemical ALE. *Applied Surface Science*, 107 (107), 153.

Madelung O, 1992. Semiconductors: other than group IV elements and III-V compounds. Germany: Springer-Verlag.

Rajpure KY, 1999. A comparative study of the properties of spray-deposited Sb_2Se_3 thin films prepared from aqueous and nonaqueous media. *Materials Research Bulletin*, 34 (7), 1079.

Santos MC, 2004. Microgravimetric, rotating ring-disc and voltammetric studies of the underpotential deposition of selenium on polycrystalline platinum electrodes. *Journal of Electroanalytical Chemistry*, 567 (2), 203.

Sun SG, 1990. Electrocatalytic properties of glassy metals: combined auger electron spectroscopy and electrochemical studies of the surface composition and electrocatalysis of CO oxidation at amorphous $Pt_{66}Sb_{34}$ alloy. *Journal of Electroanalytical Chemistry*, 278 (1-2), 205.

Trasatti S, 1991. Real surface area measurement in electrochemistry. *Pure & Applied Chemistry*, 63 (5), 353.

Wang X, 2013. Preparation and electrical transport properties of nanostructured Sb_2Se_3 films fabricated by combining spin-coating and gas-induced reduction. *Journal of Nanoparticle Research*, 15 (4), 1.

Wu QH, 2000. An EQCM study of Sb adsorption and coadsorption with CO on Pt electrode in perchloric acid solutions. *Electrochimica Acta*, 45 (22-23), 3683.

Xiao CJ, 2009. Electrodeposition and characterization of Bi_2Se_3 thin films by electrochemical atomic layer epitaxy (ECALE). *Electrochimica Acta*, 54 (27), 6821.

Xiao XB, 2006. Thermoelectrics handbook: macro to nano. Boca Raton: CRC.

Yan JW, 2004. Electrodeposition of Sb on Au (100) at underpotentials: structural transition involving expansion of the substrate surface. *Electrochemistry Communications*, 6 (8), 843.

Yang JY, 2006. Formation and characterization of Sb_2Te_3 nanofilms on Pt by electrochemical atomic layer epitaxy. *Journal of Physical Chemistry B*, 110 (10), 4599.

Yu L, 2010. Pulsed laser deposited heterogeneous mixture of Li_2Se–Sb_2Se_3 nanocomposite as a new storage lithium material. *Electrochimica Acta*, 55 (3), 1258.

Xue MZ, 2008. Pulsed laser deposited Sb_2Se_3 anode for lithium-ion batteries. *Journal of Alloys & Compounds*, 458 (1), 351.

Zhu W, 2005. Effect of potential on bismuth telluride thin film growth by electrochemical atomic layer epitaxy. *Electrochimica Acta*, 50 (20), 4041.

Zhu W, 2005. The underpotential deposition of bismuth and tellurium on cold rolled silver substrate by ECALE. *Electrochimica Acta*, 50 (27), 5465.

349: Design and analysis of an organic rankine cycle power generation system using solar energy

Ruiling GUO[1], Xiaobin LI[2]

1 School of Energy, Xi'an University of Science and Technology, Xi'an, China, ruilingguo96@163.com
2 Datong architectural design and research institute, Shanxi.China

In this paper, a solar organic Rankine cycle system with net output power of about 100 kW is designed. R600，R600a, R245ca，R245fa，R123, R113 and R227ea are selected as working fluids during the different evaporation temperature, and thermodynamic cycle characteristics of the ORC system was studied. The evaporation pressure, thermal efficiency, and irreversible loss were respectively calculated and compared. An organic radial turbine is designed and modeled for the system. The results show that R245fa, as the circulating working fluid of the solar organic rankine cycle system, creates relatively high thermal efficiency and produces relatively low total irreversible loss. According to the CFD calculation results, the internal flow state in the organic radial turbine is good and the streamline distribution is uniform, and the isentropic efficiency of turbine reaches 83.41%, which basically meets the design requirements.

Keywords: Solar energy; Organic rankine cycle; Organic working fluid; Thermal efficiency; Radial turbine

1. INTRODUCTION

With the increasingly prominent energy and environmental problems, solar energy, as a representative of clean and renewable energy, has received more and more attention.At the same time, in response to China's "energy conservation and emission reduction" policy, large-scale solar energy utilization is realised through solar power generation technology. At present, the solar organic Rankine cycle system is a new solar power generation technology after photovoltaic power generation and photothermal power generation. The working principle of the system is to use solar energy as heat source and orc as power cycle for heat work conversion. It is simple in structure, economical and environmentally friendly for this system.Due to the characteristics of low energy flow density and strong dispersion of solar energy, the utilization of high temperature of solar energy requires a large area and high collection ratio heat collecting device, which leads to high cost and increased research and development difficulty.While it is relatively easy to obtain a heat source of medium or low temperature for solar energy.

The temperature of the heat source for solar medium-low temperature power generation is about 100 - 250°C and a low-power focus load parabolic concentrator is used as the solar energy collector. The CPC collector can not only effectively receive the direct light from the sun but also collect the diffuse light from the sun because of its large receiving angle. The reflectivity of the CPC reflective material can reach more than 0.9, and the heat absorption tube can adopt a high-efficiency heat pipe vacuum tube, which is a novel solar energy medium-temperature heat collecting and assembling device with high thermal efficiency and convenient manufacture, installation, operation and management. There are the important contents of the organic Rankine cycle thermal power generation system with medium and low temperature of solar energy,the selection of organic working medium, the study of physical properties, and the design of radial turbine. The technological development of a solar thermal-driven mechanical power generation based on a solar-heated thermodynamic cycle was analysed by Lourdes et al (García-Rodríguez, 2007). A thermodynamic screening of 31 pure component working fluids for organic Rankine cycles (ORC) is given using BACKONE equation of state, it is concluded that overheating will reduce the circulation efficiency of the dry working medium under certain heat source temperature, while increasing the heat recovery measures can improve the orc heat work conversion efficiency. In the organic Rankine cycle of solar heat collection,R236ea, R245ca, R245fa,R600, R600a, R601a, RE134, and RE245 should be considered by Saleh et al. (2007).With the increasing of high demands for environmental protection, the available range of working fluids is continuously updated. Therefore, the selection of suitable organic working medium is of great significance to improve the system performance and energy utilization efficiency. A small solar medium and low temperature thermal power generation device with a power of 7.6 kW was reported by Saitoh in Japan, the device uses a compound parabolic collector with an acceptance angle of 32 degrees and uses r113 as a circulating working medium. Under the condition of an irradiation intensity of 1300 w/m^2, the power generation efficiency of the system is 19.5 % (Saitoh, 2002). The heat pipe/gas ORC cogeneration system was preliminarily explored theoretically and experimentally by Professor Saffa Riffat from the University of Nottingham.

The system uses the self-developed heat pipe as the solar energy collector and HFE-7100 as the working medium. The power generation efficiency reaches 16%, and the total thermal efficiency is 59% (Yagoub, 2006). Solar energy medium-temperature heat collection technology is booming in China. For example, the medium-temperature solar vacuum tubes and heat collectors independently developed by Shandong lino group and Tsinghua University can reach more than 45% efficiency at 150°C, and the technology is close to the international leading level (www.linuo-paradigma.com; Ma, 2010). Based on the research and manufacture of single screw compressor for many years, a new type of power machine developed by the working principle of reverse compressor is developed by the key laboratory of thermal energy of Beijing University of technology (Wen, 2009). The research work on the direction of solar low-temperature thermal power generation was carried out, the simulation and preliminary test of the system composed of flat plate/vacuum tube heat collector and expander were completed by Tianjin University (Huang, 2006). A micro distributed solar driven cogeneration system consisting of vacuum tubes, orc, adsorption refrigeration and afterburning devices was preliminarily studied and discussed at Shanghai Jiaotong University (Wang, 2010). The optimisation research on the structure and operation mode of the solar organic Rankine cycle system, organic working medium, photothermal photoelectric performance and other aspects have been carried out in China university of science and technology (Li, 2011).

2. SOLAR ORGANIC RANKINE CYCLE SYSTEM

The solar organic Rankine cycle system includes the heating subsystem, the regenerator subsystem and the ORC subsystem. The solar energy collector can gather the solar energy and convert it into heat. The phase change storage tank will store the excess heat in the collector when the solar radiation is strong, and the ORC subsystem is supplied with the.ORC system for the whole system when the radiation is insufficient. The core includes evaporator, radial turbine, condenser and working fluid pump. The schematic diagram of solar Organic Rankine Cycle system is shown in Figure 1.

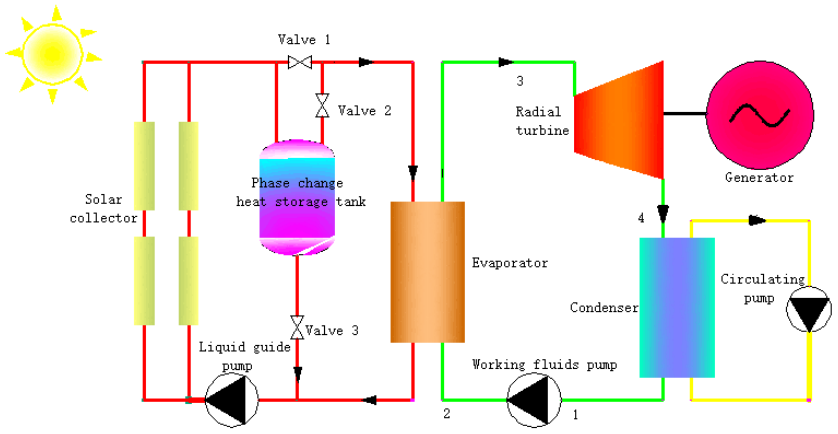

Figure 1: Solar energy ORC system

2.1. Heat collection subsystem

The main component of the collector subsystem is the collector. In this paper, the compound paraboloid condensing collector is selected. Through market research, Satioch has studied the CPC of double-layer glass cover plate and the new type of CPC collector without tracking solar energy trace. Both of them have high heat collecting effect. The efficiency of solar vacuum tube and collector developed by Shandong Linuo Group and Tsinghua University can reach more than 45% under condition of 150°C. There are many studies in this area by domestic scholars. The collector invented by Shandong Linuo Group and Tsinghua University are adopted in this paper.

Table 1: Main parameters of heat collection subsystem

	Unit	Value
Heat collection temperature	℃	120
Heat transfer working medium (mineral oil) specific heat capacity	KJ/(kg·k)	2.61
Heat source outlet temperature	℃	85
Annual solar radiation in Xi' an	MJ/m^2	5
Heat collector efficiency		45%
Working hours	h	8
Heat collecting area	m^2	2000
Mineral oil flow rate	t/h	25

2.2. Heat storage subsystem

The heat storage subsystem can ensure a relatively stable output of the solar power generation system, which can temporarily store the excess heat in the solar thermal power generation process. Such as lack of sunlight or night is to release this part of the heat for use by the ORC subsystem. In this paper, heat storage tanks, phase change material storage tanks. During the operation of the system, when the heat load provided by the collector is greater than the required heat load, the valves 1 and 2 are opened and the valve 3 is closed. At this time, the heat storage device absorbs and stores excess heat; the collector provides. When the heat load is less than the required heat load, the valves 1 and 2 are closed and the valve 3 is opened. The heat transfer fluid heated by the collector enters the heat reservoir and is heated again, and the heat released by the heat accumulator is transferred to the Rankine cycle system. With the continuous promotion of phase change materials, it has been applied to various fields. Phase change heat storage tanks can extend the heat storage time and keep the temperature change for a long time. So as to increase solar energy utilization and improve power generation efficiency.

2.3. ORC subsystem

System thermal cycle

The working principle of organic Rankine cycle system is shown in Figure 1. Solar collectors are used to collect solar energy and convert it into heat energy. Because solar energy is affected by weather conditions, it is uncertain and intermittent. To ensure the smooth operation of solar thermal power generation system, the addition of phase change thermal storage device is used to store solar heat. The organic working medium absorbs heat from the solar heat source in the evaporator to form steam with a certain pressure and temperature. The steam enters the turbine and expands to do work, thereby driving the generator to generate electricity. The pressure and temperature of the steam from the turbine

have been greatly reduced. After being condensed into a liquid, the refrigerant is sent back to the solar collector by the working fluid pump to start a new cycle.

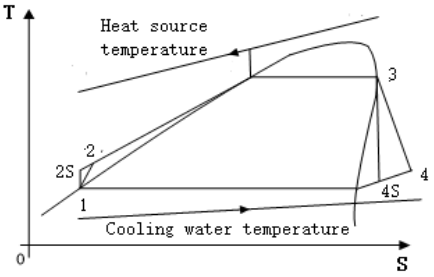

Figure 2: Thermal cycle curve of the ORC system

The schematic diagram of the organic Rankine cycle thermal cycle is shown in Figure 2. The theoretical cycle includes the following basic processes:

（1）2-3：Organic working fluid constant pressure evaporation, constant pressure endothermic process.

The heat absorbed of organic Rankine cycle system is

$$Q_{\text{eva}} = m_w\left(h_3 - h_2\right) \text{（1）}$$

Where：

- m_w =Working mass flow rate，kg/s.

（2）3-4：The organic working fluid expands in the turbine to do work, adiabatic work process;

Work done by organic working media is

$$W_{\text{T}} = W_{\text{T,ideal}}\eta_{\text{T}} = m_w\left(h_3 - h_{4\text{S}}\right)\eta_{\text{T}} \text{（2）}$$

where：

- $W_{\text{T,ideal}}$=the ideal power consumption of turbine(kw)；
- η_{T} =Turbine Isentropic Efficiency， $\eta_{\text{T}} = \dfrac{h_{\text{S}} - h_4}{h_{\text{S}} - h_{4\text{S}}}$

(3) 4-1：The organic working medium is condensed in the condenser, and the heat release process is constant pressure;

Heat released by organic media

$$Q_{\text{con}} = m_w\left(h_1 - h_4\right) \text{ (3)}$$

（4）1-2：The pump pressurises the working fluid and adiabatic compression process;

The work done by the working pump

$$W_{\text{P}} = \frac{W_{\text{P,ideal}}}{\eta_{\text{P}}} = \frac{m_w\left(h_{2\text{S}} - h_1\right)}{\eta_{\text{P}}} \text{ (4)}$$

where：

- $W_{\text{P,ideal}}$= the ideal power consumed by the pump(kw)；
- η_{P} =the pump's isentropic efficiency， $\eta_P = \dfrac{h_{2S} - h_1}{h_2 - h_1}$.

（5）System efficiency

Organic Rankine cycle thermal efficiency is

$$\eta = \frac{W_T - W_P}{Q_{eva}} \text{ (5)}$$

（6）Total irreversible loss of system

$$I = T_0 m_w \left[\frac{h_2 - h_3}{T_H} - \frac{h_1 - h_4}{T_L} \right] \quad (6)$$

where：

- T_H =the average high temperature heat source temperature (K)；
- T_L =the condensation temperature (K).

Candidates for organic media

The selection of organic working media directly affects the thermal performance and economy of organic Rankine cycle systems and needs to meet the requirements of the application environment. In principle, substances that can achieve phase change within the operating temperature range can be used as the working medium. However, considering various factors such as system thermal efficiency, safety, operation and maintenance performance, and environmental protection, only some of them are suitable as organic Rankine cycles. The working medium.

The Organic Rankine Cycle System has the following requirements for the selection of organic working fluids from the aspects of thermodynamics, physicochemical properties, safety, and equipment design feasibility: (1) Good thermodynamic performance; (2) Chemically stable, non-flammable, not easy Explosive, non-toxic; (3) Environmental friendly, will not deplete the ozone layer, the greenhouse effect is low; (4) The organic working fluid is favorable to the turbine design; (5) Easy to produce and transport, the source is abundant, the cost is low.

Table 2: Primary organic physical property

Working medium name	molecular weight	normal boiling point	critical temperature	critical pressure	critical density	ODP	GWP
	g/mol	K	K	KPa	mol/L		
R600	58.1222	272.660	425.125	3796.0	3.922769613	0	4
R600a	58.1222	261.401	407.81	3629.0	3.879756788	0	20
R245ca	191.5	298.412	447.57	3940.7	3.92	0	726.
R245fa	152.0384	271.66	398.07	3200.0	3.626	0	820
R123	152.931	300.973	456.831	3661.8	3.596417	0.01	77
R113	187.375	320.735	487.21	3392.2	2.988659	0.85	6130
R227ea	170.02886	256.81	374.9	2925.0	3.495	0	3220

Considering various factors comprehensively, seven kinds of working media such as R600, R600a, R245ca, R245fa, R123, R113 and R227ea were selected as candidate working media in the study. It contains two types of substances: alkane and HFC. The detailed characteristic parameters are shown in Table 2. The physical properties of the selected working fluid were obtained from the National Institute of Standards and Technology (NIST) fluid thermal and transport properties database REFPROP 9.1.

3. THEORETICAL CYCLE CALCULATION RESULTS

Under the same conditions, the performances of the selected R600, R600a, R245ca, R245fa, R123, and R227ea in the organic Rankine cycle were compared and analysed. Table 3 shows the organic Rankine cycle calculation conditions.

Table 3: parameters for calculation of the ORC system

Parameter	Value
Ambient temperature	20
Rated power of turbine	120
Transparent equal entropy efficiency	85
Isentropic efficiency of pumps	80
condensing temperature	35
Evaporator heat transfer temperature difference	5
Condenser heat transfer temperature difference	5

3.1. Analysis based on the first law of thermodynamics

The thermal efficiency is a performance evaluation index based on the first law of thermodynamics. It can be seen from Figure 3 that as the evaporation temperature increases, the thermal efficiency of the organic Rankine cycle system gradually increases. Taking R245fa as an example, when the evaporation temperature is 50, the thermal efficiency is 5.989%, and when the evaporation temperature rises to 75, the thermal efficiency increases to 11.35%. When the evaporation temperature is lower than 55 degrees, the thermal efficiency of each working fluid is not greatly different. When the evaporation temperature is higher than 55 degrees, the thermal efficiency of R600, R600a and R245fa is relatively close, and R227ea is the lowest.

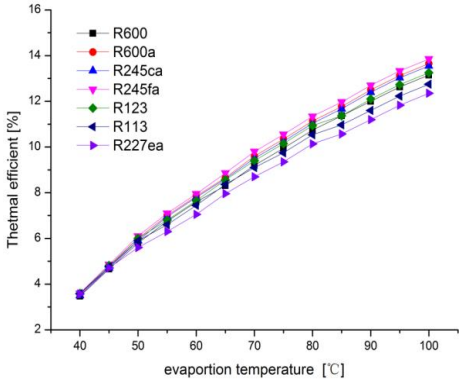

Figure 3: Thermal efficiency vs.evaporation temperature of various working fluids

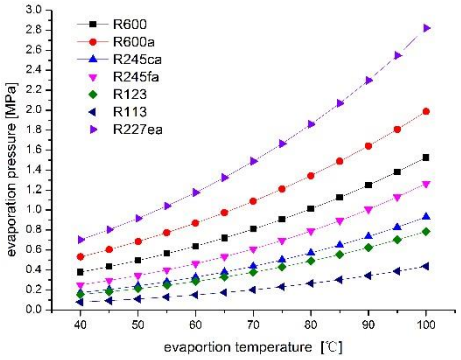

Figure 4: Evaporation pressure vs.evaporation temperature of various working fluids

Figure 4 shows the change of evaporation pressure of 7 working substance at different evaporation temperatures. We can see that, as a whole, with the increase of evaporation temperature, the pressure level of the candidate working fluid is getting higher and higher, and with the increase of temperature, the pressure rises faster and faster. For safety and equipment considerations, when the cycle reaches the maximum temperature, the corresponding saturation pressure should not be too high, because excessive pressure will lead to mechanical pressure problems, and thus increase unnecessary equipment costs. Compared to other working fluids, R123 has a lower evaporation pressure level at the same evaporation temperature.

3.2. Analysis based on the second law of thermodynamics

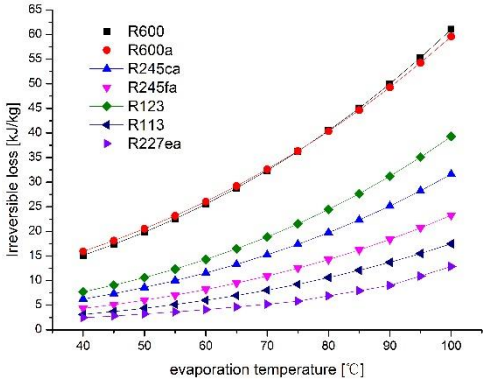

Figure 5: Irreversible loss vs.evaporation temperature of various working fluids

In fact, every practical system inevitably has irreversible losses. That is, from the perspective of the second law of thermodynamics, the amount of work and heat is not equivalent. In the actual irreversible process, the devaluation of energy occurs. Figure 5 shows the effect of working mass on irreversible losses in the system at different evaporation temperatures. As can be seen from Figure 5, as the evaporation temperature increases, the irreversible loss of the system gradually increases. Through the observation of the graph, it was found that although the working power of the alkane-type working medium is higher than that of the HFC-type working medium, the effect of the alkane-type working medium on the irreversible loss of the system is far greater than that of the HFC-type. As the evaporation temperature increases, the total irreversible loss of the system increases more and more. Taking R245fa as an example, when the temperature rises from 60 degrees to 70 degrees, the total irreversible loss of the system increases by 4.537 kJ/kg. When the temperature rises from 70 to 80, the total irreversible loss of the system increases by 5.562 kJ/kg.

4. DESIGN AND MODELING OF CENTRIPETAL TURBINE WITH ORGANIC WORKING MEDIUM

The image of the centripetal organic working fluid mainly consists of volute, guide vane and moving impeller. The volute can provide a uniform circumferential inlet airflow distribution for the vanes, reducing the impact of the airflow on the guide. The moving impeller is the core component of the centripetal turbine of the organic working fluid, which can determine the overall performance of the centripetal turbine.

According to the physical parameters of the selected organic working medium R245fa, the operating parameters of the centripetal turbine are determined. Turbine design is accomplished through design software.

Table 4: Operational parameters of radial turbine expander

Total inlet pressure/kPa	Total inlet temperature/K	Total outlet pressure/kPa	Rated power/kW
914.64	359.15	211.72	120

After software calculation and design, the design parameters are shown in Table 5.

Table 5: Design parameters of the organic radial turbine

Nozzle	NumBlade	17
	Tip Rad	109.8012mm
	Height	10.2615mm
Rotor	NumBlade	12
	Tip Rad	90.9326mm
	Height	10.2615mm
	Outlet Height	54.5596mm
	Alpha	75.48°
	Rotational speed	16358.8rad/m

5. ORGANIC WORKING CENTRIFUGAL CFD CALCULATION AND ANALYSIS

The structural mesh of the centripetal scroll is simulated by ANSYS-ICEM. Due to the complex shape of the blades, the grid is divided by the turbogrid. The grids in this paper are structured grids. The number of grids in each part is shown in Table 5. The total number of grids is 6.86 million.

Table 6: Meshing of the radial turbine

Part	Number
volute	562440
nollze	4085689
rotor	2223467

In this paper, the fixed-length calculation is used, and the wall boundary conditions are set to adiabatic and non-slip. The K-ε turbulence model is selected, the working medium is R245fa, the inlet boundary condition is a given total pressure 914.64kPa, the total temperature is 359.15K, and the outlet static pressure condition is Static pressure 193.56 kPa, the connection form of dynamic and static leaf interface adopts the built-in Frozen-rotor form of CFX-Pre.

Table 7: Comparison of CFD results and design

	Unit	Design value	Calculated value
Mass of flow	Kg/s	5.24	5.36
Total inlet pressure	kPa	914.64	914.13
Total inlet temperature	K	359.15	358.86
Static outlet pressure	kPa	196.88	197.11
Power	kW	120	122.12
Efficiency	%	89	83.41

Table 7 shows the results of centripetal CFD calculations, and compared with the design values, the deviation of the flow rate from the design value is within 5%, indicating that the design meets the requirements.

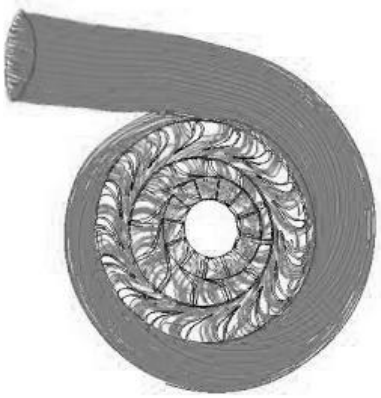

Figure 6: Streamline in the radial turbine

Figure 6 shows the overall streamline diagram of the ORC toward the turbine. The flow of the working medium in the complete machine is in good condition and there is no obvious separation in the volute, guide vane and moving impeller. The volute achieves diversion and distribution of gas. The flow lines are evenly distributed and the flow conditions are good.

6. CONCLUSION

(1) Considering various considerations, R245fa is selected as the circulator of the low-temperature solar thermal power generation Rankine cycle system with high thermal efficiency, and the irreversible loss is also relatively small.

(2) Through the centripetal turbine design and CFD simulation analysis, comparing the calculated values and design values, it has certain reference value for the subsequent turbine optimal design. The designed system basically meets the requirements and can realise the utilization of solar energy, providing reference value for future engineering practice.

7. REFERENCES

García-Rodríguez L, Blanco-Gálvez J. Solar-heated Rankine cycles for water and electricity production: POWERSOL project[J]. Desalination, 2007, 212(1):311-318.

Huang X. Research on double cycle screw expander system with organic working fluids[D]. Tianjin University, 2006.

Li J. Optimization and test of low-medium temperature solar thermal electric generation using Organic Rankine Cycle[D].University of Science and Technology of China, 2011.

Ma G, Ni C, Zhou L.Preliminary experiments of thermal performance of solar collector for medium temperature applications[J].Acta Energiae Solaris Sinica, 2010.

Saitoh T S, Proposed solar rankine cycle system with phase change steam accumulator and CPC solar collector, 2002, 37th Intersociety Energy Conversion Engineering Conference (IECEC), Paper No. 20150

Saleh B, Koglbauer G, Wendland M, et al. Working fluids for low-temperature organic Rankine cycles[J]. Energy, 2007, 32(7):1210-1221.

Wang X D, Zhao L, Wang J L, et al. Performance evaluation of a low-temperature solar Rankine cycle system utilizing R245fa[J]. Solar Energy, 2010, 84(3):353-364.

Wen K. Research on waste heat power generation technology of aluminum electrolysis cell flue gas based on organic Rankine cycle[D]. Central South University, 2009

www.linuo-paradigma.com

Yagoub W, Doherty P, Riffat S B. Solar energy-gas driven micro-CHP system for an office building[J]. Applied Thermal Engineering, 2006, 26(14):1604-1610.

351: Study on the evolution of living energy consumption structure for urban residents in China under the background of low-carbon

Fangchun PENG[1], Yuxi SHEN[1], Hao XU[1]

[1]School of Economics and Management, Hubei University of Technology

The proportion of urban residents' living energy consumption in total energy consumption is increasing, and its structural evolution is related to the sustainable development of China's energy structure and the green development. Based on 1997-2016 as samples, this paper analysis the spatial and temporal evolution of energy consumption structure for urban residents in China. After building the vector autoregressive model containing information entropy of energy consumption structure, the per capita consumer expenditure of urban residents and urbanization rate, the influence of per capita consumer expenditure and urbanization rate on the evolution of urban residents' living energy consumption structure was studied by impulse response analysis and variance decomposition. The result shows: in terms of time, the information entropy presents the "inverted U" tendency, namely the energy consumption for urban residents has gradually evolved from disorder to order and from low order to high order; in terms of space, there are significant differences in the living energy consumption structure in eastern, central and western regions of China. The impact of per capita consumer expenditure and urbanization rate on the living energy consumption structure is significantly different. The structure has obvious lag effect on the impact of per capita consumer expenditure and less fluctuation. And the response to the impact of urbanization rate has repeated fluctuations. Under the background of low-carbon, the optimisation of China's living energy structure needs not only give full play to the role of the market in energy structure adjustment, but also give full play to the role of the government in macro-control.

Keywords: living energy consumption structure; the information entropy; per capita consumer expenditure; vector autoregressive model

1. INTRODUCTION

The structure of living energy consumption restricts the development of economy and society. From 2000 to 2016, China's residential energy consumption increased from 16,695,05 to 542,0866 tons of standard coal. Over 17 years, the share of living energy in total energy consumption increased from 11.36 % to 12.44%. The adjustment of energy consumption structure can effectively reduce carbon emissions (Chen, 2011; Fang, 2016). Liu (2015) used the Markov chain model based on OLS estimation. She believes that the change of energy consumption structure is reflected in the continuous decline of the proportion of high carbon energy consumption mainly based on coal, while the proportion of high efficiency and clean energy is increasing. In view of this, exploring suitable living energy consumption structure, improving energy efficiency, reducing the pollutant emissions of energy utilization, promoting the establishment of modern power system, improving residents' quality of life, is the only way to build our living energy consumption sustainable utilization pattern (Wan, 2016; Wan, 2017). It is an urgent requirement for environmental protection, energy conservation and emission reduction to promote the upgrading of the living energy consumption. Therefore, in this paper, we analyse the changing characteristics and influencing factors of the energy structure of urban residents in China. This is of great practical significance to the analysis of living energy trends, the promotion of sustainable development of energy consumption and the formulation of energy development strategies.

The analysis of living energy consumption structure generally starts from direct and indirect consumption. Zhang (2011) divided living energy into direct and indirect parts. The trend of energy consumption structure of urban and rural households and the corresponding carbon emissions were studied by means of lifestyle analysis. Li (2013) used the co-integration theory and structural decomposition analysis model to find that the indirect living energy consumption is much greater than direct consumption at present, and the gap between urban and rural areas is decreasing day by day. Luo Guanghua et al. (2010) used structural evolution indicators such as structure entropy to analyse the characteristics of living energy consumption structure evolution from 1980 to 2007. It was found that the structure of living energy in China showed a trend towards higher and cleaner development (Luo, 2010).

From the perspective of analysis method, it varies according to the analysis perspective. Pachauri and Spreng (2002) used input-output method to analyse the energy demand of Indian households. It is found that India's direct living energy accounts for the largest proportion of non-commercial energy consumption, while half of indirect energy consumption is food demand consumption. Bin and Dowlatabadi (2005) used consumer lifestyle analysis to analyse the UK's energy use. It is found that the indirect living energy in Britain is more than twice the direct living energy. It is a more general view to analyse the energy structure of life from the perspective of energy types. Generally speaking, the early researches are mainly based on statistical data to summarise the trend. With the deepening of research, most studies start from the construction of indexes reflecting the living energy structure, and measure the change of structure (Geng, 2004; Tian, 2009; Chuai, 2009). In fact, this kind of index is mostly based on information entropy theory. This is because information entropy can effectively reflect the dynamic change of nonlinear irreversible system.

The existing research provides the theoretical basis and the method worth learning. But they're all horizontal comparisons of spatial dimensions. In this paper, we analyse the changing characteristics and influencing factors of the energy structure of urban residents in China from the perspective of time and space. The innovation of this paper is to reveal the formation factors and mechanism of "inverted U" curve. The paper puts forward the mechanism and package policy of Chinese government and market.

2. THE DESCRIPTION OF LIVING ENERGY CONSUMPTION STRUCTURE FOR URBAN RESIDENTS IN CHINA

2.1. The change of living energy consumption in time

In this paper, we adopt the energy division standard of China energy balance (standard amount) in China energy statistics yearbook. We divided the urban living energy into raw coal, gasoline, natural gas, heat power and other energy. In view of the availability of data, we analyses the development and current situation of living energy consumption structure for residents in China from 1997 to 2016. The per capita consumption of energy is shown in Figure 1.

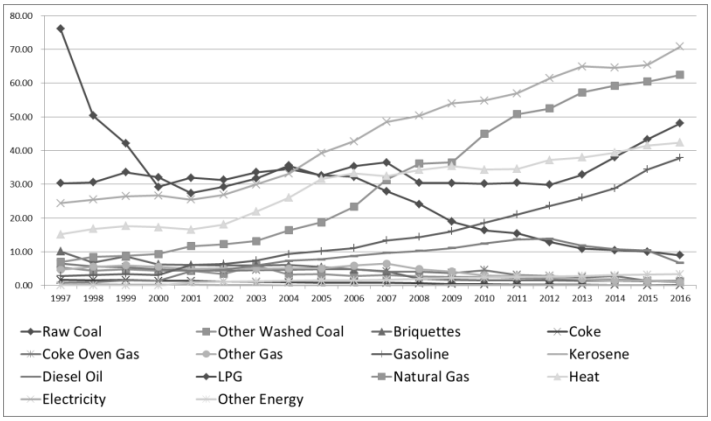

Figure 1: 1997-2016 China's per capita consumption of living energy

Data source: calculated and sorted according to China energy statistics yearbook.

In the 20 years from 1997 to 2016, except for the slight decline in 2008, the per capita living energy consumption showed a general trend of "first declining and then rising". From 1997 to 2000, it decreased from 185.08kgce to 141.61kgce. From 2000 to 2016, there was an upward trend, with the per capita living energy rising to 285.54kgce. The reason why the year 2000 became a low point is that the Asian financial crisis in 1997 aggravated the external environment of China's economic and social development. The crisis is reflected in the decline in living energy consumption. Entering the new century, China's entry into WTO enables China to participate in the global value chain comprehensively. Prosperity is reflected in a sustained rise in living energy consumption.

The total consumption of coal shows a "decline - rise - decline" trend. The proportion of raw coal consumption accounts for more than 60% of the total consumption of coal, so the trend of raw coal consumption is the determinant of the trend of the total coal consumption. The consumption of other washed coal, briquettes, coke, coke oven gas and other gases is relatively small and basically showing a downward trend. The cause of the change of coal consumption trend is similar to the reason of the total amount of energy consumption in 2000, and the reason for the high point in 2003 is that in 2003 our country put forward the "Scientific Outlook on Development", the economic and social development paid more attention to the environmental protection, so the coal consumption continued to decline.

From 1997 to 2016, the per capita consumption of petroleum, natural gas, thermal energy and electric power continued to rise. Per capita oil consumption rose from 34.2kgce in 1997 to 92.64kgce in 2016. At present, oil has become the largest per capita consumption of urban residents in China. Natural gas rose from 6.97kgce in 1997 to 62.46kgce in 2016. Thermal power increased from 15.15 in 1997 to 42.41kgce in 2016. Electric power increased from 24.4kgce in 1997 to 70.82kgce in 2016, and is now the second largest energy source for per capita consumption of urban residents in China.

From the perspective of internal structure, the ratio of various energy to total living energy presents a similar changing trend with the real scale. The share of coal consumption has fallen from 56.39% in 1997 to 4.85% in 2016. Oil consumption rose from 18.48% in 1997 to 32.44% in 2016 and is now the largest category of energy consumption. Natural gas consumption increased from 3.76% in 1997 to 21.87% in 2016, and electric power consumption increased from 13.18% in 1997 to 24.8% in 2016. It is now the second largest category of urban living energy in China. Taking into account the changing trend of various energy consumption structures, China's living energy consumption has been significantly cleaner, the consumption of coal has dropped significantly, and the consumption of natural gas and electricity has increased substantially.

The analysis of living energy consumption structure from absolute quantity or relative proportion can not accurately measure the change trend of structure. The nonlinearity and irreversibility of energy consumption structure conform to the presupposition of dissipative structure system. Entropy is the irreversible state function that describes the spontaneous evolution of a system. Based on the research methods of Geng Haiqing et al in 2004, we calculates the information entropy, equilibrium and superiority of energy structure in domestic life in China from 1997 to 2016.

Table 1: Information Entropy, Equilibrium, and Dominance of Energy Structure in China during 1997~2016

Year	Information Entropy	Equilibrium	Dominance	Year	Information Entropy	Equilibrium	Dominance
1997	1.87	0.71	0.29	2007	2.13	0.81	0.19
1998	2.00	0.76	0.24	2008	2.10	0.79	0.21
1999	2.06	0.78	0.22	2009	2.07	0.79	0.21
2000	2.08	0.79	0.21	2010	2.06	0.78	0.22
2001	2.18	0.83	0.17	2011	2.03	0.77	0.23
2002	2.17	0.82	0.18	2012	2.00	0.76	0.24
2003	2.18	0.83	0.17	2013	1.95	0.74	0.26
2004	2.16	0.82	0.18	2014	1.95	0.74	0.26
2005	2.15	0.82	0.18	2015	1.92	0.73	0.27
2006	2.14	0.81	0.19	2016	1.87	0.71	0.29

Data source: calculated and sorted according to China energy statistics yearbook.

As shown in Table 1, the information entropy of living energy consumption structure of urban residents presents an "inverted U " trend of "up-down". It rose from 1.87 in 1997 to 2.18 in 2001, basically flat in 2002 and 2003, and then fell to 1.87 in 2016. On the whole, this is consistent with the above two stages of structural change of living energy consumption in China. Before 2001, the information entropy continued to increase because coal consumption dropped rapidly and electricity consumption increased rapidly. At the same time, oil, natural gas and heat are also on the rise. This makes our family living energy consumption structure tends to balance. After 2001, consumption of electricity, oil, natural gas and heat continued to expand, while coal continued to shrink. At this stage, the consumption of oil and electricity occupies a dominant position, so the information entropy continues to decrease.

2.2. The distribution of living energy consumption in space

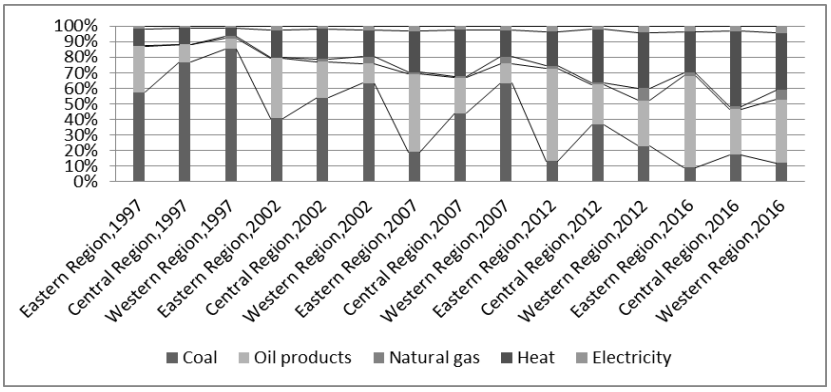

Figure 2: energy structure for living in east, middle and west regions of China

Data source: calculated and sorted according to China energy statistics yearbook.

Figure 2 shows that there are significant differences in the living energy consumption structure in eastern, central and western regions of China. At the same time, the difference varies with time. In 1997, coal accounted for the largest share of living energy consumption, but it was the smallest in the east and the largest in the west. Oil consumption is largest in the east and smallest in the west. This reflects the uneven development of the economy in 1997. This continued until 2012, when coal consumption grew smaller and energy consumption, such as oil and gas, increased. Coal consumption is still the smallest in the east after 2012, but the largest in the middle. Oil consumption is still the largest in the east, but the smallest in the middle. To some extent, this situation reflects the lag of development in central China.

3. RESEARCH DESIGN: "INVERTED U" CURVE AND ITS FORMATION FACTORS

3.1. Selected variables and utilised data

Per capita consumption expenditure and urbanization rate are undoubtedly the key factors influencing its structural evolution. Higher per capita consumer spending has prompted households to choose more convenient, safe and clean energy sources. The history shows the consumption of energy from coal to electricity and natural gas. In the context of differences between urban and rural areas, the increase of urbanization rate means that more families change from extensive rural lifestyle to intensive urban lifestyle. The change of lifestyle leads to the change of energy consumption structure. Therefore, this paper aims to analyse how per capita consumper expenditure and urbanization rate affect the living energy consumption structure in urban China. The living energy consumption structure is replaced by the information entropy of the previous text; per capita consumer expenditure is adjusted at the annual price level based on 1997; the urbanization rate is expressed as the proportion of urban population to the total population. The three variables are represented by *Entr*, *Cons*, and *Urba*, respectively. The above data are from the China statistical yearbook of previous years.

In addition to the above factors, price is also an important factor. But energy prices are largely set by the Chinese government and are not highly marketable. Therefore, the existing energy price system cannot well reflect the relationship between supply and demand in the market and the consumption level of Chinese residents. Therefore, this paper gives up the research on the influence of price factors on the living energy. There are other factors that have an impact on energy demand, such as climate, national macro-policy and lifestyle changes. However, these factors are difficult to quantify or obtain relevant data, so this paper does not consider them.

3.2. Research process

Entr and Urba are dimensionless data, and their value is relatively small, so there is no need for logarithmic processing. Therefore, only logarithmic processing is performed for Cons, and the new variable is LnCons. Since Entr, LnCons, and Urba are all time series data, the stationarity test is required. In this paper, ADF test method is adopted, and the test results are shown in Table 2.

Table 2: Results of unit root test of ADF of each variable

Variable	Inspection form	t-Statistic	1% level	5% level	10% level	Prob.	Conclusion
ΔEntr	(c , 0 , 4)	-3.4693	-4.0044	-3.0989	-2.6904	0.0261	First-order stability
ΔLnCons	(c , 0 , 0)	-3.2838	-3.8574	-3.0404	-2.6606	0.0314	First-order stability
ΔUrba	(c , 0 , 0)	-4.2291	-3.8574	-3.0404	-2.6606	0.0047	First-order stability

Table 2 shows that Entr, LnCons, and Urba are all integrated of order 1, so there may be a co-integration relationship between them. Since all three variables are integrated of order 1, if VAR model is directly established, the model is unstable and the impulse response function is not convergent. Therefore, the first difference of each variable is adopted to establish the VAR model. For the sake of brevity, the following variable differences are still expressed in the name of the original variable without affecting comprehension. Before establishing VAR model, the determination of lag order is especially important. In this paper, we refer to LR statistics, PPE final prediction error, AIC information criterion, SC information criterion and HQ information criterion to determine the lag order of 2, as shown in Table 3.

Table 3: Selection criteria of lag order of VAR model

Lag	LogL	LR	FPE	AIC	SC	HQ
0	136.1911	NA*	7.51E-11	-14.79902	-14.65062*	-14.77855
1	145.9627	15.20018	7.05e-11*	-14.88474*	-14.29116	-14.80290*

** indicates lag order selected by the criterion.*

At the same time, before establishing the VAR model, the granger causality test was conducted for Entr, LnCons and Urba to determine whether variables are suitable for dependent variables. The test results are shown in Table 4. It is worth noting that the granger causality is only a statistically causal relationship, not a causal relationship in fact.

Table 4: Granger Causality Test

Null Hypothesis:	F-Statistic	Prob.	Conclusion
LnCons dose not Granger Cause *Entr*	2.87318	0.0733	rejected
Entr dose not Granger Cause *LnCons*	0.31645	0.7313	accepted
Urba dose not Granger Cause *Entr*	7.48253	0.0025	rejected
Entr dose not Granger Cause *Urba*	0.96467	0.3934	accepted
Urba dose not Granger Cause *LnCons*	2.04641	0.1481	accepted
Lncons dose not Granger Cause *Urba*	1.22512	0.309	accepted

Table 4 shows that LnCons and Urba are the granger causes of Entr, so in the VAR model below, Entr can be interpreted variables, while LnCons and Urba are interpreted variables. Through the calculation of EViews software, the VAR model of Entr, LnCons and Urba is obtained in this paper. The VAR model needs to be tested for stability. In this paper, AR root diagram is adopted to test. The test results are shown in Figure 3. Figure 3 shows that the modules of AR root of VAR model are all less than 1 and within the unit circle, which indicates that the above VAR model is stable.

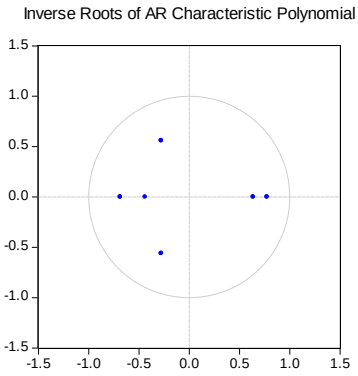

Figure 3: AR root diagram

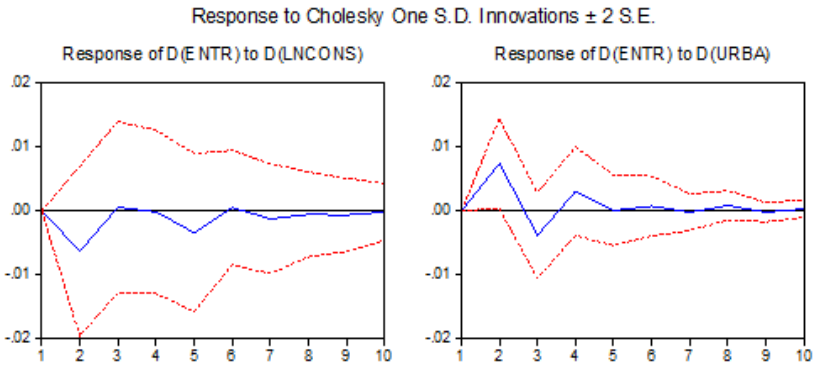

Figure 4: impulse response diagram

The impulse response function based on VAR model is used to measure the influence of the current and future values of each variable after the random disturbance term is impacted by a standard deviation. This article focuses on Entr's response to LnCons and Urba shocks. Figure 4 shows that when a positive impact is given to LnCons, Entr decreases in phase 2, increases in phase 3 and 4, decreases in phase 5, and then gradually stabilises, but the cumulative effect is negative. When a positive impact for Urba, 2 rapidly rising, 3 drops, and in the third phase of the maximum, slightly rebounded. 4, 5 after stable gradually, but the cumulative effect is negative.

Variance decomposition is to analyse the contribution of each structural shock to the change of endogenous variables. In this paper, variance decomposition method is adopted to investigate the influence of LnCons and Urba changes on the structural change of domestic living energy consumption in China. The contribution of each variable to information entropy change is shown in table 5. Table 5 shows that the change in per capita consumption expenditure contributed 6% to the change in the structure of living energy consumption in the 10th period. The change in urbanization rate contributed nearly 9% to the structural change in the 10th period. In general, per capita consumption and urbanization rate do not contribute much to the living energy of urban residents, but the impact of urbanization is relatively large.

Table 5: Variance Decomposition

Period	S.E.	*Entr*	*LnCons*	*Urba*
1	0.024028	100	0	0
2	0.025971	85.97829	5.854146	8.167565
3	0.028703	86.72483	4.831862	8.443304
4	0.02916	86.03389	4.684608	9.281506
5	0.029597	85.11897	5.870939	9.010095
6	0.029779	85.20646	5.828908	8.964636
7	0.029904	85.15621	5.949276	8.894519
8	0.029955	85.092	5.962214	8.945783
9	0.029997	85.08257	5.991506	8.925926
10	0.030015	85.08637	5.986425	8.927204

Based on the VAR model above, Johansen co-integration test was conducted. The test results are shown in Table 5. Table 5 shows that at a significance level of 5%, we reject the original assumption that at least one co-integration equation exists. There are at least two co-integration equations between variables Entr, LnCons and Urba, namely two long-term stable relationships. The first co-integration equation is adopted in this paper. The normalised co-integration relationship can be expressed as:

Equation 1: cointegration equation $$Entr = -0.1081LnCons - 3.1033Urba$$
$$(-0.088)\quad(-0.6686)$$

Table 6: Johansen Cointegration Test Results

Hypothesised No. of CE(s)	Eigenvalue	Trace Statistic	0.05 Critical Value	Prob.	Conclusion
None *	0.798453	41.26963	29.79707	0.0016	Rejected
At most 1 *	0.540876	15.64194	15.49471	0.0475	Rejected
At most 2	0.180604	3.186998	3.841466	0.0742	Accepted

** denotes rejection of the hypothesis at the 0.05 level*

Equation 1 indicates that there is a long-term co-integration relationship between per capita household energy structure, per capita consumer expenditure and urbanization rate between 1997 and 2016. From the positive and negative sign of the coefficient, both LnCons and Urba are negative, that is, per capita consumer expenditure and urbanization rate are negatively correlated with information entropy of per capita living energy structure. This is because, with the improvement of per capita consumer expenditure, households tend to consume more convenient, safe and clean energy, which makes the energy consumption structure unbalanced. Urbanization rate at the same time improve the rural life of family from extensive use can be transformed into intensive urban life with, so as to make the electricity, gas and other energy in life with the rise in the can, reduce entropy.

4. DISCUSSION

In the context of low-carbon, it is necessary to optimise China's living energy consumption structure for urban residents. We need to give full play to the role of the market in price regulation and the role of the government in macro-control.

First, governments should formulate energy policies from a global and strategic perspective. The government should strengthen the regulation of energy markets, improve the energy tax system, maintain a fair and just market environment, mobilise the parties participate in energy conservation and emissions reduction action actively, and let the public can consciously to participate in the green consumption action. At the same time, the government should improve energy utilization efficiency by means of institutional innovation and technological progress. We need to promote changes in the way energy is used, actively support the clean energy industry, and achieve low-carbon and marketization of the energy industry.

Second, the government should establish and improve the price mechanism of energy market and increase the subsidy to the research and development of efficient energy technology. At the same time, we will strengthen cooperation in energy technology between countries, absorb advanced international energy technology and realise diversified and complementary supply of various types of energy.

Finally, we will accelerate the restructuring of the living energy consumption and increase the share of clean energy consumption. In order to achieve the goal of energy conservation and emission reduction, the government should strengthen the control over coal and oil consumption and reduce its share in the total energy consumption. At the same time, the government needs to increase funding for new and renewable energy sources, mainly natural gas, primary electricity and other clean energy sources, so as to increase the proportion of clean energy in the consumption structure.

5. CONCLUSIONS

In this paper, the information entropy is used to measure the change of living energy consumption structure for urban residents. The information entropy of living energy consumption structure presents an "inverted U-shaped" curve, namely China's urban living energy consumption has experienced a process of transformation from low-end structure to high-end structure, and has gradually realised the evolution from disorder to order. This process took 2001 as the boundary. Before 2001, China's living energy consumption was mainly coal, which was a kind of extensive structure of living energy. After 2001, electric power consumption dominated, and it is a kind of efficient living energy consumption structure.

Since then, a VAR model including three variables which are the information entropy, the per capita consumer expenditure and urbanization rate was built and the impulse response analysis and variance decomposition analysis were carried on. The results showed that the impact of per capita consumer expenditure and urbanization rate on the living energy consumption structure was significantly different. The living energy consumption structure has obvious lag effect on the impact of per capita consumer expenditure and less fluctuation. However, the living energy consumption structure has repeated fluctuations in response to the impact of urbanization rate. And the results of variance decomposition show that the contribution of urbanization rate to the improvement of living energy consumption structure is significantly greater than that of per capita consumption. This also indicates that the improvement of living energy consumption structure in urban China from 1997 to 2016 is mainly the result of the increase of urbanization rate. In order to test whether there is a long-term stable relationship between the above three variables, the co-integration relationship is tested and the co-integration equation is obtained. The results show that information entropy is negatively correlated with per capita consumer expenditure and urbanization rate. In other words, the increase of per capita consumer expenditure and urbanization rate will lead to imbalance in the living energy consumption structure consumption and shift energy consumption from low-end energy to high-end energy.

With the continuous rise of per capita income, people's requirements on the quality of life are also constantly improving. However, whether the living energy consumption structure is reasonable depends not only on income growth. China is still industrializing and urbanizing, and energy consumption will continue to grow in the foreseeable future. Therefore, it is one of the important contents of current energy work to construct a reasonable energy consumption structure. In view of the above analysis, we believe that the living energy consumption structure can be improved by increasing per capita consumer expenditure and urbanization rate. At present, the improvement of urbanization rate is still an important factor for the improvement of living energy consumption structure. Therefore, we should improve the quality of urbanization by improving the living standard and quality of life, so as to improve the living energy consumption structure more quickly and efficiently. In the future when the urbanization rate reaches a certain level, it is more necessary to raise the level of per capita consumer expenditure.

6. REFERENCES

Bin S, Dowlatabadi H. Consumer Lifestyle Approach to US Energy Use and The Related CO2 Emissions[J].Energy Policy, 2005, 33(2):197~208.

Chen Q, Long Z. Econometric Analysis on the Influence Factors of Chinese Provincial Carbon Dioxide Emissions [J]. China Population, Resources and Environment, 2011,21(11):15-20.

Chuai X, Huang X, Wang Q et al. The Dynamic Analysis on The Energy Resource in China Based on Shannon’s Entropy and Its Countermeasures[J]. Resources Science,2009, 31(8):1280~1285.

Fang D, Dong W, Yu Q. Optimization of China's Energy Consumption Structure under Trend of Low-carbon Transition[J]. Technical Economy, 2015,(01):27-33.

Geng H, Gu S, Guo D. Analyses on Evolution of Household Energy Consumption Structure Based on Information Entropy. [J].Journal of Natural Resources, 2004,19(2):257~262.

Li Z. The Structure and the Influence Factors of Household Energy Consumption in China[D]. Journal of Harbin Institute of Technology,2013

Liu Y, Zhao G. The Evolution Analysis of China's Energy Consumption Structure in The Constraints Of Energy Saving and Carbon Emissions Reduction[J]. On Economic Problems, 2015 (01):27-33

Luo G, Niu S, Zhao C et al. The Evolution of Direct Living Energy Structure in Chinese Residents[J]. Inquiry into Economic Issues,2010(7):40~44.

Pachauri S, Spreng D. Direct and Indirect Energy Requirements of Households in India[J].Energy Policy,2002,30(6):511~523.

Tian Z, Guan Z, Wang S. Evolution of Energy Consumption Structure Based on Information Entropy[J].Journal of Transportation Systems Engineering and Information Technology,2009,9(1):17~121.

Wan W, Zhao X, Wang W. Spatial-temporal patterns and impact factors analysis on carbon emissions from nergy consumption of urban residents in China[J]. Acta Scientiae Circumstantiae, 2016,36(9),3445~3455.

Wan W, Zhao X, Wang W. Analysis of spatio-temporal patterns of carbon emission from energy consumption by rural residents in China[J]. Acta cologica Sinica,2017,37(19): 6390-6401.

Zhang X, Niu S, Zhao C, Hu L. The Study on Household Energy Consumption and Carbon Emissions in China's Urbanization [J]. China Soft Science,2011(09):65-75.

352: Simulation of thermal management for perovskite solar cells

Li FANG[1], Chuyun HUANG[2], Hu XIE[3]

[1] Hubei Collaborative Innovation Center for High-efficiency Utilization of Solar Energy, Hubei University of Technology, Wuhan 430068, China, 75515078@qq.com
[2]Hubei Collaborative Innovation Center for High-efficiency Utilization of Solar Energy, Hubei University of Technology, Wuhan 430068, China, 6981605@qq.com
[3] School of Science, Hubei University of Technology, Wuhan 430068, China, 2289728371@qq.com

The thermal stability of the PSCs (perovskite solar cells) is one of critical problem for its commercialization. With help of COMSOL software, we create a simplified heat transfer model of PSCs and analyse the temperature distribution and variation of PSCs by means of the numerical simulation. The results show that under the environment temperature of 45 ^{o}C and the radiation intensity of 1000 W/m^{2}, the temperature at the perovskite layer can reach around 85 ^{o}C while the copper substrate used as a heatsink is employed in the PSCs, the temperature at the perovskite layer can be decreased to 75.5 ^{o}C. The performance on the thermal management of the copper substrate with different thickness has also been investigated, from which we can conclude that the thickness of the copper should be optimised.

Keywords: Perovskite solar cells, thermal management, temperature, simulation

1. INTRODUCTION

Halide perovskites have attracted much attention for solar cell application due to their unique properties such as favorable electrical properties (Mitzi, 1994: page 467; Mitzi, 1995: page 1473), tunable optical band gap (Noh, 2013: page 1764; Pellet, 2014: page 3151), long carrier diffusion lengths (Xing, 2013: page 344; Stranks, 2013: page 341) and solution processability (Liu, 2014: page 133; Sun, 2014: page 399; Zhao, 2014: page 4175). Intensive efforts have been devoted to improving the morphology and properties of the perovskite layers, optimising the processing techniques (Heo, 2013: page 486; Leijtens, 2014: page 1096; Eperon, 2014: page 151; Barrit, 2017: page 1; Tao, 2015: page 2365), identifying new electron and hole transport materials (Yin, 2017: page 10752; Bera, 2014: page 28494; Wang, 2015: page 849; Rao, 2016: page 7800; Tong, 2016: page 34464; Yu, 2016: page 6173), aiming at enhancing the overall photovoltaic performance. A fast development was achieved by improving the certified efficiency to 22.1% in 2016 (Saliba, 2016: page 1989). For the commercialization of the perovskite photovoltaic devices, the stability of PSCs is equally important with the high efficiency. Factors affecting stability of perovskite materials and devices have been investigated. Usually, the degradation of the PSCs mainly stems from three aspects: heat, illuminations and moisture. Compositional engineering (Misra, 2015: page 326; Eperon, 2014: page 206; Saliba, 2016: page 206) advanced encapsulations (Habisreutinger, 2014: page 5561) and UV-filter (leijtens, 2013: page 2885) technologies have been developed in order to protect the PSCs from degradation. Regardless of the influence of illuminations and moisture, it is expected to be difficult to control heat accumulation inside a device which can be conducted from outside environment or generated by solar cells assembly. In outdoor condition, the accumulated heat may lead to the temperature of a device as high as 85ºC assuming the outside temperature is 45ºC (Li, 2015: page 551). Degradation of the PSCs is thus dependent on controlling the heat inside a device, which indicates that thermal stability of the PSCs is one of critical subjects. Our work focuses on the simulation of the thermal distribution in the perovskite layers by COMSOL software and the research of thermal management of the PSCs by adding a heatsink layer.

2. THERMAL MODEL OF THE PSCs

The PSCs employ a typical mesostructured (m)-TiO_2-$CH_3NH_3PbI_3$ -spiro-OMeTAD architecture. Au is used as the back contact acting as electron-blocking layer. A schematic presentation of the PSCs is shown in Figure 1, which is a sandwich-like structure. The sunlight radiates to the surface of the FTO glass, and then goes inside of the PSCs. Finite element software COMSOL Multiphysics that allows the mesh size varied in different regions of the simulation is used so that the number of elements remained manageable. Figure 2 shows the mesh diagram in different layer of PSCs.

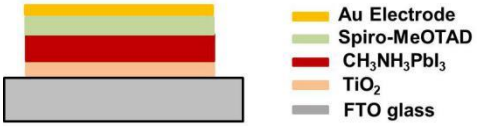

Figure 1: schematic cross section of the PSCs

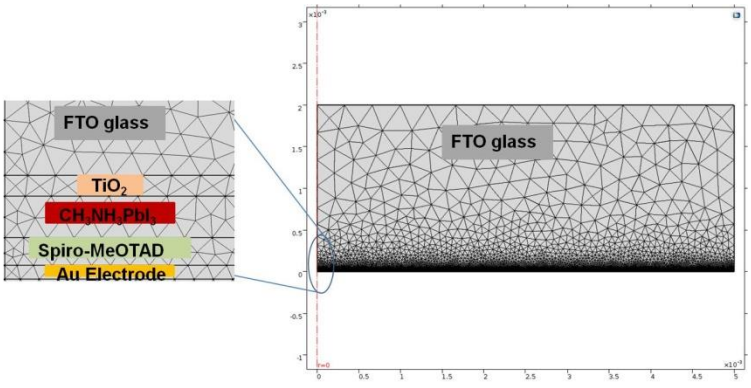

Figure 2: Mesh diagram of PSCs layers in COMSOL Multiphysics

To simplify the physical mode for PSCs chips, the physic properties related to thermal management can be defined as three parameters: heat transfer between chip and the extra environment (boundary condition), heat source, and physical parameters of different layers. Moreover, the following two assumptions are made:

(1) Considering the thin layers of the PSCs, the heat transfer on the sides of the PSCs is ignored, and the boundary condition at the sides can be set as thermal insulation;

(2) The physical properties of the layer materials of the PSCs are not varied with the temperature and the time.

2.1. Heat transfer boundary conditions

The radiation which radiated on the top surface of the PSCs is defined as a constant. The PSCs exchange the heat with the outside. With the convection at the boundary and the radiative heat transfer at the boundary, the stationary heat transfer function can be written as:

Equation 1: Stationary heat transfer equation

$$\boldsymbol{\rho c_p \nabla T + \nabla \cdot (-k \nabla T) = Q + h(T_e - T_w) + \varepsilon \sigma (T_e^4 - T_w^4)}$$

Where:

ρ = the density (Kg/m^3)
c_p = the heat capacity (J·kg^{-1}·K^{-1})
k = thermal conductivity (W·m^{-1}·K^{-1})
Q = the heat generation (W/m^3)
T = the temperature (K)
h = the heat transfer coefficient (W·m^{-2}·K^{-1})
ε = surface emissivity (%)
σ = Stefan Boltzmann constant (W·m^{-2}·K^{-4})
T_e = ambient temperature (K)
T_W = the surface temperature of the PSCs (K)

2.2. Heat source

The heat source of the PSCs mainly comes from two parts. On part is generated from the structure materials which absorb the solar radiation and convert it directly into heat. Another part is from the perovskite layer in which the absorbed radiation is lost in form of the heat energy. Considering that the most of the sunlight is absorbed in the FTO layer, TiO_2 layer and Perovskite layer, the heat loading was therefore assumed to occur in these three layers. In the multi- layers solar cell device, the heat load distribution in the parallel plane is treated as uniform. The heat load in the FTO layer, in z- coordinate (perpendicular direction) can be taken to be

Equation 2: Heat source in FTO layer

$$\boldsymbol{Q_{FTO}(z) = D_{in} \cdot \eta_{FTO} \cdot T_{FTO} \cdot \alpha_{FTO} \cdot \exp\left(-\alpha_{FTO}(z_{oFTO} - z)\right)}$$

Where:

z = the spatial coordinate
η_{FTO} = the fraction of the light power absorbed in the FTO layer converted to heat
T_{FTO} = the transmission of light through FTO, with a typical value of ~ 80%
D_{in} = the light density reaching on the solar cell
α_{FTO} = the effective light absorption coefficient in the FTO layer
z_{oFTO} = the z-coordinate of the interface between the FTO layer and air

The heat load in the TiO_2 layer can be taken to be

Equation 3: Heat source in TiO_2 layer

$$\boldsymbol{Q_{TiO_2}(z) = D_{in} \cdot \eta_{TiO_2} \cdot T_{FTO} \cdot \alpha_{TiO_2} \cdot \exp\left(-\alpha_{TiO_2}(z_{oTiO_2} - z)\right) \cdot exp(-\alpha_{FTO} \cdot t_{FTO})}$$

Where:

z = the spatial coordinate
η_{TiO2} = the fraction of the light power absorbed in the TiO_2 layer converted to heat
T_{FTO} = the transmission of light through FTO, with a typical value of ~ 80%
D_{in} = the light density reaching on the solar cell
α_{TiO2} = the effective light absorption coefficient in the TiO_2 layer
α_{FTO} = the effective light absorption coefficient in the FTO layer
z_{oTiO2} = the z-coordinate of the interface between the TiO_2 layer and the FTO layer
t_{FTO} = the thickness of FTO layer

The heat load in the perovskite layer can be taken to be

Equation 4: Heat source in perovskite layer

$$\boldsymbol{Q_{per}(\mathrm{z}) = D_{in} \cdot \eta_{per} \cdot T_{FTO} \cdot \alpha_{per} \cdot \exp\left(-\alpha_{per}\left(z_{oper} - z\right)\right) \cdot exp\left(-\alpha_{TiO_2} \cdot t_{TiO_2}\right) \cdot exp\left(-\alpha_{FTO} \cdot t_{FTO}\right)}$$

Where:

z = the spatial coordinate
η_{per} = the fraction of the light power absorbed in the perovskite layer converted to heat
T_{FTO} = the transmission of light through FTO, with a typical value of ~ 80%
D_{in} = the light density reaching on the solar cell
α_{per} = the effective light absorption coefficient in the perovskite layer
z_{oper} = the z-coordinate of the interface between the perovskite layer and TiO_2 layer
α_{TiO2} = the effective light absorption coefficient in the TiO_2 layer
α_{FTO} = the effective light absorption coefficient in the FTO layer
t_{FTO} = the thickness of FTO layer
t_{TiO2} = the thickness of TiO_2 layer

2.3. Physical parameters of the materials

In the COMSOL thermal model for the PSCs, the physical parameters of the materials are presented in Table 1 (Park, 2015: page 65).

Table 1: Thermal performance parameters of materials

Materials	Density (Kg/m^3)	Heat capacity ($J \cdot kg^{-1} \cdot K^{-1}$)	Thermal conductivity ($W \cdot m^{-1} \cdot K^{-1}$)	Thickness (um)	Fraction of heat convertion	Absorption coefficient (1/cm)
FTO	2452	645.6	1.0260	2000	1	1.08
TiO2	4230	710	6.3842	0.15	1	0.002
$CH_3NH_3PbI_3$	880	600	0.34	0.3	0.82~0.9	10^5
spiro-OMeTAD	790	500	0.156	0.2	1	1858
Au	19300	125	315	0.1	1	3.1×10^5

3. SIMULATION RESULTS

Under the environmental temperature condition of 45 ºC and the radiation intensity of 1000 W/m^2, the calculated stationary temperature distribution in the device give the highest temperature of ~85°C (385 K) as shown in Figure 3, which is same to the experimental results of 85°C (Li, 2015: page 551). This result also verifies the validity of the numerical module developed in COMSOL software. Results in Figure 3 reveal that the most part of radiation is absorbed in perovskite and transferred to heat, heat accumulated in the thin layers which cause the temperature rise. The black arrows in Figure 3 show the direction of heat dissipation. The heat dissipation mostly occurs through the bottom of device via heat flux, which limited part of heat dissipated from top surface of device because of the low heat conductivity of FTO glass.

In this work, we proposed a new type of PSCs with bottom substrate shown in Figure 4. The copper is employed as bottom substrate which can be integrated with solar cell device either by bonding or by electro-plating. The thermal conductivity of

copper material is about 400 $W \cdot m^{-1} \cdot K^{-1}$. For the flexible solar cell application, flexible substrate like graphite with high thermal conductivity may be proposed. The thermal performance of PSCs with bottom substrate structure is illustrated in Figure 4. Under the environmental temperature and the radiation intensity, the same PSCs structure as shown in Figure 3 is considered, combined with a 500 μm thick Cu substrate. The black arrows in Figure 4 show that the heat dissipation efficiently occurs through the bottom cooper substrate because of the high value of thermal conductivity, and then dissipated through the bottom surface of copper substrate via heat flux. Due to efficient heat dissipation through the bottom substrate, the calculated highest temperature in solar cell device is 75.5ºC (348.5 K), which is 9.5 K lower than PSCs devices without bottom substrates.

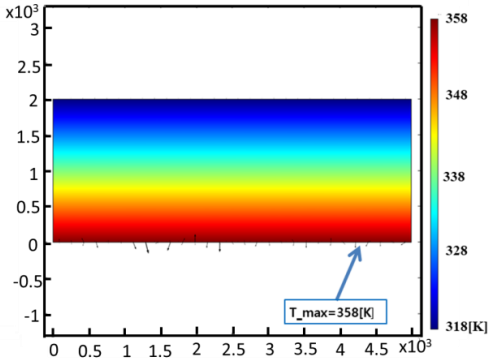

Figure 3: Simulation result of temperature distribution in different layers of the PSCs

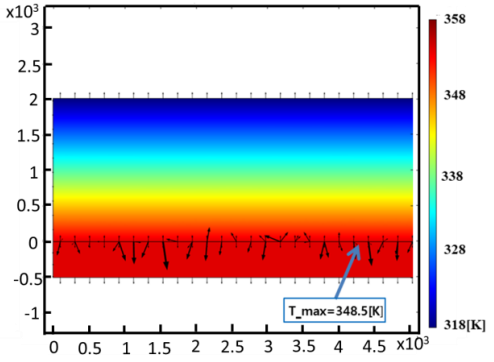

Figure 4: Simulation result of temperature distribution in different layers of the PSCs with Cu substrate

In order to optimise the thickness of the copper substrate, the maximum temperature in the perovskite layer is calculated versus copper thickness and the calculated curves are displayed in Figure 5. Simulation results reported in Figure 5 show that the copper thickness should be larger than 450 μm for efficient heat dissipation to achieve temperature decrease of 10 K by proper thermal management in the PSCs chips.

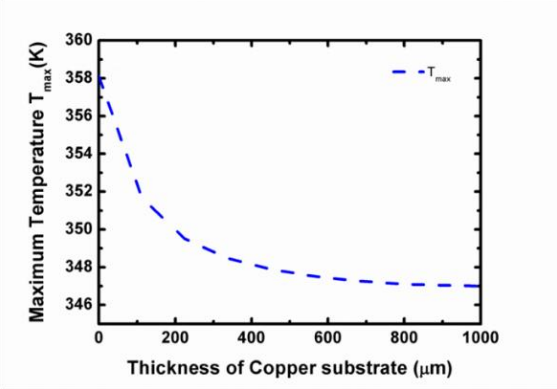

Figure 5: Heat transfer performance depends on the thickness of copper substrate

4. CONCLUSION

Based on the working principle and the structure of the PSCs, the numerical model of the heat transfer in the PSCs had been build up. The results show that under the environment temperature of 45°C and the radiation intensity of 1000 W/m^2, the temperature at the perovskite layer can reach around 85°C while the copper substrate used as a heatsink is employed in the PSCs, the temperature at the perovskite layer can be decreased to 75.5°C. Moreover, the result shows that the thicker Cu substrate had a better heat transfer performance. This study is expected to provide important insight into design thermally stable PSCs.

5. REFERENCES

Barrit Dounya, Sheikh Arif D., Munir Rahim, Barbé Jérémy M., Li Ruipeng, Smilgies Detlef-M., Amassian Aram, 2017. Hybrid Perovskite Solar Cells: In Situ Investigation of Solution Processed PbI2 Reveals Metastable Precursors and a Pathway to Producing Porous Thin Films. Journal of Materials Research, 21, 1-9.

Bera Ashok, Wu Kewei, Sheikh Arif, Alarousu Erkki, Mohammed Omar F., Wu Tom, 2014. Perovskite Oxide $SrTiO_3$ as an Efficient Electron Transporter for Hybrid Perovskite Solar Cells. The Journal of Physical Chemistry C, 118, 28494-28501.

Eperon Giles E., Burlakov Victor M., Docampo Pablo, Goriely Alain, Snaith Henry J., 2014. Morphological Control for High Performance, Solution-Processed Planar Heterojunction Perovskite Solar Cells. Advanced Functional Materials, 24, 151-157.

Eperon Giles E., Stranks Samuel D., Menelaou Christopher, Johnston Michael B., Herz Laura M., Snaith Henry J., 2014. Formamidinium Lead Trihalide: A Broadly Tunable Perovskite for Efficient Planar Heterojunction Solar Cells. Energy & Environmental Science, 7, 982-988.

Habisreutinger Severin N., Leijtens Tomas, Eperon Giles E., Stranks Samuel D., Nicholas Robin J., Snaith Henry J., 2014. Carbon Nanotube/Polymer Composites as a Highly Stable Hole Collection Layer in Perovskite Solar Cells. Nano Letter, 14, 5561–5568.

Heo Jin Heo, Im Sang Hyuk, Noh Jun Hong, Mandal Tarak N.,Lim Choong-Sun, Chang Jeong Ah, Lee Yong Hui, Kim Hi-jung, Sarkar Arpita, Nazeeruddin Md.K., Grätzel Michael, Seok Sang Il, 2013. Efficient Inorganic–organic Hybrid Heterojunction Solar Cells Containing Perovskite Compound And Polymeric Hole Conductors. Nature Photonics, 7, 486-491.

Jeon Nam Jong, Noh Jun Hong, Kim Young Chan, Yang Woon Seok, Ryu Seungchan, Seok Sang Il, 2014. Solvent Engineering For High-Performance Inorganic-Organic Hybrid Perovskite Solar Cells. Nature Material, 13, 897-903.

Leijtens Tomas, Eperon Giles E., Pathak Sandeep, Abate Antonio, Lee Michael M., Snaith Henry J., 2013. Overcoming Ultraviolet Light Instability of Sensitized TiO2 with Meso-Superstructured Organometal Tri-Halide Perovskite Solar Cells. Nature Communication, 4, 1-8.

Leijtens Tomas, Lauber Beat, Eperon Giles E., Stranks Samuel D., Snaith Henry J., 2014. The Importance of Perovskite Pore Filling in Organometal Mixed Halide Sensitized TiO2-Based Solar Cells. The Journal of Physical Chemistry Letters, 5, 1096-1102.

Li Xiong, Tschumi Manuel, Han Hongwei, Babkair Saeed Salem, Alzubaydi Raysah Ali, Ansari Azhar Ahmad, Habib Sami S., Nazeeruddin Mohammad Khaja, Zakeeruddin Shaik M., Grätzel Michael, 2015. Outdoor Performance and Stability under Elevated Temperatures and Long-Term Light Soaking of Triple-Layer Mesoporous Perovskite Photovoltaics. Energy Technology, 3, 551–555.

Liu Dianyi, Kelly Timothy L., 2014. Perovskite Solar Cells With A Planar Heterojunction Structure Prepared Using Room-Temperature Solution Processing Techniques. Nature Photonics, 8, 133-138.

Mitzi D. B., Feild C. A., Harrison W. T. A., Guloy A. M., 1994. Conducting Tin Halides with a Layered Organic-Based Perovskite Structure. Nature, 369, 467- 469.

Mitzi D.B., Wang, S., Feild C.A., Chess C.A., Guloy A.M., 1995. Conducting Layered Organic-Inorganic Halides Containing (110)-Oriented Perovskite Sheets. Science, 267, 1473-1476.

Noh Jun Hong, Im Sang Hyuk, Heo Jin Hyuck, Mandal Tarak N., Seok Sang II., 2013. Chemical Management for Colorful, Efficient, and Stable Inorganic-Organic Hybrid Nanostructured Solar Cells. Nano Letter, 13, 1764 -1769.

Pellet Norman, Gao Peng, Gregori Giuliano, Yang Tae-Youl, Nazeeruddin Mohammad K., Maier Joachim, Grätzel Michael, 2014. Mixed-Organic-Cation Perovskite Photovoltaics for Enhanced Solar-Light Harvesting. Angewandte Chemie International Edition, 53, 3151- 3157.

Rao Haixia, Sun Weihai, Ye Senyun, Yan Weibo, Li Yunlong, Peng Haitao, Liu Zhiwei, Bian Zuqiang, Huang Chunhui, 2016. Solution-Processed CuS NPs as an Inorganic Hole-Selective Contact Material for Inverted Planar Perovskite Solar Cells. ACS Applied Materials & Interfaces, 8, 7800-7805.

Saliba Michael, Matsui Taisuke, Domanski Konrad, Seo Ji-Youn, Ummadisingu Amita, Zakeeruddin Shaik M., Correa-Baena Juan-Pablo, Tress Wolfgang R., Abate Antonio, Hagfeldt Anders, Grätzel Michael, 2016. Incorporation of Rubidium Cations into Perovskite Solar Cells Improves Photovoltaic Performance. Science, 354, 206-209.

Saliba Michael, Matsui Taisuke, Ji-Youn Seo, Konrad Domanski, Correa-Baena Juan-Pablo, Nazeeruddin Mohammad Khaja, Zakeeruddin Shaik M., Tress Wolfgang, Abate Antonio, Hagfeldt Anders, Gratzel Michael, 2016. Cesium Containing Triple Cation Perovskite Solar Cells: Improved Stability, Reproducibility And High Efficiency. Energy & Environmental Science, 9, 1989-1997.

Stranks Samuel D., Eperon Giles E., Grancini Giulia,Menelaou Christopher, Alcocer,Marcelo J.P., Leijtens Tomas, Herz Laura M., Petrozza Annamaria, Snaith Henry J., 2013. Electron-Hole Diffusion Lengths Exceeding 1 Micrometer in an Organometal Misra Ravi K., Aharon Sigalit, Li Baili, Mogilyansky Dmitri, Visoly-Fisher Iris, Etgar Lioz, Katz Eugene A., 2015. Temperature-and Component-Dependent Degradation of Perovskite Photovoltaic Materials under Concentrated Sunlight. The Journal of Physical Chemistry Letters, 6, 326–330.

Sun Shuangyong, Salim Teddy, Mathews Nripan, Duchamp Martial, Boothroyd Chris, Xing Guichuan, Sum Tze Chien, Lam Yeng Ming, 2014. The Origin Of High Efficiency In Low-Temperature Solution-Processable Bilayer Organometal Halide Hybrid Solar Cells. Energy & Environmental Science, 7, 399-407.

Tao Chen, Neutzner Stefanie, Colella Letizia, Marras Sergio, Kandada Srimath Ajay Ram, Gandini Marina, Bastiani Michele De, Pace Giuseppina, Manna Liberato, Caironi Mario, Bertarelli Chiara, Petrozza Annamaria, 2015. 17.6% Stabilized Efficiency In Low-Temperature Processed Planar Perovskite Solar Cells. Energy & Environmental Science, 8, 2365-2370.

Trihalide Perovskite Absorber. Science, 342, 341-344.

Wang Hong, Sheikh Arif D., Feng Quanyou, Li Feng, Chen Yin, Yu Weili, Alarousu Erkki, Ma Chun, Haque Md Azimul, Shi Dong, Wang Zhong-Sheng, Mohammed Omar F., Bakr Osman M., Wu Tom, 2015. Facile Synthesis and High Performance of a New Carbazole-Based Hole-Transporting Material for Hybrid Perovskite Solar Cells. ACS Photonics, 2, 849-855.

Wu Qiliang, Zhou Weiran, Liu Qing, Zhou Pengcheng, Chen Tao, Lu Yalin, Qiao Qiquan, Yang Shangfeng, 2016. Solution-Processable Ionic Liquid as an Independent or Modifying Electron Transport Layer for High-Efficiency Perovskite Solar Cells. ACS Applied Materials & Interfaces, 8, 34464-34473.

Xing Guichuan, Mathews Nripan, Sun Shuangyong, Lim Swee Sien., Lam YengMing., Grätzel Michael., Mhaisalkar Subodh, Sum Tze Chien, 2013. Long-Range Balanced Electron and Hole Transport Lengths in Organic-Inorganic $CH_3NH_3PbI_3$. Science, 342, 344-347.

Yin Guannan, Ma Jiaxin, Jiang Hong, Li Juan, Yang Dong, Gao Fei, Zeng Jinghui, Liu Zhike, Liu Shengzhong Frank, 2017. Enhancing Efficiency and Stability of Perovskite Solar Cells Through Nb-Doping of TiO2 at Low Temperature. ACS Applied Materials & Interfaces, 9, 10752-10758.

Yu Weili, Li Feng, Wang Hong, Alarousu Erkki, Chen Yin, Lin Bin, Wang Lingfei, Mohamed Hedhili Nejib, Li Yangyang, Wu Kewei, Wang Xianbin, Mohammedc Omar F., Wu Tom, 2016. Ultrathin Cu_2O as an Efficient Inorganic Hole Transporting Material for Perovskite Solar Cells. Nanoscale, 8, 6173-6179

Zhao Yixin, Zhu Kai, 2014. Solution Chemistry Engineering toward High-Efficiency Perovskite Solar Cells. The Journal of Physical Chemistry Letters, 5(23), 4175-4186.

353: Modelling and optimising of the heating performance of solar assisted GWSHPS in Tibetan Plateau Airport

Jun LU[1], Meilin WANG[2], Yongcai LI[3], Lulu YANG[4], Liyue ZENG[5], Zhenyong QIAO[6,7]

[1] *Key Laboratory of the Three Gorges Reservoir Region's Eco-Environment, Ministry of Education, Chongqing, 1181367768@qq.com*
[2] *Key Laboratory of the Three Gorges Reservoir Region's Eco-Environment, Ministry of Education, Chongqing, 20161713051t@cqu.edu.cn*
[3] *Key Laboratory of the Three Gorges Reservoir Region's Eco-Environment, Ministry of Education, Chongqing, 905255911@qq.com*
[4] *Key Laboratory of the Three Gorges Reservoir Region's Eco-Environment, Ministry of Education, Chongqing, 648527308@qq.com*
[5] *Key Laboratory of the Three Gorges Reservoir Region's Eco-Environment, Ministry of Education, Chongqing, bonjourzly@qq.com*
[6] *Chongqing University，Chongqing, qzymail@163.com*
[7] *Sichuan Institute of Building Research, Chengdu, qzymail@163.com*

Tibetan Plateau in China is characterised by the shortage of conventional energy resources, fragile ecosystem and the need of space heating, which has made the renewable energy progressively more important than other parts. Therefore, solar and geothermal energy are the optimal alternatives to fossil fuels in Tibetan Plateau because of their abundance and sustainability. Solar assisted groundwater source heat pump system (GWSHPS) is an energy efficient system that could be a promising alternative to stove, boiler and electric heater for spacing heating. The system can avoid the intermittence of solar energy system and limitation of groundwater source heat pump system. In this paper, parametric optimisation was carried out in order to select the optimum size of the system based on the combination of efficiency and initial cost. Firstly, a detailed numerical model of solar assisted GWSHPS for a civil airport in Tibetan autonomous prefecture of Aba was developed in TRNSYS with typical meteorological year data. The result of numerical model corresponds well to the experimental data, with error less than 15%. Then, the total energy consumption, useful heat gain and economy of system were discussed for different combinations among water tank, solar collector, and supply hot water temperature. Finally, considering the balance between economy and performance of GWSHPS, the optimum sizing for water tank, collector, and supply hot water temperature are 80L/solar collector area, 55°, 1130m^2, and 40℃, respectively. These results may provide guidance for the design of solar assisted GWSHPS in airport building in cold plateau climate.

Keywords: Cold Plateau climate; solar assisted GWSHP; solar collector; water tank; supply hot water temperature

1. INTRODUCTION

Solar assisted GWSHP has been authenticated utilises solar energy and low enthalpy geothermal energy to supply hot water and space heating for buildings. In 1995, the feasibility of solar assisted heat pump system (SAHPS) was investigated firstly (Jordan and Threlkeld, 1954: pages 122-130). In the following year Penrod and Prasanna attempted to combine the solar collector with geothermal heat pump system (GHPs) (Penrod and Prasanna, 1962: pages 9-22). Subsequently, substantial investigators assessed the energy consumption and the energy performance of different configurations and operation modes of solar assisted GWSHPs (or GHPs) using experiments or simulation approach.

Bertram (Bertram, 2014: pages 505-514) and Rad et al. (Rad et al., 2013: pages 224-232) found the use of solar energy on cold side of heat pump can effectively short the ground heat exchangers by 20% and 15% respectively by TRNSYS, the net present value of system is lower than the conventional GHPs depending on the drilling cost. Ozgener and Hepbasli extended their studies to exergoeconomic analysis (Ozgener and Hepbasli, 2005: pages 1459-1471), and the exergetic efficiency of the overall solar assisted GHPs for a greenhouse heating reached 67.7% (Ozgener and Hepbasli, 2005: pages 101-110). The measurement results of Zhen indicated the energy conservation and economic benefit of solar assisted GWSHPs is better in comparing to boilers and air source heat pump system (Zhen et al., 2017: pages 33-42).

The coefficient of performance (COP) values of different configurations solar assisted GHPss located in an Alpine ski park at 2500 m elevation was found between 3.53 and 3.62 by TRNSYS (Fabrizio, 2015: pages 2286-2291). Experimental heating coefficient performance of the GHP and the overall solar assisted GHPs for greenhouse were obtained to be 2.64 and 2.38, respectively (Ozgener and Hepbasli, 2005: pages101-110). In addition, a high COP of GWSHP about 5 embodied in Xigaze Peace Airport (Zhen et al., 2017: pages 33-42). Bertram (Bertram, 2014: pages 505-514) also found the seasonal performance factor is increased 1.5 in comparing to a simple domestic hot water system with $5m^2$ collector area by simulated the solar assisted GHPs. These literatures have confirmed the superiority of SAHPs. However, the optimisation design of SAHPs in whole heating season for plateau cold climate is deficient.

The increasing demand for heating and double crisis of energy sources and environment in recent years, more and more scholars pay much attention to find suitable heating modes for plateau cold climate (Liu and Chen,2012: pages 461-464; Jiang, 2013: pages 1-7; Rong et al., 2013: pages 23-30). Furthermore, a number solar energy heating system experimental bases of monomer buildings have been completed for plateau cold climate in China (Pan and Jin, 2007: page53-58; Chen, 2010: pages 63-65; Xing and Wang, 2010: pages 30-33; He, 2012; Yu et al.,2017: pages 99-102). Take the case of science and technology department in Tibet, Zheng et.al (Zheng et al., 2006: pages 52-54) measured the solar energy heating system (SEHs), the results show that the economy of SAHPs is better than direct SEHs, although both systems can meet the demand of loads. What's more, Ma et.al (Ma et al., 2007: pages 69-70) found that the average indoor temperature is 19.6℃, the average COP of heat pump is 3.1, and the average daily heat collecting efficiency is 50%. However, they just selected a few days in the metaphase of heating, the experiment data cannot demonstrate the performance of SAHPs. In addition, Wang (Wang et al., 2012: pages 53-56) investigate 28 solar energy heating systems in Tibet by field tests. The results indicate that these systems design does not satisfy the requirements of owners and match the installation, operation management is improper leading to most solar energy heating systems paralyzed after running about 3 years. At present, the study on the system of SAHPs at the experimental stage basically, there is some gap with the internal level. Therefore, in order to promote SAHPs development for plateau cold climate of China, taking system configurations, economy and performance to conduct in-depth exploration is necessary.

The motivation for this investigation is to establish a complete performance model to optimise solar assisted GWSHPs for plateau cold climate, based on a civil airport in Sichuan province, Tibetan autonomous prefecture of Aba, Hongyuan County. In this model, each component is considered, and the effect of water tank size, collector tilt angle, area and heat supply water temperature on system performance and economy are studied. Furthermore, for the simulation of the system, the high accuracy program TRNSYS (Banister et al., 2014: pages 499-504; Ayompe et al., 2011: pages 1536-1542) is used and the model is verificated by experiments. Finally, the optimum allocation of each component are put forward. These findings can provide a guidance on application of SEHs for plateau cold climate.

2. SYSTEM DESCRIPTION

The complete solar assisted GWSHPs consists of a solar collector, a water tank, GWSHPs, terminal and pumps. A brief description and performance model of each of the system components is given in an upcoming section. A weather data file of a typical meteorological year for Hongyuan is used to model the long-term performance of solar assisted GWSHPs.

Dynamic simulation of solar assisted GWSHPs is carried out using TRNSYS software, which is a suitable software to simulate thermal energy systems. While heating seasonal system performance can be modelled in TRNSYS using theses detailed state property components, it is also possible to create less complex component models based on some simple energy balance formulations.

2.1. Modelling of solar collector

At present, the explosions of tubular solar collector crop up frequently, nevertheless, the flat-plate solar collector runs well, when the SEHs experimental bases in Tibet (Zhao, 2013). Moreover, the characteristics of simple structure, strong pressure-bearing ability, large heat absorption area and acceptable price are perfectly cogent reasons why flat-plate solar collector is scientific choice for plateau cold climate (Khoukhi and Maruyama, 2005: pages 1177-1194). Therefore, the flat-plate solar collector is used in civil airport of Hongyuan.

The objective of establishing mathematical model is to know the working fluid temperature of collector inlet, outlet and collector efficiency, rather than analysis the performance characteristics. Consequently, this research only needs to establish the efficiency curve fitting model of flat-plate solar collector. The efficiency of flat-plate solar collector is a ratio of effective solar energy collection to incident solar energy on the daylighting surface. And the efficiency curve fitting model divides into two parts by the phase of collector:

Heat storage phase

The constant values of efficiency curve is tested in given operating flow. When the actual flow is different from test condition, it is necessary to correct the collector efficiency by correction factor R_1. In addition, there is only one piece of flat-plate solar collector under test condition. In fact, several pieces series connection collective simultaneously, which contributes to a decrease in collector efficiency and can be corrected by correction factor R_2.

Equation 1: Collector efficiency by Hottel-Whillier-Bliss equation (Whillier,1967)

$$\eta = (a_0 - a_1 \frac{T_{f,i} - T_a}{I_\theta} - a_2 \frac{(T_{f,i} - T_a)^2}{I_\theta}) R_1 R_2$$

Equation 2: Correction factor R_1

$$R_1 = \frac{\frac{m_c C_{p,f}}{A_c F' U_L}(1 - e^{-A_c F' U_L / m_c C_{p,f}})}{\frac{m_t C_{p,f}}{A_c F' U_L}(1 - e^{-A_c F' U_L / m_t C_{p,f}})} = \frac{m_c (1 - e^{-A_c F' U_L / m_c C_{p,f}})}{m_t (1 - e^{-A_c F' U_L / m_t C_{p,f}})}$$

Equation 3: Parameter $F'U_L$

$$F' U_L = -m_t C_{p,f} \ln(1 - \frac{a_2}{m_t C_{p,f}})$$

Equation 4: Correction factor R_2

$$R_2 = (1 - (1 - \frac{A_c a_2}{m_c C_{p,f}})^{N_S}) \Big/ N_S \frac{A_c a_2}{m_c C_{p,f}}$$

where:

- η = collector efficiency
- A_c = collector area(m^2)
- I_θ = incident solar radiation intensity on an inclined plane with angle of θ°(W/m^2)
- m_c = circulated fluid flow of collector(Kg/h)
- $C_{p,f}$ = specific heat capacity of working fluid of collector(KJ/(Kg·K))
- $T_{f,i}$ = inlet working fluid temperature of collector(°C)
- T_a = air temperature surrounding collector(°C)
- a_0 = intercept efficiency
- a_1 = tilt angle efficiency
- a_2 = curvature efficiency
- m_t = circulated fluid flow on the test condition(Kg/h)
- N_S = series connection number of flat-plate solar collectors

Night and stagnation phase

In night and stagnation phase, the flow of collector is zero. It is assumed that the temperature of pipes, working fluid in the pipes and insulation material in the bottom of collector are same.

Equation 5: Thermal equilibrium of collector

$$\eta I_\theta = a_0 I_\theta - a_1 (T_{f,o} - T_a) - a_2 (T_{f,o} - T_a)^2 = 0$$

2.2. Modelling of GWSHP

The varying duty model of GWSHP is established by fitting analysis of data, which not only avoids the complex computation of theoretical model, but also is suitable for annual and full life cycle energy consumption simulation (Huang et al., 2013: pages 82-86). GWSHPs are usually selected by design load, but as it is, the unit rarely runs in full load condition. Thus the partial load is an important indicator to assess performance and calculate actual energy consumption (Fan, 2010; Yu and

Chan, 2007: page1581-1593). In the long-term heating, the water temperature and flow of source side and load side are main parameters for GWSHP's COP. For convenience application, the heating capacity and power can be corrected by water temperature and flow with quartic polynomials.

The correction of operating mode

Equation 6: Correction factor of water temperature

$$\phi_{\mathrm{HL,T}} = a_{\mathrm{HL,T}} T_{\mathrm{L,i}}^{4} + b_{\mathrm{HL,T}} T_{\mathrm{L,i}}^{3} + c_{\mathrm{HL,T}} T_{\mathrm{L,i}}^{2} + d_{\mathrm{HL,T}} T_{\mathrm{L,i}} + e_{\mathrm{HL,T}}$$

Equation 7: Correction factor of water flow

$$\phi_{\mathrm{HL,F}} = a_{\mathrm{HL,F}} r_{\mathrm{L,i}}^{4} + b_{\mathrm{HL,F}} r_{\mathrm{L,i}}^{3} + c_{\mathrm{HL,F}} r_{\mathrm{L,i}}^{2} + d_{\mathrm{HL,F}} r_{\mathrm{L,i}} + e_{\mathrm{HL,F}}$$

where:

$\Phi_{HL,T}$ = correction factor of water temperature for heating capacity of GWSHP at load side
$\Phi_{HL,F}$ = correction factor of water flow for heating capacity of GWSHP at load side
$T_{L,I}$ = inlet water temperature of GWSHP at load side (°C)
$\gamma_{L,i}$ = ratio of actual water flow to rated water flow of GWSHP at load side

Equation 8: Correction factor of water temperature

$$\phi_{\mathrm{HS,T}} = a_{\mathrm{HS,T}} T_{\mathrm{S,i}}^{4} + b_{\mathrm{HS,T}} T_{\mathrm{S,i}}^{3} + c_{\mathrm{HS,T}} T_{\mathrm{S,i}}^{2} + d_{\mathrm{HS,T}} T_{\mathrm{S,i}} + e_{\mathrm{HS,T}}$$

Equation 9: Correction factor of water flow

$$\phi_{\mathrm{HS,F}} = a_{\mathrm{HS,F}} r_{\mathrm{S,i}}^{4} + b_{\mathrm{HS,F}} r_{\mathrm{S,i}}^{3} + c_{\mathrm{HS,F}} r_{\mathrm{S,i}}^{2} + d_{\mathrm{HS,F}} r_{\mathrm{S,i}} + e_{\mathrm{HS,F}}$$

where:

$\Phi_{HS,T}$ = correction factor of water temperature for heating capacity of GWSHP at source side
$\Phi_{HS,F}$ = correction factor of water flow for heating capacity of GWSHP at source side
$T_{S,I}$ = inlet water temperature of GWSHP at source side (°C)
$\gamma_{S,i}$ = ratio of actual water flow to rated water flow of GWSHP at source side

Equation 10: Correction factor of water temperature

$$\phi_{\mathrm{HPL,T}} = a_{\mathrm{HPL,T}} T_{\mathrm{L,i}}^{4} + b_{\mathrm{HPL,T}} T_{\mathrm{L,i}}^{3} + c_{\mathrm{HPL,T}} T_{\mathrm{L,i}}^{2} + d_{\mathrm{HPL,T}} T_{\mathrm{L,i}} + e_{\mathrm{HPL,T}}$$

Equation 11: Correction factor of water flow

$$\phi_{\mathrm{HPL,F}} = a_{\mathrm{HPL,F}} r_{\mathrm{L,i}}^{4} + b_{\mathrm{HPL,F}} r_{\mathrm{L,i}}^{3} + c_{\mathrm{HPL,F}} r_{\mathrm{L,i}}^{2} + d_{\mathrm{HPL,F}} r_{\mathrm{L,i}} + e_{\mathrm{HPL,F}}$$

where:

$\Phi_{HPL,T}$ = correction factor of water temperature for GWSHP power at load side
$\Phi_{HPL,F}$ = correction factor of water flow for GWSHP power at load side

Equation 12: Correction factor of water temperature

$$\phi_{\mathrm{HPS,T}} = a_{\mathrm{HPS,T}} T_{\mathrm{S,i}}^{4} + b_{\mathrm{HPS,T}} T_{\mathrm{S,i}}^{3} + c_{\mathrm{HPS,T}} T_{\mathrm{S,i}}^{2} + d_{\mathrm{HPS,T}} T_{\mathrm{S,i}} + e_{\mathrm{HPS,T}}$$

Equation 13: Correction factor of water flow

$$\phi_{\mathrm{HPS,F}} = a_{\mathrm{HPS,F}} r_{\mathrm{S,i}}^{4} + b_{\mathrm{HPS,F}} r_{\mathrm{S,i}}^{3} + c_{\mathrm{HPS,F}} r_{\mathrm{S,i}}^{2} + d_{\mathrm{HPS,F}} r_{\mathrm{S,i}} + e_{\mathrm{HPS,F}}$$

where:

$\Phi_{HPL,T}$ = correction factor of water temperature for GWSHP power at source side
$\Phi_{HPL,F}$ = correction factor of water flow for GWSHP power at source side

The power correction of load rate

Equation 14: Correction factor of power(FAN,2010)

$$FP_{\mathrm{PLR}} = a_{\mathrm{p}} PLR^{4} + b_{\mathrm{p}} PLR^{3} + c_{\mathrm{p}} PLR^{2} + d_{\mathrm{p}} PLR + e_{\mathrm{p}}$$

where:

FP_{PLR} = correction factor of power with different load rates
PLR = load rate
a_p = 0.6993, b_p = -1.39472, c_p = 1.30536, d_p = 0.21791, e_p = 0.17333

The calculation of energy efficiency

Equation 15: Actual heating capacity of GWSHP

$$Q_{\mathrm{H},a} = PLR\phi_{\mathrm{HL,T}}\phi_{\mathrm{HL,F}}\phi_{\mathrm{HS,F}}Q_{\mathrm{H,r}}$$

Equation 16: actual power of GWSHP

$$P_{\mathrm{H,a}} = FP_{\mathrm{PLR}}\phi_{\mathrm{HPL,T}}\phi_{\mathrm{HPL,F}}\phi_{\mathrm{HPS,F}}P_{\mathrm{H,r}}$$

where:

$Q_{H,a}$ = actual heating capacity of GWSHP(kWh)
$Q_{H,r}$ = rated heating capacity of GWSHP(kWh)
$P_{H,a}$ = actual power of GWSHP (kWh)
$P_{H,r}$ = rated power of GWSHP(kWh)

2.3. Modelling of water tank

Because of convection, the distribution of water temperature in water tank is a function of space and time. In this study, the water tank is a combination of plate heat exchanger and tank resulting a decrease in temperature difference of heat transfer. The water temperature in the upper layer of water tank is higher, it can be assumed that the temperature changes just in the vertical direction. So, the water tank can be divided vertically into N layers, one layer is considered as a node, and each node sets a temperature value. Hefei Zhang (Zhang, 2004) has mentioned the hypothesis that the return water flows into the layer with an approximately same density and lower temperature.

Equation 17: Node control function

$$F_{\mathrm{i}}^{\mathrm{L}} = \begin{cases} 1, & i = N, \quad T_{\mathrm{L,r}} < T_{\mathrm{t,N}} \\ 1, & T_{\mathrm{t},i-1} < T_{\mathrm{L,r}} < T_{\mathrm{t},i} \\ 0, & \text{others} \end{cases}$$

where:

F^{L}_{i} = node control function of return water at load side entering
I = the number of node
$T_{L,r}$ = return water temperature at load side (°C)
$T_{t,i-1}$ = water temperature of water tank at i-1 node (°C)
$T_{t,N}$ = water temperature of water tank at N node (°C)
$T_{t,I}$ = water temperature of water tank at i node (°C)

When calculating the water temperature of a certain layer, it is necessary to calculate the net flow of mass transfer between two adjacent nodes in the vertical direction, and the flow is determined by F^{L}_{i} and the flow of return water. The mass transfer in the vertical direction is taken into account, instead of the return water of load side.

Equation 18: Mixing flow of 1 node

$$m_{\mathrm{m},1} = 0$$

Equation 19: Mixing flow of i+1 node enters into i node

$$m_{\mathrm{m},i} = V_i \sum_{i=1}^{N} F_{\mathrm{i}}^{\mathrm{L}}$$

Equation 20: Mixing flow of N+1 node

$$m_{\mathrm{m,N+1}} = 0$$

Equation 21: Energy balance of I node

$$V_i C_{\mathrm{P,w}} \frac{dT_{\mathrm{t},i}}{d\tau} = K_i T_{\mathrm{l},i} - F_i^{L} V_i C_{\mathrm{P,w}} (T_{\mathrm{t},i} - T_{\mathrm{L,r}}) - U_{\mathrm{t},i} (T_{\mathrm{t},i} - T_{\mathrm{a}}) + m_{\mathrm{m},i+1} C_{\mathrm{P,w}} (T_{\mathrm{t},i+1} - T_{\mathrm{t},i})$$

where:

$C_{p,w}$ = specific heat capacity of water (J/(kh/K))
V_i = fluid size at the I node (m^3)
τ = time (s)
K_i = total heat transfer coefficient between tubes and fluid at I node (W/(m^2·K))
$U_{t,i}$ = heat loss coefficient of water tank (W/(m^2·K))
$T_{l,i}$ = logarithmic mean temperature difference of heat transfer coil tubes at i node (°C)

The heat transfer of fluid and coil tubes contains convection heat transfer of fluid and internal surface of coil tubes, heat conduction of coil tubes, convection heat transfer of outer surface of coil tubes and water.

Equation 22: Overall heat transfer coefficient

$$K_i = \frac{1}{1/h_{\mathrm{i},i} + R_i + 1/h_{\mathrm{o},i}}$$

where:

$h_{i,i}$ = convective heat transfer coefficient of fluid with coil tubes of internal surface in i node (W/(m^2·K))
$h_{o,i}$ = convective heat transfer coefficient of fluid with coil tubes of outer surface in i node (W/(m^2·K))
R_i = thermal resistance of tubes in i node (m^2·k/W)

2.4. Modelling of terminal and pumps

There is no need to consider the coupling between building and heating terminal, because this investigation just concerns the temperature of supply water and return water at terminal side.

Equation 23: Mathematical model of terminal

$$T_{\mathrm{L,r}} = T_{\mathrm{L,s}} - \frac{Q_{\mathrm{L}}}{m_{\mathrm{w}} C_{\mathrm{P,w}}}$$

Equation 24: Power of pump

$$P_{\mathrm{a}} = \alpha_{\mathrm{P}} \mathrm{P}_{\mathrm{r}}$$

Equation 25: Water temperature of pump outlet

$$T_{\mathrm{P,o}} = \frac{fP_{\mathrm{a}}}{m_{\mathrm{P,w}} C_{\mathrm{P,w}}} + T_{\mathrm{P,i}}$$

where:

$T_{L,S}$ = temperature of supply water at load side (°C)
Q_L = thermal load (kW)
m_w =water flow of terminal (kg/h)
P_a = actual power of pump (kW)
α_P = correction factor of pump,
P_r = rated power of pump (kW)
$T_{P,o}$ = water temperature of pump outlet (°C)
$T_{P,I}$ = water temperature of pump intlet (°C)
F = ratio of work converts into heat of pump
$m_{p,w}$ = water flow of pump (kg/h)

2.5. Operation modes and controlling systems

The control systems contain collector and load side. Collector side mainly controls the startup and shutdown of collector circulating pump. However, the load side mainly controls the pumps and GWSHPs.The differential control is used in collector. When the fluid temperature difference between solar collector outlet and the water tank bottom is less than 2°C, or the water temperature of the top of water tank is more than 60°C, shutdown the collector circulating pump. If this fluid temperature difference is more than 5°C, startup the collector circulating pump. The load side also uses differential control. The GWSHPs must meet the requirements of load and heat supply water temperature. When the outlet water temperature of water tank ($T_{t,o}$) is lower than given heat supply water temperature (T_h), startup GWSHPs, otherwise, shutdown it.There are two GWSHPs. When the load is not more than 10% of GWSHP rated load, No.1 GWSHP is enough. If the actual load is more than one GWSHP's rated load, startup two GWSHPs. However, the precondition is that the value of controller output is 1, in other words, the heating conditions have been met.

3. MODEL VERIFICATION

To validate the developed model, TANSYS predictions are compared with field experimental data, this work has been carried out in Shigatse airport of Tibet, a typical plateau cold region in China. According to the actual situation of solar assisted GWSHPs in Shigatse Airport, the main parameters of simulated system were set as follows: the collector tilt angle is 38°, the collector area is 962m^2, the water tank size is 8m^3, and the heat supply water temperature is 42°C.The field experiments were carried out from January 20 to January 31 in 2015.

The simulated and measured results is compared from January 21 to January 22. It should be clear that the errors of collector are all within 15% and the errors of water tank are all within 10%. The results illustrate that the developed TRNSYS model predicts the temperature of collector and water tank with acceptable accuracy. The errors between simulated and measured results of daily average GWSHP's COP, heating capacity and energy consumption were checked. The simulated and measured results is compared from January 21 to January 30. It is seen that the errors of COP are within 2%, the errors of heating capacity and energy consumption are not more than 15%. These results demonstrate a good prediction of the model.

4. SYSTEM OPTIMISATION

A large number of TRNSYS simulations were carried out to optimise the various factors affecting the performance of the solar assisted GWSHPs. The effect of water tank size, collector tilt angle, collector area and heat supply water temperature on energy situation, solar fraction, collector efficiency and economics are considered. Table 1 shows a detail description of solar assisted GWSHPs components modelled in the TRNSYS simulation studio.

4.1. Optimising of water tank

According to the suggestion of《Technical code for heating system》, the suitable water tank size for collector area of short-term SEHs is 50~150L/m^2. Therefore, the each water tank size of 8.5m^3, 20m^3, 30m^3, 40m^3, 50m^3 and 60m^3 have been set, the other parameters are the same with initialization.

The variation of system parameters with the increase of water tank size are shown in Figure 1. Increasing size from 8.5m^3 to 60m^3, the solar energy heating capacity is upward trend generally. For the size of 60m^3, the solar energy collection is increased by 25%, the solar energy heating capacity is increased by 15% in comparing to 8.5m^3. However, the solar energy heating capacity of 20m^3 is less than 8.5m^3, meanwhile, the total energy consumption is more. When the water tank size is 8.5m^3, the water tank overheats frequently resulting circulating pump seldom used. On the other hand, it is easy to reach heat supply water temperature. However, the size of 8.5 m^3 is irrational, it is obvious that the solar collection stays in stagnation phase frequently in the afternoon. In addition, there is no obvious variation in energy consumption of circulating pump with the increase of water tank. That is, for a larger size, the utility time of circulating pump increases, but the energy consumption of GWSHPs reduces leading to total energy consumption erratic.

Table 1: Input component parameters for system optimisation, and TRNSYS simulation parameters.

Meteorological module	**Coefficient of ground reflective sunshine**		**Tilt Angle of collector(°)**		**Azimuth of incline(°)**
	0.2		38		0
Solar collector subsystem	Area (m^2)	Flow (kg/s)	a_0	a_1	a_2
	1130	0.02	0.761	4.106	0.012
Water tank subsystem	Size (m^3)	Height (m)	Area of heat exchange coils (m^2)	Density of fluid (kg/ m^3)	Specific heat of fluid (kJ/(kg·K))
	8.5	3.2	21.4	1000	4.19
	Step	Divided layers	Coefficient of heat loss (W/(m^2·K))	Types of fluids in heat exchange coils	size fraction of ethanediol
	6	3	0.833	3	50%
	Thermal conductivity of coil (W/(m·K))	Thermal conductivity of fluid (W/(m·K))	Nu constant in natural convection		Nu index in natural convection
	100	0.6	0.5		0.25
Controller module of collector side	Upper limit temperature (℃)		Upper limit of temperature difference (℃)		Lower limit of temperature difference (℃)
	60		5		2
Controller module of load side	Upper limit temperature (℃)	Lower limit temperature (℃)	Rated temperature (℃)	Startup load of No.2 (kW)	Temperature of groundwater (℃)
	53	47	50	780	13

In addition, the major purpose of increasing water tank size is to increase the solar fraction in the heating prophase. However, the solar fraction for each month in metaphase is an important index of the size of water tank. Figure 2 shows the variation of monthly average solar fraction with the increase of water tank size. The increase of water tank size is conducive to increase solar fraction, especially in heating prophase, but not obvious in heating metaphase, even opposite. In prophase of heating, the size of 8.5m^3 is overheated for long periods, but the size of 60m^3 hardly occurred overheating. When the size increases from 8.5 m^3 to 60 m^3, the solar fraction of October, November and April are increased by 66%, 27% and 27%, accordingly. However, in the heating metaphase, the increase of water tank size is detrimental to rapid increasing in temperature of water tank, which reduces the solar energy utilization and system performance.

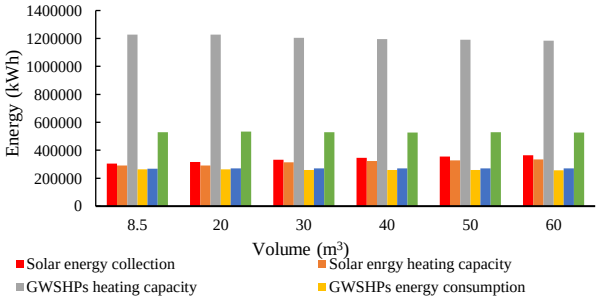

Figure 1: The effect of water tank size on system parameters

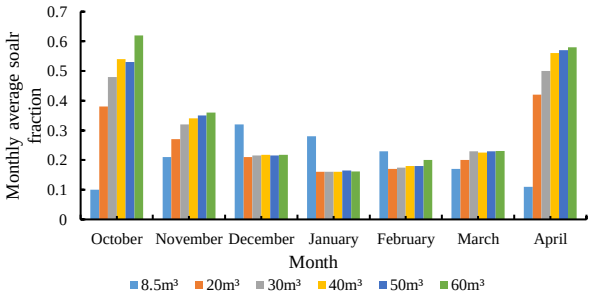

Figure 2： The effect of water tank size on monthly average solar fraction

The variation of monthly average collector efficiency is given in Figure 3. The monthly average collector efficiency increases with the increase of water tank size. Furthermore, the increment is distinct in metaphase and anaphase of heating. Increasing size from 8.5 m^3 to 60 m^3, the monthly average collector of October, April and November is increased by a percentage of 170%, 89% and 51%, accordingly. But, the collector efficiency is not significantly increased with water tank size in metaphase of heating.

The utility time ratio of solar energy increases initially then decreases with the increase of water tank size, but the utility time ratio of GWSHPs shows an opposite trend. Considering the time of solar energy direct heating, the each water tank size of 30m^3 is the best. Figure4 describes the effect of various water tank size on investment cost, operation cost, annul

cost and annual cost of per square meter collector. As shown, the annual cost is lowest when the size is 8m^3, but the collector overheated seriously. When the size increases from 20m^3 to 60m^3, the capital cost is increased, the annual cost and operation cost in heating season is fluctuant. The annual cost 60.1 thousand Yuan is minimal with the size of 30m^3. Therefore, considering the overall economy, the water tank size should be chosen as 30m^3.

4.2. Optimising of collector tilt angle

According to the suggestion of a technical code for heating system, the suitable collector tilt angle shall be within ±10℃ for local latitude (32°). Therefore, the collector tilt angle from 32° to 60° has been set, the other parameters are the same with initializations. The effect of collector tilt angle on collector efficiency is given in Figure 5. The collector efficiency increases and then deceases when the collector tilt angle is increased from 32° to 60°. The effective heat collection 358409kWh is maximum with the collector tilt angle of 55°. Nevertheless, the collector tilt angle determined by collector efficiency and space in practical projects.

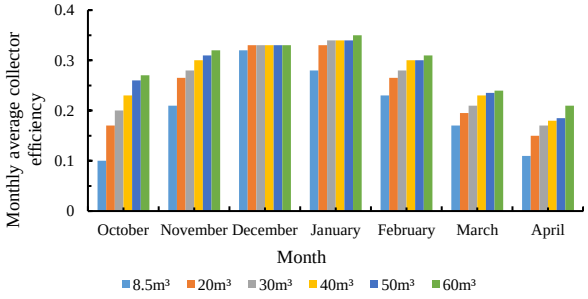

Figure 3:The effect of water tank size on monthly average collector efficiency

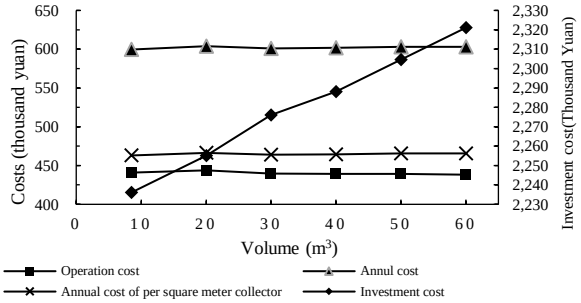

Figure 4:The effect of water tank size on economics

4.3. Optimising of collector area

In order to achieve the best economic benefits, the optimum collector area to balance the contradiction between the investment cost and energy performance is very important. According to the suggestion of《Technical code for heating system》, the collector area of 1300m^2, 1600m^2, 1900m^2, 2200m^2 has been set, the other parameters are the same with initializations.

The variation of parameters with the increase of collector area are shown in Figure 6. Increasing area from1300m^2 to 2200m^2, the quantity of solar energy collection and heating capacity are increased, while the quantity of GWSHPs heating capacity is decreased, meanwhile, the total energy consumption is decreased from 528475kWh to 483615kWh. In short, a larger collector area is contribute to solar energy utilization and energy performance.

Figure 7 describes the effect of collector area on monthly average solar fraction. When the collector area is 2200 m^2, the maximal monthly average solar fraction is 0.72 in October, while the minimum is 0.31 in January, and the solar fraction can reach 1 in number of days of heating prophase and anaphase. The solar fraction trend at October, November and April is different from other months. This is due to collector overheated in a portion time of heating prophase and anaphase, the degree of overheated for each collector is not exactly the same resulting a different solar energy utilization.

The costs of different collector areas are presented in Figure 8. With the increase of collector area 1130m^2 to 2200m^2, the investment cost is increased 935.5 thousand Yuan, the operation cost decreased 37.3 thousand Yuan. When the collector area is 1130 m^2, the investment cost of solar assisted GWSHPs is equal to GWSHPs, furthermore, the average solar fraction is only 31.86%, and even the water tank size increases to 60m^3, the average solar fraction is not more than 34%. It is obvious that the substantial growth in investment cost leading to solar assisted GWSHPs uneconomical.

4.4. Optimising of heat supply water temperature

The effect of heat supply water temperature is evaluated against heating capacity and energy consumptions. As can be seen in Figure 9, the lower heat supply water temperature the more solar energy collection and heating capacity. Simultaneously, the energy consumptions of GWSHPs decreases, while the energy consumptions of circulating pump increases resulting a decrease in overall system. When the heat supply water temperature decreases from 50°C to 40°C, the solar energy collection is increased from 314482kWh to 381061kWh, rose by 21.2%. In addition, with decreasing of heat supply water temperature from 50°C to 40°C, the energy consumption is decreased by 8.4%. That is the lower heat supply water temperature is contribute to energy performance on the premise of meeting thermal load, especially for a limited collector area.

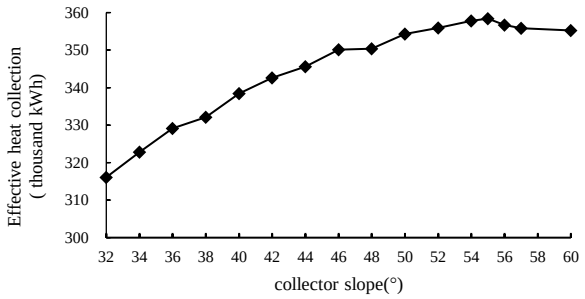

Figure 5:The effect of collector tilt angle on effective heat collection

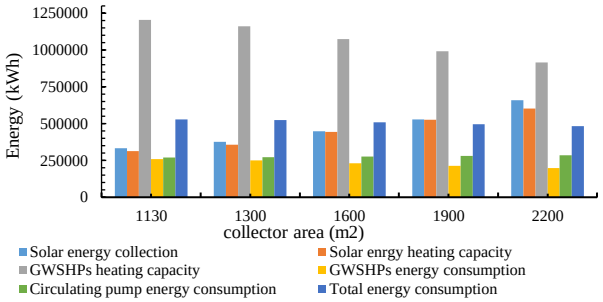

Figure 6: The effect of collector area on system parameters

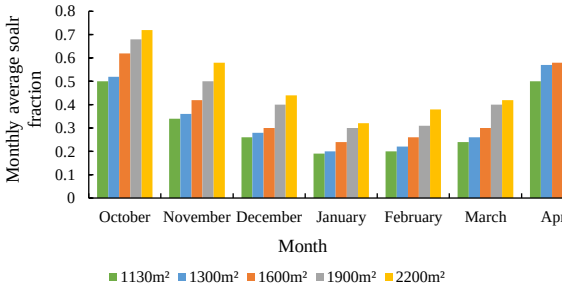

Figure 7: The effect of collector area on monthly average solar fraction

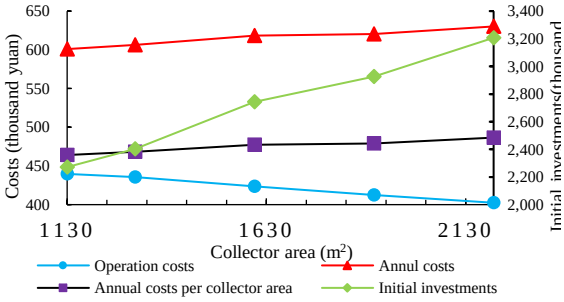

Figure 8: The effect of collector area on economics

The effect of different heat supply water temperature on operation cost and annual cost is shown in Figure 10. When the heat supply water temperature decreases from 50°C to 40°C, the operation cost is decreased by 34 thousand Yuan, and the annual cost is decreased by 37 thousand Yuan. Therefore, the lower heat supply water temperature the less costs on the premise of meeting the thermal load. However, the lower heat supply water temperature demands a larger heating terminal area. Accordingly, the terminal shall be radiant floor heating (Ma et al., 2016:page972-977) or fan coil unit.

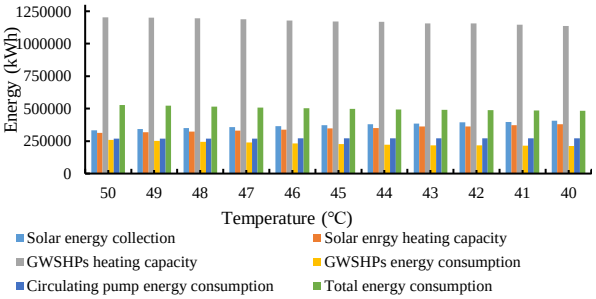

Figure 9: The effect of heat supply water temperature on system parameters

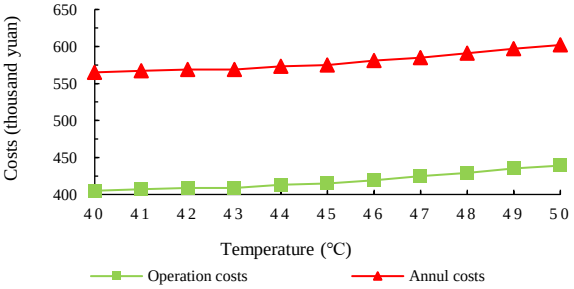

Figure 10: The effect of heat supply water temperature on economy

5. CONCLUSIONS

The optimisation of solar assisted GWSHPs for plateau cold climate was studied by using an experimentally validated TRNSYS model in this paper. The performance model is able to analyse and optimise the water tank size, collector tilt angle, collector area and heat supply water temperature. The appropriate system configurations are proposed by energy performance, economics, and performance. The optimum sizing for water tank, collector, and supply hot water temperature are 80L/solar collector area, 55°, 1130m^2, and 40°C, respectively.

6. ACKNOWLEDGEMENTS

This work is sponsored by National Science Foundation of China (No.51708054, No.51478058), 2017 Chongqing University “Graduate student research innovation project” agreement (CYS17005), The National Key R&D Program of China (2016YFC0700703) and Research Project of Sichuan Huaxi Group Co., Ltd. (HXKX2017/015).

7. REFERENCES

Ayompe, L., Duffy, A., Mccormack, S., & Conlon, M, 2011. Validated TRNSYS Model for Forced Circulation Solar Water Heating Systems with Flat Plate and Heat Pipe Evacuated Tube Collectors, Articles. Dublin Institute of Technology, 31(8–9), 1536-1542.

Banister, C. J., Wagar, W. R., & Collins, M. R, 2014. Validation of a single tank, multi-mode solar-assisted heat pump TRNSYS model, Energy Procedia, 48, 499-504.

Bertram, E, 2014. Solar assisted heat pump systems with ground heat exchanger – simulation studies ☆, Energy Procedia, 48, 505-514.

Chen, X.H, 2010. The Using of Solar Energy in a Heat Energy Supply Engineering at a Water Processing Factory in the North Suburb of Lasa, District heating, (2), 63-65.

Fabrizio, E., Ferrara, M., Urone, G., Corgnati, S. P., Pronsati, S., & Filippi, M, 2015. Performance assessment of a solar assisted ground source heat pump in a mountain site ☆, Energy Procedia, 78, 2286-2291.

Fan, Q.Y, 2010. The character analysis and program design of lake water-source heat pump system, Chongqing University.

He, Z.N, 2012. Application of solar heating system in Tibet, International Conference on green building and building energy conservation.

Huang, G., & Lu, J, 2013. Transient condition model of heat pump unit with screw compressor based on data fitting, Heating Ventilating & Air Conditioning, 43(7), 82-86.

Jiang, Y., Feng, Y., & Rong, X, 2013. Discussion on urban heating modes for Lhasa, Heating Ventilating & Air Conditioning, 43(6),1-7.

Jordan, R.C; Threlkeld, J.L, 1954. Design and economics of solar energy heat pump systems. ASEM Journal Section, Heating, Piping and Air Cond, 26, 122-130.

Khoukhi, M., & Maruyama, S, 2015. Theoretical approach of a flat plate solar collector with clear and low-iron glass covers taking into account the spectral absorption and emission within glass covers layer, Renewable Energy, 30(8), 1177-1194.

Liu, J. P., & Chen, L. B, 2012. Study on the local heating modes in north of qinghai province, Advanced Materials Research, 374-377, 461-464.

Ma, H., Li, C., Lu, W., Zhang, Z., Yu, S., & Du, N, 2016. Investigation on a solar-groundwater heat pump unit associated with radiant floor heating. Renewable & Sustainable Energy Reviews, 75.

Ozgener, O., & Hepbasli, A, 2005. Experimental performance analysis of a solar assisted ground-source heat pump greenhouse heating system, Energy & Buildings, 37(1), 101-110.

Ozgener O, Hepbasli A, 2005. Exergoeconomic analysis of a solar assisted ground-source heat pump greenhouse heating system, Applied Thermal Engineering, 25, 1459–71.

Pan, Y.G, Jin, J, 2007. Application of solar energy to heating system in Lhasa railway station, Heating Ventilating & Air Conditioning, 37(06),53-58.

Penrod, E. B., & Prasanna, K. V, 1962. Design of a flat-plate collector for a solar earth heat pump, Solar Energy, 6(1), 9-22.

Rad, F. M., Fung, A. S., & Leong, W. H, 2013. Feasibility of combined solar thermal and ground source heat pump systems in cold climate, Canada, Energy & Buildings, 61(3), 224-232.

Rong, X., & Min, X, 2013. Suitability analysis for Lhasa heating techniques, Heating Ventilating & Air Conditioning, 43(6), 23-30.

Technical code for heating system. China Architecture & Building Press, Beijing 2009.

Wang L, Yuan L, Zhu C.M, Li Z.R, Yu N.Y, 2012. Necessity of the whole process commissioning for active solar heating systems, Heating Ventilating & Air Conditioning, 42(2), 53-56.

Whillier, 1967. A, Low Temperature Engineering Applications of Solar Energy, Chap. 3, Design factors Influencing Collector Performance, ASHRAE, New York.

Xing, L. Y, 2010. Experimental study on the solar energy hot water heating system for qinghai-tibet railway line, Building Energy & Environment, 29(2), 30-33.

Ye, Y. U., Xiao-Chuan, L. I., & Song, M. A, 2017. Application of solar energy to heating system in Shigatse railway station, Building Energy & Environment, 36(1), 99-102.

Yong-Tao, M. A., Zheng, Z. H., Xin, G. E., & Wang, H. M, 2007. Performance analysis of heating system with solar energy heat pump in tibet region, Gas & Heat, 27(1), 69-70.

Yu, F. W., & Chan, K. T, 2007. Optimum load sharing strategy for multiple-chiller systems serving air-conditioned buildings, Building & Environment, 42(4), 1581-1593.

Zhang, H.F, 2004. Solar energy utilization principle and simulation, Xi'an Jiaotong University Press, Xi'an.

Zhao, J, 2013. Composite solar heating system with phase change, Chongqing University.

Zhen, J., Lu, J., Huang, G., & Zhang, H, 2017. Groundwater source heat pump application in the heating system of Tibet plateau airport, Energy & Buildings, 136, 33-42.

Zheng, Z. H., Gao, J. S., & Xin, G. E, 2006. Application of heat-supply system with solar heat pump in Tibet region, Gas & Heat, (12), 52-54.

356: The sensitivity of roof surface and envelope insulation in naturally ventilated tropical housing

Case study across three climate zones in Myanmar

May ZUNE[1], Lucelia RODRIGUES[2], Mark GILLOTT[3]

[1] *Faculty of Engineering, University of Nottingham, may.zune@nottingham.ac.uk*
[2] *Associate Professor, Faculty of Engineering, University of Nottingham, lucelia.rodrigues@nottingham.ac.uk*
[3] *Professor of Sustainable Building Design, University of Nottingham, mark.gillott@nottingham.ac.uk*

The study was aimed to investigate the impacts of the thermophysical property of the building envelopes for the present typical weather and predicted climate scenarios in Myanmar. The objective of this study was to work out the sensitivity of thermal performance of a model by varying levels of envelope u-value, solar absorptivity and thermal emissivity of the roof, coupled with the use of daytime only and nocturnal ventilation. The sensitivity analysis framed with 125 u-value matrices and eight scenarios was carried out to evaluate the impact of material variables on the indoor environment of the model. In total, 3360 dynamic simulations were performed in order to understand the sensitivity of the model to these parameters in three cities of Myanmar: Yangon, Mandalay, and Myitkyina where Koppen climates Am, Aw, and Cwa govern. The findings have found that the logical understanding of adding insulation to the roofs at first is better than adding insulation in walls and floors. In the scenario with high solar absorptivity and high thermal emissivity in the daytime ventilation mode, the overheating period above 32°C was decreased 5.18%, 2.75% and 6.89% of a year in Yangon, Mandalay, and Myitkyina when the roof u-value was reduced from 2.0 to 0.2W/m^{2}K in that scenario. However, a better result could be found in a 24-hour ventilation mode without reducing roof u-value from 2 W/m^{2}K in that scenario. It means the nocturnal ventilation model could decrease more overheating hours than low u-value. On the contrary, the overheating hours were increased when the u-value were reduced in the cool-roof scenarios. It means if the roof has low solar absorptivity and high thermal emissivity "the higher the u-value, the better" could overwrite "the lower the u-value, the better." Based on the results of all simulations, the nocturnal ventilation becomes more sensitive in future climate scenarios. From this analysis, conclusions are drawn by comparing three insulation types and their characteristic of improving the thermal performance.

Keywords: cool roof, insulation, natural ventilation, thermal performance, climate change.

1. INTRODUCTION

Besides the human factor, the challenges of designing a thermally comfortable indoor environment are to achieve energy efficiency and to define the material properties effectively. In essence, the present and future local climate contexts are critical factors to define the required material thermophysical properties; however, it remains lack of knowledge gap for the Myanmar climates fundamentally. The growing research of insulation shows that the lower the u-value, the better to slow down the flow of heat into the building. Reducing u-value provides the higher insulation against daytime in the hot and humid tropical climate, but it also hinders night-time heat loss. Cool roofs, unlike insulation, minimise solar absorption and maximise thermal emission through the exterior surface finish by increasing the reflectance value (Levinson and Akbari, 2010). The optimum roof solar reflectance varies under different climate contexts (Piselli et al., 2017), so a careful design for the material conductivity and material thickness is a concern in the cool roof application. Natural ventilation technique has been well-recognised as an efficient passive cooling technique for the non-insulated tropical housing, but the influence of the exterior condition is unavoidable and uncontrollable. Each strategy allows different levels of material property and causes different results. The context of the article was about determining the impacts and the sensitivity of the thermophysical property of the building envelope for three climate zones of Myanmar for the present typical weather and predicted climate condition up to 2070.

The concept of insulation is to isolate a building and to make it as an island in the ocean of heat or cold (Moe, 2014, page 14). The degree of insulation is measured by the thermal transmittance or u-value of building envelope. It depends upon the thermal conductivity of the various layers of materials together with the boundary heat transfer coefficient at any solid and air interface of the envelope. The boundary layer heat transfer fundamentally occurs by three agencies: free convection, forced convection and radiation (Diamant, 1965, page 29). Adding insulation layers in building envelopes approach more concerns the first two agencies, and the cool roof concerns the last agency. A super-insulated passive house aims to reduce the energy load in which thermal comfort can be achieved solely by post-heating or post-cooling of the fresh air mass (Feist, 2006). Even in the cold and temperate climates, the superinsulation approach could bring summer overheating risks despite the uses of passive and active design strategies, which ask the addition of a cooling strategy (Rodrigues et al., 2013). Technically, improving the ventilation system is the most efficient way for cooling requirements. Unlike preventing heat transfer by the use of insulation in the hot and cold climates, the natural ventilation is widely used in the tropical climates to response high humidity and high temperature. If the ventilation plays importantly in the insulated housings for overheating risks, the tropical housing will suffer more if there is no optimum amount of insulation and coupled ventilation. Garde et al. (2004) found that the differences of more than 3°C were observed between a dwelling with a well-insulated roof and another one with no insulation in the tropical climate of Saint-Pierre, Réunion. Another tropical climate case study in Puerto Rico by Alvarado and Martinez (2008) proved that the roof insulation system could reduce the typical thermal load by over 70% while efficiently controlling thermal fluctuations. However, the clear understanding of the relationship between the roof insulation and other building envelop insulation is still required for the tropical climate contexts.

In the tropical climates, the roof must perform the defensive effects of preventing precipitation and solar gains (Hyde, 2001, pages 137-138), and resist the destructive effects of heating and cooling cycles (Athienitis and Santamouris, 2002, page 6). During the day, the sun is a radiator, and the roof is an absorbent. Solar radiation falling on the surface of a house is partly reflected away and partially absorbed. It is necessary to reduce heat absorption from the surface before the heat is transferred through the building. The cool roofs radiate the heat not to be absorbed by reflecting the incident sunlight (Levinson and Akbari, 2010). A field case optical measurements study by Berdahl and Bretz (1997) reported that highly absorptive roofs receive the surface and ambient air temperature as high as 50°C while the less absorptive surface receives only about 10°C. For this reason, 'cool-coloured' roofs are effective in reducing ambient outside air temperature. A parametric analysis done by Synnefa et al. (2007) was found that an increase in roof solar reflectance by 0.65 resulting from the application of a cool-coating, the hours of discomfort by 9–100% and the maximum temperature by 1.2–3.7°C are reduced depending on the climatic conditions. These reductions were found to be more crucial for poorly or non-insulated buildings. Saber et al. (2012)'s study results showed that the white roofs could lead to longer-term moisture-related problems depend on a specific roof system under the particular climate contexts. During the night, the building envelop is another radiator, and the sky is a low-temperature environmental heat sink. Decreasing absorbed heat from daytime and allowing longwave radiation is preferable to cool down the building for the next day that asks the night-time ventilation and night-time cooling. Humidity and cloud is a barrier for the long-wave exchange in the atmosphere (Erell, 2007, page 264) that causes less efficient approach to cool down the thermal envelope by natural ventilation alone (Hindrichs and Daniels, 2007, page 235) unless a huge amount of air change is applied. Above mentioned the nature of climate asks a careful material property selection and ventilation adjustment for the tropical climate context.

According to the Koppen-Geiger climate classification for 2001-2025, Myanmar received a kind of subtropical highland climate (Cwb), a mixed humid subtropical climate (Cwa), a kind of equatorial winter dry climate (Aw), and tropical monsoon climate (Am), shown in Figure *1:* 1 (left) (Rubel and Kottek, 2010). The global climate risk index also reported that Myanmar, which was known as Burma, ranked second out of 183 countries in the long-term climate risk index from 2016 (Kreft et al., 2015, page 6). The authors generated the Koppen-Geiger climate shift figure for Myanmar shown in Figure *1:* 1 (left), in which we can see that the climate Cwa and the climate Cwb is disappearing in 2075-2100. Instead, the southern and western Myanmar would receive the climate Am. The northern and eastern Myanmar would receive the climate Aw. That prediction also means the changes of the degree-day values in Myanmar climates. Both the performance of thermal insulation and cool roof values depend on the degree-day for annual review and time-lag for the 24-hour cycle, which

differs markedly from area to area. A light roof with bracing structure is a safer selection for Myanmar housing as Myanmar lies in one of the two main earthquake belts of the world. Defining the required thermo-physical property can be more difficult when other material requirements such as physical, chemical and environmental properties are taken into account. For this reasons, it is advocated that far greater attention should be paid to understand the sensitivity of thermo-physical property for the specific climate both to meet the thermal performance and structural stability.

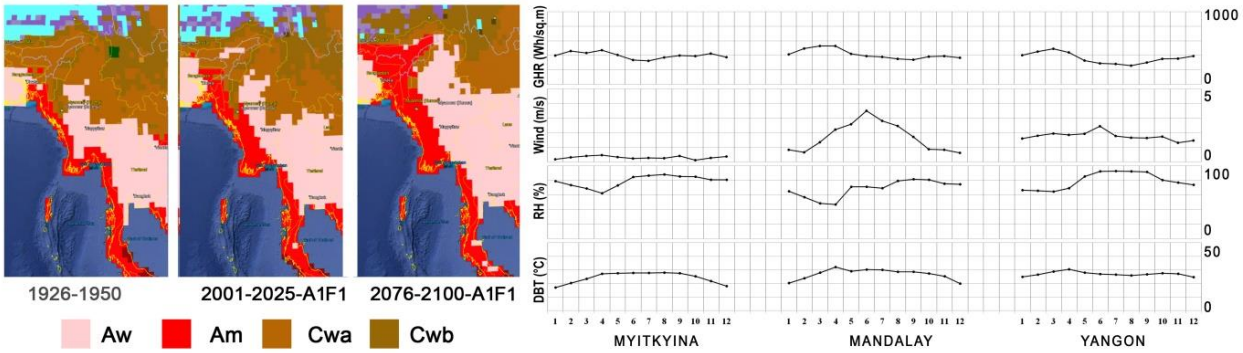

Figure 1: Koppen-Geiger climate map for Myanmar (left) (Rubel and Kottek, 2010) and weather data of case study cities (right) (White Box Technologies, 2017)

We aimed to fill the knowledge gap of understanding the relationship between envelope u-value, solar absorptivity and thermal emissivity of the roof, and the local climate contexts of Myanmar. The objective of this study was to work out the sensitivity of the thermal performance of the model by varying levels of exterior finish and insulation, coupled with the use of natural ventilation. The aspects of serviceability, structural performance, and energy calculation were left in the scope of work. Based on the above reviews and considerations, the three questions listed below were set for the investigation work.

1. Does the envelope insulation necessary in three Myanmar climates? What are the impacts of insulation?
2. How do the roof insulation and cool roof effect influence in the Myanmar climates?
3. How does the nocturnal ventilation impact the insulated and uninsulated buildings in Myanmar?
4. What are the feasible options to improve the indoor thermal environment for the future climate change scenarios?

2. METHODOLOGY

This study was conducted a sensitivity analysis to investigate the influences of roof surface and envelope insulation in naturally ventilated tropical housing. Technically, a sensitivity analysis is based on 'one-factor-at-a-time' approach and use to assess the relative importance of input factors in the presence of factors uncertainty (Saltelli et al., 2006). The series of results through the sensitivity analysis allow checking two outputs: which variables in which range are more decisive than others, and how far the result has exceeded the threshold at a given time. In the following section, all known dependent and independent variables were defined to understand the sources of uncertainty and to carry out in the sensitivity analysis with dynamic simulations.

2.1. Climate contexts and future climate change scenarios

In this study, the three cities - Yangon, Mandalay, and Myitkyina - were selected to cover the different climate contexts of Myanmar. Yangon presents the climate Am, Mandalay presents climate Aw, and Myitkyina presents climate Cwa. The climate study for this paper was used ASHRAE typical year weather files (White Box Technologies, 2017). The typical weather files here were generated from 22 years' worth of data typically spanning 1991 to 2013, and the challenge of the study was the accuracy of the typical year weather file. In Figure *1:* 1 (right), the weather data of a typical year was presented. From the typical year weather, the hottest day temperature is known as 37.12°C for Yangon, 38.16°C for Mandalay and 33.34°C for Myitkyina. Basically, the highest solar radiation occurs at the summer time when the sky is clear the cloud, and the highest temperature tends to occur at the peak summertime. The peak temperature eventually changes back to the normal when the rainy season starts, however, remains constant high temperature. The average temperature is usually above 22°C, and most of the daytime the temperature rises above 27°C. The average daily relative humidity is above 70% for the whole year except the peak summer time. Regarding wind speed, Yangon receives above 1.0m/s throughout a year. Mandalay receives above 0.5m/s, but the wind blows strongly in the rainy season in the middle of a year. Myitkyina receives a very moderate wind speed above 0.15 to 0.3m/s. Generally, the wind blows from the south and north direction according to the trade winds. Mandalay receives the highest solar radiation due to her location of flat central land. High diffuse radiation continually occurs throughout the year, and it is approximately half amount of global horizontal radiation. Direct radiation is usually lower at the early mid-year to the end of mid-year while the rainy season occurs.

The World Wild Life Fund and the Myanmar Climate Change Alliance reported in 2017 as the annual temperature of Myanmar can be increased 1.3°C to 2.7°C in 2041-2070 compared to 1980-2005 according to the NASA NEX-GDDP

(2015) sources (Horton et al., 2017). If only the summer time is considered, the report highlighted that the temperature could be increased up to 2.9ºC. The increment would cause the peak temperature above 40°C that is obvious. Thus, it is necessary to consider the increasing awareness of building thermal performance for extreme overheating risks. In this study, the authors created three future climate weather files by using a "shift" of a current hourly weather data parameter by adding increased value (Jentsch et al., 2008). The values were considered as 1.3°C dry bulb temperature (DBT) increased case annually, 2.7°C DBT increased case annually and, 2.9°C DBT increased case in the summertime. Technically, creating the future weather files requires expert knowledge of climatology. Due to the lack of availability of weather data, three customised weather files were generated by the authors by using the hourly offset method based on typical meteorological weather files. The experimental investigation aimed at observing the thermal performance of the defined fifteen scenarios in the future climate change conditions. A constraint was that the future weather files were limited to change in the dry bulb temperature alone. Hence, further work is required to take into account other parameters, such as global radiation, diffuse radiation, relative humidity, cloud cover, and wind speed and wind direction.

2.2. U-value matrix and tested variables

The u-value was chosen in this study by considering two basic construction materials. Generally, 220mm (9 inches) solid brick wall with 13mm thick plaster has the u-value of 2.09 W/m^{2}K, and the waterproof roof is covering with 19mm timber decking, ventilated airspace, vapour control layers and 12.5mm plasterboard has the u-value of 2.35 W/m^{2}K (CIBSE Guide A, 2007). Based on these assumptions, the highest range was set at 2.0 W/m^{2}K in this study. Each matrix was offset by 0.5, but the lowest range was kept at 0.2 W/m^{2}K. When one u-value of a building system was changed, there were 125 sets of u-value matrix. Considering the solar absorptance (SA or α) and thermal emittance (TE or ε) variables for cool roof function, higher and lower values were introduced. SA becomes 1 if a surface is black opaque. TE becomes 1 when a surface emits thermal radiation highly (Coolrooftoolkit, 2012). In this analysis, the high SA and high TE were set as 0.9. The low SA and low TE were set as 0.3. When the u-value was introduced as low as 0.2 W/m^{2}K, it could affect the thermal mass properties. However, it was treated as a constant value for all 125 matrices. Two ventilation modes – daytime ventilation mode and a 24-hour ventilation mode - were considered in this study. Finally, there were eight scenarios with a multivariable function to test the pre-defined 125 matrices, as shown in Table 1. The green colour represents reducing the roof u-values, the blue colour represents reducing the wall u-values, and the yellow colour represents reducing the floor u-values if the other two building envelope u-values are fixed.

Table 1: Matrix table for 125 u-value variation of roof, wall, and floor

U-value variation from 2.0W/m2K to 0.2W/m2K. [R=roof, W=wall, F=floor]				
R2.0_W0.2_F0.2	R1.5_W0.2_F0.2	R1.0_W0.2_F0.2	R0.5_W0.2_F0.2	R0.2_W0.2_F0.2
R2.0_W0.5_F0.2	R1.5_W0.5_F0.2	R1.0_W0.5_F0.2	R0.5_W0.5_F0.2	R0.2_W0.5_F0.2
R2.0_W1.0_F0.2	R1.5_W1.0_F0.2	R1.0_W1.0_F0.2	R0.5_W1.0_F0.2	R0.2_W1.0_F0.2
R2.0_W1.5_F0.2	R1.5_W1.5_F0.2	R1.0_W1.5_F0.2	R0.5_W1.5_F0.2	R0.2_W1.5_F0.2
R2.0_W2.0_F0.2	R1.5_W2.0_F0.2	R1.0_W2.0_F0.2	R0.5_W2.0_F0.2	R0.2_W2.0_F0.2
R2.0_W0.2_F0.5	R1.5_W0.2_F0.5	R1.0_W0.2_F0.5	R0.5_W0.2_F0.5	R0.2_W0.2_F0.5
R2.0_W0.5_F0.5	R1.5_W0.5_F0.5	R1.0_W0.5_F0.5	R0.5_W0.5_F0.5	R0.2_W0.5_F0.5
R2.0_W1.0_F0.5	R1.5_W1.0_F0.5	R1.0_W1.0_F0.5	R0.5_W1.0_F0.5	R0.2_W1.0_F0.5
R2.0_W1.5_F0.5	R1.5_W1.5_F0.5	R1.0_W1.5_F0.5	R0.5_W1.5_F0.5	R0.2_W1.5_F0.5
R2.0_W2.0_F0.5	R1.5_W2.0_F0.5	R1.0_W2.0_F0.5	R0.5_W2.0_F0.5	R0.2_W2.0_F0.5
R2.0_W0.2_F1.0	R1.5_W0.2_F1.0	R1.0_W0.2_F1.0	R0.5_W0.2_F1.0	R0.2_W0.2_F1.0
R2.0_W0.5_F1.0	R1.5_W0.5_F1.0	R1.0_W0.5_F1.0	R0.5_W0.5_F1.0	R0.2_W0.5_F1.0
R2.0_W1.0_F1.0	R1.5_W1.0_F1.0	R1.0_W1.0_F1.0	R0.5_W1.0_F1.0	R0.2_W1.0_F1.0
R2.0_W1.5_F1.0	R1.5_W1.5_F1.0	R1.0_W1.5_F1.0	R0.5_W1.5_F1.0	R0.2_W1.5_F1.0
R2.0_W2.0_F1.0	R1.5_W2.0_F1.0	R1.0_W2.0_F1.0	R0.5_W2.0_F1.0	R0.2_W2.0_F1.0
R2.0_W0.2_F1.5	R1.5_W0.2_F1.5	R1.0_W0.2_F1.5	R0.5_W0.2_F1.5	R0.2_W0.2_F1.5
R2.0_W0.5_F1.5	R1.5_W0.5_F1.5	R1.0_W0.5_F1.5	R0.5_W0.5_F1.5	R0.2_W0.5_F1.5
R2.0_W1.0_F1.5	R1.5_W1.0_F1.5	R1.0_W1.0_F1.5	R0.5_W1.0_F1.5	R0.2_W1.0_F1.5
R2.0_W1.5_F1.5	R1.5_W1.5_F1.5	R1.0_W1.5_F1.5	R0.5_W1.5_F1.5	R0.2_W1.5_F1.5
R2.0_W2.0_F1.5	R1.5_W2.0_F1.5	R1.0_W2.0_F1.5	R0.5_W2.0_F1.5	R0.2_W2.0_F1.5
R2.0_W0.2_F2.0	R1.5_W0.2_F2.0	R1.0_W0.2_F2.0	R0.5_W0.2_F2.0	R0.2_W0.2_F2.0
R2.0_W0.5_F2.0	R1.5_W0.5_F2.0	R1.0_W0.5_F2.0	R0.5_W0.5_F2.0	R0.2_W0.5_F2.0
R2.0_W1.0_F2.0	R1.5_W1.0_F2.0	R1.0_W1.0_F2.0	R0.5_W1.0_F2.0	R0.2_W1.0_F2.0
R2.0_W1.5_F2.0	R1.5_W1.5_F2.0	R1.0_W1.5_F2.0	R0.5_W1.5_F2.0	R0.2_W1.5_F2.0
R2.0_W2.0_F2.0	R1.5_W2.0_F2.0	R1.0_W2.0_F2.0	R0.5_W2.0_F2.0	R0.2_W2.0_F2.0

Each matrix is tested from eight scenarios:
α=0.9, = ε=0.9, Day-time ventilation mode
α=0.9, = ε=0.3, Day-time ventilation mode
α=0.3, = ε=0.9, Day-time ventilation mode
α=0.3, = ε=0.3, Day-time ventilation mode
α=0.9, = ε=0.9, 24 hours ventilation mode
α=0.9, = ε=0.3, 24 hours ventilation mode
α=0.3, = ε=0.9, 24 hours ventilation mode
α=0.3, = ε=0.3, 24 hours ventilation mode

α and ε variables are only varied for roof.

All matrices are tested for three cities: Yangon, Mandalay, and Myitkyina

The results of highlighted coloured matrices are shown in the charts.

Reduced u-value from roof
Reduced u-value from wall
Reduced u-value from floor

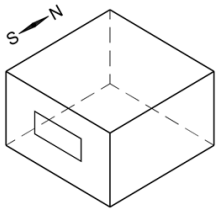

Reference Model

2.3. Reference model and simulation process

A simplify cube shape building with 5m length, 5m width, and 3m height was considered as a reference model to carry out the further dynamic simulation tasks. The 2m width and 1.125m height south-facing window were considered for the ventilation purpose in which the day-time ventilation mode was considered from 06:00 am to 18:00 pm. As regards the internal heat gain, one fluorescent lighting with 15 W/m^2 maximum sensible gains from 18:00 pm to 06:00 am was added. Three occupants with 75 W/m^2 maximum sensible gains and 55 W/m^2 latent gain were added for a 24-hour profile. The infiltration rate of 0.5 ach and ventilation rate 0.5 ach were added. In the first set of simulation, the defined 125 model simulation matrices where the geometry, internal gains, infiltration, glazing, fenestration, and thermal mass were constant, but the u-values of the roof, walls, and floor varied. The finish of the surfaces for each scenario was also fixed, meaning that absorptivity and emissivity were also constant. Then, the simulation was run for two ventilation modes. In the next set

of simulations, absorptivity and emissivity were varied following the pre-defined eight scenarios. Each of the simulations was run in three cities. In total 3360 dynamic simulations were performed to understand the sensitivity of the model to these parameters in the three climates. ApacheSim (IESVE) dynamic simulation program was used to generate dynamic simulations. IESVE offers several simulations engines for different calculation methods, and the results differ following the values of a coefficient used in the equations. In this study, the McAdams' equation of the external convention model, CIBSE fixed value for the thermal convention model, and anisotropic for solar radiation model were chosen. In the internal convection model, using the fixed value, the surface orientation, and air-surface temperature difference and mean air velocity is not considered (IESVE, 2015); therefore, the overheating hour's result would be different if they are accounted in the calculation.

2.4. Output parameters and comparison target

The results of sensitivity analyses were carried out to evaluate the impact of material variables on the thermally comfortable indoor environment. The output data was concerned to check the range that exceeded a threshold of comfortable temperature and the peak condition that reached in each scenario. In this study, the concern was the impacts of thermophysical properties for indoor environments. The human factor was not a key performance indicator here. On the other hand, the adaptable temperature can be varied by the influences of local climate contexts, building types, diverse cultural backgrounds and so forth. For the sake of convenience in this study, the authors proposed a range from 24°C to 36°C to check as a threshold and to generate quantitative results. When a 4°C interval is further separated, eg. 24°C, 28°C, 32°C and 36°C. In which, the threshold 32°C is considered as a threshold between the acceptable condition and the overheating condition. The temperature above 36°C is considered as an extreme range. It is important to note that the range here is for comparison purpose, and it is not defined as a thermal comfort benchmark for the study climates.

3. RESULTS

The simulation matrix models developed were used to generate hourly temperature through the defined level of insulation and roof exterior finishes. The results were extracted to check the sensitivities of material variables to indoor air temperature (AT), mean radiant temperature (MRT) and internal surface temperature of the roof.

3.1. Sensitivity of insulation location

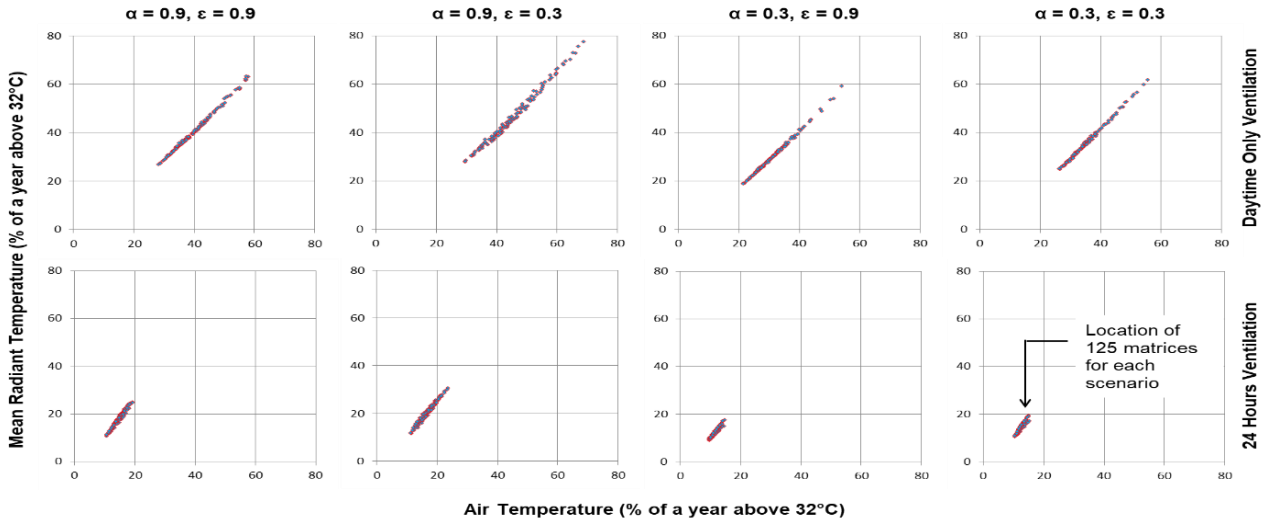

Figure 2: Percentage of a year above 32°C for eight scenarios in Yangon, as an example

In Figure *2:*e 2, the results of Yangon were presented for eight scenarios by using 32°C threshold. A very similar result was found in the other two cities although the results were not presented here. The results proved that the logical understanding of adding insulation to the roof at first is the best case. The peak temperatures were found in α=0.9 and ε=0.3 scenario, which is opposed to the cool roof variable. Impressive results were found in α = 0.3 and ε = 0.9 scenarios where the overheating hours were increased when the u-values were reduced. It means if a roof has a cool roof performance, low u-value is undesirable. The results clearly showed that reducing u-values was more effective if a roof had high SA and high TE. Impressive results were that a similar result could be seen in two cases: the R0.2_W2.0_F2.0 matrix with high SA and the R2.0_W2.0_F2.0 matrix with low SA. In a roof had a very low u-value, the internal room temperatures were increased when the wall u-values were reduced in the daytime only ventilation mode. It means as long as a building is prevented the solar heat gain by the roof, the wall insulation is not required in Myanmar. The results became worst if the floor u-value was reduced. It is understandable that the passive approach of ground cooling was lost from the floor u-value was reduced. An impressive result was that the sensitivity of 125 u-value matrices were less difference in the 24-hour ventilation, regardless the roof exterior finish variation, the intensity of overheat could reduce effectively. Based on the first 3000

simulation results, 13 set of the optimum and considerable u-value matrices were selected to present further investigation works. The selected matrices were highlighted in Table 1, where the feasible options are highlighted in green, blue and yellow colour in which the green colour is for priority consideration. The unlighted colours represent unfeasible options to consider as overheating periods were extended when the u-values were reduced.

3.2. Sensitivity of U-value, solar absorptivity, and thermal emissivity

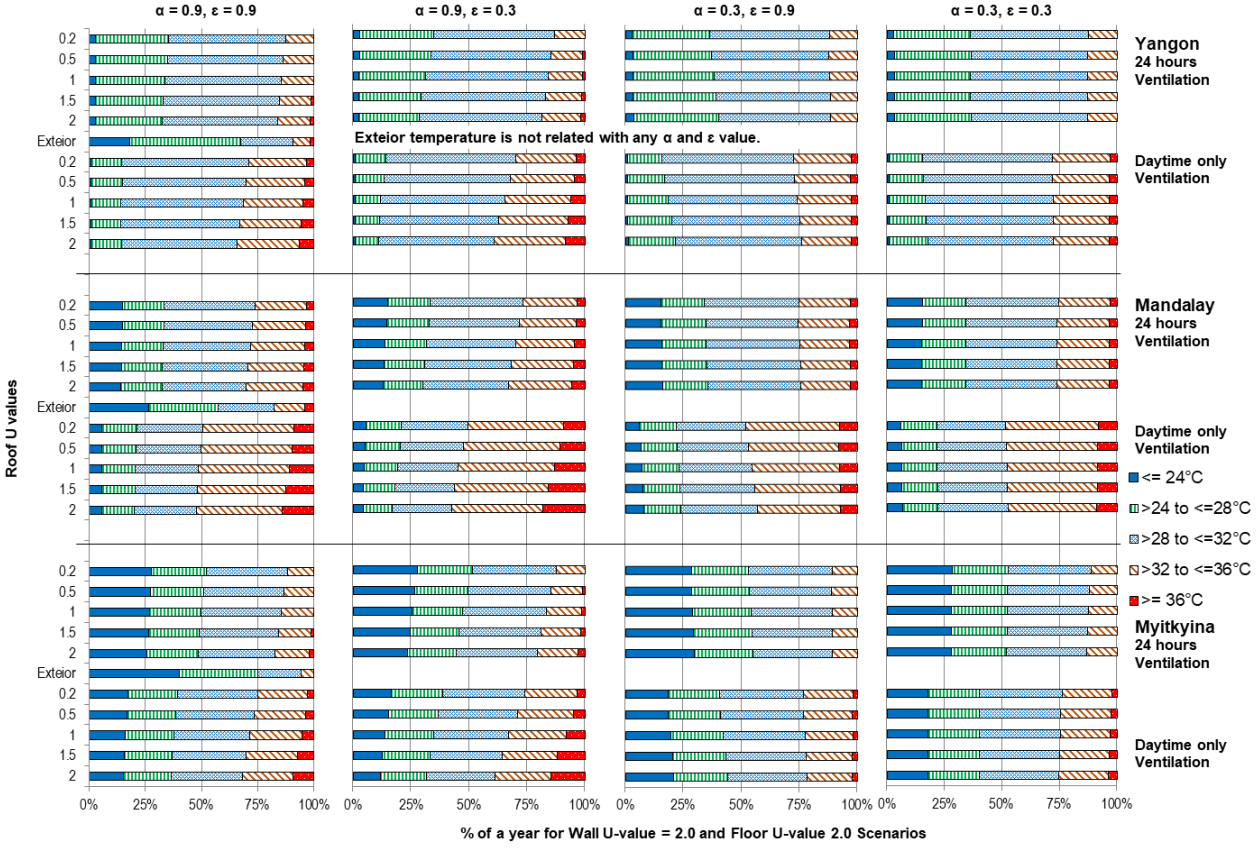

Figure 3: Room Air Temperature percentage in a typical weather year for three cities with a fixed wall and floor u-value cases

This section presents the temperature ranges of the exterior condition and eight scenarios of indoor room temperature. Since it was known that reducing roof u-value was the most efficient approach, five u-value matrices were selected for comparison here. They are R2.0_W2.0_F2.0, R1.5_W2.0_F2.0, R1.0_W2.0_F2.0, R0.5_W2.0_F2.0, R0.2_W2.0_F2.0. Among all results, Mandalay received the longest overheating period, for example, 13.95% of a year was above 36°C was dropped to 8.53% if roof u-value was reduced from 2 W/m^{2}K to 0.2 W/m^{2}K in α=0.9 and ε=0.9 scenario. In fact, only 3.82% of a year was above 36°C in the typical weather file of Mandalay. In Mandalay, 18.21% of a year was above 36°C was dropped to 9.10% if roof u-value was reduced from 2 W/m^{2}K to 0.2 W/m^{2}K in α=0.9 and ε=0.3 scenario. It means reducing u-value is more sensitive in low emissivity cases. However, high emissivity cases performed better results. In the scenario with α = 0.9 and ε = 0.9 in the daytime ventilation mode, the overheating period above 32°C was decreased 5.18%, 2.75% and 6.89% of a year in Yangon, Mandalay, and Myitkyina when the roof u-value was reduced from 2.0 to 0.2W/m^{2}K. A very similar result could be found in a 24-hour ventilation mode without reducing roof u-value, from 2 W/m^{2}K, which means a 24-hour ventilation model could decrease more overheating hours than reducing u-value. As shown in Figure *3:* 3, the effect of insulation of a roof surface about reductions of u-value is only effective in non-cool-roof condition. Once the roof surface is considered as a cool roof, the changes of interior room air temperature are insignificant and even bring worst overheating risks by reducing u-value. The impact of overheating from annual results and hottest day temperature fluctuation for this selected five u-value matrices were presented in Figure *4:* 4 and Figure 5.

3.3. Sensitivity to internal roof surface temperature and mean radiant temperature

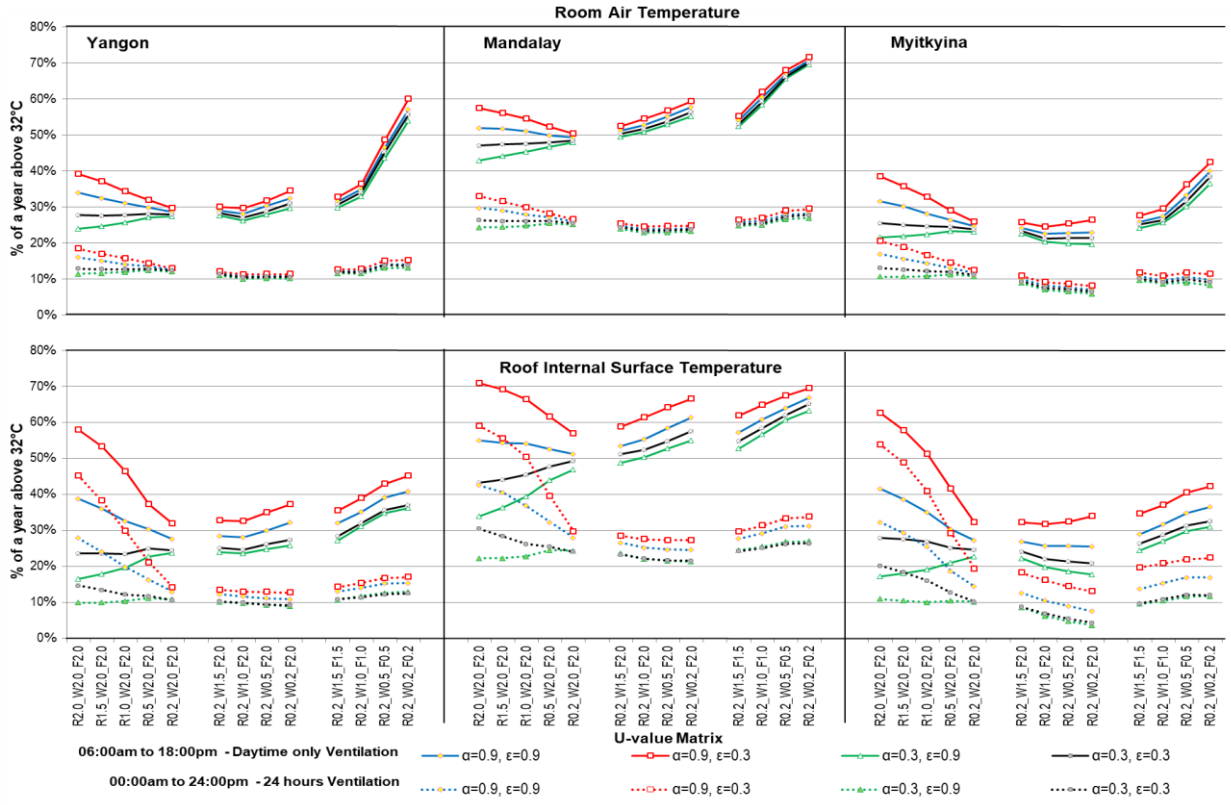

Figure 4: Room air and roof internal surface temperature percentage of a year above 32°C in a typical weather year

In Figure *4:* 4, the results of 13 u-value matrices were presented for the room air temperature and roof internal surface temperature above 32°C for the three cities. Basically, the internal roof surface received higher temperature than the temperature of air mass below. There were a shorter period of extreme overheating above 36°C in α=0.3 and ε=0.9 scenario in Figure *3:* 3, but there were unremarkable differences in reducing u-value. In fact, it can be seen in Figure *4:* 4 that the divergent chart results were found in the cases with α = 0.9 and ε = 0.3 and α = 0.3 and ε = 0.9 while the roof u-values were varied. On the other hand, the overheating period was extended when the wall and floor u-values are reduced in low SA daytime ventilation cases. Figure *4:* 4 clearly showed the importance of the surface colouration of exterior walls and roof, and a necessary to keep ground cooling without reducing floor u-value. The temperatures could be reduced effectively when the nocturnal ventilation was applied - for example, 27.16% reduction could be found in Mandalay R0.2_W2.0_F2.0 cases.

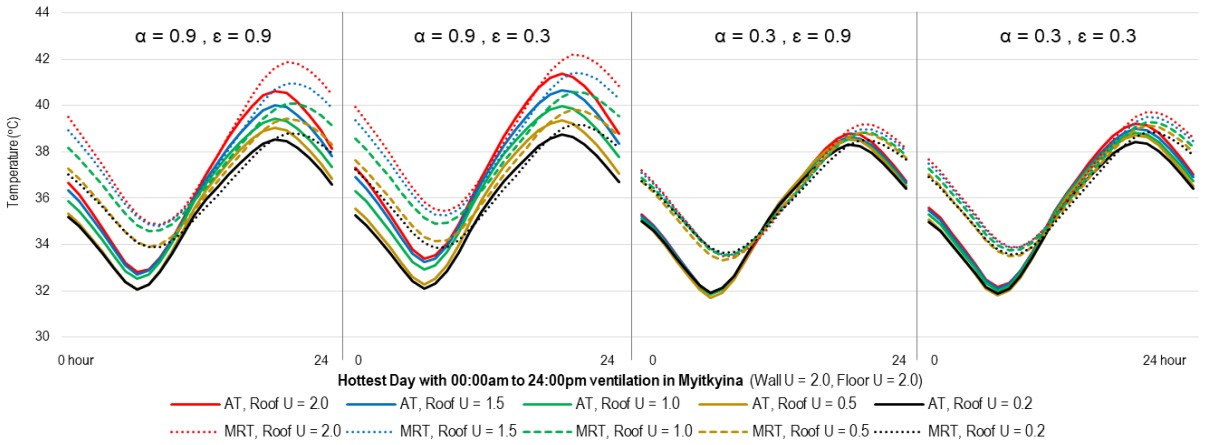

Figure 5: Comparison of the hottest day air temperature and mean radiant temperature in a typical weather year

The relationship between the air temperature (AT) and the mean radiant temperature (MRT) for the hottest day of Myitkyina was presented in Figure 5 for five u-value matrices. A very similar result was found in the other two cities, but the difference was Myitkyina received the highest and worst temperature in the hottest day of a year due to the low wind speed throughout

the year. Consistent trend lines were found for all cases, but the significant difference was between the values of exterior roof surfaces rather than u-values. The effort of reducing u-values less impacted in the AT, but hugely impacted in the MRT, especially if the roof had high SA. Although Myitkyina had a shorter period of extreme overheating above 36°C and the hottest day external air temperature was only 33.34°C, the AT was increased up to 41.38°C, and MRT was increased up to 42.2°C in α = 0.9 and ε = 0.3 when the roof had u-value 2 W/m^{2}K. On the other hand, there were remarkable differences in reducing u-value in low SA cases. Based on the results, it can be stated that the cool roof effect with low SA can give better performance for the hottest day and summertime. It also means that the radiative and convective heat transfer is more sensitive in the study climate rather than conductive heat transfer.

3.4. Comparison for the typical weather year and future climate change scenarios

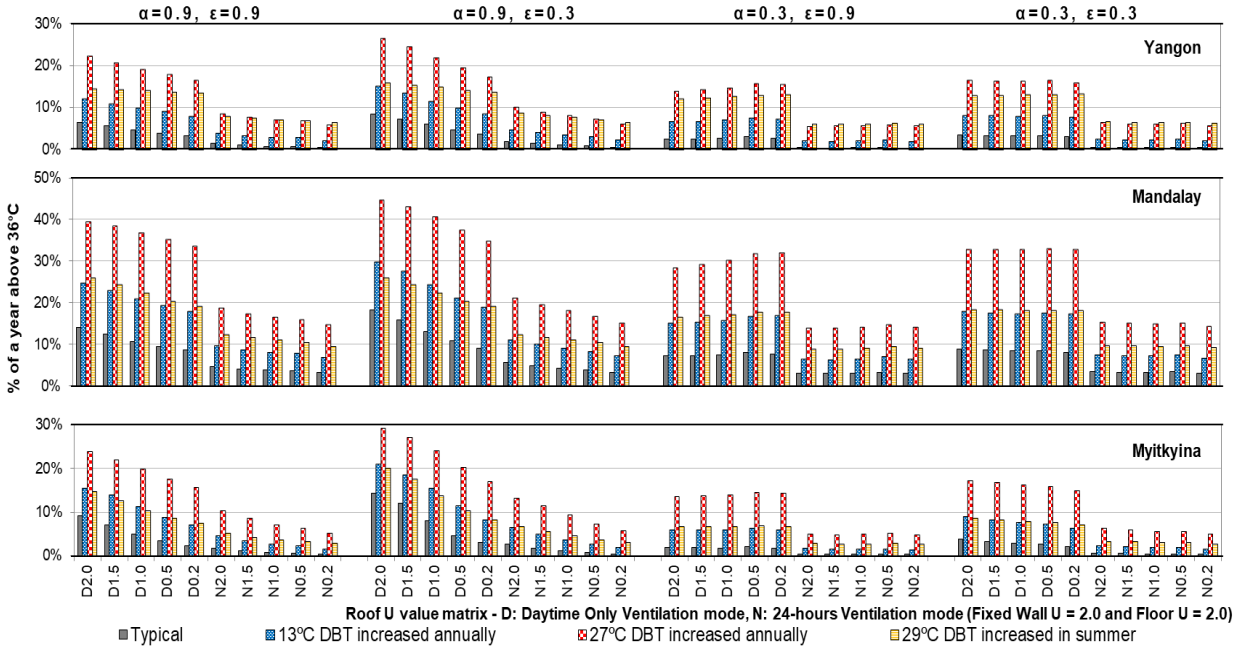

Figure 6: Comparison of the overheating hours above 36°C in the typical weather year, 1.3°C DBT annually increased cases, 2.7°C DBT annually increased cases, and 2.9°C DBT increased in summer cases

In Figure *6:* 6, the comparison of overheating hours above 36°C was presented for four cases: typical weather year and three future climate scenarios. The worst results were found in 2.7°C DBT annually increased cases as expected. If 1.3°C DBT annually increased cases and 29°C DBT increased in summer cases are compared, a small difference was found in Mandalay and Myitkyina, but there was a significant difference in Yangon, especially in α=0.3 with ε=0.9 scenario. Technically, the air in Yangon contains more vapour due to the location near the ocean. High humidity by nature and increasing global temperature is upcoming of summer overheating risks in Yangon. It also highlighted that the importance of the design-summer year for the overheating risks for the future climate scenarios. From all the findings, the nocturnal ventilation was more sensitive in high SA scenario couple with the roof u-value 2.0 W/m2K, and the more overheating hours could decrease. Although the roof had low u-value in high SA scenario, there is some amount of heat was transferred to the internal environment through the daytime ventilation. The nocturnal ventilation is more sensitivity in the TE at night rather than the values of SA. Therefore, a slight more overheating could be reduced in the α=0.3 with ε=0.9 scenario than α=0.3 with ε=0.3 scenario. Nonetheless, the nocturnal ventilation became more sensitive in both high SA and low SA scenarios in the future climate scenarios.

4. DISCUSSION OF THE RESULTS

Results of 125 u-value matrices showed that the roof insulation alone was necessary to consider in high SA scenarios in Myanmar climates. The insulations were not preferrable to the walls and floors in the studied building; otherwise, the building was overheated. That finding answered the first question that the roof u-value up to 0.2W/m^{2}K, and the wall and floor u-value up to 2.0W/m^{2}K are optimum values in the defined model. In fact, the optimum values can also be varied due to the building types and sizes.

In order to answer the second question, it is necessary to separate two perspectives: insulation in the building member or cool roof as they have a different role and different impacts. It was obvious that the roof insulation was crucial in the non-cool-roof scenarios in the studied climates. In fact, the insulation in the building members is not a priority approach due to its issue of building weight and size. Technically, preventing the heat gain through the exterior surface is more important as the predominant heat transfer mode is the radiative one for the study climates. Whatever the TE, the low SA is the priority to consider as it can reduce the own building weight and able to approach earthquake resistance light-weight roofs

rather than massive insulated building. In the low SA scenario, the u-values are required to control, means the insulation should not be a reason to extend the overheating period. Whatever the SA, the high TE is the priority to consider to increase the radiative heat transfer through the solid roof surface at night to remove the hot air effectively. On the other hand, the moisture-related problems in the white roof and trapped rains on the roof are necessary to solve in the high TE scenarios as water holds heat the white colour envelop demands higher maintenance requirements. When the roof has high SA and high TE, the lower u-value is, the better; especially it could be seen in the results of Myitkyina.

In the study climates, the radiative and convective heat transfer process are the main heat transfer process that is related with the hot and humid air mass, which asks the natural ventilation design to play a critical role. Whatever SA, TE and roof u-values, the nocturnal ventilation plays sensitively to reduce the overheating hours, and the performance is depended on the amount of heat stored in the daytime, the degree of envelope insulation and the adjacent condition to transfer heat at night. For example, if the envelope is highly insulated, a quick way to transfer heat to the sky is through the ventilation only. The different is uninsulated envelope can help a quicker heat transfer at night. For the third question, the results of all scenarios showed that coupling the nocturnal ventilation could reduce more overheating period. In this study, all models were considered south facing, but the airspeed of southwest and northeast is stronger in Myitkyina. In fact, the effectiveness of nocturnal ventilation was absolutely depended on the outdoor airspeed, external temperature fluctuations through the building envelope, the capacity of the building envelope to store heat, which is challenging to report precisely although the thermal mass values in the 125 u-value matrices were fixed.

Although the diurnal temperature swing is small, the nocturnal ventilation is one of the high potential strategies to reduce the daytime stored heat coupled with two roof types. The first roof type is cool roof without insulation. The second roof type is high SA and high TE with low u-value in the roof. Unfortunately, both roof types have limited capability in daytime only ventilation modes for the present climate and future climate change scenarios. The last question answers that a careful design with combined design strategies to achieve the effective nocturnal ventilation is the most feasible option to improve the indoor thermal environment for future climate scenarios. Nonetheless, the daytime heat gain is first to reduce and prevent to increase the efficiency of the nocturnal ventilation.

5. CONCLUSION

The present work was aimed to fill the knowledge gap of understanding the relationship between envelope u-value, solar absorptivity and thermal emissivity of the roof in Myanmar climates. The sensitivity analysis has presented the impacts of roof materials variables from different temperature ranges with two ventilation modes. Although findings of this study are limited with the scope of work and the threshold, the sensitivity analysis of this study could answer feasible solutions to improve the thermal performance both for the present and future climate change scenarios.

Moe (2014)'s explanation of the concept of insulation is, of course, applicable for the tropical climate to isolate a building in the hot and humid environment if different insulation types are applied carefully. Insulation types can be categorised as resistive insulation, reflective insulation and capacitive insulation (Roaf et al., 2003, page 56). The resistive insulation approach of "the lower the u-value, the better to slow down the flow of heat into the building" is more applicable for the roof in all Myanmar climates if the exterior finish has high solar absorption. In this case, the conductivity of the material is crucial that ask to increase the size and the own building weight, which is somehow a challenge for the earthquake resistant structural design. If the roof has cool roof effect with low solar absorptivity and high thermal emissivity, "the higher the u-value, the better" could overwrite "the lower the u-value, the better," which is a characteristic of reflective insulation. In this case, the surface colouration of roofs and exterior walls are crucial that asks the extra maintenance for the use of high albedo. Moreover, the radiation reflected back into the surrounding, and the unpleasant glares are necessary to control. No matter what, the efficiency of the resistive and reflective insulation can be increased if the nocturnal ventilation is considered in the studied climates. It is worth noting about the efficacy of the nocturnal ventilation and the data of future weather files. The files were created by adding the predicted temperature without changing other variables. Technically, the humidity of nigh time is higher than daytime that asks different thermal comfort adjustment. If the future weather files are created with changes in temperature and humidity, the results will be different. The capacitive insulation is aimed to avoid immediate heat transfer by its thermal mass. The thermal mass is critical to determine the time lag of thermal storage and always necessary to check both for the annual overheating reduction and summer overheating condition. The thermal mass value was fixed in this study; therefore, there were no findings for this insulation type. Nonetheless, it is necessary to highlight that the impacts of capacitive insulation are important to be taken into account when the resistive insulation and reflective insulation are compared. The capacitive insulation is also somehow a challenge for the earthquake resistant structural design. Additionally, it needs to consider the impact of the position of insulation; cool-walls and heat-emitting-walls as they are not investigated in this study. Finally, it needs to suggest considering the possibilities to improve the efficacy of natural ventilation that is more effective in the study climates. A careful design in fenestration and ventilation variables can further improve the indoor thermal environment. In sum, it is worth considering the importance of combining multi-variables: insulation and ventilation- are better to improving thermal environments for all Myanmar climates.

6. REFERENCES

Alvarado, J L. & Martinez, E 2008. Passive Cooling of Cement-Based Roofs in Tropical Climates. *Energy and Buildings,* 40**,** 358-364.

Athienitis, A K & Santamouris, M 2002. *Thermal Analysis and Design of Passive Solar Buildings,* London, James & James (Science Publishers).

Berdahl, P & Bretz, S E. 1997. Preliminary Survey of the Solar Reflectance of Cool Roofing Materials. *Energy and Buildings,* 25**,** 149-158.

Cibse Guide a, Environmental Design. 2007. *CIBSE GUIDE A.* Section title.

COOLROOFTOOLKIT 2012. A Practical Guide to Cool Roofs and Cool Pavements. Cool Roofs and Cool Pavements Toolkit (https://www.coolrooftoolkit.org): Global Cool Cities Alliance and R20 Regions of Climate Actions.

Diamant, R. M. E. 1965. *Insulation of Buildings: Thermal and Acoustic,* Dorst House, Stamford Street, London.

Erell, E 2007. Radiative Cooling. *In:* SANTAMOURIS, Mat (ed.) *Advances in Passive Cooling.* UK, USA: Earthscan.

Feist, W. 2006. *Definition of Passive Houses* [Online]. https://passiv.de/: Passive House Institute. Available: https://passiv.de/former_conferences/Passive_House_E/passivehouse_definition.html [Accessed December 25 2017].

Garde, F, Adelard, L, Boyer, H. & Rat, C. 2004. Implementation and Experimental Survey of Passive Design Specifications Used in New Low-Cost Housing under Tropical Climates. *Energy and Buildings,* 36**,** 353-366.

Hindrichs, D U. & Daniels, K 2007. *Plus Minus 20° / 40° Latitude: Sustainable Building Design in Tropical and Subtropical Regions,* Stuttgart / London, Edition Axel Menges.

Horton, R, Mel, M De, Peters, D, Lesk, C, Barlett, R, Helsingen, H, Bader, D, Capizzi, P, Martin, S & Rosenzweig, C 2017. Assessing the Climate Risks in Myanmar, a Contribution to Planning and Decision-Making in Myanmar.

Hyde, R 2001. *Climate Responsive Design: A Study of Buildings in Moderate and Hot Humimd Climates,* London, Spon Press.

IESVE 2015. Apachesim Calculation Methods. *In:* ENVIRONMENT, IES Virtual (ed.) *Apache.* Integrated Environmental Solutions Limited.

Jentsch, M F., Bahaj, A S. & James, P A. B. 2008. Climate Change Future Proofing of Buildings - Generation and Assessment of Building Simulation Weather Files. *Energy and Buildings,* 40**,** 2168.

Kreft, S, Eckstein, D, Dorsch, L & Fischer, L 2015. *Global Climate Risk Index 2016. Who Suffers Most from Extreme Weather Events? Weather-Related Loss Events in 2014 and 1995 to 2014.,* Bonn, Germany, Germanwatch e.V.

Levinson, R & AkbarI, H 2010. Potential Benefits of Cool Roofs on Commercial Buildings: Conserving Energy, Saving Money, and Reducing Emission of Greenhouse Gases and Air Pollutants. *Energy Efficiency,* 3**,** 53-109.

Moe, K 2014. *Insulating Modernism: Isolated and Non-Isolated Thermodynamics in Architecture,* Berlin, Germany, Birkhäuser.

Piselli, C, Saffari, M, Gracia, A De, Pisello, A L, Cotana, F & Cabeza, L F. 2017. Optimization of Roof Solar Reflectance under Different Climate Conditions, Occupancy, Building Configuration and Energy Systems. *Energy and Buildings,* 151**,** 81-97.

Roaf, S, Fuentes, M & Tomas, S 2003. *Ecohouse 2: A Design Guide*, Oxford : Architectural.

Rodrigues, L T, Gillott, M & Tetlow, D 2013. Summer Overheating Potential in a Low-Energy Steel Frame House in Future Climate Scenarios. *Sustainable Cities and Society,* 7**,** 1-15.

Rubel, F & Kottek, M. 2010. *Observed and Projected Climate Shifts 1901-2100 Depicted by World Maps of the Köppen-Geiger Climate Classification* [Online]. Available: http://koeppen-geiger.vu-wien.ac.at/shifts.htm [Accessed 7 August 2017].

Saber, H H., Swinton, M C., Kalinger, P & Paroli, R M. 2012. Long-Term Hygrothermal Performance of White and Black Roofs in North American Climates. *Building and Environment,* 50**,** 141-154.

Saltelli, A, Ratto, M, Tarantola, S & Campolongo, F 2006. Sensitivity Analysis Practices: Strategies for Model-Based Inference. *Reliability Engineering and System Safety,* 91**,** 1109-1125.

Synnefa, A., Santamouris, M. & Akbari, H. 2007. Estimating the Effect of Using Cool Coatings on Energy Loads and Thermal Comfort in Residential Buildings in Various Climate Conditions. *Energy and Buildings,* 39**,** 1167-1174.

White Box Technologies 2017. Weather Data for Energy Calculations. *In:* ASHRAE (ed.). White Box Technologies

357: Humidification-dehumidification desalination system using hollow fibre membranes

Omar RAMADAN[1], Siddig OMER[2], Saffa RIFFAT[3]

[1] University of Nottingham, Nottingham, omar.ramadan@nottingham.ac.uk
[2] University of Nottingham, Nottingham, siddig.omer@nottingham.ac.uk
[3] University of Nottingham, Nottingham, saffa.riffat@nottingham.ac.uk

The ability of many nations to sustain fresh water supply is strained due to the increased population growth and population density. Hence water desalination of sea or brackish water presents a sustainable solution to tackle the issue of increase in demand for fresh water. This article experimentally investigate water desalination, using humidification-dehumidification process. In this process, air is humidified using saline water and the subsequent condensation of the humid air at normal atmospheric pressure produces freshwater. Hollow fibre membrane bundles are employed in the humidification chamber, to humidify the air. The humidified air is cooled resulting in condensation of the water vapour to obtain distilled water using shell and tube heat exchanger. The purpose of the investigation is to assess the ability of the hollow fibre membrane to humidify the incoming air and to optimise the rate of air and water flow rates, in the humidification and dehumidification chambers.

Keywords: Water desalination, Hollow fibre membranes, Sustainable water treatment, Heat and mass transfer

1. INTRODUCTION

Fresh water is a renewable resource, however the ability of many local supplies to sustain fresh water is strained due to the increased population growth and population density (Lee et al., 2011). Over 71% of the earth's surface is covered with water, however around 97.5% of water on the earth is sea or brackish water which contains large amounts of salt (Zhang et al., 2017). The United Nations predicts that water scarcity will potentially impact 2 to 7 billion people in the next 50 years (Teow et al., 2017). Hence water desalination of sea or brackish water presents a sustainable solution to tackle the issue of the increase in demand for fresh water. However, commonly used desalination systems have some drawbacks, for example electrodialysis, reverse osmosis and distillation are capital and energy intensive with hard maintenance regularly required (Wang et al., 2012, Welgemoeda et al., 2005, Yang et al., 2005). Desalination systems can be categorised into thermal processes with phase change, membrane processes including Reverse osmosis (Gabelich et al., 2007), hybrid processes including phase change and membranes (Zhang et al., 2017). In this article water desalination using humidification-dhimmification process is investigated using experimental evaluation. In this process, saline water is evaporated by thermal energy and the subsequent condensation of the humid air that is generated (normally at atmospheric pressure) produces freshwater.

2. EXPERIMENTAL EVALUATION OF THE DESALINATION SYSTEM

Air has the ability to hold large quantities of water vapour and vapour carrying capability increases with temperature. To achieve a water-salt separation, hollow fibre membrane bundles are employed in a humidification chamber, to humidify air. The humidified air is then cooled and condensed to obtain distilled water using shell and tube heat exchanger.

2.1. System description

In the proposed system, sodium chloride solution with 3.5% salinity is used to simulate the seawater. Bundles of hollow fibres membrane are implemented using polypropylene porous fibre with pore size of 0.1 × 0.5 µm. The ambient air flows from a fan outside the fibre bundles in the shell side of the humidifier, while the hot saline water flow inside the fibre bundles. The surface tension forces between the water and the hydrophobic membrane prevent liquid molecules from entering the pores of membranes. Under trans-membrane vapour partial pressure differences, water vapour from saline water inside the fibres can pass through the pores. It is then absorbed by the air stream outside the fibres. Thus, heat and mass transfer is achieved between the hot saline water and the ambient air streams. The air becomes hotter and humid while the outlet salty water becomes cooler. The hot humid air now passes through the shell and tube heat exchanger (dehumidification unit), and heat transfer with the cool saline water results in cooling of the air and the vapour contained is condensed into distilled and collected in fresh water tank, where the salty water becomes hotter. The salty water is pumped to a stainless steel tank where it is further heated using an immersion heater. The outlet of the stored hot salty water in the stainless steel tank is the inlet to the fibre membrane humidification unit. The schematic for the design is shown in Figure **1.**

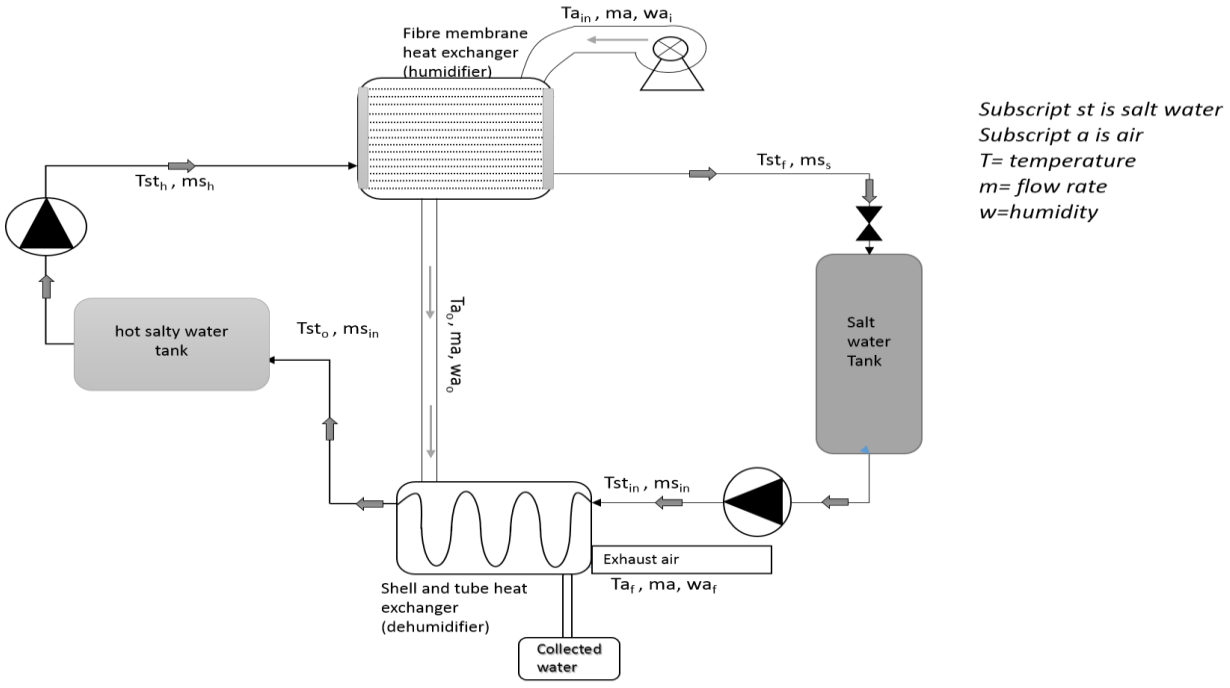

Figure 1: Schematic of the proposed system process

2.2. Experimental design

The aim of the laboratory evaluation is to optimise the system configuration using different number of bundles of fibre membranes in the humidification unit, as well as testing the impact of using different flow rates of the saline water on the heat and mass transfer and the produced fresh water. The system components include the humidification chamber consisting of 4 bundles of hollow fibre membranes provided by Zena with 1385 fibres per bundle, while the dehumidification chamber is implemented using a shell and tube heat exchanger. An immersion heater is used to further heat the salty water to the required temperature (after initial heating in the shell tube heat exchanger). Two Grundfos pumps are used to pump the salty water, the first circulating the salty water from the cold salty water storage tank to the shell and tube heat exchanger while the second pump is used to circulate the hot salty water from the storage tank with the immersion heater to the humidification unit. An in-line ducted fan integrated with an Xpelair speed controller is used to circulate air at ambient temperature and humidity to the humidification chamber. Atrato Ultrasonic Flow Meter is used to monitor the liquid flow rates, the Sensirion EK-H4 evaluation kit was used to monitor the humidity and temperature levels of the air at different locations in the experimental rig. Thermocouples were used to measure the temperature of the air and the salty water at various points on the rig and the measured data was logged into a data logger (Data Taker DT85). The experimental rig developed is shown in Figure 2. The tests were run for 15 minutes, heating the stainless steel tank up to 38°C, then pumping the water via the Grundfos pumps and the air through the in-line duct fan. The air temperature and relative humidity levels were measured every second including ambient temperature (outside the rig), inside the humidification chamber (fibre membranes heat exchanger) and at the outlet of the humidification chamber. While the salty water temperature was measured every second at the inlet to the dehumidification chamber (shell and tube heat exchanger), at the outlet of the stainless steel tank (with immersion heater) and at the outlet of the humidification chamber. The air flow was set at a constant value of 0.5 m/sec while the salty water flow rate was set to 0.5 litres/minute for the first test and the flow rate was increased to 1.3 litres/minute in the second test.

Figure 2: System experimental rig

2.3. Experimental Results

The results for the temperature and humidity levels are displayed for two tests carried out at different flow rates for the salty water: 0.5 litres/minute and 1.3 litres/minute.

The air temperature levels showed that the ambient air temperature was around 27°C for the testing day. The temperature of the inside the humidification chamber rose to around 30 °C-32°C at the outlet of the humidification chamber at flow rate of 0.5 litres/minute, while the air temperature increased to around 31.5°C -32.5°C when the flow rate was increased to 1.3 litres/minute for the salty water. These results show that the air gains some heat from the incoming salty water in the fibre membranes causing the air temperature to rise as it leaves the humidification chamber. The increase in temperature in the humidification chamber was around 5°C -6°C for this test.

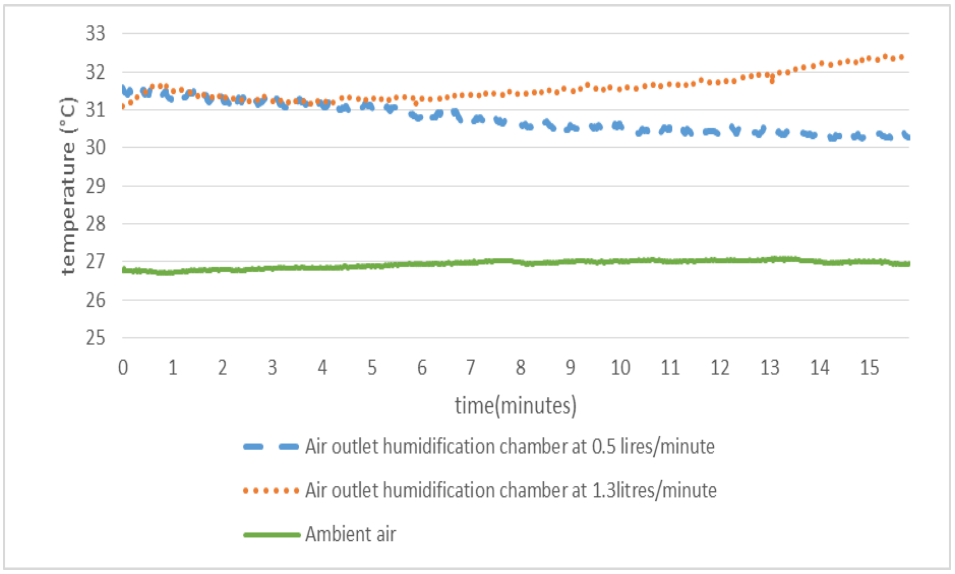

Figure 3: Temperature of the air for different flow rates of salty water

The humidity levels was again monitored in the same locations using the Sensirion humidity and temperature sensors. Figure 4 shows the increase in relative humidity levels of the air as it increases in the humidification chamber. The relative humidity of ambient air was around 51%, which increases to around 83%-87% as it leaves the humidification chamber. Hence the ambient air absorbs the moisture as it leaves the pores in the fibre membranes to increase its humidity levels.

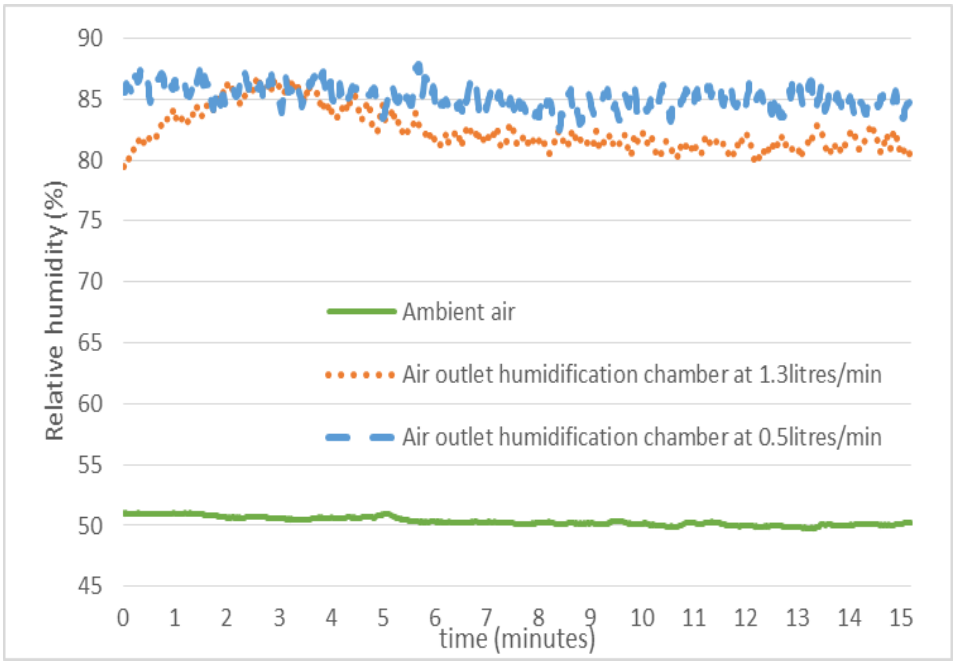

Figure 4: Relative humidity levels for air

Figure 55 shows the variation of temperature for the salty water in the humidification chamber. The immersion heater temperature was to 38°C, hence the salty water temperature leaving the hot tank (inlet to the humidification unit) ranged between 38°C-40°C. The temperature drop in the salty water between the outlet and the inlet of the humidification chamber was around 2.5°C-3.5°C when the flow rate of the salty water was around 0.5 litres/minute. On the other hand, the temperature drop in the salty water was around 1.5°C- 2°C at 1.3 litres/minute, which is slightly lower than the temperature difference when using smaller flow rate of salty water. Hence, the slower the flow rate will result in a higher heat exchange with the air in the humidification chamber.

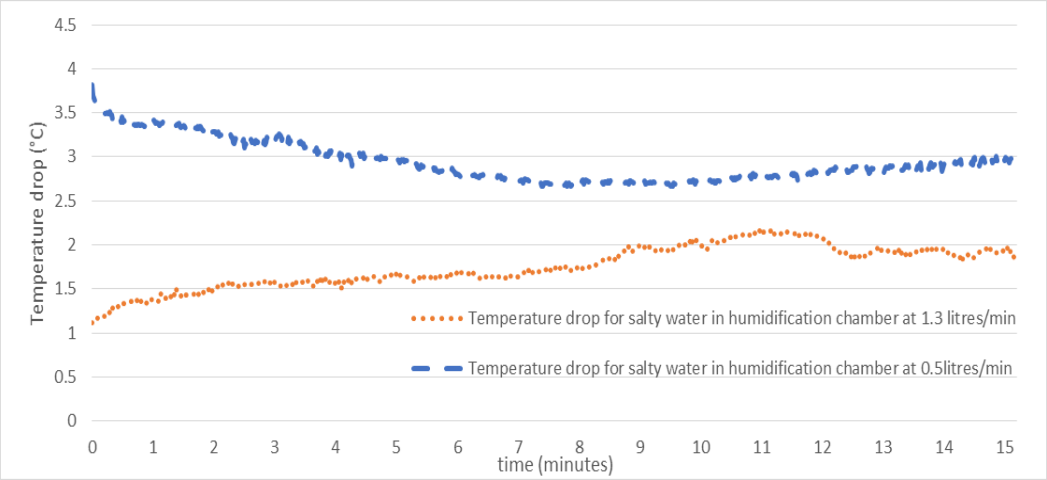

Figure 5: Temperature drop of the salty water in the humidification chamber at different flow rates

3. CONCLUSION

Experimental evaluation was carried out for humidification-dehumidification water desalination unit. The tests were performed using hollow fibre membrane bundles as a humidification unit and a shell and tube heat exchanger as a dehumidification unit. The temperature levels of the salty water, temperature and humidity levels of air were monitored at different positions in the experimental rig. Two tests were carried out at different flow rates for the salty water in the system. The tests showed that the fibre membranes has significant potential to be used in the heat and mass transfer in humidification-dehumidification water desalination systems, as air relative humidity levels were increased significantly, by absorbing the moisture which is leaked from the pores of the hollow fibre membrane bundles. Similar results in terms of humidity levels and temperature increase for the air were achieved when using different flow rates of salty water, while using a lower flow rate of salty water resulted in higher heat loss of the salty water in the humidification unit. Further work on the experimental evaluation will include controlling the water temperature in the cold salty water tank to achieve higher heat exchange levels between the salty water and the hot humid air in the shell and tube heat exchanger (dehumidification unit), to be able to optimise the system and increase the levels of condensation of the air in the dehumidification chamber. Furthermore, more bundles of fibre membranes will be added to evaluate the performance of the system when more surface area is covered with fibres to allow more heat and mass transfer between the salty water and the air in the humidification chamber.

4. ACKNOWLEDGEMENTS

This work is funded by the Newton Fund Institutional Links (Award ref 261839879)

5. REFERENCES

Gabelich, C. J., Williams, M. D., Rahardianto, A., Franklin, J. C., & Cohen, Y. 2007. High-recovery reverse osmosis desalination using intermediate chemical demineralization. *Journal of Membrane Science*, Vol. 301(1), pp. 131-141

Geng, H., Wu, H., Li, P., He, Q., 2014. Study on a new air-gap membrane distillation module for desalination. *Desalination*, Vol. 334(1), pp. 29-38

Lee, KP., Arnot, TC., Mattia D., 2011. A review of reverse osmosis membrane materials for desalination—Development to date and future potential. *Journal of Membrane Science*, Vol. 370, pp. 1-22

Teow, Y. H., Mohammad, A.W., 2017. New generation nanomaterials for water desalination: A review, *Desalination*. In Press.

Wang, Z., Dou, B., Zheng, L., Zhang, G., Liu, Z., & Hao, Z., 2012. Effective desalination by capacitive deionization with functional graphene nanocomposite as novel electrode material. *Desalination*, Vol. 299, pp. 96-102

Welgemoeda, T.J., Schutte, C.F., 2005. Capacitive deionization technology: an alternative desalination solution, *Desalination,* Vol. 83, pp. 327–340.

Yang, C.M., Choi, W.H., Na, B.K., Cho, B.W., Cho W.I. 2005. Capacitive deionization of NaC1 solution with carbon aerogel–silica gel composite electrodes, *Desalination*, Vol. 174, pp. 125–133

Zhang, LZ., Li, GP., 2017. Energy and economic analysis of a hollow fiber membrane-based desalination system driven by solar energy. *Desalination*, Vol. 404, pp. 200-214.

358: High temperature air source heat pump coupled with thermal energy storage: an analysis of demand-side management designed for flattening the grid demand

Khoa Xuan LE[1,*], Ming Jun HUANG[1], Nikhilkumar SHAH[1], Paul Mac ARTAIN[2], Raymond BYRNE[2], Neil J. HEWITT[1]

[1] Centre for Sustainable Technologies, Ulster University, Northern Ireland, United Kingdom
[2] School of Engineering, Dundalk Institute of Technology, Dundalk, Ireland
*Corresponding author: le-k@ulster.ac.uk

High temperature air source heat pumps (HT-ASHPs) have a good potential for retrofitting the domestic built environment in the UK because they can directly replace existing fossil-fuelled boilers without the requirement of modification of the heat distribution systems, which makes them cost-competitive regarding retrofit aspect and allows the UK to attain the carbon cut target. However, a widespread of these heat pumps would pose a challenge to the grid demand. In this study, a demand-side management (DSM) strategy was developed to address this issue. Thermal energy storage (TES) was integrated with HT-ASHPs to perform the developed DSM, which aimed at levelling off the grid demand by means of switching on the heat pump to charge the TES where there was low demand (midnight to 7am) and switching off the heat pump during peak hours (4pm to 7pm). The reference case was a mid-terraced dwelling equipped with traditional wet radiators, which is a typical house in Northern Ireland. TRNSYS simulations were used to run the developed DSM. Different TES sizes and set point temperatures were examined to seek the optimum values. The study also analysed with different electricity tariffs including flat rate, Economy 7 (the electricity is cheaper in night time than daytime) and Powershift (the electricity is divided into three bands: low, normal and peak). Results showed that both the tank size and setpoint temperature strongly affected the heat pump performances. The TES size of 1m^3 and set point of 75˚C were the ideal parameters because it could shift wholly the 3-hour peak demand. The effects of the developed DSM on the grid and how the tariffs affected the system have also been discussed in this paper.

Keywords: high temperature air source heat pump, thermal energy storage, demand side management, electricity tariffs.

1. INTRODUCTION

The UK has made the legally binding target of reducing carbon emissions up to 80% by 2050 compared to the 1900 figure (Parliament of the United Kingdom, 2008). Regarding domestic sector in the UK, almost 78% of space heating and hot water demands were met using fossil-fuelled boilers (DECC, 2015), and they were responsible for 40% of domestic heat-related emission (DECC, 2012). Therefore, the UK domestic sector comprising of about 26 million dwellings equipped with fossil-fuelled boilers should be decarbonised in order to acquire the carbon cut target (Abedin et al., 2011). Air source heat pumps (ASHPs) that can pair with the central electricity generation from renewable sources are a promising solution for the decarbonization target at the domestic level (Kelly et al., 2014), and furthermore, they can directly replace existing boilers without the requirement of ground work compared to ground source heat pumps.

ASHPs can be categorised based on the outlet water temperature lift according to BS-EN 14511:2013 (BSI 2013), which is described as: low temperature (35°C), medium temperature (45°C), high temperature (55°C) and very high temperature (above 65°C). In this paper, ASHPs in which the highest flow temperature is 55°C are re-defined as standard ASHPs, and the ones with the outlet water temperature above 65°C are re-defined as high temperature ASHPs (HT-ASHPs).

Considering the UK retrofit perspective, standard ASHPs are unlikely to be the feasible option for replacing existing boilers. This is because installation costs would increase due to the need of modification for the heat distribution systems such as radiators, piping, hot water tanks etc., and hence it is not an economic option. Alternatively, HT-ASHPs of which the supply temperature is the same as boilers can be a possible solution because they can help prevent those modification costs and have the ability to meet hot water demands directly. Furthermore, HT-ASHPs are suitable for retrofitting into heat large, old or listed properties in the off-gas grid area, which makes them more competitive (Department for Business Energy & Industrial Strategy, 2016).

While the current market of HT-ASHPs is niche (Department for Business Energy & Industrial Strategy, 2016), they are expected to be spreading across the UK in the next several years due to the superior for retrofitting the built environment. The future widespread uptake of these heat pumps would pose a challenge to the grid such as voltage dips and cable overloading (Kelly et al., 2014). Therefore, the form of thermal energy storage (TES) coupled with these heat pumps is needed to mitigate this issue. Such a combined system can shift the electrical demands from peak-load to low-load periods, which can help to balance the grid and reduce electricity bills for homeowners. Furthermore, this system can be designed as a demand-side management (DSM) tool for future energy systems with increased proportions of non-dispatchable renewable energy (Hewitt, 2012). According to the annual report of EirGrid and SoNi (2017), approximately 63% of wind energy was curtailed in Northern Ireland in the year 2017, and it happened mostly in night time (11pm to 8am) where the electrical demand was low. Therefore, turning on heat pumps to charge TES in the night also helps to prevent the dispatch-down of wind energy, which in turn allows more renewable energy to accommodate in the grid.

Utilizing modelling and simulations that have been validated against field trial data, this paper presents the system of a HT-ASHP coupled with TES as a DSM tool which aims to level off the curve of the electrical load in Northern Ireland, the UK by switching on the heat pump to charge the TES at night time and switching it off during the peak hours. The paper also gives insight into the performances of the system with different TES sizes and set point temperatures in order to seek the optimum parameters. Furthermore, how the designed DSM strategy affects upon the operating costs when considering different domestic electricity tariffs and the electrical demand is investigated thoroughly.

2. CASE STUDY

In this paper, the facilities and configurations of the field trials of Shah and Hewitt (2015) were investigated as a reference case. It comprised of a mid-terraced “hard-to-heat” dwelling built under the 1900s specifications, representing 27.3% of housing stock in Northern Ireland (National Statistics, 2016). The house was retrofitted with a variable capacity HT-ASHP integrated with a TES tank, providing heat for space heating and domestic hot water (DHW). The scheme of the system can be seen in Figure 1. The house had three habitants including one teenager and two adults. The central heating was controlled based on a fixed schedule (switching on at 7:00 and off at 23:00 every day) and a thermostat in the dining room where its temperature was maintained at 21°C. The flow temperatures from the heat pump to the house were fixed to 76˚C which is the same as the retrofitted boilers. The DHW tank was maintained at 60˚C.

The retrofit HT-ASHP was cascade technology employing variable speed compressor units. This HT-ASHP had a nominal COP of 2.5 with the nominal heating capacity of 11kW at 7°CDB of the outdoor unit as well as 70°C water inlet temperature and 80°C water outlet temperature of the indoor unit according to the manufacturer.

The TES was a sensible tank that was custom made with copper material, 0.6m^3 capacity, 2m height and 0.6m diameter and 75mm foam thick insulation. There were two coiled tube heat exchangers for charging and discharging the TES as well as seven temperature probes at an equal distance used for control and monitoring purposes. There was also a de-stat pump installed on the storage to mix thermally inside the tank so that the stratification effect was eliminated.

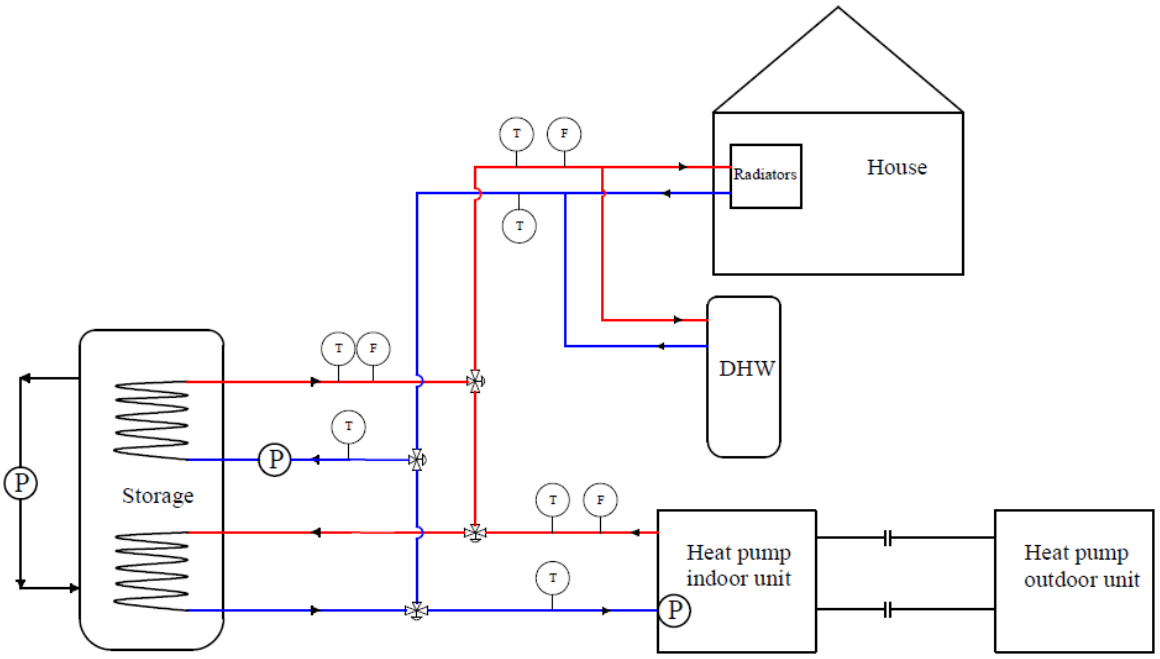

Figure 1: Schematic of the system

3. MODELLING

TRNSYS 17 (Klein et al., 2014) was used to model the system illustrated in Figure 1. The developed models have been validated against field trial results which were mentioned in the previous study (Le et al., 2017), and this paper just presents the developed models, as described as follows.

3.1. HT-ASHP model

TRNSYS Type 1231 was utilised to model the performances of the variable capacity HT-ASHP. This model just predicted the steady-state performances, whilst it could not model the transient states. This model mainly depended on a characterised performance map comprising of full load and part load curves which were obtained from the field trial data (Shah and Hewitt, 2015). The performance map informed by the measured data excluded the periods of defrost operation; therefore, an incorporating defrost model was developed outside the heat pump Type 1213 model. The following subsections describe those curves and the coupling defrost model in detail.

Full load curves

The full load curves of the heat pump model were the functions of outdoor ambient temperatures and outlet water temperatures, as expressed in the following Equation 1 and Equation 2. The electric consumption of the compressors, fans, controllers and a circulating pump inside the indoor unit were totally accounted for in the input electric power curve.

Equation 1: Function of electric power at full load (kW)

$$W = -1.01 + 0.7T_w + 0.24T_a - 0.01T_w^2 + 0.000051T_w^3 - 0.0105T_wT_a + 0.000075T_w^2T_a$$

Equation 2: Function of heat capacity at full load (kW)

$$Q = W * (-1.797 + 2.133T_w - 0.107T_a - 0.0034T_w^2 + 0.000016T_w^3 + 0.0046T_wT_a - 0.000035T_w^2.T_a)$$

Where:

T_w = outlet water temperature of the heat pump (°C)

T_a = outdoor ambient temperature (°C)

Part load curves

The variable capacity heat pump can modulate its heat output based on the thermal load required. The part load curve of the heat pump model is illustrated in Figure 2, with the part load factor (PLF) and part load ratio (PLR) being expressed in the following Equation 3 and Equation 4.

Equation 3: Part load factor (%)

$$PLF = {}^{Q}/_{Q_{full}} * 100$$

Equation 4: Part load ratio (%)

$$PLR = {}^{COP}/_{COP_{full}} * 100$$

Where:

Q = heat output at the respective ambient temperature (kW)

Q_{full} = heat output at full load at the same respective ambient temperature (kW)

COP = coefficient of performance (COP) at the respective ambient temperature (-)

COP_{full} = COP at full load at the same respective ambient temperature (-)

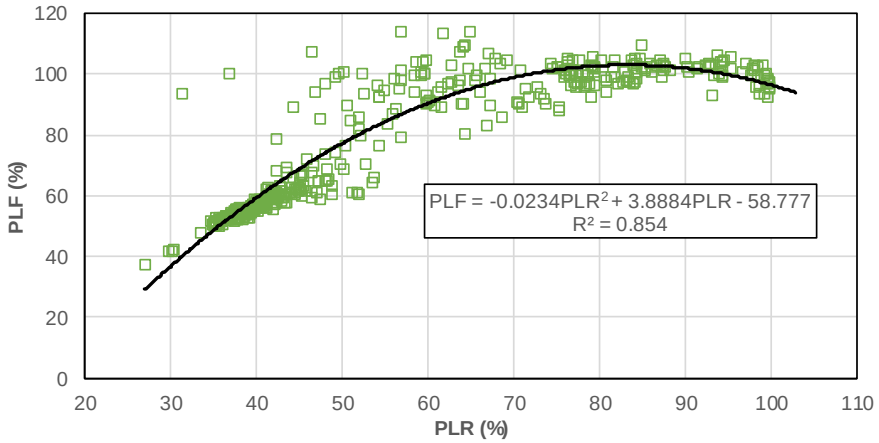

Figure 2: Part load curve of the heat pump model

Defrost_cycles

When the outdoor temperatures dropped below 7°C and the relative humidity rose above 65% for a long period, the heat pump switched to defrost mode, which was observed from the field trial data of Shah and Hewitt (2015). The time of a defrost cycle was between 1 minute and 10 minutes depending on the frosting time t_{fr} and weather conditions, as expressed in the following Equation 5 and Equation 6:

Equation 5: Frosting time (mins)

$$t_{fr} = 39 - 1.06T_a + 0.33RH + 0.13{T_a}^2 - 0.0093RH^2 - 0.018{T_a}^3 - 0.00006RH^3$$

Equation 6: Defrosting time (mins)

$$t_{def} = 56.2 - 0.34T_a - 3.56t_{fr} - 0.047{T_a}^2 + 0.079t_{fr}^2 + 0.0096{T_a}^3 - 0.00057t_{fr}^3$$

Where:

T_w = outlet water temperature of the heat pump (°C)

T_a = outdoor ambient temperature (°C)

RH = outdoor relative humidity (%)

3.2. TES model

TRNSYS Type 534 was obtained to model the sensible stratified TES. The tank was set up with seven nodes and two coiled tube heat exchangers. The heat exchanger for charging the tank occupied in three nodes placed at the tank's bottom,

while another for discharging was in the other four nodes. There was a de-stat pump forcing water convection inside the tank to prevent stratification effect so that this pump model (Type 3d) was also implemented besides the storage tank model.

3.3. Whole building simulation model

Building geometry was firstly drawn in Sketchup software and then imported into TRNSYS Type 56. U-values in the model were set with the known building envelope elements. Heat gains of occupants and equipment were set identically for weekday and weekend based on the surveys with the inhabitants.

TRNSYS Type 534 was utilised to model the DHW. Heat storage capacity of the DHW model was 3.78 kWh with 162 litres and heat loss of 2.74 kWh/24 hours. The collected data of DHW consumption (Shah and Hewitt, 2015) was used as an input profile for the DHW drawing patterns in the model.

The HT-ASHP model, TES model, building model and DHW model above were integrated with other TRNSYS component models to compose a whole system. The heat distribution system included radiators (Type 1231), valves (Type 11 and Type 647), piping (Type 31), temperature sensors (Type 911). Type 15 was utilised to initiate the weather conditions.

4. METHODOLOGY

In Figure 3, the two-day electrical demand in Northern Ireland shows that the peak load occurred between 4pm and 7pm, while the low load was from midnight to 6am. Therefore, the DSM in this study was designed to switch off the heat pump during peak hours (4pm-7pm) and switch it on during low load period (night time), while guaranteeing the thermal comfort of the house. TES therefore plays a key role in this strategy; particularly, it was used to store the energy during night time and later released heat to the house during the peak hours. It is worth to note that the TES in this research is not used as a buffering tank that is similar to other studies (e.g. Kelly et al. (2014), Arteconi et al. (2013)) because the buffering tank reduces the heat pump's performance due to the continuous operation at high flow temperature lift. According to the report of EirGrid and SoNi (2017), the figures of wind curtailment in Northern Ireland were highest from 3am to 5am, and therefore in our study, the heat pump was designed to initiate the TES top-up at 3am. By obtaining this DSM strategy, in short, the grid can be levelled off, which in turn can help to avoid the curtailment of wind energy during night time as well as the peak demand hours.

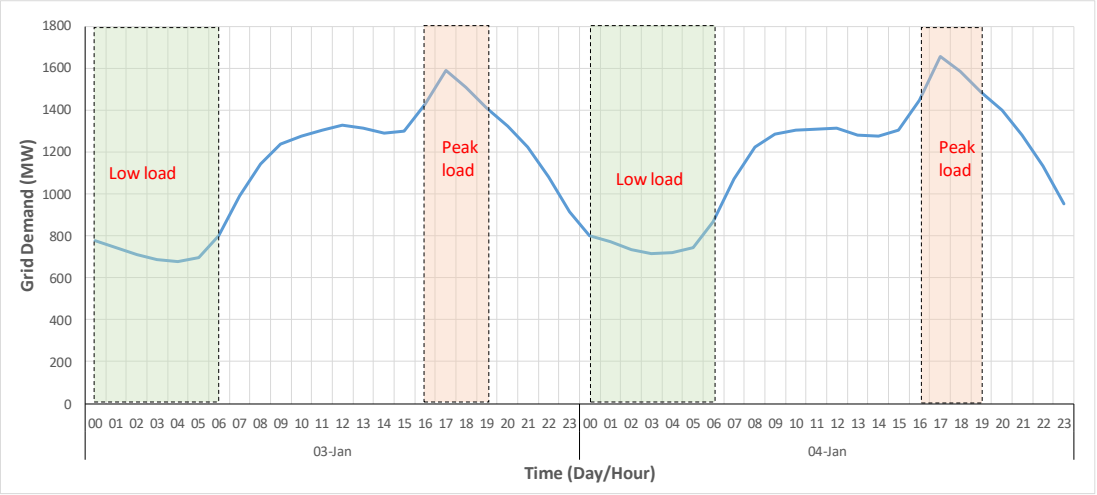

Figure 3: Grid demand in Northern Ireland (two days: 03rd and 04th January 2017) [data are adapted from Soni (2018)*]*

Based on the designed DSM above, a series of simulations were run to seek the optimum the tank sizes and set-point temperatures. Details of these factors are as follows:

- Apart from the size of 0.6m^3 mentioned in section 2, the other sizes of 0.8m^3, 1m^3 and 1.2m^3 were simulated.
- The tank set points of 70˚C and 75˚C were examined in this study. Particularly, if the tank temperature was below the desired set point during low load demand period, the heat pump was switched on to top up the tank. During the discharging period (peak hours), the tank stopped drawing heat to the house if its temperature was below 55˚C. There are two main reasons why the tank setpoint should not be higher than 75˚C and lower than 70˚C. Firstly, if the tank is topped up to the temperatures above 75˚C, the heat pump will lift its flow temperature somewhere above 85˚C to maintain the 10˚C difference between the flow and return temperatures which are designed by the manufacturer, resulting in the reduction of the performance and furthermore the overload of the

heat pump. Secondly, based on the initial analysis with the sizes mentioned above, if the tank is charged to the levels below 70˚C, it leads to the insufficient energy to shift the whole 3-hour peak load.

The tank loss coefficient was set to 1W/m^{2}K which is a common figure of the UK modern tanks. The simulations were run for one month of winter (January), with the weather data of Belfast-Aldergrove available in TRNSYS database. As mentioned in Section 2, the central heating was switched on from 7am to 11pm every day, meaning this period was the occupied hours. Hence, the simulations were set up with the same schedule. Particularly, the heat pump was turned on to provide heat to the house during the occupied period to maintain the desired room temperature, except the peak-load hours (4pm to 7pm) which was the role of the TES. In case the tank cannot satisfy the heat demand during the peak hours, the heat pump will be in charge alternatively.

This study also considered the different domestic electricity rates in Northern Ireland including flat rate tariff, Economy 7 tariff (the electricity is cheaper in nighttime than daytime) and Powershift tariff (the electricity is divided into three bands: low, normal and peak), as illustrated in Figure 4. Flat rate tariff was used to calculate the operating cost of the heat pump without the DSM, while Economy 7 and Powershift were utilised to quantify the operating costs of the heat pump controlled with the designed DSM. The purpose of this analysis was twofold. The first was to assess whether the DSM can obtain cost savings. The second was to evaluate either Economy 7 or Powershift to be best suitable for the designed system.

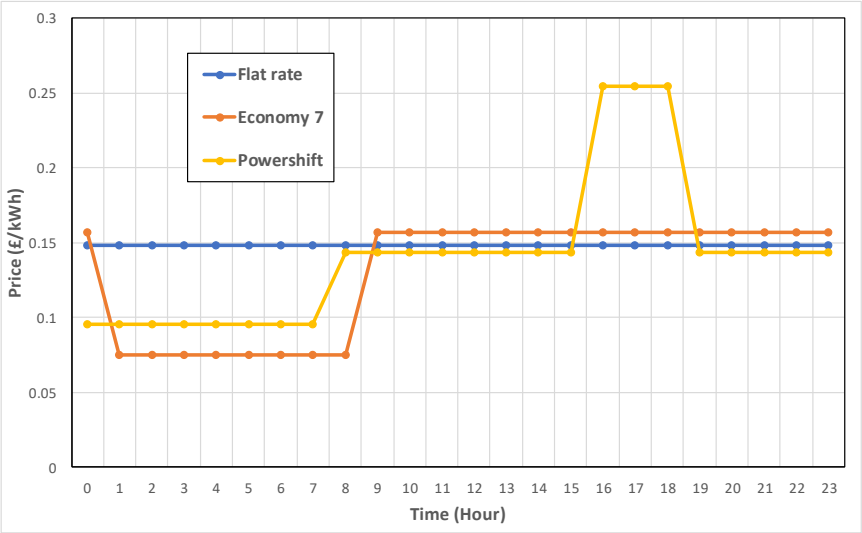

Figure 4: Domestic electricity rates of different tariffs in Northern Ireland, the UK [data are adapted from Housing Excutive (2015)]

5. RESULTS AND DISCUSSIONS

Summaries of the simulation results are reported in Table 1. The system with or without DSM can guarantee the same room temperature. Although the heat output and energy use of the heat pump without DSM were lower than those with DSM (Table 1), there was a cost penalty associated with the heat pump without demand control (£264) except the system of 70˚C set point and 0.6m^3 calculated by Powershift tariff (£268), as seen more clearly in Figure 5. Literally, the DSM can provide cost savings compared to the heat pump without the support of TES.

Table 1: Summary results of simulations for one month of winter

		Without DSM	With DSM							
			70˚C tank set point				75˚C tank set point			
			0.6m^3	0.8m^3	1m^3	1.2m^3	0.6m^3	0.8m^3	1m^3	1.2m^3
Running cost (£)	Flat rate	264	N/A	N/A		N/A	N/A	N/A	N/A	N/A
	Economy 7	N/A	260	255	252	249	257	251	247	247
	Powershift	N/A	268	259	252	245	262	250	241	240
Heat output of the heat pump (kWh)		3556	3652	3659	3666	3675	3661	3668	3679	3699
Energy use of the heat pump (kWh)		1779	1829	1837	1843	1849	1836	1845	1853	1856
Average room temperature (˚C)		19.42	19.41	19.41	19.41	19.41	19.41	19.4	19.41	19.4

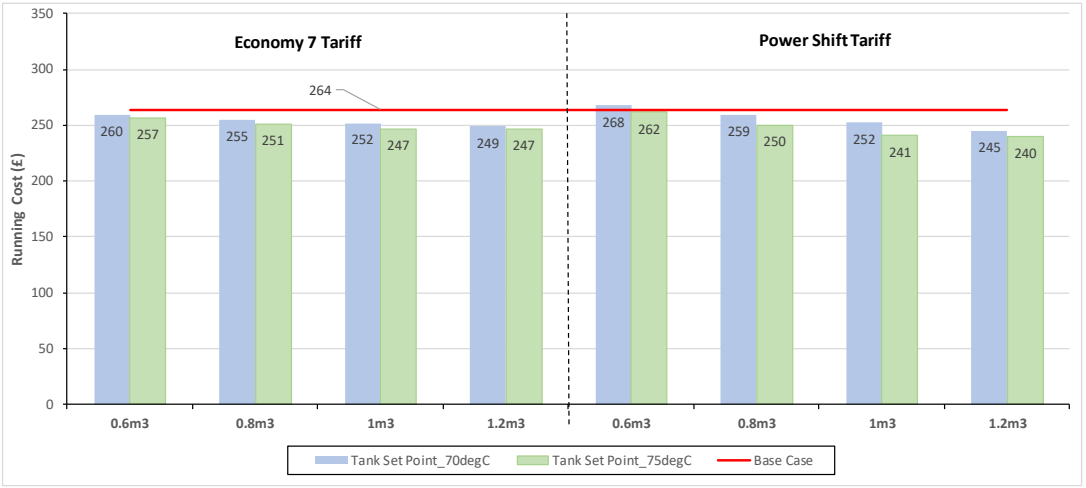

Figure 5: Operating costs of the heat pump for one month of winter (Base case represents the system without the DSM)

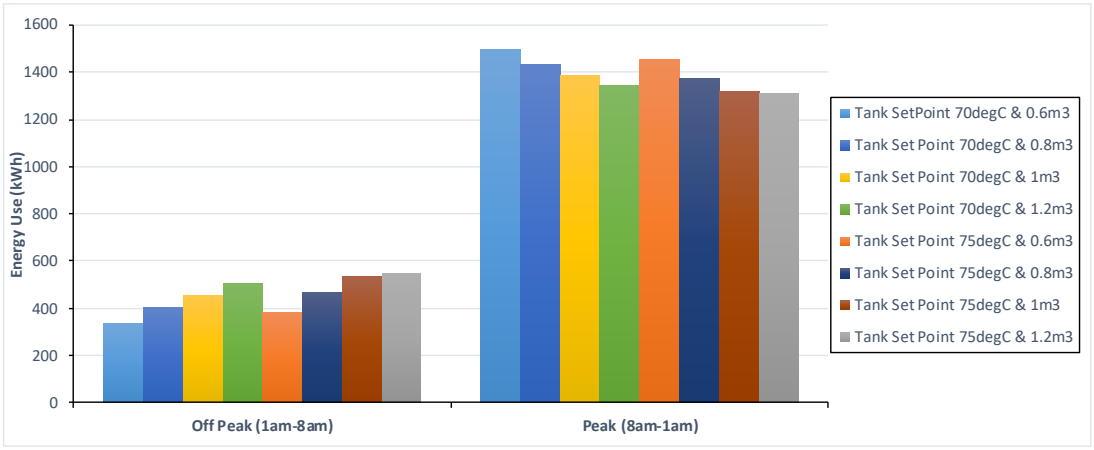

Figure 6: Breakdown of one-month energy use of the heat pump based on Economy 7 tariff

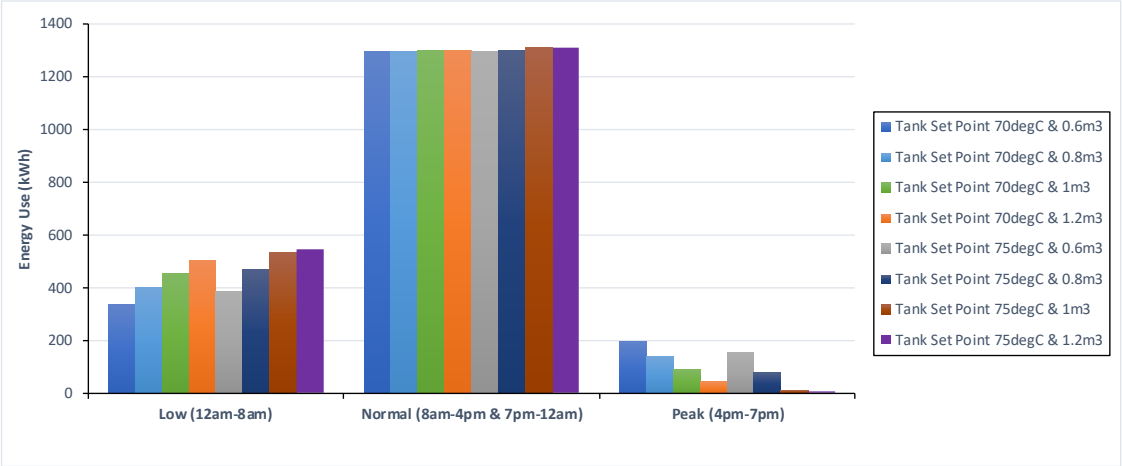

Figure 7: Breakdown of one-month energy use based on Powershift tariff

The TES set points highly influenced the heat pump performance. If the tank was topped up to 75˚C, more energy was consumed compared to the tank with the set point of 70˚C (see Table 1), but its running costs were lower than the figures of 70˚C tank set point (Figure 5). Looking at Figure 6 and Figure 7, the higher set point of the TES the lower energy use during peak hours, and vice versa, which explains why there was the cost benefit associated with the higher set point tank. Therefore, the temperature of 75˚C would be the ideal set point for the system within this study.

The performance of the heat pump with the demand control was also affected by the size of the TES. In Figure 5, the running costs of the system with the larger sizes were lower than those with the smaller sizes. To explain this result, the breakdowns of the energy use with different TES sizes are seen in Figure 6 and Figure 7, It is clear from the figures that with the larger sizes, more energy was consumed during off-peak hours, and in contrast less energy was used during peak hours, leading to the reason why the larger TES can help the system to save money. Considering the set point of 75˚C, however, there was not much different in terms of operating costs between the system with the tank size of $1m^3$ and $1.2m^3$ (Figure 5). As a result, the ideal tank size would be $1m^3$ rather than $1.2m^3$ because the larger size would not be preferred by end-users due to the higher capital costs and the larger space required to accommodate the TES. Furthermore, it can be seen in Figure 7 that the size of $1m^3$ associated with the 75˚C set point can shift wholly the 3-hour peak demand.

Different tariffs yielded different operating costs of the heat pump controlled under the designed DSM. Considering the tank with $0.6m^3$ and $0.8m^3$, Economy 7 tariff was the better choice for cost savings (Figure 5). Regarding the tank with $1m^3$ and $1.2m^2$, however, Powershift was the appropriate tariff (Figure 5). Therefore, care should be paid to end-users when choosing the appropriate tariff. Taken the system with the ideal set point and size mentioned above into consideration, it is clear from Figure 5 that Powershift was the right tariff.

To see how the designed DSM with different system parameters affected upon the electrical demand, the average one-month results of the heat pump demand were aggregated for 5% of current housing stock in Northern Ireland which was 776,526 dwellings in 2016 (Department for Communities, 2016), as depicted in Figure 8. The base case which represents the system without DSM seemed to pose the challenge for the future grid (Figure 8a). In contrast, the HT-ASHP coupled with the TES as a DSM tool can help to flatten the grid. Depending on the set point and size of the TES, its effects on the grid were different. The systems with larger size and higher set point were more grid-friendly. Regarding the ideal system (75˚C and $1m^3$), its influence on the grid was highly beneficial as it can totally avoid the peak hours and fill “the valley” low demand (Figure 8d).

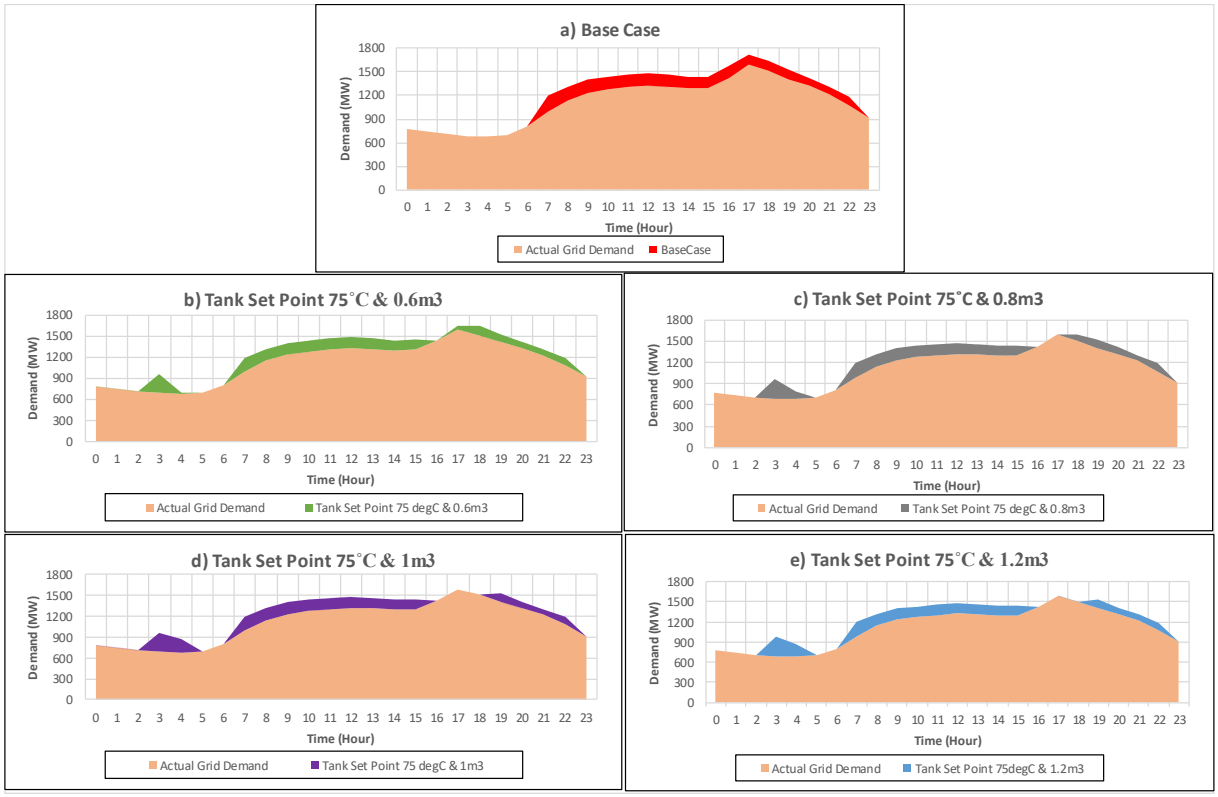

Figure 8: Impacts of the systems without and with DSM upon the electrical demand in Northern Ireland (the average one-month demand of the heat pump was aggregated with 5% of the current housing stock in Northern Ireland)

6. CONCLUSIONS

The DSM designed to flatten the electrical demand curve in Northern Ireland, the UK has been developed for the system of an HT-ASHP coupled with a TES tank. The idea of the DSM was using the TES to shift the 3-hour peak load and to fill “the valley” of low load demand during night time which can allow more wind energy to be integrated into the grid at night. TRNSYS simulations were utilised to carry out the developed DSM. Different tank sizes and set point temperatures were analysed in conjunction with the varied electricity tariffs. The results of the simulations indicate that:

- Without the developed DSM, the costs will increase, and the future grid will counter challenges.
- The setpoint temperature of the TES highly influenced the running costs of the heat pump. The higher set point (75˚C) could provide the better cost savings.
- Tank size strongly affected the heat pump's performances and the demand curve of the grid when applying the demand control. The size of $1m^3$ would be the ideal tank in association with the appropriate set point of 75˚C, which can reduce the operating cost and obtain the positive effect on the grid.
- Applying this DSM strategy should be paid attention when choosing the electricity tariff. If the TES sizes are $0.6m^3$ and $0.8m^3$, homeowners should choose Economy 7 tariff. On the other hand, Powershift is recommended if the tank sizes are larger. Regarding the ideal set point of 75˚C and the size of $1m^3$, Powershift tariff is the right choice.

Future avenue will carry out different TES types such as phase change material, with the aim to reduce the size of the storage while remaining its required capacity. Also, the DSM in this study was designed based on the electrical demand curve which is static. Future work will design the better friendly-grid DSM which considers the market price that is dynamic and reflects the correlation between the demand and renewable sources on the grid.

7. ACKNOWLEDGEMENTS

The research leading to these outcomes has funded by Research Councils UK (RCUK) under i-STUTE EPSRC project; European Union's INTERREG VA under SPIRE 2 project; and the EU H2020 CHESS-SETUP project.

8. REFERENCES

Abedin, J., Firth, S. & Eames, P., 2011. Simulation of domestic heat demand shifting through short-term thermal storage. *Proceedings of BS2013: 13th Conference of International Building Performance Simulation Association*, pp.3368–3374.

Arteconi, A., Hewitt, N.J. & Polonara, F., 2013. Domestic demand-side management (DSM): Role of heat pumps and thermal energy storage (TES) systems. *Applied Thermal Engineering*, 51(1–2), pp.155–165.

BSI, 2013. *EN14511: Air conditioners, liquid chilling packages and heat pumps with electrically driven compressors for space heating and cooling (Part 1-4), s.l.: BSI*,

Department for Communities, 2016. The Northern Ireland Housing Statistics 2015-16. Available at: https://touch.nihe.gov.uk/latest_tariffs [Accessed June 25, 2018].

DECC, 2015. *Digest of United Kingdom Energy Statistics 2015*, Available at: https://www.gov.uk/government/publications/digest-of-united-kingdom-energy-statistics-dukes-2013-printed-version-excluding-cover-pages [Accessed June 25, 2018].

DECC, 2012. *Emission from Heat: Statistical Summary*.

Department for Business Energy & Industrial Strategy, 2016. Evidence Gathering – Low Carbon Heating Technologies.

EirGrid & SoNi, 2017. All-Island Generation Capacity Statement 2012-202.

Housing Executive, 2018. Northern Ireland electricity tariffs. Available at: https://touch.nihe.gov.uk/latest_tariffs [Accessed June 25, 2018].

Hewitt, N.J., 2012. Heat pumps and energy storage - The challenges of implementation. *Applied Energy*, 89(1), pp.37–44.

Kelly, N.J., Tuohy, P.G. & Hawkes, A.D., 2014. Performance assessment of tariff-based air source heat pump load shifting in a UK detached dwelling featuring phase change-enhanced buffering. *Applied Thermal Engineering*, 71(2), pp.809–820.

Klein, S. A., et al. (2014). TRNSYS 17, *a TRaNsient SYstem Simulation and program - vol.1. Getting started*.

Le, K.X., Shah, N., Huang, M.J., & Hewitt, N.J. (2017). High Temperature Air-Water Heat Pump and Energy Storage: Validation of TRNSYS Models. *Proceedings of the World Congress on Engineering and Computer Science 2017*. Vol *II*, 754-759.

National Statistics, 2017. The Northern Ireland House Condition Survey. Avaibale at: https://www.nihe.gov.uk/nihcs_2016_preliminary_report.pdf [Accessed June 27, 2018].

Parliament of the United Kingdom, 2008. Climate Change Act 2008. *HM Government*, pp.1–103. Available at: http://www.legislation.gov.uk/ukpga/2008/27/pdfs/ukpga_20080027_en.pdf. [Accessed June 26,2018].

Shah, N. & Hewitt, N., 2015. High temperature heat pump operational experience as a retrofit technology in domestic sector. *EEE International Conference on Engineering, Technology and Innovation/ International Technology Management Conference (ICE/ITMC)*, pp.1–7.

Soni, 2018. System Information. Available at: http://www.soni.ltd.uk/__uuid/2e0badb7-e18f-47bd-8eff-865a716a3197/ [Accessed June 28, 2018].

361: Process simulation of a circulating fluidised bed and ultra-supercritical power plant system

Wenbin ZHANG[1], Decai LI[1], Hao LIU[2], Junfu LV[3], Jihong WANG[1]

[1] School of Engineering, University of Warwick, Coventry, UK, W.zhang.26@warwick.ac.uk
[2] Faculty of Engineering, University of Nottingham, Nottingham, UK, Liu.Hao2@nottingham.ac.uk
[3]Department of Thermal Engineering, Tsinghua University, China, lujf@tsinghua.edu.cn

To achieve the UK's ambitious target of reducing the greenhouse gas emissions by 80% by 2050, the UK's conventional power plants must be operated in a more flexible manner in terms of high efficiency, using alternative fuels such as biomass and integrating technologies such as energy storage and carbon capture and storage. Currently the most advanced solid fuel-based conventional power generation is the ultra-supercritical (USC) steam cycle combined with Circulating Fluidised Bed (CFB) combustion technology. USC/CFB has several advantages over pulverised coal (PC)-based USC power generation, especially regarding fuel flexibility. There are still many fundamental research and technical challenges such as the hydrodynamic behaviour when coal/biomass co-firing is used as flexible feedstock. In this study, a steady state model of power plant system using CFB technology is established using the commercial software Aspen Plus. Unlike the traditional way in which a fluidised bed is discretised into a series of reactors, a compact and more realistic module FluidBed is explored to simulate an industrial 600 MW USC/CFB power plant for the first time. The hydrodynamic behaviour inside the CFB boiler and external recirculation loop including external heat exchangers has been investigated. Ash mass balance model is constructed considering various particle size distribution of coal, ash and additional bed materials. The fluidization quality has accordingly evaluated by a number of factors when coal and/or biomass is used as the fuel feed. The simulation results such as the bed pressure drop, bubble size and velocity, bed voidage etc. have provided useful guidance on the flexible operation of a USC/CFB power plant system.

Keywords: Circulating Fluidised Bed (CFB), power plant, ultra-supercritical (USC), process simulation, Aspen Plus

1. INTRODUCTION

According to the global land-ocean temperature index measured by NASA/GISS (2017), the global temperature has been increasing continuously and the measured ambient CO_2 concentration has broken through 400ppm the first time in 2015. The current global warming trend has drawn sufficient attention by researchers and also by the public. It has been stated that the global warming is extremely likely (greater than 95 percent probability) to be the result of human activities since the mid-20th century and it is developing at a rate that is unprecedented over decades to millennia (IPCC, 2014). In order to combat the climate change, the Paris Agreement has been proposed to strengthen the global response to the threat by keeping a global temperature rise this century well below 2 degrees Celsius above pre-industrial levels and to pursue efforts to limit the temperature increase even further to 1.5 degrees Celsius (UNFCCC, 2015).

Despite the fact that renewable energy sources have been extensively developed over the recent years, coal will continue to serve as the principle fuel for electricity generation of the world for the next 20-30 years with a slight decrease from the current share of 40% to 36% in 2040 (EIA, 2016). Specifically, to achieve the UK's ambitious target of reducing greenhouse gas emissions by 80% by 2050 without compromising energy security, the UK's conventional power plants need to be operated in a flexible manner in terms of high efficiency, using alternative fuels including renewable energy sources such as biomass, and integration of carbon capture facilities. Therefore, there is a great urgency to develop highly efficient, fuel flexible and CCS-compatible coal power generation technologies.

Pulverised Coal (PC) combustion in a Rankine steam cycle has been the prevailing mode of coal utilization in power generation worldwide, since the 1920s. Efficiency of subcritical (SubC) steam plants with typical steam parameters of 168 bar, 538/538ºC (2469 psi, 1000/1000ºF) can reach up to 40% (LHV). When steam pressure and temperature increase to beyond 225 atm (3308 psi) and 374.5ºC (706ºF), the steam becomes supercritical (SC). Developments in materials and increasing demand for higher efficiencies are making the Supercritical steam plants (PC/SC) preferential choices of new coal fired power plants worldwide. Armor (2003) reviewed the performance and history of PC/SC units in the US and in Europe and concluded the efficiency improvement of about 2.9 points (from 38.6% LHV for SubC to 41.5% LHV for SC). With continuous improvements in materials, Ultra Supercritical steam (USC) parameters of higher than 300 bar and 600/600ºC (4350 psi, 1112/1112ºF) can now be approached in practical scales, resulting in efficiencies of 45% (LHV) and above for bituminous coal-fired power plants. The plant efficiency increases by about one percentage point for every 20ºC rise in superheat temperature. Higher USC steam parameters are favourable to further improvements in efficiency but are restricted by the availability of new, high-temperature alloys for boiler furnace, superheater and reheater tubes and steam turbines. An advanced 700ºC (1293ºF) USC plant constitutes a benchmark for a 50% efficiency (LHV) coal-fired power plant resulting in 25% reduction in CO_2 emissions (Booras, 2004).

Circulating Fluidised Bed (CFB) technology has been well developed since 1920's and served as efficient gas/solid contactors for many industrial applications such as fluidised bed catalytic cracking, coal/biomass combustion and gasification due to the inherent high gas-solid contact efficiency and high mass and heat transfer rates. According to Transparency Market Research, a leading U.S.-based market research firm, the global installed capacity of CFB boilers is expected to grow at an estimated CAGR of nearly 12.2% from 2012 to 2018. Unlike conventional PC steam generators that burn the fuel in a high-temperature flame, CFB serves as a clean combustion platform with low temperature combustion process that can burn flexible fuels including both high and low quality coals and carbon-neutral fuels such as biomass. The outstanding ability of pollutant control makes CFB especially environmental-friendly in that sulphur oxides can be captured in bed using limestone and formation of nitrogen oxides can also be minimised owing to the lower bed temperature comparing to PC boilers. CFB technology can also provide a potential CCS solution by operating in oxy-combustion mode which produces a CO_2 rich flue gas that can be easily captured and stored.

Although CFB boilers as large as 330 MWe are now in operation, they are mostly drum-type and subcritical pressure units. The CFB technology is now being integrated with vertical-tube, once-through unit (OUT) supercritical and ultra-supercritical steam technology, which provides a best combination of features for efficient, cost effective, and environmentally responsible power generation. A conceptual design study (Zhen, 2006) was conducted to investigate the technical feasibility and economics of USC/CFB boilers. Following this study, the world's first advanced OUT/SC units were demonstrated at the 460MWe Lagisza plant in Poland by Foster Wheeler, which entered commercial operation in 2009. The Samcheok Green Power Project in Korea, as an advanced USC/CFB technology from Foster Wheeler, has started up in June 2015. According to the reviews by International Energy Agency (IEA, 2013), the ultra-supercritical (USC) steam Rankine cycle power generation combined with Circulating Fluidised Bed (CFB) combustion technology is the most viable alternative to the pulverised coal (PC)-based USC power generation.

Since most CFB boilers are currently operating in a nominal 300 MWe size, the combination of USC and CFB needs more experience in boiler configurations for the move to bigger sizes which represents a significant scale-up in CFB components such as furnace, gas/solid separators, heat exchangers etc. Process simulation and computational modelling of such a USC/CFB power plant system has been regarded as a powerful tool to provide valuable database for the design and operation. However no publications so far have been found to address this topic. The aim of this paper is to construct a process model on a commercial platform Aspen Plus and to present preliminary simulation results on a practical 600MW USC/CFB power plant.

2. USC/CFB POWER PLANT SYSTEM

2.1. Description of a typical USC/CFB plant

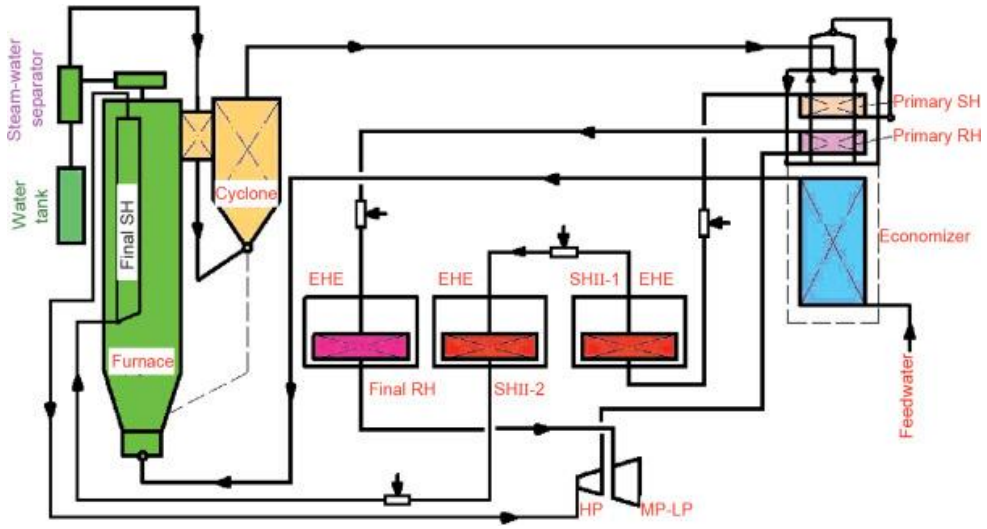

Figure 1: Sketch of a USC/CFB power plant system

A simplified schematic of a typical USC/CFB power plant system is illustrated in Figure 1, which consists mainly of the CFB boiler, several cyclones, external heat exchangers (EHE), downstream heat exchangers such as super-heaters (SH), re-heaters (RH), Economiser, air preheaters and turbines. The feedwater, after being preheated in the Economiser, was fed into the water wall inside the CFB furnace, where it is transferred directly to the supercritical steam without evaporation. Unlike a subcritical power plant, a drum is not a necessary component in the so-called once-through boiler and it can be replaced by a much smaller steam-water separator acting as the drum's role in the circumstances of low load working conditions. Cyclones are crucial components which are used to capture majority of the bed materials elutriated from the CFB. The captured bed materials are then fed back into the CFB, in which way a mass balance can be established by solid recirculation.

Application of EHEs is another major difference between a USC/CFB and a USC/PC power plant system. Recently, the load of a solid-fuel fired power plant has been significantly increased from a nominal 300 MW up to 600 MW or even higher. The load increase has resulted in an increasing demand of heat exchange area. A typical Pyroflow type CFB boiler uses additional heat exchanger tubes in the top zones of the CFB furnace. This design has however been suffered from severe attrition by the solids flow. The typical Lurgi type CFB has been proposed to move the additional heat exchange area outside the CFB and these external heat exchangers are installed underneath the cyclones. A portion of recirculating bed materials is directed into the EHEs where heat is exchanged between the superheated or reheated steam and the hot solids. The application of EHEs provides advantageous flexibility in controlling the temperatures of CFB and the steam by configuring the valve openings which are used to adjust the mass ratio of solids entering the EHEs. On the other hand, the mass balance involving the EHEs in the recirculating loop is becoming more complex and vital to the operation as the mass flow of the solids are essential factors to be considered when establishing the energy balance.

2.2. Operational parameters and fuel properties

A practical industrial 600 MW USC/CFB power plant X, which has already been commissioned in 2013, is used as a reference plant for verification of the model studied in this paper. The CFB boiler itself has a height of 55 metres and a rectangular cross section of 17.6 metres by 25.1 metres. In order to increase the capture efficiency, a total number of 6 is used for cyclones, each having an inner diameter of 8.5 metres. There are 6 EHEs in total, four of which SHII-1 and SHII-2 are used for external superheaters, while the other two are used for reheaters. The principle operational parameters measured on-site under different loads are concluded in Table 1. The load variations are mainly configured by changing the feeding rate of coal. Limestone is fed for desulphurization inside the CFB. The bed temperatures are controlled below 900 ^{o}C so that NOx formation can be effectively restrained. According to the on-site monitoring, the concentrations of dust, SO_2 and NOx in the flue gas are below 30, 380, 160 mg/Nm^3 respectively, all of which meet the local requirements of pollution emissions.

Table 1: Operational parameters of plant X under different loads

Load	BMCR	BECR	75% THA	50% THA	40% THA
Superheated Steam flow rate (t/h)	1900	1820	1222	810	667
Superheated steam temperature (°C)	571	571	571	571	571
Superheated steam pressure (MPa)	25.5	25.4	20.7	14.0	11.6
Reheated steam flow rate (t/h)	1568	1497	1037	703	583
Reheated steam inlet temperature (°C)	317	312	299	307	308
Reheated steam inlet pressure (MPa)	4.592	4.379	3.062	2.087	1.708
Reheated steam outlet temperature (°C)	569	569	569	569	543
Reheated steam outlet pressure (MPa)	4.352	4.149	2.901	1.978	1.619
Feedwater temperature (°C)	284	281	257	235	225
Average bed temperature (°C)	890	890	890	890	850
Coal feeding rate (t/h)	366.2	353.3	253.3	177.5	146.5
Limestone feeding rate (t/h)	80.5	77.7	55.7	39.0	32.2

The analysis results of the design coal for plant X are listed in Table 2, together with the corrected dry basis data needed for Aspen+ inputs. The heat of combustion indicates that the coal is Low to Medium quality with high content of ash at around 44%. The volatile matter content is relatively low which makes it difficult for the coal to be ignited. The sulphur content is as high as 3.3%. Comparing the FC and C element content, the little difference implies that almost all C element exists in the fixed carbon while the volatile matter does not contains C element. All these characteristics of the design coal make it less favourable for a typical PC boiler. Nevertheless, in a CFB boiler, ash consists of 90% of bed materials for recirculation and sulphur can be effectively removed by addition of limestone in bed. Due to the massive heat and mass transfer efficiency and large heat capacity of the bed materials, ignition of low quality coal has not been a serious issue in the CFB.

Table 2: Coal analysis results for plant X

				Design coal	Aspen+ (dry basis)
Proximate analysis	Moisture as received	M_t	%	7.58	7.58
	Ash as received	A_{ar}	%	43.82	47.41
	VM (dry and ash free basis)	V_{daf}	%	14.74	-
	VM as received (calculated)	V_{ar}	%	7.16	7.75
	FC as received (calculated)	FC_{ar}	%	41.44	44.84
Ultimate analysis	Carbon as received	C_{ar}	%	41.08	44.45
	Hydrogen as received	H_{ar}	%	1.62	1.75
	Nitrogen as received	N_{ar}	%	0.54	0.58
	Oxygen as received	O_{ar}	%	2.06	3.57
	Sulphur as received	S_{ar}	%	3.3	2.24
	Heat of Combustion	HHV	MJ/kg	15.53	15.53

In order to investigate the fuel flexibility for CFB combustion, three biomass materials (straw, miscanthus and wood chips) have been proposed as alternative feedstocks and their proximate and ultimate analysis results are listed in Table 3. Comparing with coal, biomass feedstock has much lower ash content which may expose a potential issue in maintaining the mass balance in the recirculation loop. In order to compensate the solid loss due to fly ash and slag, additional bed materials need to be supplied regularly. The high content of volatile matter in biomass leads to higher ignition and combustion rate comparing with the coal that may change the heat flow profiles along the height of CFB. Sulphur contents in the biomass are usually very low which indicates that the in-bed desulphurization by addition of limestone is not necessary.

Table 3: Proposed biomass analysis results for plant X

			Straw	Miscanthus	Wood
Proximate analysis	Moisture as received	%	6.15	5.12	6.17
	Ash (dry basis)	%	7.01	2.09	0.83
	VM (dry basis)	%	73.20	80.19	81.37
	FC (dry basis)	%	19.79	17.72	17.80
Ultimate analysis	Carbon as received	%	42.61	46.09	46.66
	Hydrogen as received	%	6.34	6.48	6.65
	Nitrogen as received	%	0.63	0.40	0.27
	Oxygen as received	%	37.69	39.92	39.48
	Sulphur as received	%	<0.01	<0.01	<0.01
	Heat of Combustion	MJ/kg	18.21	19.10	19.81

3. MODEL DESCRIPTION

3.1. Flowsheet model developed in Aspen+

Aspen+ (Advanced System for Process Engineering PLUS) is a commercial software package designed to allow a user to build a process model for a wide variety of chemical engineering tasks. It is a computer-aided platform which uses the underlying physical relationships (e.g. material and energy balances, thermodynamic equilibrium, rate equations) to predict process performance (e.g. stream properties, operating conditions, and equipment sizes). Aspen+ uses flowsheet simulator to predict the behaviour of a process using basic engineering equations. It has been well recognised by engineering researchers as a powerful process simulation tool. According to the literature search on Web of Science, there have been more than 2500 publications making use of Aspen+. Recently, with the development of packages including solids handling, it has been used in more than 200 publications to simulate coal combustion/gasification in fluidised beds.

The methodology adopted to simulate a fluidised bed in the existing publications is to use a series of Aspen built-in reactors called RCSTR (Rigorous Continuous Stirred Tank Reactor) along the height of the fluidised bed. Although the current models can produce informative results such as the voidage, bed temperature etc. at different locations of a fluidised bed, they all have noticeable limitations in representing the fundamental hydrodynamics of a fluidised bed such as the bubbles behaviour and the bed pressure drop. It is difficult to simulate a circulating fluidised bed with solids circulating in a closed loop involving EHEs using this traditional methodology. Furthermore, no such an integrated model with water wall heat exchange has been reported. For the first time, this study has proposed to use another built-in module “FluidBed” to simulate the above mentioned USC/CFB plant X. The module FluidBed was added into the Aspen+ package in 2013 but its application in coal combustion/gasification in a fluidised bed has never been explored and reported.

A flowsheet has been developed in Aspen+ to simulate the CFB boiler system including feeding of primary and secondary air, decomposition and combustion of coal particles inside the CFB furnace, solids recirculation in the loop consisting of CFB bed, cyclones and EHEs (as illustrated in Figure 2*Figure 2*). The complete power plant system with additional components including downstream heat exchangers, steam turbines is under development.

3.2. Reactions of coal/biomass inside CFB

When the solid fuel particles such as coal and/or biomass enter the CFB furnace, they subject a series of physical and chemical reactions consecutively, including drying, devolatilisation, volatile combustion, char combustion and desulphurization.

Devolatilisation

As a simplified treatment, the coal/biomass particles are first decomposed into virtual elemental substances, such as carbon (C), hydrogen (H), oxygen (O), nitrogen (N) and sulphur (S) according to the ultimate analysis results. An Aspen+ built-in reactor, RYield, is used to model this decomposition using an In-Line Fortran calculator block.

Volatile combustion

Comparing with char combustion, the volatile combustion has a much quicker reaction rate and it can be regarded to happen instantaneously once the fuel particles are fed into the CFB bed. The carbon content in the volatile matter (VM) is only oxidised to CO due to O_2-lean environment in the dense bed region. The amount of carbon in VM can be estimated by the difference between the Fixed Carbon (FC) in the proximate analysis and total C in the ultimate analysis. An Aspen+ built-in module RStoic is used to simulate the reactions including:

$$C\ (VM) + 0.5\ O_2 \rightarrow CO \quad (R1)$$
$$H_2 + 0.5\ O_2 \rightarrow H_2O \quad (R2)$$
$$S + O_2 \rightarrow SO_2 \quad (R3)$$

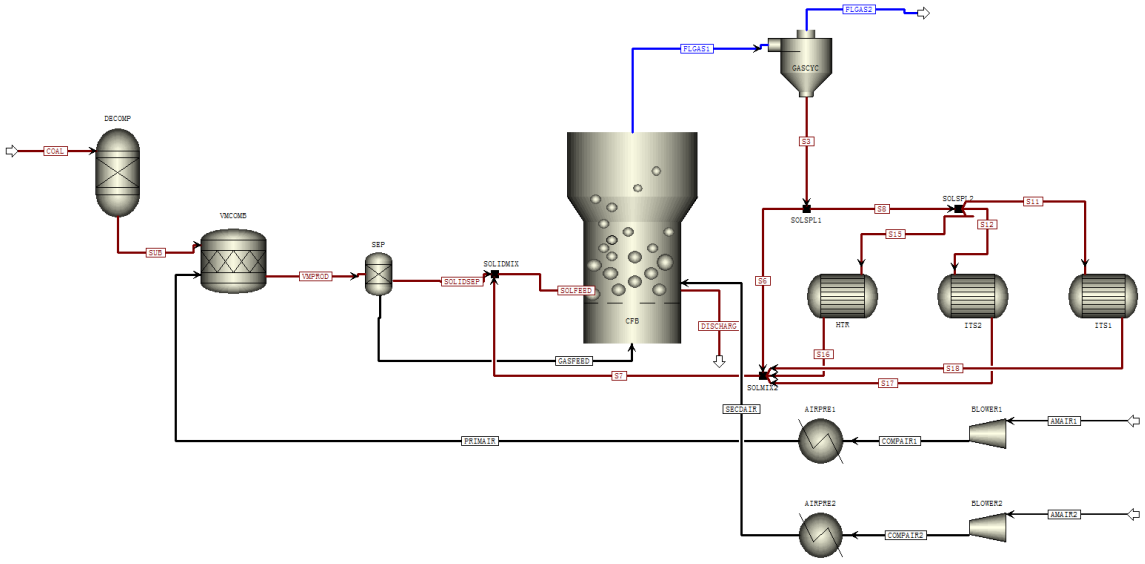

Figure 2: Aspen+ model for the CFB boiler in Plant X

Char combustion

Complete combustion of char particles takes longer time to finish depending on the size and kinetics of the particles. As particles are circulated within the loop in the CFB system, their residence time has been significantly prolonged, resulting in a nearly 100% of burnout rate and very low carbon contents in the fly ash and slag. The kinetics of char combustion can be described as:

$$C\ (FC) + \frac{1}{\varphi} O_2 \rightarrow \left(2 - \frac{2}{\varphi}\right) CO + \left(\frac{2}{\varphi} - 1\right) CO_2 \quad (R4)$$

$$CO + 0.5\ O_2 \rightarrow CO_2 \quad (R5)$$

Desulphurization

Unlike the expensive downstream flue gas desulphurization used for most PC boilers, one of the advantages of CFB boilers is that sulphur oxide can be effectively captured inside the CFB furnace by addition of limestone. The reactions can be concluded as:

$$CaCO_3 \rightarrow CaO + CO_2 \quad (R6)$$
$$CaO + SO_2 + 0.5\ O_2 \rightarrow CaSO_4 \quad (R7)$$

The optimal reaction temperature for the above reactions is around 850°C to 900ºC, which falls well within the operational temperature of a typical CFB boiler.

3.3. Mass balance model of CFB

The principles of mass balance in a CFB recirculation loop including the EHEs can be illustrated in Figure 3. In a steady-state operation condition, the input of bed materials, mainly consisting of ash from fuel and limestone, need to compensate

the loss of fly ash escaped from the cyclone and the bottom ash (slag) discharged from CFB. This balanced can be described by:

$$B = B_l + B_c \cdot A_{ar} = \alpha_f \cdot B + (1 - \alpha_f) \cdot B \tag{1}$$

where B, B_l, B_c are the solids' flow rates of the total, limestone and coal respectively; A_{ar} is the ash content in the fuel on the as received basis; α_f is the ratio of fly ash while (1- α_f) is the ratio of bottom ash. The solid flow rate of recirculation particles B_r is determined by the capturing efficiency of the cyclone:

$$\eta_c = \frac{B_r}{\alpha_f \cdot B + B_r} \tag{2}$$

The solid flow captured by the cyclone is separated by a valve into two streams, one returning into CFB directly with a mass ratio of β, while the other entering EHEs with individual ratios of γ_1, γ_2 and γ_3 for heat exchange between superheated or reheated steam. At the same time, the solid flow leaving CFB from the top needs to be calculated using a specific elutriation model (discussed in next subsection).

$$\dot{m}_e = \alpha_f \cdot B + B_r \tag{3}$$

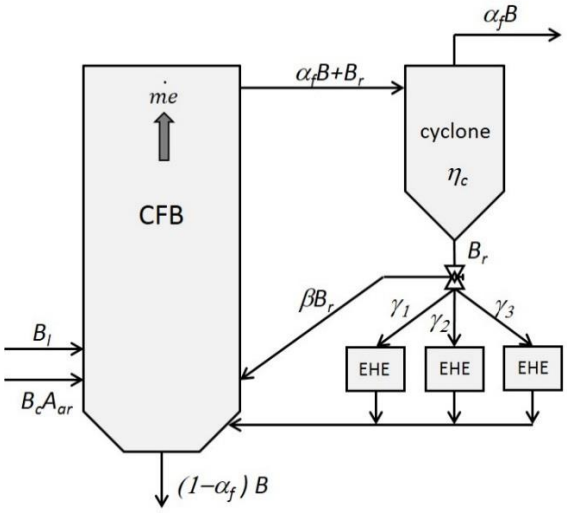

Figure 3: Schematic of mass balance in CFB with EHEs

The biggest challenge in modelling the mass balance lies in the complicated particle size distribution of various kinds of particles in the CFB loop including coal, ash, char, and limestone. When coal particles are fed into the CFB bed, they subject to a series of physical and chemical processes such as drying, explosion, breakage, combustion and attrition. The size distribution of ash and char derived from coal particles depends much on the coal properties and combustion conditions. Unfortunately, there have been very limited models and available experimental results for verification (Lv et al., 2003). In this study, various particle meshes for coal, ash, char and limestone have been defined so that these particles can be classified into a number of groups. Each group of coal particles with diameter of $d_{c,i}$ produces a vector of fractions (denoted by $\alpha_{i,j}$) in each defined group of ash meshes (as shown in Table 4). Therefore, the weight fractions in each group $d_{a,j}$ of ash particles can be calculated using:

$$d_{a,j} = \sum_{i=1}^{im} \alpha_{i,j}, \qquad where\ im\ is\ the\ total\ number\ of\ coal\ size\ groups. \tag{4}$$

Table 4: Ash particle size distribution

	$d_{c,i}$ (μm)				
$d_{a,j}$ (μm)	0~100	100~200	…	8000~9000	9000~10000
0~30	$\alpha_{1,1}$	$\alpha_{2,1}$	$\alpha_{i,1}$	$\alpha_{im-1,1}$	$\alpha_{im,1}$
30~60	$\alpha_{1,2}$	$\alpha_{2,2}$	$\alpha_{i,2}$	$\alpha_{im-1,2}$	$\alpha_{im,2}$
…	$\alpha_{1,j}$	$\alpha_{2,j}$	$\alpha_{i,j}$	$\alpha_{im-1,j}$	$\alpha_{im,j}$
8000~9000	$\alpha_{1,jm-1}$	$\alpha_{2,jm-1}$	$\alpha_{i,jm-1}$	$\alpha_{im-1,jm-1}$	$\alpha_{im,jm-1}$
9000~10000	$\alpha_{1,jm}$	$\alpha_{2,jm}$	$\alpha_{i,jm}$	$\alpha_{im-1,jm}$	$\alpha_{im,jm}$

3.4. Hydrodynamic models

Transport disengagement height

The CFB reactor can be divided into the bottom dense zone and the above freeboard or upper dilute zone. The bottom zone is modelled as a bubbling bed according to Werther and Wein (1994) and the model proposed by Kunii and Levenspiel (1991) is adopted for the upper dilute zone. The transient region in between is denoted as the splash zone, where rising bubbles from the bottom bed explode and cause a more fuzzy transition between the bottom bed and upper dilute zone. From this region, the solids hold-up gradually decays until it becomes nearly constant. The distance between this point, where the solids concentration becomes nearly constant, and the surface of the fluidised bed, is called the 'Transport Disengagement Height' (TDH). The following correlation (George and Grace, 1978) is used for determination of TDH in this study:

$$TDH = 18.2 \cdot d_b \tag{5}$$

where d_b is the diameter of a bubble at the surface of the bottom zone.

Elutriation model

If the freeboard is higher than the TDH, the elutriated mass of solids is dependent on the fluidizing gas velocity, the particle size distribution, the particle terminal velocity and the solid mass fraction in the bed inventory. The elutriation model is especially important in this study as it determines the solid recirculation rate and solid density in the CFB bed. The elutriated mass flow $\dot{m}_{e,i}$ of the particles that belong to the terminal velocity class *i* can be calculated as follows:

$$\dot{m}_{e,i} = k_{\infty,i} \cdot A_t(H_B) \cdot \Delta Q_{3,b,i} \tag{6}$$

where $k_{\infty,i}$ is a particle related elutriation coefficient (kg/(m²s)) which is the cross sectional specific mass flow of particles of terminal velocity class *i* that would be elutriated if the whole inventory contained only particles of that terminal velocity class; A_t is the cross sectional area at height of H_B and $\Delta Q_{3,b,i}$ is the mass fraction of particles of terminal velocity class *i* in the total inventory. $k_{\infty,i}$ is a function of the terminal velocity of the particles $u_{t,i}$ and the fluidizing velocity u_0 and it can be calculated using Geldart's model (1979) in this study:

$$k_{\infty,i} = 23.7 \cdot exp\left(-5.4 \cdot \frac{u_{t,i}}{u_0}\right) \cdot \rho_G \cdot u_0 \tag{7}$$

4. RESULTS AND DISCUSSION

Simulation of the industrial USC/CFB plant X based on the above models has been carried out in Aspen+ and the preliminary results are presented in this section. Figure 4 illustrates the particle size distribution for coal, bed material and recirculating ash particles. Coal particle sizes are measured and obtained from on-site data with an average diameter of around 1mm.

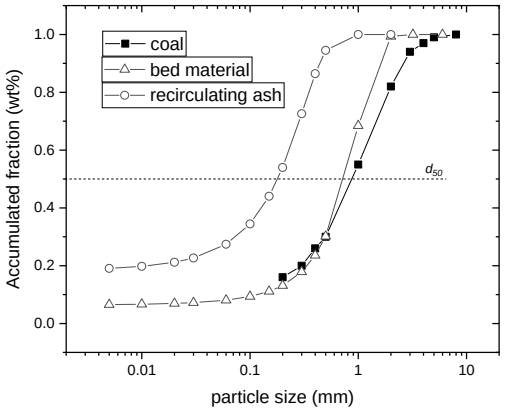

Figure 4: Particle size distribution inside CFB and EHE

The CFB bed materials, derived from coal particles, however have a wider distribution within which fines are elutriated and the coarse particles form the bottom ash and are discharged. The recirculating ash particles between CFB, cyclone and EHEs have a much smaller average diameter of around 180 μm. They belong to Geldart B classification and have good fluidization behaviour. With their terminal velocity being lower than the superficial velocity, most of the ash particles can be elutriated and form the circulating loop, resulting in a much longer residence time.

Table 5: Hydrodynamic parameters for Plant X

Height of bottom zone (dense phase)	m	1.35
Height of freeboard	m	53.65
Solid mass inventory	tonne	444.2
Distributor pressure drop	Pa	1000
Bottom zone pressure drop	Pa	9831
Freeboard pressure drop	Pa	169
Fluidised bed pressure drop	Pa	10000
Overall pressure drop	Pa	11000
Minimum fluidization velocity	m/sec	0.029
Calculated temperature	K	1163 K

Some hydrodynamic parameters in the operation of the plant X are concluded in Table 5. The CFB has been divided into a bottom zone and a freeboard zone. Their heights are determined by the superficial velocity and the ratio of primary and secondary air flow rate. The overall solid mass inventory in the CFB boiler is restricted by the available pressure head of the air supply. The total bed pressure drop consists of components from distributor, bottom zone and freeboard. The minimum fluidization velocity is calculated from the average size of bed materials.

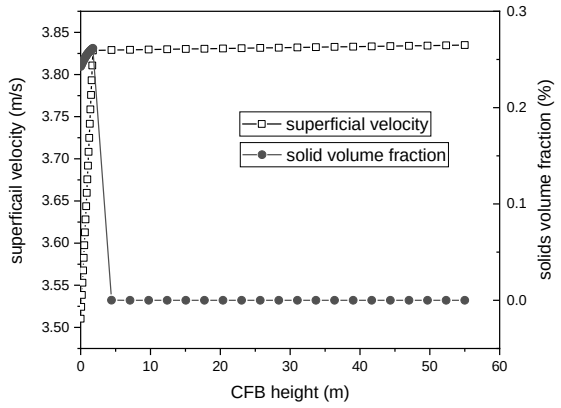

Figure 5: gas velocity and solid fraction along height of CFB

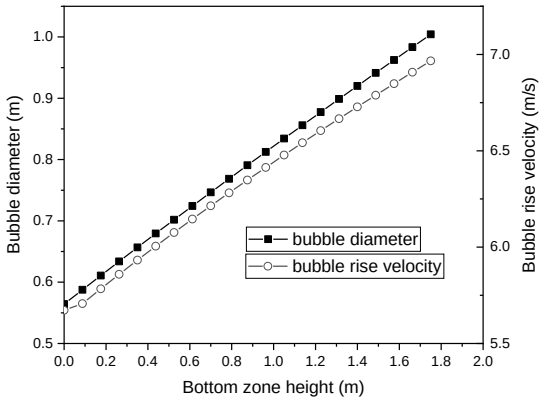

Figure 6: bubble size and rise velocity in bottom zone

The superficial gas velocity and the solid volume fraction along the total height of the CFB reactor are illustrated in Figure 5 and the bubble size and rise velocity inside the bottom dense zone are shown in Figure 6. These results represent the hydrodynamic characteristics of a CFB boiler as an entirety which cannot be simulated by the methodology using discretised RCSTRs adopted in the previous simulations by Aspen+.

5. CONCLUSION

This study has attempted for the first time to use an Aspen+ built-in module “FluidBed” to simulate an industrial 600 MW USC/CFB power plant system. This novel fluidised bed model coupled with a mass balance model comprehensively considers particle size distribution of various solids in the CFB bed, geometry of the reactor, effect of secondary gas supply, impact of heat exchangers on bed temperature and fluid mechanics, and also chemical reactions involving decomposition, volatile matter combustion, char combustion and desulphurization. It provides hydrodynamic characteristics of a CFB boiler such as bubble size and velocity, minimum fluidization velocity and terminal velocity, transport disengagement height, entrainment of solids from the bed, bed pressure drop etc. which cannot be obtained from the traditional methodology previously used in Aspen+ simulations. Apart from the preliminary results presented in this paper, more simulations on mass balance, energy balance and flexible operation of the whole USC/CFB plant system are being carried out and will be reported in the near future.

6. ACKNOWLEDGEMENTS

The authors wish to acknowledge the financial support of the UK Engineering and Physical Research Council (EPSRC, grant No. EP/M01536X/1) for the research work presented in this paper.

7. REFERENCES

Armor, A. F., Viswansthan, R., Dalton, S. M., 2003. 28th Int. Conf. on Coal Utilization & Fuel Systems, pp.1426-38 US DOE, ASME

Booras, G., And Holt, N., 2004. Pulverized coal and IGCC plant cost and performance estimates. Gasification Technologies Conference, Washington D. C.

EIA (Energy Information Administration), 2016. International Energy Outlook. https://www.eia.gov/outlooks/ieo/pdf/0484(2016).pdf. Accessed in June, 2018

Geldart, D., Cullinan, J., Georghiades, S., et al., 1979. The effect of fines on entrainment from gas fluidized beds. *Trans. Inst. Chem. Eng.*, pp. 269-275.

George, S. E., Grace, J. R., 1978. Entrainment of particles from aggregative fluidized beds. *AIChE Symp. Series*, Vol. 74, pp. 67-73.

Hu, Y., Wang, J., Tan, C. K., Sun, C., Liu, H., 2017. Coupling detailed radiation model with process simulation in Aspen Plus: A case study on fluidized bed combustor. *Applied Energy*, http://dx.doi.org/10.1016/j.apenergy.2017.08.030

IEA (International Energy Agency), 2013. World Energy Outlook 2013, https://www.iea.org/publications/freepublications/publication/WEO2013.pdf. Accessed in June, 2018

IPCC (Intergovernmental Panel on Climate Change), 2014. Summary for Policymakers, in IPCC Fifth Assessment Report.

Kunii, D., Levenspiel, O., 1991. Fluidization Engineering, Butterworth-Heinemann, Boston.

Lv, J., Yang H., Zhang, J., LIU, Q., et al., 2003. Investigation on the ash size distribution and attrition during the coal combustion in fluidized bed. *Journal of Combustion Science and Technology*, Vol. 9, pp. 1-5.

NASS/GISS (National Aeronautics and Space Administration/Goddard Institute for Space Studies), 2017. Global land-ocean temperature index. https://climate.nasa.gov/vital-signs/global-temperature/. Accessed in June, 2018.

UNFCCC (United Nations Climate Change), 2015. The Paris Agreement. https://unfccc.int/process-and-meetings/the-paris-agreement/the-paris-agreement. Accessed in June, 2018.

Werther, J., Wein, J., 1994. Expansion behaviour of gas fluidized beds in the turbulent regime. *A.I.Ch.E. Symp. Series*., Vol. 90, pp. 31-44.

Zhen, F., Goidich, S., Robertson, A., Wu, S., 2006. Ultra-supercritical pressure CFB boiler conceptual design study. Final report under U. S. Department of Energy, Cooperative Agreement No. DE-FC26-03NT41737.

368: Nanofluid Brownian motion effect of natural convection in a square enclosure subjected to a constant magnetic field

Mirsarah ABDELAZIZ[1], Wael M. El-MAGHLANY[2], Ashraf S. ISMAIL[3]

[1]*Alexandria University, Faculty of Engineering, Egypt, 11432, misarah.abdelaziz@alexu.edu.eg*
[2] *Alexandria University, Faculty of Engineering, Egypt, 11432, elmaghlany@alexu.edu.eg*
[3] *Alexandria University, Faculty of Engineering, Egypt, 11432, ashraf_s_ismail@yahoo.com*

Natural convection in a square enclosure filled with water-Al_2O_3 and water- TiO_2 nanofluids is studied numerically. Upper, and lower surfaces are insulated, left wall is at high temperature, while right wall and two heat sinks vertically attached to the horizontal walls of the enclosure are kept at low temperature. A uniform magnetic field is applied in a horizontal direction. Steady state laminar regime is considered. The transport equations for continuity, momentum and energy are solved. The numerical results are reported for the effect of solid volume fraction, Rayleigh number, and Hartmann number on the Iso-contours of streamline and temperature. Also, the results for average Nusselt are presented for various parametric conditions. In addition, heat sinks length is investigated for different configurations. This study is presented in the following ranges, Rayleigh number from 10^3 to 10^5, Hartmann number from 0 to 60, and solid volume fraction from 0 to 0.06, while the Prandtl number representing water is kept constant at 6.2. The results show that heat transfer rate decreases with the increase of Hartmann number and increases with the rise of Rayleigh number and with the increase of the nanoparticles solid volume fraction. Also, results show that the heat sinks length have great effect on heat transfer rate depending on the Hartmann number, Rayleigh number and nanoparticle solid volume fraction. In addition, water-Al_2O_3 has better effect on convective heat transfer than water- TiO_2 nanofluid.

Keywords: Nanofluid, Natural Convection, MHD

1. INTRODUCTION

The prevalent problem of natural convection in square enclosures or cavities has various engineering applications, such as electronic chip cooling systems, buildings thermal insulation systems, nuclear reactor systems, and built-in-storage solar collectors (Ostrach,1988). In some practical cases such as the crystal growth in fluids, the cast of metals, and the extraction of geothermal energy, the natural convection is influenced by a magnetic field.

There has been a growing interest to understand the flow behaviour and the mechanism of heat transfer of enclosures that are filled with electrically conducting fluids and are influenced by a magnetic field (Rudraiah et al., 1995; Vasseur and Bilgen, 1995). The common finding of all these studies is that the fluid within the enclosure, which is under the magnetic field effect, experiences a Lorentz force which, affects the buoyant flow field and the heat transfer rate. Researchers argue that the addition of nanoparticles with relatively higher thermal conductivity to the base fluid results in an increase in the thermal performance of the resultant nanofluid (Abu Nada and Chamkha, 2010; Ho et al., 2010; Alloui, Vasseur and Reggio, 2011).

A numerical investigation of the double-diffusive convective flow in a rectangular enclosure also concluded that the heat and mass transfer mechanisms and the flow characteristics in the enclosure strongly depended on the magnetic field strength and the heat generation (Teamah, Elsafty and Massoud, 2012). Mahmoudi et al. (Mahmoudi et al., 2011) investigated numerically the natural convection in an open cavity with 2 vertical thin heat sources subjected to a nanofluid. They demonstrated that the average Nusselt number rises linearly with the rise in the solid volume fraction of nanoparticles.

Mahmoodi (Mahmoodi, 2011) investigated numerically natural convection and heat transfer of different water based nanofluids in a square enclosure with an inside thin heater. The results revealed that at low Rayleigh numbers the horizontal positioned heater have higher Nusselt number compared to the vertical positioned heater, while at high Rayleigh numbers the position of the heater does not affect the heat transfer rate. Bhuiyana et al. (Bhuiyana, Alam and Alim, 2017) examined natural convection in a square enclosure that is filled with a water based nanofluid partially heated at the bottom wall. An enhancement in heat transfer rate is observed with the rise of nanoparticles volume fraction for the whole range of Rayleigh numbers. Also, it is observed that the heat transfer enhancement strongly depended on nanofluids type. It can be concluded that thermal conductivity enhancement is a strong function of φ.

Particles material is also another important key factor, which affect the nanofluids thermal conductivity. Many different studies conducted in the past concluded that particle material also greatly contributes towards the thermal conductivity enhancement of nanofluids. For a specific base fluid, thermal conductivity of particles would greatly influence thermal conductivity of one sample compared to the other one while both possess the same base fluid. Higher thermal conductivity of nanoparticles is expected to lead in higher thermal conductivity of nanofluid.

However, from the above review, and up the authors' knowledge, no studies investigate the nanoparticles Brownian motion effects on natural convection in a square enclosure that is exposed to a constant magnetic field using finite volume method have been reported. Hence, this study examines numerically natural convection in a two-dimensional square cavity filled with water-Al_2O_3 and water- TiO_2 nanofluids. A constant magnetic field is applied horizontally to the enclosure. Effective thermal conductivity and viscosity of nanofluids are obtained using Koo-Kleinstreuer (Koo and Kleinstreuer, 2005) model which implements the nanoparticles Brownian motion effect. Two heat sinks are vertically attached to the horizontal walls of the enclosure. Furthermore, the effects of parameters such as nanoparticles volume fraction, Hartman and Rayleigh numbers on heat transfer rate have been investigated on water-Al_2O_3 and water- TiO_2 nanofluids.

2. MATHEMATICAL MODELING

2.1. Problem statement

A two-dimensional square enclosure with two heat sinks vertically attached to the horizontal walls is considered for the present study with the physical dimensions shown in Figure 1. The temperatures T_h and T_c are uniformly imposed along the vertical walls (the left wall is the source of heat). The bottom and top surfaces are assumed to be adiabatic. A magnetic field with uniform strength B_o is applied in the horizontal direction. The enclosure is filled with nanofluid. The nanofluid is Newtonian and in-compressible. The flow is considered steady, two dimensional, and laminar as well as the radiation effects are negligible. The displacement currents induced magnetic field, dissipation and Joule heating are also neglected. The base fluid and the nanoparticles are in thermal equilibrium, the nanofluids were assumed to be similar to a pure fluid and then nanofluid qualities were gotten and they were applied for the equations of the considered problem.

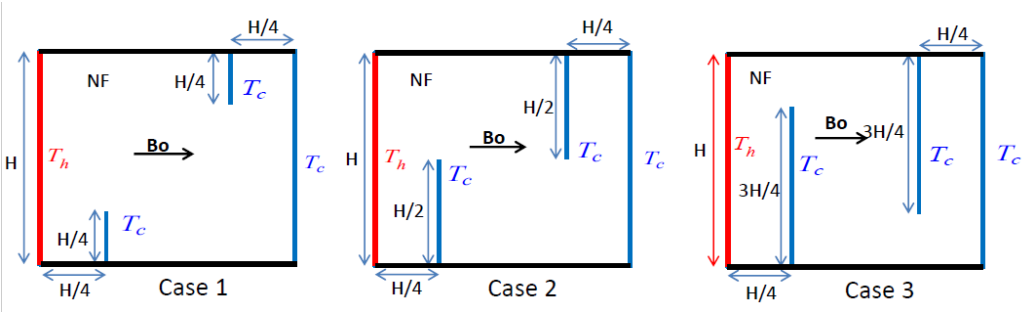

Figure 1: Geometry of the present study

2.2. **Thermal properties of nanofluids** (Teamah and El-Maghlany,2012; El-Maghlany et al., 2016)

$$\rho_{nf} = (1-\phi)\rho_f + \phi\rho_s \quad (1)$$

$$C_{p_{nf}} = \frac{(1-\phi)\rho_f C_{p_f} + \phi\rho_s C_{p_s}}{\rho_{nf}} \quad (2)$$

$$\beta_{nf} = \frac{(1-\phi)\rho_f \beta_f + \phi\rho_s \beta_s}{\rho_{nf}} \quad (3)$$

$$\sigma_{nf} = (1-\phi)\sigma_f + \phi\sigma_s \quad (4)$$

$$K_{nf} = K_{static} + K_{brownian} \quad (5)$$

$$\frac{K_{static}}{K_f} = 1 + \frac{3(\frac{K_s}{K_f} - 1)\phi}{(\frac{K_s}{K_f} + 2) - (\frac{K_s}{K_f} - 1)\phi} \quad (6)$$

$$K_{brownian} = 5*10^4 \beta\phi\rho_f C_{p,f} \sqrt{\frac{k_b T}{\rho_s d_s}} f\,(T,\phi) \quad (7)$$

$$\mu_{nf} = \mu_{static} + \mu_{brownian} \quad (8)$$

$$\mu_{static} = \frac{\mu_f}{(1-\phi)^{2.5}} \quad (9)$$

$$\mu_{brownian} = 5*10^4 \beta\phi\rho_f \sqrt{\frac{k_b T}{\rho_s d_s}} f\,(T,\phi) \quad (10)$$

$$\beta = 0.0137(100\phi)^{-0.8229} \quad \text{for } \phi < 1\% \quad (11)$$

$$\beta = 0.0011(100\phi)^{-0.7272} \quad \text{for } \phi > 1\% \quad (12)$$

$$f\,(T,\phi) = (-6.04\phi + 0.4705)T + (1722.3\phi - 134.63) \quad (13)$$

$$\alpha_{nf} = \frac{K_{nf}}{\rho_{nf} Cp_{nf}} \quad (14)$$

Where:

ρ = Density (Kg/m^3)

C_p = Specific heat ($J/Kg.k$)

β = Coefficient of thermal expansion (K^{-1})

σ = Electrical conductivity (Am/V)

K = Thermal conductivity (W/mK)

k_b = Boltzmann constant

T = Local temperature

d = diameter of solid particles (m)

μ = Dynamic viscosity (m^2/s)

α = Thermal diffusivity (m^2/s)

ϕ = Solid volume fraction

Subscript

nf = Nanofluids

f = Base fluid

s = Solid particles

The thermo-physical properties of the base fluid and the nanoparticles are given in Table1

Table 1: Thermo-physical properties of pure water and Nanofluids

	ρ (Kg/m^3)	Cp (J/KgK)	K (W/mK)	B (K^{-1})	σ (Ωm^{-1})
Al_2O_3	3970	765	40	0.85×10^{-5}	10^{-12}
TiO_2	4250	686.2	8.9538	0.9×10^{-5}	10^{-10}
Water	997.1	4179	0.613	21×10^{-5}	0.05

2.3. Dimensionless Analysis

A dimensionless analysis was performed to study the parameters that affect thermal conductivity. A list of dimensionless groups is listed in Table 2. Substitution with the dimensionless groups in the Table 2 into the governing equations have been made to get the dimensionless governing equations as follows:

$$\frac{\partial U}{\partial X}+\frac{\partial V}{\partial Y}=0 \tag{15}$$

$$(U\frac{\partial U}{\partial X}+V\frac{\partial U}{\partial Y})=-\frac{\partial P}{\partial X}+\frac{\mu_{nf}}{\rho_{nf}\alpha_f}(\frac{\partial^2 U}{\partial X^2}+\frac{\partial^2 U}{\partial Y^2}) \tag{16}$$

$$(U\frac{\partial V}{\partial X}+V\frac{\partial V}{\partial Y})=-\frac{\partial P}{\partial Y}+\frac{\mu_{nf}}{\rho_{nf}\alpha_f}(\frac{\partial^2 V}{\partial X^2}+\frac{\partial^2 V}{\partial Y^2})+\frac{\beta_{nf}}{\beta_f}R_a \mathrm{P_r}\theta-\frac{\sigma_{nf}\rho_f}{\sigma_f\rho_{nf}}H_a^2 \mathrm{P_r}V \tag{17}$$

$$U\frac{\partial \theta}{\partial X}+V\frac{\partial \theta}{\partial Y}=\frac{\alpha_{nf}}{\alpha_f}(\frac{\partial^2 \theta}{\partial X^2}+\frac{\partial^2 \theta}{\partial Y^2}) \tag{18}$$

Where:

U = Dimensionless velocity component in X direction
V = Dimensionless velocity component in Y direction
X , Y = Dimensionless coordinates
R_a = Rayleigh number
$\mathrm{P_r}$ = Prandtl number
H_a = Hartmann number
θ = Dimensionless Temperature

Table 2: Dimensionless Groups for the model.

Length	$X=\frac{x}{H}$
Height	$Y=\frac{y}{H}$
Velocity component of x direction	$U=\frac{uH}{\alpha_f}$
Velocity component of y direction	$V=\frac{vH}{\alpha_f}$
Pressure	$P=\frac{pH^2}{\rho_{nf}\alpha_f^2}$
Temperature	$\theta=\frac{T-T_c}{T_h-T_c}$
Rayleigh number	$Ra=\frac{g\beta_f H^3 T_h-T_c}{\nu_f\alpha_f}$
Hartmann number	$H_a=B_o H\sqrt{\frac{\sigma_f}{\rho_f\nu_f}}$
Prandtl number	$\mathrm{Pr}=\frac{\nu_f}{\alpha_f}$

Where:

H = Enclosure height (m)
P = Dimensionless pressure
p = pressure (N/m^2)
T = Temperature (K)
g = Acceleration of gravity (m/s^2)
B_o = Magnetic field (Tesla)

Subscript

c = cold
h = hot

Table 3: Dimensionless Boundary Conditions for the model

Bottom wall	Adiabatic	U=V=0	$\partial\theta/\partial y = 0$
Top wall	Adiabatic	U=V=0	$\partial\theta/\partial y = 0$
Left wall	Adiabatic	U=V=0	$\theta = 1$
Right wall	Cold side	U=V=0	$\theta = 0$
Left sink	Hot side	U=V=0	$\theta = 0$
Right sink	Hot side	U=V=0	$\theta = 0$

2.4. Nusselt Number Calculation

Equating the heat transfer by convection to the heat transfer by conduction yields equation (19);

$$h\Delta T = -K_{nf}\frac{\partial T}{\partial x} \tag{19}$$

Introducing the dimensionless variables,

$$Nu_L = -\frac{K_{nf}}{K_f}\left(\frac{\partial\theta}{\partial X}\right)_{X=1} \tag{20}$$

The average Nusselt number is obtained by integrating the above local Nusselt number over the cold vertical wall

$$Nu = \int_0^1 Nu_L dY \tag{21}$$

The stream function is calculated using equation (22)

$$U = \frac{\partial\psi}{\partial Y}, V = \frac{\partial\psi}{\partial X} \tag{22}$$

Where:

ΔT = Temperature difference (K)
Nu = Average Nusselt number
Nu_L = Local Nusselt number
ψ = Dimensionless stream function

3. CODE VALIDATION AND VERIFICATION

3.1. Solution procedure

The governing equations are solved using the finite volume technique developed by Patankar (Patanker, 1980). This technique is based on the discretization of the governing equations using the central difference scheme in space. Firstly, Grid dependence study is performed where various grid sizes ranging from (20, 20) to (360, 360) are used. The deviation between the results for Nusselt number on the right cold vertical wall obtained for domain (160, 160) and (200-200) were less than 0.4 %, as shown in Figure 2. Accordingly, the (160, 160) grid points in X-direction and Y-directions are found to be a good compromise between the computation cost and the accuracy, enough to resolve the thin boundary layer near the vertical walls. Secondly, the discretization equations are solved by the Gauss Seidel method. The iteration method used in this program is a line-by-line procedure, which is a combination of the direct method and the resulting Tri-Diagonal Matrix Algorithm (TDMA). Finally, the convergence of the iteration is determined by the change in the average Nusselt number as well as other dependent variables through one hundred iterations to be less than 0.01% from its initial value.

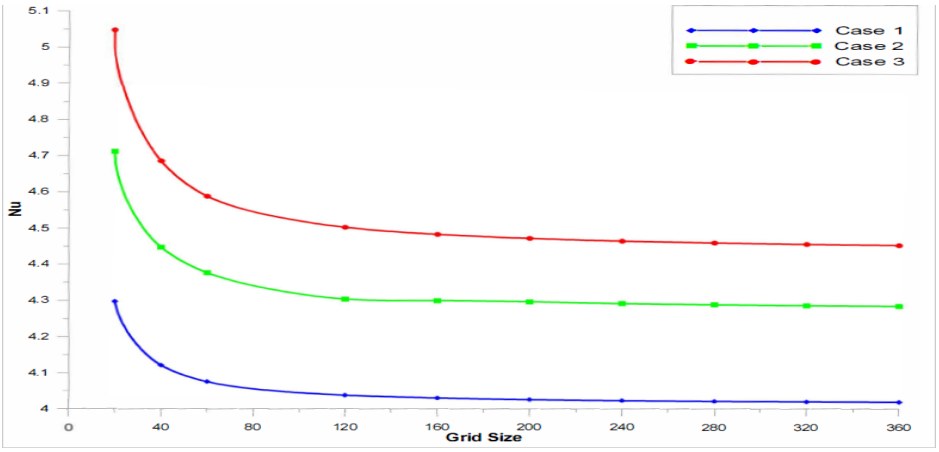

Figure 2: Mesh dependence study

3.2. Program validation and comparison with previous work

(Mahmoudi, Mejri and Omri, 2016) numerical results are used to validate the numerical technique employed in the present study. The validation is performed for the isotherms and the streamlines of nanofluid (F= 0.04) with different Rayleigh and Hartmann numbers. Same boundary conditions are used, as well as the Brownian motion effect is neglected in this validation case. The comparison in Figure 3 shows an excellent agreement between the proposed method and the results reported by Mahmoudi et al.

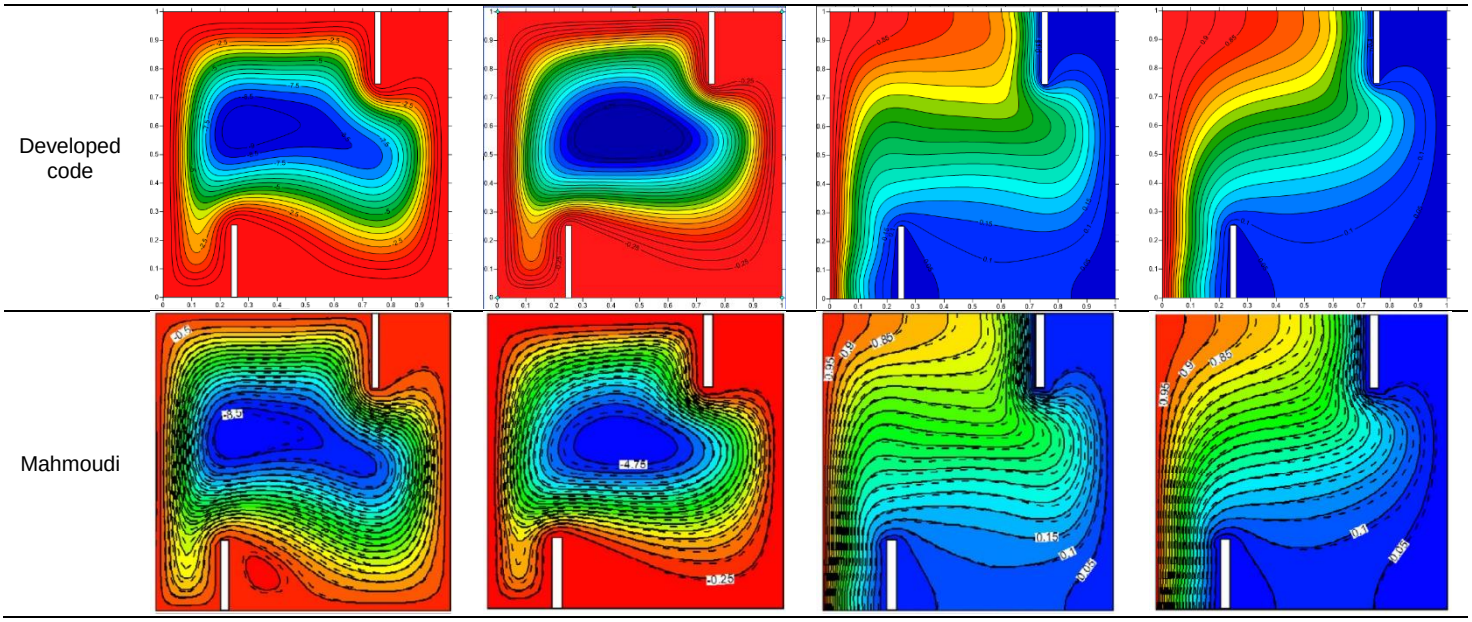

Figure 3: Streamlines & Isotherms validation for 2 different conditions

4. RESULTS AND DISCUSSION

In this study, the Prandtl number, Pr is kept constant at Pr = 6.2. The base case in this study is made with Rayleigh number $R_a = 10^5$, Hartmann number $H_a = 30$, solid volume fraction φ = 0.04 (water-Al_2O_3 and water- TiO_2 nanofluid). The numerical results for the streamline and Iso-thermals contours for various values of H_a, R_a, φ and length of heat sinks will be presented and discussed. In addition, the results for average Nusselt, at various conditions will be presented and discussed.

For all studied cases, the buoyancy-driven circulating flows with in the enclosure are evident for all values of the R_a and H_a numbers. The strength of these circulations increases as the R_a number increases and decreases as the H_a number increases. Examining equation 17 the sign of H_a is opposite to the sign of R_a in source term. Therefore, there is an

opposite effect of R_a and H_a on flow regime and Nusselt number. The results also show that the heat transfer rate increases with the increase of R_a number and decreases with the increase of H_a number. For all studied cases, the increases of R_a number increase the natural convection and stabilise the temperature in the middle of the cavity. The opposite effect is produced by increasing the number of H_a. In addition, water-Al_2O_3 enhances the heat transfer better than water-TiO_2 nanofluid in all studied cases.

4.1. streamline and isothermal Contours

Figure 4 shows the streamlines and isothermal contours of different configurations for the length of heat sink in the cavity Figure 8a shows that Nusselt number increases with increasing the length of heat sink, on the other hand max ψ decreases with the increase of the length of heat sink. Also, using water-Al_2O_3 nanofluid increases the Nusselt number than using water-TiO_2 nanofluid however, it has no effect on max ψ.

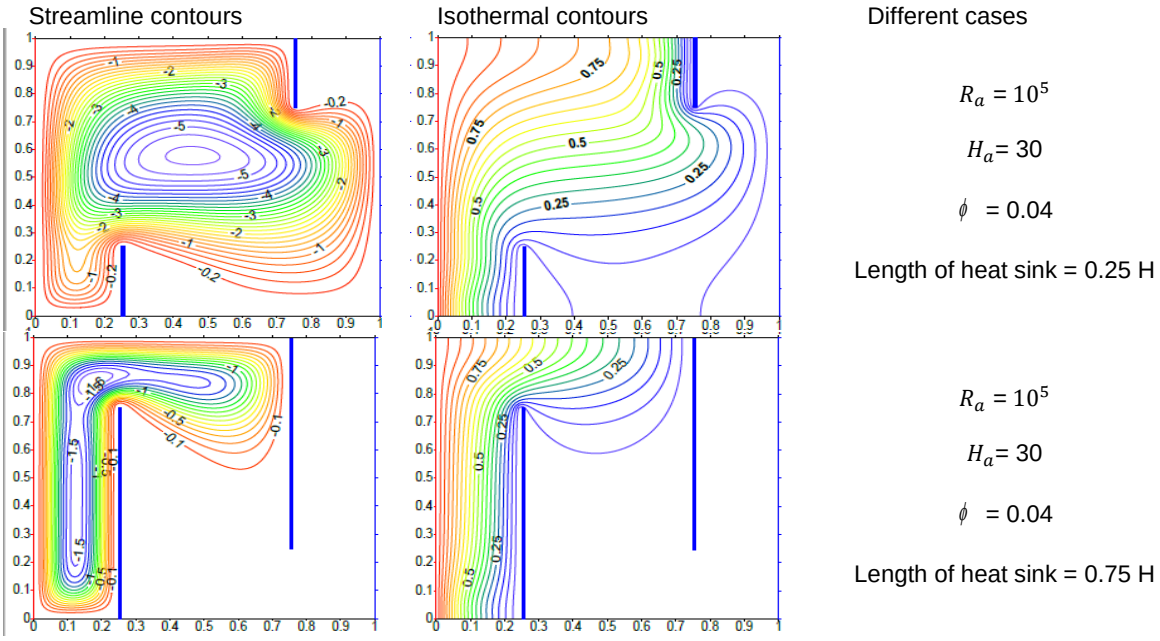

Figure 4: Effect of length of heat sinks on streamlines & isotherms

4.2. Effect of rayleigh number

Figure 5 represents the effect of R_a number on the streamline and isothermal contours for φ = 0.04 and H_a = 30 for water-Al_2O_3 nanofluid. For low R_a number (R_a = 1000), the conduction regime is dominant, weak clockwise circulation in the cavity is found. On the other hand, the isotherms are parallel (conduction domain). As the R_a number increases ($R_a = 10^5$) the convection mode is pronounced, the flow cell becomes stronger. Figure 5 shows the isothermal are closer to the hot wall in the lower region, therefore, the temperature gradient at the cavity bottom is higher than at the top. This is leads to high heat transfer rate at the cavity bottom as shown in Figure 8b. As R_a increases the Nusselt number increases for constant H_a number with exact agreement of the streamlines and isotherms contours in Figure 5. Also, as R_a increases the max. ψ increases for constant H_a . So, the overall heat transfer increases as R_a increases. In addition, using water-Al_2O_3 nanofluid increases the Nusselt number than using water-TiO_2 nanofluid even if it has no effect on max ψ. An intense temperature gradient appears between the cold sink and the hot wall indicating strong heat transfer rate in this region.

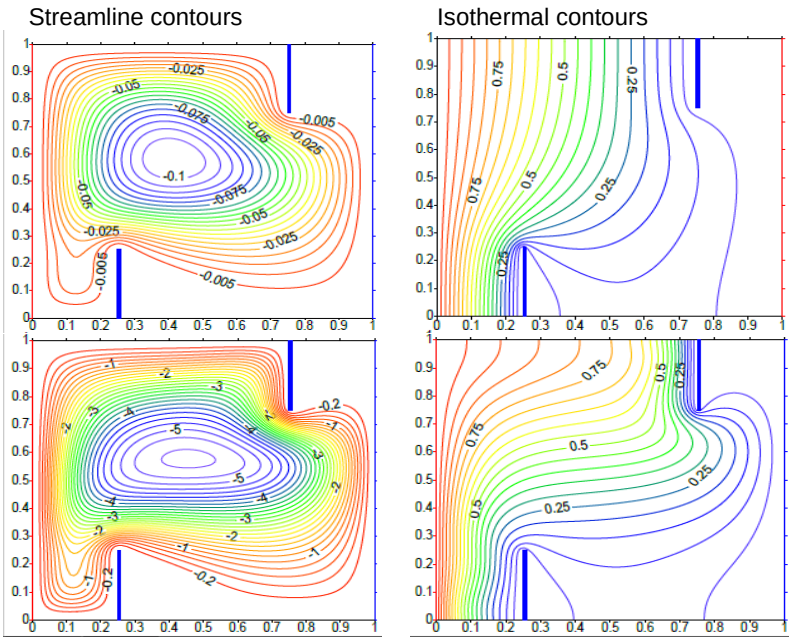

Figure 5: Effect of Rayleigh No. on streamlines & isotherms

4.3. Effect of hartmann number

For all values of R_a number, the application of the magnetic field has the tendency to slow down the movement of the fluid in the enclosure due to Lorenz force effect. As H_a number increases circulation strength is decreased as shown in Figure 6. The effect of magnetic field on the Nusselt number and max. ψ are presented in Figure 8.c. The figure shows that as H_a increases the Nusselt number as well as the max. ψ decreases for constant R_a number. Accordingly, the overall heat transfer decreases with the increase in H_a. Again, using water-Al_2O_3 nanofluid increases the Nusselt number compared to using water- TiO_2 nanofluid, while having no effect on max. ψ

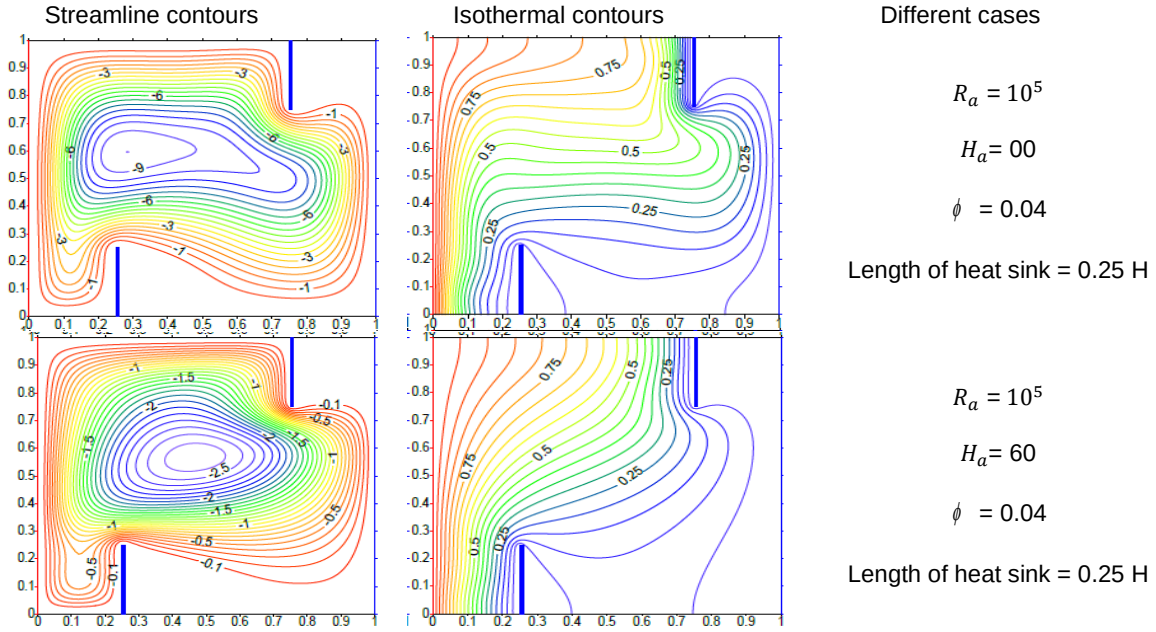

Figure 6: Effect of Hartmann No. on streamlines & isotherms

4.4. Effect of solid volume fraction

From Figure 8.d, it is observed that the addition of nanoparticles increases slightly the Nusselt number, also, the ϕ directly proportional to max. ψ. Accordingly, the overall heat transfer increases as ϕ increases. Figure 7 shows that increasing the solid volume fraction has no significant effect on isotherms and isostream contours. It is also noticed that using water-Al_2O_3 nanofluid increases the Nusselt number compared to using water- TiO_2 nanofluid and the difference between the two nanofluids increases with the increase of the solid volume fraction.

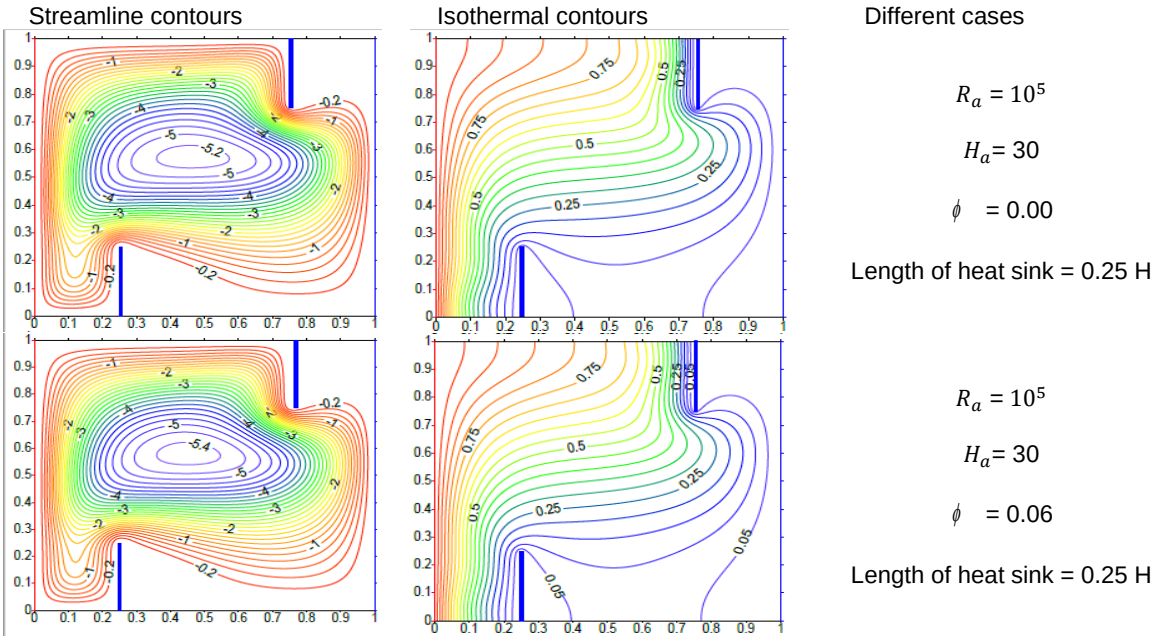

Figure 7: Effect of solid volume fraction. on streamlines & isotherms

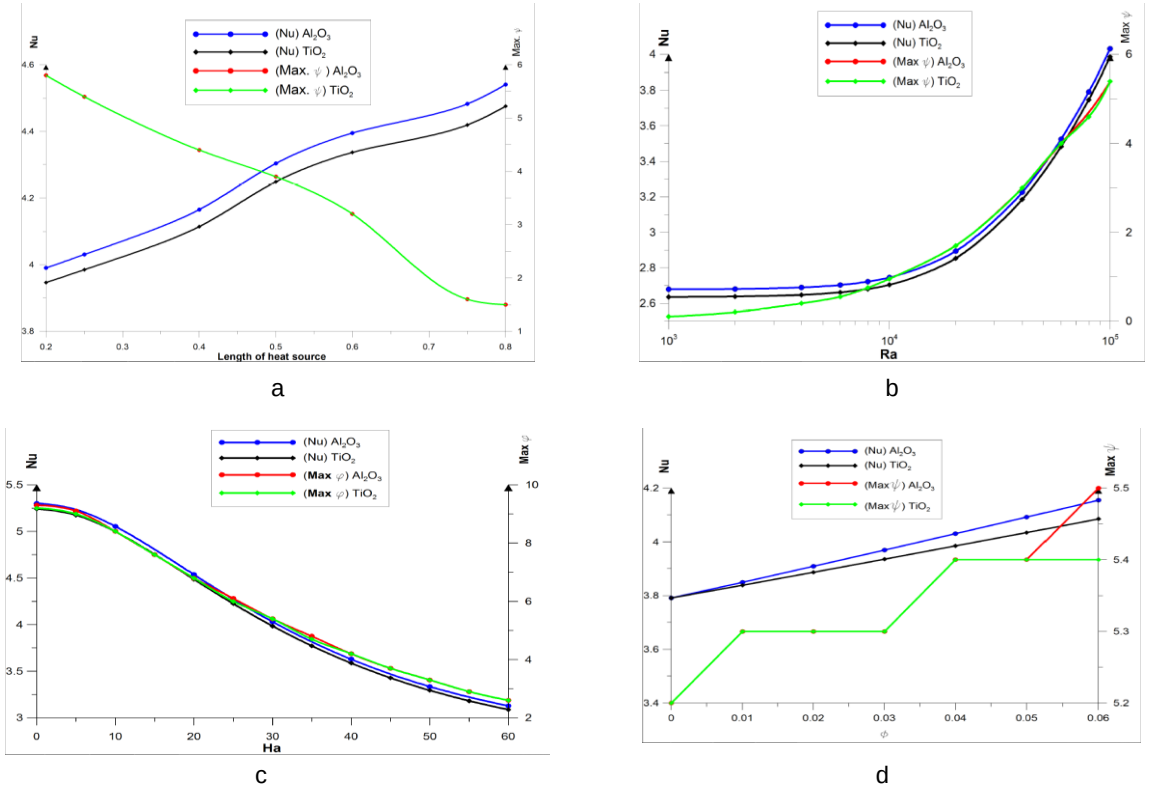

Figure 8: Effect of different parameters on Nu & Max ψ

a: effect of length of heat source b: effect of R_a No. c: effect of H_a No. d: effect of ϕ .

5. CONCLUSION

Natural convection in a square enclosure that is filled with a water-Al_2O_3 and water- TiO_2 nanofluids and is influenced by a magnetic field has been studied numerically. The effects of parameters such as: the R_a number, the H_a number, the length of heat sinks and φ on the flow & temperature fields and the heat transfer rate have been examined. The results of the numerical analysis led to the following conclusions:

- A good agreement valid with other numerical investigations demonstrates that finite volume technique developed by Patanaker is an appropriate method for different applicable problems.
- For constant φ = 0.04 and H_a = 30, as the R_a number increases the heat transfer increases and Stronger flow circulations are formed.
- For constant φ = 0.04 and $R_a = 10^5$, as the H_a number decreases the heat transfer increases and Stronger flow circulations are formed.
- For constant $R_a = 10^5$ and H_a = 30, to enhance the heat transfer, φ must be increased.
- For constant φ = 0.04, $R_a = 10^5$ and H_a = 30, water-Al_2O_3nanofluid enhances the heat transfer compared with water- TiO_2.

6. REFERENCES

Abu-Nada, E., and Chamkha, A. J., 2010, Effect of nanofluid variable properties on natural convection in enclosures filled with a cuo-eg-water nanofluid*, International Journal of Thermal Sciences*, 49(12), 2339-2352.

Alloui Z., Vasseur, P., and Reggio, M., 2011, Natural convection of nanofluids in a shallow cavity heated from below, *International journal of Thermal sciences*, 50(3), 385-393.

Bhuiyana, A., Alam, M. S., and Alim, M., 2017, Natural convection of water-based nanofluids in a square cavity with partially heated of the bottom wall, *Procedia Engineering*, 194, 435-441.

El-Maghlany, W. M., Elazm, M. M. A., Shehata, A. I., and Teamah, M. A., 2016 A novel technique for heat transfer enhancement from a horizontal heated pipe by using nanofluid restrained flow, *Journal of the Taiwan Institute of Chemical Engineers*, 68, 338-350.

Ho, C., Liu, W., Chang, Y., and Lin, C., 2010, Natural convection heat transfer of alumina-water nanofluid in vertical square enclosures: an experimental study, *International Journal of Thermal Sciences*, 49(8), 1345-1353.

Koo, J., and Kleinstreuer, C., 2005. Laminar nanofluid flow in microheat-sinks, *International Journal of Heat and Mass Transfer*, 48(13), 2652–2661

Mahmoudi, A. H., Shahi, M. A., Shahedin, M., and Hemati, N., 2011, Numerical modeling of natural convection in an open cavity with two vertical thin heat sources subjected to a nanofluid, *International Communications in Heat and Mass Transfer*, 38(1), 110-118.

Mahmoodi, M., 2011, Numerical simulation of free convection of nanofluid in a square cavity with an inside heater, *International Journal of Thermal Sciences*, 50(11), 2161-2175.

Mahmoudi, A., Mejri, I., and Omri, A., 2016. Study of natural convection cooling of a nanofluid subjected to a magnetic field, *Physica A: Statistical Mechanics and its Applications*, 451, 333–348.

Ostrach, S., 1988, Natural convection in enclosures. *Journal of Heat Transfer*, 110, 1175-1190.

Patankar, S., 1980. Numerical heat transfer and fluid flow, CRC press.

Rudraiah, N., Barron, R., Venkatachalappa, M., and Subbaraya, C., 1995, Effect of a magnetic field on free convection in a rectangular enclosure, *International Journal of Engineering Science*, 33(8), 1075-1084.

Teamah, M. A., Elsafty, A. F., and Massoud, E. Z., 2012, Numerical simulation of double-diffusive natural convective ow in an inclined rectangular enclosure in the presence of magnetic field and heat source, *International Journal of Thermal Sciences*, 52, 161-175.

Teamah, M. A., and El-Maghlany, W. M., 2012, Augmentation of natural convective heat transfer in square cavity by utilizing nanofluids in the presence of magnetic field and uniform heat generation absorption, *International Journal of Thermal Sciences*, 58, 130-142.

Vasseur, P., and Bilgen, E., 1995, Natural convection heat transfer in a rectangular enclosure with a transverse magnetic field, *Journal of Heat Transfer*, 117, 668-673.

369: Performance evaluation of heat recovery in heat generating systems based on computational analysis

Timothy LASEINDE[1], Koketso MADITSI[2]

[1] University of Johannesburg, Johannesburg, otlaseinde@uj.ac.za
[2] University of Johannesburg, Johannesburg, 201446621@student.uj.ac.za

Heat recovery is a process of converting wasted heat, which would otherwise be lost to the environment into useful work to power other thermal systems thereby, improving the power generation while saving overall energy costs. The paper is aimed at sharing the methodological approach employed in a heat recovery research based on recoverable heat computation analysis conducted on various heat recoverable systems using specific key computational indicators and comparing the results with that obtained in Heating-Ventilation and Air-conditioning (HVAC) appliances which are powered by Photovoltaic (PV) and Photovoltaic Thermal (PV/T) cells. The design elements considered in this research were informed by existing heat regeneration and conversion processes. The heat regeneration process typically found in gasoline turbines, and those found in PV cells were considered. The workability of these systems for heat reuse is an integral part of the study. The relevance of this research is that the findings informed the design of a heat recovery unit for a PV solar air-conditioning system. Through computation analysis, the benchmarks obtained forms part of the building block that supports the design phase of a heat recovery system. The principles applied as presented in this paper will guide researchers who are considering venturing into projects related to heat recovery.

Keywords: Heat Recovery, PV/T, PVT, Photovoltaic thermal, Peltier fan, Design

1. INTRODUCTION

Waste heat recovery entails capturing and reusing the wasted heat from industrial, commercial and domestic equipment processes, for heating and generating mechanical and electrical energy through semiconductor thermal converters, based on Seebeck effect. According to past studies on heat losses, approximately 20% to 50% of industrial energy consumption is ultimately discharged as wasted heat. These losses arise from both equipment inefficiencies and thermodynamic limitations of equipment's and processes. The waste heat losses may be reduced by improving equipment designs or by installing waste heat recovery mechanisms. The strategy employed for recovery of heat is entirely based on key factors such as temperature, chemical composition of the exhaust stream, the phase of the heat stream, the intended use of the recovered heat, environmental regulations, and financial factors involved. It is desirable for heat recovery technologies to be efficient, sustainable, and capable of producing considerable output of the recovered heat at reasonably acceptable cost. If these conditions cannot be achieved, then, having the heat recovery unit will be counterproductive to a thermal system, which is already inefficient. From an economic point of view, a considerable amount of wasted heat energy from primary combustion of fuel are none recoverable. However, much of the heat energy from the exhaust point of the combustion chamber are recoverable, thereby minimising the losses as discussed in this paper.

Compressor powered air conditioning systems demand considerable amount of power and in-turn absorb considerable heat from the cooled conditioned space, which is exhausted into the outer environment. The exhaust heat could otherwise be re-utilised for heating up the incoming fresh air of such systems in a typical HVAC system. The performance of a PV system degrades due to high surface panel temperature and this lowers the electrical output produced. PV surface temperature are usually regulated using a suitable fluid, air-cooling system, or heat absorption sinks. A suitable method, which focuses on reusing the recovered heat for water heating, is the Photovoltaic Thermal (PV/T) cells. PV/T technology is a system that only considers cooling the PV cells for improving their efficiency. PV/T solar systems have limitations due to their cost, applications, and their availability. A plausible method for heat recovery is by integrating systems such as thermoelectric generators, which convert the heat generated to electricity.

A typical approach for regenerating and improving the efficiency of power production systems as typical to gas turbines is the design of a cycle combining two power units with the heat rejected from the first system supplying heat to the second system. The gases leaving the gas turbine are at sufficiently high temperature to be used as a source of heat for the production of steam at suitable pressure and temperature. Performance evaluation was also carried out on other heat recovery systems and the analysis guided the design elements and hardware components selected for the design of a heat recovery system for the HVAC system considered in the next stage of this phase of the research.

1.1. Research overview and study approach

The heat recovery research is divided into phases. The first phase reviews and evaluates the performance of some common heat recovery systems, and computational analysis were conducted by considering energy consumption, efficiency and Coefficient of Performance (CoP) of selected systems. The computations further included comparative analysis of the above considerations in Photovoltaic (PV) and Photovoltaic Thermal (PV/T) solar modules, combined gas and steam turbine plant efficiencies, and the performance of the vapour absorption refrigeration systems powered by waste heat from internal combustion engine of an automobile. Other heat recovery systems briefly discussed includes shell and tube heat exchangers, heat pipes, economisers, heat wheels and waste heat boilers. The numerical investigation of waste heat losses presented in this paper is required for better understanding and for identification of heat recovery opportunities, which can be harnessed from existing thermal technologies, with the intent of adopting some of the principles for the heat recovery unit in view.

The study took a structured stepwise approach by extensive consideration of existing literature regarding current trends in power optimisation techniques, computational analysis models, and the development of heat recovery system. The paper is anchored on the computational analysis section of the research from which inferences emerged. The actions carried out in the design and build phase of the research, were based on recommendations that emerged from this phase of the study.

2. MAJOR CONSIDERATIONS AND DISCUSSION

2.1. Source of waste heat for different temperature range

Table 1: Waste heat source for high temperature range

Source of waste heat	Temperature range (°C)
Nickel refining furnace	1370 - 1650
Steel heating furnace	760 - 1100
Copper refining furnace	760 - 815
Hydrogen plants	650 - 1000
Solid waste incinerators	650 - 1000

Table 2: Waste heat source for medium temperature range

Source of waste heat	Temperature range (ºC)
Drying and baking ovens	230 – 600
Steam boiler exhausts	230 – 480
Gas turbine exhausts	370 – 540
Reciprocating engine exhausts	315 – 600
Turbo charged reciprocating engine exhausts	230 – 370

Table 3: Waste heat source for low temperature range

Source of waste heat	Temperature range (ºC)
Air conditioning & refrigeration condenser	32 - 43
Hot processed liquids & solids	32 - 232
Internal combustion engine	66 - 120
Furnace doors	32 - 55
Drying and baking ovens	93 - 230

Based on the temperature range categories stated in Tables 1 to Table 3, heat from air-conditioning and refrigeration condenser systems fall within the low temperature range heat sources. As such, solutions for recovering low temperature heat losses were considered. Since limited research on heat recovery of air conditioning systems was found from literature review within the public repository, existing heat recovery solutions that have been applied in the other four sources of waste heat mentioned in Table 4 were considered in the research.

2.2. Performance evaluation of air type Photovoltaic Thermal (PV/T) solar collector with Heat Recovery Ventilation (HRV)

Heat Recovery Ventilations (HRV's) makes the mechanical ventilation more cost effective by recapturing some of the heat from exhausts airflows, which accounts for the reclaim of approximately 40% – 85% of the conditioned temperature that would otherwise be lost to the outside environment.

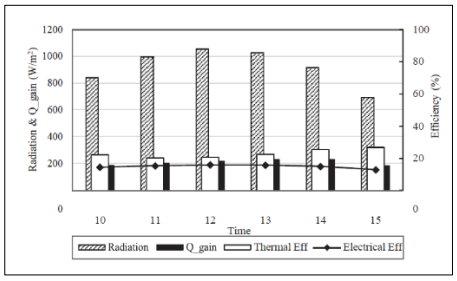

Figure 1: Daily performance of PV/T collector (Ahn, 2015)

The performance of air type PV/T collectors coupled with the heat recovery ventilation was first approached based on existing literature, and then computationally compared with the information obtained from literature. According to analysis of PV/T collectors presented by Ahn (2015), the electrical and thermal efficiencies of PV/T systems were found to be 15% and 35% respectively as illustrated in Figure 1. The higher the thermal efficiency, the lower the electrical efficiency and vice-versa. However, this varies with time and how long the cells have been exposed to the sun. The overall performance of the PV/T coupled with the HRV was found to be 38%. The heat transfer efficiency improved by the combination to an approximate 20% by pre-heating the incoming fresh air. This research was completed with a conclusive statement that PV/T collectors with HRV yields maximum efficiency as compared to conventional system (Ahn, 2015).

2.3. Comparative performance analysis of PV and PV/T systems

Lynn (2010) selected a PV module containing 72 monocrystalline cells quoted by the manufacturer in line with the approach taking. Table 4 contains the quoted manufacturer's specifications. Computation analysis was carried out to determine the sizing requirements for an air-conditioning unit, for evaluating the expected output.

Table 4: PV performance data (Lynn, 2010)

Cell operating temperature at standard conditions (25 ºC)	
Cell maximum safe temperature at a particular location (70 ºC)	
Nominal power	180 W
Open circuit voltage	43.8 V
Short circuit current	5.5 A
Voltage at maximum power	35.8 V
Current at maximum power	5.03 A
Power reduction per ºC (PV)	0.45 %
Power reduction per ºC (PV/T)	0.058 %
Length	1600 mm
Width	804 mm
Weight	18 kg
Efficiency	14 %

Calculations

Increase in cell temperature =70℃ - 25℃ (temperature rise is 45℃)

$(PV)\ power\ reduction = 0.45\% \times 45 = 20.25\ \%$

$(PV/T)\ power\ reduction = 0.058\% \times 45 = 2.61\ \%$

$(PV)\ power\ output = 180 \times (1 - 20.25\%) = 143.55\ Watts$

$(PV/T)\ power\ output = 180 \times (1 - 2.61\%) = 175.302\ Watts$

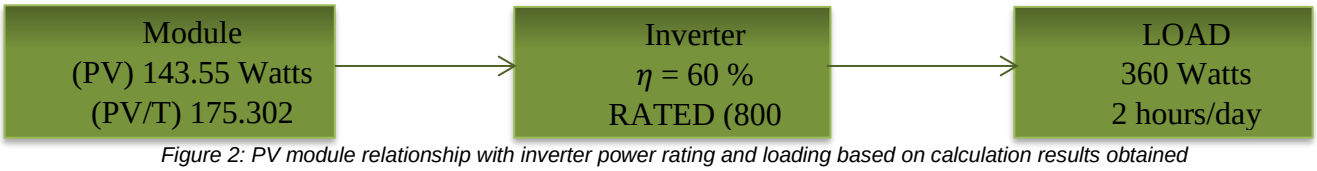

Figure 2: PV module relationship with inverter power rating and loading based on calculation results obtained

Input power to the Inverter

$$P_{input} = \frac{P_{output}}{\eta_{inverter}} = \frac{360}{0.6} = 600\ Watts$$

Since the input power is less than its rated power (800 Watts), only one inverter is required for this connection.

Energy consumption of the load

$$energy = \frac{360\ Watts \times 2\ hours \times 1\ kW}{1000\ Watts} = 0.72\ kW.hr/day$$

Energy input to the inverter

$$E_{input} = \frac{E_{output}}{\eta_{inverter}} = \frac{0.72}{0.6} = 1.2\ kW.hr/day$$

Solar radiation at the worst month of the year where the panels receives less radiation is obtainable from a program developed by the National Renewable Energy Lab. The 2.88 kW.hr/m^2/day is used in the below calculations and it is not a standard value. This is obtained from a specific location and it differs from country to country (Messenger, 2004).

PV energy consumption per panel and efficiency

$$E_{PV} = \frac{2.88\ hours \times 143.55\ Watts \times 1\ kW}{1000\ Watts \times 1\ solar\ panel} = 0.4134\ kW.hr/day/1\ solar\ panel$$

$$number\ of\ panels = \frac{1.2\ kW.hr/day}{0.4134\ kW.hr/day/1\ solar\ panel} = 2.9 \approx 3\ panels$$

$$efficiency = \frac{(PV)\ power\ output\ in\ kW}{area\ of\ the\ module} = \frac{143.55}{1000 \times 1.2864} = 11.2\ \%$$

PV energy consumption per panel and efficiency

$$E_{PV/T} = \frac{2.88\ hours\ \times 175.302\ Watts\ \times 1\ kW}{1000\ Watts\ \times 1\ solar\ panel} = 0.5049\ kW.hr/day/1\ solar\ panel$$

$$number\ of\ panels = \frac{1.2\ kW.hr/day}{0.5049\ kW.hr/day/1\ solar\ panel} = 2.4\ \approx 2/3\ panels\ may\ be\ used$$

$$efficiency = \frac{(PV/T)\ power\ output\ in\ kW}{area\ of\ the\ module} = \frac{175.302}{1000 \times 1.2864} = 13.6\ \%$$

The equation below is applicable to calculate the thermal efficiency of the module $\eta_{thermal} = \frac{m \times C_p \times (t_{outlet} - t_{inlet})}{A_{PV/T\ module}}$

Table 5: Summary of performance calculations

PERFORMANCE EVALUATION OF DIFFERENT MODULES POWERING A 360 WATTS LOAD			
	PV module at (MPP)	PV module	PV/T module
Efficiency (%)	14	11.2	13.6
Number of panels (N)	3	3	2 or 3

The comparative calculations above suggests that if the cell temperature rises above its nominal operating temperature in our case an increase by 45 ℃ will negatively affect the power output which will fall by about 20% for the PV panel and by just 2.6 % for the PV/T panel. This emphasises the need to keep the module as cool as possible with adequate ventilation. From the results in table5 above, it shows that the efficiency of the PV/T is relatively about the same as the PV module operating at its maximum power point. The PV/T acts as a heat recovery system by reclaiming excess panel temperature and uses it to heat the working fluid inside the tubes. The result is space saving as one module simultaneously generates both heat and electricity.

2.4. Heat recovery from an Internal Combustion (IC) engine of an automobile

Table 6: Performance data from IC engine

Engine	4 cylinder, 4 stroke IC Engine (diesel)
Bore x Stroke	83 mm x 99mm
Compression ratio	16.2:1
Capacity	1.5 litres
Power output	100 kW at 2500 RPM
Specific Fuel Consumption	0.2 kg/kW.hr

Table 7: Additional IC engine data

Ambient Temperature	40 ℃
Exhaust Temperature	350 ℃
Specific Heat Capacity	1.063 kJ/kg.K
Volumetric efficiency	75 %
Density for gas	1.2
Heat exchanger effectiveness	0.8

Estimation of the heat lost from the exhaust through diesel engine compression ratio (Zheng et al., 2011)

Total volume (V_{tot})

$ALn = 1.5\ l$, and $= \frac{V_s + V_c}{V_c}$, hence, $rV_c = (ALn) + V_c$. As such,$16.2V_c = (1.5 \times 10^{-3}) + V_c$, therefore, $V_c = 9.868 \times 10^{-5} m^3$

$$V_{tot} = V_s + V_c = 9.868 \times 10^{-5} + 1.5 \times 10^{-3} = 1.6 \times 10^{-3} m^3$$

Mass flow rate of fuel based on the Specific Fuel Consumption (sfc)

$sfc = \frac{m_{fuel}}{P_{output}}$ Therefore, $m_{fuel} = \frac{0.2 \times 100}{3600} = 5.56 \times 10^{-3} m^3$

Swept volume (V_s) flow rate

$V_s = (ALn) \times \frac{N}{2}$ $(2\ revolutions\ of\ cranshaft)$ $= \frac{1.5\times10^{-3}\times2500}{60\times2}$ $= 0.031\ m^3/s$

Mass flow of air

$Volumetric\ efficiency\ (\eta_{volumetric})\ \eta_{volumetric} = \frac{V_{induced}}{V_s} = \frac{m_{air}}{\rho V_s}$, therefore $0.75 = \frac{m_{air}}{1.2\times0.031}$ Therefore, $m_{air} = 0.028\ kg/s$

Mass flow rate of exhaust gas (m_{gas})

$m_{gas} = m_{air} + m_{fuel} = 5.56 \times 10^{-3} + 0.028 = 0.033\ kg/s$

Heat lost in exhaust gases (Q_{lost})

$Q_{lost} = m_{gas} \times C_p \times \Delta T = 0.033 \times 1.063 \times (350 - 40) = 10.87\ kW$

Heat supplied to the generator (Q_{gen})

$Q_{gen} = Q_{lost} \times effectiveness = 10.87 \times 0.8 = 8.7\ kW$

Estimation of the total load to be removed from the refrigerated space (car cabin)

Table 8: Numerical refrigeration load calculations

Load	Amount
Metabolic load	170 W x 5 occupants
Engine load	1000 W
Exhaust load	1200 W
Direct radiation (front glass/windscreen)	800 W
Diffuse radiation (back glass)	800 W
Total	**4650 W**

The refrigeration load is 4.65 kW

Estimation of the heat to be supplied to the generator

From research, the condenser temperature for the absorption refrigeration system used for air conditioning of a compact car ranges from 10 – 50°C and the heat rejected by the condenser is approximately 2.5% more than the refrigerating load.

Table 9: Vapour absorption refrigeration system data

Condenser Temperature (T_{con})	20 ℃ (Technical Assumption)
Absorber Temperature (T_{abs})	20 ℃
Generator Temperature (T_{gen})	50 ℃
Refrigerating Load (Q_{eva})	4650 W (Evaluated)
Heat rejected from by Condenser (Q_{con})	4750 W (Technical Assumption)

From the Ammonia (NH_3) property table, $T_{con} = 20$ ℃ and The corresponding Pressure, $P_{con} = 8.570$ bar

Estimation of the corresponding Evaporator temperature (Eastop and McConkey, 1993)

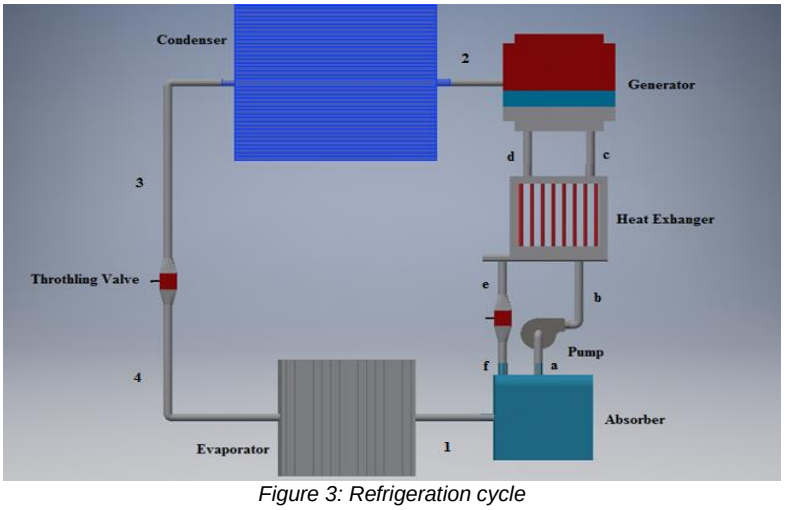

Figure 3: Refrigeration cycle

h_1, h_2, h_3, h_4 represents entry point enthalpy at different states Figure 3 clearly shows the sections 1 to 4 as shown in the subscripts associated with the calculations below.

$h_3 = h_4 = h_f \; at \; 20\,℃ \; = 275.1 \; kJ/kg$

$h_2 = \; h_g \; at \; 50\,℃ \; = 1474.7 \; kJ/kg$

$Q_{con} = m_{ref}(h_2 - h_3) = 4.75 \; kW$

$m_{ref} = \dfrac{4.75}{1474.7 - 275.1} = 3.9616 \times 10^{-3} kg/s$

$Q_{eva} = m_{ref}(h_1 - h_4) = 4.65 \; kW$

$h_1 = \dfrac{4.65}{3.961 \times 10^{-3}} + 275.1 \; = 1448.89 \; kJ/kg$

Interpolating the corresponding saturation temperature (evaporator temperature)

Table 10: Evaporator temperature interpolation

Temperature (°C)	Enthalpy (kJ/kg.K)
4	1448.5
t_{sat}	1448.89
6	1450.6

$\frac{t_{sat}-4}{6-4} = \frac{1448.89-1448.5}{1450.6-1448.5} t_{sat} = 4.4$ ℃. The evaporator temperature is approximately 4 °C

Estimation of the heat supplied to the generator (Eastop and McConkey, 1993)

The enthalpy-concentration chart for ammonia water solution was used to obtain the dryness fraction and the enthalpy of the fluid at different state points as illustrated in Figure 3.

At the evaporator pressure 4.975 bar and the absorber temperature 20 °C, $x_a = \; x_b = \; x_c = 0.69 \; and \; h_a = \; -128 \; kJ/kg$

At the condenser pressure of 10.34 bar and generator temperature of 50 °C

$x_f = \; x_e = \; x_d = 0.58 \; and \; h_d = \; -60 \; kJ/kg$

At the generator pressure of 8.570 bar and the concentration of 0.69, $h_c = -50 \; kJ/kg$

Mass balance to the absorber,$m_1 = \; m_2 = m_{ref} = \; 3.9616 \times 10^{-3} kg/s$, and $m_1 = m_a - m_f$

$0.0039616 = m_a - m_f$ ……equ1

From ammonia mass balance, $x_1 m_1 = x_a m_a - x_f m_f$

where $x_1 = 1 \;\; 0.0039616 = 0.69(0.0039616 + m_f) - 0.58 m_f$, therefore, $m_f = 0.0112 \; kg/s$

From equation 1, $m_a = 0.0039616 + 0.0112 \;\; = \; 0.0152 \; kg/s$

Energy balance to generator

$Q_{gen} = \; m_2 h_2 + m_d h_d - m_c h_c = 0.0039616 \times 1474.7 + 0.0112 \times (-60) - 0.0152 \times (-50) \;\; = 5.9 \; kW$

This based on analysis is much less than 8.7 Kw obtained from the exhaust of the car. The pressure ratio of the condenser and evaporator are acceptable. $COP = \frac{Q_{eva}}{Q_{gen}} \;\; = \frac{4.65}{5.9} \;\; = 0.79$

The coefficient of performance for this system is just around the range of 0.7 – 0.9 from literature. This suggests that the proposed heat recovery method as used by other automobiles is suitable to power the air conditioning system of a compact car.

2.5. Thermo-electric generation of electrical power

These are devices, which converts thermal energy into electrical energy. The electrical output ranges from few watts (W) to Kilowatts (kW) depending on the temperature difference between the cold and hot side. They may be used for heat recovery by using the exhaust heat from the internal combustion engine to power some of the power consuming electrical components within an automobile. Their efficiency depends on the temperature difference ranging from 5 – 8 %.There is no conclusive evidence as of today that shows these systems have been tested in industrial waste heat recovery applications, but a few have undergone prototype testing in automobile applications.

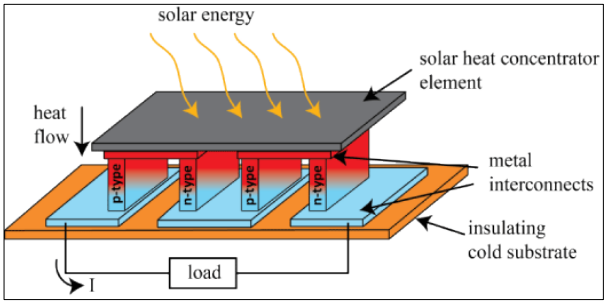

Figure 4: Thermo-electric generator (Quimtana, et al., 2013)

2.6. Comparative performance analysis of gas and steam combined power plants

Table 11: Combined gas and steam turbine operational data

Total output power (Overall plant)	12.5 MW
Temperature of gases leaving the steam generator	**160 ºC**
Gas Turbine	
Work output	61.2 kJ/kg
Heat supplied	273.5 kJ/kg
Mass flow rate of gas	105.72 kg/s
Steam Turbine	
Work output	516 kJ/kg
Heat supplied	1555 kJ/kg
Mass flow rate of steam	11.68 kg/s

Calculations of the plants efficiencies (Eastop and McConkey, 1993)

Gas turbine plant

$$\eta_{gas\ turbine} = \frac{energy\ output}{energy\ Input} = \frac{61.2}{273.5} = 22.38\ \%$$

Steam turbine plant

$$\eta_{steam\ turbine} = \frac{energy\ output}{energy\ Input} = \frac{516}{1555} = 33.18\ \%$$

Combined plants

$$P_{input\ (gas)} = E_{in\ (gas)} \times m_{gas} = 105.72 \times 273.5 = 28.92\ MW;\ \eta_{combined} = \frac{power\ output}{power\ Input} = \frac{12\ 500}{28\ 914.42} = 43.23\ \%$$

This method of heat recovery at industrial level is been used for years as you can see from the combined cycle efficiency that there is a need to use the two plants with the gas turbine supplying energy to generate steam. The overall efficiency improved by about 21% from the gas turbine and by 10% from the steam turbine.

3. COMMON HEAT RECOVERY METHODS

3.1. Shell and tube heat exchangers

Typically, when the fluid medium containing waste heat is in a liquid or vapour state, and which heats up another liquid, a heat re-utilization method often recommended is the Shell and tube heat exchangers. The shell contains the tube bundle and usually internal baffles to give direction to the working fluid in the shell over the tubes in single or multiple passes (Bureau of Energy Efficiency, 2008). Typical applications would be heating liquids with condensates from refrigeration and air conditioning systems and distillation processes, coolants from air compressors, bearings, engines and lubricants.

3.2. Heat pipes

Heat pipe is a thermal energy absorbing and transferring system. Thermal energy applied to the outer surface of the heat pipe is in thermal equilibrium with its own vapour as the container tube is sealed under vacuum. This energy applied to the outer surface forms evaporation of the working fluid. The vapour formed from evaporation absorbs the latent heat of vaporisation and this region of the pipe is now referred as an evaporator. The vapour then migrates to the other side of the

heat pipe where the heat is removed causing the vapour to condense into liquid state thereby giving off latent heat of the condensate. This region of the heat pipe is then referred as the condenser. Typical applications would be process space heating, HVAC applications for cooling and heating and process to process heating and other many industrial application as it is widely used. Heat pipes are capable of operating at temperatures as high as 315ºC with an estimated 60% to 80% recoverable heat which increases the overall efficiency of the system (BCS, 2008).

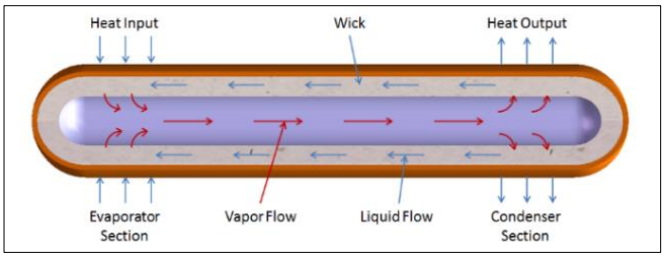

Figure 5: Heat pipe (Zheng et al., 2011)

3.3. Heat wheels

Typically used for low to medium temperature range applications, this type of waste heat recovery system is a sizable porous disk, fabricated with material having a fairly high heat capacity which slowly rotates between two compartments each having the air suction and discharge vent. One compartment consists of a hot gas while the other consists of a cold gas duct. As the disk rotates, sensible heat is transferred to the disk by the hot air at the same time on the other compartment; the air becomes dry and warm. In the case of cooling, an evaporative cooler may be installed at the discharge side to the conditioned space. The overall estimated efficiency for this kind of a regenerator for sensible heat transfer can be as high as 85% with applications such as heating and ventilation systems as well as heat recovery of the exhausts airflows from a dryer (Dean, 1980).

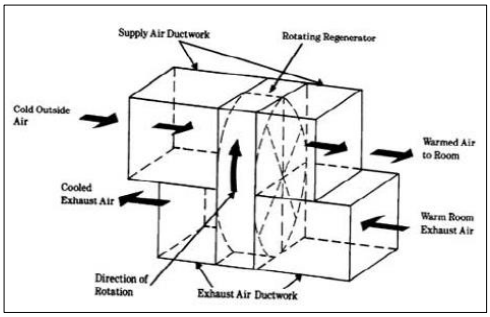

Figure 6: Heat rotary wheel (Dean, 1980; BSC, 2008)

3.4. Economisers

Economiser uses the same working principles as the waste heat boilers discussed below and in the case of boiler system economiser may be provided to utilise the flue gas heat for pre-heating feed water of the boiler and in the case of an air pre-heater system the flue gases are used to heat the combustion air. By using an economiser, there is 1% saving of the primary fuel for each temperature drop of the exhaust gases, this increases the thermal efficiency of the system (Bureau of Energy Efficiency, 2008).

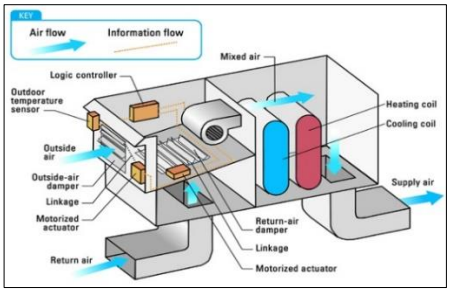

Figure 7: Airflow economiser (Zheng et al., 2011)

3.5. Waste heat boilers

These are water tube boilers, which use the medium to high temperature exhaust gases to generate steam as illustrated in Figure 8. The steam generally may be used for process heating or for turning the turbine for power generation. In the case where there is a requirement for the steam to be in a superheated state as it is in most cases, an external source of heat such as a super-heater may be added to the system. An estimated overall efficiency of the system is recorded as 80% of the recovered heat as used with other thermal systems.

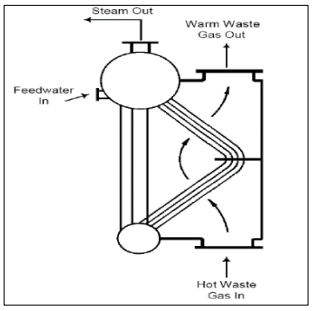

Figure 8: Waste heat boiler (Agriculture and Agri-Food Canada, 2001; Goldstick and Thumann, 1986)

4. CONCLUSION AND RECOMMENDATION

The performance evaluation of different heat recovery systems presented is based on computation analysis, by calculations and graphs with other heat recovery systems briefly discussed. From the analysis of results based on literature, the thermal and electrical efficiency of a PV/T collector was 23% and 15% respectively. For the same electrical load, the PV/T module succeeded the PV module operating at its Maximum Power Point (MPP) and the PV module with an efficiency of 13.6% for 14% of the PV at MPP. The coefficient of performance of the vapour absorption refrigeration system was found to be 0.79 using the exhaust waste heat from the internal combustion engine of a motor vehicle to power the air conditioning system. The overall efficiency of the combined plants increased by 21% from the gas turbine plant and by 10% from the steam power plant. It was concluded that the use of the heat recovery system for recapturing the wasted heat improves the thermal efficiency of different systems and lowers the energy consumption of the primary fuel used. For design purposes, it is recommended that further literature be carried out on the proposed heat recovery system of choice to improve the reliability of results at the validation phase of a developed prototype.

5. REFERENCES

Agriculture and Agri-Food Canada, 2001. Heat Recovery for Canadian Food and Beverage Industries. Departmental Electronic Publications, www.agr.gc.ca/cal/epub/5181e/5181-0007_e.html (Retrieved 10 March, 2018).

Ahn, J. K. (2015). A study on experimental performance of air-type PV/T collector with HRV, South Korea: Elsevier

BCS, I. 2008. https://www1.eere.energy.gov/manufacturing/intensiveprocesses/pdfs/waste_heat_recovery.pdf Retrieved May 6, 2018.

Bureau of energy efficiency. 2008. Waste heat recovery, book chapter 8, pp 173-189, http://www.em-ea.org/guide%20books/book-2/2.8%20waste%20heat%20recovery.pdf Retrieved May 6, 2018.

Dean, N., Energy Efficiency in Industry, Environmental Law Institute, 1st Edition, 1980.

Eastop, T., & McConkey, A., 1993. Applied Thermodynamics for Engineering Technologists. United Kingdom: Longman Group.

Goldstick, R., & Thumann, A., Principles of Waste-heat Recovery, Fairmont Press, 1st Edition, 1986.

Lynn, P., 2010. Electricity from Sunlight - An Introduction to Photovoltaics. United Kingdom : John Wiley & Sons Ltd .

Messenger, R. V., 2004. Photovoltaic Systems Engineering. New York: CRC Press LLC.

Quimtana, H., Wang, G. & Martinez, J., 2013. Heat Transport in Novel Nanostructured Materials and Thier Thermoelectric Applications, s.l.: Chem Eng Process Tech 1: 1008.

Zheng, Y., Mark, B., and Youmans, H., 2011. A Simple Method to Calculate Vehicle Heat Load," SAE Technical Paper 2011-01-0127, 2011

371: Preparation and application of $BiFeO_3$-plant fiber visible light catalytic material

Mengling WANG[1], Mengxuan HUANG, Shiju YUAN, Junjian AN*

[1] Hubei University of Technology, School of Material & Chemical Engineering, Wuhan 430068, 925148240@qq.com
* Hubei University of Technology, School of Material & Chemical Engineering, Wuhan 430068, anjunjian0000@163.com

In recent years, Advanced Oxidation processes (AOPs) possesses obvious advantages in removing organic pollutants from environmental media, causing widespread concern among researchers in related research fields around the world. In advanced oxidation technologies, the combination of several oxidation technologies can combine the advantages of these oxidation technologies to achieve higher catalytic efficiency. $BiFeO_3$ is a kind of bismuth-based catalytic material, with a bandgap energy value of 2.1 eV. It possesses high visible light catalytic activity, which greatly improves the utilization of light energy. Except that, it also possesses heterogenetic Fenton-like catalytic ability, which resulting in generating strong oxidative actives. This heterogeneous Fenton system not only can improve the catalytic performance of iron-containing catalysts, but also can recycle the catalysts, reduce the secondary pollution of iron mud in the reaction system, and greatly reduce the pressure of environmental pollution. In this paper, the $BiFeO_3$ composite catalyst was prepared through loading $BiFeO_3$ nanoparticles on plant fibres. The way of loading makes the composite catalyst better to be recycled and the catalytic effect of the composite was explored. The organic contaminant Congo red was selected as the substrate. The degraded kinetic process of Congo red was explored. And the effect of catalyst load, H_2O_2 dosage and pH value on the degradation of Congo red was explored. It was found that 96% of Conge red was degraded under the optimal reactive condition (the ratio of $BiFeO_3$ and fibre: 1:1, catalyst load: 0.8g L^{-1}, H_2O_2 concentration: 15mmol L^{-1}, and pH 6). This provides a certain theoretical and practical value for the degradation of organic pollutants. At the same time, it also provides a certain reference value for the recycling of resources and its sustainable development.

Keywords: Photocatalysis; Fenton; BiFeO3; plant fiber; degradation; catalyst

1. INTRODUCTION

Photocatalytic process is an important approach to transform light energy to chemical energy, which has been utilised widely in the domains of photocatalytic hydrogen production and the degradation of environmental pollutants. Especially, photocatalytic reaction was employed extensively to remove organic pollutants in environmental media, which possess the advantages of mild reactive condition, low treatment cost, high degradative efficiency and no secondary pollution (Gaya et al., 2008). In addition to photocatalytic process, Fenton oxidative process has also arouse the attention of researchers, which has the advantages of mild reaction conditions, easy operation, and high processing efficiency (Martínez et al., 2018; Li et al., 2016; Wang et al., 2016). However, it has a narrow pH range (PH<3), large consumption of Fe^{2+}, and low catalytic efficiency. To overcome this drawback, ultraviolet (UV), photo energy (Photo), ultrasonic (US) and other energy are introduced into the Fenton reaction to improve the treatment effect (Hassan et al., 2017; Ebrahiem et al., 2017). Especially, the combination of photo catalysis and Fenton oxidative process could improve the catalytic performance remarkably to degrade pollutants (García et al., 2017). In the combined system, light energy can significantly enhance the oxidizing ability of Fenton reagent; while the high-transition metal ions from Fenton reagent can trap photoelectrons, inhibit the recombination of photo-generated carriers, and increase the catalytic efficiency (Youping et al., 2017). Therefore, this combination technology possesses better application prospects.

As a kind of classical organic pollutant, organic dyes have aroused intensive interesting around the world. As a kind of azo dyes, Congo red is widely used in the textile industries, pharmacy and cosmetics processing (Santhosh et al., 2017). Due to their stable complex aromatic structures and potential risk of carcinogenicity and mutagenicity, it was difficult to be biodegraded (Li et al., 2009; Jana et al., 2017). Various physical and chemical techniques are used to remove the pollutant (for example, chemical oxidation (Tsitonaki et al., 2010), floatation and coagulation (Liu et al., 2010)). However, these methods could not degrade the organics completely or only transfer the contaminants from one media to another. In recent years, AOPs which activate H_2O_2 to generate strongly oxidizing species (such as •OH) are important processes for decomposing organic pollutants (Stasinakis et al., 2008; An et al., 2010). Among AOPs, Fenton oxidative (Martínez et al., 2017) and photocatalytic (Pirhashemi et al., 2017) processes are the most concerned. And the combination of photocatalytic and Fenton oxidative process may improve the catalytic ability to degrade Conge red.

$BiFeO_3$ nanoparticles are typical iron-containing catalysts which possess strong heterogeneous Fenton-like catalytic activity (Luo et al., 2010). Except that, $BiFeO_3$ possess weaker visible light catalytic properties (Liu et al., 2010). In order to improve its weak visible light catalytic performance, many efforts have been made by researchers (Guo et al., 2010). Recently, the non-toxic, porous, and soft renewable material of plant fibers has arouse the wide concern of the researchers (Kalia et al., 2013), which was utilised as a carrier to load functional nanoparticles materials. Especially, the loading of photocatalytic nanoparticles on fibers could not only enhance its photocatalytic performance but also improve the reuse rate of catalyst (Elroz et al., 2013). Therefore, $BiFeO_3$ nanoparticles which possess visible light catalytic and heterogeneous Fenton-like performance were selected as a basic catalyst. And plant fibers were utilised as carrier. The $BiFeO_3$ nanoparticles were loaded on plant fibers through Tappi papermaking process. Thus the three-dimensional composite catalysts which possess strong catalytic activity were prepared. Congo red was selected as an objective pollutant. Under the irradiation of visible light, the catalytic performance of the above composite was evaluated in the presence of H_2O_2.

2. EXPERIMENTAL

2.1. Chemicals and materials

Iron nitrate ($Fe(NO_3)_3 \cdot 9H_2O$), bismuth nitrate ($Bi(NO_3)_3 \cdot 5H_2O$) , Ethylene glycol methyl ether, nitric acid, citric acid, ethylene glycol and hydrogen peroxide were provided by Sinopharm Chemical Reagent Co, Ltd. (Shanghai, China). Wet strength agent Polyamide Epichlorohydrin (PAE) and Softwood pulp were obtained from Tianjin Chemical Co, Ltd (Tianjin, China). All chemicals were analytical grade reagents and used without further purification.

2.2. Preparation of $BiFeO_3$ nanoparticles

$BiFeO_3$ nanoparticles were prepared with a sol-gel process as reported previously (Luo et al., 2010). Firstly, Iron nitrate (0.008 mol) and bismuth nitrate (0.008 mol) were dissolved in 2-methoxyethanol (20 mL), followed by adding 20 μL HNO3 (0.1 mol L^{-1}). Then citric acid (0.008 mol) and ethylene glycol (10 mL) were added to the solution, the mixture was stirred for 1 h at 60 ºC to form a sol. The sol was heated at 100 °C for 2 h to form a brown gel. It was then placed on an electric furnace for 30 minutes and calcined in a muffle furnace at 500°C for 2 hours. After cooling to room temperature, the resulting product is ground for use.

2.3. Preparation of $BiFeO_3$-plant fiber composite

$BiFeO_3$-plant fiber composite was prepared with a Tappi papermaking process. Firstly, a certain amount of $BiFeO_3$ nanoparticles are dispersed in water, followed by ultrasonic treatment for about 5 minutes. And then the above dispersion was added to the plant fiber pulp. After that, the wet strength agent Polyamide Epichlorohydrin (2 mL) is added to the pulp and mixed uniformly. At last, the composite was prepared by Tappi papermaking process.

2.4. Degradation experiment

The degradation experiment was carried out in a cylindrical Pyrex vessel at 25 ºC. Typically, a given amount of $BiFeO_3$-plant fiber composite was added in a solution of organic pollutant (100 mL; 25mg L^{-1} Conge red,), followed by adjusting the pH to 6 with 0.1 mol L^{-1} HCl or NaOH. The dispersion was magnetically stirred for 60 min to achieve adsorption-desorption equilibrium between the catalyst and pollutant. A small volume (2.5 mL) of the dispersion was sampled. The pollutant concentration was measured and taken as its initial concentration. After H_2O_2 was added to the solution, the photocatalytic degradation was initiated by switching on a 500 W halogen lamp with a cutoff filter (λ > 420 nm). At given time intervals, aliquots of the solution (1.5 mL) were sampled to centrifuge tubes containing a certain quantity of absolute ethyl alcohol (to quench •OH radicals). And the remaining pollutant concentration was determined immediately.

3. RESULTS AND DISSCUSSION

3.1. Characterisation of $BiFeO_3$ nanoparticles and $BiFeO_3$-plant fiber composite

The SEM image of $BiFeO_3$ and $BiFeO_3$-plant fiber composite are shown as Figure 1a and b. It was found that $BiFeO_3$ exhibited a structure composed of nanoparticles with grain sizes of 100-150 nm. As showed in Figure 1b, the $BiFeO_3$ nanoparticles are tightly loaded on plant fibers to form a three-dimensional structure. This structure is conducive to the capture of pollutant molecules, which improved the catalytic efficiency of the composite. Except that, the special structure was benefit to the recycling of the composite.

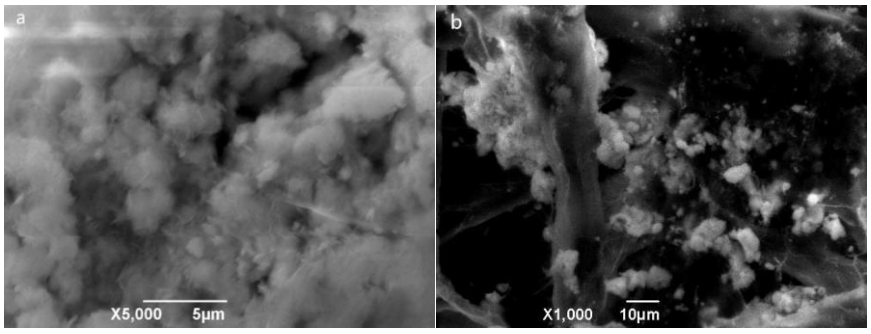

Figure 1: SEM image of BiFe03 nanoparticles (a), and $BiFeO_3$-based photocatalytic paper (b)

FT-IR spectra of $BiFeO_3$ and $BiFeO_3$-plant fiber composite have been investigated which was showed in Figure 2a and b, respectively. In the FT-IR spectrum of $BiFeO_3$ the broad band around 3129.97 cm^{-1} arises from the antisymmetric and symmetric stretching of bond H_2O and OH- groups. Two strong absorptive peaks around 557.33 cm^{-1} and 447.40 cm^{-1} are attributed to the Fe-O stretching and O-Fe-O bending vibrations (Ramezanalizadeh et al., 2016) acording to metal-Oxygen band, formation of perovskite structure can be confirmed. And the absorption peak near 3415.31 cm^{-1} (Figure 2b) is the stretching vibration absorption of OH group, which belong to the characteristic band of all cellulose. There is a strong absorption peak at 2902.34 cm^{-1} which attributed to the absorption peak of the stretching vibration of CH_2. The absorption peak at 896.74 cm^{-1} is a vibrational of C_1, which is a characteristic peak of cellulose. The absorption peak at 1639.2 cm^{-1} is the carbonyl group conjugated to aromatic nucleus. The absorption peak (1428.99 cm^{-1}) is corresponded to the absorption band of the aromatic ring. And the absorption peak of the absorption peak at 1373.07 cm^{-1} is attributed to the bending vibration of C-H bond. The peaks which located to the wavenumber region (lower than 1300 cm^{-1}) belong to the lignin fingerprint region (Shi et al., 2012). It was also found that the corresponding peaks of $BiFeO_3$ are also appeared in the corresponding position of the composite, indicating that $BiFeO_3$ has been well loaded on the plant fibers.

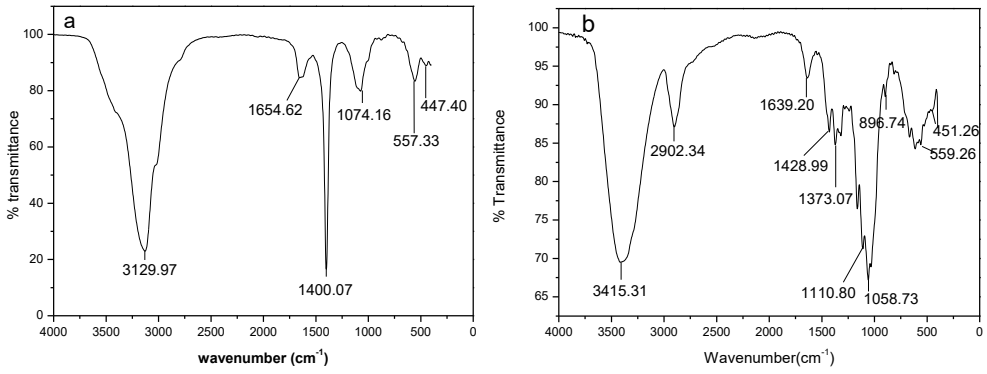

Figure 2: FTIR spectra of $BiFeO_3$ (a) and $BiFeO_3$-plant fiber composite (b)

3.2. Photo-fenton catalytic degradation of Congo red by $BiFeO_3$-plant fiber composite

The degradation of Congo red in different degradation systems (c/c_0 represents the ratio of Congo red concentration to initial concentration at a certain time) is showed as Figure 3a. It was found that the degradation of Congo red in $BiFeO_3$-Vis system is low (about 39.82% of Congo red was degraded in 60 mins). And the introduction of H_2O_2 to the above reactive system has increased the degradation efficiency of Congo red remarkably (about 92.85% of Congo red was degraded after 60 mins). The $BiFeO_3$-plant fiber composite exhibited much higher catalytic activity than $BiFeO_3$ either in catalyst-vis system or in catalyst-vis-H_2O_2 system. The degradation of Congo red approximately followed the pseudo first order kinetics ($\ln(c_0/c) = kt$). Figure 3b shows the apparent rate constants (k, min^{-1}) of Congo red degradation in different reactive systems. As can be seen in Figure 3b, the Congo red degradation constant in different system was in the following order: $BiFeO_3$-Vis (*0.00858 min^{-1}*) < $BiFeO_3$-plant fiber composite-Vis (0.01109 *min^{-1}*) <$BiFeO_3$-Vis-H_2O_2 (0.04254 *min^{-1}*) < $BiFeO_3$-plant fiber composite-Vis-H_2O_2 (0.10171 *min^{-1}*). It was further confirmed that the loading of $BiFeO_3$ nanoparticles on plant fibers could improve the catalytic performance of $BiFeO_3$.

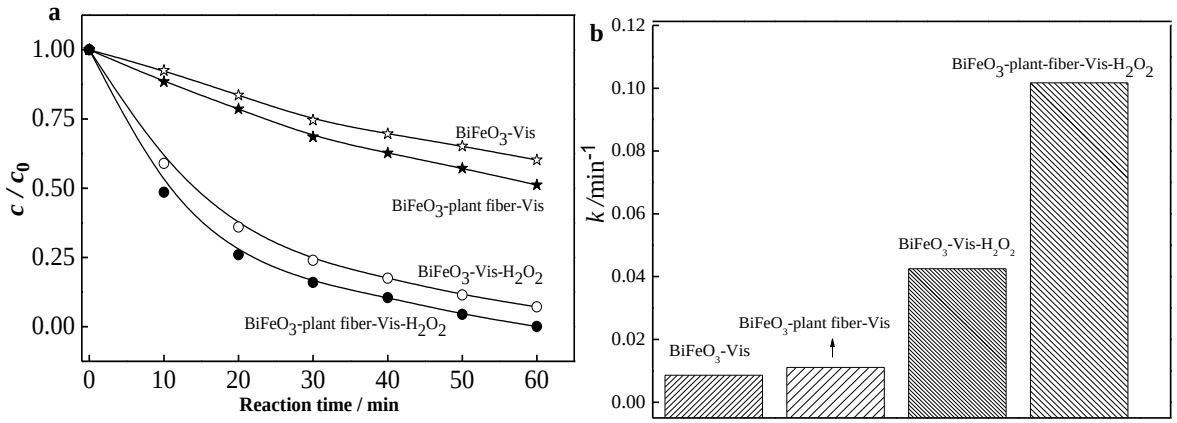

Figure 3: (a) Degradation of Congo red and (b) its rate constants in different systems of (1) $BiFeO_3$-Vis, (2) $BiFeO_3$-plant fiber-Vis, (3) BiFeO3-vis-H_2O_2, (4) $BiFeO_3$-plant fiber-Vis-H_2O_2. Reaction conditions: Congo red concentration 25mg L^{-1}, catalyst load 0.8 g L^{-1}, solution pH 5, initial H_2O_2 concentration 15 mmol L^{-1} and temperature 25 ºC.

The effect of catalyst load on the degradation of Congo red was investigated. The degradation of Congo red and its corresponding degradation rate constant with different catalyst load was showed as Figure 4a and b, respectively. It was observed that as the amount of catalyst increasing, the degradation rate constant firstly increased, passed a maximum (catalyst load: 0.8 g L^{-1}), and then decreased with the increasing of catalyst load. The initially increased catalyst load led to increased number of the reactive sites on catalyst surface, resulting in enhanced generation of hydroxyl radicals and faster degradation of Congo red. However, superabundant catalyst may produce overmuch •OH radicals, increasing the reaction between •OH radicals themselves and then leading to lower efficiency of •OH radicals for the degradation of organic pollutants. In the case of the photocatalytic catalysis, the over high catalyst load increases light filtering effect, being unfavorable to catalytic generation of •OH radicals. Therefore, the optimal load of the composite was 0.8 g L^{-1}.

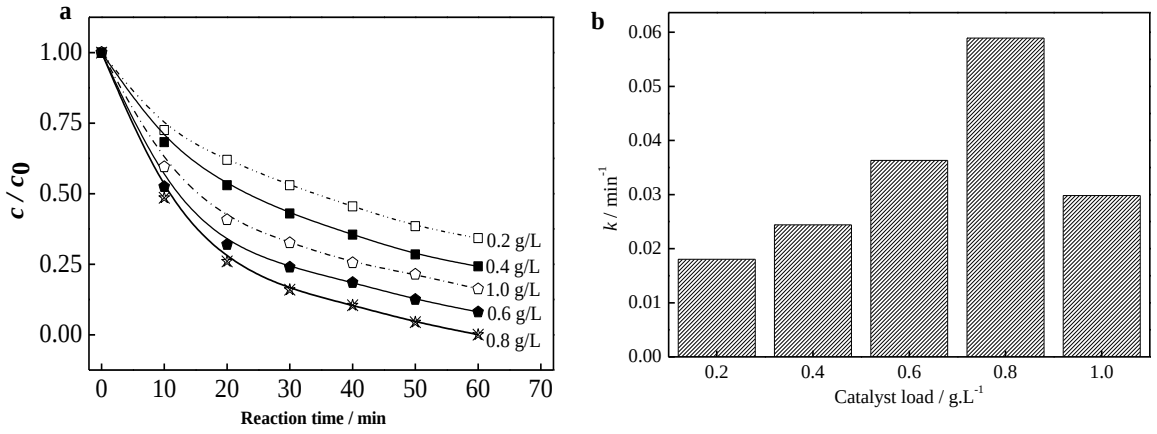

Figure 4: (a) Degradation of Congo red and (b) its rate constants with the catalyst load of 0.2、0.4、0.6、0.8、1.0 g L^{-1}. Reaction conditions: Congo red concentration 25 mg L^{-1}, the $BiFeO_3$ content in $BiFeO_3$-plant fiber composite is 50%, solution pH 5, initial H2O2 concentration15 mmol L^{-1} and temperature 25 ^{0}C.

The effect of initial H_2O_2 concentration on the degradation of Congo red was showed in Figure 5a. And its corresponding degradation rate constant with different initial H_2O_2 concentration was showed in Figure 5b. Similarly, with the increasing of H_2O_2 concentration, the generation of hydroxyl radicals was increased constantly, resulting in the increase of *k* value. However, as the decomposition of H_2O_2 at concentrations beyond 15 mmol L^{-1}, much excessive hydroxyl radicals will be generated, which may interact with themselves to quench hydroxyl radicals. In addition, the high concentration of H_2O_2 can also scavenge hydroxyl radicals. All these may result in the decrease of *k* value. Therefore, the *k* value reached to a maximum at the H_2O_2 concentration of 15 mmol L^{-1}.

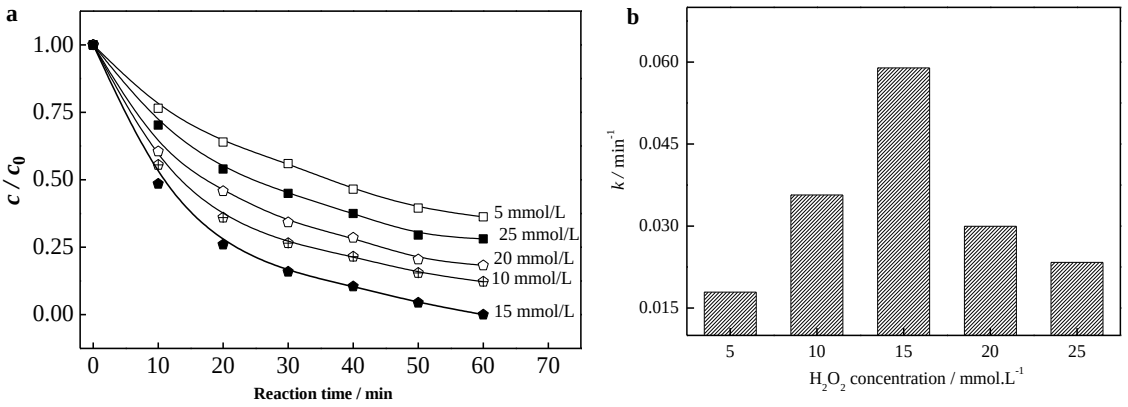

Figure 5: (a) Degradation of Congo red and (b) its rate constants with the H_2O_2 concentration of 5, 10, 15, 20, 25 mmol.L^{-1}. Reaction conditions: Congo red concentration 25 mg L^{-1}, the $BiFeO_3$ content in $BiFeO_3$-plant fiber composite is 50%, catalyst load: 0.8 g L^{-1}, solution pH 5, and temperature 25 ºC.

The effect of pH on Congo red degradation efficiency and its corresponding degradation rate constant is shown in Figure 6a and b, respectively. With the increasing of pH value (from 4 to 6), the *k* value of Conge red was increased from 0.035 to 0.06 min^{-1}. This may be the adsorption of pollutant on the Composite increases with the increasing of the pH value, which induced the improvement of the contact chance between the pollutant and oxidizing species. With the further increasing of pH (>6), the degradation efficiency of Congo red was reduced. That might be the alkaline condition was not favorable to the activation of H_2O_2. Therefore, the optimal pH value for Conge red degradation was 6.

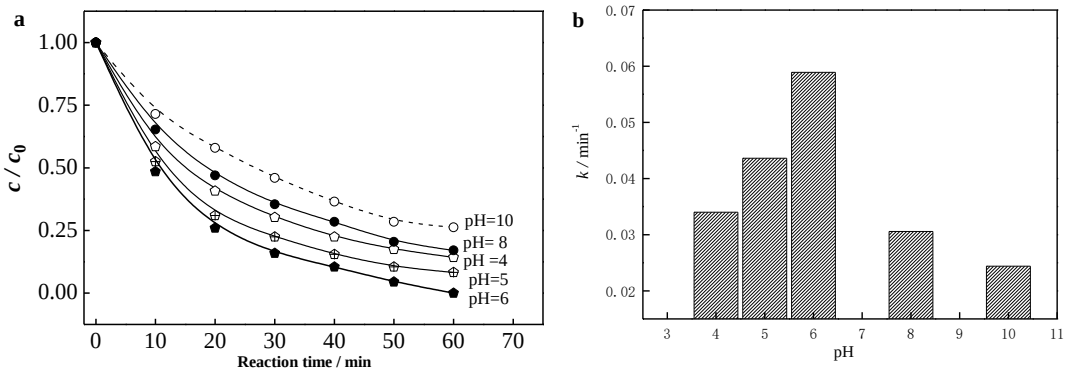

Figure 6: (a) Degradation of Congo red and (b) its rate constants with pH value of 4, 5, 6, 8, 10. Reaction conditions: Congo red concentration 25mg L^{-1}, the $BiFeO_3$ content in $BiFeO_3$-plant fiber composite is 50%, catalyst load: 0.8 g .L^{-1}, solution pH 6, initial H_2O_2 concentration 15 mmol L^{-1} and temperature 25 ºC.

The active species which induce the degradation of Conge red was also investigated. We proposed the major active species was •OH radicals, which was also confirmed preliminarily by the following study. The isopropyl alcohol (IPA) which was the quencher of •OH radicals was introduced to the $BiFeO_3$-plant fiber composite-vis-H_2O_2 reactive system. And it was found that the degradation of NP was restrained significantly compared with that without IPA (Figure 7a). The reactive rate constant in composite-vis-H_2O_2 reactive system was 0.05772 min^{-1}, while the rate constant was sharply reduced to 0.00634 min^{-1} with the introduction of isopropyl alcohol. And the generation of •OH radicals in the systems of composite-H_2O_2-vis and $BiFeO_3$-H_2O_2-Vis was further investigated by using the coumarin probe method. As shown in Figure 7b, $BiFeO_3$ can produce hydroxyl radicals under visible light irradiation. This activating ability was greatly strengthened by the catalytic effect of $BiFeO_3$-plant fiber composite, leading to the generation of much more hydroxyl radicals.

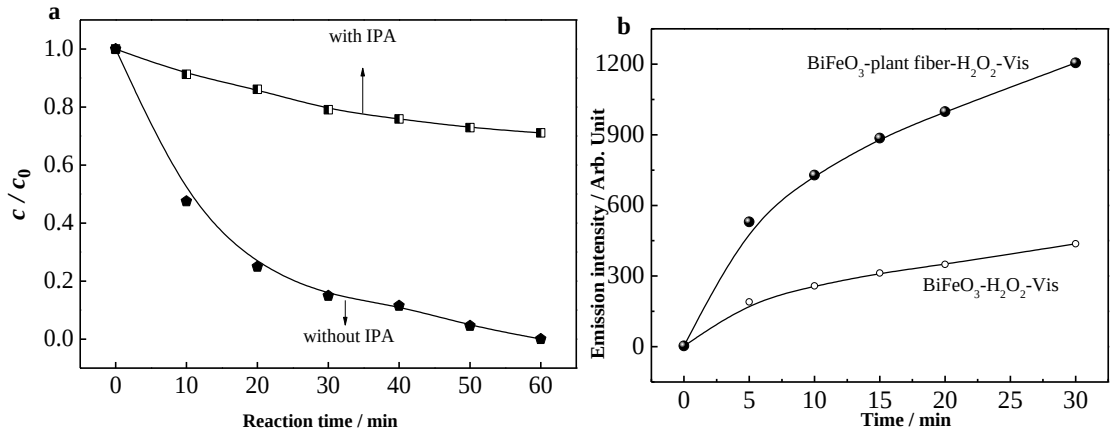

Figure 7: (a)Degradation kinetics of Conge red catalyzed by $BiFeO_3$-plant fiber composite with (1) or without (2) the introduction of isopropyl alcohol; (b)Reaction time dependences of the fluorescence intensity generated from the oxidation of coumarin by •OH radicals in the systems of (1) $BiFeO_3$-H_2O_2-vis and (2) $BiFeO_3$-plant fiber composite-H_2O_2-vis. Reaction conditions: Congo red concentration 25 mg L^{-1}, the $BiFeO_3$ content in BiFeO3-plant fiber composite is 50%, catalyst load: 0.8 g L^{-1}, solution pH 6, initial H_2O_2 concentration 15 mmol L^{-1} and temperature 25 ºC.

The stability and recyclability of $BiFeO_3$-plant fiber composite was evaluated by successive batches of Conge red degradation. It was found that the composite were able to be reutilised for at least five cycles and the reused catalyst almost retained the catalytic activity as efficient as the fresh one (Figure 8a). The rate constant for the Conge red degradation was estimated as 0.05882, 0.0587, 0.05804, 0.05794 and 0.05764 min^{-1} for the initial five cycles. Moreover, no leaching of Bi ions from the composite was detected during the Conge red degradation at pH 6.0 by AAS, and the leaching of Fe ions was less than 1% of the iron element from the composite (Figure 8b). Therefore, the composite was stable and could be reused without loss of catalytic activity.

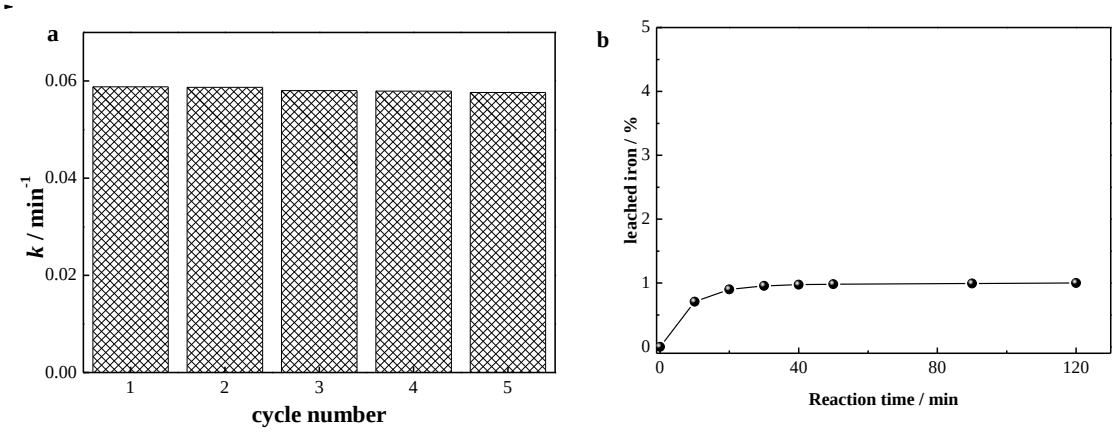

Figure 8: (a) Degradation of Conge red with the recycled $BiFeO_3$-plant fiber composite and (b) percentage of total dissolved iron during the degradation in the $BiFeO_3$-plant fiber-H_2O_2-Vis systems. Reaction conditions: Congo red concentration 25 mg L^{-1}, the $BiFeO_3$ content in $BiFeO_3$-plant fiber composite is 50%, catalyst load: 0.8 g L^{-1}, solution pH 6, initial H_2O_2 concentration 15 mmol L^{-1} and temperature 25 ºC.

The mechanism of generation of •OH in this reaction system was also analysed. The degradation of contaminants in this reaction system was mainly caused by •OH, which was mainly generated from photocatalytic and Fenton-like processes. In the photocatalytic process, electrons (e^-) were excited from the valence band (VB) to the conduction band (CB) under the irradiation of visible light. And photogenerated holes (h^+) were formed in the valence band. Photogenerated electrons undergo oxidation-reduction reactions with H_2O_2 and oxygen dissolved in water, which produced strong oxidizing hydroxyl radicals and other active species, causing the degradation of organic matter. In the Fenton-like reaction, Fe^{2+} and H_2O_2 can also produce strong oxidative species (such as •OH), which induced the degradation of organic matter.

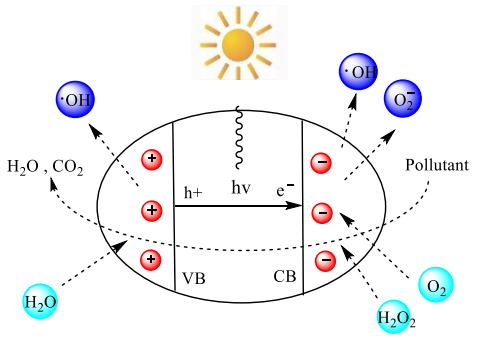

Figure 9: A proposed mechanism of visible light Fenton like process of $BiFeO_3$-plant fiber composite.

4. CONCLUSION

$BiFeO_3$ nanoparticles are able to activate H_2O_2 for the decomposition of organic pollutants under the irradiation of visible light, but their catalytic ability is rather weak towards the degradation of more resistant organic pollutants. To improving the photo-Fenton-like catalytic properties of $BiFeO_3$, we developed a TAPPI papermaking method to prepare the $BiFeO_3$-plant fiber-vis-H_2O_2 composite. It was found that the degradation rate of Conge red in the composite-vis-H_2O_2 system is about 10 times to that of $BiFeO_3$-vis system. In addition, the effect of reactive conditions (Catalyst dosage, pH value, H_2O_2 concentration) on the degradation of Conge red has also been studied. It was observed that 96% of Conge red could be degraded at the optimal reactive condition (catalyst dosage: 0.8 g L^{-1}, pH value: 6, and initial H_2O_2 concentration: 15 mmol L^{-1}). The strong enhancing effect may bring about promising applications of $BiFeO_3$-plant fiber catalytic materials as a visible light photo-Fenton like catalyst for removing organic pollutants from wastewaters.

5. REFERENCES

An, T., Yang, H., Li, G., Song, W., Cooper, W. J., & Nie, X. (2010). Kinetics and mechanism of advanced oxidation processes (AOPs) in degradation of ciprofloxacin in water. *Applied Catalysis B: Environmental*, *94*(3-4), 288-294.

Ebrahiem, E. E., Al-Maghrabi, M. N., & Mobarki, A. R. (2017). Removal of organic pollutants from industrial wastewater by applying photo-Fenton oxidation technology. *Arabian Journal of Chemistry*, *10*, S1674-S1679.

Elroz, M., Haidar, Z., Lakiss, L., Toufaily, J., & Thibaultstarzyk, F. (2013). Immobilization of TiO_2 nanoparticles on natural luffa cylindrica fibers for photocatalytic applications. *Rsc Advances, 3*(10), 3438-3445.

Gaya, I., & Abdul, H. (2008). Heterogeneous photocatalytic degradation of organic contaminants over tio2. *Journal of Photochemistry & Photobiology C Photochemistry Reviews, 9*, 1-12.

García, J. C., Pedroza, A. M., & Daza, C. E. (2017). Magnetic fenton and photo-fenton-like catalysts supported on carbon nanotubes for wastewater treatment. *Water Air & Soil Pollution, 228*(7), 246.

Liu, S., Wang, Q., Zhai, X., Huang, Q., & Huang, P. (2010). Improved Pretreatment (Coagulation-Floatation and Ozonation) of Younger Landfill Leachate by Microbubbles. *Water Environment Research*, *82*(7), 657-665.

Li, J., Zhao, L., Qin, L., Tian, X., Wang, A., & Zhou, Y., et al. (2016). Removal of refractory organics in nanofiltration concentrates of municipal solid waste leachate treatment plants by combined fenton oxidative-coagulation with photo--fenton processes. *Chemosphere, 146*, 442-449.

Luo W, Zhu L H, Wang N, Tang H Q, Cao M J, She Y B, 2010 . Efficient removal of organic pollutants with magnetic nanoscaled $BiFeO_3$ as a reusable heterogeneous Fenton-like catalyst. Environmentul Science and Technology, 44(5): 1786-1791.

Liu Z K, Qi Y J, Lu C J, 2010. High efficient ultraviole photocatalytic activity of $BiFeO_3$ nanoparticles synthesized by a chemical coprecipitation process. Jouruul of Muteriuls Science-Muteriuls in Electronics, 21(4): 380-384.

Martínez, F., Leo, P., Orcajo, G., Díaz-García, M., Sanchez-Sanchez, M., & Calleja, G. (2017). Sustainable Fe-BTC catalyst for efficient removal of mehylene blue by advanced fenton oxidation. *Catalysis Today*.

Martínez, F., Molina, R., Rodríguez, I., Pariente, M. I., Segura, Y., & Melero, J. A. (2018). Techno-economical assessment of coupling Fenton/biological processes for the treatment of a pharmaceutical wastewater. *Journal of Environmental Chemical Engineering*, *6*(1), 485-494.

Pirhashemi, M., & Habibi-Yangjeh, A. (2017). Ultrasonic-assisted preparation of plasmonic ZnO/Ag/Ag2WO4 nanocomposites with high visible-light photocatalytic performance for degradation of organic pollutants. *Journal of colloid and interface science*, *491*, 216-229.

Ramezanalizadeh, H., & Manteghi, F. (2016). Photocatalytic degradation of MB as an organic dye over a novel MOF/$BiFeO_3$ composite. *The, International Electronic Conference on Synthetic Organic Chemistry*(pp.a052).

Santhosh, A. M., Yogendra, K., Mahadevan, K. M., & Madhusudhana, N. (2017). Photodegradation of Congo Red azo dye, a Carcinogenic Textile dye by using synthesized Nickel Calciate Nanoparticles. *International Journal of Advance Research in Science and Engineering*, *6*(7), 51-64.

Stasinakis, A. S. (2008). Use of selected advanced oxidation processes (AOPs) for wastewater treatment—a mini review. *Global NEST journal*, *10*(3), 376-385.

Shi, J., Xing, D., & Jian, L. (2012). Ftir studies of the changes in wood chemistry from wood forming tissue under inclined treatment. *Energy Procedia, 16*(Part B), 758-762.

Tsitonaki, A., Petri, B., Crimi, M., Mosbæk, H., Siegrist, R. L., & Bjerg, P. L. (2010). In situ chemical oxidation of contaminated soil and groundwater using persulfate: a review. *Critical Reviews in Environmental Science and Technology*, *40*(1), 55-91.

Wang, N., Zheng, T., Zhang, G., & Wang, P. (2016). A review on fenton-like processes for organic wastewater treatment. *Journal of Environmental Chemical Engineering, 4*(1), 762-787.

Youping, Y. U., Gao, P., Liu, B., & Jinxin, H. E. (2017). Preparation and degradation properties toward tetracycline hydrochloride of a new photo-fenton-like catalyst nano $FeVO_4$. *Chinese Journal of Environmental Engineering*.

372: Investigation of novel integration of natural ventilation windcatcher and rotary passive heat recovery system

John CALAUTIT[1], Dominic O'CONNOR[2], Ben HUGHES[3], Lewis CAMERON[4]

[1] Department of Architecture and Built Environment, University of Nottingham, Nottingham NG72RD, john.calautit1@nottingham.ac.uk
[2] Free Running Buildings Ltd., Leeds Innovation Centre, 103 Clarendon Road, Leeds, LS2 9DF, dom.oconnor@freerunningbuildings.com
[3] Department of Mechanical Engineering, University of Sheffield, Sheffield S10 2TN, ben.hughes@sheffiled.ac.uk
[4] Department of Architecture and Built Environment, University of Nottingham, Nottingham NG72RD, Lewis.Cameron@nottingham.ac.uk

In this work, a novel design incorporating a passive heat recovery device into a windcatcher was proposed and investigated using numerical and experimental analysis. The proposed system incorporates a rotary thermal heat recovery in the windcatcher channel. Computational Fluid Dynamics (CFD) was used to investigate the effect of the heat recovery device on the performance of the windcatcher, highlighting the capabilities of the system to deliver the required fresh air rates. The windcatcher model was incorporated to a 5m x 5m x 3m test room model representing a small classroom. The study employed the CFD code Fluent18 with the k-epsilon model to conduct the simulations. The numerical model provided detailed analysis of the airflow and temperature distribution inside the test room. A 1:10 scale prototype of the system was created and tested experimentally in a closed-loop subsonic wind tunnel to validate the CFD investigations. Despite the blockage of the rotary heat recovery wheel, ventilation rates were able to provide adequate ventilation. In addition to sufficient ventilation, the heat in the exhaust airstreams was captured and transferred to the incoming airstream, raising the temperature up to 2K, this passive recovery has the potential to reduce demand on space heating systems. This shows that the concept has significant potential to be developed further, whereby the heat transfer properties of the system can be investigated and tested on a larger scale.

Keywords: buildings; CFD; heat recovery; natural ventilation; passive system

1. INTRODUCTION AND LITERATURE REVIEW

The government policy to reduce UK carbon emissions by at least 80% of the pre-1990 levels by 2050 is a major driving force in reducing the energy demand of the built environment (DECC, 2008). A large percentage of the energy use is due to space heating, which accounts for up to 40% of the total energy demand in both residential and service sector properties in the UK and other developed countries (WBCSD, 2008). Hence, reducing the energy required to heat domestic and commercial buildings presents one part of a solution to reach the goal of cutting carbon emissions. Recently, natural ventilation techniques such as windcatchers were increasingly being employed in buildings for increasing the supply of fresh air and reducing the mechanical ventilation consumption (Calautit et al., 2017, O'Connor et al., 2016). Windcatchers were utilised in buildings in the Middle East for many centuries and their commercialisation had increased over the years (Hughes et al., 2012; Nejat et al., 2016a). A windcatcher is divided into quadrants, which allow fresh air to enter as well as stale (used) air to escape irrespective of the prevailing wind direction (Figure 1a). The windcatchers provides fresh air driven by the positive air pressure on the wind-ward side, while exhausting stale air with the assistance of the suction pressure on the leeward side. Windcatchers also operate by a secondary action of the stack effect; the density of air decreases as the temperature increases, causing warmer air to rise and exit the windcatchers. In mild-cold climates such as in the UK, their use is generally limited to the summer, as shown in Figure 1. This is due to the potential for low incoming air temperatures to cause thermal discomfort to the occupants and the use of natural ventilation solutions will increase heat loss and lead to increased energy costs (Calautit and Hughes, 2014). While by restricting the use of natural ventilation during winter months, the concentration of pollutants have been seen to rise above the accepted guideline levels, which can lead to poor mental performance and ill health (Calautit et al., 2014a; O'Connor et al., 2014).

Recently, windcatchers have undergone a considerable amount of research to better understand the effect of airflow through and over windcatchers as well as the ventilation rates that can be provided by these systems (Calautit et al., 2014a). Further to this, attempts have been made to improve the thermal comfort that can be provided to occupants (Hosseini et al., 2016). The work has been conducted through the use of CFD modelling as well as scaled wind tunnel testing and in some cases, in situ or field testing in order to understand the effects in a real-world environment (Nejat et al., 2016b).

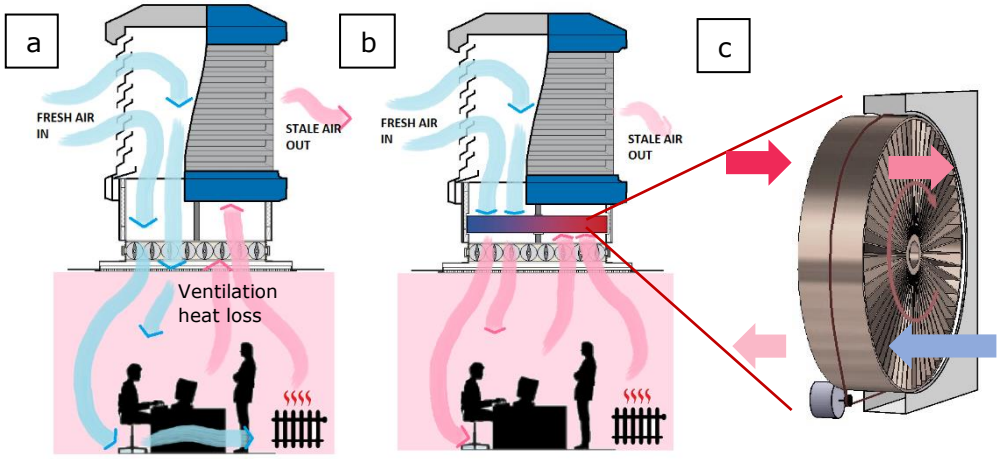

Figure 1: (a) standard windcatcher (b) passive heat recovery windcatcher (c) proposed passive heat recovery wheel

Though windcatcher cooling (Chaudhry et al., 2015; Calautit et al., 2013; Calautit et al., 2015) has had more attention in the past, little work has been carried out in the area of heat recovery or heating incoming air in windcatchers. Shao et al. (1998) noted that passive stack systems are designed without heat recovery which leads to large amounts of wasted heat. Woods et al. (2009) looked at the use of wind catchers during the winter using air mixing techniques to dilute the incoming cool air with the internal air. This system increased the incoming air temperature, thereby negating the heat demand whilst maintaining adequate pollutant levels but required very strict building design and control systems. Though this area of research is expanding with more teams exploring the potential of heat recovery in passive ventilation systems, little work has been performed on the use of the rotary thermal wheels specifically in natural ventilation. This is due to the high pressure drop across the rotary wheel which can impede the flow of air through the natural ventilation system. Rotary thermal wheels provide heat recovery at a high efficiency, even when compared to other heat recovery technology. The potential for energy savings using a rotary thermal wheel coupled with a passive ventilation system such as a wind tower are high. The lack of current research exploring a system similar to this demonstrates a key gap in existing knowledge.

To improve the year-round capabilities of windcatcher systems to enable consistent use during cooler months, a retrofit heat recovery system is desirable. This study introduces and discusses the potential of this concept using CFD analysis and wind tunnel experimental for validation. The concept is to attach a redesigned rotary heat recovery wheel system at the bottom channel of a windcatcher, as shown in Figure 1b. Using the properties of the thermal wheel as a heat exchanger,

the thermal energy in the internal exhaust air is recovered to the incoming air. This concept raises the incoming air temperature. By raising the temperature of the incoming air from the windcatcher, adequate year-round ventilation is maintained and during the heating season, energy demand for heating systems is reduced.

2. METHODOLOGY

2.1. Numerical modelling

ANSYS Fluent 18 software was used to conduct the steady-state Reynolds averaged Navier–Stokes equation) which employed a control-volume-based technique for solving the flow equations. The standard k-e turbulence model was used, which is a well-established method in research on windcatcher natural ventilation (Calautit et al., 2017). Second-order upwind scheme was used to discretise all the transport equations. The numerical code used the semi-Implicit method for pressure-linked equations algorithm for the velocity-pressure coupling of the computation. The governing equations are not repeated here but available in the ANSYS User guide. The flow domain representation of the geometry of the windcatcher and location of set boundary conditions are shown in Figure 2a. A 5 x 5 x 10 m3 enclosure was created to simulate the velocity of the outdoor wind. Furthermore, the model of the 1 x 1 m2 windcatcher was integrated to a test room located beneath it. The test room with an internal volume of 3 x 3 x 5 m3 represents a small classroom (Calautit et al. 2014a). The windcatcher was modelled with seven louvres angled at 45°. The wind tower was assumed to be supplying at 100% (fully open), therefore the volume control dampers was not added to the model. The rotary heat recovery wheel was connected below the windcatcher as a separate part. Unlike previous works, the rotary heat recovery wheel was modelled explicitly with radial plates instead of using porous zone method. A non-uniform mesh was applied to the volumes of the computational model. The computational mesh of the windcatcher and test room model is shown in Figure 2b. The mesh was refined around critical areas of interests in the simulation. Several meshes were generated to investigate the solution independency from the mesh. The mesh was refined (mesh sizes ranging from 2.8 to 7.4 million elements) until the posterior estimate error became insignificant between the number of elements and the posterior error indicator (supply velocity). The discretisation error was found to be the lowest at over 7.4 million elements.

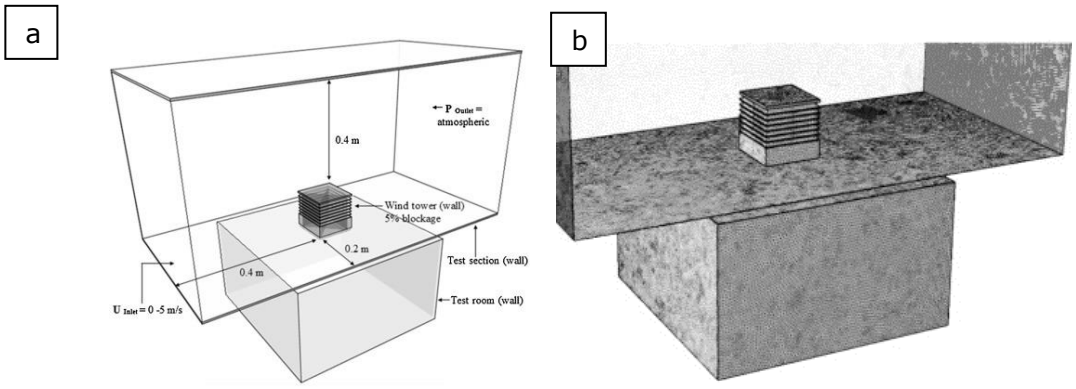

Figure 2: (a) Computational domain (b) mesh design

The rotation of the rotary heat recovery wheel was modelled using frame motion in ANSYS Fluent. The mesh motion of the rotary heat recovery wheel was orientated at the centre point and vertical axis of the wheel; this ensured that the volume rotated around the centre point at the required speeds of 15rpm (1.57 rad/s). The material of the heat recovery wheel was set to copper. The CFD analysis was performed at various outdoor wind speeds (0 - 5 m/s). The pressure outlet was set to 0 Pa (atmospheric). For the analysis of the windcatcher, the external air temperature was set to 283 K to simulate a cold outdoor environment. This was chosen as it represented the average annual air temperature in the UK according to the UK Met Office. The floor was set as a heat source with a heat flux of 75 W/m2 to simulate the internal heat gains (occupants and equipment) in a teaching space.

2.2. Experimental setup

The experimental investigation was conducted in a closed-loop wind tunnel (Calautit et al., 2014b). The size of the test section was 0.5 x 0.5 m2 and 1m length (Figure 3). A 1:10 scale model of the windcatcher with heat recovery wheel was used in the experimental study. The creation of an accurate scaled model was essential for the study; therefore, the windcatcher was constructed using 3D printing. The scale of the model of the windcatcher was selected to maintain, as close as possible, equality of model and prototype ratios of overall dimensions to the important meteorological lengths of the simulated wind. The rotary heat recovery wheel was designed to be 80mm in diameter with a depth of 20mm and porosity of 70%. The rotary heat recovery wheel was held in place in the casing by using supports which did not interfere with the rotation. In order to achieve the required rotation speed for the wheel, a rotation shaft was fitted through the test section vertically which connected to a DC motor underneath the test section. The rotation shaft was kept as thin as

possible in order to prevent the flow being affected. The scale model of the windcatcher produced a maximum wind tunnel blockage of 4.8%. The model of the windcatcher was connected to a 0.5 x 0.5 x 0.3 m3 test room, mounted underneath the test section.

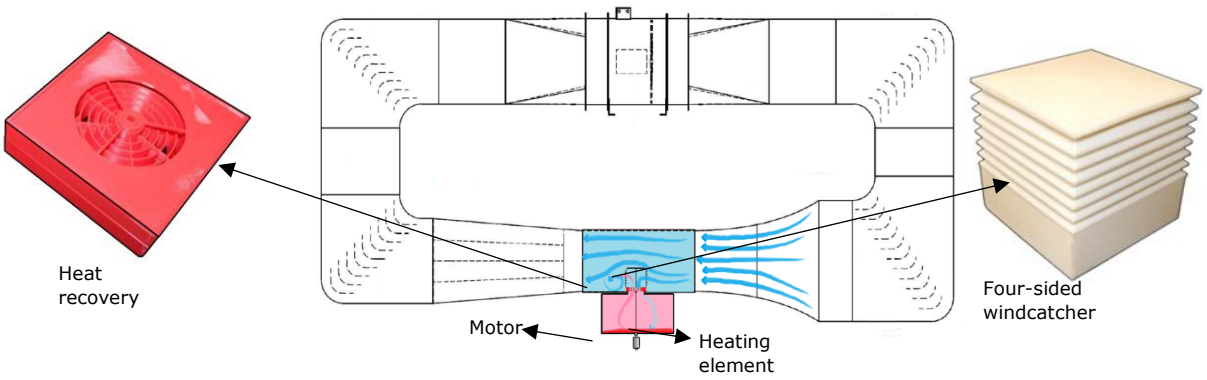

Figure 3. Experimental wind tunnel testing of the passive heat recovery windcatcher

3. RESULTS AND DISCUSSION

To validate the CFD model against the experimental model, the percentage error between the two data sets must be to an acceptable level. In addition to percentage error as an indicator of correlation, identifying equal trends in both sets of data is important to validate the CFD model. To determine the accuracy of the CFD model in relation to the wind tunnel model, first a comparison of the quantitative data was taken to calculate the numerical accuracy. The air velocity at the building model mid-height was calculated at each of the nine measurement points for the three different external air velocities. Figure 4a shows a comparison between the experimental and CFD results of the velocity measurements. This comparison showed a low difference range and the trends were to be in good agreement. Average error across the points was 7.46%. It should be noted that the boundary conditions in the CFD model were kept as similar as possible to those in the experiment, minimising the error which could be caused.

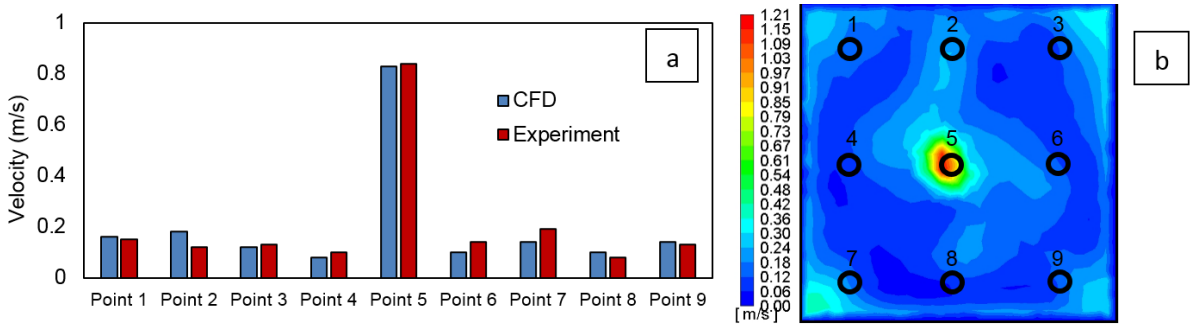

Figure 4. (a) Comparison between CFD and experiment values of air velocity (b) measurement points at a height of 150mm in the test room.

Figure 5a shows the temperature contours of the cross-sectional plane in the test room model. As observed, the addition of heat recovery had a positive effect on the indoor air temperature, raising the incoming fresh air by up to 1-2 K. It is worth noting that the temperature difference seen in the inflow and outflow of the wind tower. On the inlet stream of the wheel, the air temperature is at 283 K. On the outlet stream of the wheel, the air temperature is 290 K due to the heating effect of the floor area. This suggests that if the increased temperature in the outlet stream can be recovered and transferred to the inlet stream, the inlet temperature would reduce the demand on any heating system used. Further to this, the inlet air temperature was set at 283 K which is higher than average winter outdoor air temperature during the recorded in the UK between 1981 and 2010 of 277–279 K, meaning that the exhaust stream temperature would be even higher than the inlet stream temperature, giving great potential for thermal energy recovery and transfer.

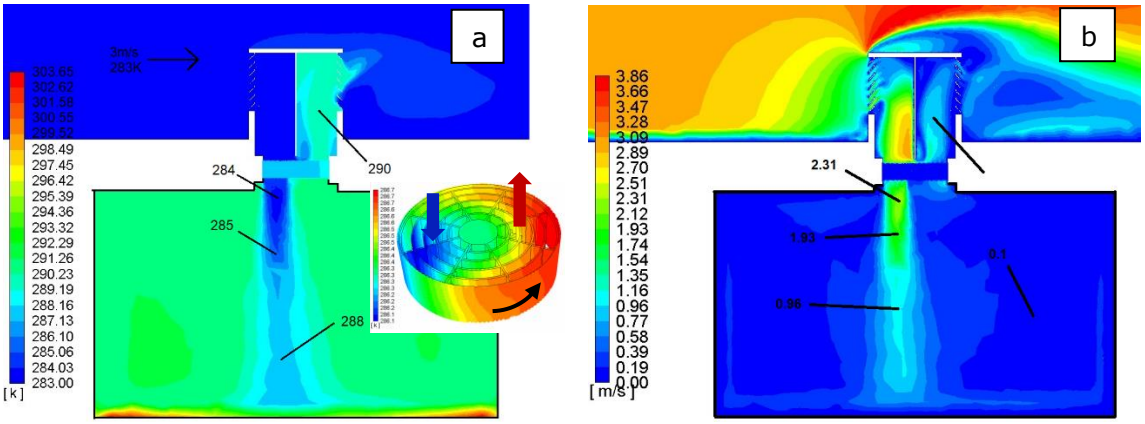

Figure 5. Cross-sectional contour planes of (a) air temperature (b) air velocity with the outdoor wind speed and temperature at 3m/s and 283K

Figure 5b illustrates the contours of velocity in the vertical plane drawn from the middle of the room which is aligned with the direction of the flow and contains the centre of the windcatcher. The airflow that entered the windcatcher via the 45˚ louvers was deflected upwards while the lower side of the flow was in reverse which formed a small recirculation region. The flow slightly accelerated as it turns sharply inside the 90° corner. Although reduction in speed was observed downstream of the heat recovery device, it did not impede the ventilation rate of the wind catcher. A column of fast moving air enters the space, where the airstream hit the floor of the room and circulated inside the structure and exited the wind catcher exhaust. A large recirculation region was observed at the leeward side of the wind tower. Figure 6a shows the effect of varying the outdoor wind speed on the indoor air temperature for standard windcatcher and windcatcher with heat recovery. As expected, the higher the outdoor wind speed, the lower resultant air temperature inside the room. The rate at which the internal temperature falls as the inlet velocity increases was of significance. A more substantial temperature increase was seen from 2 m/s to 3 m/s outdoor wind speed, than from 3 m/s to 5 m/s. Figure 6b shows the effect of varying the outdoor wind speed on the average indoor air velocity.

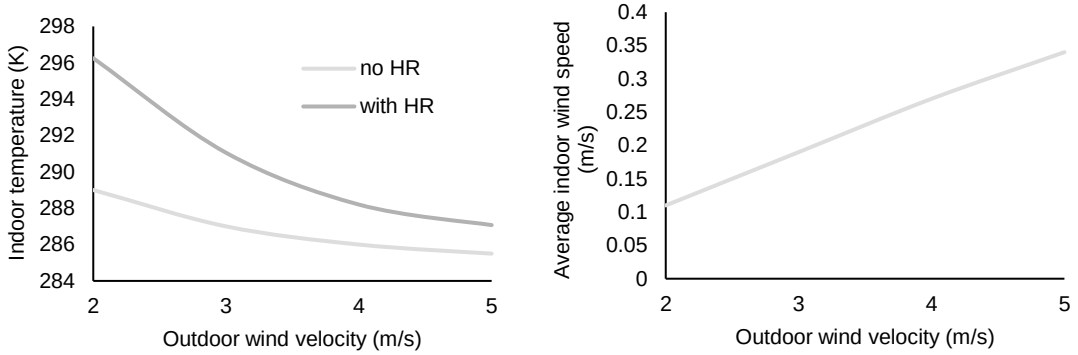

Figure 6. Effect of varying external wind speeds on average (a) indoor temperature (b) indoor velocity

4. CONCLUSION

In this study, the air flow through a windcatcher with a rotary heat recovery wheel was investigated using CFD modelling. It has been shown in previous work that windcatchers are capable of delivering the guideline levels of ventilation into a room, therefore the rotary wheel should not reduce the air supply rate to unsuitable levels to provide adequate ventilation to be an effective system. The numerical modelling was validated against experimental models tested in a closed-loop wind tunnel. The comparison between the CFD and experimental model showed a good correlation between the two sets of data. Results showed that the addition of heat recovery had a positive effect on the indoor air temperature, raising the incoming fresh air by up to 2 K with the outdoor wind speed and temperature at 3m/s and 283K. Optimising the configuration can further improve the heat recovery performance and a recovery of 3K from the exhaust stream to the inlet stream could generate energy savings up to 20% in heating costs. This shows that the concept has significant potential to be developed further, whereby the heat transfer properties of the system can be investigated and tested on a larger scale.

5. REFERENCES

Calautit, J K, Chaudhry, H, Hughes, B R, Ghani, S, 2013. Comparison between evaporative cooling and heat pipe assisted thermal loop for a commercial wind tower in hot and dry climatic conditions, Applied Energy, 101, 740-755.

Calautit, J K, Hughes, B R, 2014. Wind tunnel and CFD study of the natural ventilation performance of a commercial multi-directional wind tower. *Building and Environment*, 80, 71-83.

Calautit, J K, O'connor, D, Hughes, B R, 2014a. Determining the optimum spacing and arrangement for commercial wind towers for ventilation performance. Building and Environment, 82, 274-287.

Calautit, J K, Chaudhry, H, Hughes, B R, Sim L F, 2014b, A validated design methodology for a closed-loop subsonic wind tunnel. *Journal of Wind Engineering and Industrial Aerodynamic.* 125, 180-94

Calautit, J K, Hughes, B R, Shahzad, S, 2015. CFD and wind tunnel study of the performance of a uni-directional wind catcher with heat transfer devices. *Renewable Energy*, 83, 85-99.

Calautit, J K, Hughes, B R, Nasir, D S, 2017. Climatic analysis of a passive cooling technology for the built environment in hot countries. *Applied Energy*, 186, 321-335.

Chaudhry, H, Calautit, J K, Hughes, B R, 2015. Computational analysis of a wind tower assisted passive cooling technology for the built environment. *Journal of Building Engineering*, 1, 63-71.

DECC. Climate Change Act. London, 2008. WBCSD, Energy Efficiency in Buildings: Facts & Trends.

Hosseini, S, Shokry, E, Hosseini, A, Ahmadi, G, Calautit, J K, 2016. Evaluation of airflow and thermal comfort in buildings ventilated with wind catchers: Simulation of conditions in Yazd City, Iran. *Energy for Sustainable Development*, 35, 7-24.

Hughes, B R, Calautit, J K, Ghani, S, 2012. The Development of Commercial Wind Towers for Natural Ventilation: a review. *Applied Energy*, 92, 606-27.

O'connor, D, Calautit, J K, Hughes, B R, 2014. A Study of Passive Ventilation Integrated with Heat Recovery. *Energy and Buildings*, 82, 799-811.

O'connor, D, Calautit, J K, Hughes, B R, 2016. A novel design of a desiccant rotary wheel for passive ventilation applications. *Applied Energy*, 179, 99-109.

Nejat P, Calautit, J K, Majid, M H, Hughes, B R, Zeynali, I, Jomehzadeh, F, 2016a, Evaluation of a two-sided windcatcher integrated with wing wall (as a new design) and comparison with a conventional windcatcher. *Energy and Buildings*, 126, 287-300.

Nejat P, Calautit, J K, Majid, M Z, Hughes, B R, Jomehzadeh, F, 2016b. Anti-short-circuit device: A new solution for short-circuiting in windcatcher and improvement of natural ventilation performance. *Building and Environment*, 105, 24-39.

Shao, L, Riffat, S, Gan, G, 1998. Heat recovery with low pressure loss for natural ventilation. *Energy and Buildings,* 28, 179-184.

WBCSD, 2009. Transforming the market: Energy efficiency in buildings, World Business Council for Sustainable Development, Geneva.

Woods, A, Fitzgerald, S, Livermore, S, 2009, A comparison of winter pre-heating requirements for natural displacement and natural mixing ventilation. *Energy and Buildings*, 41, 1306-1312.

374: Exploring mobilised thermal energy storage for space heating: Policies and regulations analysis in China

Guang JIN[1], Wenxiu ZHAO[1], Li ZHANG[1], Shaopeng GUO[1,2,3], Jun ZHAO[3]

[1] School of Energy and Environment, Inner Mongolia University of Science and Technology, 014010, Baotou, China
[2] Institute of Engineering Thermophysics, Chinese Academy of Sciences, 100190, Beijing, China
[3] Key Laboratory of Efficient Utilization of Low and Medium Grade Energy, MOE, Tianjin University, 300072, Tianjin, China

Mobilised thermal energy storage (M-TES) system is considered as a promising alternative to supply heat for sparse users. It is of great importance to promote this technology for saving conventional energy and reducing greenhouse gas emission especially when introducing industrial waste heat as input source. To further develop the M-TES in China, the concerned policies and regulations are summarised and discussed in this paper including those on waste heat recovery and utilization, and transportation on road. The results obtained in this paper can helps the policy makers in developing and implementing policies that involve the utilization of M-TES technology in China.

Keywords: Mobilised thermal energy storage (M-TES); space heating; policy and regulations; China

1. INTRODUCTION

For most countries in temperate and cold regions, the energy consumption of space heating has become a main category in the list of total energy consumption. For example, in 2017, that part of energy used in China accounted for more than 40% of the total energy consumption (Lin, 2017). Thus, an effective method of heat delivery for space heating is crucial for realizing the goal of energy utilization reduction. District heating (DH) is considered as an energy efficient and cost-effective method for space heating. However, it is usually used for the users with large heat demand. For sparse user with low heat demand, it is infeasible to extend the network because of poor economic performance. In recent year, a concept called mobilised thermal energy storage (M-TES) was proposed to solve the above issue (Ma, 2009; Nomura, 2010; Wang, 2010; Köster, 2011; Li, 2013). Because it has the potential to use industrial waste heat, the M-TES technology draws much attention in many counties. In China, there have been several M-TES pilots (Zhongyineng Ltd Company, 2018 & Zhongyineng (Beijing) Ltd Company, 2018). Though the technique has been commercialised, the corresponding policies and regulations on M-TES have not been widely reported. In this paper, we summarise and discuss the concerned policies and regulations in terms of waste heat recovery and utilization, and transportation on road. The analysis presented in this paper can provide a reference for policy makers and benefits for promoting the development of M-TES in China.

2. DESCRIPTION OF M-TES CONCEPT

The concept of M-TES is shown in Figure 1. A specific container filled with storage material is transported between heat source and users by a vehicle. Using heat exchanger and heat transfer media, the heat collected from heat sources is stored in M-TES container. After the M-TES container is fully charged, it is transported over a distance and releases heat at the end-user site by employing the heat exchanger and heat transfer media.

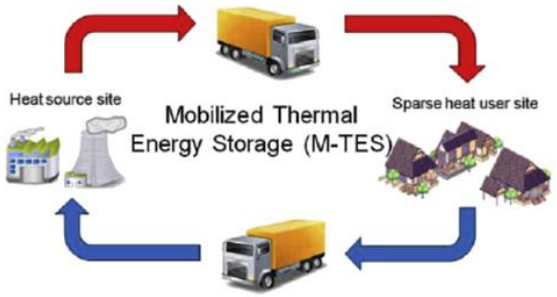

Figure.1. The concept of M-TES

3. POLICIES AND REGULATIONS ANALYSIS

As mentioned above, the operational process of the M-TES mainly consists of two steps: i) charging/discharging at heat source site/ user site and ii) transportation on road. Therefore, this section will be described based on the summarization of corresponding policies and regulations in terms of above two aspects.

3.1. Support policies on waste heat recovery and utilization

The industrial waste heat released in China accounts for 10-50% of the total energy consumption (Lu, 2016). However, only about 30% can be recovered (Zhang, 2016). Herein, the provinces of Hebei, Shandong and Henan respectively released 60.5 million tce, 58.78 million tce and 39.55 million tce of waste heat in 2015, ranked the top 3 in the regions with heating demand in China (Jiang, 2017). The abundant waste heat resources and heating demand in these regions lead to a potential of heat supply with recovered waste heat. Thus, the government has issued a series of policies to strongly support the waste heat recovery for heating.

Table 1 lists the relevant polices issued by both the central and local governments. It can be seen that there are mainly three nationwide support polices, i.e. Implementation Plan for Waste Heat and Civil Engineering issued in (2015), Cleaning Heating in Winter in the North Region (2017), and the 13th Five-year Plan for Energy-saving and Environmental Protection of Industry Sector issued in (2017). All are issued in the latest three years. Notably, the development of waste heat recovery technology for heating is repeatedly mentioned in the national policies last year. This indicates that the central government is realizing the necessity and urgency of the waste heat recovery and utilization especially with the consideration of heating demand in China. In addition, each province has also formulated relevant policies according to its own development reality. However, the heat supply with recovered waste heat cannot compete with the conventional heating method at present due to its huge investment cost. Thus, the financial subsidies are usually provided for its promotion. Herein, Beijing ranks the top in north of China and provides an extra reward of 260 RMB/tce except the 240

RMB/tce provided by the central government. Xinjiang Uygur Autonomous Region has not specified subsidy standards. Therefore, the support policies of waste heat recovery and utilization should be further improved.

Table 1: Policies of waste heat recovery and utilization in north of China

Regions	Year	Policy	Financial subsidies*
Nationwide	2017	Cleaning Heating in Winter in the North Region (2017-2021)	Eastern region: 240 RMB/tce Midwest region: 300 RMB/tce
	2017	The 13th Five-Year Plan for Energy-saving and Environmental Protection of Industry Sector	
	2015	Project Implementation Plan for Waste Heat and Civil Engineering	
Beijing	2017	Beijing's "13th Five-Year Plan" Period of Energy Development Plan	260 RMB/tce
	2016	The Civilian Building Energy-saving Development Plan in the 13th Five-Year Plan Period in Beijing	
Tianjin	2016	Energy Production and Consumption Revolution Implementation Plan of Tianjin (2016-2030)	120 RMB/tce
Hebei	2017	Implementation Plan for Controlling Greenhouse Gas Emissions in the "13th Five-Year Plan" of Hebei Province	60 RMB/tce
	2016	The 13th Five-Year Plan for Energy Development in Hebei Province	
Shandong	2017	13th Five-Year Plan for Energy Conservation in Shandong Province	1. Top 5: 1 million RMB 2. Top 50 : 100 thousand RMB
	2017	Shandong Industrial Low Temperature Waste Heat Utilization Action Plan	
Henan	2017	The 13th Five-Year Plan for Energy Saving and Low Carbon Development in Henan Province	50 thousand RMB to 150 thousand RMB
	2017	Notice on Organizing and Conducting Energy-Saving Activities in Henan Province	
Shanxi	2017	Shanxi Province's Industrial Green Low Carbon Cycle Development Project 2017 Action Plan	160 RMB/tce
	2017	Energy Conservation and Emission Reduction Implementation Plan of Shanxi Province	
Inner Mongolia	2017	13th Five-Year Plan for Energy Development in Inner Mongolia Autonomous Region	60 RMB/tce
	2017	Integrated Work Program for Energy Saving and Carbon Reduction in the 13th Five-Year Plan of Inner Mongolia Autonomous Region	
Shaanxi	2017	Implementation Plan for Controlling Greenhouse Gas Emissions in the 13th Five-Year Plan of Shaanxi Province	60 RMB/tce
Qinghai	2017	Comprehensive Work Plan for Energy Saving and Emission Reduction in the 13th Five-Year Plan in Qinghai	Exceed 500 tce: 200 RMB/tce
Gansu	2017	The 13th Five-Year Plan for Energy Development in Gansu Province	60 RMB/tce
	2014	Gansu Provincial Energy Conservation and Environmental Protection Industry Development Plan (2014-2020)	
Ningxia	2017	Comprehensive Work Plan for Energy Saving and Emission Reduction in the Thirteenth Five-Year Plan	60 RMB/tce
Liaoning	2017	Implementation Plan for Integrated Work of Energy Saving and Emission Reduction in the 13th Five-Year Plan in Liaoning	60 RMB/tce
	2017	Liaoning Province Promotes Three-Year Rolling Plan for Clean Heating in the Province (2018-2020)	
Jilin	2017	Comprehensive Implementation Plan of Energy Saving and Emission Reduction in Jilin Province in the 13th Five-Year Plan	60 RMB/tce
	2016	The 13th Five-Year Plan of Energy Development in Jilin	
Heilong jiang	2017	Action Plan for Promoting Energy Saving and Environmental Protection Industry Development in Heilongjiang Province (2017 - 2020)	60 RMB/tce
	2017	Implementation Plan of Comprehensive Energy Saving and Emission Reduction in the 13th Five-Year Plan in Heilongjiang	
Xinjiang	2016	Notice on Strengthening Project Management of Garbage, Waste heat, Residual Pressure, Residual Gas and Biomass power Generation Projects.	Depending on the situation
	2014	Environmental access conditions for key industries in the Xinjiang Uygur Autonomous Region (for Trial Implementation)	

* saving 1 ton standard coal equivalent fossil energy

3.2. Transport regulations on M-TES

At present, the commonly used storage materials for the M-TES include erythritol and sodium acetate trihydrate (SAT). Though erythritol is generally used as a food additive, it is classified as the ninth kind of dangerous substances in “Name List of Dangerous Goods” (GB12268-2012) (National Technical Committee for Standardization of Hazardous Chemicals Management, 2012), because its temperature of molten phase exceeds 100℃. As for SAT, it can be regarded as a normal transport substance. Both of the above materials are packaged inside the container. Therefore, there are no specific requirements for the issue of leakage according to the “General Specifications for Transport Packages of Dangerous Goods” (GB12463-2009) (National Technical Committee for Standardization of Hazardous Chemicals Management, 2009). Nevertheless, the transportation of dangerous goods and high-temperature goods were restricted in most provinces of China as shown in Table 2. Further, the vehicles are banned from parking in urban area except at user site. The warning signs of toxic substances and high temperature should be marked as required according to the rule of “Packing symbol of dangerous goods” (GB190-2009) (National Technical Committee for Standardization of Hazardous Chemicals Management, 2012).

In the aspect of transport vehicle, the dimension and load are nationally standardised according to the regulation GB1589-2016 (Ministry of Industry and Information Technology of the People's Republic of China, 2016). The others with respect to the M-TES including restriction and requirements are listed in Table 2. Herein, the on-board electrical devices must be concealed and have sufficient capability of thermal stress resistance. Only non-flammable materials can be used in the cab. The engine and fuel tanks should be covered by fire retardant. Besides, an over-speed governor with maximum speed under 90 km/h should be installed (China Machinery Industry Federation, 2008). During transportation, the automobile data recorder and communication devices should remain open. In terms of size, there are two specifications. One is 12,000 mm (length) × 2,550 mm (width) × 4,000 mm (height) with the corresponding maximum allowable total mass 31 t. The other is 13,750 mm (length) × 2,550 mm (width) × 4,000 mm (height) with the corresponding maximum allowable total mass 40 t. In addition, the maximum allowable total mass of low-speed trucks (with a maximum speed less than 70 km/h) can be increased to 45 t (Ministry of Industry and Information Technology of the People's Republic of China. 2016). Considering the dangerousness of M-TES container, the transport vehicle must be run with at least one escort (Ministry of Transport of the People's Republic of China, 2008).

Table 2: Regulations of road transport on M-TES

Regions	Year	Road transport regulations	Requirements
Nationwide	2016	Provisions on Technical Management of Road Transport Vehicles (2016)	1. Warning signs 2. Communication tools. 3. Recorder and satellite positioning device 4. Qualification
	2016	Provisions on The Administration of Road Dangerous Goods Transportation (2016)	
	2016	Regulations on the Management of Road Transport Employees	
	2016	Road Vehicles External Dimensions, Axle Loads and Quality Limits (2016)	
Beijing	2013	Motor Vehicle Parking Management Measures in Beijing	1. Warning signs 2. Qualification
	2009	Regulations on the Management of Road Transport in Beijing	
Tianjin	2015	Motor Vehicle Parking Management Measures in Tianjin (2015)	1. Warning signs 2. Fire Equipment 3. Qualification
	2012	Regulations on Illegal Overloading and Overloading of Vehicles in Tianjin	
	1998	Administrative Measures for the Transport of Dangerous Goods on Roads in Tianjin	
Hebei	2017	Road Transport Regulations of Hebei Province	1. Warning signs 2. Qualification
	2013	Guiding opinions of Hebei provincial road transport administration on Further Strengthening Safety Management in road transportation industry	
	2010	Regulations on Overloading and Overloading Freight Vehicles in Hebei Province	
Shandong	2015	Measures for the Technical Management of Road Transport Vehicles in Shandong	1. Warning signs 2. Qualification
	2014	Road Transport Vehicle Dynamic Monitoring Socialization Platform Service Providers Record Management Measures of Shandong Province	
	2010	Road transport regulations of Shandong Province	

Henan	2017	Implementation Plan for Comprehensive Safety Control of Road Dangerous Goods Transportation in Henan (2017)	1. Warning signs
	2004	Circular on the Prohibition of Vehicular Traffic of Dangerous Chemicals in the Highways	2. Qualification
Shanxi	2014	Notice of the Shanxi Provincial Public Security Bureau on the Transportation of Dangerous Chemicals by Vehicles on Expressways(2014)	Recorder and satellite positioning device
	2011	Road Transport Regulations of Shanxi Province (2011)	
Inner Mongolia	2010	Road Transport Regulations of the Inner Mongolia Autonomous Region	Recorder and satellite positioning device
Shaanxi	2017	Implementation Plan for Promoting Healthy and Stable Development of Road Freight Industry in Shaanxi(2017 - 2020)	1. Warning signs 2. Qualification 3. Emergency treatment and protective equipment
	2010	Regulations on the Management of Road Transport in Shaanxi	
Qinghai	2016	Regulations on the Management of Road Transport in Qinghai	1. Warning signs 2. Qualification
	2016	Implementation Plan for Quality Improvement of Road Transport Practitioners in Qinghai	
	2013	Opinions on Further Promoting Healthy and Stable Development of Road Transport Industry in the Whole Province	
Ningxia	2013	Amendment to the Regulations of the Ningxia Hui Autonomous Region on the Administration of Road Transport	1. Warning signs
	2013	Measures for the Administration of Road Freight Transport in the Ningxia Hui Autonomous Region	2. Qualification
	2010	Overrun and Overloading of Freight Vehicles in the Ningxia Hui Autonomous Region	
Gansu	2017	Measures for the Construction and Management of Road Transport Stations in Gansu Province	1. Qualification 2. Recorder and satellite positioning device
	2014	Road Transport Regulations of Gansu Province	
Liaoning	2001	Some Opinions on Speeding Up the Development of Road Transport Industry in Our Province	1. Warning signs 2. Qualification
	2015	Road Transport Regulations of Liaoning Province	
Jilin	2006	Road Transport Regulations of Jilin Province	1. Warning signs 2. Qualification
Heilongjiang	2016	Road Transport Regulations of Heilongjiang Province	1. Warning signs
	2014	Opinions on Deepening Reform and Speeding up Development of Road Transport Industry	2. Qualification
Xinjiang	2018	Main Points of Emergency Management Work for Road Transportation Industry in 2018	1. Warning signs
	2018	Measures for Overloading and Overloading Freight Vehicles in the Xinjiang Uygur Autonomous Region	
	2014	Road Transport Regulations of the Xinjiang Uygur Autonomous Region	2. Qualification

4. CONCLUSIONS

The technique of M-TES has drawn much attention in China. A series of support policies are issued to promote its development. Overall, the waste heat recovery from industry is strongly encouraged by the government especially for heat supply, which can provide sufficient heat for charging the M-TES container. The financial subsides are provided by both the central and local governments. For example, 240 RMB and 300 RMB will be issued when saving per ton standard coal equivalent fossil energy in eastern and mid-west regions of China, respectively. However, most subsides are provided for the large scale projects of waste heat recovery. The support for small scale heating system especially for that using M-TES should be further enhanced. In addition, the commercial projects of M-TES have been operated for years in China. Though there are regulations on transport of dangerous goods on road, the special regulation on M-TES is lacking resulting in a confusion of dangerous goods demarcation. Besides, the operation of M-TES requires the professional knowledge of design, installation, and operation. Therefore, the practitioner should be qualified. The storage devices should be standardised. The corresponding rules and regulations on M-TES have to be enacted.

5. ACKNOWLEDGEMENTS

Financial support provided by the National Natural Science Foundation of China (No. 51706111) is acknowledged. Shaopeng Guo also appreciates the support by the China Postdoctoral Science Foundation (No. 2017M620067) and Innovation Fund of Inner Mongolia University of Science and Technology (No. 2017YQL07). The Guidance of Scientific and Technological Innovation of Inner Mongolia Autonomous region (2017CXYD-1) is also acknowledged.

6. REFERENCES

China Machinery Industry Federation. 2008. Dangerous Goods Transportation Vehicle Structural Requirements (GB 21668-2008).

Jiang XM, Xiong HW. 2017. Potential and utilization analysis of middle and low grade industrial waste heat resources in Beijing Tianjin Hebei and its surrounding areas. China's energy. 39(9): 32-36.

Köster M, Sadek T. 2011. A Product-Service System for Industrial Waste Heat Recovery Using Mobile Latent Heat Accumulators. ASME International Mechanical Engineering Congress and Exposition. 2011: 1331-1340

Li LH, Wang WL, Yan JY, Erik Dahlquist. 2013. Economic assessment of the mobilized thermal energy storage (M-TES) system for distributed heat supply. Applied Energy. 104(2): 178-186.

Lin BQ, Lin J. 2017. Evaluating energy conservation in China's heating industry. Journal of Cleaner Production. 142: 501-512.

Lu HY, Price L, Zhang Q. 2016. Capturing the invisible resource: Analysis of waste heat potential in Chinese industry. Applied Energy. 161(6): 497-511.

Ma Q, Luo L, Wang RZ. 2009. A review on transportation of heat energy over long distance: Exploratory development. Renewable and Sustainable Energy Reviews. 13: 1532-1540.

Ministry of Industry and Information Technology of the People's Republic of China. 2016. Outline Dimensions, Axle Loads and Quality Limits for Cars, Trailers and Car Trains (GB 1589-2016).

Ministry of Transport of the People's Republic of China. 2008. Rules for Carriage of Dangerous Goods (JT 617-2004). National Technical Committee for Standardization of Hazardous Chemicals Management. 2012. Name List of Dangerous Goods (GB 12268-2012).

National Technical Committee for Standardization of Hazardous Chemicals Management. 2009. General Technical Conditions for the Transport of Dangerous Goods (GB 12463-2009).

National Technical Committee for Standardization of Hazardous Chemicals Management. 2009. Dangerous Goods Packaging Mark (GB 190-2009).

Nomura T, Okinaka N, Akiyama T. 2010. Waste heat transportation system, using phase change material (PCM) from steelworks to chemical plant. Resources Conservation and Recycling. 54(11): 1000-1006.

Wang WL, Hu YK. 2010. Combined heat and power plant integrated with mobilized thermal energy storage (M-TES) system. Frontiers of Energy and Power Engineering in China. 4(4): 469-474.

Zhang J, Zhang HH, He YL, Tao WQ. 2016. A comprehensive review on advances and applications of industrial heat pumps based on the practices in China. Applied Energy. 178: 800-825.

Zhongyineng Ltd Company. http://www.zhongyineng.com/. Accessed on May 10th 2018.

Zhongyineng (Beijing) Ltd Company. http://zhongyineng.chinajnhb.com/. Accessed on May 10th 2018.

375: To investigate thermal transmittance of building integrated photovoltaic system

Shin-Ku LEE[1], Benson LAU[2], Xiaofeng ZHENG[3], Mingtsu HO[4]

[1] Research Center for Energy Technology and Strategy, National Cheng-Kung University, Tainan, 701, Taiwan, sklee1015@gmail.com
[2] Department of Architecture & Built Environment, University of Westminster, London, W1B 2UW, UK, B.Lau@westminster.ac.uk
[3] Department of Architecture & Built Environment, University of Nottingham, Nottingham, NG7 2RD, UK, Xiaofeng.Zheng@nottingham.ac.uk
[4] Graduate School of Opto-Mechatronics and Materials, WuFeng University, Chiayi, 621,Taiwan, homt@wfu.edu.tw

Building energy consumption accounts for a large proportion of a country's total energy consumption. One approach to achieving the goals of energy conservation and greenhouse gas (GHG) reduction in the building sector is to use good thermal insulating materials in the building envelope. The thermal transmittance (U-value) of the building envelope plays a key role in the evaluation of the thermal performance of a building. Recently, many countries have been increasingly approving the planning, design, and construction of net zero energy buildings. In a net zero energy building, the energy demand from the operation of the building is met by renewable energy generated on site. The application of a renewable energy system to produce electricity is necessary for a ZEB. In particular, Building Integrated Photovoltaic (BIPV) systems are a promising strategy to integrate PV systems with building materials to reduce construction costs and add aesthetic features. BIPV systems that generate electricity can also play an important role in achieving zero energy balance in buildings. In this study, we referred to ISO 12567-1 and CNS 10523 A3197 to set up the insulating performance testing equipment and to investigate the U Value of various types of building integrated photovoltaic (BIPV) panel. The experimental results indicated that the thermal conductivity of insulation material and thickness of the BIPV system are the major factors affecting U value. Five types of photovoltaic panel selected in this study have little difference in U value. However, the insulating material inside BIPV system has a significant effect on the U value of a BIPV panel.

Keywords: Green Building, Building Integrated Photovoltaic System, thermal transmittance, thermal insulating material

1. INTRODUCTION

The photovoltaic (PV) industry and solar cell panel installation capacity are rapidly expanding in Taiwan, and the government has laid down many policies that aim to facilitate the development of green energy technologies, as shown in Figure 1. For example, the Bureau of Energy, at the Ministry of Economic Affairs, has set out a plan for “one million rooftop PVs”, with an office responsible for this project opening in May, 2012. The aim of this is for Taiwan’s rooftop PV capacity to reach 847 MW in 2015, 2120 MW in 2020, and 6,200 MW in 2030, with the focus first being on rooftop systems and then ground-based ones (Bureau of Energy, Ministry of Economic Affairs, 2018). Building integrated photovoltaic (BIPV) systems are a promising technology that aims to integrate PV systems into building materials. Compared to traditional, non-integrated PV systems, BIPV do not require any extra space to be allocated to the PV system, while also offering instant electrical power generation for buildings, supporting applications such as air-conditioning, lighting and other electrical appliances (Raugei, 2009; Strong, 2010). BIPV systems have attracted intense interest because they can replace the traditional envelopes of buildings, like windows, roofs, façades and shading devices, and thus reduce the use of architectural materials (Kim, 2010; Peng, 2011; Yoon, 2011; Wittkop, 2012; Santos, 2012; Yoon, 2013). Evaluations of the thermal insulation, optical, electrical and wind-resistance properties of BIPV systems (building's façades) have been reported in the literature in order to promote the use of this technology in Taiwan, as well as analysis of high colour rendering index (HCRI) BIPV window systems (Huang, 2014; Chen, 2012). Though BIPV systems have been developed in many countries with the aim of realizing zero energy buildings (ZEB) or nearly-zero energy buildings (NZEB), there are still very few studies of thermal properties of BIPV systems.

In general, PV module should be tested based on IEC 61730 (2016) to assess the prevention of electrical shock, fire hazards, and personal injury due to mechanical and environmental stresses. However, in accordance with the Building Technical Rules of Taiwan, if the BIPV is used as the roof, façades, or loadbearing wall, it should pass the critical criteria for thermal insulation performance. While BIPV products are more and more available in the market, it is common interest to understand the thermal and optical properties of BIPV system and to evaluate its optimisation potentials for building application. Thus, we focus on measuring the thermal characterisation of commercially available BIPV modules and investigating the thermal performance enhanced solutions of BIPV system in this study.

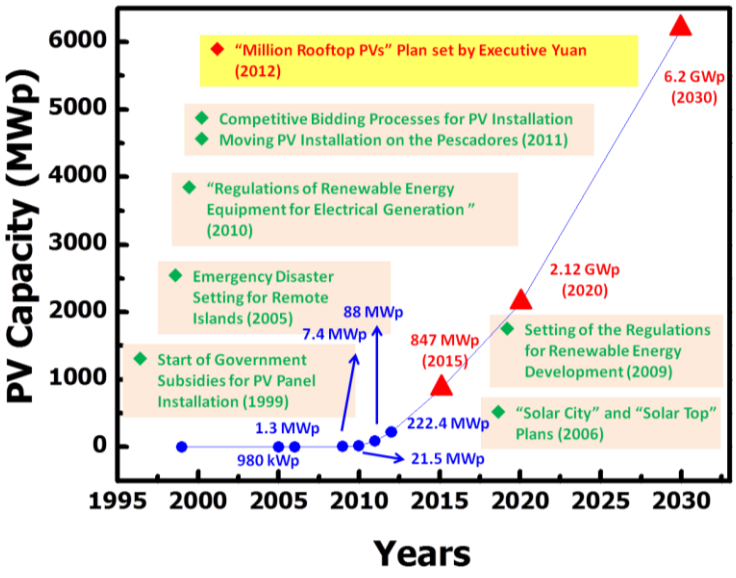

Figure 1: The installation capacity of PV systems in Taiwan

2. EXPERIMENTAL SETUP AND PROCEDURE

In this study, a full-scale testing equipment for investigating the heat insulation performance of building materials complying with ISO 12567-1 (2000) and ISO 9869 (2014), was used to measure the U value of BIPV specimen. The test specimens were placed in the middle of the indoor and outdoor environmental chamber, respectively, and the temperature of the interior and exterior surfaces of the building materials were measured by k-type thermocouple, in order to study the heat insulation properties of building materials.

2.1. Setup

In order to obtain valid assessment of heat insulation performance of the test specimens, a suitable thermal environment is created as follows:

1. Simulation of the outdoor environmental chamber: The temperature is set in a range of -20℃ - 40℃. Specifications require it to have an air cooling device to simulate the indoor environment mounted with the test specimen (opening scale 2500 × 2000 mm, depth above 700 mm). In order to achieve an even temperature distribution with a position difference within ± 1 ° C as shown in Figure 2, heating device and the uniform distribution of air flow design were employed to simulate outdoor environment with insulated and airtight envelope.
2. Simulation of the indoor environmental chamber: The temperature was set between +10℃ and 40℃. The surface temperature distribution of the specimen is the same as that of the simulated outdoor environment.
3. Pre-test preparation room: The temperature and relative humidity were set in ranges of +10 ℃~40 ℃ and 40% ~ 90% respectively. The standard requires that the size of preparation room should be able to accommodate the indoor environment chamber with a minimum 500mm gap in-between. The temperature control accuracy should be within ± 1 ℃, so that the test room temperature can achieve a good uniformity.
4. Thermocouple temperature control accuracy: ± 0.5 ℃, ± 3.0% RH.
5. Inner box size:

   Simulation outdoor environmental chamber: 160 × 310 × 340 cm (W × H × D)
   Simulation indoor environment chamber: 95 × 310 × 206 cm (W × H × D)
   Door and window Test preparation room: 145 × 310 × 340 cm (W × H × D)

6. Test box size: 600 × 335 × 360 cm (W × H × D). Maximum size of specimen: 250 × 200cm
7. Air flow speed: the outdoor side should not be less than 1.5 m/s, the indoor side must be less than 0.3 m/s.

Figure 2: Building insulation performance testing equipment.

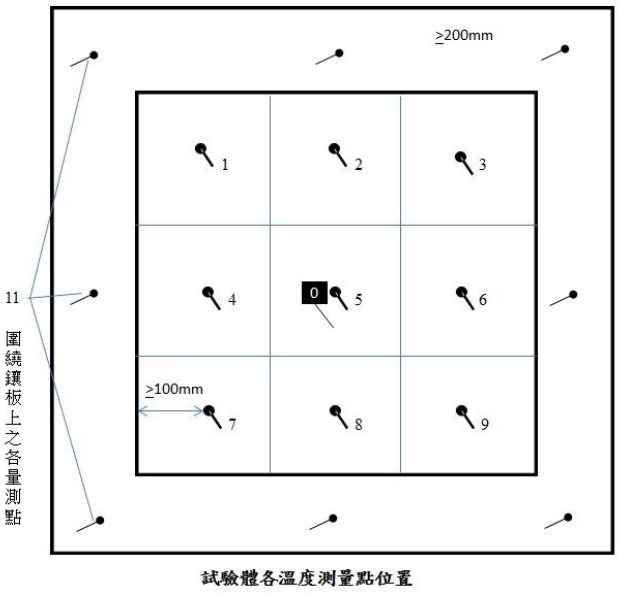

Figure 3: Schematic diagram of specimen surface temperature measuring point.

2.2. Procedure

This experiment is divided into two parts: calibration test and experiment test, the installation and the experimental procedures are as follows:

1. Preloaded the device frame, installed the test specimen in the test device in an airtight way and set on the same side with the exterior surface of the wall.
2. The test body was installed in the test device box and sealed with silicone.
3. The temperature measurement of the interior and exterior surfaces using thermocouples is shown in Figure 3, with 9 points evenly distributed on each side.
4. The thermostat, the heating chamber, the low-temperature room and the cooling towers were switched on first. The target temperature was set via the display panel and the test was commenced. After the set temperature was reached, the wind speed measurement was initiated and recorded. Finally, after the wind speed met the target, the experiment started.
5. The average summer outdoor temperature in Taiwan, according to the national standard, was set to 40°C, with indoor temperature set to 20°C (ambient temperature determination with reference to ISO 12567-1, Thermal performance of windows and doors, 2000).
6. The readings of temperature and heat flux were taken every 10 minutes, in the steady state. The steady state means that the temperature of the air on both sides of the test body tends to be stable under the heating device, and the temperature change per hour is within 3%.
7. The calibration panel with known thermal resistance was installed with the temperature in indoor and outdoor chamber reached the required level. The surface temperatures on both sides of the standard plate were measured.
8. Finally, the U value was calculated according to ISO formula using the measurements described above.

3. RESULTS AND DISCUSSION

In order to investigate the U value of various BIPV system, eight samples from different BIPV modules were selected in this study (see Figure 1). In specimen U01~U05, five types of PV modules: double-glass monocrystalline, double-glass multicrystalline, polycrystalline silicon, silicon thin film, and GIGS with aluminum frame were tested. In specimens U06~U08, heat insulation board was added in the polycrystalline silicon PV module. 30mm phenolic form board, 15mm gypsum board and 9mm Calcium Silicate board were installed in front of 1mm aluminum rear plate in specimen U06, U07, and U08, respectively.

The measured mean temperature values during the experimental campaign for the different case studies can be seen in Figure 3. The curves in Figure 3 show the data over a period in which the heat flows become stationary. The actual measurement took place in the range of 2–2.5 h. Furthermore, the obtained thermal transmittance and heat flux values are reported in Table 1. As can be seen that the U value was constant but with slight variations in U01~U05 case studies, the U values of various BIPV panel are in the range of 2.826~3.219W/m2-K. Thermal transmittance of silicon thin film BIPV is the lowest among these five types of BIPV module. In Table 4, it can be seen that the U-value is dependent on the thickness and thermal conductivity of heat insulation material in a relatively strong degree as expected. For specimens U03, U06 to U08, the U value decreases from 3.157 to 0.511 with increasing thickness of the BIPV modules from 9mm to 30mm. The comparison of measured results between U07 and U08 tests indicated that thermal conductivity of insulation material is the primary factor affecting the whole U value of BIPV system. The thermal conductivity of Calcium Silicate board (0.209 W/m-K) which is lower than that of gypsum board (0.384 W/m-K) resulted in that the U-value of U08 sample (1.066W/(m^2-K)) is lower than that of U07 (1.730W/(m^2-K)), even the thickness of Calcium Silicate board is 0.6 times the thickness of gypsum board.

The mean temperature difference between exterior and interior surface of BIPV module also reflects the thermal insulation performance of BIPV. The experimental results indicated that the largest surface temperature difference is U06 (14.7℃), followed by U08 (10.9℃) and U07 (7.9℃).

Figure 4: Photographs of BIPV modules

Table 1: Thermal performance test results of the eight BIPV modules

#	component	Temperature difference	Heat flux (W/m^2)	U-value W/(m2-K)	Area (m^2)
U01	Double-glass monocrystalline BIPV	2.24℃	56.30	3.217	1.196
U02	Double-glass multicrystalline BIPV	1.76℃	54.73	3.219	1.874
U03	Polycrystalline silicon BIPV	0.93℃	53.37	3.157	1.638
U04	Silicon thin film BIPV	1.28℃	47.49	2.826	1.430
U05	GIGS BIPV	0.91℃	54.46	3.025	0.791

U06	U03+phenolic form board+aluminum rear plate	14.7℃	9.76	0.511	1.620
U07	U03+gypsum board+aluminum rear plate	7.9℃	31.83	1.730	1.620
U08	U03+ Calcium Silicate board+aluminum rear plate	10.9℃	19.18	1.066	1.620

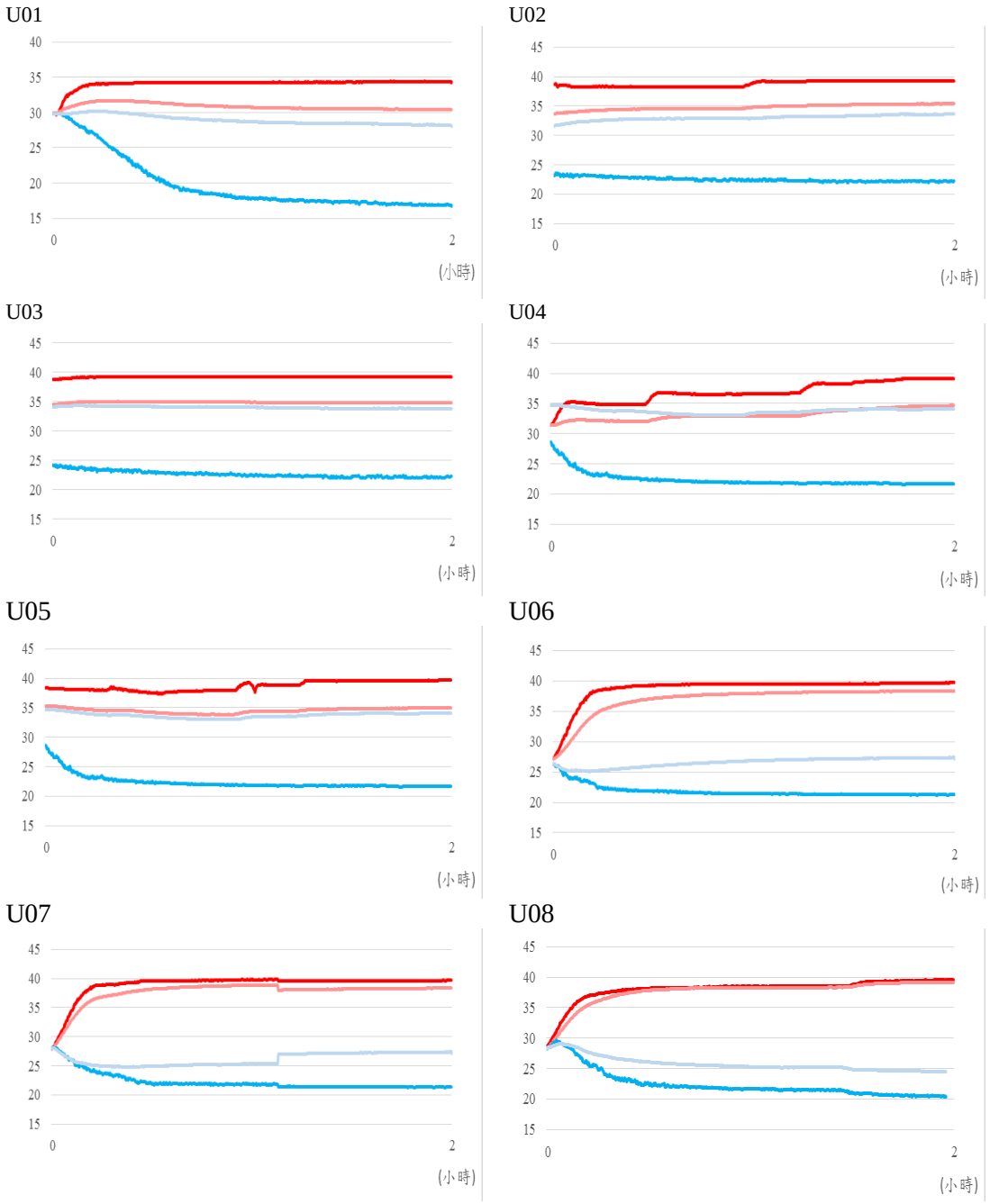

Figure 5: Values of the measured temperature: the internal air temperature (blue), the internal surface temperature of the sample (light blue), the external air temperature (red) and the internal surface temperature of the sample (light red)

4. CONCLUSION

As building regulations become more stringent and innovative BIPV systems are used in buildings, the overall thermal insulation performance of the BIPV system has become the necessary data. In this study, the U value of various types of BIPV panel combined with different composite panels were measured in full-scaled hot box U-value Measurement Facility. Experimental parameters include the type of solar cell, the type of insulation composite plate and the thickness. The experimental results indicated that the thickness dominates the U-value of BIPV system as the thermal insulation composite plate was not installed on the back surface of BIPV system. However, in the case of installing a thermal insulation plate on the back of the BIPV system, the thermal conductivity of thermal insulation plate has a significant effect on the U-value of BIPV system and temperature difference between exterior and interior surface of BIPV system.

5. REFERENCES

Bureau of Energy, Ministry of Economic Affairs. A Plan for a Million Rooftops PVs. http://mrpv.org.tw/index.php (Retrieved 1 June 2018)

Chen HJ, Chiang CM, C, Shu CM and Lee SK. Self-Power Consumption Research with the Thermal Effects and Optical Properties of the HCRI-BIPV Window System. J. of Electronic Science and Technology 2012; 10: 29-36.

Huang YC, Chan CC, Kuan SC, Wang SJ and Lee SK. Analysis and Monitoring Results of a Building Integrated Photovoltaic Façade Using PV Ceramic Tiles in Taiwan. International Journal of Photoenergy 2014; 2014: 1-12.

IEC 61730-1, Photovoltaic (PV) module safety qualification - Part 1: Requirements for construction, 2016.

ISO 12567-1, Thermal performance of windows and doors — Determination of thermal transmittance by hot box method — Part 1: Complete windows and doors, 2000.

ISO 9869-1:2014, Thermal insulation -- Building elements -- In-situ measurement of thermal resistance and thermal transmittance -- Part 1: Heat flow meter method, 2014.

Kim JJ, Jung SK, Choi YS and Kim JT. Optimization of Photovoltaic Integrated Shading Devices. Indoor Built Environ 2010; 19: 114–122.

Peng C, Huanga Y and Wu Z. Building-integrated photovoltaics (BIPV) in architectural design in China. Energy and Buildings 2011; 43: 3592–3598.

Raugei M and Frankl P. Life cycle impacts and costs of photovoltaic systems: current state of the art and future outlooks. Energy 2009; 34: 392–399.

Santos ÍPD and Rüthera R. The potential of building-integrated (BIPV) and building-applied photovoltaics (BAPV) in single-family, urban residences at low latitudes in Brazil. Energy and Buildings 2012; 50: 290–297.

Strong S. Building Integrated Photovoltaics (BIPV), Whole Building Design Guide. 2010; http://www.wbdg.org/resources/bipv.php (Retrieved on 1 June 2018)

Yoon J, Song J and Lee SJ. Practical application of building integrated photovoltaic (BIPV) system using transparent amorphous silicon thin-film PV module. Solar Energy 2011; 85: 723–733.

Yoon JH, Shim SR, An YS, and Lee KH. An experimental study on the annual surface temperature characteristics of amorphous silicon BIPV window. Energy and Buildings 2013; 62: 166–175.

Wittkop S, Valliappan S, Liu L, Ang KS and Cheng JSC. Analytical performance monitoring of a 142.5 kWp grid-connected rooftop BIPV system in Singapore. Renewable Energy 2012; 47: 9–20.

379: Study on the economic insulation thickness of external insulation construction in Xi’an

Hao DONG[1]

[1] Xi'an University of Architecture and Technology, No. 13 Yanta Road, Xi’an, Shaanxi Province, P.R. China, 349362978@qq.com

The economic insulation thickness is a thermal design method that considers both energy conservation and economy. The existing researches have often ignored the effects of solar radiation. Taking a typical three-story external thermal insulation building in Xi’an as an example, this paper introduces solar radiation through the OTTV algorithm to calculate the relationship between insulation thickness and life cycle cost of the external wall of the building. A life cycle cost analysis model was established to determine the economic insulation thickness of the external insulation building in Xi’an. The paper uses the theory of non-equilibrium heat preservation to calculate the thickness of economic insulation in different orientations and provides new ideas and methods for the study of economic insulation thickness.

Keywords: *economic insulation thickness, solar radiation, non-equilibrium heat preservation*

1. INTRODUCTION

The energy crisis of the 1980s forced people to pay attention to energy conservation, and the building energy conservation field has thus developed rapidly. Building insulation is an important means of building energy saving. The setting of building insulation will bring increase of initial investment and reduction of building energy consumption. By doing economic analysis and energy consumption calculation, the economic insulation thickness is a special point between investment and energy saving to make the building's investment and energy consumption expenses in the entire life cycle minimum.

The research on the economic insulation thickness in China began in the 1980s. However, the research on the economic insulation thickness was mainly for industrial services at the beginning. The main research objects were the transportation pipelines and heating pipelines in the petrochemical industry. In 1997, Meng Changzai (Meng, 1987: pages 39-43) used the optimisation model of the annual average cost of heating to analyse and calculate the six structural schemes of the typical buildings in Hohhot, and found out the optimum insulation thickness of external walls and roofs. Subsequently, more and more scholars have conducted studies on the economic insulation thickness in different climate regions and cities in China, such as Jin Hong (Jin, 2018: pages 37-40), Zhang Yao (Zhang, 2017: pages 149-156), Wang Houhua (Wang, 2008: pages 936-939), and Fang Lin (Fang, 2002: pages 711-716). The research methods are mainly divided into two major types. The first type is using the heating degree days and cooling degree days given in the relevant specifications to calculate the relationship between heating and cooling load and external wall insulation thickness with the building model. And then use the life-cycle economic evaluation to find the relationship between life-cycle cost and insulation thickness, so as to find out the minimum value as the economic insulation thickness, such as Huang Daren (Huang, 2017: pages 105-110), Xu Jianliu (Xu, 2008: pages 49-51), and Wang Houhua (Wang, 2008: pages 936-939), etc. The second type is to simulate the energy consumption by using building energy simulation software such as Energy Plus and Design Builder. The building energy consumption for different external wall insulation thickness is calculated by regression analysis and the fitting curve of energy consumption and insulation thickness is obtained, then brought into the full-cycle economic evaluation model for calculation to obtain the economic insulation thickness, the others' researches applies this method, Jin Hong (Jin, 2018: pages 37-40), Liu Enhai (Liu, 2017: pages 67-70), Zhang Bingli (Zhang, 2012: pages 309-311).

The first method is a steady-state calculation method. Although easy to be applied and calculated, this method does not take the solar radiation heating effect on the building into consideration, thus the research ignored the solar radiation gains in the heating season and the negative influence caused by solar radiation in the cooling season. As a result, the energy consumption calculation is inaccurate. The second type of method takes into account the radiation effects through software simulation and obtains more accurate energy consumption results, but it will take more time and efforts, on the other hand, selects different Insulation thickness is generally uniformly distributed. If the sample size is too small, no sample may exist near the extreme point, which affects the reliability of the regression curve. In addition, most of the research based on the two methods did not consider the difference of solar radiation on different orientations.

Taking a three-storey hotel building in Xi'an as an example, this article uses the OTTV method in combination with the climate data of Xi'an to calculate the energy consumption of heating and cooling seasons with different insulation thicknesses, and then use the life cycle method (LCC) to find the optimum insulation thickness despite of orientations. Finally, non-equilibrium coefficients of heat transfer are considered.

2. CALCULATION METHOD

2.1. Influence of Solar radiation on economic insulation thickness

Solar radiation is a very important parameter in a region's climatic conditions, which has a huge impact on building energy consumption. Efficient use of solar energy is also a hotspot in building energy conservation field in recent years. The effect of solar radiation on the economic insulation thickness of the building is mainly manifested in two aspects: (1) Solar radiation that enters the room through the glazing components in winter can heat indoor air and reduce heating load, while solar radiation in the summer can cause indoor air temperature rise and increase cooling load. Changes in building load will affect the value of the economic insulation thickness of the external wall. (2) Most cities in China are located in the north of the Tropic of Cancer. In winter, the total amount of radiation received by the south wall is much higher than that in the north. When the south wall is heated, the temperature difference between the inner and outer surfaces will be reduced. The south exterior wall should use a higher heat transfer coefficient limit. At present, most houses in China are constructed with the same heat transfer coefficient in four directions, which will cause unnecessary waste. In order to comprehensively consider the influence of radiation factors, the OTTV method and the theory of non-equilibrium heat preservation are introduced to analyse and calculate the building insulation.

2.2. OTTV concept

OTTV (overall thermal transfer value) is a measure of heat flux density in the building envelope. The parameter is used to evaluate the overall thermal performance of building envelopes and the relative size of building envelopes for different envelopes. It can be calculated as Equation 1.

Equation 1:

$$OTTV=(1-WWR)\times TD_{eq}\times U_w+WWR\times DT\times U_f+WWR\times SC\times SF$$

Where:

- OTTV = overall thermal transfer value (W/(m^2·K))
- WWR = window wall ratio
- TD_{eq} = equivalent temperature difference (K)
- DT = temperature difference between interior and exterior design conditions (K)
- U_w, U_f =the U value of the wall and fenestration (W/(m^2·K))
- SC = the shading coefficient of fenestration
- SF= solar factor for that orientation (W/m^2)

When using the OTTV method for energy consumption assessment, the OTTV value of each orientation of the building envelope should be calculated. And then multiply by the area of the envelope and period. The outdoor meteorological parameters used in this calculation are mostly average values. Although it will cause a certain numerical deviation in energy consumption, the purpose of this paper is to compare the full-cycle economic situation under different thermal insulation thicknesses to find the optimal thermal insulation thickness. So the purpose to find the relative relationship between different samples, and this method is feasible.

2.3. Method of measuring loads and costs

The method of measuring heating and cooling load are shown as Equation 2.

Equation 2:

$$Q=Q_h+Q_c$$

$$Q_h=\sum(OTTV_d\times A_d\times 24\times N_h\times 10^{-3})$$

$$Q_c=\sum(OTTV_d\times A_d\times 24\times N_c\times 10^{-3})$$

Where:

- Q = annual heating and cooling loads (Kwh)
- Q_h = annual heating loads (Kwh)
- Q_c = annual cooling loads (Kwh)
- $OTTV_d$ = OTTV values in different orientations (W/(m^2·K))
- A_d = total area of different orientations (m^2)
- N_h = number of heating days (d)
- N_c = number of cooling days (d)

In the cost calculation, all the costs are converted to the final value and then brought into the life cycle cost (LCC) analysis method, the highest-cost stages in the entire life cycle of a building are the construction phase and the operation phase, so the specific formula of LCC can be shown as Equation 3.

Equation 3:

$$LCC=CI+CO$$

Where:

- LCC = life circle cost (RMB)
- CI = cost of investment (RMB)
- CO = cost of operation (RMB)

The CI and CO can be calculated by Equation 4 - Equation 5.

Equation 4:

$$CI=(P_b+P_m)(1+i)^n$$

$$P_b=\delta\times A_i\times p_1$$

Where:

- P_b = material purchase cost (RMB)
- P_m= material installation cost (RMB)
- i = rate of inflation
- n = building life (y)
- δ = the thickness of insulation (m)
- A_i= the area of insulation (m^2)
- p_1= insulation material unit price (RMB)

Equation 5:

$$CO=A\frac{[(1+i)^n-1]}{i}$$

$$A=(\frac{Q_c}{EER}+\frac{Q_h}{COP})\times p_e$$

Where:

A = annual energy cost (RMB)
i = rate of inflation
n = building life (y)
EER= air conditioning refrigeration energy efficiency ratio
COP = Coefficient of Performance
p_e = electricity price (RMB)

When LCC reaches the minimum value, the corresponding wall insulation thickness is the economic insulation thickness.

3. THE EXAMPLE OF CALCULATION

3.1. The calculation and analysis of typical architectural model

A three-storey apartment building in Xi'an is selected as a model to calculate its economic insulation thickness. Figure 1 shows the layout of the building. The ratio of windows and walls of this building in south, north, east and west are 0.348, 0.336, 0.218, and 0.132 respectively. Common materials are applied in walls and the 240mm KP1 porous bricks is used as the basement of exterior wall. The coefficient of heat transfer and solar radiation absorption is 1.74 W/ (m^2·K) and 0.8 respectively when the insulation layer is not added. The exterior window adopts an empty double glass steel window in a single frame, and its heat transfer coefficient and the total solar radiation transmittance is 3.4 W/ (m^2·K) and 0.42 respectively. Based on relevant data of the China Standard Yearly Meteorological Database (CSWD) and the Design *Standard for Energy Efficiency of Residential Buildings in Severe cold and Cold Zones* (JGJ 26-2010), the period of November 15 to March 15 is set as the heating season of the following year. The calculation temperature of indoor and outdoor is 18 degrees and 2.1 degrees. The cooling period lasts from July 1 to August 31. The calculation temperature of indoor and outdoor is 26 degrees and 27.2 degrees. The air-conditioning unit has a COP of 3.3 and an EER of 3.0. The XPS board is used as the insulation materials in the model building, which has a transfer coefficient of 0.31 W/ (m^2·K) and an average price of 700 yuan/ m^3.

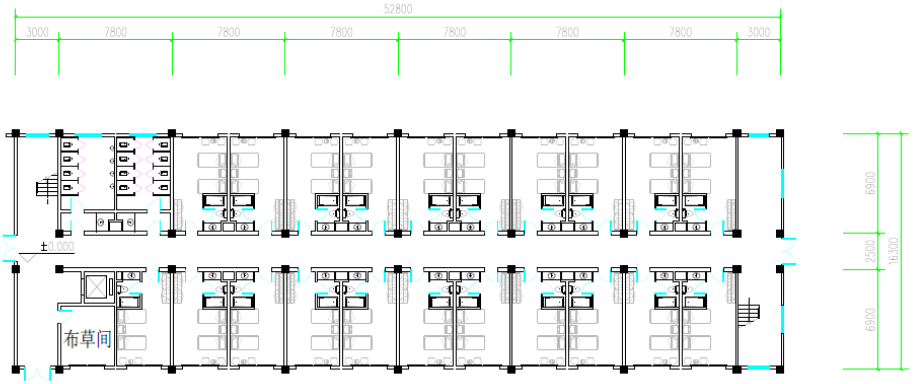

Figure 1: The layout of model building

The installation price of insulation materials is considered to be 50 *yuan*/m^2 and the lifetime of it is 10 years. The inflation rate stays 6%. The unit price of electricity is about 0.5 yuan in Xi'an. The thickness of the external wall varies from 10 to 100mm in steps of 10mm.

Substituting the conditions above into the model, the heating load and cooling load change by the insulation thickness are shown in Figure 2.

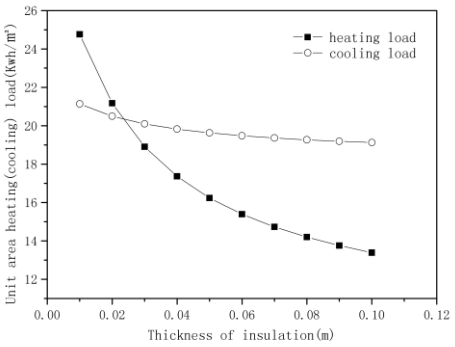

Figure 2: Unit load-thickness of insulation

It can be seen that the heating load shows a very significant downward trend as the thickness of insulation increases, while the cooling load decreases slightly. This phenomenon is caused by two reasons. Firstly, Xi'an locates in a cold climate zone and the heating season is much longer than the cooling season. Moreover, the temperature difference of indoor and outdoor during the heating season is much larger than that during the cooling season. Secondly, the intensity of solar radiation is high in summer, and the heat generated by buildings through radiation increases, which will further weaken the contribution of wall insulation to energy conservation. Therefore, the architectural insulation design focuses more on ventilation and shading in south area. Thus, the main factor of summer cooling energy consumption is neither the outdoor air temperature nor the outdoor integrated temperature in Xi'an area, and the direct radiation entering the room through the transparent envelope structure plays an important role. Meanwhile, the subjective behaviour of the building's shading and occupants tends to block the direct radiation entering the room in summer. As a result, the amount of direct radiation should be excluded and scattered radiation and reflected radiation should be considered when calculating the solar radiation in summer for each vertical plane. According to this idea to optimise the model again, the results are as Figure 3.

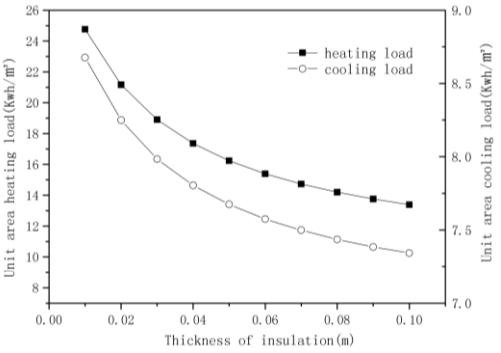

Figure 3: Unit load-thickness of insulation (revise)

And the relationships between LCC and thickness of insulation are shown as Figure 4 and Figure 5.

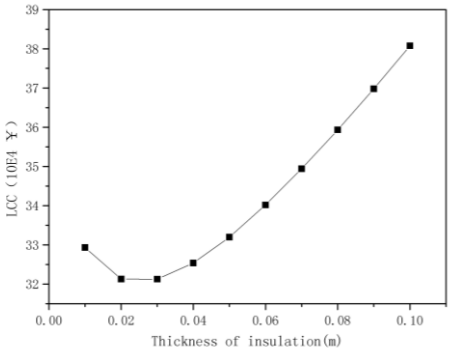

Figure 4: LCC-thickness of insulation

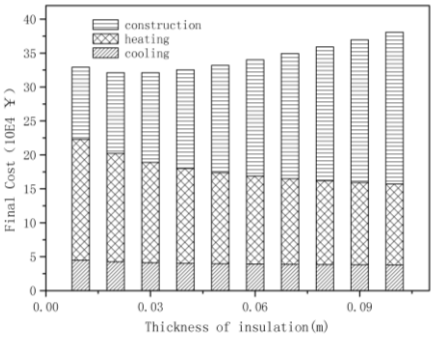

Figure 5: LCC-thickness of insulation(bar)

A regression analysis of the curve yields a regression equation of

$$y = -13873x3 + 3274.9x2 - 119.66x + 34.145$$

Equation 6:

$$R^2 = 0.9992$$

Take the derivative of the equation and make its derivative to be zero, yielding x=0.027. The economic insulation thickness of the exterior wall in Xi'an is 0.027m and the heat transfer coefficient of the wall is 0.63 W/ (m^2·K).

3.2. Non-equilibrium thermal insulation analysis

The amount of solar radiation received by buildings in different orientations is different. If the solar radiation intensity varies greatly in a region, it will lead to unequal heat fluxes in all facing walls and roofs. The south wall is exposed to more solar radiation, and its exterior equivalent temperature will be higher than the rest of the wall, and the heat flux density will be relatively small. At present, the heat transfer coefficient of buildings in most parts of northern China is determined by the heat consumption index. In the process of calculating the index, the default four-direction outdoor calculation temperatures are the same, which leads to the same calculated heat transfer coefficients. Ignoring the effect of solar energy on the heating of buildings in winter, it will result in the waste of resources and energy. Li et al. (Li, 2011: pages 56-60) proposed a non-equilibrium thermal design method based on the equal-heat-flow method through the study of Tibet. The main principle is to adjust the average heat transfer coefficient of the envelope structure in different orientations of the building, so that the heat flux density of each envelope structure is equal. It can be shown as Equation 7.

Equation 7:

$$K_n(t_i-t_{eqn})=K_s(t_i-t_{eqs})=K_e(t_i-t_{eqe})=K_w(t_i-t_{eqw})$$

Where:

$K_nK_sK_eK_w$ = the heat transfer coefficient of north south east west wall (W/ (m^2·K))

$t_{eqn}t_{eqs}t_{eqe}t_{eqw}$ = the equivalent temperature of north south east west wall (K)

t_i=the indoor design temperature (K)

The OTTV method used in this paper has already considered the influence of solar radiation, but when calculating the economic insulation thickness, the same thickness is used for the calculation, which is equivalent to the effect of the solar radiation gain on the wall being equal. In order to carry out non-equilibrium thermal insulation design, the ratio of the heat transfer coefficient of each wall must be calculated according to the design of non-equilibrium thermal insulation design and then back-calculated.

According to the previous calculation results, it can be calculated that the ratio of the heat transfer coefficient in the north and east-west wall of Xi'an and the south-to-west wall should be as Equation 8.

Equation 8:

$$\frac{K_s}{K_n}=1.17 \quad \frac{K_s}{K_e}=\frac{K_s}{K_w}=1.10$$

The economic thickness of the insulation is 0.027m and the heat transfer coefficient of the wall is 0.63 W/ (m^2·K).Considering it as the heat transfer coefficient of east/west wall, then the heat transfer coefficient of south wall should be 0.69 and the economic insulation thickness should be 0.022m. The heat transfer coefficient of south wall should be 0.58 and the economic insulation thickness should be 0.032m.

4. CONCLUSION

Enhancing the thermal insulation performance of external walls is a necessary measure for building energy conservation in cold regions. The economic insulation thickness can take into account both the energy saving and economic goals. However, most of the previous studies did not consider the effects of differences in radiation and orientation. In this paper, the OTTV method is used to calculate the heating and cooling energy consumption of a three-story apartment building in Xi'an with different insulation thickness. The gain effect of different orientation radiation is taken into account, and the economic insulation thickness of the south, north and east directions of Xi'an City is calculated to be 22mm, 27mm, 32mm respectively. The paper provides an economic insulation analysis method which can involve both temperature differences and solar factors, and the method can be used for reference in the study of economic insulation thickness in other regions.

5. REFERENCES

Fang L, Qu D, Liu F. Calculation of economical insulation thickness of external walls and roofs of air-conditioned buildings[J]. Chinese Journal of Solar Energy, 2002, 23(6):711-716.

Huang R, Li L, Wu H, et al. Economic Analysis of External Wall Insulation Material Thickness in Hot Summer and Cold W inter Regions [J]. New Building Materials, 2017(9):105-110.

Jin H, Shao T, Chen D, et al. Study on Economic Thickness of External Thermal Insulation Structural Insulation Layer of Exterior Wall in Severe Cold Area[J]. Southern Architecture, 2018(2).

Li E, Liu J, Zhang W. Research on Non-Equilibrium Insulation of Residential Buildings in Solar Energy Enrichment Area: Limit Value of Unbalanced Heat Insulation Coefficient in Lhasa City[J]. Building Science, 2011, 27(8):56-60.

Liu Y, Lam J C, Tsang C L. Energy performance of building envelopes in different climate zones in China[J]. Applied Energy, 2008, 85(9):800-817.

Liu E, Wang C, Pan J, et al. Thermal Insulation Thickness Analysis Based on Economic, Energy, and Environmental Fac tors[J]. Building Air Conditioning, 2017, 36(10):67-70.

Meng C. Calculation and Analysis of Thermal Insulation Thickness of Residential Buildings[J]. Gas & Heating, 1997(3):39 -43.

Wang H, Wu W. Optimization Analysis of External Thermal Insulation Thickness of External Structure of Residential Buil dings[J]. Journal of Chongqing University, 2008, 31(8):937-941

Xu J, He J, Sun W. Study on Calculation of Economic Thickness of Thermal Insulation of Building Envelope in Nanjing[J]. HVAC, 2008, 38(1):49-51.

Zhang B, Huang J, Feng W, et al. Determination of Economic Thickness of External Wall Insulation Layers of Public Buil dings: Taking Xuzhou District as an Example[J]. Sichuan Building Science, 2012, 38(3):309-311.

Zhang W, Niu J, Jin G. Research on Energy Saving Performance and Economic Thickness Optimization of Building Insul ation Materials[J]. Building Science, 2017, 33(10): 149-156.

381: Increasing power system flexibility through utilizing VRE curtailment and power-to-heat strategy

Sannamari PILPOLA, Vahid ARABZADEH, Peter D. LUND

Aalto University, School of Science, New Energy Technologies Group,
P.O. Box 15100, FI-00076 Aalto, Espoo, Finland,
sannamari.pilpola@aalto.fi and vahid.arabzadeh@aalto.fi

When increasing the share of variable renewable energies (VRE) such as wind or solar power, power curtailment may become necessary to balance the power system. In general, curtailment may be needed because of transmission congestion or lack of transmission capacity with a high share of VRE. Here we explore the effects of wind power curtailment utilization in Finland. The study examines the effect of curtailment on two levels: on a city level for Helsinki (Finland's capital), and on a national level (whole Finland). For each level, a specific optimisation-based model has been developed. The city-level model employs 10-minute time steps, while the national model uses 1-hour time steps. Both models aim to minimise system costs, and the main constraints of the models are the characteristics of power plants and balancing methods, in addition to securing the energy demand and supply balancing. The city-level results reveal the optimal transient operation of power plants and their CO_2 emissions, while the national-level results demonstrate the effects of wind curtailment on the whole energy system and its composition. The curtailment has been defined through 3 different scenarios, estimating the wind curtailment based on fixed percentages of the wind generation peaks, the wind generation profile, and a fixed percentage of the power demand profile. The fixed percentage of the wind power generation results in most curtailment, whereas the wind peak-shaving results in least curtailment. To increase the wind power penetration, the option of power-to-heat utilizing the curtailed wind power was applied on both levels. Increasing the amount of wind and curtailment and implementing power-to-heat conversion may not automatically lead to positive effects, but may need additional measures such as higher CO_2 emission pricing and more effective heat generation (heat pumps) to get the full benefits.

Keywords: curtailment, power-to-heat, wind power integration, energy system flexibility

1. INTRODUCTION

The Paris Climate Accord requires that most of the energy production need to be emission free by the middle of this century (United Nations Framework Convention on Climate Change, 2015). This in turn will require massive investments in clean energy production and more efficient energy use. At the same time, the market penetration of new renewable technologies, notably wind power and solar photovoltaics, is accelerating (International Energy Agency, 2012; IEA, 2016). The International Energy Agency (IEA) estimates in its future energy scenarios that solar and wind power will be the most popular alternatives for new power generation investments till 2040 (International Energy Agency, 2017). On a very long term by year 2100, the global energy company Shell estimates that close to 40% of all energy could come from solar energy alone (Shell International BV, 2018). Clearly, the energy transition towards sustainability will rely on new energy technologies, whose characteristics may differ quite much from the traditional fuel-based energy system.

A major challenge with much wind or solar power in the energy system will be the matching of supply and demand of power, as the electricity system needs to be in balance on each point of time (Koltsaklis, Dagoumas and Panapakidis, 2017). Existing balancing methods, e.g. the reserves of the power system, could manage some of the balancing, but even additional or new approaches may be necessary. Such include flexible supply (gas turbines, gas engines), demand response, strengthening transmission cables, curtailment and power-to-x (x=different final energy forms or fuels), among others (Lund et al., 2015). Basically these could help in reaching high shares of variable renewable electricity (VRE) shares, without the need of dedicated energy storage units per se (EASAC, 2017). Naturally, the development of electrical storage and Li-ion batteries in particular is an interesting option for flexibility, but most of electrical storage (>99%) is still hydropower based. Batteries could be quite attractive for small-scale distributed power options, such as photovoltaics in buildings (Lund, 2018).

A rather simple and scalable method to balance VRE could be curtailment of VRE with power-to-heat conversion (P2H), which would also be motivated by the high share of thermal energy or heat of the final energy use. Most of the final energy in Europe is heat, e.g. in Finland around 80% of the final energy consumption of households is heat (space heating and domestic hot water, (Statistics Finland, 2018). Actually, the kind of sectoral coupling of power and heating has received increasing interest in the scientific literature as an energy system flexibility measure. The heating system also provides inertia and easy solutions for energy (heat) storage, in addition to large demand, which provide effective measures for energy system balancing (Lund, 2012).

Curtailment is simple and already applied e.g. when transmission capabilities are lacking, but it would also mean a loss of VRE power, sometimes a loss of revenue if VRE is subsidised e.g. through feed-in-tariff schemes. However, with high VRE shares curtailment may be more motivated to better manage the electricity system and market.

In this paper, we analyse the use of curtailment and power-to-heat for increasing the energy system flexibility with a high share of wind power. The aim is firstly to assess the effects of three different curtailment strategies on the overall performance of the power system, when increasing the amount of wind power, and secondly, quantify the role of linking P2H to curtailment. The way curtailment is arranged would affect both the amount of curtailed wind power but also the power system and dispatch of other power plants. Basically curtailment offers an interesting option for VRE in particular, as the capacity factor of VRE is much lower compared to fuel-based traditional power plants running continuously. Therefore, in the best case, curtailing VRE may lead to only small energy loss, though the power curtailment is major. On the other hand, if the objective would be to use the curtailed power for heating through P2H, choosing a strategy which supplies adequately energy to the heating sector may be more preferable. For these reasons, choice of curtailment strategy will be important.

For the analyses, we consider two levels of the energy system, a national (Finland) and a city (Helsinki), both in a northern cold climate with a high heating demand. The national energy system represents a macro-scale case, with more inertia smoothing out some transient effects, whereas the city is a micro-scale case with stronger dynamical effects down to the power-plant level, which need to be differently modelled compared to macro-scale level. The analyses are therefore done with two dynamic energy system models: a national model with 1-hour time step and city energy system model with 10-min step resolution.

2. METHODOLOGY

The analyses were conducted with two optimisation-based models, one for national level and one for city level. The national model aims to demonstrate the effects of wind curtailment on the whole energy system, whereas the city-level model focuses on optimal transient operation of the existing power plants. Finland is used as the case study for the national analysis, whereas Finland's capital Helsinki is used as the case study for the city-level analysis.

2.1. National level model

The national-level analysis is conducted with an in-house-developed model described previously in (Pilpola and Lund, 2018). The model incorporates all aspects of an energy system, including electricity, heat and fuel. The model employs a 1-hour time step for electricity and heat, while fuel demands are considered on an annual scale. The model seeks for a cost-optimal solution of the energy system while keeping the supply-demand balance. The cost optimisation problem is mathematically stated as Minimise Total Annual Cost $= \sum_{t=1}^{tech}(\text{Investment Cost}_t + \text{O\&M}_t) + \sum_{f=1}^{fuels} \text{Fuel Cost}_f +$ Net cost of power import + Emission cost.

The variables in the optimisation are the amounts the primary energy sources and the amount of conventional conversion, i.e. CHP, separate production, and heat pumps. The model uses 2013 as the reference year for input data, and the more detailed description of the input data can be found in Pilpola and Lund (2018). The primary energy composition of the reference year is given in Table 1. As the model focuses only on the reference year, no other system flexibility measures except for power-to-heat (P2H), thermal storage, and wind power curtailment are employed. The three methods for wind power curtailment are described in Section 2.3.

Three levels of wind power are utilised in the national-level analysis: reference (0.8 TWh), 20 TWh, and 40 TWh of wind power, corresponding to 0.9%, 23.5% and 47.1% of the yearly electricity use of Finland. In the basic scenario, the amount of fossil fuel and share of conventional power are the optimisation variables. In addition, we include two additional scenarios. Firstly, we consider the effect of increasing CO_2 emission costs, using the costs of 8, 20, and 60 €/tCO_2. Secondly, we include nuclear power and bioenergy as optimisation variables. In this case, nuclear power addition is limited to the upcoming Olkiluoto 1,600 MW nuclear power plant, while the bioenergy potential is assumed to be +20% to the current use. The fossil primary resources are always considered unconstrained.

Table 1: Primary energy consumption in Finland in 2013 (Statistics Finland, 2017). The share of fossil resources was 47%, while the share of renewables was 29%. The CO_2 emissions were 49.2 MtCO_2.

	Oil	Coal	Natural gas	Peat	Nuclear	Biomass	Wind	Hydro	Other renewable	Power import	**Total**
PJ	346	135	107	57	258	345	3	46	5	57	**1 359**
%	25%	10%	8%	4%	19%	25%	0%	3%	0%	4%	**100%**

2.2. City-level model

The city-level analysis is conducted with another in-house model, which is described in (Mikkola and Lund, 2016). This optimises the local energy production system on a plant level. A mixed-integer linear programming algorithm is used to optimise the costs of the energy production mainly. The objective function is Minimise $\sum_t$(Production costs + Balancing costs + Storage costs - Revenues from sales).

The main optimisation constraints reflect the technical properties of power plants, the technical properties of balancing methods along with the balance of energy demand and supply. The main optimisation outputs are energy production, energy sold to consumers, and costs and profit from running the energy system. The analyses are done for Helsinki (60°N) with an annual heat demand of 6.1 TWh and electrical demand of 4 TWh. In Helsinki, over 90% of the heat demand is covered through a district heating (DH) system. The energy production plants for Helsinki include 3 combined heat and power (CHP) plants, 3 boilers, and a large heat pump (Mikkola and Lund, 2016).

2.3. Curtailment cases

Figure 1 illustrates the three different wind power curtailment methods used in the study. In the first method, dubbed “Peak-shaving”, curtailment is based on shaving a fixed percentage of the wind power peaks. In the second method, “Wind-following”, wind power is curtailed with a constant fixed percentage. The last method, “Load-following”, also considers the actual electricity demand: wind power is curtailed so that wind power production cannot exceed a fixed percentage of the electrical load. All three curtailment methods are studied on both national and city scale, and two curtailment rates, 10% and 30%, are used.

To increase the usefulness of the wind curtailment, we also consider the option of power-to-heat utilizing the curtailed wind power. Here, we direct all curtailed wind to heat pumps (COP=3) to be converted into heat. As wind power is a renewable and a zero-marginal-cost resource, we argue that the heat produced by this “forced” heat pump operation offers a renewable and low-cost, albeit non-dispatchable, source of heat, which in turn may have the possibility to decrease the marginal costs of energy production. In the Helsinki case, where the maximum capacity of heat pumps is limited, this “forced” heat pump operation with the curtailed wind power limits the heat pump capacity available for the dispatch optimisation, whereas in the national level, the required additional heat pump capacity is simply added to the energy system.

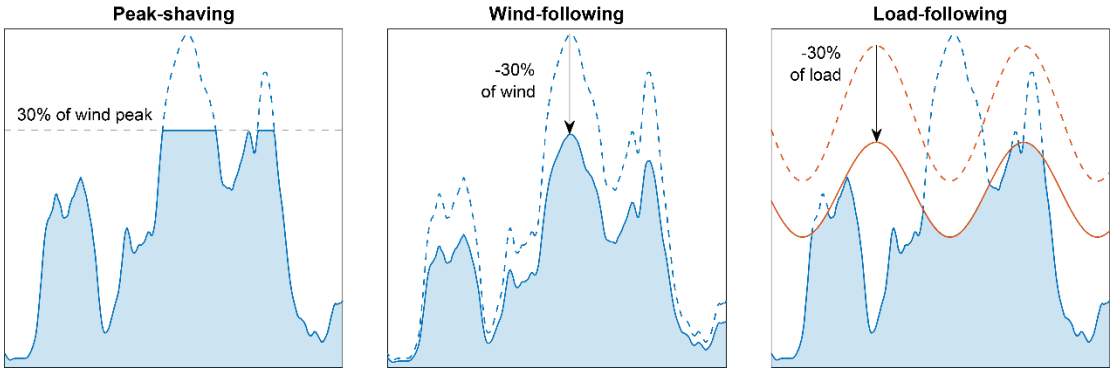

Figure 1: Schematic illustration of the different wind power curtailment methods using a curtailment rate of 30%.

3. RESULTS AND DISCUSSION

In this section, we analyse the effects of wind power curtailment on the national and city-level energy system. Both models aim to minimise annual system costs, and the main constraints of the models are the technical properties of power plants and balancing methods, in addition to securing the energy demand and supply balancing.

3.1. National case (Finland)

In the national case, the three different wind power curtailment methods, described in Section 2.3, produced very different levels of curtailed wind (Table 2). The temporal profile of the national wind power production caused the "Peak-shaving" method to curtail very little power, suggesting a highly peaking profile, whereas in the "Load-following" method, especially the lower amount of wind power (20 TWh) was too low compared with the national power demand profile to be curtailed. The "Wind-following" method produced the highest amount of curtailment.

Table 2: Curtailed wind power directed to power-to-heat (% of initial wind power) in the national case.

		Curtailment method:		
Wind power before curtailment	Curtailment rate	Peak-shaving	Wind-following	Load-following
20 TWh	10%	0.1 %	10 %	0 %
	30%	4 %	30 %	0.05 %
40 TWh	10%	0.1 %	10 %	4 %
	30%	4 %	30 %	12 %

Effects of different curtailment methods on the energy system composition

Figure 2 shows the change in the overall primary energy consumption with the different curtailment methods and wind power levels, compared to the national reference case (Finland 2013). All cases exhibit changes in fossil fuel composition: oil, gas and peat have been replaced by cheaper coal use in particular in CHP plants (here we used 2015 price for coal which was 2.3 €/GJ). Furthermore, the CO_2 emissions had a positive correlation with the level of coal use, ranging between -10 to +6 $MtCO_2$ (-20% – +11% from reference). In addition, all cases showed a decrease in power import, and in the 40 TWh wind power cases, even notable power export (3-13 TWh) resulted. This change from net importing to net exporting suggests that a high wind power addition may not always be cost-effectively utilised in the national scale power due to fuel prices and system limitations, even if a power-to-heat scheme for curtailed wind. The share of wind power in the overall power production was on average 23% for 20 TWh wind, and 35% for 40 TWh, compared to <1% in 2013. The changes in nuclear power and other renewable resources are zero in Figure 2, as these primary energy sources were not included as variables in this optimisation.

As for the energy system composition, the results show increased heat production from heat pumps (on average +3 TWh for 20 TWh wind cases, +12 TWh for 40 TWh wind cases), mostly due to the P2H scheme, which in turn decreased the heat from heat-only boilers (-7/8 TWh in the 20/40 TWh wind cases). The influx of wind power also eliminated power production from power-only plants. Interestingly, in all cases except for the "Load-following" cases, the CHP production increased, despite the large wind power additions. This CHP increase was most likely caused by the availability of low-cost coal and the comparably high electricity export prices.

Overall, the results suggest that the wind power addition caused both power-only and heat-only production to decrease, and coal-CHP production to increase. Importantly, the cost of emissions was 8 €/tCO_2 (2013) was low, which did not penalise high emissions. Consequently, in the 40 TWh wind case, the increased power production led to electricity excess,

which was then exported to international markets. The P2H scheme with curtailed wind power led to an increased share of heat pumps, but it seemed to have only a minor effect in mitigating excess electricity production, since increasing the curtailment share from 0% to 10% to 30% did not systematically decrease export. The failure of the P2H scheme to mitigate wind power excess may have partly been caused by the fact that the wind power curtailment sometimes coincided with times of low heat demand.

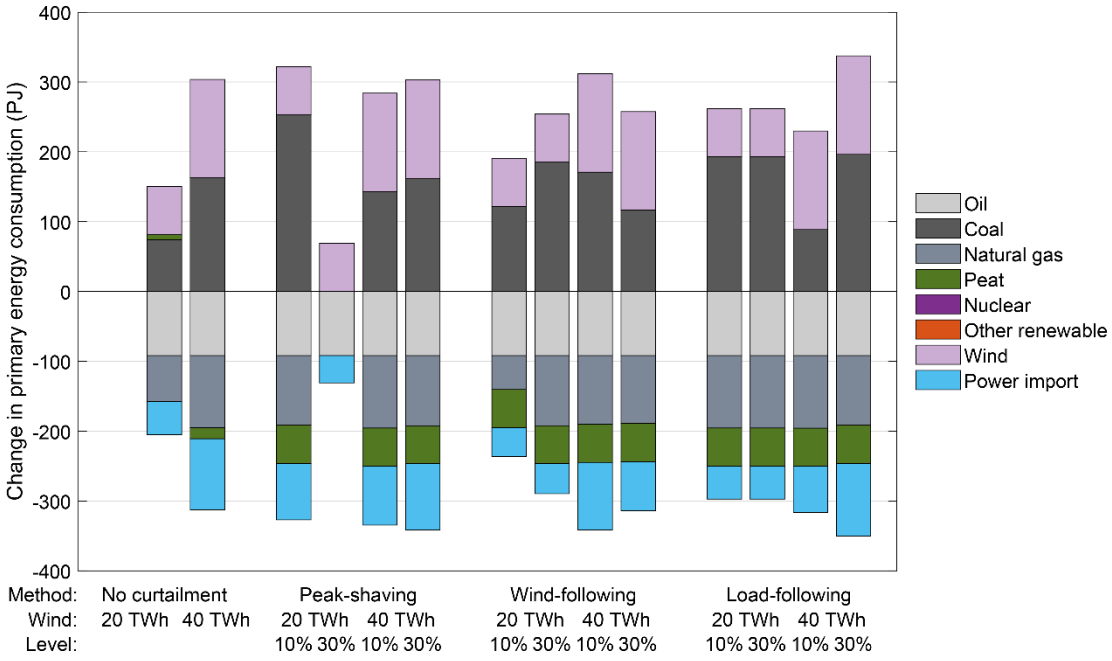

Figure 2: Change in primary energy compared to the national reference case (Finland in 2013, see Table 1 1).

Table 3 shows the change of the annualised system cost compared with the reference case (2013, see Table 1). Overall, all optimised scenarios had lower annual system costs than the reference case, suggesting that integrating wind power into the Finnish energy system may be cost-effective. However, there is no clear trend whether wind power curtailment systematically decreases costs. Furthermore, the cost effect of different curtailment methods remains ambiguous: only in the "Wind-following" method, the annual costs decreased for both levels of wind power.

Table 3: Change in annual system cost compared to the national reference case.

			Curtailment method:		
Wind power before curtailment	Curtailment rate	None	Peak-shaving	Wind-following	Load-following
20 TWh	0%	-13%			
	10%		-18%	-13%	-15%
	30%		-9%	-17%	-14%
40 TWh	0%	-14%			
	10%		-15%	-15%	-10%
	30%		-15%	-15%	-13%

Sensitivity to CO_2 price

As the carbon emission price has a significant effect on the overall system costs and mutual competitiveness of fossil-based generation, we also conducted a sensitivity analysis with a varying CO_2 price. The basic case described previously used 8 €/tCO_2 as the emission price, which is quite low and may have contributed to the increased coal use. In the sensitivity analysis, we used additional emission prices of 20 and 60 €/tCO_2. The sensitivity analysis was conducted for both levels of wind power (20/40 TWh), whereas for curtailment only two cases were studied: no curtailment and curtailment with the "Wind-following" method with a curtailment rate of 30 %. This particular curtailment case was chosen as an example because this method resulted in the highest amount of curtailed wind power (6/12 TWh) to be directed to the P2H scheme.

Figure 3 illustrates the results of the CO_2 sensitivity analysis on the primary energy composition. The results clearly show that the amount of coal decreased with an increasing CO_2 price. Simultaneously, the power export also decreased and power import increased, indicating that the power production from coal-CHP plants decreased. With a higher CO_2 price, the heat production shifted to heat pumps, using either curtailed wind power, or power import in the lower 20 TWh wind

case. Also here, the CO_2 emissions decrease with respect to the coal use (-19 to -3 $MtCO_2$, i.e. -39% –- +6% from reference). The abnormal increase in coal use in the leftmost case of Figure 3 can be explained by the simultaneously decreasing peat use.

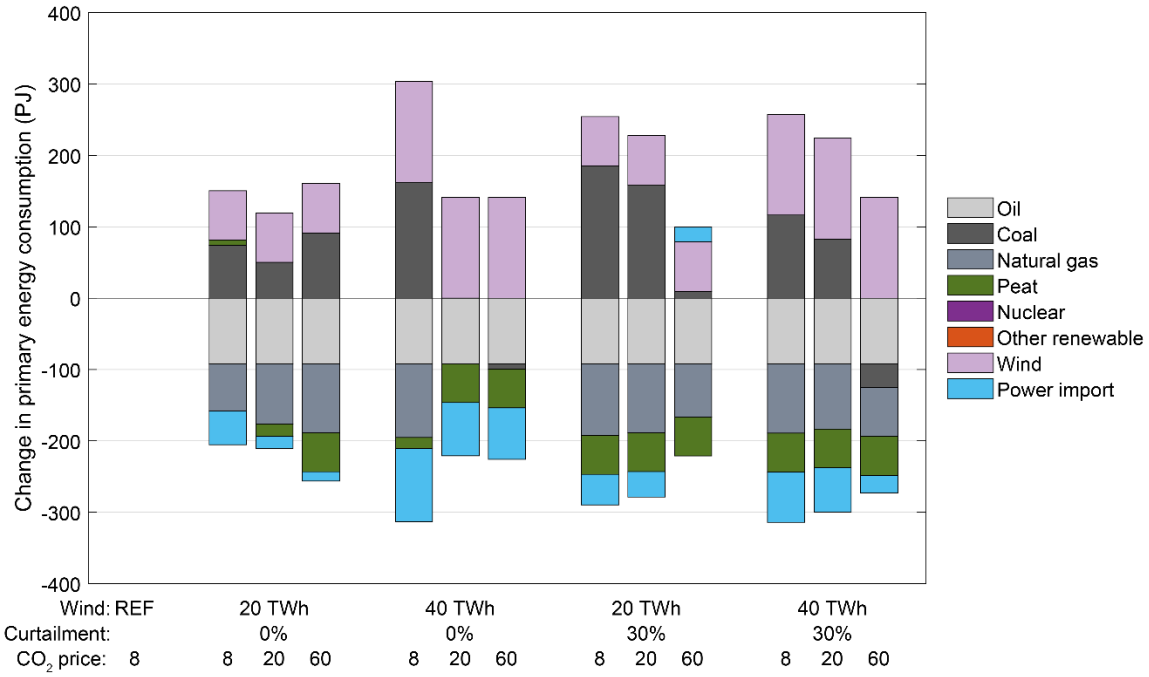

Figure 3: CO_2 price sensitivity: change in primary energy compared to the national reference case. The values of the 8 €/tCO_2 cases are the same as in Figure 2.

The changes in the annual system costs is shown in Table 4. Unsurprisingly, the annual costs increased with increasing CO_2 price, and with the highest CO_2 cost (60 €/tCO_2) both the uncurtailed and curtailed cases have higher annual costs than the reference case. This means that even though the increasing carbon price decreased the use of carbon-emitting coal, the subsequent decrease in CO_2 emissions was not enough to compensate the effect of the higher CO_2 price in overall annual costs.

Table 4: CO_2 price sensitivity: change in annual system cost compared to the national reference case.

		CO_2 price (€/tCO_2):		
Wind power before curtailment	Curtailment rate	8	20	60
20 TWh	0%	-13%	-7%	12%
	30%	-17%	-10%	10%
40 TWh	0%	-14%	-2%	17%
	30%	-15%	-9%	8%

Sensitivity analysis on bioenergy and nuclear power

As the final note, we tested the sensitivity of the results against the optimisation variables. In the two previous analyses, the level of nuclear power and bioenergy was kept constant. In this last national analysis, we include nuclear power and bioenergy as optimisation variables, and their maximum limits are given in Section 2.1. The analysis is conducted for both wind levels (20/40TWh) and for three curtailment rates (0/10/30%) with the “Wind-following” curtailment method.

The changes in the primary energy composition are shown in Figure 4. Compared with the previous cases with only fossil fuels as variables, in the new cases with nuclear and bioenergy included, the level of nuclear power increased in most cases, while the level of biomass use slightly decreased. In the uncurtailed cases, nuclear power did not increase, suggesting that the uncurtailed wind power was enough to provide the country’s power demand cost-effectively, but in the cases with wind power curtailment, the nuclear production increased by 13 TWh, which was also the maximum limit. This increase in nuclear production consequently decreased the power production from CHP plants, which in turn shifted the heat production from CHP plants to heat pumps, using the curtailed wind power. However, in two cases the level of coal-CHP remained high, even despite the nuclear increase, suggesting that most coal-CHP electricity production was exported at a comparably high price. As for the changes in bioenergy, the use of industrial wood residue increased, while the use of firewood decreased, resulting in a small 20 TJ decrease in overall bioenergy consumption.

The changes in the annual system costs are shown in Table 5. In most cases, allowing variable nuclear power and bioenergy, the annual cost decreased. Overall, this sensitivity analysis implies that adding nuclear power might be cost-effective, especially if combined with the P2H scheme utilizing curtailed wind power, but will also depend on the actual construction cost of nuclear power which has a large spread (we used 4,000 €/kW for the investments).

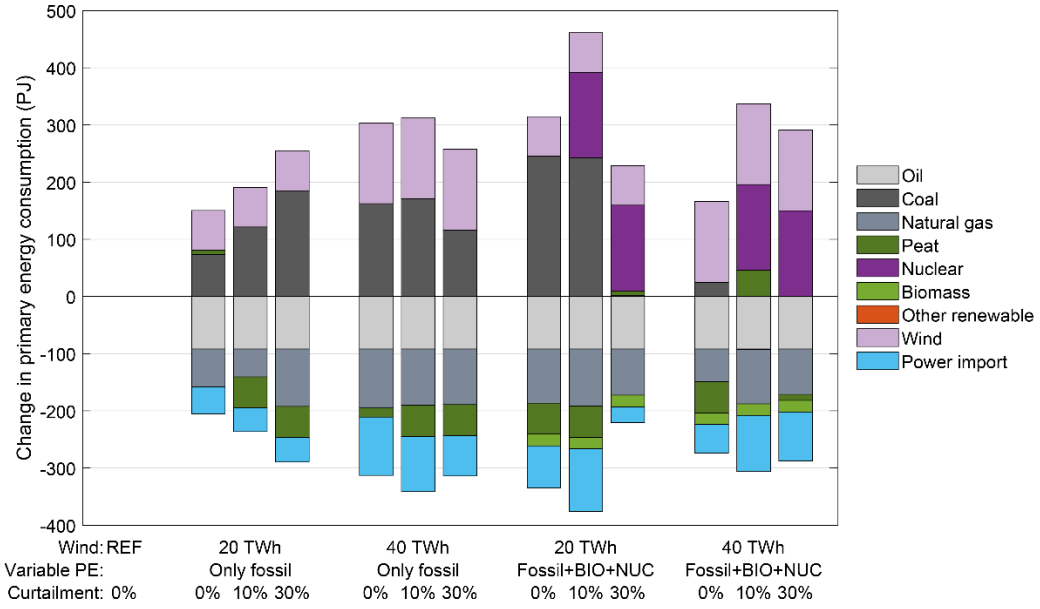

Figure 4: Nuclear and bioenergy sensitivity: change in primary energy compared to the national reference case. The values of the "Only fossil" cases are the same as in Figure 2.

Table 5: Nuclear and bioenergy sensitivity: change in annual system cost compared to the national reference case.

Wind power before curtailment	Curtailment rate	Variable primary energy: Only fossil	Variable primary energy: Fossil + nuclear + bioenergy
20 TWh	0%	-13%	-21%
	10%	-13%	-23%
	30%	-17%	-19%
40 TWh	0%	-14%	-12%
	10%	-15%	-17%
	30%	-15%	-19%

3.2. City case (Helsinki)

Two scenarios are defined to investigate the effect of the wind curtailment on optimal operation of energy production system in Helsinki. The main output of the optimisation model is the yearly fuel cost and CO_2 emissions, which are compared against different curtailment methods and wind energy shares. As reference case we consider the present energy system of Helsinki; the nominal outputs of the existing power plants and boilers linked to the district heating system are presented in Table 6.

Table 6: Nominal output of energy plants in Helsinki (MW).

	CHP gas	CHP coal	CHP coal	Boiler gas	Boiler Oil	Boiler Coal	HP
Power	630	220	160	---	---	---	---
Heat	580	420	300	360	1900	180	90

In the first scenario, 750 MW and 1,500 MW of wind power is added to the power system, representing 43% and 86% of the yearly electricity demand in Helsinki, respectively. The curtailed wind power is used only in a limited way for heat production through the existing 90 MW heat pump capacity. Three curtailment strategies explained in Section 2.3 were used. The optimisation results are shown in Table 7, which presents the yearly fuel cost and CO_2 emissions for the different cases.

Cases 5 and 11 with the highest curtailment percentage of wind power yield the lowest yearly costs (-10%) and emissions (-2%), but the differences to the existing system are not that large even with a high wind share. Figure 5 shows the details on these cases. It is noteworthy to observe that in the present case, the electricity production exceeds with almost 40% the electricity consumption, but heat production and consumption is in balance. This is because of use of CHP plants which

has a varying power-to-heat ratio, e.g. for gas-CHP 1:1 and coal-CHP 1:2. As heat demand need always be met, this may sometimes lead to power oversupply, which is sold to the Nordic electricity market.

Table 7: Annual CO_2 emissions and fuel cost for different wind power and curtailment schemes in the present energy system of Helsinki.

Case	Curt	Curtailment strategy	Wind MW	Emissions $ktCO_2/yr$	Fuel cost M€/yr
Present	0	---	---	2264	304
1	10%	Peak-shaving	750	2267	280
2	10%	Wind-following	750	2239	276
3	10%	Load-following	750	2264	279
4	30%	Peak-shaving	750	2265	280
5	30%	Wind-following	750	2217	275
6	30%	Load-following	750	2263	279
7	10%	Peak-shaving	1500	2255	271
8	10%	Wind-following	1500	2234	273
9	10%	Load-following	1500	2252	274
10	30%	Peak-shaving	1500	2255	270
11	30%	Wind-following	1500	2217	273
12	30%	Load-following	1500	2251	274

Increasing wind in an energy system such as Helsinki with CHP needs special consideration of the heating side as well. The results in Figure 5 clearly indicate that wind would mainly replace gas, as coal contributes more to heat than electricity. With 1,500MW wind, the electricity and heat production by the gas CHP shows a reduction of 24% and 20%, respectively. Also, the share of exported electricity will increase when wind is increased, as CHP is still needed to meet the heat demand. Increasing wind from 750 to 1,500 MW does not change much the emissions or fuel costs, and almost all of the added wind (750→1,500 MW) would go to power export. The price of coal (€43/MWh) is cheaper than gas (€56/MWh), which also slightly favours coal. We did not include emissions costs here (0 €/MWh), which in theory would also favour slightly gas. However, in the Helsinki case adding a €15/tCO_2 emission cost would not in practice change the results, because of the need to balance the heat demand. The role of curtailed wind power and P2H remains here small, as the heat conversion rate was limited to the heat pump capacity only, but we observe that the heat pumps would mainly be run with curtailed wind power.

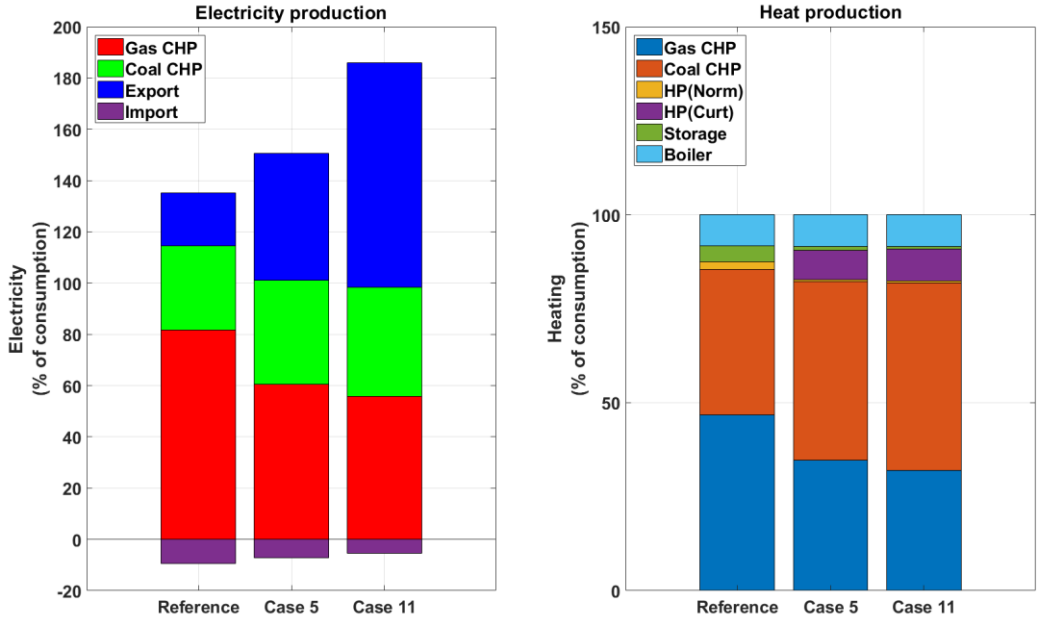

Figure 5: Electricity production and heat production of the power plants for cases 5 and 11 from Table 7.

In the second scenario, P2H was strengthened by increasing the heat pump capacity to 1,500 MW to increase the utilization of curtailed wind power for heat production. The aggregated results for this case are listed in the Table 8 as with the first scenario. Comparing Table 7 (scenario 1) and Table 8 (scenario 2) indicates a major decrease in the CO_2 emissions and yearly fuel cost (CHP plants) as the utilization rate of wind power is much higher.

With 750 MW of wind power, the largest reduction in the fuel cost and CO_2 emission was reached with the load-following curtailment method with a 10% curtailment level (case 3). Compared to the reference system (see Present in Table 7) this would represent a 57% emission reduction and to the Modified in Table 8 45% respectively. Increasing the amount of wind

power to 1,500 MW, a “Wind-following” curtailment strategy with a 30% curtailment (case 11) shows the lowest fuel cost and emissions (-65% from Present and -55% from Modified).

Table 8: Annual CO_2 emissions and fuel cost for different wind power and curtailment schemes with a modified energy system (1,500 MW of heat pumps) of Helsinki.

Case	Curt	Curtailment scenario	Wind MW	Emissions $ktCO_2/yr$	Fuel cost M€/yr
Modified	0	---	---	1778	271
1	10%	Peak-shaving	750	1228	182
2	10%	Wind-following	750	1215	182
3	10%	Load-following	750	977	144
4	30%	Peak-shaving	750	1225	182
5	30%	Wind-following	750	1705	162
6	30%	Load-following	750	991	148
7	10%	Peak-shaving	1500	1029	151
8	10%	Wind-following	1500	971	181
9	10%	Load-following	1500	871	128
10	30%	Peak-shaving	1500	1000	147
11	30%	Wind-following	1500	804	119
12	30%	Load-following	1500	848	124

Figure 6 shows the detailed electricity and heat balance for cases 3 and 11 in the second scenario. Compared to the scenario 1 (Figure 5) with very limited P2H capability, we find that curtailed wind power could now be effectively be used through the 1,500 MW heat pump capacity to replace fossil fuels. Actually, now gas CHP would be preferred over coal-CHP, the share of which drops significantly from scenario 1. Followingly, also the amount of exported power from Helsinki would be much lower than in the scenario 1.

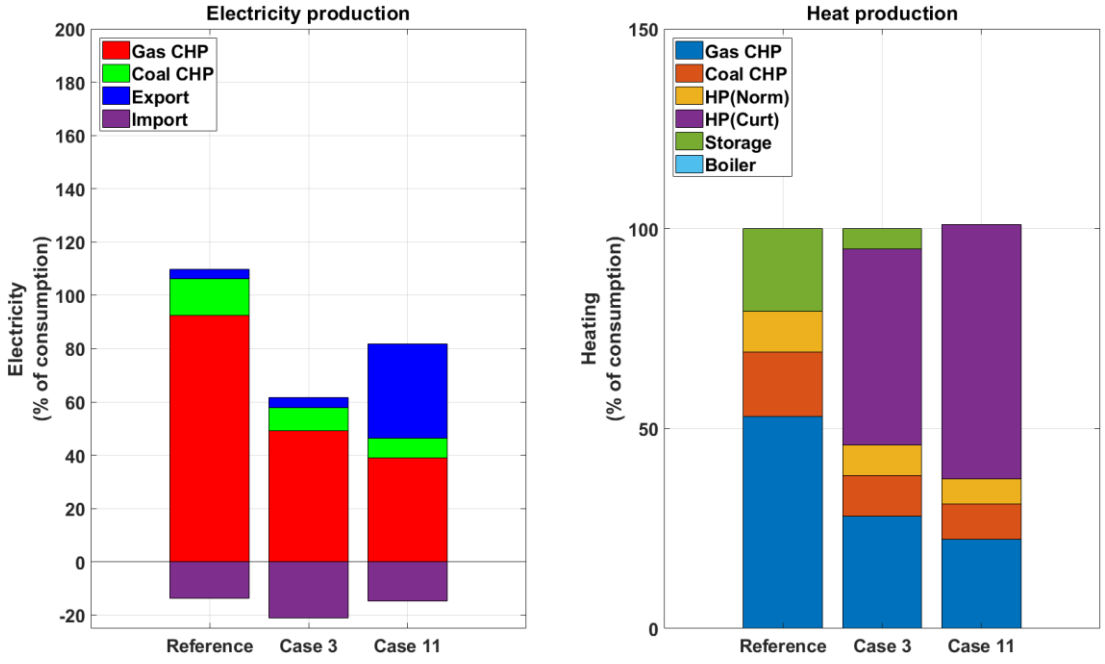

Figure 6: Electricity production and heat production of the power plants for cases 3 and 11 from Table 8.

In case 11, the electricity and heat production from the gas CHP reduces around 40% and 30% respectively from the reference (Modified). We also observe in Figure 6 that coal CHP remain almost at the same level for different curtailment and wind power share, which is explained by the important role of heat in the overall energy balance of Helsinki. In this scenario, the curtailed heat (wind+heat pump) covers over 60% of the yearly heat demand.

4. SUMMARY AND CONCLUSIONS

Here we have investigated the effects of different curtailment strategies of wind power and power-to-heat conversion (P2H) on the energy system. Two energy system topologies were considered, namely a national (Finland) and city (Helsinki) case. We used dynamic energy system models and optimisations as the method of the study.

One of the main conclusions from the analyses is that integration of wind power involves very complex energy system interactions, meaning that the impacts of wind and curtailment need to be analysed case by case. Fuel prices, market conditions and energy system limitations among others may significantly affect the outcomes from introducing large wind power and curtailment schemes. For example, we found that wind power was not always effectively used on national level even if curtailment and P2H were considered, but it rather led to increased export of power. To avoid such as a situation and revert the curtailed wind power to heating would require increasing the price of carbon emissions (€/tCO_2).

We observed that in the Helsinki city case, straightforward addition of wind power to an energy system with much CHP may not lead to wanted effects, e.g. emissions reductions, unless the energy system is considered as a whole, in particular the heating sector. Wind power replaces power generation, but in case of CHP this would also lead to reduced heat generation, which need to be compensated for. Incorporating a curtailment strategy with P2H and heat pumps could provide an effective solution to replace fossil-fuel-based CHP and result in major emission reductions. A straightforward integration of wind without such a strategy may lead to marginal impact only. The most effective strategy employed more heat pumps with a "Wind-following" curtailment and P2H strategy, which could cut well above half of the carbon emissions of heat and power production.

A "Wind-following" curtailment strategy with P2H delivers the most heat, whereas the "Peak-shaving" the least. With a "Load-following" strategy notable heat amounts are reached not until higher curtailment levels. The effects of the three strategies on the annual costs of the national energy system (Finland) and the present city-level system (Helsinki) were marginal, whereas if modifying the city energy system to more adoptive to P2H by introducing large heat pump schemes, would clearly give preference to a "Load-following" strategy ("Wind-following" was marginally better at high wind share and high curtailment only).

5. ACKNOWLEDGEMENTS

This work was supported by the Nordic Energy Research [grant 76084] and the Academy of Finland [grant 285353].

6. REFERENCES

EASAC, 2017. *Valuing dedicated storage in electricity grids*.

IEA, 2016. *Key Renewable Trends. Exerpt from¨Renewables Information*. *Renewables Trends*.

International Energy Agency, 2012. *Tracking Clean Energy Progress 2013*. *Technology*. doi: 10.1787/energy_tech-2014-en.

International Energy Agency, 2017. *World Energy Outlook 2017*. *International Energy Agency*.

Koltsaklis, N. E., Dagoumas, A. S. And Panapakidis, I. P., 2017. Impact of the penetration of renewables on flexibility needs. *Energy Policy*. Elsevier Ltd, 109(March), pp. 360–369. doi: 10.1016/j.enpol.2017.07.026.

Lund, P., 2012. Large-scale urban renewable electricity schemes – Integration and interfacing aspects. *Energy Conversion and Management*, 63, pp. 162–172. doi: 10.1016/j.enconman.2012.01.037.

Lund, P. D. *et al.,* 2015. Review of energy system flexibility measures to enable high levels of variable renewable electricity. *Renewable and Sustainable Energy Reviews*. Elsevier, 45, pp. 785–807. doi: 10.1016/j.rser.2015.01.057.

Lund, P. D., 2018. Capacity matching of storage to PV in a global frame with different loads profiles. *Journal of Energy Storage*, 18. doi: 10.1016/j.est.2018.04.030.

Mikkola, J. and Lund, P. D., 2016. Modeling flexibility and optimal use of existing power plants with large-scale variable renewable power schemes. *Energy*, 112, pp. 364–375. doi: 10.1016/j.energy.2016.06.082.

Pilpola, S. and Lund, P. D., 2018. Effect of major policy disruptions in energy system transition: Case Finland. *Energy Policy*, 116, pp. 323–336. doi: 10.1016/j.enpol.2018.02.028.

Shell International BV, 2018. *Shell and the Energy Transition*.

Statistics Finland, 2017. *Energy table service*. Available at: http://pxweb2.stat.fi/sahkoiset_julkaisut/energia2015/html/engl0000.htm (Accessed: 21 August 2016).

Statistics Finland, 2018. *Cold weather raised energy consumption in housing in 2016*.

United Nations Framework Convention on Climate Change, 2015. *Adoption of the Paris Agreement: Proposal by the President to the United Nations Framework Convention on Climate Change*. doi: 10.1002/bse.1835.

385: Clean energy transition – focus on the heating sector

Vahid ARABZADEH, Sannamari PILPOLA, Peter D. LUND

Aalto University, School of Science, New Energy Technologies Group,
P.O. Box 15100, FI-00076 Aalto, Espoo, Finland,
vahid.arabzadeh@aalto.fi and sannamari.pilpola@aalto.fi

The European Union has planned to reduce the greenhouse gas emissions about 80% to 95%, and to increase the share of renewable energy to achieve the share of renewable energy at least 55% in the gross final energy consumption by 2050. As most of the end-use energy in Europe, or well above 60 %, is for heating, these targets will put more stress on the heating sector. So far, much of the focus in the emission reduction has been on the electricity sector. Therefore, the efficient coupling of renewable energy integration to heat and heating will be part of an optimal clean energy transition. This paper develops optimisation-based models on national (Finland) and sub-national level (Helsinki) to include the heating sector in an energy transition. The models are based on transient simulation of the energy system, coupling VRE through power-to-heat schemes to the heating energy production system. We used large-scale wind power schemes as VRE in both cases. The results indicate that due to different system limitations and boundary conditions, stronger curtailment strategies accompanied by large heat pump schemes would be necessary to bring a major impact in the heating sector. On a national level, the best cases considered were able to produce wind-derived heat around 40% of the annual heat demand. On a city level, fossil-based heat and power production (CHP) could be significantly reduced leading in best cases close to 70% CO2 emission reductions. Though the results are indicative and are site dependent, they indicate major opportunities for VRE in sectoral coupling to heat production.

Keywords: power-to-heat, energy system flexibility, urban energy system

1. INTRODUCTION

Climate change mitigation relies much on renewable energies and their integration into the prevailing energy system (International Energy Agency, 2017). Also, integration of renewables on a different scale from stand-alone buildings to cities and nations or regions will be necessary. The challenges ahead are huge as major part of the carbon emissions needs to be eliminated by the middle of this century. For example, the European Union has planned to reduce its emissions by about 80% to 95% and to reach a 55% share of renewable energy in final energy consumption by 2050 (Oettinger, 2012).

While the clean energy transition is often dominated by variable renewable electricity sources such as solar PV and wind power for power production, the future focus needs also to better include the heating sector, as most of the final energy use is in the form of thermal energy. For example, in Finland over 80% of the final energy use of households is heating (Statistics Finland, 2018). Therefore, the role of the built environment in the energy transition will also be important; measures of interest include building energy efficiency and on-site renewable energy generation (Lund, 2012; Cao et al., 2013; Kayo et al., 2014).

Another interesting development is to increase energy system flexibility which may include curtailing VRE for better energy system management, but also to supply heat through power-to-heat (P2H) conversion (Lund et al., 2015). One may foresee 'oversizing' VRE for the power sector needs and use the surplus or curtailed power for heating purposes. This would also mean increased electrification of the heating sector, and if linked to e.g. heat pumps, providing large amounts of renewable-derived heat to end-use sectors. This kind of sectoral coupling of VRE would increase the energy system flexibility, but also reduce emissions in the heating sector as well. Other measures such as energy storage and demand response could also be used in this context (Arabzadeh et al., 2018; Lund, 2018).

The purpose of this paper is to investigate the effects of VRE coupling on the heating sector. The aim is to quantify the effects of large-scale wind power with curtailment, P2H conversion, and heat pumps on national and city level power and heat production. As the national case, we use Finland to see how the heat production mix would change with such schemes. For the sub-national level, we use Helsinki city. In the case of Helsinki, the interest is to see how the existing CHP-based energy production system is changed, including the running costs and emissions on a yearly scale. Also, the effects of different energy system limitations and building energy efficiency schemes are analysed. The analyses are done with dynamic energy system simulation models.

2. METHODOLOGY

The methodology employed in the study is based on an economic optimisation of the energy system, i.e. finding the system configuration which yields the minimum cost under different boundary conditions and limitations. We consider both national (Finland) and sub-national (Helsinki city) levels of the energy production system, for which different optimisation techniques will be applied.

As clean energy transitions often involve large renewable electricity usage, we take here as the starting-point a large wind power scheme. This will be accompanied by different curtailment strategies and power-to-heat conversion to produce carbon-free heat, which is of importance in northern latitudes. Curtailment may also be justified by energy system limitations and power market conditions.

2.1. National model

The national-level analysis is done with a macro-scale energy system model (Pilpola and Lund, 2018). The model includes all aspects of an energy system, including electricity, heat, and fuel. The model employs a 1-hour step for electricity and heat, while fuel demands are considered on an annual scale. The model seeks for a cost-optimal solution of the energy system while keeping the supply-demand balance. The optimisation problem is defined as *Minimise* Total Annual Cost = $\sum_{t=1}^{tech}$(Investment Cost$_t$ + O&M$_t$) + $\sum_{f=1}^{fuels}$ Fuel Cost$_f$ + Net cost of power import + Emission cost . The variables in the optimisation are the amounts the primary energy sources and the amount of conventional conversion, i.e. combined heat and power (CHP), separate production, and heat pumps (HP). The model uses 2013 as the reference year for input data. A more detailed description of the input data can be found in (Pilpola and Lund, 2018). The reference case for the heating sector of interest is in Table 1.

Table 1: Heat production in Finland 2013 (Statistics Finland, 2017).

	CHP-District heating	CHP-Industrial	Separate thermal production	Residential fuel boilers	Residential electric boilers	Heat pumps	**Total**
TWh	32.6	3.8	14.6	20.2	14.4	4.6	**90.3**
%	36	4	16	22	16	5	**100**

The hourly distribution of the conventional production, such as CHP, is based on historical production data (2013) to mimic the hourly distribution, but their values are scaled to the yearly amounts (PJ, TWh) resulting from the optimisation. The operation of power-to-heat conversion is rule-based. The level of industrial CHP and residential heat production (fuel and electric boilers), which accounted for 43% of the heat demand in 2013, are assumed non-variable. The model employs three methods for wind power curtailment (see Section 2.3). The model also assumes 60 GWh thermal storage available in the Finnish district heating networks.

2.2. Sub-national model

The objective of the sub-national model is to reduce the marginal costs of the local energy production system while introducing variable renewable electricity. The cost function is a sum of the production costs, balancing costs, storage costs, and revenues from electricity sales to the Nordic power exchange, or, *Minimise* $\sum_t$ (Production costs+Balancing costs+Storage costs-Revenues from sales). The details of the model are described in (MIKKOLA and LUND, 2016). We also incorporated several modifications to the model to enable a heating sector analysis as follows: Firstly, a limitation for heat storage charging and discharging was defined. Secondly, to account for possible heat source restrictions in case of large heat pump schemes with P2H conversion, we defined a dynamic COP, which drops when entering the peak heat demand period (HP has a COP=3 whenever the heat demand is <50% of the peak heat demand; COP=2 for heat production between 50% and 70% of the peak demand; COP=1, i.e. HP is replaced with an electric boiler, when heat demand >70% of the peak demand). The annual heat demand in Helsinki (60°N) is 6.1 TWh and the electricity use is 4 TWh. Two energy efficiency strategies in buildings will be considered leading to 8% and 16% lower heating demand, respectively. The heat demand profiles will be modified accordingly in these cases by using a scaled U-value for the temperature-dependent part of the heat load. The details of the present energy production plants in Helsinki are shown in Table 2 (MIKKOLA and LUND, 2016).

Table 2: Nominal output of energy plants in Helsinki (MW).

	CHP gas	CHP coal	CHP coal	Boiler gas	Boiler Oil	Boiler Coal	HP
Power	630	220	160	---	---	---	---
Heat	580	420	300	360	1900	180	90

2.3. Curtailment cases

Three different methods for wind energy curtailment will be employed. ‘’Peak-shaving” curtailment is based on shaving a fixed percentage of the wind power peaks. In “Wind-following”, wind power is curtailed with a constant fixed percentage. In “Load-following”, wind power is curtailed above a fixed level (percentage) of the electrical load. The curtailed wind power is used to strengthen the power-to-heat (P2H) strategy - all curtailed wind is directed to heat pumps. As wind power is a renewable and zero-marginal-cost resource, we argue that the heat produced by this “forced” heat pump operation offers a renewable and low-cost, albeit non-dispatchable, source of heat, which in turn may have the possibility to decrease the marginal costs of energy production. In the sub-national level, the forced implementation of the HP, limits the available HP capacity for the dispatch optimisation.

3. RESULTS AND DISCUSSION

In this section, we analyse the effects on the heat production system when applying large wind power schemes and curtailment with the P2H conversion. On the national level, the effect of each curtailment method is discussed in term of system operation and energy conversion. On the sub-national level, the focus is on the heating demand profile modification through building energy efficiency measures in addition to heat resource limitations for heat pumps.

3.1. National case

In the national case, the three wind power curtailment strategies described in Section 2.3 resulted in very different levels of curtailed wind power shown in Table 3. The “Peak-shaving” yielded the least heat, even at high curtailment level. The “Load-following” did not produce any heat with 20 TWh of wind, but clearly more with 40TWh than the “Peak-shaving”

strategy. “Wind-following” gave the highest level of curtailment: With 30% curtailment and 40 TWh of wind resulted in 36 TWh of heat production, which would account for 40% of the total annual heat demand. Note that the curtailed wind power was used in heat pumps (COP=3).

Table 3: Heat pump production with curtailed wind power in the national case.

		Curtailment method:		
Wind power before curtailment (TWh)	Curtailment rate (%)	Peak-shaving (TWh)	Wind-following (TWh)	Load-following (TWh)
20 TWh	10	0.1	6.0	0.0
	30	2.2	18.0	0.0
40 TWh	10	0.1	12.0	4.6
	30	4.3	36.0	14.0

Figure 1 shows the change in the heat production caused by the different curtailment and P2H schemes. Almost all cases exhibited increased CHP production and decreased separate heat production. As this was also observed in the cases without curtailment and P2H, it can be stated that this effect was caused by the overall cost optimisation, suggesting that

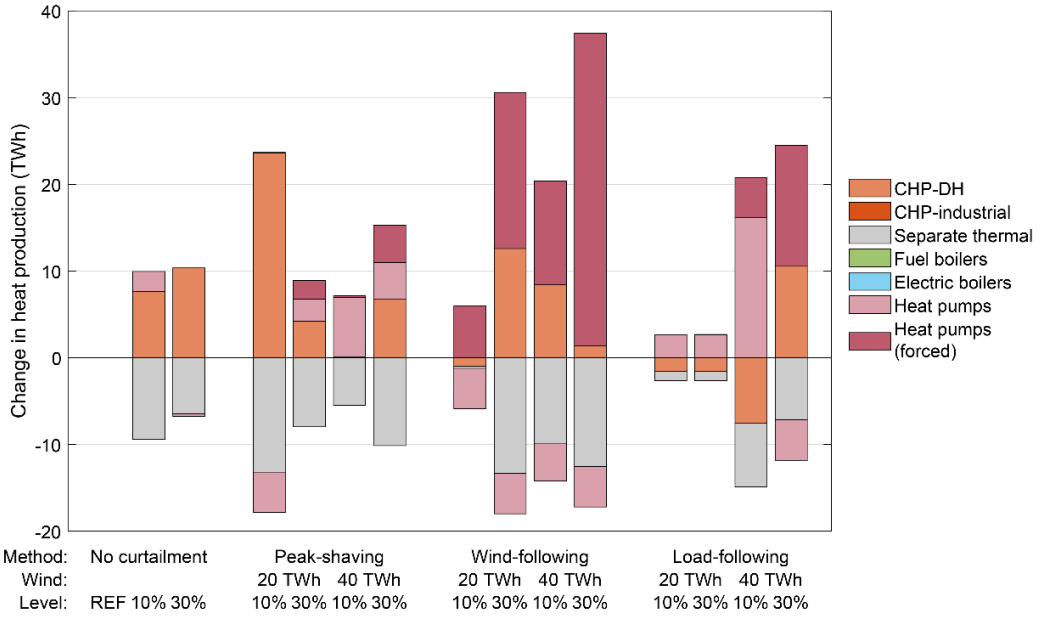

Figure 1: Change in the heat production compared to the national reference case (Finland 2013). Heat pump operation is divided into normal heat pump operation and “forced” heat pump operation using the curtailed wind power.

with increasing wind power, replacing separate heat boilers with CHP may be cost-effective even without any additional P2H measures. However, including curtailment+P2H would emphasise the role of the heat pumps, i.e. the HP heat production increased in all cases with wind power curtailment.

Figure 1 also illustrates that in cases of a higher amount of wind-power driven (“forced”) heat pump operation, the net change of heat production is positive. As the overall heat demand stayed constant in all cases, this positive net change suggests that part of the additional heat production was wasted. In the “Wind-following” curtailment case, heat production was up to 20 TWh higher than the demand. A part of the excess heat production may appear in the losses of thermal storage. But clearly forced, non-dispatchable heat pump operation was not always able to match the heat demand which leads to the oversupply of heat. Some of the surplus heat could, however, disappear if the COP of the heat pumps were lower than anticipated, which could occur in particular during the peak heating season.

3.2. Sub-national case (Helsinki)

For the sub-national level, the effect of heating demand improvement, wind curtailment, and heat source limitation are investigated through four scenarios:

1. Current energy system (90MW HP, no curtailment, no heat resource limitation);
2. 1500MW of heat pumps, no curtailment, no heat resource limitation;
3. 1500MW of heat pumps, 30% curtailment, no heat resource limitation;
4. 1500MW of heat pumps, 30% curtailment, dynamic COP (heat source limitation).

In all scenarios, building energy efficiency improvements are applied: present building U-value is improved by 10% and 20% leading to 8% and 16% lower heat demand, respectively. The necessary measures could typically involve better thermal insulation, improved heating control and/or better windows in the building stock. Moreover, 750 MW and 1,500 MW of wind power will be introduced to the energy production system, representing 43% and 86% of the yearly electricity demand in Helsinki, respectively. For comparison, the yearly fuel costs and CO_2 emissions are compared with the present system with no measures, for which the system parameters are given in Table 2. The results for Scenario 1 are shown in Table 4.

Table 4: Annual CO_2 emissions and fuel cost for different building energy efficiency improvements in the present energy system of Helsinki (Scenario 1).

Case	Efficiency Improvement (%)	Wind (MW)	Fuel cost (M€/yr)	Emissions ($ktCO_2$/yr)
Present system	---	---	327	2271
1	---	750	296	2232
2	---	1500	288	2210
3	8	750	273	2137
4	8	1500	264	2112
5	16	750	250	2027
6	16	1500	239	2000

Wind power alone would mainly reduce the gas use, but not coal, because of the need to meet the heat demand (coal-CHP produces more heat than gas-CHP). Also, the price difference between coal (€43/MWh) and gas (€56/MWh) would slightly favor coal. No emission cost was applied, but e.g. a 15 €/MWh CO_2 cost would not change the results due to these system limitations. Wind power would therefore mainly reduce fuel costs, but marginally the emissions in Helsinki case.

Building energy efficiency measures in cases 4 and 6 gave the best results with cost reductions of 19% and 26% and emissions decrease of 7% and 12%, respectively. Detailed heat and electricity production is shown in Figure 2, which clearly demonstrates that most of the wind power would go to export to the Nordic power exchange. Note that Helsinki presently produces more electricity than it needs, i.e. some 40% is sold to the market (export).

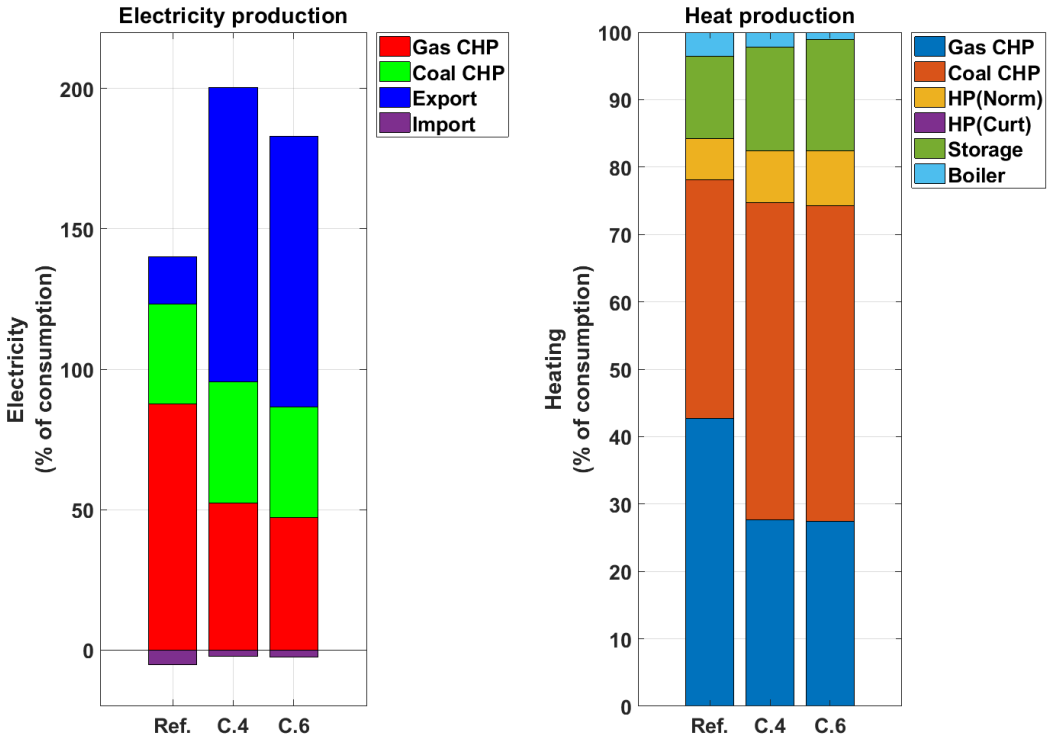

Figure 2: Electricity production and heat production of the power plants with different building energy saving levels for Scenario 1 (cases 4 and 6 in Table 4).

In Scenario 2 1,500 MW of heat pumps are added to Scenario 1. Neither curtailment nor limitation of heat sources for heat pumps is included here. Table 5 presents the key results.

Table 5: Annual CO_2 emissions and fuel cost for building energy efficiency improvements and 1,500 MW of heat pumps (Scenario 2).

Case	Efficiency Improvement (%)	Wind (MW)	Fuel cost (M€/yr)	Emissions ($ktCO_2$/yr)
Present system	---	---	327	2271
1	---	750	204	1270
2	---	1500	162	1010
3	8%	750	194	1234
4	8%	1500	154	983
5	16%	750	184	1201
6	16%	1500	146	957

Adding a large heat pump scheme would significantly reduce the yearly fuel costs and emissions, whereas adding building energy efficiency measures on the top of that had fewer effects. In the best case 6, the fuel costs and emission dropped by 55% and 58%, respectively. Figure 3 demonstrates details of the energy production system for the Scenario 2. There is no difference between case 4 and 6, which indicates that reducing the heat demand of more than 10% does not have any major effect on the operation of the energy production system. Integration of the wind power reduces the gas electricity production by about 42% and the coal electricity production about 81%. The gas heat production is reduced by 31% and coal heat production is cut 77%. The HP heat production increases by 70%. The storage use increased by 70%.

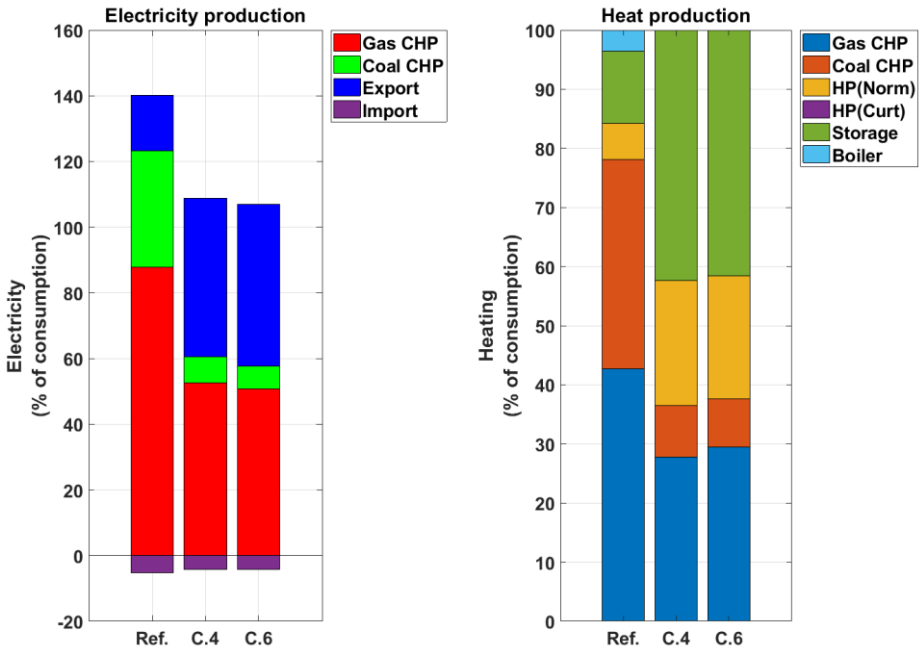

Figure 3: Electricity production and heat production of the power plants with different building energy saving levels and 1,500 MW of heat pumps for Scenario 2 (cases 4 and 6 in Table 5).

In Scenario 3, wind energy curtailment was introduced to Scenario 2. The resulting fuel cost and emissions are in Table 6.

Table 6: Annual CO_2 emissions and fuel cost for building energy efficiency improvements, 1,500 MW of heat pumps, and 1,500 MW of wind power with curtailment (Scenario 3).

Case	Efficiency Improvement (%)	Curtailment method	Curt (%)	Fuel cost (M€/yr)	Emissions ($ktCO_2$/yr)
Present system	---	---	---	327	2271
1	---	Peak-shaving	10	145	950
2	---	Peak-shaving	30	142	925
3	8	Wind-following	10	140	752
4	8	Wind-following	30	118	727
5	16	Load-following	10	111	727
6	16	Load-following	30	110	710

Figure 4 demonstrates the details of the energy production system. The largest reductions in the fuel cost and emission were for case 6, 66% and 68%, respectively when the “load-following” curtailment method was used, though the difference to “wind-following” curtailment was small. The heat production by coal was dramatically cut to less than 10% of yearly heat production (-84%); the gas use dropped below 30% (-47%), respectively. The reduced coal and gas use lead to significantly reduced emissions (66-68% from the present). Heat pumps are the dominating heat production method in cases 4 and 6, which leads to a slight increase in electricity imports.

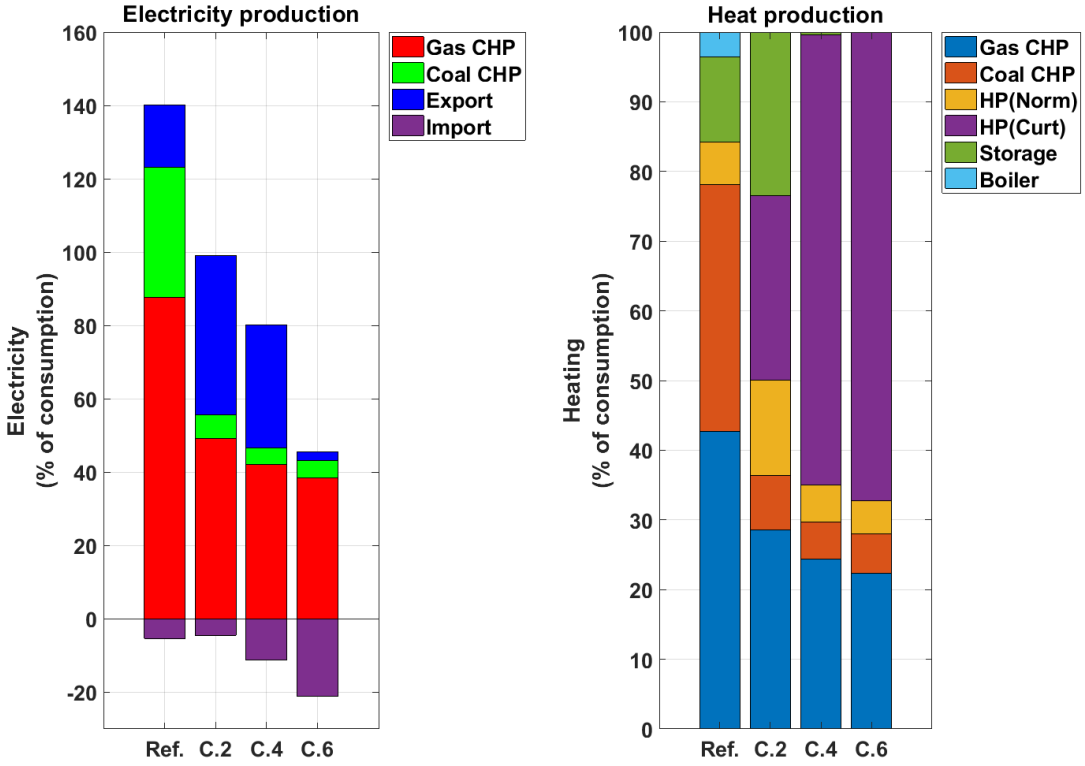

Figure 4: Electricity production and heat production of the power plants with different building energy savings, 1,500 MW of heat pumps, and wind curtailment for Scenario 3 (cases 2, 4 and 6 in Table 6).

In Scenario 4 we added a heat source limitation to heat pumps by using a dynamic COP explained earlier. An electric boiler with a maximum output of 1,500MW (equal to COP=1) was therefore added to the energy production system. Table 7 presents the results for Scenario 4.

Table 7: Annual CO_2 emissions and fuel cost for energy system with a HP with capacity as function of the heat demand (Wind energy=1500MW and curtailment = 30%) (Scenario 4)

Case	Efficiency Improvement (%)	Curtailment method	Fuel cost M€/yr	Emissions $ktCO_2$/yr
Modified system	0	---	298	1843
1	0	Peak-shaving	159	994
2	8	Peak-shaving	150	955
3	16	Peak-shaving	141	922
4	0	Wind-following	139	855
5	8	Wind-following	128	802
6	16	Wind-following	117	750
7	0	Load-following	136	841
8	8	Load-following	127	805
9	16	Load-following	119	769

The reference case in this scenario is a modified system since the nominal maximum HP output is set as 1500MW. For each curtailment method, the lowest fuel cost and emission are achieved with the highest heat demand improvement at

16% (Case 3, 6 and 9). The detail of the energy production for the scenario 4 is shown in Figure 5. In this scenario, the electric boiler is used in cases 6 and 9 due to heat source limitations. In case 9, with the load-following curtailment, there is no storage use at all. It seems that increasing the wind energy share would reduce the contribution of the heat storage in this case. Both the share of gas and coal in heat production is halved; the share of gas comes down to 25% and coal to 5% of the yearly heat production. In power production, we see the similar trend: the share of gas power production is halved to 50% of power production and coal 5%, respectively. Due to the heat resource limitation, a part of the heat production from curtailed wind power is supplied by the electric boiler. For the load-following curtailment (case 9), the electric boiler contribution is 18%.

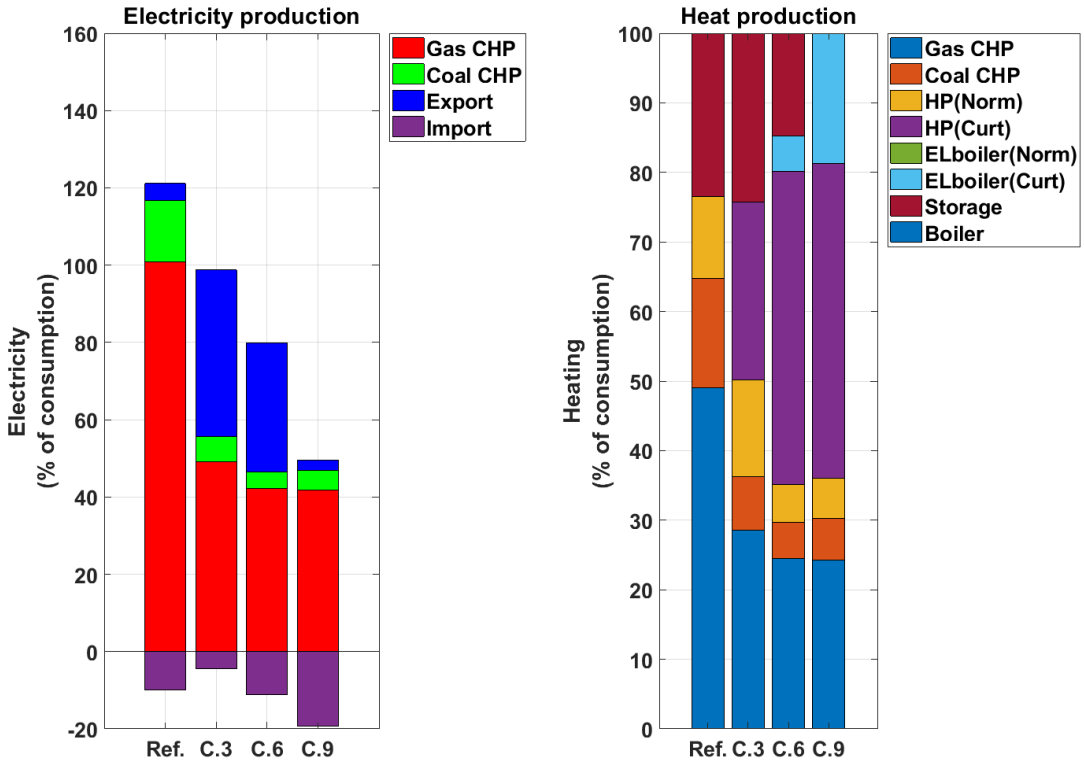

Figure 5: Electricity production and heat production of the power plants with different building energy savings, 1,500 MW of heat pumps, wind curtailment, and dynamic heat pump COP for Scenario 4 (cases 6 and 9 in Table 7). The reference system is here a modification of the present system.

For the area marked as 1 in the right side, due to heat source restriction, electric boiler starts to produce heat when there is not enough heating resource for the HP. Moreover, with the curtailed heat, the heat production by coal and gas CHP could be tackled.

4. SUMMARY AND CONCLUSIONS

In this paper, we have studied the sectoral coupling of VRE to the heating sector on a national (Finland) and city (Helsinki) level. For VRE, we used a large wind power scheme to which different curtailment & P2H strategies, building energy efficiency measures, and heat pump schemes were attached. The effects to the existing energy system were analysed with dynamic energy system models.

We observed that national (macro) and city (micro) level effects are very different. On the national scale the system inertia is typically larger and also a spatiotemporal integration of VRE is more ideal. Therefore, a sectoral coupling of VRE to heating sector produced larger impacts. The amount of VRE-based heat strongly depends on the type of curtailment strategy chosen, e.g. mere 'peak-shaving' would typically produce the least heat and 'wind-following' the most. The use of heat pumps with curtailment was important to provide leverage to electricity in heating. The most effective curtailment strategy (30%) with a heat pump P2H conversion were able to cover up to 40% of the yearly heat demand with a 40 TWh wind power in the energy system (corresponding to 47% of the yearly electricity consumption).

In the city-level analyses, the real dynamic limitations were better present, also because of the 10-min time steps used. Adding wind power as such to Helsinki case with a CHP dominated energy system, would just marginally change the energy system as most of the wind power would go to export and replace some gas-CHP, but not coal-CHP which is more important on the heat production side. This means that VRE integration would also need to better account for the heating side as well. A strategy with curtailment and heat pumps turned out to be a better case for Helsinki, which was able to cut coal and gas use, leading to main emission reductions. For an optimisation point of view, improving the building energy

efficiency from 10 to 20% of yearly heat demand did only marginally reduce the annual fuel costs and emissions, which again is a reflection of the system dynamics. With a 1,500 MW wind power scheme (corresponds to 86% of the yearly electricity use in Helsinki) and the 'best' curtailment strategy (Scenario 3 and 4), wind power and wind-power derived heat were able to radically modify the existing use of the fossil-based CHP plants, which lead to close 70% emission reductions, while still securing the operation of the energy system.

With large heat pump schemes, the question of heat source adequacy becomes highly relevant, in particular during the main heating period in the winter. In the national-level simulations, we used a constant COP for the heat pump, which could underestimate this issue. However, with high curtailment rates, we found that a lot of surplus heat in excess of heat demand was produced, which could compensate for the heat deficiency. In the case of Helsinki, we also considered a dynamic COP which accounts for heat source limitations, replacing HP use with an electric boiler during peak demand. In the scenario 4, implementing the wind curtailment for P2H and improving the building efficiency, cut the fuel cost and emission 60% and 58%.

5. ACKNOWLEDGEMENTS

This work was supported by the Nordic Energy Research [grant number 76084] and the Academy of Finland [grant number 285353].

6. REFERENCES

Arabzadeh, V., Alimohammadisagvand, B., Jokisalo, J., Siren, K., 2018. A novel cost-optimizing demand response control for a heat pump heated residential building. *Building Simulation*, 11, pp. 533-547.

Cao, S., Hasan, A., Siren K., 2013. On-site energy matching indices for buildings with energy conversion, storage and hybrid grid connections. *Energy and Buildings*, 64, pp. 423-438.

International Energy Agency, 2017. World Energy Outlook 2017. *International Energy Agency*.

Kayo, G. Hasan, A. Siren, K., 2014. Energy sharing and matching in different combinations of buildings, CHP capacities and operation strategy. *Energy and Buildings*, 82, pp. 685-695.

Lund, P., 2012. Large-scale urban renewable electricity schemes – Integration and interfacing aspects. *Energy Conversion and Management*, 63, pp. 162–172.

Lund, P. D. *ET AL.*, 2015. Review of energy system flexibility measures to enable high levels of variable renewable electricity. *Renewable and Sustainable Energy Reviews*. Elsevier, 45, pp. 785–807.

Lund, P. D., 2018. Capacity matching of storage to PV in a global frame with different loads profiles. *Journal of Energy Storage*, 18, pp. 218-228.

Mikkola, J. and Lund, P. D., 2016. Modeling flexibility and optimal use of existing power plants with large-scale variable renewable power schemes. *Energy*, 112, pp. 364–375.

Pilpola, S. and Lund, P. D., 2018. Effect of major policy disruptions in energy system transition: Case Finland. *Energy Policy*, 116, pp. 323–336.

Oettinger G., 2012, Energy roadmap 2050. 1st ed. Belgium: Publications Office of the European Union.

Statistics Finland, 2017. *Energy table service*. Available at: http://pxweb2.stat.fi/sahkoiset_julkaisut/energia2015/html/engl0000.htm (Accessed: 21 August 2016).

387: The low-carbon network consumption behaviour and guidance strategy of college students

Jihong SHAO[1] Xia WANG[2]

[1]School of Economics & Management, Hubei University of Technology, Hubei, Wuhan, 446558049@qq.com
[2] School of Economics & Management, Hubei University of Technology, Hubei, Wuhan, 707548763@qq.com

As a high knowledge community, college students are disseminators, practitioners and designers of low-carbon consumption, their online consumption view has an inestimable impacts on the future development of the Internet. The future development must be towards low carbon, they have an inescapable responsibility for the future of the Internet shopping. Through questionnaire survey, this paper studied and analysed college students' behaviour in the network consumer, and pointed out the problems and influencing factors in the low-carbon consumption of contemporary college students' network, also gives positive suggestions.

Keywords：*Internet consumption; Low-carbon consumption; the status quo; Affecting factors;*

1. INTRODUCTION

Online consumption has become an indispensable part of consumers' daily life. The convenience of the Internet consumption brings high energy consumption, high carbon life and environment degradation. The most representative example is the development of logistics industry, which develops rapidly with shopping, and the large amount of pollution caused by logistics in transportation, packaging, storage and treatment, such as CO2, CO, NOX and SO2 and dust, which make environmental worse. The environmental impacts are reflected in fossil energy consumption, global warming, acidification and eutrophication.

On November 6, 2017, Beijing--the International Environmental Greenpeace has released the report "the shopping rethink season: carbon emissions and other environmental impacts of online shopping" Online shopping generates high carbon emissions, the report says. On November 11, 2016, the carbon emissions from online clothing products alone are as high as 258,000 tons, which would require 2.58 million trees to be carbon-neutral, and is equivalent to the size of 1.5 primitive forests in Xishuangbanna.

The high carbon life brought by Internet consumption has seriously affected the ecological environment and living environment, and the number of Internet users in China continues to grow. By June 2017, it has reached 751 million, and there were 19.92 million new Internet users were registered in half of this year. The Internet penetration rate has reached 54.1%, compared with that in the end of 2016, it has increased an increase of 1.1%. In addition, the number of mobile Internet users has reached 724 million, increasing of 28.3 million in the half year, and the proportion of mobile Internet users has increased to 96.3 %. According to the statistics from China Internet Information Center (CNNIC) statistics, in China, 29.7% of netizens are between 20 and 29 years old, and 30.5 % of Internet users have a college degree or above. According to the big network platform data statistics，in 2017, the online retail sales were about 7.18 trillion, accounting for 19.6% of the total national social consumer goods, and online shopping shows a growing trend, 16 to 35 year-old users as the main force of Internet shopping, which accounted for 85.5%. Therefore, college students are the main force in the popularity of shopping.

The future development trend is building ecological civilization, energy-saving, protecting ecological environment. The construction of ecological civilization is an important way to solve the problems of environment and energy. Zhi Yi (2004) showed that, the proportion of environmental consumers among young people with higher education level will be higher. It can be seen that as the main force of future consumption and the main body of future environmental protection, whether the consumption behaviour of college students is reasonable or not is directly related to the future development of China's environment. Therefore, this study took college students as the survey objects, conducted a questionnaire survey on their low-carbon consumption awareness and low-carbon behaviour, and through SPSS software analysis, points out the existing problems and influencing factors of the contemporary college students' network consumption. This paper aims to improve the low-carbon awareness of this group, correctly guides the college students' network consumption behaviour.

2. NETWORK LOW-CARBON CONSUMPTION OVERVIEW

2.1. Low-carbon consumption concept

The connotation of low-carbon consumption

Low carbon refers to emissions of greenhouse gases, mainly carbon dioxide emissions. Low-carbon consumption is an important approach and core force to realise the development of ecological civilization. Low energy consumption and pollution are not only the driving forces of social and economic development, but also help people balance it. Pan (2010) put forward that consumption is the most important economic production and the production of the purpose and motivation, consumers' behaviour will directly affect the energy consumption, even more will indirectly affect the industrial structure. (Wang Shuxin, 2010) as the most important energy-intensive behaviour, consumers' daily life and consumption behaviour will affect the total energy consumption by 45% to 50%. Therefore, how to reduce emissions is the connotation of low carbon consumption, including direct and indirect emission reduction, which is the promotion of green, sustainable life and consumption mode. Low-carbon consumption includes the purchase, use and disposal of products throughout the process of behavioural and ideological low-carbon.

Characteristics of low-carbon consumption

For low-carbon consumption, many domestic and foreign scholars have carried out researches on it, covering a wide range of areas and methods. Different from the traditional consumption pattern, low-carbon consumption is a way of developing and improving consumption. It not only integrates material consumption into the consumer culture, but also participates in environment-friendly shopping ideas. It does not constrain consumption and does not damage the environment. This connotation of low energy consumption, low pollution and low emissions remains as the same as recognised by scholars at local and abroad. In other words, the essence of low-carbon consumption is to create the maximum benefit with the least resources without damaging the environment. Therefore, to effectively realise low-carbon consumption, we must start

from the characteristics of low-carbon consumption. At present, it is of the utmost importance to raise the awareness of low-carbon consumption and to change its consumption behaviour.

2.2. The impact of low carbon consumption on the environment

Taniguchi (2002) is taking into account some of the negative effects of pollution from trucking on the environment, such as emissions, noise and vibration，and calling for further reductions in emissions and fuel consumption in the process of logistics. Product packaging is also an important link in the production of pollutants in logistics. Based on the principle of convenient and durable, low loss, paper box, cushion bags, bubble bags, and plastic film packaging are the first choice of the express packages, which are almost all rubbish in the hands of consumers, but this is the main source of environmental pollution. And the main impacts are as following:

The impact of transportation

（1）Fog effect

The exhaust from diesel vehicles is the main source of haze weather. Fog contains more than 20 kinds of fine particles, toxic substances harmful to human body, including acids, basis, salts, amines, phenols etc, as well as dust, pollen, mites, influenza virus, Mycobacterium tuberculosis, pneumococcus, etc. Smog is more harmful to people's health, which can be directly through the respiratory system into the bronchi, and even the lungs, causing the disease mainly concentrated in respiratory disease, cerebrovascular disease, inflammatory diseases, such as nasal cavity at the same time, the high risk of disease transmission.

（2）Acidizing effect

Xuexiang Hui, according to the statistical analysis of a group of acid rain and pollutant concentration monitoring data in the atmosphere between 2006 and 2010, says large amounts of motor vehicle exhaust emission has become the important reasons for the formation of acid rain, and logistics is to use the motor vehicle with large-emissions trucks, so logistics transportation will increase acid rain.

The impact of packaging on the environment

According to the report, it is a common phenomenon that packaging bags in the soil take at least 100 years before natural decomposition, excessive packaging, low recycling efficiency is common. Although domestic and related enterprises have started to take action, measures have been taken to promote the greenness of express packages, such as developing degradable materials and promoting the recycling of packaging. However, lagging packaging standards, difficult recycling and lack of environmental awareness remain the three major bottlenecks.

The impact of recycling on the environment

Recycling is the most important part of resource recycling in transportation, but the least valued part. After receiving the package, consumers usually tear up the packaging materials. General waste disposal stations get used to burning a large number of plastic bags, paper boxes, foam which produce HCl, CO and benzene ring compounds. Most of the HCl is trapped in the mucosa of the upper respiratory tract after inhalation. Carbon monoxide poisoning is the result of incomplete combustion of carbon-containing substances through respiratory inhalation; benzene is flammable, toxic and a carcinogen.

Therefore, it can be seen that network low-carbon consumption is an important step to optimise the environment for low-carbon consumption and an important issue to promote low-carbon economy at present.

3. COLLEGE STUDENTS NETWORK LOW-CARBON CONSUMPTION STATUS

3.1. Sample selection of questionnaire

Hubei province is a big province of education, for Wuhan, it has the second largest number of colleges and universities in China, which contain 84 institutions of higher education, 46 undergraduate and 38 colleges. This study, the selected samples were investigated by means of on-site random interview and online and offline questionnaire. Two questionnaires were distributed in this study，the first is to directly cite the questionnaire of Zhou Lin's research (2005) on college students' online behaviour preference, in order to understand the consumption preference and structure of contemporary college students. The second survey is based on the questionnaire set by previous scholars, which is composed of three parts: the first part, including gender, grade, disposable amount after excluding daily expenses and educational background, the number of monthly online shopping; The second part includes students' cognition, understanding and personal attitude

and willingness to low carbon consumption on the Internet. The third part, including influence factors on students' cognition, intention and behaviour of low-carbon consumption. A total of 500 questionnaires were issued in this survey, and 464 copies were recovered, with a recovery rate of 92.80%. As a supplement, the number of random interviews was set at 50, and the recovery rate was 100%. 300 questionnaires were distributed online, 277 copies were recovered, and the recovery rate was 92.33%. 150 questionnaires were distributed offline, 137 copies were recovered, and the recovery rate was 91.33%. The sample analysis table is as follows：

Table 1: the sample analysis table

Indicators	Classification of the sample	The percentage
Gender	male	48.91%
	female	51.09%
Record of formal schooling	Specialised subject	5.43%
	Undergraduate course	63.04%
	A graduate student	26.09%
	Dr.	5.43%
Grade	In grade one	22.83%
	Second grade	45.65%
	The third grade	23. %
	In fourth grade	5.43%
	other	3.09%
The amount of disposable income after the removal of daily expenses	0—400 yuan	23.91%
	400—600 yuan	40.22%
	600—800 yuan	30.44%
	Over 800 以上	5.43%
Monthly online shopping	Less than 3 times	27.61%
	3—5 times	40.22%
	6—8 times	20.39%
	More than 8 times	9.78%

As can be seen from the table above, the proportion of male and female selected samples is 48.91% and 51.09% respectively. Among the academic degree distribution, the proportion of colleges and universities is 5.43%, that of undergraduate students is 63.04%, that of graduate students is 26.09%, and that of doctoral students is 5.43%. According to grade distribution, the proportion of the first grade is 22.83%, the second grade is 45.65%, the third grade is 23%, the fourth grade is 5.43%, and the other grade is 3.09%. After excluding the daily food expenses, the amount of disposable money, 0-400 yuan accounts for 23.91%. The proportion between 400 yuan and 600 yuan is 40.22%. The proportion of 600-800 yuan is 17.39%. The proportion above 800 is 5.43%. From the perspective of monthly online shopping times, 27.61% of online shopping times are below 3 times, 40.22% are 3-5 times, 20.39% are 6-8 times, and 9.78% are above 8 times. From the analysis of the above sample indicators, it can be seen that in the sample table selected, the proportion of males to females is moderate, and the proportion of undergraduates and graduate students is relatively high. In addition to daily expenses, most students have a disposable amount of 400 to 600 yuan and 600 to 800 yuan, accounting for nearly 60%.

3.2. Characteristics of college students' network consumption behaviour

University student network shopping is based on diversified motivations

It can be seen from the questionnaire that today's college students have diversified motivations for online consumption, including convenience, cheap price, diversified products and clear price. 76.7% of people think that the Internet consumption is very convenient and saves the time to buy at physical shop otherwise. As long as there is network, they can browse and buy goods at any time, and there is no need to take a long ride to buy; 43.1% of the students said that there was no bargaining process when they purchase on-line, it was shown that 86.5% of students did not like bargaining with businesses. 69.1% of students believe that online shopping platform products are diversified and goods that need to be purchased in multiple places in physical stores can be quickly solved on the online platform.

The network consumption structure of college students is diversified and the amount is increasing gradually

The survey results show that the consumption structure of contemporary college students presents a trend of diversification, mainly including access to information, entertainment and leisure, communication, shopping, video games and learning. Of course, some students say that sometimes they will buy something they don't need because of impulsiveness. Another important finding of the survey is that, compared with previous college students, the new college students has much more disposable money, disposable consumption at 600-800 yuan and above 800, amount to 35.87%. The proportion of shopping above 3 times per month account for 70.39%.

College students have a low awareness of low-carbon consumption

It can be seen from the survey that contemporary college students overall have a low cognition of low-carbon consumption on the Internet, and only know the general concept of low-carbon. As far as the concept is concerned, 96.83 % of students know the concept, but when it comes to low carbon consumption on the Internet, many students don't know how to answer it. 98% of the students clearly know it is necessary to recycle the waste generated in the process of shopping. Almost all students understand the environmental pollution caused by logistics and transportation during the express delivery process, as well as the environmental pollution of logistics packaging materials, also understand improper handling will pollute the environment, but when asked what harm resulting from material, what specific performance on the human body and environment, they don't know exactly. The survey results show that, in addition to the knowledge of individual students, the understanding of other students is relatively simple. Only 32.4% of students pay attention to low-carbon labeling and product classification, we also don't know whether they will pay attention to low-carbon labeling in the process of shopping online.

College students have a strong desire to consume low-carbon product online but lack practical behaviours

Asked whether they would like to take part in a low carbon environmental protection activities and logistics packaging recycling, almost all the students are willing to join in the activity, 100% of students think they have the responsibility and obligation to reduce waste generated in the network consumption. But from the behavioural analysis, 83.48% of students will throw packing bag, only 25% of the students will put it in the classification dustbin. According to the survey, when you buy an unsatisfactory product, 41% of students will choose to ignore, 63% of the students will choose to return directly. However, in real life, students still have a lot of unnecessary products piled up in the dormitory.

4. THE AFFECTING FACTORS OF LOW-CARBON NETWORK CONSUMPTION IN COLLEGE STUDENTS

According to the investigation and research, the main factors influencing college students' low-carbon consumption are:

4.1. The network low-carbon consumption cognition is low

In real life, students have a higher awareness of low-carbon consumption. However, for online consumption channels, low-carbon consumption of the Internet is still a new word for many students, which is a special channel for online consumption, because this special channel makes it easy for consumers to buy products neglecting the high carbon impact of the whole process from product to consumer. Moreover, most students don't know what is low-carbon because online shopping unlike the physical store shopping which supplies the product itself, the network channel can only provide pictures, so clearly distinguishing the low-carbon mark is a very important factor. Secondly, related to the living environment of students, many rural college students have lower low-carbon awareness than urban students, which is closely linked to the natural environment of the countryside. When college students are shopping on the internet, they will neglect the special impact to human body and environment in the process of buying goods.

4.2. A herd mentality

The herd mentality is an important factor affecting the low-carbon consumption behaviour of college students. It is also an important factor for college students to continue the online consumption frenzy after understanding the serious environmental impact of excessive network consumption. According to the survey, 49.92% of the students will buy products that are not needed under the influence of friends and classmates, and 93.59% of the students will buy things recommended by their classmates, friends and family.

4.3. Personal consumption view

The personal consumption view is another significant factor affecting college students' network consumption, in the 21st century with personalities, personal consumption influences consumers' behaviour and habits. In the survey, 67.06% of the students said that they would follow the fashion to buy some unnecessary product. Of course, there were still part of the students believed that saving was a merit for college students。

4.4. Economic ability

In the course of investigation, it was found that economic ability was also a factor that affected the low-carbon consumption of college students. Students with higher disposable money obviously went shopping more frequently than those with lower disposable money.

5. SUGGESTIONS

In view of the characteristics and influencing factors of contemporary college students' consumption behaviour, this study puts forward several suggestions：

5.1. For schools

First of all, the school should strengthen the cultivation of college students' awareness of low-carbon consumption and enhance their awareness of low-carbon online consumption. From the stage of purchase, application to treatment of packages, the school should focus on cultivating students' awareness of low-carbon consumption. At present, college students' cognition of consumption stay on the surface, but not on the deep meaning and let alone the reality. Colleges and universities should set up relevant organizations, hold regular low-carbon literacy briefing sessions. At present, most students will join social practices held by schools during the summer and winter, schools can organise network low-carbon social practice activities, let more students to participate. Because in those situations, students can understand the real meaning of network low-carbon consumption deeply, at the same time they can spread the idea to more people. Secondly, the university should cultivate the correct consumption concept and encourage them to establish the good virtue of thrift.

5.2. For families

Parents should not only care about their children's healthy but also pay attention to the cultivation of their psychology. Most parents only concerned about their children whether have enough money in school, but neglect the importance of the consumption concept. Students who graduate from high school to university have not yet developed mature self-management and self-discipline, so the influence of parents in this area is crucial. Parents should pay attention to the psychological development of college students and develop their independent ability management and self-management skills.

5.3. For college students themselves

University is a small society, the final stage before college students enter the society. It is of importance for them to set up the correct values and their own cognitive system without going with the flow.

6. REFERENCES

Crainic TG, Ricciardi N, Storchi G. Models for Evaluating and Planning City Logistics Systems[J]. Transportation Science, 2009, 43 (4): 432-454.

Gao F. Survey on College Students' Online Consumption Psychology and Behavior [J]. Undergraduate Studies, 2015(2): 100-107.

Gao Z, Li X, Zhang Y. Study on the Influential Factors of Low-carbon Consciousness and Behavior of Urumqi Residents——An Analysis of Structural Equation [J]. Journal of Xinjiang University (Philosophy, Humanities & Social Science), 2017, 459(4):1-9.

He Z, Yang S. Research on the Lifestyle Characteristics of Green Consumers [J]. Nankai Management Review. 2004(3): 4-10.

Huang F, Huang J. Influencing Factors of Online Preferences based on Flow Theory [J]. Chinese Journal of Management, 2014, 11(5): 733-739.

Li X. Study on Influence Mechanism and Guidance Strategy of Low-carbon Consumption Behavior of College Students——Based on ANP Model[J].Special Zone Economy,2014(5): 227-228.

Pan J, Zhuang G, Zheng Y et al. Concept Identification and Core Elements Analysis of Low Carbon Economy[J]. International Economic Review. 2010(4):88-101.

Taniguchi E, Yamada T, Kakimoto Y. Models for Evaluating City Logistics Measures [J]. Proceedings of the Eastern Asia Society for Transportation Studies, 2001, 3(2): 511-526.

Taniguchi E, Thompson RG. Modeling City Logistics [J] Transportation Research Record, 2002, 1790(1) : 45-51.

Wang S, He Y, Wang X et al. Transformation of China's Consumption Pattern in the Era of Low Carbon Economy [J]. Soft Science. 2010(7): 54-57.

Yang J. A Study on Low-carbon Consumption Behavior and Influence Factors of College Student Group[J].Journal of Nanjing Institute of Technology (Social Science Edition), 2017,17(2): 57-64.

Zhou L. The Research on the Internet-Behaviors Preferences of Undergraduates[D]. Shanghai：Shanghai Normal University, 2005, 9-26.

391: Development and analysis of anodic aluminium oxide composites for thermochemical energy storage systems

Zafer UTLU[1], Behiye YUKSEL[2], Bengisu YILMAZ[3], Devrim AYDIN[4], Saffa RIFFAT[5]

[1] Istanbul Gedik University, Department of Mechanical Engineering, Istanbul, Turkey, zaferutlu@aydin.edu.tr
[2]Istanbul Gedik University, Department of Mechanical Engineering, Istanbul, Turkey, behiyeyuksel@gmail.com
[3]Istanbul University, Engineering Faculty, Istanbul, Turkey, bengisu.yilmaz93@gmail.com
[4]The Eastern Mediterranean University, Gazimagusa, Cyprus, e-mail: devrim.aydin@emu.edu.tr
[5]The University of Nottingham, of Architecture and Built Environment, Nottingham, UK, e-mail: saffa.riffat@nottingham.ac.uk

Global energy demand is increasing due to improvements in the industrial world and increasing world population. The fact that existing energy sources are exhausted has led their work to renewable energy sources. However, renewable energy sources are not limitless. Supply-demand imbalance is an obstacle to the use of these resources. According to all these, 'energy storage' has become an important topic in many areas of the sector in recent years. Thermal energy storage (TES) is seen as a promising technology in renawable energy systems. As an evolving technology, TES systems are an effective way to achieve the sustainable use of energy. In this study, new composite material "high energy density storage salts with honeycomb filter form Anodic Aluminum Oxide (AAO) template" is fabricated its application for the low temperature thermal energy storage systems. Therefore AAO templates with pores were controlled were used. Then, having different energy storage capacities of salts and complex salts were absorbed by the vacuum method into these known pores of diameter and length. The energy storage capacities of these composite materials obtained using different salts were compared.

Keywords: Anodization, AAO, Termal Energy Storage

1. INTRODUCTION

Developments in the industrial world, rapid population growth and urbanization have increased the importance of energy use more effectively and energy efficiency day by day. Today, limited resources of fossil fuels that meet the vast majority of world energy resources, continuous increase of prices, negative effects on people and environment, energy studies have been directed to renewable energy sources. However, the use of renewable energy resources is not limited to continuity, and the time difference between acquisition and consumption is limited by reasons such as incompatibility. Therefore, in parallel to the studies conducted on effective use of renewable energy sources of energy also being studied. Energy storage methods used to efficiently use energy can contribute to reducing consumption of fossil fuels and finding new and renewable energy sources.

Today, a significant amount of low-temperature (< 100 C) housing buildings heat and industrial waste heat are directly discharged to the atmosphere (Liu, 2013). Therefore, low temperature advanced heat recovery technology needs to be prompted to reduce fossil fuel consumption and the impact of utilizing fossil fuel energy on environment and to increase the proportion of utilise renewable energy in energy consumption sector (Abedin, 2011). TES systems provide a means to store energy for use in heating and cooling applications at a later time (IEA-ETSAP and IRENA, 2013; Khudhair, 2004; Tay, 2017).

Materials used up to now in TES are usually porous natural rocks themselves. These self-porous rocks have absorbed high salt storage capacity, producing composite materials for use in TES systems (Kurokawa, 2011; Zhang, 2016; Posern, 2010; Zhang, 2016; Casey, 2014; Tokarev, 2002). However, some of the limiting features of natural rocks have led to the search for alternative materials. The studies about this subject of literature are limited (Jänchen, 2005). All for these reasons this works aim is the high thermal storage capacity of the new composite material that used anodic aluminum oxide (AAO) templates was produced for this new ambiance as an alternative to the other materials used for thermal storage in TES systems.

2. EXPERIMENTAL

2.1. Preparation of specimens and experimental procedure

In this work, high purity aluminum sheets (99.99%) were used to fabricate anodic aluminium oxide (AAO) samples. Before anodization, the aluminium substrates were degreased using isopropyl alcohol and then chemically polished in a mixture of 89ml H_3PO_4, 7 ml HNO_3, 40ml H_2O, and 0.5 g $CuSO_4$ at 80°C for 2 min. to remove the natural oxide layer. AAO were fabricated by using a two-step anodization method.The chemically cleaned aluminum samples were anodised in a solution of 0.6 M $C_2H_2O_4$ at a temperature of 20°C, 40 V for 30 min. Chemical etching step was carried out between first and second anodization step in a mixture of 3.5% H_3PO_4 and 2% CrO_3 (percentages in wt%) at 55°C for 15 min. The second anodization was carried out in a solution of 0.6 M C2H2O4 at a temperature of 20°C, 40 V for 30 min. After the second anodization step, the samples were treated to enlarge the pore diameter with 0.1M NaOH solution for 10 min.

In first phase of the study, obtained AAO plates were impregnated with 4 different salts as LiCl, LiNO3, CaCl2 and MgCl2. In the second phase of the study, mixtures of salts were used that the best results from the DSC results of samples made using a single type of salt.

All samples were examined with a JSM-6335F model JEOL field emission scanning electron microscope (FESEM). The FESEM micrographs were taken from top view and cross sectional view of AAO samples after anodization. The diameter and length of AAO structures were measured by FESEM.

In Figure 1, FE-SEM images of AAO templates are shown by immersing in a 3.5 wt% NaOH solution for 10 min after two-step anodization. The distance between the centres of two neighbouring pores is about 80 ± 5 nm and the distance between the outer surfaces of the pores is 30 ± 5 nm.

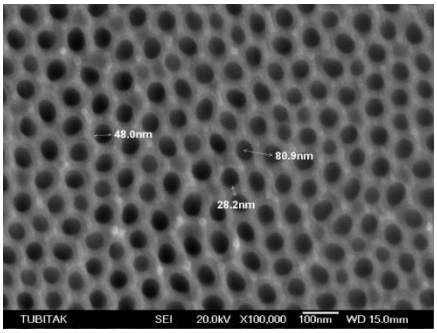

Figure1: FE-SEM image of the top of the AAO template after pore expanding

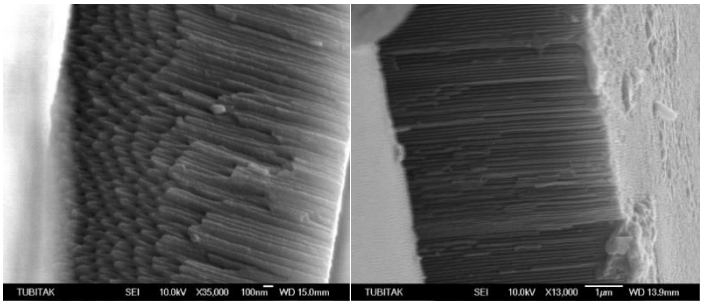

Figure 2: Cross-section view FESEM images of AAO templates

Cross sectional views of AAO structures are given in Figure 2. As can be seen, the oxide layer obtained by the anodization process consists of hollow tubes to the surface of the substrate. This allows the interior of the nanotube structures to be filled with salt solutions. The resulting nanotubes are approximately 5 μm in length.

2.2. Salt impregnation

Samples was investigated as mono-salts and salt mixtures according to the salts impregnated in the AAO templates. Among the composite materials obtained as samples of 1, 2, 3 and 4; LiCl and LiNO3 were chosen which give the best results in terms of desorption energy and energy storage density. Subsequently, LiCl and LiNO3 were mixed at different ratios and 5 and 6 samples were prepared using the solutions obtained.

Following pore expanding, the AAO templates were allowed to dry at 110° C for 24 hours. At the end of 24 hours, the samples whose nemesis has been completely removed are ready for the salt impregnation process. AAO templates with pore diameters extended to about 50 nm were filled with 4 different salts and combinations thereof by vacuum impregnation. For this purpose, LiCl, LiNO3, MgCl2 and CaCl2 salts, which give the best results, have been selected in the literature review. The salts used in this study are given in Table 1. During the preparation of the solutions, the salts are slowly added while continuously stirring.

As mentioned above, this study was carried out using two groups of AAO samples; firstly, composite materials (samples of 1, 2, 3 and 4) prepared using mono-salt, and then to investigate the change in the performance of the composites produced using combinations of the salts (samples 5 and 6) that gave the best results.

The used anodization conditions are shown in Table 1.

Table 1: Anodization conditions

Sample No.	Enlargement Time in NaOH Solution	Impregnated Salt
1	10	LiCl
2	10	LiNO3
3	10	MgCl2
4	10	CaCl2
5	10	LiCl+LiNO3 (1:1)
6	10	LiCl+LiNO3 (1:3)

For salt impregnation, AAO plates are submerged into the solutions placed in separate containers, with the AAO plates fully penetrating. The specimens thus placed in the oven were allowed to stand in salt solutions at 30° C for 48 hours under 0.1 MP vacuum. In this environment, capillary action is provided to fill the pores with the relevant salt solution.

3. RESULTS

Following the synthesise of the salt in matrix composites, according to the BS EN ISO 11357-4 standards, the Ed was carried out using a differential scanning calorimeter (DSC). For each test, 2 aluminum pans were used as reference for 30 <T <140° C temperature range. Each of the samples was stirred at 1° C / min. the scanning rate was kept constant for 10 minutes at the lowest and highest temperature values. This procedure was repeated by calibrating the DSC instrument with the certified sapphire reference standard. Then, in order to measure the desorption energy of the prepared samples, it was provided to desorb the moisture in the open atmosphere. The samples were stored for 24 hours at 23° C and 95% relative humidity for testing. First, the DSC Q2000 instrument was used to determine the specific heat capacity (Cp, J / kg K). Cp values were calculated for each sample. Therefore, the total energy values are obtained from the derivative of the Cp values according to the temperature change. The ratio of the total energy to the weight of the sample tested gives the energy storage density (Ed).

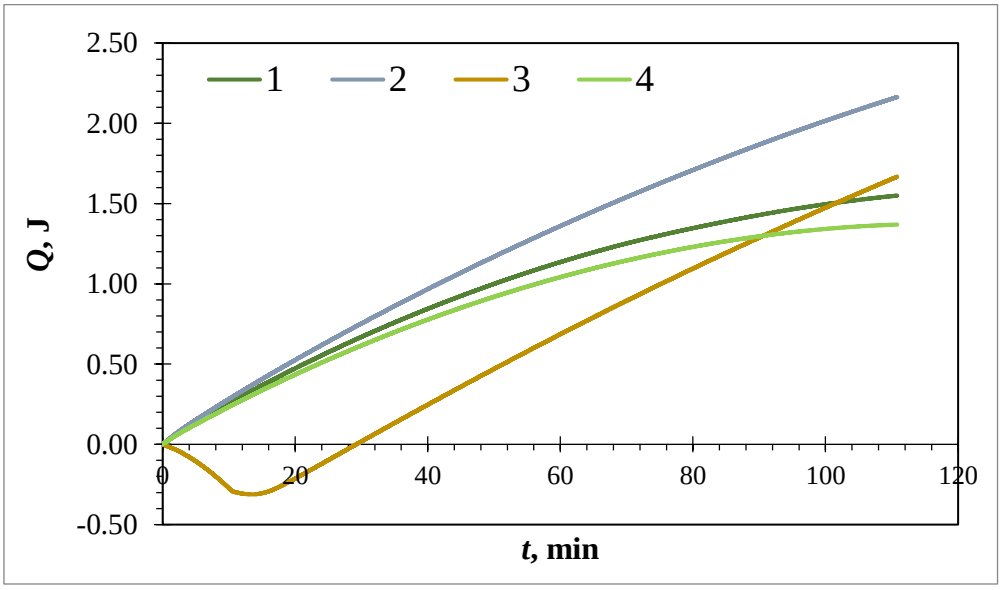

Figure 3: The amounts of desorption energy

Figure 3 shows the amount of desorption energy in the same phase of the samples. When the Q values used in the calculation of the energy density are examined, it is seen that samples of 1 and 2 have better results than others. Sample 1 is adsorbed 1,55 Joules of energy after a period of about 2 hours. The sample of 2 adsorbed 2,16 Joule energy at the same time, giving the highest value compared to the other samples.

When the calculated energy density (Ed) values in Figure 4 were examined, the highest Ed sample was 2 samples with 251,64 kJ / kg energy density. The 1 sample has the second highest value with an energy density of 242,16 kJ / kg. The expected performance from the 3-way (231,63 kJ / kg) and 4-way (220,85 kJ / kg) samples was not achieved.

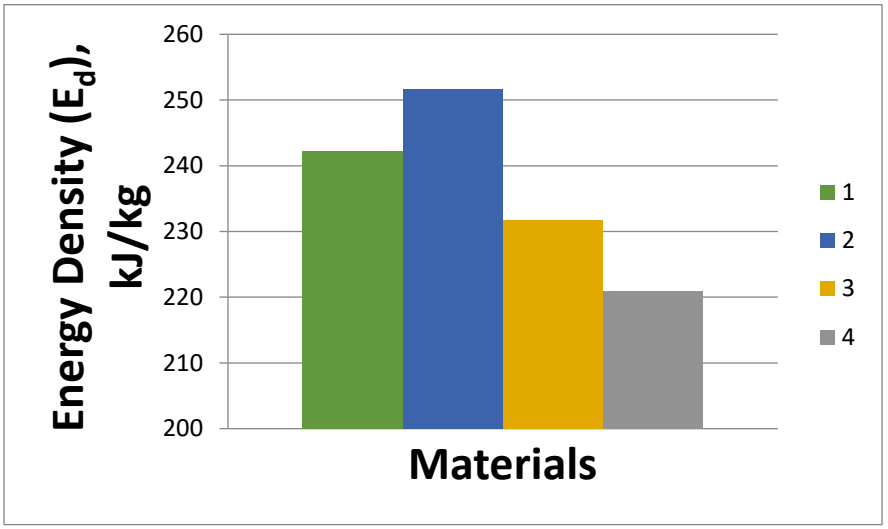

Figure 4: Energy density values of samples

At this stage of the work, the LiCl and LiNO3 salts, which gave the best results, absorbed the salt mixtures prepared by mixing in different volumes and samples 5 and 6 were obtained.

In the synthesis of salt mixtures, LiCl and LiNO3 salts for sample 5 were mixed in equal proportions while for sample 6 LiCl and LiNO3 salts were used in 1:3 ratio respectively. As in the case of mono-salts, the AAO templates were immersed in the solutions placed in individual containers for salt impregnation. The specimens thus placed in the oven were allowed to stand in salt solutions at 30° C for 48 hours under 0.1 MP vacuum. Figure 5 shows the amounts of desorption energy at the same time.

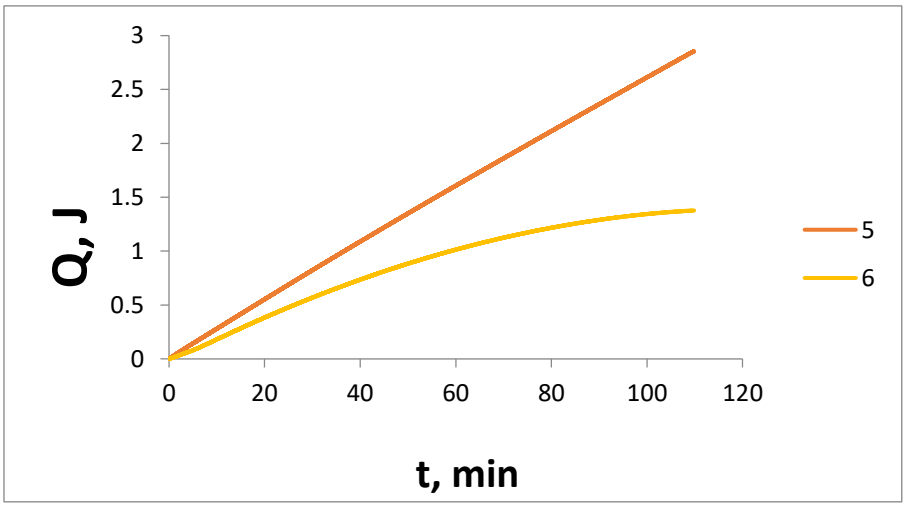

Figure 5: The amounts of desorption energy for 5 and 6

When the energy density (Ed) values were examined from the results of the DSC analysis shown in Figure 6 to determine the thermal properties of the produced composite materials, the material with the highest Ed value among all the samples was sample of 5 with an energy density of 468.14 kJ / kg. A result of samples of 6 (199.57 kJ / kg) was obtained below the expected value.

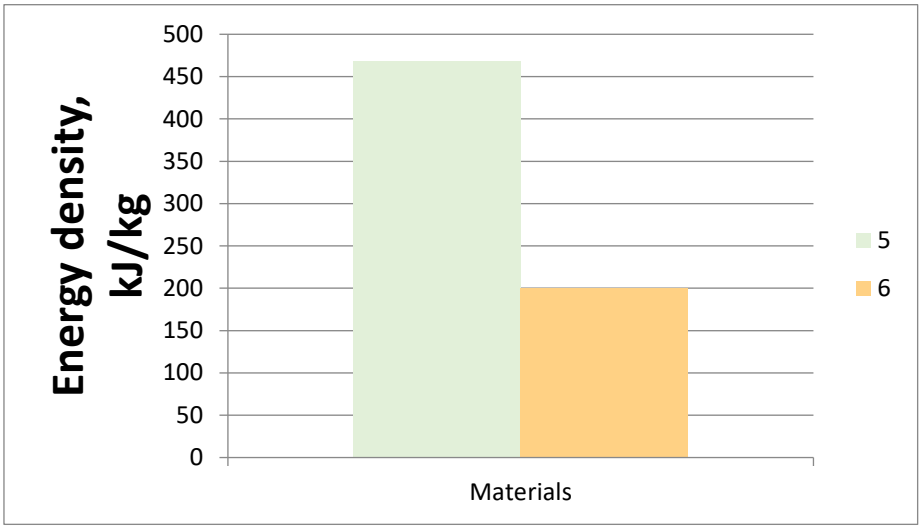

Figure 6: The energy density values for 5 and 6

4. ACKNOWLEDGEMENT

This study was supported by the Scientific and Technological Research Council of Turkey (TUBITAK) Project no: 315M524

5. CONCLUSION

All samples for using thermal storage systems were obtained in standard AAO templates by the two-step anodization process. The study was then carried out in two stages. In the first step, the nanotubes of the resulting anodization were impregnated with 4 salts which exhibited the best performance from the literature. The salt impregnated AAO templates were subjected to DSC analysis to examine the energy density (Ed). The DSC results obtained as Ed of LiCl-Al2O3, LiNO3-Al2O3, MgCl2-Al2O3 and CaCl2-Al2O3 were computed as 242,16 kJ/kg, 251,64 kJ/kg, 231,63 kJ/kg, 220,85 kJ/kg respectively. From the results of DSC, the best resultant of these four salts yielded composite materials impregnated with LiCl and LiNO3 salts. Accordingly, in the second stage of the work, LiCl and LiNO3 salts were mixed in different volumes and impregnated with standard AAO templates prepared under the same anodization conditions. Equal volume of salt mixture was computed 468.139 kJ/kg. The salt mixture prepared by mixing in a ratio of 1: 3 was computed 199,57 kJ/kg. The material impregnated with a mixture of LiCl and LiNO3 salt prepared by mixing in equal volume gave the best result when compared with the others. These parameters used this work gave satisfactory results when compared to previous studies with natural rocks (168-406 kJ/kg) (Casey, 2014).

6. REFERENCES

Abedin A.H., Rosen M.A., A critical review of thermochemical energy storage systems, The Open Renewable Energy Journal, 4 (2011) 42-46.

Casey, S. P., Elvins, J., Riffat, S., Robinson, A., (2014) Salt impregnated dessicant matrices for 'open' thermochemical energy storage-Selection, synthesis and characterisation of candidate materials.Energy and Buildings, 84, 412-425

IEA-ETSAP and IRENA© Technology Brief E17 – January 2013 Thermal Energy Storage Andreas Hauer (ZAE Bayern).

Jänchen J., Ackermann D., Weiler E., Stach H., Brösicke W., Calorimetric investigation on zeolites, AlPO4's and CaCl2 impregnated attapulgite for thermochemical storage of heat, In Thermochimica Acta, Volume 434, Issues 1–2, 2005, Pages 37-41, ISSN 0040-6031

Khudhair A M., Farid M M., *A review on energy conservation in building applications with thermal storage by latent heat using phase change materials*, Energy Conversion and Management, Volume 45, Issue 2, 2004, Pages 263-275.

Kurokawa A., Togawa J., Nabeshima Y., Nagano K., The evaluation of the moisture sorption mechanism of chloride-impregnated Wakkanai siliceous shale, Kagaku Kogaku Ronbunsyu 37 (5) (2011) 394–399.

Liu H, Nagano K, Sugiyama D, Togawa J, Nakamura M, *Honeycomb filters made from mesoporous composite material for an open sorption thermal energy storage system to store low-temperature industrial waste heat*, International Journal of Heat and Mass Transfer, Volume 65, 2013, Pages 471-480.

Posern, K.; Kaps, C. Calorimetric studies of thermochemical heat storage materials based on mixtures of MgSO4 and MgCl2. Thermochim. Acta 2010, 502, 73–76.

Tay N.H.S., Liu M., Belusko M., Bruno F., Review on transportable phase change material in thermal energy storage systems, In Renewable and Sustainable Energy Reviews, Volume 75, 2017, Pages 264-277.

Tokarev, M., Gordeeva, L., Romannikov, V., Glaznev, I., Aristov, Y., (2002) New composite sorbent CaCl2 in mesopores for sorption coolingheating. International Journal of Thermal Science, 41, 470-474

Zhang, Y. N., Wang, R. Z., Zhao Y. J., Li, T. X., Riffat, S. B., Wajid, N. M.,(2016). Development and thermochemical characterizations of vermiculit/SrBr2 composit sorbents for low-temparature heat storage. Elsevier, Energy 115, 120-128

Zhang, Y., Wang, R., Li, T., Zhao, Y., (2016) Thermochemical Characterizations of Novel Vermiculite-LiCl Composite Sorbents for Low-Temperature Heat Storage. Energies

394: People, buildings, living environment and our cities

Han LIN[1], Di YUN, Hong WANG, Xuan SHI

[1] Delos (Beijing) Building Technology Co. Ltd, Beijing 100025, Corresponding Author: han.lin@delos.com

In 2018, Tsinghua University and The Lancet jointly published the report "The Tsinghua–Lancet Commission on Healthy Cities in China: unlocking the power of cities for a healthy China". In this report, the major urban health challenges and opportunities in cities are well analysed and a system approach to urban health management with specific strategies are concluded, which provide a clear path for the realization of the Healthy China 2030 plan.

The report has four sections. In section 1, the reason why cities are the key factors to a Healthy China is described in detail. As cities in China are facing many healthy challenges caused by the fast-paced changes associated with urbanization, section 2 examined those major health challenges are from the cause, status and risk factors. For the cities that have taken actions to address urban health challenges, the health improvements and remained gaps of these actions are well summarised and discussed in section 3. With the comprehensive consideration of the aspects of urban infrastructure, environmental conditions, socio-cultural factors and government administration capabilities, a system methodology to urban management and specific actions for healthy cities are discussed and concluded in section 4.

Based on Tsinghua-Lancet's joint report, author forwards 10 Healthy Cities principles to land research results on real large scale development cases. The 10 principles include Health and Happiness, Culture and Heritage, Ecology and Biophilia, Active and Active Transportation, Climate Change and Health, Material and Waste, Verification and Transparency, Public Health Policy, Responsible Development, Innovative Economy.

Health is the fundamental right of people. The realization of Healthy China needs the active participation of the whole society, including private enterprises, NGOs and community groups, public–private partnerships, and citizens themselves. As the cornerstone of the socio-economic and human economic activities, companies should actively engage in technology innovation and corporate wellness in the development of Healthy China.

The health industry market is very huge. Technology innovation and investment in 'big health' industry cannot be ignored. It is believed that with the gradual implementation of the strategies stated in this report, a variety of health benefits will surely be obtained and contribute a lot for Healthy China.

Keywords: Healthy City, Corporate Wellness, Technical Innovation

1. INTRODUCTION

With the gradual deepening of urbanization, many problems keep emerging, such as the increasing urban population, housing shortage, traffic congestion and the lack of health resources (Luo, 2010). At the same time, the changes in lifestyle and the fierce social competition have led to an increase in mental illness among the urban population. A data shows that the risk of mental disease and anxiety disorder among urban residents is 39 percent and 21 percent higher than in rural areas, and the risk of schizophrenia is 50% higher than in rural areas (Benedictus, 2014). In order to deal with the health challenges in cities, the concept of healthy cities has gradually emerged worldwide in the 1980s. So far, Europe, the Western Pacific, the Americas, Southeast Asia, Africa, and the Mediterranean have launched the Healthy City Project under the WHO organization. In 1994, the China Ministry of Health cooperated with the Western Pacific Office of the World Health Organization to make the Beijing Dongcheng District and the Shanghai Jiading District as the “Pilot Zone for China’s Healthy Cities Project”, which kicked off the construction of healthy cities in China (Fu, Xuan and Li, 2006).

2. HEALTH CHALLENGES AND RESPONSES IN CHINA

It is estimated that by 2030, the urbanization rate in China will reach 71% (Chen, Dietzenbacher and Los, 2017). This makes the health challenges of our cities more serious. In 2016, the State Council of China promulgated the Outline of the Healthy China 2030 Plan. The promulgation of this outline reflects a clear understanding of the health challenges, health trends, and public health awakening. Given the rapid growth of the urban population and the political and economic primacy of cities, cities are the key to achieving healthy China.

In 2018, Tsinghua University and The Lancet jointly published the report “The Tsinghua–Lancet Commission on Healthy Cities in China: unlocking the power of cities for a healthy China” (Yang, 2018). In this report, it systematically examines the majoy opportunities and challenges faced by cities in the process of building a healthy China, and it proposes a system methodology and specific implementation strategies of urban health management, which provides a strong guarantee for the Healthy China 2030 Plan. The report includes four parts, including: The key to achieving healthy China, the major health challenges in Chinese cities, the response of Chinese cities to health challenges, and the development of healthy cities.

The report points out that China is in the stage of rapid urbanization. Compared with the rural society, Chinese cities have large population, strong economic strength, a wide range of administrative resources, which is the best support for implementing comprehensive health management and has become the key to healthy China. However, city brings unprecedented health benefits to the residents as well as new challenges. The report analyses the causes, status and risk factors of non-communicable diseases, infectious diseases, injuries, mental disorders, nursing care needs of the elderly, increased health expenditure, and health inequities with detailed data.

The report mentions that Chinese cities have taken a series of actions to deal with health challenges. Controlling environmental pollution, improving the liveability of urban environments, strengthening the prevention and control of diseases, promoting full coverage of health care, and establishing pilot cities for healthy cities, these actions have achieved significant health benefits and are rapidly promoted among cities. In addition to describing the series of actions taken by Chinese cities to address health challenges, the report also focuses on the health consequences and unresolved issues that these practices have. For example, how to implement the market mechanism to control environmental pollution? Whether and in what way can the public be more involved in deeper enhance the urban environment? How can the urban disease intervention program be conducted effectively and how can it attract the active participation of urban residents' personal wishes? What innovative and scalable methods are available for pilot projects in healthy cities? How can health city evaluation indicators be improved?

After comprehensively considering the aspects of infrastructure, environmental conditions, socio-cultural factors, and administrative capabilities, the report puts forward a health strategy for urban management in the fourth part, and more specifically provides five principles and strategies for the construction of healthy cities. : Integrate health in a variety of strategies, increase social participation, promote cross-sectoral cooperation, set goals according to local conditions and regularly assess, and strengthen research and education in healthy cities.

Healthy cities require extensive social participation. The report proposes that in addition to government-led planning and organization, there is a need to increase the participation of residents, the private sector, non-governmental organizations and community groups in health management. This provides very favorable conditions for private enterprises to participate more deeply and widely. In the process of building a healthy city, the active participation of private companies is mainly focused on technological innovation and corporate welfare.

The “New York Times” pointed out in the “Technical Outlook Launching the Whole City”, engineers and innovators who design integrated circuits and social networking sites are using the same methods and technologies to change cities (Badger, 2018). Looking back at 2017, the combination of science, technology, and healthy life has changed our old habits, reshaped our behaviour, and unleashed our health potential. A report in “Forbes” pointed out that the health and well-being

of the company is no longer a fashion, it is indeed there for us. Many companies believe that corporate welfare can increase the competitiveness and advancement of enterprises (Kohll, 2017).

By 2016, 80% of urban residents worked in private companies. Culture, work environment, and work style of the company all have a huge impact on the health of employees. The Well Living Lab studies quantified effects of different indoor heat, light, and sound environments on employee productivity, satisfaction, emotions, alertness, and sleep status (Jamrozik et al., 2017). Gensler's survey of workplaces shows that 88% of employees believe that the quality of the workplace's environment is important to their job satisfaction (Tompkin, 2006). Office that fully consider healthy design can improve the performance of a company by 22% (Jamrozik et al., 2017). More and more companies are paying attention to corporate welfare, investing more in employee health and occupational safety, providing a healthy indoor environment, and formulating corporate health travel plans, with a view to improving employee health, increasing employee productivity, increasing corporate income, and to improve the company's reputation.

Technological innovation is the driving force for enterprises to keep advancing. Scientific innovation and investment in health can create valuable business opportunities. The McKinsey study pointed out that welfare is the next trillion-dollar industry. "The 13th Five-Year Plan National Science and Technology Innovation Plan" proposes to focus on the development of modern industrial technology systems, including the development of a new generation of information technology, the development of advanced and efficient biotechnology, the development of population health technology, and these technical systems are related to the needs of healthy China's construction. A new generation of technologies, including cloud computing, Internet of Things, big data, and bioinformatics simulation, will become an important driving force for the entire health industry. By 2020, the scale of health industry market is expected to reach 10 trillion yuan, and it will exceed 16 trillion yuan by 2030, which is a huge opportunity for enterprises.

3. HEALTHY LIVING DEMONSTRATION ZONE AND FUNDAMENTAL HEALTHY PRINCIPLES

The process of urbanization in China keep advancing, and cities are the key to achieving healthy China. To promote the development of healthy cities, Healthy Living Demonstration Zone as a healthy model with clear theme, high sustainability and high replicability, can establish a template for creating healthy cities. Follow the Healthy China 2030 plan and the report, there are ten fundamental healthy principles should be complied in Healthy Living Demonstration Zone, which includes: Health and Happiness, Culture and Heritage, Ecology and Biophilia, Active and Active Transportation, Climate Change and Health, Material and Waste, Verification and Transparency, Public Health Policy, Responsible Development, Innovative Economy. In this way, the Healthy Living Demonstration Zone will give people a healthy environment that is inclusive, integrated, flexible, and with strong social identity and high level of participation.

3.1. Health and happiness

Health is not simply defined as having no disease. Instead, it is related to people’s overall physical, social and psychological well-being. There is a growing awareness of the complex relationship between mind and body. This interaction can significantly affect people’s health and well-being. Health and happiness are important components of sustainable life. Social, physical and psychological factors affect the overall health of individuals. In Healthy Living Demonstration Zone, we hope to see that green space in streetscape will be visible everywhere; Public art and aesthetic design will enrich the public environment; Medical services, educational facilities, elderly care facilities and other fundamental service facilities will fully cover people's need; Each community will provide residents with mental health, emergency and such support services; Art galleries, museums, houses of worship and other restorative places will be accessible; Low density of alcohol shop will reduce the crime rate; High density of parks, squares, playgrounds and other public open spaces will promote participation in public activities; The promotion of carpooling and neighbourhood association activities will bring people closer to each other, thus achieving happiness.

3.2. Culture and heritage

Culture and heritage are urban features that can stimulate people's emotional activities. With the rapid development of social productivity and science and technology, the economic strength of cities has been continuously enhanced, people’s material life has been greatly improved, and the desire and pursuit of people in spiritual life is getting stronger. The Healthy Living Demonstration Zone shall use healthy and wellness as its city brand. Its planning and construction will comply with the WELL Community Standard and the WELL Building Standard. With fully utilise of Internet, Internet of Things, cloud computing and other technologies, intelligent buildings, smart homes, road network monitoring, smart hospitals, personal health and digital living platforms will provide people a healthy, safe, comfortable, smart and convenient environment, so that the city brand of health and wellness will be an important source of urban confidence, cohesion and creativity in Health Living Demonstration Zone.

3.3. Ecology and biophilia

Land development and management are very important. The foundation of the Healthy Living Demonstration Zone is to increase the nature value and maximise the synergies of natural ecology and human health. In order to create a people-

nature integrated urban environment, biophilic design should be the primary concern. In a natural environment, people can effectively reduce stress, improve cognition and creativity, speed up healing and enhance well-being. The Healthy Living Demonstration Zone will increase natural visual, tactile, auditory, olfactory, and space perceptions to inspire positive interactions between humans and nature; Urban farms will enable people to enjoy cultivation and obtain Fresh food; The special design of rainwater management will enable the demonstration zone to have a good “flexibility” in adapting to environmental changes and responding to heavy rainfall disasters; The control of high quality air and water, as well as prevention technologies for light pollution and noise, will surely create a healthy and comfortable environment.

3.4. Active and active transportation

The World Health Organization pointed out that the movement is an important investment. The city's exercise programs and accessibility of activity spaces will increase participants' physical activity levels and physical quality, and even boost urban cohesion. Active and active transportation is the active, healthy and vibrant urban environment that people feel when they enter the demonstration zone for the first time. The environmental factors such as the mixed use of land, the residential density, the intersections density, the accessibility of bus stops and service facilities greatly affects people's travel choices. Through the perspective and experience of pedestrians and cyclists, convenience, comfort, safety, orientation and aesthetics are integrated into the design of district and street. At the same time, considering the characteristics and needs of people in different ages and their different physical conditions, individual exclusive activity spaces will be created for children, the elderly, pregnant women and disabled people. Beyond that, an urban long-time health management program will be established in Healthy Living Demonstration Zone to provide personalised health management services based on individual health records, hence achieve comprehensive protection for individuals and groups in health.

3.5. Climate change and health

In response to China’s plan of reducing its CO2 emissions per unit of GDP by 60% to 65% from 2005 by 2030, the principle of climate change and health is born. Traditional energy sources are usually accompanied by a large amount of carbon emissions. The use of renewable energy can not only help the demonstration zone to reduce overall carbon emissions, but also reduce the losses caused by energy transport. On the other hand, through the simulation of wind corridors to guide urban planning can improve air flow, relieve heat island effect, and improve the comfort of human body; Plant trees with huge crown to shade the road and square will reduce the heat island effect which caused by hard pavement. These development methods that reduce energy consumption as well as improve the heat island effect will further enhance the pioneering and demonstrative role of the demonstration zone.

3.6. Material and waste

Materials and waste is an important principle of relieving the tensions of world’s resources and creating a healthy environment. The Health Living Demonstration Zone will reduce the consumption of material resources from four aspects: source control, reuse, recycling, and energy generated by waste. The demonstration zone put the healthy materials as the primary concern during material selection. All building materials, paints and coatings, sealants and adhesives, furniture, and public facilities will be tested and verified by a third-party material testing centre, which ensures the excellent performance of materials and products. In addition, the material testing centre will also control the concentration of total volatile organic compounds, formaldehyde and other harmful pollutants to provide people a safe and stable, clean and healthy environment.

3.7. Verification and transparency

Verification and transparency is an effective way for people to obtain city information. Through establishing of network publicity platform, brochures, and display screens, people will have a clear understanding of the target, project progress, materials used, energy consumption during planning, construction and operation period; At the same time, by constructing a health monitoring platform, operational data such as air quality, water quality, comfort, light environment, and acoustic environment will be collected together. These data are all based on people’s experiences and improved to better adjust the health model and development in the demonstration zone.

3.8. Public health policy

Public health policy can support people's physical, mental and emotional well-being. By creating comprehensive and equal medical, housing and food health policies, flexible corporate policies, community’s health supporting policies, as well as the policies of encouraging public participation and feedback, an active and healthy social environment will be created which will give people a sense of belonging. Public health policy not only emphasises people's subjective feelings of wellbeing, but also improves people's livelihood and strengthening the social security system. It is a favorable guarantee for the implementation of the “Healthy China 2030” plan.

3.9. Responsible development

Healthy living cannot be separated from responsible development. The development of Healthy Living Demonstration Zone will implement a series of sustainable management measures and strategies, such as: Healthy living researchers are appointed to facilitate the setting of healthy living related performance targets and participate in the whole processes of design and development; The principal contractor will operates an Environmental Management System (EMS) covering their main construction process; Indoor air and water testing will be carried out by an independent third party; Sharing operational data with evidence-based platforms to monitor health status and guide future development. The responsible development attaches great importance to health research and innovation, and has outstanding and rich project experience, which will effectively guarantee the implementation effect and long-term development of healthy living in the demonstration zone. Responsible developers can not only successfully establish a healthy living demonstration zone, but also can replicate the healthy concept and experience in other cities, thus healthy living will trigger a trend in the industry.

3.10. Innovative economy

Innovative economy is an economic theory that emphasises entrepreneurship and innovation spirit. Markets that rely on input of resources and price signals have been unable to effectively stimulate productivity growth. The focus of corporate development and its wealth expansion have shifted to creating new business models, products and services. The Healthy Living Demonstration Zone will encourage knowledge and innovation as the main driving force. The WELL living labs will be constructed on site so that enterprises will have new intellectual properties, new technologies, new products, and new services. This will increase the core competitiveness of the demonstration zone and bring a thriving regional economy.

4. CONCLUSION

The healthy cities in the future should be healthy and fair, and everyone should enjoy the same sustainable health insurance. The realization of healthy China needs the implement of Healthy Living Demonstration Zone, the development of healthy cities nationwide, and the active participation of the whole society. We believe that with the development of health innovations, and the gradual implementation of health strategies, a number of health benefits will realised and become the basis for China's healthy development in the future.

5. REFERENCES

Badger, E., 2018. Tech envisions the ultimate start-up: An entire city [OL]. The New York Times. https://www.nytimes.com/2018/02/24/upshot/tech-envisions-the-ultimate-start-up-an-entire-city.html

Benedictus, L., 2014. Sick cities: Why urban living can be bad for your mental health. The Guardian, 25.

Chen, Q., Dietzenbacher, E. and LOS, B., 2017. The effects of ageing and urbanisation on China's future rural and urban populations. Asian Population Studies, 13(2), pp.172-197.

Fu, H., Xuan, Z.L. and Li, Y., 2006, Development and practical model of healthy city programs in China. Med Philosophy, 27: 12-15

Jamrozik, A., Ramos, C., Zhao, J., Bernau, J., Clements, N., Wolf, T.V. and Bauer, B., 2017. A novel methodology to realistically monitor office occupant reactions and environmental conditions using a living lab. Building and Environment.

Kohll, A., 2017. The top corporate wellness trends to watch for in 2017[OL]. Forbes. https://www.forbes.com/sites/alankohll/2017/01/18/the-top-corporate-wellness-trends-to-watch-for-in-2017/#19aa07797b28

Luo, Y., 2010. Health problems and solutions during the urbanization in China. Chin J Public Health, 26: 1532-1534

Tompkin, G., Vecchione, T., Williamson, J., et al., 2006. The 2006 U.S. Workplace Survey.

Yang J, José G S, Remais J V, et al. The Tsinghua-Lancet Commission on healthy cities in China: Unlocking the power of cities for a healthy China. Lancet, 2018

395: Mitigation of the impact of solar PV module exposed to partial shading condition

Akim AMINOU MOUSSAVOU[1], Marco ADONIS[2], Atanda RAJI[3]

[1] *Cape Peninsula University of Technology, Department of Electrical Engineering, cape town, South Africa, aminou-moussavou@cput.ca.za*

[2] *Cape Peninsula University of Technology, Department of Electrical Engineering, cape town, South Africa, adonisma@cput.ac.za*

[3] *Cape Peninsula University of Technology, Department of Electrical Engineering, cape town, South Africa, rajia@cput.ac.za*

This article focuses on the performance of PV modules under partial shading, which causes a variation in the output power, and the module operating temperature. To reduce this effect, it is important to take appropriate action. The partial shading affects most of the hot spots in the PV module, resulting in total energy dissipation and cracking the solar module, which can reduce up to 10% of the total power of the solar module. Reverse current due to partial shade can be increased to a high temperature on the module. The analysis conducted shows that the hot spot of solar cell components in the concentration of the element is not uniform. This paper considers the internal heat generated due to shade cells and power loss. The use of a bypass diode model in PV module significantly improves the power and the operating temperature of the solar cell under partial shading.

Keywords: Temperature effect, partial shading, bypass diode, photovoltaic systems, modelling and simulation, power production.

1. INTRODUCTION

Many countries around the world have been widely promoting the use of renewable energy, which tends to reduce greenhouse gases caused by human activities using fossil fuels (Lu, 2017; Moussavou et al., 2015). Solar photovoltaic technology is the most used renewable energy, due to its availability, sustainability and environmentally friendly energy. Several applications such as solar electric propulsion and solar desalination are derived from solar energy. The transformation of the solar radiation into electrical energy has been intensified in the past decades with wide applications for human development. Photovoltaic systems are integrated into the society to promote energy independence (autonomy), therefore requiring large-scale integration. This integration of solar components allows optimisation of solar collecting surfaces. However, the main problem of this type of conversion is its low output energy efficiency. Most of the absorbed radiation is discarded in the PV modules as wasted heat, which increases the solar cell operating temperature (Koech et al., 2012; Moussavou et al., 2016).

Photovoltaic modules are made to convert solar radiation into electrical energy which is characterised by their peak power and is determined under certain conditions in the laboratory. The performance of photovoltaics is related to the operating temperature of the modules. Solar cells in the module are connected in parallel and in series in the network to provide the desired current and voltage. When the characteristic IV curve of the photovoltaic module is different due to cell damage, radiation change, temperature inequality, local shading and pollution, the power output of the PV generator decreases considerably (Swart and Hertzog, 2016). In traditional PV module models, open-circuit voltages, short-circuit currents and different loss sources appear as shunts and resistors in series. The electrical characteristics of a solar cell depend on the temperature of the junction. The short circuit current increases with temperature. The open circuit voltage decreases approximately linear with the temperature. Consequently, the yield of a photovoltaic module decreases, when it's operating temperature increases (Chander et al., 2015). For example, crystalline silicon modules dependence is linear to strong illumination. The yield decreases by about 0.5% per degree if the climate is considered, 10% to 30% difference can be observed between the yield to STC (Standard Test Condition) and actual yield in illumination (Dupré et al., 2018). The power provided by the PV system is greatly inclined by a lower shunt resistance and higher series resistance (Zegaoui et al., 2012). Due to the reverse current through the shunt, a solar cell with a local ohmic shunt heats up under local shading conditions, creating a hot spot. Depending on the size of the hot spot and the reverse current, this can damage the solar module (Warta et al., 2011; Zaraket et al., 2017). When the module operates under partial shading, the energy conversion rate is amplified in opposite direction. In this case, all photovoltaic cells connected in series will force the same amount of current from the shading cells that generate the smallest currents. For this reason, the shadow cell can be polarised in reverse, producing high temperatures because it is charged (Humada et al., 2014; Lu et al., 2013). This article mainly studies the power dissipation on solar modules and the formation of hotspots caused by partial shading and its effect on photovoltaic performance in practical operation. The formation of photovoltaic hot spots, different types of cracks and the mode of operation of bypass diode are also discussed.

2. PARTIAL SHADING OPERATION AND HOT SPOT FORMATION

Hot spots occur in cells that generate less current in solar modules, which make the total power of the modules higher than those of the short circuits (Herrmann et al., 1997). The development of hot spots is due to various causes, such as shading, shunting behaviour of a P-N junction in a solar cell, damage to the solar cell, or when solar cells are electrically mismatched (Herrmann et al., 1997). Some shadow cells receive energy from shadow-free areas and forces all the solar cells in series to operate at the same current, The shadow cells of the module are reverse biased, resulting in power dissipation and heating effect, creating hot spots, causing permanent damage to the PV array (Rahman et al., 2014; Salem and Awadallah, 2016). The results show that there is a strong reduction in power under the shading conditions on behalf of the two highest points of the power-voltage characteristic curve (Meyer and Dyk, 2004). In order to prevent compressed local heating due to partial shade, an additional discrete component (bypass diodes) has been introduced to the photovoltaic modules. The shading causes the total voltage drop of the photovoltaic module by absorbing energy as a load; as a result, it creates hot spots that dissipate power. Variation of shunt resistance (Rsh) value has an impact on the inverse I-V slope of the cell, resulting in high power dissipation. This dissipated power introduces a sudden change in the local connection area, forming a hot spot which increases the overall temperature (Moore and Shi, 2014; You et al., 2015). The module dissipates this thermal energy through its surface in convective mode, radiative and in infrared. Some of the heat migrates in conductive mode towards the rear of the module. However, this flow is neglected in most modelling of the literature, since the gradients induced in the module plane are small compared to those caused by natural or forced convection.

3. PV PHOTOVOLTAIC LOSSES

The main factors of loss and the main physical limits of photon-electron within a photovoltaic cell are the following (Alharbi and Kais, 2015; Humada et al., 2014):

- The incomplete absorption of the incident photon spectrum (photon energy Eph less than the band gap energy hv < Eg) depends on the choice of the semiconductor materials of the module.
- The excess of photon energy greater than the band gap (hv - Eg> 0) generating an electron-hole pair is wasted as heat to the module.

- The only part of the incident flux is absorbed into the material and the other part is being reflected. This reflection on the solar surface module depends on orientation parameters (the direction of the solar module and the angle of incidence, the position of the sun, and the geographical location of the module. The absorption properties of some module surfaces are improved by adding an anti-reflection layer at the surface to reduce the loss.
- The loss depends on the chosen type of junction (homojunction, heterojunction) and the characteristics of the materials involved (purity, defects, electrical properties, residual stresses)
- Joule heating losses associated with the internal series resistance of the module depend on the electrical properties of the metals used. The combined loss in cable resistance, the contact resistance in the terminals, fuses, connectors, shunt resistance and the diode voltage drop in the array.
- Degradation of the characteristic IV is related to the shunt resistance, among other things such as the leakage currents of the cell surface or short-circuits at the edge of the cell, cell mismatching.
- Influence of temperature and influence of illumination (shading effect).
- The current is not balanced due to a portion of the array which is covered with a shade; when the current and voltage of the modules are mismatched. This results in low overall output power.
- PV cells also lose power output over time; ageing of cells can limit power to as much as 80% of original power over 20 years.
- The accumulation of dirt and other particles on the surface of the PV module reduces.

4. PHOTOVOLTAIC MODULE MODEL

Many studies have addressed the impact of temperature on photovoltaic cells performance, but most of the literature does not analyse the origin of the problem. The instantaneous decrease in performance of the photovoltaic with the rise of temperature and long-term degradation is favoured by thermal (Chander et al., 2015; Royne et al., 2005). It exists in various types of solar cell material, for instance, silicon-based mono-crystalline, polycrystalline and amorphous solar cells with an efficiency of 20%, 12% and 7% respectively (Kosyachenko, 2011). Numerous equations describe the degradation in temperature of a photovoltaic cell performance. The following solar cell efficiency equation is mostly used in practical applications without incurring a significant loss in the accuracy(Makrides et al., 2012).

The maximum surface temperature of the PV module is proportional to the amount of the induced reverse current and the leakage current. The PV modules overheating is proportional to the reverse current (Zaraket et al., 2017). These phenomena become important when some cells operate under reverse bias mode, in turn, destroys the particular cells, thus disrupting the entire photovoltaic system.

of Evans (Tiwari and Dubey, 2010):

Equation 1: The cell efficiency at the operating temperature T_C

$$\eta_{T_C} = \eta_{ref}\left[1-\beta\left(T_C - T_{ref}\right)\right]$$

Where:

T_{ref} = reference temperature(K)

β = temperature coefficient is ranging between 0.003 – 0.0063 /ºC

T_C = operating temperature (K)

η_{ref} = electrical efficiency at the reference temperature

The temperature coefficient β can be calculated by the following equation:

Equation 2: The temperature coefficient β

$$\beta = \frac{1}{\left(T_0 - T_{ref}\right)}$$

A cell with a low β is not sufficient to ensure good performance operation. It is also necessary that the cell does not operate at high temperature.

Where:

T_0 = maximum temperature (K)

T_0 (270 °C for crystalline silicon cells) represents the maximum temperature at which the efficiency of the PV cells decreases to zero.

Many authors address the problem of heating modules and excellent syntheses are proposed by (Chow et al., 2012; Meyer and Dyk, 2004; Royne et al., 2005).

When a series of a PV array is under a shadow, the current output is determined by:

Equation 3: The current output of PV array under a shadow

$$I = FI_L - I_0\left(e^{\frac{q(V_S+I_S R_{sei})}{nkT}} - 1\right) - \frac{V_S + I_S R_S}{R_S}$$

Where:

F = Ratio of the photoabsorption current generated by the shaded illuminated cells to that generated by the fully illuminated cells

I_0 = Diode reverses saturation current in the equivalent circuit of the module (A)

q =Electron charge (=1.602×10-19 C)

η = diode ideality factor

V_S - Voltage across one of the shaded illuminated cells (V)

P_{Ds} - Power dissipated by a cell under shaded illumination (W)

I_L - The current generation by absorption of photons at short circuit (A)

As the shaded and illuminated cells are connected in series, the same current is forced to flow through both. As the value of *F* declines from 1 to 0, $e^{\frac{q(V_S+I_S R_S)}{nkT}}$ lean towards to zero.

Thus the equation (3) is simplified as

Equation 4: simplification of equation (3)

$$I = I_{m1} = I_{m2}$$

$$I = FI_L - I_0\left(e^{\frac{q(V_S+I_S R_{sei})}{nkT}} - 1\right) - \frac{V_S + I_S R_S}{R_S}$$

The measured voltage across shaded cell is

Equation 5: The voltage across the shaded cell V_S

$$V_S = (FI_L + I_S)R_{shs} - IR_{shs}$$

The power degenerated by the partially shaded cells is obtained from the following equation.

Equation 6: The power degenerated

$$P_{Ds} = V_S I = (FI_L + I_S)IR_{shs} - IR_{shs}$$

4.1. Bypass diode in photovoltaic module

The voltage-current (I-V) characteristic curve of a photovoltaic generator using a bypass diode shows one or more local maximum power points (MPP) caused by the mismatch. As a result, the distortion of the I-V shadow curve is used to determine the overall MPP mismatched (Ramos-Paja et al., 2016; You et al., 2015). Bypass diodes are inserted PV modules in the junction box to avoid hot spots and high temperature on a solar cell, while the bypass diodes are forward biased under the shading conditions. The new short-circuit current flows through the bypass diode in the shaded cell, so that the bypass diode reduces local overheating in the shaded area. The shaded cells change dramatically towards the PV characteristic and reduce the output power, minimizing the mismatching effect of PV devices by using shunt diodes on PV module output performance and IV characteristics (Ramos-Paja et al., 2016).

5. DESIGN SPECIFICATION

Two PV modules system is connected in series. One of the PV modules is considered to have constant solar radiation on its surface, while others are full or partially shaded as seen in Figure 1. Various simulations will run under full illumination (1 kW/m^2) and shaded conditions to study the effect shaded cells have on the output power.

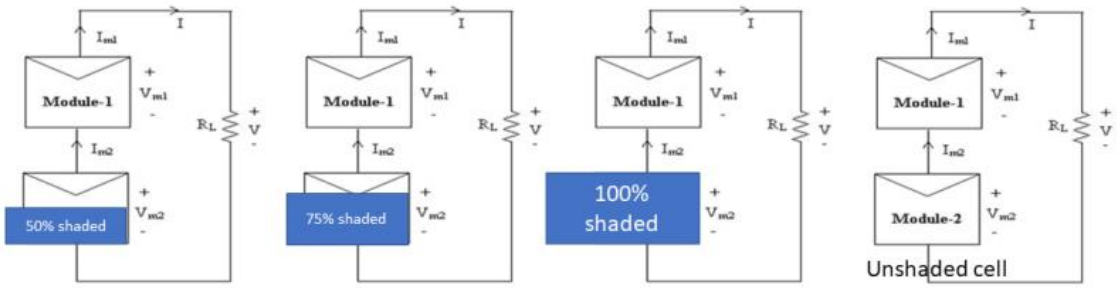

Figure 1: Solar cell under different percentage in shade

A bypass diode is connected in parallel to each PV module made of 18 cells. The function of the diode is simply to deliver power and protection to the load while some solar cells are shaded. Two sets of cells are connected to the intensity of the radiation. The behaviour under reverse bias conditions of the same type of cells (poly-Si and mono-Si cell) undergoes considerable changes. This involves the slope of the low polarization inverse characteristic and the value of the breakdown voltage. The temperature is generated through a heat port pattern and represents the heat mass of the solar cell only. The heat mass is directly connected to the heating port of the component H. The internal heat source is suitable for the flow of heat to the port and the heat mass. The internal heat generated in the solar cell is calculated according to the formulas above including ambient temperature, radiative heat transfer and convective heat transfer.

Table 1: solar module parameter

S.No.	Parameters	Single Cell	Module
1	Rated Power	1.03W	151.2W
2	Voltage at maximum Power (Vmp)	0.62V	17.V
3	Current at maximum power (Imp)	7A	7A
4	Open circuit voltage (Voc)	0.62V	22.14V
5	Short circuit current (Isc)	7.34A	7.34A

6. SIMULATION RESULTS AND DISCUSSION

All PV modules are assumed to be identical and the difference between the shaded and non-shaded cells temperature and reverse breakdown in shaded cells are considered to be uniform. The values of Rses and Rsh are assumed to be constant for a particular value F. First order temperature coefficient (TC1) for the linear term in the equation in MATLAB was used to calculated resistance value for temperature. Connecting modules in series forms the arrays and the parameters are shown in Table 1. The simulation model of the two solar cells connected in series with non-uniform solar radiation. The first PV module received full solar radiation of 1 kW/m^2, while the second received 100%, 75%, 50%, 25% and 0% of solar radiation, corresponding to 1 kW/m^2, 0.5 kW/m^2, 0.25 kW/m^2 and 0 kW/m^2. The average value of the power, current and voltage produced. In full solar radiation, one of the solar modules in series produces a fixed power value; however, power varies in the shaded solar module.

The voltage across the load resistance varies with the percentage changes in the shade solar cell connected in series with a solar cell that receives the full radiation of 1000 w/m^2. This is being presented in the simulation. In absence of bypass diode, different voltages are measured under various shaded cells as seen in Figure 2.

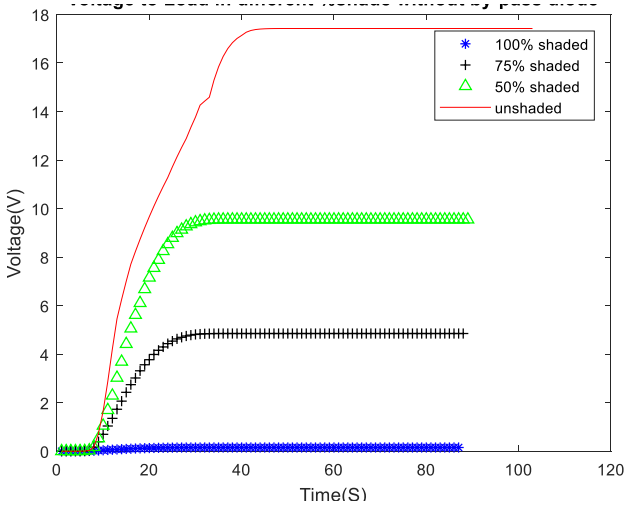

Figure 2: Voltage across the load resistance without bypass diode

Figure 2 above, the output voltage falls to 16.8 V, 9.9 V, 4.3V, and almost 0 V, when the percentage of solar cell shaded is 0%, 50%,75% and 100% with no bypass diode connected to the system.

Figure 3 below, There was a decrease in current to 6.8 A, 3.8 A, 1.9 A and 0 A when the percentage of solar cell shaded is 0%, 50%,75% and 100%. Thus the voltage and the current decrease as the shade in the solar cell increase with no bypass diode connected.

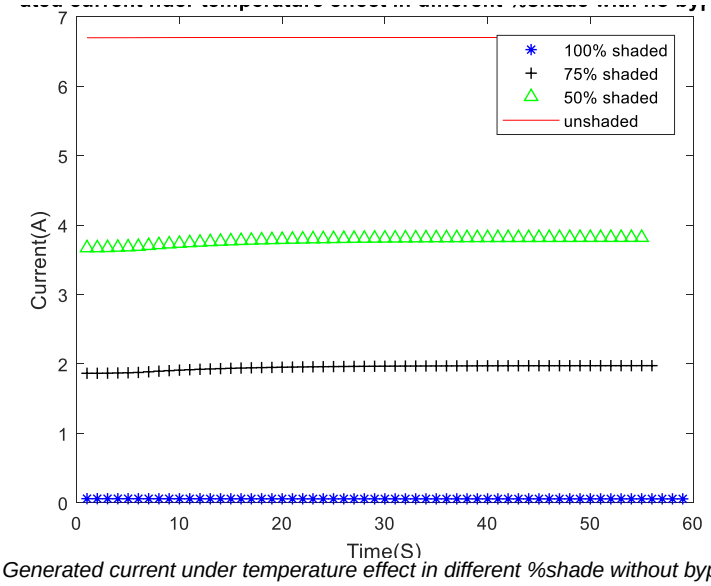

Figure 3: Generated current under temperature effect in different %shade without bypass diode

Figure 4 below, presents the overall power generated under different percentages of the shaded cell. The average power goes down considerably to 120W, 45W, 14W and barely 0 W, as the shade increase from 0% 50% 75% to 100%, respectively. The power loss is due to the shade in the second PV module.

Figure 5 below, shows the average internal temperature of the PV module. There were rapid and constant increases in temperature to 28 °C, 33 °C, 36 °C and 40 °C through the time (S), as the shade increases in the cell to 0%, 50%, 75 % and 100 %, respectively. The average temperature rises due to the hotpot effects.

When bypass diode is parallel connected to each solar cell. Figure 6 below, illustrates the output voltage produced at specific partial shade on the solar cell 50%, 75% and 100% are 9.8 V, 9.2 V, 8.5 V, respectively. When the shade on the second PV module are 50%, 75% and 100%, the currents drop to 3.8 A, 3.5 A and 0.2 A, respectively.

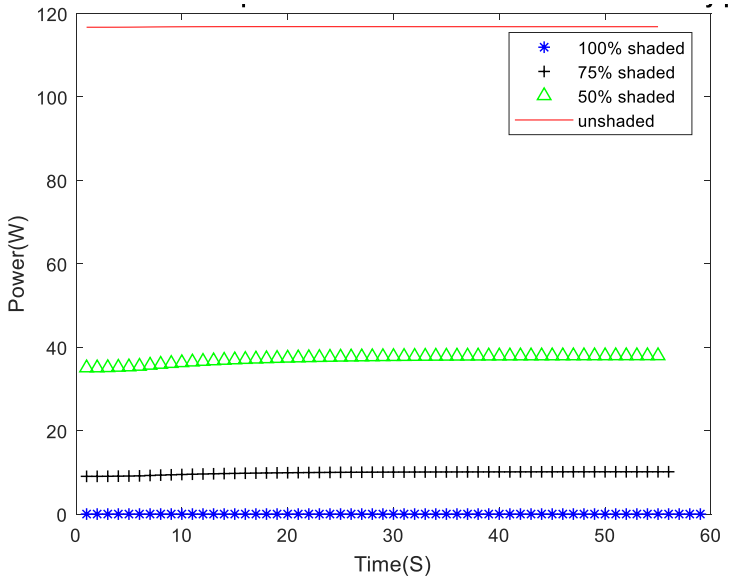

Figure 4: Generated Power under temperature effect in different %shade without bypass diode.

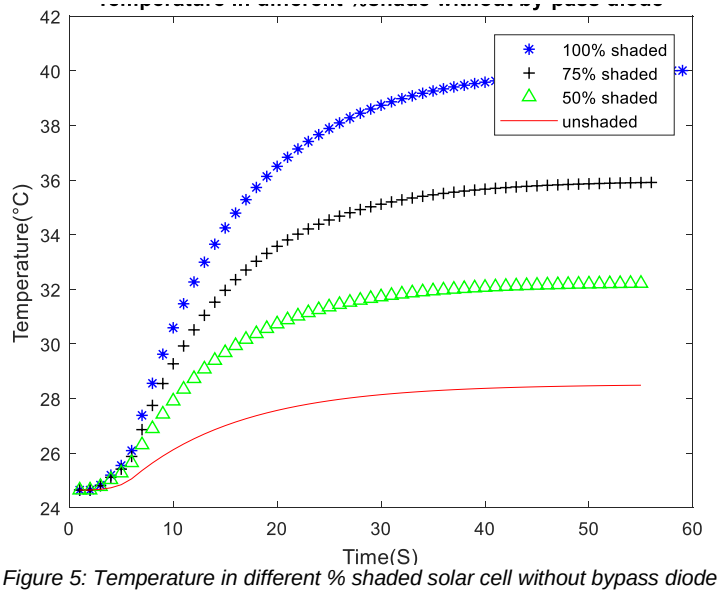

Figure 5: Temperature in different % shaded solar cell without bypass diode

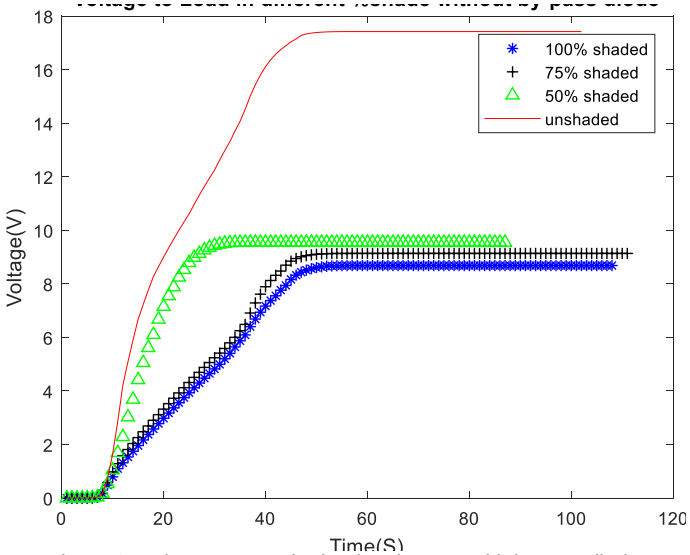

Figure 6: Voltage across the load resistance with bypass diode.

Figure 7 below, there was a decrease in current to 6.8 A, 3.8 A, 3.5 A and almost 0 A, when the percentage of solar cell shaded is 0%, 50%,75% and 100%, respectively. A slight improvement can be observed in the generated current.

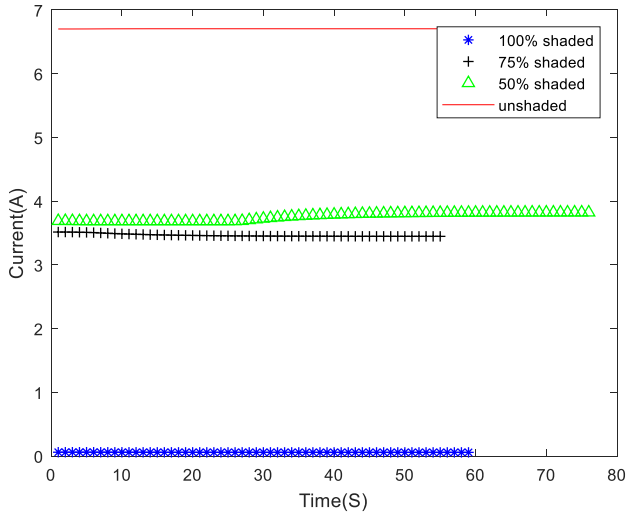

Figure 7: Generated current under temperature effect indifferent %shade with bypass diode

When bypass diode is connected to the system. Figure 8 below, there was a drop in average power produced by the PV module to 40 W, 33 W and 30 W, when the percentage in the shaded solar cell goes up to 50%, 75% and 100%, respectively.

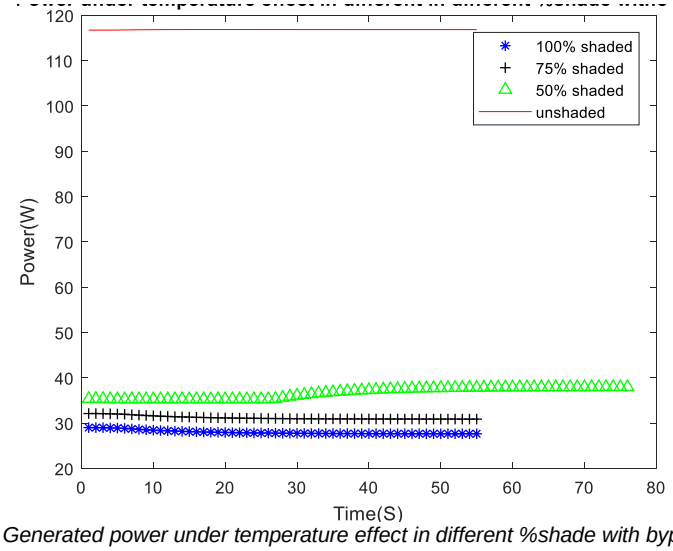

Figure 8: Generated power under temperature effect in different %shade with bypass diode

Figure 9 below, there was a slow and steady rise in the internal temperature to 31°C, 32 °C and 33°C, as the percentage in the shaded solar cell goes up to 50%, 75% and 100%, respectively.

The overall design efficiency improves (voltage, current, temperature and power), when comparing Figure 2, Figure 3, Figure 4 and Figure 5 to Figure 6, Figure 7, Figure 8 and Figure 9, respectively; the insertion of bypass diode has reduced the loss in power, current and voltage and also decreased the internal temperature of the PV module.

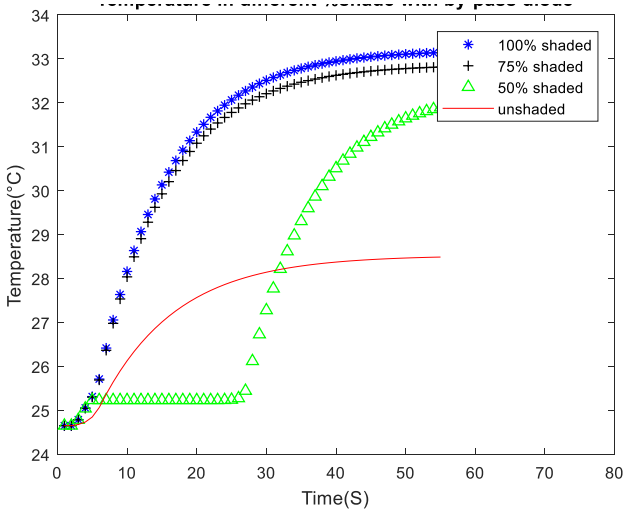

Figure 9: Temperature in different % shaded solar cell with bypass diode

7. CONCLUSION

Many of solar cells string are connected in the serial-parallel network to obtain the necessary power. All cells connected in series receive the same illumination in different shadow modes. Considerable power dissipation on solar module due to the non-uniform solar radiation is caused by shaded cells and the internal generated heat. Special care is provided for protecting the solar cell module which consists of connecting sub-modules in series and in parallel by the bypass diode protection, while total energy production will be higher. In this paper, solar cell with and without bypass diode were compared under different shading conditions and analysed. From the simulation model, the power generated by different PV modules (with and without bypass diode) of the network was evaluated with temperature. The module configuration with bypass diode was found to dominate the shadow condition as it tends to reduce the power dissipation on the module. Inclusion of bypass diode models and the use of cooling systems are possible solutions for minimizing hot spots and the effects of temperature in certain operating conditions.

8. REFERENCES

Alharbi, F.H., Kais, S., 2015. Theoretical limits of photovoltaics efficiency and possible improvements by intuitive approaches learned from photosynthesis and quantum coherence. Renew. Sustain. Energy Rev. 43, 1073–1089.

Chander, S., Purohit, A., Sharma, A., Arvind, Nehra, S.P., Dhaka, M.S., 2015. A study on photovoltaic parameters of mono-crystalline silicon solar cell with cell temperature. Energy Rep. 1, 104–109.

Chow, T.T., Tiwari, G.N., Menezo, C., Chow, T.T., Tiwari, G.N., Menezo, C., 2012. Hybrid Solar: A Review on Photovoltaic and Thermal Power Integration, Hybrid Solar: A Review on Photovoltaic and Thermal Power Integration. Int. J. Photoenergy Int. J. Photoenergy 2012, 2012, e307287. https://doi.org/10.1155/2012/307287, 10.1155/2012/307287

Dupré, O., Niesen, B., De Wolf, S., Ballif, C., 2018. Field Performance versus Standard Test Condition Efficiency of Tandem Solar Cells and the Singular Case of Perovskites/Silicon Devices. J. Phys. Chem. Lett. 9, 446–458.

Herrmann, W., Wiesner, W., Vaassen, W., 1997. Hot spot investigations on PV modules-new concepts for a test standard and consequences for module design with respect to bypass diodes, in: Conference Record of the Twenty Sixth IEEE Photovoltaic Specialists Conference - 1997. Presented at the Conference Record of the Twenty Sixth IEEE Photovoltaic Specialists Conference - 1997, pp. 1129–1132.

Humada, A.M., Samsuri, F.B., Hojabria, M., Mohamed, M.B., Sulaiman, M.H.B., Dakheel, T.H., 2014. Modeling of photovoltaic solar array under different levels of partial shadow conditions, in: 2014 16th International Power Electronics and Motion Control Conference and Exposition. Presented at the 2014 16th International Power Electronics and Motion Control Conference and Exposition, pp. 461–465.

Koech, R.K., Ondieki, H.O., Tonui, J.K., Rotich, S.K., 2012. A Steady State Thermal Model For Photovoltaic/Thermal (PV/T) System Under Various Conditions, 11.

Kosyachenko, L.A., 2011. Thin-Film Photovoltaics as a Mainstream of Solar Power Engineering. Sol. Cells - Thin-Film Technol.

Lu, F., Guo, S., Walsh, T.M., Aberle, A.G., 2013. Improved PV Module Performance under Partial Shading Conditions. Energy Procedia, PV Asia Pacific Conference 2012 33, 248–255.

Lu, W.-C., 2017. Greenhouse Gas Emissions, Energy Consumption and Economic Growth: A Panel Cointegration Analysis for 16 Asian Countries. Int. J. Environ. Res. Public. Health 14. https://doi.org/10.3390/ijerph14111436

Makrides, G., Zinsser, B., Norton, M., Georghiou, G.E., 2012. Performance of Photovoltaics Under Actual Operating Conditions. Third Gener. Photovolt.

Meyer, E.L., Dyk, E.E. van, 2004. Assessing the reliability and degradation of photovoltaic module performance parameters. IEEE Trans. Reliab. 53, 83–92.

Moore, A.L., Shi, L., 2014. Emerging challenges and materials for thermal management of electronics. Mater. Today 17, 163–174.

Moussavou, A.A.A., Adonis, M., Raji, A., 2016. Design and simulation of solar cell system under different environmental conditions, in: 2016 International Conference on the Industrial and Commercial Use of Energy (ICUE). Presented at the 2016 International Conference on the Industrial and Commercial Use of Energy (ICUE), pp. 270–277.

Moussavou, A.A.A., Adonis, M., Raji, A., 2015. Microgrid energy management system control strategy, in: 2015 International Conference on the Industrial and Commercial Use of Energy (ICUE). Presented at the 2015 International Conference on the Industrial and Commercial Use of Energy (ICUE), pp. 147–154.

Rahman, M.M., Hasanuzzaman, M., Rahim, N.A., 2014. Temperature effect of photovoltaic module under partial shading operation condition, in: 3rd IET International Conference on Clean Energy and Technology (CEAT) 2014. Presented at the 3rd IET International Conference on Clean Energy and Technology (CEAT) 2014, pp. 1–6.

Ramos-Paja, C.A., Trejos, L.A., Herrera Murcia, J., 2016. Fast calculation of the maximum power point of photovoltaic generators under partial shading. Ing. E Investig. 36, 58–65.

Royne, A., Dey, C.J., Mills, D.R., 2005. Cooling of photovoltaic cells under concentrated illumination: a critical review. Sol. Energy Mater. Sol. Cells 86, 451–483.

Salem, F., Awadallah, M.A., 2016. Detection and assessment of partial shading in photovoltaic arrays. J. Electr. Syst. Inf. Technol. 3, 23–32.

Swart, A.J., Hertzog, P.E., 2016. Varying percentages of full uniform shading of a PV module in a controlled environment yields linear power reduction. J. Energy South. Afr. 27, 28–38.

Tiwari, G.N., Dubey, S., 2010. Fundamentals of Photovoltaic Modules and Their Applications. Royal Society of Chemistry.

Warta, W., Schubert, M.C., Rein, S., Fertig, F., 2011. Impact of Junction Breakdown in Multi-Crystalline Silicon Solar Cells on Hot Spot Formation and Module Performance. 26th Eur. Photovolt. Sol. Energy Conf. Exhib. 1168–1178.

You, S., Chen, M.-W., Dlott, D.D., Suslick, K.S., 2015. Ultrasonic hammer produces hot spots in solids. Nat. Commun. 6, 6581.

Zaraket, J., Khalil, T., Aillerie, M., A. Vokas, G., Salame, C., 2017. The Effect of Electrical stress under temperature in the characteristics of PV Solar Modules. Energy Procedia, International Conference on Technologies and Materials for Renewable Energy, Environment and Sustainability, TMREES17, 21-24 April 2017, Beirut Lebanon 119, 579–601.

Zegaoui, A., Petit, P., Aillerie, M., Sawicki, J.-P., Charles, J.-P., 2012. Experimental Validation of Photovoltaic Direct and Reverse Mode Model. Influence of Partial Shading. Energy Procedia, Terragreen 2012: Clean Energy Solutions for Sustainable Environment (CESSE) 18, 1247–1253.

398: Simulation study on performance of a solar assisted heat pump drying system

Zhaohai Li, Zhenqian Chen*

School of Energy and Environment, Southeast University, Nanjing, China
**Corresponding email: zqchen@seu.edu.cn*

Solar assisted heat pump drying system has been proposed to improve the efficiency of energy using for drying process due to drying is an energy intensive process and solar drying is deeply influenced by local weather compared to heat pump drying. In this study, a new solar assisted heat pump dryer has been designed and investigated. The drying system consists of a compressor, evaporator-collector, air condenser, air collector, dryer, blower and dampers. This system can realise three kinds of working modes, including solar drying, heat pump drying and solar assisted heat pump drying, and also can switch operating condition on opening, semi-opening and closing based on heat pump according to the path of drying medium. MATLAB program has been developed to evaluate the performance of the system and the influence of different variables. Results suggest that the entire drying time of the product decreases with the increase of drying air temperature, in addition, The air temperature of each outlet varies little with the ambient temperature and solar radiation when system working with mode of solar assisted heat pump. Coefficient of performance (COP) and the specific moisture extraction rate (SMER) are two main performance indices. With the increase of ambient temperature or solar radiation, the COP slightly decreased, but the SMER increased significantly. The SMER of the system can be improved under certain environmental conditions by adjusting the refrigerant flow ratio of evaporator. Analysis reveals that the drying system with simple structure is sustainable, adaptable and good for high quality product.

Keywords: Solar assisted heat pump dryer, heat pump, evaporator-collector, Coefficient of performance

1. INTRODUCTION

Drying is an energy intensive operation that easily accounts for up to 15% of all industrial energy usage, often with relatively low thermal efficiency in the range of 25–50% (Chua *et al.*, 2001). Therefore, under the circumstances of global energy shortage and environmental pollution, it is necessary to reduce the energy consumption for drying process by using present technologies.

In the world, 97–98% of dried vegetables that made traded dry with hot air under controlled conditions (Şevik *et al.*, 2013). At present, solar drying and heat pump drying as typical hot air drying methods are widely used in the drying process. The most prominent feature of solar drying is the use of solar energy that is renewable energy, and its device construction is simple. However, its application is limited by the discontinuity and instability of solar energy. Heat pump dryers possess high coefficient of performance and potential improvements in the quality of dried products due to the ability of heat pump to operate at lower temperature (Daghigh *et al.*, 2010).The principal advantages of heat pump dryers emerge from the ability of heat pumps to recover energy from the exhaust as well as their ability to control independently the drying gas temperature and humidity (Chua, 2002). Although heat pump drying has so many advantages, its energy consumption for same drying is higher than solar drying. Combined solar dryer and heat pump can overcome these difficulties of using solar dryer systems or solely using heat pump drying separately and satisfy important demands in industrial drying with respect to product quality control, reduced energy consumption and reduced environmental impact. Solar assisted heat pump drying systems have been studied and applied since the last decades in order to increase the quality of products where low temperature and well-controlled drying conditions are needed (Daghigh *et al*., 2010).

Solar assisted heat pump drying systems can be divided into several categories according to the medium flowed through solar collectors. One is based on air and water as the medium, and the other is based on refrigerant as the medium. There is also a combination of both. Şevik (Şevik et al., 2013) proposed a solar assisted heat pump drying system with a plate collector and a water source heat pump. The hot water heated by the plate collector is used as the heat source of the evaporator to increase the energy efficiency of the system. Qiu (Qiu *et al.*, 2016) studied a solar assisted heat pump drying system with a heat exchanger coil. The hot water heated by the solar collector flows through the heat exchanger coil to further heat the drying medium already heated by the condenser. Li (Li *et al.*, 2011) studied a solar assisted heat pump in-store drying system. After the air heated by the solar collector was mixed with the air heated by the condenser, it was sent to the dryer. Yahya M et al. (Yahya *et al.*, 2016) studied solar drying and solar assisted heat pump drying. Solar collectors assisted heat pump drying by further heating the air heated by the condenser. Mohanraj (Mohanraj, 2014) proposed a solar-ambient hybrid source heat pump drying system, in which a solar collector was used as an evaporator. Hawlader (Hawlader and Jahangeer, 2006; Hawlader *et al.*, 2003) proposed a solar-assisted heat pump system for drying and water heating. This system includes both an air collector and an evaporator-collector. The drying medium was heated by air collector after treated by the dehumidifier, so the system makes full use of solar and exhaust energy. Hawlader *et al*. (Rahman *et al.*, 2013, Hawlader, 2008) also studied the performance of the air collector and evaporator-collector in this system, and the economic optimisation of the two collector areas.

However, with respect to the solar assisted heat pump drying system, few people have studied the change of the drying mode by changing the air path to adapt to the change of meteorological conditions, and in the literature review, little works on the performance of the solar assisted heat pump drying system using numerical simulation. Therefore, in the study of this paper, a new solar assisted heat pump drying system was proposed. This system can not only achieve the three basic working modes, namely solar drying, heat pump drying and solar assisted heat pump drying, but also by changing the air duct to be further subdivided into open, semi-open, and closed working modes, which can greatly improve the ability of the system to adapt to environmental changes while ensuring high energy efficiency of the system; secondly, the performance of the system on working mode of solar assisted heat pump drying was studied through MATLAB programming.

2. SIMULATION

2.1. System design

In order to study a drying device that can change the working mode according to the external environment and operating conditions, a new solar assisted heat pump drying system was proposed, as shown in Figure 1. The system can be divided into two parts according to the flow paths of air and refrigerant. The air flowed path mainly composed of various components, including air collector, condenser, evaporator, dryer, blower, duct and valves. The refrigerant flowed path consists of a vapour compression heat pump unit and evaporator-collector. The two evaporators are connected to parallel with individual expansion valves and solenoid valves. The two flow paths are connected by evaporator and condenser.

When the solar radiation is strong, and the temperature of the air passing through the air collector is higher than the drying required temperature, the dampers 1, 3, 4 are opened, the dampers 2, 5 are closed, and the heat pump is turned off. At this moment, the energy required for drying was only provided by solar energy, which is a solar drying mode. When there is no solar radiation or at night, the heat pump is turned on, the dampers 3, 4 are closed, the dampers 2, 5 are opened, the solenoid valve 9 is closed, and the solenoid valve 8 is opened, which is a solar drying mode. In addition, the three working modes, including open, closed, semi-open, can be achieved by adjusting other dampers 1, 6, 7.

When the solar radiation is weak and the air temperature of the air collector is lower than the required temperature for drying, the heat pump is opened, the damper 3 is opened, the damper 2 is closed, and the solenoid valve 8 and 9 are opened at the same time. Similarly, according to the operating and environmental conditions, the damper can be adjusted to realise open, closed and semi-open working modes. In addition, in the middle and late stages of drying, dehumidification is mainly to remove the bound water in the dried material. Removing these waters requires a long drying time and consumes more energy. Moreover, due to the small mass transfer coefficient between the air and the dry material, the air state at the inlet and outlet of the dryer changes little, which affects the dehumidification capacity of evaporator. In order to maintain the stability of the drying temperature, most of the energy input into the system was discharged out of the system in the form of heat energy, and the dehumidification efficiency of the system is low (Wang *et al.*, 2002). Therefore, the evaporator-collector can be used as the only evaporator in the middle and later stages of drying to improve the energy efficiency of the system.

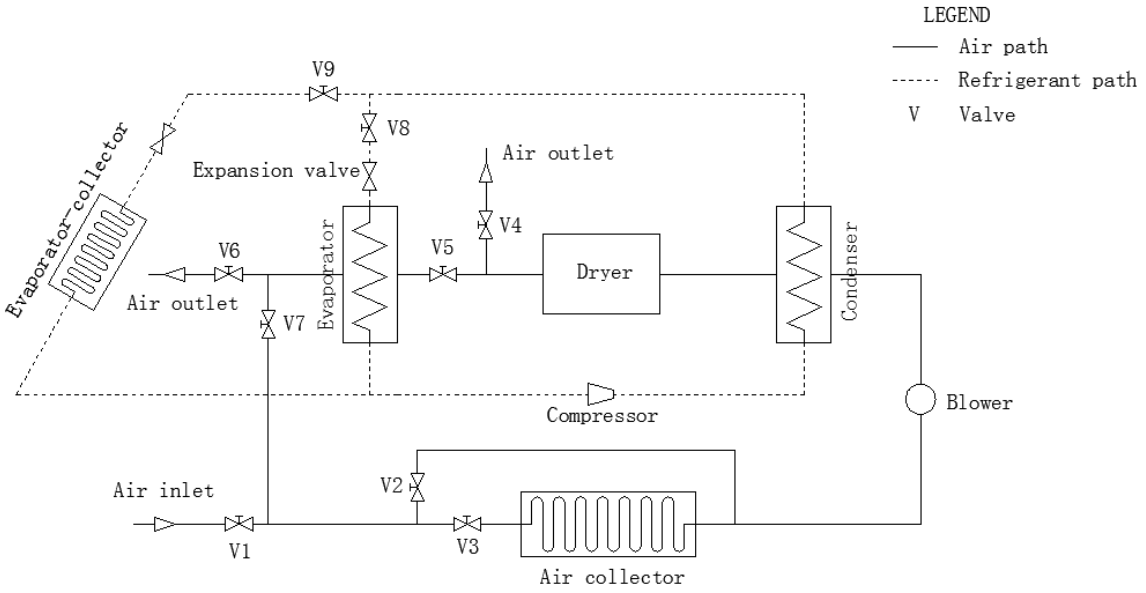

Figure 1: Schematic diagram of the solar assisted heat pump drying system

2.2. Mathematical model

Plate collector was selected as air collector，The useful energy collected by the collector can be expressed using the following equation (Duffie *et al.*, 1980)：

Equation 1: The useful energy collected by the collector

$$Q_u = A_c F_R \left[I_T (\tau\alpha) - U_L \left(T_{ai} - T_a \right) \right]$$

Where:

- Q_u = useful energy collected by the collector (W)
- A_c = area of air collector (m^2)
- F_R = collector heat removal factor (dimensionless)
- I_T = Solar radiation on the collector surface (W/m^2)
- $(\tau\alpha)$ =Transmittance absorptance effective product (dimensionless)
- U_L = collector overall loss coefficient (W/m^2K)
- T_{ai} =air temperature at inlet of collector (℃)
- T_s = ambient temperature, air temperature (℃)

The collector of the evaporator-collector is in the form of a bare plate, and the useful energy collected by the evaporator-collector can be determined by the following equation (Timoumi *et al.*, 2004):

Equation 2: The useful energy collected by the evaporator-collector

$$Q_u^{'} = A_c^{'} F^{'} \left[S^{'} - U_L^{'} \left(T_{evap} - T_a \right) \right]$$

Where:

Q_u' = useful energy collected by the evaporator-collector (W)
A_c' = area of evaporator-collector (m^2)
F' = collector efficiency factor (dimensionless)
S' = Solar radiation energy absorbed by an endothermic bare plate (W/m^2)
U_L' = evaporator-collector overall loss coefficient (W/m^2K)
T_{evap} =evaporating temperature (℃)
T_a = ambient temperature, air temperature (℃)

Rotary compressor was used in this study, and the refrigerant mass flow and input power can be expressed by the following equations (Zhang, 2013):

Equation 3: The refrigerant mass flow

$$m_{com} = \frac{\eta_v V_{th}}{v_{suc}}$$

Where:

m_{com} = refrigerant mass flow rate of compressor (kg/s)
η_v =Volume coefficient (dimensionless)
V_{th} = theory gas transmission of compressor (m^3/stroke)
v_{suc} = specific volume of compressor suction (m^3/kg)

Equation 4: The input power of the compressor

$$W = m_{com}\left(h_{dis} - h_{suc}\right) / f_Q$$

Where:

W = input power of the compressor (w)
h_{dis} =enthalpy of compressor discharge (J/kg)
h_{suc} =enthalpy of compressor suction (J/kg)
f_Q = heat loss coefficient (dimensionless)

The condenser model was based on the steady lumped parameter method according to different phase regions in the condenser, heat transfer equation (Zhang, 2013) is given as:

Equation 5: heat transfer equation

$$Q_r = UA_i\Delta T_m$$

Where:

Q_r =heat transfer rate of refrigerant side (W)
U = overall heat transfer coefficient of refrigerant side (W/m^2K)
A_i = area of refrigerant side (m^2)
ΔT_m = logarithmic mean temperature difference (℃)

With the same as condenser, the steady lumped parameter method was used in evaporator, and the heat transfer equation was also similar to condenser. However, unlike the condenser, the evaporator not only has heat transfer, but also has mass transfer. The equation for the moisture content of the humid air is given as follows (Zhang, 2013):

Equation 6: moisture content of humid air

$$-m_a dW_a = h_d\left(W_a - W_w\right)dA_a$$

Where:

W_a = moisture content of humid air (kg/kg)
W_w = saturated moisture content of humid air at the temperature of outer tube wall (kg/kg)
h_d = mass transfer coefficient (kg/m^2)
A_a =area of air side (m^2)

In this simulation study, mushroom was selected as drying material, and its drying kinetic model was expressed by following equation (Krokida *et al.*, 2003):

Equation 7: moisture content of dry material

$$X = X_e - (X_e - X_i)e^{-kt}$$

Where:

X = material moisture content in dry basis (kg water/kg dry solids)
X_e =equilibrium moisture content in dry basis (kg water/kg dry solids)
X_i = initial moisture content in dry basis (kg water/kg dry solids)
K =drying constant (1/min)
T = time (min)

R134a was selected as refrigerant in the system, and the calculation model of the refrigerant charge can be determined using the following equation (Zhang, 2013):

Equation 8: refrigerant charge

$$M = M_{TP,cond} + \int_0^{V_{SH,cond}} \rho dV + \int_0^{V_{SC,cond}} \rho dV + M_{TP,evap} + \int_0^{V_{SH,evap}} \rho dV + \rho_{com} V_{com} + M_{other}$$

Where:

M = refrigerant charge (kg)
V =volume (m^3)
TP, two phase; SH, superheat; SC, subcool; cond, condenser; evap, evaporator; com, compressor
ρ =density (kg/m^3)

In addition to the above models, the system also includes some other component models, such as the mathematical model of the expansion valve, the enthalpy of refrigerant is not changed before and after throttling. There are also some models in the system that connects the components, such as the continuity equation, mass conservation equation, energy conservation equation and momentum conservation equation. In addition, the simulation process also involves the calculation of the physical properties of refrigerant R134a, and the refrigerant properties are calculated by calling the loaded REFPROP function in MATLAB.

There are two important indices to evaluate the performance of entire system, coefficient of performance (COP) and specific moisture extraction rate (SMER). The coefficient of performance of the heat pump is defined by the following equation (Hawlader and Jahangeer, 2006):

Equation 9: COP

$$COP = \frac{Thermal\ energy\ released\ by\ the\ condenser}{Electrical\ energy\ input\ to\ the\ compressor}$$

The specific moisture extraction rate can be defined as the ratio of the moisture removed in kg to the energy input in kWh (Hawlader and Jahangeer, 2006):

Equation 10: SMER

$$SMER = \frac{Moisture\ removed\ in\ kg}{Energy\ input\ in\ kWh}$$

2.3. Simulation methodology

The simulation of the system was carried out by MATLAB. The simulation algorithm mainly assumes that the evaporating temperature, condensing temperature, subcool, superheat and inlet enthalpy of compressor, and the mathematical model of each part of the system was called in turn. Adjust the hypothetical values in turn by determining the conditions until the conditions are met. After the calculation of the cycle was completed, the calculation parameters were outputted. The simulation flow chart of the system is given in Figure 2.

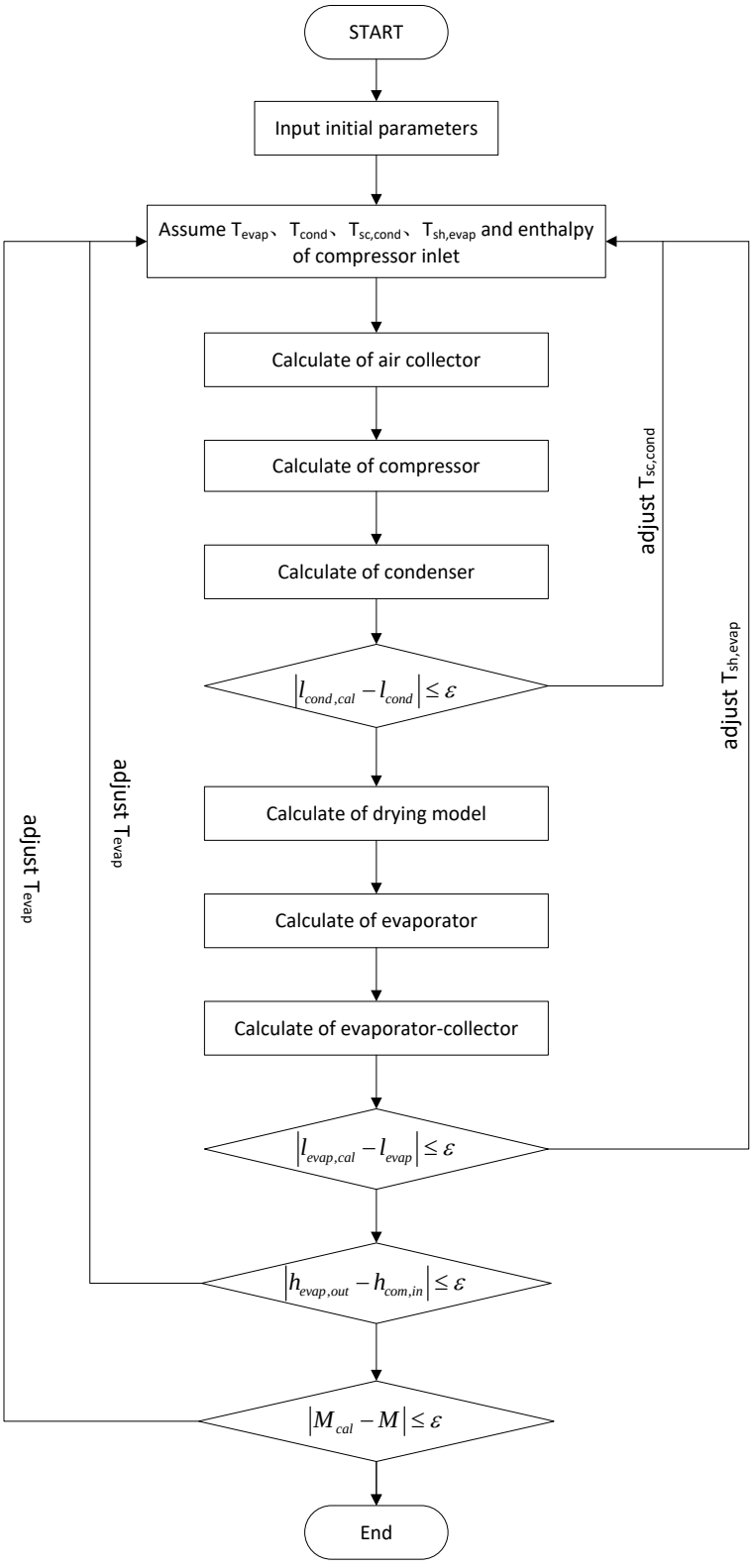

Figure 2: Simulation Flow chart of the system

2.4. Simulation parameters

Before the start of simulation, some relevant initial parameters need to be input, and in this study, solar assisted heat pump drying working modes was the primary research object. The value of each parameter is shown in Table 1 below.

According to the simulation calculation, when the solar radiation is greater than 500 W/m^2, in order to achieve the solar drying mode, the area of the air collector is supposed to be about 1.5 m^2. When the solar radiation is 200 W/m^2, to achieve drying requirements, and the evaporator-collector working as the only evaporator at the last drying stage, the area of the evaporator-collector should be about 1.0 m^2.

As can be seen from Table 1, the refrigerant charge is small due to the small design capacity of the overall system, where the input power of the compressor is about 230 W. In addition, the heat absorbed by the refrigerant in the evaporator comes from the air with relatively high temperature and humidity discharged from the dryer, which leads to the total tube length of the evaporator small, and resulting in a lower refrigerant content in the evaporator.

Table 1: Initial parameters of the system in simulation

content	symbol	unit	value
area of air collector	A_c	m^2	1.5
area of evaporator-collector	A_c'	m^2	1.0
solar radiation	I_T	W/m^2	200
ambient temperature	T_a	℃	25
refrigerant charge	M	g	143

3. RESULTS AND DISCUSSION

For mushroom drying, Figure 3 shows the variation of moisture content (dry mass) with time when the solar radiation was 200 W/m^2. As can be seen from Figure 3, when the drying time is 120 minutes, the mushrooms reach safe water content (dry basis less than 0.13).

Since there is no air volume involved in the drying mathematical model, it is difficult to calculate the air state at the outlet of the dryer based on this model. In this study, a certain simplified treatment was performed to calculate the air state at the outlet of the dryer. The average value of the air state at the outlet of the dryer during the drying time was calculated at constant air volume, so the simulation of the entire system is steady state.

Figure 4 shows air temperature at different outlet under different solar radiation, as can be seen from Figure 4, with the solar radiation increases in the range shown in the figure, the air temperature of all different outlets was little change, which is due to the variation range of solar radiation was relatively small under the working mode of solar assisted heat pump drying.

Figure 5 shows the variation of SMER and COP with solar radiation. As seen from the figure, the COP decreases slightly despite an increase in solar radiation. This can be attributed to the air temperature difference between inlet and outlet of condenser decreases slightly with the increases of solar radiation, which can be seen from Figure 4, and input power of compress remains basically unchanged. It can also be seen that as the solar radiation increases, the temperature of the air at the inlet of the dryer rises, which leads to a decrease in the drying time required to reach a safe moisture content, and as a result, SMER increases.

Figure 6 shows air temperature at different outlet under different ambient temperature. With the same as solar radiation in Figure 4, ambient temperature has little influence on air temperature at different outlet.

Figure 7 shows the variation of SMER and COP with ambient temperature. From the figure, it can be seen that, with the increase of ambient temperature, the SMER increases and the COP decreases slightly. This phenomenon may be explained by the fact that, with the increase of ambient temperature, the air temperature difference between inlet and outlet of condenser decreases and the air temperature of dryer inlet increases slightly.

Figure 8 shows the variation of SMER and COP with refrigerant flow ratio of evaporator, when the ambient temperature was 27℃. As the ratio increases in the range shown in the figure, the SMER increases slightly then unchanged, and the COP remains basically unchanged.

.

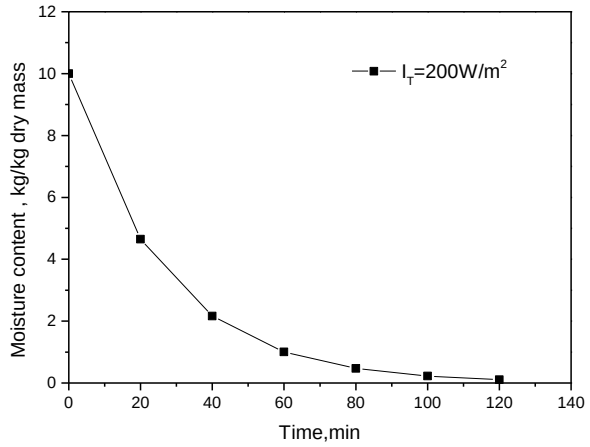

Figure 3: Variation of moisture content with time

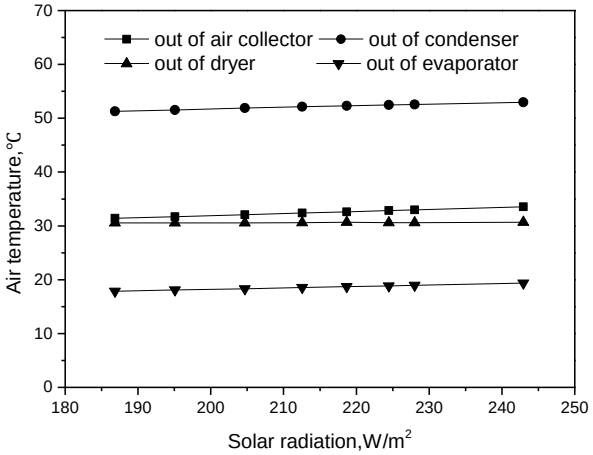

Figure 4: Air temperature at different outlet under different solar radiation

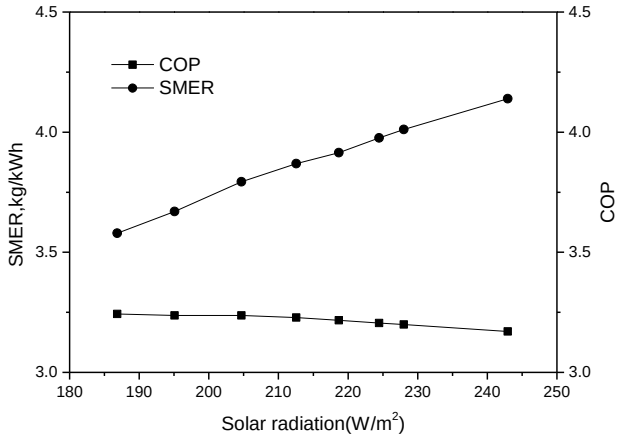

Figure 5: Variation of SMER and COP with solar radiation

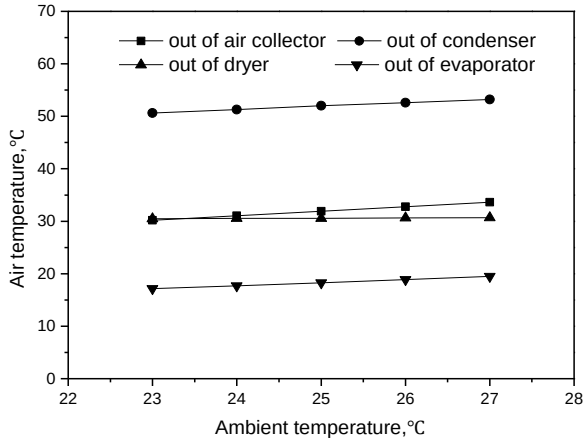

Figure 6: Air temperature at different outlet under different ambient temperature

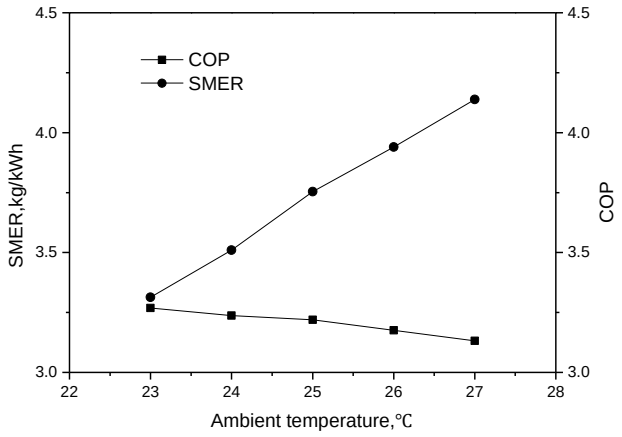

Figure 7: Variation of SMER and COP with ambient temperature

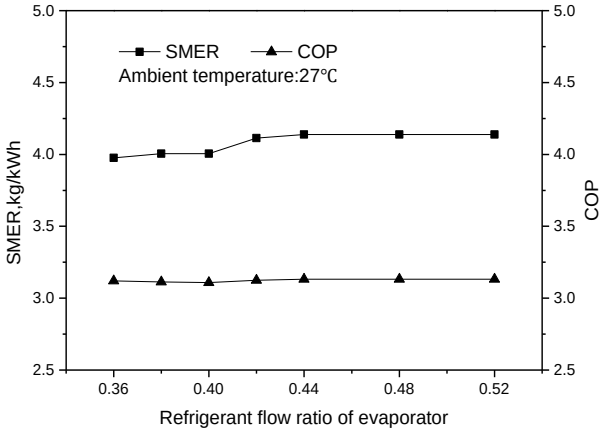

Figure 8: Variation of SMER and COP with refrigerant flow ratio of evaporator

4. CONCLUSION

A new designed of solar assisted heat pump drying system was proposed, and a simulation study was conducted on this system through MATLAB. In the solar assisted heat pump drying mode, the effects of solar radiation and ambient temperature on the air temperature at the outlet of each component in the system and the SMER and COP in the system were studied by simulation. According to the simulation results, the outlet air temperature of the condenser slightly increases with the increase of the solar radiation, and the value was about 52°C when the ambient temperature was 25°C and evaporator refrigerant flow ratio was 0.5. As the drying temperature increases, the drying time decreases, resulting in a significant increase in SMER with increase of solar radiation. However, the COP has slightly declined, and the value was

about 3.2. Under the condition that the solar radiation was 200W/m2 and the evaporator refrigerant flow ratio was 0.5, with the increase of the ambient temperature, the variation trend of each variable similar to the variation trend that they were influenced by solar radiation. According to the simulation study of the evaporator refrigerant flow ratio, it is found that under certain environmental conditions, the SMER of the system can be improved by adjusting the evaporator refrigerant flow ratio.

5. REFERENCES

Chua, K. J., Mujumdar, A. S., Hawlader, M. N. A., Chou, S. K. & Ho, J. C. (2001), "Batch drying of banana pieces - Effect of stepwise change in drying air temperature on drying kinetics and product colour", Food Research International, Vol. 34 No. 8, pp. 721-731.

Chua K. J., Chua S. K. Ho J. C. (2002), "Heat pump drying: Recent developments and future trends", Drying Technology, Vol. 20 No. 8, pp. 1579-1610.

Daghigh, R., Ruslan, M. H., Sulaiman, M. Y. & Sopian, K. (2010), "Review of solar assisted heat pump drying systems for agricultural and marine products", Renewable & Sustainable Energy Reviews, Vol. 14 No. 9, pp. 2564-2579.

Duffie, J. A., Beckman, W. A. & Worek, W. M. (1980), Solar Engineering of Thermal Processes, 2nd ed., Wiley.

Hawlader, M. N. A. & Jahangeer, K. A. (2006), "Solar heat pump drying and water heating in the tropics", Solar Energy, Vol. 80 No. 5, pp. 492-499.

Hawlader, M. N. A., Chou, S. K., Jahangeer, K. A., Rahman, S. M. A. & Eugene, L. K. W. (2003), "Solar-assisted heat-pump dryer and water heater", Applied Energy, Vol. 74 No. 1–2, pp. 185-193.

Hawlader, M. (2008), "Performance of evaporator-collector and air collector in solar assisted heat pump dryer", Energy Conversion & Management, Vol. 49 No. 6, pp. 1612-1619.

Krokida, M. K., Karathanos, V. T., Maroulis, Z. B. & Marinos-Kouris, D. (2003), "Drying kinetics of some vegetables", Journal of Food Engineering, Vol. 59 No. 4, pp. 391-403.

Li, Y., Li, H. F., Dai, Y. J., Gao, S. F., Wei, L., Li, Z. L., Odinez, I. G. & Wang, R. Z. (2011), "Experimental investigation on a solar assisted heat pump in-store drying system", Applied Thermal Engineering, Vol. 31 No. 10, pp. 1718-1724.

Mohanraj, M. (2014), "Performance of a solar-ambient hybrid source heat pump drier for copra drying under hot-humid weather conditions", Energy for Sustainable Development, Vol. 23165-169.

Qiu, Y., Li, M., Hassanien, R. H. E., Wang, Y., Luo, X. & Yu, Q. (2016), "Performance and operation mode analysis of a heat recovery and thermal storage solar-assisted heat pump drying system", Solar Energy, Vol. 137225-235.

Rahman, S. M. A., Saidur, R. & Hawlader, M. N. A. (2013), "An economic optimization of evaporator and air collector area in a solar assisted heat pump drying system", Energy Conversion & Management, Vol. 76 No. 1, pp. 377-384.

Şevik, S., Aktaş, M., Doğan, H. & Koçak, S. (2013), "Mushroom drying with solar assisted heat pump system", Energy Conversion & Management, Vol. 72 No. 72, pp. 171-178.

Timoumi, S., Mihoubi, D. & Zagrouba, F. (2004), "Simulation model for a solar drying process", Desalination, Vol. 168 No. 1, pp. 111-115.

Wang, J., Ouyang, Y., Zhu, Y. & Liu, J. (2002), "Experimental study on heat pump drying system with phase change material", Acta Energiae Solaris Sinica, Vol. 78 No. 1, pp. 60-67.

Yahya, M., Fudholi, A., Hafizh, H. & Sopian, K. (2016), "Comparison of solar dryer and solar-assisted heat pump dryer for cassava", Solar Energy, Vol. 136606-613.

Zhang, C. (2013), Fundamentals of Vapor-Compression Refrigeration and Air-Conditioning System Modeling, Chemical Industry Press.

399: Research on the operation and maintenance management technologies of offshore wind farms

Tingxin SONG[1], YimingTONG, Tian ZHANG

[1]School of Mechanical Engineering, Hubei University of Technology, Wuhan, China
stx@hbut.edu.cn

With the rapid development of offshore wind power industry, the operation and maintenance (O&M) requirements of wind turbine are continuously increasing. And the existing low-efficient of extensive O&M management restricts healthy development of the wind power industry. Hence, in order to improve the automatic management level of the offshore wind farms and optimise the coordination of resources, the O&M management technologies were implemented with the idea of lean maintenance, repair and overhaul/operations (MRO) in this paper. With the analysis of the O&M business characteristics and the management status of offshore wind farms, the main business functions and workflows of the MRO system were designed. And the maintenance bill of material (BOM), MRO planning and an improved AB2C inventory control strategy which was proposed and applied to spare parts inventory management were researched to optimise the O&M business processes. As a case, the MRO management software has been applied to the Shanghai Donghai Offshore Wind Farm, which effectively achieve lean management of the wind farm.

Keywords: Offshore wind farms; Maintenance, repair and overhaul/operations (MRO); MRO planning; The AB2C inventory control strategy

1. INTRODUCTION

In order to alleviate the energy crisis, wind energy, which involves the most mature of technologies and the largest scale development conditions and commercial development prospects, has been widely valued and developed as a new energy source (Martin, 2016:1226-1236). Compared to onshore wind power, offshore wind power has the characteristics of abundant resources, greater wind speed, wind direction stability and less environmental pollution. It can be expected that offshore wind power will gradually become the new development direction of wind power in the coastal countries (Huang, 2016:1557-1567). However, behind the rapid development of the domestic wind power industry, some existing problems are manifested in the following aspects: lacking an advanced management method of wind power equipment, attaching more importance to construction and ignoring the management of O&M, high O&M costs and backward information. These problems have greatly hindered the further development of China's offshore wind power industry (Kandukuri, 2016:1557-1567).

Maintenance, repair and overhaul/operation (MRO) of offshore wind farms plays an important role in the whole life cycle of wind power products and MRO technologies are the core of data management and supporting service businesses. In offshore wind farms, the MRO system, with the application of MRO technologies, conducts the O&M service management between product manufacturers, users and service providers to ensure the efficient operation of wind farms and prolong the service life of equipment (Hofmann, 2001:1-16). Meantime, with the increase in maintenance costs and equipment complexity, the concept of lean MRO has received the publics' attention. Implementing lean maintenance in the O&M processes can not only effectively reduce waste and save O&M costs, but also make a great contribution at the equipment manufacturing level (Cheng, 2010:2026-2037).

Based on the support of a national 863 project, this paper applies lean MRO to the wind power field, optimises and integrates all the work involved in the O&M from the management level of wind farms, summarises the O&M management status and offshore wind farms main daily businesses for the domestic and foreign wind farms and focuses on the three key technologies of lean MRO which include; the maintenance bill of material (BOM) of wind turbines, MRO planning and maintenance business processes and spare parts inventory control strategy.

2. O&M MANAGEMENT STATUS OF OFFSHORE WIND FARMS

From the beginning of the 1980s, the world began the large-scale development of the wind power industry. With the planning, construction and operation of a legion of wind farms, the wind power industry chain, which takes the wind turbine manufacturers as the leader, has gradually formed and is being continuously developed; the wind power industry has ushered in a golden 30 years of development. As an emerging industry, the technological innovation of core products, such as wind turbines, has received enough attention but the supporting technologies and management innovation for the whole industrial chain have been seriously neglected (Li, 2010:2064-2072). The lack of innovation in the O&M processes can be embodied in the following points:

(1) Lacking advanced management methods and information technologies: The wind power industry is a typical equipment industry. Under the environment of modern management and information technologies, the equipment industry, such as advanced equipment manufacturing, generally has an O&M management system which is similar to the enterprise resources management (ERP), however, there is no such system in the wind power industry.

(2) Attaching more importance to construction and ignoring the management of O&M: In order to quickly occupy a favorable market position and share in the initial stages of the wind power industry, whether wind turbine manufacturers or wind power operators, they all place high importance on the production of wind turbines and the construction of wind power generation, but ignore the lean management of O&M.

(3) There is a disconnect exists between the operation and maintenance: Due to the inherent technical barriers which are introduced by wind turbine suppliers, wind power owners are less independent to control the operation and management of wind farms. Further, the operation system and maintenance system are considered separately to the technical requirements of sales contract yet it is not straight forward for the owners to carry out the deep-level of analysis required for the optimum utilization of information resources.

(4) Problems of O&M costs: The construction of large-scale wind farms requires billions of RMB, due to the high costs of purchasing equipment and construction. Meanwhile, the O&M costs are also rising and account for more than 20% of the total costs. Despite this high level of running cost, most importance is still attached to the former rather than the latter.

3. MAIN BUSINESSES OF OFFSHORE WIND FARMS

In order to achieve the optimum benefits of wind power enterprises, the core work of offshore wind farms is to carry out the lean MRO management of wind turbines in a scientific and effective way. The lean MRO management system must focus on the whole life cycle of the wind turbines, which comprises the various stages from the design, production, testing,

purchasing, installation, operation and maintenance until equipment retirement. As the core businesses of the MRO system, the ordinary O&M businesses can be divided into following four categories:

(1) Production and operation management: Production and operations includes the three aspects of production planning, production reporting and operation recording for the management and statistical analysis of operational data in wind farms. In this way the personnel can immediately know the operational state of the wind turbines and deal with failures in a timely manner. Further, the wind farms can operate in safe and effective way through the management of the different stages of production planning and reporting.

(2) Routine maintenance: Based on the marine weather conditions, operation states and the technical requirements of wind turbines, personnel can formulate an appropriate maintenance cycle and make routine maintenance of wind turbines over a large area to keep the wind turbines in a stable state of operation.

(3) Repair: By real-time monitoring of the operational state and collecting operational data, personnel can monitor the health of the wind turbines with failure diagnosis technology, allowing immediate identification of failures, implementation of a timely repair scheme resulting in a reduction in the frequency and duration of failures thereby improving the operational benefit of the wind turbines.

(4) Check/inspection: Based on the characteristics of the production process, O&M manual requirements and related maintenance experience, personnel can formulate the check / inspection cycle allowing regular checks on the operational state of wind turbines, the elimination of hidden equipment failure, replace the expired components and so reduce the frequency of emergency repairs to ensuring the safe operation of the wind turbines and their system.

4. KEY TECHNOLOGIES OF O&M BASED ON LEAN MRO

As the application of the lean concept to maintenance, Lean MRO can eliminate waste in maintenance processes thereby improving the value of maintenance through a series of principles, concepts and techniques. The "waste" in maintenance is reflected not only in the costs of waste e.g. untimely material transportation, unreasonable maintenance process design and planning, but also in the uneconomical spare parts inventory allocations. Therefore, in order to eliminate these kinds of "waste", one must strive for the achievement of the optimal scheduling of maintenance resources including spare parts inventory, maintenance personnel and materials thereby saving maintenance costs and improving the "value" of maintenance. This paper, based on lean MRO, discusses the three key technologies of O&M which include maintenance BOM, MRO planning and maintenance business processes, and spare parts inventory control strategy.

4.1. Maintenance BOM

The maintenance BOM is the Bill of Material related to the spare parts maintenance businesses within the MRO processes and it also contains the technical information used to describe information pertaining to the spare part’s structure, maintenance procedure and other basic attribute information. Different from the design and manufacture BOMs, the maintenance BOM has the following features:

(1) Management system must be accurate to a single specific product: In the maintenance processes and including product failures, wind turbines require regular maintenance, emergency repair, product upgrading and other MRO activities. These MRO activities mean that components are constantly being repaired, replaced and increased resulting in changes to the product structure or component properties and hence to a change in the maintenance BOM. The failure conditions and the actual situation of maintenance that each product may confront are different leading inevitably to differences between corresponding maintenance BOMs. Therefore, the MRO system’s management accuracy must be accurate to a single specific product (Roy, 2013:172-175), that is to say, each wind turbine must have their separate corresponding maintenance BOM.

(2) Basic maintenance unit’s schedule must be formulated with the actual maintenance requirements: The Production BOM must be accurate to each part which is indivisible in the structure but the maintenance BOM is formulated based on the specific assembling conditions and maintenance requirements. It usually only contains materials for the maintenance, and the basic unit of product maintenance can be parts or components which cannot be repaired and disassembled. In terms of the actual maintenance situation, when a gearbox, primarily composed of gear, bearing and wind wheel, fails, maintenance personnel can choose to undertake maintenance or change some parts of the gearbox depending on the actual cause of failure, to achieve the maintenance goal. But if the frequency converter, a component of wind turbines, is damaged, it cannot be repaired and must be exchanged for a new one. In addition, during the operation stage of products, the maintenance state of identical components distributed in different positions is hard to keep consistent due to the different wear conditions experienced. Therefore, the basic maintenance unit’s schedule must be formulated based on the actual maintenance requirements.

(3) The Maintenance BOM must have continuous timely feedback: During the operation of an MRO system, products are implemented with a variety of MRO service activities as a result of functional decline and these activities change the

product structure, component properties and business state. So that maintenance BOM must keep continuous feedback over time, in other words, the new data information caused by MRO activities must be directly used to update the corresponding maintenance BOM, and the history information of MRO businesses should exist to facilitate query and trace. In making a maintenance schedule, exact and real-time information of the maintenance BOM can provide accurate reference data to support decision making. The maintenance BOM structure is showed in Figure 1, it can be divided into three levels: wind turbines, components and parts.

4.2. MRO planning and maintenance business processes

MRO planning

The formulation of processes for a whole maintenance schedule are based on the maintenance BOM. During normal operation, there will be various failures resulting in the need to conduct many different types of maintenance work. To resolve these failures, firstly, maintenance personnel need to submit the failure codes of the wind turbines to the MRO system, and call up the corresponding maintenance schedule through the automatic matching of failure databases.

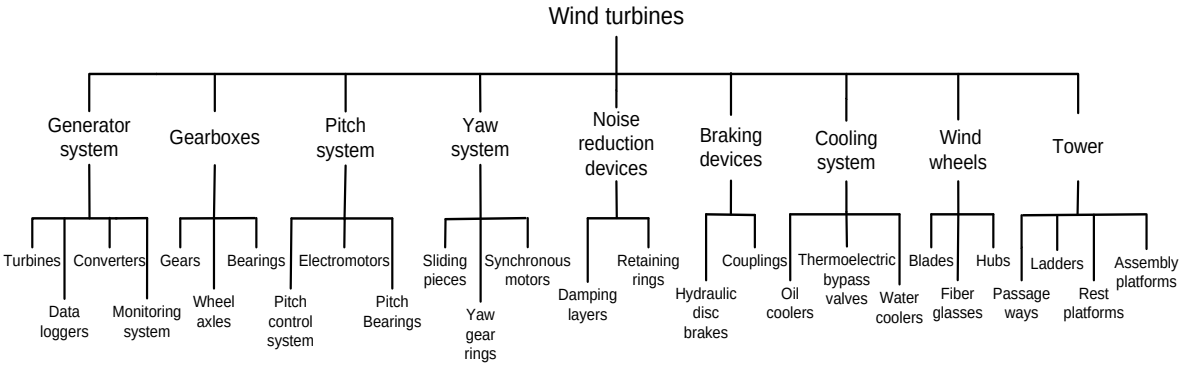

Figure 1: Maintenance BOM structure

When there is new failure mode, the maintenance personnel need to check the maintenance manual, make a specific maintenance schedule by means of failure detection and diagnosis, and archive it at all at the same time. The system will then apply and allocate the manpower, tooling, spare parts and other resources required this particular maintenance issue and develop a final maintenance schedule.

The annual maintenance schedule of routine maintenance is shown in Table 1. As can be seen, although the maintenance cycle of different components varies with their operational losses, the maintenance tasks of all components which include the maintenance tools, ship scheduling, staffing and other related works should be arranged one month in advance to timely execute MRO businesses (Sood, 2013:99-104). In addition, the different components required can be coordinated and different departments can cooperate to complete the maintenance works in a highly efficient manner.

Table 1: the annual maintenance schedule for main components

Main components		Time（Month）												Maintenance period（Month）
		1	2	3	4	5	6	7	8	9	10	11	12	
Turbines	Preparation period	√	√	√	√	√	√	√	√	√	√	√	√	1
	Execution period	√	√	√	√	√	√	√	√	√	√	√	√	
Gearboxes	Preparation period	√	√	√	√	√	√	√	√	√	√	√	√	1
	Execution period	√	√	√	√	√	√	√	√	√	√	√	√	
Pitch system	Preparation period	√		√		√		√		√		√		2
	Execution period		√			√			√		√		√	
Yaw system	Preparation period	√		√		√		√		√		√		2

	Execution period	√	√	√	√	√	√	
Wind wheels	Preparation period	√		√		√		√	3
	Execution period		√		√		√		
Monitoring system	Preparation period	√		√		√		√	3
	Execution period		√		√		√		

Maintenance business processes

Due to the marine climate constraints, it is difficult for offshore wind farms to adopt the real-time maintenance methods of onshore wind farms. The system, therefore, needs to be able to comprehensively analyse the maintenance costs, marine climate conditions and equipment failure losses in order to formulate a specific MRO plan. When maintenance requirements reach a certain threshold or there is a serious failure warning, the system will begin to execute the maintenance tasks. The maintenance business processes are shown in Figure 2.

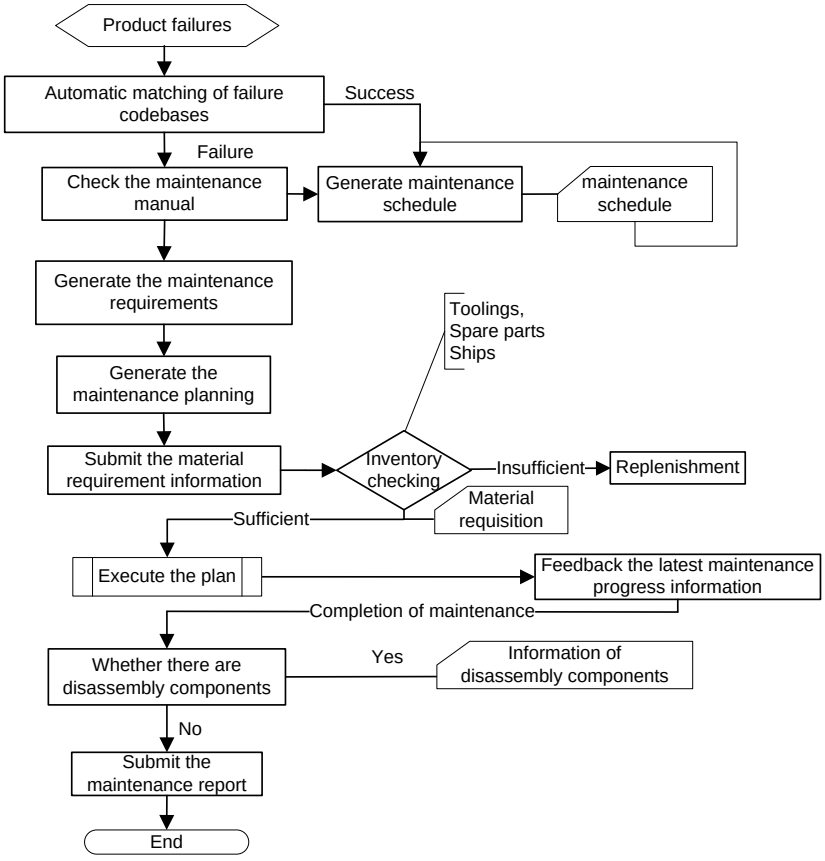

Figure 2: Maintenance business processes

After the examination and approval of MRO planning by technical personnel and department heads, maintenance personnel will submit the tooling, spare parts and other material requirements to the MRO management system, and the system will carry out comparative analysis through automatically scanningthe inventory information. When inventories fully meet the MRO material requirements, the system will automatically generate material requisitions, however, if inventories are insufficient, it will submit an application for replenishment based on the amount of stock out, andafter the completion of procurement, warehouse managers will conduct the inventory register. During maintenance implementation processes, maintenance personnel should submit timely information feedback about the latest maintenance progress to the MRO management system. If there are some components that couldn't be repaired and need to be exchanged for a new one,

data about both the broken component andnew component should be submitted and at the same time the new components' information should be updated to the BOM structure of the wind turbinesproviding continuous feedback between the maintenance BOM and the condition of each wind turbine ensuring the consistency and timeliness of the next maintenance schedule. Finally, after summarizing and reporting the maintenance activities, the whole maintenance task complete.

4.3. Spare parts inventory control strategy

In offshore wind farms, it is critical to manage and maintain an adequate level of spare parts. However, there are no specific data that can serve as the basis for procurement and forecast of spare parts at the initial stage of wind farm and, although there some mature inventory management software exists in market, the kind of software available is not quite suitable for wind farms and application can result in overstocking or understocking for the maintenance processes.

In order to solve the above problems, lean MRO inventory management can be applied to the O&M management of offshore wind farms ensuring not only the smooth operation of equipment and reduction in failure losses, but also the improved utilization equipment by reducing downtime from failure. Through the analysis of the importance of spare parts relative to wind turbines, this paper proposes a new inventory control strategy based on combining the analytic hierarchy process (AHP) (Schneider, 2016:209-216) and the activity based classification (ABC). This AB2C (activity based twice classification) inventory control strategy is a method which is consistent with the characteristics of offshore wind farms inventory management (Geng, 2014:200-209).

The traditional ABC methodology is commonly applied to inventory control and management with the characteristics of simple, flexible and strong operability, but its classification criteria is unilateral and oversimplified hence it doesn't take account of the purchasing difficulty and purchasing lead-time of spare parts. Further, there are a wide range of spare parts with complex structures in offshore wind farms which can result in the loss of resources within inventory management. Therefore, based on the method of AHP and ABC, this paper puts forward a new inventory control strategy which is suitable for the characteristics of offshore wind farms—AB2C inventory control strategy.

In AB2C inventory control strategy, class A spare parts are the components which are robust and demand little attention; class B spare parts are the fragile components of wind turbines with high maintenance frequency, and according to the purchasing cycle of spare parts, class B can be divided into B1 and B2 two categories to optimise the traditional ABC method and achieve a more rational and efficient inventory management. In addition, as the auxiliary components of wind power equipment, class C spare parts, with low value, have little importance to the normal operation of wind turbines. Therefore the AB2C classification of spare parts can be conducted as follows: turbines which rank in the top 15% are divided into class A; ranking in the intermediate 65% of spare parts are classified as class B in which hydraulic disc brakes and yaw gear rings are grouped into class B1, gears and bearings are grouped into class B2; and sensors which rank in the last 20% are divided into class C.

Under the premise that the failure rates and annual consumption rates are a definite value K, this paper analyses the inventory control strategy of class A, B1, B2, and C respectively, among which class C spare parts with little importance can be purchased in bulk within a given time frame.

Class A spare parts are the key components of wind turbines, and they are not easily damaged, but once damaged, they are hard to repair. Therefore, the inventory management of class A should be strictly controlled under a conditioncapable of meeting the demands of the required service level, hence it is better to compress the purchasing lead-time (L) and increase the purchasing frequency as much as possible to reduce the single purchasing quantity. The inventory control strategy of class A is shown in Figure 3, where R represents the reorder point, Q is the quantity of spare parts for each order and T is time. When the inventory consumption decreases to R, the personnel need to immediately send an order with the order quantity is Q to keep class a spare parts in a normal and reasonable level after the period of purchasing lead-time.

Class B1 spare parts are easily damaged but the shortage costs are low, and they can be replenished readily from outside with a short purchasing cycle which means that the periodic inventory control strategy can be applied to class B1 items to reduce the frequency of inventory counts and appropriately increase the order quantity. The inventory control strategy of class B1 is shown in Figure 4, where S represents the maximum inventory and C is the inspection cycle. When the inventory reaches the period C, the personnel should conduct an inventory count and send the application for replenishment to make the inventory of class B1 items back to S.

As the secondary important components of wind turbines, the difference between class B1 and class B2 is the purchasing cycle. With the long purchasing cycle, the minimum inventory of class B2 spare parts should be formulated, and when the inventory consumption decreases to the minimum inventory, the MRO system will issue a warning to remind the personnel to conduct the replenishment of class B2 to keep the stability of the quantity of spare parts. The inventory control strategy of class B2 is shown in Figure 5, where S represents the maximum inventory and S is the minimum inventory.

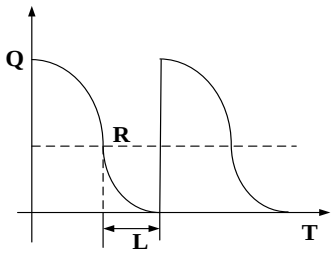

Figure 3: Class A inventory control strategy

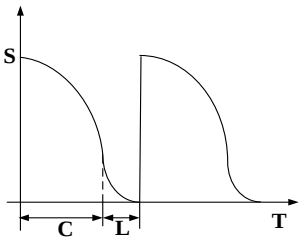

Figure 4: Class B1 inventory control strategy

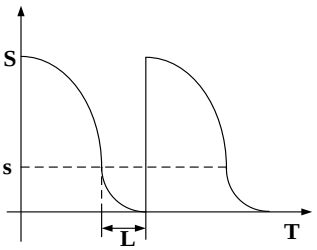

Figure 5: Class B2 inventory control strategy

5. CASE STUDY

Considering all the information above, an O&M management (MRO) system of offshore wind farms was developed and applied to an offshore wind farm consisting of 34 3MW turbines. Shanghai DongHai offshore wind farm, located in the east of the DongHai Bridge and south of the PuDong new area was chosen for the analysis. This is the first large-scale offshore wind power project in China and can therefore be considered as the representative of current and future offshore wind farms in Asia.

The main businesses of Shanghai DongHai offshore wind farm are operation and maintenance. The operation segment contains production planning, operation monitoring and production data analysis, and the maintenance segment contains routine maintenance, regular inspection and repair. In view of these businesses, the MRO management system developed in this paper takes the wind turbines as mainline and designs several modules such as production and operation management, maintenance management, spare parts management, ship management and maintenance process management. Therefore, the whole system guided by a workflow engine can carry out lean management and monitoring on maintenance processes of wind farms. The main interface is shown in Figure 6.

Figure 6: Main interface of MRO management system

In the verification application, the system makes it possible for DongHai offshore wind farm to implement the standard, lean management and promote better coordination between various departments. With the improvement of information management at the wind farm, the original fragmented document management system has developed into a comprehensive information management system where the information of components and equipment can be updated in a timely manner and the spare parts inventory can be well regulated. The production and maintenance efficiency of DongHai offshore wind farm has significantly improved and the level of O&M has ascended to a new dimension.

6. CONCLUDING REMARKS

The application of lean MRO in the O&M processes can bring significant benefits to offshore wind farms. First of all, the lean MRO system has changed the traditional management mode and can carry out information management on each structure component (BOM) of wind turbines from the view of the whole life cycle; this helps to formulate accurate

maintenance planning and material requirements planning. With the supervision and feedback of the implementation processes of the maintenance plan, the transparency and efficiency of maintenance works has shown great progress. In addition, the key technologies of lean MRO studied in this paper have further enhanced the management level of spare parts inventory, and the improved AB2C inventory control strategy has realised economic and practical inventory control.

7. REFERENCES

Cheng YA, Zhang L, Liu YB, M0 XN, 2010. Solution of MRO support system for large complex equipment. Computer Integrated Manufacturing System 16(10):2026-2037

Geng JH, Tian XT, Bai MX, Jia XL, Liu XW, 2014. A design method for three-dimensional maintenance, repair and overhaul job card of complex products. Computers in Industry 65(1):200-209

Kandukuri ST, Robbersmyr KG, Karimi HR, 2016.Towards farm-level health management of offshore wind farms for maintenance improvements. Int J Adv Manuf Techno 83(9):1557-1567

Hofmann M, 2011. A Review of Decision Support Models for Offshore Wind Farms with an Emphasis on Operation and Maintenance Strategies. WIND ENGINEERING 35(1):1-16

Huang BQ, Zhang Y, Yi XC, 2014. Operation and maintenance systems for offshore wind farms. Journal of Tsinghua University (Science and Technology) 54(4):522-529

Li H, Ji YJ, Qi GN, Gu XJ, Zhang D, Chen JX,2010. Integration model of complex equipment MRO based on lifecycle management. Computer Integrated Manufacturing Systems 16(10):2064-2072

Martin R, Lazakis I, Barbouchi S, Johanning L, 2016. Sensitivity analysis of offshore wind farm operation and maintenance cost and availability. Renewable Energy 85:1226-1236

Roy R, Shaw A, Erkoyuncu JA, Redding L, 2013. Through-life engineering services. Meas. Control 46(6):172-175

Schneider D, Tracht K, Meyer-Stender M, Mederer M, 2016.Customer stock in repairable item systems. Prod. Eng. Res. Devel 10(2):209-216

Sood V, Sant S, Parmar CS, 2013. Design Considerations and Selection of Equipment for Assured Life Cycle Support. J. Inst. Eng. India Ser. C 94(1):99-104

400: Study on Al-Ga-In-SnCl2 composites for hydrogen production by hydrolysis

Kang LIU[1,2], Shijie DONG[1,2],Yufei ZUO[1,2], Xiaohan XU[1,2], Cheng CHEN[1,2], Zhen CHEN[1,2], Ping LUO[1,2*]

[1] *Hubei Provincial Key Laboratory of Green Materials for Light Industry, Hubei University of Technology, Wuhan 430068 P. R. China*

[2] *Collaborative Innovation Center of Green Light-weight Materials and Processing. Hubei University of Technology Wuhan 430068 P. R. China*

**Corresponding author, E-mail addresses: blueknight_0930@163.com*

Hydrogen energy is increasingly attracting the attention of all countries in the world because of its green, clean and efficient characteristics. Hydrolysis of aluminium is a highly efficient, convenient and green method for hydrogen production. Due to passivation, aluminium does not react with water at room temperature. Low-melting metals such as gallium, indium can activate aluminium through mechanical ball milling method. X-ray diffraction (XRD), scanning electron microscopy (SEM), and energy dispersive spectroscopy (EDS), analysis of composition and morphology of aluminium alloys. The results show the formation of In_3Sn or InSn4 phases, indicating that this reaction occurred during the milling process: $Al+SnCl_2 \rightarrow AlCl_3+Sn$ $In+Sn \rightarrow InSn_4$. When mechanical milling, $SnCl_2$ can be used as a grinding aid to eliminate agglomeration. At the same time, the aluminium-salt ball mill produces a large amount of fresh surface and defects, which helps to promote the hydrolysis reaction. As far as we know, our composite materials have not been reported. The experimental results show that our composite material has good hydrogen production performance and can be used as a hydrogen fuel cell hydrogen donor material. This paper studied the effect of different $SnCl_2$ content on the hydrogen production performance of Al alloys in order to find the best Al alloy composition with the best hydrogen production performance. The maximum hydrogen production of alloy Al-3%Ga-3%In-5%$SnCl_2$ reaches 1225ml, and the maximum hydrogen production rate is 1225ml/g min. The mechanical alloying parameters at this time were as follows: ratio of ball material 15:1, ratio of size ball 2:1, ball milling time 1 h, ball grinding speed 450 r/min.

Keywords: Al alloys; ball milling; Hydrolysis; hydrogen production performance

1. INTRODUCTION

Hydrogen energy has a wide range of sources, is clean and environmentally friendly, and is renewable. It is regarded as the most promising clean energy in the 21st century, and all countries in the world use hydrogen energy as a strategic energy source. Hydrogen production from aluminium alloy hydrolysis has attracted the attention of researchers. Compared to traditional hydrogen production technology, hydrogen production from aluminium hydrolysis has a wide range of raw materials, easy control of reaction, low power consumption, simple equipment, and wide application (Kotay, 2008; Lattin, 2007; Wang, 2012; Wang, 2012; Huang, 2011; Alinejad, 2009). The product of aluminium hydrolyzed hydrogen can be recycled and used, with little pollution to the environment. Therefore, hydrogen production from aluminium alloys is considered to be a commercial hydrogen production technology (Xu, 2016; Grigoriev, 2006).

Under standard conditions, 1g of aluminium reacts with water and releases 1244ml of hydrogen. However, a passive layer forms on the surface of aluminium. At room temperature, aluminium does not react with water by hydrolysis. Therefore, how to remove the passivation layer is the key to study the hydrogen production of aluminium. Mechanical milling is a common method for activating metallic aluminium. Adding a low-melting point metal (Ga, In, Sn, Hg, Bi, etc.) during ball milling effectively removes the passivation layer, allowing aluminium to rapidly react with water (Wang, 2013; Wang, 2014). Mechanical milling is an effective means of activating metallic aluminium.

In the ball milling process, in order to eliminate the agglomeration phenomenon, a small amount of salt is often added as a grinding aid. This method can generate a large amount of fresh surface and defects, which helps to promote the hydrolysis reaction (Alinejad, 2009). Fan et al. (Fan, 2010; Fan, 2009; Fan, 2007; Fan, 2013; Fan, 2011) studied the effect of adding Zn, Ga, Bi, Hg, In, and Sn to aluminium by means of a mechanical alloying method on the hydrolysis reaction of aluminium. Xun Fen et al. (Xu, 2017; Xu, 2007) prepared a series of aluminium alloys by ball milling and studied the hydrogen production of aluminium alloys by hydrolysis. The experimental results show that the addition of Zn and Ga promotes the hydrolysis of aluminium. For aluminium-tin alloys, partial replacement of Sn in the alloy with Zn can reduce the agglomeration of aluminium powder. The hydrogen production performance of the product was increased when the inorganic salts such as $MgCl_2$ and NaCl were added to the ball-milled Al-Bi alloy

Based on previous research, this paper studies the hydrogen production performance of Al-Ga-In-$SnCl_2$ quaternary system. Introducing $SnCl_2$ into Al-Ga-In system to prepare highly active aluminium matrix composites with excellent hydrogen production performance. The Al alloy with the best hydrogen production performance can be prepared by milling for 1 h.

2. EXPERIMENTAL

2.1. Material preparation

The raw materials used to prepare aluminium alloys are: Al (200 mush, 99 wt.%), Ga (99 wt.%), In (200 mush,99 .9wt.%), $SnCl_2$ (200 mush, 99.9 wt.%). The equipment used to prepare the aluminium alloy in this paper is model QM-3SP4 planetary ball mill (Manufacturer: Nanjing University Instrument Factory). Weigh Al, Ga, In, and $SnCl_2$ in the ratio required by the experiment. The mechanical milling parameters are as follows: the ratio of balls to balls is 15:1, the ratio of balls to balls is 2:1, the grinding time is 6h, and the grinding speed is 450r/min. The ball mill jar was sealed in an argon-filled vacuum glove box.

2.2. Hydrogen production performance test

The hydrolysis of the aluminium alloy takes place in a three-necked flask with a volume of 500 ml. Hydrogen is collected by drainage at room temperature until the reaction is complete. This study uses the drainage method to collect the hydrogen produced.

2.3. X-ray diffraction and scanning electron microscope analysis

The X-ray diffraction (XRD) measurements were performed to investigate the crystallographic structure using a Bruker D8 Discover X-ray diffractometer with Cu Kα radiation (λ = 1.5418 Å). The SEM images were collected by a JEOL-7100F microscope at an acceleration voltage of 20 kV.

3. RESULTS AND DISCUSSION

3.1. Effect of different contents of $snCl_2$ on hydrogen production performance of Al alloys

Table 1 shows the experimental scheme of the effect of $SnCl_2$ content on the hydrogen performance of Al alloys. The Al alloy material was prepared according to the experimental scheme of Table 1, and the ball milling parameters were as described in section 2.1, and finally the hydrogen production performance was tested at room temperature.

Table 1: Elements composition of ternary Al alloys and its hydrogen yields.

NO.	Elements composition(wt.%)				Hydrogen yields (ml)
	Al	Ga	In	$SnCl_2$	
1	94	3	3	0	0
2	93	3	3	1	0
3	91	3	3	3	910
4	89	3	3	5	1140
5	87	3	3	7	1110
6	85	3	3	9	770

Figure 1 shows the hydrogen production curve of aluminium alloys with different contents of $SnCl_2$. The results show that when the $SnCl_2$ content is 0% and 1%, the aluminium alloy hardly reacts with water. As the $SnCl_2$ content increases, the amount of hydrogen produced first increases and then decreases, When the $SnCl_2$ content was 5%, the hydrogen production amount was 1140 ml, the conversion rate was 93%, and the maximum rate was 840 ml/g min. Due to the higher rotational speed and longer ball milling time, the prepared Al alloy material is agglomerated into blocks. Then when using this bulk alloy for hydrogen production, the rate in Figure 1 suddenly increased. The reason is that when the reaction is started, the contact area of the alloy with water is small, and as the reaction progresses, the bulk alloy is decomposed into small pieces, and the contact area becomes large, so that the reaction rate is accelerated.

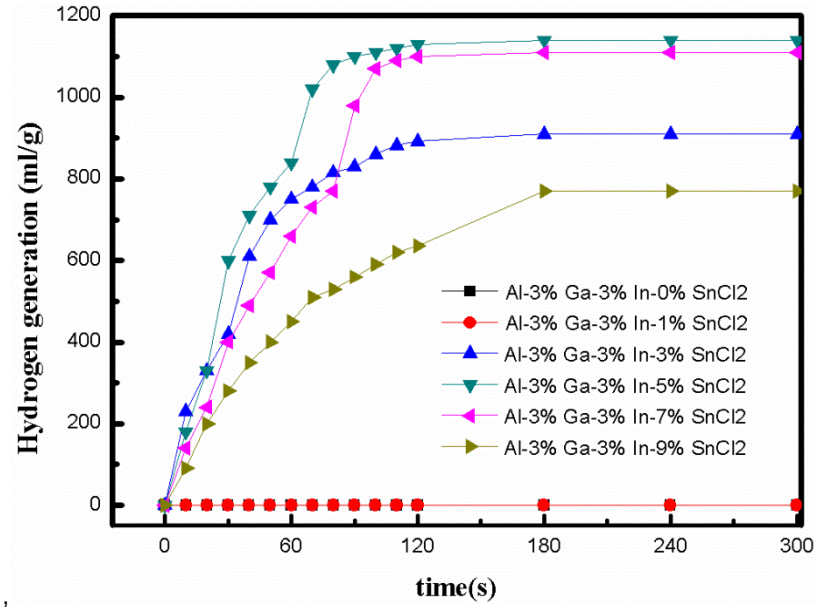

Figure 1: Hydrogen production performance curves of composites with different $SnCl_2$ contents

3.5. Effect of different milling time on hydrogen production performance of Al alloys

The parameters of other milling parameters were unchanged, and the selected system Al-3%Ga-3%In-5%$SnCl_2$ was ball milled for 1 h, 2 h, 3 h, 4 h, 5 h, and 6 h, respectively. The performance of hydrogen production was also tested at room temperature. The experimental results show that when the milling time gradually decreases from 6h to 1h, the agglomeration phenomenon decreases. And the Al alloy particles prepared by ball milling for 1 h are uniform in size and no agglomeration occurs. Figure 2 is the hydrogen production performance curve of Al alloy prepared by using different milling time. It can be seen from the figure that the larger the hydrogen production capacity of Al alloy is, the less the milling time is. The Al alloy prepared by ball milling for 1 h has an extremely fast hydrolysis reaction. The reaction can be completed within one minute. The maximum hydrogen production is 1225 ml, the conversion rate is close to 100%, and the maximum hydrogen production rate is 1225 ml/g min.

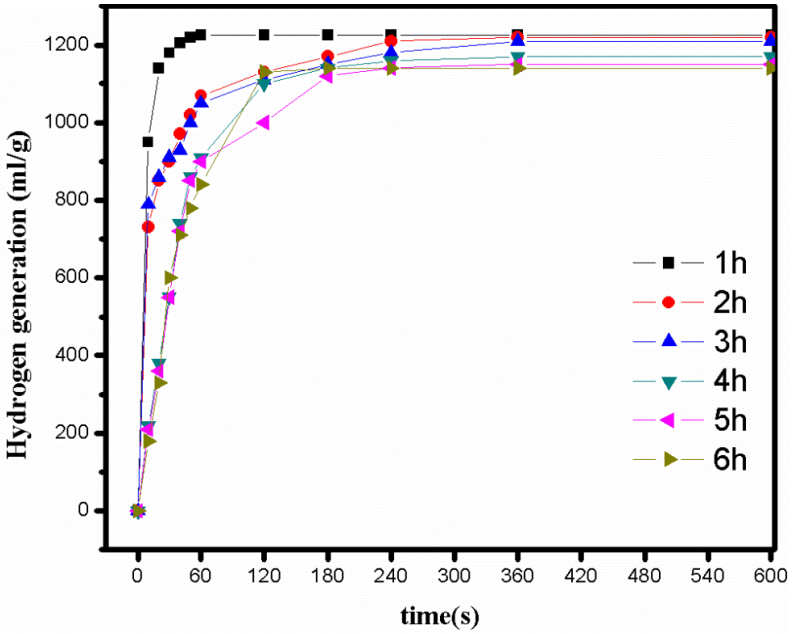

Figure 2: Hydrogen-producing performance curve of composites reacting with water for 1 h under different milling time

3.3 Phase and micromorphology analysis of composites

Figure 3 shows the XRD patterns of Al alloys with different $SnCl_2$ contents. When the $SnCl_2$ content is higher than 3%, InSn4 diffraction peaks appear in the XRD patterns. The following reaction occurred during the ball milling: $Al+SnCl_2 \rightarrow AlCl_3+Sn$. Then, newly generated Sn reacts with In to produce $InSn_4$ during ball milling Xu 2014). Intermetallic compound $InSn_4$ becomes active point of aluminium hydrolysis reaction. Aluminium easily dissolves in the crucible and forms an aluminium-niobium alloy with it. The aluminium dissolved in the metal crucible is a very uniform dispersed phase, and the degree of dispersion reaches an atomic level, so that a dense passivation layer cannot be formed on the surface of the aluminium particles. Aluminium hydrolysis activity is greatly enhanced.

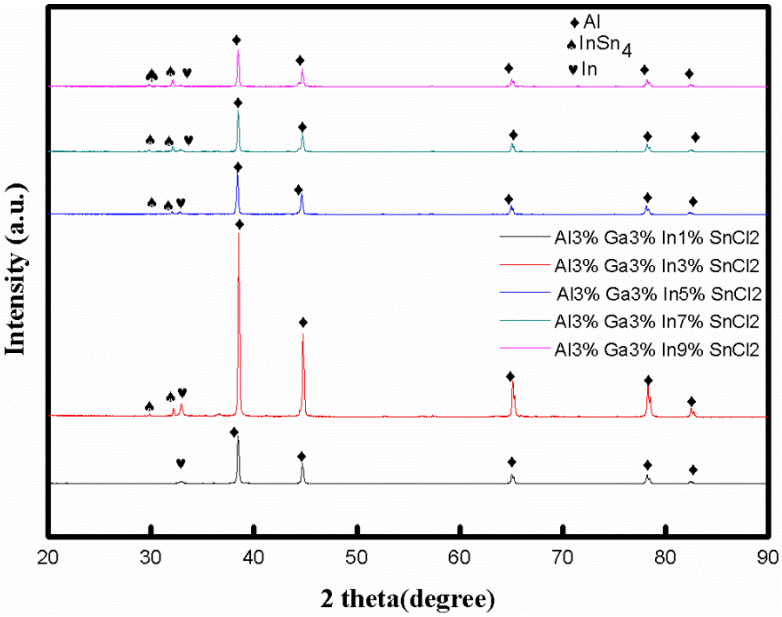

Figure 3: XRD patterns of Al alloys with different $SnCl_2$ contents

The micro-morphologies of Al alloy materials with different $SnCl_2$ contents are shown in Figure 4. Figure 4a shows the micro-morphology of Al. Figures 4b, 4c, 4d, 4e and 4f show the micro-morphologies of Al alloys with $SnCl_2$ contents of 1%, 3%, 5%, 7%, and 9%, respectively. In the ball milling process, aluminium powder undergoes strong plastic deformation, cold welding, and crushing under the action of mechanical force, which causes structural defects and increased free energy of the system on the surface of the aluminium powder, thereby destroying the dense oxide film and enhancing the

aluminium hydrolytic activity. Figure 5 is an EDS pictures of an Al-3% Ga-3% In-5% $SnCl_2$ composite. It can be seen from the figure that the ball milling process makes Ga, In and Sn evenly distributed around the Al particles. Chloride salt covers the fresh surface of aluminium particles, which prevents oxidation and enhances the hydrolytic activity of aluminium.

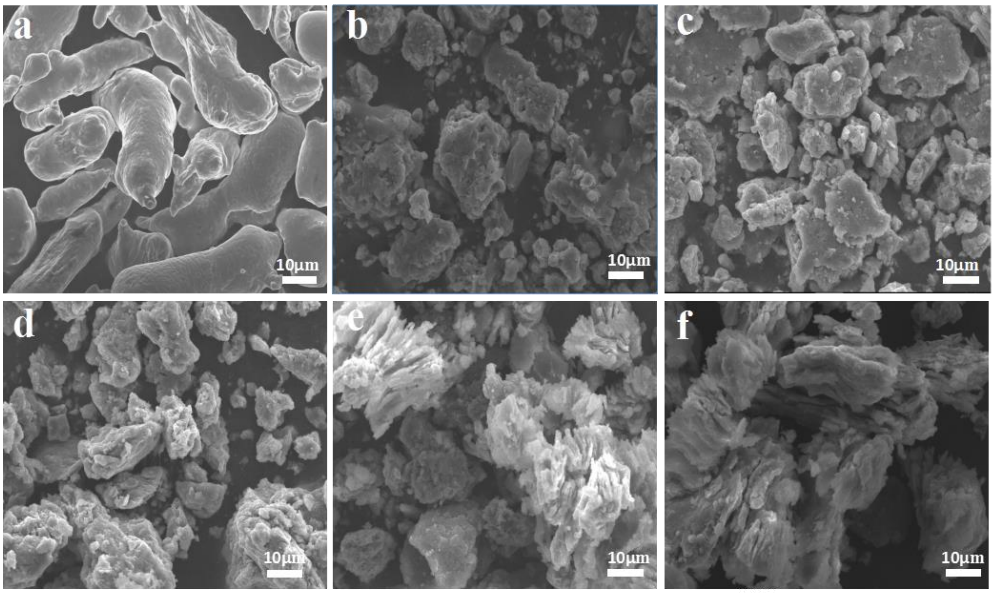

Figure 4: SEM images of Al alloys with different $SnCl_2$ contents (4a - 100%Al, 4b - 1%, 4c - 3%, 4d - 5%, 4e - 7%, 4f - 9%)

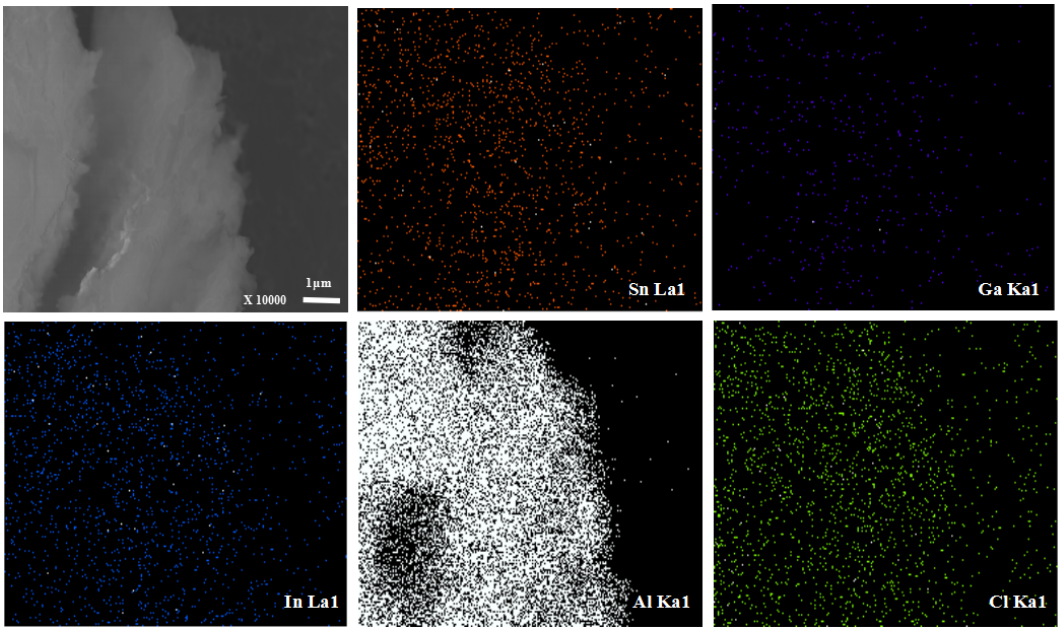

Figure 5: EDS pictures of composites

4. CONCLUSION

1. The effect of $SnCl_2$ content on the hydrogen production performance of Al alloys is very obvious. When the $SnCl_2$ content is less than 1%, the Al alloy hardly reacts with water at room temperature. When the content of $SnCl_2$ is increased to 5%, the hydrolytic activity of Al alloy is greatly increased, and the amount of hydrogen produced reaches a maximum value. However, when the $SnCl_2$ content is increased to 9%, the amount of hydrogen produced decreases.

2. After selecting the optimal Al alloy composition and ratio, the effect of milling time on the hydrogen production performance was studied. The reaction rate and hydrogen production rate of Al alloy prepared by ball milling for 1 h are the largest. As the milling time increases, the amount of hydrogen produced and the reaction rate decrease. The reason

is that the ball mill 1h Al alloy is in a uniform powder state, continue to increase the ball milling time, Al alloy appears agglomeration phenomenon.

3. The following reactions occur during ball milling: $Al+SnCl_2 \rightarrow AlCl_3+Sn$ $In+Sn \rightarrow InSn_4$. Since the electrode potential of Sn (-0.136 V) is significantly higher than that of aluminium (-1.66 V), Sn formed in situ can form a micro-cell with Al, thereby enhancing the hydrolytic activity of the Al alloy. In addition, the aluminium and chlorinated salt ball milling products produce a large amount of fresh surface and defects, so that the dense passivation layer is destroyed, thereby enhancing the hydrolytic reaction activity of the Al alloy composites.

5. ACKNOWLEDGEMENTS

This work was financially supported by the National Natural Science Foundation of China (Grant No. 51771071).

6. REFERENCES

Alinejad B., Mahmoodi K. A novel method for generating hydrogen by hydrolysis of highly activated aluminum nanoparticles in pure water [J]. International Journal of Hydrogen Energy, 2009, 34(19):7934-7938

Fan M. Q., Xu F., Sun L. Studies on hydrogen generation characteristics of hydrolysis of the ball milling Al-based materials in pure water [J]. International Journal of Hydrogen Energy, 2007, 32(14): 2809-2815

Fan M. Q., Sun L. X., Xu F. Feasibility study of hydrogen generation from the milled Al-based materials for micro fuel cell applications [J]. Energy Fuel, 2009, 23: 4562- 4566

Fan M. Q., Sun L. X., Xu F. Feasibility study of hydrogen production for micro fuel cell from activated Al-In mixture in water [J]. Energy, 2010, 35(3):1333-1337

Fan M. Q., Sun L. X., Xu F. Hydrogen production for micro-fuel-cell from activated Al-Sn-Zn-X (X: hydride or halide) mixture in water [J]. Renewable Energy, 2011, 36(2): 519-524

Fan M. Q., Wang Y., Tian G. L., et al. Hydrolysis of AlLi/NaBH4 system promoted by Co powder with different particle size and amount as synergistic hydrogen generation for portable fuel cell [J]. International Journal of Hydrogen Energy, 2013, 38(25): 10857-10863

Grigoriev S A, Porembsky V I, Fateev V N. Pure hydrogen production by PEM electrolysis for hydrogen energy [J]. International Journal of Hydrogen Energy, 2006, 31(2): 171-175

Huang XN, L v CJ, Huang YX, Liu S, Wang C, Chen D. Effects of amalgam on hydrogen generation by hydrolysis of aluminium with water. Int J Hydrogen Energy 2011; 36:15119-24.

Kotay SM, Das D. Bio hydrogen as a renewable energy resource-prospects and potentials. Int J Hydrogen Energy 2008; 33(1):258-63.

Lattin WC, Utgikar VP. Transition to hydrogen economy in the United States: a 2006 status report. Int J Hydrogen Energy 2007; 32:3230-7.

Wang W, Zhao XM, Chen DM, Yang K. Insight into the reactivity of Al-Ga-In-Sn alloy with water. Int J Hydrogen Energy 2012; 37:2187-94

Wang W, Chen W, Zhao XM, Chen DM, Yang K. Effect of composition on the reactivity of Al-rich alloys with water. Int J Hydrogen Energy 2012; 37:18672-8.

Wang H. H., Chang Y., Dong S. J. *, et al. Investigation on hydrogen production using multicomponent aluminum alloys at mild conditions and its mechanism [J]. International Journal of Hydrogen Energy, 2013, 38 (3): 1236-1243

Wang H. H., Lu J., Dong S. J. *, et al. Preparation and Hydrolysis of Aluminum Based Composites for Hydrogen Production in Pure Water [J]. Materials Transactions, 2014, 55 (6): 892-898.

Xu F., Fan M. Q., Sun L. X. A hydrogenated hydrogen produced aluminum alloy and its preparation [P]. Chinese Invention Patent, CN 200710011042.5

Xu F, Sun L, Lan X, et al. Mechanism of fast hydrogen generation from pure water using Al–SnCl 2, and bi-doped Al–SnCl 2, composites [J]. International Journal of Hydrogen Energy, 2014, 39(11):5514-5521Xu L, Ashraf S, Hu J P, et al. Ball-milled Si powder for the production of H2 from water for fuel cell applications [J]. International Journal of Hydrogen Energy, 2016, 41: 12730-12737

Xu F., Fan M. Q., Sun L. X. Research on hydrogen production from aluminum alloys for mobile hydrogen sources [C]. The 2nd China Academic Forum on Energy Storage and Power Battery and Key Materials, Chen Du,2017.11

403: Design of an axial-flux electric machines with amorphous alloy for flywheel energy storage system

Xiaoguang WANG[1,2], Xiong HU[1,2], Lingyun LIU[1,2,3]

[1] *Hubei Collaborative Innovation Center for High-efficiency Utilization of Solar Energy, Hubei University of Technology, Wuhan 430068, China; xgwang84@qq.com*
[2] *Hubei Key Laboratory for High-efficiency Utilization of Solar Energy and Operation Control of Energy Storage System, Hubei University of Technology, Wuhan, 430068, P. R. China;*
[3] *Hubei Power Grid Intelligent Control and Equipment Engineering Technology Research Center, Hubei University of Technology, Wuhan, 430068, P. R. China*

This paper presents an axial flux permanent-magnet (AFPM) machine used in flywheel energy storage system (FESS). Amorphous alloy is used in the stator, which can reduce coreloss remarkablely when the FESS is working in high-frequency. A new multi air-gap AFPM machine with multi-rotor and multi-stator is proposed, and the different numbers of motors can make up different power of the FESS. A 3-D finite element method was used to analyses the design and performances of AFPM, the result shows that the AFPM machine with amorphous alloy have lower iron loss than that with silicon lamination, with can improve the efficiency of FESS effectively.

Keywords: Axial flux permanent-magnet (AFPM) machine; flywheel energy storage system (FESS); 3-D finite element method; Amorphous alloy.

1. INTRODUCTION

Flywheel Energy Storage System (FESS) has the advantages of large capacity, long service life, large energy storage density, no pollution, simple maintenance and no requirement to the environment (Daoud, 2016; Kondoh, 2016; Itoh, 2016; Wang, 2015), so it has become the most promising new energy storage technology. FESS can be used for wide applications , such as aerospace, wind power station, power system peaking, communication system, solar power station (Daoud, 2015), which is of great significance to national economy and national defense construction (Krings, 2017; Stannard, 2017).

A highly active field of innovative and improved soft magnetic materials for present and future use in electrical machine applications was presented in Stannard (2017). With the ever broadening choice of materials, it is incumbent on the machine designer to investigate in detail the many available steels that may offer the best combination of performance properties, whether magnetic or mechanical, as well as the cost and availability restrictions that may affect nonperformance parameters such as time-to-market for new designs or the cost of manufacturing machines across differing geographical regions. This paper three high aspect ratio axial field topologies for traction applications employing soft magnetic composite (SMC) was compared in Pei (2017). Several important aspects of designing axial flux machines using SMC was discussed, and the results shows that the yokeless and segmented armature topology has the best overall performance due to its shorter iron circuit. In Zhang (2016), this paper presents a novel structure of in-wheel AFPMSM with a higher torque density compared with the traditional structure and proposes a design method of the new structure by analysing the material utilization rate (MUR) of yokes. The sizing equations of the new structure are also given in this paper. In Wang (2015), this paper is about the mechanical design and analysis of a yokeless and segmented armature axial flux permanent magnet synchronous machine, a reliable mechanical construction is developed and performed based on finite element method (FEM), the proposed construction is reliable and the measured data match well with the results of the electromagnetic analysis. In Jung (2015), an analytical approach was studied, in order to evaluate both stator types including the respective winding configurations. The result reveals that the N-N- machine is likely to produce more iron and copper losses, if the SPP is near to 1/3, as it is compulsory for tooth-wound coils. A design of an axial flux machine was investigated in Fei (2009), which comprises a segmented stator made of SMC (Soft Magnetic Composite). In contrast to conventional machines, the stator iron is not coherent. An optimised stator segmentation concept is derived. It is shown that the number of turns in series per phase is halved and therefore the copper losses decrease significantly. A new closed form solution of toroid and overlapping windings for axial flux permanent magnet machines was found in Ju (2014). Finite element analysis is used to validate the accuracy of the proposed analytical calculations. The proposed solution should assist machine designers to ascertain benefits and limitations of toroid and overlapping winding types as well as to get faster results.

At present, most scholars use soft magnetic material instead of silicon steel sheet as the stator of an axial flux machine. Compared with soft magnetic material, the amorphous materials have more ability to reduce iron loss. Amorphous magnetic materials (also called metallic glass) have the advantage of very low iron losses due to their very thin foil structure (the typical thickness is 0.025 mm) and low manufacturing process costs. This paper, a 29.4kW and axial flux permanent magnet synchronous machine which has 24 poles and 36 slots is designed by using the amorphous materials. Also, the electromagnetic performance of the machine is simulated by the finite element method in this paper.

2. THE FLYWHEEL ENERGY STORAGE SYSTEM

2.1. Configuration of the flywheel energy storage system

The simplified structure of the FESS is shown in Figure 1. Power electronic converter input power from power grid, which can drive motor rotation. The mechanical energy is stored in the flywheel. When the power grid or the other external load needs energy, flywheel working in the generation state, and then the mechanical energy is converted into electrical energy by the power electronic conversion device. The structure of flywheel energy storage system consists of four parts: the system housing, the magnetic bearing, the AFPM machine, and the power converter.

The motor/generator that transferred electricity to the rotating energy is an AFPM machine. In order to reduce the air friction, the rotor was enclosed in a vacuum vessel. The core of the FESS is the proposed AFPM machine with amorphous alloy, which can have two or more stators and rotors. The different numbers of AFPM machines can make up different power of the FESS.

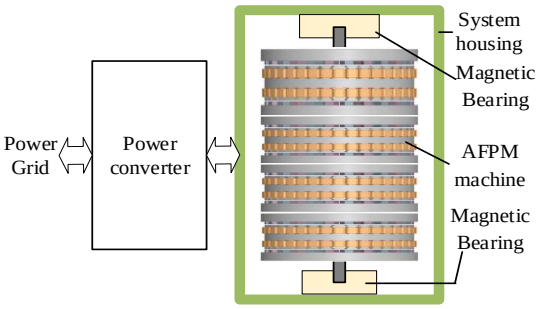

Figure 1: Simplified structure of FESS

2.2. Analysis of iron loss

The machine are constructed on one of two types of core-loss. One type is eddy current losses. The second type is hysteresis. Iron core material is not only the permeability magnetic material, but also the conducting material.It will be produced induced current in the time-varying electromagnetic field, the current is also called eddy current. It should be noted that the resistance of iron core material can lead to energy loss under the effect of eddy current, this energy loss is defined as eddy current loss. The eddy current loss factor is given by:

$$P_e = C_e f^2 B_m{}^2 \Delta^2 V \tag{1}$$

Where:

C_e = eddy current loss factor, it is inversely proportional to resistivity

B_m = maximum of flux density (T)

Δ = thickness of ferromagnetic material (mm)

V = Volume of iron core (mm^3)

It can be seen from the Equation (1) that the eddy current losses are both proportional to the thickness squared of material and volume.However, this paper uses amorphous alloy material, and the thickness of silicon steel material is 1/12 larger than them. And the eddy current losses are inversely proportional to the resistivity of material, the resistivity of amorphous alloy material is greater than silicon steel material by about 4 times. Through the above analysis, as we have seen that the eddy current losses of amorphous alloy material significantly decrease when they compare with ordinary silicon steel material.

When ferromagnetic material is magnetised by an applied magnetic field, the magnetic flux density B shows a special curve relationship with the change of magnetic field strength H, or simply call hysteresis loop. Since the change of magnetization intensity of ferromagnetic material always lags behind the change of magnetic field strength, energy losses will be produced during the magnetization process. We call these energy losses as hysteresis loss. The hysteresis losses are given by:

$$P_h = K_h f \oint HdB = C_h f B_m^n V \tag{2}$$

Where:

K_h = constant depended on material property

f = frequency of alternating magnetic field (Hz)

C_h = the coefficient of hysteresis loss

B_m = maximum of flux density (T)

n = constant

V = Volume of iron core (mm^3)

The hysteresis loop area of amorphous alloy material is obviously less than silicon steel material due to the amorphous alloy material has the feature of small coercive force and low remanence. So it is demonstrated that the hysteresis loss of amorphous alloy material is much less than that of ordinary silicon steel sheet.

3. THE ELECTROMAGNETIC PERFORMANCE OF MACHINE

This paper presents the design and analysis of a new multi-rotor and multi--stator AFPM machine, the material of the stator core is amorphous alloy. Its application in a FESS is realised by orientating its axial direction vertically, and the different numbers of motors can make up different power of the FESS. The structure of the AFPM is shown in Figure 1. Based on the design requirement data shown in Table 1, the motor design results can be obtained as in Figure 2.

Table 1: Performance parameters of AFPM

Parameter	Value	Parameter	Value
Rate Power	14.7kW	Rated Voltage	380V
Rate Current	15.6A	Rate Torque	35Nm
Rate Speed	4000r/min	Efficiency	96%

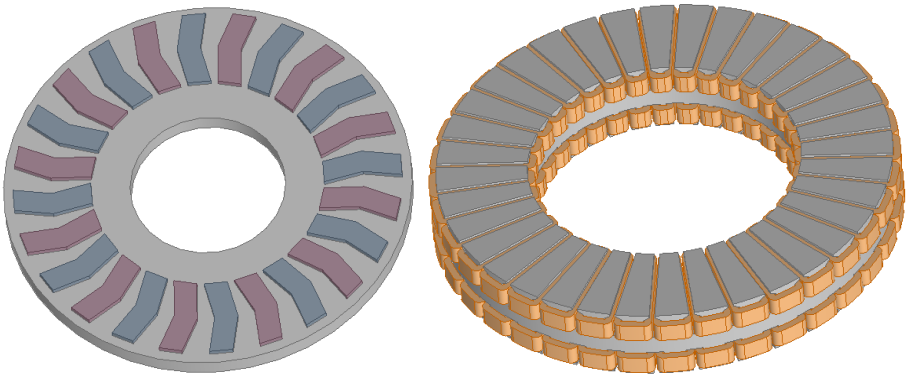

(a) Rotor *(b) Stator*

Figure 2: Proposed AFPM machine

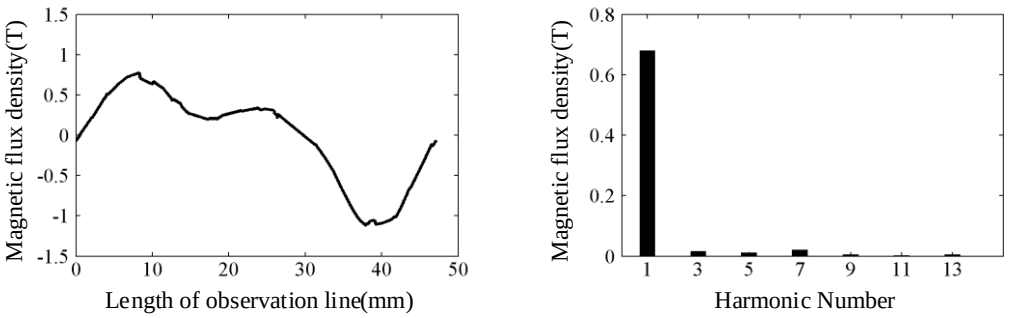

(a) Air gap flux density *(b) Spectrum analysis*

Figure 3: Magnetostatic flux density

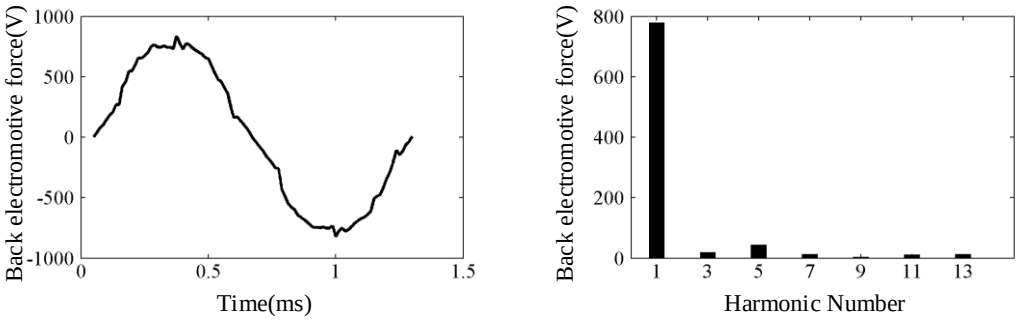

(a) Back EMF *(b) Back EMF spectrum analysis*

Figure 4: No-load back EMF

According to the electromagnetic performance of the machine model, the oscillogram can be obtained as Figures 3 and 4. The oscillogram of the air-gap flux density as known from Figure 3 is asymmetrical due to the permanent magnet shape of rotor is designed to look like a arrow. Therefore, rregular shape leads to the incomplete symmetry of the air-gap flux density waveform. But the distortion factor of waveform is only 4.3% and fundamental amplitude is 0.68T. As we can see from Figure 4, because the distortion factor is only 6.7% and the effective value of counter electron-motive force is 550V, the symmetry of empty counter electron-motive force waveform is better.

To summarise, through the simulation of static field, the axial flux machine which is used arrow structure has great sinusoidal property. But for verifying the electromagnetic performance of the machine, we need to make dynamic field simulation. The oscillogram of the torque performance and iron loss are shown by Figure 5 and these figures are based on two different stator materials.

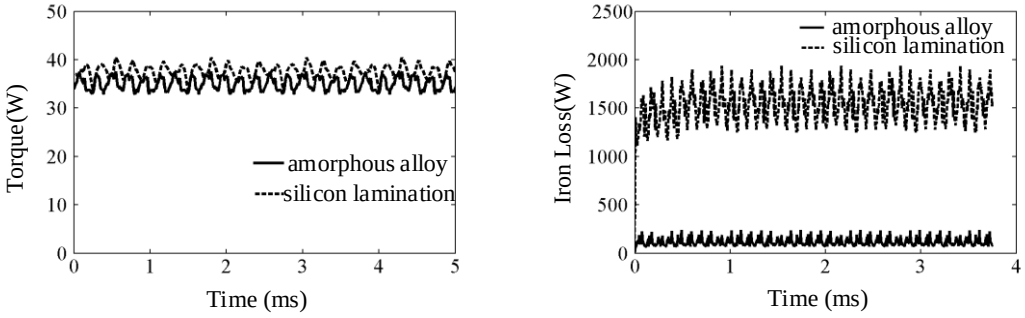

(a) Torque *(b) Iron Loss*

Figure 5: Transient field performance

Figure 5(a) compares the torque performance between silicon steel sheet and amorphous alloy material. Under these two kinds of materials, the machines can both reach the rated torque. However, the saturated magnetic density of ordinary silicon steel sheet is much higher than amorphous alloy material so when the silicon steel sheet is used as stator material that the torque is larger than 2N*m. We can conclude that the available ratio of the silicon steel sheet stator material is higher for permanent magnet under the same same structure of rotor. The torque pulsation coefficient of the amorphous material is 13%, which is lower than the silicon steel sheet stator. There is difference on the air-gap magnetic field strength due to the saturated degree of the stator is different. It's worth noticing that air-gap magnetic flux density is low and its harmonic content is low, too. As a result, the torque pulsation coefficient is relatively low.

Figure 5(b) shows that the iron loss of machine which is made up by amorphous magnetic materials is much lower than ordinary silicon steel sheet machine. The iron loss between amorphous machine and ordinary machine range between 114W at amorphous and 1523W at ordinary machine. It is clear that the latter is 13 times as much as the former.

4. CONCLUSION

A new structure of FESS with unit AFPM machine was proposed and designed in this paper, different power of FESS demands can be met by adjusting the number of unit AFPM machines. In order to reduce friction loss, the vacuum system is usually adopted in flywheel energy storage system, which causes poor heat dissipation of the motor. The simulation

result shows that the AFPM machine with amorphous alloy have lower iron loss than that with silicon lamination, with can improve the efficiency of FESS effectively.

5. ACKNOWLEDGEMENT

This work has been supported by Hubei Province Department of Education Science Research Supporting Program Q20161403.

6. REFERENCES

Daoud M., Abdel-khalik A, Elserougi A., Ahmed S., and Massoud A., 2015. Flywheel Energy Storage Systems. Handbook of Clean Energy, vol. 5, pp. 1-14.

Daoud M.I., Massoud A., Khalik A.A., and Ahmed S., 2016, 19th Int. Conf. on Electrical Machines and Systems (ICEMS 2016)/An asymmetrical six-phase induction machine based flywheel energy storage system using modular multilevel converters. Chiba (Japan), pp.1-6.

Fei W, Luk P C K, 2009. Energy Conversion Congress and Exposition/Torque ripple reduction of axial flux permanent magnet synchronous machine with segmented and laminated stator. IEEE, pp:132-138.

Itoh J.I., Masuda T., Nagano T., and Higa H., 2016. 19th Int. Conf. on Electrical Machines and Systems (ICEMS 2016)/Hybrid sixstep operation for matrix converter in flywheel energy storage system. Chiba (Japan), pp.1-4.

Ju H K, Choi W, Sarlioglu B, 2014. Energy Conversion Congress and Exposition/Closed-form solution for winding types of axial flux permanent magnet machines. IEEE, pp:5877-5884.

Jung J, Hofmann W, 2015. European Conference on Power Electronics and Applications/Comparison of two concentrated winding topologies applied on an axial flux permanent magnet machine. IEEE, pp:1-10.

Kondoh J., Takeshima K., Ishida Y., and Satoh H., 2016. 19th Int. Conf. on Electrical Machines and Systems (ICEMS 2016)/Energy balance analysis for fixed-speed flywheel energy storage system. Chiba (Japan), pp.1-4.

Krings A, Boglietti A, Cavagnino A, et al., 2017. Soft Magnetic Material Status and Trends in Electric Machines. IEEE Transactions on Industrial Electronics, 64(3):2405-2414.

Pei Y, Wang Q, Bi Y, et al., 2017. Conference of the IEEE Industrial Electronics Society/A novel structure of axial flux permanent magnet synchronous machine with high torque density for electrical vehicle applications. IEEE, pp,1717-1722.

Stannard N J, Washington J G, Atkinson G J, 2017. International Conference on Electrical Machines and Systems/A comparison of axial field topologies employing SMC for traction applications. IEEE.

Wang G., Qiu Q.L., Wang P., and Wang X.Y., 2015. 18th Int. Conf. on Electrical Machines and Systems (ICEMS 2016)/Analysisof the rotor loss in a high speed permanent magnet motor for flywheel energy storage system. Pattaya (Thailand), pp.2040-2044.

Zhang B, Seidler T, Dierken R, et al., 2016. Development of a Yokeless and Segmented Armature Axial Flux Machine. IEEE Transactions on Industrial Electronics, 63(4):2062-2071.

407: Modelling cooling loads and impact of PV deployment in middle income domestic buildings in Saudi Arabia

Nouf ALBARRAK[1], Patrick JAMES[2], Abubakr BAHAJ[3]

[1] *Energy and Climate Change Division / Sustainable Energy Research Group, University of Southampton, Southampton SO17 1BJ, N.A.Albarrak@soton.ac.uk*
[2] *Energy and Climate Change Division / Sustainable Energy Research Group, University of Southampton, Southampton SO17 1BJ, P.A.James@soton.ac.uk*
[3] *Energy and Climate Change Division / Sustainable Energy Research Group, University of Southampton, Southampton SO17 1BJ, A.S.Bahaj@soton.ac.uk*

Energy efficiency and conservation are important areas of consideration in many developed and developing countries. Over the last 5 years, electricity consumption in Saudi Arabia has grown at a compound annual growth rate of 6%; due to population growth and industrial activities. Such growth is predicted to be sustained at a similar rate over the next decade. The residential sector alone is responsible for over 50% of the total national electricity consumption. Recently, electricity prices rose by 35% to 253% depending on consumption levels. Around 65% of Saudi residents, mainly of middle-income families, live in either modern villas or traditional houses. This type of housing is the target of the research presented here, which aims to understand the effect of residents' behaviour and its impact on internal temperatures and electricity use. A selection of residences in the Khobar city in Saudi Arabia is used as a case study. TRNSYS modelling estimated the annual cooling loads in the case study based on detailed characteristics of the buildings including architectural form, envelope, occupancy profile and local weather data. The results indicate 20,350 kWh annual electrical loads are expected of which 52% are associated with cooling. Deploying solar photovoltaic (PV) systems to displace some of such loads is considered effective due to the 6 kWh/m^2 average daily solar irradiance in Khobar city. A 4-kWp solar PV system, which could be deployed in such homes, was also modelled. These results show that such a system would generate around 7000 kWh/year which could displace approximately 34% of such a load. The estimated payback period for the solar system is 21 years for the 0.048 $/kWh tariff rate without any additional subsidies. Further technical and economic assessment are also included in the paper.

Keywords: Electricity consumption, Domestic building, Middle-income, PV, Saudi Arabia.

1. INTRODUCTION

The Kingdom of Saudi Arabia (KSA), occupies the larger part of the Arabian Peninsula and has a population of around 27 million (Global Alliance of SMEs, 2016). Saudi Arabia has the world's second largest oil reserves which are concentrated mostly in the Eastern Province (BP, 2017). The economy is petroleum-based; around 75% of budget revenues and 90% of export incomes come from the oil industry, the oil industry accounts for around 45% of Saudi Arabia's nominal gross domestic product (Global Alliance of SMEs, 2016).

KSA is characterised by its hot climate and geographical location in a global region renowned for its high energy consumption and carbon emission rates. The Kingdom of Saudi Arabia is now committed to effectively implementing a programme of sustainable growth within its national development plan (Saudi Vision 2030, 2016). KSA's vision for 2030 is to increase national income from non-oil-based energy resources. Today, more than 80% of global energy consumption is attributable to fossil fuels, and the global population is currently dealing with a significant issue in terms of the environment and the energy we use (Alrashed, 2015)). One of the countries most associated with this issue is Saudi Arabia, where the lack of energy conservation regulations coupled with the speed of economic development has led to the rise of electricity consumption, which has increased by around 50% over the last 10 years (Al-Ajlan et al., 2006; KAPSARC, 2018). In 2001, KSA's had a peak electrical load of approximately 24 GW; which is 25 times higher than that of 1975. This electrical load is projected to grow to 60 GW by 2023. Over the last 5 years, the electricity consumption in Saudi Arabia has grown at a compound annual growth rate of 6% and this is predicted to continue at a similar pace over the next few years (Jones, 2012). Taleb and Sharples (2011) explain that one of the main reasons for the KSA's rising electricity consumption is the widespread use of air conditioning to cope with the country's high ambient temperatures especially in the summer. Saudi Arabia also has corresponding high levels of CO_2 emission and is amongst the world's largest producers and exporters of oil. In 2016, the Kingdom spent a total of $29.6 billion on fossil fuel consumption subsidies, making it the third highest in the world after China and Iran (IEA, 2018). Recently Saudi Arabia announce plans to cut energy subsidies and to this end the government increased energy prices in early 2018, so that residential and commercial electricity prices will increase gradually between 2018 and 2025 to reach 100 percent of international levels (Nereim, 2017).

As indicated earlier, cooling is a major contributor to the electrical consumption in Saudi Arabia, especially for residential buildings. To reduce energy consumption, buildings will need to be more efficient, this may require retrofits including improvements of insulation, the use of shading devices, and the installation of solar photovoltaic systems to shave off some of the electrical cooling loads. There is a paucity of information and understanding of how people use and interact with their homes, resulting in poor predictions of energy use at the building level. This research is part of a wider study which aims to increase our understanding of the electrical consumption in buildings including the role of residents' behaviour, building design and the needed interventions to provide clear energy use reductions. In KSA, the residential sector alone is responsible for over 50% of the total national electricity consumption where most of the residents prefer European house designs and architecture. Some of the utilised architectural features such as high glass facades, pitched roofs and the shape of the building or its orientation are however, not suitable for the Saudi hot climate environment. This leads to the following research questions:

- What are the determinants of electricity consumption in typical existing homes in Saudi Arabia?
- Can we understand occupants' behaviour from their electricity consumption data?
- Under what energy cost development scenarios will low energy building concepts become adopted as the standard approach in the KSA context?

1.1. Saudi Arabia climate

Saudi Arabia is primarily characterised by its desert climate, which follows a pattern of low rainfall annually, high temperatures during the day and quickly descending temperatures at nightfall. It is typical for summer temperatures to reach 45°C when the sun is at its peak, they can reach a high of 54°C; the winters are warm and rarely fall below freezing (0°C). Spring and autumn both have an average temperature of 29°C, which is temperature in comparison (Weather Online, 2016).

Electricity consumption is split between a host of different sectors and for a number of different purposes: the major contributors are industrial, agricultural, desalination plants, commercial, governmental, and residential. The latter sector consumes the overwhelming majority of electricity produced by fossil fuel based generation in Saudi Arabia (in the form of gas and oil) (Sankey IEA, 2015). Jeg and Sa (2016) note that industrial consumption (18.76 percent), commercial consumption (15.37 percent), governmental consumption (thirteen percent) agricultural consumption (1.75 percent), and desalination efforts (1.01 percent) follow as the highest-use sectors after residential. Figure 1 below represents power consumption levels between 2005 and 2016 (expressed as annual consumption in TWh) by sector:

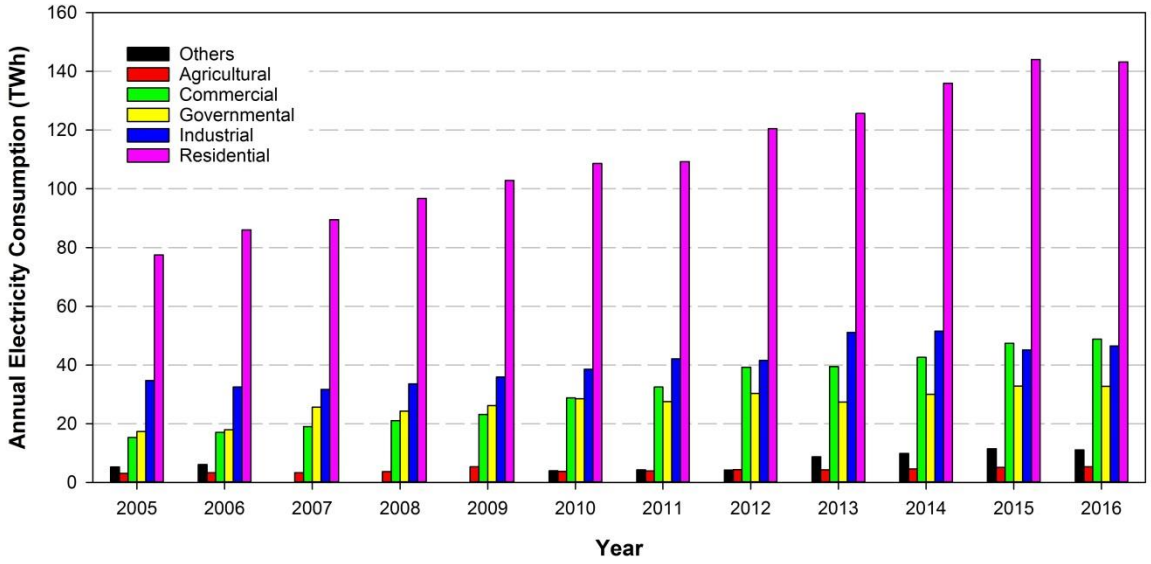

Figure 1: Annual electricity consumption in Saudi Arabia by sector (TWh). Source : http://www.sama.gov.sa/ar-sa/EconomicReports/Pages/YearlyStatistics.aspx

The Saudi Arabian governmental report outlines updated price points for electricity, which has resulted from the Council of Ministers proclamation that they would implement a national conservation programme for water and energy resources (ECRA, 2016). According to Jeg and Sa (2016), this would involve auditing prices for diesel kerosene, sewage, electricity, and water, and then amending prices to make their usage more sustainable. The New Tariff started from January 2018 and electricity prices rose 35% to 253% depending on the consumption level. Table 1 shows a comparison of a monthly household electricity bill before and after the introduction of the new tariff. It is interesting to note that the significant burden falls on low electricity consumers, there is no change in tariff for usage above 6000 kWh per month.

Table 1: Comparison between the monthly household Bill before and after the New Tariff for The Residential Sector. Source: www.se.com.sa.

Consumption (kWh)	Old Tariff		New Tariff	
	Unit rate ($/kWh)	Total bill ($)	Unit rate ($/kWh)	Total bill ($)
1000	0.01	13.33	0.048	48.00
2000	0.01	26.67	0.048	96.00
3000	0.03	80.00	0.048	144.00
4000	0.03	106.67	0.048	192.00
5000	0.048	240.00	0.048	240.00
6000	0.048	288.00	0.048	288.00
7000	0.08	560.00	0.08	560.00
8000	0.08	640.00	0.08	640.00
9000	0.08	720.00	0.08	720.00
10000	0.08	800.00	0.08	800.00

1.2. Overview of housing in Saudi Arabia

Saudi Arabian families live in different types of housing, including villas, duplex villas, penthouses, apartments, etc. These housing types are differentiated according to the influence of many factors, such as family income, resident's needs, and Saudi community traditions and customs (Alhubashi & Roca Cladera, 2016).

Table 2: General Authority for Statistics, Kingdom of Saudi Arabia 2010 (last statistics).

Type of housing	Percentage
Apartments	34.3%
Traditional House	26.9%
Villa (modern house)	25.5%
Floor in a Villa	10.9%
Floor in a Traditional House	1.2%
Other	1.3%

Table 2 illustrates the different types of housing available in Saudi Arabia and the percentage of how many of each type is present. Around sixty-five percent of Saudi residents live in either a modern villa or traditional house, which represents the majority of Saudi citizens, who are mainly middle-income families. This type of housing should thus be considered as a key factor in studies relating to low energy and sustainable housing in Saudi Arabia.

2. SUSTAINABLE DOMESTIC AND LOW ENERGY DESIGN IN HOT CLIMATIC REGIONS

There are a number of studies relating to the subject of domestic sustainable and low energy design in hot climatic regions especially in Saudi Arabia. The following section briefly summarises these and findings in provides an insights into gaps in knowledge.

Taleb (2011) said that houses in Saudi Arabia are heavily reliant on cooling, most of the families target a luxurious style and the principles of low energy buildings are rarely considered. She argues that the application of sustainable architectural practices is important to improve the efficiency of electricity use and water consumption in Saudi buildings. Taleb (2011) demonstrated through simulation of case study buildings located in Jeddah City, that the per capita electricity consumption for the apartment complex was around 8,047 kWh, while for villa it was 14,377 kWh per year. Taleb (2011) showed a significant reduction in the total electricity consumption for two case studies after adopting the suggested energy conservation measures and applying changes to the DesignBuilder (a building simulation software) models. It was shown that the calculated annual electricity use and resulting CO_2 emissions for the apartment complex which contains six apartments was estimated to have been reduced to around 76,446 kWh and 52.36 tonnes (from 144,850 kWh and 99.22 tonnes as a base case). With regard to the second case study the villa, the consumption was estimated to be around 122,785 kWh and 84.11 tonnes of CO_2 per year (compared to 186,901 kWh and 128.03 tonnes as a base case).

Another study focused on establishing a low carbon domestic design framework for Saudi Arabia (Aldossary, 2015). The research methods used in this study are: site visit, modelling and simulations of existing homes in different locations across Saudi Arabia (Riyadh city, Jeddah city, Abha city). 3 different houses and 3 apartments in each city were selected as case studies. The suggested solutions for the existing homes were retrofitting, remodelling and simulation the investigated homes in the three climatic regions. In addition, expert interviews were conducted to assist establishing a low carbon domestic design framework for sustainable homes in Saudi Arabia. Finally, the results suggest that an energy reduction of up to 71.6 % is achievable.

Alshaikh (2016) has reviewed and reported on different aspects to improve residents' thermal comfort in homes in a Saudi Arabia context. The approach used in this study was by measuring and analysing the thermal performance of the buildings, the thermal satisfaction and comfort responses of the residents and the electricity consumption during the summer period and the winter period. The comfort of residents was evaluated using the adaptive thermal comfort method. Alshaikh (2016) found that indoor air temperatures for several homes were high. In addition, most of the studied houses were not considered to be thermally comfortable as described within either by Predicted Mean Vote or Adaptive comfort limits. The study reviewed numerous influencing actors that included the houses properties, resident behaviour towards high electricity use, loads and charges. The result of the study found that lifestyle, attitudes and other socio-cultural factors have a strong influence on the comfort and energy use in individual houses.

Although (Aldossary, 2015; Taleb, 2011) studies show a significant reduction in electricity consumption there are some limitations in both of the studies. The building sample used for the case study in Taleb (2011) research may not be representative of the majority of housing or the residents lifestyle in Saudi Arabia. While, (Aldossary, 2015) research studied a larger sample size that may overcome this limitation his case studies are categorised under different types of houses in terms of house area, resident income, lifestyle. In addition, middle income families and residents behaviours in energy use were not explicitly considered in (Aldossary, 2015; Taleb, 2011) research . Alshaikh (2016) focused on improving residents' thermal comfort in Saudi homes, the study did not measure electricity use and household modelling through simulation programs was not conducted. It is clear that middle-income level of citizens is an important grouping to study as they represent the majority of families.

3. STUDY APPROACH

The approach in this study is to understand the effect of residents' behaviour on internal temperatures and electricity use. The following sub-sections provide an overview of the case study, initial research including thermal/electrical modelling. A

model was created for the case study using the TRNSYS simulation tool to predict the electricity consumption and calculate the annual cooling loads.

3.1. Case study

The case study is the AlShablan development in AL Khobar city in the eastern region in Saudi Arabia. It contains 19 typical villas and 30 typical apartments that are newly built (2015) from precast concrete, residents are middle-income families. Khobar is a large city located in the Eastern Province of the Kingdom of Saudi Arabia on the coast of the Arabian Gulf. Khobar experiences clear weather consistently, and temperatures generally fall between 11°C and 42°C. It doesn't exceed 45°C or fall below 8°C (Weathersparks, 2018). Figure 2 below shows the psychrometric chart analysis from ClimateConsultant for the nearest city to Khobar city. Thermal comfort without additional strategies will only be achieved for 11.6% of the hours of the year. Air conditioning with dehumidification is seen as the dominant intervention strategy in this climate, being required for 35.1% of the hours.

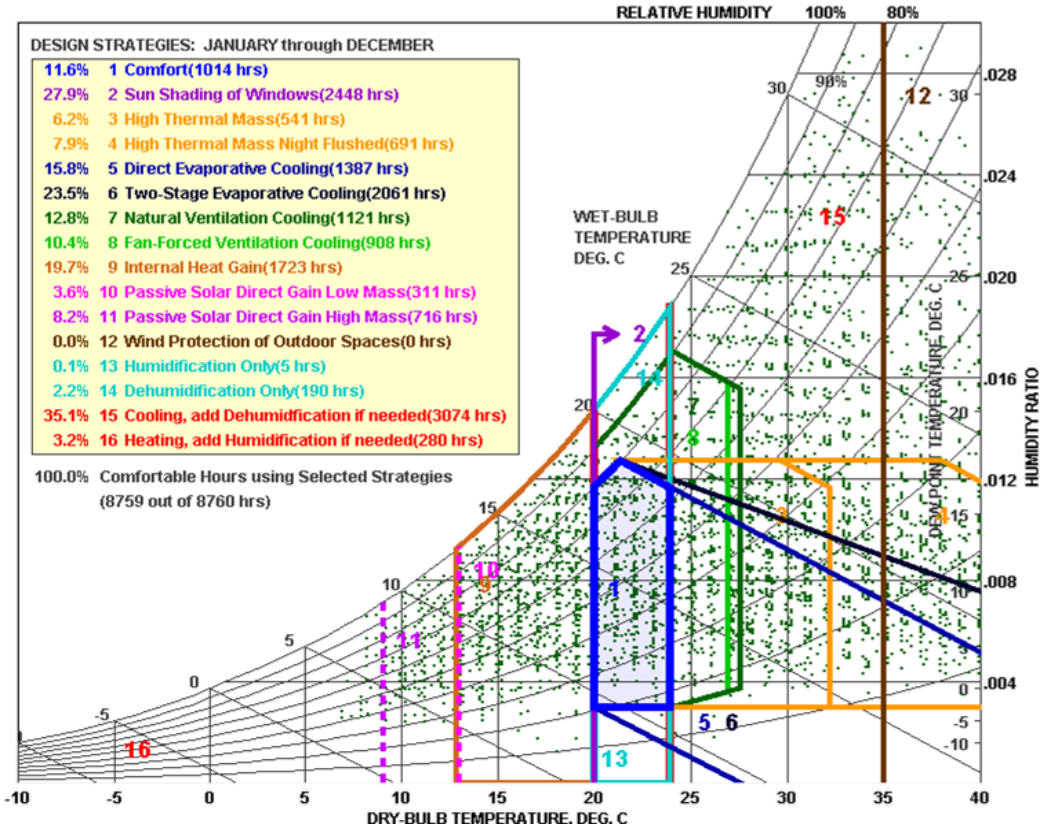

Figure 2: PSYCHROMETRIC chart for the nearest city to Khobar city (lat 26.27 deg N, long 50.17 deg East). Solid blue region (1) = comfort region without additional strategies applied, 11.6% of all hours. Source: ClimateConsultant.

3.2. Building simulation using (TRNSYS)

The case study (villa) was modelled, simulated and analysed using TRNSYS to estimate the annual cooling loads. The following elements were taken into consideration in this process of analysis: Building architectural form, building envelope, occupancy profile and local weather data (see Figure 3). The base reference case was created as a model using TRNSYS, based on building dimensions, the construction materials used, occupants' profile and energy consumption per appliance to calculate the internal gains of the weekday and the weekend. The area of each window, and the overall orientation of the building were considered.

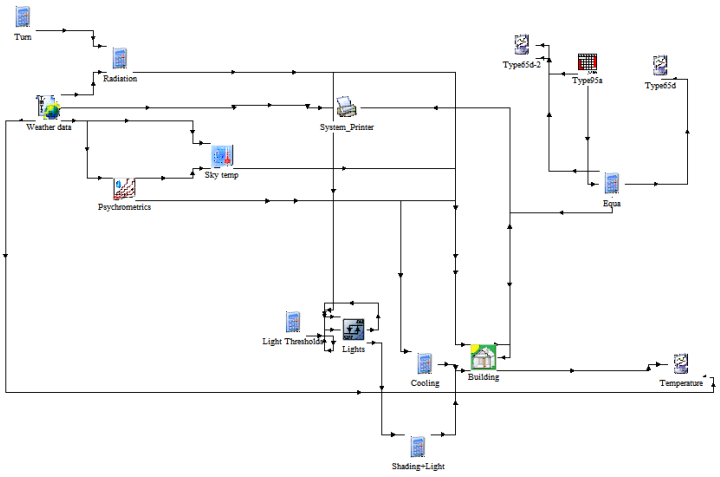

Figure 3: TRNSYS component model for KSA villa complex. Source: researcher.

The modelled building has a living area of 200m^2 across two storeys. The key parameters of the building model simulation are given in Table 3. The residence is assumed to have a combined infiltration and ventilation rate of 1 air change per hour.

Table 3: TRNSYS model parameters of residence.

Parameter	U-value (W/m^{2}K)	Area (m^2)
External wall	0.36	240
Roof	0.23	100
Ground floor	0.31	100
Glazing	1.40	23.8

The electrical appliance loads and lighting loads are estimated to have a consumption of 24 and 34 kWh per day for a weekday and weekend day respectively. The annual electrical appliance and lighting loads is 9800 kWh, the majority of which becomes additional cooling load for the air conditioning (AC) system. The AC system is assumed to maintain an upper limit of 21 deg C at all times in the dwelling and provide dehumidification above 80% RH. The temperature in the house drops below 21 deg C at the start and end of the year due to low ambient temperatures during this period.

The TRNSYS model estimates the annual cooling load to be 31,691 kWh thermal, which for a split unit AC system with a Coefficient of Performance (CoP) of 3.0 (Fujitsu General, 2017), corresponds to an annual electrical load of 10,564 kWh. Air conditioning is therefore estimated to represent 52% of the annual electricity consumption of the dwelling (20,350 kWh). Figure 4 below shows the ambient temperature and modelled dwelling temperature over the year alongside the thermal cooling load.

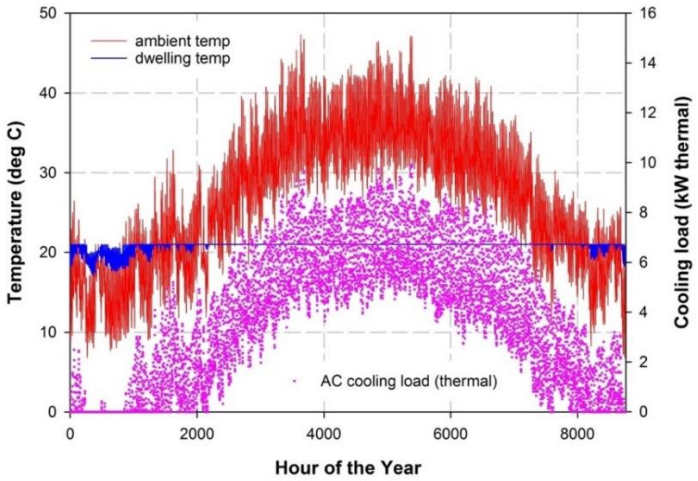

Figure 4: Ambient temperature and modelled dwelling temperature over the year alongside the thermal cooling load.

The TRNSYS model also considers 1 kWp of PV roof mounted at a slope of 20 degrees. For a typical inverter efficiency of 93% the annual AC generation is estimated to be 1750 kWh/kWp or 8% of the household electricity use. NOTE: This estimate does not consider the cumulative effects of dust or module mismatch (~1%) or dc cable losses (~1%) in the system yield. PV-GIS estimates 1 kWp at a slope of 20 degrees to generate 1720 kWh/kWp per annum (European Commission, 2018). 1 kWp of PV requires approximately 7m^2 of roof area, a 4kWp system is therefore a realistic deployable system which would meet around 32% of electrical demand of the dwelling. Khan et al (2017) have assessed the rooftop potential of PV in KSA considering the available roof areas due to building form self-shading etc. Their work suggests 30% of the nominal roof area is useable for PV deployment, which equates to our 4kWp estimate. As would be expected there is a very good seasonal and daily match between PV generation and cooling demand. Figure 5 shows the hourly PV generation (kW/kWp) across the year in comparison to the modelled cooling load.

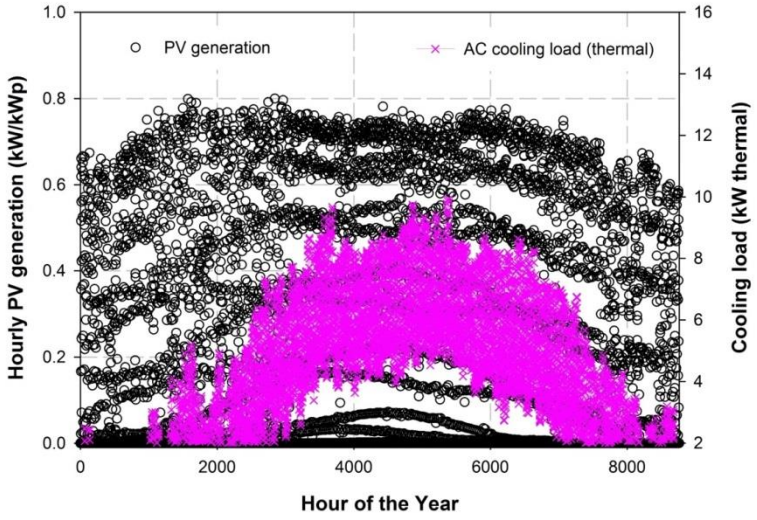

Figure 5: Hourly PV generation (kW/kWp) across the year in comparison to the modelled cooling load (kW thermal).

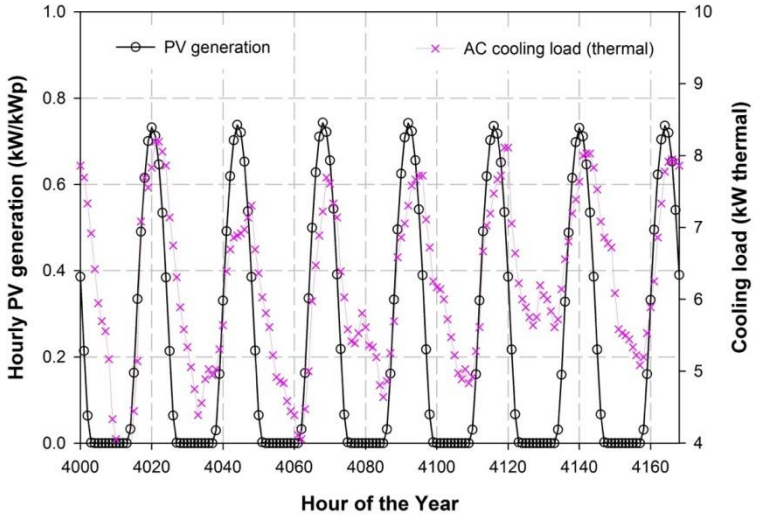

Figure 6: Hourly PV generation (kW/kWp) across a summer week in comparison to the modelled cooling load (kW thermal)

The summer cooling loads (Figure 6: 1-week example hours of the year 4000-4168) vary between 4 and 8kW thermal. For a CoP of 3.0, this corresponds to an electrical load of 1.3-2.7 kW. 4kWp of PV is estimated to have a peak electrical output of 3.2 kW, which when the additional electrical loads of the dwelling are considered means that export to the utility grid from the dwelling will be minimal.

4. RESULTS

4kWp of PV is a good sizing match to the electrical load of the dwelling if avoidance of export is considered important. The dramatic increases in electricity prices in KSA mean there is an opportunity for PV to be economically deployed. Here, by calculating the electricity bill for a year we compare the old tariff with the new tariff (see table 4), the new cost of the bill is raised by around 365%.

Table 4: Annual electricity bill by comparing the old tariff with the new tariff. Source: researcher.

Electricity Consumption (kWh/year)	Old tariff		New tariff	
	Unit rate (US$/kWh)	Annual bill (US$)	Unit rate (US$/kWh)	Annual bill (US$)
20,350	0.013	264.5	0.048	976.8

Table 5 represents the case study annual electricity consumption if 4 kWp of PV system is used, the system will generate annually 7000 kWh. The residential rooftop PV market is still relatively new in KSA and so we have considered turnkey CAPEX costs between 1000 and 1600 US$/kWp. We assume the annual maintenance cost is 2% of CAPEX. At a CAPEX cost of 1200 US$/kWp and a discount rate of 0% on the financing a system would have a payback time of 21 years, just less than the typical 25 year PV lifetime for the 0.048 $/kWh tariff rate.

The payback period is reduced to 11 years if the annual electricity consumption of the dwelling reaches 72,000 kWh, because at this consumption level, the tariff rate is 0.08 $/kWh. There are likely to be further increases in the electricity price as KSA tries to eliminate electricity subsidies. Figure 7 shows the payback time for PV CAPEX between 1000 and 1600 US$/kWp as a function of electricity tariff increase to up to 2X the new tariff. Payback times of as little as 7 years are predicted (Figure 7).

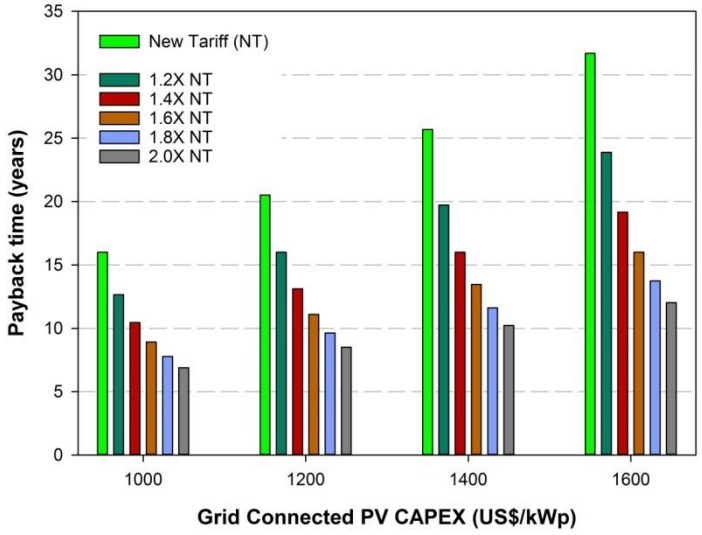

Figure 7: Estimated payback time for rooftop PV in KSA as a function of CAPEX and multiplier of the New Tariff KSA. Maintenance cost is 2% of CAPEX per annum, 0% discount rate on CAPEX.

Table 5: Case study annual electricity consumption before and after reduction and payback period in years. Source: researcher.

consumption (kWh/year)	consumption (kWh/year) after reduction	Tariff (US$/kWh)	annual bill before reduction (US$)	annual bill after reduction (US$)	Reduction per year (US$)	Payback period in years
20,350	13,350	0.048	976.8	640.8	336	21

5. CONCLUSIONS AND FUTURE WORK

This study focused on the residential buildings of middle-income Saudi's families and their electricity consumption. A case study development of villas and flats in Khobar city was adopted. This was achieved by modelling the existing case study through TRNSYS simulation tool and calculating the annual cooling loads, the model estimated a 20,350 kWh annual electricity consumption. Using solar photovoltaic system was considered as an effective solution to reduce electricity import and avoid grid export as results showed, a 4-kWp solar PV system would generate around 7000 kWh/year which could cover around 34% of such a load. The estimate payback period for the solar system is 21 years, but because residential rooftop PV market is still quite new in KSA and there are possible further increases in the electricity price. The payback time for PV CAPEX between 1000 and 1600 US$/kWp as a function of electricity tariff increase to up to 2X the new tariff. Payback times of as little as 7 years are expected.

Future work will use a mixed methods approach of environmental and energy usage monitoring combined with surveys of participants in the case study development. The participant study will determine patterns in behaviour, actual electricity

demand profiles through analysing collected data and relate these to internal environmental conditions and energy use in middle income domestic buildings. This approach will provide model validation and enable the exploration of the real world impact of a range of building form changes such as shading and alternative cooling strategies.

6. REFERENCES

Al-Ajlan, S. A. *et al.* (2006) 'Developing sustainable energy policies for electrical energy conservation in Saudi Arabia', *Energy Policy*, 34(13), pp. 1556–1565. doi: 10.1016/j.enpol.2004.11.013.

Aldossary, N. A. R. (2015) *Domestic Sustainable and Low Energy Design in Hot Climatic Regions*.

Alhubashi, H. and Roca Cladera, J. (2016) 'Housing types and choices in Saudi Arabia', *Back to the Sense of the City: International Monograph Book*. Centre de Política de Sòl i Valoracions, pp. 233–244. Available at: http://upcommons.upc.edu/handle/2117/90896 (Accessed: 23 November 2017).

BP (2017) 'BP Statistical Review of World Energy 2017'. Available at: https://www.bp.com/content/dam/bp/en/corporate/pdf/energy-economics/statistical-review-2017/bp-statistical-review-of-world-energy-2017-full-report.pdf (Accessed: 4 April 2018).

Climate Scorecard (2018) *Saudi Arabia Subsidies - Climate Scorecard*. Available at: https://www.climatescorecard.org/2018/01/saudi-arabia-subsidies/ (Accessed: 28 March 2018).

ECRA (2016) *Data and Statistics*. Available at: http://www.ecra.gov.sa/en-us/dataandstatistics/Pages/DataAndStatistics.aspx (Accessed: 13 July 2018).

European Commission, J. R. C. (2018) *PV potential estimation utility*. Available at: http://re.jrc.ec.europa.eu/pvgis/apps4/pvest.php?map=africa (Accessed: 15 July 2018).

Fujitsu General (2017) *Air Conditioners Line-Up Product Catalogue 2017*. Available at: https://www.fujitsu-general.com/shared/g-mea/pdf-gmea-ctlg-3mgs07-1701ea-01.pdf (Accessed: 15 July 2018).

Global Alliance of SMEs (2016) *Brief Introduction of Saudi Arabia*. Available at: http://www.globalsmes.org/news/index.php?func=detail&detailid=1061&catalog=20&lan=en&search_keywords=.

IEA (2018a) *Energy Subsidies*. Available at: https://www.iea.org/statistics/resources/energysubsidies/ (Accessed: 13 July 2018).

IEA (2018b) *IEA Sankey Diagram*. Available at: https://www.iea.org/Sankey/#?c=Saudi Arabia&s=Balance (Accessed: 13 July 2018).

Jeg, W. W. W. and Sa, O. R. G. (2016) 'Saudi Arabia – Public Utilities Report February 2016 Saudi Arabia – Public Utilities Report', (February).

Jones, S. (2012) 'Saudi Arabia, an unlikely, but lucrative country for New Energy investments'. Available at: http://jherrerosdc.typepad.com/jhsdc/2012/11/.

Khan, M., Asif, M. and Stach, E. (2017) 'Rooftop PV Potential in the Residential Sector of the Kingdom of Saudi Arabia', *Buildings*. Multidisciplinary Digital Publishing Institute, 7(4), p. 46. doi: 10.3390/buildings7020046.

Mohammed, A., Alshaikh, A. and Arch, B. (2016) 'Design Principles for Thermally Comfortable and Low Energy Homes in the Extreme Hot-Humid Climatic Gulf Region, with reference to Dammam, Saudi Arabia'.

Nereim, V (2017) *Saudi Arabia Slows Pace of Energy Subsidy Cuts to Boost Economy - Bloomberg*. Available at: https://www.bloomberg.com/news/articles/2017-12-19/saudi-arabia-slows-pace-of-energy-subsidy-cuts-to-boost-economy (Accessed: 28 March 2018).

OpenEnergyMonitor (2018) *OpenEnergyMonitor*. Available at: https://openenergymonitor.org/ (Accessed: 13 July 2018).

Saudi Vision 2030 (2016) *Saudi Vision 2030*. Available at: http://vision2030.gov.sa/en (Accessed: 11 January 2018).

Taleb, H. M. *et al.* (2011) 'Developing sustainable residential buildings in Saudi Arabia: A case study', *Applied Energy*. Elsevier, 88(1), pp. 383–391.

Taleb, H. M. (2011) 'Hanan M. Taleb', (September).

Tech, M. (2018) *MadgeTech*. Available at: shorturl.at/iwKR7.

Weather Online (2016) *Saudi Arabia climate*. Available at: http://www.weatheronline.co.uk/reports/climate/Saudi-Arabia.htm.

Weathersparks (no date) *Average Weather in Khobar, Saudi Arabia, Year Round - Weather Spark*. Available at: https://weatherspark.com/y/104952/Average-Weather-in-Khobar-Saudi-Arabia-Year-Round (Accessed: 1 February 2018).

410: Experimental analysis of thermophotovoltaic applications in waste heat recovery systems: example of GaSb cell

Zafer UTLU[1]; Büşra Selenay ÖNAL[2]

[1] İstanbul Gedik University İstanbul, Turkey,zafer.utlu@gedik.edu.tr
[2] İstanbul Gedik University İstanbul, Turkey, selenay.onal@gedik.edu.tr

In this study, it is aimed to evaluate real data in high temperature GaSb cell thermophotovoltaic systems. The thermophotovoltaic system can be defined as a system that converts the waste heat energy emitted from the heat sources into electrical energy at high temperature. The thermophotovoltaic energy conversion system consists of heat source, selective emitter, filter and photovoltaic cell module.In the study, the conversion of the high temperature applied to the cell to electrical energy has been investigated by selecting the GaSb photovoltaic cell as the cell type. According to have done analysis TPV high temperature real graphics have been obtained using GaSb cell. The temperature parameters used are cell temperature and source temperature. With these graphs, energy efficiency, fill factor, effect of open circuit voltage and short circuit current values have been determined. While the efficiency value of the GaSb thermophotovoltaic cell systems was calculated, the radiation source temperature values have been taken in increments of 300 K between 1300 K and 3100 K. In the real (lossy analysis, the optimum energy conversion efficiency value of GaSb solar cell structure was found to be 21.5763%. As a result of the obtained results, opinions about the feasibility, efficiency and development of thermophotovoltaic energy conversion systems have been stated and suggestions are presented.

Keywords: Thermophotovoltaic, waste heat, photovoltaic cell, GaSb cell, electricity generation, real data analysis.

1. INTRODUCTION

Electricity generation is possible by using existing waste heat in thermal systems. In industrial systems, the waste heat from the production phase can be recovered to the system and transformed into thermal energy electricity by thermophotovoltaic systems. Thus, electricity production from high-temperature waste heat is carried out, contributing to the current generation of electricity as clean and renewable energy. This method offers an alternative in terms of cost, efficient use of waste heat and energy saving, at the same time it is considered as an environmentally friendly production model by reducing greenhouse effect.

The main objectives are to maximise efficiency and minimise energy cost. The next generation TPV system has become a research topic as an alternative to existing electricity generation (Utlu and Parali, 2013; Utlu, 2014).

TPV's origins date back to the early 1970s (Coutts, 2001). Thermophotovoltaic has been as intensively researched this technology for heat / electricity accumulation in the last decade of the 20th century. However, there is still no wide commercialization (Barnett et al., 1997). Nelson, Kolm have been give information about a TPV system and a publication entitled "Power supplies for solar batteries" (Bauer, 2001). Industrial waste heat recovery using TPV conversion was proposed by Coutts at the end of 1990s (Yamaguchi and Yamaguchi, 1999). In addition, at the end of the 1990s, basic research in the field of Near Field TPV (NF-TPV) started. From the beginning of the 2000s, the development of miniature TPV generators under 10 W of electric power has been accelerated. These studies show that TPV applications are increasingly increasing, contributing greatly to energy conversion and efficiency (Bauer, 2001; Coutts, 2001; Colangelo et al., 2006).

2. THERMOPHOTOVOLTAIC SYSTEMS

Thermophotovoltaic systems are systems that convert thermal energy into electrical energy. These systems are an alternative to current electrical energy production. In this system, heat source, selective emitter, filters and photovoltaic cells are among the main components. In thermophotovoltaic systems, the sun can be used as a heat source as well as other heat sources such as combustion systems and fuels. The heat source is used to obtain photons in TPV systems. While the selective emitter is used to increase the system efficiency, the filter sends back the selective emitter by reflecting back the non-energised radiation. Photovoltaic cells convert photon energy from the emitter into electricity energy. Thermophotovoltaic systems, which are considered as alternatives to the existing electricity generation, are cycles that generate electricity from heat and provide waste heat recycling. Figure 1 shows general structure of TPV system.

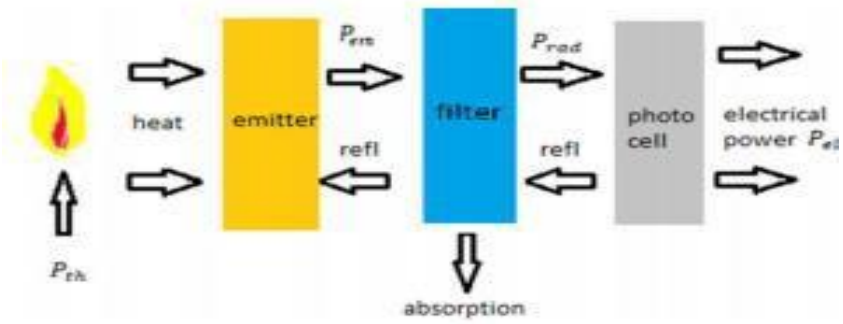

Figure 1: General structure of TPV system

2.1. Heat source

The heat source is the source of photons. Heat sources with operating temperatures between 1000°C and 1400°C can be used in TPV systems (Laroche, et. al., 2006). These sources include sunlight, radioactive isotopes (β-photons) and flaming combustion. The heat energy from the heat source passes through the selective emitter, filter and cells by radiation. The heat source comes from the photovoltaic cells and allows photons to be obtained (Mardiana-Idayua and Riffat, 2012).

Waste heat temperatures from iron and steel processes in industrial systems are suitable for TPV systems. Alkaline oxygen furnace, electric arc furnace and coke oven gas can be used as waste heat sources. The temperatures of these sources are given below: Alkaline oxygen furnace: 1973K; Electric arc furnace: 1473K; • Coke oven gas: 1247K.

Figure 2: Heat Source

2.2. Selective emitter

The system is used to increase system efficiency. The selective emitter translates the heat to the emission spectrum by providing the appropriate receiver cell sensitivity before transferring to the filters. Because the receiving cells can only use an energy absorber above the band spacing. This leads to less electricity generation (Shoaei, 2016).

Selective emitters radiate photons in a specific wavelength band that is spectrally matched to PV cells and increase the efficiency of the system. Yb_2O_3 can be used as the selective emitter. In addition, various spectral selective emitters such as earth selective emitter, micro structure emitter can be used. Also selective emitters such as Wu, MgO + NiO, Er + TiO_2 may be used. These selective emitters need to adapt to the photovoltaic cells (Utlu et al., 2017).

2.3. Filter

The photons from the selective emitter reach the filter before they reach the cells. The filters have the same characteristics as the selective emitter. Reflects non-energised radiation and sends the selective emitter back. Thus, the system efficiency is increased (Utlu et al., 2017).

2.4. Photovoltaic cells

Photovoltaic cells; Absorb photons from the emitter and convert them into thermal energy electrical energy. The necessity of absorbing as many photons as possible obligates the use of materials with low band gap (Xu et al., 2014).

In general, GaInAs and GaInAsSb cells are used. The bandwidths of these semiconductor materials are different from each other. The GaInAs band gap equals 0.7 eV. This band gap has a very large scale for optimum efficiency and energy. In addition to these cells, InGaSb and InGaAsSb are formed by forming quaternary alloys. InGaSb has a band gap of 0.5 eV, which is a very narrow band gap. InGaAsSb can be adjusted between 0.38 eV and 0.7 eV depending on the ratio of the elements.

In this study GaSb cells have been selected for TPV prototype. The band spacing of these cells is suitable for actual study. The GaSb cells are connected in series and placed on the inner surface of the cooling system.

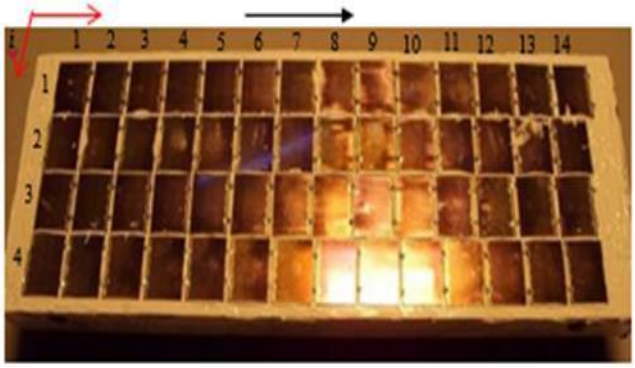

Figure 3: GaSb Cell

The working mechanism of TPV can be summarised as follows:

• The thermal energy (photons) obtained from the heat source (waste heat) is transferred to the selective emitter by radiation.

• The selective emitter translates the incoming heat to the appropriate emission spectrum to increase the efficiency of the system. A selective emitter is used to increase the amount of electricity generated. The photons passing through the selective diffuser pass through the filters.

• Filters have a feature similar to a selective emitter. The filter sends back the selective emitter by reflecting back the non-energised radiation. Thus, the system efficiency is increased. The radiation from the selective emitter has enough energy to reach the cells. Filters also help to protect the selective emitter's temperature.

• Photons with sufficient energy come from photovoltaic cells and are converted directly into electricity.

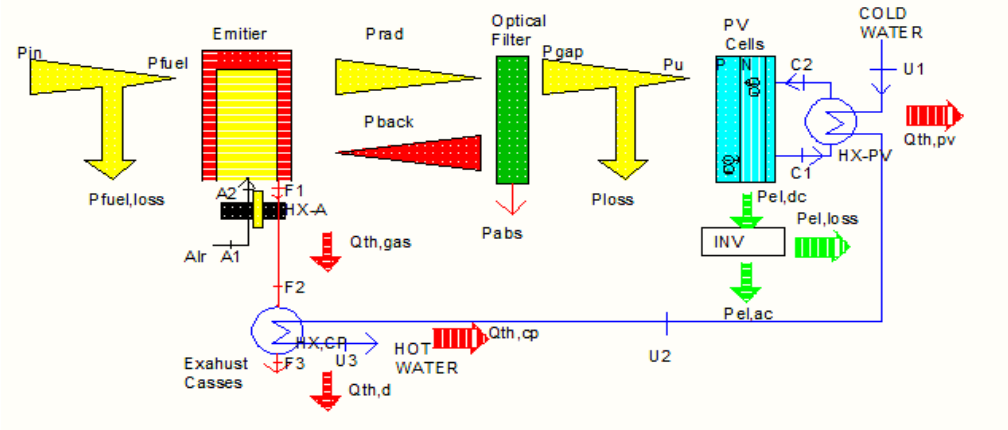

Figure 4: Schematic representation of the TPV system

Figure 4 is a schematic representation of the TPV system. According to this demonstration fuel is used as heat source. The fuel mixes with the air to form a selective emitter. Exhaust gas is thrown out of the system. The photons emitted from the selective emitter come to the optical filter by radiation, and are reflected to the selective emitter, which filters the low-energy photons. Photons, which have an appropriate band gap in terms of energy, reach the photovoltaic cell. In a photovoltaic cell, thermal energy turns into electrical energy. This Electrical energy is direct current. The inverter converts the direct current (DC) to alternating current (AC). The coolant attached to the system maintains the temperature of the cell by reducing the overheating of the photovoltaic cell. Both the cooling system and the filter prevent the cell from overheating.

3. REAL ANALYSIS OF THERMOFOTOVOLTAIC SYSTEMS

Within the scope of the analysis, GaSb cell thermophotovoltaic solar cell structure applied to industrial systems with high temperature waste heat is designed. Graphical representations of the basic parameters against cell temperature, such as open circuit voltage (Voc), short circuit current (Jsc), fill factor (FF) and energy conversion efficiency values (η), have been presented graphically depending on the changing radiation source temperature.

In the theoretical analysis, the efficiency value of GaSb thermophotovoltaic cell systems was calculated while the radiation source temperature values were increased by 300 K between 1300 K and 3100 K. Cell temperature values were taken from 300 K to 400 K with 25 K increments. According to the final design, the optimum energy conversion efficiency value of the GaSb solar cell structure was found to be 33.14 % at T_{source} = = 2200 K and at T_{cell} = 300 K.

In the real (lossy) analysis of the GaSb-cell TPV system installed on the industrial system as can be seen in the Figure 5, the efficiency value was calculated while the radiation source temperature values were taken in increments of 250 K between 1000 K and 3000 K. Cell temperature values were taken from 300 K to 400 K with 25 K increments. According to the final design, the optimum energy conversion efficiency value of the GaSb solar cell structure was found to be 21.5763 % at T_{source} = 2500 K and at the T_{cell}= 300 K.

Figure 5: Cell temperature and voltage values at 949 ° C and 950 ° C source temperature

3.1. Real analysis of thermophotovoltaic systems

In the real (lossy) analysis of the GaSb-cell TPV system installed on the test system, the radiation temperature values are 1000 K, 1750 K, 2500 K and 3000 K, and the cell temperature values are 300 K, 325 K, 350 K, 375 K and 400 K It was obtained. Graphs have been obtained using the cell values for each radiation temperature.

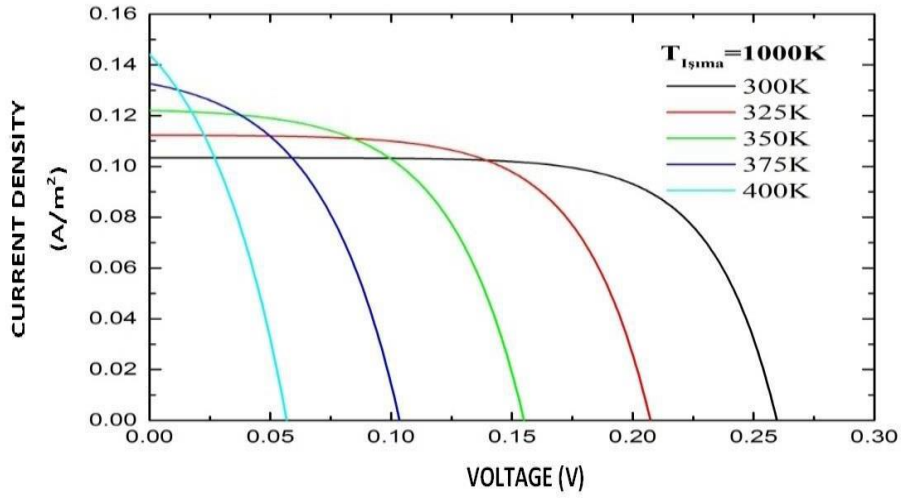

Figure 6: Flow dependence of different cell temperature for radiation temperature - voltage graph

At 1000 K radiation temperature, current densities are seen according to the changing voltage values at different cell temperatures as given Figure 6. For example, at 350 K cell temperature, when the voltage value is 0.05 V, the current density is 0.12 A / m² whereas when the voltage value is 0.12 V, the current density drops to 0.08 A / m². At 300 K source temperature, when the voltage value is 0.10, the current density is 0.10 A / m² whereas when the voltage value is 0.25 V, the current density drops to 0.04 A / m². In this case, as the voltage increases, the current density decreases.

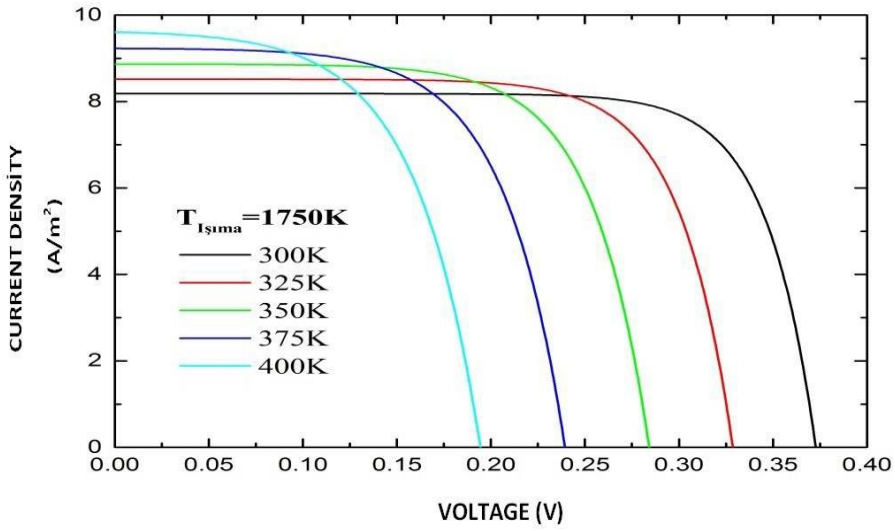

Figure 7: Flow Dependence of Different Cell Temperature for 1750 K Radiation Temperature - Voltage Graph

At 1750 K radiation temperature, current densities are seen according to the changing voltage values at different cell temperatures, as indicated Figure 7. For example, at 400 K cell temperature, when the voltage value is 0.05 V, the current density is 9.8 A / m² whereas when the voltage value is 0.15 V, the current density drops to 8 A / m². In this case, as the voltage increases, the current density decreases.

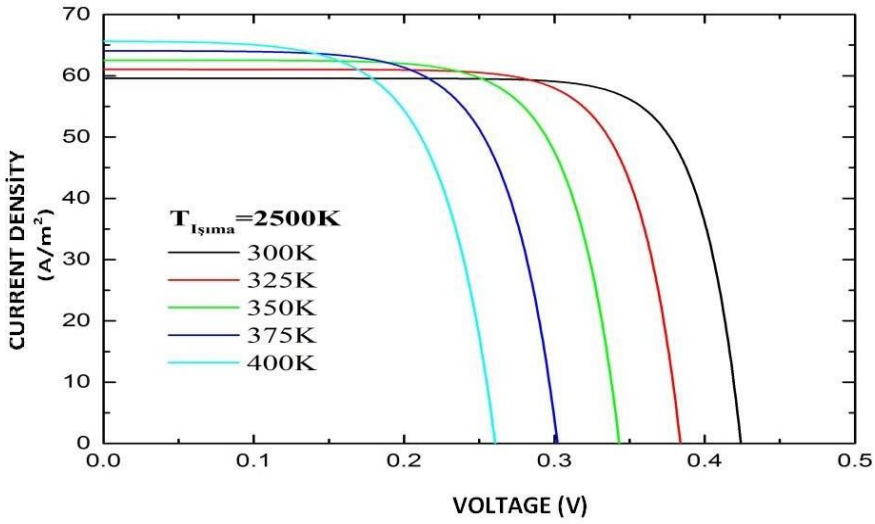

Figure 8: Flow dependence of different cell temperature for radiation temperature - voltage graph

At 2500 K radiation temperature, current densities are seen according to the changing voltage values at different cell temperatures as shown Figure 8. For example, at 400 K cell temperature, when the voltage value is 0.1 V, the current density is 66 A / m² whereas when the voltage value is 0.2 V, the current density drops to 60 A / m². In this case, as the voltage increases, the current density decreases.

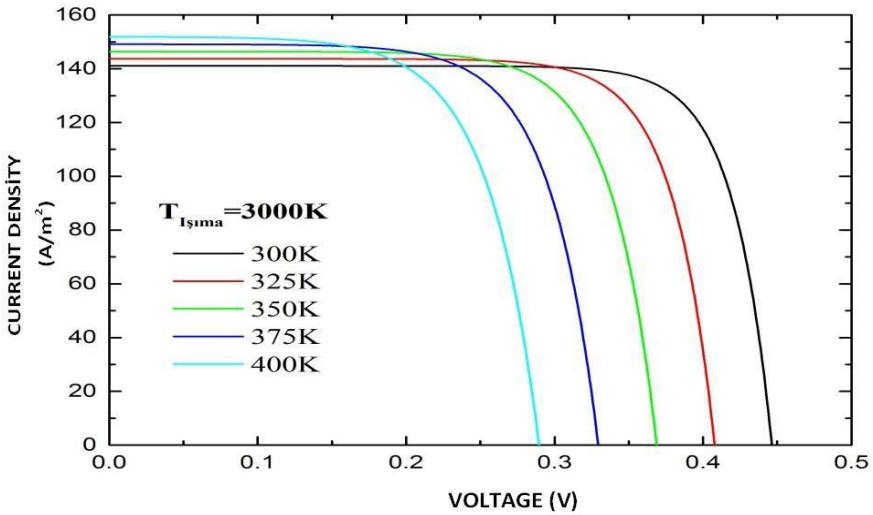

Figure 9: Flow dependence of different cell temperature for radiation temperature - voltage graph

At 3000 K radiation temperature, current densities are observed according to varying voltage values at different cell temperatures as given Figure 9. For example, at a cell temperature of 375 K, when the voltage value is 0.1 V, the current density is 150 A/m² whereas when the voltage value is 0.3 V, the current density drops to 110 A / m^2. In this case, as the voltage increases, the current density decreases.

4. RESULT AND DISCUSSION

According the real analysis of GaSb cell thermophotovoltaic systems have been compared the behaviour of values. This value is open circuit voltage (Vc), short circuit current (Jsc), fill factor (FF) and energy conversion efficiency value (η), which are basic parameters against cell temperature. This value varies depending on the radiation source temperature.

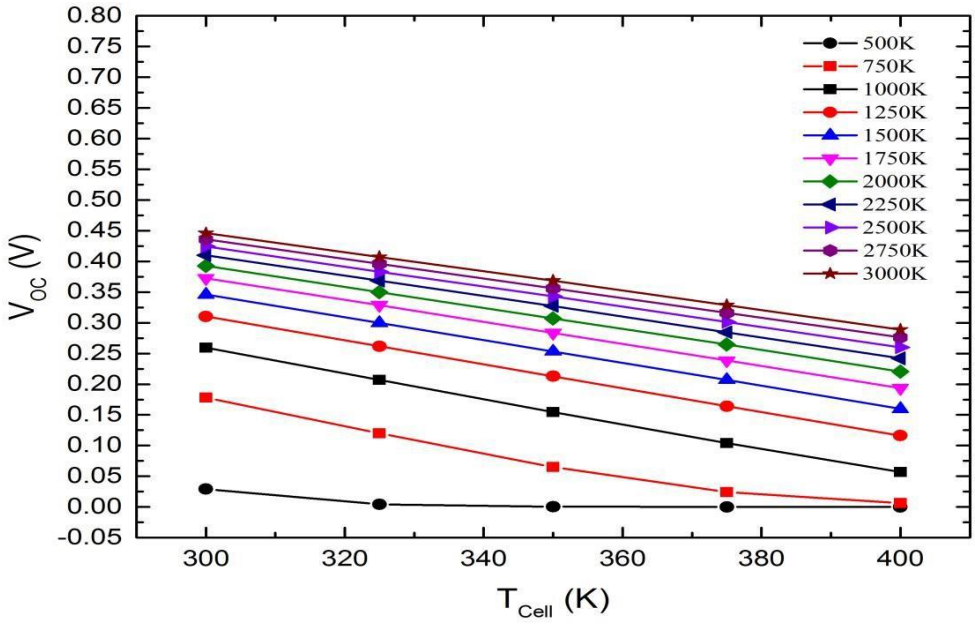

Figure 10: Effect of cell temperature change on open circuit voltage

As a result of the real analysis made, the relationship between cell temperature and open circuit voltage is shown depending on the changing radiation temperature as indicated figure 10. For example, when the cell temperature is 300 K at the 2000 K source temperature, the open circuit voltage decreases to 0.25 V when the cell temperature is 0.4 V while the cell temperature is 400 K. In this case, as the cell temperature increases, the open circuit voltage decreases.

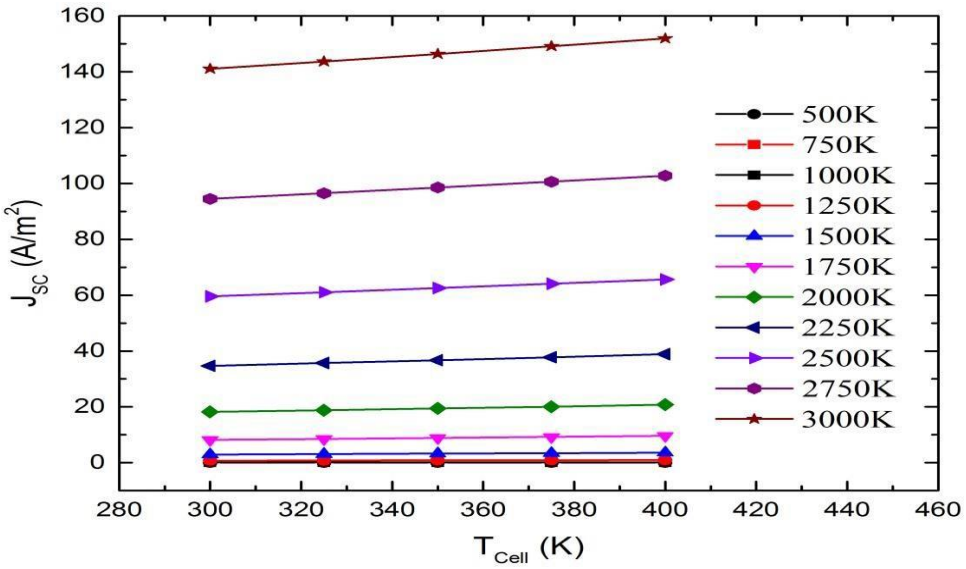

Figure 11: Effect of cell temperature change on short circuit current

As a result of the actual analysis made, the relationship between cell temperature and short circuit current is shown depending on the changing radiation temperature as seen Figure 11. For example, when the cell temperature is 300 K at 3000 K source temperature, the short circuit current is about 140 A / m² while when the cell temperature is 400 K, the short circuit current is about 150 A / m². In this case, it is observed that the short circuit current rises as the cell temperature increases.

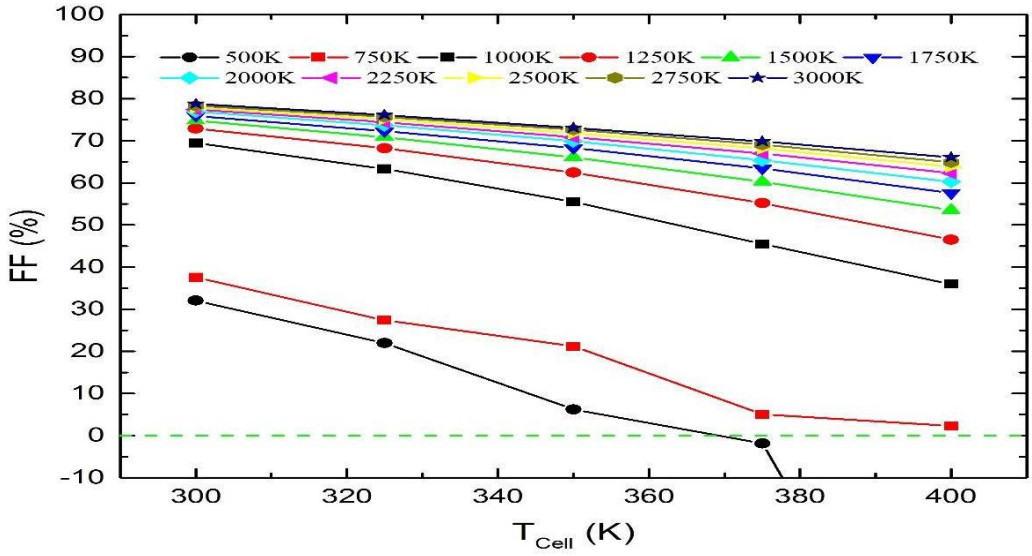

Figure 12: Effect of cell temperature change on fill factor

In the real analysis made, the relationship between cell temperature and filling factor is shown depending on the changing radiation temperature as shown Figure 12. For example, when the cell temperature is 300 K at a 1000 K source temperature, the filling factor is about 70% while the filling factor is about 40% when the cell temperature. İs 400 K. In this case, as the cell temperature increases, the short cuircuit current decreases.

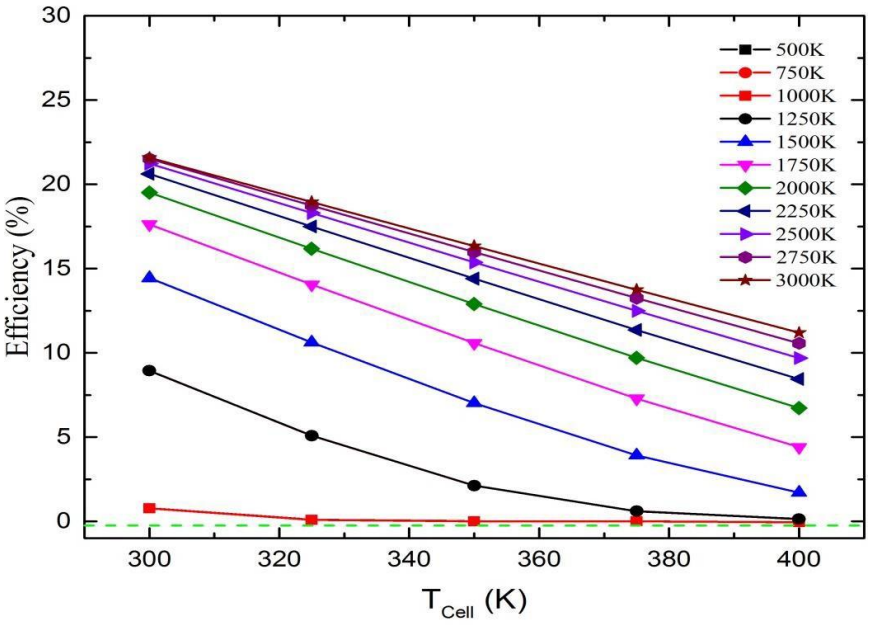

Figure 13: Effect of cell temperature change on filling factor

According to the real analysis made, the relationship between the cell temperature and the energy efficiency is shown depending on the changing radiation temperature as given Figure 13. For example, when the cell temperature is 300 K at the 3000 K radiation temperature, the energy efficiency is 21.29163% while when the cell temperature is 400 K, the energy efficiency falls to 15%. In this case, as the cell temperature increases, the energy efficiency decreases.

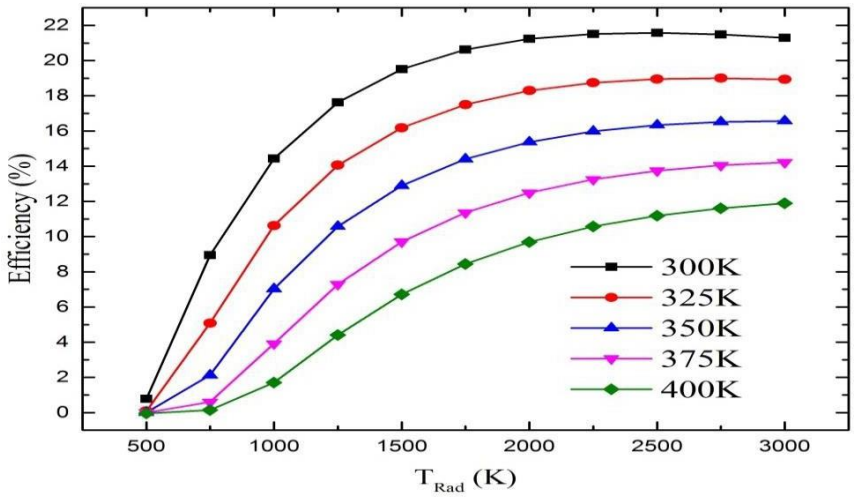

Figure 14: As Depend on varying cell temperature, radiation temperature- efficiency graph

According to real analysis made, the relationship between the radiation temperature and the energy efficiency is shown depending on the changing cell temperature as given Figure 14 and Figure 15. For example, when the radiation temperature is 2000 K at 400 K cell temperature, the energy efficiency is 9.6894%, while when the radiation temperature is 3000 K, the energy efficiency is 11.89359%. In this case, it is observed that the energy efficiency increases as the radiation temperature increases.

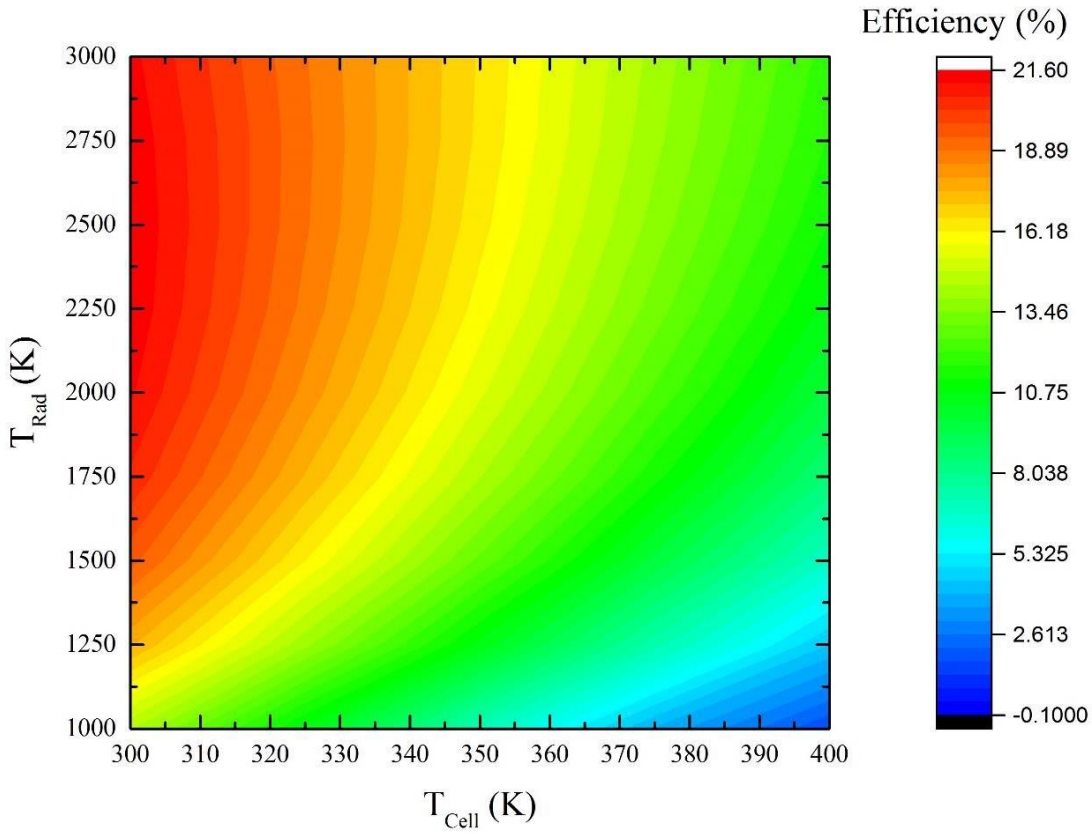

Figure 15: As depend on varying cell temperature, radiation temperature- efficiency graph

5. CONCLUSION

The thermophotovoltaic energy conversion system has gained great importance in terms of recovery of existing waste heat to the system and generation of electricity. By saving waste heat in the system, saving energy and cost is ensured.

In this study, thermophotovoltaic system applied on high temperature GaSb cell was really analysed and data were obtained.

- The optimum energy efficiency obtained as a result of the prototype result on the industrial system is 21.5763%.
- The highest filling factor is 79.39943% while the lowest filling factor is 71.00556%. As the temperature of the cell increases, the short circuit current decreases.
- The highest energy efficiency is 21.57% at 3000 K radiation temperature, while the lowest energy efficiency at 1000 K radiation temperature is 10.02%.
- When cell temperature is increased, energy efficiency is reduced. As the temperature of the cell decreases, the energy efficiency increases.
- As the temperature of the cell increases, the band gap decreases, and the TPV decreases the open circuit voltage of the cell. In addition, the filling factor and efficiency are reduced due to increased cell temperature.
- Compared to the ideal and ideal analysis, the highest open circuit voltage has been 0.464 V at the 3000 K radiation temperature in the theoretical (ideal) analysis, but this value decreased to 0.4459 V at 3000 K radiation temperature for the highest open circuit voltage.
- In the real analysis, the short circuit current has been 151.9016 A / m² at 3000 K radiation temperature.
- When the filling factor was examined, the highest value in the real analysis was 78.7718%.

In general, it is seen that the values obtained in the actual analysis are slightly lower than the theoretical data. The thermophotovoltaic system installed in the industrial system in accordance with the actual analysis obtained can contribute to the current electricity production with an efficiency of approximately 21.5763%.

6. ACKNOWLEDGEMENTS

This study was produced from the project 114R088 which is carried out within the scope of Scientific and Technological Research Council of Turkey (TUBITAK) 1001 from the project titled "Development of Electricity Energy Production Technology by Thermophotovoltaic Methods Utilizing Existing Waste Heat Potential in Thermal Systems". We would like to thank TUBITAK for their support to the Project.

7. REFERENCES

Barnett, A. M., Coutts, T. J., Kazmerski, L. L., Ramakumar, R., & Benner, J. P. 1997. Power Systems and Generation. In The Electrical Engineering Handbook, Second Edition. CRC Press.

Bauer T., 2001. Overview of the technology in: Thermionics Quo Vadis, an assessment of the DTRAs advanced thermionics researchand development program, Chap. 3. National Academy Press, pp 15–32, [Online] Available at: http://books.nap.edu/.

Bendig M., Maréchal F., Favrat D. 2013. Defining “Waste Heat” for industrial processes. Applied Thermal Engineering 61,134-142.

Colangelo A. de Risi A. Laforgia A. 2006, Experimental study of a burner with high temperature heat recovery system for TPV applications. Energy Conversion and Management, 2006, 47, 1192 - 1206.

Coutts, T. J. 2001. An Overview of Thermophotovoltaic Generation of Electricity. Solar Energy Materials and Solar Cells, 66(1), 443-442.

Ferrari, C., Melino, F., Pinelli, M., & Spina, P. R., 2014. Thermophotovoltaic energy conversion: Analytical aspects, prototypes and experiences. Applied Energy, 113, 1717-1730.

Ferrari, C., Melino, F., Pinelli, M., Spina, P. R., & Venturini, M., 2014. Overview and status of thermophotovoltaic systems. Energy Procedia, 45, 160-169.

Fraas LM., Avery JE., Huang HX., Martinelli RU., 2003. Thermophotovoltaic system configurations and spectral control. Semicond Sci Technol 18:165–173.

Horne E., 2002. Hybrid thermophotovoltaic power systems. EDTEK, Inc., US, Consultant Report, P500-02-048F.

Hugues L.T., Beyene A., Heat recovery from automotive engine. Applied Thermal Engineering, 2009. 29, 439– 444.

Laroche, M., Carminati, R., & Greffet, J. J. 2006. Near-field Thermophotovoltaic Energy Conversion. *Journal of Applied Physics*, 100(6), 063704.

Lodhi Mak., Vijayaraghavan P., Daloglu A., 2001. An overview of advanced space/ terrestrial power generation device: AMTEC. J Power Sources 103(1):25–33.

Mardiana-Idayua A., Riffat S.B. 2012; Review on heat recovery technologies for building applications. Renewable and Sustainable Energy Reviews 16, 1241– 1255.

Reay D, Kew P. Heat pipes. 5th ed. Oxford: Elsevier; 2006

Shoaei, E., 2016. Performance assessment of thermophotovoltaic application in steel industry. Solar Energy Materials and Solar Cells, 157, 55-64.

Steinhüser A., Hille G., Kügele R., Roth W., Schulz W 1999. Photovoltaic-Hybrid Power Supply for Radio Network Components. Proceeding of the Intelec’99, Kopenhagen, 6–9. Juni.

Swithenbank J., Finney, KN., Chen Q., Yang Y.B., Nolan A., Sharifi.VN. 2013. Waste heat usage, Applied Thermal Engineering, 60, (1-2), 430-440.

Tobler, W. J., Durisch, W. 2008. High-Performance Selective Er-Doped Yag Emitters for Thermophotovoltaics. *Applied Energy*, *84*(6), 483-493.

Utlu Z., Hepbaşlı A., 2007. A Review And Assessment Of The Energy Utilization Effeciency In The Turkish Industrial Sector Using Energy And Exergy Analysis Method, Renewable and Sustainable Energy Reviews11, 1438–1459.

Utlu, Z., & Parali, U., 2013. Investigation of the potential of thermophotovoltaic heat recovery for the Turkish industrial sector. Energy Conversion and Management, *74*, 308-322.

Utlu, Z., 2015. Investigation of the potential for heat recovery at low, medium, and high stages in the Turkish industrial sector (TIS): An application. *Energy*, *81*, 394-405.

Utlu, Z., Kınacı B., Önal, B.S. 2017. Investigation of The Use of Waste Heat in Central Heating Systems in The Thermophotovoltaic Technology; GaSb Cell Application. 12th Conference on Sustainable Development of Energy, Water and Environment Systems – SDEWES Conference /Pp:774:1-16, ISSN 1847-7186 (book of abstracts) ISSN 1847-7178 (digital proceedings). September 04-08, Dubrovnik.

Utlu, Z.,Parali, U., Gültekin Ç., 2018, Applicability of Thermophotovoltaic Technologies in the Iron and Steel Sectors, 6, 6, 1039-1051.

Volz W., 2001. Entwicklung und Aufbau eines thermophotovoltaischen Energiewandlers (in German), Doctoral thesis, Universität Gesamthochschule Kassel, Institut für Solare Energieversorgungstechnik (ISET).

Xu, X., Ye, H., Xu, Y., Shen, M., Zhang, X., & Wu, X. 2014. Experimental and Theoretical Analysis of Cell Module Output Performance for a Thermophotovoltaic System. Applied Energy, 113, 924-931.

Yamaguchi H., Yamaguchi M., 1999. Thermophotovoltaic potential applications for civilian and industrial use in Japan. Proceeding of the 4th NREL conference on thermophotovoltaic generation of electricity, Denver, Colorado, 11–14 Oct 1998. American Institute of Physics, pp 17–29.

411: Research on intelligent control system of solar LED street lights

Kun KE[1], ZhengWang XU[2], Guozhang JIANG[3], Jiarui ZHANG[4], Daiwei FENG[5]

[1]Hubei University of Technology, Wuhan, China, 1029360275@qq.com
[2]Hubei University of Technology, Wuhan, China, 69628025@qq.com
[3]Hubei University of Technology, Wuhan, China, 1047315944@qq.com
[4]Hubei University of Technology, Wuhan, China, 695922893@qq.com
[5]Hubei University of Technology, Wuhan, China,1140439455@qq.com

This paper proposes to use mobile terminal equipment as the monitoring and management platform of solar LED street lighting system to realise remote control, centralised and fine-grained monitoring and management of solar LED street lighting system. Firstly, a set of selective ad hoc network multi-hop transmission scheme is designed based on CC2530 to build a wireless ad hoc network to maximise the wireless communication distance. Secondly, the three major sections of the solar LED street lighting monitoring and management system: the mobile terminal node, the transit node and the controller node are respectively designed with hardware. Then the software design of the system's selective ad hoc network multi-hop scheme was carried out. Finally, the experimental platform of the solar LED street lamp monitoring and management system designed in this paper is built and experimentally analysed to verify the feasibility of the selective self-organizing network multi-hop transmission scheme and the stability when using CC2530 for wireless transmission.

Keywords: Solar LED light; Wireless ad hoc network; CC2530

1. INTRODUCTION

At present, non-renewable energy sources are over-exploited and used, and then renewable renewable energy is increasingly favored by people. Solar LED street lamps show an efficient and energy-saving and green lighting method, which not only saves resources such as manpower and material resources, but also returns High, system security is also strong (Zang, 2012). However, the existing street lamp system has problems such as complicated layout, difficulty in unified management, single control mode, unreasonable power distribution, and methods and methods of networking (Gao, 2017), so the future development tends to energy-saving control, remote control and refinement control. In the development of solar energy, in order to improve energy efficiency, the system of chasing the sun has been proposed. However, motion sensors require complex motion mechanisms and are costly, so they are not intended to be used in our streetlight system.The scale of use of solar LED street lighting systems continues to expand, and the management of lighting systems has also appeared more and more problems. This paper mainly designs a set of mobile terminal-based lighting monitoring and management system for solar LED street lighting system on rural roads instead of the traditional mobile monitoring and management platform that cannot be moved and is more cumbersome to solve the current management of solar LED street lighting system. Defects.

2. SYSTEM DESIGN

The lighting monitoring management platform designed in this paper includes three parts, mobile terminal nodes, transit nodes and controller nodes. First, we compare the advantages and disadvantages of wireless communication technologies such as Bluetooth, Wi-Fi, and Ir DA. We chose to build a wireless ad hoc network system using the CC2530 module based on the ZigBee protocol. The wireless ad hoc network topology variable network contains four basic structures: central control structure, hierarchical central control structure, fully distributed control structure and hierarchical distributed control structure (Goseling, 2017). The system chooses a hierarchical distributed control structure, but in order to maximise the scope of wireless communication, a selective wireless ad hoc network multi-hop transmission scheme is designed to maximise the range of wireless communication.

2.1. Selective ad hoc network multi-hop scheme design

The CC2530 module used in the wireless communication scheme can perform automatic multi-hop transmission, and the multi-hop transmission scheme is designed based on two transit node-based systems. As shown in Figure 1, the M number and the street lamp controller node in front of it are all within the transmittable range of the transit node 1, so by obtaining the address, the data packet is directly sent to the corresponding target street lamp controller node through the transit node 1, M number to M+ The streetlight controller node between the 14th is outside the transmission range of the transit node 1, so the transit node selects the address of the M number as the first hopping point, and then transmits it to the target streetlight controller node in order. The streetlight controller node after M+14 exceeds the range in which the M-lamp controller node is transmitted in order after the first hopping point. Therefore, the transit node 2 is used to increase the transmission distance and reduce the packet transmission. The number of times, after receiving the data packet, the M street lamp controller node selects the address of the transit node 2 as the next hop point, and then transfers the node 2 to the street lamp after the M+14.

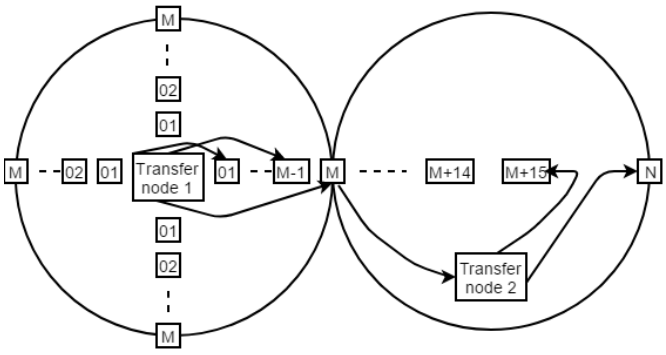

Figure 1: Flow chart of selective ad hoc network multi-hop transmission scheme

2.2. Functional design

The wireless ad hoc network system designed in this paper will configure a CC2530 module on each street light controller. Each CC2530 module has an address, and each address number is unique. The address numbers are in the order of street lights. Arrange, manage the address to achieve real-time control of each street light.In this paper, the wireless ad hoc network system selects the CC2530 module as the medium for wireless communication, and its chip model is CC2530F256. The chip has 256KB of flash memory and includes an RF transceiver, an enhanced 8051 CPU, 8KB of RAM,

programmable flash memory and a host of other powerful features. The chip integrates a 2.4GHz RF transceiver, the 8051MCU. The chip's operating currents in transmit mode and receive mode are 29mA and 24mA, respectively, making it ideal for low-power systems (Kang, 2017). The CC2530 module complies with the IEEE802.15.4 protocol and does not require the design of a complex protocol stack. The address can be configured independently. When the module works, the module and the surrounding modules form a wireless multi-hop network. This network is a peer-to-peer network. It does not need a central node. The maximum transmission distance between the two modules can reach 75m. It has a confirmation transmission function between CC2530 modules. It can automatically perform wireless multi-hop transmission. When the transmission distance exceeds the maximum transmission distance between two modules, it can automatically select the nearest module for jump transmission, thereby achieving the purpose of long-distance transmission.

3. OVERALL HARDWARE DESIGN

3.1. Mobile terminal hardware design

The mobile terminal is the monitoring and management platform of the whole solar street lighting monitoring and management system. Its hardware structure includes: HMI human-machine interface touch screen, control circuit, CC2530 module and power supply circuit. The HMI human-machine interface consists mainly of the processor, storage unit, communication interface, input and display. In this paper, the solar LED street lighting monitoring management system selects the HMI human-machine interface touch screen of model TJC4832T035-011R as the core of the mobile control terminal. The controller selects a high-performance, low-cost ARM processor as the core controller. The control circuit of the mobile terminal node and the transit node in the solar LED street lighting monitoring and management system designed in this paper finally selects the STM32 series STM32F103C8T6 as the main control chip. The CC2530 module uses the UART as the interface data interaction interface. Before configuring the ad hoc network, configure the basic information of all CC2530 modules so that they are all in the same network. In the same network, the CC2530 module needs to have the same network. ID, same baud rate and a separate network address (Feng, 2018). The 3.3V voltage required by the CC2530 wireless ad hoc network module is converted by the ASM1117.

3.2. Controller node hardware design

The hardware components of the street lamp controller node include: street lamp controller and CC2530 module. The CC2530 module communicates with the street lamp controller through UART3. The solar LED street light system is mainly composed of LED street lights, solar panels, batteries and intelligent controllers (Huang, 2017). Since the low-end mode is adopted on the switch, the negative pole of the solar panel and the ground of the main circuit are cut off by Q24. When Q24 is turned off, the voltage of the solar panel cannot be directly detected by the partial pressure method. The detection result of the solar panel voltage is directly related to the conversion of the controller in the charging or discharging state. To solve this problem, the circuit is designed with a differential detection circuit to detect the solar panel voltage, as shown in Figure 2. By detecting the voltage of the solar panel, we judge the day and night alternate time to prevent the weather conditions, so the daylight sensor is not used here.

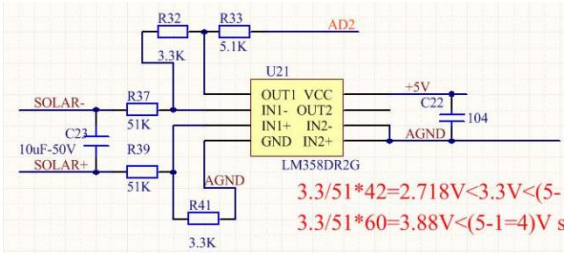

Figure 2: solar panel voltage detection circuit

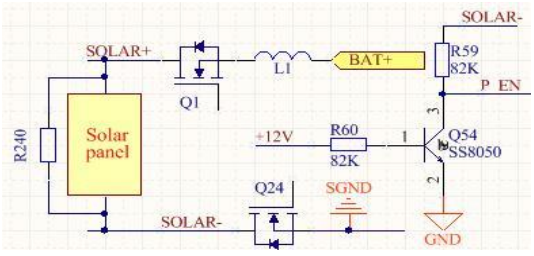

Figure 3: solar panel boot circuit

After in-depth analysis, the power supply of the controller is obtained from the solar panel and the battery through the XL1509-12E1 chip. Since the 4th pin of the XL1509-12E1 chip is the enable terminal, when the pin is floating or grounded, the chip works normally. When the pin is pulled high, the chip stops working. Once the chip stops working, the entire control circuit loses power and enters the standby state, and the power consumption is extremely low. Using the enable terminal in conjunction with the circuit shown in Figure 3 above, the required P_EN enable signal can be generated to implement the solar panel boot function.

3.3. Relay node hardware design

The role of the transit node is to carry out data transfer in the solar street lighting wireless ad hoc network system, which plays a bridge role in the communication process. The hardware part mainly includes CC2530 plus RF amplifier circuit, power supply circuit, control circuit and antenna. Based on CC2530 module, this paper adds a RF amplification circuit

based on CC2591 RF front-end chip to improve the transmit power of wireless communication part and further improve Receive sensitivity to extend wireless communication distance (Mai, 2015). There are roughly three types of antennas commonly used in wireless communication systems: PCB antennas, on-chip antennas, and whip antennas. The transfer node is added to the antenna mainly to increase the distance of wireless communication. The requirements for the size and the size are not strict, and the number of transit nodes is small and the cost is not large. Therefore, this paper chooses a whip antenna to improve performance to a greater extent. First, the transmit power and the receive sensitivity are estimated, and then the approximate distance of the wireless transmission of the transit node is further estimated.

4. SYSTEM SOFTWARE DESIGN

4.1. Mobile terminal operating platform software design

The mobile terminal uses the HMI human-machine interface as the operating platform. The system switching, sending data commands, receiving data commands and data input interface control programs on the HMI human-machine interface are all written by the host computer USARTHMI. The HMI human-machine interface touch screen receives the parameter data sent by the controller node. The control circuit of the mobile terminal receives the controller operating parameters transmitted from the CC2530 wirelessly, and displays the operating parameters of the controller on the HMI human-machine interface touch screen through the program. The corresponding text box in the interface (Li, 2011).

4.2. System software design

In this paper, the design of the solar street lighting monitoring and management system is designed in the transmission mode, receiving mode, street lamp dual control mode switching, alarm prompt and selective ad hoc network multi-hop scheme. Here, only the software design of the ad hoc network multi-hop scheme is described in detail. The software implementation flow chart of the selective ad hoc network multi-hop scheme designed on the basis of the existing wireless ad hoc network system is shown in Figure 4.

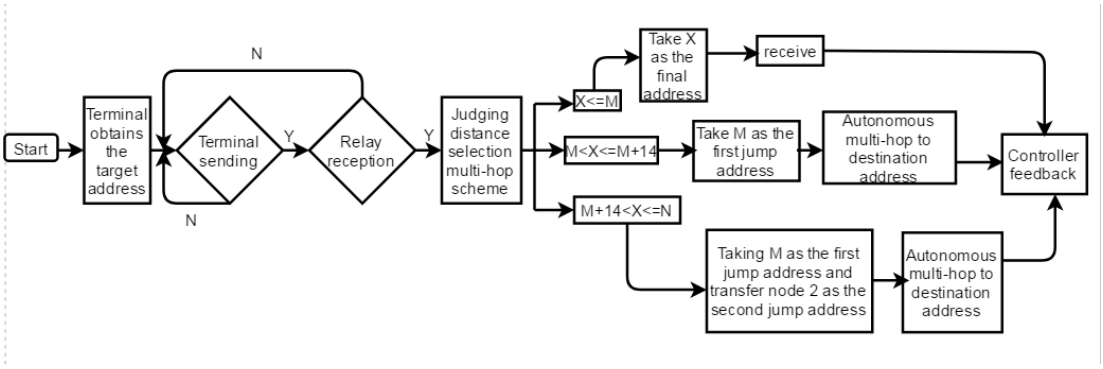

Figure 4: Software design flow chart of selective ad hoc network multi-hop scheme

Based on the street lamp controller node M at the maximum transmission range of a transit node, after the mobile control terminal selects the address of the target street lamp controller, the transit node determines the positional relationship between the target address and M, and selects the above according to different positional relationships. Three multi-hop schemes. The effect of using these three schemes is to expand the range of communication, and to control the number of transmissions of one data packet within 15 times, and to coordinate the nodes with long transmission distance and nodes with short transmission distance to achieve an optimised transmission scheme.

5. SYSTEM EXPERIMENTAL TEST

In this paper, the transmission power and receiving sensitivity of the CC2530 are added to the RF amplifying circuit. The estimated wireless transmission distance of the transit node is about 1200 metres. The actual distance of the wireless transmission of the transit node obtained through experimental test is 1020 metres. Therefore, in this experiment, the distance between the mobile terminal node and the transit node is tested to be 500~950 metres, and the packet loss rate is obtained without occlusion. The number of experiments in each case is 2,000, and the results of the packet loss test between the mobile terminal node and the transit node are shown in Table 1.

Table 1: Experimental test of packet loss rate between mobile terminal nodes and transit nodes

Test program	Packet loss rate	Test program	Packet loss rate
500 metres unobstrutedc	0%	800 metres unobstrutedc	0.25%
500 metres blocked	0%	800 metres blocked	0.25%
600 metres unobstrutedc	0%	900 metres unobstrutedc	0.30%
600 metres blocked	0%	900 metres blocked	0.30%

Long-distance packet loss rate test: When the distance between the terminal node and the transit node reaches 800 metres and above, packet loss will start to occur, but the packet loss rate is very low, which has little impact on the operation of the entire system.

In this paper, the test results of three experimental cases on the experimental platform are used to verify the feasibility of the scheme. The three schemes are to select the one of the streetlight controller nodes farthest from the transit node as the target node. The experimental scheme is 1:1 relay. Node, 2 streetlight controller nodes, controller nodes are within the transmission range of the transit node, respectively, the distance from the transit node is 730 metres and 760 metres; experimental scheme 2: 1 transit node, 2 street light controller nodes One controller node is on the maximum transmission range of the transit node, and the other controller node is outside the transmission range of the transit node, and the distance from the transit node is 950 metres and 980 metres respectively; experimental scheme 3: 2 relays node, 2 street light controller nodes, the left side of the figure is the transit node 1, the right side is the transit node 2, one controller node is on the maximum transmission range of the transit node 1, and the other controller node is in the transit node 1 Outside the transmission range, but within the transmission range of the transit node 2, the distance between the two street lamp controllers is 800 metres, and the mobile terminal in the experimental project is experimental 1 send 01 02 03 04; send 05 06 07 08 to experiment 2; send 09 10 11 12 to experiment 3, and send feedback data 00 after successful reception. After receiving the data sent by the mobile terminal, the target controller node uniformly returns a feedback instruction, and the result is shown in Figure 5.

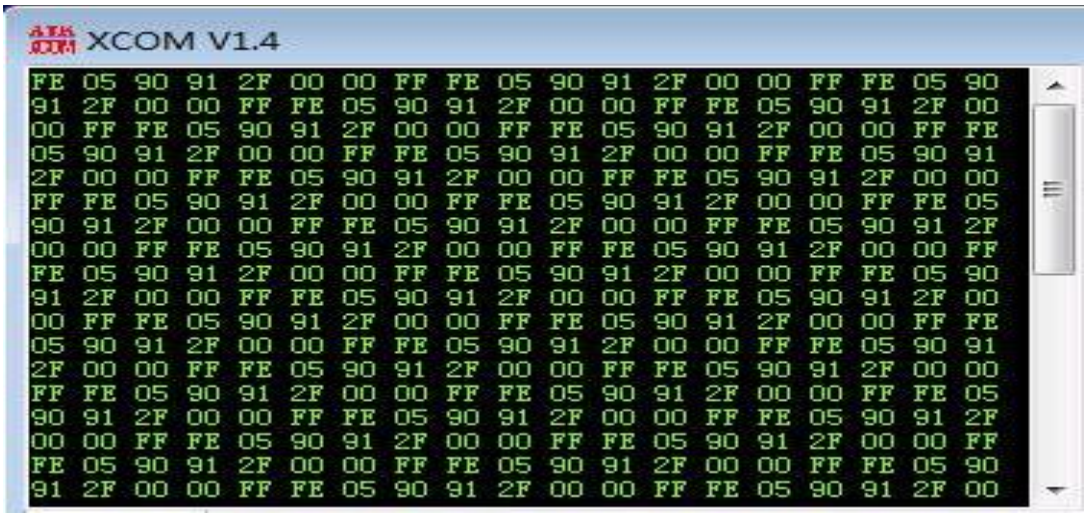

Figure 5: feedback results

Selective ad hoc network multi-hop scheme experiment: The controller node can completely receive the mobile terminal. The data verifies the feasibility of the selective ad hoc network multi-hop transmission scheme proposed in this paper.

6. CONCLUSION

Through the design of the whole solar street lighting monitoring management system, the monitoring management system designed in this paper can basically realise the following functions: receiving function, sending function, alarm function, storage function, display function and dual control mode switching function. The research done in this paper is based on the experimental platform. The designed monitoring and management system has not been fully transplanted into the solar street lighting system. The debugging experiment in the solar street lighting system has not been fully completed. In the later work, the entire monitoring management system is ported to the solar street lighting system.

7. REFERENCES

Feng, D. 2018. Research on Solar Street Light Monitoring and Management System Based on Mobile Terminal. Hubei University of Technology.

Gao, Y. 2017. Design of Urban Lighting Street Lamp Monitoring System. Electromechanical Information,27 (6): 14-19.

Goseling, J. Boucherie RJ, Jan-Kees OV, 2017. Queueing analysis of wireless network coding.Huisarts En Wetenschap.

Huang, Z. 2017. Design of solar LED intelligent control system . Hubei University of Technology.

Kang, P. 2016 Design of intelligent street lamp monitoring system based on ZigBee technology . Harbin University of Science and Technology.

Li, J., Hu, Y. 2011. Application Design of ZigBee Communication Network Based on CC2530. Electronic Design Engineering, 19(16): 108-111.

Mai, J., Deng, Q., Wan, Z. 2015. Design of ZigBee wireless network temperature monitoring system based on CC2530. Electronic Design Engineering, 23(22): 117-121.

Zang, LL., Li, S., Tian, DJ. 2012 Energy Saving Analysis of Solar-Powered LED Street Lighting Systems.Advanced Materials Research.2254-2258.

412: Research on LED intelligent lighting system

Guozhuang JIANG[1], Zhengwang XU[2], Kun KE[3], Jiarui ZHANG[4], Zhangjie HU[5]

[1] Hubei University of Technology, Wuhan, China,1047315944@qq.com
[2] Hubei University of Technology, Wuhan, China,69628025@qq.com
[3] Hubei University of Technology, Wuhan, China,1029360275@qq.com
[4] Hubei University of Technology, Wuhan, China,695922893@qq.com
[5] Hubei University of Technology, Wuhan, China, 452662133@qq.com

With the rapid development of society, the traditional lighting system has not been able to meet the green concept advocated by people for energy conservation and environmental protection. In recent years, the application of semiconductors has become more and more extensive, gradually replacing the traditional lighting system. LED intelligent lighting systems are one of the most common semiconductor applications today.

In this paper, the fuzzy expert library is used to process multi-sensor data, and the illumination state of the LED can be intelligently processed according to different environments to meet the requirements of adjustment at any time. The fuzzy expert library decision module uses the single-chip STM32F103C8T6 as the main controller, and uses multi-sensor data fusion technology to control the current output of the HV9910B chip by outputting appropriate PWM waves through various control strategies, so as to realise dimming of the LED. Moreover, the intelligent lighting system can make full use of the sunlight, and fully intelligentises the power consumption of the lighting system to a minimum, thereby playing the role of energy saving and environmental protection.

Keywords: LED intelligent lighting system; fuzzy expert library; energy saving and environmental protection

1. INTRODUCTION

Modern annual lighting consumes a large proportion of energy, and lighting power consumption is increasing every year, which creates a gap in energy and needs to save energy consumption to solve this problem. However, at present, many lighting equipment control systems need to be manually operated, so that unavoidable management is unavoidable, and the lighting system is not shut down in time, resulting in great energy loss, thereby designing an intelligent lighting system, according to the indoor situation. Automatically switch lighting tools to adjust the brightness to save energy, which not only saves energy, but also saves a lot of manpower and material resources (Li, 2014: page 519).Secondly, most of the current LED lighting systems are limited to illuminate indoors. They do not make good use of the adjustable brightness of LED lights, and do not meet the requirements of brightness and comfort of the lighting system. In this paper, LED lights and fuzzy intelligent control systems are combined to intelligentise the lighting system. One of the most important aspects is the fuzzy expert library to process the collected information. Through multi-sensor fusion technology, real-time monitoring of environmental changes to achieve intelligent control effects.

In this paper, the LED intelligent lighting system combines comfort and energy saving to meet the diverse needs of modern people in their living and working environments.

2. SYSTEM DESIGN REQUIREMENTS

The significance and advantages of the design of LED intelligent lighting system are:

(1) Long-term energy saving, reducing the duration of use of lamps. First of all, the LED intelligent lighting system can automatically adjust the lighting equipment according to the brightness of the environment and whether it needs to be turned on. Under the premise of ensuring illumination, the natural light is fully utilised to reduce the working time of electricity and lamps, especially those with long lighting time and many lighting equipment. Public places. Secondly, the system has designed various protection schemes, which can prevent LED light decay in advance and effectively extend the service life of LEDs. This reduces power consumption, and open source and throttling eases huge energy demands.

(2) Improve the living and working environment and better meet the diverse needs of people. The important point of the LED intelligent lighting system proposed in this paper is to combine lighting comfort and energy saving to meet the diverse needs of modern people for the living and working environment. The brightness required in the library reading room is large and the light in the corridor does not need to be too strong; when you need to turn on the bedroom lights when you wake up at night, the sudden glare will make people feel uncomfortable. These scenarios require LED intelligent lighting system to achieve.

(3) In different indoor environments, the demand for ambient brightness is different. The intelligent lighting system of LED can adapt to various indoor environments according to the settings. One of the advantages of LED lighting is that it does not produce glare and stroboscopic. In the lighting environment, it can help to protect vision, and can use PWM to dim.

(4) The LED lamp is packaged with epoxy resin filling technology. The principle of illumination does not require filament heating like traditional light sources, such as incandescent lamps. Fluorescent lamps also need to be protected by a glass casing, and the mechanical strength is poor, the casing is fragile, and it may hurt people. Therefore, the LED lighting system is also convenient and reliable when used (Wu, 2014: page 130).

3. SYSTEM DESIGN

In this paper, the lighting comfort is integrated into the expert database data. The design system mainly has the following parts: the measuring module includes the illuminance sensor to monitor the intensity of the indoor light, the infrared sensor detects the characteristics of the human body, and the automatic closing of the lighting system can be realised by detecting the human body characteristics. The temperature sensor detects the LED temperature; the fuzzy expert library module integrates the lighting comfort into the multi-sensor data of the measurement module according to different indoor environments, controls the PWM wave, determines the brightness of the LED lamp, meets the different needs of people for the environment, and the LED lighting module provides stable Current, LED colour temperature is normal, no flickering occurs.The overall structure of the designed system is shown in Figure 1.

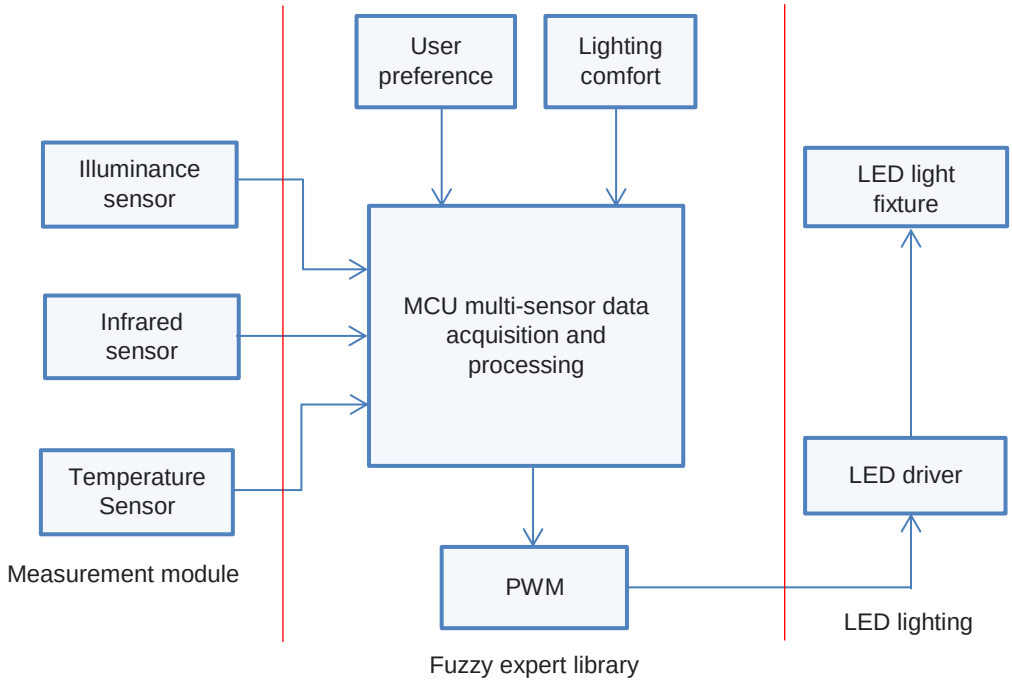

Figure 1: The overall structure of the designed system

In the system hardware structure, the single-chip microcomputer system is the control core, and the infrared detecting part of the human body can detect whether there is someone on the working area. The ambient brightness detection part is mainly used to detect the ambient brightness, and converts the detected indoor light illuminance signal to the single chip system through A/D. The MCU controls the LED illumination driver module according to the detected infrared signal and illuminance signal. Combined with the control strategy based on illumination comfort in this paper, the output current is regulated by PWM mode, and the brightness of the LED lamp is adjusted by the constant current drive circuit. At the same time, the temperature detection module is designed in the circuit, the temperature detection module is installed on the LED lamp, and the detected temperature signal is transmitted to the controller. After receiving the temperature signal, the STM32 determines whether the temperature of the LED lamp is too high, and the lighting system. If there is a possibility of light decay, the controller will reduce the PWM to reduce the current, and the heat of the LED will gradually decrease as the current decreases.

4. DETECTION CIRCUIT DESIGN

4.1. Environmental brightness detection circuit design

The function of the ambient brightness detection circuit is to detect the brightness of the indoor environment. Under a given bias condition, as the light intensity increases, the photoresist increases, and the optical properties of the curve are mostly nonlinear (Liu, 2016: page 149). The characteristics of the photoresistor are convenient to use, but its shortcoming is that its response speed is slow, and it is not possible to directly output digital quantities. It is necessary to perform AD conversion data for the single chip microcomputer to use. The essence of a photodiode is a PN junction, so it has a good output linearity, its response characteristics and the range of the wavelength of the incident light are better than the photoresistor and phototransistor. The ambient brightness detection circuit of this paper mainly uses the characteristics of the photodiode S5052 to work. The working voltage of the photodiode S5052 is 3.3V~5V, and the wavelength range of the incident light is 320nm~1000nm, which is good for the light. The photocurrent is formed in the S5052 when the daytime illumination is strong, and this current varies with the illumination intensity. In order to meet the needs of the MCU read, the analog signal detected by the S5052 circuit needs to be converted into a digital signal by A/D. The ambient brightness detection circuit is shown in Figure 2.

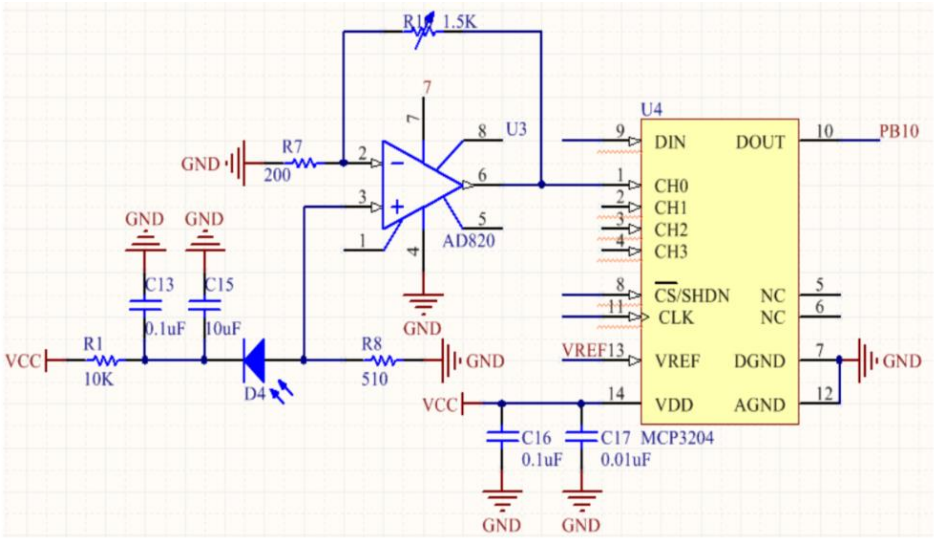

Figure 2: Ambient brightness detection circuit

In order to amplify the light intensity signal measured by the S5052, a low-power transistor input operational amplifier AD820 is selected in the detection circuit, and converted into a digital signal by the AD conversion to the MCU. When the system is working, the photodiode S5052 detects the current signal of the circuit. In order to facilitate the MCU processing, the current signal is converted into a voltage signal output through the resistor R8. The converted voltage signal has a small value and is amplified by the AD820 of the operational amplifier and output to the A/D converter through its 6-pin.

4.2. Temperature detection circuit design

The function of the temperature detection circuit is to detect the temperature of the LED lamp. The LED can only dissipate heat by conduction. Therefore, it is necessary to prevent the temperature of the LED lamp from continuously rising, causing harmful light decay to affect its service life. At present, commonly used temperature measuring devices include thermistors, thermocouples, etc., but in the process of measuring the temperature of these devices, it is necessary to design an AD conversion circuit (Zhang, 2015: page 19). In this paper, the digital temperature sensor DS18B20 is selected as the main component of the temperature detecting circuit. The DS18B20 is a single-bus digital temperature sensor with a temperature measurement range of -55 to +125°C and an accuracy of ±0.5°C. Temperature detection circuit design shown in Figure 3.

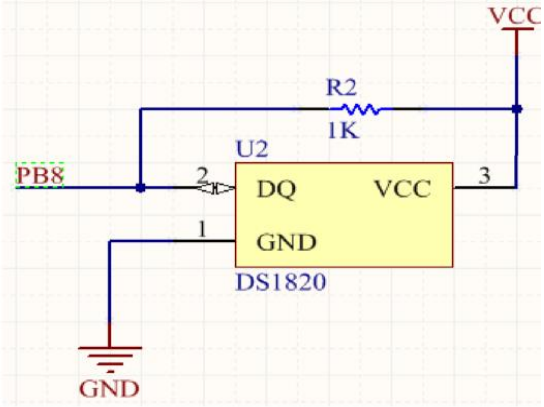

Figure 3: Temperature detection circuit design

The DS18B20 is designed with three pins. One pin GND is directly grounded. The 2-pin DQ is a single bus data transfer bus port. It is not necessary to design other peripheral circuits when measuring temperature. Only a single bus port is used to connect to the I/O port of the MCU. This greatly simplifies the hardware structure of the temperature detection circuit, and the 3-pin VCC is powered by a +5V power supply. In the temperature measurement circuit, the PB8 port of the STM32F103 is connected to the pin DQ. The MCU controls the DS18B20 to work. The single bus accepts the measured temperature data, and R2 is a single-line pull-up resistor.

5. FUZZY EXPERT LIBRARY MODULE DESIGN

This article uses several different types of sensors. The controller needs to analyse and process a variety of external factors, so it is necessary to design a fuzzy expert library control strategy to process multiple detection information. The control module designed in this system does not need to know the exact model, so it has a relatively simple design, and has the advantages of accurate data processing results and high stability.

5.1. Data fusion based on expert knowledge

In this paper, there are multiple sensor detection information, which combines temperature, illuminance and infrared detection factors, analyse and process in the controller, and finally output PWM signal. Therefore, analysis and processing of multiple detection information needs to be considered. Data fusion based on expert knowledge integrates and analyses data transmitted from multiple sensors (Algazar, 2012: page 21) and sends processing instructions to each module. This is the core of the humanised adjustment rules of the LED lighting system. The current expert system mainly includes two parts: the expert database and the inference engine. The knowledge base provides coordination rules, the speculative machine implementation decision, and the overall reliability can be provided through speculation and data fusion. . The model block diagram of data fusion based on expert knowledge is shown in Figure 4.

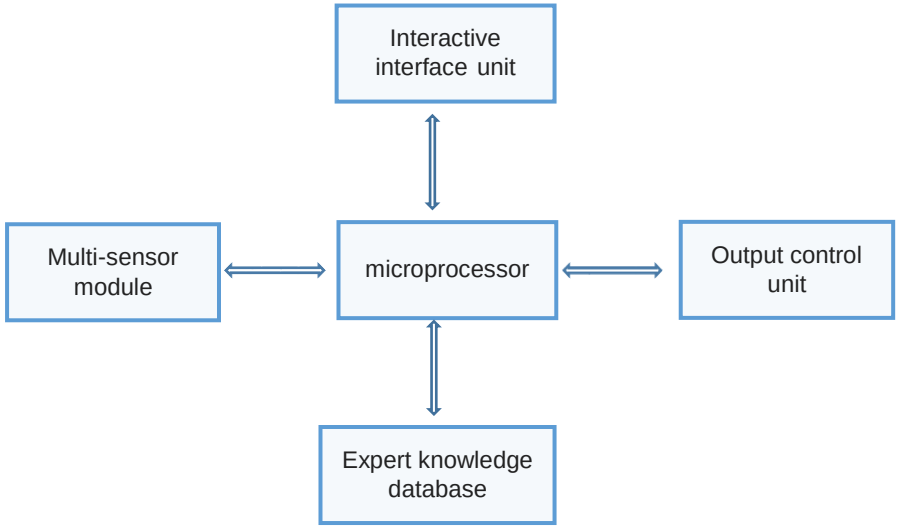

Figure 4: Model block diagram of data fusion of expert knowledge

5.2. Expert knowledge base design

The design method of the expert knowledge base used in this paper is the production rule of knowledge, which consists of the premise and conclusion pairs of “IF-THEN”. If the data set of the sensor is premised, the result generated by the expert database is a conclusion, which is used to express the one-to-one correspondence. The multi-sensor data fusion technology is used to conclude that each sensor data group corresponds to a rule, so the form of expression is as follows: IF<premise> THEN<conclusion>. Assuming that P is used to indicate the condition and the condition of the production formula is available, and Q is the result of data fusion, the expression can be rewritten as: IF P, THEN Q or P→Q. The data fusion table based on expert knowledge designed in this paper is shown in Table 1. The human infrared sensor is used in the LED intelligent lighting system with Ai (i=1,2), where i=1 means that the human body infrared signal is detected, i= 2 means no detection. The brightness sensor is represented by Bi (i=1, 2, 3, 4), where the value of i represents the range of ambient brightness, and the temperature detected by the LED is judged to be too high according to the temperature sensor detection signal Ci (i=1, 2). Di represents brightness comfort feedback, and finally Ei (i = 1, 2, ..., 15, 16) represents the result of data fusion of multiple sensors.

Table 1: Expert library design rules

rules	Human body infrared signal	Light intensity signal	LED temperature signal	Comfort signal	result
1	A1	B1	C1	Di	E1
2	A1	B1	C2	Di	E2
3	A1	B2	C1	Di	E3
4	A1	B2	C2	Di	E4
5	A1	B3	C1	Di	E5
6	A1	B3	C2	Di	E6
7	A1	B4	C1	Di	E7
8	A1	B4	C2	Di	E8
9	A2	B1	C1	Di	E9
10	A2	B1	C2	Di	E10
11	A2	B2	C1	Di	E11
12	A2	B2	C2	Di	E12
13	A2	B3	C1	Di	E13
14	A2	B3	C2	Di	E14
15	A2	B4	C1	Di	E15
16	A2	B4	C2	Di	E16
17	Q	W	R	D	E

6. SYSTEM EXPERIMENT TEST

6.1. Light intensity test

Firstly, the indoor light intensity is detected. In order to ensure the reliability of the system, firstly, an illuminometer is used to perform multiple sets of experiments under the conditions of light intensity at different times in the same scene. The results of the desktop illumination are shown in Table 2.

Table 2: Desktop illuminance results

lab environment	Illumination size(1x)
night	0
Cloudy day indoors (unturned light)	83
Cloudy day indoors(lights on)	170
Cloudy outdoor	150
Sunny day indoors (unturned light)	208
Sunny day indoors (lights on)	297
Sunny day outdoor	380

6.2. PWM dimming test

LED lighting systems must meet different lighting requirements according to different lighting requirements, that is, to achieve different illumination levels. Taking the studio as an example, the results of the studio dimming experiment are shown in Table 3.

Table 3: Studio dimming experiment results

Light intensity before dimming(1x)	Adjusting duty cycle	Light intensity after dimming(1x)
0	100	349
10	84	338
60	75	345
138	53	336
196	25	348
250	15	337
315	0	315

According to the measured illuminance before and after dimming, the voltage and current of the LED driving circuit, etc., the error between the LED intelligent lighting system and the design target is very small, and the expected design goal is achieved. Through the actual operation, the system the work is stable and the studio can adapt to various environments and meet the design requirements. The system designed in this paper can give the most comfortable illumination in the adaptive environment. It is proposed in the most energy-saving situation of the system. Therefore, after the actual operation, the percentage of energy saving in the actual operation of the system is measured (Hu, 2018: page 45), and the energy consumption curve is drawn. Figure 5 shows Illustration and photographs.

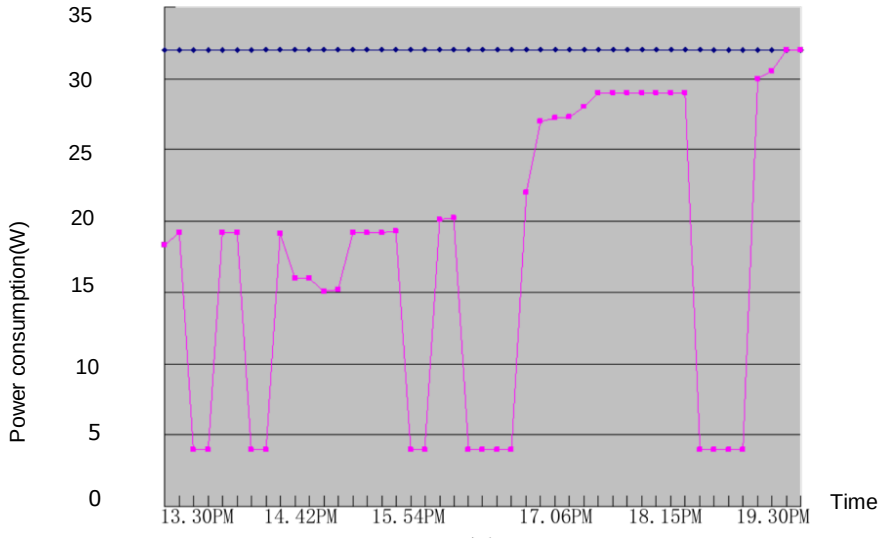

Figure 5: Energy consumption graph

7. CONCLUSION

This paper introduces several components of LED intelligent lighting system, mainly introduces the fuzzy expert library, proposes that the system can control the constant lighting source dimming by PWM, and can automatically adapt to the lighting needs of various environments, through the knowledge of expert database. Combined with PWM technology, the LED lighting system is intelligent, and the lighting energy saving requirements are greatly realised under the illumination of suitable lighting locations. The function of the intelligent lighting system in this paper is not perfect enough. In the subsequent research process, the functions of colour grading, time-sharing segmentation control, multi-channel LED control, etc. can be added, which is more widely used in practical applications.

8. REFERENCES

Algazar M M, AL-monier H, EL-halim H A, and EL Kotb Salem M E, 2012. Maximum power point tracking using fuzzy logic control. Int. J. Electr. Power Energy Syst, 9(1) :21–28.

Hu Z, 2018. Research and Design of LED Intelligent Lighting System. Hubei University of Technology.30-50.

Li X, Wang H, Li G, 2014.Design and Research of LED Intelligent Lighting System. Applied Mechanics and Materials. 519-522.

Liu D, Xie Q, Fang D, 2016. Research on characteristics of photoresistor. Electronic Technology and Software Engineering. (20): 149-150.

Wu T, 2014. Application and development of LED intelligent lighting system. Electronic Technology and Software Engineering. (02): 130-131.

Zhang Y, 2015. Research on Temperature Detection Technology of Electronic Products. Metrology and Testing Technology, 42 (1): 19-20.

413: Intelligent meter reading system based on LoRa

Cheng CHEN[1], Zhengwang XU[2], Jiarui ZHANG[3], Yuchun YI[4], Wei MEI[5], Jiaqi YU[6]

[1] *Hubei University of Technology, Wuhan, China, 1510795214@qq.com*
[2] *Hubei University of Technology, Wuhan, China, 69628025@qq.com*
[3] *Hubei University of Technology, Wuhan, China, 695922893@qq.com*
[4] *Hubei University of Technology, Wuhan, China, 1042048803@qq.com*
[5] *Hubei University of Technology, Wuhan, China, 790534374@qq.com*
[6] *Hubei University of Technology, Wuhan, China, 757345365@qq.com*

In the age of the Internet of things, more and more objects are connected to the Internet, gradually realizing the grand blueprint of "everything connected". Low power consumption wan LPWAN technology, as an effective complement to cellular M2M connections. It has accelerated the development of the Internet of things in terms of low power consumption, low cost, wide coverage and large capacity. Traditional way of manual meter reading was time-consuming, laborious, accuracy and timeliness of protected, aimed at the present stage ZigBee communication distance is short in the wireless network and complex network routing, the problem of weak anti-interference ability , this paper proposes a design of wireless smart meter reading system based on LoRa, LoRa modulation technology of the system with SX1301 as the core, Star - shaped and chain network is adopted to design self - organizing network, build an intelligent meter reading system with long communication distance and resistance to many kinds of interference sources ; Introduce that design process of the system network topology, the LoRa node's software and hardware and the custom communication protocol, realise the energy consumption data acquisition and the remote management of the smart meter, and finally the system carries out the test and analysis; The experimental results show that the system has the features of long communication distance, low power consumption, convenient networking and good real time, and has wide application prospects.

Keywords: Smart meters; Self networking technology; SX1278; LoRa; data acquisition

1. INTRODUCTION

Internet of things technology has developed rapidly in recent years, and the corresponding Internet of things industry is also growing rapidly. However, there are also many problems behind the rapid development. The existing communication technology was designed for the communication between people at the beginning, which cannot meet the needs of Internet of things communication. Therefore, LoRa, a wireless communication technology based on spread spectrum technology, came into being. The features of low power consumption and wide coverage are very suitable for large-scale deployment of the Internet of things. LoRa, as a long distance communication technology of LPWAN, solves the problem that the transmission distance of traditional wireless sensor network cannot be obtained simultaneously with low power consumption. It is a new kind of wireless communication technology, use the advanced technology of spread spectrum modulation and decoding scheme, and increase the link budget and better anti-jamming performance, with deep fading and Doppler frequency shift has better stability. The SX1278 radio frequency module adopts LoRa remote modem, which is suitable for the Internet of things network environment requiring long distance communication, anti-interference capability and low power consumption.

Due to the high communication frequency of ZigBee technology and the fast attenuation in signal transmission (Wang and Tian, 2015: pages 14-18), the use of WIFI and bluetooth signals (Zhou, Zhu and Yu, 2013: pages 31-33) in the same frequency band leads to the short transmission distance of ZigBee (Xu, Zhou and Guo, 2013: pages 51-53), easy interference and complex network structure. LoRa communication technology is applied to remote wireless meter reading in the article, implement a series of intelligent management, such as the remote copy meter, remote management and troubleshooting, solve the trouble that the artificial meter reading will cost a lot of manpower material resources and financial resources, extremely convenient when the wrong leakage happens (Min, Cheng, Huang, etc., 2014: pages 639-642), convenient for residential electricity automation management. Long-distance communication greatly of LoRa reduces the use of relay and saves cost. This system can be applied to residential areas, schools, industrial production and other scenes, realizing remote centralised management and control of electricity meters.

2. THE SYSTEM OVERALL DESIGN

System overall network topology structure as shown in Figure 1, mainly includes the rf transmission module base on LoRa, LoRa gateway, network nodes and electric meter management platform, network node including relay nodes and terminal nodes. In the system, terminal acquisition node distribute by electric meter in the building, electricity meter information collected and status information. The specific topology is that the acquisition node is connected down to the intelligent electricity meter through RS485 according to the Modbus communication protocol (Wang and Wang, 2015: pages 4202-4206), upward with LoRa gateway communication, which will be collected by the meter data back to the electric meter management platform. If the terminal acquisition node cannot communicate normally due to serious obstruction, the relay node can be added to complete the work of collecting node data and forward it to the platform.

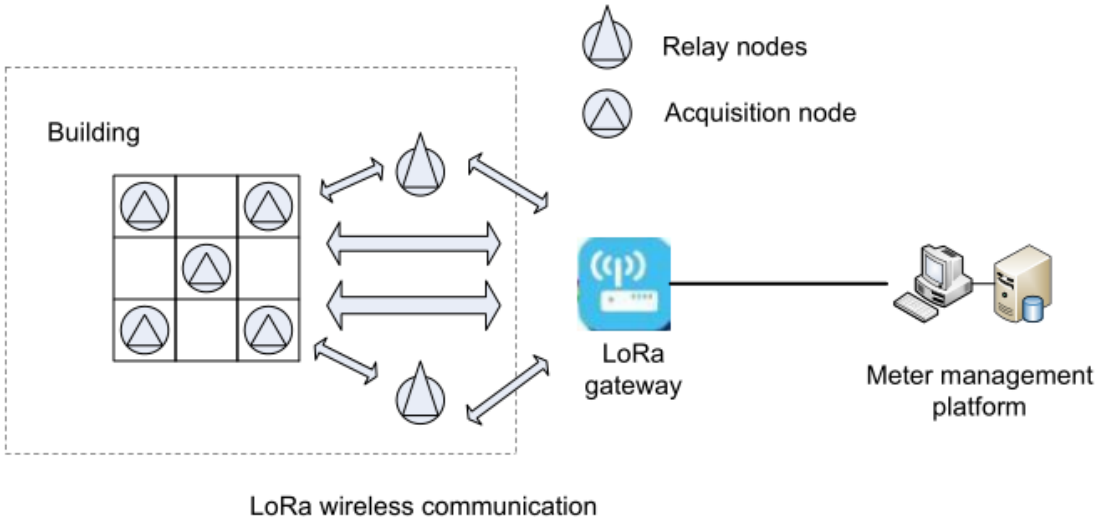

Figure 1: System architecture

3. SYSTEM HARDWARE DESIGN

The MCU main control chip STM32L151CBU6 of this system is a microprocessor based on the arm32-bit cortex-m3 architecture (Wang, Xu and Hao, 2008: page 4), with a maximum operating frequency of 32MHz, a built-in 128K byte high-

capacity memory and 16K byte RAM, which can easily meet the space required by the power wireless set copying system. At the same time, STM32L151CBU6 sleep, stop and standby are three low-power working modes, which facilitate the system's low-power design, and have superior computing performance and interrupt response system. In hardware design, the SX1278 rf module is a highly integrated wireless data transmission module with low power consumption, half duplex and small power. It has the characteristics of long transmission distance, strong penetration of signals, stable data reception and transmission.

3.1. Design of acquisition node and relay node

Electronic meter, which is consistent with the national power grid, with the power meter, data storage, and the rs-485 interface to the outside world. The hardware structure of the design acquisition node and relay node is shown in figure 2. Relay node is mainly used to forward the instruction and data information between the management platform and the acquisition node and expand the wireless meter reading transmission range. The task of the acquisition node, on the one hand, is responsible for the collection and control of the electricity meter data; on the other hand, it responds to the instructions issued by the meter management platform end and uploads the collected data to the management platform system, realizing the functions of electricity data acquisition and remote charge control of the electricity meter. The rs-485 interface of the acquisition node is designed with ADM2483 chip.

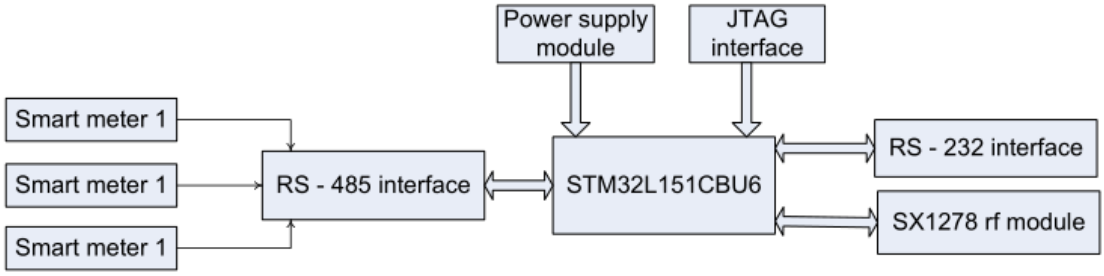

Figure 2: Acquisition/relay node structure diagram

3.2. LoRa gateway

The gateway core chip adopts Semtech company SX1301. LoRa/LoRaWAN gateway module with high performance, small volume and other features which can provide robust star base stations for a wide range of wireless nodes because of its reception sensitivity up to -142.5dbm, 49 LoRa "virtual" channels and ADR technologies. There is a public cloud platform on the LoRa gateway, and we can upload the data from the collection node and the relay node to this platform, logging on to the platform where Internet access is available, accessing the data we've collected in real time. We can also issue instructions through the platform window to realise remote control operations.

4. SYSTEM SOFTWARE DESIGN

4.1. Application layer communication protocol design

The advantages and disadvantages of protocol design directly determine the intelligence degree of the system (Hou, Zhao, Feng, etc. 2014: pages 108-114). The system has a custom protocol design for the application layer, and it is packed and parsed with the data, and it's a transparent transmission of data. The data transmission mode adopts data frame mode, and the transmission sequence is binary byte stream. At the same time, CRC16 verification algorithm is adopted in data transmission to ensure the accuracy of data transmission. In meter, electricity meter management centre issued by relay nodes, acquisition nodes which meet with watt-hour meter communication protocols DL/T645-2007 protocol instructions, waiting for a period of time after being meter response, will be returned to the data acquisition node, and data acquisition nodes will packaging uploaded to the electric meter management centre.

4.2. Node software design

The acquisition node not only needs to collect the data of the electricity meter, but also needs to upload and receive the data and commands through the LoRa network. After receiving the command issued by the management platform, the acquisition node first verifies the data with CRC16 to ensure the accuracy of the data. Then, according to the frame command in the message, the corresponding operation is performed, and the corresponding data information is uploaded to the meter management platform after execution.Software acquisition node work process is shown in Figure 3.

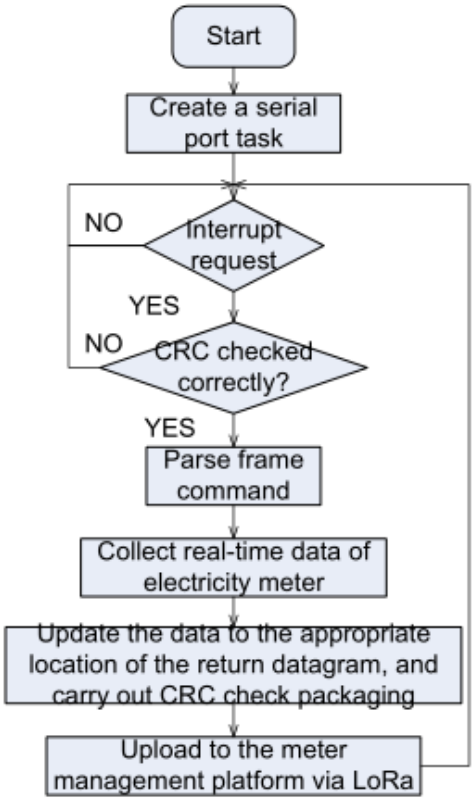

Figure 3: Acquisition node flow chart

5. SYSTEM TEST AND ANALYSIS

The system test environment is built to verify the actual operation effect of the intelligent meter reading system. The simulation network consists of three acquisition nodes, which send data message to the acquisition node in the electricity meter management platform and query the real-time power condition of the electricity meter. In the test, the rf centre frequency of the device node is 470MHz, the transmitting power is 20dbm, and the serial port baud rate is 15200bps, etc.

In order to test the effective transmission distance between LoRa gateway and the acquisition node, a large number of data transmission and transmission tests were conducted at different locations in the building (starting from the first floor of the stairs), with 100 packets sent at a time. The test results are shown in Table 1.

Table 1: Test results in buildings

Group number	Test scenarios	Receiving packet	Packet loss rate
1	2 Floor	100	0%
2	3 Floor	98	2%
3	4 Floor	90	10%
4	5 Floor	78	22%
5	6 Floor	45	55%

As shown in Table 1, data packet loss rate increases with the increase of communication distance. Good communication between the first and fourth floors within the building. In addition, the system power consumption was tested by using the simplest method of series ammeter. When using low power consumption design mode, the power consumption of system current is much lower than that of non-use low power consumption mode.

The test results show that the system has long communication distance, strong anti-interference ability, low power consumption and high system stability. It can improve work efficiency, management level and quality of service for that electric department remote intelligent management electric energy meter.

6. CONCLUSION

In this paper, the low-power wan technology is applied to remote wireless intelligent meter reading. The communication between the meter management platform and the meter can be realised through the low power consumption and remote LoRa wireless network, so as to achieve the management platform's remote power data acquisition and the operation status of each meter. The system architecture, application layer communication protocol and hardware and software design of nodes are analysed in detail. From the experimental results, the system runs in good condition, communication distance, low power consumption, convenient networking, and low cost, can well meet the demand of wireless intelligent meter reading system, has extensive application prospect.

7. REFERENCES

Hou C, Zhao Q, Feng H, etc. 2014. Research and Implementation of an Intelligent Data Acquisition System for the Internet of Things. Electronic Measurement and Technology, 37 (6), 108-114.

Min HS, Cheng Z, Huang L, etc. 2014.Design of Wireless Meter Reading System Based on RF . Computer Measurement and Control, 2, 639-642.

Wang Y, Xu W, Hao L. 2008. Principle and Practice of Stm32 Series Arm Cortex-m3 Microcontroller .1. Place: Beijing University of Aeronautics and Astronautics Press.4

Wang P, Wang W. 2015. Design of Energy Consumption Data Collector Based on 3G. Computer Measurement and Control, 12, 4202-4206.

Wang X, Tian H. 2015. International Telecommunication Operators Have Stepped Up Their Distribution in the Field of Industrial Internet. World Telecom, 5, 14-18.

Xu S, Zhou X, Guo Q. 2013. ZigBee Gateway Design Based on ARM Platform. Microcomputers and Applications, 16, 51-53.

Zhou X, Zhu X, Yu X. 2013. Design of ZigBee Remote Wireless Meter Reading System. Automatic Instrument, 3, 31-33.

414: Summary of different forms of air-to-air heat exchanger and a new type of exhaust heat recovery system

Ren JIA, Waqar AHMAD, Chen JIUFA[1*]

[1*]*Corresponding Author: School of Energy and Environment, Southeast University, Nanjing, China, 210096.*
Email: chen.jiufa@seu.edu.cn

With the increasing waste of energy and the reduction of energy become serious. It is necessary to take effective measures to save energy. Exhaust heat recovery technology is an effective way to reduce energy consumption in air conditioning. It introduced the different forms of exhaust heat recovery, such as rotary wheel heat and mass exchanger, plate type heat exchanger, run around heat exchanger and heat pipe heat exchanger in this paper, which finally proposed a new system of exhaust air heat recovery called window type heat recovery system.

Keywords: Thermoelectric module, vapor chamber, spreading resistance, effective thermal conductivity, COP.

1. INTRODUCTION

In the present, the pollution problem is ever important and the consumption of energy is even bad than before. Therefore, saving energy and protecting the environment is an eternal issue of our society, no matter at home and aboard. And building energy accounts for a large proportion of energy consumption. In china, the consumption of building energy accounts for more than 27% of all energy consuming, and the ratio is increasing at a rate of 1 percentage every year. In building energy consumption, heating and refrigeration are the most energy consuming, accounting for more than 60% of the all proportion (Tang, 2010). In the present, buildings are responsible for approximately 40% of energy consumption and 36% of CO2 emission in the European Union (EU) (Burlacu, 2018). Air conditioning system is one of the main energy consumption of buildings. At present, the energy consumption of air conditioning has reached more than 60% of the building energy consumption. The total amount of energy consumed by the air conditioning system has exceeded 20% of the total energy of China (Yang, 2016). Therefore, reducing the energy consumption of air conditioning system is of great significance.

In order to ensure good indoor air quality, a certain amount of outdoor fresh air must be introduced into the air conditioning system (Zhang, 2012). It is necessary to dissipate energy to deal with these fresh air. At the same time, the indoor air exhausting needs to be discharged to the outside environment. It always contains cold or heat. Therefore, if the energy is recovered well, it will greatly reduce the energy consumption needed to deal with the fresh air, so as to achieve the purpose of energy saving. The use of heat pipes for waste heat recovery is an excellent way to save energy and prevent global warming. Therefore, exhaust heat recovery technology is an effective way to reduce energy consumption in air conditioning.

2. ANALYSIS OF ENERGY SAVING

Such as what the Figure 1 shows is a typical air conditioning system with exhaust heat recovery equipment.

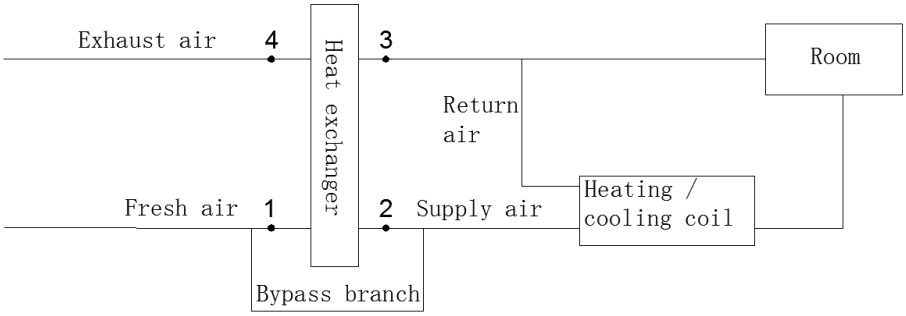

Figure 1: Air conditioning system with exhaust air heat recovery

The points 1, 2, 3 and 4 in the figure represent four states of the air: fresh air, supply air, return air and exhaust air. So that the efficiency of the heat recovery can be represented by the equations as following.

$$\varepsilon\_T=(m\_s\ (T\_1-T\_2))/(m\_min\ (T\_1-T\_3)) \quad (2\text{-}1)$$

$$\varepsilon\_h=(m\_s\ (h\_1-h\_2))/(m\_min\ (h\_1-h\_3)) \quad (2\text{-}2)$$

The equation (2-1) and (2-2) shows the sensible heat recovery efficiency and the total heat recovery efficiency respectively. The ms is the airflow rate of air supply; the T1, T2, T3 and T4 are the temperatures of the fresh air, supply air, the return air and the exhaust air; the mmin is the minimum airflow rate between supply air and exhaust air; also, the h1, h2, h3 and h4 are the enthalpies of the fresh air, supply air, the return air and the exhaust air.

If the air flow rate of supply air and exhaust air are the same, the ms and the mmin are same too. So that the equations showed before can be simplified as the equations (2-3) and (2-4) shows.

$$\varepsilon\_T=(T\_1-T\_2)/(T\_1-T\_3\ ) \quad (2\text{-}3)$$

$$\varepsilon\_h=(h\_1-h\_2)/(h\_1-h\_3\ ) \quad (2\text{-}4)$$

In China, most of the areas are hot in summer and cold in winter. The Figure 2 shows the curve of varieties of temperature and enthalpy in one year.

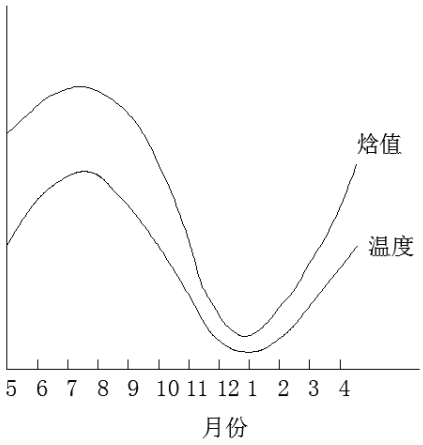

Figure 2: the varieties of temperature and enthalpy in one year

For the convenience of analysis, the indoor air supply conditions in summer and winter are set the same. According the Figure 2, we can get two curves below, as Figure 3 shows.

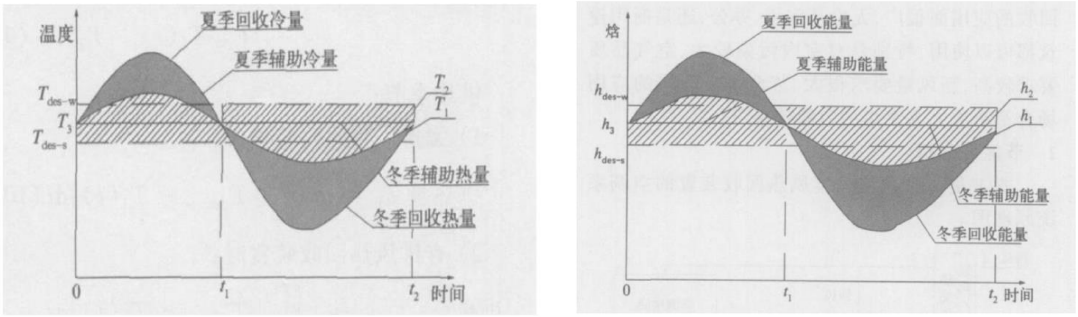

(a) Sensible heat recovery *(b) Total heat recovery*

Figure 3: Energy saving diagram of heat recovery

Suppose: (1) All year operation of air conditioning, the operation time of summer is t1 and the operation time of winter is t1~t2. (2) The mass flow of fresh air and supply air are the same, represented by m. (3) T3 is a constant value, but T1, T2 and T4 all vary with time. As Figure 3 shows, before adding the exhaust heat recovery device, the cold (heat) load of the air conditioning system should be the sum of the shaded and slash parts; after joining, the air conditioning system only needs to provide cold (heat) amount of the slash part, and the shaded part is the energy recovered. Hence, heat recovery from exhaust is a good way to reduce energy consumption.

3. FORMS OF EXHAUST HEAT RECOVERY

There are many advantages of exhaust air heat recovery: (1) the fresh air is pretreated to reduce the operation load of the air conditioner and save the running cost. (2) Reduce the maximum load and the size of the air conditioning system, and save the initial investment. (3) While saving energy, we can also increase indoor fresh air ratio and improve indoor air quality. (4) In summer, the exhaust temperature decreases, which reduces the heat discharged outwards, reduces the heat pollution and alleviate the heat island effect.

Therefore, in the present we already have many types of air-to-air heat recovery device, which can be classified according to heat transfer, number of fluids, geometry, construction type and etc. (Zeng, 2016).The following discussion is based on the classification of construction type. Several studies have been reported on rotary wheel, heat pipe, plate type, and run around heat exchanger and are presented below as follows.

3.1. Rotary wheel heat and mass exchanger

Rotary wheel heat and mass exchanger is a rotating porous wheel driven by a motor and works as a thermal storage mass. Two air streams alternatively pass through the wheel when heat and moisture exchange takes place (Figure 4) (Mardiana-Idayu, 2012).

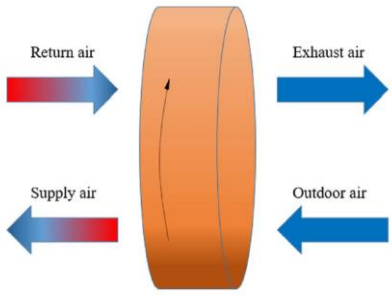

Figure 4: working principle of rotary wheel heat and mass exchanger

As the figure shows, the fresh air and exhaust air are respectively pass through two halves of the revolving wheel core from the opposite direction, and the core is made of asbestos, paper, aluminum, or other materials. It looks like honeycomb (where the peak of the corrugated plate is about 1.6 ~ 2.6mm) and it obtains the energy from the exhaust air, and when it turns on the other side, the energy is taken away by the fresh air. The lithium bromide hygroscopic agent is soaked on the base material such as asbestos and paper to make the asbestos, paper and other materials not only exchange heat with the air, but also have wet exchange, which greatly improves the efficiency of heat recovery.

The rotary heat exchanger has small resistance, high efficiency of heat recovery, and self- purification which can prevent the occurrence of clogging. But it also has limitations. The limitations of rotary wheel heat and mass exchanger are the potential of air short circuiting and cross contamination (Roulet, 2001). Air short circuiting can dwarf system efficiency due to air recirculating in an unintended direction. Cross contamination causes the technology unsuitable for hospitals and other buildings where isolated air streams are required.

3.2. Plate type heat exchanger

Plate type heat exchanger is built with thin plates stacking together to form flow channels, shown as Figure 5 (Mardiana-Idayu, 2012). Two different air streams pass through each other when heat transfer occurs. Airflow arrangements can be counter flow, cross flow and parallel flow (Library, 2012).

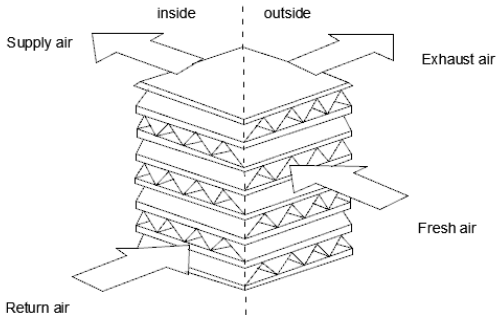

Figure 5: Fixed plate heat recovery exchanger

Typical effectiveness of sensible heat transfer ranges from 50% to80% (Mardiana-Idayu, 2012; Sammeta, 2011). The performance of plate type heat exchangers can be influenced by: 1) plate types and configurations (different height, pitch and orientation of corrugation and chevron angles); 2) flow pattern; 3) heat and mass exchange material. It has no cross contamination between fresh air and exhaust air and the device without driving unit. But the possible of producing dew, frost and the blockage of the wind pipe limit its development.

3.3. Run around heat exchanger

Run around heat exchanger is consisted of two separate heat exchangers and a coupling liquid, depicted diagrammatically in Figure 6 (Mardiana-Idayu, 2012). The pumped liquid gains heat from one air stream and releases the heat to the other one.

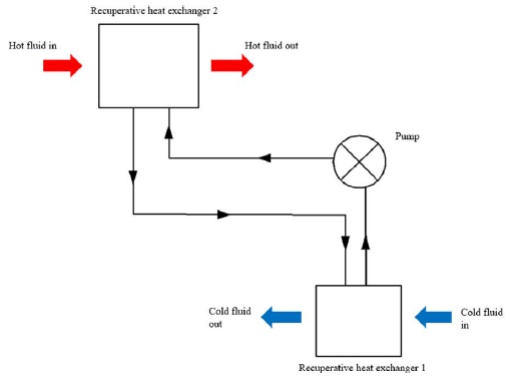

Figure 6: Principle of run round heat exchanger

When working on the exhaust side, the heat (winter) or the cold (summer) is transferred to the working fluid, and the working fluid conveyed the working medium to the coil of the fresh air side to heat the fresh air (winter) or to cool the fresh air (summer). It advantages are with no cross contamination between fresh air and exhaust air and flexible piping. But it also have problems on low efficiency of heat recovery and only sensible heat recovery.

3.4. Heat pipe heat exchanger

Heat pipe which has the advantages of the superior heat superconducting ability, steady property, small-sized and controllable structure has been widely used in central AC system (Wang, 2016). There are two kinds of HPHE AC system, the common one and the secondary one which structure as shown in Figures 7 and 8.

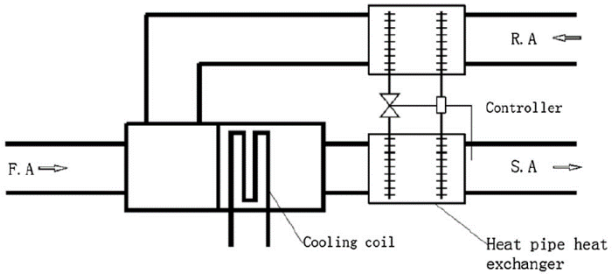

Figure 7: Common heat recovery HPHE AC system

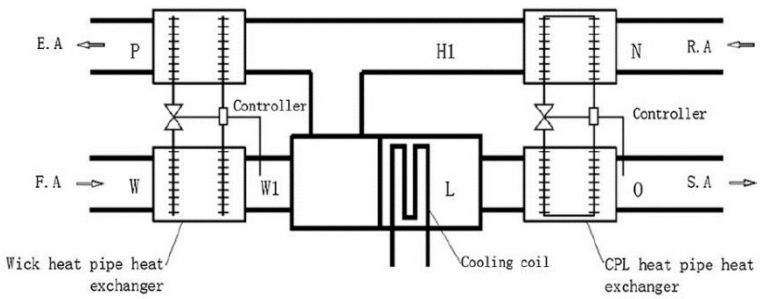

Figure 8: Secondary heat recovery HPHE AC system

In the common heat recovery HPHEAC system, return air and supply air can obtain the goal of energy saving with heat pipe. The fresh air mixed with return air in cooling coil can reduce the reheating capacity in air treatment and as well the energy consumption of fresh air in summer, and only can be used in summer.

In the secondary heat recovery HPHE AC system, the heat exchanger can both be used during winter and summer. In summer, the heat exchange between return air and supply air is of the same volume, so the heat that the heat pipes draw from return air should suffice the reheating capacity that supply air requires. The heat transfer between exhaust and fresh air is also of the same volume, it can maximally reduce the energy consumption in the process of handling fresh air. In winter the wick heat exchanger works solely, by adjusting the percentage of fresh air to control the energy saving issues.

4. WINDOW TYPE HEAT RECOVERY SYSTEM

The forms of air-to-air heat recovery system we talked before all need apply to the AC system. But there are a new type air-to-air heat recovery device which can work independently called window type heat recovery system. Its structure show in the Figure 9.

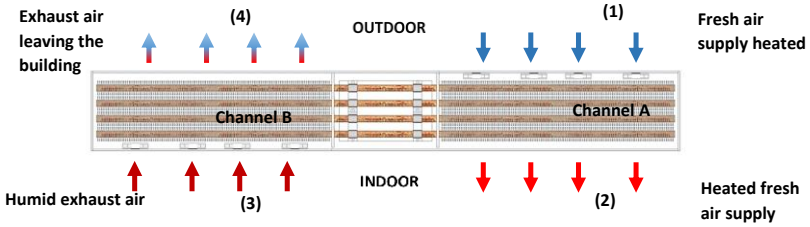

Figure 9: working principle of the window type heat recovery system

The system is comprised of 8 high efficiency heat pipes combined with 16 thermoelectric and small size fans which drive air flow. In summer, the cold was obtained from the exhaust air then was transferred by the heat pipes to the fresh air. The heat pipes occupied with the thermoelectric which can strengthen the heat exchange. Through changing the current of the thermoelectric the temperature of fresh air can be changed, until get a temperature we required. In winter the heat from the exhaust air was transferred. During the transitional season the mode to choose depend on the temperature of fresh air and exhaust air. If the temperature of fresh air is higher than the exhaust air, choose the summer mode, if lower choose the opposite. If only using ventilation can achieve the temperature wanted, then we can only start fans.

This system can working separately and with thermoelectric its efficiency of heat recovery will be improved. It will have a good effect of reducing energy of AC system.

5. CONCLUSION

Adding a heat recovery device of AC system can effectively save the energy of the air conditioning. There also a lot of heat exchangers was used in AC system, such as rotary wheel heat and mass exchanger, plate type heat exchanger, run around heat exchanger and heat pipe heat exchanger. But we still should pay attention to the development of find a more effective way of saving energy. In this paper, it proposed a new system which can work independently and can increase the efficiency.

6. REFERENCES

Burlacu A, Sosoi G, Vizitiu R Ș, et al. Energy efficient heat pipe heat exchanger for waste heat recovery in buildings [J]. 2018, 22:714-721.\

Library W E. American society of heating, refrigerating and air-conditioning engineers [J]. International Journal of Refrigeration, 2012, 2(3):56–57.

Mardiana-Idayu A, Riffat S B. Review on heat recovery technologies for building applications [J]. Renewable & Sustainable Energy Reviews, 2012, 16(2):1241-1255.

Roulet C A, Heidt F D, Foradini F, et al. Real heat recovery with air handling units [J]. Energy & Buildings, 2001, 33(5):495-502.

Sammeta H, Ponnusamy K, Majid M A, et al. Effectiveness charts for counter flow corrugated plate heat exchanger [J]. Simulation Modelling Practice & Theory, 2011, 19(2):777-784.

Tang W, 2010. Talking about the current situation of energy consumption in China, [J]. Urban and rural construction. 25.

Wang H, Zhou S, Wei Z, et al. A study of secondary heat recovery efficiency of a heat pipe heat exchanger air conditioning system [J]. Energy & Buildings, 2016, 133:206-216.

Yang F, Dong T. Analysis of Separate Heat Pipe Heat Recovery Air Conditioning System [J]. Times Report, 2016(20).

Zhang H, Lan X, Wang Y. Talking about the Application of Heat Recovery Technology in Air Conditioning System [C]// Architectural Technology and Management Academic Exchange Conference. 2012.

Zeng C, Liu S, Shukla A. A review on the air-to-air heat and mass exchanger technologies for building applications [J]. Renewable & Sustainable Energy Reviews, 2016, 75.

416: A study on condensation simulation for a building integrated with a capillary ceiling HVAC system

Jianchao MA, Waqar AHMAD, Jiufa CHEN[1*], Jia REN

[1]Corresponding Author: School of Energy and Environment, Southeast University, Nanjing, China, 210096.*
Email: chen.jiufa@seu.edu.cn

In this study, the condensation of capillary ceiling embedded with capillary radiant network (CRN) was simulated. Two types of condensation in capillary ceiling will be produced (i.e., surface and internal condensation of the enclosure). Temperature, humidity distribution and condensation of ceiling in both summer and winter were studied based on principle of coupled heat and moisture transfer. In this study, the effect of Expanded Polystyrene (EPS) insulation board thickness has been carefully analysed. In summer, the thickness of EPS must be greater than 10 mm to avoid wall surface condensation. If the thickness of EPS exceeds 20 mm, the surface relative humidity can be reduced to below 95%. In winter, in order to prevent the ceiling condensation at the internal interface between EPS and concrete, the thickness of EPS should better be less than 20 mm or more than 45 mm. Considering the fact that no condensation occurs within the 30 days in summer and winter, the thickness of the EPS should be greater than 45 mm. The results indicate that even if no condensation occurs on the surface of the capillary ceiling, the risk of internal condensation still exists, especially in winter. Increasing thickness of EPS insulation board can reduce the possibility of the radiant ceiling condensation.

Keywords: capillary radiant network, capillary ceiling, internal condensation.

1. INTRODUCTION

Currently, energy consumption in buildings mainly consists of domestic hot water, heating, cooling, ventilation, lighting and electrical appliances, over one-third of China's total energy is used in buildings in which energy consumption for heating and cooling is about 63% of the overall energy consumption of buildings in China (Cui, Wang & Zhu, 2015). Both energy conservation and indoor thermal comfort are main concerns for architects to select an appropriate HVAC system for their building development (Hesaraki & Holmberg, 2013). The radiant air-conditioning system (RACS) with CRN as terminal has become prevalent. The CRN composed of micro-plastic tubes (ø 3.0-5.0 mm) made of polypropylene. RACS is noiseless and use less building space without causing any draughts. It has very short distance (10 – 30 mm) between each capillary tube. When properly designed, the RACS can also add an aesthetic to buildings as it doesn't disrupt the designed space and therefore increase the architectural value (Mikeska & Svendsen, 2013).

The supply water temperature with RACS for heating/cooling is 28-32°C /18-22°C which can be used to meet the demand of indoor thermal comfort. Temperature difference between supply and return water is commonly in range of 2- 4°C. It can be used by low grade energy, combined with heat pump which could save energy in range of 40 - 70% (Wen, Yang, Chen, Li & Wei, 2014). When using RACS in buildings, the radiant heating system can maintain room air temperature lower than convective systems. This means that energy can be saved on heat losses and transmission losses for ventilation. Similarly, the radiant cooling can maintain room air temperature higher convective systems, resulting in low energy consumption.

However, building envelope is made of porous materials in which heat and moisture transfer can exist. When CRN is embedded in the ceiling, two types of condensation in ceiling will be produced (i.e., surface and internal condensation of the enclosure). There is no difference between internal condensation and surface condensation. When the temperature is lower than the dew point temperature, condensation occurs. Wet accumulation and condensation are usually easy to occur in the places with large thermal insulation board and temperature gradient. The moisture transfer and condensation of the enclosure structure cause many hazards. The performance of thermal insulation in building enclosure can be reduced by moisture which can increase energy consumption of the building (Maliki, Laredj, Hassan, Bendani and Missoum, 2014). It shows an important subject again in connection with necessary reduction carbon dioxide emissions in housing construction. There are also important hygienic reasons why excess moisture in building component must be avoided. If insulation material of building becomes wet (eg. due to condensation), fungi will grow and release spores into the ventilation (Pasanen P, Pasanen A L and Jantunen, 1993). And high indoor spore levels of fungi such as cladosporium and the dry rot fungus sepula have been associated with cases of hypersensitivity pneumonitis. Fungal spores and vegetative mycelium are also known to contain toxic substances (mycotoxins) that can lead to respiratory symptoms unrelated to allergic mechanisms (Flannigan et al., 1991).

In practice, most researchers didn't consider the condensation inside the radiant wall under the effect of heat and humidity coupling transfer. A radiant cooling system always works together with a fresh air system to meet the latent load and even part of sensible load. To prevent the condensation of moisture on a radiant surface, the surface temperature of a radiant panel needs to be higher than the indoor dew point temperature (Song et al.). Yin et al. (2014) have compared three radiant cooling model (pure CRN model, the CRN model with metal covering and the CRN model with gypsum covering) the performance of heat transfer and moisture condensation, found the upper limit of sub-cooling degree by gradually decreasing the chilled water temperature from 17 °C until the condensation of moisture occurred. It was concluded that the upper limit of sub-cooling degree for the pure tube, gypsum panel and metal panel were 3.2°C, 6.5°C and 5.4°C, respectively. However, it is inaccurate to determine the upper limit of sub-cooling degree by observing the surface condensation of the model. The internal condensation of the gypsum should be considered. At present, the research mainly focuses on the surface condensation of radiation, and very few studies on the overall condensation of the wall, especially on the wall embedded with CRN.

This paper has mainly studied condensation of the ceiling embedded with CRN, in the hot summer and cold winter areas of China. Temperature, humidity distribution and condensation of ceiling in both summer and winter were studied based on principle of coupled heat and moisture transfer. The influence of the thickness of the insulation board has also been analysed. This research study has provided a practical way in order to prevent formation of dew in ceiling.

2. PHYSICAL MODEL (CAPILLARY NETWORK EMBEDDED IN CEILING)

A radiant air conditioning room with ceiling is used as physical model whereas an adjacent room without air conditioning is present above that ceiling. The two dimensional model was built of ceiling, as shown in Figure 1, this ceiling consists of 20 mm cement mortar + EPS + 100 mm reinforced concrete + 20 mm cement mortar, and capillary network of PVC material is laid in the cement mortar of the radiation air conditioning room side. The thickness of the EPS is d mm. The section is at the middle of two micro tubes.

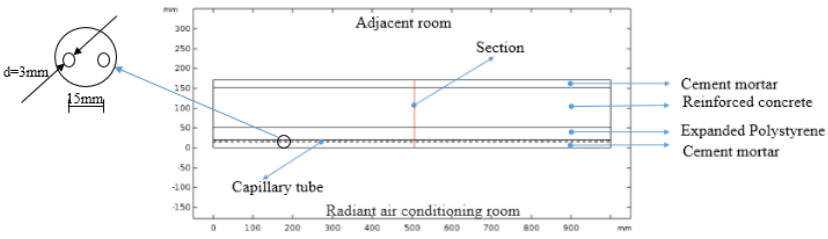

Figure 1: The ceiling structure embedded with radiant capillary network

3. MATHEMATICAL MODEL

3.1. Dynamic modeling of heat and moisture transport

In the present study, the phase change occurring within porous materials acts as a heat source or sink, which results in the coupled relationship between moisture transfer and heat transfer. The heat of absorption or desorption is generally one of the sources or sinks as well. Two-dimensional governing equations with coupled temperature and moisture for a multi-layer porous wall are considered with the effect of the absorption or desorption heat has been added. The moisture diffusivity is dependent on temperature and moisture. A local thermodynamic equilibrium between the fluid and the porous matrix is assumed as shown in given equations: (Künzel, 1995)

Equation 1: Moisture transfer governing equation.

$$\xi \frac{\partial \varphi}{\partial t} = \nabla((\delta_v P_s + D_w \xi)\nabla\varphi + \delta_v \varphi \frac{dP_s}{dT}\nabla T)$$

Equation 2: Heat transfer governing equation.

$$(\rho_m c_{p,m} + w c_{p,l})\frac{\partial T}{\partial t} = \nabla\left((\lambda \nabla T) + h_{lv}[\delta_v(\varphi \frac{dP_s}{dT}\nabla T + P_s \nabla\varphi)]\right)$$

Where:

- δ_v = the permeability coefficient of water vapor in porous materials (s),
- P_s = the saturated water vapor pressure (Pa),
- φ = relative humidity (%),
- ξ = the slop of sorption moisture retention curve, (kg/m^3),
- D_w = the moisture diffusion coefficient with the moisture content as the gradient (m^2/s),
- ρ_m = dry material density (kg/m^3),
- $c_{p,m}$ = specific heat of dry materials (J/(kg·K)),
- $c_{p,l}$ = the specific heat of liquid water (J/(kg·K)),
- λ = thermal conductivity coefficient (W/(m·K)),
- h_{lv} = latent heat of evaporation (2500 kJ/kg),
- T = object temperature (K),
- W = moisture content (kg/m^3),
- T = time (s),
- H = specific enthalpy of material (J/kg),
- h_v = specific enthalpy of water vapor (J/kg),
- h_l = specific enthalpy of liquid water (J/kg),
- q_c = heat flux density (W/m^2).

P_{sat} is the single value function of temperature T (Hartwig M. Kunzel.1995.).

Equation 3: The saturated water vapour pressure.

$$P_{sat} = 611 \cdot exp(\frac{a \cdot T}{T_o + T})$$

Where:

- a = the constant,
- T_o = Reference temperature (K),

When T<0, a=22.44, T_o=272.44 K; T≥0, a=17.08, To=234.18 K.

Equation 4: Moisture storage capacity.

$$\frac{\partial w}{\partial \varphi} = \xi$$

Water vapor pressure P_v can be expressed as follows:

Equation 5: Water vapour pressure.

$$P_v = \varphi P_{sat}$$

4. BOUNDARY CONDITIONS

The heat flux at the building elements surface can be calculated as：

Equation 6: The heat changes at the ceiling surface.

$$q = h(T_{air} - T_{surf}) + h_{lv}g$$

Where:

- q = heat flux density (W/m^2),
- h = total heat transfer coefficient (W/(m^2·k)),
- T_{air} = temperature of the ambient air (K),
- T_{surfe} = temperature of the building elements surface (K).

The moisture flux through the building surfaces can be calculated as follows：

Equation 7: Moisture transfer governing equation.

$$g = \beta(\varphi_{air}P_{sat,air} - \varphi_{surf}P_{sat,surf})$$

Where:

- g = water vapor diffusion flux density (kg/(m^2·s)),
- β = water vapor transfer coefficient (kg/(m^2·s·Pa)),
- φ_{air} = relative humidity of air (%),
- φ_{surfe} = Relative humidity on the surface of the ceiling (%),
- $P_{sat,air}$ = saturated pressure of water vapor in the ambient air (Pa),
- $P_{sat,surf}$ = saturated pressure of water vapor of the ceiling surface (Pa).

Water vapor transfer coefficient β can be carried out by the Lewis criterion correlation formula reflecting the relationship between the thermal boundary layer and the concentration boundary layer (Hagentoft et al., 2003.)

Equation 8: Lewis's principle of analogy.

$$\beta = \left(\frac{h}{461.4 \times c_{p,a} \times \rho_a \times T}\right)$$

Where:

- $c_{p,a}$, ρ_a= air specific heat capacity, density, (J/(kg·K)), (kg/m^3).

The heat transfer coefficient of the surface in the air conditioning room and adjacent floor surface is 11 W/(m^2·K), 5.3 W/(m^2·K), respectively. The air temperature on both sides was 26ºC, 32ºC, respectively with the relative humidity of both sides was 60% and 85% respectively in summer. The heat transfer coefficient of the surface in the air conditioning room and adjacent floor surface is 6 W/(m^2·K), 9 W/(m^2·K), respectively. The air temperature on both sides were 18ºC, -2ºC, respectively with relative humidity of both sides were 60% and 80% respectively in winter. Detailed boundary conditions are presented in Table 1 and Table 2.

Table 1: Both sides boundary conditions of ceiling in summer

Position	h (W/(m^2·K))	β×10^8 (s/m)	T_{air} (ºC)	φ_{air}
Floor surface of adjacent room(Non radiation air conditioning)	5.3	3.7	32	85%
Ceiling surface of room (Radiation air conditioning)	11	8.4	26	60%

Table 2: Both sides boundary conditions of ceiling in winter

Position	h (W/(m^2·K))	β×10^8 (s/m)	T_{air} (°C)	φ_{air}
Floor surface of adjacent room(Non radiation air conditioning)	9	7.2	-2	80%
Ceiling surface of room (Radiation air conditioning)	6	4.8	18	60%

5. PHYSICAL PARAMETERS OF THE CEILING

The selection of performance parameters of the ceiling are as shown in Table 3.

Table 3: Properties of the ceiling components (M.K.Kumaran, 1996.)

Component	Cement mortar	Reinforced concrete	EPS
ρ (kg/m^3)	1800	2500	30
c_p (J/(kg·K))	840	940	1470
ω (kg/m^3)	$\frac{\varphi}{-0.022\varphi^2+0.025\varphi+0.0001}$	$\frac{\varphi}{0.018\varphi^2-0.027\varphi+0.020}$	$\frac{\varphi}{-0.5277\varphi^2+0.9647\varphi+0.07086}$
δ_v (10^{-12}s)	16.67	6.76	11.00
λ (W/(m·k))	$0.854+4.5\times10^{-3}w$	$2.7+0.0032\times10^{-3}w$	$0.0331+1.23\times10^{-3}w$
D_w (m^2/s)	$1.4\times10^{-9}\exp(0.027w)$	$1.8\times10^{-11}\exp(0.0582w)$	N/A

6. NUMERICAL SOLUTION

The capillary tubes wall temperature is assumed as mean value of water supply and return temperature. In summer, the water supply/return temperatures are 18/22 °C. Similarly in winter, water supply/return temperatures are 30/32°C. The multi physical field coupling simulation software COMSOL Multiphysics is used to solve the coupled heat and moisture transfer model of the enclosure structure. COMSOL Multiphysics uses the finite element method to discretise the model automatically and solve the discrete algebraic equations with the numerical solver. The capillary network is laid on the ceiling of 140 mm, and another 32 mm EPS is formed. 53749 domains and 4247 boundary elements are formed. The model temperature, relative humidity initial value is set to be the same as radiation air conditioning room

7. RESULTS AND DISCUSSIONS

7.1. Effect of EPS thickness on condensation in summer

To evaluate the impact of EPS on the condensation of ceiling, the temperature and moisture content distribution calculated by the model presented in this paper. Figures 2 and 3 show the temperature and humidity distribution of the whole ceiling, display the relative humidity and water vapor pressure distribution at the section when 0 mm and 10 mm EPS were laid in summer, respectively. Since moisture transfer is very slow, the temperature and humidity distribution on day 1, day 7, and day 30 were studied. Figure 4 shows the Relationship between the ceiling surface relative humidity on the adjacent room side and EPS thickness.

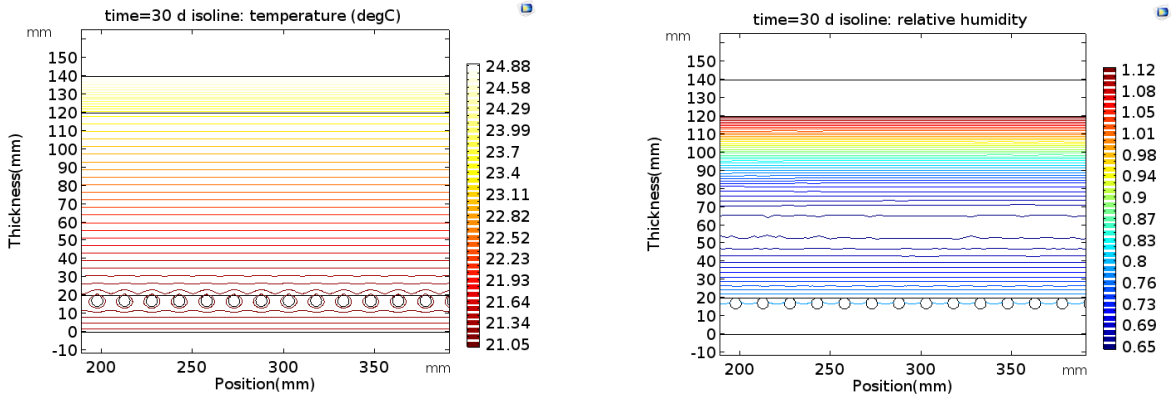

(a) *(b)*

Figure 2: Temperature and humidity distribution when EPS thickness is 0 mm (a: temperature distribution at the 30th day, b: relative humidity distribution at the 30th day.

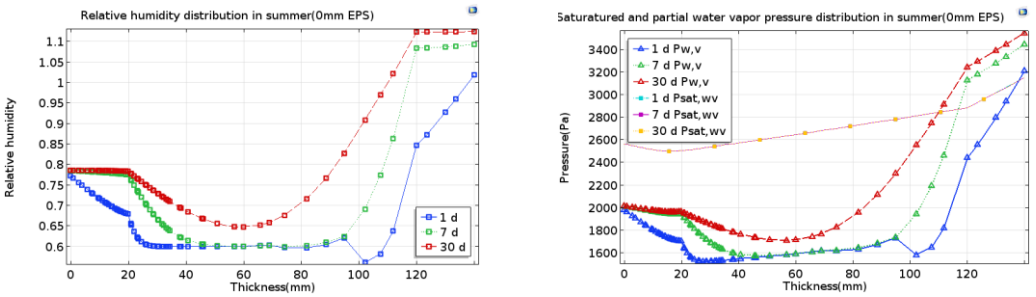

(c) *(d)*

Figure 2: Temperature and humidity distribution when EPS thickness is 0 mm: c: relative humidity distribution at the section, d: saturated and partial water vapor pressure distribution at the section)

In summer, from Figures 2 (a, b), the ceiling surface temperatures on radiant air-conditioning room side and the adjacent room side are 21.05ºC, 24.88ºC respectively, and the relative humidity of ceiling surface on the adjacent room side reaches maximum, the numerical solution of relative humidity is greater than 1, indicating that surface condensation occurs. Figure 2 (c) shows the relative humidity distribution at the 1st, 7th and 30th day. The ceiling's moisture transfer inertia is very strong, and it is not stable after 30 days, especially at the position of 50-70mm. it can be found from Figure 2 (d), $P_{w,v}$ and $P_{sat,wv}$ represent the partial water vapor pressure and the saturated water vapor pressure, respectively, when EPS is not laid, $P_{sat,wv}$ of the ceiling surface on the adjacent side is less than the $P_{w,v}$, which results in condensation. The saturated vapor pressure is a single value function of temperature. Since the heat transfer inertia is very small, the ceiling temperature quickly becomes stable, and the temperature changes very little between the 1st, 7th and 30th days, so the saturated vapor pressure lines almost coincide. The temperature curves almost coincide. Since the rate of heat transfer through the ceiling is faster than moisture transfer, moisture content distribution changes over time slowly, the temperature distribution varies little with time.

In order to prevent the condensation of ceiling on the adjacent room side, EPS was laid under the CRN. Figure 3 shows the temperature and moisture content distribution of the ceiling when 9mm EPS was laid. Figure 3 (a, b) shows that the ceiling surface temperature at the adjacent room side rise to 29ºC, meanwhile, the relative humidity is down to 100%. Figure 3 (c, d) shows the relative humidity from the interface between EPS and reinforced concrete to the adjacent room side is reduced, $P_{sat,wv}$ of the ceiling surface on the adjacent side is equal to the corresponding $P_{w,v}$, This means that EPS can be used to prevent condensation of the ceiling on the adjacent room side in summer. The ceiling surface on the adjacent room side is still the most prone to condensation.

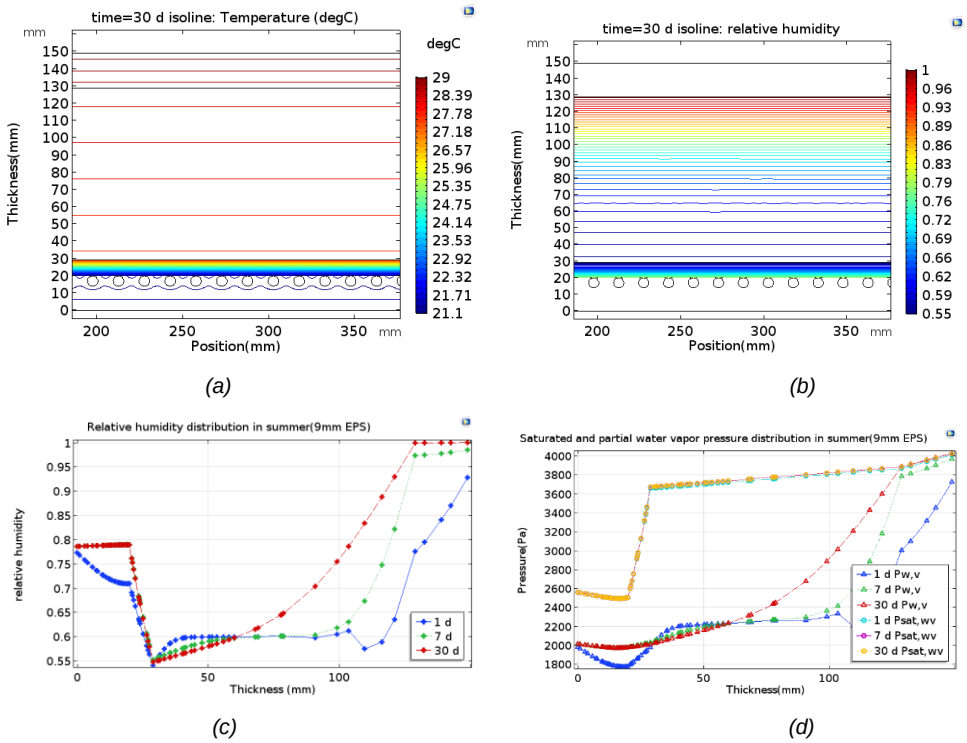

(a) *(b)*

(c) *(d)*

Figure 3: Temperature and humidity distribution when EPS is 10 mm (a: temperature distribution at the 1st day, b: relative humidity distribution at the 30th day, c: temperature and moisture content distribution at the section, c: temperature and relative humidity distribution at the section, e: saturated and partial water vapor pressure distribution at the section)

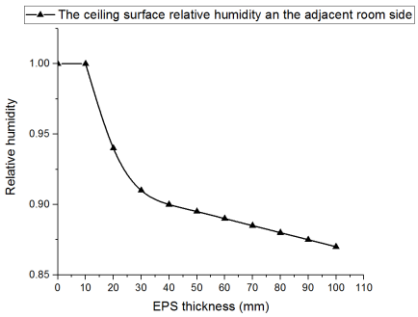

Figure 4: Relationship between the ceiling surface relative humidity on the adjacent room side and EPS thickness in summer

In order to prevent the ceiling surface condensation within 30 days on the adjacent room side, the thickness of EPS has been changed. It can be concluded from Figure 4 that as the thickness of the insulation board increases, the surface relative humidity gradually decreases. When the thickness of EPS is 10 mm, the numerical value of the relative humidity drops to 100%, indicating that 10 mm is the minimum thickness to prevent surface condensation within 30 days, to reduce the risk of condensation, the relative humidity should be reduced to 95%, at which time the thickness of EPS is 20 mm.

7.2. Effect of EPS thickness on condensation in winter

In winter, Figures 5 and 6 show the temperature and humidity distribution of the whole ceiling, the relative humidity and water vapor pressure distribution at the section when 0 mm and 32 mm EPS were laid, respectively. From Figure 5 (a, b, c), the ceiling surface temperature on air-conditioning room side and adjacent room side are 29.09ºC, 19.37ºC respectively. Due to the initial relative humidity of the model was set to 60% and the moisture transfer is very slowly, the relative humidity inside the ceiling gradually decreases after 30 days. The relative humidity of the ceiling surface on the adjacent room side and the radiation air conditioning room side were 0.2 and 0.3 respectively. By simulating the heat and humidity distribution of the ceiling after 1, 7 and 30 days, it is found from Figure 5 (d), when EPS is not laid, the vapor pressure of radiant air-conditioning rooms is higher than that of adjacent rooms, so water vapor permeates from the radiant air-conditioning room to adjacent room. The saturated water vapor pressure is greater than the corresponding water vapor pressure on the entire ceiling, so no condensation occurs.

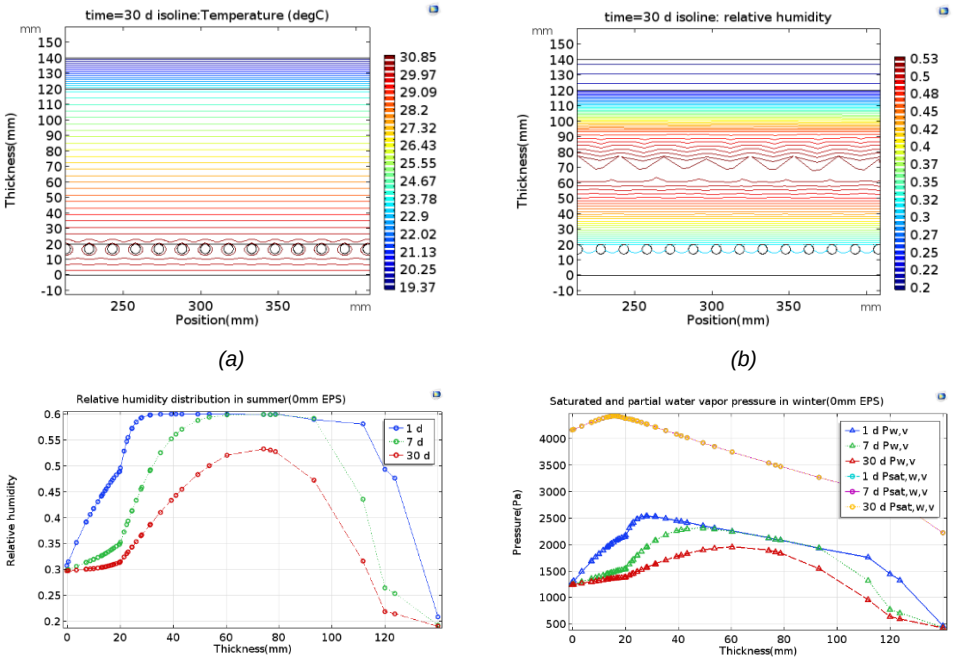

(a) *(b)*

(c) *(d)*

Figure 5: Temperature and humidity distribution when EPS thickness is 0 mm (a: temperature distribution at the 1st day, b: relative humidity distribution at the 30th day, c: relative humidity curve of the section, d: saturated and partial water vapor pressure curve of the section)

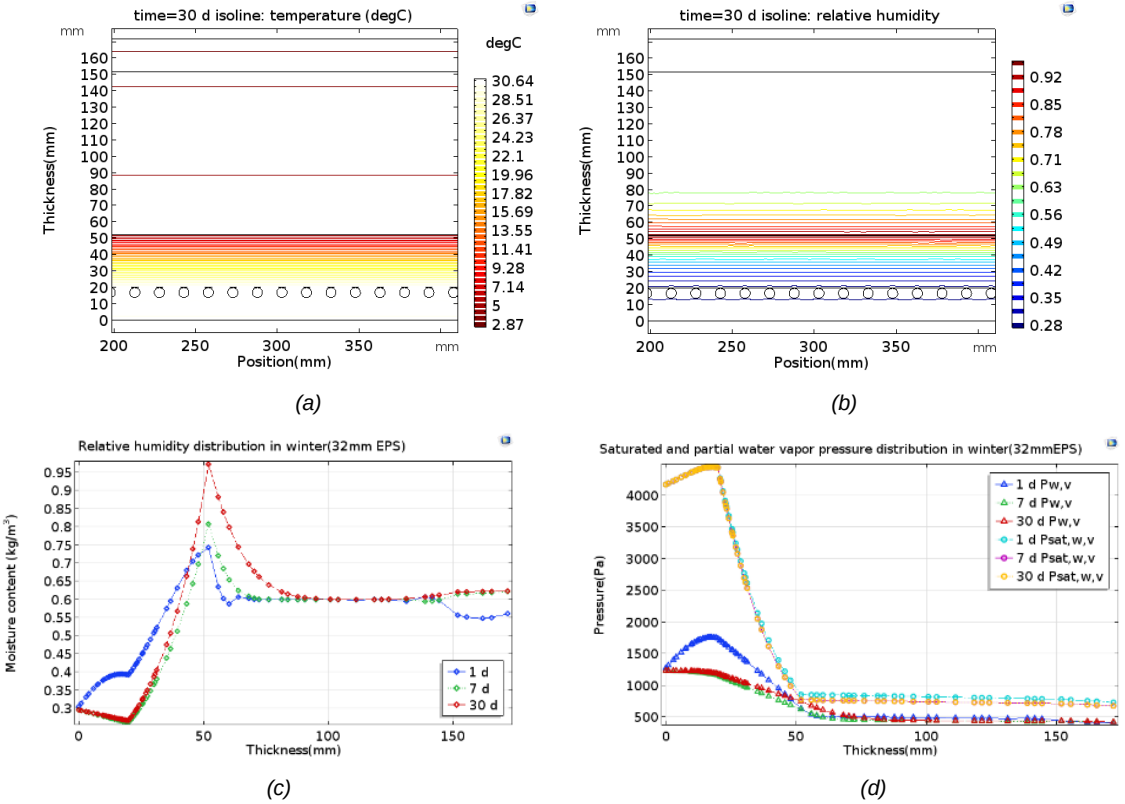

Figure 6: Temperature and humidity distribution when EPS thickness is 32 mm (a: temperature distribution at the 1st day, b: relative humidity distribution at the 30th day, c: relative humidity curve of the section, d: saturated and partial water vapor pressure curve of the section)

In winter, when the EPS is not laid, the ceiling is in a high temperature state because of CRN heating the whole ceiling, so the ceiling is not easy to condensation. However, Figure 6 shows that, when the EPS is laid, which the heat and moisture resistance of the insulation board forms a high humidity area at the interface between EPS and concrete. This area has the highest relative humidity on the whole ceiling. This paper mainly studies preventing the capillary ceiling condensation within 30 days. When the thickness of EPS is 32 mm, the relative humidity increases with time and finally reaches 99% at the 30th day, causes condensation inside the ceiling.

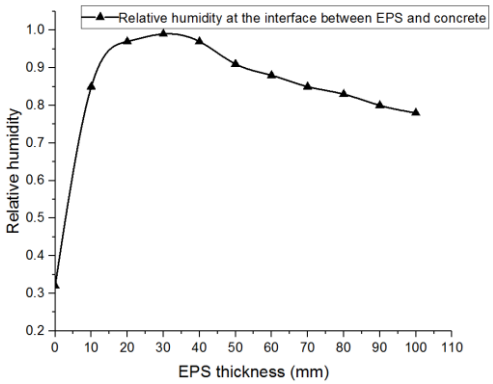

Figure 7: Relationship between relative humidity at the interface and EPS thickness in winter

Figure 7 shows that, as the thickness of EPS increases, the relative humidity at the interface increases first and then decreases on the 30th day. When the thickness of EPS is increased to 32 mm, the relative humidity reached the maximum, up to 99%, and the relative humidity is more than 95%, when the thickness of EPS is between 20 mm and 45 mm. In order to prevent the ceiling condensation at the interface between EPS and concrete in winter, the thickness of EPS should be less than 20 mm or more than 45 mm. Considering the situation of summer and winter, the thickness of insulation board should be greater than 45 mm.

8. CONCLUSIONS

In summer, increasing the thickness of EPS prevents the ceiling surface condensation on the ambient room side. The thickness of EPS should be greater than 10 mm to avoid condensation. If the thickness of EPS exceeds 20 mm, the surface relative humidity can be reduced to below 95%.

In winter, compared with not laying the insulation board, laying the insulation board will instead cause to produce condensation inside the ceiling. When the thickness of EPS is between 20 mm-45 mm, the relative humidity at the interface is over 95%. In order to prevent the ceiling condensation at the internal interface between EPS and concrete, the thickness of EPS should be less than 20 mm or more than 45 mm. Considering the situation of summer and winter, the thickness of insulation board should be greater than 45 mm. Under the design working condition, in order to ensure that no condensation occurs in the capillary radiant ceiling within 30 days in summer and winter, the thickness of EPS shall be over 45 mm.

9. REFERENCES

Cui, Y., Wang, Y., & Zhu, L. 2015. Performance analysis on a building-integrated solar heating and cooling panel. *Renewable Energy, 74*(C), 627-632.

Flannigan, B., Mccabe, E. M., & Mcgarry, F. 1991. Allergenic and toxigenic micro-organisms in houses. *Society for Applied Bacteriology Symposium, 20*(1), 61S.

Glaser H. 1958. Simplified calculation of vapor diffusion through stratified walls with precipitation of water and ice. *Refrigeration technology; 10(11):358–64 and (12) 386–90. (In German)*

Hagentoft, C. E., Adan, O., Adl-Zarrabi, B., Becker, R., Brocken, H., & Carmeliet, J., et al. 2003. Assessment method of numerical prediction models for combined heat, air and moisture transfer in building components: benchmarks for one-dimensional cases. *Journal of Building Physics*, 27(4), 327-352.

Hartwig M. Kunzel. 1995. Simultaneous Heat and Moisture Transport in Building Components, PhD Thesis. London: Wiley IRB Verlag, Stuttgart.

Hesaraki, A., & Holmberg, S. 2013. Demand-controlled ventilation in new residential buildings: consequences on indoor air quality and energy savings. *Indoor & Built Environment, 24*(2).

Künzel, H. M. 1995. Simultaneous heat and moisture transport in building components: one- and two-dimensional calculation using simple parameters. *Irb Verlag*.

M.K.Kumaran, 1996. Heat, Air and Moisture Transfer in Insulated Envelope Parts, Final Report, Vol 3, Task 3: Material Properties, IEA Annex24, Laboratorium Bouwfysica, KU Leuven, Belgium.

Maliki, M., Laredj, N., Hassan, N., Bendani, K., & Missoum, H. 2014. Numerical modelling of hygrothermal response in building envelopes. *Gradevinar*, 66(11), 987-995.

Mikeska, T., & Svendsen, S. 2013. Study of thermal performance of capillary micro tubes integrated into the building sandwich element made of high performance concrete. *Applied Thermal Engineering, 52*(2), 576-584.

Pasanen P, Pasanen A L, Jantunen M. 1993. Water Condensation Promotes Fungal Growth In Ventilation Ducts [J]. *Indoor Air*, 3(2):106-112.

Philip, J. R., & Vries, D. A. D. 1957. Moisture movement in porous materials under temperature gradients. *Eos Transactions American Geophysical Union,* 38(2), 222–232.

Qin, M., Belarbi, R., Aït-Mokhtar, A., & Nilsson, L. O. 2008. Simultaneous heat and moisture transport in porous building materials: evaluation of nonisothermal moisture transport properties. *Journal of Materials Science*, 43(10), 3655-3663.

Wen, Q. M., Yang, D., Chen, M. J., Li, Y. A., & Wei, S. J. 2014. Analysis of the heating and energy saving effect of capillary radiant, ceiling in hot summer and cold winter area. *Advanced Materials Research*, 960-961(960-961), 599-602.

Yin, Y. L., Wang, R. Z., Zhai, X. Q., & Ishugah, T. F. 2014. Experimental investigation on the heat transfer performance and water condensation phenomenon of radiant cooling panels. *Building & Environment*, 71(1), 15-23.

422: A technology platform for monitoring homes within a community energy scheme

Design and implementation challenges

Rob SHIPMAN[1], Mark GILLOTT[2]

[1] University of Nottingham, University Park, Nottingham, UK, rob.shipman@nottingham.ac.uk
[2] University of Nottingham, University Park, Nottingham, UK, mark.gillott@nottingham.ac.uk

This paper describes a technology platform for monitoring homes within a community energy scheme. A range of sensors were deployed to measure in-home environmental conditions, occupancy, electrical power, electrical energy, thermal energy, heating behaviour and boiler performance to better understand and predict energy consumption in individual homes and across the community. The community assets include solar photovoltaic panels that are deployed in an urban solar farm and on rooftops to generate energy that is used to charge a central battery. This community scale storage supports participation in grid services to help balance the national grid and in future phases to power a community heat network, electric vehicle charging and self-consumption within individual properties. The monitoring data aims to help develop insights to help optimise this multifaceted system and to provide feedback to residents to help visualise and control their energy consumption to encourage reductions in demand. It was found that a diverse range of Internet of Things technologies was required to generate this data and make it available for subsequent access and analysis, which are described together with associated challenges that were experienced during the system design and implementation. The diversity in the monitoring technology was consolidated in the cloud to provide a common data structure for consumption by other services via industry standard APIs. The cloud infrastructure developed to achieve this is described, which utilised scalable and easily deployable services that are readily available from the major technology companies. The paper concludes by highlighting promising areas of focus for community-level monitoring in related projects.

Keywords: Community energy, Internet of Things, energy monitoring

1. INTRODUCTION

The Sustainable Community Energy Networks (SCENe) project aims to accelerate the adoption of community energy schemes through research and development of the necessary technological platforms and associated business models. It is centred on a new low-carbon housing development in the Trent Basin area of Nottingham, UK that will result in several hundred new homes as part of a wider regeneration initiative (Project SCENe, 2016). Integral to this development are the components necessary to facilitate community energy. A 2.1 MWh Tesla battery has been installed that will be charged in part through solar photovoltaic panels that are installed on the roof tops of participating homes and an urban solar farm. This battery will allow participation in grid services that help balance the UK's National Grid while generating revenue for the scheme. In future phases of the project it will also be used for the direct benefit of the community to power a heat network, electric vehicles and potentially homes through behind the meter services.

To optimise the use of these assets it is important to understand the energy demands within the community so that decisions can be made as to when to import from the grid, export to the grid or consume generated electricity within the community. In addition, it is important for participants to understand their own energy behaviour, its impact on the overall operation of the scheme and any behavioural changes they may be able to make to enhance their energy efficiency. For these reasons, each participating home was equipped with a range of monitoring equipment to help measure and predict associated usage of electricity and demands for space and water heating.

This paper details the technological platform developed to facilitate the monitoring, the challenges encountered and the lessons learned that may be of value to related initiatives. Section 2 of the paper describes the monitoring devices that were deployed, section 3 shows how these devices were brought together in a system architecture, section 4 discusses the design and implementation challenges before the paper concludes.

2. MONITORING DEVICES

A key requirement of the monitoring equipment was the ability for it to be installed and maintained in properties that were already built and occupied. It was important therefore that it could be retrofitted as unobtrusively as possible and with a minimum of disruption. The equipment deployed falls into 3 categories; indoor environment, electricity consumption, heating and thermal energy as detailed below.

2.1. Indoor environment

Indoor environmental conditions were monitored using a range of EnOcean sensors. This technology utilises low bandwidth and low power wireless transmissions from sensors that are typically designed to harvest their energy requirements from the environment in the form of solar energy, thermal differentials or kinetic energy for example (EnOcean, 2015). This feature reduced the need for battery replacements and hence maintenance visits to the properties.

Indoor temperature and relative humidity were measured using batteryless sensors with small solar panels that could be easily wall-mounted. Sensors were installed in the main bedroom and the landing of another floor within the property. Data was sent whenever the temperature changed by at least 0.5 degrees, the relative humidity changed by at least 2% or otherwise every 15 minutes. This data provided an historical view of how warm the participants maintain their property and therefore the likely energy required to satisfy this demand. It also provides the opportunity to present feedback to the user as to how their heating requirements relate to others in the community and the likely impact of any changes they may wish to make.

Changes in internal CO_2 concentration are primarily the result of human activity i.e. breathing out, and without adequate ventilation CO_2 can rise to unhealthy levels, which in extreme circumstances can result in symptoms such as drowsiness and headaches. It is important to understand therefore whether energy efficiency measures taken to reduce heat loss in energy efficient homes such as those on the Trent Basin development are at the expense of internal air quality. As internal CO_2 concentration is correlated with human activity, together with other data it can also help us develop a view of occupancy patterns within a property and across the community. This data can in turn help to predict likely energy demand. A single sensor, powered by ambient light with a battery backup, was thus installed in the main living area. CO_2 concentration together with temperature and relative humidity was measured and transmitted at least every 15 minutes.

Although CO_2 concentration in the main living area provides some insight into occupancy patterns, more data was required to enhance the ability to measure and predict occupancy given its importance to likely energy demand. A more direct measure was also introduced therefore using a motion sensor installed on the ceiling of the main hallway. This EnOcean sensor was powered by a small battery that was specified to last for at least the 2-year duration of the project. It transmitted a signal whenever motion was detected with a minimum interval of 1 minute.

2.2. Electricity consumption

As part of the UK's rollout of smart meters, the Trent Basin properties were equipped with first generation smart meters that promise to provide consumers with near real-time information on their energy use. However, access to this data is limited to the energy provider and the consumers own in-home display. It was not possible therefore to interface with the meters for the purposes of the project. The specification of second generation UK smart meters provides for a Consumer Access Device (BEAMA, 2015) that allows more flexibility with data access, however these meters were not available in the project timescales. In addition, smart meters only provide data on overall household consumption and do not support finer-grained categorisation that allows energy use to be disaggregated into potential areas of interest such as lighting or cooking.

For these reasons electricity was monitored at the consumer unit, which receives the main incoming supply and distributes this to individual circuits within the property. Although there was variance in the specific wiring of each property, a typical pattern was for the electrical sockets to be separated in to 2 to 3 circuits, lighting separated in to a further 2-3 circuits and the electric cooker and electric hob to have their own individual circuits. These were all monitored therefore together with the main incoming supply. To facilitate retrofitting, PowerTag technology (Schneider Electric, 2018) was selected that allows circuits to be easily and accurately monitored without the need for any rewiring. A small single-pole Schneider PowerTag was attached to each circuit of interest that transmitted power data to a concentrator, which due to space constraints was installed externally but close to the consumer unit.

2.3. Heating and thermal energy

Space and water heating accounts for around 80% of the energy consumed in a typical UK property (BEIS, 2018: page 21). It therefore plays a dominant role in the energy demands of the community and, following introduction of the heat network, operation of the community energy scheme. This also presents an opportunity for better understanding heating behaviour with a view to providing residents with actionable information to make potentially significant reductions in their usage.

To help develop this understanding and provide residents with more control of their heating, each participating property was equipped with a Honeywell Evohome system (Honeywell, 2018). By controlling each radiator separately this system allows temperature control of individual rooms helping to ensure that rooms are only heated when necessary. This zonal control provides greater scope for energy saving over more traditional single zone thermostats. Evohome is also a connected thermostat allowing access and control through a website or smartphone app, which provides further opportunities for residents to better control their heating. This connectivity allows data to be collected on the temperatures of each zone and a richer picture of the house temperature to be developed. In addition, data can be collected on heating behaviour such as choice of target temperatures, schedule use and overrides.

Boilers within participating properties were equipped with OpenTherm technology (OpenTherm Association, undated), which is an open standard for communication between a boiler and a thermostat. This technology allows the modulation rate of a boiler to be controlled to more precisely satisfy heating demand and can be more efficient than simple on/off controls. It also provides access to a rich dataset from the boiler including boiler on times, calls for hot water, water temperatures and fault conditions.

Given the dominance of thermal energy in a typical domestic property, it was important to develop a richer understanding of this demand to help specify future developments of the scheme such as the heat network and to highlight opportunities for optimisation and behaviour change. In phase 1 of the development, space and water heating demand was satisfied by a gas fired combination boiler. As this was the only gas using appliance in a property, gas meter data therefore provided a picture of total thermal energy demand. However, this data did not provide disaggregated data for space and water heating. In addition, it was not possible to directly interface with the first-generation UK smart meters installed in the properties.

For these reasons, heat meters were installed to measure specific energy use for both space and water heating. For central heating, these meters measured flow and return temperatures together with flow rate to provide an accurate calculation of energy consumption. Hot water was heated on demand using an independent water circuit within the boiler and energy consumption was therefore measured using the temperature differential between the cold water inlet and hot water outlet together with flow rate.

3. SYSTEM ARCHITECTURE

There are two key aspects to the system architecture; the in-home monitoring system that generated the data and the cloud infrastructure that received, processed and exposed this data for consumption by other services. These are detailed in the remainder of this section.

3.1. Monitoring equipment architecture

The architecture of the in-home equipment is shown in Figure 1. EnOcean telegrams transmitted by the indoor environment sensors were received by a gateway device specifically developed for the project. This gateway was based on a Raspberry Pi 3 Model B+ with an EnOcean Pi board that provided a radio and serial interface for interacting with EnOcean sensors in the property.

Schneider PowerTag sensors transmitted power data using proprietary wireless communications to the associated Schneider concentrator, which also calculated energy consumption for each monitored circuit. This device was connected to the Project SCENe gateway using a wired Ethernet connection and the power and energy for each tagged circuit were read every 15 seconds using the Modbus TCP/IP protocol. The gateway was connected to the Internet using a Wi-Fi connection to the participants existing wireless router and broadband connection.

The Honeywell Evohome heating controller used proprietary wireless communications to interact with the controllers installed on each radiator within the property and with an OpenTherm bridge that in turn was wired to the OpenTherm controls within the boiler. The heating controller was also connected to the Internet using the participants existing Wi-Fi router and broadband connection allowing remote control and data storage and access from the Honeywell cloud.

Heat meters were equipped with Wireless M-Bus, which is a European standard that specifies the communication between utility meters and gateways and has a range of up to several kilometres in urban areas. The meters were installed close to the boiler and wirelessly transmitted data to an external receiver that was installed in a community energy centre, which also housed the battery and other control equipment. This receiver transmitted data to the University of Nottingham's cloud using General Packet Radio Service (GPRS) on the mobile network.

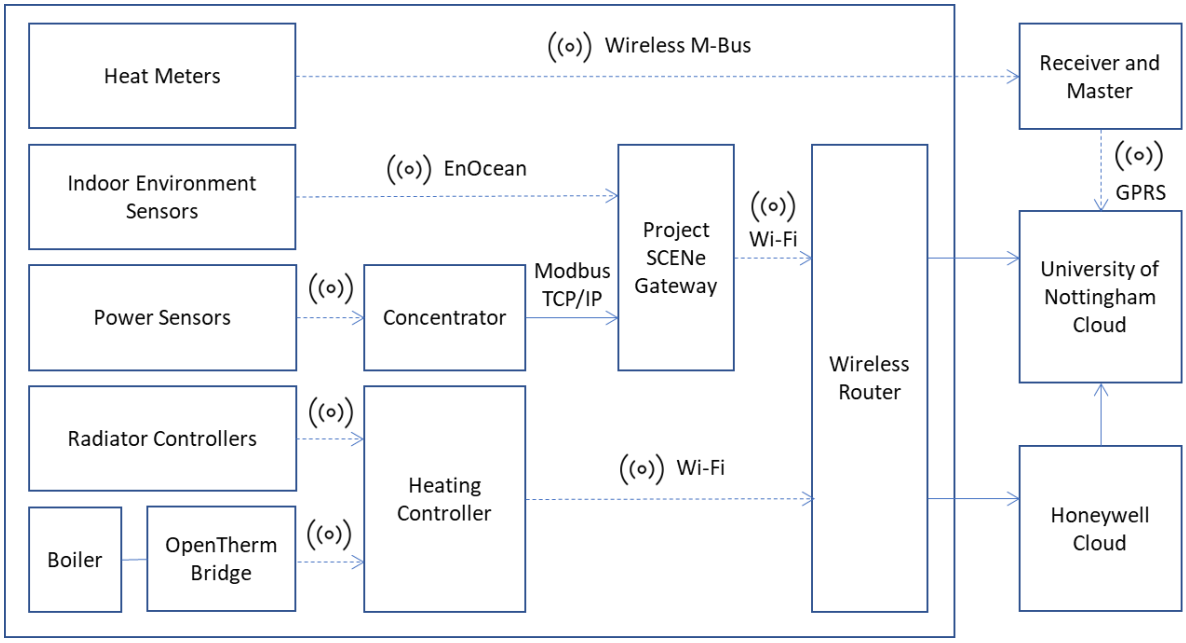

Figure 1: Architecture of the in-home monitoring equipment and cloud connections. Data leaves the property over the public Internet via the router's broadband connection or wirelessly for the heat meters. Dashed lines show wireless connections and solid lines physical connections.

3.2. Cloud architecture

The University of Nottingham's cloud was built on top of Microsoft Azure and provided the hub for data storage and access while laying the foundation for subsequent data analysis. Message Queue Telemetry Transport (MQTT) was chosen to send data from the SCENe gateway to the cloud (Banks and Gupta, 2014). This is a standardised Internet of Things connectivity protocol designed to be very lightweight. It therefore places minimal data requirements on the participant's broadband connection. It uses a publish/subscribe pattern in which received messages are published to a central broker, which in turn sends the message on to all relevant subscribers. In this case an Azure Internet of Things (IoT) Hub was used as the broker, which accepts messages from any registered device over a connection secured using Transport Layer Security. JavaScript Object Notation (JSON) was adopted as a lightweight format for sensor data interchange and each received message triggered a function app on Azure, which was responsible for persisting the data. Such stateless functions that are quickly started on a defined trigger are an example of a serverless architecture sometimes known as

Functions as a Service (FaaS). Data was stored using Azure Cosmos DB, a document-based NoSQL database that is scalable and responsive and does not require a fixed schema.

It was not possible to interface directly with the Evohome heating data as this was sent directly to Honeywell's own cloud infrastructure, which was also based on Microsoft Azure. However, it was possible to retrieve data from participants who had granted access through cloud-to-cloud interaction in two ways. Firstly, Representational State Transfer (REST) APIs provided access to in-home temperature data, target temperatures, heating schedules and boiler data collected through the OpenTherm interface. Secondly, an Azure Event Hub was used to provide a publish/subscribe capability for all heating data. A serverless function app running in the cloud was again triggered that parsed the data into JSON documents, which were stored in the same Cosmos DB instance. Boiler monitoring data was not available through the Event Hub and could only be accessed using the REST API.

Heat meter data was sent from the Wireless M-Bus receiver over the mobile network using GPRS. Data files were transferred using HTTP to Azure where another serverless function app was used to parse the data into JSON documents and store in Cosmos DB. All monitoring data was therefore stored in this database, which facilitated subsequent analysis using other services. A REST API was also developed that provided access to anonymous data to research partners. This made use of Azure API Management to provide a front-end that could be managed and secured. This service used another serverless function app to query Cosmos DB for the requested data. Key elements of the resulting architecture are shown in Figure 2.

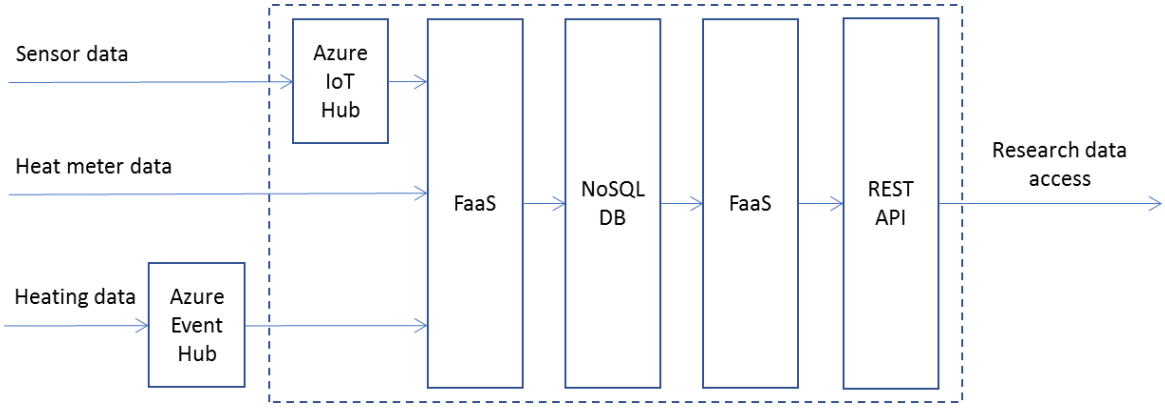

Figure 2: Key elements of the cloud service architecture. Services shown within the dotted area are part of the University of Nottingham's cloud infrastructure hosted on Microsoft Azure. The heating data Event Hub is part of the Honeywell cloud infrastructure, which is also hosted on Microsoft Azure. Data is stored and retrieved as documents using serverless functions or Functions as a Service (FaaS).

4. DISCUSSION

It is clear from the previous section that a broad range of technologies and protocols were required to implement the monitoring architecture described in this paper. This is consistent with the fragmented nature of the Internet of Things technology space at the time of writing. Although some consolidation is likely given the initiatives of the large technology companies such as Google and Apple, this fragmentation is likely to persist for the foreseeable future and a successful architecture will thus need to be flexible to a range of different technologies.

However, such diversity at the device and protocol level can be consolidated at the cloud level. Data generated can be ingested using a common structure in such a way that the complexity of the underlying system can be made invisible to services that consume this data. In this work, JSON documents with a common core of objects were used for storage in a document-based NoSQL database. Data retrieved from the API by consuming services could therefore work with this common structure independently of the underlying technology. To reach this point however a number of challenges and learnings were encountered that will be discussed in the remainder of this section.

EnOcean technology was chosen for monitoring of the indoor environment. The key feature of this technology is the ability for devices to harvest the energy they need for data transmission from their environment. In this project ambient light was used to power devices via embedded photovoltaic cells thus alleviating the need for batteries. The attraction of this approach from a maintenance perspective is clear as in theory devices can be installed and left to run for long periods without further intervention. However, in practice batteryless devices used in this work were sometimes unable to generate and store enough power for consistent data transmission even in relatively well-lit rooms. In some cases, this resulted in no data transmissions during the night and therefore any maintenance advantages were overshadowed by data quality issues. Other EnOcean devices with a battery backup proved more reliable and thus the advantage of this technology was

to extend battery life rather than remove the need for them. It should be noted however that these findings are specific to the sensors used in this work and therefore should not necessarily be generalised across all EnOcean devices.

As previously highlighted, it was not possible to interface with the smart meters installed in the Trent Basin properties and sub-metering was therefore necessary. This proved impractical in a retrofit scenario for gas meters however electricity sub-metering was achieved using PowerTags installed in the consumer unit. Such use of wireless sensors has the potential to be problematic where the consumer units are metal-clad, which is now a requirement for new properties in the UK for example, and the receiver is externally installed. In this scenario, as was the case in this work, wireless data transmissions must penetrate the metal-clad box. However, consumer units typically have holes designed for cable connections that can be exposed to create a more radio friendly environment. Very few packet errors were therefore registered when the receiver was installed close to the consumer unit in this way.

The power sensors also allowed monitoring of individual circuits such as lighting and cooking. Such disaggregated data is of potential value in helping to build a finer-grained understanding of energy consumption. It was however limited in several ways. Firstly, circuits within individual homes were not consistent and therefore it was not always possible to directly compare consumption of a given circuit across the community, which may have been useful for analysis and feedback for residents. This will always be the case in a retrofit scenario but for future developments specification of consistent circuit wiring across properties of the same type would be useful to facilitate subsequent monitoring and analysis. Secondly, it was not typically possible to directly monitor the consumption of individual appliances such as the washing machine or dryer as these were not powered by individual circuits. However, circuit power sensors provide more focussed data on an area of interest such as kitchen sockets, which is likely to increase the efficacy of any subsequent algorithmic analysis to identify specific devices (Armel, Gupta, Shrimali et al., 2013). Over time this issue is likely to become redundant as smart appliances are adopted that report their own energy consumption.

The OpenTherm connection to the boiler provided access to a range of data that allowed monitoring of boiler performance. This dataset included modulation rate expressed as a percentage of maximum firing rate, flame-on times and whether the boiler was firing due to a call for heating or hot water. In theory therefore, this data could be used in conjunction with the capacity of the boiler to estimate energy consumed for heating and hot water individually. However, there are several issues with this approach. Firstly, modulation rate is an optional OpenTherm parameter and cannot therefore be relied on across all boiler types. Secondly, the resolution of the data may not be sufficient to make accurate calculations. With the Evohome thermostat used in this work, the maximum resolution of data was every minute and thus the data was not fully representative of actual boiler operation. This approach may be possible however using other thermostats that more frequently poll for boiler data.

Thermal energy consumption can also be calculated using flow rate, flow temperature and return temperatures. However, only 2 of these data points were available via OpenTherm. For central heating, flow and return temperatures were provided but not flow rate. For hot water in a combination boiler, flow rate and flow temperature are provided but not inlet water temperature. In both cases therefore it was not possible to calculate energy consumption thus necessitating the use of heat meters.

Although providing accurate data, heat meters are far more difficult to retrofit often requiring draining of the entire central heating system. In addition, in some properties installation was difficult due to space constraints and length of exposed pipe work. However, to alleviate these difficulties, certified compact ultrasonic heat meters were used that can be used in scenarios with limited upstream and downstream piping, which in some cases can adversely impact the accuracy of this type of meter.

A key issue in the design of a monitoring system is access to data. It was important therefore to choose protocols that provide open access to data. EnOcean telegrams conform to a publicly available specification and can thus be interpreted and used by any compatible receiver. Power and energy data was available via Modbus TCP/IP, which is another open protocol. Similarly, the wireless M-Bus data transmissions used by the heat meters could be received and used without restriction.

However, although the availability of connected home products is proliferating, data from such products is often not available either through an open interface or a negotiated commercial agreement. This is the case for many smart thermostats and it was important therefore to ensure that any such products used also provided access to the associated data. In general, this issue limited the option of utilising off-the-shelf connected products.

Another important issue to consider was data transfer from a monitored home to the backend cloud infrastructure. There were several possibilities considered including use of the mobile network however an advantage of the advent of the connected home is that consumers are becoming more accustomed to the use of their existing Internet connection for these products. A similar approach for this project was thus adopted and in keeping with this general market trend.

This approach does however require consent for the use of an existing Internet connection and introduce the risk of data acquisition failing due to changes in the homes Internet connectivity that are not visible or directly controllable. This is a

key advantage of technologies such as Wireless M-Bus and other Low-Power Wide-Area Network (LPWAN) technologies (Centenaro, Vangelista, Zanella et al., 2016). These technologies are designed to facilitate low-power, long range data transmission so that communal receivers can be used removing the need for individual receivers in each property. This architecture is a good fit for geographically constrained areas such as community energy projects and a fruitful area of investigation for subsequent projects.

The advent of managed cloud services from the major technology companies is a great asset in the development of IoT systems. It is now possible to easily create scalable, robust services with high availability. In this project a number of such services were used including serverless functions that performed many important roles within the system. These functions are spun-up on demand following a defined trigger and have the significant advantage of not requiring a dedicated server. In many cases, this architecture served its purpose well. However, in cases where rapid response was required it was found to be problematic due to the inherent delays in the spin-up process. This was particularly apparent when a rapid response from the API was required to answer a user request for data for example. On first execution of the function significant delays were often apparent that were detrimental to the user experience. Careful consideration should thus be made before employing serverless functions for scenarios in which functions may not be used for some time but require rapid response on first use.

5. CONCLUSIONS

In this paper we have described a system architecture for monitoring homes in a community energy scheme. The monitoring includes indoor environmental conditions, electric power, thermal energy and heating. A diverse range of technologies and protocols were required to implement this system, which given the fragmented nature of Internet of Things technology, is likely to be commonplace for the foreseeable future. However, consolidation was possible in the cloud to provide a consistent data structure for other services that consume the data.

Much of the technology deployed used short range wireless sensors that require a local gateway to receive, process and transmit the data to the backend cloud services. These sensors were easy to install and retrofit but placed a requirement on network connectivity in each individual home. Heat meters however used the low-power, long-range Wireless M-Bus protocol thus alleviating the need for a receiver in each home. This technology is an example of a Low Power Wide Area Network of which there are several examples including LoRa and NB-IoT (Sinha, Wei and Hwang, 2017). These technologies are designed for IoT applications that typically require low power consumption and low data rates but long range. They are thus a natural fit for community energy schemes and as more devices utilising these technologies emerge provide a fruitful area of focus for associated monitoring.

6. ACKNOWLEDGEMENTS

This research is supported by Innovate UK and ERA (Energy Research Accelerator). The partners of the project are: The University of Nottingham, Blueprint, ATKearney, Smartklub, Stickyworld, Solar Ready, Loughborough University, Slam Jam, Urbed and Siemens.

7. REFERENCES

Armel, C., Gupta, A., Shrimali, G. and Albert, A. (2013) Is disaggregation the holy grail of energy efficiency? The case of electricity. Energy Policy 52: pp.213–234.

Banks, A. and Gupta, R. (2014) MQTT Version 3.1.1, OASIS Standard [online]. Available at: http://docs.oasis-open.org/mqtt/mqtt/v3.1.1/csprd02/mqtt-v3.1.1-csprd02.html. [Accessed on 26 July 2018].

BEAMA (2015) Consumer Access Devices a BEAMA Guide [online]. Available at: http://www.beama.org.uk/resourceLibrary/consumer-access-devices-a-beama-guide.html. [Accessed on 26 July 2018]

BEIS (2018) Energy Consumption in the UK (ECUK) [online]. Available at: https://www.gov.uk/government/statistics/energy-consumption-in-the-uk. [Accessed on 26 July 2018]

Centenaro, M., Vangelista, L., Zanella, A. and Zorzi, M. (2016) Long-range communications in unlicensed bands: the rising stars in the IoT and smart city scenarios. IEEE Wireless Communications 23(5): pp.60-67.

EnOcean (2015) EnOcean – The World of Energy Harvesting Wireless Technology [online]. Available at: https://www.enocean.com/en/technology/white-papers/. [Accessed on 26 July 2018]

Honeywell (2018) evohome Wi-Fi [online]. Available at: https://getconnected.honeywell.com/en/evohome. [Accessed on 26 July 2018]

OpenTherm Association (undated) Why OpenTherm? [online]. Available at: https://www.opentherm.eu/why-opentherm/. [Accessed on 26 July 2018]

Project SCENe (2016) Trent Basin [online]. Available at: https://www.projectscene.uk/trentbasin/. [Accessed on 26 July 2018].

Schneider Electric (2018) PowerTag Wireless Energy Sensor [online]. Available at: https://www.schneider-electric.com/en/product-range-presentation/63626-powertag. [Accessed on 26 July 2018]

Sinha, R., Wei, Y., Hwang, S. (2017) A survey on LPWA technology: LoRa and NB-IoT. ICT Express 3(1): pp.14-21,

425: Improving Honghu Lake environment with the implementation of the River Chief System

Peng XIANZE[1], Li PENGFEI[2]

[1] Peng Xianze, Hubei University of Technology,China,407732051@qq.com
[2]Li Pengfei, Hubei University of Technology,China,2269012988@qq.com

The River Chief System plays an important role in protecting water environment. Honghu Lake is the largest lake in Hubei Province, however, as time passes, many problems arise: water pollution is getting worse; the area of Honghu Lake is shrinking; biodiversity is being destroyed. To solve these problems, the River Chief System should be implemented by making relevant laws and regulations; cleaning the water flowing into Honghu Lake; clarifing the duties of the River Chief System at all levels; strengthening water ecological restoration; strengthening supervision and law enforcement; and developing red and green culture coordinately. Only by implementing these strategies can the sustainable development of Honghu Lake be boosted.

Keywords: The River Chief System, Honghu Lake, sustainable development

1. INTRODUCTION

Honghu Lake, the largest lake in Hubei Province, is China's seventh largest freshwater lake. Honghu Lake crosses Honghu Lake County and Jianli County, N29°38′--29°59′, E113°11′--113°28′, it lies to the north of the Yangtze River. Previously, it belonged to Yun-meng Lakes. The water level in Hong Lake is 25.00m, its length is 23.4km and maximum width is 20.9km.Honghu Lake is located in the subtropical humid monsoon climate. The annual average temperature is 16.6°C, and the average annual precipitation is 1343.3 mm.

Honghu Lake was originally the main place to accumulate floods of the following counties: Jiangling, Jianli, Qianjiang, Shashi and Honghu. The main rivers connected to Honghu lakes are Yangtze River, Dongjing River, Neijing River, Hongpai River, Nangang River and Taohong River, forming a water network that extends in all directions (Wang Sumin; Dou Hongshen, 1998). Honghu Lake is a lake with various functions such as irrigation, fishing, shipping and water supply. It is also one of the Jingjiang flood diversion areas. The planned flood storage capacity is 94.58 x $108m^3$ to prevent Wuhan from flood. The mileage of the navigation route in the lake is 81.0 km which can be used for ships of 5--20t. Honghu Lake is one of the important old revolutionary base areas. During the second domestic revolutionary war, it was the birthplace of the Hunan and Hubei revolutionary bases and the Chinese Workers' and Peasants' Red Army.

Honghu Lake is a freshwater lake and an important aquatic production base with the most abundant organic matter in Hubei Province. It is famous for its rich resources: fish, shrimp, lotus root and wild duck.

2. THE ORIGIN AND DEVELOPMENT OF THE RIVER CHIEF SYSTEM

In the early summer of 2007, due to the deterioration of water quality in Taihu Lake and bad meteorological conditions, not only did Taihu Lake suffer an outbreak of blue algae, but it also caused drinking water crisis in Wuxi City, which attracted national attention. The Jiangsu provincial government attached great importance to the problem and determined to improve water quality. In September 2007, Wuxi government issued *Wuxi City's River Cross Section Water Quality Control Targets and Assessment Measures*, including water quality test results of the river cross section into the principal person's career performance and achievements. Then, both Jiangsu Province government and Wuxi City government came up with credible packages to protect water resources. What the Jiangsu Province government did was a big success, and the practices were then promoted and used in other areas with remarkable results.

In December 2016, Central Committee of the Communist Party of China and General Office of the State Council issued *the Opinions on the Full Implementation of the River Chief System*, pointing out that "government officials will be hired as River Chief System at provincial, city, county and township levels and heads of provincial regions will be general chiefs that are responsible for all rivers and lakes in the region". The strategy including the following tasks the River Chief System should do: resource protection; shoreline management and protection; water pollution prevention and control; water environment management; ecological restoration law enforcement monitoring.

Hubei Province is known as the "Thousand Lakes Province". In recent years, Hubei Provincial government has continuously strengthened the protection of lakes. In 2011, it began to explore the implementation of the River Chief System in Wuhan. In 2014, the River Chief System was in full operation in Hubei Province. The strategy lay a foundation for the anti-water-pollution efforts and also helps with the management of Honghu Lake.

3. THE SIGNIFICANCE OF THE IMPLEMENTATION OF THE RIVER CHIEF SYSTEM

The implementation of the River Chief System is a necessary requirement for the development of an ecological civilization. General Secretary Xi Jinping emphasised at the 19th Congress of the Communist Party of China the importance of ensuring harmony between human and nature: building an ecological civilization is vital to sustain the Chinese nation's development. We must realise that lucid waters and lush mountains are invaluable assets and act on this understanding, implement our fundamental national policy of conserving resources and protecting the environment, and cherish the environment as we cherish our own lives. Rivers and lakes are the pulse of the earth, the source of life, the cradle of civilization, and it is also an important support for economic and social development. China's rivers and lakes are widespread and water net clouds. As an important part of the ecosystem, it plays an important role in resource, ecological and economic aspects. The River Chief System incorporates the management and protection of rivers and lakes into the construction of ecological civilization, and proposes a good plan for the problems existing in rivers and lakes. It is also an inevitable requirement for the Beautiful China initiative to create good working and living environments for our people and play our part in ensuring global ecological security.

The implementation of the River Chief System is an important part in ecological advancement. The River Chief System not only constructs a complete river and lake management and protection mechanism, but also point out that mayors and county heads are responsible for their areas, River Chiefs will be responsible for the management and protection of the watercourses. On one hand, it can urge all parties to combine the ecological protection and water-clean tasks into performance evaluation system and join forces to solve the problem, on the other hand, implementing the River Chief System will raise the leader's awareness on the importance of protecting the environment. And the cadres of the party and

the government carry out the Party's principles and policies to improve the environment of the lake, meet the needs of the people for a better and better life, and realise the modernization of harmonious coexistence between man and nature as soon as possible.

4. THE PROBLEMS AND ITS CAUSES ABOUT HONGHU LAKE

4.1. The main problems of Honghu Lake

The lake water pollution is serious. In 1990, the water quality of Hong Lake Lake was Grade II (Hu Xueyu et al., 2006). The Report on the State of the Environment in China (2017) show, the water quality of Honghu Lake is Grade IV, and the water is medium eutrophication. The water quality of Honghu Lake has dropped by two grades in 17 years; The area of Hong Lake has been reduced from 661.9km2 in 1950s to 344.2km2 in 2010s; The biodiversity has decreased, according to the Records of Lakes in China (Wang Sumin, Dou Hongshen,1998), there are 55 species of zoobenthos and 148 species of plankton in Hong Lake.Department of Ecology and Environmental of Hubei Province and Environmental Monitoring Center of Hubei Province jointly released the Report on Major Lake Library Biological Monitoring of Hubei Province (2010), showing that 20 species of zoobenthos and 48 species of zooplankton in Honghu Lake were detected.

4.2. Causes of the existing problems in Honghu Lake

Industrial pollution and unreasonable building

Since the reforming and opening up, China has developed in all aspects and great changes has taken place, especially a series of policies to promote the rapid development of the Yangtze River Economic Belt, accelerating the development of Honghu Lake. Not only has the number of surrounding industrial enterprises increased and the scale of enterprise is expanding, but also many residents build houses on the bank or fill the lake up to build houses. In addition, the supervision and the awareness of citizens' environmental protection is poor. As a result, untreated sewage is draining directly into Honghu Lake making the water quality of Honghu Lake increasing bad and the area increasingly small.

Agricultural irrigation and living pollution

The Jianghan Plain, where Honghu Lake is located, is an important base for grain production in China. In order to increase the fertility of the land to increase the grain output, a large amount of chemical fertiliser is used. According to the statistics of the agricultural department of Honghu City, about 1 million tons of nitrogen fertiliser is used every year. Some fertilisers that are not absorbed by the land contaminate surface water and groundwater by irrigation, rainfall and infiltration. At the same time, many fishermen lived around Honghu Lake dump sewage and solid waste into Honghu Lake. In addition, sewage especially from Jingzhou city is pumped into the lake through some canals. All in all, environmental and resource capacity is overloading with many ways of pollution and the water quality of Honghu Lake is going from bad to worse.

Overfishing and fish breeding by netting box

In order to earn more money and lead a better life, fishermen in Honghu Lake are doing something that is bad for Honghu Lake's environment. Fishing nets are becoming heavier with fish no matter the size of fish, fish therefore become fewer and fewer. In addition, fishermen have started to cage-culture fish. By the end of 2004, the area of cage-culture fishing has reached more than 240km^2, accounting for 70% of the surface of Honghu Lake. With the growing scale of cage-culture fishing, natural bait cannot meet the overloaded fish. To combat this, people dump chemical fertilisers into the lake to promote the growth of natural bait, and they begin to use synthetic bait to raise fish, which causes serious pollution. Gradually, fish has begun to die out so to make money, fishermen have begun to catch wild duck for example. All the above unreasonable behaviour both pollutes the lake and destroys biodiversity.

Reclaiming land from lake

In 1955, dams around Honghu Lake were built to stop the flooding of the Dongjing River and the Yangtse River. Since then, flooding of Honghu Lake have been effectively controlled. A series of water conservancy projects have been built to reduce floods and disasters. It also provids conditions for reclamation of land from the lake. In the 1950s to 1970s, large-scale farming activities are taken in Honghu Lake. However, water conservancy projects reduce the water from rivers to lake and reduce water inflow, the connectivity of rivers and lakes is weakened, which is bad for the living and egg-laying for fish, besides, the bad connection between river and lake has a bad effect on environmental self-purification abilities.

5. HOW TO DEAL WITH THE PROBLEMS

The deeper problem is a lack of supervision and management by government. The management of river and lake is a complex work and it needs all levels of government and office to take action together. Therefore, implementing the River Chief System as soon as possible is important for a better Honghu Lake.

5.1. Making relevant laws and regulations

Putting the guiding principles from 19th National Congress of the Communist Party of China and the Opinions on the Full Implementation of the River Chief System into action. Hubei Province has many leading universities and research institutes and could take advantage of talents in law, economic and other relevant experts to formulate laws that meet the specific circumstances of Honghu Lake. During the process of making laws, the following things should be attention: experts must adhere to the principle of seeking truth from facts and problem-oriented. Only in these principles can they make laws more reasonable, and in good operation. Ultimately, they can provide a scientific basis for the governance of Honghu Lake.

5.2. Introducing cleaning water flow into Honghu Lake

There are many rivers flowing into Honghu Lake, and the management of Honghu Lake will improve its condition if all the rivers that connect with Honghu Lake are clean. So government should attach equal importance to both Honghu Lake and the rivers that connect with it; establishing River Chief Offices in the districts where the rivers are located; drawing up plans, clarifying duties and identyifying responsible parties. In addition, they should call for people to join the effort by publicising widely, making river chief's board to make sure the water flow into Honghu Lake meets quality standard.

5.3. Clarify the duties of the river chief system at all levels

Honghu Lake located in Honghu County and Jianli County,according to the river chief system, governor of Hubei Province took the chair of The general river chief, and set up the river chief office at Honghu County and Jianli County,and they should take the major tasks to protect Hong Lake. What should pay attention is Honghu Lake is a whole instead of dividing by different administrative division.Therefor, making laws or taking actions should in a more systematic, holistic and coordinated way.

5.4. Strengthen water ecological restoration.

While ensuring the water flow into Honghu Lake is good, actions clean the water of Honghu Lake should be taken, for example, clearing away sludge and algae, connecting rivers and lake and so on, among them, the most effective way to improve water ecological is connect rivers and lake (Xiongwen and Peng Xianze, 2017). Also, planting some vegetation and aquatic plants to improve water environmental capacity. With these strategies, can Honghu Lake restore its original appearance as soon as possible?

5.5. Strengthen supervision and law enforcement

On one hand, to strengthen the internal supervision of the administrative system, the River Chief should regularly report the work about what they do to protect Honghu Lake, on the other hand, to strengthen the external supervision of the administrative system, the most important thing is to make full use of people, anyone who destroy the environment should be tipped-off by people, if the officers cannot finish the goal, they will be penalised. Besides, forming a joint law enforcement mechanism with department of justice, water resource or something is a must to crack down all kinds of illegal fishing or other illegal activities, and no one is allowed in any way to override the law with his or her own orders.

5.6. Develop red and green culture coordinately

Xi Jinping pointed out, as socialism with Chinese characteristics has entered a new era, the principal contradiction facing Chinese society has evolved. What we now face is the contradiction between unbalanced and inadequate development and the people's ever-growing needs for a better life. Honghu Lake has rich Red Culture and green culture. The Red Culture refers to the revolutionary history and culture formed by the Communist Party of China during the revolutionary war (Maming, 2002). "Endeavor, perseverance, courage and overcoming any difficulties, which is the spirit cherished by Honghu Lake people", this is the spirit of Honghu Lake interpreted by Rewi Alley, an American reporter. Honghu Lake is the birthplace of the Hunan and Hubei revolutionary bases, there are many historical relics, such as site groups of the Western of Huna-Hubei Revolutionary Base in Zhoulaozui Town. Green culture is a culture which ensures harmony between human and nature, eventually, it can help social development in a sustainable way (Che Shegnquan, 1998). Honghu Lake's lotus is a beautiful sight famous throughout China. Honghu Lake can develop tertiary industry by using the rich red and green culture.

6. CONCLUSION

Regulating rivers and watercourses has played an important role in the development of China. The River Chief System is the better measure to protect the water environment; it is a good way of ensuring sustainable development in Honghu Lake by implementing the River Chief System.

7. REFERENCES

Che S (1998). Analysis of Green Culture [J]. Environment Herald,(04):4-6.

Hu X, Chen D, Ai Tiancheng (2006). Changes of Water Environment of Honghu Lake from 1990-2003. Wetland Science, (02): 115-120.

Mamin (2002). Chinese culture course [M]. Wuhan: Huazhogn Normal University Press.

Wang S, Dou H (1998). The Records of Lakes in China [M]. Beijing: Science Press.

Xiongwen, Peng X (2017). Harness water by implementing the river chief system [M]. Wuhan: Chang Jiang Press.

427: On ecological water restoration under the "River Chief System"

Peng XIANZE[1], Xia YI[2]

[1] *Peng Xianze, Hubei University of Technology, China, 407732051@qq.com*
[2] *Xia Yi, Hubei University of Technology, China, 549170021@qq.com*

Starting from water ecological restoration and considering overall water ecological management.This paper puts forward the current problems of water ecological restoration from several aspects, such as the characteristics of water ecological system, and puts forward some analysis on the impact of "river length system" on urban water ecological construction.

Keywords: The river chief system, Ecological development, Water resources

1. INTRODUCTION

Discussion on the comprehensive implementation of “river length system" points out that the main task of water ecological restoration is to promote the ecological restoration and protection of rivers and lakes, and any encroachment on water conservation spaces such as natural rivers, lakes and wetlands should be prohibited. In terms of planning, measures such as returning farmland to the lake and returning fish to the lake will be gradually adopted to restore the natural connection of river and lake water systems. Other measure include strengthening the conservation of aquatic biological resources, improving the diversity of aquatic organisms, and carrying out health assessment of rivers and lakes.

2. OVERVIEW OF ECOLOGICAL WATER RESTORATION

Water ecological system refers to the interaction and restriction between aquatic communities and aquatic habitats. Through a series of material circulation and energy flow, they form a dynamic balance system, which has certain structure and function. The water ecosystem consists of both a freshwater ecosystem and a seawater ecosystem. The freshwater ecosystem is composed of a lake as a typical hydrostatic ecosystem and a river as a typical hydrological ecosystem, both of which have the following characteristics:

(1) The consistency between the biological community and the habitat: water is the carrier of community life, and so is the medium of energy flow and material circulation. Different types of ecosystems, such as forests, grasslands, deserts and wetlands are nurtured because of different rainfall and surface runoff in different regions of the earth;

(2) Integrity of water ecosystem structure: the internal analysis of the biological community shows that a very important feature of the ecosystem structure is the integrity of the community. In terms of the biodiversity of the biological community, a stable ecosystem not only ensures a wide variety of biological species, but also is relatively balanced in terms of quantity, so that the ecosystem reaches a certain equilibrium state, i.e., steady state. Such an ecosystem must be perfect;

(3) Self-repairing ability of water body: as a part of the self-regulation function of water ecosystem, it relies on self-repair to reduce the external influence and realise water self-purification. The self-regulation and repair ability of a water body ensures the stability of water ecosystem. Stability here has two meanings: first, adaptability to external influences (also called elasticity); second, the ability to return to the original state after interference.

When aquatic organisms live in a water ecosystem, they are classified into the following ecological groups according to the external environment and its own series of lifestyles: declared plankton; parliamentary native species; CNN anchor; superior peripheral living things; alien plankton; and microbes in water include fungi and bacteria. The ecosystem has no absolute stability, so its adaptability to various effects is limited. In a word, if the water ecosystem remains healthy and stable, the biodiversity of the biological community must be relatively rich, the food chain structure is relatively complex and perfect, and the material circulation, energy flow and even information flow will be relatively smooth.

Water is the goal of ecological protection in the water ecological system; to protect the system of biological communities and aquatic habitat build dynamic balancing system structure and function; to ensure the water ecological system in the rational flow of the material cycle and energy by means of information feedback; to maintain relative stability and development of water ecosystem and participate in the cycle of the biosphere. Specifically, water ecological protection includes the following contents:

(1) Maintain the reasonable spatial structure of the water ecosystem, ensure the appropriate ecological flow of rivers, maintain the appropriate water level of lakes, reservoirs and groundwater, prevent the depletion of water resources and the pollution of water environment, and maintain a good aquatic habitat.

(2) To protect the composition of aquatic communities, it is necessary to protect their structural and functional diversity, and maintain the integrity and coordination of the community structure.

(3) To protect the normal basic functions of energy flow, material circulation and information exchange between aquatic communities and aquatic habitats, maintain the normal nutritional connection between functional groups of water ecosystems, and maintain the mutual adaptability between aquatic communities and habitats in the process of long-term evolution and development.

(4) Maintain the short-term periodic changes of water ecosystem, and the dynamic changes of community succession and water ecosystem evolution develop in a positive way.

Water ecological restoration involves the improvement or restoration of the living environment under polluted, damaged or threatened conditions and its survival and development through the principles of ecological engineering, ecological environment balance, material circulation and other related technologies. The targets of water ecological restoration are

aquatic communities and their habitats, as well as various kinds of restoration or restoration. The aim is to provide a good environment for the survival and development of aquatic organisms or other endemic species.

3. EXISTING PROBLEMS IN ECOLOGICAL WATER RESTORATION

With the rapid growth of population and the rapid development of economy and society, the water ecosystem has been under increasing pressure and a series of problems have emerged. It is mainly reflected in the following four parts:

(1) Water resource depletion; the proper ecological flow rate of rivers and the appropriate ecological water level of lakes and reservoirs are not guaranteed. The river lakes, wetlands and river valleys where the river water is the main source of supply are short of ecological water, and the reasonable exploitation rate of groundwater is low.

(2) Water pollution and eutrophication are prominent; the water quality of water functional areas is not up to the standard, the lake eutrophication index is not controlled at a reasonable level, and the low temperature water temperature of the reservoir is not within the acceptable range of the water ecosystem.

(3) River closure; River and lake connectivity is not good enough, wetland reserve rate needs to be increased, and the density of rare aquatic organisms and communities has been improved. The enhanced protection of habitat conditions has stabilised or increased the number of species, and fish have been effectively protected to adapt to the habitats.

(4) Over-extraction of groundwater and shrinking of wetlands; the utilization rate of water resources development and utilization rate of water energy development do not meet the needs of ecological security in water areas.

First of all, water quality should be improved to eliminate or reduce water pollution so that water quality can meet the growth conditions of aquatic organisms. To meet the needs of economic and social development and people's life; It is necessary to restore the original biodiversity and continuity of water body, make full use of the effective production potential of resources, and turn it into a virtuous cycle, so as to achieve the synchronous development of economy and ecology.

4. MAIN CONTENTS OF ECOLOGICAL WATER RESTORATION

(1) Scientific and reasonable allocation of water resources to ensure the reasonable demand for water in the water ecosystem.

On the basis of rational allocation of water resources, the total control index of water intake permit is defined. According to the investigation and evaluation results of the current situation of water ecology, combined with the control index of water resource exploitation and utilization and the characteristics of ecological water demand of ecological protection target, the requirements and safeguard measures of the main control section of ecological water demand are clarified. We will strengthen the unified allocation of water resources, improve the mechanism and means of allocation, and ensure a reasonable demand for ecological water use.

(2) To build a sound planning system for water ecological protection and restoration

Based on the investigation and evaluation of the current situation of water ecology, the typical water ecology problems in the region are analysed and identified. The aim of water ecological protection and restoration is clarified, and the overall layout of water ecological protection and restoration measures is proposed. To formulate the allocation and guarantee scheme of ecological water demand, as well as various water ecological protection and repair engineering measures and non-engineering measures.

(3) Strengthen the supervision and management of water functional areas, scientifically verify the capacity of water pollution storage, and maintain a reasonable ecological water demand

According to the water quality objectives of water functional areas, the capacity of water pollution tolerance should be scientifically verified, and the total amount of water pollution should be limited to ensure the water quality of water functional areas meets the standards. We will accelerate the delineation of groundwater overdraft zones, gradually reduce the amount of groundwater mined, curb the over-exploitation of groundwater, maintain the reasonable ecological flow of rivers, and maintain the reasonable water level of lakes, reservoirs and groundwater.

(4) Improve the efficiency and efficiency of water use and promote the construction of a water-saving society

We will establish and improve the national water quota standards and the market quota system for water-saving products. We will establish a national system for evaluating and evaluating water efficiency and efficiency, and improve the accountability and performance appraisal system for water conservation. We will improve the mechanism for public participation, guide and mobilise all sectors of society to take an active part in building a water-saving society, reduce the exploitation and utilization of water resources, reduce sewage discharge and mitigate the impact on water ecosystems.

(5) Protecting important water ecosystems

We will protect water-related landscape, nature reserves and water ecosystems with important ecological significance (estuaries, important wetlands, lakes, rivers and lakes, habitats of important aquatic species, etc.), improve relevant regulations, formulate strict red lines for protection, and coordinate the development and utilization of water resources and the protection of water ecosystems.

(6) Protect aquatic biological habitats and biodiversity, and protect and repair water ecosystems

In view of the conservation and diversity of aquatic habitats and the protection of water ecosystems in rivers, lakes and important wetlands, water ecological protection and restoration engineering measures shall be implemented according to local conditions. Protect or repair the water ecosystem by building or utilizing existing engineering measures, and at the same time give full play to the self-repairing ability of nature to protect and repair the water ecosystem.

(7) Improve the technical support system, policies, regulations and standards system for water ecological protection

We will strengthen technical research on establishing water ecological protection, select hot spots, and carry out pilot projects to protect and repair water ecological system according to typical problems. Through the pilot study, the results of the system can be popularised and applied to provide technical support for water ecological protection. The health index system and evaluation and assessment index system of water ecosystem were established to provide scientific basis for water ecological protection.

5. THE INFLUENCE OF "RIVER CHIEF SYSTEM" TO PROMOTE URBAN WATER ECOLOGICAL CONSTRUCTION

"Long river system" the implementation of the purpose is to "respect for nature, comply with the nature, protect the natural ecological civilisation concept, rational utilisation of natural, advocate harmony with water, strengthen the management of river system, to solve because of increased population and economic and social development of floods, drought, soil erosion and water pollution, such as water, promote regional water ecological civilisation construction.

Measures are taken to ensure urban water quality at the source by means of regular silt removal and control of sewage discharge in large and small river systems in cities, establishing rain and sewage diversion measures, and reducing and controlling the amount of sewage entering the river. To adjust the peak flow rate, the collection, storage and arrangement should be reasonable and orderly, and each link should be controlled strictly, and the responsibility scope of each middle position should be defined, so as to achieve the responsibility. Combined with urban landform and topography, the rainwater "reservoir" is constructed to strengthen the rainwater cleaning function and improve the rainwater resources. We will implement the policies formulated in the strictest possible way, strictly control the quality of water resources, and emphasise the safety and cleanliness of water systems.

The urban water system is interrelated and inseparable, and the improvement of urban water ecological restoration is the important content and necessary precondition of urban construction. The implementation of the "river length system" can significantly improve the urban water ecology and water environment, which provides the basic conditions for the solution of water resources and water security problems.

6. REFERENCES

Che S (1998).Analysis of Green Culture[J].Environment Herald,(04):4-6

Mamin (2002).Chinese culture course[M].Wuhan:Huazhogn Normal University Press.

Xiongwen, Peng X (2017).harness water by implementing the river chief system[M]. Wuhan: Chang Jiang Press

428: Study on promoting the sustainable development of Honghu East Block Flood Storage Area by paying attention to the construction of ecological city

Peng XIANZE[1], Liu TING[2]

[1] *Peng Xianze, Hubei University of Technology, China, 407732051@qq.com*
[2]*Liu Ting, Hubei University of Technology, China, 396828595@qq.com*

As one of the 172 major national water conservancy projects designated by the state council, the flood storage and detention area of Honghu east sub-block is an important part of the overall flood control system in the middle and lower reaches of the Yangtze River. It is an important engineering facility to deal with the excessive flood in Chenglingji area and ensure the flood control safety of Jingjiang embankment and Wuhan City for the sub-storage areas, it is particularly important to protect the river ecosystem and the wetland ecosystem so that it can fully utilise the ecological service functions and achieve sustainable development of the green industry through investigation and analysis, this paper also provides several suggestions for solving problems while analysing the problems.

Keywords: Sustainable Development, Honghu East Block Flood Storage Area, Construction of Ecological City

1. INTRODUCTION

Due to the long summer and autumn flood season in the middle reaches of the Yangtze River, it is one of the areas with the most frequent rainstorm and the largest rainstorm intensity in China. The river channel is criss-cross, the lake star is spread, the topography is low, the population is numerous, the economy is developed, also is our country rainstorm flood and waterlogging disaster frequently occurrence area. The completion of the three gorges project, for the middle and lower reaches of the Yangtze River has played a key role. However, the flood control situation near the Chenglingji in the middle reaches is complicated, and the flood storage project is seriously lagging behind. It is one of the weakest links in the Yangtze River flood control system. According to experts' estimates. In case of flood in 1998, Chenglingji area still has some 10 billion cubic meters of excess flood can't handle. Therefore, in 1999, Honghu east block flood storage area began planning and construction as an important project to properly handle these excess floods, and was included by the state council as one of 172 major national water conservancy projects in 2014.

2. AN OVERVIEW OF HONGHU EAST BLOCK FLOOD STORAGE AREA

According to the geographical location conditions of Honghu flood storage area, three block schemes are proposed, namely eastern block, middle block and west block scheme. The Honghu east block flood storage area is located in the eastern part of the Honghu sub-storage area, in Hubei. Within the territory of Honghu City, Jingzhou City. The project consists of a waist section, a Honghu Jianli Yangtze River embankment, a Dongjing River embankment, and a Honghu main embankment. The total length of the dike is 155 kilometers, the total area of the flood storage area is 883.62 square kilometers, and the designed flood level is 32.50 meters (frozen surface); the effective flood storage volume is 6.186 billion cubic meters.

After the completion of the Honghu east block flood storage project, on the basis of effectively protecting the Jingjiang levee and the safety of Wuhan City, it will also help improve the infrastructure of water conservancy and transportation in Honghu City, accelerate the urbanization process of Honghu City, and promote the social and economic development of Honghu City.

3. FACTORS AFFECTING SUSTAINABLE DEVELOPMENT OF HONGHU EAST BLOCK FLOOD STORAGE AREA

3.1. Backward management system

At present, the management framework of Honghu flood storage area is respectively undertaken by the Yangtze River water conservancy commission, the water administration department of Honghu local government, as well as other management departments and professional management departments. On the one hand, the management objectives of all departments are not completely consistent. "Dividing troops and guarding" will easily lead to conflicts of interests and contradictions among all departments. In the case where the legal provisions of related matters are not clear, it is easy to lead to mutual inducement and other dispute. In management, on the other hand, usually more than just a single department, a single region, the management of the comprehensive coordination ability request is very high. However, under the management system, there is no reasonable coordination mechanism to make all involved departments work together to jointly cope with flood water storage, economic development, ecological protection and environmental governance, as well as the area, area of various relations and other issues. Obviously, this kind of management system lacking overall planning has become incompatible with the comprehensive management requirements of the flood storage areas, which are more rapid in economic development and more complex and changeable in governance.

3.2. Unsuitable economic development

Economic and social development is limited. Honghu east block flood storage area and Wuhan are not far away from each other. After the Hannan area was transferred to the Zhuankou in Wuhan, the Honghu east block flood storage area is getting closer and closer to the central area of Wuhan. Honghu east block flood storage area is vulnerable to the economic radiation impact of Wuhan and its location advantage is obvious. However, on the one hand, so far, Wuhan city circle has not covered Honghu, and the system barrier of Honghu is significantly higher than that of other neighbouring cities in Wuhan, making it difficult to give full play to regional advantages. On the other hand, due to the topographical conditions of natural reservoirs, it has also become a flood protection barrier to protect Wuhan from flood risks. It belongs to Honghu Lake, which is a key development area. It has little investment in the country, no major projects, and it is difficult to attract investment. The risk of loss is high, talents are weak, and there is no good employment platform. At the same time, the agricultural production base is poor, the investment in sub-storage infrastructure is too large, and traffic is blocked, resulting in very slow economic development.

Economic and social development is disorderly. Over the years, there have been different understandings on the status and functions of the east Honghu sub-block flood storage area, and little attention has been paid to the construction and management of the east Honghu sub-block flood storage area, which has resulted in a weak sense of social management in the east Honghu sub-block flood storage area. The Honghu east sub-block flood storage area lacks a management system with obvious overall planning effect. The optimisation and upgrading of the industrial structure that should be led by the government have not played a substantive role. At the same time, blind development and construction, population growth is too fast, the natural population growth rate of the region is far greater than the surrounding areas and other phenomena that are not conducive to the sustainable development of flood storage areas, resulting in the difficulty of Honghu East Block Flood Storage Area.

Urbanisation is difficult. In order to ensure the safety of floods, the State Council and the Yangtze River Water Resources Commission have made specific restrictions on the urban construction of the Honghu Lake flood storage area. The urbanization of the flood storage areas is more bound, costly and difficult. Although the construction of the first and second phases of the Honghu Lake flood storage area has begun to take shape, the degree of safe use still falls short of requirements, so that the construction of the Honghudong block flood storage area must not only improve the production and living conditions of local residents, but also It is also necessary to have the function of sub-storage and flood storage. Therefore, the local urbanization planning and construction and flood storage project construction are integrated, the urbanization cost is relatively high, and urbanization is difficult. The flood storage area of the Honghudong block is characterised by scattered living, single industrial structure, and lagging construction of urban infrastructure and flood storage projects. Moreover, due to the construction of the flood storage area project, the construction of four digging trenches and the construction of a safe area in the district has caused the original water system to be destroyed again and again, and the flat and complete fields have been torn apart. It broke the original pattern in the area and increased the difficulty of planning and construction.

4. SUGGESTIONS FOR SUSTAINABLE DEVELOPMENT OF HONGHU EAST BLOCK FLOOD STORAGE AREA

4.1. Establishing a unified comprehensive management organization

The management of flood storage areas should be globally aware. The management of rivers, dikes and related environmental facilities should be centralised in one institution, and cooperation with other institutions should be carried out to realise the integration of flood storage area management. On the basis of the existing management structure and system, we will further strengthen the comprehensive coordination management function of the flood storage and storage areas through institutional construction, and establish corresponding flood storage area management teams from different levels to implement watershed planning, flood control and disaster reduction planning, and ecological environment planning. The overall planning of the flood storage area and the local town planning and land use planning are effectively linked to achieve the goal of multi-regulation. The establishment of a unified and comprehensive management organization is conducive to strengthening social management, improving the quality of public services, and ultimately achieving the sustainable development of social and economic development in flood storage areas.

4.2. Transforming the form of flood management

The idea of flood control needs to change from "control flood" to a new concept of "management flood" and "human water harmony". On the one hand, it is necessary to enhance the tolerance to flood risks and losses; on the other hand, it is necessary to strengthen the natural ecological functions of flood storage areas. The flood storage area should be regarded as part of the large ecosystem of the river basin, and the understanding of the human, historical and ecological values of the flood storage area should be enhanced and enhanced. n all actions related to flood storage areas, both social and environmental factors should be considered. The various plans for protecting and improving the flood storage area and the river basin environment should be revised or re-engineered to speed up the improvement of the living environment.

4.3. Comprehensive utilization of flood resources

Floods are a valuable and available freshwater resource. As China's drought and water shortages become more and more prominent, the frequency, scope and impact areas of droughts continue to expand, lasting for a long time, causing large losses, which have become serious constraints affecting economic and social development. The economic losses caused by water shortages are about 180 billion yuan per year, and the ecological disasters caused by water shortages are even more serious. In China, where water resources are scarce, floods in flood seasons are causing disasters, and their characteristics as resources should be taken seriously. It should be transferred from the traditional single-function protection of flood storage area to the multi-ecological function protection based on flood storage area, highlighting its functions of purification, self-organization, landscape, leisure recreation and characteristic breeding. We must do our utmost to make harm to the interests, make full use of flood resources, and vent and pay equal weight to solve the problem of water shortage.

4.4. Develop wetland resources and strengthen the tertiary industry

The flood has two sides. It is both a natural phenomenon that causes disasters and an ecological process that is essential to maintain natural ecological balance. Restoring the low-lying land in the flood storage area to natural wetland, as compensation for the ecological environment of the river basin, can maintain the important and beneficial effects of washing, purifying, replenishing groundwater, maintaining lakes and improving soil in the natural ecological environment. The lush reeds and water plants, the flocks of waterfowl and amphibians form a beautiful and comfortable ecological landscape, which is an ideal place for future tourism. It can be combined with large-scale water conservancy projects in the surrounding areas, as well as the construction of Zhuangtai, Baozhuanghao and flood prevention buildings in the area, to build water conservancy scenic spots with water conservancy projects, waterscapes and water activities as the mainstay, to carry out water conservancy projects and water recreation activities, and to develop tourism. Third industry such as service, catering and so on. At the same time, it is possible to raise ducks moderately, collect diamonds and dragonflies, and develop tourism products. In addition, we can build wetlands, attract migratory birds to settle down, build ecological protection zones, and build elevated bird-watching and holiday lodges around the wetlands, and build ecological science research bases.

Accelerate the development of tourism projects including Honghu Ecology, Red Education and Hot Spring Leisure, and start the construction of Honghu Tourism Port; continue to strive for the dredging project of the Great Lakes Channel and complete the navigation light setting from the tourist port to the Lantian Scenic Area. Utilise Honghu's characteristic resources to develop tourism products with distinctive regional characteristics and extend the tourism industry chain. Encourage towns and villages such as Daijiachang to develop local characteristic rural tourism and support the development of tourism such as sightseeing agriculture and ecological agriculture. Carefully build Honghu tourism boutique routes, and actively build a tourism lending development platform, unified packaging and unified promotion of the major scenic spots in the city, and promote Honghu tourism deep into the Central South Tourism Alliance.

4.5. Paying attention to ecological protection and achieving sustainable development

Attaching great importance to the ecological environment protection of resources in flood storage areas, under the premise of analysing the impact of flood storage construction on the ecological environment, considering the constraints of local ecological environment fragility, the specific ideas of industrial development and environmental protection synergy are proposed. Due to its special function and status, the Honghudong block flood storage area is not suitable for the development of large-scale industries, but it can develop the ecological industry according to local conditions, and at the same time recycle the ecological environment to achieve sustainable development. For example, using the natural resource conditions of the Honghudong block flood storage area, vigorously develop green agriculture and high-quality agriculture, to fill the shortage of quantity, and become unfavorable, create a green ecological brand, and transfer green agricultural products from the flood storage area to the whole province. And even the country to promote.

5. CONCLUSION

The Honghu east block flood storage area is an important component of the Honghu Lake flood storage area. It is responsible for both strategic and economic reasons. Efforts to achieve “human and water harmony” are the new mission and new requirements for the construction of the Honghudong block.

6. REFERENCES

Jin Z (2015). Difficulties and Countermeasures of Quality Management of Hydraulic Engineering [J]. Heilongjiang Water.

Xiongwen, Peng X (2017). Harness water by implementing the river chief system [M]. Wuhan: Chang Jiang Press.

429: A bi-fluid PV/T solar collector and its potential application in solar drying

Hasila JARIMI[1], Mohd Nazari ABU BAKAR[2] and Saffa RIFFAT[3]

[1] The University of Nottingham, United Kingdom, Hasila.jarimi@nottingham.ac.uk
[2] Department of Applied Sciences, Universiti Teknologi MARA (Perlis), Perlis, Malaysia 02600 Arau, mohdnazari@perlis.uitm.edu.my
[3] The University of Nottingham, United Kingdom, Saffa.Riffat@.nottingham.ac.uk@nottingham.ac.uk

A bi-fluid PV/T solar collector incorporates two types of working fluid (air and water) under the same PV/T solar collector. In addition to the electricity generated, this type of collector enables the production of thermal energy in the form of heated air and water. The use of both fluids (bi-fluid) also creates a greater range of thermal applications and offers options in which three modes of fluid operation namely: the air mode, the water mode, and the simultaneous mode (air and water) can be produced depending on the energy needs and applications. In this paper using a validated mathematical model, we have simulated the performance of a glazed single pass bi-fluid PVT solar collector in terms of its temperature output, and thermal energy performance when operated simultaneously. In the simulation we have used amorphous silicon polycrystalline PV panels operated under typical hot climatic conditions, of Perlis, Malaysia. We found that, when both working fluids are operated at its optimum flow rate (air mass flow rate of 0.027 kg/s and water mass flow rate of 0.0066 kg/), the PV/T solar collector could produce an average of 40 to 53 °C air output temperature in addition to hot water output between 50 to 70 °C. By taking into account both thermal and electrical energy of the collector, for 2 m^2 collector aperture area, on average, the PV/T collector could produce in total of 11 kWh thermal energy, and 1.2 kWh electrical energy during the day. Important to note that, the working fluid cools down the PV cells temperature which leads to increase in electrical efficiency. In hot climate, space heating is not required for typical residential and commercial building applications. The potential application of the PV/T bi-fluid solar collector is seen in a solar drying system for fruits, crops, vegetables, and marine products. From the simulation, the air temperature range is clearly within the average temperature requirement for solar drying. In addition to air heating, the heat output from the hot water can be supplied into the chamber via water to air heat exchanger arrangement thus, enhancing the drying rate by reducing the moisture content inside the drying chamber. The warm water leaving the chamber can be stored for later usage or for different useful application. In this paper two designs of bi-fluid PV/T solar collector integrated with a greenhouse drying chamber are presented. Future studies will include detail simulation and experimental work of the proposed drying systems.

Keywords: Photovoltaic/thermal; greenhouse drying; simulation; bi-fluid

1. INTRODUCTION

Theoretical and experimental studies of PV/T solar collectors were carried out and documented as early as in the mid-1970s. Wolf (1976) investigated the performance of a combined solar heating and photovoltaic electric power generation system for a single family residence. The study was carried out in Boston, USA. Florschuetz (1979) came up with the famous extension of the well-known Hottel-Whillier-Bliss model for thermal analysis of flat-plate collectors to the analysis of combined photovoltaic/thermal collectors. More studies were carried out by S. D. Hendrie (1982) to prove the technical feasibility of the collectors. Since then, studies have continued on collector designs and performance analysis, including development of thermal and electrical modelling together with the influence of various parameters on the overall performance of the collectors. This chapter reviews the development of some of the important and related PV/T solar collector which may include four key elements namely: the design concept, type of modelling, experimental analysis, and the collector overall performance. The PV/T systems being reviewed are mainly segregated into three groups based on the collector's working fluid namely: air type, water type, and bi-fluid type (dual mode). While the first two types of PV/T solar collectors have been widely researched, the bi-fluid type (with dual mode of operation) was first introduced by Tripanagnostopoulos (2007), in the 17th European PV Solar Conference in Munich Assoa, Menezo et al. (2007). Tripanagnostopoulos (2007) proposed three different basic configurations of PV/T dual mode operations which are: the water heat exchanger (WHE) placed directly behind the PV module, placed inside the air channel, and placed on the back plate of air channel. In order to test the designed solar collector, experiments were performed with the solar collector. However, to the best of this author's knowledge, the focus of his research is the independent mode of fluid operation such that the mass flow rate of each of the fluid is fixed at 0.02 kg/s. The experimental results indicate that, when operated independently, the first design with WHE placed directly behind the PV module, the electrical efficiency and thermal efficiency of the system is considered as satisfactory for the PV component and both water and air, respectively.

Also, Assoa, Menezo et al. (2007) conducted a study on a PV/T solar collector which utilised both air and water as the working fluids. The PV cells act as the thermal absorber component for the air heat exchange component but not for the water heat exchange component. In their study, a 2-D steady-state analysis are developed. Indoor experimental studies were performed and the results were compared with the simulation results and shown to be in good agreement. Several parametric studies were conducted using the validated mathematical model. The significant advantage of this configuration is that high water temperature production is feasible when compared to the conventional hybrid solar collector without causing undesirable effect on the PV cells. In addition, such system can also be integrated with solar cooling devices which are extremely appealing during summertime. Later, some of the current authors (Abu Bakar, Othman et al., 2014, Jarimi, Abu Bakar et al., 2016, Bakar and Jarimi, 2017) have introduced a bi-fluid PVT system with both water and air heating component. The researchers introduced the design concept of the collector, and its performance was simulated using 2D finite difference equations solved in MATLAB, and validated against both indoors and outdoors testing. Air, water and the simultaneous air and water mode were considered for the analysis. The primary energy savings of bi-fluid PVT system were 58.10% and 62.31% for air and water mode respectively. In bi-fluid mode, it was observed that, as the fluid flow of one fluid increased, the thermal efficiency of other fluid tends to decreased. When the flow rate of water was varied and air flow rate was fixed, the total experimental thermal efficiency was increased from 51.88% to 65.70% and primary energy saving was increased from 64.02% to 77.90% in comparison to water mode. However, when flow rate of air was varied keeping constant water flow rate, the total experimental thermal efficiency was increased from 51.88% to 66.12% and primary energy saving increased from 64.02% to 78.98%.

Othman, Hamid et al. (2016) proposed a new design of Photovoltaic/thermal solar collector integrating transparent solar panels with double pass flat plate solar air heating system and water heating segments made of copper pipe. The performance of the system is calculated based on Hottel-Whillier-Bliss equation. Under controlled indoor environment at radiation level of 800 W/m^2, air flow rate at 0.05 kg/s and water flow rate at 0.02 kg/s; the average outlet temperature indicated reading of 27.4 °C, Su, Jia et al. (2016) introduced a photovoltaic/thermal (PV/T) solar collector with dual channels for different fluids. In their research, when the PV/T solar collector was operated under water mode configuration, the performance of the PV/T collector is the highest and the performance of the bi-fluid configuration always dominates. Baljit, Chan et al. (2017). Investigate a PV/T bi-fluid solar collector that integrates a PV panel with a serpentine-flow stainless steel tube as the water-heating component and a double pass air channel as the air-heating component. They have also used a Fresnel lens as the glazing and primary concentrator. Meanwhile, compound parabolic concentrators (CPCs) are used as the secondary concentrator. The system can simultaneously generate hot air and hot water in addition to electricity, and the total energy generated per unit area is higher than that of a single-fluid system. The simulated results have shown that the total equivalent efficiencies for single fluid condition have ranged from approximately 30 to 60%, and increased to a maximum efficiency of near to 90% for the case of the dual fluids. They have concluded that the dual fluids operation mode has reduced the solar cells temperature and hence increased the electrical output

Bi-fluid type PVT solar collector may be considered as the most recent developed PVT techniques (Joshi and Dhoble, 2018). Researchers are interested to investigate this type of PVT collector since the idea of integrating both type of the common working fluids, air and water into the same PV/T solar collector is considered appealing due to its space-saving design and potential applications. The use of both fluids (bi-fluid) also creates a greater

range of thermal applications and offers options in which three modes of fluid operation namely: the air mode, the water mode, and the simultaneous mode (air and water) can be produced depending on the energy needs and applications. However, similar to typical PVT technologies, the main limitation to the wide used of PV/T collector is being the environmental conditions especially in cold climates. Although some researchers claimed that, the low grade air and water have limited applications, the statement are not very accurate since the thermal output of the collector can be at accepted level depending on the climatic conditions. Based on the current authors published articles, this paper simulates the performance of a glazed single pass bi-fluid PV/T solar collector at 2 m^2 aperture area under tropical climate conditions. From the simulation, we then evaluate the potential application of the bi-fluid type PV/T solar collector.

2. DESIGN CONCEPT AND MATHEMATICAL MODEL

The design concept of the bi-fluid type PV/T solar collector is illustrated in Figure 1. The collector comprises of a single glazing with a single pass air channel and serpentine shaped copper tube as the water heating element.

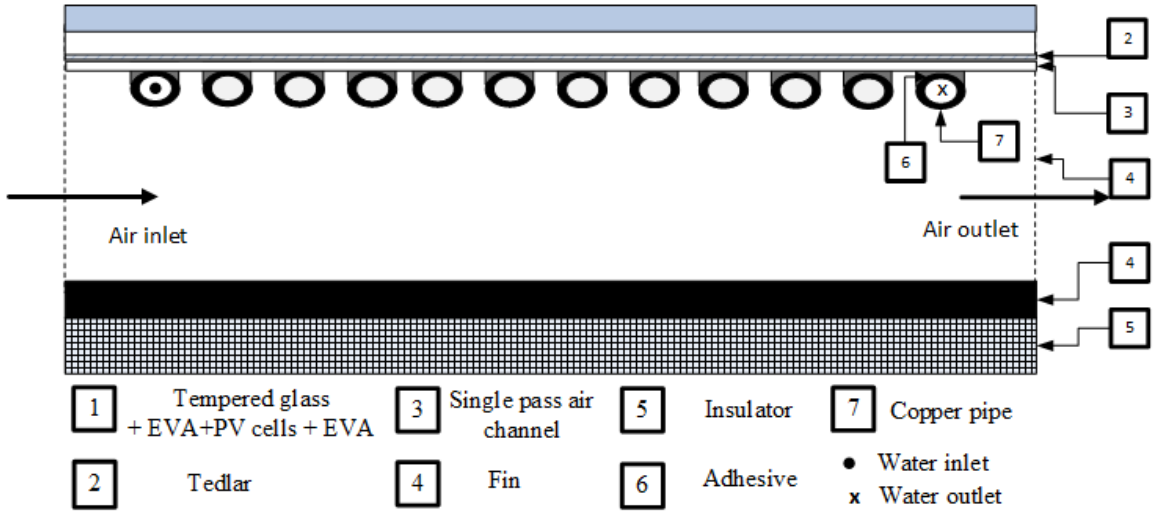

Figure 1: The design concept of the single pass glazed PV/T bi-fluid solar collector.

The current authors have discussed the mathematical modelling of the collector design without the glazing in detail in several publications (Abu Bakar, Othman et al., 2014, Jarimi, Abu Bakar et al., 2016). A set of energy balance equations were developed and solved in MATLAB using finite difference equations. In this paper, in order to take into account the additional single glazing element of the PV/T solar collector, the energy balance equations in the aforementioned publications were modified. Equation (1) and (2) represent the energy balance for the single glazing and the modified equation for the PV layer of the solar cells components of the PV/T solar collector.

Equation 1

$$\underbrace{\alpha_g G}_{1} = \underbrace{U_{t,m}\left(T_{g\,m} - T_a\right)}_{2} + \underbrace{h_{rpg,m}\left(T_{g,m} - T_{PV,m}\right)}_{3}$$

Where; α_g is the absorptance of the glass sheet, *G* is the incident solar radiation, $U_{t,m}$ is the Overall top heat loss coefficient for sub-segment $T_{g\,m}, T_{PV,m}$ are the temperature nodes of the glass sheet and the PV cells (at the centre of the cells) respectively.

The heat transfer terms are defined as follows:

1: the rate of the solar energy absorbed by the single glazing, 2: The rate of the top heat lost to the ambient per unit area, and 3: The rate of radiative heat transfer between the single glazing and the PV panel.

$$\underbrace{\tau_g \alpha_c(\beta_c) G}_{4} - \underbrace{\tau_g \alpha_c \beta_c(\eta_{ele}) G}_{5} + \underbrace{h_{rpg,m}\left(T_{g,m} - T_{PV,m}\right)}_{3} = \underbrace{h_{pvbs,m}\left(T_{pv,m} - T_{bs,m}\right)}_{6} - \underbrace{\frac{k_{PV}\delta_{PV}}{(\Delta x)^2}\left(T_{PV,m+1} - T_{PV,m}\right) + \frac{k_{PV}\delta_{PV}}{(\Delta x)^2}\left(T_{PV,m} - T_{PV,m-1}\right)}_{7} \quad \textbf{(2)}$$

Where; τ_g is the glazing transmittance, α_c is the abosrptance of solar cells, (β_c) is the solar cells packing factor, η_{ele} is the PV cells electrical efficiency, $h_{pvbs,m}$ is the Conduction heat transfer coefficient from the centre of PV cell to the back surface of Tedlar, k_{PV} is the thermal conductivity of photovoltaic cells (W/m K), δ_{PV} is the Thickness of the PV module, Δx is the Distance between temperature nodes (Δx= 1 cm) and $T_{bs,m}$ is the temperature nodes of the back surface of Tedlar

The heat transfer terms are defined as follows:

4: The rate of the solar energy received by solar cells of the PV module after transmission per unit area; 5: The rate of electrical energy available per unit area; 6: The rate of heat transferred to the back surface of Tedlar per unit area; and 7: The rate of heat conducted along the x- direction aside the tube per unit area.

3. PVT BI-FLUID POTENTIAL APPLICATION

3.1. Simulation analysis

The energy balance equations were solved using the inverse matrix solution procedure, with Newton Raphson iteration implemented to compute the unknown temperature nodes using MATLAB. The performance of the PV/T solar collector was simulated for total collector area of 2 m^2 in size, against hourly weather data for Arau Perlis, Malaysia (See Figure 2), with a latitude of 6.5224816° N and a longitude of 100.2308224°E, between 9:30 a.m. to 5:30 p.m. in a typical day of January, 2015. The simulation is important to get an overview on the thermal and electrical performance of the PV/T solar collector to determine its potential application.

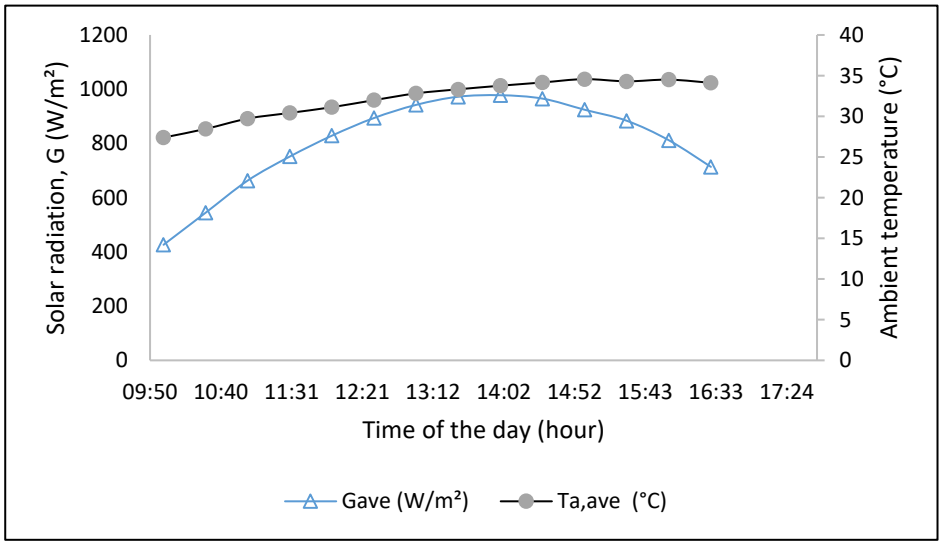

Figure 2: Hourly variation of average solar radiation Gave for the solar collector facing south and average ambient temperature Ta,ave on 13th of January 2015.

Figure 3 shows an hourly variation of solar cell temperature and its electrical efficiency. From morning to afternoon, while the mean temperature of the PV cells increases, the electrical efficiency η_{ele} clearly decreases with time, and this condition becomes very obvious during peak solar radiation between 11:00 a.m. to 3:00 p.m. The electrical η_{ele} gives a negative parabolic curve with time of the day. This is due to the temperature dependency of the open circuit voltage of the PV cells with its temperature which in turns influences the amount of power produced by the collector.

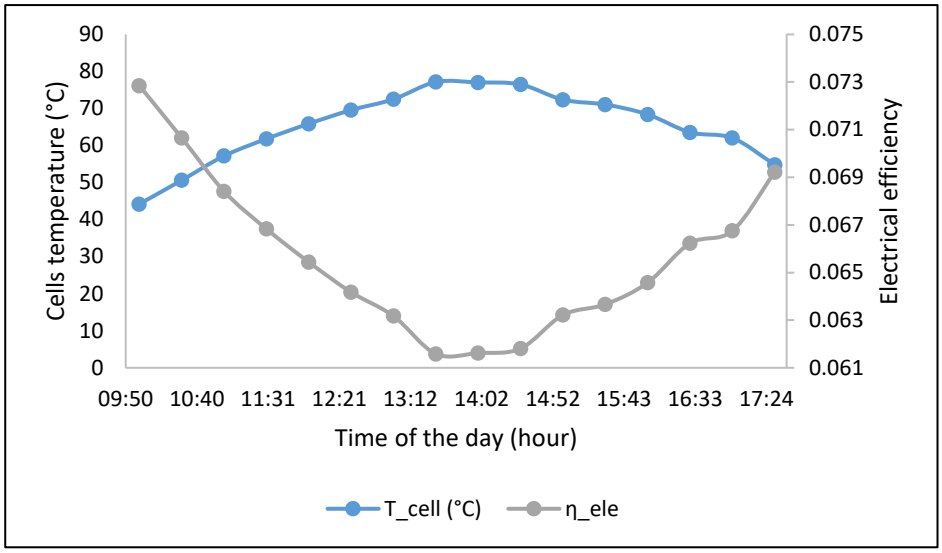

Figure 3: The hourly variation of solar cell temperature T_cell, and electrical efficiency with time of the day η_ele.

Figure 4 shows the hourly variation of outlet air and outlet water temperature from the PV/T solar collector at the fluids' optimum flow rates which are 0.0066 kg/s and 0.027 kg/s respectively. Clearly, the output temperature of air is lower in comparison to water due to the lower heat capacity as the working fluid. The air and water output temperature increases with the increase in solar radiation. At average solar radiation of 977 W/m^2, the output temperature of air and water is 56°C and 67°C respectively, meanwhile during minimum incident solar radiation, the air and water output temperature is 34°C and 40°C respectively. From a psychometric chart, if the initial inlet air temperature is 30°C, and heated in the solar collector to 40°, the relative humidity will reduce from around 90% to 40%.

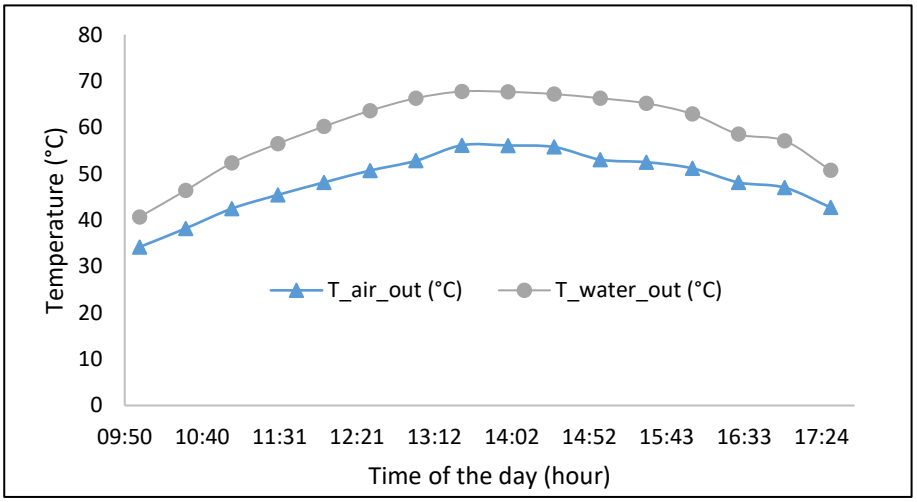

Figure 4: The hourly variation of air T_air and water output T_water temperature.

Figure 5 shows the hourly variation in the air, water and total thermal and electrical energy output from the PV/T solar collector at air and water mass flow rate of 0.027 kg/s and 0.0066 kg/s respectively. The calculated thermal energy found to be 4.2 kWh/day and 7.4 kWh/day for air and water output respectively. Meanwhile, the total electrical energy was found to be 1.2 kWh/day. The produced electricity will be stored in a battery for useful application such as powering the low dc fan. When comparing the simulation results with a greenhouse dryer design studied in (Tiwari, Agrawal et al., 2018), such energy produced by the current PV/T bi-fluid solar collector should be sufficient for self-sustainable drying system application.

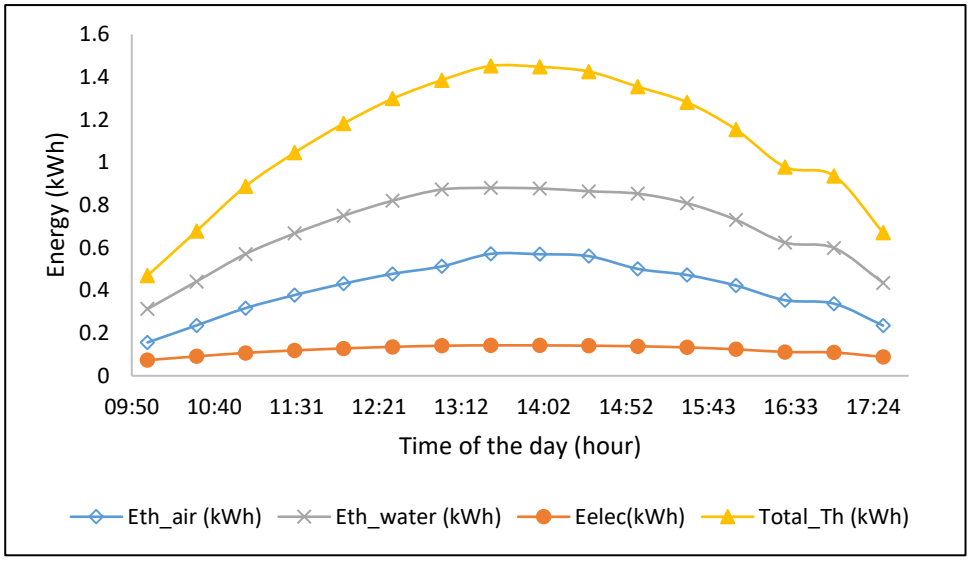

Figure 5: The hourly variation of thermal energy Eth, electrical energy Eelec and overall thermal energy gain Total_Th with time of the day.

3.2. PVT bi-fluid solar collector integrated with a greenhouse dryer

Considering the air output temperature of the PVT bi-fluid solar collector, the temperature is considered suitable for crop drying application with average maximum allowable temperature of 55°C (Ekechukwu, 1999). Therefore, in this paper, an integrated PV/T bi fluid solar-greenhouse drying system is introduced. In a typical tray dryer chamber which has been widely used in a hot climate countries, non-uniform distribution of heat transfer causes variation in the moisture level of the drying chamber tray. A tray dryer consists of level of trays placed in an insulated chamber. The heat transfer is either via forced convection of natural convection. The non-uniformity drying throughout the chamber must be avoided to get an efficient drying conditions.

In this paper we are proposing two designs of a PV/T bi-fluid solar collector integrated with a greenhouse dryer-see Figure 6 and 7. In design as shown in Figure 6, instead of using heated air from the PV/T solar collector as the main heat source, crops drying will be performed via heated air from the water to air heat exchanger installed below the bottom tray. Low dc fans are used to circulate the air in the chamber. The heated water for the water to air heat exchanger is obtained from the water output of the PV/T water solar collector. When the heated air leaving the first tray, the air will increase in its absolute humidity and decrease in temperature.

In a typical tray dryer chamber, this will cause the tray at the top chamber low in temperature and high in moisture level. In this drying chamber design, the incoming hot air from the PV/T solar collector will complement the heating process thus the temperature and moisture difference between the crops in the bottom and top trays will be reduced. In addition to that, the crop drying will also be assisted by solar heat gained through the glass chamber body. Air with lower in humidity and higher in temperature will dry the crops in the first tray. The warm water that leaves the water to air heat exchanger configuration can be stored in a water tank. At times of low solar radiation, the valve for the water piping from the solar collector can be closed and hot water from the water tank can be used as the backup heating element via floor heating.

One of the significant disadvantages of solar assisted drying system is the unavailability of solar radiation at night. In design 2 as shown in Figure 7, the PV/T solar dryer is integrated with a low temperature phase change materials (PCM) thermal storage. Although the PCM storage will not be able to provide heating as efficient as during the day, the heat output is considered sufficient to allow continuous drying for at least 3-4 hours at times without solar radiation. The working concept of the dryer may be explained as follows: during the day, the heated water charged the PCM thermal storage. With water temperature of approximately 70 °C, efficient heat transfer is assumed can be achieved to melt the PCM at 40-50°C During the day, the crops drying is mainly via hot air output from the solar collector. At night, PCM thermal storage will be discharged of which temperature of up to 55°C can be achieved. The heat released by the PCM storage from its container will be circulated in the drying chamber using a low dc fan powered by the PV power stored in the battery and an arrangement of fins is introduced to enhance heat transfer rate from the PCM to the air flow.

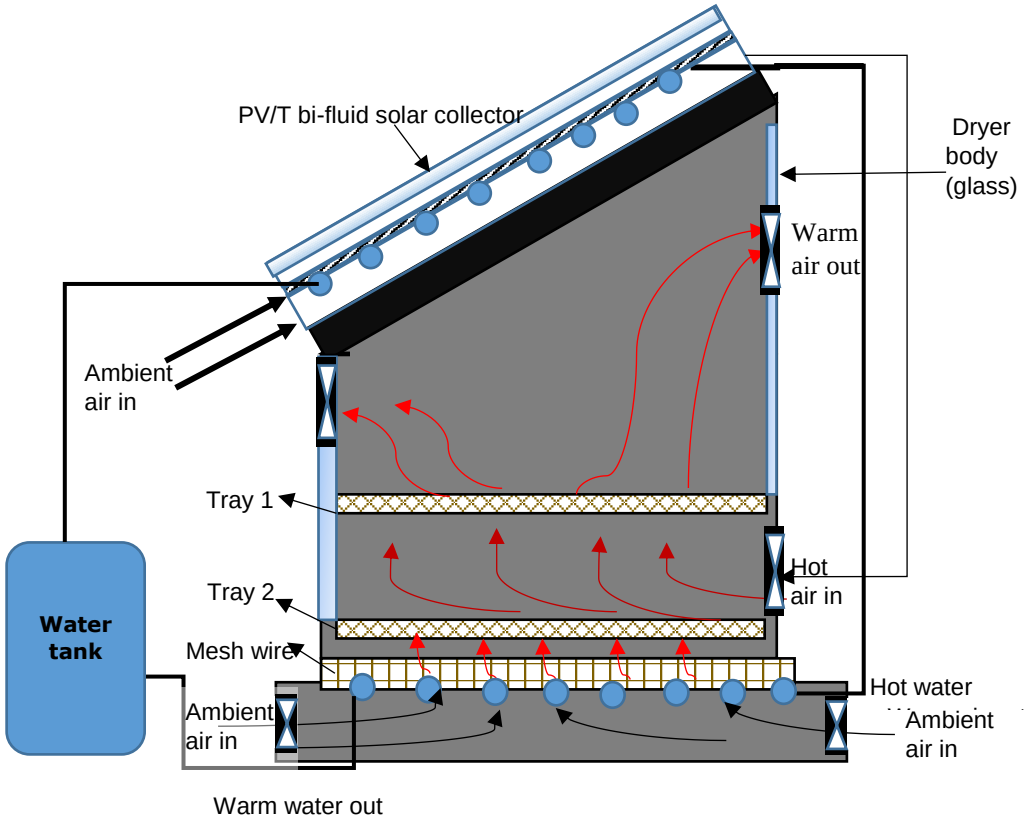

Figure 6: The integrated PV/T bi-fluid solar collector with a greenhouse dryer

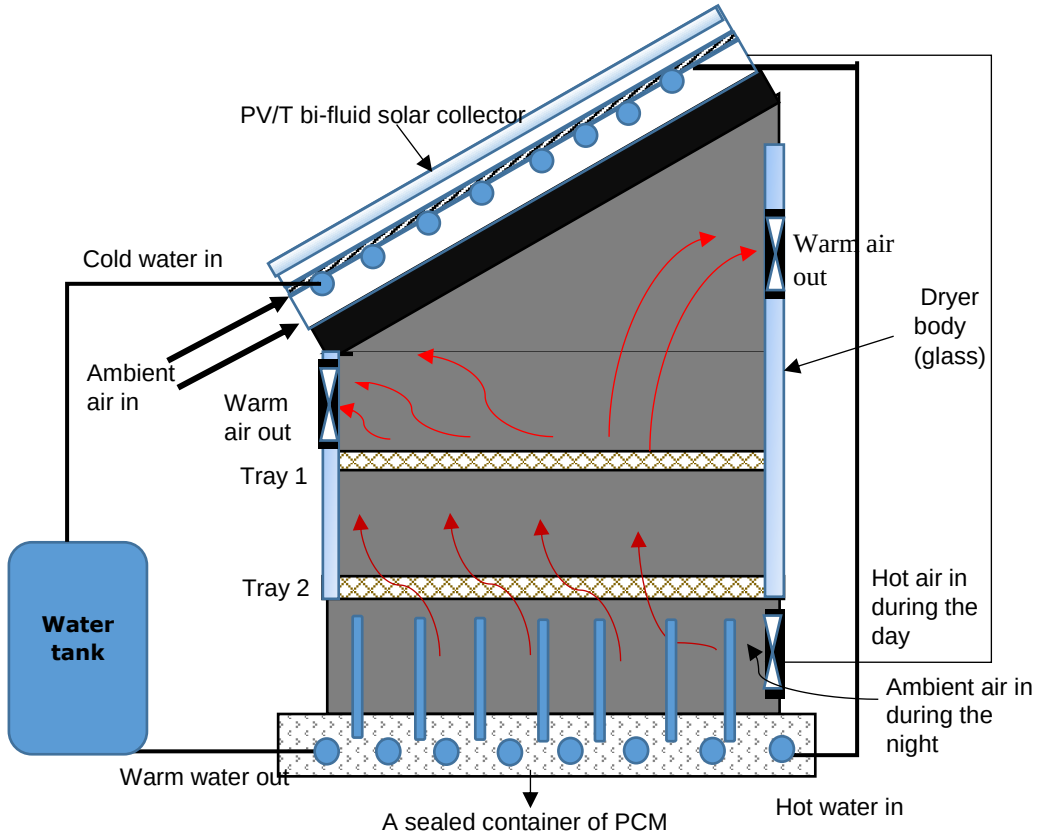

Figure 7: The integrated PV/T bi-fluid solar collector with a greenhouse dryer and PCM thermal storage

4. CONCLUSIONS AND FUTURE STUDIES

This paper presents a simulation analysis on the thermal performance of a PV/T bi-fluid solar collector using a validated mathematical model. The PV/T solar collector can be operated under three different modes of operation namely; water mode, air mode and bi-fluid mode, depending on the energy needs and application. In hot climate, space heating is not required for typical residential and commercial building applications. The potential application of the PV/T bi-fluid solar collector is seen in a solar drying system for fruits, crops, vegetables, and marine products. From the computer simulation, the air temperature range is clearly within the average temperature requirement for solar drying. Therefore, two designs of autonomous solar drying system by integrating the PV/T bi-fluid solar collector with a greenhouse dryer are proposed. The main objective of the proposed solar drying system is to create a drying system which is self-sustainable. This is usually needed at rural area or area with limited access to power. In the current research, the suitable application of the designed PV/T bi-fluid solar collector is made based on the comparison between its thermal performance and temperature requirement in solar drying application. Future studies will involve detail modelling of the crop drying in the chamber and also experimental work to prove the concept.

5. REFERENCES

Abu Bakar, M. N., M. Othman, M. Hj Din, N. A. Manaf and H. Jarimi (2014). "Design concept and mathematical model of a bi-fluid photovoltaic/thermal (PV/T) solar collector." Renewable Energy **67**: 153-164.

Assoa, Y. B., C. Menezo, G. Fraisse, R. Yezou and J. Brau (2007). "Study of a new concept of photovoltaic–thermal hybrid collector." Solar Energy **81**(9): 1132-1143.

Bakar, M. N. A. and H. Jarimi (2017). Performance Analysis of a bi-fluid type photovoltaic/thermal (PV/T) Solar Collector under low-cost solar simulator and tropical climate conditions. 16th International Conference on Sustainable Energy Technologies, Bologna, Italy.

Baljit, S. S. S., H. Y. Chan, V. A. Audwinto, S. A. Hamid, A. Fudholi, S. H. Zaidi, M. Y. Othman and K. Sopian (2017). "Mathematical modelling of a dual-fluid concentrating photovoltaic-thermal (PV-T) solar collector." Renewable Energy **114**: 1258-1271.

Ekechukwu, O. V. (1999). "Review of solar-energy drying systems I: an overview of drying principles and theory." Energy Conversion and Management **40**(6): 593-613.

Florschuetz, L. W. (1979). "Extension of the Hottel-Whillier model to the analysis of combined photovoltaic/thermal flat plate collectors." Solar Energy **22**(4): 361-366.

Jarimi, H., M. N. Abu Bakar, M. Othman and M. H. Din (2016). "Bi-fluid photovoltaic/thermal (PV/T) solar collector: Experimental validation of a 2-D theoretical model." Renewable Energy **85**: 1052-1067.

Joshi, S. S. and A. S. Dhoble (2018). "Photovoltaic -Thermal systems (PVT): Technology review and future trends." Renewable and Sustainable Energy Reviews **92**: 848-882.

Othman, M. Y., S. A. Hamid, M. A. S. Tabook, K. Sopian, M. H. Roslan and Z. Ibarahim (2016). "Performance analysis of PV/T Combi with water and air heating system: An experimental study." Renewable Energy **86**: 716-722.

Hendrie S. D. (1982). "Photovoltaic/thermal collector development program"." Rapport Final, Massachusetts Institute of Technology, Cambridge, Mass, USA.

Su, D., Y. Jia, X. Huang, G. Alva, Y. Tang and G. Fang (2016). "Dynamic performance analysis of photovoltaic–thermal solar collector with dual channels for different fluids." Energy Conversion and Management **120**: 13-24.

Tiwari, S., S. Agrawal and G. N. Tiwari (2018). "PVT air collector integrated greenhouse dryers." Renewable and Sustainable Energy Reviews **90**: 142-159.

Tripanagnostopoulos, Y. (2007). "Aspects and improvements of hybrid photovoltaic/thermal solar energy systems." Solar Energy **81**(9): 1117-1131.

Wolf, M. (1976). "Performance analyses of combined heating and photovoltaic power systems for residences." Energy Conversion **16**(1-2): 79-90.

430: Characterisation of irreversibility in the heat and mass transfer process involving liquid absorbents

An alternative approach based on entransy theory

Xiaoyue ZHANG[1,2], Zhen LI[1,2], Junda WU[1,2], Yang SUN[3]

[1] Key Laboratory of Thermal Science and Power Engineering of Ministry of Education, Tsinghua University, Beijing, China, lizh@tsinghua.edu.cn
[2] Beijing Key Laboratory of Heat Transfer and Energy Conversion, Tsinghua University, Beijing, China
[3] Hebei Mobile Communication Co.,Ltd.

The absorber and generator are the key components of the absorption system, where heat transfer and mass transfer is coupled along with the concentration change of the solution mixtures. Quantifying the irreversible dissipation in the transfer processes is of guiding significance for further optimisation. As there is no heat-work conversion in the processes, it is appropriate to characterise the irreversibility using entransy dissipation. However, the current entransy analysis is not fully developed when dealing with concentration change of liquid absorbents. The mass transfer irreversibility between the vapour and the absorbent was not considered and the entransy was not balanced. In such case, the role played by the absorbent is analysed and the "concentration entransy" is defined in this paper based on the saturation temperature of the absorbent. It associates vapour transfer with latent heat transfer and enables entransy dissipation to characterise mass transfer irreversibility. Owing to the unified dimension, the entransy balance equation is derived by taking into account the concentration entransy change and the entransy dissipation in the mass transfer process. Then, an integral method and a simplified method based on the entransy balance equation to calculate entransy dissipation are presented. According to a calculation example, the results can tell whether the heat transfer or the mass transfer is more crucial to strengthen. Further, the entransy balance equation in the dehumidifier involving liquid desiccants is deduced based on the new concept of concentration entransy. The present work provides an alternative view of the simultaneous heat and mass transfer processes and lays the foundation for the future entransy analysis of systems concerning liquid absorbents or desiccants.

Keywords: irreversibility; mass transfer; absorber; liquid desiccant; concentration entransy

1. INTRODUCTION

The absorption system has been widely applied to waste heat recovery, seawater desalination and other fields. The absorber and generator are the key components where simultaneous heat and mass transfer occurs involving the concentration change of the absorbent. To improve the system performance, it is significant to strengthen the heat and mass transfer and reduce the irreversible loss of the processes, especially in the absorber and generator.

The falling film absorber is a commonly used type of absorber at present. For the enhancement of the heat and mass transfer in the falling film absorber, current research focused on the surface improvement of heat transfer tubes and the addition of the surfactant (Kim, 2003: page 575; Hoffmann, 1996: page 331) to strengthen the convection or wettability. Apart from the optimisation of the absorber, improving measures of generators and heat exchangers were also studied. But for the absorption system as a whole, it is important to figure out how much room is left for the system's performance promotion and which component is more worthy of optimisation. Therefore, Chua et al. (Chua, 1997: page 179) used the entropy production to analyse the absorption system. Other researchers (Talbi, 2000: page 619; Kerme, 2017: page 60) conducted exergy loss and exergy efficiency analyses based on thermal power conversion. It needs to be noted that chemical exergy must be taken into account when calculating the exergy of the absorbent due to its concentration change in the process. Reynaldo et al. (Reynaldo, 2012: page 166) presented a methodology to calculate LiBr-H_2O solution's chemical exergy, which is directly related to the concentration. Fartaj et al. (Fartaj, 2004: page 1219) made a comparative analysis of the above methods and concluded that they could help to locate system non-irreversibility that was not identified by energy analysis. In fact, the entropy generation and exergy analysis methods are both based on the second law or thermal power conversion and thus they are essentially identical. But in absorption systems, there only exist heat and mass transfer processes instead of thermal power conversion process. Accordingly, characterising the irreversibility from the perspective of transfer rather than conversion might be more appropriate. Moreover, exergy efficiency varies with the reference state, and the choice of reference state tends to be unfixed. If the reference state is not well-chosen, especially when dealing with liquid absorbents or desiccants, the inlet exergy flow may be even smaller than the outlet exergy flow (Zhang, 2014: page 320), which is apparently misleading.

Recently, for heat transfer processes without heat-work conversion, the entransy-dissipation-based analysis has become a possible approach to characterising the irreversibility. Entransy, originally called heat transport potential capacity, is a product of heat and temperature (Guo, 2007: page 2547). Correspondingly, entransy dissipation is the product of heat transfer quantity and heat transfer temperature difference. It can reflect the irreversible loss caused by the temperature difference in the heat transfer process and is independent of the reference point. It has been proved that, for the heat transfer process of a given heat flow, the minimum of the entransy dissipation corresponds with the smallest average heat transfer temperature difference. As an analogy, mass entransy was defined to analyse the mass transfer process (Chen, 2009: page 2863) and the concept of moisture entransy was introduced for air handling process (Chen, 2010: page 2451). Entransy analysis method has already been used in the optimisation of the heat exchangers (Guo, 2012: page 227) and HVAC systems (Zhang, 2013: page 332). Furthermore, some researchers adopted this method to analyse coupled heat and mass transfer processes. Zhang et al. (Zhang, 2012: page 103) investigated the parameter and flow match properties of liquid desiccant dehumidification system. Wang et al. (Wang, 2014: page 712) optimised the absorption temperature transformer and proposed that the flow mismatch should be reduced as much as possible. However, this analysis did not involve the internal characteristics of the absorber, i.e., the dissipation of the mass transfer between the water vapour and solution was not discussed. Li (Li, 2016: page 27) established a three-way flow heat and mass transfer model of the absorber. In this model, the mass transfer dissipation was associated with the heat entransy dissipation by a hypothetical fluid. For the single absorber, when the amount of vapour absorption was constant, the smaller the total entransy dissipation was, the higher the heat was elevated.

Actually, the current entransy-dissipation-based method is not fully developed for the analysis of heat and mass transfer processes involving concentration change of the absorbent. For instance, in the entransy analysis, there is no such quantity as chemical exergy, which describes the role played by the solution concentration. In consequence, the irreversibility characterisation of the absorption process is incomplete, leading to the entransy imbalance of the process. Moreover, the heat transfer and mass transfer is coupled in the process and obviously the irreversibility is not caused by the heat transfer alone. Nevertheless, previous entransy analyses seldom take into account the mass transfer irreversibility. This is because there lacks comparability between the irreversibility in the mass transfer and in the heat transfer. In such case, the concentration entransy will be introduced in this paper. Furthermore, the equivalent entransy dissipation of the mass transfer process will be derived based on the concentration entransy.

2. DEFINITION OF CONCENTRATION ENTRANSY

The absorber or the generator is relatively complicated for its simultaneous heat and mass transfer process along with the concentration change of the solution mixture. It is essential to cognize the process by analysing the role the solution mixture plays. It is also necessary to take into account the mass transfer dissipation between the

vapour and the solution and compare it with the heat transfer dissipation since the investment for improvement is limited.

2.1. Roles played by the solution mixture

Absorption system usually use solution mixtures as the working fluids, such as the LiBr-H_2O solution and ammonia aqueous solution. Binary solutions differ from pure water in surface vapour pressure and saturation temperature, which vary with the solution concentration. Figure 1 shows a cluster of curves representing relations between the saturation temperature and the composition of LiBr-H_2O under different pressure. The curves are drawn with the EES (Engineering Equation Solver) software using correlations provided by Patek et al. (Patek, 2006: page 569).

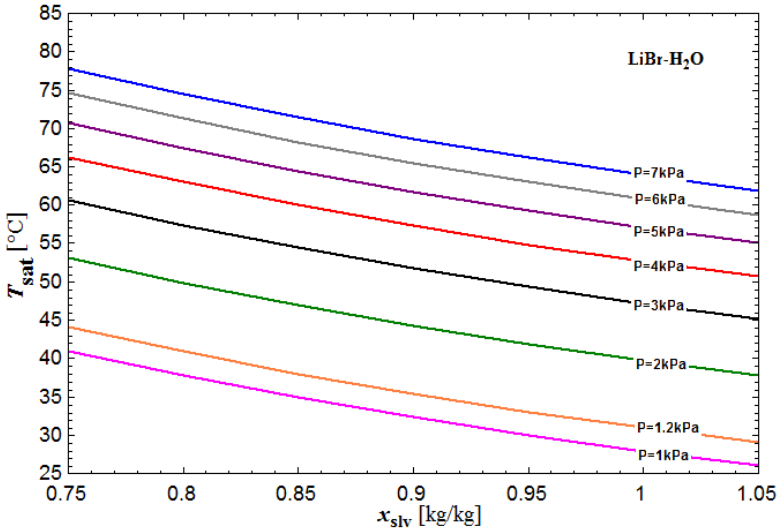

Figure 1: Relations between the saturation temperature and composition of the LiBr-H_2O under different pressure

In Figure 1, the vertical axis is the saturation temperature of the solution. The horizontal axis, represented by x_{slv}, is the solute water content, which is a new expression form of concentration and has already been used in dehumidification systems (Zhang, 2014: page 322). It is similar to the definition of adsorption ratio in solid desiccant and refers to the solvent content per kilogram of the solute. For the LiBr-H_2O solution, it means the water content per kilogram of the LiBr. The solute-based water content expression facilitates the calculation since the mass flowrate of the solute keeps unchanged in the absorption system. As can be seen from Figure 1, the saturation temperature changes approximately linearly with the solute water content. Although the saturation temperature of the solution drops with the increase of the solute water content, it is still higher than that of the pure water under the same pressure. This property of saturation temperature elevation, also called boiling point elevation, is one of the core characteristics of the electrolyte solutions. Elevating saturation temperature is the exact role the solution plays in the absorption system. This will be illustrated below by taking the evaporator and absorber as an example.

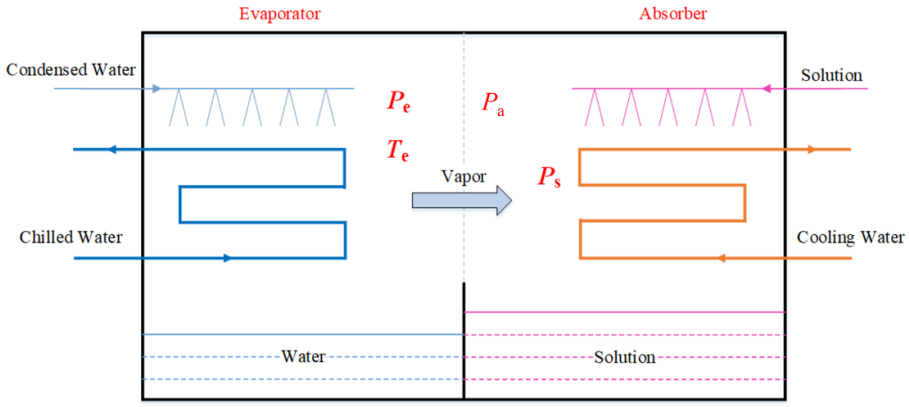

Figure 2: Diagram of the falling film absorber and evaporator of an absorption chiller

Figure 2 is the diagrammatic sketch of the absorber and evaporator of an absorption chiller. P_e, P_a and P_s stand for the pressure in the evaporator, absorber and the saturation vapour pressure of the solution, respectively. In the ideal case, the mass transfer area is assumed infinitely large and the pressure drop caused by the flow resistance

of the vapour is ignored. Thus, there is no irreversible loss in the mass transfer process and P_e, P_a and P_s are equal. In the ideal mass transfer process, the surface pressure of the solution is kept the same value as the evaporation pressure. So the temperature of the solution must be accordingly reduced by the cooling water as the solution is getting diluted with the vapour absorption. As the liquefaction of the water vapour happens at the surface of the solution, the latent heat is ultimately released at the saturation temperature of the solution instead of the evaporation temperature T_e. This is why the grade or quality of the heat from the evaporator is elevated. It also explains why the ultimate quality of the heat varies with the concentration change of the solution. Hence, the temperature at which the heat is absorbed significantly correlates with the solution and its concentration under certain pressure.

2.2. Concentration entransy and entransy dissipation of mass transfer in absorption process

The LiBr-H_2O solution is one of the most widely used working pairs in the absorption system. Taking a typical process in the absorber as an example, the LiBr-H_2O solution is diluted from x_1 to x_2 under the pressure of 1.2 kPa as shown in Figure 3. The solution's saturation temperature decreases along the orange line.

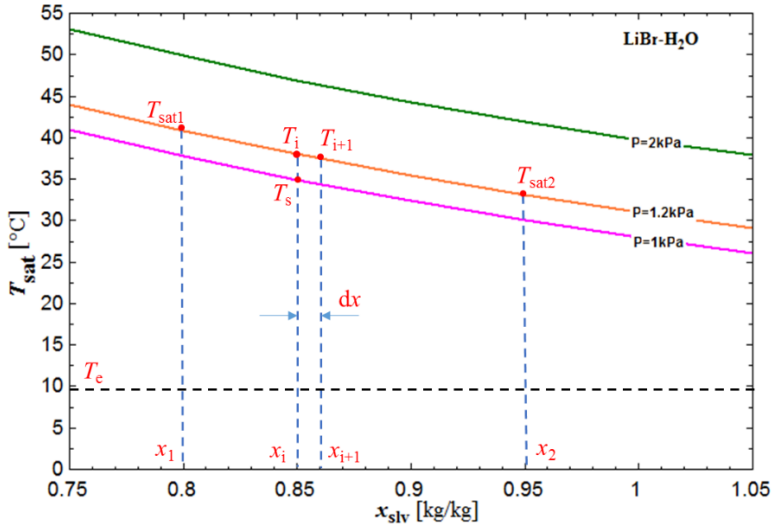

Figure 3: Ultimate temperature of the absorbed heat and its relation with the solute water content

Imagine the water vapour is divided into many small portions and the mass of each portion is dm_v. The solute water content of the solution has an infinitesimal change from x_i to x_{i+1} after absorbing one portion of vapour. In the ideal mass transfer process, the latent heat of the vapour is released at the temperature of T_i (T_{i+1} approximately equals T_i). The entransy of the absorbed heat dG_a can be formulated as Equation 1, where T_i is the saturation temperature of the solution and γ is the phase change heat of the water per kilogram. According to Wang et al. (Wang, 2015: page 538), the latent heat entransy of vapour was expressed as Equation 2, where T_e is the evaporation temperature under certain pressure.

$$\mathrm{d}G_a = T_i \gamma \mathrm{d}m_v \tag{1}$$

$$\mathrm{d}G_v = T_e \gamma \mathrm{d}m_v \tag{2}$$

The difference between dG_a and dG_v is due to the saturation temperature elevation effect of the solution. It can be integrated in the whole process as below:

$$\Delta G = \int (T_i - T_e)\gamma \mathrm{d}m_v = \int_{x_1}^{x_2} (T_{sat} - T_e)\gamma m \mathrm{d}x_{slv} \tag{3}$$

Where dx_{slv} is the change of the solute water content. Correspondingly, m is the mass flowrate of the solute rather than the solution. T_{sat} is used in place of T_i to represent the saturation temperature of the solution, which is a function of concentration under certain pressure.

As we all know, the quality of energy cannot increase spontaneously, nor can the entransy in any process. The increased entransy ΔG in the absorption process does not come out of the void but from the solution mixture because the solution mixture not only serves as the absorbent but also elevates the grade of heat. As Equation 3 depicts, ΔG is exactly a function of the grade elevation effect, which depends on the concentration of the solution. Moreover, the concentration decreases with the increase of entransy in the process. Therefore, the increased heat entransy can be considered to be converted from concentration potential or chemical composition potential, which could be equivalently defined as concentration entransy. Equation 4 describes the concentration entransy change.

$$\Delta G_{\mathrm{x}} = -\Delta G = -\int_{x_1}^{x_2} \left(T_{\mathrm{sat}} - T_{\mathrm{e}}\right) m\gamma \mathrm{d}x_{\mathrm{slv}} \tag{4}$$

The minus sign in Equation 4 indicates that the concentration entransy decreases as it converts into more heat entransy. Although derived from the analysis of the absorber, the equation still holds for the solution in the generator. In the absorber, the concentration entransy converts into heat entransy while in the generator the solution gains concentration entransy from heat entransy input. Based on Equation 4, the concentration entransy is expressed as:

$$G_{\mathrm{x}} = -\int_{x_{\mathrm{j}}}^{\infty} \left(T_{\mathrm{sat}} - T_{\mathrm{e}}\right) m\gamma \mathrm{d}x_{\mathrm{slv}} \tag{5}$$

It is the negative value of the heat entransy converted from the solution when the solute water content changes from x_{j} to ∞ (infinite dilution) in ideal mass transfer process. The concentration entransy is an equivalent concept, which guarantees the consistency of its dimension with heat entransy. It can be seen from Equation 5 that the concentration entransy is a state function of the concentration under a certain pressure. As people are generally interested in calculating the entransy in relative sense, the expression in Equation 5 is less useful than Equation 4.

The above definition of the concentration entransy derives from the analysis of ideal mass transfer process. In the actual process, the mass transfer area is limited. The existence of irreversible factors calls for a lower solution surface pressure, like 1 kPa, to absorb the water vapour, which lowers the vapour's phase change temperature from T_{i} to T_{s} as shown in Figure 3. This means that the irreversibility of the mass transfer process leads to the degradation or depreciation of the heat quality. Equation 6 depicts this degradation of quality from the perspective of entransy dissipation. T_{s} is the actual temperature of the solution.

$$G_{\mathrm{m,dis}} = \int_{x_1}^{x_2} \left(T_{\mathrm{i}} - T_{\mathrm{s}}\right) m\gamma \mathrm{d}x_{\mathrm{slv}} = \int_{x_1}^{x_2} \left(T_{\mathrm{sat}} - T_{\mathrm{s}}\right) m\gamma \mathrm{d}x_{\mathrm{slv}} \tag{6}$$

3. ENTRANSY BALANCE EQUATION AND ENTRANSY DISSIPATION CALCULATION

The concentration entransy has the same dimension with heat entransy. So the irreversibility in the heat and mass transfer processes becomes comparable and the entransy in the processes become additive. Based on this, the entransy balance equations in the absorber and generator can be derived. The entransy balance equation can be used to indirectly obtain the entransy dissipation by calculating the total entransy change in the processes.

3.1. Entransy balance equation in the absorber

Taking the differential element absorption process as the analysis process, the change of the cooling water entransy, solution heat entransy, solution concentration entransy, vapour entransy and the entransy dissipation of the heat transfer and mass transfer are listed in Equations 7~12, respectively. The sensible heat of the vapour is neglected. T_0 (usually 0 K) is the reference temperature and δQ is the heat transferred from the solution to the cooling water.

$$\mathrm{d}G_{\mathrm{w}} = \left(T_{\mathrm{w}} - T_0\right)\delta Q \tag{7}$$

$$\mathrm{d}G_{\mathrm{s}} = \left(T_{\mathrm{s}} - T_0\right)\left(m\gamma \mathrm{d}x_{\mathrm{slv}} - \delta Q\right) \tag{8}$$

$$dG_x = -\left(T_{sat} - T_e\right) m\gamma dx_{slv} \tag{9}$$

$$dG_v = -\left(T_e - T_0\right) m\gamma dx_{slv} \tag{10}$$

$$\delta G_{h,dis} = \left(T_s - T_w\right)\delta Q \tag{11}$$

$$\delta G_{m,dis} = \left(T_{sat} - T_s\right) m\gamma dx \tag{12}$$

By combining Equations 7~12, the entransy balance equation in the absorber can be derived as Equation 13.

$$\delta G_{m,dis} + \delta G_{h,dis} = -\left(dG_w + dG_s + dG_x + dG_v\right) \tag{13}$$

The entransy balance equation of the generator is basically the same except that the equivalent entransy dissipation of mass transfer in the generator tends to be zero because T_s equals T_{sat} when the solution is boiling.

3.2. Simulation of the absorber and entransy dissipation calculation

To calculate the entransy change and dissipation in the heat and mass transfer process, a mathematical model is demanded to get parameters of key state points. Li (Li, 2016: page 27) established a model for counter flow vertical falling film absorber. The absorber is simplified as a one-dimension model and the sensible heat of the vapour is neglected. LiBr-H_2O servers as the absorbent. Table 1 lists the input parameters of the counter-flow absorber. The evaporation temperature is 24.1°C (P_e=3.0 kPa) and the flow resistance of the water vapour is neglected.

Table 1: Input parameters of the absorber

m (kg/s)	m_w (kg/s)	x_{in} (kg/kg solute)	$T_{s,in}$ (°C)	$T_{w,in}$ (°C)	k(kW·m^{-2}·K)	k_m (m/s)	A (m^2)
0.27	3.5	0.852	43.0	30.0	2	5×10^{-5}	5

Based on Equation 11 and 12, the entransy dissipation of the differential element absorption process can be gained and the total entransy dissipation of the whole process is just an integral of it. Actually, the dissipation can be gained by calculating the difference between the inlet and the outlet entransy. For the LiBr-H_2O solution, its saturation temperature changes approximately linearly with the solute water content under certain pressure as shown in Figure 1. Accordingly, concentration entransy change of the LiBr-H_2O solution can be simplified as Equation 14, where Q_L is the latent heat absorbed from the water vapour. T_{sat1} and T_{sat2} are the saturation temperature of the solution at the initial/inlet and final/outlet state, which can be easily gained by the EES software.

$$\Delta G_x = \left(T_{sat1} + T_{sat2} - 2T_e\right) m\gamma\left(x_1 - x_2\right)/2 = -\left(T_{sat1} + T_{sat2} - 2T_e\right) Q_L/2 \tag{14}$$

Table 2 lists the calculation results of the entransy changes and dissipation using the two methods. In comparison with the integral method, the error of the simplified method is less than 1%. So the simplified method is reliable and can be adopted to analyse complex systems. But because the simplified method is based on the entransy balance equation, only the total entransy dissipation can be gained by calculating the entransy change. It cannot separate the total entransy dissipation into heat transfer dissipation and mass transfer dissipation. As can be seen from the results of the integral method, the entransy dissipation of mass transfer is larger than that of heat transfer, which indicate that strengthening the mass transfer is more worthwhile if the investment for improvement is limited.

Table 2: Entransy changes and dissipation (kW·K) of the absorber (T_0=273.15 K)

	ΔG_w	ΔG_s	ΔG_x	ΔG_v	$G_{h,dis}$	$G_{m,dis}$
Integral Calculation	2503.4	-254.5	-1935.4	-1694.4	587.4	793.5
Simplified Calculation	2495.5	-253.5	-1938.7	-1694.4	1391.0	
Error (%)	-0.32	-0.39	0.17	0	0.73	

4. EXTENDED APPLICATION IN LIQUID DESICCANT DEHUMIDIFICATION SYSTEMS

The liquid desiccant dehumidification system is similar to the absorption system in that the heat transfer and mass transfer between coexist and the concentration of the liquid desiccant changes in the dehumidifier and regenerator. Taking the dehumidifier as an example, the humidity ratio of air and the partial pressure of the water vapour in the air is reduced. So the dehumidification process can be regarded as the absorption process with infinite stages of evaporation pressure. The dew point of air is the corresponding evaporation temperature T_e. If the initial air state is marked as *a* and the mass concentration of the solution is 40% as shown in Figure 4, the vapour in the air will be absorbed by the solution at the state point of s_1 in the ideal mass transfer condition. So the latent heat will be released at the temperature of T_{sat}, which is the saturation temperature of the solution under the partial pressure of water vapour in the air. This means the grade of the latent heat of the vapour is elevated from T_e to T_{sat}. But in the actual dehumidification process, the temperature of the solution T_s should be lower than T_{sat} so that the vapour pressure of the thin air layer on the surface of the solution is lower than the partial vapour pressure of the processed air. So the latent heat is degraded from T_{sat} to T_s, which can also be characterised by entransy dissipation.

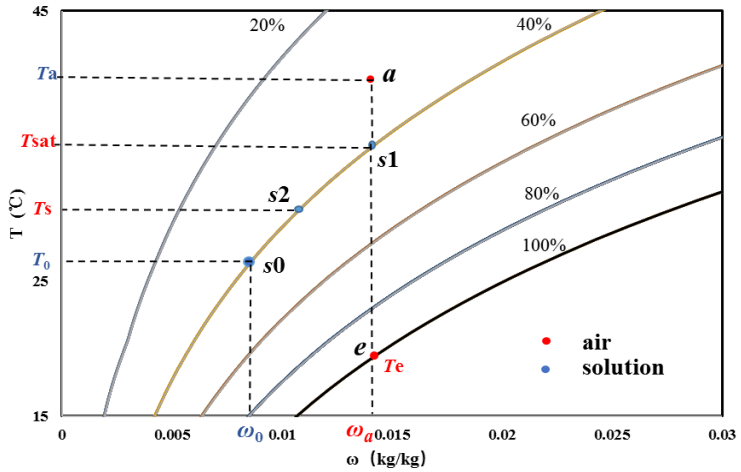

Figure 4: Psychrometric chart of air dehumidification process

For an adiabatic counter-flow dehumidifier, the change of the air's sensible heat entransy, air's vapour latent heat entransy, solution's heat entransy, concentration entransy and the entransy dissipation of the heat transfer and mass transfer process are listed in Equations 14~19. The entransy balance equation is derived as Equation 20.

$$\mathrm{d}G_{\mathrm{a,s}} = -\left(T_{\mathrm{a}} - T_0\right) m_{\mathrm{a}} c_{\mathrm{pa}} \mathrm{d}T_{\mathrm{a}} \tag{14}$$

$$\mathrm{d}G_{\mathrm{a,l}} = -\left(T_{\mathrm{e}} - T_0\right) m\gamma \mathrm{d}x_{\mathrm{slv}} \tag{15}$$

$$\mathrm{d}G_{\mathrm{s}} = \left(T_{\mathrm{s}} - T_0\right)\left(m_{\mathrm{a}} c_{\mathrm{pa}} \mathrm{d}T_{\mathrm{a}} + m\gamma \mathrm{d}x_{\mathrm{slv}}\right) \tag{16}$$

$$\mathrm{d}G_{\mathrm{x}} = -\left(T_{\mathrm{sat}} - T_{\mathrm{e}}\right) m\gamma \mathrm{d}x_{\mathrm{slv}} \tag{17}$$

$$\delta G_{\mathrm{h,dis}} = \left(T_{\mathrm{a}} - T_{\mathrm{s}}\right) m_{\mathrm{a}} c_{\mathrm{pa}} \mathrm{d}T_{\mathrm{a}} \tag{18}$$

$$\delta G_{\mathrm{m,dis}} = \left(T_{\mathrm{sat}} - T_{\mathrm{s}}\right) m\gamma \mathrm{d}x_{\mathrm{slv}} \tag{19}$$

$$\mathrm{d}G_{\mathrm{a,s}} + \mathrm{d}G_{\mathrm{a,l}} + \mathrm{d}G_{\mathrm{s}} + \mathrm{d}G_{\mathrm{x}} + \delta G_{\mathrm{h,dis}} + \delta G_{\mathrm{m,dis}} = 0 \tag{20}$$

5. CONCLUSION

The strong solution elevates the grade of latent heat in vapour absorption processes at the cost of the decrease of its concentration. The diluted solution consumes high quality energy from the heat source to get concentrated in the generator. This means the concentration of solutions is closely connected with the grade of heat. The saturation temperature of the solution is the key physical quantity that associates heat grade with solution concentration. Proceeding from this point, concentration entransy is defined and the entransy balance equation is derived. Further, the irreversibility in the mass transfer process is characterised by the equivalent entransy dissipation, whose dimension coincides with that of the heat transfer entransy dissipation. The irreversibility of the mass transfer process and the heat transfer process can thus be compared directly. The comparison results can offer guidance about which transfer process's enhancement is more crucial. The entransy balance equation based on concentration entransy and the method to calculate the entransy dissipation lay a foundation for the future optimisation of absorption or dehumidification system involving liquid absorbents or desiccants.

6. ACKNOWLEDGEMENTS

The research was sponsored by the National Natural Science Foundation of China (Grant No. 51776103).

7. REFERENCES

Chen, Q. Chen, J.X. Ren and Z.Y. Guo, 2009. The extremum principle of mass entransy dissipation and its application to decontamination ventilation designs in space station cabins. Chinese Science Bulletin, 54 (16), 2826-2870.

Chen, Q. Chen, K.D. Yang, M.R. Wang, N. Pan and Z.Y. Guo, 2010. A new approach to analysis and optimization of evaporative cooling system I: Theory. *Energy,* 35 (6), 2448-2454.

Chua, H.T. Chua, J.M. Gordon, K.C. Ng and Q. Han, 1997. Entropy production analysis and experimental confirmation of absorption systems. *International Journal of Refrigeration,* 20 (3), 179-190.

Fartaj, S.A. Fartaj, 2004. Comparison of energy, exergy, and entropy balance methods for analysing double‐stage absorption heat transformer cycles. *International Journal of Energy Research,* 28 (14), 1219-1230.

Guo, Z.Y. Guo, H.Y. Zhu, X.G. Liang, 2007. Entransy-A physical quantity describing heat transfer ability. *International Journal of Heat and Mass Transfer,* 50 (13-14), 2545-2556.

Guo, J.F. Guo, M.T. Xu, 2012. The application of entransy dissipation theory in optimization design of heat exchanger. *Applied Thermal Engineering,* 36, 227-235.

Hoffmann, L. Hoffmann, I. Greiter, A. Wagner, V. Weiss and G. Alefeld, 1996. Experimental investigation of heat transfer in a horizontal tube falling film absorber with aqueous solutions of LiBr with and without surfactants. *International Journal of Refrigeration,* 19 (5), 331-341.

Kerme, E.D. Kerme, A. Chafidz, O.P. Agboola, J. Orfi, A.H. Fakeeha, A.S. Al-Fatesh, 2017. Energetic and exergetic analysis of solar-powered lithium bromide-water absorption cooling system. *Journal of cleaner production,* 151, 60-73.

Kim, J.K. Kim, C.W. Park and Y.T. Kang, 2003. The effect of micro-scale surface treatment on heat and mass transfer performance for a falling film H_2O/LiBr absorber. *International Journal of Refrigeration,* 26 (5), 575-585.

Li, J.Y. Li, 2016. Research on heat and mass transfer and match properties of absorber in absorption heat pump. Beijing: Tsinghua University.

Patek, J. Pátek and J. Klomfar, 2006. A computationally effective formulation of the thermodynamic properties of LiBr–H2O solutions from 273 to 500K over full composition range. *International Journal of Refrigeration,* 29 (4), 566-578.

Reynaldo, P.B. Reynaldo, R. Gonzales and S.A. Nebra, 2012. Exergy calculation of lithium bromide–water solution and its application in the exergetic evaluation of absorption refrigeration systems LiBr-H_2O. *International Journal of Energy Research,* 36 (2), 166-181.

Talbi, M.M. Talbi and B. Agnew, 2000. Exergy analysis: an absorption refrigerator using lithium bromide and water as the working fluids. *Applied Thermal Engineering,* 20 (7), 619-630.

Wang, S. Wang, X.Y. Xie and Y. Jiang, 2014. Optimization design of the large temperature lift/drop multi-stage vertical absorption temperature transformer based on entransy dissipation method. *Energy,* 68, 712-721.

Wang, W.H. Wang, X.T. Cheng and X.G. Liang, 2015. Entransy definition and its balance equation for heat transfer with vaporization processes. *International Journal of Heat and Mass Transfer*, 83, 536-544.

Zhang, T. Zhang, X.H. Liu, L. Zhang and Y. Jiang, 2012. Match properties of heat transfer and coupled heat and mass transfer processes in air-conditioning system. *Energy Conversion and Management,* 59, 103-113.

Zhang, L. Zhang, X.H. Liu and Y. Jiang, 2013. Application of entransy in the analysis of HVAC systems in buildings. *Energy,* 53, 332-342.

Zhang, L. Zhang, X.H. Liu, J.J. Jiang and Y. Jiang, 2014. Exergy calculation and analysis of a dehumidification system using liquid desiccant. *Energy and Buildings,* 69, 318-328.